frontiers | Research Topics

Emerging technologies for the construction of renewable energy-dominated power system

Edited by
Liansong Xiong, Haitao Zhang, Flavia Grassi, Sergio Amedeo Pignari, Yushuai Li, Anant Kumar Verma, Yonghui Liu and Jin Ye

Coordinated by
Chaoran Zhuo

Published in
Frontiers in Energy Research

ISSN 1664-8714
ISBN 978-2-8325-5750-1
DOI 10.3389/978-2-8325-5750-1

About Frontiers

Frontiers is more than just an open access publisher of scholarly articles: it is a pioneering approach to the world of academia, radically improving the way scholarly research is managed. The grand vision of Frontiers is a world where all people have an equal opportunity to seek, share and generate knowledge. Frontiers provides immediate and permanent online open access to all its publications, but this alone is not enough to realize our grand goals.

Frontiers journal series

The Frontiers journal series is a multi-tier and interdisciplinary set of open-access, online journals, promising a paradigm shift from the current review, selection and dissemination processes in academic publishing. All Frontiers journals are driven by researchers for researchers; therefore, they constitute a service to the scholarly community. At the same time, the *Frontiers journal series* operates on a revolutionary invention, the tiered publishing system, initially addressing specific communities of scholars, and gradually climbing up to broader public understanding, thus serving the interests of the lay society, too.

Dedication to quality

Each Frontiers article is a landmark of the highest quality, thanks to genuinely collaborative interactions between authors and review editors, who include some of the world's best academicians. Research must be certified by peers before entering a stream of knowledge that may eventually reach the public - and shape society; therefore, Frontiers only applies the most rigorous and unbiased reviews. Frontiers revolutionizes research publishing by freely delivering the most outstanding research, evaluated with no bias from both the academic and social point of view. By applying the most advanced information technologies, Frontiers is catapulting scholarly publishing into a new generation.

What are Frontiers Research Topics?

Frontiers Research Topics are very popular trademarks of the *Frontiers journals series*: they are collections of at least ten articles, all centered on a particular subject. With their unique mix of varied contributions from Original Research to Review Articles, Frontiers Research Topics unify the most influential researchers, the latest key findings and historical advances in a hot research area.

Find out more on how to host your own Frontiers Research Topic or contribute to one as an author by contacting the Frontiers editorial office: frontiersin.org/about/contact

Emerging technologies for the construction of renewable energy-dominated power system

Topic editors
Liansong Xiong — Xi'an Jiaotong University, China
Haitao Zhang — Xi'an Jiaotong University, China
Flavia Grassi — Polytechnic University of Milan, Italy
Sergio Amedeo Pignari — Polytechnic University of Milan, Italy
Yushuai Li — Aalborg University, Denmark
Anant Kumar Verma — Universidad de O'Higgins, Chile
Yonghui Liu — Hong Kong Polytechnic University, Hong Kong, SAR China
Jin Ye — University of Georgia, United States

Topic coordinator
Chaoran Zhuo — Xi'an University of Technology, China

Citation
Xiong, L., Zhang, H., Grassi, F., Pignari, S. A., Li, Y., Verma, A. K., Liu, Y., Ye, J., Zhuo, C., eds. (2024). *Emerging technologies for the construction of renewable energy-dominated power system*. Lausanne: Frontiers Media SA.
doi: 10.3389/978-2-8325-5750-1

Table of contents

frontiers | Frontiers in Energy Research

TYPE Original Research
PUBLISHED 16 January 2024
DOI 10.3389/fenrg.2024.1344749

OPEN ACCESS

EDITED BY
Yonghui Liu,
Hong Kong Polytechnic University, Hong Kong SAR, China

REVIEWED BY
Zhanghai Shi,
Southwest Jiaotong University, China
Chunyu Chen,
China University of Mining and Technology, China
Zhengyang Xu,
Tianjin University, China

*CORRESPONDENCE
Jianhui Meng,
mengjianhui2008@163.com

RECEIVED 26 November 2023
ACCEPTED 04 January 2024
PUBLISHED 16 January 2024

CITATION
Wang D, Sun Y, Ge Y, Li J, Yan C and Meng J (2024), A smooth grid connection strategy for compressed air energy storage based on adaptive PI control.
Front. Energy Res. 12:1344749.
doi: 10.3389/fenrg.2024.1344749

A smooth grid connection strategy for compressed air energy storage based on adaptive PI control

Dajiang Wang[1], Yaxin Sun[2], Yaming Ge[3], Jie Li[3], Chaoyang Yan[3] and Jianhui Meng[2]*

[1]State Grid Jiangsu Electric Power Company Ltd. Research Institute, Nanjing, China, [2]State Key Laboratory of Alternate Electrical Power System with Renewable Energy Sources, North China Electric Power University, Baoding, China, [3]State Grid Jiangsu Electric Power Company Ltd., Nanjing, China

In the context of the application of compressed air energy storage system participating in power grid regulation, a large capacity of compressed air energy storage accessed to or off from the power grid will bring instability to the system, and there will be voltage and current impact during off-grid operation, which will pose a threat to system security. Therefore, this paper puts forward the control strategy of compressed air energy storage for both grid-connected and off-grid, and proposes a smooth grid-connected strategy of compressed air energy storage based on adaptive PI control, which can better improve the problem of excessive impulse current during the connection of compressed air energy storage. Finally, a simulation model is built in MATLAB/Simulink to verify the effectiveness and superiority of the proposed control strategy.

KEYWORDS

compressed air energy storage1, grid-connected and off-grid control strategies2, smooth grid connection3, PI control4, impulse current5

1 Introduction

Compressed air energy storage, due to its large energy storage capacity and high conversion efficiency, is suitable for commercial application in large-scale energy storage power plants. It is one of the key technologies to solve the problems of volatile renewable energy consumption, power grid peak shaving, carbon compliance, and carbon neutrality (Mei S et al., 2017; Liu et al., 2023; Chen et al., 2016; Attarha et al., 2018). Compressed air energy storage has the characteristics of storing and converting three forms of energy: cold, heat, and electricity (R. Khatami et al., 2020). Through multi-energy cogeneration, high energy comprehensive utilization efficiency (70%–80%) can be achieved to make up for the lack of low power conversion efficiency of compressed air energy storage, thereby effectively improving the application economy of compressed air energy storage (A. Azizivahed et al., 2020).

In terms of the application of compressed air energy storage in power grid regulation, compressed air energy storage is used to smooth the fluctuations of wind power and improve the quality of wind power, so as to increase the utilization level of wind power and its penetration rate in the power grid (Cleary et al., 2015; Cheng et al., 2019; Zhu et al., 2023). Reference (Wen X et al., 2021) studies the participation of compressed air energy storage systems in primary frequency regulation and proposed a method for the compressed air

energy storage system to participate bidirectionally in response to the primary frequency regulation of the power grid in the two stages of energy storage and energy release. Reference (Li G et al., 2021) proposes a phase modulation operation mode based on compressed air energy storage power plants, which achieves the function of supporting reactive power and voltage of the power grid and verifies the rationality of phase modulation operation of salt cavern compressed air energy storage power plants. Reference (Aldaadi et al., 2021) proposes a grid-connected power optimization strategy based on segmented real-time wind power and electricity price data averaging to ensure continuous and stable output of power to the grid. Reference (Xu W et al., 2022) proposes a new configuration that uses compressed air energy storage to assist wind turbines to increase the total power generation and schedulability of wind power generation, and verifies its effectiveness in realizing a schedulable wind energy conversion system through case studies. Reference (Meng et al., 2023) proposes a compressed air energy storage multi-energy co-supply system coupled with thermal power, evaluates its thermal performance and technical economy, and provides a new development idea for the large-scale commercial application of compressed air energy storage. Reference (Cheng J et al., 2018) proposed an advanced adiabatic compressed air energy storage multi-energy flow optimization scheduling model based on energy hub matrix modeling, proving that advanced adiabatic compressed air energy storage can realize daily hot spot joint supply and improve regional energy utilization efficiency.

Compressed air energy storage can operate independently with load and can also be connected to the power grid to participate in grid regulation. However, during the grid connection process, if the conditions of equal phase frequency to the grid voltage are not met, large impulse currents and voltages will usually be generated, threatening the safe and stable operation of equipment. Therefore, a smooth grid connection strategy is needed to ensure the smooth and safe connection of compressed air energy storage to the power grid. For smooth switching, reference (Xiong et al., 2016) adopts the methods of V/f control and PQ control switching, and introduces current compensation to reduce the transient impact before and after switching the control strategy. References (Wang et al., 2016; Zheng F et al., 2019) use a virtual synchronous generator to switch to PQ control, and controls the current loop instructions to ensure that the inner loop parameters are consistent when the control mode is switched to achieve smooth switching. Reference proposes a smooth grid connection strategy for optical storage virtual synchronous machines based on adaptive model predictive control. On the basis of the model predictive control strategy, frequency variation is introduced to adaptively adjust the weighting coefficient, which effectively improves the voltage and current surge problem during the switching process. Reference (Yuan et al., 2017) proposes a smooth switching control strategy for microgrid operation mode based on linear active disturbance rejection control technology, achieving the effect of quickly eliminating disturbances and smoothing the switching process. Reference (Xiong et al., 2016) proposes a new phase-locked loop suitable for microgrid systems based on the smooth switching control method of microgrid under master-slave control conditions to ensure smooth switching of microgrid operation modes and enhance system stability. At present, research on smooth switching focuses on microgrids, and there is little research on the issue of compressed air energy storage and smooth grid connection to reduce impulse voltage and current.

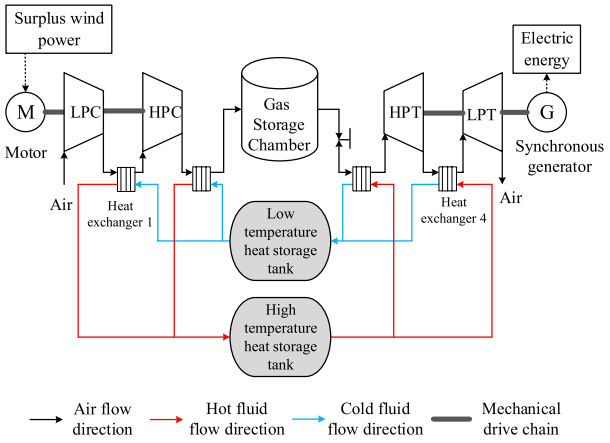

FIGURE 1
Topological structure of non-complementary compressed air energy storage system.

In order to solve the impact problem caused by the grid connection of compressed air energy storage, this paper proposes a smooth grid connection control strategy based on adaptive PI control after proposing control strategies for the compressed air energy storage system in both grid-connection and off-grid modes. Finally, a simulation model of compressed air energy storage was built on the MATLAB/SIMULINK simulation platform, and the proposed control strategy was experimentally verified.

2 Structure and modeling of compressed air energy storage system

Compressed air energy storage refers to the use of low valley electricity, wind power curtailment and photovoltaic power, *etc.*, to compress the air through a compressor, and store high-pressure air in a sealed storage chamber. During peak electricity consumption period, the air is released to drive a turbine to generate electricity.

2.1 Structure of compressed air energy storage system

This paper builds an advanced adiabatic compressed air energy storage system, and the topology diagram of the system is shown in Figure 1. The system consists of an electric motor, a compressor unit, a gas storage tank, a heat storage system, an expansion unit, and a generator. During the low period of electricity consumption, surplus wind power is used to drive the compressor to compress the air through two stages of compression, generating high-temperature and high-pressure air that enters the heat exchanger on the compression side for heat exchange with the heat transfer oil. The heat transfer oil absorbs heat and heats up before entering the high-temperature heat transfer oil tank. The compressed air releases heat and cools down to the environmental temperature before entering the salt cavern gas storage tank for storage; During

electricity peak period, high-pressure air is released from the gas storage, heated by high-temperature thermal oil in the oil-gas heat exchanger on the power generation side, and then enters the secondary air turbine with an intermediate reheater to expand and perform work to complete the power generation process (Shengwei et al., 2022).

2.2 Modeling of compressed air energy storage system

This paper establishes a mathematical model for the operation of advanced adiabatic compressed air energy storage system under reasonable simplified conditions based on the thermodynamic, heat transfer, fluid mechanics, and electrical mechanisms of the main devices in the system (I. Calero et al., 2020; Mirzapour-Kamanaj et al., 2022). The mathematical model of each device is shown in Eqs 1–21.

1) Mathematical model of compressor

The continuous equation is as follows:

$$m_{i.c} = m_{e.c} \tag{1}$$

The compressor outlet air temperature equation is as follows:

$$T_{e.c} = T_{i.c}\left(1 + \frac{\pi^{\frac{k-1}{k}} - 1}{n_s}\right) \tag{2}$$

The compressor power equation is as follows:

$$N_c = m(h_{e.c} - h_{i.c})n_s \tag{3}$$

The compressor outlet pressure equation is as follows:

$$P_{e.c} = \pi P_{i.c} \tag{4}$$

The number of compression stages is expressed as follows:

$$S = \ln \pi_z / \ln \pi \tag{5}$$

where mi. c and me. c are the air mass flow rates at the inlet and outlet of the compressor, kg/min; Ti. c and Te. c are the inlet and outlet air temperatures of the compressor, K; k is the specific heat ratio of air; ns is the adiabatic efficiency of the compressor; m is the air mass flow rate inside the compressor, kg/min; Nc is the input power of the compressor, kW; hi. c and he. c are the specific enthalpies of the inlet and outlet air of the compressor, kJ/kg; Pi. c and Pe. c are the inlet and outlet air pressures of the compressor, MPa; π is the single stage pressure ratio of the compressor, πz is the total pressure ratio of the compressor; S is the number of compressor stages.

2) Mathematical model of heat exchanger

The heat exchanger model in the energy storage stage is basically the same as the heat exchanger model in the energy release stage, with the difference being that the air in the heat exchanger during the energy storage stage releases heat, while the water absorbs heat; During the energy release stage, the air in the heat exchanger absorbs heat, while the water releases heat.

The air energy balance equation is as follows:

$$M_a C_{pa}\frac{dT_{ae.c}}{dt} = mC_{pa}(T_{ai.c} - T_{ae.c}) - Q_1 \tag{6}$$

The metal heat storage equation is as follows:

$$M_t C_t \frac{dT_t}{dt} = Q_1 - Q_2 \tag{7}$$

The cooling water energy balance equation is as follows:

$$M_w C_{pw}\frac{dT_{we.c}}{dt} = G_{w.c}C_{pw}(T_{wi.c} - T_{we.c}) + Q_2 \tag{8}$$

The heat transfer equation is as follows:

$$\begin{aligned} Q_1 &= \alpha_1 A\left(\frac{T_{ai.c} + T_{ae.c}}{2} - T_t\right) \\ Q_2 &= \alpha_2 A\left(T_t - \frac{T_{wi.c} + T_{we.c}}{2}\right) \end{aligned} \tag{9}$$

The energy efficiency equation is as follows:

$$\varepsilon = \frac{T_{ae.c} - T_{ai.c}}{T_{wi.c} - T_{ai.c}} \tag{10}$$

The pressure drop equation is as follows:

$$\begin{aligned} \Delta P &= \left(\frac{0.0083\varepsilon}{1-\varepsilon}\right)P_{ai.c} \\ P_{ae.c} &= P_{ai.c} - \Delta P \end{aligned} \tag{11}$$

Where, Ma, Mt, Mw are the air mass in the heat exchanger, the metal pipe mass of the heat exchanger, and the water mass inside the heat exchanger, kg; Cpa, Ct, and Cpw are the specific heat capacity of the air at constant pressure, metal tube specific heat capacity, and water specific heat capacity in the heat exchanger, kJ/(kg*K); m is the air mass flow rate inside the heat exchanger, kg/min; Gw. c is the mass flow rate of water inside the heat exchanger; Tai. c and Tae. c are the inlet and outlet air temperatures of the heat exchanger, K; Tt is the temperature of the metal tube of the heat exchanger, K; Twi. c and Twe. c are the temperatures of the inlet and outlet water in the heat exchanger, K; Q1 is the energy released by air, kJ; Q2 is the energy absorbed by water, kJ; α1 and α2 are the heat transfer coefficient of air and water, kJ/(m2*min*K); A is the heat exchange area, m2; ε is the energy efficiency of the heat exchanger; Pai. c and Pae. c are the air pressure at the inlet and outlet of the heat exchanger, MPa.

3) Mathematical model of gas storage tank

In this paper, the process of storing high-pressure gas in advanced adiabatic compressed air storage system is regarded as a constant volume process, energy is not released during storage, and air liquefaction is not considered. The pressure and temperature changes in the storage tank are mainly studied, and air is regarded as an ideal state.

The energy balance equation of gas storage tank in energy storage stage is as follows:

10.3389/fenrg.2024.1344749

$$\frac{d(M_v v)}{dt} = C_{pa} m_c T_{vi} - \alpha_3 A_v (T_v - T_h) \tag{12}$$

The energy balance equation of gas storage tank in energy release stage is as follows:

$$\frac{d(M_v v)}{dt} = -C_{pa} m_s T_{ve} - \alpha_3 A_v (T_v - T_h) \tag{13}$$

The change trend of air pressure and temperature in storage tank during energy storage stage is expressed as follows:

$$\frac{dp_v}{dt} = \frac{C_{pa} m_c T_{vi} - \alpha_3 A_v (T_v - T_h)}{C_{va} V} R_g \tag{14}$$

$$\frac{dT_v}{dt} = \frac{C_{pa} m_c T_{vi} - \alpha_3 A_v (T_v - T_h) - C_{va} m_c T_v}{C_{va} V P_v} R_g T_v \tag{15}$$

The change trend of air pressure and temperature in the tank during energy release is expressed as follows:

$$\frac{dp_v}{dt} = \frac{-C_{pa} m_s T_v - \alpha_3 A_v (T_v - T_h)}{C_{va} V} R_g \tag{16}$$

$$\frac{dT_v}{dt} = \frac{-C_{pa} m_s T_{ve} - \alpha_3 A_v (T_v - T_h) + C_{va} m_s T_v}{C_{va} V P_v} R_g T_v \tag{17}$$

Where, Pv is the air pressure of the air storage tank, kPa; V is the volume of the air storage tank, m3; mc and ms are the air mass flow at the inlet and outlet of the air storage tank, kg/min; α3 is the heat exchange coefficient of the air storage tank, W/(m2*K); Mv is the gas mass in the air storage tank, kg; v is the internal energy per unit mass of the gas in the air storage tank, kJ/kg; AV is the heat exchange area of the air storage tank, m2; Th is the ambient temperature, K; Tvi and Tve are the air temperature at the inlet and outlet of the air storage tank, K; Cva is the specific heat capacity of air at constant volume, kJ/(kg*K); Rg is the gas constant, kJ/(kg*K). Tv is the air temperature in the tank, K.

4) Turbine mathematical model

The operation mechanism of turbine can be understood as the inverse process of compressor. The mathematical model of turbine is established by compressor modeling method.

$$m_{i.s} = m_{e.s} \tag{18}$$

The turbine outlet air temperature equation is as follows:

$$T_{e.s} = T_{i.s}\left(1 - \left(1 - \frac{1}{\pi^{\frac{k-1}{k}}}\right) n_s\right) \tag{19}$$

The turbine power equation is as follows:

$$N_s = m_s (h_{i.s} - h_{e.s}) n_s \tag{20}$$

The turbine outlet pressure equation is as follows:

$$P_{e.s} = \frac{P_{i.s}}{\pi} \tag{21}$$

Where, mi.s and me. s are the air mass flow at the inlet and outlet of turbine, kg/min; Ti. s, Te. s are the air temperature at the inlet and outlet of turbine, K; k is the specific heat ratio of air; ns is the adiabatic efficiency of turbine; m is the mass flow in turbine, kg/min; Ns is the output power of turbine, kW; hi. s and he. s are the air specific enthalpy at the inlet and outlet of turbine, kJ/kg; Pi. s and Pe. s are the air pressure at the inlet and outlet of turbine, MPa.

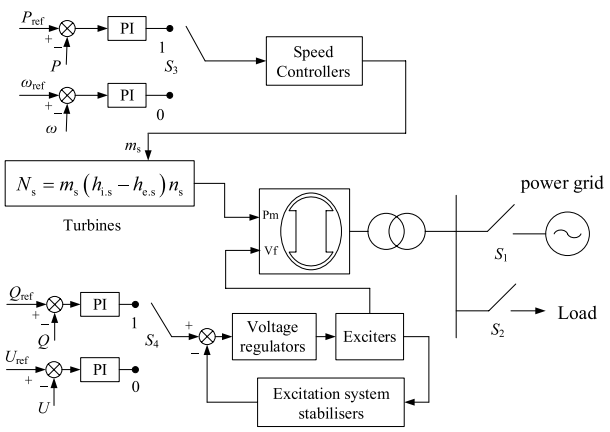

FIGURE 2
Grid-connected and off-grid control structure of compressed air energy storage system.

3 Compressed air energy storage smooth grid-connection strategy based on PI control

3.1 Grid-connected control structure and off-grid control structure of compressed air energy storage system

PQ control strategy is adopted when the compressed air energy storage system is connected to the grid, and V/f control strategy is adopted when the compressed air energy storage system is off the grid.

The coordinated control of grid-connected and off-grid modes enhances power supply reliability. Based on the above two control strategies, a control structure for compressed air energy storage systems operating in both grid-connected and off-grid modes is constructed, as shown in Figure 2.

3.2 Control strategy of compressed air energy storage system connected to grid

PQ control strategy is adopted for grid-connected mode operation of compressed air storage. The fluctuation of load, frequency and voltage carried by compressed air storage are borne by the large power grid. Compressed air storage does not need to consider the regulation of voltage and frequency, but is directly controlled and regulated according to the voltage and frequency of the power grid. Compressed air storage outputs active and reactive power according to a given reference value. In this way, compressed air energy storage only needs to emit or absorb power, which can avoid interference to the power system caused by compressed air energy storage participating in voltage regulation of the power grid.

The active pow P output by that synchronous generator is compared with a reference value Pref to make a difference, then PI regulation is carry out, after PI regulation, the active power P enters a speed governor link to obtain air mas flow ms, ms is then input into a turbine for compressed air energy storage, wherein the turbine is equivalent to a prime mover in a conventional generator set, the air mass flow ms is equivalent to a steam valve opening of the turbine, and mechanical power Pm generated by expansion air of the turbine drives the synchronous generator to complete power generation. The process of generating power by compressed air energy storage system can be expressed by Equation 20.

The output reactive power Q and the reference value Qref of the synchronous generator are compared. After PI regulation, the excitation voltage of the exciter is obtained to control the output voltage of the exciter, that is, the excitation voltage Vf of the generator, and then input into the synchronous generator. In order to stabilize the operation of the excitation system and improve its dynamic quality, the negative feedback link of the excitation system is introduced, that is, the excitation system stabilizer, which is generally a soft feedback link, also known as speed feedback.

3.3 Off-grid control strategy for compressed air energy storage system

V/f control strategy is adopted for compressed air storage off-grid mode operation. When the power grid fails or scheduled maintenance occurs, the compressed air storage system needs to disconnect the common connection point with the power grid to realize off-grid operation, providing voltage and frequency support to ensure that the amplitude of frequency and output voltage is always controlled within the allowable range, regardless of how the output power changes, so as to ensure the normal and stable operation of the compressed air storage system off-grid.

When the compressed air energy storage system operates off-grid with V/f control strategy, the amplitude of output voltage V is obtained by measuring module, and then the frequency f is obtained by phase-locked loop. The amplitude of output voltage V is compared with reference value Vref, and then the excitation voltage Vf is obtained by exciter and input to synchronous generator. The frequency f is compared with the reference value fref, and after PI regulation, the air mass flow ms is obtained through the speed governor and input into the turbine for compressed air energy storage. The mechanical power generated by the turbine expansion air is used as the mechanical power Pm of the prime mover to drive the synchronous generator to complete power generation.

3.4 Compressed air energy storage smooth grid-connection strategy based on adaptive PI control

When the compressed air energy storage system is connected to the grid, the compressed air energy storage system voltage needs to be the same as the grid voltage in amplitude, phase and frequency. If the conditions cannot be met, there will be a large voltage difference

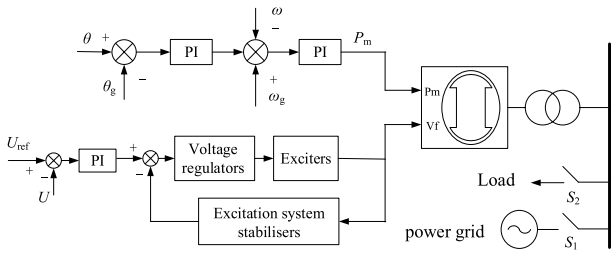

FIGURE 3
Compressed air energy storage smooth grid-connection strategy based on PI control.

when the grid switch is closed, which will lead to excessive grid impulse current and pose a threat to the system safety. Therefore, the output voltage of the compressed air energy storage system needs to match the grid voltage in amplitude, frequency and phase before grid-connection. In the voltage control of compressed air energy storage, the reference voltage has been set as the grid side voltage, so this paper mainly studies the control strategy of frequency and phase Angle. The control block diagram of compressed air energy storage smooth grid connection strategy based on PI control is shown in Figure 3.

In Figure 3, θ is the compressed air energy storage side voltage phase angle, θg is the grid side voltage phase angle, ω is the compressed air energy storage side angular frequency, and ωg is the grid side angular frequency. The phase difference between the compressed air storage output phase and the power grid is first controlled by PI, and its deviation value is introduced into the angular frequency deviation, and then Pm is obtained through PI control. This process can pre-synchronize the phase difference and frequency difference between the compressed air energy storage and the power grid, so that the phase difference and frequency difference between the compressed air energy storage and the power grid can be minimized when connected to the grid, so as to reduce the impulse current of the grid-connection.

In order to control the phase and frequency synchronization process of compressed air energy storage more accurately, the kp and ki parameters of PI regulator are adjusted adaptatively on the basis of PI control, so as to achieve the purpose of rapid response of the system and precise adjustment of phase and frequency pre-synchronization. kp and ki are proportional coefficients and integral coefficients respectively. The larger kp is, the faster the system responds, but too large kp will cause the instability of the system. ki improves the stability of the system, but the larger ki increases the overshoot and even the oscillation of the system. Therefore, in the pre-synchronization process, when the phase difference between the energy storage side and the network side is large, kp and ki are increased to improve the system response speed and reduce the pre-synchronization time. When the phase difference between the energy storage side and the network side is small, and the phase difference is close to the grid-connected requirements, in order to reduce the phase difference too fast and cause the system frequency instability, reduce kp and ki at this time. The adaptive PI control designed in this paper is shown in Eqs 22, 23:

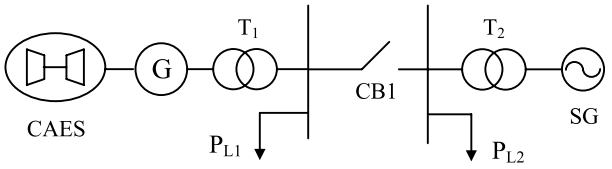

FIGURE 4
Compressed air energy storage grid-connected system topology.

$$k_p = \begin{cases} k_{p0} + \Delta k_p & \Delta\ \theta > 15^\circ \\ k_{p0} - \Delta k_p & \Delta\ \theta < 15^\circ \end{cases} \tag{22}$$

$$k_i = \begin{cases} k_{i0} + \Delta k_i & \Delta\ \theta > 15^\circ \\ k_{i0} - \Delta k_i & \Delta\ \theta < 15^\circ \end{cases} \tag{23}$$

In the formula, kp0 and ki0 are proportional coefficients and integral coefficients at the initial moment, respectively, which are set to 1 and 0.1; Δkp and Δki are increments of scale and integration coefficients, respectively, set to 0.2 and 0.02, respectively.

4 Virtual inertial control based on fuzzy logic control

In order to verify the effectiveness of the grid connection and off-grid control strategies of the compressed air energy storage system and the smooth grid connection strategy of compressed air energy storage based on adaptive PI control, this section establishes the compressed air energy storage grid connection as shown in Figure 4 on the MATLAB/simulink platform. The system model verified the grid-connected and off-grid control strategies of the compressed air energy storage system and the smooth grid-connected strategy of compressed air energy storage based on PI control.

In Figure 4, the rated power of compressed air energy storage is 200 MW, the rated voltage is 13.8 kV; the rated power of transformer T1 is 210MVA, the voltage level is 13.8/35 kV, the load PL1 is 150 MW; the rated power of the grid-side synchronous machine SG is 100 MW. The rated voltage is 13.8 kV; the rated power of transformer T2 is 210MVA, the voltage level is 13.8/35 kV, and the load PL2 is 10 MW. When the system starts, the compressed air energy storage adopts the PI control strategy shown in Figure 3 for pre-synchronization. When the phase angle difference between the compressed air energy storage and the grid side reaches the minimum, the grid is connected, and the compressed air energy storage control mode is switched to V/f control strategy and complete grid connection. The synchronous generator on the grid side adopts V/f control strategy before grid connection and PQ control strategy after grid connection.

Under the premise of the same system, the impulse voltage and current and phase Angle difference synchronization speed under adaptive PI control pre-synchronization and non-adaptive PI control are compared. In order to facilitate comparison, the output waveforms under different working conditions are displayed on the same interface. The compressed air energy storage and grid-side phase difference during the pre-synchronization and grid connection processes are shown in Figure 5.

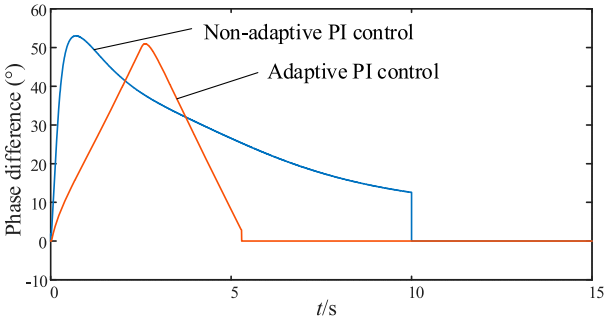

FIGURE 5
Phase difference between compressed air energy storage and power grid.

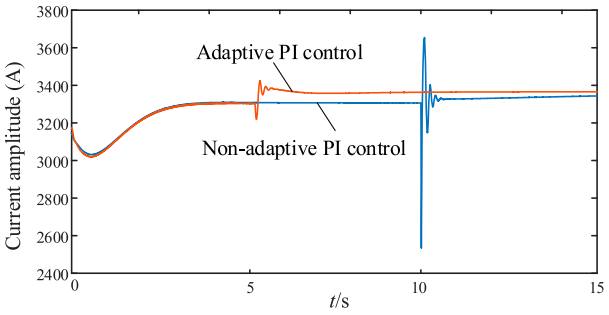

FIGURE 6
Compressed air energy storage grid connection point current amplitude.

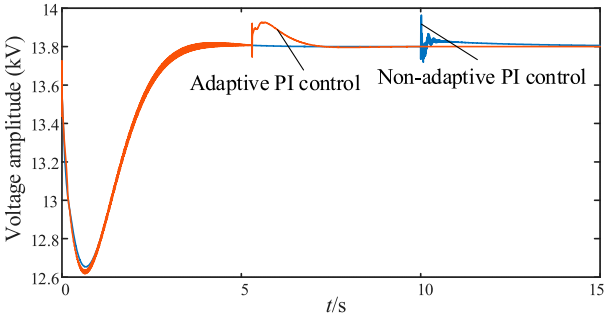

FIGURE 7
Compressed air energy storage grid connection point voltage amplitude.

As shown in Figure 5, when adaptive PI control is adopted to reduce the phase difference in the pre-synchronization mode, the phase difference between the compressed air energy storage and the network side will eventually be reduced to 0. The reason why

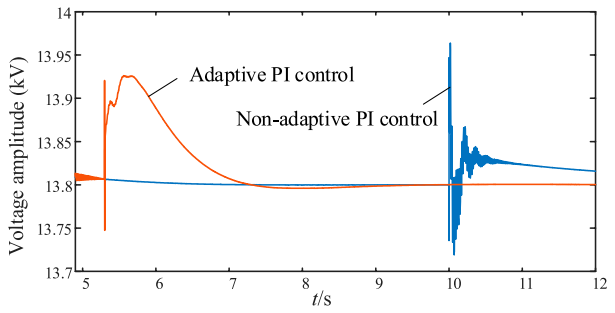

FIGURE 8
Partial amplification waveform of voltage amplitude at the compressed air energy storage grid-connection point.

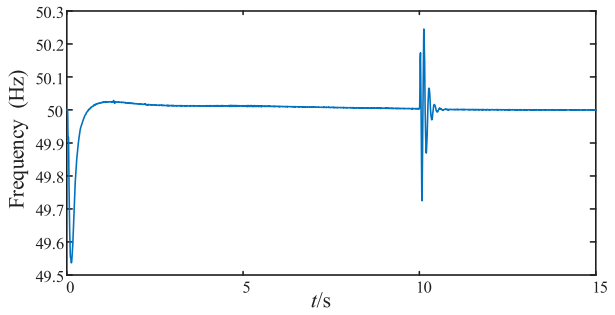

FIGURE 9
System frequency under non-adaptive PI control.

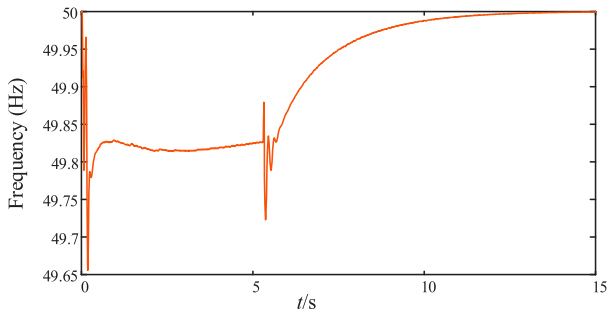

FIGURE 10
System frequency under adaptive PI control.

the phase difference of the curve in the figure jumps to 0 is that the grid connection switch is closed at this moment, the compressed air energy storage is connected to the grid, the two run synchronously, and the phase difference becomes 0. By comparison, it can be found that the phase difference of compressed air energy storage and grid side will eventually be reduced to the value that meets the requirements of grid connection when adaptive PI control is used for pre-synchronization and non-adaptive PI control for pre-synchronization. However, the phase difference decreases faster under adaptive PI control, and the phase difference decreases to 0 at about 5.3s. When conventional non-adaptive PI control is adopted, the phase difference stabilizes at 12° at about 10s, and the phase difference reduction speed under adaptive PI control is obviously better than that under conventional PI control.

Figure 6 and Figure 7 show grid-connected current and grid-connected voltage under adaptive PI control and non-adaptive PI control. Due to the difference of grid-connection time between adaptive PI control and non-adaptive PI control, the time of impulse current and impulse voltage will be different. As can be seen from the figure, after grid-connection, the impulse current under non-adaptive PI control is about 3646A, and large amplitude oscillation occurs, and it takes about 1s to reach a stable state from the beginning of grid-connection. The impulse current under adaptive PI control is about 3420A, the oscillation amplitude is small, and it takes about 0.6 s from the beginning of grid connection to stability. As for the impulse voltage at the moment of grid connection, it can be seen from the voltage amplitude at the junction point in Figure 7 and the local amplification waveform in Figure 8 that the impulse voltage amplitude under adaptive PI control is smaller, the maximum impulse voltage is about 13.93kV, and the time taken to recover to stability is shorter, during which the voltage does not oscillate. However, the impact voltage amplitude under non-adaptive PI control is larger, and the maximum value of the impact voltage amplitude is about 13.96kV, and the recovery time is longer, and the voltage oscillates more seriously during the recovery.

Figure 9 and Figure 10 show the system frequency under non-adaptive PI control and adaptive PI control respectively. It can be seen from the figure that the system frequency under non-adaptive PI control will have a large oscillation amplitude at the grid-connected time, with the maximum oscillation exceeding 50.2 Hz and the minimum oscillation approaching 49.7 Hz. When adaptive PI control is adopted, the frequency oscillation amplitude of the system is small and there is no overshoot at the grid-connected time, and the maximum frequency is about 49.85 Hz during the oscillation process. It can be seen that the frequency stability is taken into account while the phase Angle synchronization is accelerated.

Based on the experimental results, it can be concluded that the smooth grid-connection strategy proposed in this paper based on adaptive PI control has a good control effect on the reduction rate of phase difference and the suppression of impulse current and voltage during the pre-synchronization process of compressed air energy storage grid-connection, and the voltage, current and frequency have smaller fluctuations when compressed air energy storage is connected to the grid, improving the safe and stable operation ability of the system.

5 Conclusion

Compressed air energy storage has broad application prospects. In order to reduce the impact current and voltage when compressed air energy storage is connected to the power grid and enable smooth grid-connection, this paper proposes a smooth grid-connection

strategy based on adaptive PI control. The conclusions drawn are as follows.

1) A smooth grid-connection strategy based on adaptive PI control is proposed, which optimizes the frequency, phase and voltage response characteristics during the pre-synchronization process, reduces the impact current and voltage during compressed air energy storage connecting to power grid, and improves the ability of the system to operate safely.
2) Aiming at the problem of smooth grid connection of compressed air energy storage, a pre-synchronization strategy based on adaptive PI control is proposed, which can effectively solved the impact problem caused by mode switching during grid-connection and has good practical engineering application value.

Data availability statement

The raw data supporting the conclusion of this article will be made available by the authors, without undue reservation.

Author contributions

DW: Data curation, Writing–review and editing. YS: Investigation, Software, Writing–original draft. YG: Project administration, Resources, Writing–review and editing. JL: Methodology, Validation, Writing–review and editing. CY: Funding acquisition, Resources, Writing–review and editing. JM: Investigation, Writing–review and editing.

Funding

The author(s) declare financial support was received for the research, authorship, and/or publication of this article. This work was supported by the Science and Technology Project of State Grid Jiangsu Electric Power Company Limited (J2022064).

Conflict of interest

Author DW was employed by State Grid Jiangsu Electric Power Company Ltd. Research Institute. Authors YG, JL, and CY were employed by State Grid Jiangsu Electric Power Company Ltd.

The remaining authors declare that the research was conducted in the absence of any commercial or financial relationships that could be construed as a potential conflict of interest.

Publisher's note

References

Aldaadi, M., Al-Ismail, F., Al-Awami, A. T., and Muqbel, A. (2021). A coordinated bidding model for wind plant and compressed air energy storage systems in the energy and ancillary service markets using a distributionally robust optimization approach. *IEEE Access* 9, 148599–148610. doi:10.1109/access.2021.3123792

Attarha, A., Amjady, N., Dehghan, S., and Vatani, B. (2018). Adaptive robust self-scheduling for a wind producer with compressed air energy storage. *IEEE Trans. Sustain. Energy* 9 (4), 1659–1671. doi:10.1109/tste.2018.2806444

Azizivahed, A., Razavi, S. E., Arefi, A., Ghadi, M. J., Li, L., Zhang, J., et al. (2020). Risk-oriented multi-area economic dispatch solution with high penetration of wind power generation and compressed air energy storage system. *IEEE Trans. Sustain. Energy* 11 (3), 1569–1578. doi:10.1109/tste.2019.2931670

Calero, I., Cañizares, C. A., and Bhattacharya, K. (2020). Implementation of transient stability model of compressed air energy storage systems. *IEEE Trans. Power Syst.* 35 (6), 4734–4744. doi:10.1109/tpwrs.2020.2995787

Chen, L., Zheng, T., Mei, S., Xue, X., Liu, B., and Lu, Q. (2016). Review and prospect of compressed air energy storage system. *J. Mod. Power Syst. Clean Energy* 4 (4), 529–541. doi:10.1007/s40565-016-0240-5

Cheng, J., Li, R., Choobineh, F. F., Hu, Q., and Mei, S. (2018). Dispatchable generation of a novel compressed-air assisted wind turbine and its operation mechanism. *IEEE Trans. Sustain. Energy* 10 (4), 2201–2210. doi:10.1109/tste.2018.2883068

Cheng, J., Li, R., Choobineh, F. F., Hu, Q., and Mei, S. (2019). Dispatchable generation of a novel compressed-air assisted wind turbine and its operation mechanism. *IEEE Trans. Sustain. Energy* 10 (4), 2201–2210. doi:10.1109/tste.2018.2883068

Cleary, B., Duffy, A., OConnor, A., Conlon, M., and Fthenakis, V. (2014). "Assessing the economic benefits of compressed air energy storage for mitigating wind curtailment," in *IEEE transactions on sustainable energy* 6 (3), 1021–1028. doi:10.1109/TSTE.2014.2376698

Khatami, R., Oikonomou, K., and Parvania, M. (2020). Look-ahead optimal participation of compressed air energy storage in day-ahead and real-time markets. *IEEE Trans. Sustain. Energy* 11 (2), 682–692. doi:10.1109/tste.2019.2903783

Li, G., Wang, G., Xue, X., Chen, L., et al. (2021). Design and analysis of condenser mode for jintan salt cavern compressed air energy storage plant of China. *Automation Electr. Power Syst.* 45 (19), 91–99. doi:10.7500/AEPS20210120006

Liu, X., Mei, S., Ding, R., et al. (2023). Current situation, development trend and Application Prospect of compressed air energy storage Project. *Electr. Power Autom. Equip.* 43 (10), 38–47+102. doi:10.16081/j.epae.202309005

Mei, S., Gong, M., Qin, G., et al. (2017). Advanced adiabatic compressed air energy storage system with salt cavern air storage and its application prospects. *Power System Technology* 41 (10), 3392–3399. doi:10.13335/j.1000-3673.pst.2017.1992

Meng, J., Zhang, Z., Zhang, G., Ye, T., Zhao, P., Wang, Y., et al. (2023). Adaptive model predictive control for grid-forming converters to achieve smooth transition from islanded to grid-connected mode. *Transm. Distribution* 17 (12), 2833–2845. doi:10.1049/gtd2.12859

Mirzapour-Kamanaj, A., Talebi, A., Zare, K., Mohammadi-Ivatloo, B., Abdul-Malek, Z., and Anvari-Moghaddam, A. (2022). Optimal look-ahead strategic bidding/offering of integrated renewable power plants and CAES with stochastic-robust approach. *IEEE Access* 10, 107901–107912. doi:10.1109/access.2022.3210033

Shengwei, M. E. I., Tong, Z., Xuelin, Z., et al. (2022). Research and engineering practice of non-supplementary combustion compressed air energy storage: taking Jintan national demonstration project as an example. *Exp. Technol. Manag.* 39 (05), 1–8. doi:10.16791/j.cnki.sjg.2022.05.001

Wang, M., Luo, An, Chen, Y., et al. (2016). The dual-mode control and seamless transfer control method of three-phase inverter. *Trans. Chin. Soc. Electr. Eng.* 31 (16), 124–134. doi:10.19595/j.cnki.1000-6753.tces.2016.16.015

Wen, X., Zhang, H., Yang, D., Zhong, J., and Feng, T. (2021). Research on the bidirectional participation of compressed air energy storage in primary frequency regulation of power grid. *Autom. Instrum.* 42 (12), 67–70+76. doi:10.16086/j.cnki.issn1000-0380.2021010071

Xiong, L., Zhuo, F., Wang, F., Liu, X., Chen, Y., Zhu, M., et al. (2016). Static synchronous generator model: a new perspective to investigate dynamic characteristics and stability issues of grid-tied PWM inverter. *IEEE Trans. Power Electron.* 31 (9), 6264–6280. doi:10.1109/tpel.2015.2498933

Xiong, L., Zhuo, F., Wang, F., Liu, X., Zhu, M., and Yi, H. (2016). A novel fast open-loop phase locking scheme based on synchronous reference frame for three-phase non-ideal power grids. *J. Power Electron.* 16 (4), 1513–1525. doi:10.6113/jpe.2016.16.4.1513

Xu, W., Zhang, W., Hu, Y., et al. (2022). Advanced adiabatic compressed air energy storage multi-energy flow optimization scheduling Model. *Trans. China Electrotech. Soc.* 37 (23), 5944–5955. doi:10.19595/j.cnki.1000-6753.tces.220772

Yuan, X., Lou, G., Liang, C., et al. (2017). Control strategy for microgrid seamless switching via linear active disturbance rejection. *Power Syst. Technol.* 41 (12), 3824–3831. doi:10.13335/j.1000-3673.pst.2017.0748

Zheng, F., Lin, X., Lin, Y., Zhang, Y., and Zhang, Y. (2019). Design of a novel hybrid control strategy for ES grid-connected inverter for smooth microgrid transition operation. *IEEE Access* 7, 171950–171965. doi:10.1109/access.2019.2955713

Zhu, J., Wei, C., Zhang, Y., Hu, D., Zheng, T., and Shan, L. (2023). "Thermal and electric characteristics of mine compressed air energy storage system based on stepped gas compression," in *2023 5th asia energy and electrical engineering symposium* (Chengdu, China: AEEES), 1722–1727. doi:10.1109/AEEES56888.2023.10114342

frontiers | Frontiers in Energy Research

TYPE Original Research
PUBLISHED 26 January 2024
DOI 10.3389/fenrg.2023.1342854

OPEN ACCESS

EDITED BY
Haitao Zhang,
Xi'an Jiaotong University, China

REVIEWED BY
Zhiqiang Zhang,
Hefei University of Technology, China
Jice Wang,
University of Chinese Academy of Sciences, China
Lin Ma,
Hong Kong Polytechnic University, Hong Kong SAR, China

*CORRESPONDENCE
Wei Cui,
abcuiglad@139.com

RECEIVED 22 November 2023
ACCEPTED 18 December 2023
PUBLISHED 26 January 2024

CITATION
Liao X, Bao B, Cui W and Liu D (2024), Load balancing and topology dynamic adjustment strategy for power information system network: a deep reinforcement learning-based approach.
Front. Energy Res. 11:1342854.
doi: 10.3389/fenrg.2023.1342854

Load balancing and topology dynamic adjustment strategy for power information system network: a deep reinforcement learning-based approach

Xiao Liao, Beifang Bao, Wei Cui* and Di Liu

State Grid Information and Telecommunication Group Co., LTD., Beijing, China

As power information systems play an increasingly critical role in modern society, higher requirements are placed on the performance and reliability of their network infrastructure. In order to cope with the growing data traffic and network attack threats in the power information system, we select the power information system data center network as the research object and design an overall system solution based on software defined network, including the application layer, control layer and infrastructure layer. A typical fat tree network topology is simulated and analyzed. We define the load balancing and network topology dynamic adjustment problem as a Markov decision process, and design a data flow path acquisition method based on breadth-first search to construct the action space of each host. Then, a deep reinforcement learning algorithm based on deep Q-network, priority experience replay and target network is introduced to provide solutions for optimizing the performance of power information systems and responding to network attacks. Simulation results show that the proposed method is better than the traditional equal-cost multi-path algorithm in terms of average bandwidth utilization, average jitter and average packet loss, and can reduce the probability of network nodes being attacked by more than 11%.

KEYWORDS

power information systems, load balancing, flood attack, Markov decision process, deep reinforcement learning

1 Introduction

The smart grid (Fanlin and Wei, 2020; Gunduz and Das, 2020; Tufail et al., 2021) is the core of power grid modernization. The burgeoning evolution of power systems necessitates advanced capabilities in data acquisition, transmission, and processing. This evolution fosters a mutually beneficial relationship between information systems and power systems, marking their integration as a key feature of smart grid development. The power information system (PIS) exemplifies this trend by enhancing the interconnectedness of various power system components. This integration facilitates a seamless operational harmony across the spectrum of power generation, transmission, distribution, and consumption.

Alongside these power system developments, the expansion of the Internet has also occurred, which has precipitated an exponential increase in network devices and, correspondingly, network traffic. Such growth imposes substantial demands on network

resource allocation and management. As a new type of network architecture (Hamdan et al., 2021), software defined network (SDN) has a more flexible, dynamic, and frequent form of network resource allocation compared to traditional networks. SDN, characterized by its decoupled control and forwarding functions, centralized management, programmability, and open interfaces, embodies a stratified design. This idea of layered decoupling divides the network into application, control and infrastructure layers. OpenFlow, a standardized communication protocol (Nisar et al., 2020; Wazirali et al., 2021), operates at the intersection of the control and forwarding layers, enabling their disentanglement. The demarcation of control and forwarding planes, alongside features like resource virtualization and programmability, yields multiple advantages. It allows network hardware to concentrate on forwarding efficiency, thus diminishing costs; enables network intelligence through programmable software; and empowers a centralized controller to tailor network configurations in real-time, thereby enhancing service adaptability.

Unbalanced distribution of network traffic not only leads to congestion on a certain link of the network, but also leads to the suboptimal use of available resources. In the context of smart grids, load balancing technology is pivotal, as it allocates the load across operational units, thereby leveraging finite resources to accomplish a broader array of tasks. Using load balancing technology can maximize the use of network resources and improve the performance of the network. The problem of load balancing in SDN is an important research direction for power information systems. Deep reinforcement learning (DRL), a technique that has recently gained traction in artificial intelligence, is increasingly being employed to resolve various challenges in PIS due to its exceptional learning and adaptive capabilities, making it a robust solution for refining SDN load balancing.

However, potential attack risks pose great challenges to the stable operation of power information systems (Dash et al., 2022). External attackers can launch attacks through terminal nodes in the network, such as common flooding attacks, which will have a negative impact on network performance. Current research on the resistance of power information systems to external attacks is lacking. The application of deep reinforcement learning algorithms, which devise optimal strategies through environmental interactions, is significant. Their inherent intelligence and adaptability are critical in identifying, mitigating, and safeguarding against malicious traffic intrusions, thereby bolstering network robustness.

In short, using DRL to solve SDN load balancing and defense attack problems is a very promising research direction. It can maximize the utilization of network resources and improve network performance, which has important practical significance for the development of power information systems and SDN networks. This paper proposes a load balancing and topology dynamic adjustment strategy based on deep reinforcement learning for power information systems. To the best of our knowledge, this is the first work that considers both load balancing and defense against external traffic attacks. The main contributions of this article are as follows:

(1) The problem of load balancing and network topology dynamic adjustment is modeled as a Markov decision process, and both traffic forwarding and defense against flooding attacks are paid attention to under the SDN framework.
(2) This paper proposes a load balancing and network topology dynamic adjustment method based on deep reinforcement learning, and introduces deep Q network, priority experience replay and target network to improve the performance and anti-attack capabilities of the power information system.
(3) Experimental simulations are conducted on the common fat tree topology of power information system data center networks to verify the effectiveness of the method proposed in this article.

The remainder of this article is organized as follows. Section 2 briefly reviews the research efforts related to load balancing and attack defense. In Section 3, we introduce the system architecture of our study. Section 4 presents a detailed description of our proposed method. In Section 5, we provide the simulation results. Finally, in Section 6, we conclude this article.

2 Related work

The escalation of power system capacities inevitably leads to an upsurge in data processing and transmission, thereby intensifying the informational network's transmission burden. To circumvent network link congestion and enhance network performance, the SDN load balancing algorithm has emerged as a pivotal research area within the SDN domain. Scholars globally have delved deeply into SDN load balancing research. The study in Priyadarsini et al. (2019) introduces a self-adaptive load balancing scheme that dynamically distributes load across multiple controllers, effectively managing high-load conditions while accounting for the proximity between switches and target controllers. In Jamali et al. (2019), Genetic Programming based Load Balancing (GPLB) is proposed to select the most efficient path by integrating real-time load data. The study by Chakravarthy and Amutha (2022) presents an innovative algorithm for load balancing that proactively computes the capacity of switches along a packet's routing path. Rupani et al. (2020) proposed a load balancing solution in SDN that utilizes a global network view to select the optimal data transmission path, significantly reducing latency through a neural network model. In Ejaz et al. (2019), explored traffic load balancing within SDN and NFV frameworks, achieving enhanced network performance by deploying a virtual SDN controller as a VNF that dynamically adds secondary controllers to distribute increased traffic loads. The study by Xue et al. (2019) introduces the Genetic-Ant Colony Optimization (G-ACO) scheme, which synergizes Genetic Algorithm (GA) for a rapid global search with ACO for efficient optimal solution finding, significantly enhancing pathfinding efficiency and reducing round-trip times and packet loss rates. Xu et al. (2019) demonstrated enhanced traffic management efficiency through dynamic switch-to-controller mapping in SDN. They introduced the 'BalCon' and 'BalConPlus' migration schemes that balance loads across controllers with minimal migration costs. In Fang et al. (2019), a reinforcement learning-based load balancing algorithm is put forward, applying neural learning for SDN routing and crafting a Q-learning based routing protocol. Nonetheless, such algorithms face challenges like high computational demands and limited scalability in extensive networks. How to design reliable

algorithms with good real-time performance and strong robustness is the focus of this article.

The stable operation of the power system can not be separated from the network security protection. Beyond firewall applications, real-time monitoring through intrusion detection is vital for timely anomaly detection and power system protection. Literature Haghnegahdar and Wang (2020) presents a novel intrusion detection model utilizing a whale optimization algorithm-enhanced artificial neural network to effectively classify various levels of cyber-attacks and incidents within power systems. Li et al. (2020) introduced 'DeepFed', a novel federated deep learning approach for detecting cyber threats in industrial CPSs, utilizing a unique combination of CNNs and GRUs within a privacy-preserving federated learning framework secured by Paillier cryptosystem protocols. A study in Choi et al. (2019) showcases a network intrusion detection system developed using an autoencoder, an unsupervised learning algorithm, boasting a 91.70% accuracy rate. Addressing DDoS attacks, Mendonça et al. (2021) proposes an IDS based on a Tree-CNN with a Soft-Root-Sign (SRS) activation function, enhancing model generalization and expediting training through batch normalization. Literature Pontes et al. (2021) presents the Energy-based Flow Classifier (EFC), an innovative anomaly-based classifier using inverse statistics for flow-based network intrusion detection. Khalid et al. (2019) proposed novel, resource-efficient algorithms that integrate distributed and intrusion detection systems to mitigate flood attacks. This paper innovatively introduces deep reinforcement learning methods to defend against external malicious traffic attacks from the perspective of dynamic adjustment of network edge topology of power information systems.

3 System architecture

In this section, we elaborate on the system architecture of our study. This section is divided into two subsections: the first subsection provides an overview of the overall system architecture, including the application layer, control layer, and infrastructure layer, while the second subsection delves into the details of the fat-tree topology commonly used in power information system data centers.

3.1 Overall system architecture

Power information system plays a vital role in the emerging landscape of smart grid, and its efficient operation relies heavily on a well-constructed system architecture. The core concept of SDN is to separate the control layer and data forwarding layer in the network. The logically centralized control layer uses communication interfaces to implement centralized control of network devices in the data forwarding layer. The application layer can flexibly control network devices in the data forwarding layer by writing software. It requires its own control network to achieve programmable control. Based on the current SDN research, this paper introduces deep reinforcement learning to achieve load balancing and resist attacks in PIS network.

The system architecture of the load balancing and dynamic adjustment strategy studied in this article is shown in Figure 1, which includes three main layers: application layer, control layer and infrastructure layer. These layers work synergistically to create an adaptive and efficient network infrastructure tailored for the unique challenges posed by the PIS data center environment.

Application Layer: The application layer resides at the top of the entire architecture, running trained deep reinforcement learning agents for real-time decision-making. The goal of this layer is to generate load balancing and topology adjustment strategies, ultimately deployed to the infrastructure layer to instruct the underlying terminal devices, ensuring efficient data forwarding and rapid responsiveness in the PIS. Each agent employs the DQN algorithm, using network terminal node information as state input, and leveraging deep Q-networks to select actions. During interaction with the environment, they learn strategies that maximize reward values.

Control Layer: The control layer serves as the central command center for the entire network. It is mainly composed of SDN controllers, bridging the application layer and the infrastructure layer. SDN controllers are responsible for managing network policies, traffic engineering, and routing. The control layer transfers network information collected from the infrastructure layer and terminal requests to the application layer via a northbound interface, and forwards load balancing and topology adjustment strategies received from the application layer to the infrastructure layer via a southbound interface.

Infrastructure Layer: The infrastructure layer resides at the bottom, responsible for data processing, forwarding, and state collection. The infrastructure layer comprises network devices such as switches, routers, etc., often referred to as the data plane. These underlying network devices lack control capabilities and possess only basic data processing functions, such as data forwarding and state collection based on flow tables issued by the controller. In the SDN environment, communication between switches and controllers is facilitated through the OpenFlow protocol, allowing the controller to instruct switches on where to forward data packets, processing packets based on the combination of packet content and switch configuration state.

3.2 Fat-tree topology in power information system data centers

In the power information system, data centers play a critical role. For many power distribution and power consumption end equipment, the switches within the power information system data centers need to process the traffic requests of each terminal equipment in real time and select appropriate communication paths for forwarding. The currently commonly used network architecture in data centers is the fat-tree topology, which is the backbone of network communication and data exchange. It is carefully designed to meet the requirements of high performance, fault tolerance, and scalability, and has become the cornerstone of modern data center architecture. The fat tree topology is an improvement over the traditional three-layer tree topology. Its essence is a three-layer cascaded multi-root tree topology with a switch as the core (switch-only). The entire topology can be described using a single parameter k (k represents the number of ports on a single switch). A classic

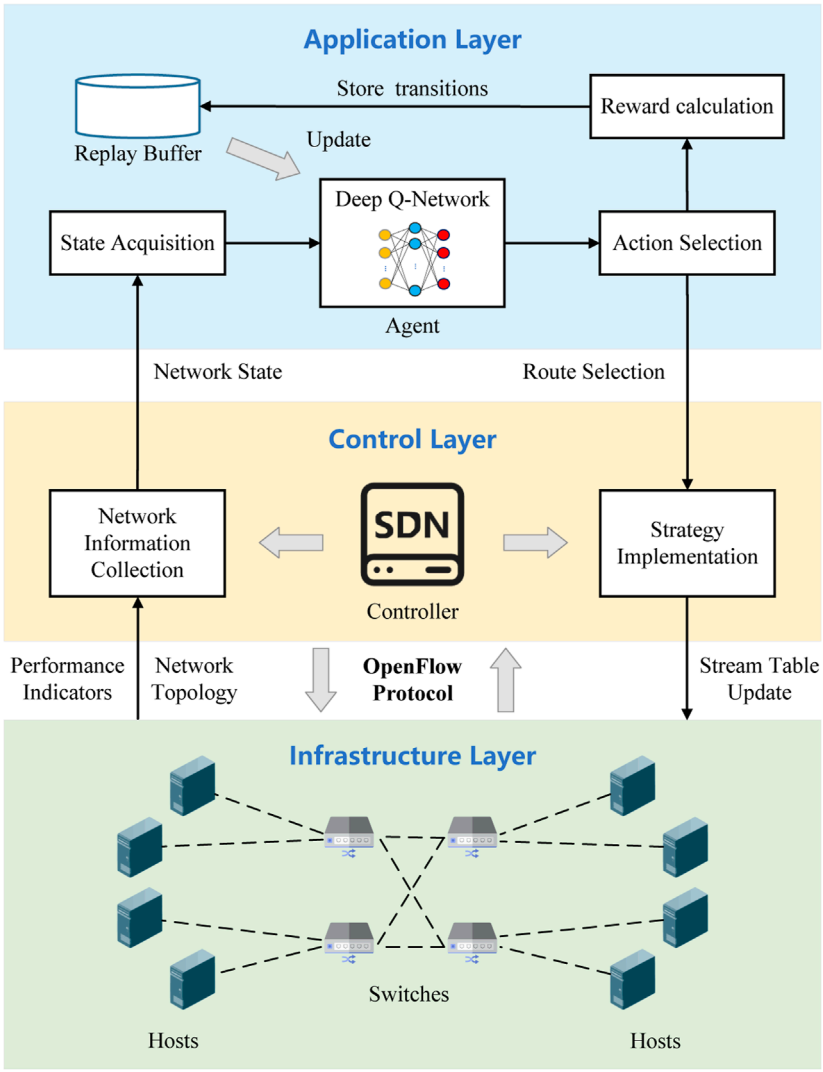

FIGURE 1
Overall system architecture.

quad-tree fat tree topology ($k = 4$) is shown in Figure 2. The three switch layers from top to bottom are the core layer, the aggregation layer and the edge layer.

Core Layer Switches: The core layer serves as the central hub of the fat-tree topology, ensuring high-speed and low-latency connections within the data center. Core layer switches aggregate data from different parts of the data center and are responsible for consolidating and forwarding network traffic. They play a crucial role in facilitating efficient flow of critical information, such as real-time grid monitoring data, between different segments of the data center.

Aggregation Layer Switches: Aggregation layer switches act as an intermediate layer, connecting core layer and edge layer switches. They are pivotal in facilitating communication between various edge switches and the core layer, enabling the efficient flow of data between different sections of the data center. Aggregation switches enhance network scalability and flexibility and are integral to load balancing and redundancy, ensuring optimal data transmission.

Edge layer switches: At the edge layer, network switches are directly connected to end-user devices, sensors, etc. in the power information system. Edge layer switches handle the initial data processing and routing, ensuring that data from different devices can be efficiently transferred to the aggregation layer. These switches play a vital role in managing diverse data sources within the data center, ensuring that incoming data is efficiently directed to its appropriate destination.

Hosts: Host devices include servers, workstations, sensors, and other end-user devices. They are directly connected to edge layer switches and serve as the terminal devices responsible for generating, processing, and consuming data within the power information system. Hosts constitute both the ultimate source and destination of data flows, making them an essential component of the power information system.

As shown in Figure 2, the fat-tree network topology systematically allocates edge layer switches and aggregation layer

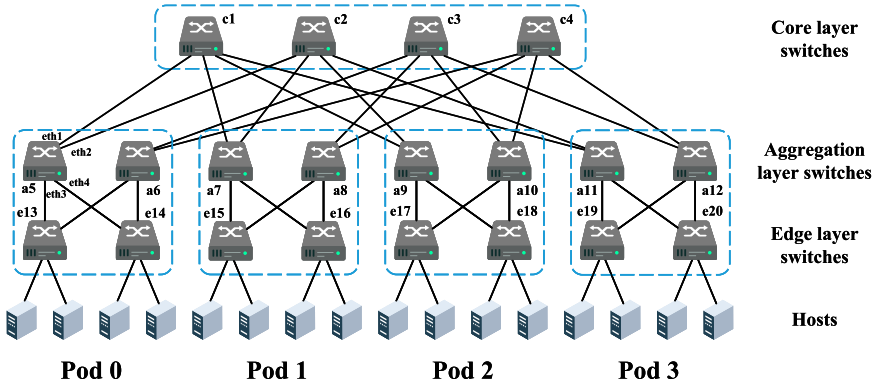

FIGURE 2
Quadruple fat tree topology.

switches to different arrays, referred to as "Pods." A k-fork fat-tree topology consists of k pods, with each pod capable of accommodating $(k/2)^2$ host devices. Each pod's aggregation layer and edge layer contain $k/2$ switches with k interfaces. Each edge layer switch is connected to $k/2$ hosts and $k/2$ aggregation layer switches, while each aggregation layer switch is connected to $k/2$ edge layer switches and $k/2$ core layer switches. Consequently, a k-fork fat-tree structured network can accommodate $k^3/4$ host devices.

Due to its excellent scalability, connectivity, and cost-effectiveness, the fat-tree topology finds widespread application in large-scale system-level network centers, providing high-throughput transmission services for data center networks. This paper focuses on load balancing and flood attack mitigation in the fat-tree topology of data center networks within the power information system, and experimental investigations are conducted using a 4-fork fat-tree topology on a network simulation platform.

4 Proposed method

In this section, we provide a detailed description of our proposed load balancing and dynamic network topology adjustment methodology. Initially, based on the characteristics of the system architecture, a Markov Decision Process is constructed. Subsequently, to determine the action space of each agent, we designed a data flow path acquisition method based on BFS (Breadth-First Search). Following that, we employ Deep Q-Network and Priority Experience Replay techniques to establish the load balancing and topology adjustment algorithm. Lastly, we elaborate on the training process and application details of the introduced algorithms.

4.1 MDP model

Existing SDN routing methods struggle with low efficiency and high computational complexity. Reinforcement learning, known for optimizing strategies, could solve these problems. In reinforcement learning, an agent interacts with an environment over discrete time steps. Reinforcement learning problems are commonly modeled as a Markov Decision Process (MDP), which typically comprises four main components: state, action, transition probability, and a reward function. The state provides a holistic description of the agent's current situation within the environment. An action refers to the decision made by the agent. Transition probability denotes the likelihood of the agent transitioning into a new state after taking a specific action in the current state. The reward function reflects the environment's feedback based on the outcome resulting from an action taken by the agent.

During the interaction with the environment, the expected cumulative reward obtained by the agent in state s_t after taking action a_t according to policy π can be represented by the state-action value function $Q^{\pi}(s_t, a_t)$:

$$Q^{\pi}(s_t, a_t) = E_{\pi}\left[\sum_{t=t_0}^{T} \gamma^{t-1} r_t | s_t, a_t\right] \tag{1}$$

where t_0 denotes the starting time, T represents the ending time, γ is the reward discount factor satisfying the range [0,1], and r_t is the immediate reward obtained at time t.

The primary objective of reinforcement learning is to adjust strategies based on feedback from interactions with the environment, aiming to derive an optimal policy that maps states to the best corresponding actions. This ensures that the value function $V(s)$ for each state s is maximized under this policy. The value function for state s can be represented as:

$$V^{\pi}(s) = E\left[\sum_{t=t_0}^{T} \gamma^{t-1} r_t | s_0 = s\right] \tag{2}$$

Traditional Q-Learning method utilizes tables to store Q-values for state-action pairs. However, such tabular methods are infeasible for problems with large scales, especially for continuous state and action spaces, due to the curse of dimensionality. Integrating with deep learning and using deep neural networks to approximate the Q-value function offers an effective solution to this challenge.

For the fat-tree network in the power information system studied in this paper, our goal is to formulate the optimal traffic

forwarding strategy based on real-time flow requests from each terminal host and to defend against potential flooding attacks. For regular flow requests, the optimal strategy trained using reinforcement learning is used to select forwarding paths. For abnormally high traffic requests (considered as external attacks), communication links between the edge-layer switch and the host should be promptly severed, adjusting the end network topology to prevent attack traffic from entering the power information system. We consider each terminal host as an agent and accordingly train a deep Q-network to guide the flow table policy. For each agent, we construct a Markov decision process, represented by the tuple $\{S, A, P, R\}$, with each element defined as follows:

(1) S represents the state space, with s_t denoting the environment state of the agent at time step t. In the system studied in this paper, considering that each host can access the traffic request information of all hosts. Their acquired state at each moment is identical. The environment state comprises two pieces of information: the target host of each source host and the traffic request. If the target host of the *ith* host is denoted as u_i and the traffic request as w_i, then the environment state at time t can be represented as $s_t = [u_1, \ldots, u_{16}, w_1, \ldots, w_{16}]$.

(2) A denotes the action space, with a_t representing the action taken by the agent at time step t. For each agent, its action space can be represented as $A = [A_0, A_1, \ldots, A_m]$, where A_0 indicates cutting off the communication link with the edge-layer switch (topology adjustment), and $A_1, \ldots, A_m$ represent all shortest paths for forwarding traffic to other hosts.

(3) P indicates the state transition probability. The probability of transitioning from state s_t to s_{t+1} can be represented as $p_t: s_t \times a_t \rightarrow s_{t+1}$.

(4) R signifies the reward function. Through the design of the reward function in this study, we aim to guide agents to achieve load balancing and defend against flooding attacks. Our designed reward function consists of four parts. During the training process, if a host launches a flooding attack, producing an exceptionally high bandwidth request at the current moment, we decide the value of the first part of the reward r_1, based on whether the agent severs the link to adjust the topology. If it successfully adjusts the topology to defend against the attack, then r_1 is 5; otherwise, it is −5. That is:

$$r_1 = \begin{cases} 5, if\ resist\ attacks\ successfully \\ -5,\ else \end{cases} \tag{3}$$

The value of r_1 is designed to incentivize the network's defensive mechanism against flooding attacks. In our model, when a host is under a flooding attack, exhibiting abnormally high bandwidth requests, the network needs to respond effectively. If the network successfully adjusts its topology to mitigate the attack, r_1 is set to a positive value (+5) to reward this effective response. Conversely, if the network fails to adjust and resist the attack, r_1 is set to a negative value (−5) to penalize this failure. This binary reward structure helps in reinforcing the desired behavior of the network in the face of potential threats.

To achieve a regular load balancing effect, we introduce the second part of the reward r_2. Let the designated traffic bandwidth of the host be denoted as $w_{applied}$, and the actual bandwidth of this data stream be w_{actual}. Based on whether the endpoint of the path selected by the agent is the target host, r_2 can be designed as follows:

$$r_2 = \begin{cases} 1 + w_{actual}/w_{applied},\ if\ the\ path\ ends\ at\ destination\ host \\ -3,\ else \end{cases} \tag{4}$$

The value of r_2 is aligned with the goal of achieving optimal load balancing. It is structured to reward actions that lead to efficient traffic distribution across the network. When the endpoint of the path selected by the agent matches the target host (indicating efficient routing), a positive reward (1) is given. This reward is proportionate to the ratio of actual bandwidth to the designated traffic bandwidth, encouraging not only accurate but also efficient bandwidth utilization. In cases where the selected path does not end at the destination host, a negative reward (−3) is assigned to discourage inefficient routing decisions.

Let the data transmission delay be d_j and the packet loss rate be l_p, then the reward for the agent during time interval t can be represented as:

$$r_t = r_1 + r_2 - \beta_1 d_j - \beta_2 l_p \tag{5}$$

where β_1, β_2 are the weight coefficients.

4.2 Data flow path acquisition method

Based on the MDP model established above, determining the action space for each host is the first issue to address. Specifically, the shortest transmission path from a host to all other hosts needs to be defined. Considering the characteristics of the Fat-Tree topology, this paper designs a data flow path acquisition method based on Breadth-First Search (BFS) to construct the action space for each host.

By analyzing the Fat-Tree topology structure, a notable feature emerges: once the data flow reaches the highest node of the transmission path, the downstream path becomes unique. Referring to the Fat-Tree topology in Figure 2, the shortest forwarding paths for different target hosts can be categorized into three types: (1) There is only one shortest path for traffic exchange between two terminal hosts on the same edge switch in the same pod, that is, through the edge switch. (2) For traffic interchange between terminal devices under different edge switches within the same pod, it is only necessary to identify the aggregation switch within that pod, resulting in two shortest paths. (3) For traffic interchange between terminal devices across different pods, identification is needed up to the core switch, leading to four shortest paths. Thus, in the quad-tree Fat-Tree topology shown in Figure 2, we identify 53 shortest paths to all hosts, making the action space dimension 54.

Breadth-First Search (BFS) is an algorithm used for traversing or searching tree structures. We employ BFS to find all potential shortest paths from a source host to other target hosts. When searching within a tree, BFS visits the current node first and then accesses all nodes adjacent to the current node. This approach ensures that during the search

```
Input: source host
Output: action space
Initializes a queue, a collection, and an empty dictionary.
The source host enqueues.
Set collection visited[source] = 1.
while queue is not empty do
    node = queue.dequeue().
    Mark the node as accessed, namely visited[node]=1.
    for neighbor=0 to len(MA[neighbor])-1 do
        if MA[node][neighbor]==1 and visited[i]==0 then
            Add the new path to the queue.
            if neighbor is not source host then
                Adds the path to the shortest path dictionary.
            end
        end
    end
end
```

Algorithm 1. The data flow path acquisition method based on BFS.

process, nodes closest to the source node are visited first. The rationality behind employing BFS in our context stems from its efficiency in identifying all possible shortest paths within a tree-like structure. Given the Fat-Tree topology's hierarchical and layered nature, BFS is particularly adept at systematically exploring this network and identifying optimal paths for data transmission.

The data flow path acquisition method based on BFS proposed in this paper is illustrated as Algorithm 1. Firstly, we define the adjacency matrix M_A for the Fat-Tree network topology. We initialize a queue where each element contains a current node and a path list from the source host to that node. A set is created to keep track of nodes that have already been visited. An empty dictionary is also established to store the shortest paths from target hosts to the source host. Next, the source host is selected as the starting point. In each iteration, a node is popped from the queue, marked as visited, and all its adjacent nodes are traversed. For each adjacent node, if it has not been visited and a connection exists, a new path is appended to the queue. If the adjacent node is not the source host, the found path is added to the shortest path dictionary. This process is repeated until the queue is empty.

We store all discovered paths to construct the action space from the source host to other target hosts. This action space will serve as the foundation for our deep reinforcement learning model, enabling it to efficiently select paths to achieve the objectives of load balancing and network topology adjustment.

4.3 Load balancing and topology adjustment strategies

In electric power information systems, due to the uncertainty of user traffic requests and the potential threat of flooding attacks, network congestion can easily arise, affecting user experience and even system stability. To this end, building upon the established MDP model, we have enhanced the classic DQN algorithm and proposed a strategy based on deep reinforcement learning for load balancing and dynamic network topology adjustment. This strategy dynamically adjusts the data flow forwarding path and network terminal topology in real-time, thereby achieving adaptive and attack-resistant network performance.

Deep neural networks possess powerful representational capabilities. We employ a deep neural network to approximate the Q-function, using the current state of the agent during a given time period as input, and the state-action value $Q(s,a) \approx Q(s,a,\theta)$ as the output, where θ represents the neural network parameters. In each decision-making step, the agent chooses an action based on the current network state, aiming to maximize the expected cumulative reward. By fitting the Q-function using a deep neural network, the agent can handle large-scale and continuous state spaces.

During the training process of the deep Q-network, each interaction with the environment results in an experience transition consisting of the state, action, reward, and next state. The classical DQN algorithm employs a replay buffer to store these transitions. During training, mini-batches of samples are randomly drawn from this buffer to learn, which breaks the temporal correlation between data and stabilizes the learning process. In this paper, we introduce an enhancement by adopting the prioritized experience replay technique, where experiences are drawn based on their importance rather than at random. When storing experience transitions, the temporal difference (TD) error is calculated concurrently. Each experience is assigned a priority based on the magnitude of the TD error, with experiences having larger errors receiving higher priorities. Consequently, when drawing from the replay buffer, experiences with higher priorities are more likely to be chosen. Since priority sampling introduces a bias, importance sampling weights are employed to correct this bias, ensuring that the learning process remains unbiased. Through the prioritized experience replay technique, those experiences that are "challenging" or "unexpected" can be reviewed and learned more frequently, thereby accelerating the learning process and potentially enhancing the network's convergence rate and overall performance.

In addition, we introduce a target network with the same structure as the deep Q-network to solve the correlation and stability problems. Initially, both the deep Q-network and the target network share the same parameters. Throughout the training process, every C steps, the parameters θ' of the target network are updated to θ. After sampling a minibatch of size B from the prioritized experience replay buffer, we can compute the estimated Q-value:

$$Q_{evel} = Q(S_t, A_t, \theta) \tag{6}$$

The target Q-value is:

$$Q_{tar} = r_t + \gamma^* Q\left(s_{t+1}, \arg_{a'} Q(s_{t+1}, a', \theta), \theta'\right) \tag{7}$$

The loss function is calculated based on the difference between the target Q-value and the estimated Q-value. Gradient descent is then applied to update the main network parameters θ. The loss function is defined as:

$$L(t) = \sum_{i=1}^{B} (Q_{tar} - Q_{evel})^2 \tag{8}$$

Through the aforementioned techniques, the agent can more effectively learn the mapping between network states and actions, thereby identifying the optimal strategies for load balancing and topology adjustments. With adequate

Initialize the parameters of deep Q-network θ and target network θ' randomly.
Initialize the prioritized experience replay buffer and the greedy coefficient.
for *episode = 1 to E* **do**
  for *t = 1, 2, , T* **do**
    Initialize the target host and traffic request.
    Receive the initial state s_t.
    Select an action according to the ε-greedy rule.
    The SDN controller sends instructions to update the flow table, then gets the reward r_t and the next state s_{t+1}.
    Calculate the priority and store the transitions $\{priority, (s_t, a_t, r_t, s_{t+1})\}$ in the prioritized experience replay buffer.
    Update the deep Q-network parameters by sampling transitions from the buffer.
    Update the greedy coefficient.
    Set $\theta' = \theta$ every C steps.
  end
end

Algorithm 2. Training Process of the Deep Q-Network.

training, the deep Q-network can provide real-time, dynamic, adaptive, and attack-resistant strategies for load balancing and network topology adjustments in the electric power information system network.

4.4 Training procedure and application

The pseudocode for the training process of the Deep Q-Network is presented in Algorithm 2, which primarily outlines the procedure to update neural network parameters using experience tuples acquired from interactions. We set the total number of training episodes to E. In each episode, interactions are carried out over T discrete time steps. Initially, the target hosts and bandwidth requests of each host are initialized, forming the current state s_t. Subsequently, each agent selects an action a_t from its action space based on the ε-greedy rule. The SDN controller issues commands to update the flow table based on this action, yielding the immediate reward r_t and the subsequent state s_{t+1}. After computing the priority, the transition $\{priority, (s_t, a_t, r_t, s_{t+1})\}$ is stored in the prioritized experience replay buffer. Then, a minibatch of tuples is sampled from the prioritized experience replay buffer for updating the parameters of the deep Q-network. Finally, the greedy coefficient is updated. Every C steps, the parameters of the target network are synchronized with those of the deep Q-network.

After training, each host can make real-time routing planning and topology adjustment decisions based on its own deep Q-network. The application process of the proposed method in this paper is shown in Algorithm 3. In each time interval, the target hosts and bandwidth requests of each host are initialized first, forming the current state s_t. Then, each host selects the optimal action a_t based on the deep Q-network. The SDN controller issues instructions according to a_t to update the flow table, followed by a state transition. Relying on a well-trained deep Q-network, each host can make real-time optimal decisions for load balancing and topology adjustments.

5 Case studies and analysis

In this section, we evaluate the performance of the proposed load balancing and topology adjustment strategy. We first show the experimental settings and metrics. Then, the convergence process of deep Q-networks is present. Finally, we carry out

```
Initialize the well-trained deep Q-networks for
each host.
Receive the target hosts and bandwidth requests of
each host.
Input the state s_t to respective deep Q-network
and get the output a_t with the largest Q-value.
The SDN controller sends instructions to update
the flow table. Load balancing and dynamic network
topology adjustment are completed.
```

Algorithm 3. The application process of the proposed method.

TABLE 1 The hyperparameters for training the deep Q-networks.

Parameter	Value
Number of training episodes	3,000
Time steps in one episode	3
Learning rate	0.001
Discount factor	0.9
Replay buffer size	5,000
Minibatch size	16

simulation experiments under different traffic loads and analyze the results.

5.1 Experimental settings

In the experiments, the computer operating system used is Ubuntu 22.04. The experimental simulation environment utilizes the Mininet simulation software, the Ryu controller, and the OpenFlow 1.3 protocol. We construct a four-fork fat-tree network structure for experimentation, as shown in Figure 2. The number of hosts is 16, with 20 switches, and all link bandwidths are set to 100 Mbps/sec. The simulations were completed by a PC with an Intel Core (TM) i5-12500 CPU @ 3.0 GHz with 16.00 GB RAM, RTX GeForce 2060 SUPER.

During the training of each deep Q-network, we set each episode to consist of three discrete time steps, with a total of 3,000 training episodes. The deep Q-network adopts a uniform fully connected deep neural network. The number of neurons in the input and output layers are 32 and 54, respectively, while the middle layer is a hidden layer with 128 neurons. The learning rate of the deep Q-network is set to 0.001. The reward discount factor is set to 0.9. The exploration coefficient is initially set to 1 and is reduced by 0.0006 after each time step. After decreasing to 0.01, it remains constant. Every 10 steps, the parameters of the target network are synchronized with the deep Q-network. Furthermore, the capacity of the priority experience replay buffer is set to 5,000 with the minibatch size is set to 16. The hyperparameters for training the deep Q-networks are presented in Table 1.

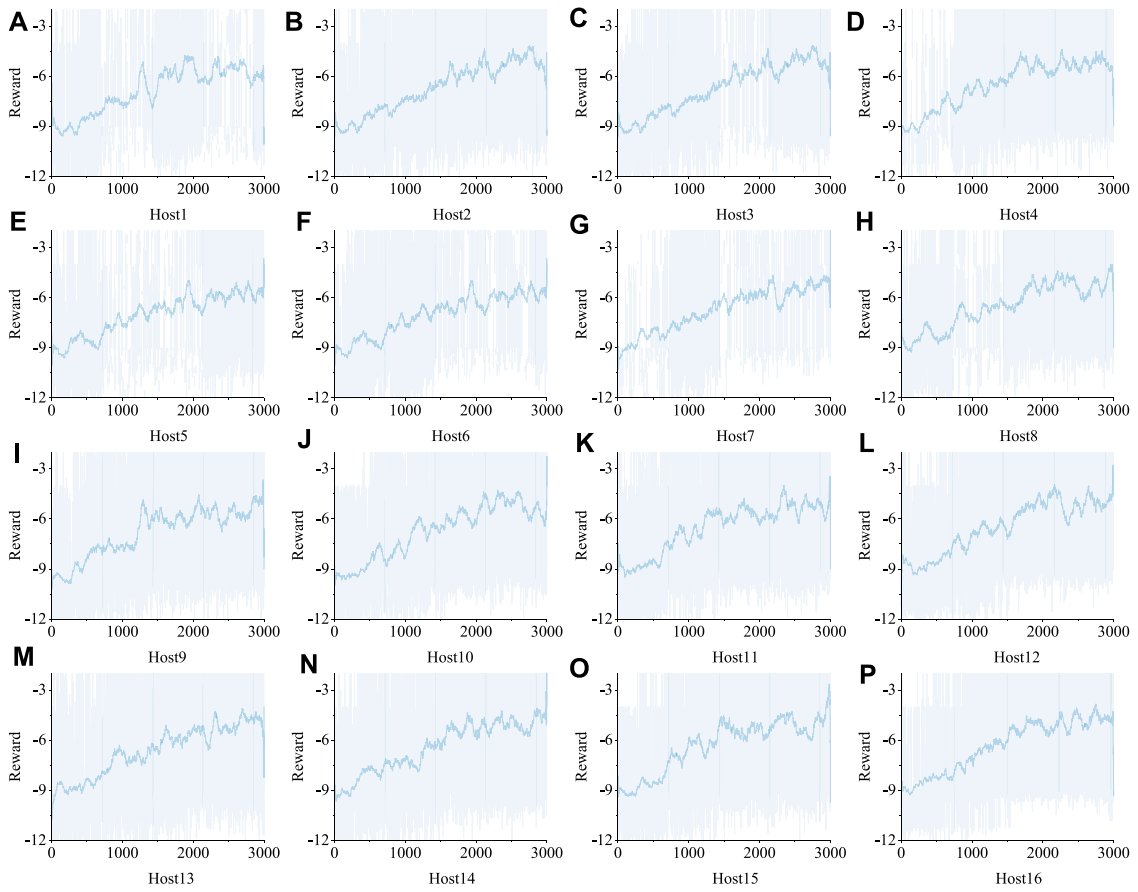

FIGURE 3
The convergence of the DNN training. **A–P** represent the convergence curves of Host1 to 16 respectively.

5.2 Neural network training convergence

First, we evaluate the convergence of the DNN training, with results presented in Figure 3. We have plotted the cumulative rewards for each of the 16 hosts using the deep Q-network over the course of the training episodes. As shown in Figure 3, during the initial phase of training, the cumulative rewards are relatively low, with agents predominantly adopting random strategies for extensive exploration. As training progresses and agents accumulate more experience, the cumulative rewards gradually increase. Notably, after 2,000 episodes, the rewards attained by each agent begin to stabilize and converge. This indicates that during the training process, the agents have learned the optimal strategy. The trained deep Q-networks can thus provide decision-making guidance for load balancing and topology adjustment for each host.

5.3 Load balancing effect analysis

To best restore the actual traffic conditions in the data center network of the power information system, this paper selects the random traffic pattern for simulation experiments. Specifically, each host injects a UDP data stream into any target host in the network with an equal probability. In Mininet, we set the traffic load ratio of each host to the link bandwidth between 0.1 and 0.9 to evaluate network performance under different traffic stress levels. The Iperf tool is used to obtain network testing metrics. Experiments are conducted multiple times under the premise of regular network link allocation, and the average measurement values are taken.

Equal-cost multi-path (ECMP) is a classic routing technique used to forward data traffic along multiple equivalent paths. The path selection strategy of ECMP has various methods such as hashing, polling, and based on path weights. The shortest path for traffic forwarding is usually set with the same routing priority, and each switch makes independent decisions for each hop. To comprehensively evaluate the performance of the algorithm proposed in this paper, we use three metrics: average bandwidth utilization, average jitter, and average packet loss. These metrics are then compared between ECMP and the algorithm proposed in this paper.

(1) Average Bandwidth Utilization: The average bandwidth utilization refers to the ratio of the data volume actually received by the target host to the data volume sent by the source host. The data volume received by the target host varies depending on the network conditions, reflecting the

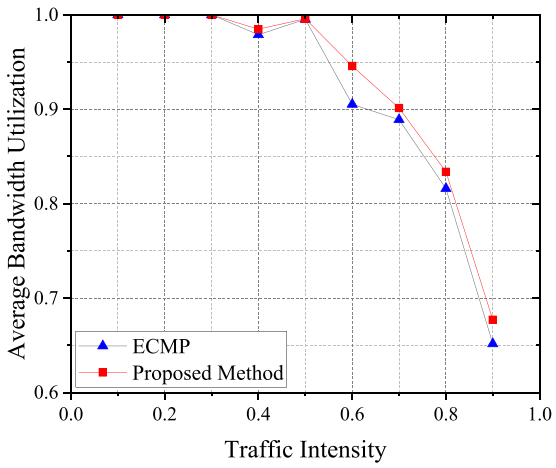

FIGURE 4
Average bandwidth utilization.

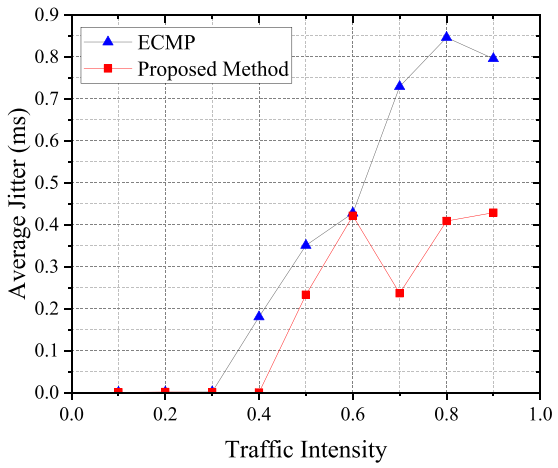

FIGURE 5
The variation of average jitter.

actual bandwidth resources enjoyed by the data stream during network transmission. The data volume sent by the source host corresponds to the designated sending bandwidth. The formula for calculating the average bandwidth utilization is as follows:

$$\eta = \frac{1}{16}\sum_{i=1}^{16}\frac{w_{i,actual}}{w_{i,applied}} \tag{9}$$

Where η represents the average bandwidth utilization, $w_{i,actual}$ denotes the actual bandwidth value of the data transmission for the *ith* host, and $w_{i,applied}$ represents the bandwidth request value of the *ith* host. The average bandwidth utilization is compared to assess the quality of network performance; the larger its value, the better the network performance and the more effective the load balancing.

(2) Average Jitter: The average jitter refers to the average time taken for all data streams in the network to travel from the sender to the receiver. The formula for its calculation is as follows:

$$\varphi = \frac{1}{16}\sum_{i=1}^{16}\left(t_{i,r} - t_{i,s}\right) \tag{10}$$

Where φ is the average jitter, $t_{i,r}$ denotes the reception time of the data stream for the *ith* host, and $t_{i,s}$ represents the starting transmission time of the data stream for the *ith* host. The average transmission delay can be used to measure the degree of link congestion. The smaller its value, the less likely it is for network congestion to occur, indicating a more effective load balancing.

(3) Average Packet Loss: The average packet loss is the ratio of the volume of data that failed to transmit within a unit of time to the volume of data sent. The formula for its calculation is as follows:

$$\delta = \frac{1}{16}\sum_{i=1}^{16}\frac{d_{i,l}}{d_{i,s}} \tag{11}$$

Where δ is the average packet loss, $d_{i,l}$ denotes the volume of data that failed to transmit for the *ith* host, and $d_{i,s}$ represents the volume of data sent by the *ith* host. Serving as a crucial metric for evaluating network performance, the average packet loss rate reflects the system's processing capability. The smaller its value, the better the load balancing effect.

Experiments are conducted at different traffic intensities and the variation of average bandwidth utilization is obtained as shown in Figure 4. As can be seen from the figure, the average bandwidth utilization is close to 1 when the traffic intensity is lower than 0.3. This is due to the relatively low network traffic during this phase, resulting in a minimal probability of link congestion. As the traffic intensity increases, the average bandwidth utilization gradually decreases, indicating a high-load state in the links. Under these circumstances, the method proposed in this paper achieves a higher average bandwidth utilization rate compared to the ECMP algorithm, signifying superior load balancing performance of our method over ECMP.

The variation of average jitter are shown in Figure 5. The graph reveals that at low traffic intensities, both the traditional ECMP algorithm and the method proposed in this paper deliver commendable data transmission outcomes, with the transmission jitter nearly being zero. As the traffic intensity surges, the overall network load increases, potentially leading to link congestion and consequently a general rise in the average transmission jitter. Compared to the ECMP algorithm, our proposed method is adept at selecting the optimal transmission path, effectively minimizing the rate of delay escalation.

Changes in the average packet loss are portrayed in Figure 6. As evident from the graph, in comparison with the ECMP algorithm, the proposed approach effectively reduces the packet loss. This is because the ECMP algorithm evenly distributes the traffic load on each link, overlooking the demands of individual hosts and the network's condition, which can easily lead to network congestion. In contrast, our proposed approach dynamically selects routing paths by comprehensively considering the traffic requests of each host, thereby reducing the probability of link congestion. Summing up

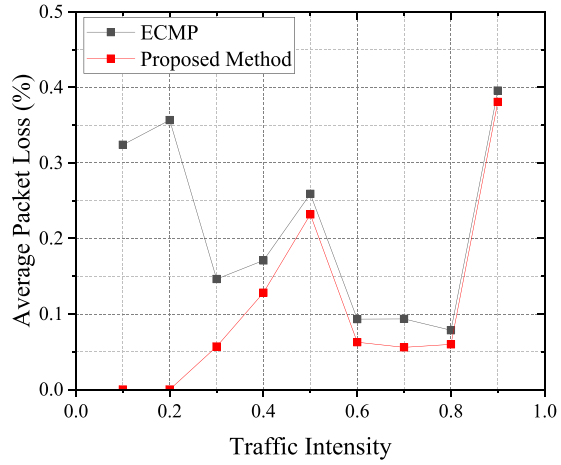

FIGURE 6
The convergence of the DNN training.

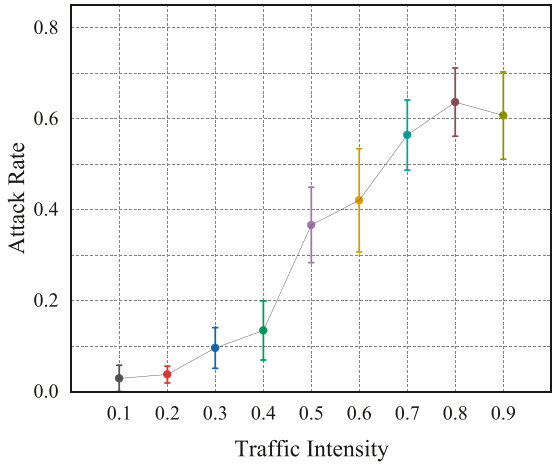

FIGURE 8
The attack rate of the proposed method.

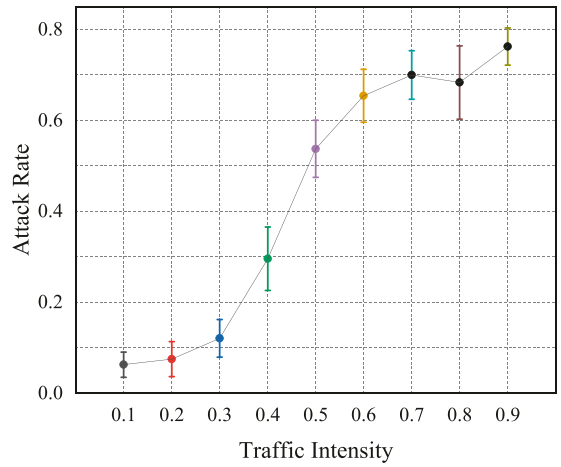

FIGURE 7
The attack rate of the ECMP algorithm.

the analysis, it is evident that the method proposed in this paper achieves superior load balancing results compared to the traditional ECMP algorithm.

5.4 Topology adjustment effect analysis

In addition to load balancing, another significant objective of the method proposed in this paper is to defend against potential attacks by dynamically adjusting network topology. To assess its defense capabilities against flood attacks, we conduct experiments under various traffic intensities. We select a single host as the attacker and adjust the topology using our method, subsequently comparing the success rates of flood attacks before and after the topological adjustments. The success rate of a flood attack is defined as the ratio of the number of other hosts experiencing a decline in average bandwidth utilization to the total number of other hosts. Each host is selected in turn as an attacker for the experiments under different traffic intensities. Experiments were conducted using both the ECMP algorithm and the method proposed in this paper, with results depicted in Figures 7, 8.

In Figures 7, 8, the circular markers represent the average success rate of flood attacks at that particular traffic intensity, while the box area indicates the 95% confidence interval for the flood attack success rate. Comparing the results from Figures 7, 8, it becomes apparent that, at identical traffic intensities, our proposed method effectively reduces the flood attack success rate. This is because our study employs a topology dynamic adjustment strategy based on deep reinforcement learning, which allows for real-time decision-making in accordance with the current network traffic request status. This timely cuts off links connected to terminal nodes that might be under attack, preventing flood attacks from affecting other hosts in the network at the source. Calculations revealed that the average probability of being affected by a flood attack using the ECMP algorithm is 43.244%, while it is 32.159% when employing our method. In comparison to the conventional ECMP algorithm, our method reduces the probability of being attacked by over 11%. This result validates the effectiveness of the approach proposed in this paper in defending against flood attacks.

6 Conclusion

This paper models the problem of load balancing and network topology dynamic adjustment as a Markov decision process, and proposes a method based on deep reinforcement learning to improve the performance, availability and attack resistance of power information systems. According to the characteristics of fat tree topology, we design a data flow path acquisition method based on breadth-first search to construct the action space of each host. Subsequently, we introduce deep Q-network to provide guidance for the optimal strategy of each host. In addition, we also introduce priority experience replay and target network to improve the convergence speed and overall performance of deep

Q-network training. In order to verify the effectiveness of our proposed strategy, we used Mininet to build a typical power information system fat-tree network topology, and conduct a series of case studies and analyses. Experimental results show that our strategy can significantly improve system performance and quickly adjust network topology in the face of network attacks to maintain system stability and availability. The proposed method holds significant promise for broader application in various network infrastructures, particularly in sectors demanding high levels of reliability and attack resilience, thus paving the way for its future adoption in more complex and dynamic network environments.

Data availability statement

The original contributions presented in the study are included in the article/Supplementary Material, further inquiries can be directed to the corresponding author.

Author contributions

XL: Conceptualization, Data curation, Formal Analysis, Methodology, Visualization, Writing–original draft. BB: Investigation, Project administration, Resources, Supervision, Validation, Writing–original draft. WC: Funding acquisition, Resources, Software, Writing–review and editing. DL: Funding acquisition, Project administration, Resources, Supervision, Writing–review and editing.

Funding

The author(s) declare financial support was received for the research, authorship, and/or publication of this article. The work was supported in part by State Grid Information and Telecommunication Group scientific and technological innovation projects “Research on Power Digital Space Technology System and Key Technologies” (SGIT0000XMJS2310456).

Conflict of interest

Authors XL, BB, WC, and DL were employed by State Grid Information and Communications Industry Group Co., Ltd.

Publisher’s note

All claims expressed in this article are solely those of the authors and do not necessarily represent those of their affiliated organizations, or those of the publisher, the editors and the reviewers. Any product that may be evaluated in this article, or claim that may be made by its manufacturer, is not guaranteed or endorsed by the publisher.

References

Chakravarthy, V. D., and Amutha, B. (2022). A novel software-defined networking approach for load balancing in data center networks. *Int. J. Commun. Syst.* 35, e4213. doi:10.1002/dac.4213

Choi, H., Kim, M., Lee, G., and Kim, W. (2019). Unsupervised learning approach for network intrusion detection system using autoencoders. *J. Supercomput.* 75, 5597–5621. doi:10.1007/s11227-019-02805-w

Dash, B., Ansari, M. F., Sharma, P., and Ali, A. (2022). Threats and opportunities with ai-based cyber security intrusion detection: a review. *Int. J. Softw. Eng. Appl. (IJSEA)* 13, 13–21. doi:10.5121/ijsea.2022.13502

Ejaz, S., Iqbal, Z., Shah, P. A., Bukhari, B. H., Ali, A., and Aadil, F. (2019). Traffic load balancing using software defined networking (sdn) controller as virtualized network function. *IEEE Access* 7, 46646–46658. doi:10.1109/ACCESS.2019.2909356

Fang, C., Cheng, C., Tang, Z., and Li, C. (2019). Research on routing algorithm based on reinforcement learning in sdn. *J. Phys. Conf. Ser.* 1284, 012053. doi:10.1088/1742-6596/1284/1/012053

Fanlin, M., and Wei, Y. (2020). “Summary of research on security and privacy of smart grid,” in 2020 International Conference on Computer Communication and Network Security (CCNS), Xi’an, China, 21-23 August 2020 (IEEE), 39–42. doi:10.1109/CCNS50731.2020.00017

Gunduz, M. Z., and Das, R. (2020). Cyber-security on smart grid: threats and potential solutions. *Comput. Netw.* 169, 107094. doi:10.1016/j.comnet.2019.107094

Haghnegahdar, L., and Wang, Y. (2020). A whale optimization algorithm-trained artificial neural network for smart grid cyber intrusion detection. *Neural Comput. Appl.* 32, 9427–9441. doi:10.1007/s00521-019-04453-w

Hamdan, M., Hassan, E., Abdelaziz, A., Elhigazi, A., Mohammed, B., Khan, S., et al. (2021). A comprehensive survey of load balancing techniques in software-defined network. *J. Netw. Comput. Appl.* 174, 102856. doi:10.1016/j.jnca.2020.102856

Jamali, S., Badirzadeh, A., and Siapoush, M. S. (2019). On the use of the genetic programming for balanced load distribution in software-defined networks. *Digital Commun. Netw.* 5, 288–296. doi:10.1016/j.dcan.2019.10.002

Khalid, W., Ahmed, N., Khalid, M., Din, A. U., Khan, A., and Arshad, M. (2019). Frid: flood attack mitigation using resources efficient intrusion detection techniques in delay tolerant networks. *IEEE Access* 7, 83740–83760. doi:10.1109/ACCESS.2019.2924587

Li, B., Wu, Y., Song, J., Lu, R., Li, T., and Zhao, L. (2020). Deepfed: federated deep learning for intrusion detection in industrial cyber–physical systems. *IEEE Trans. Industrial Inf.* 17, 5615–5624. doi:10.1109/TII.2020.3023430

Mendonça, R. V., Teodoro, A. A., Rosa, R. L., Saadi, M., Melgarejo, D. C., Nardelli, P. H., et al. (2021). Intrusion detection system based on fast hierarchical deep convolutional neural network. *IEEE Access* 9, 61024–61034. doi:10.1109/ACCESS.2021.3074664

Nisar, K., Jimson, E. R., Hijazi, M. H. A., Welch, I., Hassan, R., Aman, A. H. M., et al. (2020). A survey on the architecture, application, and security of software defined networking: challenges and open issues. *Internet Things* 12, 100289. doi:10.1016/j.iot.2020.100289

Pontes, C. F., De Souza, M. M., Gondim, J. J., Bishop, M., and Marotta, M. A. (2021). A new method for flow-based network intrusion detection using the inverse potts model. *IEEE Trans. Netw. Serv. Manag.* 18, 1125–1136. doi:10.1109/TNSM.2021.3075503

Priyadarsini, M., Mukherjee, J. C., Bera, P., Kumar, S., Jakaria, A., and Rahman, M. A. (2019). An adaptive load balancing scheme for software-defined network controllers. *Comput. Netw.* 164, 106918. doi:10.1016/j.comnet.2019.106918

Rupani, K., Punjabi, N., Shamdasani, M., and Chaudhari, S. (2020). “Dynamic load balancing in software-defined networks using machine learning,” in Proceeding of International Conference on Computational Science and Applications: ICCSA 2019 (Springer), 283–292. doi:10.1007/978-981-15-0790-8_28

Tufail, S., Parvez, I., Batool, S., and Sarwat, A. (2021). A survey on cybersecurity challenges, detection, and mitigation techniques for the smart grid. *Energies* 14, 5894. doi:10.3390/en14185894

Wazirali, R., Ahmad, R., and Alhiyari, S. (2021). Sdn-openflow topology discovery: an overview of performance issues. *Appl. Sci.* 11, 6999. doi:10.3390/app11156999

Xu, Y., Cello, M., Wang, I.-C., Walid, A., Wilfong, G., Wen, C. H.-P., et al. (2019). Dynamic switch migration in distributed software-defined networks to achieve controller load balance. *IEEE J. Sel. Areas Commun.* 37, 515–529. doi:10.1109/JSAC.2019.2894237

Xue, H., Kim, K. T., and Youn, H. Y. (2019). Dynamic load balancing of software-defined networking based on genetic-ant colony optimization. *Sensors* 19, 311. doi:10.3390/s19020311

frontiers | Frontiers in Energy Research

TYPE Original Research
PUBLISHED 21 February 2024
DOI 10.3389/fenrg.2024.1363267

OPEN ACCESS

EDITED BY
Liansong Xiong,
Xi'an Jiaotong University, China

REVIEWED BY
Fei Jiang,
Changsha University of Science and Technology, China
Xiaokang Liu,
Polytechnic University of Milan, Italy

*CORRESPONDENCE
Congshan Li,
543627767@qq.com

RECEIVED 30 December 2023
ACCEPTED 05 February 2024
PUBLISHED 21 February 2024

CITATION
Li C, Zhang X, He P, Zhao K and Liu L (2024), Improved coordinated control strategy for VSC-MTDC system with DC voltage secondary regulation.
Front. Energy Res. 12:1363267.
doi: 10.3389/fenrg.2024.1363267

Improved coordinated control strategy for VSC-MTDC system with DC voltage secondary regulation

Congshan Li[1]*, Xiaowei Zhang[1], Ping He[1], Kefeng Zhao[1] and Libing Liu[2]

[1]College of Electrical and Information Engineering, Zhengzhou University of Light Industry, Zhengzhou, China, [2]Henan Xuji Instrument Co. Ltd., Xuchang, China

Droop control is widely used in multi-terminal flexible DC (VSC-MTDC) transmission systems by virtue of the advantage of multi-station cooperative unbalanced power dissipation, however, the essence of the droop control strategy is to change the DC current to realize the unbalanced power dissipation, and the resulting DC voltage deviation will affect the normal operation of the system. Firstly, this paper theoretically analyses the working characteristics of the conventional droop control and proposes a control method to realize the quasi-differential-free regulation of DC voltage by translating the droop curve. Second, according to the power margin of the converter station, the feedforward compensation amount of each converter station is reasonably set to avoid the power impact on the converter station. Finally, for the problem that the actual value of DC voltage still deviates from the rated value, a control strategy containing secondary regulation of DC voltage is proposed to further restore the DC voltage to the initial value on the basis of ensuring the effect of power regulation, which improves the stability of the operation of the VSC-MTDC system. The final simulation results verify the effectiveness of the proposed method.

KEYWORDS

droop control, VSC-MTDC, DC voltage deviation, power margin, secondary regulation

1 Introduction

Compared to the line-commutated converter based multi-terminal direct current (LCC-MTDC) in traditional direct current grids, the voltage source converter based multi-terminal flexible direct current transmission (VSC-MTDC) system, which connects multiple converters through direct current lines, has gained extensive use due to independent control of active and reactive power, and flexible control of tidal currents (Wang et al., 2021; Ma et al., 2022; Yang et al., 2022). Droop control can take advantage of the power regulation capability of multiple converter stations simultaneously to absorb unbalanced power, which is widely used in VSC-MTDC systems. However, an obvious drawback of droop control is that it inevitably leads to DC voltage deviation while absorbing unbalanced power at converter stations, which negatively affects the stable operation of the system (Wang et al., 2020; Li et al., 2022).

Aiming to address the inherent DC voltage deviation issue arising from the use of conventional droop control for eliminating unbalanced power at converter stations,

academia has proposed three improvement approaches. The first method involves achieving rational distribution of unbalanced power and mitigating DC voltage deviation by improving the droop coefficient. Refs (Liu et al., 2020; He et al., 2023; Wang et al., 2023). propose various adaptively adjusted droop control methods to suppress DC voltage deviation through the adjustment of the droop coefficient. However, after the completion of the dynamic regulation process, the converter station still experiences a deviation in active power and DC voltage. Furthermore, the aforementioned control method is highly dependent on the droop coefficient; a larger calculated droop coefficient may result in a smaller power fluctuation, yet cause a larger DC voltage deviation, ultimately impacting the overall stability of the system. If the calculated droop coefficient is small, it indicates greater active power distribution capability with a lower likelihood of power fluctuation, however, the DC voltage regulation capability is comparatively weak. Hence, the accuracy of the droop coefficient is crucial when implementing the above control method.

The second method involves overlaying the deviation of the DC voltage onto the droop control and continually optimizing the active power reference to reduce the DC voltage deviation. Refs (Fu Y. et al., 2021; Yu et al., 2022). respectively superimpose the DC voltage deviation onto the active power reference value to achieve non-error DC voltage regulation. However, the essence of the above methods is to transform the droop control station into a DC voltage control station, which loses the advantage of droop control for cooperative unbalanced power dissipation by multiple stations.

The third method is to adjust the active power value of the converter station proactively to achieve quasi non-error DC voltage regulation by shifting the droop curve. Refs (Zhu et al., 2018; Li et al., 2019a). gather the unbalanced power of the DC system, overlay it onto the reference value of active power at the converter station, and shift the droop curve during the dynamic regulation process for quasi non-error DC voltage regulation. The above control method solves the problem that the second control method loses the droop control multi-station coordinated consumption of unbalanced power. However, when the system returns to a stable state, there is still a deviation between the actual value of the DC voltage and the initial value, and the distribution of unbalanced power is not effectively controlled.

Aiming at the problems existing in the above control methods, this paper proposes an improved multi-point DC voltage coordinated control strategy based on the third method. Additionally, to tackle the problem of deviation in actual DC voltage values from the initial value, the paper suggests a control approach incorporating secondary DC voltage regulation, which continually corrects the DC voltage to its initial value. The primary focus of this paper encompasses the following aspects:

(1) An improved coordinated control strategy for multipoint DC voltage is proposed to achieve quasi non-error DC voltage regulation by injecting the unbalanced power as a feed-forward compensation quantity into the droop control.
(2) A power balance allocation scheme is proposed, which uses the available power margin of the converter station to reasonably allocate the unbalanced power of the system, to avoid the problem that the converter station with a smaller power margin is full and other converter stations still have power margin.
(3) A control method with secondary regulation of the DC voltage is proposed, where after the dynamic adjustment process of the system is completed, the DC voltage is restored to the initial value by using the non-static error characteristics of the PI controller.

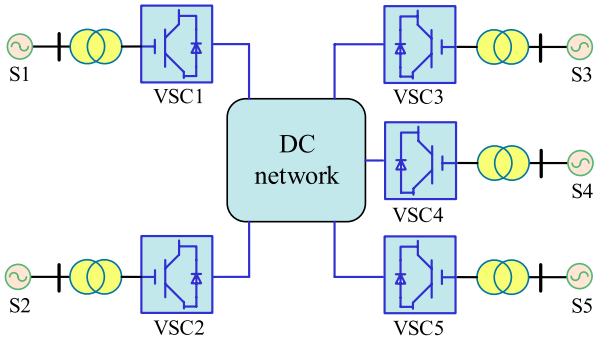

FIGURE 1
VSC-MTDC system structure diagram.

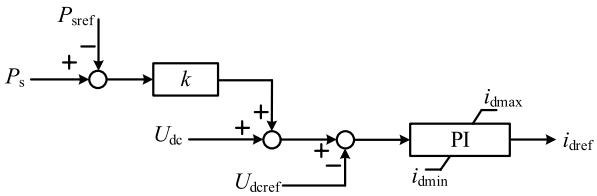

FIGURE 2
DC voltage droop Controller structure diagram.

Finally, a five-terminal VSC-MTDC simulation model is established by PSCAD/EMTDC, and the simulation results verify the effectiveness of the proposed control strategy.

2 Conventional droop control voltage deviation analysis

2.1 VSC-MTDC system model and control principle

The five-terminal VSC-MTDC system's structure is presented in Figure 1. VSC1~VSC5 depict voltage-source type converter stations. The DC side is connected through a DC network in parallel, and the AC side is connected to its corresponding AC grid, and the resistance of the lines between converter stations is 0.25 Ω.

Analogous to the primary frequency regulation characteristics of a conventional generator, droop control avoids the reliance on inter-station communication and leverages the characteristic curves of DC voltage and active power to rapidly distribute unbalanced power and maintain stable control of DC voltage. Figure 2 illustrates the structure of the DC voltage-active power (U_{dc}-P_s) controller.

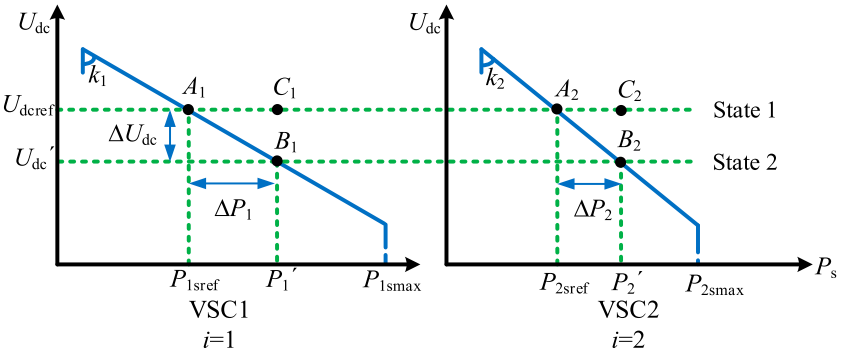

FIGURE 3
DC voltage droop control characteristic diagram.

$$e(t) = U_{dc} - U_{dcref} + k(P_s - P_{sref}). \quad (1)$$

where U_{dc} and U_{dcref} represent the measured and reference values of DC-side voltage, respectively; P_s and P_{sref} represent the measured and reference values of the active power of the converter station, respectively; k is the droop coefficient; and $e(t)$ is the PI controller input (Song et al., 2021; Xiong et al., 2022).

When the system is in a stable state, the input of the PI controller is zero, and Eq. 1 can be simplified to:

$$U_{dc} = U_{dcref} + k(P_{sref} - P_s). \quad (2)$$

2.2 Conventional droop control DC voltage deviation analysis

It is assumed that the DC system has N converter stations, of which 1~m converter stations use conventional droop control; m+1~n converter stations use constant active power control, and n+1~N converter stations use constant AC voltage control.

The sum of the active power reference values of 1~m droop stations P_r is

$$P_r = \sum_{i=1}^{m} P_i. \quad (3)$$

where $1 \le i \le m$.

The sum of active power P_t of m+1~n constant power stations is

$$P_t = \sum_{b=m+1}^{n} P_b. \quad (4)$$

where $m+1 \le b \le n$.

The sum of active power P_w of n+1~N constant AC voltage converter stations is

$$P_w = \sum_{j=n+1}^{N} P_j. \quad (5)$$

where $n+1 \le j \le N$.

The conventional droop control operating curve is shown in Figure 3.

According to Figure 3, at the initial steady state, the system should be operated in state 1. If a power disturbance, ΔP, occurs in the DC system, the m droop stations will use their own droop characteristics to dissipate the unbalanced power while the system operating point moves. When the steady state is reached again, the system is set to run in state 2 and the DC voltage deviation is ΔU_{dc}. From Figure 3, it is apparent that the unbalanced power ΔP_i borne by the droop station i has the following relationship with the DC voltage deviation ΔU_{dc}.

$$\Delta P_i = \frac{\Delta U_{dc}}{k_i}. \quad (6)$$

According to the principle of energy conservation, the sum of the active power variation of each droop station should be equal to ΔP

$$\Delta P = \sum_{i=1}^{m} \Delta P_i. \quad (7)$$

Combining Eq. 6 with Eq. 7, we can obtain

$$\Delta U_{dc} = \frac{\Delta P}{\sum_{i=1}^{m} \frac{1}{k_i}}. \quad (8)$$

$$\Delta P_i = \frac{\Delta P}{k_i \sum_{i=1}^{m} \frac{1}{k_i}}. \quad (9)$$

From Eq. 8, it is apparent that ΔU_{dc} is proportional to ΔP and inversely proportional to the sum of the reciprocals of the droop coefficients of m droop stations. This shows that when the power of the DC system fluctuates, all droop stations will cooperatively dissipate the unbalanced power according to their own droop curves (Li et al., 2019b; Liu et al., 2023).

From Eq. 9, it is evident that the droop coefficient determines how much unbalanced power is borne by the droop station in the dynamic regulation process. If each converter station adopts the same droop coefficient, all converter stations share the unbalanced power; if each converter station adopts different droop coefficients, converter stations with smaller droop coefficients will bear more unbalanced power, and converter stations with larger droop coefficients will bear less unbalanced power.

10.3389/fenrg.2024.1363267

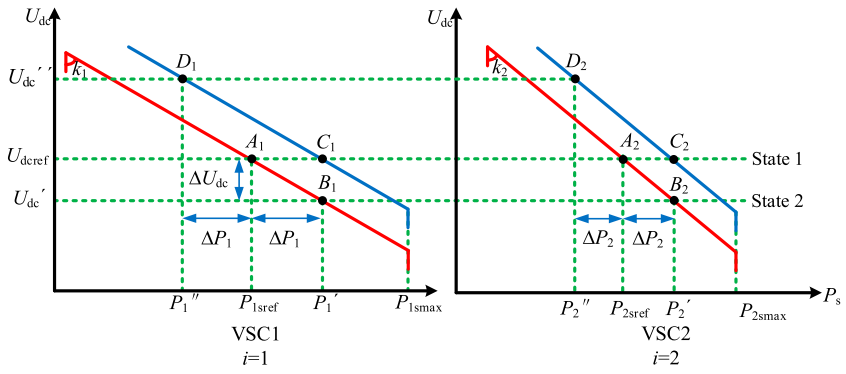

FIGURE 4
Improved coordinated control schematic.

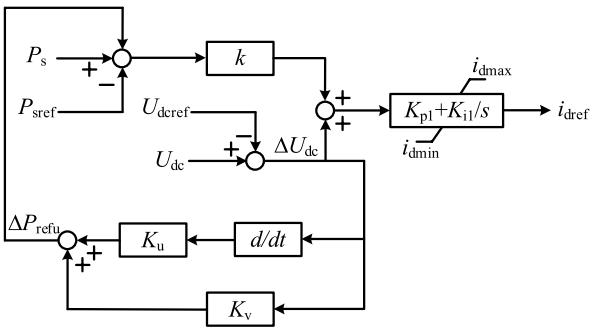

FIGURE 5
Additional DC voltage stabilizer structure.

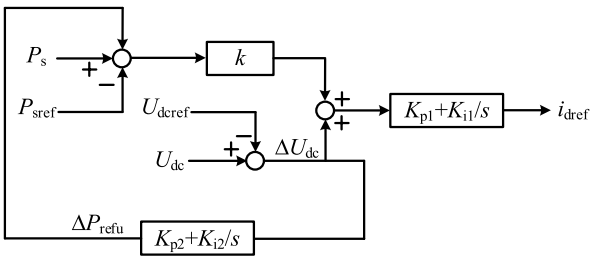

FIGURE 6
DC Voltage secondary regulation controller structure.

3 Improved coordinated control strategy for multi-point DC voltage

3.1 Improved droop control

Aiming at the DC voltage deviation problem inherent in the conventional droop control for dissipating the unbalanced power at the converter station, this paper proposes an improved coordinated control strategy for the multipoint DC voltage of the VSC-MTDC system, in which the unbalanced power is injected as a feed-forward compensation quantity into the droop control, and quasi non-error DC voltage regulation is realized by shifting the droop curve. The characteristic curve of the improved coordinated control strategy is shown in Figure 4.

Let the system be in state 1 at the initial steady state. When power disturbance ΔP occurs in the DC system, each droop station is given a feed-forward compensation amount of magnitude ΔP_i, at this time, the stable operation point of the system is changed from A_i to D_i to realize the flattening of the droop curve. P_{isref} and P_i" are the reference values of active power before and after adjustment of the converter station, respectively, which satisfies

$$P_i'' = P_{isref} - \Delta P_i. \tag{10}$$

And then the converter station dissipates the unbalanced power according to the droop characteristic, and finally the system operates stably near the C_i point, realizing the quasi non-error DC voltage regulation. Compared with the conventional droop control, the active power transmitted by the converter station does not change, while the DC voltage deviation is approximately zero, and the stability of the system is greatly improved (Fu Q. et al., 2021; Liu Q. et al., 2022).

It is worth stating that when the DC network has a power surplus, the system DC voltage will increase, and under the improved droop control strategy in this paper, the droop curve will be shifted to the upper right, and the DC voltage will first rise and then fall to about the initial value. When the system has a power deficit, the system DC voltage decreases, and under the improved droop control strategy in this paper, the droop curve will level off to the lower left, and the DC voltage first decreases and then increases, and finally stabilizes at the initial value.

3.2 Power balance distribution program

To reasonably allocate the unbalanced power in the DC system to each droop station, this paper introduces the available power margin of the converter station to the power allocation coefficients and quickly adjusts the active power reference value. The power balance allocation scheme is shown in Eq. 11.

$$P_i'' = P_{i\text{sref}} - (P_{i\max} - P_{i\text{sref}}) \times \frac{[P_t(t+\Delta t) + P_w(t+\Delta t)] - [P_t(t) + P_w(t)]}{\sum_{i=1}^{m}(P_{i\max} - P_{i\text{sref}})}. \quad (11)$$

where Δt system sampling time. Under this power balance allocation scheme, the control system only needs to collect the active power value of the non-droop station, and update the active power reference value to the droop station when, and only when, the DC system current changes. In the rest of the cases, the droop station only needs to operate stably according to the latest updated active power reference value. At the same time, this power balance allocation scheme requires very low inter-station communication, and even when the communication of each converter station is interrupted, it can still operate normally according to the conventional droop control method.

3.3 DC voltage secondary regulation

According to the above analysis, the unbalanced power of the converter station is injected into the droop control as a feed-forward compensation quantity, and the quasi-differential-free regulation of the DC voltage can be realized by shifting the droop curve. However, when the system returns to the steady state again, the DC voltage deviation still exists, which is not conducive to the stable operation of the system. To address this problem, Res (Liu H. Y. et al., 2022) designs an additional DC voltage stabilizer with the control structure shown in Figure 5.

$$\Delta P_{\text{refu}} = K_u \frac{d\Delta U_{dc}}{dt} + K_v \Delta U_{dc}. \quad (12)$$

where ΔP_{refu} represents the value of additional power generated by the controller; ΔK_u refers to the equivalent inertia coefficient; and ΔK_v is the equivalent damping coefficient.

Analogous to the synchronous generator inertia and damping, the controller takes ΔU_{dc} as the input, and reduces the DC voltage deviation by adjusting the active power reference value during the power perturbation process. However, the DC voltage deviation is generally large in the early stage of power disturbance occurrence, and if ΔK_u and ΔK_v take larger values, it is easy to trigger overshooting of the converter station and generate power oscillations; if ΔK_u and ΔK_v take smaller values, the improvement of DC voltage is generally effective.

Aiming at the above problems, this section proposes an improved control method for the secondary regulation of DC voltage to restore the DC voltage to the initial value in case of slight changes in the active power of the converter station to realize the non-error DC voltage regulation. The structure of the improved DC voltage secondary regulation controller designed in this paper are shown in Figure 6 and Eq. (13):

$$\Delta P_{\text{refu}} = \left(K_{p2} + K_{i2}/s\right)(U_{dc} - U_{dcref}). \quad (13)$$

Similarly, the DC voltage secondary regulation controller takes ΔU_{dc} as input and utilizes the steady state static-free characteristic of the PI controller to realize the static-free regulation of the DC voltage. Unlike the Res. (Liu H. Y. et al., 2022), the DC voltage secondary regulation controller does not have ΔK_u and ΔK_v parameters, so there is no need to worry about the influence of ΔK_u and ΔK_v values on the effect of improving the DC voltage. Meanwhile, to avoid the effect of ΔP_{refu} on the droop control at the early stage of the disturbance occurrence, the DC voltage secondary regulation controller can be operated again to restore the DC voltage to the initial value after some time of the improved droop control action in Section 3.1. Therefore, in this paper, the PI parameters for the droop control and the improved PI parameters for the DC voltage secondary regulation are set reasonably, K_{p1} and K_{i1} are set to 0.2 and 0.5 respectively, and K_{p2} and K_{i2} are set to 0.05 and 0.1 respectively. The step response times of the two PI controllers are differentiated to achieve the purpose of the successive response of the two controllers.

TABLE 1 Main parameters of the VSC-MTDC systems.

Parameters	Numerical value
The nominal capacity of VSC1~VSC5 stations (MW)	250/200/200/150/150
Initial-setting reference power of VSC1~VSC5 (MW)	−220/-100/115/85/100
DC capacitance (μF)	1,000
Nominal DC voltage (kV)	400
Coupling transformer ratio	220/200
VSC1/VSC2 droop coefficient	0.3/0.15
K_{p1}/K_{i1}	0.2/0.5
K_{p2}/K_{i2}	0.05/0.1

4 Simulation and analysis

In this paper, a five-terminal VSC-MTDC system as shown in Figure 1 is built based on PSCAD/EMTDC simulation software, and the specific simulation parameters are shown in Table 1.

4.1 Validation of the effectiveness of an improved coordinated control strategy for multi-point DC voltage

To verify the effectiveness of the improved droop control strategy proposed in Section 3.1 of this paper, the comparative simulations set up in this section are as follows

Control Method 1 (CM1): conventional droop control; Control Method 2 (CM2): the control method proposed in Res. (Li and Gao, 2020); Control Method 3 (CM3): the improved droop control proposed in this paper.

At t = 3 s, the active power command value of VSC3 increased from 115 MW to 175 MW. Figure 7 presents a comparison of the simulation outcomes under the three control methods.

(a) Active power of VSC1
(b) Active power of VSC2
(c) Active power of VSC3, VSC4 and VSC5
(d) System DC voltage

10.3389/fenrg.2024.1363267

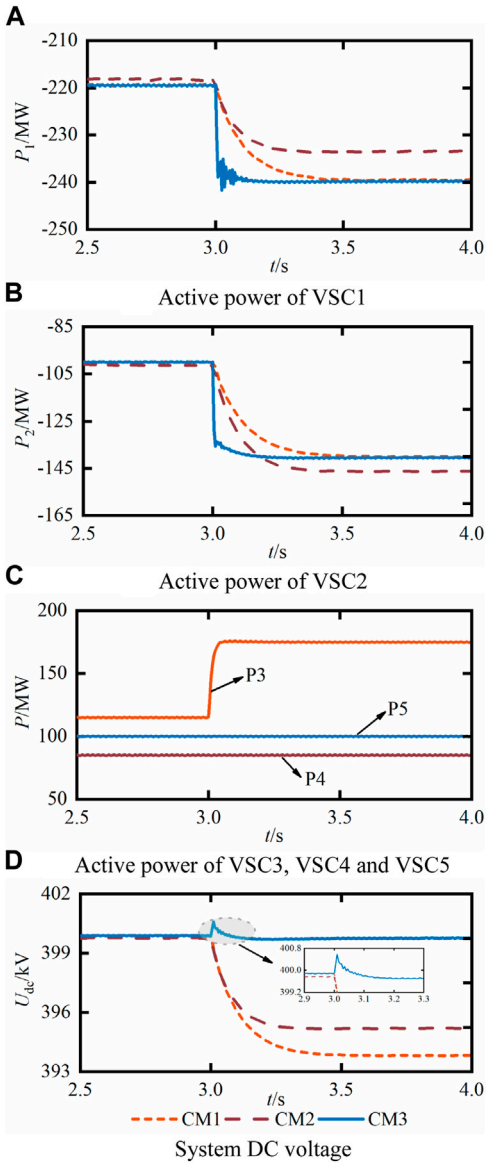

FIGURE 7
VSC3 power increase simulation.

As can be seen in Figures 7A–D, in the initial state, the actual power values of VSC1 and VSC2 under the three control methods are close to the power command value because of the existence of losses in the system, but there is a slight difference. After the change of the active power command value of VSC3 at the moment of 3 s, it is equivalent to the power surplus of the DC system, and the DC voltage of the system is gradually reduced. Under the control of CM1, the droop stations VSC1 and VSC2 adjust their active power command values according to the amount of change in DC voltage by a fixed droop coefficient, and the transmitted power changes from −219.5 MW and −100 MW to −239.5 MW and −140 MW, respectively, with a sharing amount of 20 MW and 40 MW, and a DC voltage deviation of 6.08 kV.

Under CM2 control, the droop coefficient is obtained by calculating according to the fixed margin of the converter station, which optimizes the power distribution of the DC system compared

TABLE 2 Simulation results.

Control strategy	CM1	CM2	CM3
Initial DC voltage/kV	399.89	399.77	399.88
Steady-state DC voltage/kV	393.81	395.20	399.76
DC voltage deviation/kV	6.08	4.57	0.12
DC voltage deviation rate/%	1.52	1.14	0.03

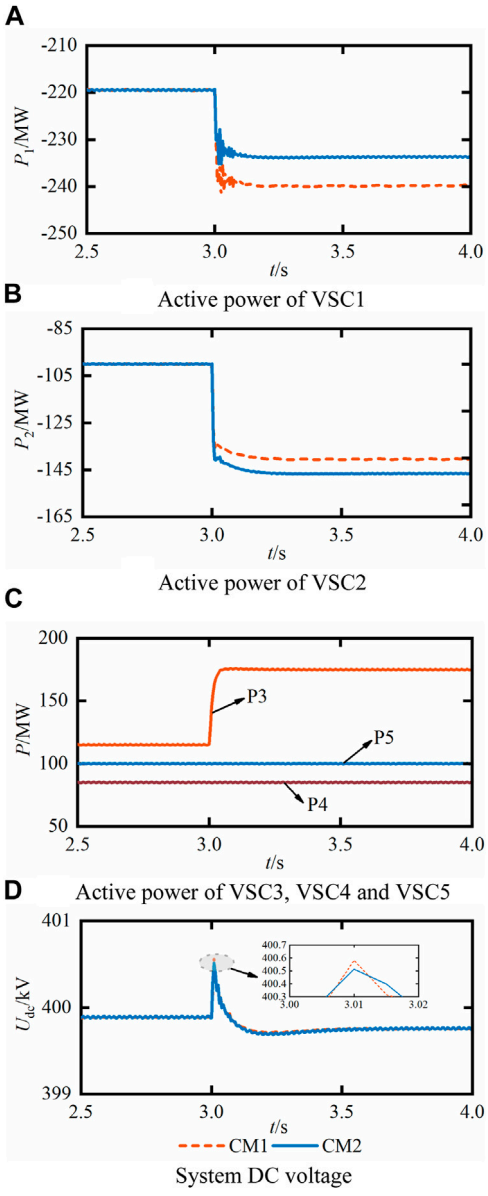

FIGURE 8
VSC3 power increase simulation.

to CM1 control, thus reducing the deviation of the DC voltage. The sharing of VSC1 and VSC2 is 15.2 MW and 44.8 MW, respectively, and the deviation of the DC voltage is 4.57 kV.

Under the control of CM3, it can be seen from Figure 7D that the DC voltage first rises and then decreases, which is in line with the

10.3389/fenrg.2024.1363267

TABLE 3 Simulation results.

Control strategy	CM1	CM2
Initial DC voltage/kV	399.89	399.89
Steady-state DC voltage/kV	393.76	393.76
DC voltage deviation/kV	0.12	0.12
DC voltage deviation rate/%	0.03	0.03

analysis in Section 3.1 of this paper. By feedforward compensation of unbalanced power to the active power command value of VSC1 and VSC2, the sharing of VSC1 and VSC2 are 20 MW and 40 MW, respectively, and the DC voltage deviation is 0.12 kV. Compared with CM1, the active power sharing of VSC1 and VSC2 does not change, while the DC voltage deviation is approximately zero, and quasi non-error DC voltage regulation is realized. The simulation results are shown in Table 2.

4.2 Validation of the effectiveness of the power balance allocation scheme

To verify the effectiveness of the power balance allocation scheme proposed in Section 3.2 of this paper, the comparison simulation set up in this section is as follows

Control Method 1 (CM1): Improved droop control; Control Method 2 (CM2): Improved droop control + power balance allocation scheme.

At t = 3 s, the VSC3 active power instruction value has increased from 115 MW to 175 MW. Figure 8 illustrates the comparison between simulation outcomes obtained with the two control methods.

As can be seen from Figures 8A–D, under CM1 control, the system's unbalanced power is allocated to VSC1 and VSC2 through a fixed ratio without considering the actual power margin of the converter stations, which may easily cause some converter stations to be fully loaded and thus lose the ability to control the DC voltage when the unbalanced power is too large. The unbalanced power allocated to VSC1 and VSC2 is 20 MW and 40 MW, respectively, and the DC voltage deviation is 0.12 kV.

Under CM2 control, the system's unbalanced power is reasonably allocated to VSC1 and VSC2 according to the power margin of the converter station, which avoids the problem that VSC1, which has a small power margin, can easily reach full load. The unbalanced power allocated to VSC1 and VSC2 are 14 MW and 46 MW, respectively, and the deviation of the DC voltage is 0.12 kV the simulation results are shown in Table 3.

4.3 Validation of the effectiveness of secondary regulation control of DC voltage

To verify the effectiveness of the DC voltage secondary regulation control strategy proposed in Section 3.3 of this paper, the comparative simulations set up in this section are as follows:

At t = 3 s, the active power command value for VSC3 is reduced from 115 MW to 45 MW. Figure 9 presents a comparison of the simulation outcomes across the three control methods.

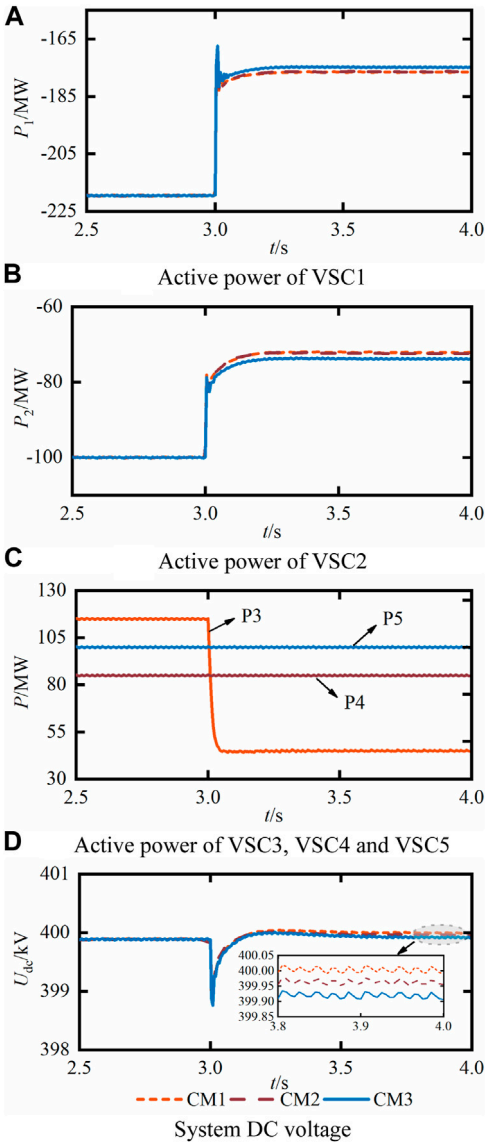

FIGURE 9
VSC3 power reduction simulation.

From Figures 9A–D, it can be seen that when the system has a power deficit, the DC voltage first decreases and then increases, which is consistent with the analysis in Section 3.1 of this paper. Under CM1 control, since the system does not have a DC voltage recovery controller, the DC voltage stabilization value still deviates from the initial value, with a deviation value of 0.11 kV. Under CM2 control, it can be seen from Figure 9D that the additional DC voltage stabilizer can further reduce the DC voltage deviation, with a deviation value of 0.08 kV. Since the ΔK_u and ΔK_v parameters are fixed values, which limits the DC voltage recovery effect, the DC voltage is gradually recovered under CM3 control by adjusting the active power reference values of VSC1 and VSC2 in small increments using the static-free characteristic of the PI controller. When the system reaches the steady state again, the DC voltage deviation is 0.02 kV. Simulation results are shown in Table 4.

TABLE 4 Simulation results.

Control strategy	CM1	CM2	CM3
Initial DC voltage/kV	399.89	399.89	399.89
Steady-state DC voltage/kV	399.99	399.96	399.90
DC voltage deviation/kV	−0.1	−0.07	−0.01
DC voltage deviation rate/%	0.025	0.018	0.0025

5 Conclusion

In this paper, we propose an enhanced coordinated control approach for VSC-MTDC systems, which includes secondary regulation of DC voltage. The aim is to address the inherent DC voltage deviation issue that arises from conventional droop control in the presence of unbalanced power dissipation at converter stations. Our findings suggest that this approach provides superior outcomes.

(1) The quasi non-error DC voltage regulation can be realized by compensating the active power reference value of the converter station through the feed-forward and shifting the droop curve.
(2) The unbalanced power is allocated according to the power margin of converter stations, which can effectively avoid the situation that some converter stations are overloaded while other converter stations still have a power margin.
(3) The DC voltage deviation can be further reduced by the DC voltage secondary regulation controller to improve the stability of system operation.

Data availability statement

The raw data supporting the conclusions of this article will be made available by the authors, without undue reservation.

Author contributions

CL: Writing–original draft. XZ: Writing–original draft. PH: Writing–original draft. KZ: Writing–review and editing. LL: Writing–review and editing.

Funding

The author(s) declare financial support was received for the research, authorship, and/or publication of this article. This work is jointly supported by the Key Programs of Higher Education Institutions in Henan Province (No. 23A470011), and National Natural Science Foundation of China project (No. 52377125), and the Smart Grid Sichuan Key Laboratory 2022 Open Fund Project (No. 2022-IEPGKLSP-KFYB01).

Conflict of interest

Author LL was employed by Henan Xuji Instrument Co. Ltd.

The remaining authors declare that the research was conducted in the absence of any commercial or financial relationships that could be construed as a potential conflict of interest.

Publisher's note

References

Fu, Q., Du, W. J., Wang, H. F., Ren, B. X., and Xiao, X. Y. (2021b). Small-signal stability analysis of a VSC-MTDC system for investigating DC voltage oscillation. *IEEE Trans. Power Syst.* 36 (6), 5081–5091. doi:10.1109/TPWRS.2021.3072399

Fu, Y., Shao, X. Y., and Li, H. (2021a). Transient voltage stability control strategy of DC distribution network. *High. Volt. Eng.* 47 (4), 1354–1362. doi:10.13336/j.1003-6520.hve.20200040

He, P., Zhang, X. W., Li, C. S., Yun, L., Yang, H., and Yan, Y. B. (2023). Smooth regulation of DC voltage in VSC-MTDC systems based on optimal adaptive droop control. *Tech. Gaz.* 30 (4), 1234–1240. doi:10.17559/TV-20220806130349

Li, H., Meng, K., Li, X., and Peng, Y. F. (2022). Simulation of wind power integration with modular multilevel converter-based high voltage direct current. *Tech. Gaz.* 29 (1), 301–307. doi:10.17559/TV-20210729043234

Li, Y. H., and Gao, L. (2020). Control strategy of flexible DC distribution system based on droop characteristics. *Mod. Electr. Power* 37 (4), 391–399. doi:10.19725/j.cnki.1007-2322.2019.0574

Li, Z., Li, Y. Z., Lu, Y. P., Zhan, R. P., He, Y., and Zhang, X. P. (2019b). Active power balance oriented coordinating control strategy for VSC-MTDC system. *Automation Electr. Power Syst.* 43 (17), 117–124. doi:10.7500/AEPS20181224003

Li, Z., Li, Y. Z., Zhan, R. P., He, Y., and Zhang, X. P. (2019a). AC grids characteristics oriented multi-point voltage coordinated control strategy for VSC-MTDC. *IEEE Access* 7, 7728–7736. doi:10.1109/ACCESS.2018.2890406

Liu, C. R., Liu, H. Y., Jiang, S. W., and Zheng, L. (2023). Dynamic frequency support and DC voltage regulation approach for VSC-MTDC systems. *CSEE J. Power Energy Syst.* 9 (2), 645–658. doi:10.17775/CSEEJPES.2021.01790

Liu, H. Y., Liu, C. R., Zheng, L., and Wang, Q. Q. (2022b). Cooperative optimal droop control for VSC-MTDC system with quasi non-error DC voltage regulation. *Automation Electr. Power Syst.* 46 (6), 117–126. doi:10.7500/AEPS20210706007

Liu, Q., Wang, Y. Z., Wang, S. X., Liang, D., Zhao, Q. Y., and Zhao, X. S. (2022a). Voltage regulation strategy for DC distribution networks based on coordination of centralized control and adaptive droop control. *IEEE Trans. Power Deliv.* 37 (5), 3730–3739. doi:10.1109/TPWRD.2021.3135884

Liu, Y. P., Xie, S., Liang, H. P., and Xie, Q. (2020). Adaptive droop control strategy for VSC-MTDC system considering DC voltage errors among converter stations. *Trans. China Electrotech. Soc.* 35 (15), 3270–3280. doi:10.19595/j.cnki.1000-6753.tces.190722

Ma, W. Z., Guang, Z. J., Zhang, K. T., Zhang, J., Yao, Y. X., and Li, M. S. (2022). Live test technology for metal shielding of medium and low voltage power cables in continuous state. *Electr. Power Eng. Technol.* 41 (06), 75–81+139. doi:10.12158/j2096-3203202206.009

Song, S. G., Roy, M., and Gilsoo, J. (2021). Cost-based adaptive droop control strategy for VSC-MTDC system. *IEEE Trans. Power Syst.* 36 (1), 659–669. doi:10.1109/TPWRS.2020.3003589

Wang, W. Y., Yin, X., Cao, Y. J., Jiang, L., and Li, Y. (2021). A distributed cooperative control based on consensus protocol for VSC-MTDC systems. *IEEE Trans. Power Syst.* 36 (4), 2877–2890. doi:10.1109/TPWRS.2021.3051770

Wang, Y. Z., Qiu, F. L., Liu, G. W., Lei, M., Yang, C., and Wang, C. S. (2023). Adaptive reference power based voltage droop control for VSC-MTDC systems. *J. Mod. Power Syst. Clean Energy* 11 (1), 381–388. doi:10.35833/MPCE.2021.000307

Wang, Z. J., He, J. H., Xu, Y., and Zhang, F. (2020). Distributed control of VSC-MTDC systems considering tradeoff between voltage regulation and power sharing. *IEEE Trans. Power Syst.* 35 (3), 1812–1821. doi:10.1109/TPWRS.2019.2953044

Xiong, Y. X., Yao, W., Shi, Z. T., Fang, J. K., Ai, X. M., Wen, J. Y., et al. (2022). Adaptive dual droop control of MTDC integrated offshore wind farms for fast frequency support. *IEEE Trans. Power Syst.* 38 (3), 2525–2538. doi:10.1109/TPWRS.2022.3179504

Yang, L., Zhao, J. J., Liu, H., Kong, Q. K., Zhao, Y. H., Cheng, L., et al. (2022). Adaptive droop control of the VSC-MTDC distribution network considering power–voltage deviation. *Front. Energy Res.* 9. doi:10.3389/fenrg.2021.814489

Yu, X., Lu, J., Dong, Y. L., Zhang, Q. W., Gan, Z. Y., and Wang, Y. Z. (2022). A steady-state voltage control method for a multi-terminal hybrid UHVDC transmission system. *Power Syst. Prot. Control* 50 (1), 174–180. doi:10.19783/j.cnki.pspc.210206

Zhu, H. Q., Li, Y., Wang, Z. Y., Li, C., and Cao, Y. J. (2018). Coordinated droop control strategy considering indifference regulation of DC voltage for MMC-MTDC system. *Electr. Power Autom. Equip.* 38 (7). doi:10.16081/j.issn.1006-6047.2018.07.027

frontiers | Frontiers in Energy Research

TYPE Original Research
PUBLISHED 06 March 2024
DOI 10.3389/fenrg.2024.1370585

OPEN ACCESS

EDITED BY
Liansong Xiong,
Xi'an Jiaotong University, China

REVIEWED BY
Yangbin Zeng,
City University of Hong Kong, Hong Kong SAR, China
Jiajie Luo,
Siemens Gamesa Renewable Energy, United Kingdom

*CORRESPONDENCE
Conghuan Yang,
conghuanyang@foxmail.com

RECEIVED 15 January 2024
ACCEPTED 29 January 2024
PUBLISHED 06 March 2024

CITATION
Yang C, Zhang Q and Zhao Z (2024), Filtering characteristics of parallel-connected fixed capacitors in LCC-HVDC considering the variations of system strength.
Front. Energy Res. 12:1370585.
doi: 10.3389/fenrg.2024.1370585

Filtering characteristics of parallel-connected fixed capacitors in LCC-HVDC considering the variations of system strength

Conghuan Yang[1]*, Qingtao Zhang[2] and Zhiyi Zhao[3]

[1]Guangzhou Maritime College, Guangzhou, China, [2]Logistics Engineering College, Shanghai Maritime University, Shanghai, China, [3]School of Electric Power Engineering, South China University of Technology, Guangzhou, China

The AC power system strength exhibits time-varying characteristics during operation, thereby affecting the filtering performance of filters in the system. Failure to account for this variability may result in the harmonic levels exceeding permissible limits under specific power system strength, thereby affecting the normal operation of the power system. Consequently, building upon the existing filtering technique based on parallel-connected fixed capacitors for LCC-HVDC systems, a method for tuning the parameters of parallel-connected capacitors is proposed, thereby the capacitance range meets the filtering requirements under various system strengths.

KEYWORDS

AC/DC system, HVDC, harmonic filtering, AC power system strength, power electronics-dominated network

1 Introduction

High voltage direct current (HVDC) transmission technology plays an important role in large-capacity and long-distance transmission applications (Agelidis et al., 2006; Tang and Xu, 2014). However, with the increasing number of converter stations in the power system, the harmonic levels in the power grid are also rising (Xin et al., 2020). Excessive harmonics can lead to distortion of the AC waveform and reactive power deficits (Xue et al., 2019), posing a serious threat to the safe operation of the power system (Geng et al., 2018). To address this issue, power grid companies have established the corresponding harmonic content standard (IEEE, 2014), specifying that the Total Harmonic Distortion (THD) value of harmonic voltage and current should not exceed 1.5%. To meet the standards, effective measures need to be taken. AC filters are essential components in HVDC transmission system for mitigating harmonics (Lee et al., 2015). In addition, the AC power system strengths have a significant impact on the operation of the power grid and the strengths can be quantified using the short-circuit ratio (SCR) (Li et al., 2020). Li et al. (2022) provide the typical variation of the SCR and its impact on the frequency and voltage stability. Lower AC strength corresponds to lower resonance frequencies and an increasing risk of resonance, leading to the degradation of the system's normal performance and distortion of voltage. In summary, weak AC power system strength can weaken the system's robustness and stability. Increasing the AC power system strength is beneficial for raising the system's resonant frequency and stability, while achieving the better filtering effects (Chen et al., 2018).

For LCC-HVDC systems, it is necessary to consider both the reduction of AC harmonics and the compensation of reactive power (Liu and Zhu, 2013). Traditionally, active or passive filters are commonly employed to achieve these objectives. The circuit topology of passive filters is relatively simple, but they suffer from drawbacks such as large space requirements and poor filtering effectiveness due to the resonance points shifting. Consequently, research and application of active filter have become more extensive. Various design approaches for active filters have been proposed (Yang et al., 2022; Farghly et al., 2022; Du et al., 2022), addressing aspects such as optimizing the multi-topology structure of passive filters, parallel filtering structures based on hybrid systems, and adopting two-parallel single-tuned LC structures while considering the time-delay effect of controllers. The designed filters can effectively reduce harmonics and simultaneously reduce the size of capacitor banks to reduce reactive power compensation. Liu et al. (2020) consider the coordination between hybrid active filters and existing reactive power compensation devices. They introduce a novel AC filtering system that utilizes a series-connected passive resonance topology and a control scheme for active filtering. This not only enhances the harmonic suppression performance of LCC-HVDC, but also optimizes the reactive power compensation between different filter groups thereby reducing HVDC costs.

The above filtering technologies typically require the addition of AC filter stations. This entails significant space occupation, and the necessity to address issues such as losses and maintenance. Therefore, novel filtering technique have been proposed. Huang et al. (2022) introduce a hybrid active power filter with simple combination of passive filters and IGBT valves. The selected passive filter capacity and topology effectively enhance the filtering efficiency while ensuring independence between the filter and AC system, preventing resonance. However, the system configuration cost is high and the control of IGBT valves is difficult. A novel induction filtering technique based on the field-circuit coupling calculation method is proposed by Li et al. (2012), which greatly reduces the harmonic current content, enhances the excitation performance, improves the electromagnetic environment, and reduces the harmonic losses of HVDC converter transformers. Zhai et al. (2017), Zhao et al. (2022), and Xue et al. (2018) propose a novel filtering technique based on parallel-connected fixed capacitors in HVDC converters, which effectively suppresses harmonics without external AC filters and reactive power compensation devices. It also provides reactive power compensation and suppresses the commutation failure. This filtering method successfully address the issues associated with traditional filters. Nevertheless, the above studies do not take into account the impact of AC power system strength on the filtering performance of the filters. Power system strength is a crucial indicator of power system stability and play a vital role in power system operation. For the novel filtering technique involving the addition of parallel-connected fixed capacitors, it is crucial to consider whether the capacitance of the parallel capacitor can still maintain the system stability and meet the harmonic requirement under the varying system strengths.

To address aforementioned problems, this paper analyzes the impact of system strength on the filtering. Additionally, a tuning method for parallel-connected capacitors is proposed considering power system strength, establishing a capacitance range that meets filtering standards. This method not only contributes to the fault and transient analysis of novel filtering technique involving parallel-connected fixed capacitors but also provide valuable guidance for the configuration of capacitance parameters in practical engineering.

The filtering methods of different references are classified in Table 1.

The rest of the paper is organized as follows: Section 2 introduces the operation principle of novel filtering technology. Section 3 proposes a parameter tuning method for parallel-connected fixed capacitors. Section 4 validates the theoretical result and determines the range of capacitor capacitance. Section 5 combines the simulation to further determine the range of capacitor capacitance. Brief conclusions are drawn in Section 6.

2 Operation principle of novel filtering technique

In response to the shortcomings associated with the traditional filters, Xue et al. (2018) propose a novel filtering technology by adding parallel-connected fixed capacitors to the inverter side of the converter station.

The circuit diagrams for the novel filtering technique are shown in Figures 1, 2, where L_s is the smooth inductance, L_c is the transformer equivalent inductance, R_s is the DC resistance, *TY(D)1~TY(D)6* are the thyristors of the converter bridge, *CapY(D)ab, CapY(D)bc, CapY(D)ac* are the parallel-connected fixed capacitors, *LY(D)abc* are series inductance, mainly used for absorbing surplus reactive power. C_a is the DC filtering capacitor, Z_{inv} is the equivalent impedance of AC system at the inverter side, and $Z_{sys}(n)$ is the grid impedance at the n_{th} harmonic frequency.

It can be seen from Figure 2 that the impedance of the capacitor branch will be small at high-frequencies, allowing a large AC current to flow through this branch. This causes the high-frequency AC harmonics to be "short-circuited" by the capacitors, achieving harmonic reduction. This further achieves the dual purpose of harmonic filtering and reactive power compensation. Xue et al. (2018) compare the simulation results between traditional and novel filtering technique, demonstrating that the latter can achieve similar filtering effects.

The *novel* filtering technique not only addresses the limitations of traditional filtering but also achieves filtering effort with a reduced amount of reactive power compensation. Therefore, studying the influence of power system strength on filtering effectiveness based on this novel filtering technique is of significance.

3 Tuning method for capacitance parameter

In this section, taking into account the AC system strength for system reactive power and harmonic content are derived. Additionally, the capacitance tuning method is introduced.

3.1 Reactive power calculation

Figure 3 highlights the definitions of reactive power at different parts of the system. In Figure 3, *TY(D)1~6* are the thyristors of the converter bridge, *CapY(D)ab,CapY(D)bc,CapY(D)ac* are the

TABLE 1 Classification of different filtering methods.

References	Filtering method
Yang et al. (2022), Farghly et al. (2022), Du et al. (2022)	Active power filter
Liu et al. (2020)	New AC filtering system
Huang et al. (2022)	Hybrid active power filter
Li et al. (2012)	New induction filter
Zhai et al. (2017), Zhao et al. (2022), Xue et al. (2018)	Parallel-connected fixed capacitor

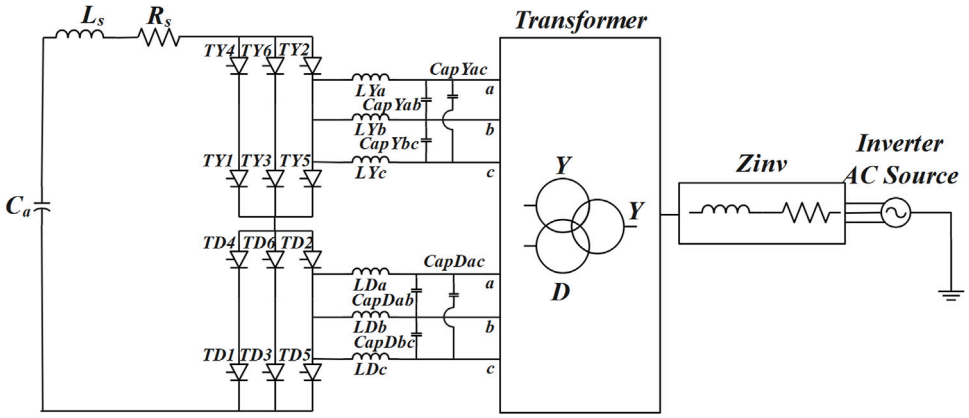

FIGURE 1
Circuit topology at the inverter side of the system.

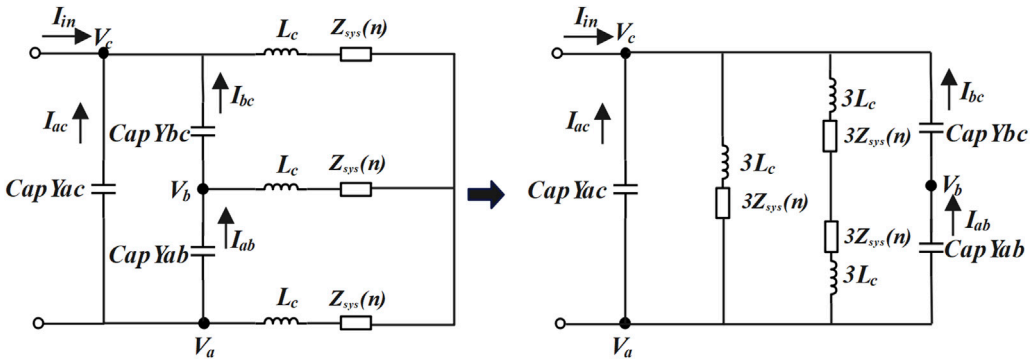

FIGURE 2
Equivalent circuit.

parallel-connected fixed capacitors, *LY(D)abc* are the series inductance, and Z_{inv} is the equivalent impedance of AC system at inverter side.

The reactive power absorbed by the converter can be calculated by Equation 1:

$$Q_S = \frac{3 \times (V_{dc})^2 \times P_{max}}{2 \times \pi \times f \times (V_{ac})^2} \quad (1)$$

where V_{ac} is the phase voltage amplitude, V_{dc} is the DC-side voltage, and P_{max} is the maximum rated power.

The reactive power absorbed by the transformer can be calculated by (2):

$$Q_t = S \times \tan(\arccos(pf)) \quad (2)$$

where S is the capacity of the transformer and pf is the power factor.

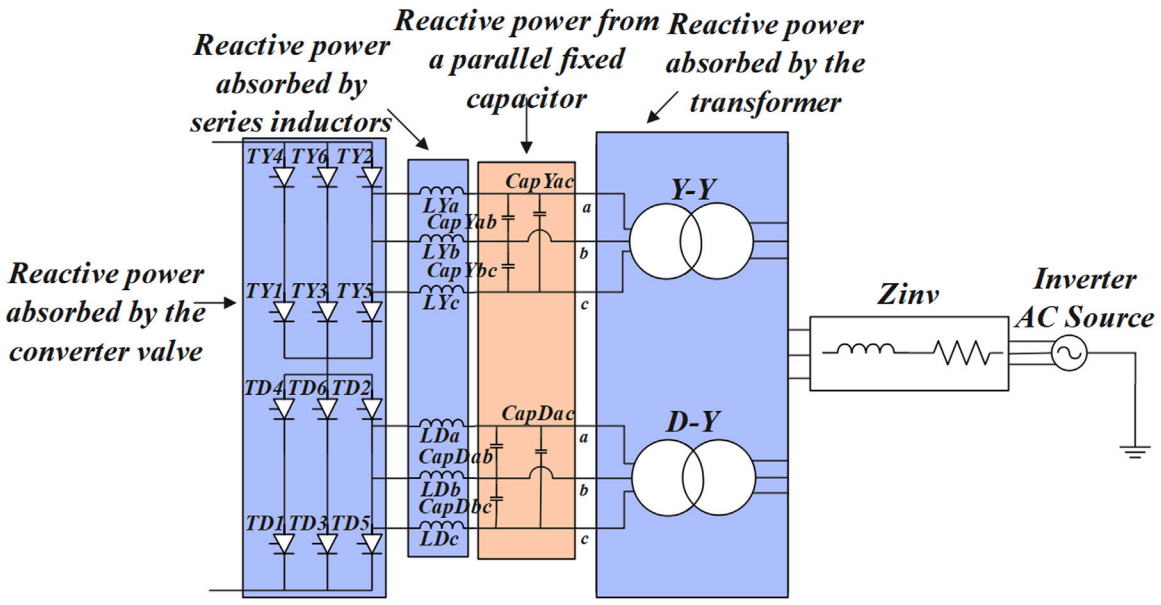

FIGURE 3
Circuit diagram with reactive power measurements.

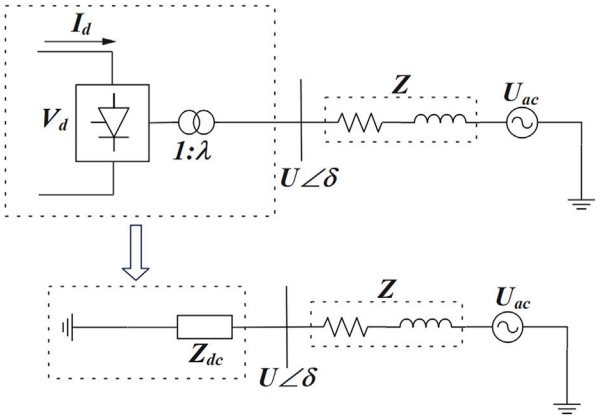

FIGURE 4
Equivalent impedance model.

The transformer power factor is shown in (3):

$$pf = \cos(arc\tan(L_c)) \tag{3}$$

where L_c is the transformer equivalent inductance.

If the ratio of the transformer is k, the reactive power generated by the parallel-connected fixed capacitor is shown in (4) and (5):

$$V_c = \frac{V_2}{k} \tag{4}$$

$$Q_c = \omega C V_c^2 \tag{5}$$

where V_2 is the phase voltage amplitude of bus.

The reactive power absorbed by the series inductance changes with the variation of capacitance and its value is relatively small. Therefore, to simplify the calculation, its impact is not considered in the theoretical calculations.

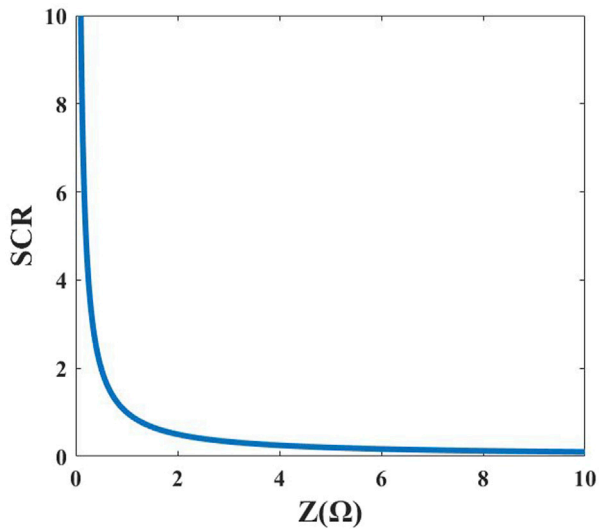

FIGURE 5
Relationship between Z and SCR

3.2 Harmonic content calculation

Xue et al. (2018) provide the harmonic amplitude expressions with AC power system strength of 2.5. Based on the twelve-pulse bridge, the expressions for *C-phase* harmonic current and voltage amplitude are shown in (6) and (7):

$$\overline{I_c} = \frac{-1}{jn\omega C \times \left(3jn\omega L_c + 3Z_{sys}(n)\right) + 1}\overline{I_{in(12)}} \tag{6}$$

$$\overline{V_{sys\_n}} = 2 \times \frac{-Z_{sys}(n)}{jn\omega C \times \left(3jn\omega L_c + 3Z_{sys}(n)\right) + 1}\overline{I_{in(12)}} \tag{7}$$

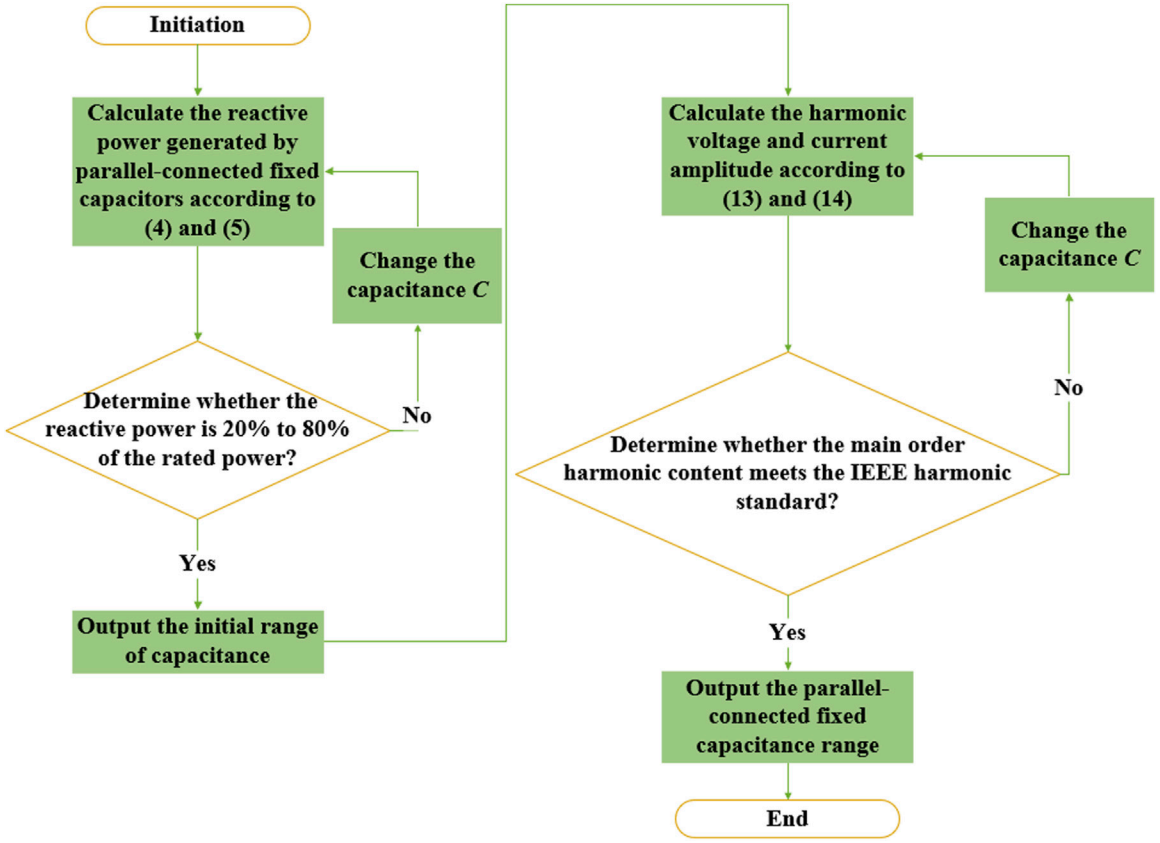

FIGURE 6
Capacitance tuning process.

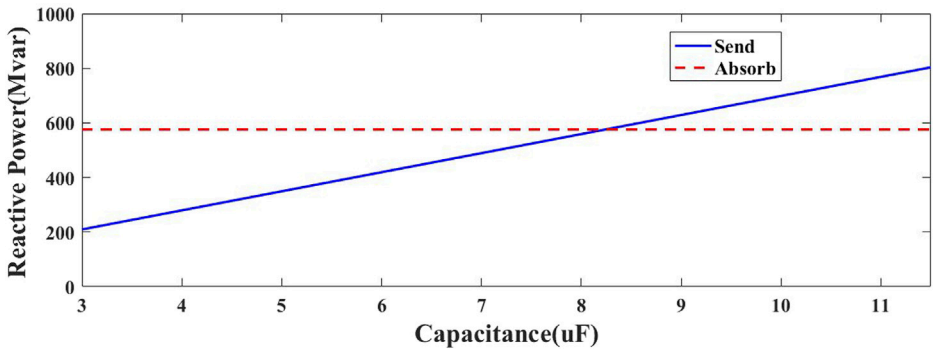

FIGURE 7
Reactive power change curve.

Where, $Z_{sys}(n)$ is the grid impedance at the n_{th} harmonic frequency, C is the capacitance of the parallel-connected fixed capacitor, $\overline{I_{in(12)}}$ is the input harmonic current corresponding to the twelve-pulse bridge, and L_c is the equivalent inductance of the transformer.

HVDC transmission system interaction are largely determined by the AC power system strength relative to the DC transmission capacity. The degree of strength is often assessed using the short-circuit ratio (*SCR*).

The definition of the Multiple Input Short Circuit Ratio (*MISCR*) is given by Wang et al. (2021) as (8):

$$MISCR_i = \frac{S_{aci}}{P_{diN} + \sum_{j \in L} MIIF_{ji} P_{djN}} \tag{8}$$

Where, S_{aci} is the short-circuit capacity of bus i, P_{diN} is the rated power of bus i, *MIIF* indicates the interaction between the converter buses.

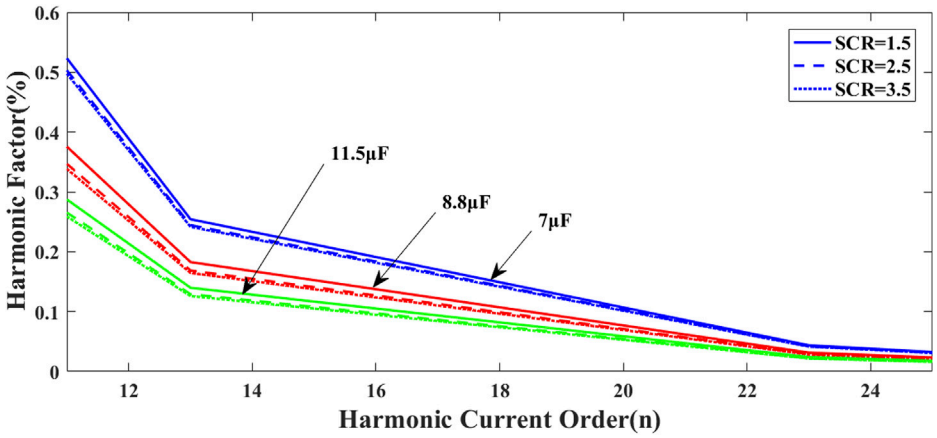

FIGURE 8
The harmonic content under different AC power system strengths.

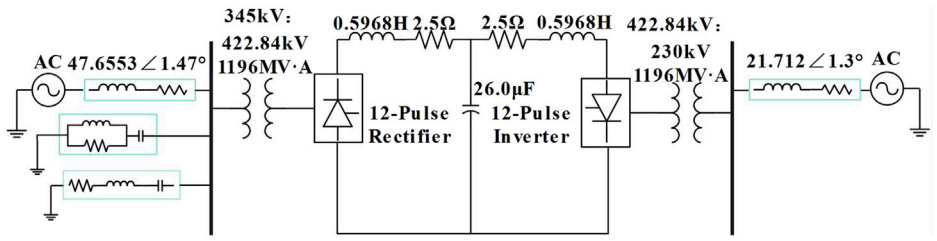

FIGURE 9
System model A.

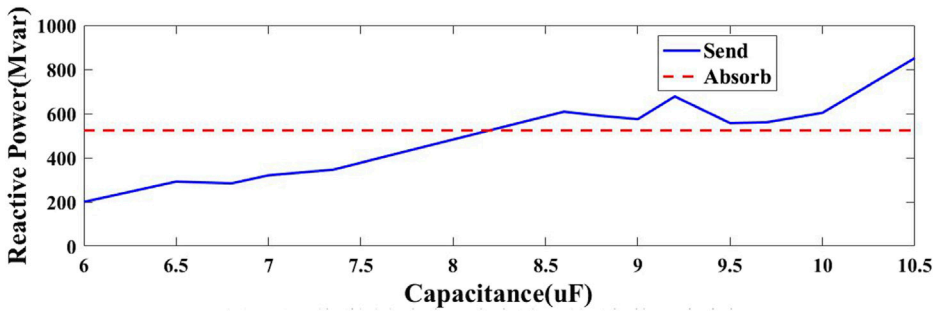

FIGURE 10
Reactive power change curve.

For single-infeed system, the *SCR* can be derived as shown in (9):

$$SCR = \frac{S_{ac}}{P_{dN}} = \frac{Z_{dc}}{Z} \tag{9}$$

Where, Z is the inherent impedance of grid, Z_{dc} is the grounding impedance. Figure 4 is the HVDC equivalent impedance model at the inverter side. In Figure 4, the grounding impedance (Z_{dc}) includes the equivalent impedance of the converter valves and transformer. The inherent impedance (Z) is the equivalent impedance of the system. The grounding impedance can be considered fixed as the network frequency normally does not vary. Thus, the relationship between the *SCR* and the equivalent impedance Z of the power grid according to (9) can be expressed as shown in Figure 5. It can be seen from the relationship curve in Figure 5 that the *SCR* is inversely proportional to the equivalent impedance (Z) of the power

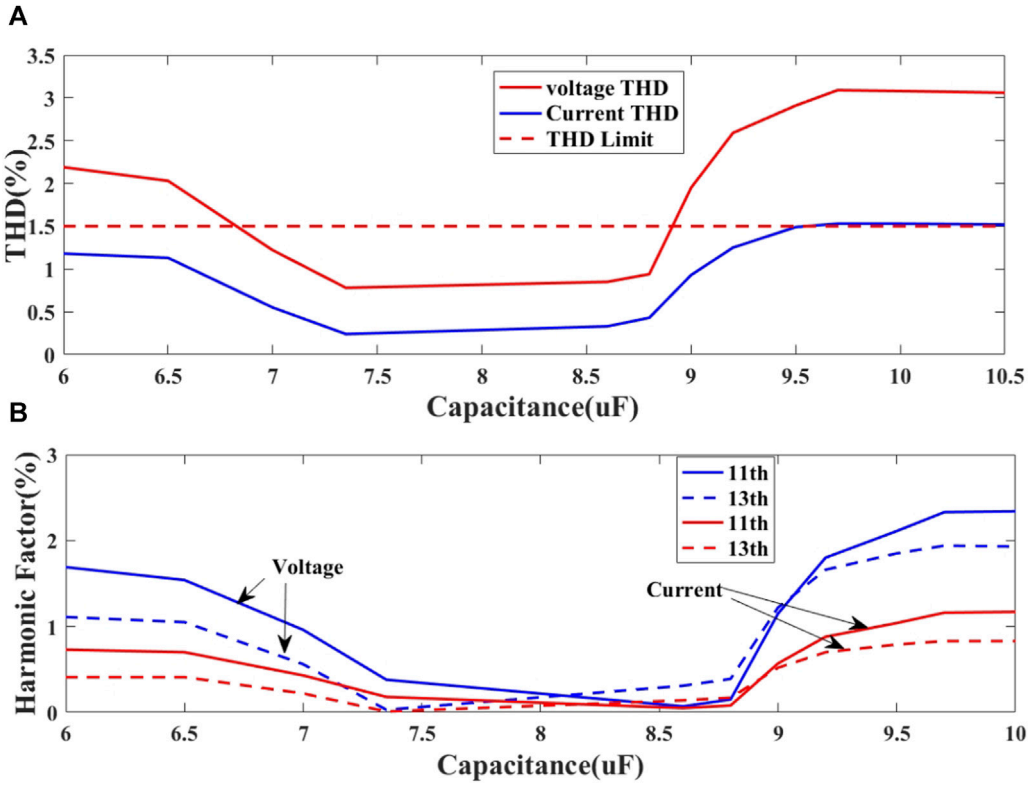

FIGURE 11
Harmonic content under varying capacitance. **(A)** THD values under varying capacitance. **(B)** Main orders harmonic content under varying capacitance.

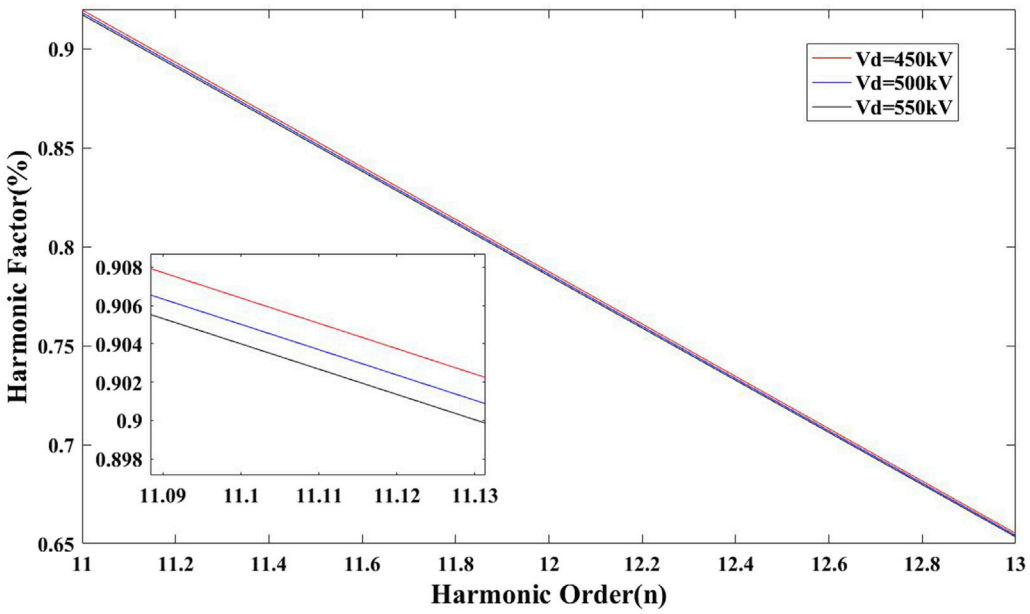

FIGURE 12
Harmonic content under different DC voltages.

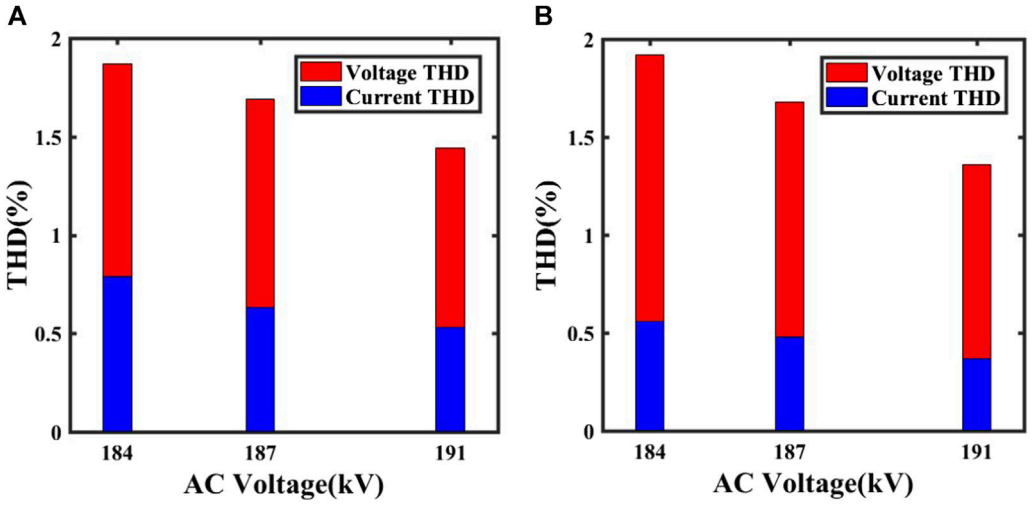

FIGURE 13
Filtering effect under different AC voltages. **(A)** SCR=1.5 **(B)** SCR=2.

TABLE 2 Comparison of filtering effect under different filtering techniques.

n_{th}	*IEEE Limits*(V/I)		PPF		Parallel-connected fixed capacitor			
	v (%)	I (%)	V (%)	I (%)	7.35 μF 8.8 μF			
					V (%)	I (%)	V (%)	I (%)
11_{th}	1	0.5	0.11	0.04	0.64	0.29	0.33	0.18
13_{th}	1	0.5	0.08	0.04	0.27	0.11	0.56	0.25
23_{th}	1	0.15	0.32	0.07	0.29	0.06	0.60	0.15
25_{th}	1	0.15	0.25	0.05	0.28	0.06	0.53	0.12
THD	1.5	1.5	0.94	0.97	0.90	0.42	1.10	0.48

grid. Since the grounding impedance (Z_{dc}) includes the equivalent impedance of the transformer, and Xue et al. (2018) separate the equivalent impedance of the transformer and the impedance of the capacitor for calculation, this paper adopts the following methods to calculate the harmonic amplitude under the different system strengths to simplify the calculation.

The basic short-circuit ratio (*SCR*) accounts for the inherent strength of AC power system, and the corresponding expression is given by Jia et al. (2012) as (10):

$$SCR = \frac{S_{sc}(MVA)}{P_{dN}(MW)} \tag{10}$$

Short-circuit capacity $S_{SC}(MVA)$ is defined as (11):

$$S_{sc}(MVA) = \frac{E_{ac}^2}{Z_{th}} \tag{11}$$

Where, E_{ac} is the commutation bus voltage under rated DC power, Z_{th} is the grid impedance at the n_{th} harmonic frequency and P_{dN} is the rated DC power.

The relationship between grid impedance and AC power system strength can be expressed as (12):

$$Z_{th} = Z_{sys}(n) = \frac{E_{ac}^2}{SCR \times P_{dN}} \tag{12}$$

Where, $Z_{sys}(n)$ represents the grid impedance at the n_{th} harmonic frequency. It can be seen from (12) that grid impedance is inversely proportional to the short-circuit ratio (*SCR*).

By substituting (12) into (6) and (7), the expressions for *C-phase* harmonic current and voltage amplitude associated with system strength based on the twelve-pulse converter bridge can be obtained as follows:

$$\overline{I_c} = \frac{-1 \times SCR \times P_{dN}}{3jn\omega CE_{ac}^2 + SCR \times P_{dN} - 3n^2\omega^2 CL_C \times SCR \times P_{dN}} \overline{I_{in(12)}} \tag{13}$$

$$\overline{V_{sys\_n}} = \frac{-2E_{ac}^2}{3jn\omega CE_{ac}^2 + SCR \times P_{dN} - 3n^2\omega^2 CL_C \times SCR \times P_{dN}} \overline{I_{in(12)}} \tag{14}$$

From (13) and (14), it can be observed that when the other parameters are constant and the equivalent inductance of the

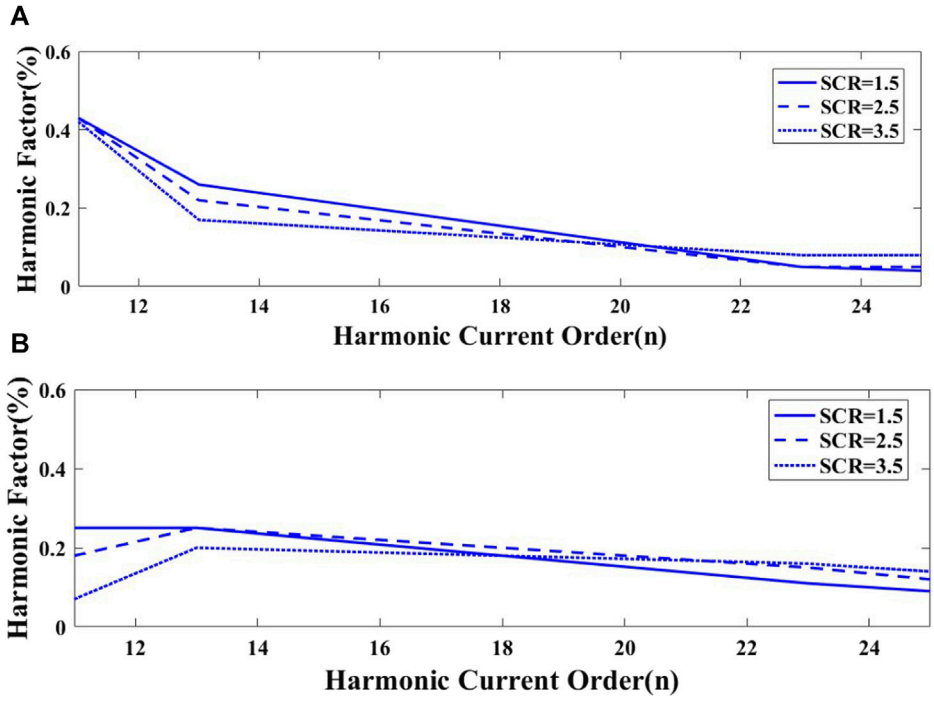

FIGURE 14
Harmonic current content with different capacitance. **(A)** Harmonic current content with a capacitance of 7 μF **(B)** Harmonic current content with a capacitance of 8.8 μF.

transformer is small enough to be negligible, the change of SCR with respect to harmonic current and voltage is as follows: As SCR increase, the amplitude of harmonic current and voltage decreases.

3.3 Capacitance parameter tuning process

This section introduces the tuning of capacitance considering the system strength. As shown in Figure 6, the process primarily involves two aspects: 1) Reactive power compensation. 2) Filtering effect. The priority is: Reactive power compensation and then the filtering effect. The tuning method is suitable for the conventional LCC-HVDC system.

3.3.1 Reactive power compensation

According to (5), the reactive power is generated by the capacitor. Typically, the reactive power compensation at the inverter side falls within the range of 40%–60% of the rated power. To fully study the impact of small capacitance on filtering performance, the range of the reactive power compensation is extended to 20%–80% of the rated DC power. If the reactive power compensation exceeds this range, the capacitance is not considered. Otherwise, it can be considered.

3.3.2 Filtering effect

According to the capacitance range initially determined by the reactive power compensation, the filtering effect of the capacitance in this range is further tested. According to the harmonic amplitude expressions (6) and (7), the harmonic content under different system strengths is calculated. Then, compared with the IEEE harmonic standard, the capacitance range is further determined.

4 Theoretical results of capacitance tuning method

The range of capacitance is determined using the tuning method from Section 3. The results are calculated based on CIGRE HVDC benchmark model.

4.1 Results of reactive power under the system strength of 2.5

Firstly, the capacitance range is initially determined by the reactive power compensation.

Figure 7 shows the change of reactive power under varying capacitance. It can be seen that the reactive power generated by the capacitors increases with the increase of capacitance, following a positive trend. Reactive power balance is achieved when the capacitance reaches 8.25 μF. In addition, the capacitance range that fulfills the reactive power compensation is approximately 3 μF–11.5 μF, in consistence with the initial capacitance range.

4.2 Results of harmonic content under the system strength of 2.5

From the relationships shown in (6) and (7), the harmonic content decreases with the increase of capacitance. Besides, the capacitance is not limited in a certain range. Xue et al. (2018) also provide the harmonic content under the system strength of 2.5, and this paper calculates the harmonic content under the same

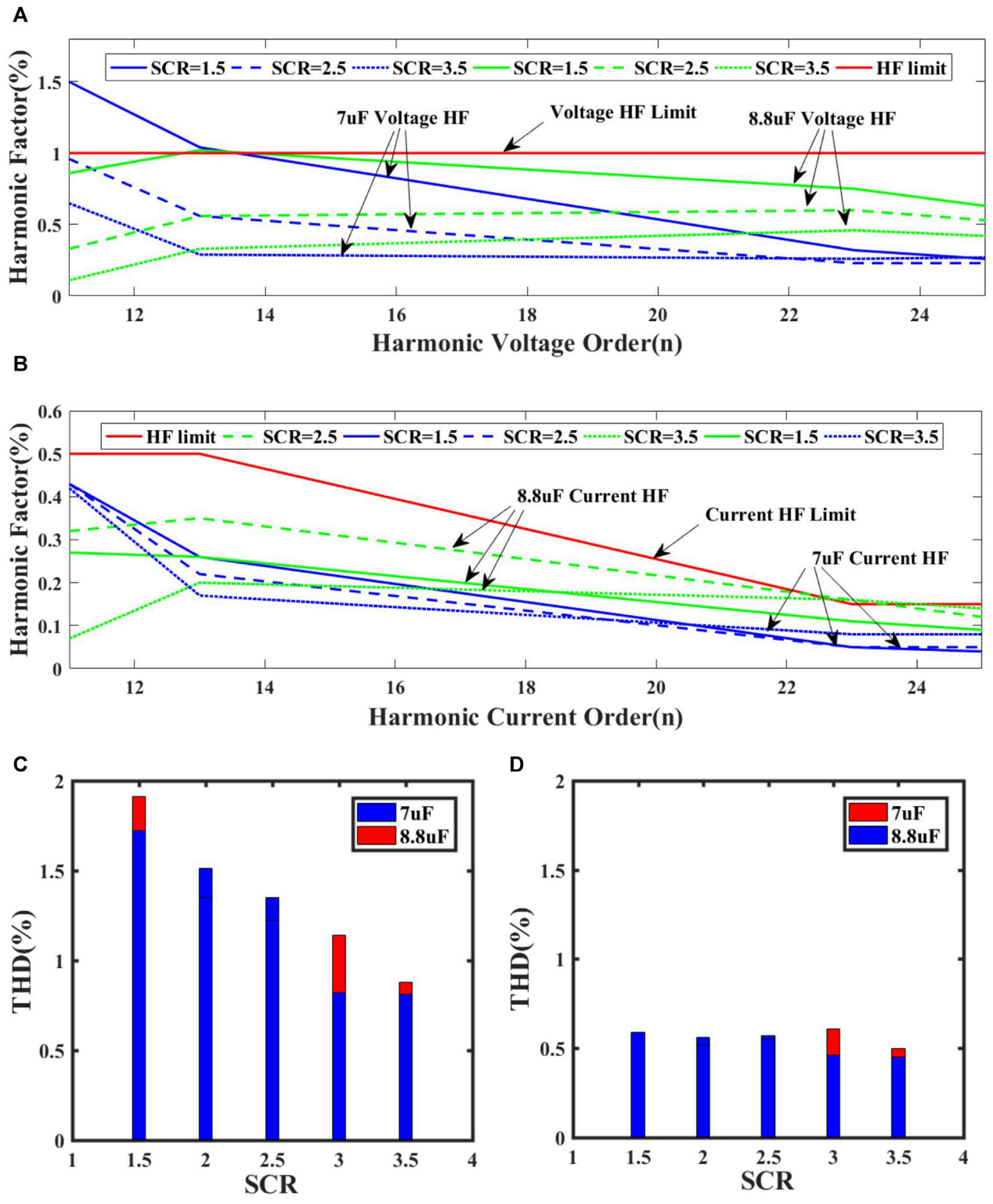

FIGURE 15
Simulation results of harmonic content and THD values with the capacitance of 7 μF and 8.8 μF under different system strengths. **(A)** Simulation results of harmonic voltage content **(B)** Simulation results of harmonic current content **(C)** Harmonic voltage THD **(D)** Harmonic current THD.

condition. According to the IEEE grid harmonic standards, the capacitance range that meets the requirements is approximately 7 μF to +∞μF.

In summary, the capacitance range that meets the reactive power compensation requirement and harmonic standard is 7 μF–11.5 μF when the AC power system strength is 2.5.

4.3 Results of harmonic content under different AC power system strengths

Based on the obtained capacitance range under the system strength of 2.5, the harmonic content of capacitors within this range is analyzed for different system strengths. Figure 8 illustrates the filtering performance of capacitors with capacitances of 7 μF, 8.8 μF and 11.5 μF under varying AC power system strengths. The selection method of the capacitance of 8.8 μF is as follows: Based on the compromise of the capacitance range of 7 μF–11.5 μF obtained in part A and B above and combined with the simulation test that can achieve stable capacitance value under rated working conditions. It can be observed that the harmonic content for 7 μF, 8.8 μF and 11.5 μF capacitors generally complies with the harmonic standards. Moreover, for a fixed capacitance, as the strength increases, the harmonic content decreases, indicating better filtering effectiveness.

In conclusion, the capacitance range for parallel-connected fixed capacitors that meets the requirement is 7 μF–11.5 μF.

5 Simulation results of capacitance tuning method

The analysis and calculation methods discussed above are applicable to systems with any strength.

This paper utilizes MATLAB/Simulink software to construct the LCC-HVDC system based on the parameters of the CIGRE benchmark model. The system model is shown in Figure 9.

5.1 Simulation results of reactive power under the system strength of 2.5

In this section, simulation results are employed to validate and analyze the reactive power generated by capacitors with different capacitance.

Figure 10 shows the relationship between capacitance and reactive power for capacitance value ranging from 20% to 80% of the rated DC power. It is evident that the capacitance and the generated reactive power exhibit an approximate correlation. The system achieves the reactive power balance when the capacitance reaches 8.25 μF.

Observing the simulation result, the acceptable capacitance range is 6 μF–10.5 μF. By comparing with the theoretical results from Figure 7, there is a small discrepancy between them. The reasons are as follows:

Equation 15 is derived from (4) and (5). It shows the reactive power generated by the capacitor.

$$Q_c = \frac{\omega C V_2^2}{k^2} \tag{15}$$

It can be observed that when capacitance and frequency are constant, factors affecting reactive power include the phase voltage on the primary side of the transformer (V_2) and the transformer turns ratio (k). In theoretical calculations, the values of both are derived based on the benchmark model parameters. In the simulation test, to ensure the system adjusts to the rated operating conditions, the grid side is equivalent to an ideal voltage source, and the transformer turns ratio may vary, leading to discrepancies between the theoretical and simulated values. Additionally, when capacitance reaches a certain level, series inductance is required to absorb additional reactive power, which is not considered in the theoretical calculations.

5.2 Simulation results of harmonic content under the system strength of 2.5

This section begins with the analysis of the filtering effect, conducting simulation analysis on the harmonic content with different capacitance. Furthermore, by combining theoretical analysis with simulation results, the discrepancies between the two are analyzed.

Figure 11 depicts the variation in THD and Figure 12 illustrates the simulation results for the main harmonic content when the capacitance is between 6μF and 10.5 μF.

5.2.1 Results analysis

Figure 11A depicts the THD variation for voltage and current. It can be observed that the THD of harmonic current are lower than those of harmonic voltage, and both exhibit similar trends. The THD values of the harmonic current are generally within the required harmonic range, whereas voltage is not. It is obvious that capacitance within a certain range complies with the IEEE harmonic standards.

Comparing Figure 10 and Figure 11A, it can be observed that when the system does not reach reactive power balance or when the capacitance is small, the reactive power compensation is much less than the reactive power absorbed by the converter station. The filtering effect also falls within the IEEE harmonic standard range. The main reasons are explained as follows:

A. High frequency harmonic currents pass through the capacitor: When the capacitance is small, its impact on the clamping circuit is reduced, leading to a reduction of the reactive power compensation provided by the capacitor. At the same time, the filtering effect of the harmonic currents on the AC side is enhanced because the frequency of harmonic current is usually high, allowing them to pass through the capacitor more easily.
B. Improve the system stability: Although the added capacitance is small, the power factor of the system is still improved, enhancing system stability. This result in that more effective reduction of harmonic current on the AC side after passing through the capacitor, thereby reducing the demand for reactive power on the AC side.

Figure 11B shows the simulation results of the main harmonic content for capacitance ranging from 6 μF to 10.5 μF. It can be observed from Figure 11B that the variation has a concave distribution, and the capacitance range that meets the IEEE harmonic standard is 7 μF–8.8 μF.

Comparing these results with theoretical analysis, there are difference in their variations. Moreover, in the simulation results, a larger capacitance does not necessarily lead to better

filtering performance. The main reasons are explained as follows:

A. During the system simulation, the generated reactive power exceeds the reactive power absorbed by the converter station when the capacitance is large. Under this condition, it is necessary to connect a parallel grounding inductor on the AC side of the converter station or connect the series inductor on the AC side of the converter bridge to absorb the surplus reactive power. At this point, the capacitor C and the inductor L form a LC resonant loop. According to the theory of series/parallel resonant circuit, the resonant frequency of the LC resonant circuit can be calculated as shown in (16):

$$f = \frac{1}{2\pi\sqrt{LC}} \tag{16}$$

Where, f is the resonance frequency, L is the inductance, and C is the capacitance.

B. The resonance frequency will decrease when the capacitance increases. Moreover, the resonance frequency becomes close to or equal to the system's resonant frequency when it reaches a certain level, causing resonance and resulting in an increase in harmonic content.

C. The internal impedance of the capacitor also affects the level of harmonic current and voltage. When the capacitance is too large, its losses will increase and the internal impedance also increase, leading to an increase in power consumption and an increase in the harmonic content.

5.2.2 Error analysis

A. During the simulation, the DC voltage do not reach exactly the rated value of 500 kV. Based on this, the relationship between different DC voltages and harmonic current content when other factors are constant is studied. The simulation results are shown in Figure 12, in which, it can be observed that the harmonic current content changes inversely with the DC voltage. The higher the DC voltage, the lower the harmonic current content. Although the variations in DC voltage have a small effect on the change in the harmonic current, the differences in DC voltage will still affect the filtering effect.

B. In the simulation process, the AC voltage is within a certain rated value range, but the AC voltage may not always match the rated value during simulation, and its variation may lead to result deviations. Below is the testing of the THD values for different AC voltage with the same fixed capacitor capacitance.

Figure 13 shows the variation of THD values for different AC voltages with the same fixed capacitor capacitance. Figure 13A, B show the THD values for a capacitance of 7 μF under the system strength of 1.5 and 2, respectively. It can be observed that the harmonic content decreases with the increase in AC voltage, indicating that a higher AC voltage leads to better filtering effect. The rated value of the AC voltage is 187 kV, and the numerical values used in theoretical calculation are based on this rating. However, in the simulation results, the filtering effect for some capacitor capacitances are measured within the range of ±2% of the rated AC voltage (184 kV–191 kV), which introduces deviations in the results.

5.2.3 Potential solutions

A. Optimize the design of the converter station structure: In the design of the converter station structure, it is possible to mitigate resonance between capacitors and line inductors by setting appropriate parameters such as capacitance and inductance. For instance, in the case of a multi-terminal filter structure, the introduction of two small resistors in series between the capacitor and inductor can prevent resonance.

B. Use controllable capacitors: Controllable capacitors can autonomously adjust their capacitance based on the system's operating conditions, thereby preventing the occurrence of resonance.

C. Dynamically adjust capacitance: Dynamically adjust the capacitance based on the actual operating conditions of the system to ensure system stability and safety.

D. Add additional inductance: Add a certain inductance between capacitors and line inductance to reduce the resonance frequency and thereby avoid resonance.

In summary, the acceptable capacitance range is 7 μF–8.8 μF for the AC power system strength of 2.5.

It should be noted that the methods mentioned above are equally applicable to systems with other system strengths.

5.3 Comparative with existing passive filtering techniques

Table 2 shows the harmonic content using different filtering techniques, with the novel filtering technique provided for capacitor capacitance of 7.35 μF and 8.8 μF. The choice of 7.35 μF is based on the fact that, at this capacitance, the reactive power compensation generated by the capacitor is comparable to the reactive power compensation achieved with a passive filter. This selection allows for a more meaningful comparison of the filtering effects of different techniques.

From Table 2, it is observed that the 11th and 13th harmonic content is higher than that of the passive filter, but the high-frequency harmonic content is lower for the capacitance of 7.35 μF. In terms of THD values, with the same reactive power compensation, the filtering effect of the novel filtering technique is superior to that of the passive filter.

For capacitance of 8.8 μF, the reactive power generated by the capacitor is much larger than the reactive power compensation of the passive filter. However, the filtering effects for some harmonics orders is worse than the passive filter, the main reasons are as follows:

A. Impedance of the parallel-connected fixed capacitor itself: The fixed capacitor has a certain internal impedance in the system. When the capacitance is large, the internal impedance also increases, leading to higher losses and increased harmonic content.

B. Resonance issues: When the capacitance is large, it requires series or parallel-connected grounding inductance to absorb the surplus reactive power. In this case, a resonant circuit is formed by the capacitor C and inductor L. With a large capacitance, the resonance frequency decreases, and if it

becomes close or equal to the resonance frequencies of other circuits in the system, it may cause resonance issues, leading to a reduction in filtering effectiveness.

C. High-performance broadband of the passive filter: Passive filter can choose different parameters according to requirements to meet the harmonic reduction. By adjusting the parameters of circuit components, better harmonic suppression can be achieved. In contrast, the filtering effect of parallel-connected fixed capacitors can only be effective within a specific frequency range, making it difficult to filter out harmonic signals at other frequencies, and adjustment is challenging.

In summary, both traditional filtering and novel filtering techniques can effectively suppress harmonic interference. However, due to limitations such as the impedance of capacitors, resonance issues and the filtering frequency range, the filtering effects vary under different capacitances. In practical engineering, it is advisable to choose different filtering methods based on actual requirements and grid conditions.

5.4 Simulation result of harmonic content under different system strengths

This section further analyzes the filtering effects under different system strengths.

Figures 14A, B show the simulation results of harmonic current content with the capacitance of 7μF and 8.8 μF under different AC power system strengths. It can be observed that, under various power system strengths, the simulation results for a capacitance of 7 μF are close to the theoretical analysis results, while the results for a capacitance of 8.8 μF differ significantly. The filtering effect on low-frequency harmonics is more obvious, but the filtering effect on high-frequency harmonics is less effective. The main reason for this includes: Parallel-connected fixed capacitors can only filter a certain range of harmonic frequencies, and when the capacitance reaches a certain level, parallel grounding inductance or series the inductance is needed to absorb surplus reactive power. The capacitor may resonate with the inductance, leading to an increase in harmonic content at that frequency.

Besides, the variation follows the following trend under different AC power system strengths: A higher system strength leads to better filtering performance.

Figure 15A, B show the variation of harmonic content with the capacitance of 7 μF and 8.8 μF under different AC power system strengths. It can be observed that the harmonic content for 7 μF and 8.8 μF capacitance can meet the harmonic standard. Except for the case of an AC power grid strength of 1.5, where the 11th harmonic voltage content exceeds the limit for a 7 μF capacitor.

Figure 15C, D illustrates the variation of THD for the capacitance of 7 μF and 8.8 μF under different AC power system strengths. It can be observed that the THD values for both 7μF and 8.8 μF capacitors are within the specified range, expect for the THD under an AC system strength of 1.5.

Based on the above analysis, it can be concluded that the harmonic level for capacitance ranging from 7 μF to 8.8 μF generally complies with the IEEE standard under different system strengths. Additionally, it is evident that a lower system strength can affect the filtering effectiveness.

In summary, take into account the filtering effect under different system strengths, the parallel-connected fixed capacitance range that meets the requirements for both reactive power compensation and the filtering effectiveness is approximately 7 μF–8.8 μF. In practical applications, when taking into account the reactive power balance of the system, the ideal range of capacitance is 8.25 μF–8.8 μF observing Figure 10.

6 Conclusion

This paper proposed a tuning method for the parameter of parallel-connected fixed capacitors considering the system strength based on the novel filtering technique. The method enables the calculation of the range of required capacitance for filtering under varying power system strengths. By analyzing the filtering performance under various power system strengths, this paper reveals that the variation in power system strength affects the filtering performance of the novel filtering technique. Specifically, within a certain range of power system strengths, weaker AC system leads to a reduction of filtering performance. Consequently, a tuning method for the capacitor parameters' range is proposed for the novel filtering technique considering the power system strengths. This method is effective for LCC-HVDC systems with varying power system strengths. It provides guidance for the selection of filtering capacitance in practical applications.

Data availability statement

The original contributions presented in the study are included in the article/supplementary material, further inquiries can be directed to the corresponding author.

Author contributions

CY: Writing–original draft, Writing–review and editing. QZ: Writing–original draft, Writing–review and editing. ZZ: Writing–review and editing.

Funding

The author(s) declare that financial support was received for the research, authorship, and/or publication of this article. This work was supported in part by the National Natural Science Foundation of China under Excellent Young Scientists Fund (overseas) (A4230010), in part by the Fundamental Research Funds for the Central Universities under Grant 2023ZYGXZR105, in part by the Research Startup Funding from the Guangzhou Maritime University (K42022121).

Conflict of interest

The authors declare that the research was conducted in the absence of any commercial or financial relationships that could be construed as a potential conflict of interest.

Publisher's note

References

Agelidis, V. G., Demetriades, G. D., and Flourentzou, N. (2006). "Recent advances in high-voltage direct-current power transmission systems," in *2006 IEEE International Conference on Industrial Technology, Mumbai, India, 15-17 December, 2006*, 206–213.

Chen, K., Luo, J., Zhou, T., Luo, K., Wang, S., and Zang, D. (2018). "Summary of research on multi-infeed short circuit ratio in AC and DC systems," in 2018 2nd IEEE Conference on Energy Internet and Energy System Integration (EI2), Beijing, China, 22 October 2018, 1–9.

Du, X., Zhao, C., and Xu, J. (2022). The use of the hybrid active power filter in LCC-HVDC considering the delay-dependent stability. *IEEE Trans. Power Deliv.* 37 (1), 664–673. doi:10.1109/tpwrd.2021.3068411

Farghly, A., El Habrouk, M., Ahmed, K. H., Abdel-khalik, A. S., and Hamdy, R. A. R. (2022). "Active power filter for12-pulse LCC converter employed in LCC-MMC hybrid HVDC system," in 2022 23rd International Middle East Power Systems Conference (MEPCON), Cairo, Egypt, 13-15 December 2022, 1–7.

Geng, X., Wen, J., Wang, S., He, D., Zhang, L., Cai, Y., et al. (2018). "Modeling and analysis of AC side equivalent harmonic impedance of HVDC converter," in 2018 2nd IEEE Conference on Energy Internet and Energy System Integration (EI2), Beijing, China, 22 October 2018, 1–6.

Huang, Y., Song, S., Li, M., Wu, F., Zhu, Q., Ji, Y., et al. (2022). "Design of hybrid active filter applied in LCC HVDC project," in 2022 IEEE International Conference on High Voltage Engineering and Applications (ICHVE), Chongqing, China, 25-29 September 2022, 1–4.

IEEE (2014). *IEEE Recommended Practice and Requirements for Harmonic Control in Electric Power Systems. IEEE std 519-2014 (revision of IEEE std 519-1992)*, 1–29.

Jia, C. C., Wen, J., and Bie, X. Y. (2012). "Study of the effect of AC system strength on the HVDC startup characteristics," in International Conference on Sustainable Power Generation and Supply (SUPERGEN 2012), Hangzhou, 8-9 September 2012, 1–5.

Lee, T. L., Wang, Y. C., Li, J. C., and Guerrero, J. M. (2015). Hybrid active filter with variable conductance for harmonic resonance suppression in industrial power systems. *IEEE Trans. Industrial Electron.* 62 (2), 746–756. doi:10.1109/tie.2014.2347008

Li, C., Yang, Y., Cao, Y., Wang, L., and Blaabjerg, F. (2022). Frequency and voltage stability analysis of grid-forming virtual synchronous generator attached to weak grid. *IEEE J. Emerg. Sel. Top. Power Electron.* 10 (3), 2662–2671. doi:10.1109/jestpe.2020.3041698

Li, Y., Luo, L., Rehtanz, C., Wang, C., and Ruberg, S. (2012). Simulation of the electromagnetic response characteristic of an inductively filtered HVDC converter transformer using field-circuit coupling. *IEEE Trans. Industrial Electron.* 59 (11), 4020–4031. doi:10.1109/tie.2011.2175673

Li, Y., Xu, Q., Dai, P., Xin, H., and Yuan, H. (2020). "The Impact of PV converter on the grid strength of receiving AC system in MIDCS," in The 16th IET International Conference on AC and DC Power Transmission (ACDC 2020), Online Conference, 2-3 July 2020, 2090–2095.

Liu, X., Ma, W., Jia, H., and Dong, C. (2020). System adaptive AC filter for a line commutated converter high voltage DC transmission system. *CSEE J. Power Energy Syst.* 6 (4), 901–910. doi:10.17775/CSEEJPES.2018.01480

Liu, Y., and Zhu, Y. (2013). "The harmonic characteristics of HVDC system and reduction," in 2013 Third International Conference on Intelligent System Design and Engineering Applications, Hong Kong, China, January 16 2013 to January 18 2013, 1452–1455.

Tang, G., and Xu, Z. (2014). A LCC and MMC hybrid HVDC topology with DC line fault clearance capability. *Int. J. Electr. Power Energy Syst.* 62, 419–428. doi:10.1016/j.ijepes.2014.04.045

Wang, S., Gao, S., Chen, Z., Zhao, X., Song, T. E., Liu, Y., et al. (2021). Analysis of the operating margin evaluation of multi-infeed LCC-HVDC systems based on the equivalent impedance. *IEEE Access* 9, 66268–66281. doi:10.1109/access.2021.3075328

Xin, Q., Zhao, X., Huang, Y., Guo, L., Li, Y., and Li, Z. (2020). "A novel design method of AC filter based on polygon-shape harmonic impedance," in The 16th IET International Conference on AC and DC Power Transmission (ACDC 2020), Online Conference, 2-3 July 2020, 550–555.

Xue, Y., Zhang, X. P., and Yang, C. (2019). Series capacitor compensated AC filterless flexible LCC HVDC with enhanced power transfer under unbalanced faults. *IEEE Trans. Power Syst.* 34 (4), 3069–3080. doi:10.1109/tpwrs.2019.2899065

Xue, Y., Zhang, X. P., and Yang, C. (2018). AC filterless flexible LCC HVDC with reduced voltage rating of controllable capacitors. *IEEE Trans. Power Syst.* 33 (5), 5507–5518. doi:10.1109/tpwrs.2018.2800666

Yang, Y., Yang, P., Du, X., Wu, F., and Ji, Y. (2022). "Passive filter design research in hybrid active filter design," in 18th International Conference on AC and DC Power Transmission (ACDC 2022), Online Conference, China, 3 July 2022, 1697–1701.

Zhai, C., Zhang, Z., Luo, L., Sun, X., and Sun, S. (2017). "Characteristic analysis of HVDC system with shunt capacitance commutated converter," in 2017 IEEE PES Asia-Pacific Power and Energy Engineering Conference (APPEEC), Bangalore, India, 8-10 November 2017, 1–5.

Zhao, L., Luo, L., Li, Y., Zhang, H., and Xiang, J. (2022). Capacitive filter based HVDC converter for reducing the vibration and noise of converter transformer. *IEEE Access* 10, 78634–78642. doi:10.1109/access.2022.3190006

frontiers | Frontiers in Energy Research

TYPE Original Research
PUBLISHED 12 March 2024
DOI 10.3389/fenrg.2024.1363323

OPEN ACCESS

EDITED BY
Liansong Xiong,
Xi'an Jiaotong University, China

REVIEWED BY
Xiaokang Liu,
Polytechnic University of Milan, Italy
Wenzhou Lu,
Jiangnan University, China
Longjun Wang,
South China University of Technology, China

*CORRESPONDENCE
Huachun Han,
hanhuachun_sgcc@163.com

RECEIVED 30 December 2023
ACCEPTED 06 February 2024
PUBLISHED 12 March 2024

CITATION
Han H, Li Q and Li Q (2024), Cooperative control of the DC-link voltage in VSC-MTDC grid via virtual synchronous generators. *Front. Energy Res.* 12:1363323. doi: 10.3389/fenrg.2024.1363323

Cooperative control of the DC-link voltage in VSC-MTDC grid via virtual synchronous generators

Huachun Han*, Qun Li and Qiang Li

Electric Power Research Institute, State Grid Jiangsu Electric Power Co., Ltd., Nanjing, China

Introduction: Virtual Synchronous Generators (VSGs) are used in Voltage Source Converter-based Multi-Terminal High-Voltage Direct Current (VSC-MTDC) systems to enhance power system stability. However, the MTDC framework can lead to instability due to reduced inertia in certain grid areas, especially during load switching at VSC stations. This instability is exacerbated by untimely adjustments of the VSG's power setpoint, leading to voltage and frequency oscillations.

Methods: This study introduces a cooperative control approach for the DC voltage of the VSG, employing a consensus algorithm and Model Predictive Control (MPC). This method aims to achieve incremental power for the VSG and provide interactive power commands for both the grid side and the wind farm side. The consensus algorithm ensures coherent system adjustments, while the MPC algorithm tracks DC-side voltage changes in real time.

Results: The application of this cooperative control approach significantly enhances DC voltage regulation performance. It effectively reduces the extent of frequency drops and mitigates secondary frequency drop (SFD) issues, particularly those arising from the use of wind farms for frequency regulation and the associated speed recovery in wind turbine units.

Discussion: The increase in supplemental power effectively utilizes the energy stored in DC-side capacitors for power balance regulation and introduces additional inertial power into the system. Electromagnetic transient simulations have confirmed the effectiveness of the Consensus MPC-VSG method, demonstrating its ability to optimize the dynamic performance of VSC-MTDC systems and promote stability in DC voltage and frequency.

Conclusion: The findings suggest that employing the Consensus MPC-VSG method offers a promising solution for enhancing the stability and operational efficiency of VSC-MTDC systems, addressing the challenges posed by the inherent segmentation of the grid and the integration of renewable energy sources like wind farms.

KEYWORDS

VSC-MTDC, VSG, DC voltage, MPC, consensus algorithm, SFD

1 Introduction

Wind energy, a quintessential form of renewable energy, has been experiencing a consistent annual increase in power generation capacity (Howlader et al., 2014). Offshore Wind Farms (OWFs), in particular, have garnered considerable attention in the renewable energy sector due to their minimal land usage, superior wind speeds, and extensive annual operation hours. However, their remote location necessitates considerable power transmission to connect with onshore grids. The use of Voltage Source Converter-based Multi-Terminal High-Voltage Direct Current (VSC-MTDC) has emerged as an effective solution for this problem (Lee et al., 2021; Xu et al., 2007). Compared to point-to-point High-Voltage Direct Current (HVDC) transmission systems, the formation of MTDC grids can reduce wind power curtailment, enhance reliability during equipment failures, and decrease capacity requirements for MTDC connections to asynchronous AC grids. However, MTDC divides the AC grid into regions with lower inertia, leading to a decoupling effect between OWFs and the main grid. The lack of mutual support capability among the ports can easily lead to frequency oscillations when the system is perturbed (Zhu et al., 2014; Zhu et al., 2021). Thus, while offering multiple benefits, MTDC integration of OWFs introduces certain challenges that must be addressed to ensure the reliable and stable operation of power systems.

The operation of MTDC grids is largely contingent on the active power control methods employed (Kirakosyan et al., 2023). Consequently, numerous studies have proposed improved active power regulation control techniques aimed at ensuring the continuous, reliable functioning of MTDC systems and providing grid support services. Among them, the Virtual Synchronous Generator (VSG) control strategy has garnered extensive attention in VSC-MTDC systems (Zhong and Weiss, 2011; Huan et al., 2018; Wang et al., 2020; Leon and Mauricio, 2023; Huang et al., 2017; Liu et al., 2023; Li et al., 2018; Wu et al., 2017a; Liu et al., 2022a; Cao et al., 2018; Liu et al., 2022b). The utilization of VSGs in MTDC systems introduces unique stability concerns, exacerbated during load switching events. The segmentation of the grid in the MTDC framework, leading to areas with reduced inertia, amplifies the impact of continuous power fluctuations at VSC stations during load transitions. Furthermore, the modern trend of utilizing wind farms for frequency regulation introduces an additional layer of complexity. Wind turbine units, while contributing to renewable energy generation, may inadvertently cause secondary frequency drops (SFD) during the speed recovery process. This phenomenon poses a significant threat to the overall stability of power systems. In the contemporary landscape of power systems, where the integration of renewable energy sources is gaining prominence, the significance of addressing these challenges becomes paramount. As renewable energy, including wind farms, contributes a substantial share to the overall power generation, the effective utilization of VSGs in MTDC systems becomes crucial for maintaining grid stability. In order to enhance the stability of VSG in MTDC operation (Huan et al., 2018), proposed a unified VSG control strategy aimed at improving the stability of very weak AC grids (Wang et al., 2020). put forth a VSG control method with adaptive parameter tuning to suppress low-frequency oscillations in VSC-MTDC systems (Leon and Mauricio, 2023). introduced a dual-degree of freedom VSG method to enhance inertia emulation and reference tracking constraints. However, these VSG methods primarily serve to provide frequency support to the system, thereby requiring at least one VSC for voltage control in MTDC systems. In order to apply VSG control in DC transmission system (Huang et al., 2017), presented a self-synchronizing VSG control exploiting the dynamic characteristics of the DC link capacitor to provide frequency support while also ensuring voltage control. Nonetheless, this approach only considered the frequency response and voltage control of a single VSC. For multiple interconnected VSCs, a significant risk of voltage collapse has been revealed once uneven power allocation causes VSG-controlled VSC to enter current saturation mode (Liu et al., 2023). Thereby, in MTDC systems, Grid Side VSC-Stations (GSVSC) may need to consider multiple VSCs for power sharing and voltage control. Therefore (Li et al., 2018; Wu et al., 2017a), proposed a VSG control strategy for suppressing DC side oscillations in VSC-MTDC systems, thereby providing inertia and damping characteristics while controlling DC side voltage. This DC-side VSG voltage control method retains the characteristics of droop control, allowing multiple VSCs to control DC voltage and power sharing. A coordinated VSG control proposed in Liu et al. (2022a) brought a new prospective to realize damping and inertia control according to the DC voltage (Cao et al., 2018). employed a V^2-P-ω droop characteristic VSG control method to emulate system inertia and damping, redistributing DC power among GSVSCs through additional power generated by virtual rotating inertia and virtual speed regulators. In these applications, the converter station is involved in DC voltage regulation, necessitating the VSG to precisely track the power reference of the external DC voltage control loop. However, solely utilizing local variable operations and VSG controllers, power injected into the VSC station tends to fluctuate persistently without timely adjustment of the output power command when system loads switch. This can lead to significant frequency drops and substantial DC-side voltage oscillations (Li et al., 2017).

Wind turbine units participate in frequency regulation primarily by utilizing additional power injection. The frequency response control of these wind turbines, which relies on the inertia of their rotors, involves rapidly releasing rotor kinetic energy to provide brief frequency support (Attya and Hartkopf, 2013; Yang et al., 2023). However, this approach can lead to a SFD issue when wind turbine units reduce rotor speed while releasing energy to support the frequency. After exiting frequency regulation, the rotor must absorb energy to return to its initial operational state, potentially resulting in SFD, which can be even more severe than the primary frequency drop if left uncontrolled. To address the SFD issue (Ullah et al., 2008), proposes a method where, during the rotor speed recovery phase, the wind turbine unit reduces its power output by a constant value. However, this approach still encounters a significant degree of SFD (Wu et al., 2017b). suggests using energy storage systems to solve the SFD problem, but this solution increases investment costs (Kang et al., 2016). presents an improved strategy based on torque limits and introduces rotor speed as a reference for additional power, slightly below the power output at the end of the frequency regulation period, which reduces SFD to some extent. Some studies have attempted to reduce SFD to some extent by tuning frequency control parameters like inertia response control coefficients or droop control coefficients, but their effectiveness is limited (Lee et al., 2016). Most of the prior research has focused on improving wind turbine control from the wind farm side, without considering the power output balance among all VSC stations in the global MTDC system. As wind power integration continues to expand, the issue of unbalanced power output during wind turbine exit from frequency regulation can worsen, potentially exacerbating SFD problems. Therefore, this study aims to enhance DC voltage control

performance to reduce the magnitude of frequency and DC voltage oscillations during load transitions and mitigate SFD in the system. This approach seeks to coordinate power balance among all VSC stations within the MTDC system.

The Model Predictive Control (MPC) optimization method has been gaining attention for its ability to handle constraints. MPC computes a series of control modifications to minimize multiple objectives and meet constraints in future time steps (Maciejowski, 2002). In HVDC systems, the application of MPC spans fast power tracking (Mariethoz et al., 2014)., electromechanical oscillation damping suppression (Fuchs et al., 2014), and secondary frequency control (Namara et al., 2016), thus playing a crucial supportive role in multi-objective coordinated control.

Currently, in the realm of enhancing control strategies for VSG within MTDC systems, the predominant focus lies on optimizing the control difference strategy at individual VSC stations. However, this approach lacks a simultaneous consideration of the influence exerted by wind farms on the frequency regulation of VSC stations. The inadequacy of attention to factors such as DC voltage regulation and coordinated control methods poses challenges in sustaining optimal dynamic performance for VSC stations within the MTDC framework. This limitation underscores the necessity for a more comprehensive and integrated control methodology to address the complexities inherent in MTDC systems and promote effective cooperation among VSC stations. In response to limitations in existing VSG control and MTDC systems, coupled with the advantages of MPC, this study proposes VSG control refinements. This approach integrates consensus variables to add interactions among VSC stations and bolstering mutual inertia effects within the system. The principal contributions of this cooperative control methodology can be summarized as follows:

1. Taking into consideration the VSG's role in mitigating DC voltage fluctuations within the MTDC network, this study established an evaluation function for voltage stability. This function serves as a foundation for deriving the relationship between DC voltage and the injection of active power.
2. Based on the discrete model of VSG, this study formulated an objective function to facilitate the optimization control of DC voltage and active power. By utilizing the MPC method to calculate incremental power, this study derive instructions for interactive power, thereby enhancing the mutual inertia effects between system.
3. Recognizing the SFD that can arise due to the inherent comprehensive inertia control mechanisms of OWFs, the introduction of additional inertia power effectively mitigates the oscillatory effects of frequency compensation. In the presence of load disturbances, this enhanced approach optimizes the convergence of power and DC voltage output, simultaneously effectively raising the minimum point of frequency descent.

The structure of this chapter unfolds as follows: Section 2 provides a comprehensive overview of the control scheme for MTDC systems. Section 3 introduces a cooperative control approach for DC voltage regulation, which leverages consensus and MPC strategies to mitigate power fluctuations. Moreover, the stability of the controller is ascertained using Lyapunov stability theory. In Section 4, a parameter analysis methodology is established, employing the Krasovskii's method. Section 5 applies the aforementioned DC voltage cooperative approach to the optimization control of the MTDC system, the effectiveness of which is subsequently validated through rigorous simulation studies.

2 VSC-MTDC system structure and traditional control strategies

The VSC-MTDC system encompasses various different topological structures (Rahman et al., 2016; Wang et al., 2018). A typical topology is illustrated in Figure 1, where the power generation from an OWF is collected by the Wind Farm Side VSC (WFVSC) and injected into the VSC-MTDC system. Electrical power is transmitted through long subsea cables to the Point of Common Coupling (PCC), after which the power is distributed to each GSVSC based on the control strategy.

Within the VSC-MTDC system, the WFVSC and GSVSC implement distinct control strategies as shown in Figure 2. Here, L_f and C_f denote the filtering inductance and capacitance of the VSC output respectively; r_f represents the equivalent resistance of the VSC filter; e_{abc} and i_{labc} are the terminal voltage and current of the VSC; u_{oabc} and i_{oabc} are the output voltage and current of the VSC; v_{dc} is the voltage of the DC-side capacitor. The subscript abc (dq) signifies the corresponding variables within the abc (dq) coordinate axes. Given that the OWF is considered as a weak AC grid, it requires the WFVSC to provide voltage and frequency support as depicted in Figure 2A.

For the GSVSC, the primary task is to ensure the power transmission from the OWF to the grid. Current research primarily focuses on single-point voltage control or multi-machine droop control strategies to achieve master-slave or distributed control. Employing droop control strategies within a networked control system ensures good dynamic stability of the DC voltage (Wang et al., 2018), as depicted in Figure 2B.

3 MTDC cooperative DC voltage control

3.1 DC voltage control based on VSG

Traditional droop control strategies do not provide inertia and damping for the DC system. To effectively mitigate fluctuations in DC voltage, this study adopts the strategy of implementing VSG control on the GSVSC side. The governing equation for the VSG control of DC voltage is as follows (Li et al., 2018):

$$C_v\frac{dv_{dc}^{vir}}{dt}+D_v\left(v_{dc}^{vir}-v_{dcn}\right)=\frac{P_m}{v_{dcn}}-\frac{P_e}{v_{dcn}} \tag{1}$$

Where C_v and D_v represent the virtual capacitance and damping coefficient, respectively; v_{dc}^{vri} and v_{dcn} denote the virtual voltage on the DC side and the rated voltage value, respectively. P_m and P_e represent the mechanical input power and electrical output power of the synchronous machine.

According to Eq. 1, it can be seen that the term for simulated inertia power is $C_v dv_{dc}^{vir}/dt$, while the term for simulated damping power is D_v (v_{dc}^{vir}–v_{dcn}). Within the MTDC network, the VSG

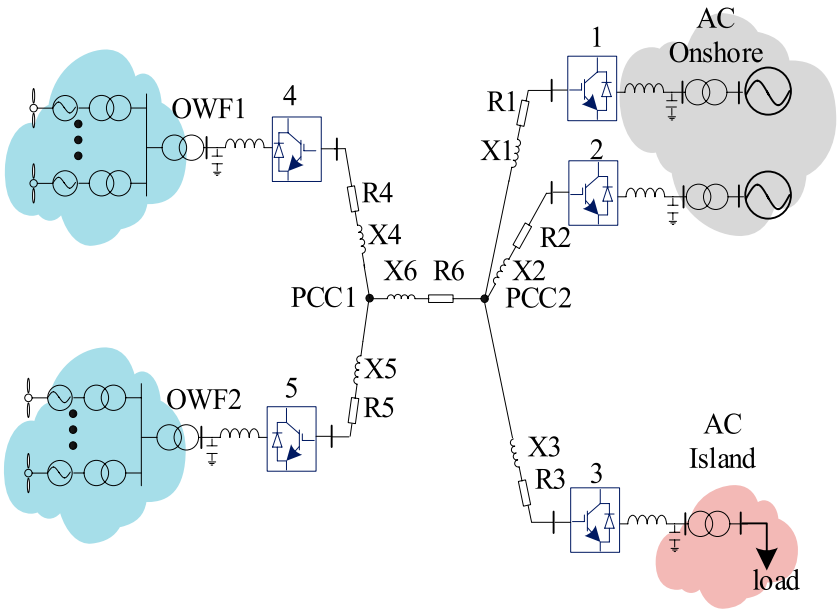

FIGURE 1
VSC-MTDC system topology diagram.

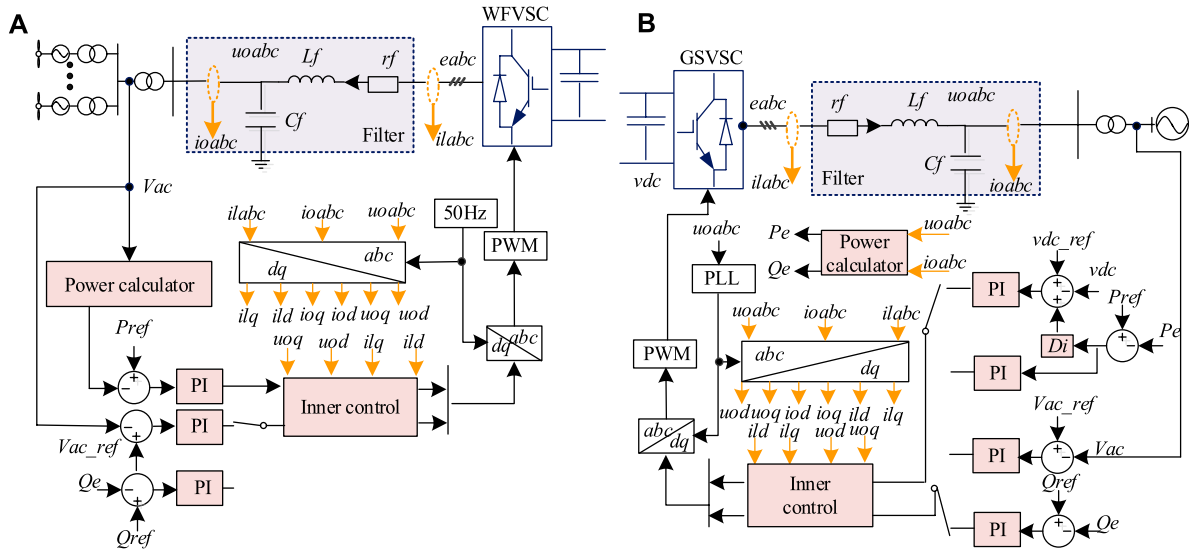

FIGURE 2
MTDC control Schematic: **(A)** WFVSC, and **(B)** GSVSC.

functions primarily to stabilize the DC voltage. In instances where the DC voltage experiences oscillations, the VSG will produce virtual inertia power to counter these fluctuations. This means that the generation of virtual inertia power is for the purpose of suppressing oscillatory phenomena. The speed of oscillations in DC voltage has a direct relationship with the generation of virtual inertia power within the system. Specifically, faster oscillations lead to an increased production of virtual inertia power, which offers inertia support during transient processes. Additionally, a larger virtual inertia constant equates to a slower rate of change in DC voltage, which is synonymous with a lower frequency of oscillation. The inertia power and damping power of the VSG are adjusted according to the changes in the DC side voltage. When the system tends toward stability, $dv_{dc}^{vir}/dt = 0$. The damping power of the VSG is proportional to the offset of the DC side voltage, and as long as there is a voltage offset ($v_{dc}^{vir} - v_{dcn}$), there will be a contribution from the damping power.

According to the direction of power flow, the charging and discharging of the DC capacitor control the value of the DC-side voltage, which can be obtained as follows:

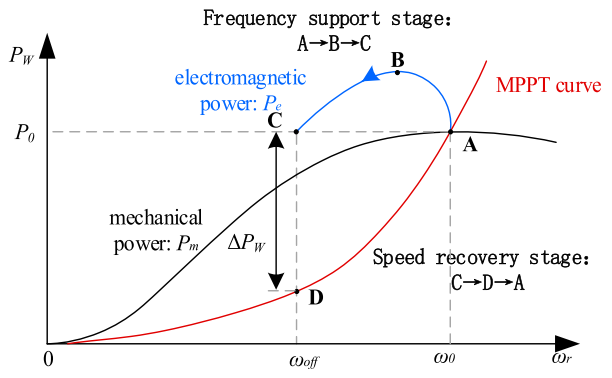

FIGURE 3
Frequency response procedure of wind turbine based on rotor kinetic energy.

$$\frac{NCv_{dci}}{S_{VSCi}} \cdot \frac{dv_{dci}}{dt} = P_{dc} - P_{ac} = P_{in} - P_{out} = \Delta P_C \tag{2}$$

Where N is the number of DC capacitors in the VSC-MTDC; C is the capacitance of a single DC capacitor; v_{dci} is the actual DC line voltage of the ith GSVSC controlling the DC-side voltage; S_{VSCi} is the apparent capacity of a single converter station; P_{in}/P_{dc} and P_{out}/P_{ac} are the input and output power of the VSC-MTDC system respectively; ΔP_C is the per-unit value of the electromagnetic power absorbed or released by the DC capacitor.

Equation 2 reveals that in order to ensure power balance between the GSVSC and the WFVSC, the DC voltage must be controlled to be constant. However, as a capacitor is an energy storage component, it can release or absorb power by adjusting the voltage. Therefore, it is feasible to use this characteristic of the DC capacitors in the VSC-MTDC system to balance power transmission (Liu and Chen, 2015). By regulating the DC link voltage through power compensation, the VSC-MTDC system can inject more or less active power into the onshore grid than the active power collected from the OWF.

3.2 Comprehensive inertia control and SFD

Additionally, addressing the frequency regulation problem of OWF, a comprehensive inertia control method enables the wind turbine units to have an inertia response and primary frequency regulation ability (Liu and Chen, 2015; Wang and Tomsovic, 2019). In the active control loop of the wind turbine units, the rate of frequency change and frequency deviation Δf are introduced, thereby realizing the additional active power reference value in the frequency response process, as shown in Eq. 3.

$$\Delta P_{add} = -K_d \frac{df}{dt} - K_p \Delta f \tag{3}$$

Where f represents the system frequency; Δf denotes the frequency deviation; K_d is the inertia control coefficient; K_p is the droop control coefficient; ΔP_{add} is the additional active power.

In cases of increasing frequency, wind turbine units can easily reduce their power output through wind curtailment. However, this study chiefly addresses situations in which units augment their output power by releasing rotor kinetic energy during frequency decreases. Using comprehensive inertia control as an exemplar, this response process primarily comprises two pivotal phases: the frequency support and rotor speed recovery stages, as illustrated in Figure 3. The entire response process can be categorized into two key phases: the frequency support phase and the rotor speed recovery phase. Here, ω_0 and P_0 denote the initial rotor speed and unit power, respectively; ω_{off} signifies the rotor speed at the conclusion of frequency regulation; P_W represents the unit's power output, while ΔP_W indicates the power variation observed at the conclusion of the frequency support phase.

This process can be delineated into four distinct stages:

1. Stage A: This represents the wind turbine unit's normal operational state, where it operates in Maximum Power Point Tracking (MPPT) mode, producing the optimal power level, denoted as *P0*.
2. Stage B: When the system encounters power insufficiency, the wind turbine unit responds by augmenting its power output to support the frequency, introducing supplementary power as per Eq. 3. During this stage, the output P_e surpasses the P_m, prompting the rotor to release kinetic energy and consequently reduce its speed.
3. Stage C: The unit exits the frequency regulation phase, reducing its power output by ΔP_W, and gradually restores rotor speed by following the MPPT curve.
4. Stage D: As wind turbine unit output power P_e falls below mechanical power Pm, the rotor absorbs energy. Rotor speed gradually recovers to the optimal level, reinstating an equilibrium state, and reverts to MPPT mode operation (effectively returning to Stage A).

Figure 3 illustrates that when ΔP_W exceeds a certain threshold, the system inevitably experiences secondary frequency drops.

3.3 DC voltage cooperative control

Accounting for the intrinsic variability of OWF power output and the dynamic switching of grid-side loads, continuous adjustments are needed in the power of the VSC station. Without timely adaptation of the VSC station's output power command, potential disturbances to the power balance may instigate significant frequency variations, potentially jeopardizing system stability.

Within this context, the OWF is modeled as a SG that provides supplementary power to the AC onshore grid. The balance of power in the SG is governed by the swing equation, P_m-$P_e = J\omega d\omega/dt$, where J represents the moment of inertia parameter. Upon disturbance in the AC onshore gird, this balance is disrupted, prompting the energy stored in the capacitor to automatically offset the unbalanced power, leading to a reduction or oscillation in the DC voltage. Combining (3), OWF participates in system frequency regulation. From the principle of energy conservation, the following can be deduced:

$$\int_{\omega 1}^{\omega 2} J_{\mathrm{OWF}} \omega \frac{d\omega}{dt} + \int_{vdc1}^{vdc2} C v_{dc} \frac{dvdc}{dt} = \int_{\omega 1}^{\omega 2} J_{\mathrm{AC}} \omega \frac{d\omega}{dt} \tag{4}$$

When energy changes are defined as ΔE_c and ΔE_J, the subsequent derivation from Eq. 4 is:

$$\begin{cases} \Delta E_c = \frac{1}{2}Cv_{dc2}^2 - \frac{1}{2}Cv_{dc1}^2 \\ \Delta E_{JOWF} = \frac{1}{2}J_{OWF}\omega_2^2 - \frac{1}{2}J_{OWF}\omega_1^2 \\ \Delta E_{JAC} = \frac{1}{2}J_{AC}\omega_2^2 - \frac{1}{2}J_{AC}\omega_1^2 \end{cases} \tag{5}$$

Equation 5 encapsulates the actual physical dynamics of the DC-side capacitor. Fundamentally, the energy stored in the rotor must be fully utilized during the control process to emulate the inertia stored in the virtual capacitor. For MTDC systems, this involves harnessing energy both from the OWF grid and the capacitor itself. Furthermore, voltage distribution within the MTDC system demonstrates non-uniform properties across the entire DC system. While some voltages within the MTDC grid may be well-regulated, other ports may display significant deviations from expected values (Kirakosyan et al., 2023).

In this study, to ensure fairness among VSCs participating in control tasks with VSG voltage control, the inertia power $\Delta P_{iner} = C_v dv_{dc}^{vir}/dt$ is introduced as a consensus variable in the voltage control strategy. This variable is incorporated into the VSC station with voltage control as an additional power command, bolstering the DC-side voltage balancing capability, facilitating mutual inertia support, and improving frequency stability.

In the system's initial operational phase, the power injection of the ith converter, denoted as P_i, aligns with its reference power, P_{ref}. However, in the event of active power imbalance, the actual power injection will diverge from its reference value. If there is an overabundance of active power in the DC system, the VSC will increase its drawn power from the MTDC system. Conversely, if the DC system's active power is lacking, the VSC will decrease its drawn power. As such, this paper proposes the introduction of power deviation, as resolved by MPC, as an adjustment variable. This adjustment pre-distributes power injection values among the VSCs, in accordance with the VSC's output power.

For the voltage control group, let the DC-side voltage it is about to control be v_{dci}, and this voltage can be measured in real-time. Based on the consensus protocol, the method of updating the supplemental power for the *ith* VSC in the group is presented as Eq. 6:

$$\varphi_i(k+1) = \sum_{j=1}^{N_i} d_{ij}(\varphi_i(k) - \varphi_j(k)) + \varepsilon d_{ij}\Delta\varphi_i^{ref}(k) \tag{6}$$

Where $\varphi_i(k)$ is the inertia power variable calculated by VSCi in the voltage control group after the kth iteration, which can be described as $\varphi_i = \Delta P_{ineri}$. N_i is the total number of VSCs using DC-side voltage control; ε is the convergence factor (Li et al., 2019). Equation 6 provides interactive power instructions for both the grid side and wind power. d_{ij} represents the weight, and its value can be calculated using Eq. 7:

$$d_{ij} = a_{ij} \Big/ \left(\sum_{j=1}^{N_i} a_{ij}\right) \tag{7}$$

If there is a communication link between VSCi and VSCj, then $a_{ij} = 1$, otherwise $a_{ij} = 0$. $\Delta\varphi_i^{ref}$ is the reference value of the unbalanced power of the ith VSC at the kth iteration. In order to regulate it, the voltage control performance evaluation function is first defined in Eq. 8:

$$f_v = \frac{1}{2}(v_{dci} - 1)^2 \tag{8}$$

Let $\Delta\varphi_i^{ref}(k)$ be the negative value of the partial derivative of the performance evaluation function f_v with respect to φ_i. Then, we have:

$$\begin{aligned} \Delta\varphi_i^{ref} &= -\frac{\partial f_v}{\partial \varphi_i|_{\varphi_i(k)}} = -\left(\frac{\partial f_v}{\partial v_{dci}} \cdot \frac{\partial v_{dci}}{\partial \varphi_i}\right) \\ &= -(v_{dci} - 1)\left(\frac{\partial v_{dci}}{\partial \Delta P_{iner}}\right) \end{aligned} \tag{9}$$

Where $\partial v_{dci}/\partial\varphi_i$ represents the sensitivity of voltage to changes in injected active power, reflecting the sensitivity of VSCi's voltage to variations in injected active power. The reflection value of active power on voltage change can be obtained from Eq. 9. As Eq. 1 indicates, the direct voltage of the VSC station plays a similar role in reflecting power balance within the DC grid. Considering that the direct voltage determines the flow of DC power, the correlation between voltage and injected power can be determined by constructing objective functions for voltage and power. Therefore, a method combining MPC for solving VSG has been proposed.

According to Eq. 1, the rotor motion equation of the VSG can be described as a state equation, as shown in Eq. 10.

$$\begin{cases} \dot{v}(t) = \frac{P_m(t)}{C_v v_{dcn}} - \frac{P_e(t)}{C_v v_{dcn}} - \frac{D_v}{C_v} v(t) \\ y(t) = v(t) \end{cases} \tag{10}$$

Where $v(t)$ is defined as the difference between v_{dc}^{vir} and v_{dcn}, which represents the voltage-related term in the state equation. P_m represents the control input variable, and P_e can be considered as the disturbance variable.

The discrete state equation is presented in Eq. 11:

$$\begin{cases} \Delta v(k+1) = \mathbf{A}_z \Delta v(k) + \mathbf{B}_u \Delta P_m(k) + \mathbf{B}_d \Delta P_e(k) \\ y_c(k+1) = \mathbf{C}_c \Delta v(k+1) + y_c(k) \end{cases} \tag{11}$$

The coefficients in Eq. 11 are detailed in Eq. 12.

$$\begin{aligned} &\mathbf{A}_z = e^{\left(-\frac{D_v}{C_v}\right)T_s}, \mathbf{B}_u = \frac{1}{C_v v_{dcn}} \int_0^{T_s} e^{\left(-\frac{D_v}{C_v}\right)\tau} d\tau, \\ &\mathbf{B}_d = \frac{1}{C_v v_{dcn}} \int_0^{T_s} e^{\left(-\frac{D_v}{C_v}\right)\tau} d\tau, \mathbf{C}_c = 1 \end{aligned} \tag{12}$$

Where T_s represents the sampling period. In this study, a three-step model prediction method due to its capacity for an extended prediction horizon is utilized. This allows for a more accurate representation of the system's dynamic behavior and a stronger response to disturbances, as it can foresee changes further ahead and adjust the control strategy accordingly. The three-step prediction output vector is presented in Eq. 13:

$$\Delta \mathbf{Y}_p(k+1 \mid k) \triangleq \begin{bmatrix} y_c(k+1 \mid k) \\ y_c(k+2 \mid k) \\ y_c(k+3 \mid k) \end{bmatrix} \tag{13}$$

The voltage prediction equation is presented in Eq. 14:

$$\Delta \mathbf{Y}_p(k+1\,|\,k) = \mathbf{S}_z \Delta v(k) + \mathbf{I}_p y_c(k) + \mathbf{S}_u \Delta P_m(k) + \mathbf{S}_d \Delta P_e(k) \tag{14}$$

The coefficients in Eq. 14 are detailed in Eq. 15:

$$\begin{aligned}
\mathbf{S}_z &= \left[\mathbf{C}_c\mathbf{A}_z \;\; \sum_{i=1}^{2}\mathbf{C}_c\mathbf{A}_z{}^{i} \;\; \sum_{i=1}^{3}\mathbf{C}_c\mathbf{A}_z{}^{i} \right] \\
\mathbf{I}_p &= \left[1 \;\; 1 \;\; 1 \right]^T \\
\mathbf{S}_d &= \left[\mathbf{C}_c\mathbf{B}_d \;\; \sum_{i=1}^{2}\mathbf{C}_c\mathbf{A}_z{}^{i-1}\mathbf{B}_d \;\; \sum_{i=1}^{3}\mathbf{C}_c\mathbf{A}_z{}^{i-1}\mathbf{B}_d \right]^T \\
\mathbf{S}_u &= \begin{bmatrix} \mathbf{C}_c\mathbf{B}_u & 0 & 0 \\ \sum_{i=1}^{2}\mathbf{C}_c\mathbf{A}_z{}^{i-1}\mathbf{B}_u & \mathbf{C}_c\mathbf{B}_u & 0 \\ \sum_{i=1}^{3}\mathbf{C}_c\mathbf{A}_z{}^{i-1}\mathbf{B}_u & \sum_{i=1}^{2}\mathbf{C}_c\mathbf{A}_z{}^{i-1}\mathbf{B}_u & \mathbf{C}_c\mathbf{B}_u \end{bmatrix}
\end{aligned} \tag{15}$$

The objective function aims to minimize the weighted sum of the squared deviations of the voltage, Δv, and the change in the rated power, ΔP_m, as shown in Eq. 16:

$$V_p = \sum_{i=1}^{3}\left[(\tau \Delta v(k+i|k))^2 + (\upsilon \Delta P_m(k+i|k))^2 \right] \tag{16}$$

Where τ and υ are the weighting coefficients for voltage and power variations, respectively. Additionally, $\Delta v\,(k+i|k)$ and $\Delta P_m\,(k+i|k)$ represent the errors between the predicted voltage and power at instant k. Based on the predicted inputs, Eq. 16 can be described as follows:

$$V_p(\Delta v(k), \Delta P_m(k)) = \min\left\{ \left\| \mathbf{T}_y\left(\mathbf{Y}_p(k+1\,|\,k) - \mathbf{R}(k+1)\right) \right\|^2 + \left\| \mathbf{T}_P \Delta \mathbf{P}_m(k) \right\|^2 \right\} \tag{17}$$

Where $\mathbf{T_y} = \mathrm{diag}\,(\tau, \tau, \tau)$ and $\mathbf{T_P} = \mathrm{diag}\,(\upsilon, \upsilon, \upsilon)$. $\mathbf{T_y}$ and $\mathbf{T_P}$ are the error weighting matrices for voltage and active power, respectively. $\mathbf{R}\,(k+1)$ represents the reference values for the control outputs at time $k+1$. The desired steady-state Δv is zero, hence $\mathbf{R}\,(k+1) = [0,0,0]$.

Due to the presence of constraints, it is not possible to obtain an analytical solution for the optimization problem in Eq. 17. Therefore, a numerical solution method is employed, transforming the constrained MPC optimization problem into a quadratic programming (QP) formulation. To facilitate the solution of the optimization problem in Eq. 17, auxiliary variables are defined:

$$\mathbf{E}_p(k+1\,|\,k) = \mathbf{R}(k+1) - \mathbf{S}_z \Delta v(k) - \mathbf{I}_p y_c(k) - \mathbf{S}_d \Delta P_e(k) \tag{18}$$

By substituting Eq. 14 into Eq. 17, and in conjunction with Eq. 18, it can be obtained that:

$$\begin{aligned}
V_p(\Delta v(k), \Delta P_m(k)) &= \left\| \mathbf{T}_y\left(\mathbf{S}_u \Delta \mathbf{P}_m(k) - \mathbf{E}_p(k+1\,|\,k)\right) \right\|^2 + \left\| \mathbf{T}_P \Delta \mathbf{P}_m(k) \right\|^2 \\
&= \Delta \mathbf{P}_m(k)^T \mathbf{S}_u{}^T \mathbf{T}_y{}^T \mathbf{T}_y \mathbf{S}_u \Delta \mathbf{P}_m(k) + \Delta \mathbf{P}_m(k)^T \mathbf{T}_P{}^T \mathbf{T}_P \Delta \mathbf{P}_m \\
&\quad - 2\mathbf{E}_p(k+1\,|\,k)^T \mathbf{T}_y{}^T \mathbf{T}_y \mathbf{S}_u \Delta \mathbf{P}_m(k) + \mathbf{E}_p(k+1\,|\,k)^T \mathbf{T}_y{}^T \mathbf{T}_y \mathbf{E}_p(k+1\,|\,k)
\end{aligned} \tag{19}$$

Given that $\mathbf{E}_p(k+1\,|\,k)^T \mathbf{T}_y{}^T \mathbf{T}_y \mathbf{E}_p(k+1\,|\,k)$ is independent of the variable $\Delta \mathbf{P}_m(k)$, for the optimization problem, Eq. 19 is equivalent to Eq. 20:

$$V_p = \Delta \mathbf{P}_m(k)^T \mathbf{H} \mathbf{P}_m(k) - \mathbf{G}(k+1\,|\,k)^T \Delta \mathbf{P}_m(k) \tag{20}$$

The coefficients in Eq. 20 are detailed in Eq. 21
Where

$$\begin{aligned}
\mathbf{H} &= \mathbf{S}_u{}^T \mathbf{T}_y{}^T \mathbf{T}_y \mathbf{S}_u + \mathbf{T}_P{}^T \mathbf{T}_P \\
\mathbf{G}(k+1\,|\,k) &= 2\mathbf{S}_u{}^T \mathbf{T}_y{}^T \mathbf{T}_y \mathbf{E}_p(k+1\,|\,k)
\end{aligned} \tag{21}$$

By transforming the voltage constraint in Eq. 14 into the form $\mathbf{C}z \geq \mathbf{b}$, Eq. 13 can be reformulated as Eq. 22:

$$\Delta \mathbf{Y}_{pmin}(k+1) < \Delta \mathbf{Y}_p(k+1\,|\,k) < \Delta \mathbf{Y}_{pmax}(k+1) \tag{22}$$

$$\begin{bmatrix} -\mathbf{S}_u \\ \mathbf{S}_u \end{bmatrix} \Delta \mathbf{P}_m(k) \geq \mathbf{b}(k)$$

$$\mathbf{b}(k) = \begin{bmatrix} \left(\mathbf{S}_z \Delta v(k) + \mathbf{I}_p y_c(k) + \mathbf{S}_d \Delta P_e(k)\right) - \Delta \mathbf{Y}_{pmax}(k+1) \\ -\left(\mathbf{S}_z \Delta v(k) + \mathbf{I}_p y_c(k) + \mathbf{S}_d \Delta P_e(k)\right) + \Delta \mathbf{Y}_{pmin}(k+1) \end{bmatrix} \tag{23}$$

From Eq. 23, it can be seen that the MPC optimization problem is transformed into the following QP problem description:

$$\min_{\Delta P_m(k)} \Delta \mathbf{P}_m(k)^T \mathbf{H} \Delta \mathbf{P}_m(k) - \mathbf{G}_m(k+1\,|\,k) \Delta \mathbf{P}_m(k) \quad satisfy:\ \mathbf{C}_u \Delta \mathbf{P}_m(k) \geq \mathbf{b}(k) \tag{24}$$

The coefficients in Eq. 24 are detailed in Eq. 25.

$$\mathbf{C}_u = \left[-\mathbf{S}_u \;\; \mathbf{S}_u \right] \tag{25}$$

By combining Eq. 21 and Eq. 24, the solution for MPC, denoted as $\Delta \mathbf{P}_m{}^*(k)$, can be obtained. According to the working principle of MPC, an initial control sequence will be applied to the system. In the next sampling period, the constraint optimization problem will be updated, and the solution to $\Delta \mathbf{P}_m{}^*(k)$ will be recalculated. According to Eq. 24, the power increment in a single VSG can be quickly solved, which is the correlation value of voltage and injected power. The variation of power increment for VSG can be written as:

$$\Delta P(k) = \Delta P_m{}^*(k) \tag{26}$$

Through Eq. 26, the association value between voltage and active power can be obtained, where $\Delta \varphi_i{}^{ref} = (\nu_{dci} - 1)\Delta \mathrm{P}\,(k)$. The inertia of the system serves as a buffer against abrupt shifts in DC voltage, aiding in damping oscillations and allowing adequate time for the MTDC network to adjust active power. Based on the aforementioned analysis, it can be deduced that surplus power from consistency calculations always exhibits an inverse relationship with the rate of DC voltage change. Therefore, it is concluded that this supplemental power functions as a counterforce to DC voltage fluctuations, supplying inertia power to the system. This mechanism assists in mitigating voltage and power instabilities. Consequently, the proposed cooperative method can timely adjust the output power of GSVSC on the VSC-MTDC side when it is disturbed, increasing the system's inertia, and reducing the rate of frequency change and voltage deviation. At the same time, the supplemental power provides second power error tracking for control, enhancing the convergence of power output. The proposed DC Voltage cooperative control based on VSG is illustrated as in Figure 4.

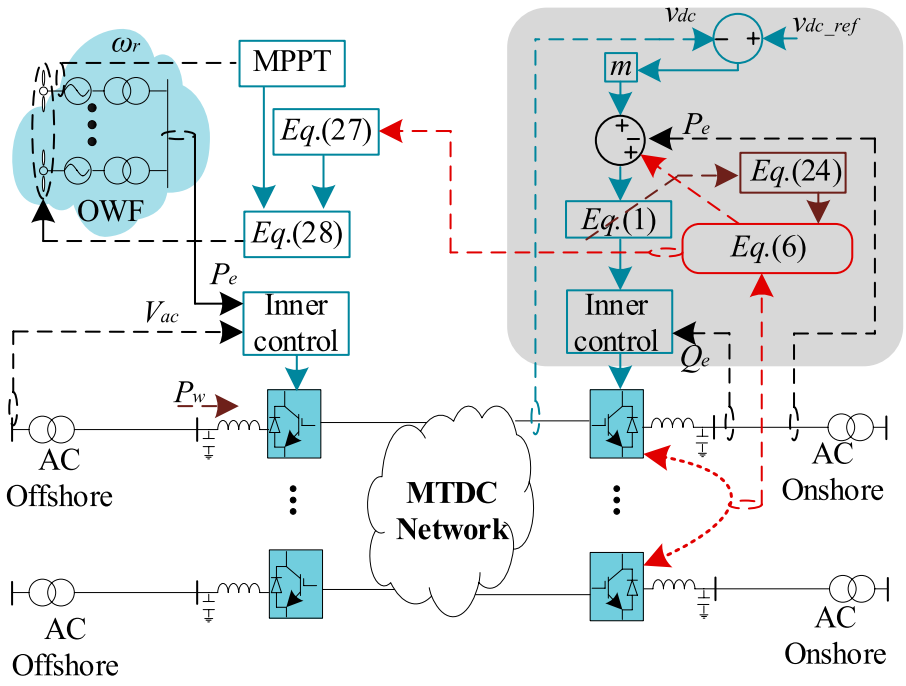

FIGURE 4
Schematic of the proposed DC voltage cooperative control.

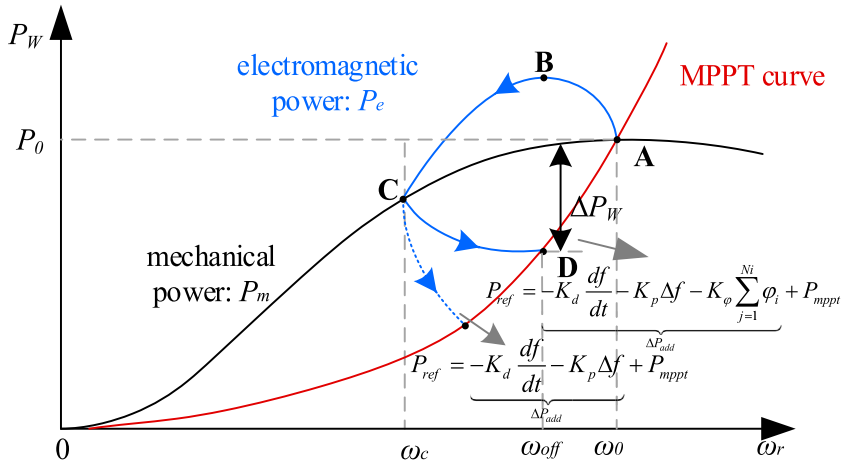

FIGURE 5
Frequency response control strategy for wind turbine units considering cooperative control.

Figure 4 illustrates the control schematic of the proposed method. In addition, in accordance with the description in Eq. 5, to fully utilize the energy from the OWF, the frequency regulation equation for the OWF is further depicted as:

$$\Delta P_{add} = -K_d\frac{df}{dt} - K_p\Delta f - K_\varphi\sum_{j=1}^{Ni}\varphi_i \tag{27}$$

$$P_{ref} = -K_d\frac{df}{dt} - K_p\Delta f - K_\varphi\sum_{j=1}^{Ni}\varphi_i + P_{mppt} \tag{28}$$

Where K_φ is the adjustment coefficient. P_{ref} denotes the reference value of wind farm units. Equation 27 represents the formula for the OWF to participate in frequency modulation, while Eq. 28 defines the operating reference value for the OWF. The introduction of the optimal power value P_{mppt} enables these units to effectively respond to variations in wind speed during the frequency support phase, particularly when coordinated with the interactive power parameter $K_\varphi\sum_{j=1}^{Ni}\varphi_i$. In comparison to Figure 3, the inclusion of cooperative power in Figure 5 leads to a further decrease in the parameter ΔP_W, consequently resulting in a diminished amplitude of SFD. As the system frequency gradually returns to normalcy and the rotor speed decreases, reaching a pivotal point C, P_m aligns with P_e. Subsequently, as P_e falls below P_m, the

wind turbine's rotational speed ascends gradually, ultimately returning to a stable state.

In response to frequency fluctuations in the AC grid caused by disturbances, the VSC station will adjust its output power. This adjustment is made by leveraging the energy from the OWF and the voltage of the DC-side capacitor to compensate for power imbalance, thereby enabling quick convergence of frequency. Simultaneously, leveraging the *V*–*P* characteristic, the total power generated by the OWF will be automatically distributed to the VSC station based on the state of DC voltage and AC power.

4 MTDC parameter stability analysis

To analyze the parameters of the MTDC, a small signal analysis method is employed for parameter analysis (Kalcon et al., 2012). On the synchronous *dq* frame, the state-space equation of the *LC* filter can be expressed as:

$$\begin{cases} L_f \dot{i}_{ld} = -r_f i_{ld} + \omega L_f i_{lq} + u_d{}^{\star} - u_{od} \\ L_f \dot{i}_{lq} = -r_f i_{lq} - \omega L_f i_{ld} + u_q{}^{\star} - u_{oq} \\ C_f \dot{u}_{od} = \omega C_f u_{oq} + i_{ld} - i_{od} \\ C_f \dot{u}_{oq} = -\omega C_f u_{od} + i_{lq} - i_{oq} \end{cases} \tag{29}$$

where u_{odq} and i_{odq} are the *dq*-axis output voltage and the *dq*-axis output current of VSG, respectively. i_{ldq} and $u_{dq}{}^{\star}$ are the *dq*-axis terminal current and the voltage reference of VSG, respectively.

The state-space equations of the transmission line on the *dq* frame are given as follows:

$$\begin{cases} L_c \dot{i}_{od} = -r_c i_{od} + \omega L_c i_{oq} + u_{od} - u_{bd} \\ L_c \dot{i}_{oq} = -r_c i_{oq} - \omega L_c i_{od} + u_{oq} - u_{bq} \end{cases} \tag{30}$$

where u_{bdq} is the *dq*-axis voltage of power grid.

The voltage reference value ($u_d{}^{*}$,$u_q{}^{*}$) and current reference value ($i_{ld}{}^{\star}$,$i_{lq}{}^{\star}$) of the VSG controlled inverter are defined as follows:

$$\begin{cases} i_{ld}{}^{\star} = k_{dv1p}\dfrac{dx_{12}}{dt} + k_{dv1i}x_{12} + i_{od} - \omega_0 C_f u_{oq} \\ i_{lq}{}^{\star} = k_{qv1p}\dfrac{dx_{13}}{dt} + k_{qv1i}x_{13} + i_{oq} + \omega_0 C_f u_{od} \\ u_d{}^{\star} = k_{dc1p}\dfrac{dx_{14}}{dt} + k_{dc1i}x_{14} + u_{od} - \omega_0 L_f i_{lq} \\ u_q{}^{\star} = k_{qc1p}\dfrac{dx_{15}}{dt} + k_{qc1i}x_{15} + u_{oq} + \omega_0 L_f i_{ld} \end{cases} \tag{31}$$

Where $k_{d\text{-}qv1p}$ and $k_{d\text{-}qv1i}$ are the PI gains of the outer loop, and $k_{d\text{-}qc1p}$ and $k_{d\text{-}qc1i}$ are PI gains of the inner loop. The state variables x_{12} to x_{15} are defined to assess the modelling of controllers.

By combining Eqs 1, 2, 29, 30, 31, the small signal model of the linearized system can be delineated as follows:

$$\begin{cases} \Delta\dot{\mathbf{x}}_{n\times1} = \mathbf{A}_{n\times n}\Delta\mathbf{x}_{n\times1} + \mathbf{B}_{n\times k}\Delta\mathbf{u}_{k\times1} \\ \Delta\dot{\mathbf{y}}_{m\times1} = \mathbf{C}_{m\times n}\Delta\mathbf{x}_{n\times1} + \mathbf{D}_{m\times k}\Delta\mathbf{u}_{k\times1} \end{cases} \tag{32}$$

Where $\Delta\mathbf{x}$ represents the state variable, $\Delta\mathbf{u}$ signifies the controller input, and $\Delta\mathbf{y}$ is defined as the output of the VSC-MTDC system. $\mathbf{A}_{nxn}$, $\mathbf{B}_{nxk}$, $\mathbf{C}_{mxn}$ and $\mathbf{D}_{mxk}$ are respectively the state matrix, input matrix, output matrix, and direct transmission matrix of the linearized model.

TABLE 1 Initial parameters.

	Name	Value
VSC-station	Rated VSC power/MVA	450
	Nominal dc voltage/kV	±160
	Nominal ad voltage/kV	160
	C/mF	7.5
dc cable	R1-R5/Ω	0.15
	X1-X5/Ω	6
	R6/Ω	0.2
	X6/Ω	8

TABLE 2 Control parameters.

Parameters	GSVSC1	GSVSC2	GSVSC3	WFVSC3/4
Voltage control loop	[5 60]	[5 60]	[5 60]	[2 10]
Current control loop	[3 150]	[3 150]	[3 150]	[1.5 60]

Stability analysis of system parameters belongs to the broad spectrum of stability analysis issues. The stability of system parameters and the determination of parameters that satisfy system stability can be ascertained through the Lyapunov direct method. The selection of an appropriate Lyapunov function becomes crucial in determining system stability and resolving the range of control parameters. This study intends to construct a Lyapunov function using the Krasovskii method (Shuai et al., 2019; Haidar and Pepe, 2021).

According to the state equation of the system, the Lyapunov function $V(\Delta\mathbf{x})$ and the derivative function $V(\Delta x)$ are constructed by the Krasovskii method.

$$\begin{cases} V(\Delta x) = f^T(\Delta x, \Delta u) f(\Delta x, \Delta u) \\ \dot{V}(\Delta x) = f^T(\Delta x, \Delta u)\hat{J}(\Delta x) f(\Delta x, \Delta u) \end{cases} \tag{33}$$

Where $f(\Delta\mathbf{x},\Delta\mathbf{u})$ is the nonlinear steady n-dimensional function of the system; $f^T(\Delta\mathbf{x},\Delta\mathbf{u})$ is the transpose matrix of $f(\Delta\mathbf{x},\Delta\mathbf{u})$; $J(\Delta\mathbf{x})$ is the Jacobian matrix of the system, and $\hat{J}(\mathbf{x}) = J^T(\mathbf{x}) + J(\mathbf{x})$. When $V(\Delta\mathbf{x}) > 0$ and $\dot{V}(\Delta x) < 0$, the system is asymptotically stable.

5 Simulink

To verify the efficacy of the proposed method, the five-port VSC-MTDC model depicted in Figure 1 is simulated using MATLAB/Simulink software. This includes two asynchronous land-based power grids and two networks of OWFs. The system parameters are based on (Wang et al., 2018), and the PI controller has been adjusted following the method proposed in (Yazdani and Iravani, 2010) to provide fast reference signal tracking. The total wind power of each OWF is 240 MW. The initial power distribution

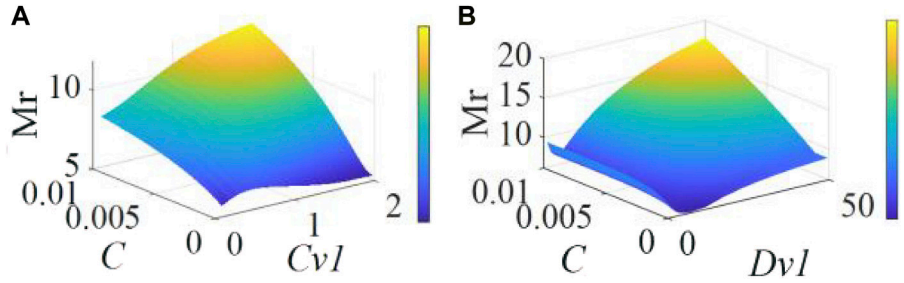

FIGURE 6
Resonant peak of system. **(A)** C and C_{v1}, and **(B)** C and D_{v1}.

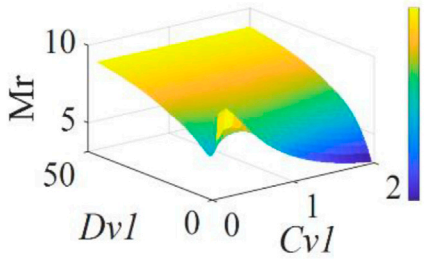

FIGURE 7
Resonant peak of system.

ratio of GSVSC is 3:1:2, as shown in Table 1. The control parameters are delineated in Table 2.

5.1 Influence of the DC-Link capacitors' size

Different DC-side capacitors can contribute differently to the system's power, thus the relationships between various virtual capacitors C_v, damping coefficients D_v, and DC-side capacitor C are analyzed. The given power of VSG1 is taken as the input variable, while the active power of VSG1 is set as the output variable. The feasible parameter domain for variables is solved based on Eqs 32 and 33, and the system's resonance peak Mr under various parameters is obtained using the direct transmission matrix of the linearized model, as shown in Figure 6. The color gradient serves as a visual representation denoting the magnitude of the resonance peak Mr, which is applied here as an indicator for assessing the system's comparative stability. Typically, a heightened resonance peak tends to correlate with diminished relative stability.

Figure 6 reveals the significant impact of capacitor capacity on system stability. As the capacitor size increases, the system's stability correspondingly decreases. This phenomenon occurs because, despite a larger DC link capacitor's ability to greatly reduce DC voltage fluctuations, under these conditions, the GSVSC unable absorb more power from the DC network to provide the necessary power support. Furthermore, grid frequency deviation increases with the growth of the DC link capacitor, which further exacerbates the decline in stability.

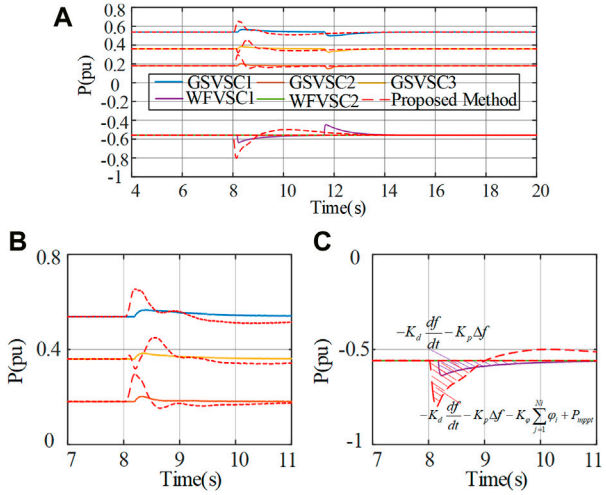

FIGURE 8
Power output comparison: **(A)** active power, **(B)** enlarged view of GSVSC, and **(C)** enlarged view of WFVSC.

Figure 7 shows the schematic diagram of the effects of changes in C_{v1} and D_{v1} parameters on system stability. Although the system can maintain asymptotic stability within a large range, larger inertia parameters require matching with larger capacitors. Overall, the size of the capacitor, virtual capacitor, and damping coefficient directly affect the system's stability. In order to achieve optimal performance, these factors need to be considered comprehensively and adjusted appropriately. In this paper, C_{v1} = 1.3,D_{v1} = 7.5; C_{v2} = 1.1, D_{v2} = 2.5; C_{v3} = 1.2, D_{v3} = 5 are selected.

5.2 Performance during load switching

To assess the effectiveness of the control strategy, a load switching experiment was conducted at 8 s. The assigned values for the parameters in this context are as follows: K_p = 1.5,K_d = 0.5, K_φ = 1. Figure 8 depicts a comparison of power output curves for VSC stations in response to load switching between the conventional method and the proposed approach. Figure 8A presents a global comparison of the active power output curves. Amplified views of the output power for corresponding VSCs are

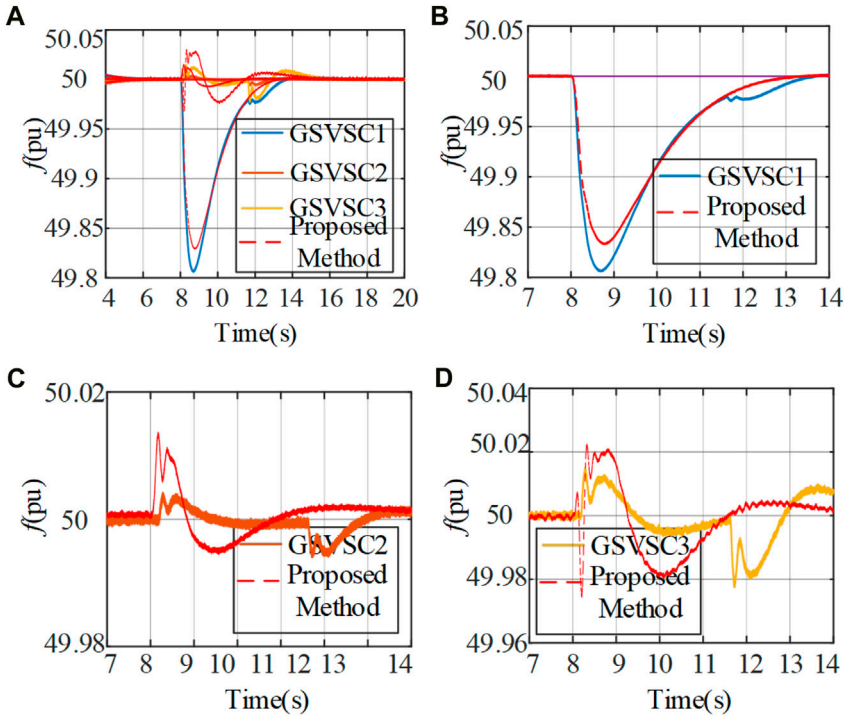

FIGURE 9
Dynamic performance of load change: **(A)** output frequency, **(B)** enlarged view of GSVSC1, **(C)** enlarged view of GSVSC2, and **(D)** enlarged view of GSVSC3.

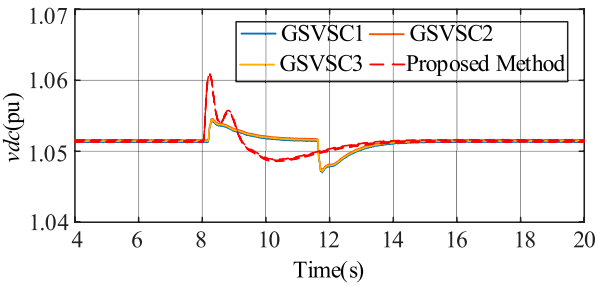

FIGURE 10
Dynamic performance under load change of DC voltage.

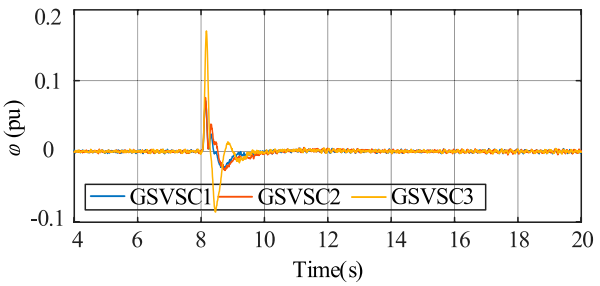

FIGURE 11
Consensus variable.

displayed in Figures 8B, C. Notably, the red dashed line is indicative of the output corresponding to the proposed method. It is important to note that in subsequent test results, the red dashed line consistently represents the output curve associated with the proposed method. At t = 8 s, the load was introduced into AC onshore grid 1. As delineated in Figure 8, subsequent to the application of the proposed voltage cooperative control, the GSVSC side gains additional active power from the OWF for equilibrium adjustment, as depicted in Figures 8B, C.

Figure 9 presents the frequency variations during load switching in the system. Load switching in AC onshore grid 1 introduces noticeable frequency fluctuations in GSVSC1. Traditional control strategies maintain a minimum frequency point at 49.8 Hz, while the proposed cooperative control approach achieves 49.83 Hz, as shown in Figure 9B. When OWF performs secondary frequency adjustment for GSVSC, relying solely on traditional comprehensive inertia control may lead to SFD. However, the introduction of the proposed voltage cooperative control effectively mitigates SFD, as shown in Figures 9B–D. These figures display before-and-after comparisons of the frequencies for GSVSC1-3 when employing the proposed method. After the adoption of the proposed method, the overall frequency variations in the system exhibit improved convergence, accompanied by a reduction in the impact of SFD.

Regarding fluctuations in DC voltage, the effectiveness of the proposed coordinated control method in leveraging the stored energy within DC-side capacitors to mitigate power

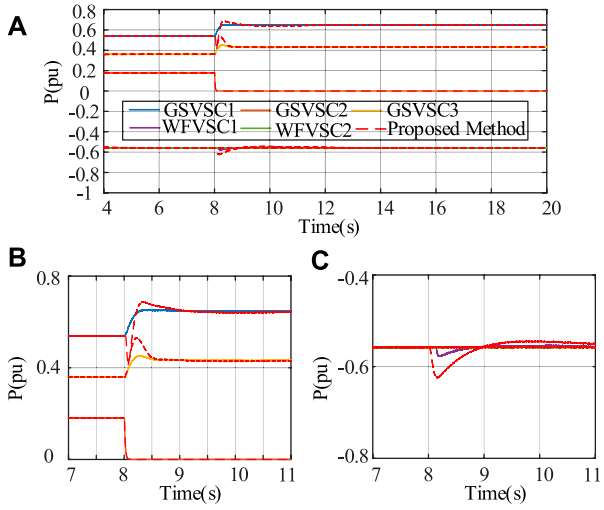

FIGURE 12
Dynamic performance under agent loss: **(A)** active power, **(B)** enlarged view of GSVSC, and **(C)** enlarged view of WFVSC.

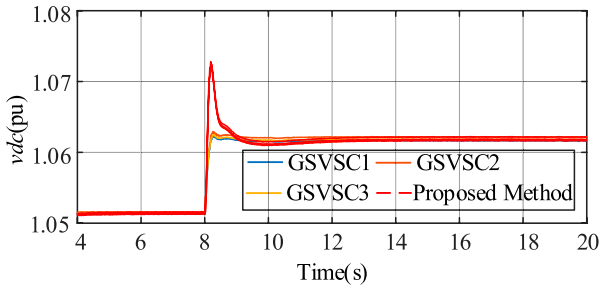

FIGURE 14
Dynamic performance under agent loss of DC voltage.

variations is illustrated in Figure 10. Through coordinated control, there is efficient utilization of the energy reserves stored in the DC-side capacitors for power regulation. This results in reduced frequency variations, thereby achieving a smoother output.

Figure 11 illustrates the corresponding supplemental power output. It is evident from Figure 11 that when the system attains stability, the supplemental power reaches zero, having no impact on the system's output. Furthermore, by utilizing the correlation values between voltage and injected power, calculated through MPC, the system effectively tracks changes in active power. This verification underscores the efficacy of the proposed method under load switching conditions and its robustness in response to variations in load.

During the regulation process, only OWF1 participates in frequency regulation. In previous research, the frequency dead zone is generally selected to be (±0.02~0.05) Hz, while in this paper, ±0.02 Hz is chosen. As shown in Figure 8, at t = 11.8 s, OWF1 exits frequency regulation work. Meanwhile, to ensure that the unit has certain frequency regulation capabilities and to reduce instances of unit stall and shutdown, this study stipulates that the output power of the unit involved in frequency response from OWF1 should not be less than 20% of the rated capacity.

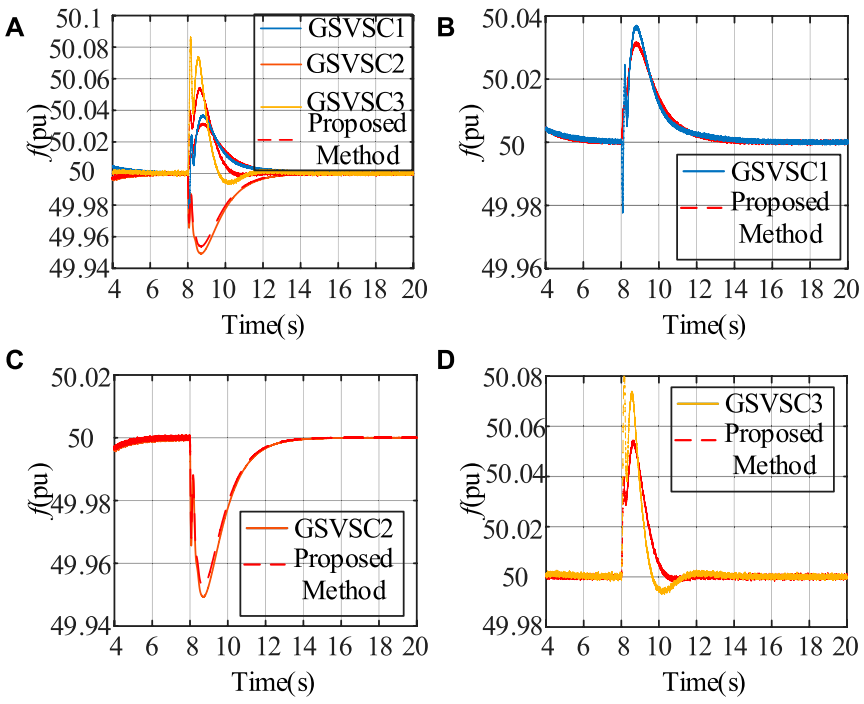

FIGURE 13
Dynamic performance under agent loss: **(A)** output frequency, **(B)** GSVSC1, **(C)** GSVSC2, and **(D)** GSVSC3.

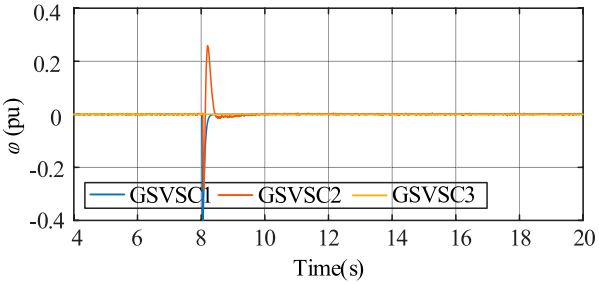

FIGURE 15
Consensus variable of the proposed method.

5.3 Performance analysis in agent loss scenarios

Figures 12–15 showcase the assessment of the proposed method's performance in the case of agent loss. Within this set, Figure 12A presents a global comparison chart of active power output, while Figures 12B, C offers a detailed enlargement of the power. At t = 10 s, GSVSC2 loses communication with others, signifying an agent loss scenario. It is noteworthy that GSVSG2 can continue to function normally based on the predefined default reference (0 kW). Concurrently, the remaining VSGs can continue to function normally. Under cooperative control, the OWF also contributes additional active power for system balance regulation, as depicted in Figure 12C.

Figure 13 illustrates the frequency variation output curve. Given GSVSC2's limited frequency fluctuations during power output changes, traditional control strategies yield reduced SFD. Nonetheless, the adoption of the proposed coordinated control method improves frequency convergence for GSVSC1 and GSVSC3 while mitigating the frequency drop in GSVSC2. This results in an overall enhancement of frequency convergence and system stability.

Figure 14 displays a comparative plot of voltage output curves. With the adoption of the proposed coordinated control method, DC-side capacitors release additional energy to fulfill the system's power demands and expedite convergence to a stable state when the system reaches equilibrium. This highlights the efficient utilization of energy stored in the DC-side capacitors. Figure 15 illustrates the corresponding supplemental power output.

The simulation results reveal the effectiveness and robustness of the proposed method in cases of agent loss. Although the communication capabilities of the agent may be interrupted due to malfunctions, the proposed method ensures the stable operation of the power system and successfully suppresses excessive voltage and frequency fluctuations. This also highlights the superiority and potential of the method when faced with system imbalances and uncertainties.

5.4 Performance analysis under non-ideal communication

In a communication system, latency encompasses various components, including system fault detection and trip time, transmission delay, and control total delay. These components can be quantified as follows: fault detection time is 3 ms, and the

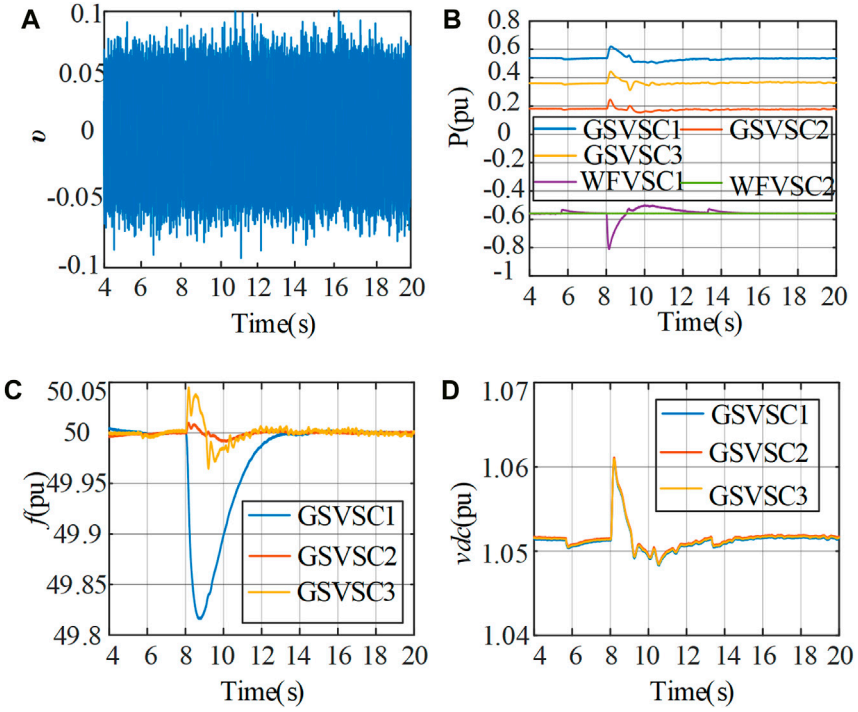

FIGURE 16
Dynamic performance under non-ideal communication: **(A)** communication noise, **(B)** active power, **(C)** output frequency, and **(D)** DC voltage.

average trip time is 6 ms. Transmission delay is directly proportional to the length of the communication line, represented as 2 times the line length divided by the speed of light. The control total delay, which encompasses network power flow calculations, is fixed at 10 ms. For instance, assuming a VSC interstation line length of 150 km, the resulting communication delay τ_{ij} is calculated as 20 ms. To assess the algorithm's effectiveness in the presence of communication delays, a total delay of τ_{ij} = 1,000 ms is designated within the MTDC for validation purposes. In a suboptimal communication setting, the reception of information from node j to node i can be described as follows:

$$x_{ij}(k) = x_j\left(k - \xi_{ij}(k)\right) + \mu_{ij}(k) \tag{34}$$

Where $\xi_{ij}(k)$ is the communication delay; $\mu_{ij}(k)$ is the channel noise using Gaussian noise simulation. Integrate (34) into the system's input signal to simulate the scenario of operating in a non-ideal communication environment.

Figure 16 provides a robustness assessment in a non-ideal communication network environment, specifically with ξ_{ij} = 1000 ms. Figure 16A visualizes μ_{ij}(k). As illuminated by Figures 16B–D, the proposed method sustains its performance effectively amidst substantial communication delays. These figures underscore that the system retains its stability notwithstanding the pronounced communication delays. By demanding less data transmission, the proposed method enhances the communication delay margin, demonstrating the robustness and resilience of this control strategy under non-ideal network conditions.

6 Conclusion

This paper has explored a VSC-MTDC voltage operation control strategy based on the VSG consensus MPC algorithm. Within the MTDC system, a challenge emerges during power regulation–the absence of inertial interaction support at the VSC station. To address this issue, this paper proposes a cooperative control strategy, incorporating MPC for VSG power increment acquisition, and employing a consensus algorithm to enhance inter-MTDC system inertia. After in-depth research and analysis, the main conclusions are as follows:

1) The proposed cooperative control strategy employs MPC to manage VSG power increments as an adjustment parameter for DC voltage control, effectively utilizing the DC-side capacitor voltage energy for power imbalance regulation. Importantly, this strategy demands minimal communication information for implementation.
2) Under the influence of supplementary power, the convergence rates of system DC voltage, active power, and output frequency have all been enhanced. Simultaneously, the adverse effects of SFD resulting from OWF frequency regulation have correspondingly decreased.
3) Simulation results demonstrate that, in comparison to the conventional DC voltage VSG control method, the cooperative control strategy presented in this study significantly mitigates frequency droop, improves power balance among different VSC stations, and maximizes the utilization of energy from DC-side capacitors. Notably, even in scenarios characterized by agent loss or non-ideal communication, the algorithm remains effective, showcasing notable attributes of high latency tolerance and robust convergence.

Data availability statement

The original contributions presented in the study are included in the article/supplementary material, further inquiries can be directed to the corresponding author.

Author contributions

HH: Conceptualization, Data curation, Investigation, Methodology, Writing–original draft. QuL: Conceptualization, Formal Analysis, Methodology, Resources, Writing–review and editing. QiL: Investigation, Software, Validation, Writing–review and editing.

Funding

The author(s) declare financial support was received for the research, authorship, and/or publication of this article. This research was funded by the Science and Technology Project of State Grid Corporation of China, grant number 5100-202118472A-0-5-ZN.

Conflict of interest

Authors HH, QuL, and QiL were employed by State Grid Jiangsu Electric Power Co., Ltd.

Publisher's note

References

Attya, A., and Hartkopf, T. (2013). Control and quantification of kinetic energy released by wind farms during power system frequency drops. *IET Renew. Power Gener.* 7 (3), 210–224. doi:10.1049/iet-rpg.2012.0163

Cao, Y., Wang, W.-Y., Li, Y., Tan, Y., Chen, C., He, L., et al. (2018). A virtual synchronous generator control strategy for VSC-MTDC systems. *IEEE Trans. Energy Convers.* 33 (2), 750–761. doi:10.1109/tec.2017.2780920

Fuchs, A., Imhof, M., Demiray, T., and Morari, M. (2014). Stabilization of large power systems using VSC-HVDC and model predictive control. *IEEE Trans. Power Del* 29 (1), 480–488. doi:10.1109/tpwrd.2013.2280467

Haidar, I., and Pepe, P. (2021). Lyapunov—Krasovskii characterizations of stability notions for switching retarded systems. *IEEE Trans. Autom. Control.* 66 (1), 437–443. doi:10.1109/tac.2020.2979754

Howlader, A.-M., Urasaki, N., and Saber, A.-Y. (2014). Control strategies for wind-farm-based smart grid system. *IEEE Trans. Ind. Appl.* 50 (5), 3591–3601. doi:10.1109/tia.2014.2304411

Huan, L.-B., Xin, H.-H., Yang, H., Wang, Z., and Xie, H. (2018). Interconnecting very weak AC systems by multiterminal VSC-HVDC links with a unified virtual synchronous control. *IEEE J. Emerg. Sel. Top. Power Electron.* 6 (3), 1041–1053. doi:10.1109/jestpe.2018.2825391

Huang, L.-B., Xin, H.-H., and Yang, H. (2017). A virtual synchronous control for voltage-source converters utilizing dynamics of DC-link capacitor to realize self-synchronization. *IEEE J. Emerg. Sel. Top. Power Electron.* 5 (4), 1565–1572. doi:10.1109/jestpe.2017.2740424

Kalcon, G.-O., Adam, G.-P., Anaya-Lara, O., Lo, S., and Uhlen, K. (2012). Small signal stability analysis of multi-terminal VSC-based DC transmission systems. *IEEE Trans. Power Syst.* 27 (4), 1818–1830. doi:10.1109/tpwrs.2012.2190531

Kang, M., Kim, K., Muljadi, E., Park, J., and Kang, Y.-C. (2016). Frequency control support of a doubly-fed induction generator based on the torque limit. *IEEE Trans. Power Syst.* 3 (6), 4575–4583. doi:10.1109/tpwrs.2015.2514240

Kirakosyan, A., Ameli, A., Tarek, H.-M., Fouly, E. L., Salama, M. M. A., and El-Saadany, E. F. (2023). A novel control technique for enhancing the operation of MTDC grids. *IEEE Trans. Power Syst.* 38 (1), 559–571. doi:10.1109/tpwrs.2022.3155692

Lee, G. S., Moon, S. I., and Kwon, D. H. (2021). DC current and voltage droop control method of hybrid HVDC systems for an offshore wind farm connection to enhance AC voltage stability. *IEEE Trans. Energy Convers.* 36 (1), 468–479. doi:10.1109/TEC.2020.3005777

Lee, J., Muljadi, E., Sørensen, P., and Kang, Y.-C. (2016). Releasable kinetic energy-based inertial control of a DFIG wind power plant. *IEEE Trans. Sustain. Energy.* 7 (1), 279–328. doi:10.1109/tste.2015.2493165

Leon, A.-E., and Mauricio, J.-M. (2023). Virtual synchronous generator for VSC-HVDC stations with DC voltage control. *IEEE Trans. Power Syst.* 38 (1), 728–738. doi:10.1109/tpwrs.2022.3164027

Li, C., Li, Y., Cao, Y., Zhu, H., Rehtanz, C., and Hager, U. (2018). Virtual synchronous generator control for damping DC-side resonance of VSCMTDC system. *IEEE J. Emerg. Sel. Top. Power Electron.* 6 (3), 1054–1064. doi:10.1109/jestpe.2018.2827361

Li, D., Zhu, Q., Lin, S., and Bian, X.-Y. (2017). A self-adaptive inertia and damping combination control of VSG to support frequency stability. *IEEE Trans. Energy Convers.* 32 (1), 397–398. doi:10.1109/tec.2016.2623982

Li, Q., Gao, D.-W., Zhang, H., Wu, Z., and Wang, F. (2019). Consensus-based distributed economic dispatch control method in power systems. *IEEE Trans. Smart Grid.* 10 (1), 941–954. doi:10.1109/tsg.2017.2756041

Liu, H., and Chen, Z. (2015). Contribution of VSC-HVDC to frequency regulation of power systems with offshore wind generation. *IEEE Trans. Energy Convers.* 30 (3), 918–926. doi:10.1109/tec.2015.2417130

Liu, Y., Wang, Y., Liu, H., Xiong, L., and Peng, Y. (2022b). An LVRT strategy with quantitative design of virtual impedance for VSG. *Int. J. Electr. Power Energy Sys.* 140, 107661. doi:10.1016/j.ijepes.2021.107661

Liu, Y., Wang, Y., Liu, X., Wang, M., Xu, Z., and Liu, H. (2023). Steady-state angle stability analysis of parallel grid-forming converters in current saturation mode. *IEEE Trans. Power Electron* 38 (7), 8039–8044. doi:10.1109/tpel.2023.3267624

Liu, Y., Wang, Y., Wang, M., Xu, Z., Peng, Y., and Li, M. (2022a). Coordinated VSG control of photovoltaic/battery system for Maximum power output and grid supporting. *IEEE J. Emerg. Sel. Top. Power Electron.* 12 (1), 301–309. doi:10.1109/JETCAS.2022.3143716

Maciejowski, J.-M. (2002). *Predictive control: with constraints*. London, U.K.: Pearson Education.

Mariethoz, S., Fuchs, A., and Morari, M. (2014). A VSC-HVDC decentralized model predictive control scheme for fast power tracking. *IEEE Trans. Power Del.* 29 (1), 462–471. doi:10.1109/tpwrd.2013.2265277

Namara, P.-Mc., Negenborn, R.-R., Schutter, B.-D., Lightbody, G., and McLoone, S. (2016). Distributed MPC for frequency regulation in multi-terminal HVDC grids. *Control Eng. Pract.* 46, 176–187. doi:10.1016/j.conengprac.2015.11.001

Rahman, M.-H., Xu, L., and Yao, L. (2016). Protection of large partitioned MTDC networks using dc-dc converters and circuit breakers. *Prot. Control Mod. Power Syst.* 1 (2), 19–9. doi:10.1186/s41601-016-0030-0

Shuai, Z.-K., Shen, C., Liu, X., Li, Z., and Shen, Z. J. (2019). Transient angle stability of virtual synchronous generators using lyapunov's direct method. *IEEE Trans. Smart Grid.* 10 (4), 4648–4661. doi:10.1109/tsg.2018.2866122

Ullah, N.-R., Thiringer, T., and Karlsson, D. (2008). Temporary primary frequency control support by variable speed wind turbines—potentialand applications. *IEEE Trans. Power Syst.* 23 (2), 601–612. doi:10.1109/tpwrs.2008.920076

Wang, S., and Tomsovic, K. (2019). Fast frequency support from wind turbine generators with auxiliary dynamic demand control. *IEEE Trans. Power Syst.* 34 (5), 3340–3348. doi:10.1109/tpwrs.2019.2911232

Wang, W.-Y., Jiang, L., Cao, Y.-J., and Li, Y. (2020). A parameter alternating VSG controller of VSC-MTDC systems for low frequency oscillation damping. *IEEE Trans. Power Syst.* 35 (6), 4609–4621. doi:10.1109/tpwrs.2020.2997859

Wang, W.-Y., Li, Y., Cao, Y.-J., Häger, U., and Rehtanz, C. (2018). Adaptive droop control of VSC-MTDC system for frequency support and power sharing. *IEEE Trans. Power Syst.* 33 (2), 1264–1274. doi:10.1109/tpwrs.2017.2719002

Wu, W.-H., Chen, Y.-D., Luo, A., Zhou, L., Zhou, X., Yang, L., et al. (2017a). A virtual inertia control strategy for DC microgrids analogized with virtual synchronous machines. *IEEE Trans. Ind. Electron.* 64 (7), 6005–6016. doi:10.1109/tie.2016.2645898

Wu, Z.-P., Gao, D.-W., Zhang, H., Yan, S., and Wang, X. (2017b). Coordinated control strategy of battery energy storage system and PMSG-WTG to enhance system frequency regulation capability. *IEEE Trans. Sustain. Energy.* 8 (3), 1330–1343. doi:10.1109/tste.2017.2679716

Xu, L., Yao, L., and Sasse, C. (2007). Grid integration of large DFIG-based wind farms using VSC transmission. *IEEE Trans. Power Syst.* 20 (3), 976–984. doi:10.1109/tpwrs.2007.901306

Yang, D., Wang, X., Chen, W., Jin, Z., and Jin, E. (2023). Adaptive frequency droop feedback control-based power tracking operation of a DFIG for temporary frequency regulation. *IEEE Trans. Power Syst. Early access* 2023, 1–10. doi:10.1109/TPWRS.2023.3277009

Yazdani, A., and Iravani, R. (2010). *Voltage-sourced converters in power systems: modeling, control and applications*. New York, NY, USA: Wiley.

Zhong, Q.-C., and Weiss, G. (2011). Synchronverters: inverters that mimic synchronous generators. *IEEE Trans. Ind. Electron.* 58 (4), 1259–1267. doi:10.1109/tie.2010.2048839

Zhu, J.-B., Guerrero, J.-M., Hung, W., Booth, C. D., and Adam, G. P. (2014). Generic inertia emulation controller for multi-terminal voltage-source-converter high voltage direct current systems. *IET Renew. Power Gener.* 8 (7), 740–748. doi:10.1049/iet-rpg.2014.0109

Zhu, J.-B., Shen, Z., Bu, S., Li, X., Booth, C. D., Qiu, W., et al. (2021). Coordinated flexible damping mechanism with inertia emulation capability for MMC-MTDC transmission systems. *IEEE J. Emerg. Sel. Top. Power Electron.* 9 (6), 7329–7342. doi:10.1109/JESTPE.2020.3025690

frontiers | Frontiers in Energy Research

TYPE Original Research
PUBLISHED 27 March 2024
DOI 10.3389/fenrg.2024.1374467

OPEN ACCESS

EDITED BY
Liansong Xiong,
Xi'an Jiaotong University, China

REVIEWED BY
Shun Sang,
Nantong University, China
Ning Li,
Xi'an University of Technology, China
Yujun Li,
Xi'an Jiaotong University, China

*CORRESPONDENCE
Bai Zhang,
zhangbai19810321@163.com

RECEIVED 22 January 2024
ACCEPTED 13 March 2024
PUBLISHED 27 March 2024

CITATION
Hu T, Zhang B, Liu P and Chang X (2024), Modeling and analysis of distribution network with photovoltaic cells based on Markov global sensitivity.
Front. Energy Res. 12:1374467.
doi: 10.3389/fenrg.2024.1374467

Modeling and analysis of distribution network with photovoltaic cells based on Markov global sensitivity

Tingting Hu[1], Bai Zhang[2]*, Pengyuan Liu[1] and Xingzhi Chang[3]

[1]State Grid Ningxia Electric Power Company Marketing Service Center, Yinchuan, China, [2]School of Electrical and Information Engineering, North Minzu University, Yinchuan, China, [3]Ningxia Longji Ningguang Instrument Co., Ltd., Yinchuan, China

When multiple distributed PV (photovoltaic) systems are integrated into multiple nodes of the distribution network, this will lead to the significant influence of the grid-tied node voltage of the power distribution network resulting from the uncertainty of PV power. Therefore, this aspect needs to be further studied in terms of how to effectively characterize the uncertainty of the voltage influence in a grid-tied multi-PV system distribution network. Focusing on this problem, a modeling and analysis method for distribution networks with PV cells based on Markov global sensitivity is proposed in this paper. Firstly, a global Markov chain is constructed using the Markov chain and the power flow equation to model the uncertainty of PV power. Furthermore, a Markov global sensitivity function is proposed to characterize the influence degree of the voltage on the distribution network nodes while multi-point PV system are grid-tied to system. The case study results show that the uncertainty model of multi-point PV grid-connection can be effectively constructed using the proposed method in this paper, and the uncertainty influence analysis is accurate. This is of great significance for grid connection planning and the optimization control of new energy systems, as well as for the new energy consumption increase.

KEYWORDS

distributed PV, grid connection, Markov chain, sensitivity, uncertainty

1 Introduction

With the development of society, the demand for energy is increasing. Currently, the development of new energy is a dependable way to improve energy supply sustainability. Within new energy developments (Pan al., 2019; Tang et al., 2021; Liang et al., 2023), the PV system is attracting more and more attention.

A small or medium-sized PV cell constructed near load usually called distributed PV system, which is one of the main research directions. The distributed PV system is generally directly connected into the multiple nodes of low-voltage distribution networks.

In this grid-tied mode, on the one hand, the PV power is mostly used by the load of the distribution network, which improves the absorption rate of new energy (Li et al., 2023; Xuan et al., 2020; Reshikeshan et al., 2021; Xing and Mu, 2023); on the other hand, the multi-point integration into the distribution network mode will cause the changing of the node voltage of the distribution network. Further, the PV power is volatile and intermittent, resulting from climate factors, and the large and fluctuant PV power may result in an uncertain power flow and power quality problems in the distribution network, especially at

the end of the low-voltage distribution network, which will cause power scheduling difficulties. In addition, the distribution network generally connects the load, which is also uncertain. Therefore, power uncertainty arises in the source side and the load side at the same time, which causes the stability to be challenged in lower voltage distribution networks (Jafari et al., 2022; Liu et al., 2022).

Therefore, the study on the PV power uncertainty is of great significance for distribution networks, in terms of the planning and construction of power systems, the consumption and improvement of new energy, etc.

In traditional research, PV power prediction and load power prediction are attracting more attention and lots of prediction methods have been proposed, which are useful for reducing the power uncertainty of PV cells and the load (Wang et al., 2022; Goh et al., 2023; Zhang et al., 2023; Zhou et al., 2023). Further, the PV power prediction results can be used to analyze its influence on a distribution network connected to PV cells.

In relevant research on the power uncertainty of PV cells connected to power systems, the output power uncertainty probability model of PV or other DG (distributed generation) systems can be modeled (Constante-Flores and Illindala, 2019; Palahalli et al., 2021; Rayati et al., 2022; Reddy et al., 2023), and then the power uncertainty probability model can be used for power flow calculations or power planning calculations. In (Constante-Flores and Illindala, 2019), a non-Gaussian model of DG is developed, namely, its output power uncertainty is represented in the form of a probability. Further, the PV power probability model and the control strategy can be combined together to optimize the control of the system power (Rayati et al., 2022).

On the network side, a probabilistic model of the distribution network's voltage can be established and used. The power flow calculation is probabilistic and the optimal control of the reactive power and voltage can be achieved (Baptista et al., 2019; Chu et al., 2022). Further, focusing on the power uncertainty of DG systems, an ESS (energy storage system) can also be used to restrain the power uncertainty to achieve the optimal control of the system power (Hong and Wu, 2019).

In a distribution network, the power flow uncertainty caused by the uncertainty of PV power that can be analyzed from the perspective of control and scheduling; for example, economic optimal scheduling can be achieved based on deterministic mixed integer linear programming (L. Meng et al., 2022). And machine learning can also be used to estimate the power flow (A. Demazy et al., 2020). From the perspective of system scheduling, by coordinating the PV power and load, the optimal power flow of the system can be obtained (Widén et al., 2017; Hu et al., 2021).

However, while a large number of PV systems are connected into distribution networks, these DG systems are multi-coupled with distribution networks and loads; each node voltage of the distribution network is related to all the grid-tied PV. This means there is global uncertainty displayed between the photovoltaic and the distribution network, and this uncertainty is enhanced with the increase of PV connected to the network.

In traditional studies, global uncertainty modeling for PV systems and the impact analysis for distribution networks need to be studied further. Therefore, how to develop global uncertainty modeling for PV systems, and how to comprehensively represent the degree of influence on the distribution network tied in with multiple PV cells in a multi-node manner is the key content of this paper. Focusing on the above problems, a modeling and analysis method for a distribution network with multi-PVs based on the Markov global sensitivity for a multi-photovoltaic grid-tied network is proposed, in which a global Markov sensitivity function is established to be associated with the grid-tied PV and the distribution network, to accurately characterize the influence of the distribution network resulting from the PV power uncertainty.

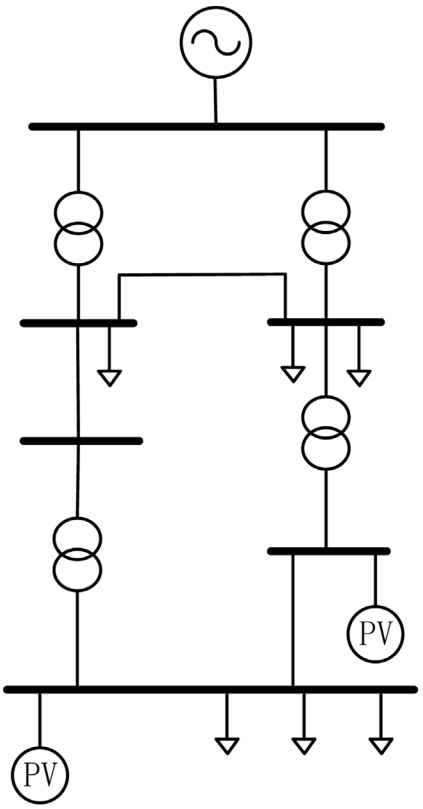

FIGURE 1
Diagram of a distribution network.

This paper is organized as follows. In Section 2, the uncertainty analysis of PV connected into distribution network is carried out. In Section 3, the model based on global Markov sensitivity for multiple grid-tied PV cells is proposed. In Section 4, the case study is developed. Section 5 gives the conclusion of this paper.

2 Uncertainty analysis of PV connected into distribution network

2.1 Principle of distributed multi-node PV grid-tied network

Shown in Figure 1 is a diagram of a distribution network.

As shown in the Figure 1, the network contains multiple buses and nodes. The PV cells and loads are connected into the distribution network in different nodes. The output power of the

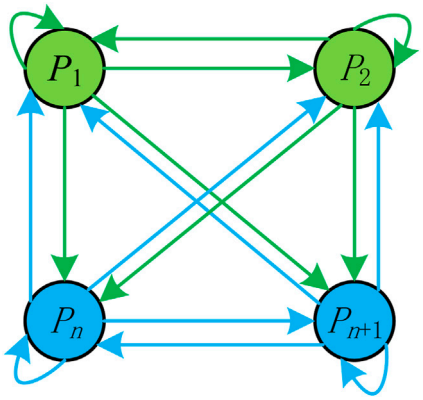

FIGURE 2
Diagram of the state transfer of power sequence.

PV is affected by a variety of climate factors, as shown below (Wang and Yang, 2017):

$$U_{OC} = \frac{A_0 KT}{q} \ln\left(\frac{I_{sc}}{I_{DO}} + 1\right) \tag{1}$$

where A_0 is a constant; μ is the Boltzmann constant; q is the electronic charge; I_{SC} is the short circuit current varied with irradiation intensity; I_{DO} is the equivalent saturation current of the diode; T is the environment temperature.

It can be seen from the above formula that the climate factors are the main factors to result in the strong uncertainty of PV power.

The PV system can be equivalent to a PQ node if the PV system is connected into a power system. With the fluctuation of grid-connected power, the power quality problem may be generated, such as voltage fluctuations, flicker, and other problems.

2.2 Principle of uncertainty modeling for grid-tied PV

Uncertainty modeling is helpful to quantitatively understand the uncertainty of PV power. In this paper, a Markov chain is used to model the power state of PV cells.

The Markov chain is one of the typical algorithms used to describe the uncertainty of a random variable process, in which the present state can be used to describe the future state of the variable; the state of the variable at different times can present the variable development uncertainty. For a discrete power sequence $\{p_1, p_2 \ldots \ldots p_t, p_{t+1}\}$, the state in t+1 can be described by the following probabilities (He, 2008; Tabone and Callaway, 2015; Zhang et al., 2021):

$$\begin{aligned} &P\left[x_{t+1} = p_{t+1} \middle| x_t = p_t, x_{t-1} = p_{t-1}, \cdots x_1 = p_1\right] \\ &= P\left[x_{t+1} = p_{t+1} \middle| x_t = p_t\right] \end{aligned} \tag{2}$$

where p is the probability of each state.

Figure 2 shows the process transfer between various random states:

As can be seen from Figure 2, each power state can be transferred to its own initial state or other states, and the transition uncertainty can be described by the transition probability. All the state transition processes can be represented as a state transition matrix:

$$A = \begin{bmatrix} A_{11} & A_{12} & \cdots & A_{1n} \\ A_{21} & A_{22} & \cdots & A_{2m} \\ \vdots & \vdots & \ddots & \vdots \\ A_{m1} & A_{m2} & \cdots & A_{mn} \end{bmatrix} \tag{3}$$

where A_{mn} is the transition probability. Namely, in the state transition matrix, each element corresponds to the transition probability of a variable state.

When modeling the power uncertainty of a PV cell, the historic data of the PV cell's power are classified first to obtain different states. And then, the transfer probability matrix of the Markov chain is trained to obtain the uncertain Markov chain model for the target PV system.

However, in the case where multiple PV systems are connected into the distribution network in different nodes, the impact on the network from the PV cells is global and comprehensive, in other words, the node voltage of the distribution network is affected by all the grid-connected PV cells, to present the mutual coupling, which increases the difficulty of the relational analysis.

Therefore, how to intuitively and accurately characterize the effect caused by the grid-connected PV is one of the key aspects addressed in this paper.

3 Proposed model and analysis based on global Markov sensitivity for multiple grid-tied PV cells

Focusing on the mutual coupling of the node voltage and the multiple grid-tied PV, an uncertainty modeling and analysis method based on the Markov global sensitivity is proposed, in which the Markov chain is used to describe the uncertainty of PV power firstly, and then the Markov chain is combined with the node voltage distributed, to present the uncertainty between the PV power and the node voltage. Further, a sensitivity function is developed to quantitatively characterize the effect of the node voltage resulting from the multiple grid-tied PV cells.

3.1 Modeling of node voltage of distribution network

The power flow of a traditional distribution network is in the form of a feeder line; the voltage of node i is related to the power and the line impedance, as in the following (Demazy et al., 2020; Wan, 2022; Yang et al., 2023):

$$U_i \approx U_{i-1} - \frac{PR - QX}{U_i} \tag{4}$$

where P is the active power; Q is the reactive power; R and X are the equivalent line impedance of the node i-1 and node i, respectively.

In traditional distribution networks, most of time, the load R_L is connected into a node. However, with the development of new energy, more and more DGs are connected into distribution networks. The connected node is usually called PCC (point of

common coupling). The modeling for the PCC voltage can be shown as the following:

$$U_{PCC} = U_{i-1} - \frac{(P_{PV} - P_L)R - (Q_{PV} - Q_C)X}{U_{PCC}} \tag{5}$$

where P_{PV} and Q_{PV} are the active power and reactive power of the PV system into the PCC, respectively; Q_C is the reactive power of the local compensation.

It is assumed that the reactive power demand in PV systems and the load can be compensated completely by the local compensation device. Thus, the above formula can be simplified as the following:

$$U_{PCC} = U_{i-1} - \frac{(P_{PV} - P_L)R_{(i-1)PCC} - QX_{(i-1)PCC}}{U_{PCC}} \tag{6}$$

where Q is the reactive power flow in the bus.

For the next node i+1, its active power can be obtained as the following:

$$P_{PCC(i+1)} = p_{(i-1)PCC} - P_{LPCC} + P_{PVPCC} \tag{7}$$

The above discussion is about a distribution network connected a single PV. In cases where multiple PVs are connected into the distribution network, the modeling for node voltage is as follows:

$$U_1 = U_N - U_{e01} = U_N - \frac{P_{01}R_{01} - Q_{01}X_{01}}{U_1} \tag{8}$$

where P_{01} and Q_{01} are the active power and reactive power of the initial node and its successive node, respectively; R_{01} and X_{01} are the equivalent line impedance between the initial node and its successive node, respectively.

Similarly, the voltage of node two and node three of the system is as follows:

$$\begin{aligned} U_2 &= U_1 - U_{e12} = U_1 - \frac{P_{12}R_{12} - Q_{12}X_{12}}{U_2} \\ &= U_N - \frac{P_{01}R_{01} - Q_{01}X_{01}}{U_1} - \frac{P_{12}R_{12} - Q_{12}X_{12}}{U_2} \end{aligned} \tag{9}$$

$$U_3 = U_2 - U_{e23} = U_2 - \frac{P_{23}R_{23} - Q_{23}X_{23}}{U_3} = U_N - U_{e01} - U_{e12} - U_{e23} \tag{10}$$

And then, the voltage of node j can be obtained as the following:

$$U_j = U_N - \sum U_{eij} = U_N - \frac{P_{ij}R_{ij} - Q_{ij}X_{ij}}{U_j} \tag{11}$$

If there are multiple PV cells connected into the node of a distribution network, the power between the node i and node j is as follows:

$$P_{ij} = p_{(i-1)i} - P_{Li} + P_{PVi} = P_{01} - \sum P_{Li} + \sum P_{PVi} \tag{12}$$

$$Q_{ij} = Q_{(i-1)i} - (Q_{Li} - Q_{PVi} - Q_{Ci}) \tag{13}$$

where $P_{(i-1)i}$ is the active power; $Q_{(i-1)i}$ is the reactive power; P_{Li}, Q_{Li}, and Q_{Ci} are the real power, reactive power, and the compensation reactive power of node i, respectively. P_{PVi} is the real power of the PV cells in node i. Assuming that the reactive power of the node can be compensated completely and locally, the above, Formula (13), can be simplified as follows:

$$Q_{ij} \approx Q_{01} \tag{14}$$

Taking Formula (14) and Formula (12) into Formula (11), the voltage model for node j is as follows:

$$U_j = U_N - \sum \frac{(P_{01} - \sum P_{Li} + \sum P_{PVi})R_{ij} - Q_{01}X_{ij}}{U_j} \tag{15}$$

3.2 Modeling for multiple grid-tied PV based on Markov chain

As mentioned above, the output power of a PV can be seen as a discrete process. Therefore, the Markov chain can be used to describe the uncertainty in power transition. For the PV system in node i of a network, the PV power can be presented as a time series:

$$P_{PVj} = [P^0_{PV}, P^1_{PV}, P^2_{PV}, \cdots, P^n_{PV}] \tag{16}$$

where n is the time number; P_{PVj} is the output power in each time.

The output power P_{PVj} can be converted to the power state as follows:

$$M_{PVj} = \left[M^0_{PV}, M^1_{PV}, M^2_{PV}, \cdots, M^k_{PV}\right] \tag{17}$$

where k is the number of state; M_{PVj} is the power state.

In this case, a T function can be defined to achieve the conversion between the PV power and the power state:

$$\left[M^k_{PVj}\right] = T\left[P^{n-1}_{PVj}\right] \tag{18}$$

As mentioned above, the state transition processes of the PV power state can be represented as a state transition matrix $\boldsymbol{A}$ in Formula (3). Therefore, the PV power state conversion can be presented as follows:

$$\left[M^r_{PVj}\right] = \left[M^k_{PVj}\right]A \tag{19}$$

And the PV power in the nth time can be obtained by the inverse transformation, as follows:

$$\left[P^n_{PVj}\right] = T^{-1}\left[M^r_{PVj}\right] + \sigma \tag{20}$$

where σ is the correction factor. In the above process, the power error may be appear, therefore this correction factor is used to correct the PV power. While the Markov chain is constructed for a PV system, the transition error distribution can be extracted and it is used to generate the correction factor, namely, the correction factor can be obtained using the historical error statistics.

As can be seen from the above formulas, the Markov chain is used to describe the PV power uncertainty transfer process; the power uncertainty is represented as a probability function.

Taking Formula (20) into Formula (15), the voltage of node j can be obtained as follows:

$$U_j = U_N - \sum U_{eij} \tag{21}$$

The voltage error is as follows:

$$U_{eij} = \sum \frac{\left(P_{01} - \sum P_{Li} + \sum (T^{-1}((T\left[P^{n-1}_{PVj}\right])A) + \sigma))R_{ij} - Q_{01}X_{ij}}{U_j} \tag{22}$$

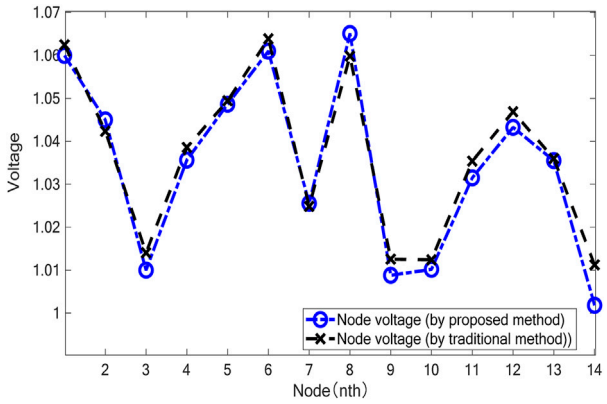

FIGURE 3
Voltage distribution.

As can be seen from the above formulas, the PV power uncertainty is represented by the Markov chain, and then, Formula (22) shows the global voltage effect of the distribution network resulting from the PV power uncertainty.

Generally, In this paper, the Markov chain is used to present the uncertainty of PV power, in which the PV power in time t+1 can be obtained by the PV power in time t. Furthermore, the Markov model is combined with the above mentioned voltage model of distribution network, to describe influence of the voltage on the distribution network nodes resulted from the uncertainty of PV power.

3.3 Development of Markov global sensitivity function

A sensitivity function is usually used to describe the relationship among the variables quantificationally, as in the following (Xiong et al., 2021; Zhou and Zhang, 2021):

$$S = \frac{dy}{dx} \tag{23}$$

where y is dependent variable; x is the independent variable.

In this paper, in order to describe the relationship between the node voltage and the grid-tied PV power, the sensitivity function is developed as follows:

$$S^{U_e}_{eP_{PVj}} = \frac{\partial U_{eij}}{\partial P_{PVj}} = \frac{\partial \sum \frac{\left(P_{01} - \sum P_{Li} + \sum (T^{-1}((T\left[P^{n-1}_{PVj}\right])A) + \sigma))R_{ij} - Q_{01}X_{ij}}{U_j}}{\partial P_{PVj}} \tag{24}$$

The above function is called the Markov global sensitivity, in which the power uncertainty of all the PV systems in a distribution network can be represented by the Markov chain.

As seen from the above mentioned, the proposed model is combined with the Markov chain, the voltage model of distribution network, and the sensitively function. By using the proposed model, the influence of the distribution network resulting from the PV power uncertainty can be characterized.

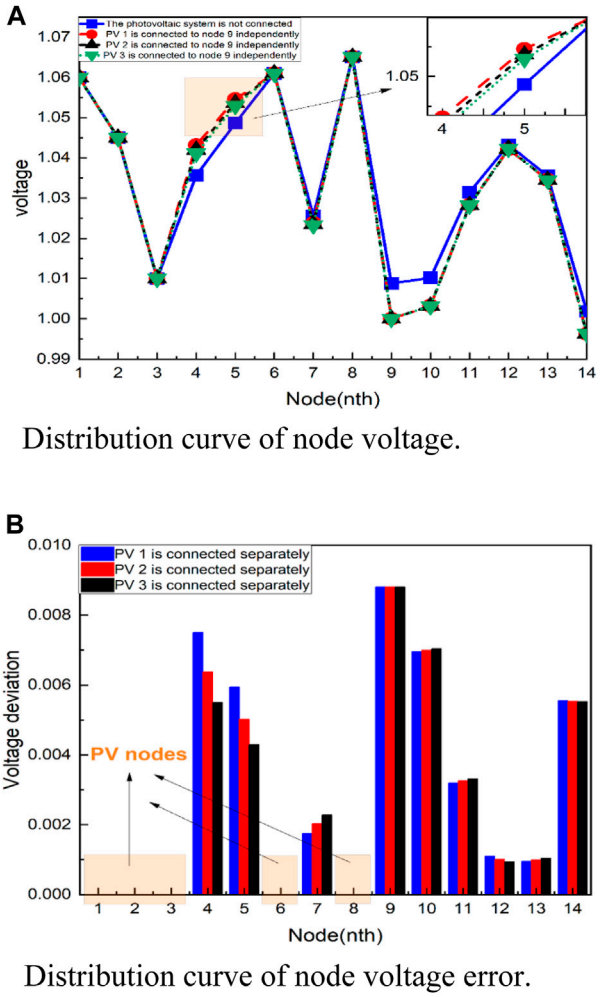

FIGURE 4
Voltage distribution for PV cell connected to a single node in distribution network. **(A)** Distribution curve of node voltage. **(B)** Distribution curve of node voltage error.

4 Example verification

In order to verify the effectiveness of the proposed modeling method, an example is developed based on the IEEE 14-node model, in which three PV systems are grid-tied into the system, as 3 MW, 5 MW, and 10 MW. Several test cases are carried out as follows.

4.1 Testing between the proposed method and the traditional method

In order to test the feasibility of the proposed method, the voltage distribution of network is calculated by the proposed method and the traditional method, as shown in Figure 3.

It can be seen that the voltage distribution is basically consistent by using the proposed method and the traditional method, this verify the feasibility of the proposed method. Further, comparing with the traditional method, the proposed method combines the uncertainly analysis and the sensitivity analysis in the following test expediently.

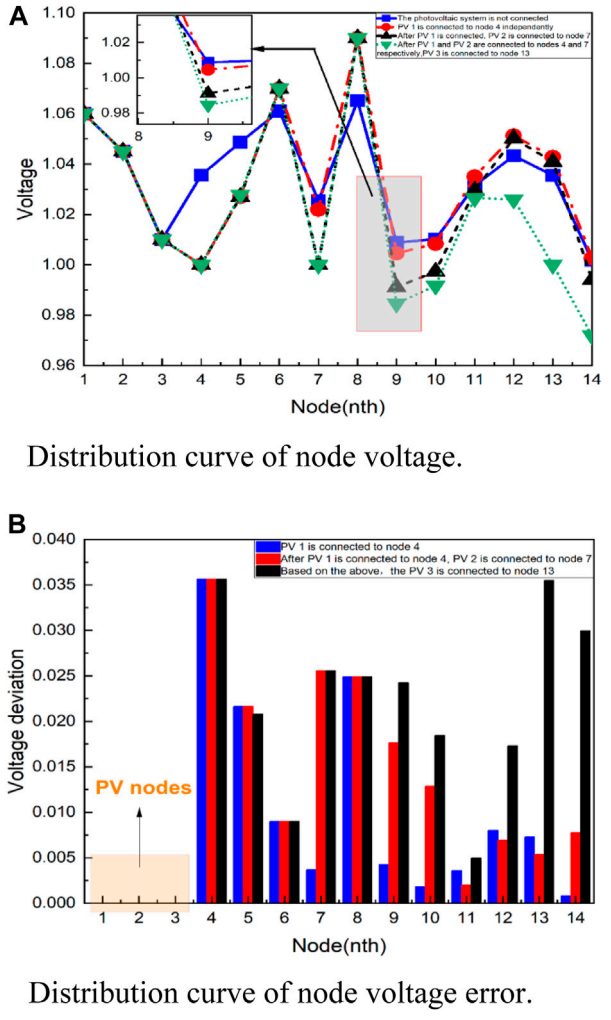

FIGURE 5
Voltage distribution for PV cells connected to multiple nodes in distribution network.

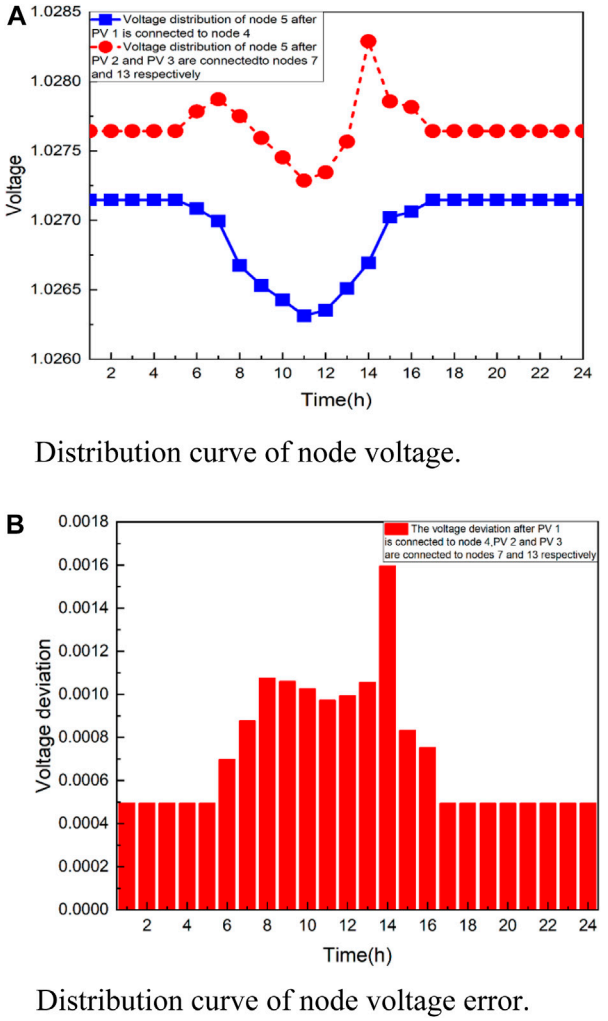

FIGURE 6
Voltage distribution of fifth node while PV cells are connected to multiple nodes in the distribution network.

4.2 Test case with single PV is grid-tied to the distribution network

The PV systems are connected into node nine of the distribution network. In this case, the power flow of the network will change, resulting in changing of the voltage distribution of the nodes; the voltage distribution and the voltage deviation are shown in Figure 4.

It can be seen that the effect on the voltage is finite because the capacity of a single PV system is not large compared with the distribution network. It can be seen that though the voltage of the grid-tied node is mainly affected, the voltage of the other nodes are also effected by a grid-tied PV system.

4.3 Test case with multiple PV are grid-tied to the distribution network

In this case, the three PVs are connected into the distribution network in node 4, node 7, and node 13, respectively. The voltage distribution of the nodes and the voltage deviation is shown in Figure 5.

It can be seen that, in terms of the connection of the PV system, the power flow of system is changed, leading the voltage distribution changing. And the effect of the node voltage is increasing, especially for the nodes which are grid-tied in the PV system.

From the sensitivity analysis of the node voltage, it can be seen that the node voltage will be affected by the all grid-tied PV system; the degree of influence can be estimated by the proposed Markov global sensitivity in this paper. For example, the voltage of node five is effected by the grid-tied PV cells, though it is not a node that is connected to a PV.

In order to analyze the voltage of node 5, in the experiment, the grid-tied node of the PV cell is changed to observe the voltage change, as shown in Figure 6.

As can be seen from the figures, the voltage distributed of node is different as the PV system are connected into the system. The changing trend of the node voltage is different, which can be described by the voltage sensitivity by using the proposed Markov global sensitivity, as shown in Figure 7 from the sensitivity analysis, it can be seen that the node voltage will

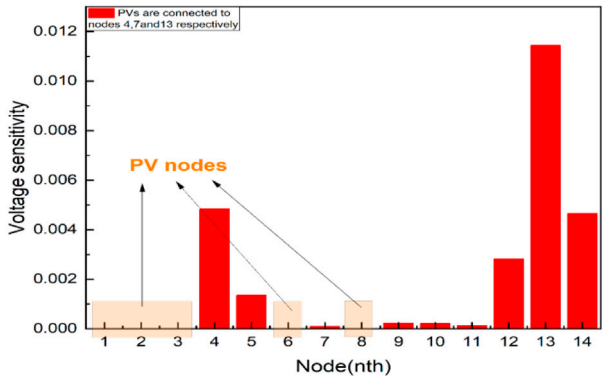

FIGURE 7
Voltage sensitivity analysis distribution network.

effected by all the grid-tied PV cells, and the degree of influence is different.

5 Conclusion

A modeling and analysis method for a distribution network with PV cells based on Markov global sensitivity is proposed in this paper. Comparing with the traditional method, the Markov chain and voltage modeling of the distribution network are combined to obtain the Markov global sensitivity function to describe the degree of the influence of the node voltage resulting from the grid-tied PV cells. The example has verified the effectiveness and plausibility of the proposed method. And the example results show that the node voltage is effected by all the grid-tied PV cells, and the degree of influence is different, due to the different grid-tied nodes. The analysis results can be used in the design and planning of distribution networks, the grid-tied node evaluation of PV cells, and the optimization control of distribution networks. The modeling method can be used to developed corresponding model for meshed network in the future work.

Data availability statement

The raw data supporting the conclusion of this article will be made available by the authors, without undue reservation.

Author contributions

TH: Data curation, Investigation, Methodology, Validation, Writing–original draft, Writing–review and editing. BZ: Data curation, Formal Analysis, Software, Validation, Writing–review and editing, Writing–original draft. PL: Software, Validation, Writing–review and editing. XC: Data curation, Writing–review and editing.

Funding

The author(s) declare financial support was received for the research, authorship, and/or publication of this article. This research is funded by 2022 Innovation and Efficiency Projects: Research and Application of Low Voltage Distributed Photovoltaic Data Interaction Technology, grant number (JG29YX220038).

Conflict of interest

Authors TH and PL were employed by State Grid Ningxia Electric Power Company Marketing Service Center. Author XC was employed by Ningxia Longji Ningguang Instrument Co., Ltd.

The remaining author declares that the research was conducted in the absence of any commercial or financial relationships that could be construed as a potential conflict of interest.

Publisher's note

All claims expressed in this article are solely those of the authors and do not necessarily represent those of their affiliated organizations, or those of the publisher, the editors and the reviewers. Any product that may be evaluated in this article, or claim that may be made by its manufacturer, is not guaranteed or endorsed by the publisher.

Supplementary material

The Supplementary Material for this article can be found online at: https://www.frontiersin.org/articles/10.3389/fenrg.2024.1374467/full#supplementary-material

References

Baptista, J. E. R., Rodrigues, A. B., and da Guia da Silv, M. (2019). Probabilistic analysis of PV generation impacts on voltage sags in LV distribution networks considering failure rates dependent on feeder loading. *IEEE Trans. Sustain. Energy* 10 (3), 1342–1350. doi:10.1109/TSTE.2018.2866931

Chu, Zh., Sun, J., Zhao, L., and Sun, X. (2022). Optimal configuration of distributed power generation in active distribution network considering the characteristics of wind power and load time series. *Electr. Power Constr.* 43 (11), 53–62. (in Chinese). doi:10.12204/j.issn.1000-7229.2022.11.006

Constante-Flores, G. E., and Illindala, M. S. (2019). Data-driven probabilistic power flow analysis for a distribution system with renewable energy sources using Monte Carlo simulation. *IEEE Trans. Indus. App.* 55 (1), 174–181. doi:10.1109/TIA.2018.2867332

Demazy, A., Alpcan, T., and Mareels, I. (2020). A probabilistic reverse power flows scenario analysis framework. *IEEE Open Access J. Power Energy* 7, 524–532. doi:10.1109/OAJPE.2020.3032902

Goh, H. H., Luo, Q., Zhang, D., Liu, H., Dai, W., Lim, C. S., et al. (2023). Hybrid SDS and WPT-IBBO-DNM based model for ultra-short term photovoltaic prediction. *CSEE J. Power Energy Syst.* 9 (1), 66–76. doi:10.17775/CSEEJPES.2021.04560

He, S. (2008). *Stochastic process*. Beijing University Press. (in Chinese).

Hong, Y.-Y., and Wu, M.-Y. (2019). Markov model-based energy storage system planning in power systems. *IEEE Syst. J.* 13 (4), 4313–4323. doi:10.1109/JSYST.2019.2900081

Hu, W., Hu, X., Wang, M., Zeng, S., Yang, Z., and Yi, H. (2021). Research on distributed photovoltaic multi-mode coordinated control algorithm for distribution

network overvoltage suppression. *Adv. Tech. Electr. Eng. Energy* 40 (9), 18–28. (in Chinese). doi:10.12067/ATEEE2103033

Jafari, M. R., Parniani, M., and Ravanji, M. H. (2022). Decentralized control of OLTC and PV inverters for voltage regulation in radial distribution networks with high PV penetration. *IEEE Trans. Power Del* 37 (6), 4827–4837. doi:10.1109/TPWRD.2022.3160375

Li, Z., Cheng, Z., Si, J., and Xu, S. (2023). Distributed event-triggered hierarchical control of PV inverters to provide multi-time scale frequency response for AC microgrid. *IEEE Trans. Power Syst.* 38 (2), 1529–1542. doi:10.1109/TPWRS.2022.3177593

Liang, W., Liu, Y., and Shen, Y. (2023). Active power control integrated with reactive power compensation of battery energy stored quasi-Z source inverter PV power system operating in VSG mode. *IEEE J. Emerg. Sel. Top. Power Electron* 11, 339–350. doi:10.1109/JESTPE.2021.3137397

Liu, Y., Wang, Y., Wang, M., Xu, Z., Peng, Y., and Li, M. (2022). Coordinated VSG control of photovoltaic/battery system for maximum power output and grid supporting. *IEEE J. Em. Sel. Top. C* 12 (1), 301–309. doi:10.1109/JETCAS.2022.3143716

Meng, L., Yang, X., and Zhao, Z. (2022). An economic optimal dispatch strategy for active distribution networksconsidering photovoltaic-load uncertainty and rotating reserve constraints. *Electr. Power Constr.* 43 (11), 63–72. (in Chinese). doi:10.12204/j.issn.1000-7229.2022.11.007

Palahalli, H., Maffezzoni, P., and Gruosso, G. (2021). Gaussian copula methodology to model photovoltaic generation uncertainty correlation in power distribution networks. *Energies* 14, 2349. doi:10.3390/en14092349

Pan, Y., Chen, L., Lu, X., Wang, J., Liu, F., and Mei, S. (2019). Stability region of droop-controlled distributed generation in autonomous microgrids. *IEEE Tran. Smart Grid* 10 (2), 2288–2300. doi:10.1109/TSG.2018.2849084

Rayati, M., Bozorg, M., Cherkaoui, R., and Carpita, M. C. (2022). Distributionally robust chance constrained optimization for providing flexibility in an active distribution network. *IEEE Trans. Smart Grid* 13 (4), 2920–2934. doi:10.1109/TSG.2022.3154023

Reddy, Y., Jithendranath, J., Chakraborty, A. K., and Guerrero, J. M. (2023). Stability constrained optimal operation of standalone DC microgrids considering load and solar PV uncertainties. *IEEE Trans. Power Del.* 38 (4), 2673–2681. doi:10.1109/TPWRD.2023.3253623

Reshikeshan, S. S. M., Matthiesen, S. L., Illindala, M. S., Renjit, A. A., and Roychowdhury, R. (2021). Autonomous voltage regulation by distributed PV inverters with minimal inter-node interference. *IEEE Trans. Indus. App.* 57 (3), 2058–2066. doi:10.1109/TIA.2021.3064911

Tabone, M. D., and Callaway, D. S. (2015). Modeling variability and uncertainty of photovoltaic generation: a hidden state spatial statistical approach. *IEEE Trans. Power Syst.* 30 (6), 2965–2973. doi:10.1109/TPWRS.2014.2372751

Tang, C.-Y., Chen, P.-T., and Jheng, J.-H. (2021). Bidirectional power flow control and hybrid charging strategies for three-phase PV power and energy storage systems. *IEEE Trans. Power Electron* 36 (11), 12710–12720. doi:10.1109/TPEL.2021.3083366

Wan, J. (2022). *Research on the influence of photovoltaic grid connection on voltage quality of distribution network*. Shaanxi university of technology. (in Chinese).

Wang, F., Li, J., Zhao, Z., Wang, C., Ren, H., Ma, H., et al. (2022). Cloud feature extraction and fluctuation pattern recognition based ultrashort-term regional PV power forecasting. *IEEE Trans. Indus. App.* 58 (5), 6752–6767. doi:10.1109/TIA.2022.3186662

Wang, M., and Yang, S. (2017). *New energy generation and grid-connected technology*. China Electric Power Press. (in Chinese).

Widén, J., Shepero, M., and Munkhammar, J. (2017). Probabilistic load flow for power grids with high PV penetrations using copula-based modeling of spatially correlated solar irradiance. *IEEE J. Photovolt.* 7 (6), 1740–1745. doi:10.1109/JPHOTOV.2017.2749004

Xing, J., and Mu, L. (2023). A novel islanding detection method for distributed PV system based on μPMUs. *IEEE Trans. Smart Grid* 14 (5), 3696–3706. doi:10.1109/TSG.2023.3236790

Xiong, Z., Chen, T., Du, L., Dai, Z., Chen, J., and Xu, L. (2021). Optimal allocation of soft open point in active distribution network based on improved sensitivity analysis. *Automation Electr. Power Syst.* 45 (8), 129–137. (in Chinese). doi:10.7500/AEPS20191021004

Xuan, Z., Gao, X., Li, K., Wang, F., Ge, X., and Hou, Y. (2020). PV-load decoupling based demand response baseline load estimation approach for residential customer with distributed PV system. *IEEE Trans. Indus. App.* 56 (6), 6128–6137. doi:10.1109/TIA.2020.3014575

Yang, S., Li, Q., Ming, Z., Ma, Q., and Luo, Q. (2023). Multi-objective probabilistic reactive power optimization of distribution network considering the randomness of source and load. *South. Power Syst. Technol.* 17 (1), 125–135. (in Chinese). doi:10.13648/j.cnki.issn1674-0629.2023.01.013

Zhang, B., Ge, S., and Li, C. (2021). Markov chain wind speed prediction model based on copula function. *Smart Power* 49 (11), 24–30+37. (in Chinese).

Zhang, X., Zhen, Z., Sun, Y., Wang, F., Zhang, Y., Ren, H., et al. (2023). Prediction interval estimation and deterministic forecasting model using ground-based sky image. *IEEE Trans. Indus. App.* 59 (2), 2210–2224. doi:10.1109/TIA.2022.3218758

Zhou, T., and Zhang, H. (2021). *Electrical network theory*. China Machine Press. (in Chinese).

Zhou, X., Pang, C., Zeng, X., Jiang, L., and Chen, Y. (2023). A short-term power prediction method based on temporal convolutional network in virtual power plant photovoltaic system. *IEEE Trans. Instrum. Meas.* 72, 1–10. doi:10.1109/TIM.2023.3301904

frontiers | Frontiers in Energy Research

TYPE Original Research
PUBLISHED 17 April 2024
DOI 10.3389/fenrg.2024.1385029

OPEN ACCESS

EDITED BY
Liansong Xiong,
Xi'an Jiaotong University, China

REVIEWED BY
Leilei Guo,
Zhengzhou University of Light Industry, China
Hao Yi,
Xi'an Jiaotong University, China
Jianzhong Xu,
North China Electric Power University, China

*CORRESPONDENCE
Hui Zhang,
zhangh@xaut.edu.cn

RECEIVED 11 February 2024
ACCEPTED 25 March 2024
PUBLISHED 17 April 2024

CITATION
Cheng Y, Zhang H, Xing J and Xiao Z (2024), An improved two-beat deadbeat synchronous predictive current control strategy for MMC based on Newton interpolation method. *Front. Energy Res.* 12:1385029. doi: 10.3389/fenrg.2024.1385029

An improved two-beat deadbeat synchronous predictive current control strategy for MMC based on Newton interpolation method

Yuan Cheng[1,2,3], Hui Zhang[1]*, Jing Xing[2] and Zihan Xiao[4]

[1]School of Electrical Engineering, Xi'an University of Technology, Xi'an, China, [2]School of Electronics Information, Xi'an Polytechnic University, Xi'an, China, [3]Xi'an Key Laboratory of Interconnected Sensing and Intelligent Diagnosis for Electrical Equipment, Xi'an, China, [4]State Grid Tongchuan Electric Power Supply Company, Tongchuan, China

Modular Multilevel Converter (MMC) is widely used in applications such as High Voltage Direct Current (HVDC) transmission, AC/DC power conversion centers, and large-scale power quality management in electrical grids due to its highly modular structure, strong redundancy and low harmonic content in AC output. The application of the traditional deadbeat predictive current control to MMC enhances the fast tracking ability of the output current, but it still has the problems of low output current accuracy and high dependence on bridge arm inductor. Based on this, this paper proposes an improved two-beat deadbeat synchronous predictive current control based on Newton interpolation method. By improving the two-beat deadbeat synchronous predictive current control strategy, the accuracy of the output current can be further improved and its fast tracking ability can be enhanced. Newton interpolation is introduced to improve the accuracy of the output current while reducing the dependence on the bridge arm inductor. The results show that the control strategy proposed in this paper reduces the output current THD by 2.88% compared with the two-beat deadbeat predictive current control, thus improving the accuracy; the bridge arm inductor value is reduced by 1.28%, thus reducing the dependence; and under the transient environment, the output current can be tracked to its predicted reference value 843 μs in advance, which enhances the fast tracking capability.

KEYWORDS

modular multilevel converter, Newton interpolation method, deadbeat predictive current control, dependency, fast tracking

1 Introduction

In 2020, in order to face the threat of climate changes and achieve the sustainable development together with the world, the Chinese government put forward the goal and vision of "carbon peak by 2030 and carbon neutrality by 2060" (Yuan et al., 2023). In order to accelerate the realization of this goal, China is building a new type of power system which coexists with multiple new forms of power generation and includes energy storage. Due to its highly modular structure, easy expansion and strong redundancy, MMC converters are currently commonly used in medium and high voltage applications in the industry and have shown good performance. In the new type of power system, MMC converters can not only achieve flexible interconnection of medium and high voltage AC/DC power grids, but also

have derived topology for energy storage access. MMC can also be used to participate in energy scheduling, power quality management, and buffer power fluctuations caused by new energy generation in the power grid. This puts higher requirements on the speed of system response and output accuracy.

MMC converters are the same as conventional two and three-level converters in that they are both voltage-source converters (Zheng et al., 2016). The main control system is often used in the dual closed-loop control based on the PI controller (Xu et al., 2019). Although it can achieve independent control of active/reactive power and has good output effect, a double frequency circulation will occur between phases during stable operation, and additional circulation suppressors need to be added to reduce the system loss (Reddy and Shukla, 2020). The introduction of a large number of circulation suppressors causes the complexity of the control system and affects the calculation control time. The feed-forward decoupling of the current inner loop increases the complexity of the control system, and its filter inductor parameters lead to dependence, reduce the output accuracy and stability. Compared with the classic PI controller-based double closed-loop control, some optimized controls, such as model predictive control, internal mode control, sliding mode control, and deadbeat current predictive control, are also used in voltage source converters. The application of two-stage model predictive control to MMC in Ref (Ma et al., 2020). improved the accuracy of AC current tracking, but it is premised on sacrificing greater optimization iteration complexity and computational cost. In Ref. (Yanchao et al., 2015), an internal mode control using the Mrmin criterion for parameter tuning was proposed, which can quickly respond to stabilize the DC-side voltage and improve the robustness of the system when responding to load changes, but when the MMC level and current sampling time change, the current inner loop open-loop transfer function needs to be re-derived, which is not universal. In Ref. (Yang and Fang, 2022), the sliding mode parameters were optimized by introducing the radial basis function RBF neural network algorithm, which does not require any circuit model and controller parameters, and does not affect the performance of the controller when the external environment changes, but the introduction of the RBF neural network algorithm will increase the complexity of the control system.

In recent years, the traditional deadbeat control has been widely used in the industry due to its advantages of simple principle and structure, and strong current tracking ability. In Ref. (Song et al., 2018), the deadbeat control based on Newton interpolation method and power feedforward was applied to the single-phase rectifier, which reduced the dependence on the filter inductor and improves the output current accuracy. Ref (Kang et al., 2017). studied the deadbeat control of photovoltaic grid-connected inverter based on Lagrange interpolation, which reduces the harmonic content of the output current and improves the overall efficiency of the system. In Ref. (Wang et al., 2020), a combination of deadbeat predictive current and model prediction was used to reduce the mismatch of circuit parameters and improve the dynamic response of the system output. The above methods can reduce the dependence on the circuit model, but do not consider the influence of delay on the output of the converter. In Ref. (Chen et al., 2020), the modulation strategy of deadbeat predictive current control and nearest level approximation was adopted, and the selection principle is added to the number of sub-modules in the phase unit, so as to reduce the influence of circulation on the output and improve the accuracy. Ref (Jiang et al., 2017; Ge et al., 2018). reduced the effect of time delay on the output of the converter by predicting the output current of two periods, but the control performance of the converter still depends on accurate circuit model parameters. In Ref. (Chen et al., 2021), the first-order forward difference method is used to predict the output current of two periods to improve the output current accuracy of the active power filter. In Ref. (Abdel-Rady Ibrahim Mohamed and El-Saadany, 2007), Adaptive deadbeat predictive current control with delay compensation is used to reduce the impact of time delay and reduce the dependence on the circuit model. The above methods have the ability of fast tracking of transient current, which reduces the dependence on the circuit model and improves the output accuracy, but does not consider the synchronous prediction of output voltage and output current.

Based on the above, this paper analyzes the time delay of the actual control system. For the MMC output voltage, there exists the time delay of one control period, and for the output current, there exists the time delay of two control periods. In order to compensate for the effect of the time delay on the output accuracy, the output current tracking ability is enhanced while the dependence on the bridge arm inductor is reduced. An innovative MMC improved two-beat deadbeat synchronous predictive current control strategy based on the Newton interpolation method is proposed. The details are as follows:

(1) The first-order forward difference method is used to complete the prediction of one control period of the output voltage, and the improved two-beat deadbeat predictive current control system model is constructed and its mechanism is analyzed. On the basis of retaining the characteristics of traditional deadbeat predictive current control, the introduction of voltage correction improves the accuracy of output.
(2) The Newton interpolation method is used to complete the prediction of the two control periods of the output current, so as to match and improve the two-beat deadbeat predictive current control system model to achieve the purpose of synchronous prediction with the output voltage. The output current tracking capability is enhanced to further improve the accuracy of the output current and reduce the inductor dependence of the bridge arm.

The remaining work of this paper is as follows: Section 1 analyzes the working principle of MMC and establishes the single-phase equivalent circuit model; Section 2 analyzes the traditional deadbeat predictive current control and the time delay of the actual control system; Section 4 simulates and verifies the proposed strategy.

2 MMC working principle and single-phase equivalent circuit modeling

2.1 Main circuit topology and working principle

The MMC main circuit topology is shown in Figure 1A. The three-phase structure is the same, with a total of six bridge arms. Each phase can be divided into upper and lower bridge arms, and each bridge arm is composed of n sub-modules with the same

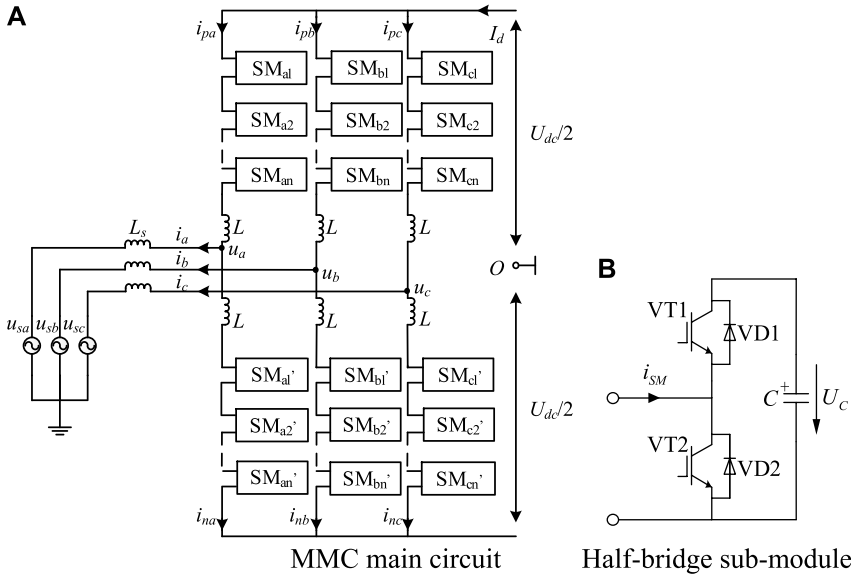

FIGURE 1
Topology of the MMC main circuit and its sub-modules. **(A)** MMC main circuit. **(B)** Half-bridge sub-module.

TABLE 1 Working status of sub-modules.

State / Current direction	Input (u_{SM} = U_c)	Cut-off (u_{SM} = 0)
1→2	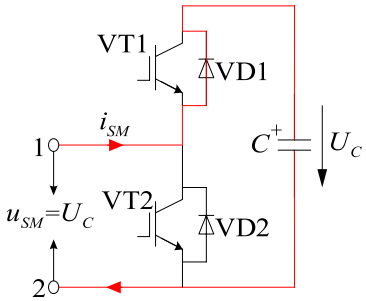	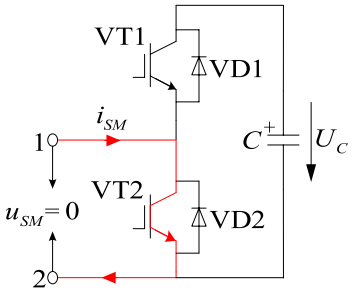
2→1	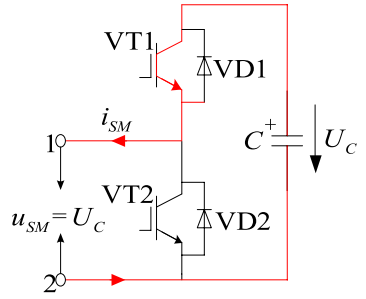	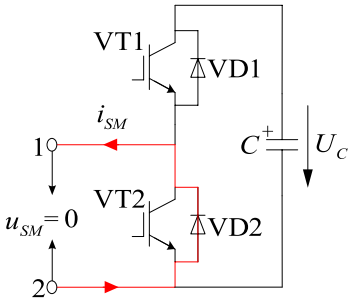

structure cascaded with the bridge arm inductor L. In Figure 1A, U_{dc} is the DC output voltage; u_{Px} and $_{uNx}$ are the output voltages of the upper and lower bridge arms of the x phase, respectively. Phase x = a,b,c; i_{Px} and i_{Nx} represent the current flowing through the upper and lower bridge arms of the phase x, respectively; u_x is the output voltage of the MMC AC port; u_{sx} and i_x are AC-side phase voltage and phase current, respectively; L_s is the filter inductor for the energy interaction between the AC power supply and the MMC.

In this paper, MMC uses a half-bridge sub-module, and the topology is shown in Figure 1B. When running, according to different modulation and sub-module equalization sequencing algorithms, it can work in three states: input, cut-off and latching. When it is running stably, it only works in the state of input and cut-off. The current i_{SM} flowing path and its port voltage u_{SM} are shown in Table 1. 1 and 2 are the outlet ports of the sub-module; in the input state, u_{SM} = U_c; in the cut-off state, u_{SM} = 0.

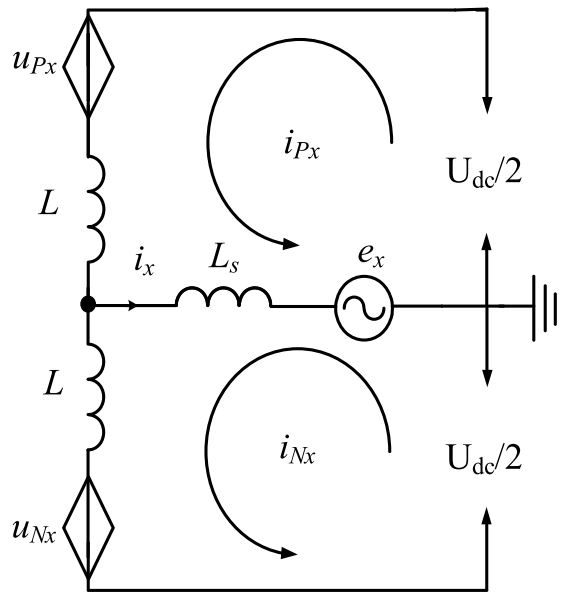

FIGURE 2
MMC single-phase equivalent circuit.

2.2 Modeling of single-phase equivalent circuits

MMC single-phase equivalent circuit is shown in Figure 2. Ignore the effects of AC power and AC-side filter inductors. Taking a single-phase as an example, the KVL equation is established for the upper and lower bridge arms (Tan et al., 2021):

$$\begin{cases} \frac{U_{dc}}{2} - u_{Px} - L\frac{di_{Px}}{dt} - u_x = 0 \\ \frac{U_{dc}}{2} - u_{Nx} - L\frac{di_{Nx}}{dt} + u_x = 0 \end{cases} \tag{1}$$

The MMC three-phase structure is symmetrical, and the DC-side current is evenly distributed among the three phases. The capacitor voltage of the sub-module of the phase unit fluctuates, resulting in the voltage difference among the phase units, forming a double frequency circulation. Therefore, the interphase circulation icir in this paper includes the DC circulation and the interphase double frequency circulation that are evenly distributed among the three phases. Thereby, the current equations of the single-phase upper and lower bridge arm nodes are established:

$$\begin{cases} i_{Px} = \frac{i_x}{2} + i_{cir} \\ i_{Nx} = -\frac{i_x}{2} + i_{cir} \end{cases} \tag{2}$$

The circulation current in the bridge arm current intensifies the fluctuation of the capacitor voltage of the sub-module, resulting in a decrease in the accuracy of the DC output voltage and an increase in the system loss (Bahrani et al., 2016). Therefore, it is necessary to introduce circulation suppression when designing the deadbeat predictive current control system applied to MMC.

3 Delay analysis of traditional deadbeat predictive current control and actual control system

Not only will the circulation affect the accuracy of the output, but the actual control system has a certain delay, which will also affect the accuracy of the system output. Therefore, the innovation proposed in this paper is an improvement on the delay analysis of the traditional deadbeat predictive current control model and actual control system.

3.1 Conventional deadbeat predictive current control applied to MMC

By discretizing formula (1), the formula for the output voltage of the upper and lower bridge arms of the MMC in the kth control period (Zhang et al., 2021) is obtained:

$$\begin{cases} u_{Px}(k) = \frac{U_{dc}(k)}{2} - u_x(k) - L\frac{i^*_{Px}(k+1) - i_{Px}(k)}{T_s} \\ u_{Nx}(k) = \frac{U_{dc}(k)}{2} + u_x(k) - L\frac{i^*_{Nx}(k+1) - i_{Nx}(k)}{T_s} \end{cases} \tag{3}$$

where $U_{dc}(k)$ and $u_x(k)$ are the DC-side voltage and the AC-port output voltage in the kth control period, respectively; $u_{Px}(k)$ and $u_{Nx}(k)$ are the sum of the voltages of all submodule capacitors of the control cascaded

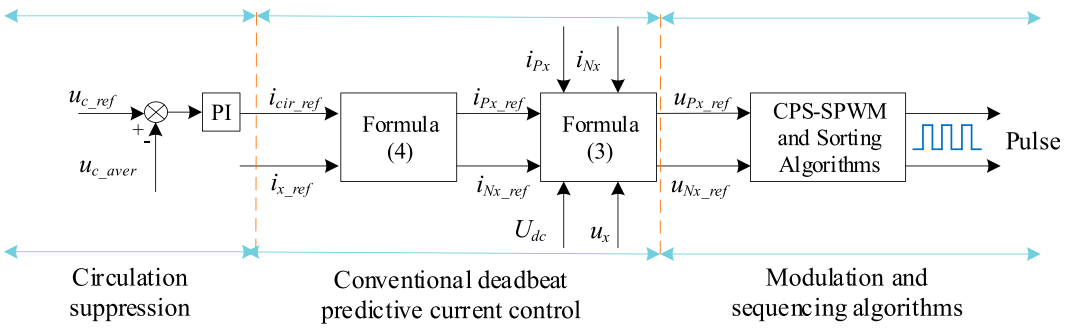

FIGURE 3
Traditional deadbeat predictive current control applied to MMC.

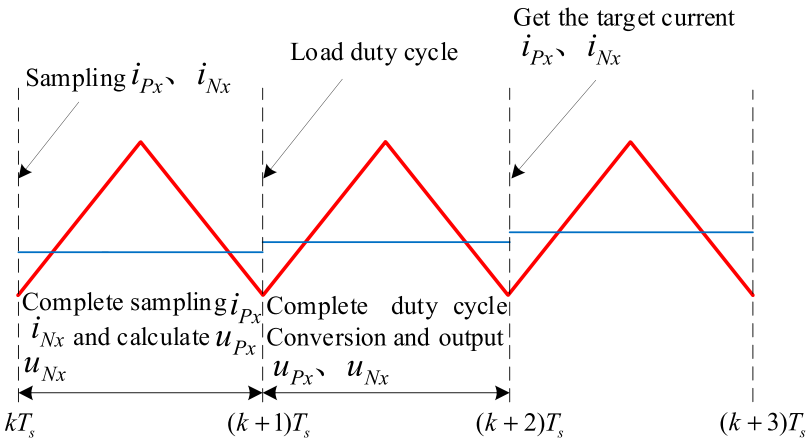

FIGURE 4
Schematic diagram of delay of the actual control system.

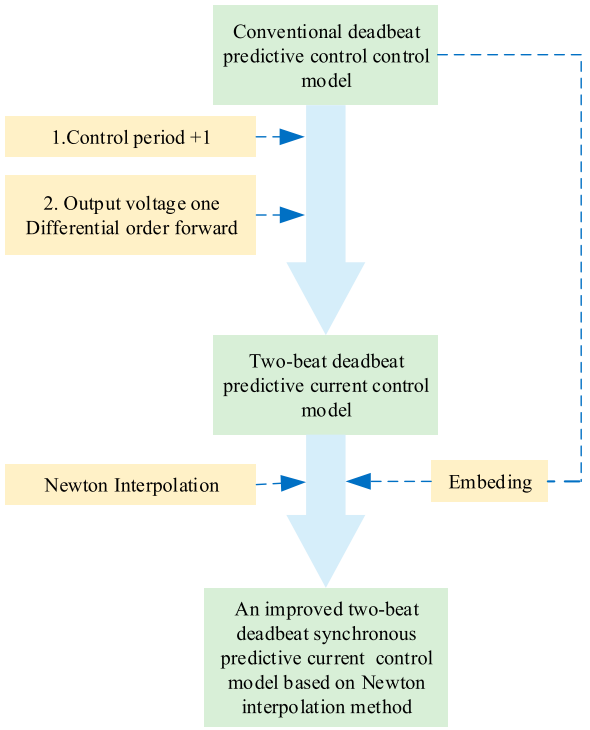

FIGURE 5
The technical route of the improved two-beat deadbeat synchronous predictive current control based on Newton interpolation method.

into the upper and lower bridge arms of the MMC main circuit in the *k*th control period; $i_{Px}(k)$ and $i_{Nx}(k)$ are the currents flowing through the upper and lower bridge arms, respectively; $i^*_{Px}(k+1)$ and $i^*_{Nx}(k+1)$ are the upper and lower bridge arm currents at the beginning of the $k+1$ control period, that is, the reference values for the prediction of the upper and lower bridge arm currents. According to formula (2), formula (4) can be obtained:

$$\begin{cases} i^*_{Px}(k+1) = i_{Px\_ref} = \dfrac{i_{x\_ref}}{2} + i_{cir\_ref} \\ i^*_{Nx}(k+1) = i_{Nx\_ref} = -\dfrac{i_{x\_ref}}{2} + i_{cir\_ref} \end{cases} \tag{4}$$

where i_{x_ref} is the AC current reference value; i_{cir_ref} is the reference value for interphase circulation to suppress the system circulation and reduce the voltage fluctuation of the capacitor of the sub-module. The interphase circulation reference value i_{cir_ref} can be obtained by PI control of the difference between capacitor voltage reference value U_{c_ref} of the sub-module and its average value U_{c_aver}.

$$i_{cir\_ref} = \left(U_{c\_ref} - U_{c\_aver}\right) \times \left(k_p + \frac{k_i}{s}\right) \tag{5}$$

where kp and ki are proportional and integral coefficients, respectively.

Formula (4) is substituted into formula (3) and formula (5) to construct a deadbeat predictive current control system, as shown in Figure 3. The MMC deadbeat predictive current control system is divided into three parts: voltage outer loop (circulation current suppression), current inner loop (deadbeat predictive current control), carrier phase-shift modulation and sequencing algorithm. The reference value of the interphase circulation is obtained by the voltage outer loop i_{cir_ref} and the reference value of the AC current is substituted together with the reference value of the AC current i_{x_ref} into formula (4) to get the reference value of the output current of the upper and lower arms of each phase i_{Px_ref} and i_{Nx_ref}. The reference values $u_{Px}(k)$ and $u_{Nx}(k)$ of the voltage of the upper and lower bridge arms of each phase in the *kth* control period can be obtained by substituting i_{Px_ref} and i_{Nx_ref} into formula (3). The sub-modules that should be put in the upper and lower bridge arms of each phase are obtained by the carrier phase-shifting modulation and sequencing algorithm, and the trigger pulse of the sub-module of each phase is generated.

Note: The u_{Px_ref} and u_{Nx_ref} in Figure 3 are $u_{Px}(k)$ and $u_{Nx}(k)$ in formula (3)

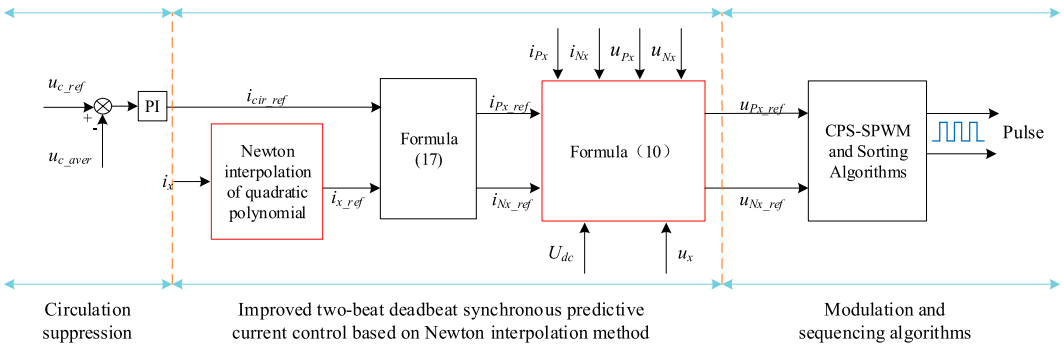

FIGURE 6
Improved two-beat deadbeat synchronous predictive current control system based on Newton interpolation method.

TABLE 2 System simulation parameters.

Parameter	Numeric value
Capacity S/MVA	1
DC-side voltage U_{dc}/kV	10
AC-phase voltage peak 1.414U_s/V	3,266
Bridge arm sub-module n	10
Arm inductor L/mH	3.23 (Improved two-beat deadbeat synchronous predictive current control)
	3.29 (Two-beat deadbeat predictive current control)
AC filter inductor L_s/mH	1.5
Sub-module capacitors C/mF	6.6
Switching frequency f_s/Hz	5,000

3.2 Delay analysis of the actual control system

Normally, we want to complete the sampling, computational control, and output of each physical quantity of the system at the same time. However, in the actual control system, there are delays in the process of system sampling, calculation control, and loading duty cycle, which cannot be completed at the same time, so the influence of time delay should be considered when designing the control system (Wang et al., 2015a). Figure 4 is a schematic diagram of the time delay of considering system sampling, calculating control, loading duty cycle, and generating target signals. i_{Px} and i_{Nx} were used as the control variables, u_{Px} and u_{Nx} were the controlled variables, and T_s was approximately equivalent to the carrier period (i.e., one beat). At the time of kT_s, start sampling i_{Px} and i_{Nx}; During the control period from kT_s to $(k+1)T_s$, the sampling of i_{Px} and i_{Nx} is completed, and the calculation of u_{Px} and u_{Nx} is completed. At the time of $(k+1)T_s$, start loading duty cycle; During the control period from $(k+1)$ T_s to $(k+2)$ T_s, the duty cycle conversion is completed and the voltages of the upper and lower bridge arms of the MMC, u_{Px} and u_{Nx}, are output. At the time of $(k+2)T_s$, the target current (MMC upper and lower arm currents) i_{Px} and i_{Nx} can be obtained.

Through the above analysis, it can be seen that there is a delay of one beat between the output voltage u_{Px} and u_{Nx}, that is, the delay of one control period T_s from the start time of current sampling to the start time of loading duty cycle. There is a delay of two beats between the output current i_{Px} and i_{Nx}, that is, the delay is $2T_s$ (two beats) between the start time of current sampling and the time when the target current signal is obtained, resulting in a lag in the control effect.

Previous studies have shown that the delay of the control system will reduce the output accuracy, affect the stability, and reduce the follow-up performance (Zhang et al., 2017). Therefore, the delay of the output voltage/current is compensated by the control period at the same time to achieve a good control effect.

4 Improved two-beat deadbeat synchronous predictive current control based on Newton interpolation method

In order to solve the problem of circulation and delay, this paper proposes an improved two-beat deadbeat synchronous predictive current control based on Newton interpolation method. On the basis of the control period plus one of the traditional deadbeat predictive current control model, the first-order forward difference method and Newton interpolation method are introduced to predict the output voltage and output current in one beat and two beats,

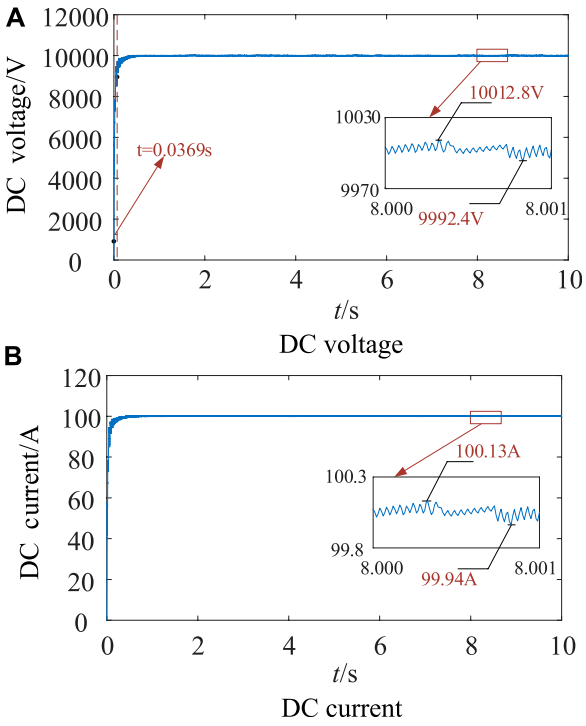

FIGURE 7
Improved two-beat deadbeat synchronous predictive current control, DC voltage/current. **(A)** DC voltage. **(B)** DC current.

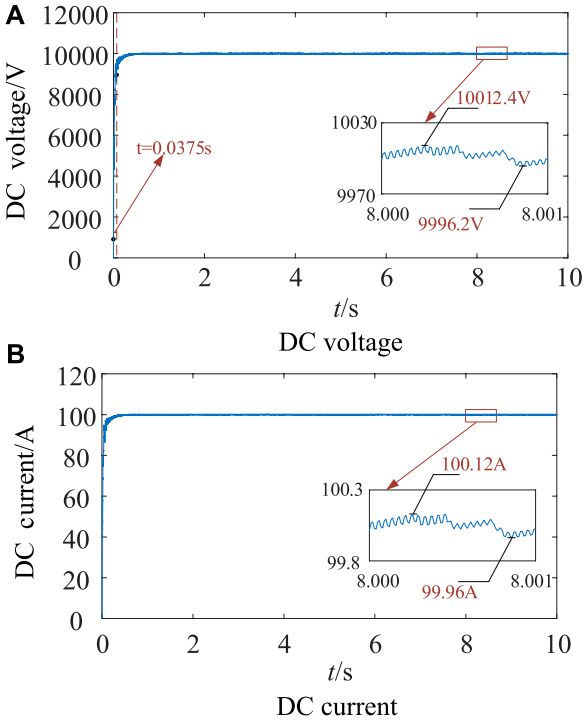

FIGURE 8
Two-beat deadbeat predictive current control, DC voltage/current. **(A)** DC voltage. **(B)** DC current.

respectively. Not only can it achieve synchronous prediction, but it can also improve output accuracy and enhance output current tracking ability. Figure 5 shows the technical route for the realization of the control strategy proposed in this paper.

4.1 Two-beat deadbeat predictive current control

In order to compensate for the influence of the delay on the control effect, the output voltage of the AC port is predicted one beat in advance, and the output current of the upper and lower bridge arms is predicted two beats in advance, so the control period plus one can be processed for formula (3) to obtain (Zhang et al., 2021):

$$\begin{cases} u_{Px}(k+1) = \dfrac{U_{dc}(k+1)}{2} - u_x(k+1) - L\dfrac{i^*_{Px}(k+2) - i_{Px}(k+1)}{T_s} \\ u_{Nx}(k+1) = \dfrac{U_{dc}(k+1)}{2} + u_x(k+1) - L\dfrac{i^*_{Nx}(k+2) - i_{Nx}(k+1)}{T_s} \end{cases} \tag{6}$$

When the MMC is running stably, the DC voltage fluctuation is relatively small, and it can be considered that:

$$U_{dc}(k) = U_{dc}(k+1) = U_{dc\_ref} \tag{7}$$

From formula (3) and formula (6), it can be seen that the output voltage u_x of the AC port is a linear relationship with the predicted currents i^*_{Px} and i^*_{Nx} of the upper and lower bridge arms, and the control period plus one. Since T_s is approximately equivalent to the carrier period, and its value is small, it can be considered that the increments of u_x in each control period are equal, and the first-order forward difference method is used to predict and downtime u_x, and it can be obtained (Abdel-Rady Ibrahim Mohamed and El-Saadany, 2007):

$$u_x(k+1) - u_x(k) = u_x(k) - u_x(k-1) \tag{8}$$

The predicted reference values of ux in the k+1 control period are:

$$u_x(k+1) = 2u_x(k) - u_x(k-1) \tag{9}$$

First, substituting formula (9) into formula (6); Secondly, $i^*_{Px}(k+1)$ and $i^*_{Nx}(k+1)$ in formula (3) are replaced by $i_{Px}(k+1)$ and $i_{Nx}(k+1)$, and the expressions $i_{Px}(k+1)$ and $i_{Nx}(k+1)$ are obtained by formula (3) and substituted into formula (6). Finally, in combination with formula (7), formula (10) is obtained:

$$\begin{cases} u_{Px}(k+1) = \underbrace{\dfrac{U_{dc\_ref}}{2} - u_x(k) - L\dfrac{i^*_{Px}(k+2) - i_{Px}(k)}{T_s}}_{\text{Conventional Deadbeat Current Predictive Control}} + \underbrace{\left[\dfrac{U_{dc\_ref}}{2} - u_x(k) - u_{Px}(k)\right]}_{\text{Arm Inductance Voltage Correction Term}} - \underbrace{[u_x(k) - u_x(k-1)}_{\text{AC port output voltage correction term}} \\ u_{Nx}(k+1) = \underbrace{\dfrac{U_{dc\_ref}}{2} + u_x(k) - L\dfrac{i^*_{Nx}(k+2) - i_{Nx}(k)}{T_s}}_{\text{Conventional Deadbeat Current Predictive Control}} + \underbrace{\left[\dfrac{U_{dc\_ref}}{2} + u_x(k) - u_{Nx}(k)\right]}_{\text{Arm Inductance Voltage Correction Term}} + \underbrace{[u_x(k) - u_x(k-1)}_{\text{AC port output voltage correction term}} \end{cases} \tag{10}$$

From formula (10), it can be seen that the mechanism of two-beat deadbeat predictive current control is to add the correction terms of bridge arm inductor voltage and AC-port output voltage on the basis of the traditional deadbeat predictive current control, so as to increase the speed and accuracy of the control system. The traditional deadbeat predictive current control can realize the fast tracking of the bridge arm current, so that the system can run stably.

TABLE 3 Comparison of metric parameters.

Control system \ The metric parameter	DC voltage (kV)	DC current(A)	Rise time(s)	Steady-state error (%)	Arm inductor value (mH)
Improved two-beat deadbeat synchronous predictive current control	10	100	0.0369	+0.13	3.23
				−0.08	
Two-beat deadbeat predictive current control	10	100	0.0375	+0.12	3.29
				−0.04	

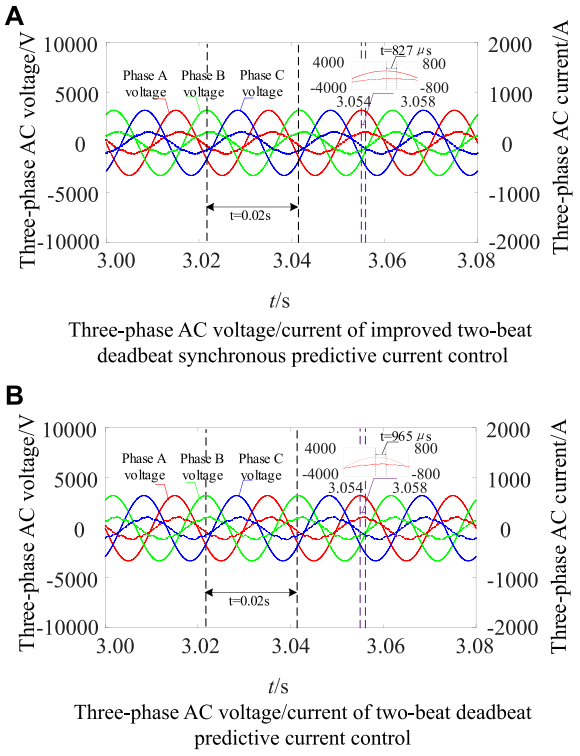

FIGURE 9
Three-phase AC voltage/current of MMC. **(A)** Three-phase AC voltage/current of improved two-beat deadbeat synchronous predictive current control. **(B)** Three-phase AC voltage/current of two-beat deadbeat predictive current control.

In the actual circuit, the bridge arm inductor current will cause the bridge arm inductor value to change, and the bridge arm inductor voltage correction term can be used to correct this change; Similarly, the AC-port output voltage correction term can be used to correct changes in the grid-side voltage.

4.2 Newton interpolation method and its quadratic/tertiary interpolation polynomials

In order to reduce the dependence of the predicted current of the bridge arm on the inductor of the bridge arm and further improve the accuracy of the control system, in this paper, the Newton interpolation method is used to predict the output current of the bridge arm. There is a series of unequal independent variables (z_0,z_1,z_2. . .,z_n, where $m\neq n$,$z_m\neq z_n$) and their function $f(z)$. $f(z_n)$-$f(z_m)$/(z_n-z_m) becomes the first-order difference quotient of the function $f(z)$ at the point z_m and z_n, which is denoted as $f[z_n,z_m]$; $f[z_1,z_2,\ldots,z_k]$-$f[z_0,z_2,\ldots,z_{k-1}]$/($z_k$-$z_0$) is the k-order difference quotient.

According to the definition of the difference quotient (Zhang et al., 2017), the Newton interpolation first-order polynomial is obtained:

$$f_1(z) = f(z_0) + f[z_0, z_1](z - z_0) \tag{11}$$

The quadratic polynomial is:

$$f_2(z) = f(z_0) + f[z_0, z_1](z - z_0) + f[z_0, z_1, z_2](z - z_0)(z - z_1) \tag{12}$$

Therefore, the nth degree polynomial of f(z) is:

$$\begin{aligned} f_n(z) = {} & f(z_0) + f[z_0, z_1](z - z_0) + f[z_0, z_1, z_2](z - z_0)(z - z_1) + \cdots \\ & + f[z_0, z_1, \cdots, z_n](z - z_0)\cdots(z - z_{n-1}) \end{aligned} \tag{13}$$

According to formula (4), the reference value of the bridge arm current prediction is related to the AC current reference value and the circulation reference value, and the circulation reference value can be obtained by the voltage outer loop, so the prediction of the bridge arm current can be converted into the prediction of the AC current reference value. Therefore, the reference values of AC current prediction at $(k+1)T_s$ and $(k+2)T_s$ can be predicted according to formula (13) and the sampling values of AC current at $(k\text{-}2)T_s$, $(k\text{-}1)T_s$ and kT_s respectively.

Newton interpolation quadratic polynomial is used to establish the AC current prediction expression, shown as follows:

$$\begin{aligned} i_{x\_ref}(t_{k+1}) &= i_x(t_{k-2}) + i_x[t_{k-2}, t_{k-1}](t_{k+1} - t_{k-2}) \\ &\quad + i_x[t_{k-2}, t_{k-1}, t_k](t_{k+1} - t_{k-2})(t_{k+1} - t_{k-1}) \\ &= i_x(t_{k-2}) - 3i_x(t_{k-1}) + 3i_x(t_k) \end{aligned} \tag{14}$$

The expression for the prediction of the AC current established by Newton interpolation cubic polynomial is:

$$\begin{aligned} i_{x\_ref}(t_{k+2}) &= i_x(t_{k-2}) + i_x[t_{k-2}, t_{k-1}](t_{k+2} - t_{k-2}) \\ &\quad + i_x[t_{k-2}, t_{k-1}, t_k](t_{k+2} - t_{k-2})(t_{k+2} - t_{k-1}) \\ &\quad + i_x[t_{k-2}, t_{k-1}, t_k, t_{k+1}](t_{k+2} - t_{k-2})(t_{k+2} - t_{k-1})(t_{k+2} - t_k) \\ &= -i_x(t_{k-2}) + 4i_x(t_{k-1}) - 6i_x(t_k) + 4i_x(t_{k+1}) \end{aligned} \tag{15}$$

Substituting the AC current value at time t_{k+1} predicted by formula (14) into formula (15), formula (16) can be obtained:

$$i_{x\_ref}(t_{k+2}) = 3i_x(t_{k-2}) - 8i_x(t_{k-1}) + 6i_x(t_k) \tag{16}$$

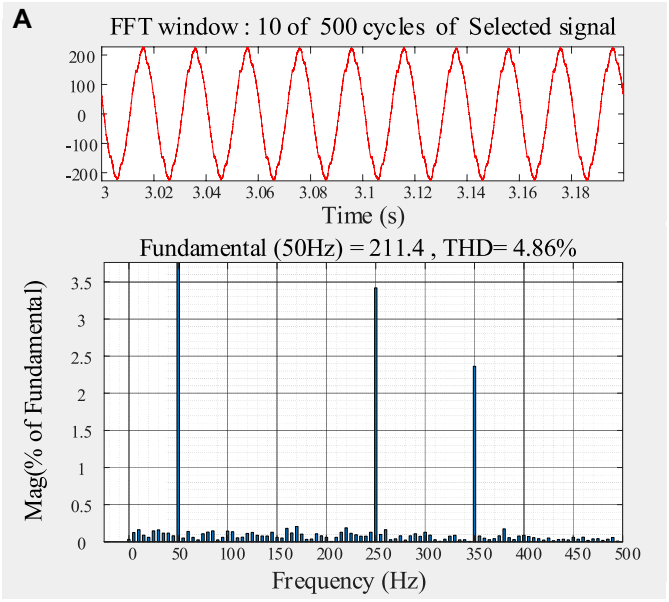

Phase-A current THD of improved two-beat deadbeat synchronous predictive current control

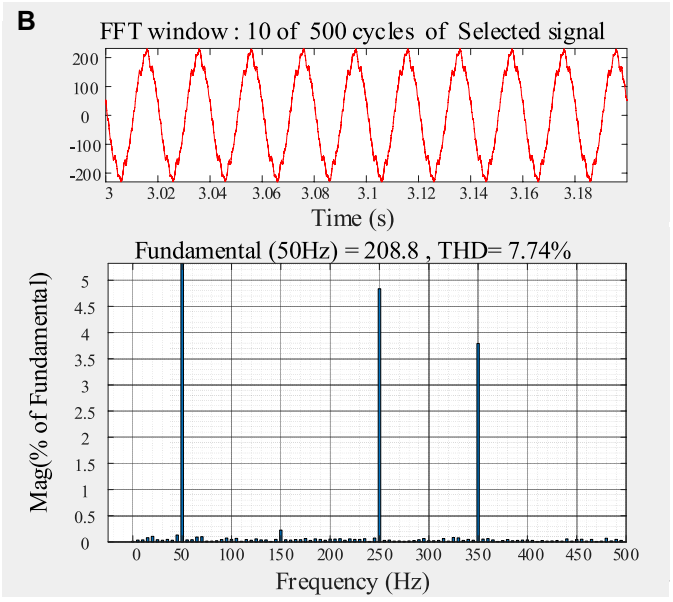

Phase-A current THD of two-beat deadbeat predictive current control

FIGURE 10
Total harmonic distortion rate of phase-A AC current of MMC. **(A)** Phase-A current THD of improved two-beat deadbeat synchronous predictive current control. **(B)** Phase-A current THD of two-beat deadbeat predictive current control.

TABLE 4 Comparison of phase-A AC current THD of two controls from 1 to 8s.

Control system	time(s)	1–1.2	2–2.2	3–3.2	4–4.2	5–5.2	6–6.2	7–7.2	8–8.2
Improved two-beat deadbeat synchronous predictive current control	THD (%)	4.90	4.80	4.86	4.82	4.87	4.81	4.74	4.85
Two-beat deadbeat predictive current control		7.78	7.74	7.74	7.79	7.79	7.73	7.77	7.80

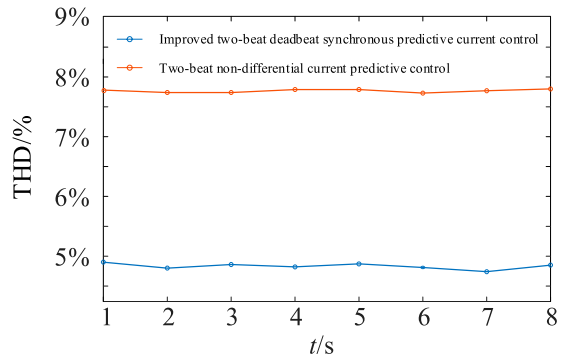

FIGURE 11
Comparison of phase-A AC current THD for two control.

Substituting i_{x_ref} (t_{k+2}) with the i_{x_ref} in formula (4), formula (17) can be obtained:

$$\begin{cases} i^{*}_{Px}(k+2) = i_{Px\_ref} = \dfrac{i_{x\_ref}}{2} + i_{cir\_ref} \\ i^{*}_{Nx}(k+2) = i_{Nx\_ref} = -\dfrac{i_{x\_ref}}{2} + i_{cir\_ref} \end{cases} \tag{17}$$

Substituting formula (17) into formula (10) constructs an improved two-beat deadbeat synchronous predictive current control system based on Newton interpolation method, and the structure is shown in Figure 6.

5 Simulation verification

In order to verify the effectiveness of the improved two-beat deadbeat synchronous predictive current control based on Newton interpolation method, a three-phase 11-level MMC rectifier converter model was built in Matlab/Simulink environment, and the parameters are shown in Table 2. In practical applications, due to the scalability of MMC, more input sub-modules can share the DC voltage in per phase. In this paper, we focus on the rectifier state of MMC: 1) Under steady-state condition, with the goal of stabilizing the DC voltage at 10 kV, compared with the two-beat deadbeat predictive current control, the method proposed in this paper has a less dependence of the output current on the inductor of the bridge arms and achieves higher accuracy. 2) Under transient conditions, the output AC current increases suddenly, and the method proposed in this paper

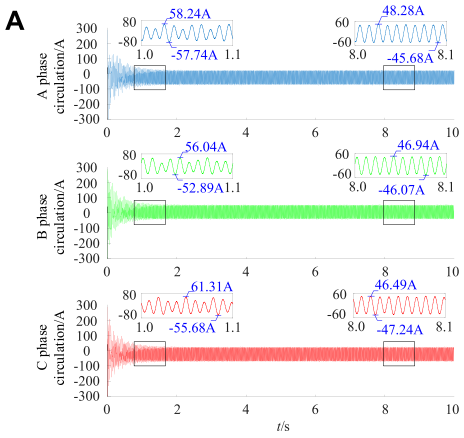

Three-phase circulation of improved two-beat deadbeat synchronous predictive current control

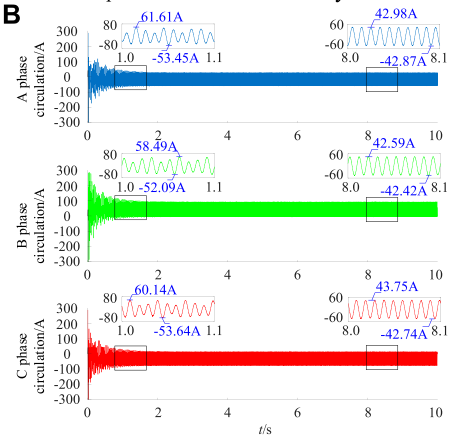

Three-phase circulation of improved two-beat deadbeat predictive current control

FIGURE 12
Three-phase circulation of MMC. **(A)** Three-phase circulation of improved two-beat deadbeat synchronous predictive current control. **(B)** Three-phase circulation of two-beat deadbeat predictive current control.

10.3389/fenrg.2024.1385029

has a faster tracking ability than the two-beat deadbeat predictive current control.

5.1 Steady-state conditions

The improved two-beat deadbeat synchronous predictive current control system is applied to MMC, and the DC voltage and current waveforms during stable operation are shown in Figure 7. The two-beat deadbeat predictive current control system is applied to MMC, and Figure 8 shows the DC voltage and current waveforms during stable operation.

As can be seen from the comparison of Figure 7 and Figure 8, both control systems can stabilize the DC voltage at 10 kV and the DC current at 100 A. The two-beat deadbeat synchronous predictive current control is improved, the rise time is 0.0369s, and the steady-state error is about +0.13% and −0.08% at about 3s. In order to stabilize the DC voltage at 10 kV, the inductor value of the bridge arm needs to be set from 3.23mH to 3.29 mH in the simulated environment with the same parameters. The two-beat deadbeat predictive current control has a rise time of 0.0375s and a steady-state error of about +0.12% and −0.04% at about 3s. Table 3 shows the comparison of the above parameters.

Figure 9A is the improved two-beat deadbeat synchronous predictive current control of three-phase AC voltage/current, and the three-phase AC phase voltage peak is 3266 V; the phase current peak is 224.2A, the phase current lag phase voltage is 827 μs, and the power factor cos (14.89°)≈0.9664 is improved. Figure 9B is a two-beat deadbeat predictive current control of three-phase AC voltage/current, and the three-phase AC phase voltage peak is 3266 V; the phase current peak is 228.2A, the phase current lag phase voltage is 965 μs, and the power factor cos (17.37°) ≈ 0.9543.

Figure 10A shows the total harmonic distortion rate of the AC current in phase A of the improved two-beat deadbeat synchronous predictive current control based on Newton interpolation method. 10 power frequency periods are selected for measurement starting from 3s, and the total harmonic distortion rate is 4.86%. As shown in Figures 10B, 10 power frequency periods are selected for measurement at the same time starting from 3s, and the total harmonic distortion rate is 7.74%. From formula (6) and formula (8), it can be seen that the two-beat deadbeat predictive current control system only uses the first-order forward difference method to predict the output voltage of the AC port for one control period, but formula (6) contains i^*_{Px} (k+2) and i^*_{Nx} (k+2), so it is necessary to predict the AC current i_x for two control periods, therefore, this paper uses Newton interpolation quadratic and cubic interpolation polynomials to predict the AC current for two periods to form i^*_{Px} (k+2) and i^*_{Nx} (k+2). Under the same system simulation parameters, the inductor of the bridge arm is reduced by 0.06 mH, which reduces the dependence of the predicted current of the bridge arm on the inductor of the bridge arm and improves the accuracy.

Table 4 shows the comparison of the THD data of phase-A AC current measured by 10 power frequency periods from 1 to 8s, and Figure 11 shows the data reconstruction curve of Table 4. From the comparison of the data in Table 4, it can be seen that the improved two-beat deadbeat synchronous predictive current control for three-phase AC current THD fluctuates between 4.7% and 4.9%, and the two-beat deadbeat predictive current control for three-phase AC current THD fluctuates between 7.7% and 7.8%.

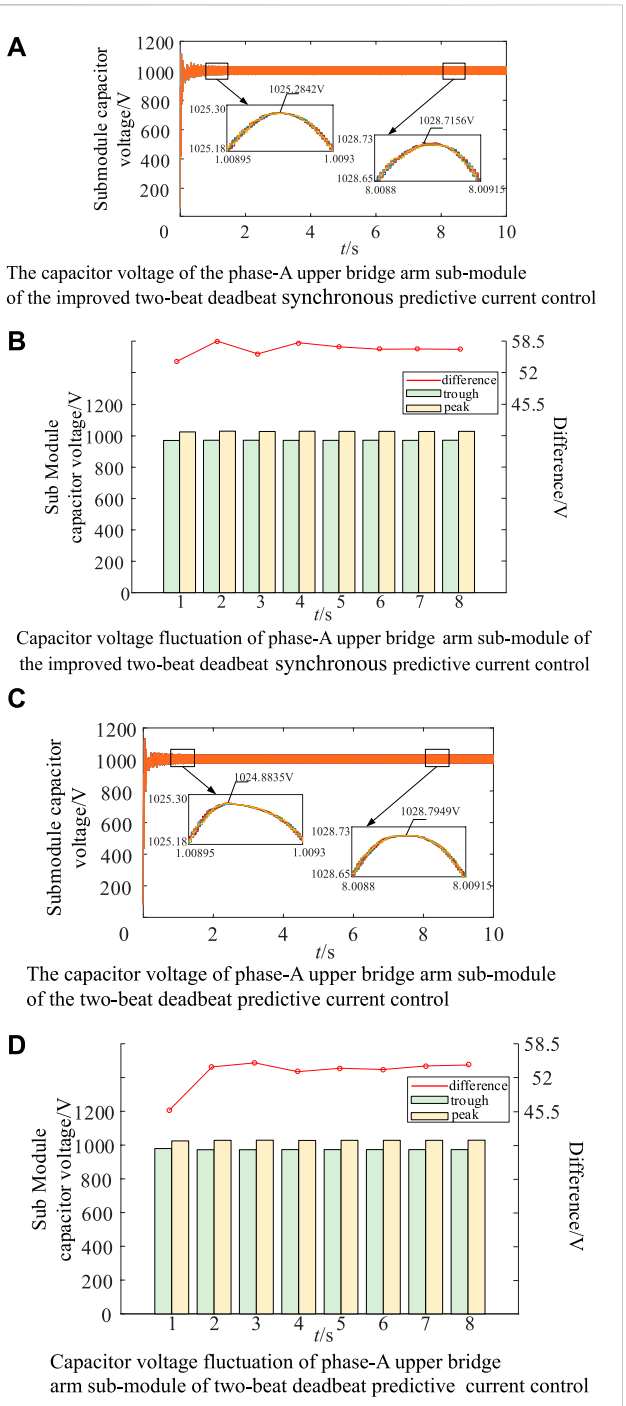

The capacitor voltage of the phase-A upper bridge arm sub-module of the improved two-beat deadbeat synchronous predictive current control

Capacitor voltage fluctuation of phase-A upper bridge arm sub-module of the improved two-beat deadbeat synchronous predictive current control

The capacitor voltage of phase-A upper bridge arm sub-module of the two-beat deadbeat predictive current control

Capacitor voltage fluctuation of phase-A upper bridge arm sub-module of two-beat deadbeat predictive current control

FIGURE 13
Capacitor voltage and its fluctuation of phase-A upper bridge arm sub-module. **(A)** The capacitor voltage of the phase-A upper bridge arm sub-module of the improved two-beat deadbeat synchronous predictive current control. **(B)** Capacitor voltage fluctuation of phase-A upper bridge arm sub-module of the improved two-beat deadbeat synchronous predictive current control. **(C)** The capacitor voltage of phase-A upper bridge arm sub-module of the two-beat deadbeat predictive current control. **(D)** Capacitor voltage fluctuation of phase-A upper bridge arm sub-module of two-beat deadbeat predictive current control.

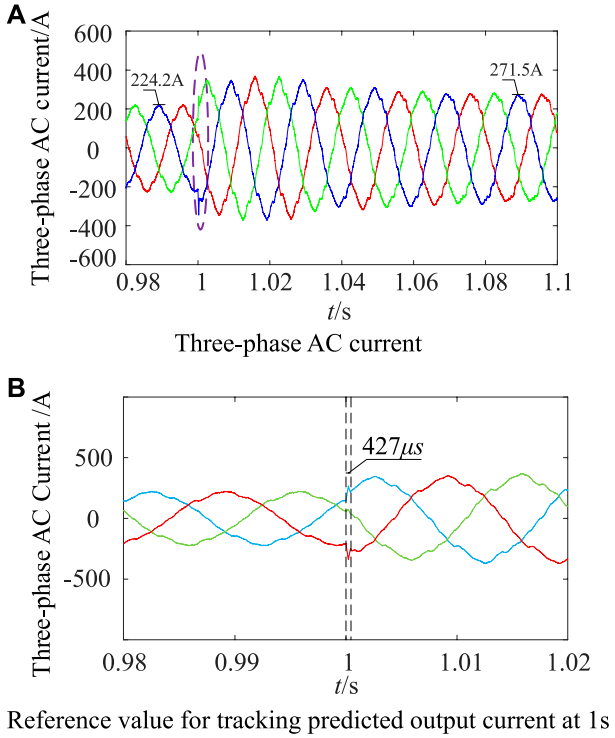

FIGURE 14
Improved two-beat deadbeat synchronous predictive current control, three-phase AC current burst. **(A)** Three-phase AC current. **(B)** Reference value for tracking predicted output current at 1s.

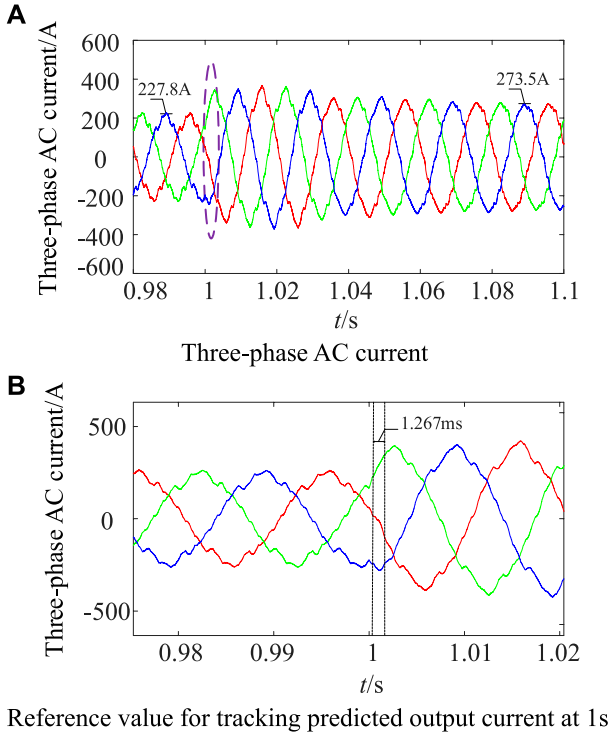

FIGURE 15
Two-beat deadbeat predictive current control, three-phase AC current burst. **(A)** Three-phase AC current. **(B)** Reference value for tracking predicted output current at 1s.

As shown in Figure 12A, with the improved two-beat deadbeat synchronous predictive current control, the system circulation is gradually decreasing. In the range of 1–8s, the positive peak value of phase A circulation attenuates from 58.24 A to 48.28A, and the circulation inhibition rate is 17.10%. The positive peak value of phase B circulation attenuates from 56.04 A to 46.94A, and the circulation inhibition rate is 16.24%. The positive peak value of phase C circulation attenuates from 61.31 A to 46.49A, and the circulation inhibition rate is 24.17%. As shown in Figure 12B, with the two-beat deadbeat predictive current control, the three-phase circulation is also gradually decreasing. In the range of 1–8s, the positive peak of phase A circulation attenuates from 61.61 A to 42.98A, and the circulation inhibition rate is 30.24%. The positive peak value of phase B circulation attenuates from 58.49 A to 42.59A, and the circulation inhibition rate is 27.18%. The positive peak value of phase C circulation attenuates from 60.14 A to 43.75A, and the circulation inhibition rate is 27.25%. From the above analysis, it can be seen that the circulation of the system is well suppressed by the two control systems, and the effectiveness of the control of the voltage outer loop (circulation suppression) is verified.

Figure 13 shows the capacitor voltage and fluctuation of the MMC Phase-A upper bridge arm sub-modules. Phase A of the improved two-beat deadbeat synchronous predictive current control is shown in Figure 13A. At 1s, the sub-module capacitor voltage fluctuation rate is 2.5%. At 8s, the sub-module capacitor voltage fluctuation rate is 2.9%. The capacitor voltage of phase-A upper bridge arm sub-module of the two-beat deadbeat predictive current control is shown in Figure 13C. At 1s, the sub-module capacitor voltage fluctuation rate is 2.5%. At 8s, the sub-module capacitor voltage fluctuation rate is 2.9%. The analysis shows that the capacitor voltage fluctuation rate of the MMC sub-module meets the requirement of ±10% for both control systems. The effectiveness of the control of the voltage outer loop (circulation current suppression) is indirectly verified.

5.2 Transient working conditions

In order to verify the dynamic performance of the two control systems, the transient working conditions are simulated. As can be seen from Figures 14A, B, the improved two-beat deadbeat synchronous predictive current control achieves the peak value of three-phase AC current of 224.2 A before 1s. At 1s, the AC current burst is set, and the output current is tracked to the predicted reference value after 427 *μs* After entering the steady state, the peak value of the three-phase AC current is 271.5A, and it can be seen from Figures 15A, B that the peak value of the three-phase AC current is 227.8 A before 1s. At 1s, the AC current burst is set, the output current is tracked to the predicted reference value after 1.267 *ms*. After entering the steady state, the peak value of the three-phase AC current is 273.5 A. Therefore, the method proposed in this paper has better current fast tracking ability than the two-beat deadbeat predictive current control.

6 Conclusion and prospects

Firstly, the traditional deadbeat predictive current control model is established according to the MMC single-phase equivalent circuit model; secondly, on the basis of analyzing the time delay of the actual control system, the control period plus one, and the two-beat deadbeat synchronous predictive current control model is given by using the first-order forward difference method for the output voltage; thirdly, the traditional deadbeat predictive current control model is embedded into the two-beat deadbeat predictive current control model to complete the improved two-beat deadbeat predictive current control model and its mechanism is analyzed. In order to achieve the purpose of synchronous prediction of output voltage and output current, the Newton interpolation method is used to predict the output current, and its prediction reference value is substituted into the improved two-beat deadbeat synchronous predictive current control model. Finally, the validity of the method proposed in this paper is verified through simulation by comparing it with the two-beat deadbeat predictive current control. After reviewing the work content of this paper, the following work can be carried out in the future (Wang et al., 2015b):

1) According to formula (1) and formula (3) in this paper, the influence of the equivalent internal resistance of the bridge arm is not considered in modeling the traditional deadbeat predictive current control system. In order to further improve the performance of the control system, the combination of the method proposed in this paper and the model predictive control can be considered to further improve the performance of the control system.
2) The carrier phase-shift modulation strategy used in this paper is replaced by the nearest level approximation modulation strategy. The numerator of the rounding function in the nearest level approximation modulation strategy is the voltage modulation wave output by the improved two-beat deadbeat synchronous predictive current control, and the denominator can be a method of equalizing the capacitor voltage and switching frequency of the sub-module. The aim is to ensure the efficiency of the whole machine while making the rounding function in the nearest level approximation modulation strategy more accurate.

Data availability statement

The original contributions presented in the study are included in the article/supplementary material, further inquiries can be directed to the corresponding authors.

Author contributions

YC: Writing–original draft, Writing–review and editing, Validation. HZ: Conceptualization, Funding acquisition, Writing–review and editing. JX: Investigation, Writing–review and editing. ZX: Data curation, Writing–review and editing.

Funding

The author(s) declare that no financial support was received for the research, authorship, and/or publication of this article.

Conflict of interest

Author ZX is employed by State Grid Tongchuan Electric Power Supply Company.

The remaining authors declare that the research was conducted in the absence of any commercial or financial relationships that could be construed as a potential conflict of interest.

Publisher's note

References

Abdel-Rady Ibrahim Mohamed, Y., and El-Saadany, E. F. (2007). An improved deadbeat current control scheme with a novel adaptive self-tuning load model for a three-phase PWM voltage-source inverter. *IEEE Trans. Industrial Electron.* 54 (2), 747–759. doi:10.1109/tie.2007.891767

Bahrani, B., Debnath, S., and Saeedifard, M. (2016). Circulating current suppression of the modular multilevel converter in a double-frequency rotating reference frame. *IEEE Trans. Power Electron.* 31 (1), 783–792. doi:10.1109/tpel.2015.2405062

Chen, J., Shao, H., and Liu, C. (2021). An improved deadbeat control strategy based on repetitive prediction against grid frequency fluctuation for active power filter. *IEEE Access* 9, 24646–24657. doi:10.1109/access.2021.3057386

Chen, X., Liu, J., Song, S., and Ouyang, S. (2020). Circulating harmonic currents suppression of level-increased NLM based modular multilevel converter with deadbeat control. *IEEE Trans. Power Electron.* 35 (11), 11418–11429. doi:10.1109/tpel.2020.2982781

Ge, L., Gu, J., and Wang, C. (2018). Research on grid-connected resonance suppression based on improved photovoltaic. *Power Syst. Prot. Control* 46 (19), 66–73.

Jiang, W., Lei, WANG, Yan, G., et al. (2017). An improved beat free control method for inner loop current tracking. *Proc. CSEE* 37 (08), 2370–2383.

Kang, J., Xia, W., and Yang, C. (2017). Lagrangian interpolation method for grid-connected photovoltaic inverter without differential beat. *Acta Solar-Energy Sin.* 38 (03), 751–757.

Ma, W., Sun, P., Zhou, G., et al. (2020). Predictive control of two-stage model of modular multilevel converter. *Power Syst. Technol.* 44 (04), 1419–1427.

Reddy, G. A., and Shukla, A. (2020). Circulating current optimization control of MMC. *IEEE Trans. Industrial Electron.* 68 (4), 2798–2811. doi:10.1109/tie.2020.2977565

Song, Z., Xiong, C., Huang, L., et al. (2018). Power feedforward control of single-phase rectifier based on Newton interpolation. *Power Syst. Technol.* 42 (11), 3623–3629.

Tan, X., Ren, L., Tang, Y., Li, J., Shi, J., Xu, Y., et al. (2021). Comparative analysis of three types of SFCL considering current-limiting requirement of MMC-HVDC system. *IEEE Trans. Appl. Supercond.* 31 (8), 1–5. doi:10.1109/tasc.2021.3107816

Wang, J., Song, Y., and Monti, A. (2015b).Design of a high performance deadbeat-type current controller for LCL-filtered grid-parallel inverters. 2015 IEEE 6th International Symposium on Power Electronics for Distributed Generation Systems (PEDG). Aachen, Germany, IEEE, 1–8.

Wang, J., Tang, Y., Lin, P., Liu, X., and Pou, J. (2020). Deadbeat predictive current control for modular multilevel converters with enhanced steady-state performance and stability. *IEEE Trans. Power Electron.* 35 (7), 6878–6894. doi:10.1109/tpel.2019.2955485

Wang, J., Yan, J. D., Jiang, L., and Zou, J. (2015a). Delay-dependent stability of single-loop controlled grid-connected inverters with LCL filters. *IEEE Trans. Power Electron.* 31 (1), 743–757. doi:10.1109/tpel.2015.2401612

Xu, Y., Xu, Z., Zhang, Z., and Xiao, H. (2019). A novel circulating current controller for MMC capacitor voltage fluctuation suppression. *IEEE Access* 7, 120141–120151. doi:10.1109/access.2019.2933220

Yanchao, C., Huang, S., Kong, F., et al. (2015). Steady-state control of MMC-HVDC based on internal mode controller. *Power Syst. Technol.* 39 (08), 2223–2229.

Yang, X., and Fang, H. (2022). RBF neural network-based sliding mode control for modular multilevel converter with uncertainty mathematical model. *Energies* 15, 1634. doi:10.3390/en15051634

Yuan, K., Zhang, T., Xie, X., Du, S., Xue, X., Abdul-Manan, A. F., et al. (2023). Exploration of low-cost green transition opportunities for China's power system under dual carbon goals. *J. Clean. Prod.* 414, 137590. doi:10.1016/j.jclepro.2023.137590

Zhang, Y., Huang, R., Li, H., and Cai, J. (2017). Handling qualities evaluation of time delay and predictive model on teleoperation docking. *J. Spacecr. Rockets* 54 (4), 936–944. doi:10.2514/1.a33704

Zhang, Y., Yang, X., Pan, Z., et al. (2021). Modular Multilevel Converter improves the predictive control of undifferentiated current. *J. Beijing Jiaot. Univ.* 45 (06), 43–50.

Zheng, Xu, et al. (2016). *Flexible DC transmission system*. 2nd edition. Beijing, China: China Machine Press, 2.

frontiers | Frontiers in Energy Research

TYPE Original Research
PUBLISHED 02 May 2024
DOI 10.3389/fenrg.2024.1375888

OPEN ACCESS

EDITED BY
Liansong Xiong,
Xi'an Jiaotong University, China

REVIEWED BY
Donghai Zhu,
Huazhong University of Science and Technology, China
Yueshi Guan,
Harbin Institute of Technology, China

*CORRESPONDENCE
Dongbo Guo,
guodongbo@neepu.edu.cn

RECEIVED 24 January 2024
ACCEPTED 04 April 2024
PUBLISHED 02 May 2024

CITATION
Yu Q, Liu C, Li R, Pei Z, Guo D, Mao T and Shao X (2024), Input-parallel output-series Si-SiC hybrid inverter with fractional harmonic elimination.
Front. Energy Res. 12:1375888.
doi: 10.3389/fenrg.2024.1375888

Input-parallel output-series Si-SiC hybrid inverter with fractional harmonic elimination

Qinhai Yu, Chuang Liu, Ruifeng Li, Zhongcheng Pei, Dongbo Guo*, Tingrui Mao and Xinming Shao

School of electrical engineering, Northeast Electric Power University, Jilin, China

This paper proposes an input-parallel output-series (IPOS) Si-SiC hybrid inverter with dual-frequency harmonic elimination modulation strategy. The proposed topology composed of two power conversion cells and a three-phase five-column medium-frequency step-down transformer, the low-frequency power conversion cell (LFPC-C, 1 kHz) leverages strong current-carrying capacity of silicon-based devices for dealing with the system main power, and the high-frequency power conversion cell (HFPC-C, 30 kHz) based on wide-bandgap semiconductor SiC devices is used to addressing the fractional harmonics compensation power. This topology combines the strong current carrying capability of Si devices with the low switching loss of SiC devices at high frequency and achieves high quality power conversion at low cost and low loss. Compared to existing "IPOP" Si-SiC hybrid inverters, this topology adopts a coupling step-down transformer on the output side of both LFPC-C and HFPC-C, which can effectively reduce current stress of HFPC-C SiC devices. Additionally, a dual-frequency harmonic elimination modulation strategy based on the topology is proposed to solve the fractional harmonics caused by the LFPC-C. The paper establishes a mathematical model according to the harmonic distribution characteristics of the LFPC-C and HFPC-C, and designs the system control schedules. Building upon the derivation of the voltage ripple model and the design of hardware parameters, Si IGBT and SiC MOSFET were selected for constructing a 7.5 kW prototype for testing, and the experimental results validate the feasibility of this topology and the accuracy of theoretical analysis.

KEYWORDS

fractional power processing, harmonic compensation, dual-frequency harmonic elimination modulation strategy, multiple quasi-proportional resonance control, recursive discrete fourier transform, SHEPWM, Si-SiC inverter

1 Introduction

SiC MOSFET devices, leveraging their superior material properties, have become a key factor in enhancing the efficiency and power density of inverters, especially in high-frequency applications (Millán et al., 2014). The efficiency of inverters can reach as high as 99.4% (Miyazaki et al., 2018). Currently, SiC MOSFET devices have been successfully applied in naval and equipment power supply (Jones et al., 2016; Anurag et al., 2022), microgrids (Burkart and Kolar, 2017), and MMC (He et al., 2022).

However, SiC devices are costly and have a smaller current capacity, resulting in their rated power being lower than Si devices at the same voltage level. As shown in Figure 1, at

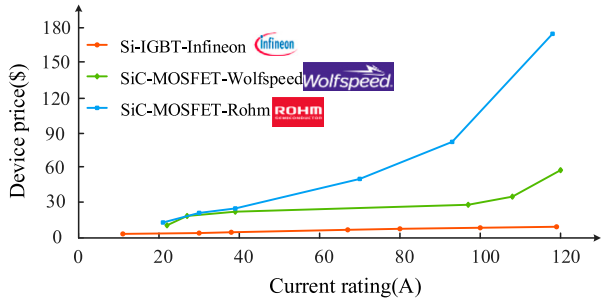

FIGURE 1
Price comparison between Si IGBT and SiC MOSFET from mainstream manufacturer.

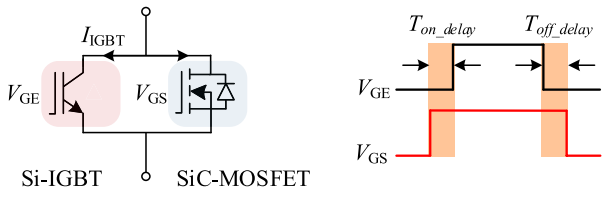

FIGURE 2
Si-SiC hybrid switch.

high currents, the current cost of SiC devices is significantly higher than that of Si devices. Therefore, it is necessary to maximize the advantages of SiC devices in high-power scenarios while reducing the cost of the inverter. Currently, to overcome the limitation of the low rated current of SiC devices, scholars are combining Si devices with SiC devices. This combination leverages the low switching loss characteristics of SiC devices and the strong current-carrying capacity and cost-effectiveness of Si devices. The design approach of using both types of devices together brings about good electrical power quality and efficiency at a cost lower than a full SiC device design. There are two solutions to address this: one is to parallel SiC devices with Si devices at the switch device level to form a Si-SiC hybrid switch (Rahimo et al., 2015; Song et al., 2015; Zhao and He, 2015; Zhang et al., 2018); the other is based on the principle of Fractional Power Processing (Di Gioia and Brown, 2015; Kundu et al., 2020) at the topology level, constituting a Si-SiC hybrid inverter.

The Si-SiC hybrid switch, as shown in Figure 2, can apply gate-source drive voltage to the SiC MOSFET and gate-emitter drive voltage to the Si-IGBT respectively. The turn-on delay and turn-off delay ensure zero voltage turn-on and turn-off of Si-IGBT, reducing switching losses and improving the efficiency and load capacity of the entire system (Li et al., 2020a). Reference (Deshpande and Luo, 2019) proposed an algorithm using dynamic junction temperature prediction to select the optimal Si-SiC current ratio, ensuring reliable operation of the hybrid switch. Reference (Li et al., 2020b) introduced an active gate delay control strategy based on an electro-thermal coupling loss model. This strategy dynamically adjusts and optimizes the gate delay time according to the operating conditions of the power converter, minimizing the working junction

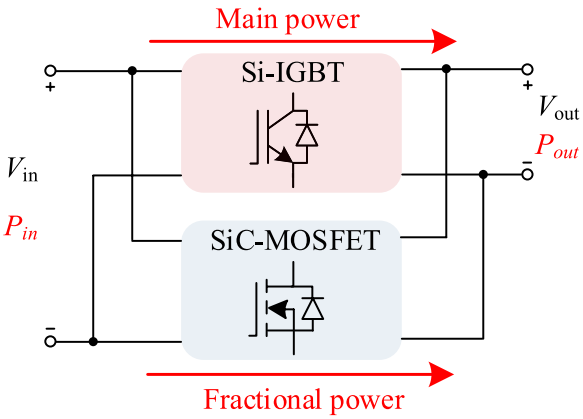

FIGURE 3
Si-SiC hybrid converter.

temperature difference between the two internal devices. Reference (Woldegiorgis et al., 2023) provided a comprehensive review and performance comparison of existing gate control strategies, gate driver designs, and packaging methods for Si-SiC hybrid switches. Design principles and guidelines were given for gate control strategies. However, significant progress in the commercial manufacture of Si-SiC hybrid switch modules has yet to be achieved.

Currently, most Si-SiC hybrid converters based on the Fractional Power Processing (FPP) principle consist of two parallel parts, as shown in Figure 3: one part comprises Si IGBT devices operating at low frequency to handle the main power, while the other part consists of SiC MOSFET devices operating at high frequency to process only a small portion of the total power. Both parts are connected in parallel on the input and output sides, forming an input-parallel and output-parallel structure. The Si-SiC hybrid converter divides the power processing path into two parallel paths. By setting the switching information of the S IGBT and SiC MOSFET devices, the continuous energy signal is converted into two discrete energy signals with different numerical values. These signals are then reconstructed and combined into the final continuous energy output through passive components (Kundu et al., 2021; Wang et al., 2022). Compared to topologies with all SiC MOSFET devices, this kind of topology achieves a reduction in circuit cost while maintaining almost the same efficiency and power quality. Based on intelligence particle swarm optimization (PSO), reference (Zhang et al., 2023) propose a novel adaptive power-sharing and switching frequency control, it can reduce the power losses of the Si-SiC hybrid converter through a simple fitness function. Reference (Endres and Ackva, 2015) proposes a combination topology where the converter composed of Si-IGBT devices carries the main load current, while the converter composed of SiC MOSFET devices is used for ripple current compensation. A common-mode current suppression strategy for this combined topology is also proposed. Reference (Judge and Finney, 2019) verifies that the parallel hybrid converter significantly increases the effective switching frequency at the megawatt power level, reducing the need for external filters and increasing the current control bandwidth of the converter. References (Wu et al., 2022; Wu et al., 2019) design a ripple compensation direct digital control

strategy that attenuates low-frequency current ripple to a small level and increases the frequency of the output current ripple, thereby reducing the volume and weight of the filter. Reference (Zhang et al., 2022) summarizes the characteristics of the input-parallel and output-series hybrid topology based on the FPP principle and proposes a hybrid bridge arm design method based on current harmonic elimination. The proposed design method can be implemented in various converters and has been validated in a bidirectional DC/DC converter. Unlike the "input-parallel and output-series "structure in the aforementioned references, the converter proposed in reference (Liu et al., 2022) has a parallel DC input and a series AC output through a transformer on the AC side, forming a "input-parallel and output-series" structure, aimed at harmonic control of the inverter output voltage.

Based on the concept of Fractional Power Processing (FPP), this paper introduces a hybrid Si-SiC three-phase inverter composed of Si IGBT and SiC MOSFET devices, following the "input-parallel and output-series" topology structure. The low-frequency power conversion cell (LFPC-C) consists of Si IGBT devices and LC filters to handle the main power output. The high-frequency power conversion cell (HFPC-C) is composed of SiC MOSFET devices and LC filters, designed to compensate for the harmonics generated in the LFPC-C. The outputs of the LFPC-C and HFPC-C are connected in series through a three-phase five-column intermediate voltage transformer, reducing the current stress on SiC MOSFET in the HFPC-C. This topology leverages the strong conduction capabilities of Si IGBT and the low switching losses of SiC MOSFET during high-frequency operation. The proposed hybrid modulation strategy and coordinated control method, "LFPC-C open-loop, HFPC-C closed-loop" reduce the complexity of the control system. Hardware design methods are also presented based on the frequency characteristics of the LFPC-C and HFPC-C.

The rest of this article is organized as follows. Section 2 introduces the topology principle and dual-frequency harmonic elimination modulation strategy. In Section 3, it derives the frequency-domain mathematical model and proposes the control method. Section 4 analyzes its hardware characteristics, proposes a voltage ripple analysis model, and outlines the design principles for the filter and three-phase five-column medium-frequency step-down transformer. In Section 5, the feasibility of the topology is validated through the experimental setup. Finally, Section 6 concludes this article.

2 Topology of proposed inverter and harmonic elimination methods

2.1 Topology of proposed inverter

The proposed hybrid Si-SiC three phase inverter topology, as shown in Figure 4, consists of a low-frequency power conversion cell (LFPC-C),a high-frequency power conversion cell (HFPC-C) and a three-phase five-column medium-frequency step-down transformer. The input side is parallel and shared by a common DC source, and the outputs are coupled in series through the transformer. The LFPC-C employs Si IGBT devices as switching devices denoted as S1 ~ S6, operating at a low switching frequency to deal with the main power of the proposed three-phase inverter. The HFPC-C uses SiC MOSFET devices as switching devices denoted as Q1 ~ Q6, operating at a high switching frequency to handle fractional power. The transformer turns ratio is denoted as k, with the primary side parallel-coupled to the output filtering capacitor of the HFPC-C and the secondary side series-coupled and connected to the LFPC-C.

This topology realizes power sharing in two power conversion cells. Under the same DC side voltage, this topology reduces the switching losses of Si IGBT devices in the LFPC-C. Additionally, the step-down transformer ensures that the working current in the HFPC-C is less than the output current in the LFPC-C, reducing the current stress on SiC MOSFET devices and lowering on-state losses in the HFPC-C. The switching losses are concentrated on SiC MOSFET devices, and leveraging their excellent characteristics helps reduce the system's overall switching losses.

2.2 Dual-frequency harmonic elimination modulation strategy

The LFPC-C is responsible for the energy output of the system. However, due to its operation at a low frequency, it can lead to lower electrical energy quality in the final output of the system. Therefore, the HFPC-C needs to compensate and eliminate some of the harmonics present in the LFPC-C t to enhance the overall electrical energy quality of the system. The final output voltage of the system is composed of the voltage in the LFPC-C and the voltage on the secondary side of the transformer. The voltage in the LFPC-C is composed of the fundamental voltage and the harmonic voltage, while represents the output voltage of the HFPC-C. The relationship between these variables can be expressed as follows

$$\begin{cases} V_{out} = u_h - v_{SiC} \\ u_h = u_h^{(1)} + u_h^{(h)} \\ v_{SiC} = V_{SiC}/k \end{cases} \tag{1}$$

The bridge arm output characteristics of the LFPC-C significantly impact the overall system performance. Specific Harmonic Elimination Pulse Width Modulation (SHEPWM) technology can eliminate particular harmonics, and the switching angles can be calculated through computations. SHEPWM operates at a low switching frequency, which helps in reducing the switching losses of the Si-IGBT devices. When using traditional SHEPWM to eliminate harmonics in the mid to low frequency range, it results in a large number of switching angles and necessitates a higher switching frequency. By serially connecting the HFPC-C and the transformer to the output circuit of the LFPC-C, certain harmonics in the bridge arm output of the LFPC-C can be eliminated. This approach ensures a reduction in the switching frequency of Si-IGBT devices in the LFPC-C, thus reducing switching losses while maintaining the total amount of eliminated output harmonics. In the HFPC-C, a Hybrid Sinusoidal Pulse Width Modulation (Hybrid SPWM) is employed. Hybrid SPWM refers to modulating the waveform, which is not a single-frequency sine wave but is determined by the superposition of multiple harmonic waves.

The collaborative elimination of mid to low-frequency harmonics by the LFPC-C and the HFPC-C involves segmenting the mid to low-frequency harmonics. Two technical approaches can be considered based on the harmonic distribution characteristics in the LFPC-C:

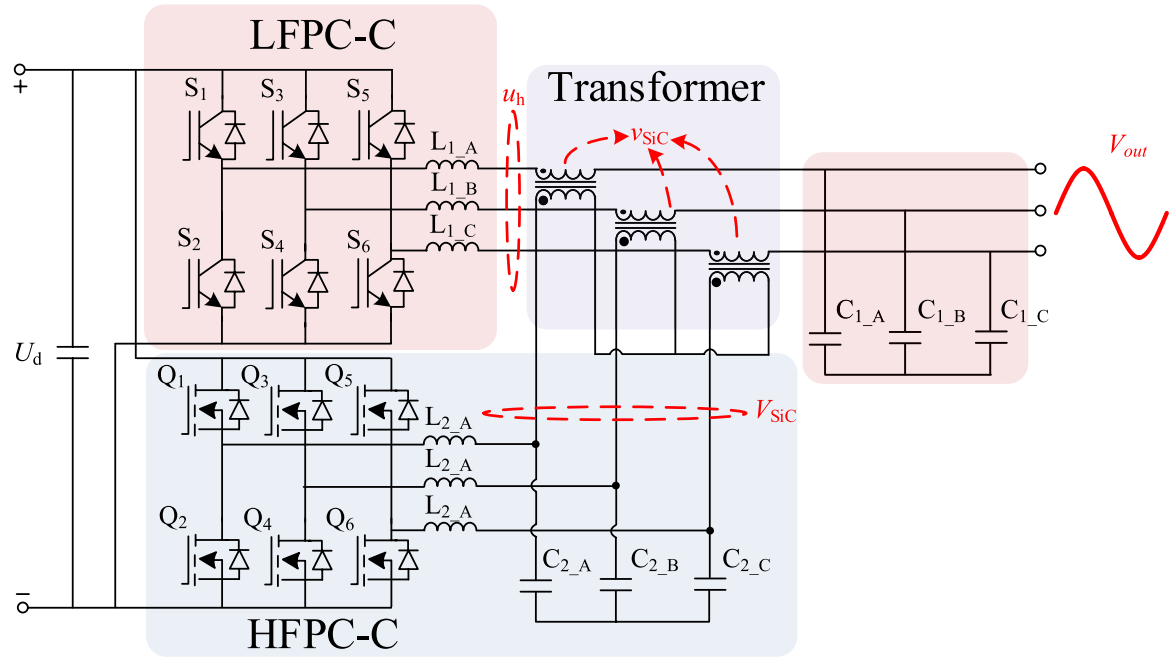

FIGURE 4
The proposed hybrid Si-SiC three phase inverter topology.

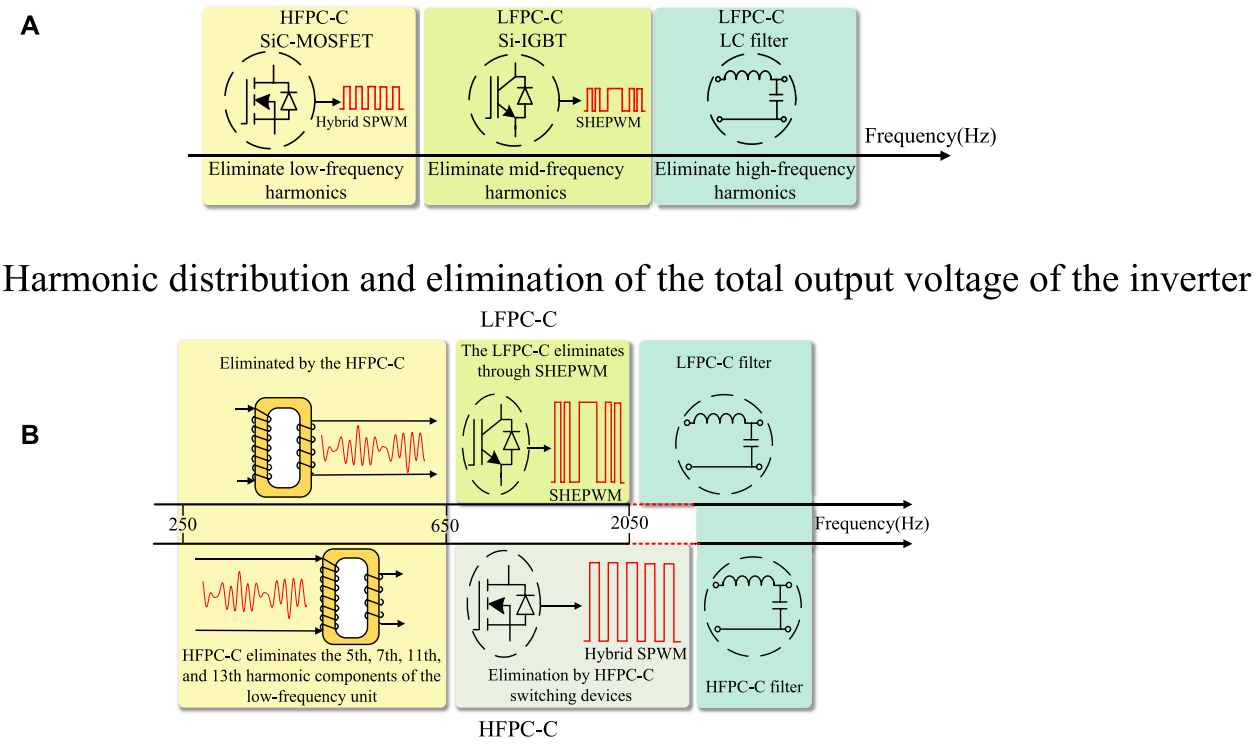

FIGURE 5
Harmonic distribution and elimination of the inverter.

Method 1: The LFPC-C eliminates mid-frequency and high-frequency harmonics, while the HFPC-C eliminates low-frequency harmonics.

Method 2: The LFPC-C eliminates low-frequency and high-frequency harmonics, and the HFPC-C eliminates mid-frequency harmonics.

According to the residual harmonic distribution characteristics of SHEPWM (Cheng, 2021), both methods merely shift the harmonic energy to other frequency bands. However, when employing Method 2, where the LFPC-C eliminates low-frequency and high-frequency harmonics, and the mid-frequency harmonics are eliminated by the HFPC-C, it results in the HFPC-C handling harmonics excessively. The equivalent harmonic frequency within one power cycle can reach several kilohertz, demanding higher requirements for the control system and switching frequency of SiC MOSFET devices in the HFPC-C, thus increasing the switching losses of SiC MOSFET devices. Therefore, Method one is adopted, where the LFPC-C eliminates mid-frequency and high-frequency harmonics while the HFPC-C eliminates low-frequency harmonics. As illustrated in Figure 5A, the LFPC-C is responsible for system energy output, using SHEPWM to remove mid-frequency harmonics. The low-frequency harmonics are eliminated by the HFPC-C, and the high-frequency harmonics are eliminated by the LFPC-C's filter. The HFPC-C compensates and eliminates low-frequency harmonics in the LFPC-C.

When employing the first technical approach, the specific division of mid to low-frequency harmonics and the modulation degree of the hybrid modulated waves m_x in the HFPC-C, as well as the selection of transformer turns ratio k, pose constraints. The effective division and treatment of mid to low-frequency harmonics in the LFPC-C and determining the appropriate modulation degree in the HFPC-C are essential for achieving effective harmonic elimination. Additionally, the choice of transformer turns ratio is crucial as it impacts the coupling between the high-frequency and LFPC-C, thereby influencing the overall harmonic elimination performance and system efficiency. Careful consideration and proper optimization of these parameters are necessary to ensure optimal performance in mitigating harmonics and achieving efficient energy conversion in the system.

The low-frequency harmonics to be eliminated in the LFPC-C represent a modulation signal composed of multiple harmonics for the HFPC-C. In SHEPWM modulation, once the fundamental modulation degree and switching angles are determined, the remaining harmonic superposition waveform becomes fixed. The LFPC-C uneliminated low-frequency harmonic family can be represented as $u_h^{(h\_low)}$.

When a three-phase inverter is connected to a balanced load on the output side, The third harmonic and its multiples cancel each other out in the line-to-line voltage, hence we only need to focus on eliminating 6k±1 harmonics (k = 1, 2, 3, ...).

In a three-phase half-bridge configuration, peak value of the output phase voltage U_{phm} is:

$$U_{phm} = 0.5 m_{SiC}(t) U_d \tag{1a}$$

The variable $m_{SiC}(t)$ represents the modulation index for the hybrid sinusoidal carrier modulation in the HFPC-C. The expression for the hybrid modulated wave $m_{SiC}(t)$ is:

$$m_{SiC}(t) = m_5 \sin(5\omega t + \theta_5) + \cdots + m_i \sin(i\omega t + \theta_i) \tag{2}$$

The transformer is a crucial coupling component connecting the LFPC-C and the HFPC-C. Through its turns ratio k, a relationship between Eqs 1, 2 is established, yielding the following correlation

$$k \le \frac{m_{SiC}(t) U_d}{2 u_h^{(h\_low)}} \tag{3}$$

The modulation index of the HFPC-C and the transformer turns ratio constrain each other. If the turns ratio k is chosen to be too large, it can lead to over-modulation in the HFPC-C. This over-modulation can introduce harmonics from other frequency bands into the output voltage of the LFPC-C, thereby degrading the quality of the output waveform. On the other hand, if the turns ratio k is chosen to be too small, it can cause the current in the HFPC-C to approach the output current in the main circuit, increasing the current cost of SiC MOSFET devices.

The LFPC-C in this paper is responsible for eliminating harmonics from the 17th to the 41st order. Meanwhile, the HFPC-C compensates and eliminates the fifth, seventh, 11th, and 13th order harmonics.

The bridge arm output voltage waveform of the LFPC-C using SHEPWM is shown in (Supplementary Figure S1).

The output waveform in Figure 6 is symmetric about a 1/4 period, and it can be represented using a Fourier series as follows

$$u(\omega t) = \sum_{n=1,17\cdots}^{41} a_n \sin n\omega t \tag{4}$$

In the equation, a_n represents the amplitude of harmonics. The expressions for the fundamental and the 17th to 41st harmonic components are as follows:

$$\begin{cases} a_1 = \dfrac{2V_d}{n\pi} \sum_{i=1}^{10} (-1)^{i+1} \cos n\alpha_i = \mathrm{U}_1 \\ a_{17} = \dfrac{2V_d}{n\pi} \sum_{i=1}^{10} (-1)^{i+1} \cos n\alpha_i = 0 \\ a_{19} = \dfrac{2V_d}{n\pi} \sum_{i=1}^{10} (-1)^{i+1} \cos n\alpha_i = 0 \\ \vdots \\ \vdots \\ a_{41} = \dfrac{2V_d}{n\pi} \sum_{i=1}^{10} (-1)^{i+1} \cos n\alpha_i = 0 \end{cases} \tag{5}$$

In the equation, α_i represents the switching angle. The modulation ratio m is defined as (Dong et al., 2024)

$$m = \frac{U_1}{U_d/2} \tag{6}$$

The HFPC-C employs hybrid sinusoidal pulse width modulation technique, where the modulation wave is composed of fifth, seventh, 11th, and 13th harmonic sinusoidal waves. The expression is:

$$\begin{aligned} m_{SiC}(t) = {} & m_5 \sin(5\omega t + \theta_5) + m_7 \sin(7\omega t + \theta_7) \\ & + m_{11} \sin(11\omega t + \theta_{11}) + m_{13} \sin(13\omega t + \theta_{13}) \end{aligned} \tag{7}$$

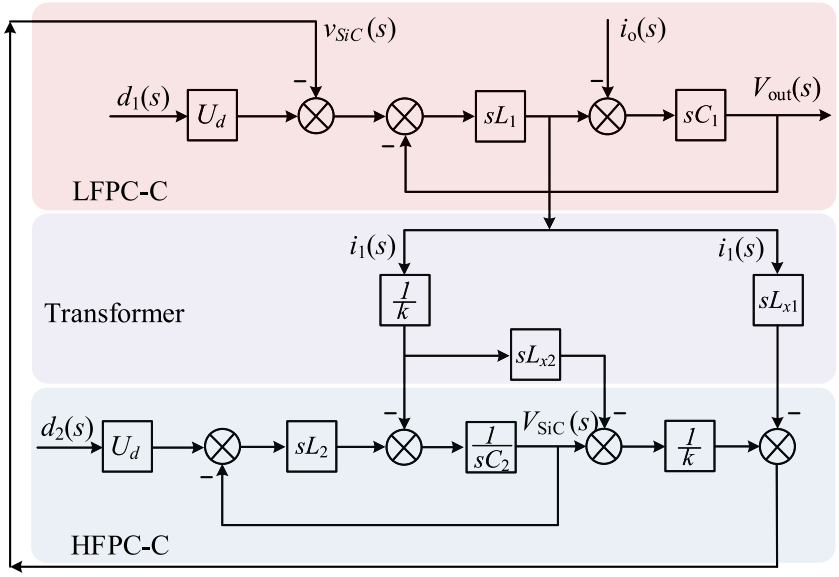

FIGURE 6
Mathematical model in frequency domain.

Taking the modulation index m = 0.97 as an example, the schematic diagram of the modulated wave and the triangular carrier wave for the HFPC-C is shown in (Supplementary Figure S2).

3 Mathematical model and control methods of the proposed inverter

In this section, based on the time-domain coupling relationship of the 2 cells mentioned above, a frequency-domain mathematical model is established. Frequency domain analysis of the system is conducted, and a control method for the system is proposed.

3.1 Mathematical models

The mathematical model is as shown in Figure 6, and there are two switch degrees of freedom, denoted as $d_1(s)$ and $d_2(s)$, in the overall control circuit. and L_{x1}、 L_{x2} respectively refer to the leakage inductance on the secondary and primary sides of the transformer.

The relationship between $V_{SiC}(s)$, $d_2(s)$ and $i_1(s)$ can be deduced from the block diagram.

$$V_{SiC}(s) = \frac{U_d}{1 + L_2C_2s^2}d_2(s) + \left(\frac{L_2s}{1 + L_2C_2s^2} - L_{x2}s\right)\frac{i_1(s)}{k} \tag{8}$$

$H(s)$ can be represented as:

$$H(s) = \frac{\frac{L_2s}{1+L_2C_2s^2} - L_{x2}s}{k} \tag{9}$$

and

$$v_{SiC}(s) = \frac{V_{SiC}(s)}{k} + sL_{x1}i_1(s) \tag{10}$$

The relationship between $v_{SiC}(s)$, $d_2(s)$ and $i_1(s)$ can be derived as follows:

$$v_{SiC}(s) = \frac{U_d}{k(1 + L_2C_2s^2)}d_2(s) + \left(\frac{H(s)}{k} + L_{x1}s\right)i_1(s) \tag{11}$$

If the secondary-side leakage inductance is attributed to the LFPC-C filter inductance, $L_1' = L_1 + L_{x1}$, If we consider $v_{SiC}(s)$ as an input for the LFPC-C, we can create an equivalent system diagram.

Let $d_2(s)$ and $i_o(s)$ be 0 separately, and determine the relationship between $V_{out}(s)$ and $d_1(s)$

$$V_{out}(s) = \frac{U_d d_1(s)}{1 + \frac{C_1H(s)}{k}s + L_1'C_1s^2} \tag{12}$$

Let $d_1(s)$ and $i_o(s)$ be 0 separately, and determine the relationship between $V_{out}(s)$ and $d_2(s)$

$$V_{out}(s) = \frac{-U_d d_2(s)}{k(1 + L_2C_2s^2)\left(1 + \frac{C_1H(s)}{k}s + L_1'C_1s^2\right)} \tag{13}$$

Let $d_1(s)$ and $d_2(s)$ be 0 separately, and determine the relationship between $V_{out}(s)$ and $i_o(s)$

$$V_{out}(s) = -\frac{L_1's + \frac{H(s)}{k}}{1 + L_1'C_1s^2 + \frac{H(s)C_1}{k}s}i_o(s) \tag{14}$$

Finally, we can obtain the following expression:

$$V_{out}(s) = G(s)\left[U_d\left(d_1(s) - \frac{d_2(s)}{k(1 + L_2C_2s^2)}\right) - \left(L_1's + \frac{H(s)}{k}\right)i_o(s)\right] \tag{15}$$

$G(s)$ can be expressed as

$$G(s) = \frac{1}{1 + L_1'C_1s^2 + \frac{H(s)C_1}{k}s} \tag{16}$$

3.2 Integrated coordinated control method

From Eqs 13, 14, it can be seen that the circuit has two degrees of freedom, $d_1(s)$ and $d_2(s)$. The choice of closed-loop control target is also related to the level of control difficulty. If the overall output voltage V_{out} of the system is chosen as the closed-loop target voltage, we need to consider not only $d_2(s)$ but also the impact of $d_1(s)$. Here, $d_1(s)$ represents the SHEPWM modulation of the LFPC-C, which has drawbacks such as real-time complex computation and poor dynamic adjustment performance. Having two input variables significantly increases the difficulty of closed-loop control.

Since the control objective is to compensate for the secondary-side voltage of the transformer, fundamentally, the closed-loop control aims to control the secondary-side voltage of the transformer. Therefore, in designing the closed-loop control circuit, the effect of the LFPC-C current on the HFPC-C can be considered as a disturbance. We propose a coordinated control method, "LFPC-C open-loop, HFPC-C closed-loop". In this approach, the LFPC-C uses open-loop SHEPWM control to adjust the voltage by only adjusting the fundamental modulation ratio, reducing the control difficulty for the HFPC-C. The HFPC-C achieves precise voltage regulation, compensating for the limitations of SHEPWM.

When processing the fifth, seventh, 11th, and 13th harmonic components in the HFPC-C and extracting the control system's reference signal, the following two points need to be considered:

1) The physical sampling point is located between the inductance of the LFPC-C and the secondary side of the transformer. The sampled voltage still contains the uneliminated high-frequency harmonics, which are not the target of the HFPC-C tracking control.
2) Regarding the selected fifth, seventh, 11th, and 13th harmonic components frequency domain characteristics: zero gain and zero phase shift.

Considering the above two points, Recursive Discrete Fourier Transform is used to meet the aforementioned requirements. The expression is as follows:

$$G^i_{RDFT} = \sum_{i=5、7、11、13} \frac{2}{N} \frac{\left(1-z^{-N}\right)\left(1-z^{-1}\cos 2\pi\frac{i}{N}\right)}{\left(1-z^{-1}e^{j2\pi\frac{i}{N}}\right)\left(1-z^{-1}e^{-j2\pi\frac{i}{N}}\right)} \tag{17}$$

Amplitude-frequency response and phase-frequency response of $G^i_{RDFT}(s)$ is shown in (Supplementary Figure S3).

The above equation yields the reference signal v_{ref} for the closed-loop control of the HFPC-C, which is then compared with the output voltage v_{SiC} of the transformer secondary side, and obtain the error signal Δv.The control loop consists of voltage and current double loops. Due to the presence of multiple harmonic voltages in the output voltage and the need for high precision, a multiple Quasi-Proportional Resonant (QPR) voltage outer loop is employed to process the error signal Δv, the transfer function is given by:

$$G_{QPR}(s) = K_{pv} + \sum_{i=5、7、11、13} \frac{2K_{iv}w_c s}{s^2 + 2w_c s + w_i^2} \tag{18}$$

ω_i is the angular frequency of the 5th to 13th harmonic components, ω_c is the damping coefficient. K_{iv} is the resonance coefficient, K_{pv} is the proportional coefficient.

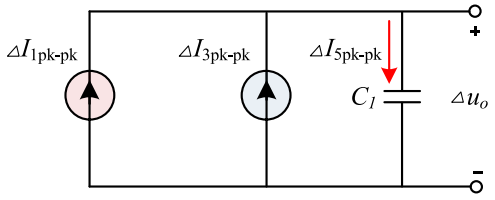

FIGURE 7
Equivalent circuit of LFPC-C ripple current source.

Obtaining the current inner-loop reference signal i_{ref}, sampling the capacitor current to obtain i_c, The inner loop adopts proportional control of the capacitor current to improve

The response speed. Controlling the inner loop with the capacitor current as the control target can increase system damping, suppress resonance, and reduce the difficulty of voltage outer loop control.

$$G_i(s) = K_i \tag{19}$$

The transfer function of the closed-loop control for the HFPC-C is

$$G_v(s) = \frac{K_i U_d}{L_2 C_2 s^2 + C_2 K_i U_d s + 1} G_{QPR}(s) \tag{20}$$

The overall control policy is shown in Supplementary Figure S4.

4 Key parameters design of proposed inverter

4.1 Voltage ripple analysis

When considering voltage compensation by the HFPC-C for the LFPC-C, it is necessary to establish a steady-state voltage ripple model. The primary side of the series-coupled transformer is connected in parallel across the filtering capacitor of the HFPC-C. Neglecting the fundamental component in the circuit, the ripple in the primary-side voltage is equivalent to a voltage source ΔU_2 on the secondary side, As shown in (Supplementary Figure S5), there are two voltage sources in the LFPC-C circuit, and the corresponding ripple currents are shown in Figure 7, the ripple current generated by the output voltage U_{Si} and the inductance L_1 in the LFPC-C bridge arm is denoted by ΔI_{3pk-pk} (Mao et al., 2009), and its expression is as follows:

$$\Delta I_{1pk-pk} = \frac{U_d T_{s1}}{L_1}\left[1 - D_{Si}(t)\right] D_{Si}(t) \tag{21}$$

In the equation, T_{s1} represents the switching period, $D_{Si}(t)$ denotes the average duty cycle. Due to the adoption of SHEPWM modulation in the LFPC-C, by calculating for different switching signal sequences, $D_{Si}(t)$ for one complete switching action can be obtained.

$$D_{Si}(t) = \frac{\sum_{i=1}^{N-1}(\alpha_{i+1} - \alpha_i)}{2\pi} T_s \tag{22}$$

ΔI_{3pk-pk} represents the ripple current generated in the LFPC-C circuit under the excitation of ΔU_2, and its expression is:

$$\begin{cases} \Delta I_{3\,pk-pk} = \dfrac{\Delta U_2}{z} \\ z = w_x L - \dfrac{1}{w_x C} \end{cases} \tag{23}$$

The total ripple current ΔI_{5pk-pk} in the LFPC-C is constituted by the two equivalent ripple current sources ΔI_{1pk-pk} and ΔI_{3pk-pk}:

$$\Delta I_{5pk-pk} = \Delta I_{1pk-pk} + \Delta I_{3pk-pk} \tag{24}$$

The expression for the total output ripple voltage ΔU_o is given by:

$$\Delta U_o = \frac{T_{s1}^3 U_d (\omega_x L_1 C_1 - 1)\left[2\pi - \left(\sum_{i=1}^{N-1} \alpha_{i+1} - \alpha_i\right)\right]\left(\sum_{i=1}^{N-1} \alpha_{i+1} - \alpha_i\right) + 4\pi^2 L_1 C_1 \omega_x \Delta U_2}{32 L_1 C_1 f_{s1} \pi^2 \left(\omega_x^2 L_1 C_1 - 1\right)} \tag{25}$$

The ripple analysis for the HFPC-C is illustrated in Figure 10.

The parameter ΔI_{2pk-pk} is determined by the output voltage U_{SiC} of the HFPC-C bridge arm, the inductance L_2, and the amplitude m_{SiC} of the non-sinusoidal fundamental modulation wave. The expression is as follows:

$$\Delta I_{2pk-pk} = \frac{U_d T_{s2}}{L_2} (1 - m_{SiC}|\sin \omega t|) m_{SiC}|\sin \omega t| \tag{26}$$

The ripple in the output current of the LFPC-C bridge arm is represented by ΔI_{5pk-pk}, and it can be equivalently modeled as ΔI_{6pk-pk} on the primary side of the series-coupled transformer.

$$\Delta I_{6pk-pk} = \frac{\Delta I_{5pk-pk}}{k} \tag{27}$$

The total ripple current ΔI_{4pk-pk} in the HFPC-C is formed by the combination of the two equivalent ripple current sources ΔI_{2pk-pk} and ΔI_{6pk-pk}.

$$\Delta I_{4pk-pk} = \Delta I_{2pk-pk} + \Delta I_{6pk-pk} \tag{28}$$

The ripple voltage on the filter capacitor of the HFPC-C is represented by ΔU_1

$$\Delta U_1 = \frac{\Delta I_{4pk-pk}}{8 C_2 f_{s2}} \tag{29}$$

Based on $\Delta U_2 = \Delta U_1/k$, ΔU_2 can be determined as follows:

$$\Delta U_2 = \frac{k U_d T_{s2} (\omega_x{}^2 L_1 C_1 - 1)(1 - m_{SiC}|\sin \omega t|)}{8 L_2 C_2 f_{s2} k^2 \left(\omega_x^2 L_1 C_1 - 1\right) - \omega_x C_1} m_{SiC}|\sin \omega t| \tag{30}$$

Substituting into Eq. 26, ΔU_o is determined as follows:

$$\begin{cases} \Delta U_o = \dfrac{Y \bullet [8 L_2 C_2 f_{s2} k^2 (\omega_x^2 L_1 C_1 - 1) - \omega_x C_1] + 4\pi^2 L_1 C_1 \omega_x k U_d T_{s2} (\omega_x{}^2 L_1 C_1 - 1)(1 - m_{SiC}|\sin \omega t|) m_{SiC}|\sin \omega t|}{[32 L_1 C_1 f_{s1} \pi^2 (\omega_x^2 L_1 C_1 - 1)] \bullet [8 L_2 C_2 f_{s2} k^2 (\omega_x^2 L_1 C_1 - 1) - \omega_x C_1]} \\ Y = T_{s1}^3 U_d (\omega_x L_1 C_1 - 1)\left[2\pi - \left(\sum_{i=1}^{N-1} \alpha_{i+1} - \alpha_i\right)\right]\left(\sum_{i=1}^{N-1} \alpha_{i+1} - \alpha_i\right) \end{cases} \tag{31}$$

Supplementary Figure S7, Figure 8 in Additional files illustrates the ratio of output voltage ripple to DC voltage on the direct current (DC) side based on Eq. 31 for different parameters chosen for L_1 and L_2.

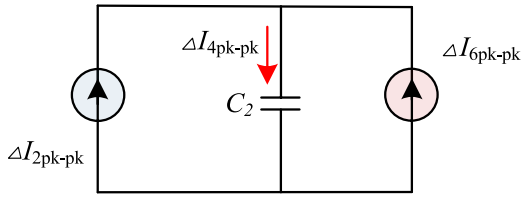

FIGURE 8
Equivalent circuit of ripple current source in HFPC-C.

4.2 Design of second-order filters for LFPC-C and HFPC-C

As shown in Figure 5B above, the filters in the low-frequency and HFPC-C filter different ranges of harmonics. Additionally, the compensation of voltage ripples in the HFPC-C and the final circuit output ripples in the LFPC-C, as analyzed in the previous section, are closely related to the selection of passive components L_1、L_2、$C_1$and C_2 in the circuit. Considering the constraints mentioned above, frequency domain constraints also need to be taken into account.

For the LFPC-C, as shown in Figure 5B above, the harmonics from the 5th to the 13th order are eliminated through the HFPC-C, and the harmonics from the 17th to the 41st order are already eliminated through SHEPWM. The remaining harmonics in the high-frequency range are eliminated through a second-order low-pass LC filter. The cutoff frequency f_{Si} of the second-order filter should be set in the mid-frequency range, specifically between 650 Hz and 2050 Hz:

$$\begin{aligned} f_{Si} &= \frac{1}{2\pi\sqrt{L_1 C_1}} \\ 650Hz < f_{Si} &< 2050Hz \end{aligned} \tag{32}$$

Simultaneously, to prevent resonance peaks in the LFPC-C filter and to amplify the fifth, seventh, 11th, and 13th harmonics, increasing the compensation difficulty for the HFPC-C, requirements are imposed on the damping coefficient of the filter ζ:

$$\begin{aligned} \zeta &= \frac{1}{2R_1}\sqrt{\frac{L_1}{C_1}} \\ \zeta &\le 0.7 \end{aligned} \tag{33}$$

The HFPC-C compensates for the highest harmonic frequency at 650 Hz. The selected switching frequency is 30 kHz, and the upper limit for the filter cutoff frequency f_{SiC} is set to 3000 Hz, with a lower limit of 1000 Hz. This setting ensures that the highest compensating harmonic (650 Hz) can pass through without attenuation, providing an allowance:

$$\begin{aligned} f_{SiC} &= \frac{1}{2\pi\sqrt{L_2 C_2}} \\ 1000Hz < f_{SiC} &< 3000Hz \end{aligned} \tag{34}$$

4.3 Design of three-phase five-column medium-frequency step-down transformer

Due to the non-sinusoidal periodic components of the input terminal voltage injected into the transformer, which is a

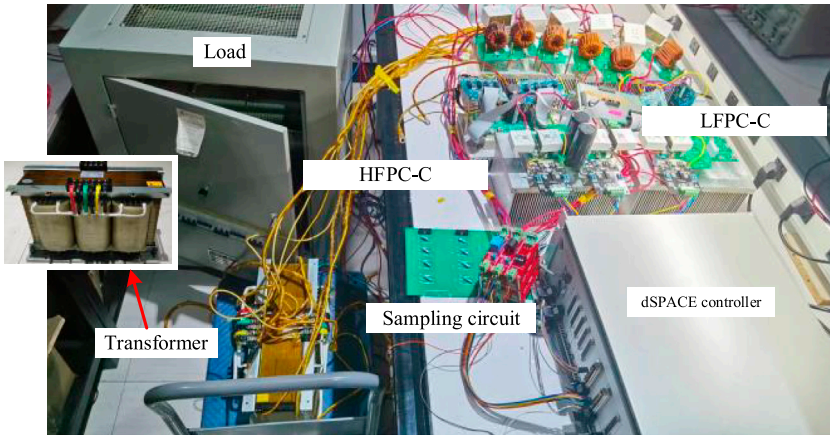

FIGURE 9
Experimental prototype.

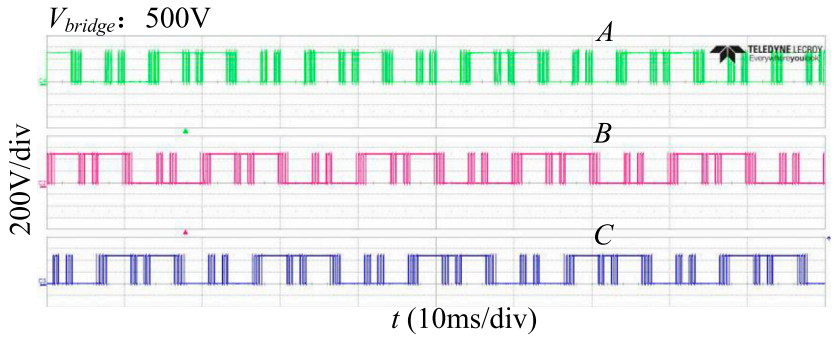

FIGURE 10
LFPC-C bridge arm output voltage.

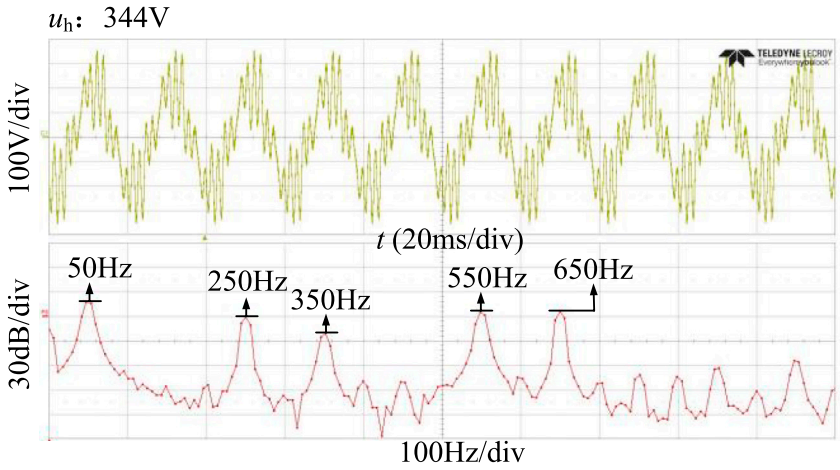

FIGURE 11
The voltage u_h between the inductor of the LFPC-C and the inlet end of the secondary side of the transformer.

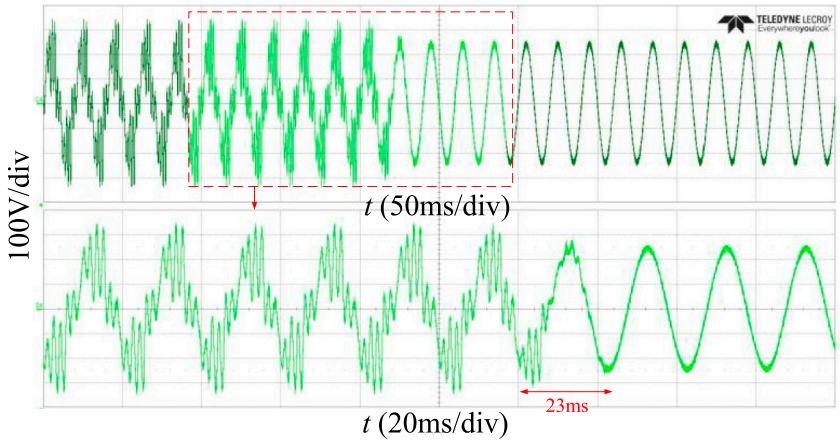

FIGURE 12
Dynamic response of HFPC-C compensation.

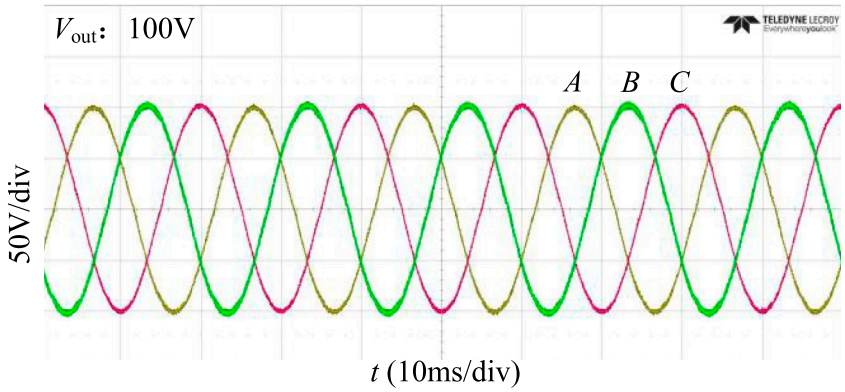

FIGURE 13
When m = 0.4, the final output voltage V_{out} waveform of Inverter.

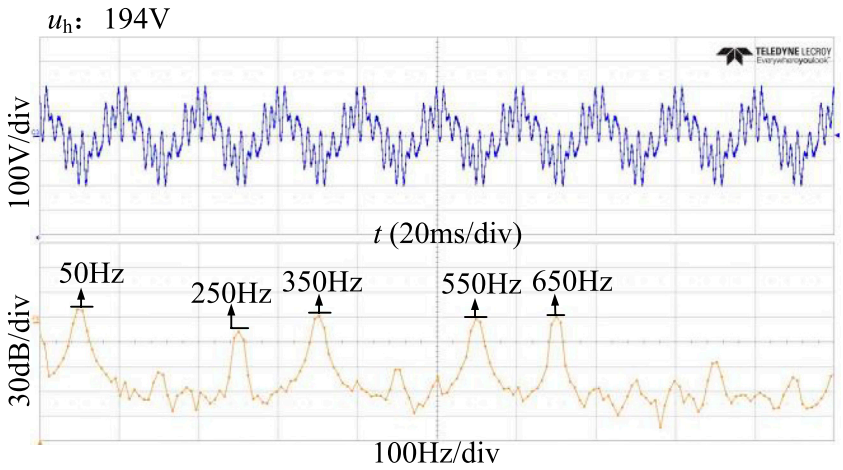

FIGURE 14
The voltage u_h between the inductance of the LFPC-C and the transformer.

superposition of fifth, seventh, 11th, and 13th harmonic voltages, a three-phase five-column medium-frequency transformer is used. This ensures that the high-order harmonic flux can circulate smoothly, and harmonics can flow in the independent magnetic circuits of the three-phase five-column medium-frequency transformer (Leung et al., 2010). When the circuit operates normally, the highest harmonic frequency allowed to pass through is 650 Hz. This necessitates the transformer to have a relatively high passband. Additionally, due to the higher frequency of voltage polarity conversions, losses will increase. Therefore, thin silicon steel sheets are used for the transformer core. Thin silicon steel offers advantages such as high saturation magnetic flux density, ideal loss performance, and low noise. Transformer model is displayed in (Supplementary Figure S9). The length of the transformer is 45cm, the height is 25 cm and the width is 19 cm.

To ensure minimal voltage distortion, it is crucial to maintain the magnetic flux of the transformer in a non-saturated state and operate within the linear region (Li et al., 2011). The magnetic flux density B_i corresponding to each frequency component is:

$$B_i = \frac{U_i}{4.44 f_i N A_c} \tag{35}$$

U_i and f_i represent the effective values and frequencies of each component, N is the turns of the transformer, and A_c is the effective magnetic area of the magnetic circuit. According to the superposition principle, the composite flux density $B_{\max}$ at its maximum can be obtained as follows:

$$B_{\max} = B_5 + B_7 + B_{11} + B_{13} \tag{36}$$

5 Experimental validation

Based on the proposed inverter and control method in this paper, a laboratory prototype with a power rating of 7.5 kW was set up in this section. The experimental setup, as shown in Figure 9, includes a dSPACE controller, a LFPC-C, a HFPC-C, a load, a transformer, and a sampling circuit. The parameters and values used in the experiment are listed in Additional files (Supplementary Table 1).

The output voltage of the LFPC-C bridge arm is shown in Figure 10. It can be observed from Additional files (Supplementary Figure S10) that the bridge arm output voltage V_{bridge} conforms to the SHEPWM modulation principle proposed in Section 2.2, as referenced in Additional files (Supplementary Figure S11).

During steady-state operation, the waveforms of the final output voltage V_{out} and output current I_1 for the LFPC-C, as well as the current I_2 for the HFPC-C, are shown in Additional files (Supplementary Figure S11). Additionally, I_2 and I_1 represent the currents on the primary and secondary sides of the transformer. It can be observed from Additional files (Supplementary Figure S12) that the current in the HFPC-C is approximately half of the current in the LFPC-C.

Figure 11 presents the Fourier Transform (FFT) analysis of u_h. Experimental results demonstrate that the harmonics in the LFPC-C circuit without compensation include a significant amount of 5th to 13th harmonics

Additional files (Supplementary Figure S13) shows the three phase voltage at the primary side of the transformer. Through FFT decomposition, it can be observed that the voltage contains harmonics at 250 Hz, 350 Hz, 550 Hz, and 650 Hz.

Figure 12 verifies the dynamic performance of the system. From the figure, it can be observed that the transient duration for the compensation of the LFPC-C by the HFPC-C is 23 m, demonstrating the rationality of the harmonic extraction and control design.

Supplementary Figure S14 displays the Fourier Transform (FFT) analysis of the output voltage V_{out}. The total harmonic distortion of the output voltage is approximately 1.02%.

Supplementary Figure S15 shows the waveforms of total output voltage, output current, and transformer primary and secondary side voltages for phase A.

Figure 13 depicts the voltage waveform at a low modulation index of m = 0.4, with a peak value of 100V.

Figure 14 and (Supplementary Figure S15) represent the FFT of u_h and the primary side voltage V_{SiC} of the transformer when m = 0.4. The sequence from Figures 13, 14, (Supplementary Figure S16) demonstrate that the proposed inverter can operate effectively under low modulation ratios.

6 Comparative analysis

To demonstrate the efficiency of the proposed converter, a theoretical comparison was made between the proposed converter, a hybrid switch converter, and an Si-IGBT converter. Considering high-power applications, the theoretical converter's DC voltage was set to 800 V, and the efficiency curves are shown in Additional files (Supplementary Figure S17).

From (Supplementary Figure S17), it can be observed that the highest efficiency of the converter proposed in this paper is 98.3%. As the load percentage exceeds 50%, the efficiency of the proposed converter is even higher, demonstrating its advantages under high-power conditions.

From (Supplementary Figure S18), it is evident that under full load conditions, the switching losses of the low-frequency unit Si-IGBT account for only 4% of the total losses. Device losses are primarily concentrated in conduction losses. On the other hand, the device losses of the high-frequency unit SiC-MOSFET account for only 22% of the total losses.

7 Conclusion

In this article, based on fractional power processing, a "input-parallel and output-series" hybrid three-phase inverter consisting of Si IGBT and SiC MOSFET devices is proposed. The LFPC-C is formed by Si IGBT devices, and it employs SHEPWM modulation along with the HFPC-C to eliminate low-frequency and mid-frequency harmonics. This approach allows Si IGBT to handle the main power with minimal switching losses. The HFPC-C consists of SiC MOSFET devices, enabling it to accurately compensate for the LFPC-C low-frequency harmonics while operating with low switching losses. Three-phase five-column medium-frequency step-down transformer reduces the current flowing through the HFPC-C to approximately half of the inverter's output current, minimizing the current stress on SiC

MOSFET devices. This topology leverages the strong conduction capability of Si IGBT and the low switching losses of SiC MOSFET in high-frequency states to reduce device losses in high power conversion applications. Additionally, the proposed "LFPC-C open-loop, HFPC-C closed-loop" coordinated control method simplifies the control system. The ripple voltage analysis model, based on circuit characteristics, guides the passive component design. Task allocation for filtering and transformer components is determined according to the circuit's requirements for harmonics elimination and compensation. Furthermore, a 7.5 kW experimental prototype is constructed to validate the feasibility of this proposed topology.

Data availability statement

The original contributions presented in the study are included in the article/Supplementary Material, further inquiries can be directed to the corresponding author.

Author contributions

QY: Writing–original draft, Writing–review and editing. CL: Writing–original draft, Writing–review and editing, Conceptualization, Data curation, Formal Analysis, Funding acquisition, Investigation, Methodology, Project administration, Resources, Software, Supervision, Validation, Visualization. RL: Writing–original draft, Writing–review and editing, Conceptualization, Data curation, Formal Analysis, Funding acquisition, Investigation, Methodology, Project administration, Resources, Software, Supervision, Validation, Visualization. ZP: Writing–original draft, Writing–review and editing, Conceptualization, Data curation, Formal Analysis, Funding acquisition, Investigation, Methodology, Project administration, Resources, Software, Supervision, Validation, Visualization. DG: Writing–original draft, Writing–review and editing, Conceptualization, Data curation, Formal Analysis, Funding acquisition, Investigation, Methodology, Project administration, Resources, Software, Supervision, Validation, Visualization. TM: Conceptualization, Data curation, Formal Analysis, Funding acquisition, Investigation, Methodology, Project administration, Resources, Software, Supervision, Validation, Visualization, Writing–original draft, Writing–review and editing. XS: Writing–original draft, Writing–review and editing, Conceptualization, Data curation, Formal Analysis, Funding acquisition, Investigation, Methodology, Project administration, Resources, Software, Supervision, Validation, Visualization.

Funding

The author(s) declare that no financial support was received for the research, authorship, and/or publication of this article.

Conflict of interest

The authors declare that the research was conducted in the absence of any commercial or financial relationships that could be construed as a potential conflict of interest.

Publisher's note

All claims expressed in this article are solely those of the authors and do not necessarily represent those of their affiliated organizations, or those of the publisher, the editors and the reviewers. Any product that may be evaluated in this article, or claim that may be made by its manufacturer, is not guaranteed or endorsed by the publisher.

Supplementary material

The Supplementary Material for this article can be found online at: https://www.frontiersin.org/articles/10.3389/fenrg.2024.1375888/full#supplementary-material

References

Anurag, A., Acharya, S., Bhattacharya, S., Weatherford, T. R., and Parker, A. A. (2022). A gen-3 10-kV SiC MOSFET-based medium-voltage three-phase dual active bridge converter enabling a mobile utility support equipment solid state transformer. *IEEE J. Emerg. Sel. Top. Power Electron.* 10 (2), 1519–1536. doi:10.1109/jestpe.2021.3069810

Burkart, R. M., and Kolar, J. W. (2017). Comparative η– ρ– σ pareto optimization of Si and SiC multilevel dual-active-bridge topologies with wide input voltage range. *IEEE Trans. Power Electron.* 32 (7), 5258–5270. doi:10.1109/tpel.2016.2614139

Cheng, J. (2021). *Improved SHEPWM technology and its application in high-power grid-connected inverter*. Hangzhou, China: Zhejiang Univ. Ph.D. dissertation, Dept. Electron. Eng.

Deshpande, A., and Luo, F. (2019). Practical design considerations for a Si IGBT + SiC MOSFET hybrid switch: parasitic interconnect influences, cost, and current ratio optimization. *IEEE Trans. Power Electron.* 34 (1), 724–737. doi:10.1109/tpel.2018.2827989

Di Gioia, A., and Brown, I. P. (2015). "Silicon and hybrid Si-SiC tandem inverter analytical loss characterization and comparison to PWM-modulated voltage source inverter," in Proc. IEEE Energy Convers. Congr. Expo, Montreal, QC, Canada, 4664–4670. doi:10.1109/ecce.2015.7310319

Dong, Z., Wang, C., Zhou, M., Liu, M., and Li, K. (2024). Active NP voltage balance control strategy for three-level three phase inverter under SHEPWM. *Transactions of China Electrotechnical Society* 39 (04), 1147–1158. doi:10.19595/j.cnki.1000-6753.tces.222093

Endres, J., and Ackva, A. (2015). "A parallel three-phase converter system for ripple current compensation and passive filter reduction," in Proc. 17th Eur. Conf. Power Electron, 1–9. Appl. doi:10.1109/epe.2015.7309135

He, Z., Lu, M., Hang, L., Zeng, P., and Liu, Y. (2022). Capacitor voltage imbalance mechanism and balancing control of MMC when riding through PTG fault. *CSEE J. Power Energy Syst.* to be published. doi:10.17775/CSEEJPES.2022.03810

Jones, E. A., Wang, F. F., and Costinett, D. (2016). Review of commercial GaN power devices and GaN-based converter design challenges. *IEEE J. Emerg. Sel. Top. Power Electron.* 4 (3), 707–719. doi:10.1109/jestpe.2016.2582685

Judge, P. D., and Finney, S. (2019). "2-level Si IGBT converter with parallel part-rated SiC converter providing partial power transfer and active filtering," in Proc. 20th Workshop Control Model. Power Electron, 1–7. doi:10.1109/compel.2019.8769710

Kundu, A., Na, R., Amir, A., and Shen, Z. J. (2021). "Optimization strategy of WBG fractional power processing," in Proc. IEEE Appl. Power Electron. Conf. Expo, 896–901. doi:10.1109/apec42165.2021.9487447

Kundu, A., Na, R., Amir, A., Zhou, Y., Brown, I. P., and Shen, Z. J. (2020). "WBG fractional power processing: a new Si-SiC hybrid voltage source inverter design," in Proc. IEEE Energy Convers. Congr. Expo, 6226–6231. doi:10.1109/ecce44975.2020.9236129

Leung, C., Dutta, S., Baek, S., and Bhattacharya, S. (2010). "Design considerations of high voltage and high frequency three phase transformer for Solid State Transformer application," in Proc. IEEE Energy Convers. Congr. Expo, 1551–1558. doi:10.1109/ecce.2010.5618234

Li, P., Dong, J., and Li, T. (2011). Design of coupling transformer in shunt active power filter. *Electrotech. Appl.* 30 (22), 25–27+35.

Li, Z., Wang, J., Deng, L., He, Z., Yang, X., Ji, B., et al. (2020b). Active gate delay time control of Si/SiC hybrid switch for junction temperature balance over a wide power range. *IEEE Trans. Power Electron.* 35 (5), 5354–5365. doi:10.1109/tpel.2019.2942044

Li, Z., Wang, J., He, Z., Yu, J., Dai, Y., and Shen, Z. J. (2020a). Performance comparison of two hybrid Si/SiC device concepts. *IEEE J. Emerg. Sel. Top. Power Electron.* 8 (1), 42–53. doi:10.1109/jestpe.2019.2947252

Liu, C., Zhuang, K., Pei, Z., Zhu, D., Li, X., Yu, Q., et al. (2022). Hybrid SiC-Si DC–AC topology: SHEPWM Si-IGBT master unit handling high power integrated with partial-power SiC-MOSFET slave unit improving performance. *IEEE Trans. Power Electron.* 37 (3), 3085–3098. doi:10.1109/tpel.2021.3114322

Mao, X., Ayyanar, R., and Krishnamurthy, H. K. (2009). Optimal variable switching frequency scheme for reducing switching loss in single-phase inverters based on time-domain ripple analysis. *IEEE Trans. Power Electron.* 24 (4), 991–1001. doi:10.1109/tpel.2008.2009635

Millán, J., Godignon, P., Perpiñà, X., Perez-Tomas, A., and Rebollo, J. (2014). A survey of wide bandgap power semiconductor devices. *IEEE Trans. Power Electron.* 29 (5), 2155–2163. doi:10.1109/tpel.2013.2268900

Miyazaki, T., Otake, H., Nakakohara, Y., Tsuruya, M., and Nakahara, K. (2018). A fanless operating trans-linked interleaved 5 kW inverter using SiC MOSFETs to achieve 99% power conversion efficiency. *IEEE Trans. Ind. Electron* 65 (12), 9429–9437. doi:10.1109/tie.2018.2816004

Rahimo, M., Canales, F., Minamisawa, R. A., Papadopoulos, C., Vemulapati, U., Mihaila, A., et al. (2015). Characterization of a silicon IGBT and silicon carbide MOSFET cross-switch hybrid. *IEEE Trans. Power Electron.* 30 (9), 4638–4642. doi:10.1109/tpel.2015.2402595

Song, X., Huang, A. Q., Lee, M., and Peng, C. (2015). "High voltage Si-SiC hybrid switch: an ideal next step for SiC," in Proc. IEEE 27th Int. Symp. Power Semicond. Devices IC's, 2015 IEEE 27th International Symposium on Power Semiconductor Devices IC's, 289–292. doi:10.1109/ispsd.2015.7123446

Wang, L., Sun, W., Xu, H., Dong, J., Li, C., and Li, W. (2022). "A three-phase-module-parallel Si and SiC hybrid inverter with smaller filter size and low cost," in Proc. IEEE Transp. Electrific. Conf. Expo., Asia-Pacific, 1–6. doi:10.1109/itecasia-pacific56316.2022.9942026

Wang, Z., and Liu, J. (2009). "PWM control technology," in *Power electronics*. 7th ed. (Beijing, China: China Machine Press), 167–168.

Woldegiorgis, D., Hossain, M. M., Saadatizadeh, Z., Wei, Y., and Mantooth, H. A. (2023). Hybrid Si/SiC switches: a review of control objectives, gate driving approaches and packaging solutions. *IEEE J. Emerg. Sel. Top. Power Electron.* 11 (2), 1737–1753. doi:10.1109/jestpe.2022.3219377

Wu, T.-F., Huang, Y.-H., Cheng, W.-C., and Gao, X.-C. (2019). "Ripple-compensation improvement of direct digital controlled 3Φ4W grid-connected hybrid-frequency inverter system," in Proc. IEEE Appl. Power Electron. Conf. Expo, 284–289. doi:10.1109/apec.2019.8722232

Wu, T.-F., Huang, Y.-H., Temir, S., and Chan, C.-C. (2022). 3Φ4W hybrid frequency parallel uninterruptable power supply for reducing voltage distortion and improving dynamic response. *IEEE Trans. Ind. Electron* 10 (1), 906–918. doi:10.1109/jestpe.2021.3099061

Zhang, C., Wang, J., Qu, K., Hu, B., Li, Z., Yin, X., et al. (2022). WBG and Si hybrid half-bridge power processing toward optimal efficiency, power quality, and cost tradeoff. *IEEE Trans. Power Electron.* 37 (6), 6844–6856. doi:10.1109/tpel.2021.3138464

Zhang, C., Yuan, X., Wang, J., Chen, W., Hu, B., and Shen, Z. J. (2023). Adaptive power sharing and switching frequency control for power loss optimization in WBG/Si hybrid half-bridge converters. *IEEE Trans. Power Electron* 38 (4), 4440–4450. doi:10.1109/tpel.2022.3230747

Zhang, Z., Zhang, L., and Qin, J. (2018). "Optimization of delay time between gate signals for Si/SiC hybrid switch," in Proc. IEEE Energy Convers. Congr. Expo, 1882–1886. doi:10.1109/ecce.2018.8557569

Zhao, T., and He, J. (2015). "An optimal switching pattern for "SiC+Si" hybrid device based voltage source converters," in Proc. IEEE Appl. Power Electron. Conf. Expo, Charlotte, NC, USA, 1276–1281. doi:10.1109/apec.2015.7104512

frontiers | Frontiers in Energy Research

TYPE Original Research
PUBLISHED 10 May 2024
DOI 10.3389/fenrg.2024.1403346

OPEN ACCESS

EDITED BY
Haitao Zhang,
Xi'an Jiaotong University, China

REVIEWED BY
Fabio Corti,
University of Florence, Italy
Andrea Toscani,
University of Parma, Italy

*CORRESPONDENCE
Li Daxi,
lidaxi1983@163.com

RECEIVED 19 March 2024
ACCEPTED 12 April 2024
PUBLISHED 10 May 2024

CITATION
Shulin C, Daxi L, Siyu S, Xinyu Y, Qiang Z and Peiyuan C (2024), A digital hysteresis control method for three-level grid-tie inverter based on online prediction of sampling time without inductance.
Front. Energy Res. 12:1403346.
doi: 10.3389/fenrg.2024.1403346

A digital hysteresis control method for three-level grid-tie inverter based on online prediction of sampling time without inductance

Cai Shulin, Li Daxi*, Shao Siyu, Yang Xinyu, Zhang Qiang and Cheng Peiyuan

Air Force Engineering University Air and Missile Defense College, Xi'an, China

This article proposed a digital hysteresis control method for three-level grid-tie inverter based on online prediction of sampling time without inductance. The proposed method eliminated the effect on the control accuracy of the inductor changing with the current in the LCL filter of the grid-tie inverter, and reduced the equivalent sampling rate in digital hysteresis control by predicting and correcting the sample time. The simulations and experimental tests confirm the effectiveness of the proposed digital hysteresis control method.

KEYWORDS

three-level inverter, grid-tie inverter, digital hysteresis control, online prediction of sampling time, robustness of inductor parameters

1 Introduction

GRID-TIE inverters are widely used in various distributed generation (DG) systems powered by solar photovoltaic (PV) arrays or wind power. Among the control algorithms used in the grid-tie inverters, the hysteresis control algorithm has many advantages compared with the traditional PID (Proportion Integration Differentiation) control algorithm: it can track any form of the command signal, the tracking error accuracy can be controlled and adjusted, and the control bandwidth is extremely high (Chavali et al., 2022). Therefore, it is widely used in harmonic suppression, noise filtering, and other occasions to improve power quality and electromagnetic protection in micro-grid (Viswadev et al., 2020; Wang et al., 2014). Hysteresis control algorithms have undergone development from analog hysteresis control to digital hysteresis control. Analog hysteresis control has high tracking accuracy and good control effect because the controlled signal is a real-time continuously changing analog quantity, but it relies heavily on the performance and cost of analog chips, which leads to its application being limited (He et al., 2013). In contrast, digital hysteresis control is the future direction because of its flexibility and low dependence on the microchip, which has great demand in many applications (Acuna et al., 2015; Davoodnezhad et al., 2014a). However, the accuracy of digital hysteresis control is limited by the discretization and sampling rate (Wang and Wang, 2013), which has a great influence.

As shown in Figure 1, the blue and orange waveforms in the first graph of figure (a) and (b) represent the bandwidth of the hysteresis control, indicating the upper and lower limits of the error tolerance. The red waveform indicates the command signal and the green

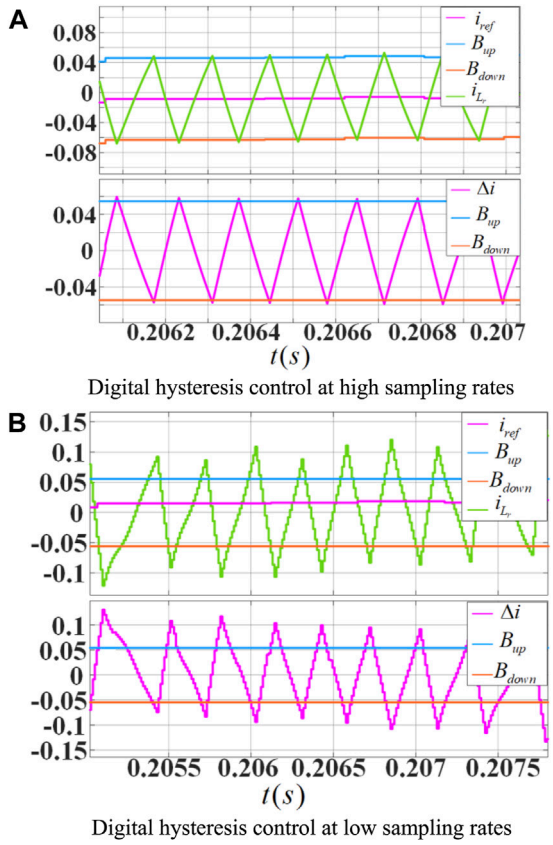

FIGURE 1
Digital hysteresis control at different sampling rates. **(A)** Digital hysteresis control at high sampling rates, **(B)** Digital hysteresis control at low sampling rates.

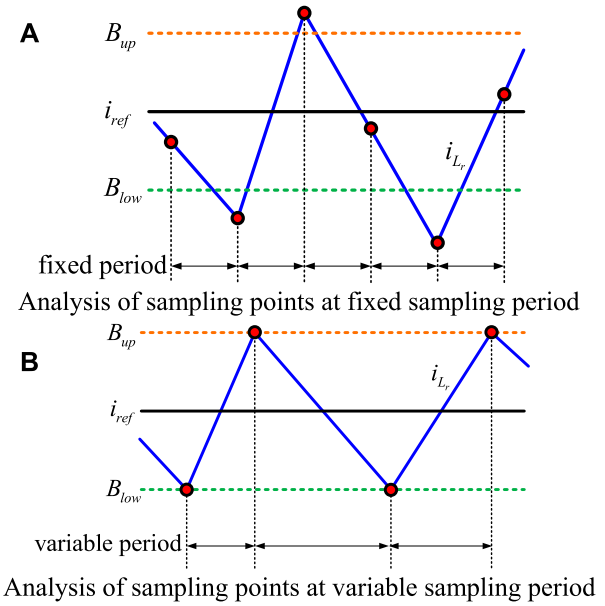

FIGURE 2
Analysis of sampling points at different sampling periods. **(A)** Analysis of sampling points at fixed sampling period, **(B)** Analysis of sampling points at variable sampling period.

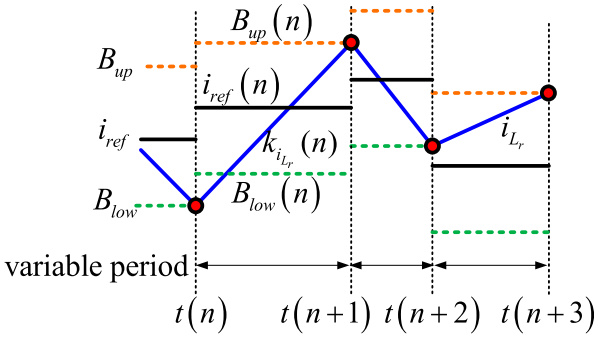

FIGURE 3
Schematic diagram of sampling time prediction at a minimum sampling rate.

waveform indicates the actual controlled signal. The red waveform in the second graph of figure (a) and figure (b) indicates the error signal. The blue signal indicates the absolute value of the bandwidth. From the comparison of the graphs, it can be seen that under a high sampling rate, the error current is close to a continuous analog signal, and the error is always kept within the hysteresis bandwidth during all the control process. While under a low sampling rate, it is difficult to accurately capture the signal at the moment of intersection of the error signal and the bandwidth, making the error signal greatly exceed the allowed boundary range, showing low precision and poor control effect.

In actual products, the ADC sampling rate of the digital controller cannot be too high, otherwise the control algorithm cannot be completed during one control period before the next data refresh. Therefore, it is of great practical importance to study how to reduce the impact of sampling rate on digital hysteresis control under the premise of ensuring control accuracy.

In the past few years, several improvements have been proposed, particularly focusing on reducing the hysteresis control equivalent sampling frequency and improving the current tracking effect (Malesani et al., 1997; Carl et al., 2009). In (Malesani et al., 1997; Stefanutti and Mattavelli, 2006; Hu et al., 2014), several digital hysteresis control methods based on oversampling and virtual sampling were proposed, but the sampling rates are high, the amount of data is too large, and the authenticity of the virtual sampling data needs to be further verified. In (Chen and Kang, 2011), a hysteresis control method with online prediction of sampling time is used, which can predict the next sampling time to ensure the effect of current tracking at a reduced sampling rate, but this method does not take into account the problem of inductor parameters changing with current, making the predicted values deviate in the practical application. In Carl et al. (2009), the error of the hysteresis control at different stages is analyzed and a method to increase the current tracking accuracy by changing the number of switch levels at the moment of maximum error is proposed, but the switching process of this method is complicated and the loss to the device is great.

In this paper, a novel online sampling prediction control method without inductance is proposed. With the proposed scheme, the

10.3389/fenrg.2024.1403346

TABLE 1 Three-level converter switching state modulation relationship.

S_{1a}	S_{2a}	$\overline{S_{1a}}$	$\overline{S_{2a}}$	E_g	V_x	$\frac{di_{Lr}}{dt}$
1	1	0	0	>0	$\frac{U_{dc}}{2}$	$1\times\frac{\frac{U_{dc}}{2}-E_g}{L_r}$
0	1	1	0	>0	0	$0\times\frac{\frac{U_{dc}}{2}-E_g}{L_r}$
0	1	1	0	<0	0	$0\times\frac{\frac{U_{dc}}{2}-E_g}{L_r}$
0	0	1	1	<0	$-\frac{U_{dc}}{2}$	$-1\times\frac{\frac{U_{dc}}{2}-E_g}{L_r}$

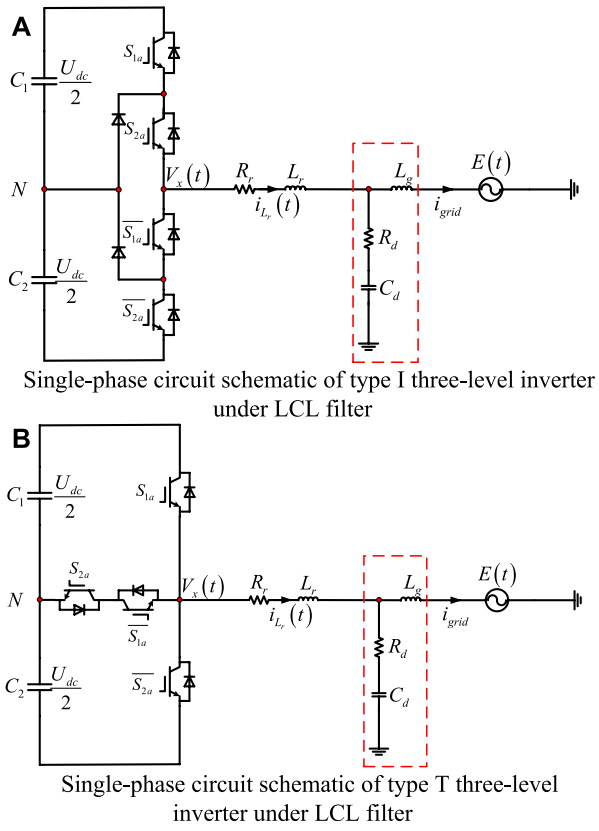

FIGURE 4
Single-phase circuit schematic of different type three-level inverter under LCL filter. **(A)** Single-phase circuit schematic of type I three-level inverter under LCL filter, **(B)** Single-phase circuit schematic of type T three-level inverter under LCL filter.

following advantages are obtained. (1) the digital hysteresis equivalent sampling frequency is reduced compared with the oversampling digital hysteresis method by the prediction control method. (2) the control accuracy is guaranteed by analyzed the error current within and beyond the hysteresis bandwidth so that the hysteresis error is fixed. (3) the problem of inductor parameters changing with current to the hysteresis control is solved.

The rest of this paper is organized as follows. In Section 2, the sampling prediction method of the digital hysteresis control for the three-level inverter is derived and the effect of inductor parameters on the control accuracy is analyzed. In Section 3, the inductance-free

TABLE 2 Simulation main circuit parameters table.

Main components	Parameters
DC Capacity C_1、 C_2	9840uF
Converter side Inductor L_r	0.7 mH
Grid side Inductor L_g	0.05 mH
AC Filter Capacitor C_d	30 uF
DC voltage U_{dc}	750 V
Grid voltage RMS E_{grid}	380 V
Grid frequency f_{grid}	50 Hz
Target switching frequency f_s	15 kHz

A. Simulation results of conventional three-level digital hysteresis control.

sampling time online prediction control method is derived. In Sections 4 and 5, the simulation and experimental results are presented in detail.

2 Principle of digital hysteresis control with sampling time prediction algorithm based on three level inverter

According to the traditional hysteresis control algorithm (Chen et al., 2012; Jiao et al., 2014) (take the current-source power electronic converter as an example), if the current sampling value is located on the boundary of the hysteresis bandwidth at each sampling moment, the converter will act at this time, and the sampling moment is valid; On the contrary, if the current sampling value at the sampling moment is within the bandwidth of the hysteresis control, the converter does not act, so the sampling point does not affect the control system, then it is meaningless. Therefore, the minimum sampling rate occurs at the moment when all the sampling points of the controlled current are located at the intersection of the bandwidth boundary of the hysteresis control (Liu and Maswood, 2006; Mohseni and Islam, 2010; Wang and Li, 2013), as shown in Figure 2.

As shown in Figure 2A, the red sampling points are inside the upper and lower boundary of the hysteresis bandwidth, which cannot trigger the converter to switch, and the sampling value is meaningless to the hysteresis control system; on the contrary, in Figure 2B, as each sampling current value is located on the upper and lower boundary of the bandwidth, it just makes the converter to switch, which is timely

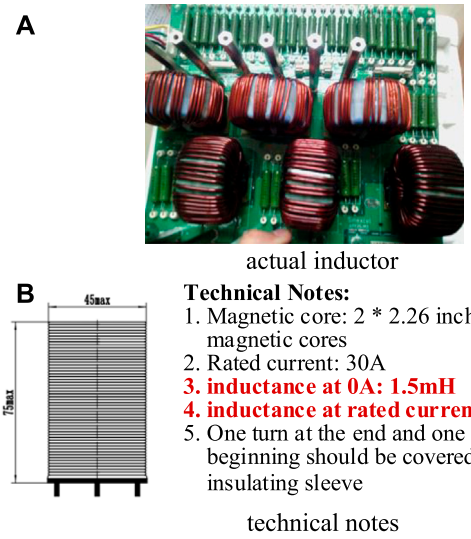

FIGURE 5
Actual inductor fabrication process. **(A)** actual inductor, **(B)** technical notes.

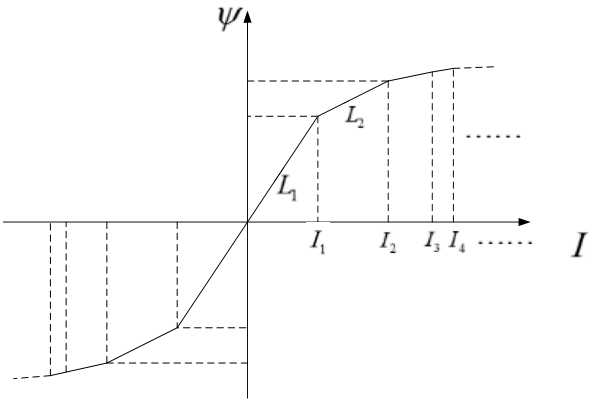

FIGURE 6
Variation curve of actual inductor flux versus inductance at different current.

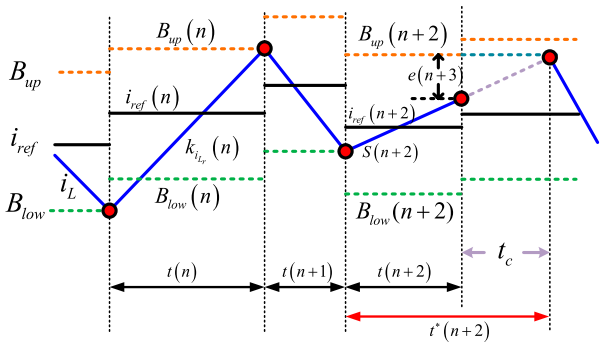

FIGURE 7
Schematic diagram of sampling time prediction correction.

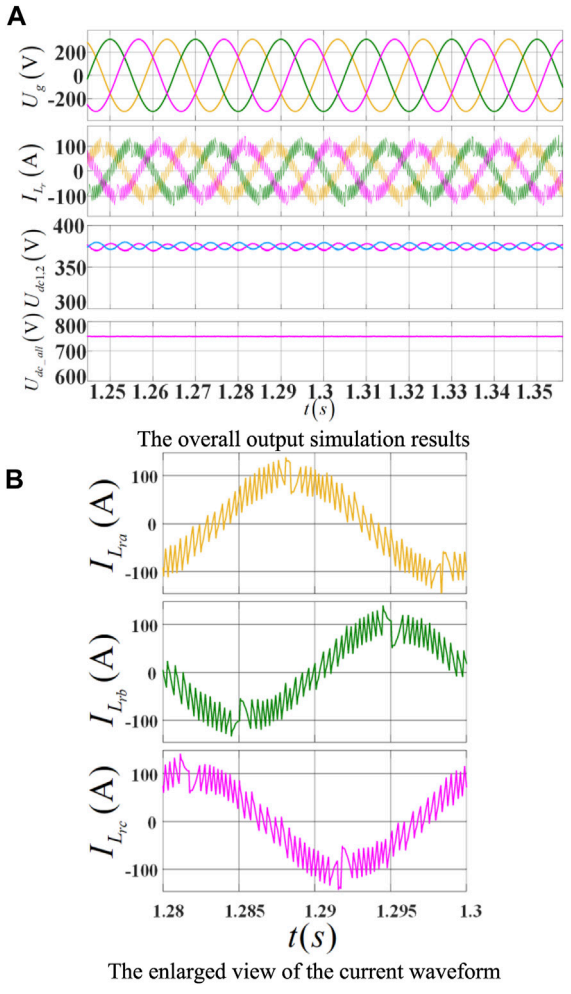

FIGURE 8
Inverter output simulation results under conventional digital hysteresis control. **(A)** The overall output simulation results, **(B)** The enlarged view of the current waveform.

and effective. Due to the changes in the control reference, hysteresis bandwidth, and hardware parameters as well as external disturbances in the actual control system, the interval between sampling points or the sampling rate, is bound to change constantly if all sampling points are located on the bandwidth boundary of the hysteresis control, as shown in Figure 2B. Therefore, simply using the traditional ideal fixed sampling rate as shown in Figure 2A cannot meet the requirements of the actual sampling interval changes, which poses a challenge to reduce the sampling rate while ensuring the control accuracy. Therefore, it is important to study how to improve the effectiveness of digital hysteresis control and how to reduce the equivalent sampling rate.

According to the analysis, it can be known that: at each sampling point, the time required for the current to reach the next bandwidth intersection position can be deduced from the actual sampled current value, as well as the commanded current given by the algorithm, the upper and lower limits of the hysteresis

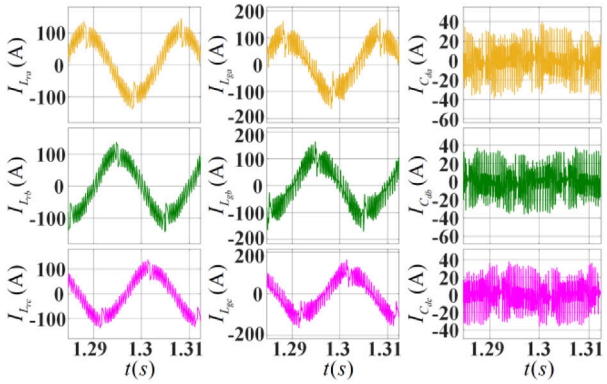

FIGURE 9
Waveform of LCL filter current of the three-level inverter under traditional digital hysteresis control algorithm.

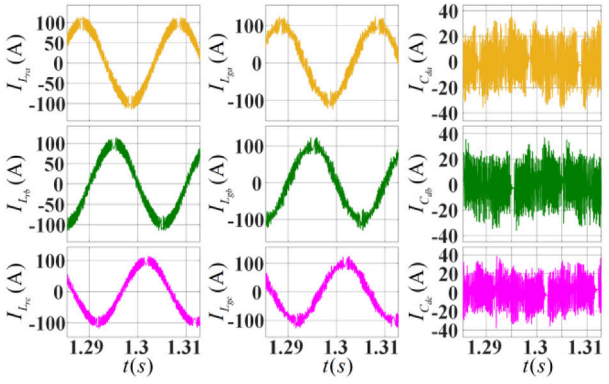

FIGURE 11
Inverter LCL filter current waveform under the proposed inductance-free digital hysteresis sampling time online prediction algorithm.

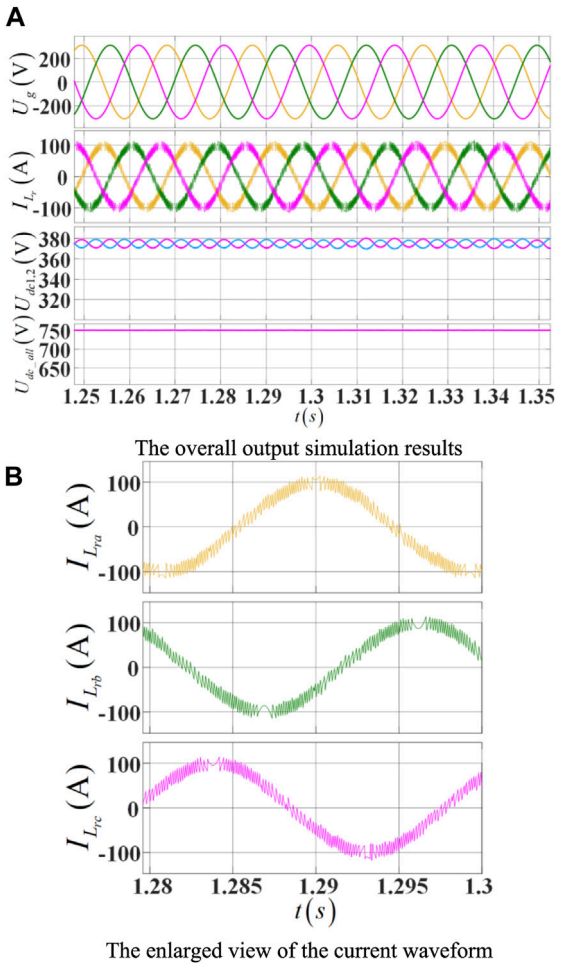

FIGURE 10
Inverter output results under the proposed digital hysteresis prediction algorithm. **(A)** The overall output simulation results, **(B)** The enlarged view of the current waveform.

bandwidth, and this time will be set as the next sampling period, then the ideal equivalent minimum sampling rate can be obtained in Eq. 1, as shown in Figure 3.

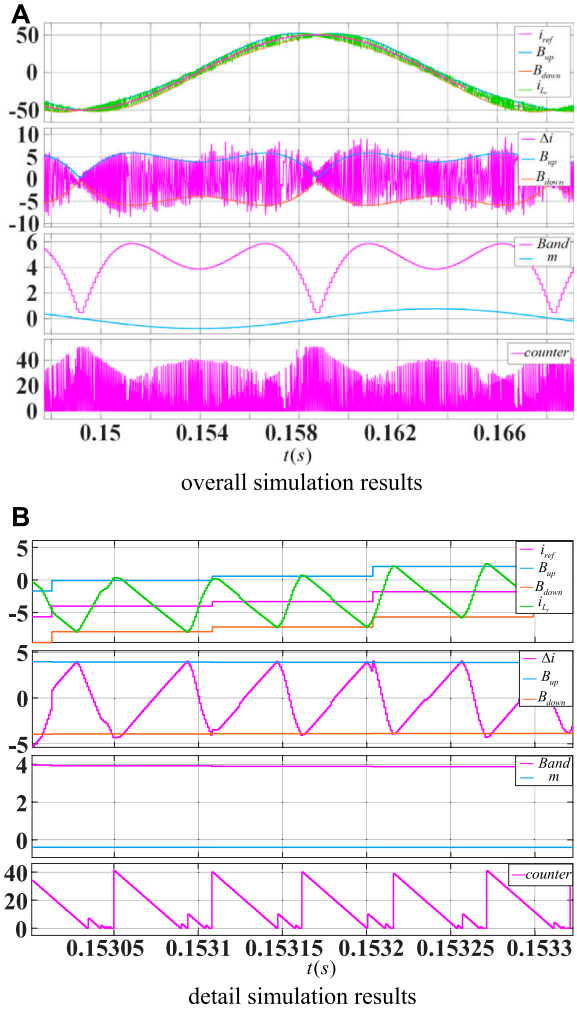

FIGURE 12
Simulation results of bandwidth versus error current and prediction time variation under the proposed digital hysteresis sampling time online prediction algorithm. **(A)** overall simulation results, **(B)** detail simulation results.

TABLE 3 Experimental main circuit parameters table.

Main components	Parameters
DC Capacity C_1、 C_2	9840uF
Converter side Inductor L_r	0.7 mH
Grid side Inductor L_g	0.05 mH
AC Filter Capacitor C_d	30 uF
DC voltage U_{dc}	750 V
Grid voltage RMS E_{grid}	380 V
Grid frequency f_{grid}	50 Hz
Target switching frequency f_s	15 kHz

A. experimental results of conventional digital hysteresis control.

$$\Delta T = t(n+1) - t(n) = \frac{B_{up}(n) - i_{L_r}(n)}{k_{i_{L_r}}(n)}. \tag{1}$$

Where $B_{up}(n) = i_{ref}(n) + H$, and H is the hysteresis bandwidth. $k_{i_{L_r}}(n)$ indicates the slope of current at sampling time $t(n)$.

As can be seen from the above equation, the slope of the current has a critical impact on the sampling rate.

The following is an example of a Type I and Type T three-level inverter.

From the single-phase topology of the three-level inverter, the series equivalent resistance R_r of the inverter-side inductor L_r is neglected, and the general LCL-type filter is usually designed with a grid-side inductor $L_g \ll L_r$, so the voltage drop on the grid-side inductor L_g can also be neglected, which leads to:

$$L_r \frac{di_{L_r}(t)}{dt} = V_x(t) - E(t) \tag{2}$$

In Eq. 2, the L_r represents the inverter-side inductor in Figure 4, the $V_x(t)$ represents the terminal voltage of the inverter, typically the PWM (pulse width modulation) voltage, and the $E(t)$ represents the grid voltage.

Then, according to the modulation law of the three-level switching state (Shen et al., 2011; Stefanutti and Mattavelli, 2006), the following Table 1 of switching states can be obtained.

In Table 1, S_x $(x = 1a, 2a)$ represent the state of the switch in one arm at the bridge of the three-level inverter. E_g represent the grid voltage. And the first row of Table 1 in orange color represents the positive level of the three level inverter, the last row in blue color represents the negative level, and the middle two rows in gray color represents the zero level of the three level inverter.

From this, it can be seen that:

$$k_{i_{L_r}} = \frac{di_{L_r}}{dt} = \begin{cases} \dfrac{S_{1a} \times \dfrac{U_{dc}}{2} - E_g}{L}, \left(E_g > 0\right) \\ \dfrac{(S_{2a} - 1) \times \dfrac{U_{dc}}{2} - E_g}{L}, \left(E_g < 0\right) \end{cases} \tag{3}$$

In Eq. 3, $k_{i_{L_r}} = \frac{di_{L_r}}{dt}$ indicates the slope of the current of the inverter-side inductor. The S_{1a} and S_{2a} represents the switching state of the first two of four switching devices in one arm of the inverter in Figure 4. And the U_{dc} represents the total voltage of the DC capacity in inverter.

Thus, the conventional sampling time prediction algorithm for digital hysteresis control of three-level converter can be obtained as follows:

$$\begin{cases} \Delta T = t(n+1) - t(n) = \dfrac{B_{up}(n) - i_{L_r}(n)}{k_{i_{L_r}}(n)} \\ k_{i_{L_r}}(n) = \dfrac{S_0 \times \dfrac{U_{dc}}{2} - E_g}{L} \\ S_0 = \begin{cases} S_{1a}, E_g(t) > 0 \\ S_{2a} - 1, E_g(t) < 0 \end{cases} \end{cases} \tag{4}$$

where S_0 is the switch state corresponding to the moment of the sampling point. The ΔT is the period of the digital hysteresis control.

Combined with the above analysis, it can be seen that the sampling moment predicted by the traditional digital hysteresis control algorithm is closely related to the inductance L. However, in actual products, due

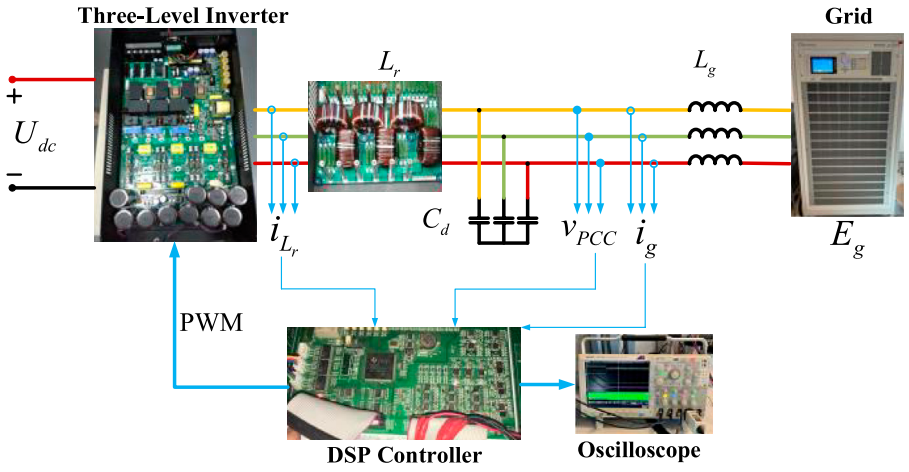

FIGURE 13
Configuration of the experimental setup.

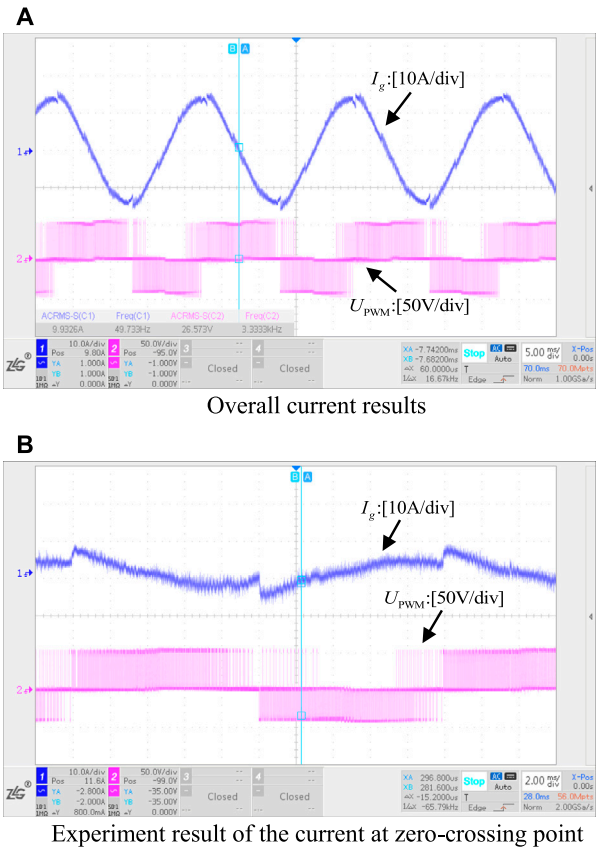

FIGURE 14
Output current and switch voltage of experiment results on conventional digital hysteresis control method. **(A)** Overall current results, **(B)** Experiment result of the current at zero-crossing point.

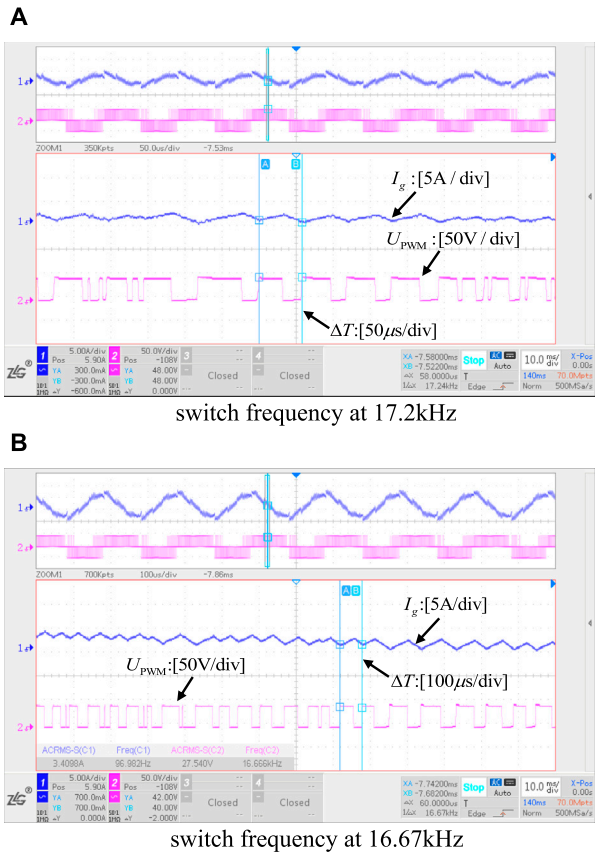

FIGURE 15
Different switching state of convention digital hysteresis control. **(A)** switch frequency at 17.2 kHz, **(B)** switch frequency at 16.67 kHz.

to cost and process limitations, the total amount of flux that the core of the inductor can hold is certain, and when the flux is saturated, it makes the inductance change drastically. Therefore, the corresponding inductance is different for various current output conditions. Usually, manufacturers design the nominal inductance according to the empty load current, which can cause the actual inductance to drop sharply to less than one-third of the nominal inductance when working at full load current. This brings inaccuracy to the digital hysteresis sampling time prediction. As shown in Figures 5, 6.

3 Online sampling time prediction algorithm based on inductance-free

From the previous analysis, it can be seen that how to accurately predict the sampling time when the actual inductor changes due to various current becomes a key step in reducing the equivalent sampling rate and improving the effectiveness of digital hysteresis control. Moreover, from the previous analysis, it is known that the predicted sampling rate varies due to a series of factors such as external disturbances in the sampling of controlled current, which inevitably cause changes in the control frequency (Ramchand et al., 2012; Shukla et al., 2011). Thus, it creates a big problem in the thermal loss of the converter, and the design of the LCL filter, especially the design of the inductance. Therefore, how to work with a relatively fixed switching frequency when both sampling time and inductance of the filer inductor change becomes a top priority. According to the literature (Davoodnezhad et al., 2014b), the bandwidth of the digital hysteresis control can be designed to change to ensure a fixed switching frequency when the sampling rate varies (Song et al., 2014; Zeng et al., 2004). Then, the bandwidth of the quasi-fixed frequency digital hysteresis control based on three-level converter with LCL filter can be expressed in Eq. 5 as follows:

$$H = \frac{U_{dc}}{2L \times f_s}|m|\,(1 - 2|m|), m = \frac{E_g(t)}{U_{dc}} \tag{5}$$

Where U_{dc} indicates the total DC voltage value on the DC side of the three-level converter, f_s indicates the desired fixed target switching frequency, L indicates the total AC side filter inductance, and $m = \frac{E_g(t)}{U_{dc}}$ indicates the control modulation index at time t.

From the equation, it can be seen that the variation of the bandwidth in the hysteresis control can be inferred from the target expectation fixed switching frequency f_s. Moreover, the bandwidth H is changed at a frequency of 2 times the grid frequency (the square function of the control modulation index, which is the same as the AC grid voltage $E_g(t)$). Since the switching frequency of the hysteresis control is typically in tens kHz, which is much larger than 2 times the grid frequency, the bandwidth can be approximated as constant within each switching cycle. Moreover, for the inverter, the frequency of the command signal it tracks is also the same as grid, which can also be considered approximately constant during each switching cycle.

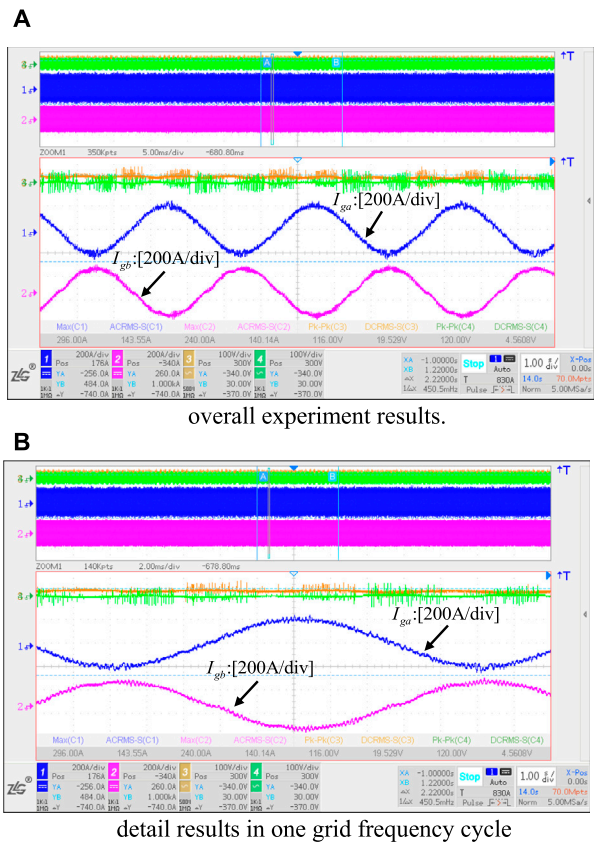

FIGURE 16
Output current waveform of proposed digital hysteresis control. **(A)** overall experiment results. **(B)** detail results in one grid frequency cycle.

So, assume: $H(k-1) \approx H(k)$, $i_{ref}(k-1) \approx i_{ref}(k)$, the upper and lower limits of the bandwidth: $B_{up} = i_{ref} + H$ and $B_{down} = i_{ref} - H$ can also be expressed as:

$$\begin{cases} B_{up}(k-1) \approx B_{up}(k) \\ B_{down}(k-1) \approx B_{down}(k) \end{cases} \tag{6}$$

Thus, when the sampling point is at the intersection of the current and the bandwidth, there is

$$\Delta T_{pre} = \frac{\left|B_{down}(k) - B_{up}(k-1)\right|}{\left|k_{i_{Lr}}\right|} = \frac{\left|B_{up}(k) - B_{down}(k-1)\right|}{\left|k_{i_{Lr}}\right|} = \frac{2H}{\left|k_{i_{Lr}}\right|} \tag{7}$$

By substituting Eqs (6), (7) into the previous Eq. 4, we can get:

$$\Delta T_{pre} = \begin{cases} \dfrac{2 \times \dfrac{U_{dc}}{2L \times f_s}|m|(1-2|m|)}{\left|\dfrac{S_{1a} \times \dfrac{U_{dc}}{2} - E_g}{L}\right|}, E_g(t) > 0 \\ \dfrac{2 \times \dfrac{U_{dc}}{2L \times f_s}|m|(1-2|m|)}{\left|\dfrac{(S_{2a}-1) \times \dfrac{U_{dc}}{2} - E_g}{L}\right|}, E_g(t) < 0 \end{cases} \tag{8}$$

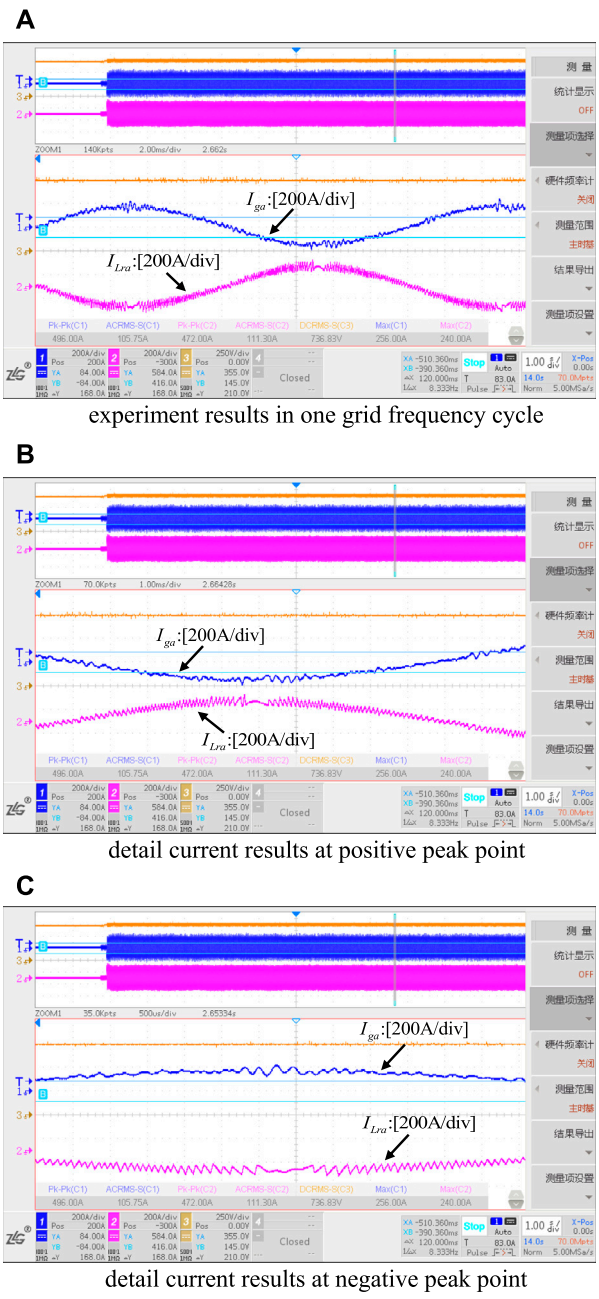

FIGURE 17
Inverter LCL filter current waveform under the proposed inductance-free digital hysteresis sampling time online prediction algorithm. **(A)** experiment results in one grid frequency cycle, **(B)** detail current results at positive peak point, **(C)** detail current results at negative peak point.

After simplification, Eq. 8 can be expressed as:

$$\Delta T_{pre} = 2T_s \frac{|m|(1-2|m|)}{|S_0 - 2m|} \tag{9}$$

Where $S_0 = \begin{cases} S_{1a}, E_g(t) > 0 \\ S_{2a} - 1, E_g(t) < 0 \end{cases}$.

As can be seen from Eq. 9, the predicted sampling time is only related to the desired switching period and the control modulation index function m, independent of parameters such as the inductor L.

Therefore, the problem of the nonlinearity between the inductance and the output current is solved for the prediction time at steady state.

The previous equation is derived to be effective when the sampling point is just at the intersection of the current and the bandwidth, and after analysis, it is also effective when the current at the sampling moment exceeds the upper or the lower limits of the bandwidth, which can be corrected to:

$$\Delta T_{pre} = 2T_s \frac{|m|(1-2|m|)}{|S_0 - 2m|}, |\Delta i(k)| \geq H \tag{10}$$

where $\Delta i(k)$ indicates the error current.

However, the sampling point is likely to deviate from the bandwidth because of the delay in the sampling process, the inertia of the system, and the actual presence of delay in the PWM control. Thus, at some moments when the current value is less than the hysteresis bandwidth, a correction to the prediction Eq. 10 is required:

From Figure 7, it can be seen that:

when $|\Delta i(k)| < H$, since $|\Delta i(k)| = |i_{ref}(k) - i(k)|$, we can get: $e(k) = H - |\Delta i(k)|$.

then, the correction of sampling period is $t_c = \frac{e(k)}{|k_{i_{L_r}}(k-1)|}$.

Due to $|k_{i_{L_r}}(k-1)| = \frac{|i(k)-i(k-1)|}{\Delta T_{pre}(k-1)}$, according to the above equations:

$$t_c = \frac{H - |\Delta i(k)|}{|i(k) - i(k-1)|} \times \Delta T_{pre}(k-1) \tag{11}$$

Therefore, t_c is the correction formula when the error current is less than the band.

According to Eq. 10 and Eq. 11, the online prediction algorithm based on inductance-free sampling time can be expressed as

$$\Delta T_{pre}(k) = \begin{cases} 2T_s \frac{|m|(1-2|m|)}{|S_0 - 2m|}, |\Delta i(k)| \geq H \\ \frac{H - |\Delta i(k)|}{|i(k) - i(k-1)|} \times \Delta T_{pre}(k-1), |\Delta i(k)| < |H| \end{cases} \tag{12}$$

Where: $\begin{cases} \Delta i(k) = i_{ref}(k) - i(k) \\ S_0 = \begin{cases} S_{1a}, E_g(t) > 0 \\ S_{2a} - 1, E_g(t) < 0 \end{cases} \end{cases}$,

S_x $(x = 1a, 2a)$ indicates the current switch status at the sampling moment, as described in Table 1.

4 Simulation analysis

In order to verify the above proposed control method, a simulation comparison analysis was conducted with a LCL type filter based on three-level neural-point-clamped inverter as an example, and the simulation parameters are listed in Table 2.

4.1 Simulation results of conventional three-level digital hysteresis control

The simulation results in Figure 8 show the three-phase grid voltage, three-phase inverter-side inductor current, three-level DC-side upper and lower bus capacitor voltage, and overall DC voltage ripple from top to bottom. It is evident that the traditional hysteresis control algorithm has a sudden change in inductor current at the zero-crossing point of the grid voltage, which causes the output waveform to change significantly, the total current harmonic distortion to increase, the hysteresis control error to exceed the bandwidth, and the control effect to be poor.

From left to right in Figure 9, the results of the three-phase grid-side inductor current, the three-phase inverter-side inductor current, and the AC-side filter capacitors are shown in that order. As can be seen from Figure 9, due to the limitation of sampling rate and control frequency, the error current exists in a large range near the command current than the bandwidth, and the overall digital hysteresis control is less effective.

4.2 The proposed digital hysteresis control based on online prediction simulation results

In Figure 10, from top to bottom, the grid voltage, the inverter output current, the upper and lower bus capacitor voltages on the DC side of the three-level inverter and the total DC voltage simulation results are shown. It can be seen from the simulation results that the output inverter current is better sinusoidal, the control effect is significantly improved, there is no obvious change in output current waveform at the zero-crossing point of the grid, the error of the hysteresis current control is reduced and limited within the hysteresis band.

From left to right in Figure 11, the results of the three-phase grid-side inductor current, the three-phase inverter-side inductor current, and the AC-side filter capacitors are shown in that order. As can be seen from Figure 11, the controlled inductor current is better sinusoidal, and the capacitor current is less ripple and there is a better control effect compared with the conventional digital hysteresis control method.

The simulation results in Figure 12 from top to bottom represent the reference current and the controlled current, the hysteresis bandwidth and the error current, the bandwidth and the counter needed to correct the period of sample time. From the simulation results, it can be seen that the controlled current is everywhere almost within the bandwidth and follows the reference current exactly with the proposed digital hysteresis sampling time online prediction algorithm. With the sample time correction algorithm, almost every sample point locates at the intersection of the bandwidth boundary exactly, and the current is controlled by the need sinusoidal reference.

5 Experimental verification

In order to further verify the theoretical feasibility of the proposed method and the accuracy of the simulation analysis, an experimental verification was conducted. The selected experimental equipment is a 100 kW type I three-level APF. The experimental parameters are shown in Table 3.

The instrumentations used in the experimental setup in Figure 13 are list as follows: the grid-tie inverter is a 100 kW Type I three-level NPC inverter. The inductors are custom-made magnetic core inductors with 1.5 mH at empty load. The controller is used with a DSP 28335 control board with maximum 16 ADC channels and 12 PWM channels. The Oscilloscope is a ZLG

3024PLUS 4 channel scope with 300 MHz bandwidth. And the grid is connected through an isolated transformer with 500 kV A.

5.1 Experimental results of conventional digital hysteresis control

The waveform in blue color in Figure 14 is the output inductor current and the red color is the inverter output PWM pulse voltage.

It is evident from the experimental results in Figure 14 that the conventional digital hysteresis control produces a poor output current waveform, with a noticeable current change at the grid zero-crossing point. As a result, there is little control effect and significant current distortion.

The switching process of the experimental waveform results in Figure 15 demonstrate how the sampled inductor current causes the traditional hysteresis control to be inaccurate. This results in frequent switching frequency adjustments and makes it challenging to adjust the output current within the hysteresis control bandwidth, both of which have an impact on the quality of the inverter's final output current.

5.2 Experimental results of proposed digital hysteresis control

The above Figure 16 shows the results of the grid-side output waveform obtained by the proposed digital hysteresis control method without inductance using online time prediction. The blue one is the phase A grid-side current and the red one is the phase B grid-side current (the direction of the current transformer is reversed in the experiment). It can be seen that with this control method, the harmonic of the output current is obvious reduced, the distortion of the current is greatly reduced, and the quality of the output current is significantly controlled.

The experimental findings of the inverter-side current switching procedure are displayed in Figure 17. In the experiment, the direction of the current transformer (shown in red) was reversed. The figure shows that there are no shocks in the current at the grid zero-crossing point, the overall inductor current is sinusoidal, and the inverter-side inductor current varies within the hysteresis bandwidth. The total power quality of the output current is efficiently managed and enhanced.

6 Conclusion

In this paper, a digital hysteresis control method for three-level inverter based on online prediction of sampling time without inductance is proposed. Through the sample time prediction and correction, the dependence on high sampling rate in traditional hysteresis control is reduced, while the accuracy is improved by keeping the error within the hysteresis band all the time. Furthermore, the impact of inductor parameter changing with different current is eliminated by cancelling the use of inductance during the control process. The effectiveness and robustness of the proposed control method are not only carried out by theoretical analysis and mathematical derivation, but also validated by simulation and experiment.

Data availability statement

The raw data supporting the conclusion of this article will be made available by the authors, without undue reservation.

Author contributions

CS: Writing–original draft, Writing–review and editing. LD: Writing–review and editing. SS: Funding acquisition, Writing–review and editing. YX: Writing–review and editing. ZQ: Writing–review and editing. CP: Writing–review and editing.

Funding

The author(s) declare that financial support was received for the research, authorship, and/or publication of this article. This research was funded by the Natural Science of Shaanxi Province of China (No.2022JQ-344).

Conflict of interest

The authors declare that the research was conducted in the absence of any commercial or financial relationships that could be construed as a potential conflict of interest.

Publisher's note

All claims expressed in this article are solely those of the authors and do not necessarily represent those of their affiliated organizations, or those of the publisher, the editors and the reviewers. Any product that may be evaluated in this article, or claim that may be made by its manufacturer, is not guaranteed or endorsed by the publisher.

References

Acuna, P., Mor´an, L., Rivera, M., Aguilera, R., Burgos, R., and Agelidis, V. G. (2015). A single-objective predictive control method for a multivariable single-phase three-level NPC converter-based active power filter. *IEEE Trans. Ind. Electron.* 62 (7), 4598–4607. doi:10.1109/tie.2015.2393556

Carl, N. H., Victor, S. P., and Chung, H. S. (2009). Constant-frequency hysteresis current control of grid-connected VSI without bandwidth control. *IEEE Trans. Power Electron.* 24 (11), 2484–2495. doi:10.1109/tpel.2009.2031804

Chavali, R. V., Dey, A., and Das, B. (2022). A hysteresis current controller PWM scheme applied to three-level NPC inverter for distributed generation interface. *IEEE Trans. Power Electron.* 37 (2), 1486–1495. doi:10.1109/TPEL.2021.3107618

Chen, Y., and Kang, Y. (2011). The variable-bandwidth hysteresis-modulation sliding-mode control for the PWM–PFM converters. *IEEE Trans. Power Electron.* 26 (10), 2727–2734. doi:10.1109/tpel.2011.2158852

Chen, Z., Luo, Y., and Chen, M. (2012). Control and performance of a cascaded shunt active power filter for aircraft electric power system. *IEEE Trans. Ind. Electron.* 59 (9), 3614–3623. doi:10.1109/tie.2011.2166231

Davoodnezhad, R., Holmes, D. G., and McGrath, B. P. (2014a). A novel three-level hysteresis current regulation strategy for three-phase three-level inverters. *IEEE Trans. Power Electron.* 29 (11), 6100–6109. doi:10.1109/tpel.2013.2295597

Davoodnezhad, R., Holmes, D. G., and McGrath, B. P. (2014b). "A fully digital hysteresis current controller for current regulation of grid connected PV inverters," in presented at the IEEE 5th Int. Symp. IEEE Power Electronics for Distributed Generation Systems (PEDG), 2014 IEEE 5th International Symposium on, Galway, Ireland, Ireland, Jun. 2014 (IEEE), 1–8.

Gunter, S., and Fuchs, F. W. (2022). "Switching time prediction for digital hysteresis control for high frequency current in grid impedance measurement application," in presented at the 16th Eur. Conf. Power Electronics and Applications (EPE'14-ECCE Europe), 2014 16th European Conference on, Lappeenranta, Finland, Finland, Aug. 26–28, 2014 (IEEE), 1–8.

He, J., Li, Y. W., Bosnjak, D., and Harris, B. (2013). Investigation and active damping of multiple resonances in a parallel-inverter-based microgrid. *IEEE Trans. Power Electron.* 28 (1), 234–246. doi:10.1109/tpel.2012.2195032

Hu, Y., Deng, Y., Liu, Q., and He, X. (2014). Asymmetry three-level gird-connected current hysteresis control with varying bus voltage and virtual oversample method. *IEEE Trans. Power Electron.* 29 (6), 3214–3222. doi:10.1109/tpel.2013.2272466

Jiao, Y., Lee, F. C., and Lu, S. (2014). Space vectormodulation for three-level NPC converter with neutral point voltage balance and switching loss reduction. *IEEE Trans. Power Electron.* 29 (10), 5579–5591. doi:10.1109/tpel.2013.2294274

Liu, F., and Maswood, A. I. (2006). A novel variable hysteresis band current con trol of three-phase three-level unity PF rectifier with constant switching frequency. *IEEE Trans. Power Electron.* 21 (6), 1727–1734. doi:10.1109/tpel.2006.882926

Malesani, L., Mattavelli, P., and Tomasin, P. (1997). Improved constant-frequency hysteresis current control of VSI inverters with simple feedforward band width prediction. *IEEE Trans. Ind. Appl.* 33 (5), 1194–1202. doi:10.1109/28.633796

Mohseni, M., and Islam, S. M. (2010). A new vector-based hysteresis current control scheme for three-phase PWM voltage-source inverters. *IEEE Trans. Power Electron.* 25 (9), 2299–2309. doi:10.1109/tpel.2010.2047270

Ramchand, R., Gopakumar, K. K., Patel, C., Sivakumar, K. K., Das, A., and Abu-Rub, H. (2012). Online computation of hysteresis boundary for constant switching frequency current-error space-vector-based hysteresis controller for VSI-fed IM drives. *IEEE Trans. Power Electron.* 27 (3), 1521–1529. doi:10.1109/tpel.2011.2120624

Shen, J., Schroder, S., Rosner, R., and El-Barbari, S. (2011). A comprehensive study of neutral-point self-balancing effect in neutral-point-clamped three-level inverters. *IEEE Trans. Power Electron.* 26 (11), 3084–3095. doi:10.1109/tpel.2011.2138161

Shukla, A., Ghosh, A., and Joshi, A. (2011). Hysteresis modulation of multilevel inverters. *IEEE Trans. Power Electron.* 26 (5), 1396–1409. doi:10.1109/tpel.2010.2082001

Song, W., Feng, X., and Smedley, K. M., (2014). "A carrier-based PWM strategy with the offset voltage injection for single-phase three-level neutral point clamped converters," *IEEE Trans. Power Electron.*, vol. 28, no. 3, pp. 1083–1095. doi:10.1109/tpel.2012.2210248

Stefanutti, W., and Mattavelli, P. (2006). Fully digital hysteresis modulation with switching-time prediction. *IEEE Trans. Ind. Appl.* 42 (3), 763–769. doi:10.1109/tia.2006.873665

Viswadev, R., Mudlapur, A., Ramana, V. V., Venkatesaperumal, B., and Mishra, S. (2020). A novel AC current sensorless hysteresis control for grid-tie inverters. *IEEE Trans. Circuits Syst. II Express Briefs* 67 (11), 2577–2581. doi:10.1109/tcsii.2019.2960289

Wang, X., Blaabjerg, F., and Chen, Z. (2014). Autonomous control of inverterinterfaced distributed generation units for harmonic current filtering and resonance damping in an islanded microgrid. *IEEE Trans. Ind. Appl.* 50 (1), 452–461. doi:10.1109/tia.2013.2268734

Wang, Y., and Li, R. (2013). Novel high-efficiency three-level stacked-neutralpoint-clamped grid-tied inverter. *IEEE Trans. Ind. Electron.* 60 (9), 3766–3774. doi:10.1109/tie.2012.2204712

Wang, Y., and Wang, F. (2013). Novel three-phase three-level-stacked neutral point clamped grid-tied solar inverter with a split phase controller. *IEEE Trans. Power Electron.* 28 (6), 2856–2866. doi:10.1109/tpel.2012.2226475

Zeng, J., Yu, C., Qi, Q., Yan, Z., Ni, Y., Zhang, B., et al. (2004). A novel hysteresis current control for active power filter with constant frequency. *Elect. Power Syst. Res.* 68 (1), 75–82. doi:10.1016/s0378-7796(03)00158-5

frontiers | Frontiers in Energy Research

TYPE Original Research
PUBLISHED 23 May 2024
DOI 10.3389/fenrg.2024.1381950

OPEN ACCESS

EDITED BY
Liansong Xiong,
Xi'an Jiaotong University, China

REVIEWED BY
Zhifeng Qiao,
Tianjin University of Technology, China
Fei Jiang,
Changsha University of Science and Technology, China
Kai Zhang,
Zhongyuan University of Technology, China

*CORRESPONDENCE
Cai Hui,
416846749@qq.com

RECEIVED 04 February 2024
ACCEPTED 28 March 2024
PUBLISHED 23 May 2024

CITATION
Hui C, Yanjie H, Yinbin P and Tao Z (2024), A method for reducing torque ripple of switched reluctance motor based on partitioned TSF.
Front. Energy Res. 12:1381950.
doi: 10.3389/fenrg.2024.1381950

A method for reducing torque ripple of switched reluctance motor based on partitioned TSF

Cai Hui[1]*, Han Yanjie[2], Pan Yinbin[3] and Zean Tao[4]

[1]School of Electrical and Electronic Engineering, Huazhong University of Science and Technology, Wuhan, China, [2]BYD Company Ltd., Shenzhen, China, [3]Ruili Group Rui'an Auto Parts Co. Ltd., Rui'an, China, [4]College of Automotive Engineering, Hu Nan Mechanical & Electrical Polytechnic, Changsha, China

In this paper, a new torque sharing function control strategy is proposed to reduce the torque ripple. The traditional torque ripple methods, such as exponential and linear torque allocation strategies, the torque generation capacity of each phase and the power limitation of the power converter is not taken into account, in this paper, the communication region is divided into three intervals by establishing a new partitioning standard. According to the re-established reference function of torque generation, the torque deviation caused by phase current tracking error is compensated according to the torque generation capacity. Both optimization of torque ripple suppression and copper loss minimization are taken into consideration in this paper. To verify the validity and performances of the proposed TSF methods, simulations and experiments have been implemented in a 12/8 structure Switched Reluctance Motor prototype. This method can be applied to other switched reluctance motors with different topologies. Result shows lower current tracking error and better performance of torque ripple minimization compared with the conventional two-interval compensation method.

KEYWORDS

switched reluctance motor, torque sharing function, torque ripple minimization, torque control, optimization

1 Introduction

A Switched Reluctance Motor (SRM) is widely used in modern industry, electric vehicles (EV), agricultural machinery equipment (Li et al., 2018; Sun et al., 2018; 2019; Cheng et al., 2022; Cao et al., 2024), and in other fields, owing to its simple structure, strong fault tolerance, wide speed range, and not requiring rare earth materials. However, the high torque ripple and noise caused by the double salient pole structure and nonlinear mapping characteristics of switched reluctance motors limit their application in high-end fields such as servo control.

Recently, the torque ripple problem of a switched reluctance motor (Marcsa and Kuczmann, 2017; Ma et al., 2018; Kuang et al., 2019; Qing et al., 2020) has been investigated through several strategies, such as Direct Torque Control (DTC) (Kim and Kim, 2018; Yan et al., 2019), Direct Instantaneous Torque Control (DITC) (Sun et al., 2020), artificial neural network control (Dang et al., 2020), and torque distribution function control (TSF) (Li et al., 2021). Among them, the torque distribution function poses an effective solution in reducing the torque ripple of SR motors by reasonably distributing the reference torque of each phase to preserve the synthetic instantaneous torque constant.

For instance, (Dowlatshahi et al., 2013), introduces a multiphase-compensate torque distribution function control strategy to compensate the phase torque tracking error to the other phase generated by each phase during commutation. This method achieves constant synthetic torque, but the comprehensive operating efficiency and the influence of other performance indicators have not been considered. In (Xia et al., 2020), the authors optimize the current reference curve to reduce torque ripple and copper loss and use a multi-objective genetic algorithm to find the optimal turn-on and turn-off angles. However, this method requires complex iterative calculations. Furthermore, (Xi-Lian et al., 2015), develops a comprehensive torque distribution control method that minimizes torque ripple and copper loss of SR motors based on an exponential function. Additionally, this method uses the weighting function to balance torque ripple suppression and the operating efficiency. Besides, (Liu et al., 2019), proposes a TSF control strategy based on pulse width modulation (PWM), which adjusts the excitation voltage of the phase winding by the duty cycle of PWM and divides different control intervals through the inductance linear model to achieve good current tracking performance. In (Chen et al., 2018), the authors suggest a TSF control scheme that does not require a preset torque distribution function and compensates for the excitation phase by feedbacking the deviation of the real-time torque of the off phase. This strategy distributes the torque of each phase more reasonably and reduces the torque ripple. A TSF control method with a single weight factor is proposed in (Li et al., 2018)to reduce the control complexity. The motor flux characteristics are obtained to find the optimal current curve from finite element analysis and experiments, which ensures low copper loss while torque ripple is reduced. The work of (?) studies and evaluates four conventional TSF methods, including linear, sinusoidal, exponential, and cubic TSFs, and uses genetic algorithms to optimize opening and overlapping angles, minimize copper loss while minimizing torque ripple, and selects the best distribution curve among the four methods. In (Sun et al., 2016), a control method based on online correction of the torque distribution function is developed to compensate its TSF positively during the outgoing phase and negatively during the incoming phase according to the torque error generated during commutation. This method optimizes the TSF function and reduces the torque ripple effectively. In [21], the authors divide the commutation interval into two intervals according to the absolute value of the flux rate of change. Besides, this work uses the proportional integration (PI) controller to compensate for the torque error to suppress torque ripple in different intervals.

This paper proposes a new torque distribution function control strategy based on existing research methods, aiming to reduce the torque ripple of switched reluctance motors effectively, generate the best reference torque curve with low torque ripple, and improve the motor's performance. Based on the motor structural parameters, the finite element analysis method is used to obtain the electromagnetic data of the motor. Furthermore, the main factors affecting the electromagnetic torque are analyzed, the basis of partition of the motor's commutation period is re-established, and the phase with strong torque generation ability is optimally selected online as the torque compensation phase in the preset partition interval. Additionally, the torque distribution function is optimized according to the real-time torque tracking error to improve the current controllability and optimize torque ripple suppression. The torque ripple can be further reduced compared with the two-interval compensation method in commutation. Finally, the effectiveness of the proposed method is verified by simulation and experiment.

2 SRM mathematical model

2.1 Voltage equation

According to Kirchhoff's voltage law, the voltage balance equation of the kth phase winding of a switched reluctance motor can be expressed as:

$$U_k = R_k i_k + \frac{d\psi_k}{dt} \tag{1}$$

where U_k is the voltage of the kth phase winding, R_k is the resistance of the kth phase winding, i_k is the current of the kth phase winding, and ψ_k is the flux linkage of the kth phase winding.

2.2 Flux linkage equation

Considering that SRM mainly operates in the magnetic saturation region and the highly nonlinear electromagnetic characteristics in this region, it is challenging to establish an accurate nonlinear model of an SR motor based on common electromagnetic characteristics and mathematical formulas. Based on the nonlinear model analyzed in (?), the flux linkage profile of SRM can be expressed:

$$\Psi(i,\theta) = \left[L_{dsat} i + A\left(1 - e^{-Bi}\right) - L_q i\right] f(\theta) + L_q i \tag{2}$$

where $L-q$ is the inductance of stator and rotor salient pole misalignment (q axis), and L_{dsat} is the saturation inductance for stator and rotor salient pole alignment (d axis). $A, B, f(\theta)$ are defined as presented in 3, 4, and 5, respectively.

$$A = \Psi_m - L_{dsat} I_m \tag{3}$$

$$B = \frac{L_d - L_{dsat}}{\Psi_m - L_{dsat} I_m} \tag{4}$$

$$f(\theta) = \left(\frac{2N_r^3}{\pi^3}\right)\theta^3 - \left(\frac{3N_r^3}{\pi^3}\right)\theta^3 + 1 \tag{5}$$

where L_d is the unsaturated inductance of the d axis, I_m is the rated current corresponding to flux linkage Ψ_m, and N_r is the number of rotor poles.

2.3 Torque equation

The electromagnetic torque of the motor is equal to the sum of the torque generated in each interval. Due to the nonlinearity of the magnetization profile, the generated torque is a nonlinear function of phase current and rotor position. According to the principle of virtual displacement, the

TABLE 1 Parameters of motor structure.

Parameter	Numerical value	Parameter	Numerical value
rated power (W)	1,500	rotor outer diameter(mm)	69
rated voltage(V)	72	rotor inner diameter(mm)	30
stator pole number	12	stator polar arc coefficient	0.5
rotor pole number	8	rotor polar arc coefficient	0.355
stator outer diameter(mm)	120	overlapping coefficient	0.95
stator inner diameter(mm)	69.8	silicon steel sheet model	50W270_2DSF0.950
core length(mm)	82.8		

instantaneous electromagnetic torque at any operating point can be expressed as:

$$T_e(i,\theta) = \left.\frac{\partial W'(\theta,i)}{\partial \theta}\right|_{i=const} \tag{6}$$

where W' is the magnetic common energy of the winding, its expression is:

$$W'(\theta,i) = \int_0^i \Psi(\theta,i)\,di \tag{7}$$

Substituting Equation (1) into Equation (7), the expression of torque T_e is:

$$T_e(i,\theta) = f'(\theta)\left[\frac{\left(L_{dsat}-L_q\right)i^2}{2} + Ai - \frac{A\left(1-e^{-Bi}\right)}{B}\right] \tag{8}$$

where $f'(\theta)$ can be expressed as:

$$f'(\theta) = \left(\frac{6N_r^3}{\pi^3}\right)\theta^2 - \left(\frac{6N_r^3}{\pi^2}\right)\theta \tag{9}$$

2.4 Mechanical equation

According to the laws of mechanics, the rotor mechanical motion equation of SRM under the action of electromagnetic torque and load torque is expressed as follows:

$$T_e = J\frac{d^2\theta}{dt} + D\frac{d\theta}{dt} + T_L \tag{10}$$

where T_e is electromagnetic torque, T_L is load torque, J is the rotary inertia, and D is the friction factor, among $\frac{d\theta}{dt}$.

3 Torque modeling and analysis

The torque share function partition compensation strategy depends on the torque generation capacity. However, the nonlinear mapping relationship between torque, current, and inductance derivatives is acquired. Using the finite element analysis of Maxwell software, the torque-current characteristic and its derivative profile, inductance characteristic profile, and torque-inductance derivative characteristic profile can be obtained, and the factors affecting the torque generation capacity are analyzed.

This paper uses a 12/8 three-phase switched reluctance motor as the prototype, with the specific structural parameters reported in Table1.

3.1 Static finite element analysis

The prototype model's static finite element analysis uses ANSYS software. Considering the A-phase winding as an example, to analyze the torque generation capacity, the step is set as 0.5, the angle value is set from 0 to 45, and the Maxwell software calculates the torque and inductance values under the fixed phase current. The characteristic profiles of the inductor-rotor position and torque-inductor derivative are plotted using Matlab, as illustrated in Figures 1A,B.

Under the linear model, the magnetic saturation characteristic is ignored, and the phase current is fixed. Thus, the inductance derivative is linearly related to the torque. In order to analyze the influence of the inductance value on torque in practical applications, the step of the phase current is set to 1A. Figures 1A,B highlight that the coincidence degree of the inductance curves is high when the phase current is 1 6A. When the current exceeds 6 A, the motor is operated at the magnetic circuit saturation state, and the inductance value in the central area gradually decreases, showing a concave state. When the center lines of the stator's and rotor's salient poles are completely aligned, the motor enters a saturation state of the magnetic circuit. Then, the saturation effect increases as the phase current increases, the inductance value decreases, and the torque generation ability becomes weaker. When the front edge of the salient poles of the stator and rotor approach, the sensitivity of inductance increases, and the torque generation strengthens. Therefore, when the phase current is constant, the torque gradually increases as the inductance derivative increases and the relation between the inductance derivative and torque tends to be linear.

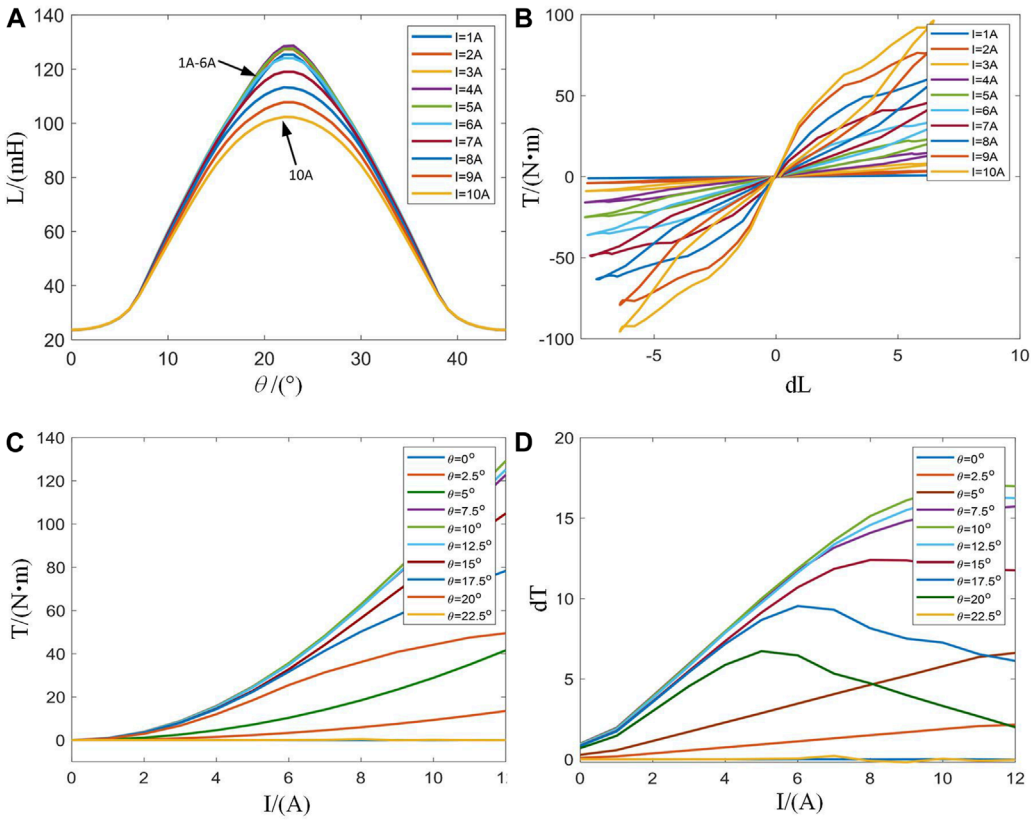

FIGURE 1
SRM static characteristic 2-D profiles. **(A)**: Characteristic profiles of inductance *versus* rotor position. **(B)**: Characteristic profiles of inductance derivative *versus* torque. **(C)**: Characteristic profiles of current *versus* torque. **(D)**: Characteristic profiles of current *versus* torque derivative.

In order to analyze the influence of phase current on the torque generation capacity, the phase A winding is given a phase current 12A with a step of 1A, and the torque value varying with the phase current at a fixed angle is acquired. The torque-current and torque derivative-current characteristics profiles are plotted in Matlab, as depicted in Figures 1C,D.

In order to analyze the influence of phase current on torque in practical application, the step is set to 2.5, and the angle value of 0 22.5 is selected. When the angle is 0–7.5, the trailing edge of the stator pole is gradually approaching the leading edge of the rotor pole. When the angle is 7.5–22.5, the salient poles of the stator and rotor gradually coincide. Figures 1C,D highlight that the A-phase winding of the motor is conducting when the rotor position is 0–15, and the torque gradually increases as the current increases. At this time, the torque generation ability is strong. When the rotor position is 15–22.5, the A-phase winding of the motor is operated at the turn-off freewheeling state, the torque derivative-current value decreases obviously as the phase current exceeds 6A, and the torque generation ability weakens. Therefore, when the angle is fixed, the torque value gradually increases with the increase of phase current, and the relationship between current and torque tends to be square.

The torque profile is obtained by a two-dimensional static field analysis, as illustrated in Figure 2. By analyzing the influence of the current and inductance on the torque generation capacity, it is demonstrated that the torque generation capacity is stronger at points A and B.

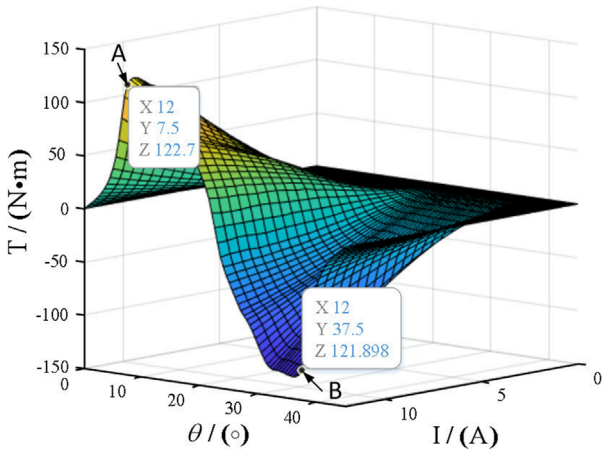

FIGURE 2
Value of torque with the change of parameters θ and current.

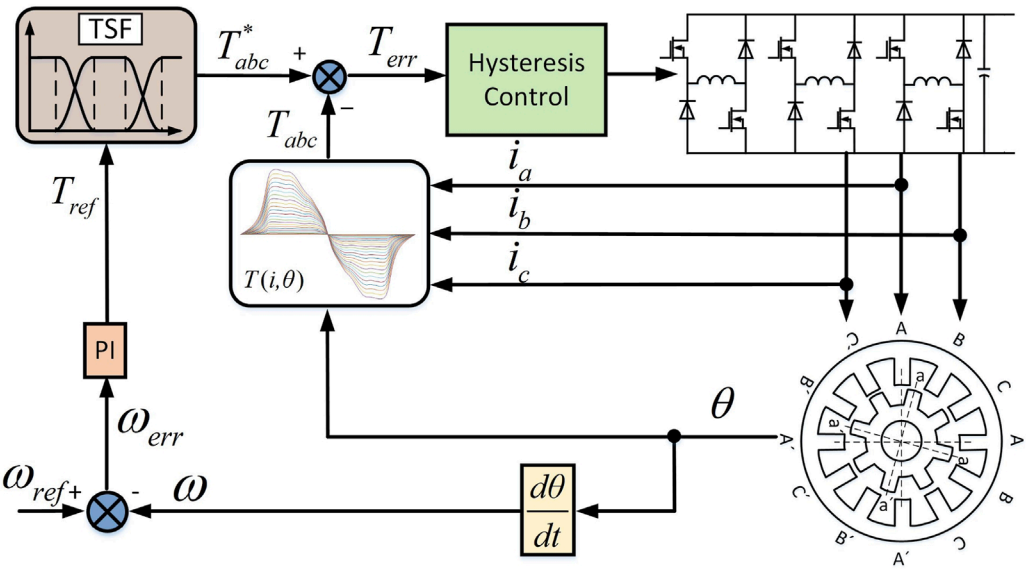

FIGURE 3
SRM control block diagram of DITC method.

4 Torque share function control strategy

The SRM control block diagram of direct instantaneous torque control based on a torque closed loop is shown in Figure 3, which mainly includes the torque calculation unit, hysteresis control unit, power converter, SRM, position detector, and current sensor. As shown in Figure 3, the total reference torque T_{ref} is divided into reference torques T_{k_ref} of each phase at different positions according to the torque share function. The look-up table module calculates the instantaneous output torque. The error between the reference torque and the instantaneous output torque is converted into the driving signal of the power converter by torque hysteresis control, and the control scheme is based on the torque share function.

4.1 Torque share module

To realize the control goal of the TSF method based on constant synthetic instantaneous torque, the following equation must be satisfied:

$$\begin{cases} T_k(\theta) = T_{ref} f_k(\theta), & k = 1,2,\cdots\cdots,m, \\ \sum_{k=1}^{m} f_k(\theta) = 1, & 0 \le f_k(\theta) \le 1 \end{cases} \tag{11}$$

where $T_k(\theta)$ is the instantaneous torque of the kth phase winding, T_{ref} is the synthesized instantaneous reference torque, $f_k(\theta)$ is the torque share function of the kth phase winding, and m is the number of phases of SRM.

The torque share function directly affects the torque ripple and the reference peak current of each phase. Hence, the TSF function can effectively improve the steady-state performance of SRM. The common TSF functions include linear, cosine, cubic, and exponential. This paper analyzes the linear and cosine types, with their profiles and current diagrams depicted in Figure 4.

In a single rotor angular period, the reference torque of the kth phase can be expressed as:

$$T_{k\_ref}(\theta) = \begin{cases} 0, & 0 \le \theta \le \theta_{on} \\ T_{ref} f_{rise}, & \theta_{on} \le \theta \le \theta_{on} + \theta_{ov} \\ T_{ref}, & \theta_{on} + \theta_{ov} \le \theta \le \theta_{off} \\ T_{ref} f_{fall} & \theta_{off} \le \theta \le \theta_{off} + \theta_{ov} \\ 0, & \theta_{off} + \theta_{ov} \le \theta \le \tau_r \end{cases} \tag{12}$$

where T_{ref} is the total reference torque, f_{rise} is the slope of the rising phase of the input phase, and f_{fall} is the slope of the falling phase of the output phase. θ_{on}, θ_{off}, and θ_{ov} represent the turn-on, turn-off, and overlapping angles, respectively, and τ_r is the rotor angle period. The relationship between f_{rise} and f_{fall} is defined as:

$$f_{fall}(\theta) = 1 - f_{rise}(\theta - \varepsilon) \tag{13}$$

θ_{ov} should satisfy the following relational equation:

$$\theta_{ov} \le \frac{\tau_r}{2} - \theta_{off} \tag{14}$$

4.2 Partition torque correction control strategy

Generally, the tracking ability of the current is constrained by the power converter, and the traditional torque share function ignores the influence of current tracking characteristics. Therefore,

the output torque of each phase cannot track the reference torque, resulting in a large torque ripple. This paper considers this limitation in the proposed torque distribution curve design. Figure 5A illustrates the schematic diagram of the TSF control strategy based on cosine, where the solid line presents the reference torque distributed by the TSF function, and the dotted line is the actual torque generated in the motor running process. The diagram reveals that the torque at the position with a small inductance cannot track the given torque in time, resulting in a large torque error. Aiming to solve the torque ripple problem, this paper proposes a method based on the partition correction of the torque share function. According to Figure 5B, the commutation period is divided into three sub-intervals (intervals I, II, and III) with $\theta_{c1}$and θ_{c2} denoting the midpoints. The torque generation capacity of each phase at a different rotor position is analyzed, and the phase with a strong torque generation capacity is selected as the torque compensation phase. The performance of the torque share function is optimized according to the real-time torque tracking error, and the control ability of the actual current is improved. Thus, the optimization goal of torque ripple suppression is achieved.

$$\theta_{c1} = \theta_{on} + \frac{1}{3}\theta_{ov} \tag{15}$$

$$\theta_{c2} = \theta_{on} + \frac{2}{3}\theta_{ov} \tag{16}$$

The torque characteristic at different rotor positions is presented in Figure 6, and the difference in torque generation capacity between the adjacent phases during commutation is presented in Figure 7. By analyzing the rate of change for the torque at the commutation, the torque share function is constructed by partition optimization for the torque ripple minimization.

(1) Interval I: At the initial stage of commutation, the torque generation capacity of the K phase is lower than the K-1 phase. The torque of the K-1 phase is used as compensation instead of the K phase. For correcting TSF, the control block diagram of interval I is presented in Figure 8A, suggesting that the torque generation capacity of the k-1 phase is greater than that of the K phase in interval I. At this time, the K phase is at the stage of establishing an excitation current. Thus, the current value is small, and the change rate of winding inductance is low. Therefore, the actual torque generated cannot track the reference torque. At this time, the torque generation capacity of the k-1 phase is strong, and the k-1 phase can compensate for the torque error generated by the k phase.

The torque error of the K phase equation is

$$\Delta T_I = T_{k\_ref} - T_k \tag{17}$$

In the overlapping area, the total electromagnetic torque equals the sum of the electromagnetic torques of the input and output phases. The updated total reference torque can be expressed as:

$$\begin{aligned} T_{ref} &= T_{k-1}^{new} + T_k \\ &= T_{ref} f_{fall}^{new} + T_{ref} f_{rise}(k) \\ &= T_{ref}\left(f_{fall}(k-1) + \Delta f_I\right) + T_{ref} f_{rise}(k) \end{aligned} \tag{18}$$

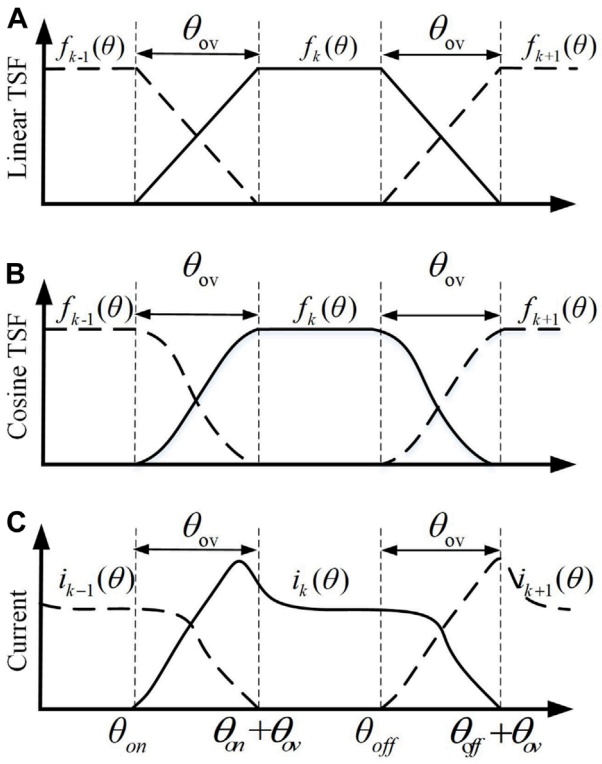

FIGURE 4
Profiles and current diagrams of linear and cosine TSF functions. **(A)**: Profiles of linear TSF. **(B)**: Profiles of cosine TSF. **(C)**: Diagram of phase current and rotor position.

The relationship between f_{rise} and f_{fall} is defined as

$$f_{fall}(\theta) = 1 - f_{rise}\left(\theta + \theta_{on} - \theta_{off}\right) \tag{19}$$

(2) Interval II: In the middle of commutation, the torque generation capacity of the k-1 phase is similar to that of the K phase. The K phase is in the current conduction interval, with strong control ability. The K phase compensates for the torque error caused by commutation.

The control block diagram of interval II correction TSF is depicted in Figure 8B, highlighting that the torque-generating capacity of the k-1 phase is similar to that of the K phase. At this time, the k-1 phase is at the turn-off freewheeling state, the current gradually decreases, the torque is in a state with a fixed profile decline, and the current control ability is weak. The k-phase current in this interval is rising, and the controllability is strong. Therefore, the k-phase is selected for torque compensation in interval II.

The torque error generated in this interval is:

$$\Delta T_{II} = \left|T_{k\_ref} - T_{k/(k-1)}\right| \tag{20}$$

The compensation function Δf_{II} can be expressed as:

$$\Delta f_{II} = a_{II}\left(\frac{\theta - \theta_{on}}{\theta_{ov}}\right)^{b_{II}} + a_{II}\Delta T_{II}^{c_{II}} \tag{21}$$

10.3389/fenrg.2024.1381950

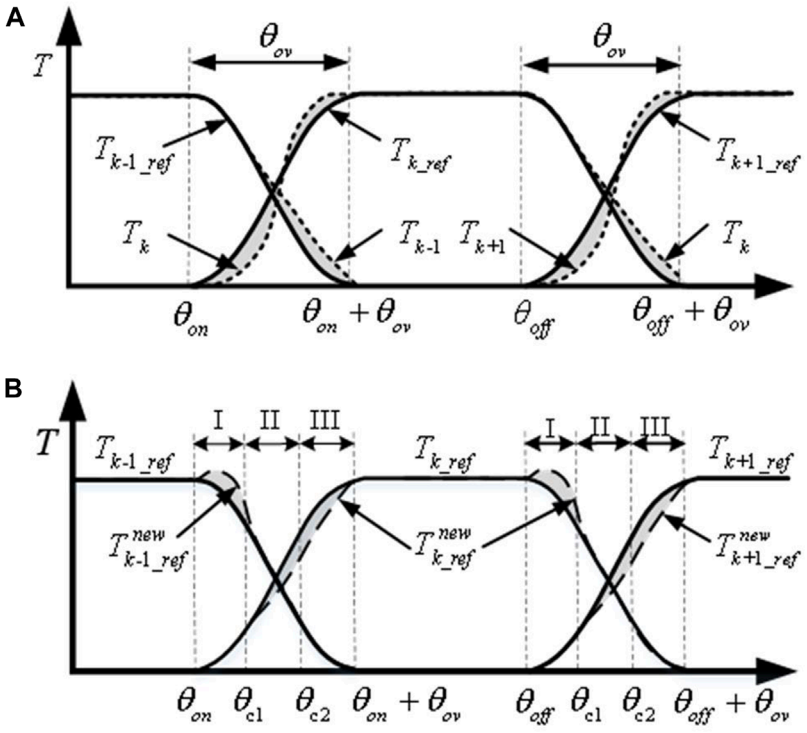

FIGURE 5
Schematic diagram of conventional and proposed TSF control strategy. **(A)**: Cosine TSF control strategy. **(B)**: Correction TSF strategy.

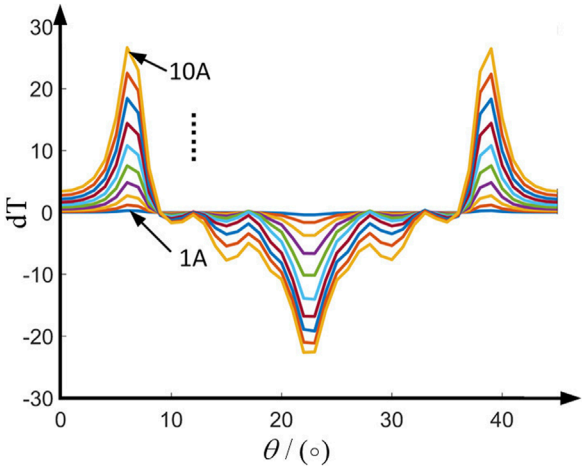

FIGURE 6
Simulation profiles of the torque characteristic at different rotor position.

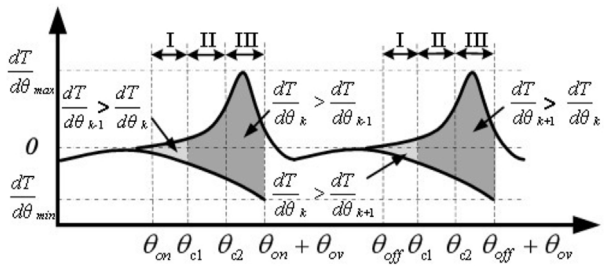

FIGURE 7
Diagram of torque generation capacity of different phases during commutation period.

(3) Interval III: In the later stage of commutation, the torque generation capability of the k-1 phase is lower than that of the k-phase. The block diagram of the interval III correction TSF control is illustrated in Figure 8C, revealing that the torque-generating capability of the k-phase is greater than that of the k-1 phase. At this time, the rate of change of the k-1 phase winding inductance is small. Thus, the phase torque is large, which causes the actual torque to exceed the reference torque, resulting in torque ripples. Additionally, the torque generation capability of the k-phase is relatively strong, so the k-phase compensates for the torque error generated by k-1.

The torque error of the k-1 phase can be expressed as:

$$\Delta T_{III} = T_{k-1} - T_{k-1\_ref} \tag{22}$$

The modified torque share function expression with adding the compensation function in sections is presented below:

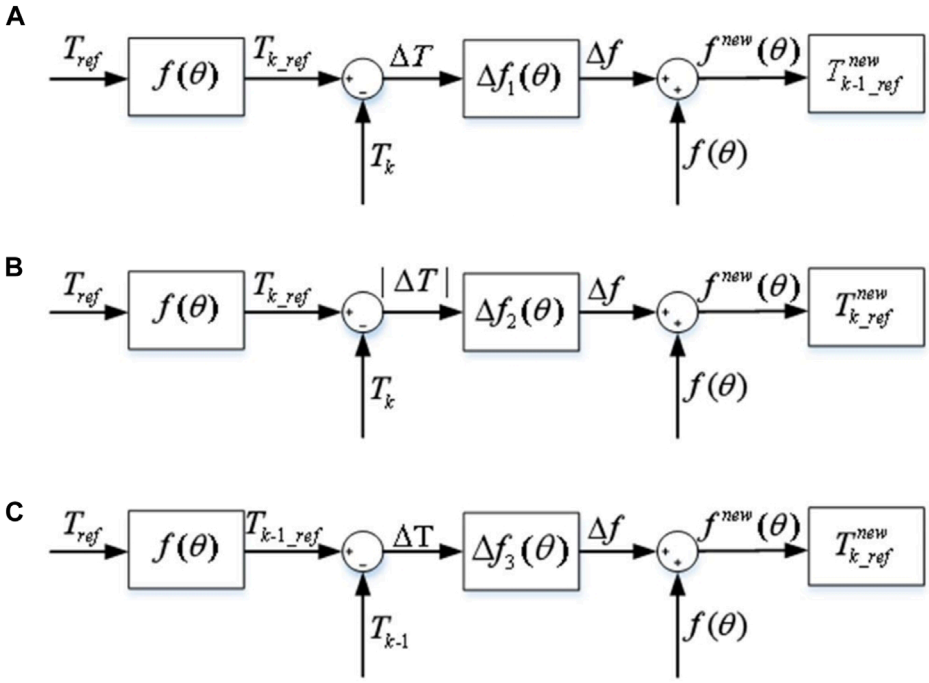

FIGURE 8
Control block diagram of correction TSF of three sub-intervals. **(A)**: Control block diagram of correction TSF of interval I. **(B)**: Control block diagram of correction TSF of interval II. **(C)**: Control block diagram of correction TSF of interval III.

$$f(\theta)=\begin{cases}0, & 0\le\theta\le\theta_{on}\\ f_{rise}, & \theta_{on}\le\theta\le\theta_{on}+\frac{1}{3}\theta_{ov}\\ f_{rise}+\Delta f_{II}, & \theta_{on}+\frac{1}{3}\theta_{ov}\le\theta_{on}+\frac{2}{3}\theta_{ov}\\ f_{rise}+\Delta f_{III} & \theta_{on}+\frac{2}{3}\theta_{ov}\le\theta\le\theta_{on}+\theta_{ov}\\ 1, & \theta_{on}+\theta_{ov}\le\theta\le\theta_{off}\\ f_{fall}+\Delta f_{I}, & \theta_{off}\le\theta\le\theta_{off}+\frac{1}{3}\theta_{ov}\\ f_{fall}, & \theta_{off}+\frac{1}{3}\theta_{ov}\le\theta\le\theta_{off}+\frac{2}{3}\theta_{ov}\\ f_{fall}, & \theta_{off}+\frac{2}{3}\theta_{ov}\le\theta\le\theta_{off}+\theta_{ov}\\ 0, & \theta_{off}\le\theta\le\tau_r\end{cases}\tag{23}$$

4.3 Evaluation criteria of torque share function control strategy

In order to ensure the stable operation of the motor in speed and torque output, this paper comprehensively considers the torque share function control strategy indicators.

The torque ripple of the motor T_r is defined as:

$$T_r=\frac{T_{max}-T_{min}}{T_{av}}\times 100\%\tag{24}$$

where T_{max} is the maximum torque, T_{min} is the minimum torque, and T_{av} is the average torque.

Copper loss is one of the important factors affecting the operating efficiency of the motor, which can be expressed by the RMS value I_{rms} during the conduction period:

$$I_{rms}=\sqrt{\frac{1}{\theta_p}\left(\int_{\theta_{on}}^{\theta_{off}}i_k^2d\theta+\int_{\theta_{on}}^{\theta_{off}}i_{k-1}^2d\theta\right)}\tag{25}$$

The copper loss of SRM is proportional to the square of the phase current, and the copper loss generated by the motor operation can be reduced by reducing the motor's phase current.

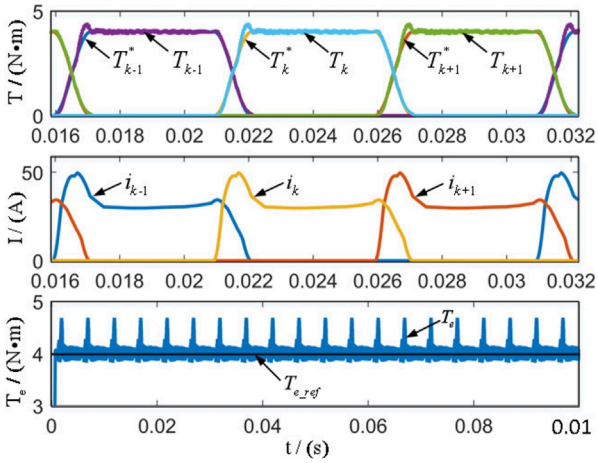

FIGURE 9
Simulation results of cosine TSF control strategy.

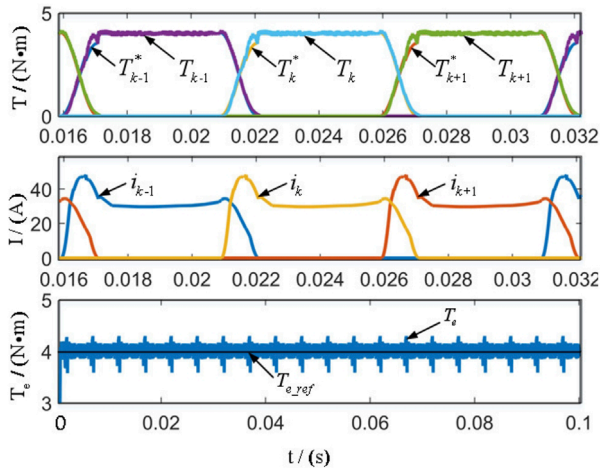

FIGURE 10
Simulation results of proposed TSF control strategy.

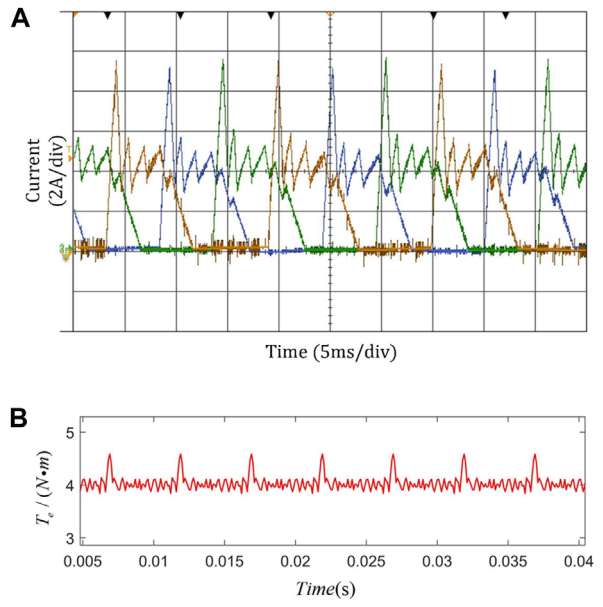

FIGURE 11
Experimental results of cosine TSF control strategy. **(A)**: Current waveform. **(B)**: Torque waveform.

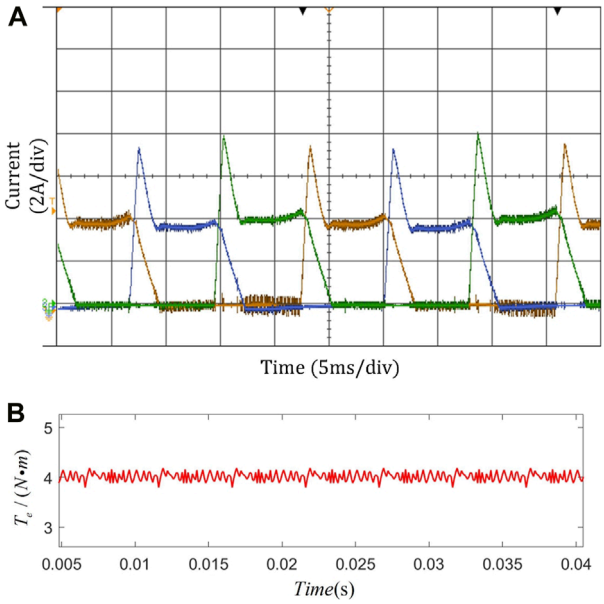

FIGURE 12
Experimental results of cosine TSF control strategy. **(A)**: Current waveform. **(B)**: Torque waveform.

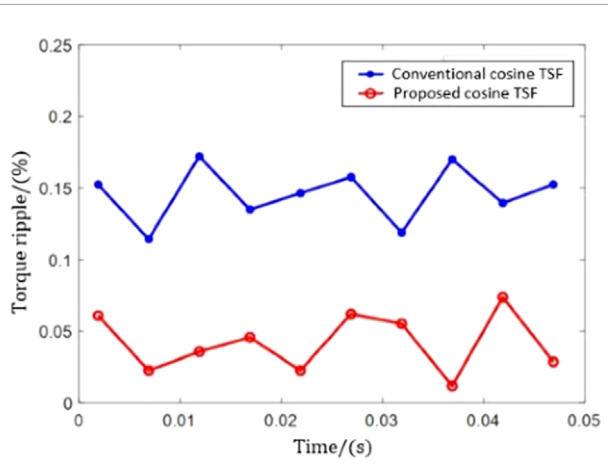

FIGURE 13
Torque Ripple Comparison of cosine TSF and correction TSF.

The flux linkage change rate of the motor is expressed as:

$$\frac{d\Psi_k}{d\theta} = \frac{U_k - R_k i_k - L\frac{di}{dt}}{\omega} \tag{26}$$

where the voltage drop $R_k I_k$ of the winding resistance is usually small compared to the dc-link voltage, and thus, the term $R_k I_k$ can be ignored in qualitative analysis. The above formula highlights that the flux linkage change rate is only affected by the DC-link voltage, the current change rate, and rotational speed.

5 Simulation analysis

The effectiveness of the proposed control strategy is verified using a three-phase 12/8 switched reluctance motor, where the flux linkage and torque characteristics of the switched reluctance motor are obtained using the Maxwell software. Figure 9, Figure 10, and Figure 11 illustrate the results of the traditional linear TSF, cosine TSF, and improved cosine TSF in the simulation test. For this trial, the parameters are configured as follows: dc-link voltage 72 V, given rotating speed 500r/min, turn-on angle, and turn-off angle are 0° and 22.5°.

According to the simulation results, the torque ripple of traditional linear TSF and cosine TSF is 25% and 23%, respectively.

Compared with the traditional TSF method, the torque ripple is reduced when using the proposed TSF, and the tracking ability of the torque is improved. The torque ripple is reduced from 23% to 18.6%. The simulation shows the motor has stronger torque ripple suppression ability using the modified torque share function partition control strategy.

6 Experimental analysis

An experimental platform for SR motor control is set up to verify the feasibility of the proposed torque ripple suppression control strategy. The experimental platform employs an STM32F103C8T6 chip as the control core and a 12/8 three-phase switched reluctance motor as the research object. The power converter adopts a three-phase asymmetric half-bridge circuit, and its rated speed is 2000r/min.

The experiment considers fixed turn-on and turn-off angles, and the reference speed is 500r/min. The results of the traditional cosine TSF and the improved cosine TSF are compared, and the experimental results are shown in Figures 12A,B, and Figure 13. The results infer that the improved cosine TSF adopted in this paper can improve the torque ripple during commutation and that the control index is better in a wide speed range.

7 Conclusion

In order to reduce the torque ripple effectively, a torque ripple suppression control strategy of switched reluctance motor based on partitioned TSF is proposed in this paper. In this control strategy, the torque share function is modified partitionally by using the difference of two-phase torque generation capacity during commutation. This method fully considers the problem of torque generation ability, which reduces the dependence of power converter, and achieves low torque ripple index, it also can be widely applied to other switched reluctance motors with different topologies. The simulation and experimental results show that the proposed control strategy can significantly reduce the torque ripple during commutation in a wide speed range and improve the reliability of motor operation.

Data availability statement

The original contributions presented in the study are included in the article/Supplementary material, further inquiries can be directed to the corresponding author.

Author contributions

CH: Writing–original draft, Writing–review and editing, Conceptualization, Data curation, Formal Analysis, Funding acquisition, Investigation, Methodology, Project administration, Resources, Software, Supervision, Validation, Visualization. HY: Conceptualization, Data curation, Funding acquisition, Investigation, Methodology, Resources, Software, Validation, Visualization, Writing–original draft. PY: Conceptualization, Formal Analysis, Funding acquisition, Investigation, Project administration, Resources, Software, Supervision, Validation, Writing–original draft. TZ: Conceptualization, Data curation, Funding acquisition, Investigation, Methodology, Project administration, Resources, Supervision, Validation, Visualization, Writing–original draft.

Funding

The author(s) declare that no financial support was received for the research, authorship, and/or publication of this article.

Conflict of interest

Author YH is employed by BYD Company Ltd.

PY is employed by Ruili Group Rui'an Auto Parts Co. Ltd.

The remaining authors declare that the research was conducted in the absence of any commercial or financial relationships that could be construed as a potential conflict of interest.

Publisher's note

References

Cao, Y., Zhou, B., Chung, C., Wu, T., Zheng, L., and Shuai, Z. (2024). A coordinated emergency response scheme for electricity and watershed networks considering spatio-temporal heterogeneity and volatility of rainstorm disasters. *IEEE Trans. Smart Grid* 1, 1. doi:10.1109/TSG.2024.3362344

Chen, F., Jianhu, Y., Pan, W., and Zhao, Y. (2018). Torque ripple suppression of switched reluctance motor based on modified torque sharing function. *Trans. China Electrotech. Soc.* 33, 394–400. doi:10.19595/j.cnki.1000-6753.tces.180593

Cheng, H., Zhang, D., Liao, S., Shao, D., and Hu, Y. (2022). Integrated drive converter of sds-srm with isolation and nonisolation charging capabilities for electric vehicle. *IEEE Trans. Industrial Electron.* 69, 8679–8691. doi:10.1109/tie.2021.3116569

Dang, X., Shi, Y., and Peng, H. (2020). Torque–flux linkage recurrent neural network adaptive inversion control of torque for switched reluctance motor. *IET Electr. Power Appl.* 14, 1612–1623. doi:10.1049/iet-epa.2020.0105

Dowlatshahi, M., Nejad, S. M. S., and Ahn, J.-W. (2013). "Torque ripple minimization of switched reluctance motor using modified torque sharing function," in *2013 21st Iranian conference on electrical engineering (ICEE)* (IEEE), 1–6.

Kim, J.-H., and Kim, R.-Y. (2018). Sensorless direct torque control using the inductance inflection point for a switched reluctance motor. *IEEE Trans. Industrial Electron.* 65, 9336–9345. doi:10.1109/TIE.2018.2821632

Kuang, S., Zhang, X., Zhang, Z., and Jiang, H. (2019). Sensorless control of switched reluctance motor based on intersection angle compensation of phase inductance. *Trans. China Electrotech. Soc.* 34, 4909–4917. doi:10.19595/j.cnki.1000-6753.tces.181491

Li, C., Zhang, C., Liu, J., and Bian, D. (2021). A high-performance indirect torque control strategy for switched reluctance motor drives. *Math. Problems Eng.* 2021, 1–15. doi:10.1155/2021/6618539

Li, H., Bilgin, B., and Emadi, A. (2018). An improved torque sharing function for torque ripple reduction in switched reluctance machines. *IEEE Trans. Power Electron.* 34, 1635–1644. doi:10.1109/TPEL.2018.2835773

Liu, D., Zhao, Y., and Fan, Y. (2019). "Subsection pwm variable duty cycle control of switched reluctance motor based on torque sharing function," in *2019 Chinese control conference (CCC)* (IEEE), 3243–3247.

Ma, M., Yu, F., Yang, Q., Wang, R., and Zhang, X. (2018). Control strategy of minimizing torque ripples of the switched reluctance motor by injecting piecewise harmonic currents. *Zhongguo Dianji Gongcheng Xuebao/Proceedings Chin. Soc. Electr. Eng.* 38, 285–291. doi:10.13334/j.0258-8013.pcsee.170276

Marcsa, D., and Kuczmann, M. (2017). Design and control for torque ripple reduction of a 3-phase switched reluctance motor. *Comput. Math. Appl.* 74, 89–95. doi:10.1016/j.camwa.2017.01.001

Qing, L., Wang, H., Ge, X., and Jiang, H. (2020). A high efficiency torque ripple suppression method for switched reluctance motor. *Trans. China Electrotech. Soc.* 35, 1912–1920. doi:10.19595/j.cnki.1000-6753.tces.190035

Sun, Q., Wu, J., and Gan, C. (2020). Optimized direct instantaneous torque control for srms with efficiency improvement. *IEEE Trans. Industrial Electron.* 68, 2072–2082. doi:10.1109/TIE.2020.2975481

Sun, Q., Wu, J., Gan, C., Hu, Y., and Si, J. (2016). Octsf for torque ripple minimisation in srms. *IET Power Electron.* 9, 2741–2750. doi:10.1049/iet-pel.2016.0270

Sun, X., Diao, K., Lei, G., Guo, Y., and Zhu, J. (2019). Direct torque control based on a fast modeling method for a segmented-rotor switched reluctance motor in hev application. *IEEE J. Emerg. Sel. Top. Power Electron.* 9, 232–241. doi:10.1109/JESTPE.2019.2950085

Sun, X., Shen, Y., Wang, S., Lei, G., Yang, Z., and Han, S. (2018). Core losses analysis of a novel 16/10 segmented rotor switched reluctance bsg motor for hevs using nonlinear lumped parameter equivalent circuit model. *IEEE/ASME Trans. Mechatronics* 23, 747–757. doi:10.1109/TMECH.2018.2803148

Xia, Z., Bilgin, B., Nalakath, S., and Emadi, A. (2020). A new torque sharing function method for switched reluctance machines with lower current tracking error. *IEEE Trans. Industrial Electron.* 68, 10612–10622. doi:10.1109/TIE.2020.3037987

Xi-Lian, W., Zhen-Liang, X. U., and Cui, W. (2015). Torque ripple and copper losses minimization control study of switched reluctance motor. *Electr. Mach. Control* 19, 7. doi:10.15938/j.emc.2015.07.008

Yan, N., Cao, X., and Deng, Z. (2019). Direct torque control for switched reluctance motor to obtain high torque–ampere ratio. *IEEE Trans. Industrial Electron.* 66, 5144–5152. doi:10.1109/TIE.2018.2870355

frontiers | Frontiers in Energy Research

TYPE Original Research
PUBLISHED 30 May 2024
DOI 10.3389/fenrg.2024.1400285

OPEN ACCESS

EDITED BY
Liansong Xiong,
Xi'an Jiaotong University, China

REVIEWED BY
Huangqing Xiao,
South China University of Technology, China
Xi Wu,
Southeast University, China

*CORRESPONDENCE
Zheren Zhang,
3071001296zhang@zju.edu.cn

RECEIVED 13 March 2024
ACCEPTED 19 April 2024
PUBLISHED 30 May 2024

CITATION
Ma J, Wu Z, Sun K, Wang C, Lu C, Gu Y, Liu J, Zhu C, Guo H, Zhang Z and Xu Z (2024), Research on variable pairing scheme for V/f controlled MMC station.
Front. Energy Res. 12:1400285.
doi: 10.3389/fenrg.2024.1400285

Research on variable pairing scheme for V/f controlled MMC station

Junchao Ma[1], Zhe Wu[2], Ke Sun[2], Chenxu Wang[1], Chengyu Lu[1], Yilei Gu[2], Jianing Liu[1], Chengzhi Zhu[1], Hanlin Guo[3], Zheren Zhang[3]* and Zheng Xu[3]

[1]State Grid Zhejiang Electric Power Co., Ltd. Research Institute, Hangzhou, China, [2]State Grid Zhejiang Electric Power Co., Ltd., Hangzhou, China, [3]Department of Electrical Engineering, Zhejiang University, Hangzhou, China

Grid-forming control is a promising solution for renewable power integration. This work presents a variable pairing scheme for the voltage controller of V/f controlled modular multilevel converter in an islanded network with a synchronous machine, which is a special type of grid-forming control. Based on the concept of the relative gain array (RGA), it is found that the RGA can be derived using steady-state sensitivity analysis. Then, the steady-state characteristics of the typical electrical components in the islanded network are considered, and the analytical expression for calculating the RGA is derived. Based on a typical system, a variable pairing scheme is then suggested using the calculated RGA elements. The time-domain simulations are conducted using PSCAD/EMTDC, and the results verify the feasibility and advantages of the suggested variable pairing scheme.

KEYWORDS

modular multilevel converter, grid-forming control, voltage controller, variable pairing scheme, relative gain array

1 Introduction

The need for carbon neutralization is rapidly driving transition from non-renewable to renewable energy utilization (Abbott, 2010). The bottleneck with utilizing renewable energy depends on large-scale exploitation and wide-area allocation (Blaabjerg et al., 2023). As predicted, the renewable power capacity in China is expected to increase to approximately 1070 GW during 2022–2027, and 90% of this is in the form of wind power and photovoltaics (PVs) (IEA, 2022). The large-scale renewable energy bases are mainly distributed in the north and west regions of China, and high-voltage direct current (HVDC) is expected to play a crucial role in transmitting the generated renewable energy to the load center in the eastern part of China (Rao et al., 2019).

With the increase in converter-interfaced power sources, load centers are facing serious security and stability issues as the proportion of synchronous machine sources has decreased. The first issue is the weak grid integration of HVDC stations (Yang et al., 2018); one possible solution to this issue is the use of the voltage-source converters (VSCs) that can operate in weak or even passive systems without commutation failure risks (Yazdani and Iravani, 2010; Zhou et al., 2014). Modular multilevel converters (MMCs) are considered as the most promising VSC topology (Debnath et al., 2015; Xiao et al., 2024a) and have been successfully implemented in many bulk-power HVDC

projects (Xu et al., 2020; Guo et al., 2022). The second issue is the deterioration of inertia, voltage, and frequency support; a possible solution to this issue is the use of grid-forming converters (Rosso et al., 2021; Xiao et al., 2024b). With proper grid-forming control, these converters can mimic the dynamics of the conventional synchronous generator, including the damping, inertia, voltage support, and frequency regulation characteristics (Beck and Hesse, 2007; Zhong and Weiss, 2011; Xiong et al., 2016a).

The technological evolution of grid-forming control has roughly experienced the following stages. Initially, droop control was proposed for load sharing (De Brabandere et al., 2007); then, the concept of a virtual synchronous generator was proposed for inertia emulation (Beck and Hesse, 2007). Power synchronization control was introduced to realize stable operation of converters in weak grids (Zhang et al., 2010). The design of grid-forming control is not as physically constrained as that of the synchronous generator and has greater flexibility. Thus, large amounts of research are still being conducted with the aim of improving the performances of grid-forming control schemes for the following aspects: synchronization stability, fault ride-through, and transition between control modes (Rosso et al., 2021). Pan et al. (2020) proved the equivalence of the above typical grid-forming control schemes. Droop control can be simplified to V/f control by setting the droop coefficient to 0, and V/f control is essentially a special type of grid-forming control (Yazdani, 2008). In MMC-HVDC projects, the grid-forming MMCs play important roles in islanded network connection scenarios, such as passive load supply and offshore wind-farm integration (Xiong et al., 2016b; Vidal-Albalate et al., 2016). Theoretically, grid-forming MMCs provide voltage and frequency support for islanded networks, acting as the "slack bus" or "PV bus." Hence, grid-forming MMCs can also be connected to islanded networks with local synchronous machines. A typical scenario of this type is an offshore island power system supplied with parallel AC and DC links; when the AC link trips, the offshore island power system can continue operating if the MMC is switched to the grid-forming mode (Liu et al., 2015).

Compared to a synchronous generator, the overcurrent capability of an MMC is limited. The maximum overcurrent capability of the MMC-HVDC is usually set to 1.2 p.u. as insulated-gate bipolar transistors (IGBTs) with a rated current of more than 3 kA are extremely expensive and are not widely used in MMC-HVDC projects. To protect the MMCs from overcurrents, grid-forming control always comprises an outer voltage loop and an inner current loop in practical MMC-HVDC projects (Guan and Xu, 2012). The inner current loop is the same as that in the conventional vector current control scheme and is cascaded with the outer voltage loop.

For the grid-forming MMC in an islanded network with a synchronous machine, determining the input–output pairing scheme of the outer voltage loop is an important concern. Most grid-forming MMC-HVDC projects directly adopt the default input–output pairing scheme, where the d-axis and q-axis voltage loops generate the d-axis and q-axis current references, respectively. Although this scheme has been proven to be effective in practical MMC-HVDC projects, it remains unclear whether there exist other reasonable input–output pairing schemes or whether the extant scheme is optimal. To solve these problems, the main focus and contributions of this work considering V/f control are as follows:

(1) The variables for the input–output pairing of the voltage controller in the grid-forming MMC were clarified, and the calculation method for the index matrix of the input–output pairing scheme is proposed. With the proposed method, the complex derivation of the state-space model can be avoided via steady-state sensitivity analysis.
(2) Based on steady-state sensitivity analysis, the recommended input–output pairing scheme of the voltage controller in the grid-forming MMC is proposed. The advantages of the recommended pairing scheme are examined through time-domain simulations.

The remainder of this article is organized as follows. Section 2 introduces some basic information, such as the topology and mathematical model of the grid-forming MMC. Section 3 describes the necessity and principle of variable pairing. Section 4 describes the detailed calculation method of the index matrix for variable pairing. Section 5 presents some case studies conducted on the basis of a typical system. Section 6 presents the conclusions of this work.

2 Basics of the grid-forming MMC

Supplementary Figure S1 illustrates the typical topology of an MMC that comprises three phase units, and each phase unit is composed of an upper arm and a lower arm. Each arm contains N cascaded submodules (SMs) and an arm inductance. According to Kirchhoff's theorem, the mathematical model of phase k (=a, b, c) can be written as Eq. (1):

$$\begin{cases} v_a + L_0\dfrac{di_{pk}}{dt} + u_{pk} = \dfrac{U_{dc}}{2} \\ v_a - L_0\dfrac{di_{nk}}{dt} - u_{nk} = -\dfrac{U_{dc}}{2} \end{cases} \tag{1}$$

Rewriting Eq. (1) with the common- and differential-mode components in phase k results in Eq. (2):

$$\begin{cases} \dfrac{L_0}{2}\dfrac{di_k}{dt} = u_{diffk} - v_k \\ L_0\dfrac{di_{cirk}}{dt} = \dfrac{U_{dc}}{2} - u_{comk} \end{cases}, \tag{2}$$

where

$$\begin{cases} u_{diffk} = \frac{1}{2}\left(u_{nk} - u_{pk}\right), u_{comk} = \frac{1}{2}\left(u_{nk} + u_{pk}\right) \\ i_{cirk} = \frac{1}{2}\left(i_{nk} + i_{pk}\right) \end{cases}. \tag{3}$$

According to the differential-mode model, the equivalent circuit of a grid-forming MMC station connected to an islanded network with a synchronous machine can be generalized as shown in Supplementary Figure S2, where the connected AC network is represented by its Thevenin equivalent circuit (Zhang et al., 2016). In Supplementary Figure S2, $E\angle\delta$ and Z_s (=R_s + jX_s) are the Thevenin equivalent voltage and impedance of the connected

AC network, respectively. The voltage at the point of common coupling (PCC) is denoted as $U\angle 0$; and $(P_s + jQ_s)$ indicates the output power of the MMC station. The transformer leakage inductance is given by L_T.

The blocks of the conventional grid-forming control scheme in the dq reference frame are shown in Supplementary Figure S3. The phase angle signal θ for the abc-dq reference frame transform is generated using the phase angle generator in Supplementary Figure S3A via V/f control or the power synchronization loop (PSL) in power synchronization control; here, ω_0 is the rated angular frequency, while T_J and D_J are the time constant and damping coefficient of the PSL, respectively. The proportional–integral controller is denoted as PI. Furthermore, u_d and u_q are the d- and q-axis components of the PCC voltage while i_d and i_q are the d- and q-axis components of the MMC output current in the dq reference frame, respectively. The superscript "*" indicates the reference signals; u^*_{diffd} and u^*_{diffq} are the reference signals of the d- and q-axis components of the MMC differential-mode voltage.

The voltage controller in Supplementary Figure S3B generates i^*_d and i^*_q, which are also the inputs to the current controller. The current controller in Supplementary Figure S3C generates u^*_{diffd} and u^*_{diffq}, and L is equal to the sum of L_T and $L_0/2$. In PI controllers, the d- and q-axis components can accurately track their references in steady state. If the time delays in the controllers are neglected, u^*_{diffd} and u^*_{diffq} can be treated as the d- and q-axis components (u_{diffd} and u_{diffq}) of the MMC differential-mode voltage. By regulating u_{diffd} and u_{diffq}, the target of grid-forming control can be achieved.

From Supplementary Figure S3, it is seen that V/f control is a special type of grid-forming control; given the basic voltage and current controllers, it has the most fundamental characteristic of grid-forming control, i.e., the voltage source behavior. Its difference with other types of control is that the phase angle is obtained by integrating the fixed angular frequency rather than through the droop regulator or PSL. In fact, when the droop coefficient is set to 0 or T_j is considered to be infinity, the droop control and power synchronization control will degenerate into V/f control.

3 Variable pairing for the voltage controller of grid-forming MMC

3.1 Necessity of input–output pairing in the outer loop

As a special type of grid-forming control, the block diagram of the V/f-controlled MMC station is illustrated in Supplementary Figure S4, where the connected AC system is labeled as $G_{grid}(s)$. Moreover, the voltage controller of the grid-forming MMC adopts the widely used default $u^*_d - i^*_d$ and $u^*_q - i^*_q$ pairing scheme (Scheme 1) shown in Supplementary Figure S4. In the most common passive load supply scenario, there are two typical cases: (1) purely resistive load supply and (2) purely inductive load supply. Passive loads with other power factors are situated between these two cases. The following analysis aims to qualitatively explain the small-disturbance stability of Scheme 1.

Scheme 1 is stable with a small disturbance. Suppose that this system is already operating in a steady state. When there is a small increase in u^*_d, the d-axis current reference i^*_d increases due to the voltage controller, leading to increase in i_d. For a resistive load, the increase in i_d means increase in the load current, causing an increase in the d-axis component u_d of the PCC voltage.

For an inductive load, the increase in i_d causes an increase in u_q because of the inductive load characteristics. Subsequently, under regulation by the voltage controller, the q-axis current reference i^*_q decreases, causing a decrease in i_q. Consequently, there is an increase in the d-axis component u_d of the PCC voltage by the inductive load characteristics.

The aforementioned two processes are plotted in Supplementary Figure S5A,B, where the blue and red arrows respectively indicate the changes in the reference voltage and response characteristics. However, when there is a synchronous machine in the islanded network, the physical meaning of Scheme 1 is not intuitive. Considering the example of Supplementary Figure S2, the output active and reactive powers of the MMC station can be calculated as in Eq. (4):

$$\begin{cases} P_s = \dfrac{U^2}{|Z_s|}\cos\alpha - \dfrac{UE}{|Z_s|}\cos(\delta-\alpha) \\ Q_s = \dfrac{U^2}{|Z_s|}\sin\alpha + \dfrac{UE}{|Z_s|}\sin\alpha(\delta-\alpha) \end{cases}, \tag{4}$$

where α is the impedance angle of Z_s. It is noted that α is usually close to $\pi/2$, so it can be concluded that the active power is closely related to the voltage phase angle difference between the PCC and Thevenin equivalent voltages and that the reactive power is closely related to the PCC voltage magnitude. Considering that the steady-state phase angle of the PCC voltage is 0, the voltage phase angle difference and PCC voltage magnitude are dominated by the q- and d-axis components of the PCC voltage, respectively.

The output active and reactive powers of the MMC station can be also calculated using the d- and q-axis components of the PCC voltage and current as in Eq. (5):

$$\begin{cases} P_s = u_d i_d + u_q i_q \\ Q_s = -u_d i_q + u_q i_d \end{cases}. \tag{5}$$

Since u_d and u_q are approximately 1.0 p.u. and 0 p.u., respectively, the output active and reactive powers are dominated by the d- and q-axis components of the MMC output current. The above analysis indicates that the $u^*_d - i^*_q$ pairing scheme would be more reasonable than the default $u^*_d - i^*_d$ pairing scheme since the MMC station output reactive power is dominated by u_d and i_q. The effect of i_d in the reactive power control is not as significant as that of i_q. Similarly, the $u^*_q - i^*_d$ pairing scheme would be more reasonable than the default $u^*_q - i^*_q$ scheme. For simplicity, the $u^*_d - i^*_q$ and $u^*_q - i^*_d$ pairing scheme for the voltage controller is denoted as Scheme 2.

3.2 Input–output pairing method for the outer loop

Based on Supplementary Figure S4, the block diagram of variable pairing for the voltage controller is outlined in Supplementary Figure S6, where the connected AC system,

voltage controller, and MMC station plus current controller are labeled as $G_{grid}(s)$, $G_v(s)$, and $G_{MMC}(s)$, respectively. It is noted that the aim of the voltage controller is to make u_d (u_q) track its reference u_d^* (u_q^*) and that the variable pairing for the voltage controller $G_v(s)$ essentially helps determine the pairing scheme between the input (u_d, u_q) and output (i_d^*, i_q^*).

This work aims to determine the variable pairing scheme based on concept of the relative gain array (RGA) (Bristol, 1966). The RGA relies on calculating the coupling degree between the input and output of the system's remaining part, except for the controller whose variables are to be paired. Here, the system's remaining part includes the connected AC system and MMC station plus current controller, which is denoted as $G(s)$ in Supplementary Figure S6. $G(s)$ is a typical two-input two-output system, and the relative gain between the jth input and ith output (element in row i and column j of the RGA $\mathbf{\Lambda}$) of $G(s)$ is defined as Eq. (6):

$$\lambda_{ij} \triangleq \frac{g_{ij}}{\hat{g}_{ij}} = \frac{\left(\frac{\partial y_{out_i}}{\partial u_{in_j}}\right)_{\Delta u_{in_k}=0\,(k\neq j)}}{\left(\frac{\partial y_{out_i}}{\partial u_{in_j}}\right)_{\Delta y_{out_i}=0\,(i\neq j)}}, \tag{6}$$

where u_{in_j} and y_{out_i} are the jth input and ith output of system $G(s)$; the numerator is the open-loop gain when all other loops are open, and the denominator is the open-loop gain when all other loops are closed with perfect control.

The variable paring can be selected on the basis of the RGA according to the following criteria: (1) when λ_{ij} is closer to 1, u_{in_j} and y_{out_i} are paired better; (2) when λ_{ij} is between 0.8 and 1.2, then u_{in_j} and y_{out_i} form a suitable pair, but λ_{ij} beyond this range does not necessarily mean an infeasible pair. However, the RGA does not provide any information on the stability of the system. The RGA $\mathbf{\Lambda}$ can be calculated as

$$\Lambda = \mathbf{G}(0).*\left(\mathbf{G}(0)^{-1}\right)^T, \tag{7}$$

where $\mathbf{G}(0)$ is defined as $\mathbf{G}(s)|s=0$; the operation ".*" indicates the Hadamard product; $\mathbf{G}(0)^{-1}$ is the inverse matrix of $\mathbf{G}(0)$; and the superscript "T" is the matrix transpose.

4 Calculation of RGA for V/f-controlled MMC in an islanded network with a synchronous machine

A multi-input multi-output system can be linearized for a specified working point and generalized in its state-space form as

$$\begin{cases} \dfrac{d\Delta\mathbf{x}}{dt} = \mathbf{A}\Delta\mathbf{x} + \mathbf{B}\Delta\mathbf{u} \\ \Delta\mathbf{y} = \mathbf{C}\Delta\mathbf{x} + \mathbf{D}\Delta\mathbf{u} \end{cases}, \tag{8}$$

where $\mathbf{x}$ is the set of state variables; $\mathbf{y}$ and $\mathbf{u}$ are the sets of outputs and inputs; Δ is a small disturbance; and $\mathbf{A}$, $\mathbf{B}$, $\mathbf{C}$, and $\mathbf{D}$ are the coefficient matrices. Therefore, the transfer function between $\Delta\mathbf{u}$ and $\Delta\mathbf{y}$ can be derived as

$$\begin{cases} \Delta\mathbf{y} = \mathbf{G}(s)\Delta\mathbf{u} \\ \mathbf{G}(s) = \mathbf{C}(s\mathbf{I} - \mathbf{A})^{-1}\mathbf{B} + \mathbf{D} \end{cases}. \tag{9}$$

As noted in Section 3, only $\mathbf{G}(0)$ is needed to calculate the RGA $\mathbf{\Lambda}$, and Eq. (9) can be written as Eq. (10) after setting s to 0:

$$\begin{cases} \Delta\mathbf{y} = \mathbf{G}(0)\Delta\mathbf{u} \\ \mathbf{G}(0) = -\mathbf{C}\mathbf{A}^{-1}\mathbf{B} + \mathbf{D} \end{cases}. \tag{10}$$

Theoretically, the most intuitive method of calculating $\mathbf{G}(0)$ is based on the second expression in Eq. (10), which requires developing the detailed state-space model of the complete system to obtain matrices $\mathbf{A}$, $\mathbf{B}$, $\mathbf{C}$, and $\mathbf{D}$. However, these matrices are no longer needed when $\mathbf{G}(0)$ is calculated, and there exists another method wherein the calculation of matrices $\mathbf{A}$, $\mathbf{B}$, $\mathbf{C}$, and $\mathbf{D}$ can be avoided.

According to the first expression in Eq. (10), $\mathbf{G}(0)$ indicates the relationship between the steady-state small disturbances in the input $\mathbf{u}$ and output $\mathbf{y}$. In other words, $\mathbf{G}(0)$ is essentially the steady-state sensitivity matrix between $[i_d^*, i_q^*]^T$ and $[u_d, u_q]^T$. Hence, $\mathbf{G}(0)$ can be calculated based on the steady-state sensitivity analysis.

Four types of typical electrical components are considered in this work: the MMC station, load, synchronous machine, and power grid network. The steady-state characteristics of these components and the complete system will be discussed separately. For simplicity, the common xy reference frame is aligned with the V/f-controlled MMC dq reference frame, and the derivations below are based on the V/f-controlled MMC's dq reference frame. The coordinate transformation between the xy and dq frames is shown in Supplementary Figure S7; it should be noted that the real and imaginary parts in the current/voltage phasor correspond to the d- and q-axis components of the current/voltage since the common xy reference frame is already aligned with the V/f-controlled MMC's dq reference frame.

4.1 MMC station

For the scheme shown in Supplementary Figure S4, the mathematical model of the MMC station plus current controller is described by Eqs. (11, 12):

$$\begin{cases} u_{diffd}(s) = u_d(s) - \omega L i_q(s) + \left[i_d^*(s) - i_d(s)\right]\left(k_{p2} + \dfrac{k_{i2}}{s}\right) \\ u_{diffq}(s) = u_q(s) + \omega L i_d(s) + \left[i_q^*(s) - i_q(s)\right]\left(k_{p2} + \dfrac{k_{i2}}{s}\right) \end{cases}, \tag{11}$$

$$\begin{cases} i_d(s) = \left[u_{diffd}(s) - u_d(s) + \omega L i_q(s)\right]/sL \\ i_q(s) = \left[u_{diffq}(s) - u_q(s) - \omega L i_d(s)\right]/sL \end{cases}, \tag{12}$$

where k_{p2} and k_{i2} are the proportion and integral gains of the current controller, respectively.

After substituting Eq. (11) into Eq. (12), $\mathbf{G}_{\mathrm{MMC}}(s)$ can be derived as in Eq. (13), and $\mathbf{G}_{\mathrm{MMC}}(0)$ is a 2 × 2 identity matrix. Therefore, the steady-state sensitivity matrix between $[i_d^*, i_q^*]^T$ and $[u_d, u_q]^T$ becomes the steady-state sensitivity matrix between $[i_d, i_q]^T$ and $[u_d, u_q]^T$.

$$\mathbf{G}_{MMC}(s) = \begin{pmatrix} \dfrac{sk_{p2} + k_{i2}}{s^2L + sk_{p2} + k_{i2}} & 0 \\ 0 & \dfrac{sk_{p2} + k_{i2}}{s^2L + sk_{p2} + k_{i2}} \end{pmatrix}. \tag{13}$$

4.2 Load

Three types of load models are considered in this work: constant impedance, constant current, and constant power loads. Suppose that the voltage and current phasors of the load node are $\dot{U}_l$ and $\dot{I}_l$ (flowing out of the load), respectively; the steady-state voltage–current characteristics of the constant impedance load can be generalized as in Eq. (14):

$$\dot{I}_l = -Y_l \dot{U}_l, \tag{14}$$

where Y_l ($Y_l = G_l + jB_l$) is the admittance of the load. Thus, the steady-state voltage–current small-disturbance characteristics of the constant impedance load is as follows:

$$\begin{bmatrix} \Delta I_{ld} \\ \Delta I_{lq} \end{bmatrix} = -\begin{bmatrix} G_l & -B_l \\ B_l & G_l \end{bmatrix} \begin{bmatrix} \Delta U_{ld} \\ \Delta U_{lq} \end{bmatrix}, \tag{15}$$

where ΔI_{ld} and ΔI_{lq} are the real and imaginary parts of vector $\Delta \dot{I}_l$, respectively; ΔU_{ld} and ΔU_{lq} are the real and imaginary parts of vector $\Delta \dot{U}_l$, respectively.

For the constant current load, the steady-state voltage–current small-disturbance characteristics are described by Eq. (16):

$$\begin{bmatrix} \Delta I_{ld} \\ \Delta I_{lq} \end{bmatrix} = \begin{bmatrix} 0 \\ 0 \end{bmatrix}. \tag{16}$$

For the constant power load, the steady-state active and reactive powers can be calculated using Eq. (17), and the derived steady-state voltage–current small-disturbance characteristics are given by Eq. (18).

$$\begin{cases} -P_l = U_{ld} I_{ld} + U_{lq} I_{lq} \\ -Q_l = -U_{ld} I_{lq} + U_{lq} I_{ld} \end{cases}, \tag{17}$$

$$\begin{bmatrix} \Delta I_{ld} \\ \Delta I_{lq} \end{bmatrix} = -\begin{bmatrix} U_{ld} & U_{lq} \\ U_{lq} & -U_{ld} \end{bmatrix}^{-1} \begin{bmatrix} I_{ld} & I_{lq} \\ -I_{lq} & I_{ld} \end{bmatrix} \begin{bmatrix} \Delta U_{ld} \\ \Delta U_{lq} \end{bmatrix}. \tag{18}$$

4.3 Synchronous machine

Given the existence of the V/f-controlled MMC station (slack bus), a synchronous machine can be treated as either the PQ or PV bus in the steady-state analysis. Therefore, both the steady-state active power and steady-state reactive power (or terminal voltage) should be taken into account. The synchronous machine's steady-state electrical power P_g is approximately equal to its mechanical power P_m provided the equivalent damping of the synchronous machine is small enough. For synchronous generators, P_m has a linear relationship with the rotor angular frequency as given in Eq. (19), where P_{m0}, ω_0, ω_g, and R_d are the reference mechanical power, rated rotor speed, steady-state rotor speed, and rotor speed-governor speed droop coefficient, respectively. For synchronous condensers, P_g is approximately equal to zero.

$$P_g = P_m = P_{m0} + \left(\omega_0 - \omega_g\right)/R_d. \tag{19}$$

Considering the frequency support from the V/f-controlled MMC station, ω_g is always equal to ω_0 in the steady state, and the synchronous machine's steady-state electrical power remains constant. Therefore, the small disturbance of the synchronous machine's steady-state active power is 0.

$$\Delta P_g = \Delta P_{m0} = 0. \tag{20}$$

Based on the above analysis, the steady-state voltage–current small-disturbance characteristics in accordance with the active power are derived as in Eq. (21), where the subscripts d and q respectively mean the real and imaginary parts of the phasor in the V/f-controlled MMC's dq reference frame (also the d- and q-axis components).

$$\begin{bmatrix} U_{gd} & U_{gq} \end{bmatrix} \begin{bmatrix} \Delta I_{gd} \\ \Delta I_{gq} \end{bmatrix} = -\begin{bmatrix} I_{gd} & I_{gq} \end{bmatrix} \begin{bmatrix} \Delta U_{gd} \\ \Delta U_{gq} \end{bmatrix}. \tag{21}$$

The next step involves modeling the steady-state voltage–current small-disturbance characteristics based on the reactive power (or terminal voltage). The first mode is the constant reactive power control mode, where the synchronous machine's steady-state reactive power Q_g is constant. The steady-state voltage–current small-disturbance characteristics are as shown in Eq. (22):

$$\begin{bmatrix} U_{gq} & -U_{gd} \end{bmatrix} \begin{bmatrix} \Delta I_{gd} \\ \Delta I_{gq} \end{bmatrix} = \begin{bmatrix} I_{gq} & -I_{gd} \end{bmatrix} \begin{bmatrix} \Delta U_{gd} \\ \Delta U_{gq} \end{bmatrix}. \tag{22}$$

The second mode is the constant terminal voltage control mode, where the steady-state terminal voltage U_g is constant. Equation (23) gives the steady-state voltage–current small-disturbance characteristics in this mode.

$$\begin{bmatrix} U_{gd} & U_{gq} \end{bmatrix} \begin{bmatrix} \Delta U_{gd} \\ \Delta U_{gq} \end{bmatrix} = 0. \tag{23}$$

The third mode is the constant reactive power control mode, where the steady-state reactive power Q_g has a linear relationship with the terminal voltage U_g, as shown in Eq. (24). The steady-state voltage–current small-disturbance characteristics are described by Eq. (25), where Q_{g0} and K_q represent the output reactive power reference and terminal voltage output reactive power droop coefficient.

$$Q_g = K_q\left(U_{g0} - U_g\right) + Q_{g0}, \tag{24}$$

$$\begin{bmatrix} U_{gq} & -U_{gd} \end{bmatrix} \begin{bmatrix} \Delta I_{gd} \\ \Delta I_{gq} \end{bmatrix} = \begin{bmatrix} I_{gq} - \dfrac{K_q U_{gd}}{U_g} & -\dfrac{K_q U_{gq}}{U_g} - I_{gd} \end{bmatrix} \begin{bmatrix} \Delta U_{gd} \\ \Delta U_{gq} \end{bmatrix}. \tag{25}$$

4.4 Power grid network

The power grid network acts as a bridge to connect the individual components and establish the relationship between i_{dq} and u_{dq}. The steady-state analysis is based on the nodal voltage equations of Eq. (26), where the power grid network is represented by the nodal admittance matrix $\mathbf{Y}$ ($= \mathbf{G} + j\mathbf{B}$). By expanding Eq. (26) into the real and imaginary parts, Eq. (27) can be derived.

$$\begin{cases} (\mathbf{I} + \Delta\mathbf{I}) = \mathbf{Y}(\mathbf{U} + \Delta\mathbf{I}) \\ \mathbf{I} = \mathrm{YU} \end{cases}, \tag{26}$$

$$\begin{cases} \Delta\mathbf{I}_d = \mathbf{G}\Delta\mathbf{U}_d - \mathbf{B}\Delta\mathbf{U}_q \\ \Delta\mathbf{I}_q = \mathbf{B}\Delta\mathbf{U}_d + \mathbf{G}\Delta\mathbf{U}_q \end{cases}. \tag{27}$$

In Eqs. (26, 27), $\mathbf{I}(=[\dot{I}_1, \dot{I}_2, \ldots, \dot{I}_n]^{\mathrm{T}})$ and $\mathbf{U}(=[\dot{U}_1, \dot{U}_2, \ldots, \dot{U}_n]^{\mathrm{T}})$ are the injecting current phasor vector and node voltage vector of the power grid network, $\Delta\mathbf{I}$ and $\Delta\mathbf{U}$ are small disturbances in vectors $\mathbf{I}$ and $\mathbf{U}$, $\Delta\mathbf{I_d}$ and $\Delta\mathbf{I_q}$ are the real and imaginary parts of the vector $\Delta\mathbf{I}$, and $\Delta\mathbf{U_d}$ and $\Delta\mathbf{U_q}$ are the real and imaginary parts of the vector $\Delta\mathbf{U}$, respectively.

With the exception of the constant current load nodes and V/f-controlled MMC station, suppose that there are k load nodes and r synchronous machine nodes in the islanded network. By rearranging Eq. (27) in the order of the V/f-controlled MMC station, load, and synchronous machine nodes, Eq. (28) can be derived. For compactness, the subscript "dq" indicates vectors containing both the d-axis and q-axis components in the V/f-controlled MMC station's dq reference frame.

$$\begin{bmatrix} \frac{\Delta I_{1dq}}{\Delta I_{l1dq}} \\ \vdots \\ \frac{\Delta I_{lkdq}}{\Delta I_{g1dq}} \\ \vdots \\ \Delta I_{grdq} \end{bmatrix} = \begin{bmatrix} \mathbf{Y}_{11} & \mathbf{Y}_{12} & \mathbf{Y}_{13} \\ \mathbf{Y}_{21} & \mathbf{Y}_{22} & \mathbf{Y}_{23} \\ \mathbf{Y}_{31} & \mathbf{Y}_{32} & \mathbf{Y}_{33} \end{bmatrix} \begin{bmatrix} \frac{\Delta U_{1dq}}{\Delta U_{l1dq}} \\ \vdots \\ \frac{\Delta U_{lkdq}}{\Delta U_{g1dq}} \\ \vdots \\ \Delta U_{grdq} \end{bmatrix}. \tag{28}$$

For brevity, the load current and voltage small-disturbance vectors are denoted by $\Delta\mathbf{I}_{Ldq}$ and $\Delta\mathbf{U}_{Ldq}$, and the synchronous machine current and voltage small-disturbance vectors are denoted by $\Delta\mathbf{I}_{Gdq}$ and $\Delta\mathbf{U}_{Gdq}$, respectively. Then, Eq. (28) can be expanded into Eqs. (29–31).

$$\Delta I_{1dq} = \mathbf{Y}_{11}\Delta U_{1dq} + \mathbf{Y}_{12}\Delta\mathbf{U}_{Ldq} + \mathbf{Y}_{13}\Delta\mathbf{U}_{Gdq}, \tag{29}$$

$$\Delta\mathbf{I}_{Ldq} = \mathbf{Y}_{21}\Delta U_{1dq} + \mathbf{Y}_{22}\Delta\mathbf{U}_{Ldq} + \mathbf{Y}_{23}\Delta\mathbf{U}_{Gdq}, \tag{30}$$

$$\Delta\mathbf{I}_{Gdq} = \mathbf{Y}_{31}\Delta U_{1dq} + \mathbf{Y}_{32}\Delta\mathbf{U}_{Ldq} + \mathbf{Y}_{33}\Delta\mathbf{U}_{Gdq}. \tag{31}$$

4.5 Steady-state sensitivity calculation

As noted in Section 4.2 and Section 4.3, the relationships between $\Delta\mathbf{I}_{Ldq}$ and $\Delta\mathbf{U}_{Ldq}$ as well as $\Delta\mathbf{I}_{Gdq}$ and $\Delta\mathbf{U}_{Gdq}$ can be generalized in compact form as Eqs. (32, 33), respectively.

$$\Delta\mathbf{I}_{Ldq} = \mathbf{E}\Delta\mathbf{U}_{Ldq}, \tag{32}$$

$$\mathbf{F}\Delta\mathbf{I}_{Gdq} = \mathbf{H}\Delta\mathbf{U}_{Gdq} + \mathbf{J}\Delta I_{1dq} + \mathbf{K}\Delta U_{1dq}. \tag{33}$$

By substituting Eqs (32, 33) into Eqs (30, 31), $\Delta\mathbf{I}_{Gdq}$ and $\Delta\mathbf{I}_{Ldq}$ can be eliminated, and the vectors $\Delta\mathbf{U}_{Gdq}$ and $\Delta\mathbf{U}_{Ldq}$ can be solved as linear combinations of ΔU_{1dq} and ΔI_{ldq}, as shown in Eq. (34):

$$\begin{cases} \Delta\mathbf{U}_{Ldq} = \mathbf{N}\Delta I_{1dq} + \mathbf{W}\Delta U_{1dq} \\ \Delta\mathbf{U}_{Gdq} = \mathbf{M}^{-1}\mathbf{J}\Delta I_{1dq} + \mathbf{M}^{-1}\mathbf{L}\Delta U_{1dq} \end{cases}, \tag{34}$$

where

$$\begin{cases} \mathbf{L} = \mathbf{K} - \mathbf{F}\mathbf{Y}_{31} + \mathbf{F}\mathbf{Y}_{32}(\mathbf{Y}_{22} - \mathbf{E})^{-1}\mathbf{Y}_{21} \\ \mathbf{M} = \mathbf{F}\mathbf{Y}_{33} - \mathbf{H} - \mathbf{F}\mathbf{Y}_{32}(\mathbf{Y}_{22} - \mathbf{E})^{-1}\mathbf{Y}_{23} \\ \mathbf{N} = (\mathbf{E} - \mathbf{Y}_{22})^{-1}\mathbf{Y}_{23}\mathbf{M}^{-1}\mathbf{J} \\ \mathbf{W} = (\mathbf{E} - \mathbf{Y}_{22})^{-1}(\mathbf{Y}_{21} + \mathbf{Y}_{23}\mathbf{M}^{-1}\mathbf{L}) \end{cases}. \tag{35}$$

Substituting Eq. (34) into Eq. (29), the steady-state characteristics between ΔI_{ldq} and ΔU_{1dq} can be derived as Eq. (36), where $\mathbf{I}$ is the identity matrix. Thus, the matrix $\mathbf{G}(0)$ (also the steady-state sensitivity matrix) can be calculated using Eq. (37).

$$(\mathbf{I} - \mathbf{Y}_{12}\mathbf{N} - \mathbf{Y}_{13}\mathbf{M}^{-1}\mathbf{J})\Delta I_{1dq} = (\mathbf{Y}_{11} + \mathbf{Y}_{12}\mathbf{W} + \mathbf{Y}_{13}\mathbf{M}^{-1}\mathbf{L})\Delta U_{1dq}, \tag{36}$$

$$\mathbf{G}(0) = (\mathbf{Y}_{11} + \mathbf{Y}_{12}\mathbf{W} + \mathbf{Y}_{13}\mathbf{M}^{-1}\mathbf{L})^{-1}(\mathbf{I} - \mathbf{Y}_{12}\mathbf{N} - \mathbf{Y}_{13}\mathbf{M}^{-1}\mathbf{J}). \tag{37}$$

5 Case studies

5.1 Description of the test case

The test case is shown in Supplementary Figure S8, where the power load in the islanded network is supplied by an MMC station and an AC tie line. When the AC tie line L_1 is tripped, there is a need for control-mode switching (PQ to V/f mode) in the MMC station. G_C in Supplementary Figure S8 represents a synchronous condenser. The parameters of this system are listed in Table 1. In this case, the constant impedance load model is adopted, and the synchronous condenser regulates the terminal voltage (20 kV side) at 1.0 p.u. The PCC voltage and frequency that are regulated by the MMC station in the V/f mode are set as 1.0 p.u. and 50 Hz, respectively. Before disconnection of AC tie line L_1, both the active and reactive powers of the MMC station are both set to 0.

5.2 Input–output pairing based on RGA

First, the RGA $\mathbf{\Lambda}$ is calculated for different operating conditions with the load power restricted within 100 MVA, and the calculated elements of $\mathbf{\Lambda}$ are plotted in Supplementary Figure S9. It is observed that the default $u_d^* - i_d^*$ and $u_q^* - i_q^*$ pairing of Scheme 1 has certain areas where the elements of $\mathbf{\Lambda}$ can be equal to 1, but these areas are very small. Thus, this pairing is only effective for very limited operating conditions. In contrast, the $u_d^* - i_q^*$ and $u_q^* - i_d^*$ pairing of Scheme 2 can achieve values of the elements of $\mathbf{\Lambda}$ equal to 1 in most areas, meaning that it is effective for most operating conditions and is therefore more reasonable.

The voltage controller for Scheme 2 is depicted in Supplementary Figure S10. To demonstrate the advantages of Scheme 2, simulation comparisons are performed between the two pairing schemes under two typical operating scenarios wherein the load is set to 80 MW + j50 MVar. Accordingly, an electromagnetic transient model of the system in Supplementary Figure S8 was built in the time-domain simulation software PSCAD/EMTDC.

5.3 Control switching from PQ to V/f modes

Before 1.0 s, the island is connected to the external system, and the MMC station operates in the PQ mode in which both the active and reactive powers are 0. At 1.0 s, the island is disconnected from the external system by tripping the AC tie line L_1, and the MMC station switches to the V/f control mode at 1.05 s. The system

10.3389/fenrg.2024.1400285

TABLE 1 System parameters of the islanded network supply scenario.

Item	Value				
MMC station					
Transformer ratio/kV	110/208				
Transformer capacity/MVA	120				
Transformer leakage reactance/p.u.	0.14				
Rated DC voltage/kV	±200				
Submodules (SMs)	236				
SM capacitance/μF	1967				
Arm reactance/mH	135				
MMC rated power/MW	100				
Load					
Transformer ratio/kV	110/35				
Transformer capacity/MVA	100				
Transformer leakage reactance/p.u.	0.1				
Synchronous condenser					
Rated capacity/MVA	200				
Transformer ratio/kV	110/20				
Transformer leakage reactance/p.u.	0.11				
$x_d''(=x_q'')$	0.111	x_d'	0.165	x_q'	0.317
x_d	1.53	x_q	1.48	H	1.495

response characteristics for the two input–output pairing schemes for the outer loop are plotted in Supplementary Figures S11, S12.

As seen from Supplementary Figures S11, S12, Scheme 2 is stable during control-mode switching while Scheme 1 loses stability. After the AC tie line is tripped, the rotor speed of G_C decreases because the active power absorbed by the load is supplied by the rotor kinetic energy; at the same time, the PCC voltage decreases. When the MMC station switches to the V/f control mode, the system shows different dynamics for the two pairing schemes.

From the perspective of active power and frequency, since the steady-state frequency is set to the rated frequency, the active power of the MMC station should increase to accelerate the rotor and supply the load. From the perspective of reactive power and voltage, the MMC station should increase the output reactive power immediately after the 1.05 s mark since the steady-state PCC voltage is larger than the voltage during the 1.0–1.05 s period.

For Scheme 2, it is seen in Supplementary Figure S11 that the active and reactive powers of the MMC station generally increase during the 1.05–1.5 s period, which coincides with the active and reactive power demand mentioned above. For Scheme 1 shown in Supplementary Figure S12, as the d-axis and q-axis voltages are smaller than their reference values shortly after 1.05 s, both the q-axis and d-axis currents increase as shown in Supplementary Figure S12B. The increase in the d-axis current means increase in active power, which meets the MMC active power increase demand. However, the increase in q-axis current decreases the MMC station reactive power and conflicts with its increased demand. Thus, the reactive power is insufficient in this system, and the voltage collapse occurs as shown in Supplementary Figure S12C. The system is therefore unstable with Scheme 1. The advantage of the $u_d^* - i_q^*$ and $u_q^* - i_d^*$ pairing of Scheme 2 in the control-mode switching scenario is thus proved.

5.4 Load step-change scenario

In this scenario, the AC tie line is assumed to be switched off, and the MMC station operates in the V/f control mode. Before 1.0 s, the islanded system already enters steady state. At 1.0 s, an equivalent 35 MVar of reactive power load is tripped, and the system response characteristics for the two input–output pairing schemes for the outer loop are shown in Supplementary Figures S13, S14.

According to Supplementary Figures S13, S14, since the equivalent reactive power load is tripped, the reactive power output from the MMC station should also decrease to achieve balance. For Scheme 2, the system quickly reaches a steady state without any large oscillations in the process. However, the system is unstable with Scheme 1. Therefore, the simulation results prove the advantage of the $u_d^* - i_q^*$ and $u_q^* - i_d^*$ pairing of Scheme 2 for the load step-change scenario.

5.5 PCC AC fault in the islanded mode

In this case, the AC tie line is assumed to be switched off, and the MMC station operates in the V/f control mode. Before 1.0 s, the islanded system already enters steady state. At 1.0 s, a solid three-phase-to-ground fault occurs at the PCC bus and is cleared 100 ms later. The system response characteristics of the two input–output pairing schemes for the outer loop are shown in Supplementary Figures S15, S16. During PCC AC fault, the PCC voltage decreases, and the PCC voltage and rotor speed decrease at the same time. When the fault is cleared, the active power of the MMC station increases to accelerate the rotor speed, and the reactive power of the MMC station should also increase to supply the load.

For Scheme 2, it is seen in Supplementary Figure S15 that the active and reactive powers of the MMC station increase when the fault is cleared, coinciding with the active and reactive power demand mentioned above. However, the system is unstable with Scheme 1. In Supplementary Figure S16, the reactive power continues decreasing to negative when the fault is cleared (during 1.1–1.4 s) regardless of the fact that the q-axis voltage keeps decreasing. The positive feedback between the reactive power and q-axis voltage deteriorates the voltage stability, and the voltage collapse at approximately 1.4 s is seen in Supplementary Figure S16. Therefore, the simulation results prove the advantage of the $u_d^* - i_q^*$ and $u_q^* - i_d^*$ pairing of Scheme 2 in the PCC AC fault scenario.

6 Conclusion

This study presents and discusses the variable pairing scheme for the voltage controller of the grid-forming MMC in an islanded network with a synchronous machine based on V/f control. The conclusions of this work are summarized as follows:

1) Based on steady-state sensitivity analysis, the analytical expression for calculating the RGA is derived, and the RGA elements corresponding to the $u_d^* - i_q^*$ and $u_q^* - i_d^*$ pairing scheme are closer to 1 than those of the $u_d^* - i_d^*$ and $u_q^* - i_q^*$ pairing scheme, indicating that the $u_d^* - i_q^*$ and $u_q^* - i_d^*$ pairing scheme is more reasonable for the voltage controller.
2) The feasibility and advantages of the $u_d^* - i_q^*$ and $u_q^* - i_d^*$ pairing scheme are verified through time-domain simulations. The simulation results demonstrate that the $u_d^* - i_d^*$ and $u_q^* - i_q^*$ pairing scheme loses stability in typical scenarios, whereas the $u_d^* - i_q^*$ and $u_q^* - i_d^*$ pairing scheme operates stably.

Data availability statement

The original contributions presented in the study are included in the article/Supplementary Material; further inquiries can be directed to the corresponding author.

Author contributions

JM: conceptualization, methodology, and writing–original draft. ZW: formal analysis, methodology, validation, and writing–original draft. KS: formal analysis, methodology, validation, and writing–review and editing. CW: formal analysis, methodology, and writing–review and editing. CL: supervision and writing–review and editing. YG: supervision and writing–review and editing. JL: formal analysis and writing–review and editing. CZ: formal analysis and writing–review and editing. HG: visualization and writing–review and editing. ZZ: conceptualization, and writing–original draft. ZX: writing–review and editing.

Funding

The author(s) declare that no financial support was received for the research, authorship, and/or publication of this article.

Conflict of interest

Authors JM, CW, CL, JL, and CZ were employed by the State Grid Zhejiang Electric Power Co., Ltd. Research Institute. Authors ZW, KS, and YG were employed by the State Grid Zhejiang Electric Power Co., Ltd.

The remaining authors declare that the research was conducted in the absence of any commercial or financial relationships that could be construed as a potential conflict of interest.

Publisher's note

All claims expressed in this article are solely those of the authors and do not necessarily represent those of their affiliated organizations, or those of the publisher, the editors, and the reviewers. Any product that may be evaluated in this article, or claim that may be made by its manufacturer, is not guaranteed or endorsed by the publisher.

Supplementary material

The Supplementary Material for this article can be found online at: https://www.frontiersin.org/articles/10.3389/fenrg.2024.1400285/full#supplementary-material

References

Abbott, D. (2010). Keeping the energy debate clean: how do we supply the world's energy needs? *Proc. IEEE* 98, 42–66. doi:10.1109/JPROC.2009.2035162

Beck, H.-P., and Hesse, R. (2007). "Virtual synchronous machine," in *2007 9th international conference on electrical power quality and utilisation*, 1–6. doi:10.1109/EPQU.2007.4424220

Blaabjerg, F., Yang, Y., Kim, K. A., and Rodriguez, J. (2023). Power electronics technology for large-scale renewable energy generation. *Proc. IEEE* 111, 335–355. doi:10.1109/JPROC.2023.3253165

Bristol, E. (1966). On a new measure of interaction for multivariable process control. *IEEE Trans. Autom. Contr.* 11, 133–134. doi:10.1109/TAC.1966.1098266

Debnath, S., Qin, J., Bahrani, B., Saeedifard, M., and Barbosa, P. (2015). Operation, control, and applications of the modular multilevel converter: a review. *IEEE Trans. Power Electron.* 30, 37–53. doi:10.1109/TPEL.2014.2309937

De Brabandere, K., Bolsens, B., Van Den Keybus, J., Woyte, A., Driesen, J., and Belmans, R. (2007). A voltage and frequency droop control method for parallel inverters. *IEEE Trans. Power Electron.* 22, 1107–1115. doi:10.1109/TPEL.2007.900456

Guan, M., and Xu, Z. (2012). Modeling and control of a modular multilevel converter-based HVDC system under unbalanced grid conditions. *IEEE Trans. Power Electron.* 27, 4858–4867. doi:10.1109/TPEL.2012.2192752

Guo, C., Wu, Z., Yang, S., and Hu, J. (2022). Overcurrent suppression control for hybrid LCC/VSC cascaded HVDC system based on fuzzy clustering and identification approach. *IEEE Trans. Power Deliv.* 37, 1745–1753. doi:10.1109/TPWRD.2021.3096954

IEA (2022) "Renewables 2022 analysis and forecast to 2027,". Paris France: IEA. Available at: https://www.iea.org/reports/renewables-2022.

Liu, S., Xu, Z., Tang, G., Hua, W., and Zhang, J. (2015). Study on MMC-HVDC switching scheme between grid-connected and passive islanding mode. *Proc. CSEE* 35, 2152–2161. doi:10.13334/j.0258-8013.pcsee.2015.09.007

Pan, D., Wang, X., Liu, F., and Shi, R. (2020). Transient stability of voltage-source converters with grid-forming control: a design-oriented study. *IEEE J. Emerg. Sel. Top. Power Electron.* 8, 1019–1033. doi:10.1109/JESTPE.2019.2946310

Rao, H., and Zhou, Y. (2019). Key technologies of ultra-high voltage hybrid LCC-VSC MTDC systems. *CSEE JPES*. doi:10.17775/CSEEJPES.2019.01140

Rosso, R., Wang, X., Liserre, M., Lu, X., and Engelken, S. (2021). Grid-forming converters: control approaches, grid-synchronization, and future trends—a review. *IEEE Open J. Ind. Appl.* 2, 93–109. doi:10.1109/OJIA.2021.3074028

Vidal-Albalate, R., Beltran, H., Rolan, A., Belenguer, E., Pena, R., and Blasco-Gimenez, R. (2016). Analysis of the performance of MMC under fault conditions in HVDC-based offshore wind farms. *IEEE Trans. Power Deliv.* 31, 839–847. doi:10.1109/TPWRD.2015.2468171

Xiao, H., Gan, H., Yang, P., Li, L., Li, D., Hao, Q., et al. (2024a). Robust submodule fault management in modular multilevel converters with nearest level modulation for uninterrupted power transmission. *IEEE Trans. Power Deliv.* 39, 931–946. doi:10.1109/TPWRD.2023.3343693

Xiao, H., He, H., Zhang, L., and Liu, T. (2024b). Adaptive grid-synchronization based grid-forming control for voltage source converters. *IEEE Trans. Power Syst.* 39, 4763–4766. doi:10.1109/TPWRS.2023.3338967

Xiong, L., Zhuo, F., Wang, F., Liu, X., Chen, Y., Zhu, M., et al. (2016b). Static synchronous generator model: a new perspective to investigate dynamic characteristics and stability issues of grid-tied pwm inverter. *IEEE Trans. Power Electron.* 31, 6264–6280. doi:10.1109/TPEL.2015.2498933

Xiong, L., Zhuo, F., Wang, F., Liu, X., and Zhu, M. (2016a). A fast orthogonal signal-generation algorithm characterized by noise immunity and high accuracy for single-phase grid. *IEEE Trans. Power Electron.* 31, 1847–1851. doi:10.1109/TPEL.2015.2478155

Xu, S., Song, Q., Zhou, Y., Meng, J., Yang, W., Zhao, B., et al. (2020). Dynamic model of the DC fault clearing process of a hybrid modular multilevel converter considering

commutations of the fault current. *IEEE Trans. Power Electron.* 35, 6668–6672. doi:10.1109/TPEL.2019.2958495

Yang, J., Hong, C., Zhou, B., Li, H., Zhang, Y., Zhang, F., et al. (2018). "Research on the mechanism of affecting the transmission capability of HVDC connected to weak AC system considering STATCOM," in *2018 international conference on power system technology (POWERCON)* (Guangzhou, China: IEEE), 2524–2532.

Yazdani, A. (2008). "Control of an islanded Distributed Energy Resource unit with load compensating feed-forward," in *2008 IEEE power and energy society general meeting* (Pittsburgh, PA, USA: IEEE), 1–7.

Yazdani, A., and Iravani, R. (2010) *Voltage-sourced converters in power systems: modeling, control, and applications*. New Jersey: Wiley.

Zhang, L., Harnefors, L., and Nee, H.-P. (2010). Power-synchronization control of grid-connected voltage-source converters. *IEEE Trans. Power Syst.* 25, 809–820. doi:10.1109/TPWRS.2009.2032231

Zhang, Z., Xu, Z., Jiang, W., and Bie, X. (2016). Operating area for modular multilevel converter based high-voltage direct current systems. *IET Renew. Power Gener.* 10, 776–787. doi:10.1049/iet-rpg.2015.0342

Zhong, Q.-C., and Weiss, G. (2011). Synchronverters: inverters that mimic synchronous generators. *IEEE Trans. Industrial Electron.* 58, 1259–1267. doi:10.1109/TIE.2010.2048839

Zhou, J. Z., Ding, H., Fan, S., Zhang, Y., and Gole, A. M. (2014). Impact of short-circuit ratio and phase-locked-loop parameters on the small-signal behavior of a VSC-HVDC converter. *IEEE Trans. Power Deliv.* 29, 2287–2296. doi:10.1109/TPWRD.2014.2330518

Nomenclature

N	Number of submodules
k	Denotes phase (a, b, c)
$E\angle\delta$	Thevenin equivalent voltage of the connected AC network
$Z_s(=R_s + jX_s)$	Thevenin equivalent impedance of the connected AC network
$U\angle 0$	Voltage at PCC.
$P_s + jQ_s$	Output power of the MMC station
L_T	Transformer leakage inductance
θ	Phase angle signal
ω_0	Rated angular frequency
T_J	Time constant of the PSL.
D_J	Damping coefficient of the PSL.
u_d/u_q d-/q-axis	Components of the PCC voltage
i_d/i_q d-/q-axis	Components of the MMC output current
u^*_{diffd}/u^*_{diffq} d-/q-axis	Reference signals of the MMC differential-mode voltage
$i^*_d/\ i^*_q$ d-/q-axis	Inputs to the current controller
u_{diffd} and u_{diffq} d- and q-axis	Components of the MMC differential-mode voltage
α	Impedance angle of the connected AC network
$G_{grid}(s)$	Denotes the connected AC system in the block diagram
$G_v(s)$	Denotes voltage controller in the block diagram
$G_{MMC}(s)$	Denotes MMC station plus current controller in the block diagram
G(s)	Denotes a two-input two-output system
λ_{ij}	Relative gain between the *j*th input and *i*th output
Λ	RGA
u_{in_j} j-th	System input
y_{out_i} i-th	System output
x	State variables of the system
y	System output
u	System input
A, B, C, D	Coefficient matrices
k_{p2}/k_{i2}	Proportional/integral gains of the current controller
$\dot{U}_l/\ \dot{I}_l$	Voltage/current phasors of the load node
Y_l	Admittance of the load
P_g/P_m	Steady-state electrical/mechanical powers of the synchronous machine
P_{m0}	Reference mechanical power
R_d	Rotor speed-governor speed droop coefficient
Q_g	Steady-state reactive power of the synchronous machine
U_g	Steady-state terminal voltage of the synchronous machine
Q_{g0}	Output reactive power reference
K_q	Terminal voltage-output reactive power droop coefficient
Y	Nodal admittance matrix
I	Injecting the current phasor vector of the power grid network
U	Node voltage vector of the power grid network
$\Delta I_{Ldq}/\Delta U_{Ldq}$	Load current/voltage small-disturbance vectors
ΔI_{Gdq} and ΔU_{Gdq}	Synchronous machine current/voltage small-disturbance vectors

frontiers | Frontiers in Energy Research

TYPE Opinion
PUBLISHED 03 June 2024
DOI 10.3389/fenrg.2024.1406654

OPEN ACCESS

EDITED BY
Yonghui Liu,
Hong Kong Polytechnic University, Hong Kong SAR, China

REVIEWED BY
Guibin Wang,
Shenzhen University, China
Shiwei Xia,
North China Electric Power University, China

*CORRESPONDENCE
Chongming Yang,
yangchongming318@szpu.edu.cn

RECEIVED 25 March 2024
ACCEPTED 13 May 2024
PUBLISHED 03 June 2024

CITATION
Su Z, Yang C, Liu Y and Mu Z (2024), Opinions on hosting capacity evaluation of distribution network with zonotope power flexibility aggregation.
Front. Energy Res. 12:1406654.
doi: 10.3389/fenrg.2024.1406654

Opinions on hosting capacity evaluation of distribution network with zonotope power flexibility aggregation

Ziao Su[1], Chongming Yang[2]*, Yutong Liu[3] and Zhiying Mu[1]

[1]College of Electrical and Information Engineering, Hunan University, Changsha, China, [2]Industrial Training Centre, Shenzhen Polytechnic University, Shenzhen, China, [3]School of Mathematics, Shandong University, Jinan, China

KEYWORDS

diversified flexibility resources, flexibility space boundaries, hosting capacity, two-stage adaptive robust, zonotope aggregation

1 Introduction

The installation of solar photovoltaic (PV) systems has been stimulated by governmental incentive mechanisms and the continual reduction in technology costs in recent years (Chattopadhyay and Alpcan, 2015). However, with the substantial integration of distributed PV systems at high penetration levels (Chen et al., 2019a), reverse power flow in the distribution network has been observed, thus triggering issues such as voltage violations and reverse overloads (Ismael et al., 2019; Wu et al., 2021). Therefore, the evaluation of maximum PV hosting capacity of the distribution network can assist distribution network planners in making decisions regarding PV generation (SUN et al., 2021). The current evaluation method considering safe operation constraints is traditional planning method of optimal power flow (Chen et al., 2016) and random scenario simulation method (Ding and Mather, 2016) which can ensure the randomness of PV configuration. To enhance the PV hosting capacity, strategies such as reactive power control (Astero and Söder, 2018), voltage control using OLTC (Wang et al., 2016), energy storage technologies (Hashemi and Østergaard, 2016), and network reconfiguration (Fu and Chiang, 2018) are continuously proposed. With the increasing proliferation of distributed resources, a promising approach to enhancement is also presented by power aggregation (Müller et al., 2017; Wang and Wu, 2021) and proactive control of diversified flexibility resources along feeders. Therefore, this research aims to provide insightful viewpoints and discussions on the assessment method of the maximum PV hosting capacity of the distribution network based on the aggregation of diversified flexibility resources.

The main contributions of this work can be twofold as listed: (1) A highly constrained zonotope aggregation model for diversified flexibility resources is proposed, and a two-stage adaptive robust framework is employed to innerly approximate the projection region of the high-dimensional original space of diversified flexibility resources; (2)A PV hosting capacity evaluation method with flexibility space boundaries is presented to accommodate distributed PV by maximizing the net load during peak PV output on the load side.

2 Highly constrained zonotope aggregation model of diversified flexibility resources

Due to diversified flexibility resources' small scale, dispersion, and large number, coordinating their control is highly challenging (Chen and Li, 2021). Aggregating flexibility resources on feeders can fully utilize the potential flexibility, reduce invocation difficulty, and lower computational complexity. Specifically, the process of flexibility aggregation can be described as the projection of the power feasible domain of all flexibility resources onto the total power feasible domain of feeders (Wei et al., 2015; Tan et al., 2019; Chen and Li, 2021). Based on the acquisition of the power feasible domain of all flexibility resources on feeders, upon observation of the strong constraints imposed by the network of the distribution network when the aggregation scale is large (Wang and Wu, 2021), the high-dimensional precise original space of flexibility resources is constituted. The analytical form of computing its dimensionality reduction projection onto the precise power flexibility space of the feeder is highly challenging; thus, most studies are focused on approximation methods (Chen and Li, 2021).

Firstly, the power-adjustable range of individual flexibility resources, including energy storage devices, electric vehicles, and HVAC-like energy storage devices, is described through a virtual energy storage model in this paper (Hughes et al., 2016). Given the discrete scheduling decision cycle with N scheduling points and a time interval of Δt and a quantity of M flexibility resources, we consider $P_{i,t}^{\mathrm{flx}}$ and $E_{i,t}^{\mathrm{flx}}$ representing the power and energy of individual flexibility resources within the scheduling interval $t \in [k\Delta t, (k+1)\Delta t]$, where $(k = 0, ..., N-1)$, the corresponding quantification model is established as follews:

$$\Omega_i = \left\{ \begin{array}{c} P_{i,t}^{\mathrm{flx,\,min}} \le P_{i,t}^{\mathrm{flx}} \le P_{i,t}^{\mathrm{flx,\,max}} \\ E_{i,t}^{\mathrm{flx,\,min}} \le E_{i,t}^{\mathrm{flx}} \le E_{i,t}^{\mathrm{flx,\,max}} \\ E_{i,t+1}^{\mathrm{flx}} = E_{i,t}^{\mathrm{flx}} + P_{i,t}^{\mathrm{flx}} \Delta t \end{array} \right\} \tag{1}$$

$$\chi = \{\Omega_1, \Omega_2, ..., \Omega_M\} \tag{2}$$

Where $i \in \{\mathrm{EV}, \mathrm{ESS}, \mathrm{HVAC}\}$, $P_{i,t}^{\mathrm{flx,\,max}}$ and $P_{i,t}^{\mathrm{flx,\,min}}$ respectively represent the upper and lower limits of the power of flexibility resource i during time period t; and $E_{i,t}^{\mathrm{flx,\,min}}$ respectively represent the upper and lower limits of the energy; Ω_i denotes the operational feasible region of flexibility resource i, χ denotes the operational feasible region of the whole flexibility resource, which can be described as the convex polytope characterized by the aforementioned set of M constraints.

The linear method outlined in (Bernstein et al., 2018) is employed to derive the network power flow model, whereby the magnitudes of node voltage $\boldsymbol{v}$, branch current $\boldsymbol{i}$, and feeder line aggregated active power $\boldsymbol{p}_{\mathrm{agg}}$, can be expressed as the following linear expressions:

$$\boldsymbol{v} = \boldsymbol{D}\boldsymbol{p}^{\mathrm{flx}} + \boldsymbol{d} \tag{3}$$

$$\boldsymbol{i} = \boldsymbol{F}\boldsymbol{p}^{\mathrm{flx}} + \boldsymbol{f} \tag{4}$$

$$\boldsymbol{p}_{\mathrm{agg}} = \boldsymbol{H}\boldsymbol{p}^{\mathrm{flx}} + \boldsymbol{h} \tag{5}$$

Where $\boldsymbol{D}, \boldsymbol{d}, \boldsymbol{F}, \boldsymbol{f}, \boldsymbol{H}, \boldsymbol{h}, \boldsymbol{J}$ and $\boldsymbol{j}$ are the system parameters. It is necessary to ensure that node voltages and branch currents are not exceeded, as follows:

$$\left\{ \begin{array}{l} \underline{\boldsymbol{v}} \le \boldsymbol{v} \le \bar{\boldsymbol{v}} \\ \underline{\boldsymbol{i}} \le \boldsymbol{i} \le \bar{\boldsymbol{i}} \end{array} \right. \tag{6}$$

Where $\underline{\boldsymbol{v}}$ and $\bar{\boldsymbol{v}}$ represent the upper and lower limits of node voltages respectively, and $\bar{\boldsymbol{i}}$ and $\boldsymbol{i}$ denote the upper and lower limits of branch currents respectively. The convex polytope formed by Eq. 2 is intersected by Eq. 6's constraints, resulting in irregular polytopes, while the high-dimensional strong constraint primal space $\boldsymbol{Z}$ of flexibility resources is formed by Eqs 1–6.

Then, the feeder power flexibility space $\boldsymbol{P}$, representing the dimensionality reduction projection of the high-dimensional constrained space $\boldsymbol{Z}$, is approximately obtained using the zonotope $\boldsymbol{U}$ as shown in Figure 1A. For the N-dimensional zonotope (Müller et al., 2017), its representation can be established with the central point $\boldsymbol{c}$, a specific generator matrix $\boldsymbol{G}$, and a scaling factor $\bar{\boldsymbol{\beta}}$. N_{g} denotes the number of generator vectors. The directions along which the zonotope can be extended are described by the generator matrix $\boldsymbol{G} = [g_1, ..., g_{N_g}]^T \in \mathbb{R}^{N \times N_g}$. The extension range along each generator vector direction is determined by the scaling factor by Eqs 7, 8:

$$\boldsymbol{U} = \left\{ \boldsymbol{p}_{\mathrm{agg}} \in \mathbb{R}^N \middle| \boldsymbol{p}_{\mathrm{agg}} = \boldsymbol{c} + \boldsymbol{G}\boldsymbol{\beta}, -\boldsymbol{\beta}_{\max} \le \boldsymbol{\beta} \le \boldsymbol{\beta}_{\max} \right\} \tag{7}$$

$$\boldsymbol{G} = \left\{ \begin{array}{l} g_i = \left[0, ..., 0, \underset{1}{i}, 0, ..., 0 \right]^{\mathrm{T}} \in \mathbb{R}^N \\ g^{N+i'} = \left[0, ..., 0, \underbrace{-1/\sqrt{2}}_{i'}, \underbrace{1/\sqrt{2}}_{i'+1}, 0, ..., 0 \right]^{\mathrm{T}} \in \mathbb{R}^N \end{array} \right. \tag{8}$$

The advantage of zonotope projection approximation over ellipsoidal projection (Cui et al., 2021) and cuboidal projection (Chen et al., 2019b) lies in its generator vectors g_i and $g_{N+i'}$, which can respectively depict the power and energy constraints of flexibility resources. Therefore, the operationally feasible region of flexibility resources aligns more closely with the characteristics of the zonotope shape.

3 Two-stage adaptive robust method for inner approximation of power flexibility space

The feeder power flexibility space obtained after dimensionality reduction projection becomes more intricate and challenging to obtain. The inner approximation requires ensuring that the approximated flexibility space is optimally bounded internally. Simultaneously, it is imperative to ensure that any aggregated power trajectory within the approximated flexibility space can be realized through scheduling without violating operational constraints, thereby guaranteeing the feasibility of the disaggregation (Chen and Li, 2021).

In this paper, the power flexibility aggregation and disaggregation problem are formulated as a two-stage adaptive robust optimization problem as shown in Figure 1B, where power aggregation is treated as uncertain variables, and the requirement to ensure the feasibility of disaggregation is regarded as adaptive robust constraints (Hua et al., 2024). In the first stage, the objective is to determine the optimal approximation space for the aggregated

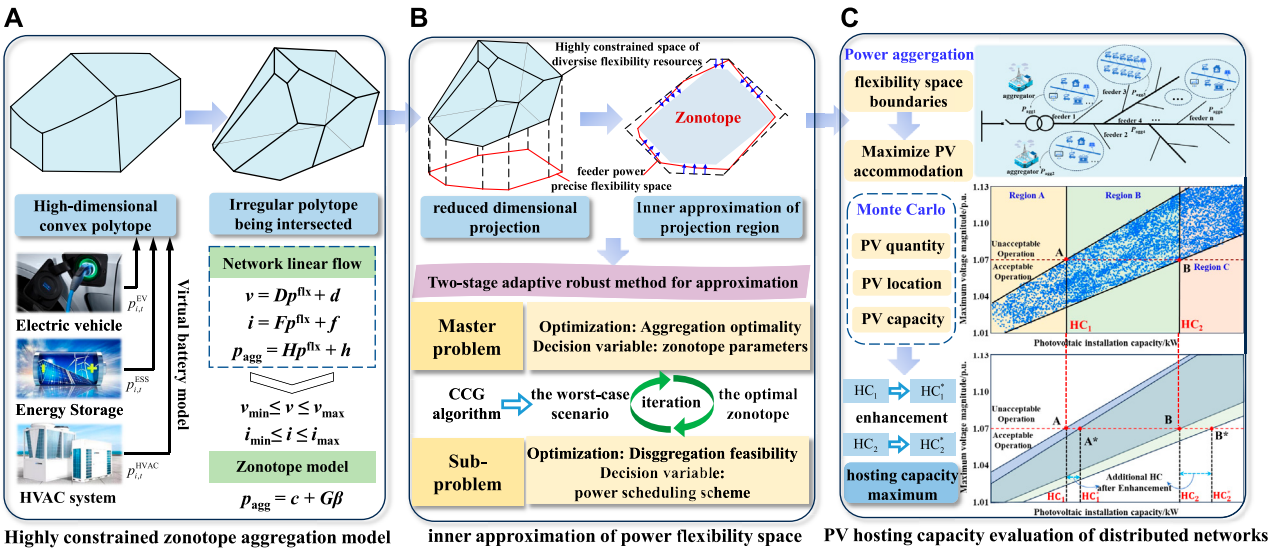

FIGURE 1
The proposed model, approximation method and PV hosting capacity evaluation. **(A)** Highly constrained zonotope aggregation model. **(B)** Inner approximation of power flexibility space. **(C)** PV hosting capacity evaluation of distributed networks.

TABLE 1 Comparison of PV hosting capacity evaluation method.

Method	Inherent hosting capacity total(MW)	Maximum hosting capacity total(MW)	Maximum hosting capacity of feeder(MW)	Computational time(s)
Our method	7.12	12.25	0.63	574
Demand response enhancement (SUN et al., 2021)	-	12.34	0.64	755
Stochastic scenario simulation (Ding and Mather, 2016)	6.10	11.14	0.56	193

feeder power. In the second stage, the objective is to ensure the feasibility of disaggregation.

The construction of any S normal vectors, denoted as $\boldsymbol{\alpha_s} \in \mathbb{R}^N\ (s = 1, ..., S)$, is performed. The diameter, denoted as ρ_κ, of the zonotope $\boldsymbol{U}$ in the direction of the normal vectors is calculated by Eq. 9. The problem of determining the diameter, denoted as ρ_τ, of the feeder power flexibility space $\boldsymbol{P}$ in the direction of the normal vectors can be addressed using Eqs 10, 11. Thus, the similarity between the approximate and the original region is defined as shown in Eq. 12. As its value increases, the zonotope's approximation to the power flexibility space of the feeder becomes larger (Müller et al., 2017).

$$\rho_\kappa = 2|\boldsymbol{\alpha_s} \boldsymbol{G}|\boldsymbol{\beta}_{\max} \tag{9}$$

$$\rho_\tau = \left|\max_{\boldsymbol{p}_{agg}} \left(\boldsymbol{\alpha_s} \boldsymbol{p}_{agg} - \varepsilon\right) - \min_{\boldsymbol{p}_{agg}} \left(\boldsymbol{\alpha_s} \boldsymbol{p}_{agg} - \varepsilon\right)\right| \Big/ \|\boldsymbol{\alpha_s}\|_2 \tag{10}$$

$$\text{s.t.} \tag{11}$$

equation (1)–(6)

$$\eta_s = \frac{\rho_\kappa}{\rho_\tau} \tag{12}$$

The introduction of ξ as an uncertain variable acting on scaling factors applied to each generator vector of the zonontope, the uncertain set is denoted as $\mathbb{C} = \left\{\xi | 0 \le |\xi_i \le 1, i = 1, ..., N_g\right\}$. An uncertain zonotope region is constructed, with its parameter feasible domain as $\mathbb{Q} = \left\{\boldsymbol{p}_{agg} \in \mathbb{R}^N : \boldsymbol{p}_{agg} = c + \boldsymbol{G\beta} \cdot \xi, \xi \in \mathbb{C}\right\}$. Therefore, a two-stage adaptive robust power aggregation solution model is established as shown in Eqs 13–16.

$$\text{Obj.} \max_{c,\ \beta} \frac{1}{S} \sum_{s=1}^{S} \frac{\rho_\kappa}{\rho_\tau} + \min_{\xi \in U_2} \max_{p^{flx}(\xi)} 0 \tag{13}$$

$$\boldsymbol{c} + \boldsymbol{G\beta} \cdot \boldsymbol{\xi} = \boldsymbol{H}\boldsymbol{p}^{flx}(\boldsymbol{\xi}) + \boldsymbol{h} \tag{14}$$

$$\boldsymbol{E}\boldsymbol{p}^{flx}(\boldsymbol{\xi}) \le \boldsymbol{\sigma} \tag{15}$$

$$\boldsymbol{Q}\boldsymbol{p}^{flx}(\boldsymbol{\xi}) \le \boldsymbol{\gamma} \tag{16}$$

In the first stage, the zonotope parameters ($\boldsymbol{c}$、$\boldsymbol{\beta}$) are decision variables, and the optimal inner approximation region is so the uncertain set ught using Eq. 13. In the second stage, the power scheduling scheme $\boldsymbol{p}^{flx}(\boldsymbol{\xi})$ is the decision variable, ensuring the feasibility of disaggregation. Eqs 15 and (16) represent the linear compact form of the highly constrained space of diversified flexibility resources $\boldsymbol{p}^{flx}$ mentioned earlier. Eq. 14 represents the projection of the highly constrained space of diversified flexibility resources $\boldsymbol{p}^{flx}$ onto the lower-dimensional space of feeder aggregated power $\boldsymbol{p}_{agg}$. The solution of this model can be implemented using the column-and-constraint generation

algorithm. This process is not further elaborated in this paper (Hua et al., 2024).

4 PV hosting capacity evaluation of distributed networks with flexibility space boundaries

As the penetration rate of PV systems in distribution networks continues to increase, the occurrence of peak PV output not coinciding with peak load power (Xiong et al., 2020) may lead to phenomena such as reverse power flow and overvoltage in low-voltage distribution networks (Zhang et al., 2018; Li et al., 2020). The increase in node voltages within distribution networks becomes the primary factor limiting the integration of distributed PV systems (Lee et al., 2020). Reference (Cao et al., 2024) ensures magnitudes of each bus are maintained within the safety range due to the load shedding. Therefore, effectively increasing the net load during periods of high PV output on the load side helps mitigate the risk of operational constraints exceeding limits, thereby enhancing the hosting capacity of distributed PV systems (Zhou et al., 2021).

In a low-voltage distribution network with H feeders, $p_{\mathrm{agg},i,t}$ represents the aggregated power of the feeder i at time t, while $p^{\min}_{\mathrm{agg},i,t}$ and $p^{\max}_{\mathrm{agg},i,t}$ represent the upper and lower limits of power at that time, respectively. $t_{\mathrm{pv},0}$ and $t_{\mathrm{pv,end}}$ represent the starting and ending times of PV output. During this period, each feeder utilizes the upper boundary of the aggregated power flexibility space, maximizing distributed PV integration (Ding and Mather, 2016). In subsequent periods, the lower boundary is employed to reduce the load on the distribution network, ensuring its stable and safe operation, as depicted in Eqs (17), (18).

$$p^{\min}_{\mathrm{agg},i,t} \le p_{agg,i,t} \le p^{\max}_{\mathrm{agg},i,t} \tag{17}$$

$$p_{agg,i,t} = \begin{cases} p^{\max}_{\mathrm{agg},i,b}\, t \in \left[t_{\mathrm{pv},0}, t_{\mathrm{pv,end}}\right] \\ p^{\min}_{\mathrm{agg},i,b}\, t \notin \left[t_{\mathrm{pv},0}, t_{\mathrm{pv,end}}\right] \end{cases} \tag{18}$$

The PV penetration rate range selected in this paper is 0%–300%, with an incremental step size of 10%. Using the Monte Carlo method, the quantity, location, and capacity of PV grid connections are randomly simulated, with the PV grid connection capacity increasing according to the PV penetration rate (Ding and Mather, 2016). The steady-state power flow of the system is then calculated. For each PV penetration rate λ_{PV}, multiple samples are drawn to compute the total installed PV capacity and maximum voltage of system nodes for each random scenario. These values serve as the abscissa and ordinate to construct a scatter plot of random simulations, depicted in Figure 1C, where each point represents one simulation result. In the low-voltage distribution network, the voltage per unit value (V_i^t) of each feeder line must satisfy the constraint given by Eq. 19, and the scatter plot intersects with the upper voltage constraint of 1.07 per unit at points HC_1 and HC_2.

$$0.93\text{p.u.} \le \left|V_i^t\right| \le 1.07\text{p.u.} \tag{19}$$

Two lines parallel to the vertical axis are drawn respectively at points HC_1 and HC_2 to divide the coordinate graph into three regions: A, B, and C. In region A, points represent scenarios where the capacity of PV systems connected to the distribution network is less than HC_1. Regardless of the node in the distribution network where PV systems are connected, the system voltage remains within the permissible range of the supply voltage. In region B, points represent scenarios where the capacity of PV systems connected to the distribution network falls between HC_1 and HC_2. If the selection of PV integration positions and capacity allocation is unreasonable, it may lead to excessively high or even over-limit system voltage levels. In such cases, the distribution network planner must ensure that the PV systems are appropriately allocated. In region C, points represent scenarios where the capacity of PV systems connected to the distribution network exceeds HC_2. Regardless of the installation scheme employed, it will lead to over-limit system voltage. The aggregation and regulation of flexibility resources on the load side result in the accommodation of distributed photovoltaics, leading to the rightward shift of HC_1 and HC_2, with HC_1 increasing to HC^*_1 and HC_2 increasing to HC^*_2.

5 Case studies

In this section, the enhancement effect of PV hosting capacity by aggregated and coordinated diversified flexibility resources is demonstrated through numerical simulations based on the proposed method. IEEE 33-bus distribution network system is employed as a case study for simulation verification, with a radial configuration and a standard voltage level set at 12.66 kV. All the algorithms are executed with an AMD Ryzen 7 5800H with Radeon Graphics CPU running at 3.20 GHz, and 16.0 GB RAM. The optimization model involved in the proposed method is programmed and solved using the commercial solver Gurobi 10.0.3. The comparison between results of PV hosting capacity and computational time under different algorithms is shown in Table 1.

As shown in Table 1, it can be seen that the proposed method, compared to the random scenario simulation, can increase the PV hosting capacity by over 9.96%. Due to the necessity of considering flexible resource power aggregation and proactive control, the computational time is comparatively longer. When the scale of flexible resources is large, aggregation can shorten the computational time compared to distributed scheduling. However, our method show a slight decrease in the PV hosting capacity compared to the demand response enhancement method, which is attributed to the approximate feasible domain of the aggregation solution, leading to certain accuracy errors. Overall, the method proposed can effectively assess the PV hosting capacity of the distribution network.

6 Discussion and conclusion

In this paper, the flexibility resource power regulation model, feeder power aggregation model, two-stage robust aggregation solution method, and PV hosting capacity assessment strategy is elaborately investigated. The key findings are summarized as follows: 1) A highly constrained zonotope aggregation model of diversified flexibility resources is proposed, and a two-stage adaptive robust method is introduced to internally approximate the power flexibility space, ensuring the optimality of aggregation and the feasibility of disaggregation; 2) The aggregation and control of flexibility resource power on the load side can accommodate high

peak output from distributed PV, thereby enhancing the PV hosting capacity of the distribution network and simultaneously reducing the computational complexity of dispatch decision-making.

Author contributions

ZS: Writing–original draft, Conceptualization. CY: Writing–review and editing, Formal Analysis, Data curation. YL: Writing–review and editing, Visualization. ZM: Writing–review and editing, Investigation.

Funding

The author(s) declare that no financial support was received for the research, authorship, and/or publication of this article.

Conflict of interest

The authors declare that the research was conducted in the absence of any commercial or financial relationships that could be construed as a potential conflict of interest.

Publisher's note

All claims expressed in this article are solely those of the authors and do not necessarily represent those of their affiliated organizations, or those of the publisher, the editors and the reviewers. Any product that may be evaluated in this article, or claim that may be made by its manufacturer, is not guaranteed or endorsed by the publisher.

References

Astero, P., and Söder, L., Improving PV dynamic hosting capacity using adaptive controller for STATCOMs[J]. *IEEE Trans. Energy Convers.*, 2018, 34(1): 415–425. doi:10.1109/TEC.2018.2873057

Bernstein, A., Wang, C., Dall'Anese, E., Le Boudec, J. Y., and Zhao, C. (2018). Load flow in multiphase distribution networks: existence, uniqueness, non-singularity and linear models. *IEEE Trans. Power Syst.* 33, 5832–5843. doi:10.1109/TPWRS.2018.2823277

Cao, Y., Zhou, B., Chung, C. Y., Wu, T., Zheng, L., and Shuai, Z. (2024). A coordinated emergency response scheme for electricity and watershed networks considering spatio-temporal heterogeneity and volatility of rainstorm disasters. *IEEE Trans. Smart Grid*, 1. doi:10.1109/TSG.2024.3362344

Chattopadhyay, D., and Alpcan, T. (2015). Capacity and energy-only markets under high renewable penetration. *IEEE Trans. Power Syst.* 31, 1692–1702. doi:10.1109/TPWRS.2015.2461675

Chen, X., Dall'Anese, E., Zhao, C., and Li, N. (2019b). Aggregate power flexibility in unbalanced distribution systems. *IEEE Trans. Smart Grid* 11, 258–269. doi:10.1109/TSG.2019.2920991

Chen, X., and Li, N. (2021). Leveraging two-stage adaptive robust optimization for power flexibility aggregation. *IEEE Trans. Smart Grid* 12, 3954–3965. doi:10.1109/TSG.2021.3068341

Chen, X., Mcelroy, M. B., Wu, Q., Shu, Y., and Xue, Y. (2019a). Transition towards higher penetration of renewables: an overview of interlinked technical, environmental and socio-economic challenges. *J. Mod. Power Syst. Clean Energy* 7, 1–8. doi:10.1007/s40565-018-0438-9

Chen, X., Wu, W., Zhang, B., and Lin, C. (2016). Data-driven DG capacity assessment method for active distribution networks. *IEEE Trans. Power Syst.* 32, 3946–3957. doi:10.1109/TPWRS.2016.2633299

Cui, B., Zamzam, A., and Bernstein, A. (2021). "Network-cognizant time-coupled aggregate flexibility of distribution systems under uncertainties," in 2021 American Control Conference (ACC), New Orleans, LA, USA, May, 2021, 1723–1728.

Ding, F., and Mather, B. (2016). On distributed PV hosting capacity estimation, sensitivity study, and improvement. *IEEE Trans. Sustain. Energy* 8, 1010–1020. doi:10.1109/TSTE.2016.2640239

Fu, Y. Y., and Chiang, H. D. Toward optimal multiperiod network reconfiguration for increasing the hosting capacity of distribution networks[J]. *IEEE Trans. Power Deliv.*, 2018, 33(5): 2294–2304.doi:10.1109/TPWRD.2018.2801332

Hashemi, S., and Østergaard, J. Efficient control of energy storage for increasing the PV hosting capacity of LV grids[J]. *IEEE Trans. Smart Grid*, 2016, 9(3): 2295–2303. doi:10.1109/TSG.2016.2609892

Hua, Z., Zhou, B., Or, S. W., Zhang, J., Li, C., and Wei, J. (2024). Robust emergency preparedness planning for resilience enhancement of energy-transportation nexus against extreme rainfalls. *IEEE Trans. Industry Appl.* 60, 1196–1207. doi:10.1109/TIA.2023.3274615

Hughes, J. T., Domínguez-García, A. D., and Poolla, K. (2016). Identification of virtual battery models for flexible loads. *IEEE Trans. Power Syst.* 31, 4660–4669. doi:10.1109/TPWRS.2015.2505645

Ismael, S. M., Aleem, S. H. E. A., Abdelaziz, A. Y., and Zobaa, A. F. (2019). State-of-the-art of hosting capacity in modern power systems with distributed generation. *Renew. energy* 130, 1002–1020. doi:10.1016/j.renene.2018.07.008

Lee, J., Bérard, J. P., Razeghi, G., and Samuelsen, S. (2020). Maximizing PV hosting capacity of distribution feeder microgrid. *Appl. Energy* 261, 114400. doi:10.1016/j.apenergy.2019.114400

Li, R., Wong, P., Wang, K., and Yuan, F. (2020). Power quality enhancement and engineering application with high permeability distributed photovoltaic access to low-voltage distribution networks in Australia. *Prot. Control Mod. Power Syst.* 5, 18. doi:10.1186/s41601-020-00163-x

Müller, F. L., Szabó, J., Sundström, O., and Lygeros, J. (2017). Aggregation and disaggregation of energetic flexibility from distributed energy resources. *IEEE Trans. Smart Grid* 10, 1205–1214. doi:10.1109/TSG.2017.2761439

Sun, W., Huang, F., and Zhang, W. (2021). Evaluation of feeder available capacity considering demand response. *Electr. Power Autom. Equip.* 41 (06), 156–165. doi:10.16081/j.epae.202101008

Tan, Z., Zhong, H., Wang, J., Xia, Q., and Kang, C. (2019). Enforcing intra-regional constraints in tie-line scheduling: a projection-based framework. *IEEE Trans. Power Syst.* 34, 4751–4761. doi:10.1109/TPWRS.2019.2913876

Wang, S., Chen, S., Ge, L., and Wu, L. Distributed generation hosting capacity evaluation for distribution systems considering the robust optimal operation of OLTC and SVC[J]. *IEEE Trans. Sustain. Energy*, 2016, 7(3): 1111–1123. doi:10.1109/TSTE.2016.2529627

Wang, S., and Wu, W. (2021). Aggregate flexibility of virtual power plants with temporal coupling constraints. *IEEE Trans. Smart Grid* 12, 5043–5051. doi:10.1109/TSG.2021.3106646

Wei, W., Liu, F., and Mei, S. (2015). Real-time dispatchability of bulk power systems with volatile renewable generations. *IEEE Trans. Sustain. Energy* 6, 738–747. doi:10.1109/TSTE.2015.2413903

Wu, H., Yuan, Y., Zhu, J., Qian, K., and Xu, Y. (2021). Potential assessment of spatial correlation to improve maximum distributed PV hosting capacity of distribution networks. *J. Mod. Power Syst. Clean Energy* 9, 800–810. doi:10.35833/MPCE.2020.000886

Xiong, L., Liu, X., Zhang, D., and Liu, Y. (2020). Rapid power compensation-based frequency response strategy for low-inertia power systems. *IEEE J. Emerg. Sel. Top. Power Electron.* 9, 4500–4513. doi:10.1109/JESTPE.2020.3032063

Zhang, D., Li, J., and Hui, D. (2018). Coordinated control for voltage regulation of distribution network voltage regulation by distributed energy storage systems. *Prot. Control Mod. Power Syst.* 3, 3. doi:10.1186/s41601-018-0077-1

Zhou, B., Zou, J., Chung, C. Y., Wang, H., Liu, N., Voropai, N., et al. Multi-microgrid energy management systems: architecture, communication, and scheduling strategies[J]. *J. Mod. Power Syst. Clean Energy*, 2021, 9(3): 463–476. doi:10.35833/MPCE.2019.000237

frontiers | Frontiers in Energy Research

TYPE Original Research
PUBLISHED 18 June 2024
DOI 10.3389/fenrg.2024.1418229

OPEN ACCESS

EDITED BY
Liansong Xiong,
Xi'an Jiaotong University, China

REVIEWED BY
Xiaokang Liu,
Polytechnic University of Milan, Italy
Xin Li,
Southeast University, China

*CORRESPONDENCE
Qun Li,
qun_li@sina.com
Weijia Tang,
tang_jsepc@126.com

RECEIVED 16 April 2024
ACCEPTED 22 May 2024
PUBLISHED 18 June 2024

CITATION
Li Q, Li Q, Tang W and Wang C (2024), Capacitor virtual inertia control and equivalent inertia analysis for a grid-forming wind generation system.
Front. Energy Res. 12:1418229.
doi: 10.3389/fenrg.2024.1418229

Capacitor virtual inertia control and equivalent inertia analysis for a grid-forming wind generation system

Qun Li*, Qiang Li, Weijia Tang* and Chenggen Wang

State Grid Jiangsu Electric Power Co., Ltd Research Institute, Nanjing, China

A grid-forming wind generation system exhibits exceptional grid frequency support abilities. The DC capacitor of the grid-forming wind generation system, which is characterized by rapid response and high sensitivity to minor disturbances, can provide short-term inertia support for the power system. This paper proposes the capacitor virtual inertia control for the grid-forming wind generation system, coupling the DC capacitor voltage with the power system frequency, which enables the DC capacitor to participate in the system frequency response process and reduces the rate of change of the system frequency during the disturbance. To analyze the inertia of the wind power generation system, this paper establishes an equivalent Philips–Heffron model for the grid-forming wind generation system and uses the equivalent inertia constant to quantify the inertia of the wind power generation system. The effectiveness of the proposed control strategy and the reasonableness of the inertia assessment method are verified through simulations in the single-turbine system and the IEEE four-machine two-area system.

KEYWORDS

wind generation system, grid-forming control, capacitor virtual inertia control, system frequency response, Philips–Heffron model, equivalent inertia

1 Introduction

To address the escalating energy crisis and environmental pollution, the power industry is undergoing a transformation toward high integration of renewable energies and power converters Xiong et al. (2020). According to the Global Wind Energy Council, global wind power capacity additions in 2023 will be 118 GW, a 36% year-on-year increase. Among renewable energies, full-power wind turbines provide less inertia to the power grid Wu et al. (2017). With the increasing proportion of wind power, the power system frequency security faces a serious challenge. Therefore, the grid codes explicitly require wind farms to have inertial response ability.

Currently, the mainstream types of wind generation are mainly doubly-fed induction generation and permanent-magnet synchronous generator (D-PMSG)-based directly driven wind generation. D-PMSG has better grid compatibility and greater speed range due to the introduction of a full-power converter that completely isolates the generator from the grid. Consequently, it has better wind condition adaptability and is widely used in the power system. The control methods for grid-tied converters of wind generation systems are categorized into grid-following (GFL) control and grid-forming (GFM) control.

The GFM control is favored by scholars due to the advantages of not needing phase-locked loop synchronization and being able to provide inertia and damping to the power system Xiong et al. (2019).

In wind generation systems, there are several sources of inertia. The wind turbine rotor, energy storage module, and DC capacitor within the system contribute to the inertia of the wind generation system. Focusing on the GFM control of the wind generation system, scholars have compared various virtual synchronization and inertia control methods and pointed out that the voltage source type control represented by virtual synchronous generator (VSG) control can make the wind generation system have good adaptability in the weak grid Bhende et al. (2011) Yazdi et al. (2019). Zhong et al. (2015) applied the VSG control to the full-power converter in which the rotor-side converter (RSC) is used to achieve DC-side voltage stabilization and the grid-side converter (GSC) is used to achieve maximum wind power tracking, while the disadvantage is that the wind turbine cannot respond to the system frequency. Wang et al. (2015) utilized grid voltage to obtain the voltage reference, directly synthesized the rotor excitation voltage, and provided current limited control using a virtual resistor. Muftau et al. (2020) used constant voltage control for RSC and VSG control for the GSC, which realizes the GFM control of wind generation and maintains DC voltage stabilization, but the disadvantage is that the DC capacitor of the wind generation system cannot provide inertia support for the power system. de Oliveira et al. (2023) used droop control to maintain DC voltage stabilization of the RSC by using torque and power as control objectives. Rodríguez-Amenedo et al. (2021) proposed a control method based on rotor magnetic chain orientation, where the magnetic chain phase angle and amplitude reference are obtained through the torque synchronization link and the voltage droop link, respectively. So it can acquire the rotor excitation voltage control reference, and finally the generator's internal potential is established to realize GFM control, while the disadvantage of this method is that the fan cannot provide inertia support for the power system. Yazdi et al. (2023) analyzed the coupling relationship between the power angle and rotor speed to elucidate rotor instability characteristics and the influence of control parameters and proposed a D-PMSG GFM frequency-supported control strategy considering rotor stability constraints, which enhanced system frequency stability under various disturbances. Meng et al. (2023) presented a cooperative control scheme for wind farms, along with GFM energy storage devices installed on the AC side. This scheme aims to endow the combined system of renewable energy and energy storage with a voltage source effect, enhancing system damping and inertia. Avazov et al. (2022) proposed an active damping support control strategy. This strategy activates the wind turbine power controller when the DC voltage fluctuation exceeds the designated threshold, subsequently enhancing system damping by using turbine-side resources.

To address the inertial response problem of wind power systems, a GFM control method for D-PMSG-based wind generation system was proposed in Davari and Mohamed (2016). The GSC achieves self-synchronization through DC voltage control, and the RSC employs additional inertia transfer control. However, this method exhibits limited performance in weak grid conditions. Thakallapelli et al. (2019) achieved inertial synchronization control by controlling the DC voltage of the GSC, enabling the wind turbine system to behave as a virtual voltage source for the power grid. Lai et al. (2017) demonstrated the potential of integrating flywheel energy storage on the DC side of the D-PMSG, where the DC bus voltage control of the flywheel aids in realizing virtual synchronous control for the GSC during grid connection. This not only enhances the system inertia response but also ensures DC bus voltage stability. Sang et al. (2021) configured flywheel energy storage on the DC side of the D-PMSG in which the flywheel energy storage adopts DC bus voltage control during grid-tied operation, the GSC realizes virtual synchronous control, and finally it realizes the purposes of improving the system inertia response ability, smoothing the active power of the wind generation system, and maintaining DC voltage stability. Pazmiño et al. (2021) proposed a novel approach to energy storage GFM frequency active support control. This approach combines constant frequency control with frequency modulation state transfer control, thereby departing from traditional control methods such as virtual inertia and primary frequency modulation. He et al. (2024) developed a system frequency response model incorporating a wind turbine with integrated inertia control. The study derives an analytical equation for the effective inertia time constant in the wind turbine frequency modulation process and assesses its inertia support capacity.

In this paper, a GFM control method for the D-PMSG-based wind generation system is proposed, where the DC capacitor voltage is coupled with the system frequency, enabling the DC capacitor to participate in the system frequency response process. The remainder of this manuscript is structured as follows: Section 2 introduces the basic GFM control strategy of the D-PMSG-based wind generation system. Section 3 introduces the proposed capacitor virtual inertia control. Section 4 presents the equivalent Philips–Heffron model of the wind power system and analyzes the equivalent inertia of the system. Finally, Section 5 verifies the sophistication and effectiveness of the proposed control method.

2 GFM control strategy for the D-PMSG-based wind generation system

The specific structure of the D-PMSG-based wind generation system is shown in Figure 1, which consists of the wind turbine, D-PMSG, and back-to-back converter. The RSC maintains DC capacitor voltage stabilization, and the GSC controls the magnitude and frequency of the voltage tied to the grid.

2.1 Modeling of the wind turbine

The mechanical power of a D-PMSG-based wind generation system Liu et al. (2016) can be expressed as

$$\begin{cases} P_{\mathrm{wm}} = \dfrac{1}{2}\rho\pi R_{\mathrm{w}}^2 C_{\mathrm{p}}(\lambda,\beta)\, v_{\mathrm{m}}^3 \\ C_{\mathrm{p}}(\lambda,\beta) = 0.5176\left(\dfrac{116}{\lambda_1} - 0.4\beta - 5\right) e^{\frac{-21}{\lambda_1}} + 0.0068\lambda \\ \dfrac{1}{\lambda_1} = \dfrac{1}{\lambda + 0.08\beta} - \dfrac{0.035}{\beta^3 + 1} \\ \lambda = \dfrac{\omega_{\mathrm{w}} R_{\mathrm{w}}}{v_{\mathrm{w}}} \end{cases}, \quad (1)$$

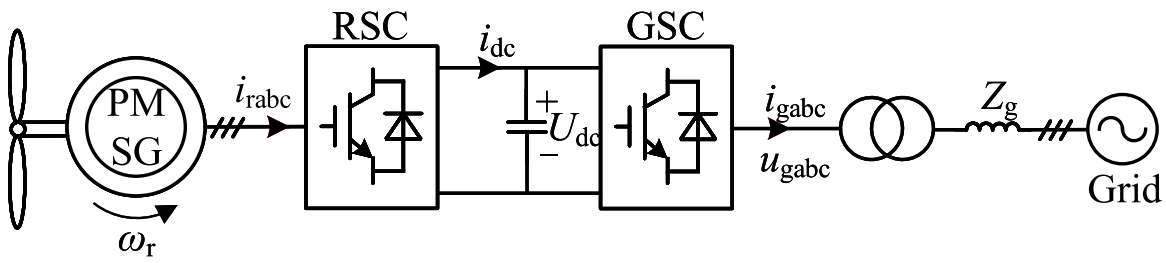

FIGURE 1
Structure of the D-PMSG-based wind generation system.

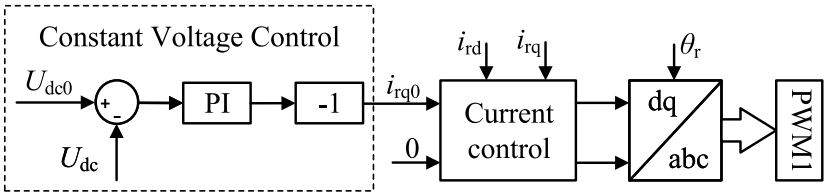

FIGURE 2
Constant voltage control strategy of the RSC.

where P_{wm} is the mechanical power of the wind turbine; ρ is the air density; R_w is the blade radius of the wind turbine; λ is the tip speed radio of the wind turbine; C_p is the wind energy utilization factor; β is the pitch angle of the wind turbine; ω_w is the angular velocity of the wind turbine; v_w is the inlet wind speed.

In (1), it is clear that P_{wm} is influenced by C_p, and C_p is the function of λ and β. When β increases, C_p decreases. At the same time, there exists a unique λ that maximizes C_p when β is the same, and when R_w and v_w are constant values, λ is in direct proportion to ω_w. So, for each v_w, there is a ω_w corresponding to the maximum P_{wm}. Therefore, to obtain the maximum power and wind energy utilization factor, the rotational speed of the wind turbine must be adjusted according to the wind speed correspondingly.

2.2 RSC control strategy

For the conventional GFM wind generation system, the GSC adopts a constant capacitor voltage control to ensure the stability of the DC capacitor voltage U_{dc}, as shown in Figure 2.

The generator stator phase voltage can be expressed as

$$U_s = \omega_s \sqrt{\left(L_{sq} i_{sq}\right)^2 + \varphi_f^2}, \tag{2}$$

where ω_s is the rotor angular frequency; L_{sq} is the stator q-axis inductance; i_{sq} is the stator current q-axis component; φ_f is the stator magnetic chain.

The electromagnetic torque and active power of D-PMSG are only related to i_{sq}. Therefore, adjusting i_{sd} does not affect the active power output of the wind turbine. In vector control, the d-axis current i_{sd} usually has the value of 0, to hence using all of the current to generate electromagnetic torque.

2.3 GSC control strategy

The GSC adopts virtual synchronous generator (VSG) control that can support the frequency and magnitude of the grid voltage Xiong et al. (2015), as shown in Figure 3.

The VSG control is composed of two primary components: *P-f* control and *Q-U* control. The former introduces the concept of virtual inertia in the GSC by simulating the rotor motion equations of the synchronous machine. The *P-f* control equation for the VSG control of the GSC is

$$2H\frac{d\omega}{dt} = P_0 - P - D(\omega - \omega_0), \tag{3}$$

where H is the inertia time constant; D is virtual damping; ω is the grid angular velocity; ω_0 is the grid rated angular velocity; P is the grid-side output power; P_0 is the power command value.

The *Q-U* control obtains the command value of the output voltage magnitude by simulating the reactive power droop characteristic of the synchronous machine. The *Q-U* control equation for VSG control of the GSC is

$$U_{ref} = U_0 + K_q(Q_0 - Q), \tag{4}$$

where U_{ref} is the commanded value of the grid-side voltage; U_0 is the rated value of the grid-side voltage; K_q is the *Q-U* control coefficient; Q is the grid-side reactive power; Q_0 is the reference value of reactive power.

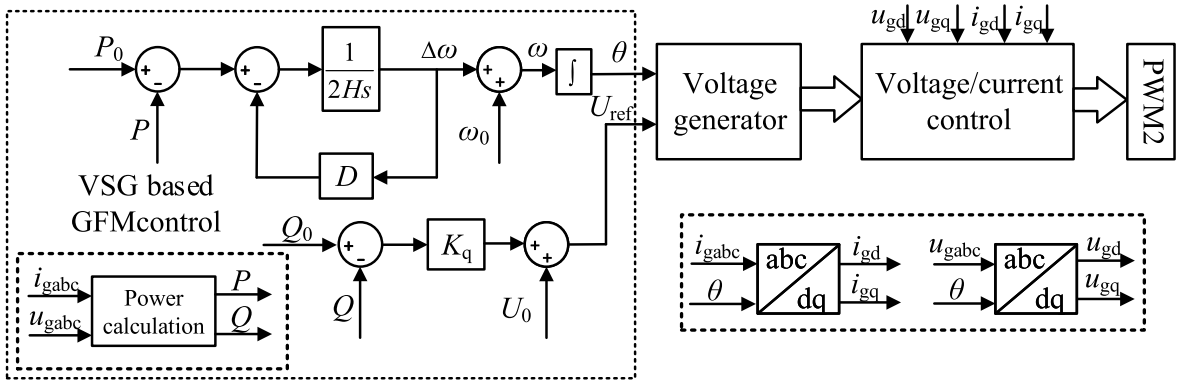

FIGURE 3
GSC control strategy.

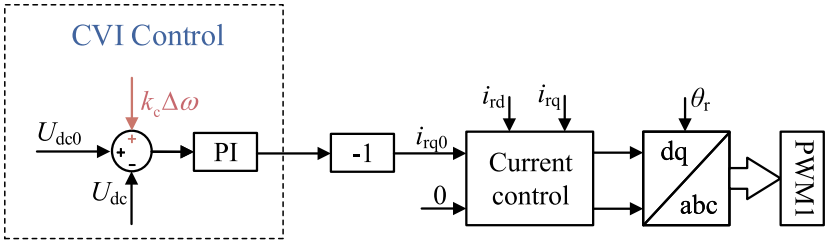

FIGURE 4
CVI control.

The GSC adopts VSG control to realize the wind generation system externally, being the voltage source characteristics, and effectively support the grid-side voltage and frequency.

3 Capacitor virtual inertia control

3.1 Control strategy

The GSC of the conventional GFM control for D-PMSG utilizes constant capacitor voltage control, where the entirety of inertia support is sourced from the wind turbine rotor. To enable the DC capacitor to contribute to the frequency response, this manuscript proposes a novel capacitor virtual inertia (CVI) control, illustrated in Figure 4.

This control strategy adds an auxiliary voltage regulation command to the constant voltage control loop, changing the reference voltage from U_{dc0} to U_{dcref}, i.e.,

$$U_{dcref} = U_{dc0} + \Delta U = U_{dc0} + k_c\Delta\omega, \tag{5}$$

where k_c is the regulation coefficient; $\Delta\omega$ is the angular frequency deviation; U_{dc0} is the initial value of the capacitor voltage; ΔU is the capacitor voltage deviation.

The CVI control couples the DC capacitor voltage to the grid frequency deviation. When the grid is disturbed, the proposed control can make the DC capacitor provide the inertia support, thus reducing the rate of change of frequency.

3.2 Capacitor equivalent inertia analysis

Normally, constant capacitor voltage control is implemented to keep the DC capacitor voltage stable, but it does not integrate the capacitor into the frequency response. As a result, under constant voltage control, the equivalent inertia provided by the capacitor is negligible. However, with the introduction of CVI control in the RSC, the interplay between capacitor voltage and grid frequency allows the capacitor to contribute to inertia support, thereby enhancing equivalent inertia. The analysis process is detailed below.

During steady-state operation, the energy stored by the capacitor is

$$E_{ck} = \int C_{dc}U_{dc}\mathrm{d}U_{dc} = \frac{1}{2}C_{dc}U_{dc}^2, \tag{6}$$

where C_{dc} is the DC capacitor value and U_{dc} is the DC capacitor voltage.

When the DC capacitor responds to the frequency deviation, the electric energy deviation of the capacitor is given by

$$\begin{aligned}\Delta E_{ck} &= \frac{1}{2}C_{dc}\left[(U_{dc0}+\Delta U_{dc})^2 - U_{dc0}^2\right] \\ &= \frac{1}{2}C'_{dc}\left[(\omega_0+\Delta\omega)^2 - \omega_0^2\right],\end{aligned} \tag{7}$$

where C'_{dc} is the equivalent capacitor under virtual inertia control.

The value of the equivalent capacitor is

$$C'_{dc} = C_{dc}\frac{(2U_{dc0}+\Delta U_{dc})\Delta U_{dc}}{(2\omega_0+\Delta\omega)\Delta\omega} \approx C_{dc}\frac{\Delta U_{dc}U_{dc0}}{\Delta\omega\omega_0}. \quad (8)$$

Define the equivalent adjustment coefficient k'_c as

$$k'_c = \Delta U_{dc}U_{dc0}/\Delta\omega\omega_0. \quad (9)$$

The relationship between k'_c and k_c is

$$k'_c = k_c U_{dc0}/\omega_0. \quad (10)$$

Under CVI control, the equivalent inertia time constant of the capacitor is

$$H_c = \frac{C'_{dc}U^2_{dc0}}{2S_B} = \frac{\Delta U_{dc}C_{dc}U^3_{dc0}}{2\Delta\omega\omega_0 S_B} = \frac{k_c C_{dc}U^3_{dc0}}{2\omega_0 S_B} = \frac{k'_c C_{dc}U^2_{dc0}}{2S_B} = k'_c H'_c, \quad (11)$$

where S_B is the rated capacity of the wind turbine and H'_c is the capacitor inertia time constant.

Eq 11 reveals that under CVI control, the dynamic regulation range of the DC capacitor is significantly broader and its inertia characteristics not only depend on its value but also on the regulation coefficient kc and the steady-state operating point. To exemplify, Figure 5 depicts the interdependence between the capacitor equivalent inertia time constant H_c, DC capacitor C_{dc}, regulation coefficient k_c, and the steady-state operating point U_{dc0} in a grid rated at 300 kW.

Figure 5 illustrates that under CVI control, the equivalent inertia provided by the capacitor is related to multiple parameters, and the equivalent inertia can be greater than its inherent inertia. The proposed control enables the capacitor to provide the energy required for the frequency response of the grid.

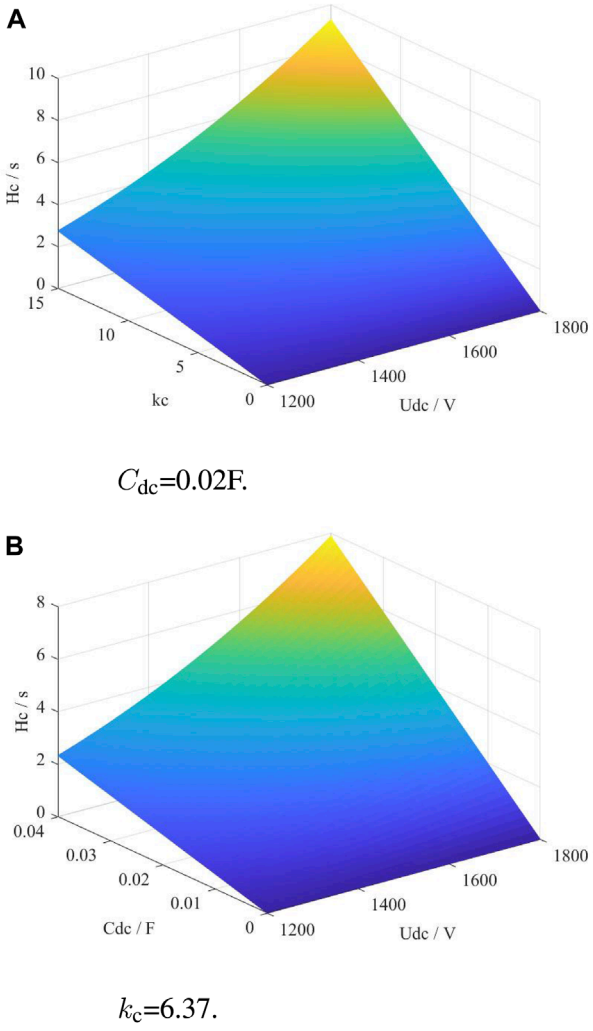

FIGURE 5
Analysis of factors affecting capacitor equivalent inertia. **(A)** C_{dc} = 0.02F. **(B)** k_c = 6.37.

4 Wind power system equivalent inertia analysis

4.1 Philips–Heffron model of the power system with GFM wind generation

In the preceding section, this manuscript proposed a GFM control strategy for the wind generation system that employs CVI control for RSC and VSG control for the GSC. To investigate the equivalent inertia of the entire power system with the wind generation controlled by the proposed GFM strategy, an equivalent Philips–Heffron model is developed, as illustrated in Figure 6.

Under the CVI control, the mathematical expression of the equivalent Philips–Heffron model of the entire power system with wind generation controlled by the proposed GFM strategy is as follows:

$$\begin{cases} \frac{d\Delta\delta}{dt} = \omega_0\Delta\omega \\ T_J\frac{d\Delta\omega}{dt} = -T_D\Delta\omega - T_s\Delta\delta \end{cases}. \quad (12)$$

According to (12), T_J is the equivalent inertial time constant, increasing T_J can reduce the frequency rate of system during

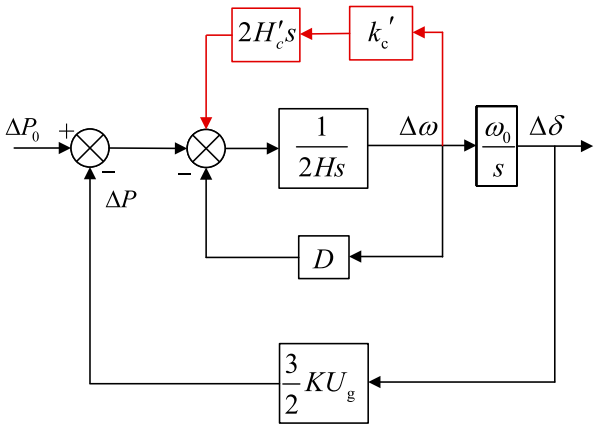

FIGURE 6
Equivalent Philips–Heffron model.

disturbances. T_D is the equivalent damping time constant, increasing T_D reduces the frequency deviation of the system during disturbances. T_S is the equivalent synchronization time constant, reflecting the self-synchronization capability of the GFM D-PMSG.

$$\begin{cases} T_J = 2(H + H_c) = \dfrac{1}{S_B}\left(J\omega_0^2 + \dfrac{k_c C_{dc} U_{dc0}^3}{\omega_0}\right) \\ T_D = D \\ T_S = \dfrac{3}{2}\dfrac{U_s U_g}{X}\cos\delta_0 \end{cases}, \quad (13)$$

where U_s is the converter side voltage, U_g is the grid-side voltage, X is the system impedance, and δ_0 is the rated power angle.

According to (13), T_J is intricately linked to both the VSG control equivalent inertia time constant H and the capacitor equivalent inertia time constant H_c, wherein H depends on the VSG control parameter in the GSC and its energy support source is the rotor; H_c is determined by the proposed CVI control parameter, and its energy source is the DC capacitor. T_D depends on the virtual damping parameter D in the VSG control. T_S depends on the electrical parameters of the converter and the grid.

4.2 Analysis of factors affecting the equivalent inertia of D-PMSG

According to the equivalent Philips–Heffron model of the entire power system with the wind generation controlled by the proposed GFM strategy, the composite equivalent inertia is composed of two distinct components. In the subsequent analysis, we will delve into the individual influencing factors of H_c and H.

4.2.1 Equivalent capacitor inertia time constant

According to 11, the equivalent inertia time constant H_c under virtual inertia regulation is related to the regulation coefficient k_c, the DC capacitor capacity C_{dc}, the initial DC capacitor voltage U_{dc0}, and the rated capacity of the wind turbine S_B.

1. The larger the adjustment coefficient k_c is, the larger the equivalent inertial time constant is. It can be seen from 5 that with the increase of k_c, the voltage deviation ΔU_{dc} of the DC capacitor also increases gradually. Since the converter is limited by voltage, the DC capacitor voltage should be greater than 1.23 U_g. Consequently, excessive voltage deviation is prohibited, constraining the viable range for selecting the adjustment coefficient k_c.
2. An increase in C_{dc} leads to a larger H_c, but practical considerations limit the choice: a larger capacitor implies larger and more expensive components. Although the supercapacitors' value can reach the farad level, the economy is poor in engineering application. Moreover, the larger the capacitor value, the lower the capacitor voltage, and the reduction in voltage leads to a reduction in the equivalent inertia time constant.
3. Higher U_{dc0} contributes to a larger H_c. However, in operational scenarios, it is crucial to maintain a reasonable initial voltage to prevent converter overvoltage, which can disrupt normal functioning and cause economic losses.
4. A smaller S_B value increases the H_c. However, in the case of the selected wind turbine, the rated capacity S_B is a fixed value.

TABLE 1 Simulation parameters.

Parameter	Value	Parameter	Value
S_B	300 kW	J_{VSG}	4.05 kg · m^2
U_{dc0}	1800 V	D_{VSG}	75.99
f_0	50 Hz	C	20 mF
P_{load}	200 kW	R_s	0.001 Ω
ΔP_{load}	15 kW	L	3 mF

4.2.2 Equivalent inertial time constant of VSG control

The VSG control mechanism facilitates the converter's participation in the frequency response by emulating synchronous machine dynamics. Its equivalent inertia constant, H, can be adjusted by changing the control parameters. However, it is important to note that the inertia support power derived from the rotors of the wind turbine comes at the expense of rotor speed during disturbances. Consequently, the inertia parameters of VSG control need to be reasonably set according to the actual situation and can not only consider the need to increase the gird inertia, while ignoring the frequency response costs.

5 Verification

5.1 Single-turbine grid-connected system

To verify the effectiveness of the proposed CVI control and the correctness of the equivalent Philips–Heffron model, a simulation model of the single D-PMSG wind generation system, as shown in Figure 1, is constructed in MATLAB/Simulink. The main parameters of the simulation model are given in Table 1.

The simulation model is built according to the control strategy described in Sections 2, 3, with CVI control for the RSC and VSG control for the GSC. Under the initial conditions, the local load at the grid side is 200 kW, and the 15 kW additional disturbance is introduced at 10 s. The system frequency waveforms and DC capacitor voltage waveforms of CVI control and constant voltage control are compared, as shown in Figure 7.

The system frequency waveforms under CVI control and constant voltage control are depicted in Figure 7A. The rate of change of the system frequency is smaller under CVI control, indicating that the proposed control increases the equivalent inertia. The steady-state frequency under both controls remains at 49.9 Hz. This consistency arises because the system inertia affects only the transient characteristics of the frequency without influencing its steady-state behavior. Additionally, the system frequency waveform under CVI control is lower than that under constant voltage control from 10.2 s to 11.2 s, corresponding to the overshooting of the DC capacitor voltage under CVI control. This occurs because the DC capacitor undergoes a discharging process to provide inertial support power to the system during the initial stage of the disturbance, necessitating a subsequent charging process.

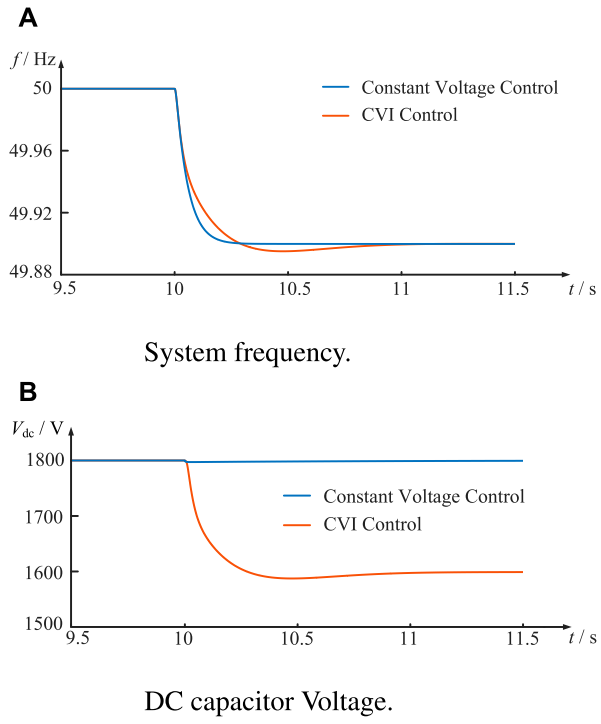

FIGURE 7
Waveform comparison of constant voltage and CVI control in single-turbine system. **(A)** System frequency. **(B)** DC capacitor voltage.

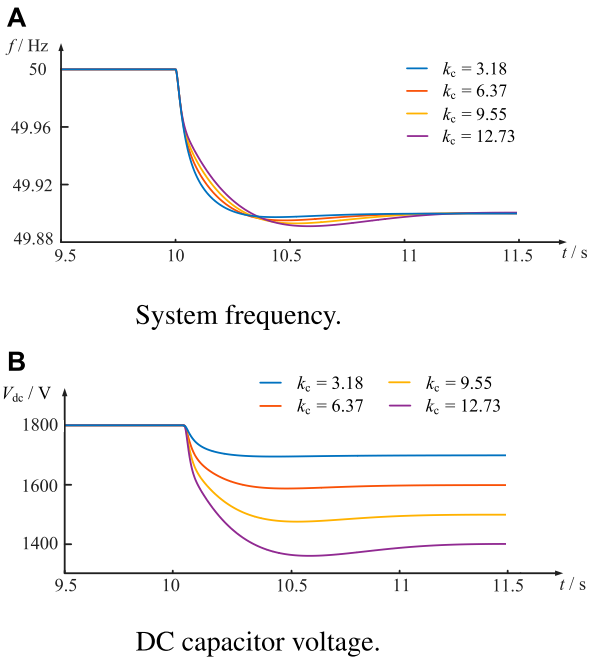

FIGURE 8
Waveform comparison of constant voltage and CVI control under different k_c. **(A)** System frequency. **(B)** DC capacitor voltage.

Figure 7B illustrates the DC capacitor voltage waveforms under both control strategies. When a load disturbance occurs, the DC capacitor voltage under constant voltage control has only a small fluctuation and recovers to 1800 V quickly. In contrast, the DC capacitor voltage under CVI control drops from 1800 V to 1600 V and subsequently keeps stabilizing due to the coupling between the DC capacitor voltage and the system frequency deviation. This dynamic behavior under CVI control has provided inertia support for the power system and enhanced the equivalent inertia of the power system.

To verify the specific impact of CVI control on frequency dynamics, the system frequency and DC capacitor voltage waveforms are conducted under the same operating condition at different regulation coefficients k_c. The results are shown in Figure 8.

Figure 8A shows that the rate of change of the frequency decreases with the increase of the regulation coefficient k_c, indicating that the stronger the coupling between the regulated DC capacitor voltage and the frequency deviation of the system, the larger the equivalent inertia provided by the CVI control to the system. In addition, the overshooting of the frequency waveform between 10.2 s and 11.2 s also increases with the increase in the regulation coefficient k_c because the overshooting of the DC capacitor voltage drop process becomes larger with the increase in the regulation coefficient k_c, and more energy is required in the charging process before it reaches the steady state. The DC capacitor voltage waveforms under different regulation coefficients k_c are shown in Figure 8B, and it reveals that the larger the regulation coefficient k_c is, the more inertia-supporting power is provided by the DC capacitor, corresponding to a larger voltage drop.

5.2 Multi-machine system

The IEEE four-machine two-area (4M2A) system is a commonly used theoretical model in the power system to study the power transmission and control between neighboring regions in a power system. To further verify the correctness and effectiveness of the control method proposed in this paper, an IEEE 4M2A simulation model with a wind generation system is constructed, as shown in Figure 9.

Area 1 consists of two synchronous generators SG1 and SG2 and stational load, whereas area 2 consists of synchronous generator SG3, D-PMSG single-turbine system replacing synchronous machine SG4, and variable load where PCC is the wind generator merging point. Initially, the load demand is 225 MW, with a variable load of 119.5 MW. At 40 s, a sudden disturbance of 50 MW is imposed on the variable load. The comparative analysis of system frequency and DC capacitor voltage waveforms under CVI and fixed-voltage control conditions is shown in Figure 10.

Figure 10A shows that in the multi-machine power system, the rate of change of system frequency is smaller under CVI control, indicating that this control increases the equivalent inertia of the wind power system. However, due to the relatively slow frequency response process of the synchronizer in the system, there is a small recovery when the system frequency drops to

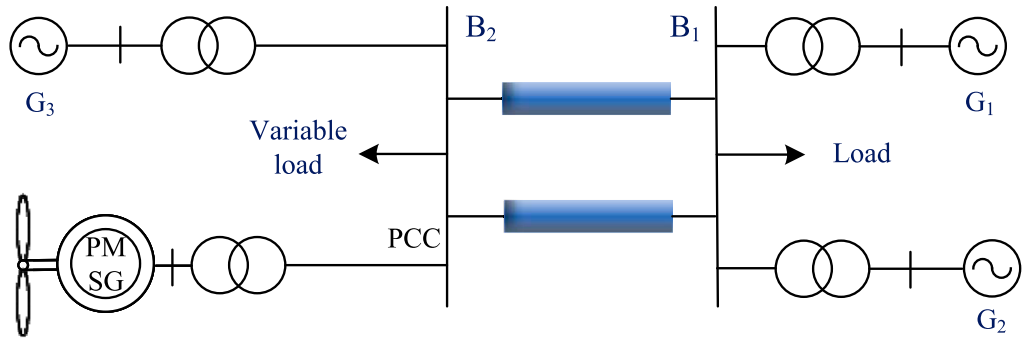

FIGURE 9
4M2A system with the wind generation system.

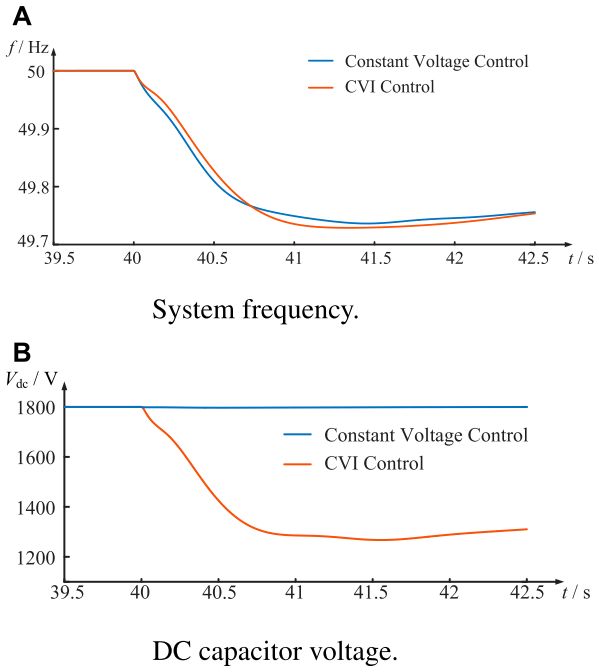

FIGURE 10
Waveform comparison of constant voltage and CVI control in multi-machine system. **(A)** System frequency. **(B)** DC capacitor voltage.

its lowest point. The DC capacitor voltage waveform is shown in Figure 10B, where the capacitor voltage remains stable under constant voltage control, while the DC capacitor voltage drops to about 1300 V under CVI control to provide inertia support to the power system.

In summary, analysis of simulation results for both the single-turbine and 4M2A systems under CVI control demonstrates its superiority over constant voltage control. CVI control facilitates the DC capacitor responsiveness to system frequency changes, effectively delaying system frequency decrease. This response aligns with the demands of the frequency response, providing the system with a reasonable level of inertia support.

6 Conclusion

This paper proposes a CVI control strategy for the GFM wind generation system and employs the Philips–Heffron model to analyze the equivalent inertia of the entire power system with the wind generation controlled by the proposed GFM strategy. The corresponding single-turbine test system and 4M2A test system are constructed to carry out the simulation validation. The main conclusions are as follows:

1. The CVI control effectively couples the DC capacitor voltage to the grid frequency deviation. When the power grid is disturbed, the CVI control can make the DC capacitor participate in the frequency response, provide the inertia support for the power grid, and reduce the rate of change of frequency.
2. The equivalent Philips–Heffron model was established to analyze the equivalent inertia of the entire power system with the wind generation controlled by the proposed GFM strategy.
3. The single-turbine and 4M2A test system models are constructed to verify the effectiveness of the proposed GFM control strategy and the correctness of the inertia analysis results.

Data availability statement

The original contributions presented in the study are included in the article/Supplementary Material; further inquiries can be directed to the corresponding authors.

Author contributions

QuL: conceptualization, data curation, formal analysis, investigation, methodology, software, writing–original draft, and writing–review and editing. QiL: conceptualization, data curation, software, supervision, and writing–original draft. WT: validation, visualization, and writing–review and editing.

CW: project administration, resources, and writing–review and editing.

Funding

The author(s) declare that financial support was received for the research, authorship, and/or publication of this article. This work was supported by the Science And Technology Project of State Grid Jiangsu Electric Power Co., Ltd (J2023021).

Acknowledgments

The authors wish to thank the project funding from the Science And Technology Project of State Grid Jiangsu Electric Power Co., Ltd (J2023021).

Conflict of interest

Authors QuL, QiL, WT, and CW were employed by State Grid Jiangsu Electric Power Co., Ltd. Research Institute.

The authors declare that this study received funding from State Grid Jiangsu Electric Power Co., Ltd. The funder had the following involvement in the study: the study design, collection, analysis, interpretation of data, and the writing of this article.

Publisher's note

References

Avazov, A., Colas, F., Beerten, J., and Guillaud, X. (2022). Application of input shaping method to vibrations damping in a type-iv wind turbine interfaced with a grid-forming converter. *Electr. Power Syst. Res.* 210, 108083. doi:10.1016/j.epsr.2022.108083

Bhende, C., Mishra, S., and Malla, S. G. (2011). Permanent magnet synchronous generator-based standalone wind energy supply system. *IEEE Trans. Sustain. energy* 2, 361–373. doi:10.1109/tste.2011.2159253

Davari, M., and Mohamed, Y. A.-R. I. (2016). Robust dc-link voltage control of a full-scale pmsg wind turbine for effective integration in dc grids. *IEEE Trans. Power Electron.* 32, 4021–4035. doi:10.1109/tpel.2016.2586119

de Oliveira, J. D. A., de Araújo Lima, F. K., Tofoli, F. L., and Branco, C. G. C. (2023). Synchronverter-based frequency control technique applied in wind energy conversion systems based on the doubly-fed induction generator. *Electr. Power Syst. Res.* 214, 108820. doi:10.1016/j.epsr.2022.108820

He, H., Xiao, H., and Yang, P. (2024). Analysis and quantitative evaluation of wind turbine frequency support capabilities in power systems. *Front. Energy Res.* 12, 1363198. doi:10.3389/fenrg.2024.1363198

Lai, J., Song, Y., and Du, X. (2017). Hierarchical coordinated control of flywheel energy storage matrix systems for wind farms. *IEEE/ASME Trans. Mechatronics* 23, 48–56. doi:10.1109/tmech.2017.2654067

Liu, J., Wen, J., Yao, W., and Long, Y. (2016). Solution to short-term frequency response of wind farms by using energy storage systems. *IET Renew. Power Gener.* 10, 669–678. doi:10.1049/iet-rpg.2015.0164

Meng, J., Wang, D., Wang, Y., Guo, F., and Yu, J. (2023). An improved damping adaptive grid-forming control for black start of permanent magnet synchronous generator wind turbines supported with battery energy storage system. *IET Generation, Transm. Distribution* 17, 354–366. doi:10.1049/gtd2.12753

Muftau, B., Fazeli, M., and Egwebe, A. (2020). Stability analysis of a pmsg based virtual synchronous machine. *Electr. Power Syst. Res.* 180, 106170. doi:10.1016/j.epsr.2019.106170

Pazmiño, I., Martinez, S., and Ochoa, D. (2021). Analysis of control strategies based on virtual inertia for the improvement of frequency stability in an islanded grid with wind generators and battery energy storage systems. *Energies* 14, 698. doi:10.3390/en14030698

Rodríguez-Amenedo, J. L., Gómez, S. A., Martínez, J. C., and Alonso-Martinez, J. (2021). Black-start capability of dfig wind turbines through a grid-forming control based on the rotor flux orientation. *IEEE Access* 9, 142910–142924. doi:10.1109/access.2021.3120478

Sang, S., Pei, B., Huang, J., Zhang, L., and Xue, X. (2021). Low-voltage ride-through of the novel voltage source-controlled pmsg-based wind turbine based on switching the virtual resistor. *Appl. Sci.* 11, 6204. doi:10.3390/app11136204

Thakallapelli, A., Kamalasadan, S., Muttaqi, K. M., and Hagh, M. T. (2019). A synchronization control technique for soft connection of doubly fed induction generator based wind turbines to the power grids. *IEEE Trans. Industry Appl.* 55, 5277–5288. doi:10.1109/tia.2019.2917654

Wang, S., Hu, J., and Yuan, X. (2015). Virtual synchronous control for grid-connected dfig-based wind turbines. *IEEE J. Emerg. Sel. Top. power Electron.* 3, 932–944. doi:10.1109/jestpe.2015.2418200

Wu, Z., Gao, D. W., Zhang, H., Yan, S., and Wang, X. (2017). Coordinated control strategy of battery energy storage system and pmsg-wtg to enhance system frequency regulation capability. *IEEE Trans. Sustain. Energy* 8, 1330–1343. doi:10.1109/tste.2017.2679716

Xiong, L., Liu, X., Zhang, D., and Liu, Y. (2020). Rapid power compensation-based frequency response strategy for low-inertia power systems. *IEEE J. Emerg. Sel. Top. Power Electron.* 9, 4500–4513. doi:10.1109/jestpe.2020.3032063

Xiong, L., Liu, X., Zhao, C., and Zhuo, F. (2019). A fast and robust real-time detection algorithm of decaying dc transient and harmonic components in three-phase systems. *IEEE Trans. Power Electron.* 35, 3332–3336. doi:10.1109/tpel.2019.2940891

Xiong, L., Zhuo, F., Wang, F., Liu, X., Chen, Y., Zhu, M., et al. (2015). Static synchronous generator model: a new perspective to investigate dynamic characteristics and stability issues of grid-tied pwm inverter. *IEEE Trans. Power Electron.* 31, 6264–6280. doi:10.1109/tpel.2015.2498933

Yazdi, S. S. H., Milimonfared, J., Fathi, S. H., Rouzbehi, K., and Rakhshani, E. (2019). Analytical modeling and inertia estimation of vsg-controlled type 4 wtgs: power system frequency response investigation. *Int. J. Electr. Power and Energy Syst.* 107, 446–461. doi:10.1016/j.ijepes.2018.11.025

Yazdi, S. S. H., Shokri-Kalandaragh, Y., and Bagheri, M. (2023). Power system stability improvement considering drive train oscillations of virtual synchronous generator-regulated type-4 wind turbines. *IET Renew. Power Gener.* 17, 579–603. doi:10.1049/rpg2.12616

Zhong, Q.-C., Ma, Z., Ming, W.-L., and Konstantopoulos, G. C. (2015). Grid-friendly wind power systems based on the synchronverter technology. *Energy Convers. Manag.* 89, 719–726. doi:10.1016/j.enconman.2014.10.027

frontiers | Frontiers in Energy Research

TYPE Original Research
PUBLISHED 05 July 2024
DOI 10.3389/fenrg.2024.1424389

OPEN ACCESS

EDITED BY
Yonghui Liu,
Hong Kong Polytechnic University, Hong Kong SAR, China

REVIEWED BY
Chen Yang,
Chongqing University, China
Weibin Zhang,
Nanjing University of Science and Technology, China
Zhiwu Li,
Macau University of Science and Technology, Macao SAR, China

*CORRESPONDENCE
Huaizhong Hu,
huhuaizhong@xjtu.edu.cn

RECEIVED 28 April 2024
ACCEPTED 07 June 2024
PUBLISHED 05 July 2024

CITATION
Hu H, Ma Y, Zhang X, Han C and Hao Y (2024), Day-ahead and hour-ahead optimal scheduling for battery storage of renewable energy power stations participating in primary frequency regulation.
Front. Energy Res. 12:1424389.
doi: 10.3389/fenrg.2024.1424389

Day-ahead and hour-ahead optimal scheduling for battery storage of renewable energy power stations participating in primary frequency regulation

Huaizhong Hu[1]*, Yanzhao Ma[1], Xiaoke Zhang[2], Chongshang Han[1] and Yiran Hao[1]

[1]School of Automation Science and Engineering, Faculty of Electronics and Information Engineering, Xi'an Jiaotong University, Xi'an, China, [2]State Grid Henan Electric Power Company, State Grid Corporation of China (SGCC), Electric Power Research Institute, Henan, China

Due to the fast response characteristics of battery storage, many renewable energy power stations equip battery storage to participate in auxiliary frequency regulation services of the grid, especially primary frequency regulation (PFR). In order to make full use of the battery capacity and improve the overall revenue of the renewable energy station, a two-level optimal scheduling strategy for battery storage is proposed to provide primary frequency regulation and simultaneously arbitrage, according to the peak-valley electricity price. The energy storage output is composed of the droop-based primary frequency regulation output and the economic output, according to the electricity price. First, day-ahead optimization defines the economic output profile and an appropriate droop coefficient, considering regulation needs, with the goal of maximizing the overall return. The scheduling result is then adjusted for hour-ahead optimization based on the updated regulation information to ensure more durable and reliable performance. Simulation results show that the proposed scheduling strategy can fully utilize the battery capacity, realize peak-valley arbitrage while assuming the obligation of primary frequency regulation of the renewable energy power station, and then improve the overall income of the power station.

KEYWORDS

battery storage, renewable energy station, primary frequency regulation, droop control, time-of-use electricity price, optimal scheduling

1 Introduction

Nowadays, many countries in the world are vigorously developing renewable energy power generation, such as wind power and photovoltaic (PV) power. Compared with traditional thermal power generation, renewable energy power generation is more environmentally friendly due to the use of clean and renewable energy. However, most renewable energy power units are connected to the grid through inverters, which decrease the inertia and damping of the grid (Xiong et al., 2022). Moreover, renewable energy units often operate in the maximum power tracking mode, which makes it difficult for them to cope with active power instantaneous fluctuations in the grid; in other words, they lack primary frequency regulation (PFR) capability. Related research equips renewable energy

units with the primary frequency regulation ability by improving their control algorithms, but they still have certain shortcomings (Mahish and Pradhan, 2020; Li et al., 2021). For instance, wind turbines need to operate at the right speed to participate in PFR (Ma et al., 2024). PV units are mostly involved in PFR through load shedding, which greatly reduces their operating economy (Cristaldi et al., 2022).

Under the above context, the use of the battery energy storage system (BESS) to undertake the primary frequency regulation task of renewable energy power stations has emerged. It is shown that BESS participating in PFR can effectively improve the system frequency (Turk et al., 2019). With the coordination of energy storage and renewable energy power stations, renewable energy units do not need to participate in PFR, and all generated electricity is connected to the grid. BESS utilizes its speed and flexibility to actively respond to primary frequency regulation signals. As more countries start to implement time-of-use electricity pricing policies, BESS can also perform peak shaving and valley filling based on the output of renewable energy generation when its capacity is sufficient. The combination of the renewable energy power station and BESS mentioned above can not only improve the grid-connected characteristics but also further increase the revenue of the integrated station (IS).

A lot of studies have been conducted on BESSs providing PFR services. Zhu and Zhang (2019) divided the PFR control into frequency regulation and state-of-charge (SOC) recovery phases. For frequency regulation, it optimizes the charge and discharge power of the BESS online based on the determined frequency regulation requirements of the grid. Most of the PFR power of BESSs is obtained by a droop-based control mechanism, according to the system frequency difference (Arrigo et al., 2020; Fang et al., 2020; Xiong et al., 2021; Zhao et al., 2022). Most BESSs under droop control set a fixed droop coefficient in their factory settings, but a fixed droop coefficient cannot satisfy various frequency regulation conditions (Xiong et al., 2021). Schiapparelli et al. (2018); Feng et al. (2024) dynamically adjusted the droop coefficient based on the prediction of future system frequency differences or the SOC of BESSs to maintain a long-term reliable operation. The above research mainly focuses on BESSs participating solely in PFR, while the relevant literature has studied BESSs providing multiple auxiliary services, including PFR. Ma et al. (2022) considered a shared BESS performing PFR and automatic generation control (AGC) for multiple renewable energy power stations. This paper only describes the formulation of the hour-ahead optimization strategy and does not involve the content of the day-ahead optimization strategy. According to Schiapparelli et al. (2018), the BESS capacity in Conte et al. (2020) is divided into PFR sub-battery and PV sub-battery: the former compensates for PV prediction errors, and the latter is for frequency regulation. The proposed method realizes the economic optimal of the IS under the premise of keeping SOC safe in both day-ahead and intra-day markets. However, the sub-battery compresses the available capacity of BESSs, which does not take into account that the effect of sub-batteries on SOC may counteract each other. Wang et al. (2022) proposed a bi-level joint optimization model of BESSs to arbitrage in the energy market and provide PFR services to make profits. The optimization of BESSs in energy and PFR markets helps improve the frequency security and stabilize the clearing price. In this model, the dynamic frequency nonlinear constraints are constructed to ensure the safety of the rate of change of frequency (RoCoF) and the frequency nadir. These constraints are related to the given power imbalance of the system and do not take into account the randomness of actual frequency regulation occurrences.

In this work, an IS containing several renewable energy units and a small-capacity BESS with PFR are considered. Usually, small-capacity BESSs in renewable energy stations are mostly just involved in PFR services (Meng et al., 2021; Li et al., 2022). Here, BESSs participate in PFR without affecting renewable energy generation and utilize the remaining capacity to arbitrage through time-of-use electricity prices. In summary, existing research on BESS optimization scheduling has not paid enough attention to the energy consumption of primary frequency regulation, and most of it has not considered the uncertainty of primary frequency regulation signals. We proposed a two-level optimization strategy for BESSs providing PFR services based on the acquired forecast PFR information. First, day-ahead scheduling (DAS) tunes a suitable droop coefficient and optimizes a preliminary BESS charge and discharge plan for the day to achieve the economic goal of the IS. Because there may be great differences in PFR action between the before-day forecast and actual operation, hour-ahead scheduling (HAS) corrects the results of DAS using updated SOC and PFR forecast to keep the BESS operation safer and more reliable. Due to the strong randomness of the PFR action by units in the real grid, both DAS and HAS use the prediction of system frequency difference integral to construct probability constraints for BESS energy offset in order to describe PFR behavior more accurately.

The remainder of this article is organized as follows: Section 2 presents the modeling of ISs and BESSs. Section 3 and Section 4 introduce the DAS and HAS optimization algorithms, respectively. Section 5 shows the simulation result analysis, and Section 6 provides a summary of our whole work.

2 IS modeling

2.1 System architecture

Figure 1 shows the system architecture of the IS. The IS mainly consists of three parts: renewable energy units, BESSs, and an integrated station dispatch center (ISDC). The power grid dispatch center (PGDC) is responsible for communication with the IS, and the total power output P_t from the IS is delivered to the grid at the grid coupling point (GCP). P_{new} and P_b represent the output of all renewable energy units and BESSs, respectively. Here, renewable energy units are composed of several wind turbines or PV plants. We assume these renewable energy units operate in the maximum power tracking mode, with their output decoupled from the system frequency. Therefore, P_{new} is fully connected to the grid.

The output P_t from the IS is the sum of the output from BESSs and renewable energy units, which is given by Eq. 1.

$$P_t = P_b + P_{new}. \tag{1}$$

In the IS above, the PFR service is only provided by BESSs, and the power from the PFR service of BESSs is P_f, which will be

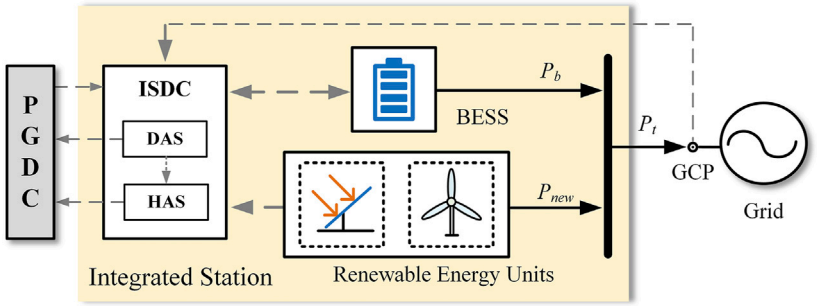

FIGURE 1
System architecture of the IS.

elaborated in Section 2.2. Furthermore, BESS arbitrages through the time-of-use electricity price, and this power is indicated by P_e. P_e can be obtained through DAS or HAS. At this point, the BESS output P_b is given by

$$P_b = P_f + P_e. \tag{2}$$

The ISDC gathers a variety of information from the power station and the grid and then performs scheduling algorithms (DAS and HAS) to plan the operation for the BESS. For running DAS, the ISDC collects the time-of-use electricity price of the day, the forecast PFR needs from PGDC, the initial capacity of BESSs, and the output forecast from renewable energy units. Through DAS, we can obtain the droop coefficient for PFR and the charge and discharge plan for BESSs before the day operation, with the goal of maximum profit. For running HAS during the day, the ISDC adds the newest PFR needs and the real-time SOC of BESSs to correct the DAS results in order to maintain a lasting and reliable operation.

The DAS and HAS optimization results will be sent back to PGDC in order to schedule the operation of other units at the grid level. During the real-time operation of BESSs, the ISDC also needs to obtain information, such as system frequency, from the GCP to provide PFR services.

2.2 Modeling of BESSs

According to droop-based control (Ma et al., 2022), the PFR output P_f from BESSs can be calculated as Eq. 3.

$$P_f = -K_f \times \frac{\Delta f}{f_N} \times P_n, \tag{3}$$

where K_f is the droop coefficient; Δf is the system frequency difference from f_N; f_N is the rated system frequency value; and P_n is the operating power of the renewable energy power station, which we consider to be the rated power of the renewable energy station.

Suppose we have a BESS with output $P_{b,k}$ at time step k and capacity E_n, then the SOC variation in the BESS satisfies the following equation in a discrete process:

$$\mathrm{SOC}_{k+1} = \mathrm{SOC}_k - \frac{\tau}{3600 \cdot E_n} \times P_{b,k}, \tag{4}$$

where τ refers to the scheduling interval during optimization. According to the above text, we can conclude that $P_{b,k}$ is composed of $P_{f,k}$ and $P_{e,k}$. $P_{e,k}$ is obtained by DAS and HAS, which we will discuss in detail in Sections 3.1 and 3.2. Because P_f is real-time dependent on Δf, in order to get the energy exchange $E_{f,k}$ caused by $P_{f,k}$, we have

$$E_{f,k} = -K_f \cdot \int_{k\tau}^{(k+1)\tau} \Delta f\,(t)\mathrm{d}t = -K_f \cdot W_{f,k}, \tag{5}$$

where $W_{f,k}$ is the integral of the frequency difference over time period $[k\tau,\ (k+1)\tau]$. Schiapparelli et al. (2018) showed that time series $\{W_{f,k}\}$ collected through a large amount of real measurement data can be expressed using an autoregressive (AR) process model and that the predicted value $\hat{W}_{f,k}$ can be used to improve SOC management of BESSs under droop control. Based on this research, in our work, the before-day and intra-day forecast $\hat{W}_{f,k}$ represents the estimation of system frequency regulation needs for DAS and HAS. According to the AR model, $W_{f,k+1}$ is given by Eq. 6.

$$W_{f,k+1} = \hat{W}_{f,k+1} + \zeta_{k+1} = \left(a_1 W_{f,k} + \ldots + a_n W_{f,k-n-1}\right) + \zeta_{k+1}, \tag{6}$$

where $W_{f,k}, \ldots W_{f,k-n-1}$ are the real measurements of the integral during the last n time steps; $\hat{W}_{f,k+1}$ refers to the prediction at time step $k+1$; $a_1, \ldots, a_n$ are the AR coefficients obtained from the database; ζ_{k+1} represents a zero-mean Gaussian random variable with standard deviation σ, which is closely related to integral intervals. Here, we consider the integral interval to be equal to the scheduling interval τ as this ensures that more accurate PFR demand information is provided for DAS and HAS under a certain amount of data. An excessively long integral interval may cause the optimization to blur or ignore the PFR demand during this time interval, leading to overly aggressive or conservative BESS operations.

3 Day-ahead scheduling

3.1 DAS objective function

The DAS optimization has the objective of maximizing the overall revenue of the IS by obtaining an appropriate droop

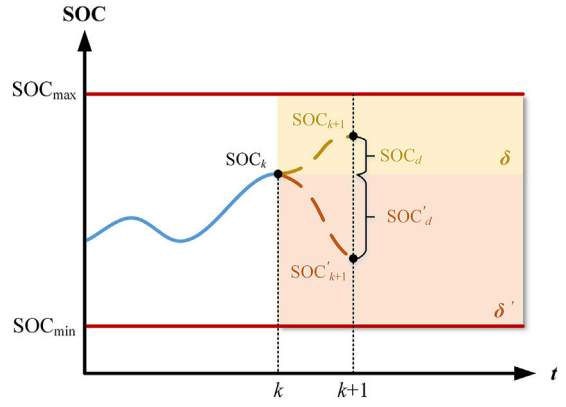

FIGURE 2
SOC offset constraint.

coefficient K_f and the daily power delivery plan $\{P_{e,k}\}$. The objective function of DAS is as follows:

$$J_{\mathrm{DAS}} = \max_{\{P_{e,k}\},K_f} c_{pfr}K_f + \sum_{k=0}^{N-1} c_{t,k}P_{e,k} - \sum_{k=0}^{N-1} P_{e,k}^2, \tag{7}$$

where c_{pfr} is the PFR profit coefficient; $c_{t,k}$ is the time-of-use electricity price; and N is the total length of the scheduling interval with $N = 24 \cdot 3600/\tau$. Since the renewable energy output is not our decision variable, we consider the overall revenue of the IS to be composed of the PFR revenue and the electricity price revenue from the BESS. Zhang et al. (2018) showed the profit BESS receives by providing PFR is proportional to its standby reserve capacity rather than the actual PFR output. Referring to Conte et al. (2020), we use the droop coefficient K_f to represent the PFR capability of BESSs and let $c_{pfr}K_f$ represent the PFR revenue. In Eq. 7, $c_{t,k}P_{e,k}$ refers to the electricity price revenue of the BESS output. So, the sum of the first two items in Eq. 7 is equal to the total revenue. The square of $P_{e,k}$ is added as a penalty to make the BESS power smoother and avoid sudden changes in the output. For running DAS before-day, the following data should be available in advance:

(a) the initial SOC of the BESS SOC_0;
(b) the PFR profit coefficient c_{pfr};
(c) the time-of-use electricity price $\{c_{t,k}\}$;
(d) the forecast frequency integral $\{\hat{W}_{f,k}\}$ and the standard deviation σ;
(e) the forecast renewable energy power $\{\hat{P}_{new,k}\}$.

The solution to the DAS problem should also satisfy a certain number of constraints, which are elaborated in detail in the following.

3.2 DAS constraints

- SOC constraints

Combining Eqs 2, 4 and Eq. 5, we can obtain SOC variation as Eq. 8.

$$\mathrm{SOC}_{k+1} - \mathrm{SOC}_k = -\frac{\tau P_{e,k} - K_f W_{f,k}}{3600 \cdot E_n}. \tag{8}$$

Define $\mathrm{SOC}_d = \mathrm{SOC}_{k+1} - \mathrm{SOC}_k$ as the SOC offset between time steps k and $k+1$. During the daily operation of the BESS, we consider the SOC deviation between every two steps to be within an allowable range to avoid SOC being too close to the operating boundary. Here, we introduce δ to describe the allowable SOC deviation, similar to Eq. 9. Because the SOC offset between two periods could be either positive or negative, there are two possible situations for SOC deviation like Eq. 10.

$$\mathrm{SOC}_d \le \delta, \tag{9}$$

$$\delta = \begin{cases} \mathrm{SOC}_{\max} - \mathrm{SOC}_k, \mathrm{SOC}_{k+1} \ge \mathrm{SOC}_k \\ \mathrm{SOC}_k - \mathrm{SOC}_{\min}, \mathrm{SOC}_{k+1} < \mathrm{SOC}_k \end{cases}. \tag{10}$$

Figure 2 shows two situations that satisfy our SOC constraint: variations from SOC_k to SOC_{k+1} and SOC'_k to SOC'_{k+1} correspond to two possible increasing or decreasing cases. For example, assume that the SOC at time step k is SOC_k; as long as the SOC at $k+1$ is within the yellow or red range, the operation of SOC is safe.

From Eq. 6 we can derive that $W_{f,k}$ is a Gaussian random variable, and it is the only random variable in the definition of SOC_d. Therefore, SOC_d is a Gaussian random variable, and its randomness comes from the uncertainty of $W_{f,k}$. In order to maintain the SOC of the BESS safe, we have the following probability constraint:

$$\mathbf{P}(\mathrm{SOC}_d \le \delta) \ge \rho, \tag{11}$$

where ρ is the confidence level. Eq. 11 means the probability that the SOC offset during every two steps of the BESS is within δ should be greater than ρ. By applying such a probability constraint, the uncertainty of PFR action is taken into account, making the optimization more adaptable and in line with the energy requirements of PFR action in real scenarios. Now, we will convert this chance constraint into a deterministic constraint through derivation.

Eq. 11 can be rewritten as follows:

$$\mathbf{P}\left(\frac{K_f W_{f,k} - \tau P_{e,k}}{3600 \cdot E_n} \le \delta\right) \ge \rho. \tag{12}$$

Obviously, if K_f and E_n are greater than zero, then we can normalize the coefficients of $W_{f,k}$ as Eq. 13.

$$\mathbf{P}\left(W_{f,k} - \tau P_{e,k}/K_f \le 3600 \cdot \delta E_n/K_f\right) \ge \rho. \tag{13}$$

In addition, the random events included in the above probability inequality are

$$\begin{cases} W_{f,k} - \tau P_{e,k}/K_f \le 3600 \cdot (\mathrm{SOC}_{\max} - \mathrm{SOC}_k)E_n/K_f, \mathrm{SOC}_{k+1} \ge \mathrm{SOC}_k \\ W_{f,k} - \tau P_{e,k}/K_f \ge -3600 \cdot (\mathrm{SOC}_k - \mathrm{SOC}_{\min})E_n/K_f, \mathrm{SOC}_{k+1} < \mathrm{SOC}_k \end{cases}. \tag{14}$$

Clearly, $W_{f,k} - \tau P_{e,k}/K_f$ is a Gaussian random variable and it follows Eqs 15, 16.

$$\left(W_{f,k} - \tau P_{e,k}/K_f\right) \sim \mathcal{N}(m_k, \sigma_k), \tag{15}$$

where

$$m_k = \hat{W}_{f,k} - \tau P_{e,k}/K_f, \sigma_k = \sigma. \tag{16}$$

Since we have known the mean and standard variance of $W_{f,k} - \tau P_{e,k}/K_f$, Eq. 12 can be solved based on probability theory. The idea is to convert the random variable on the left in Eq. 14 into a standard Gaussian random variable and solve it according to the percentile table. Therefore, we obtain the following inequality:

$$\begin{cases} \left(\dfrac{3600 \cdot E_n(\mathrm{SOC}_{\max} - \mathrm{SOC}_k)}{K_f} - W_{f,k} + \dfrac{\tau P_{e,k}}{K_f}\right) \Big/ \sigma \geq \mu \\ \left(\dfrac{3600 \cdot E_n(\mathrm{SOC}_k - \mathrm{SOC}_{\min})}{K_f} - W_{f,k} + \dfrac{\tau P_{e,k}}{K_f}\right) \Big/ \sigma \leq -\mu \end{cases}, \quad (17)$$

where μ is ρth percentile of the zero-mean standard Gaussian random variable. Eq. 17 can be further simplified:

$$\begin{cases} \left(3600 \cdot E_n(\mathrm{SOC}_{\max} - \mathrm{SOC}_k) + \tau P_{e,k}\right) \geq K_f\left(\mu\sigma + W_{f,k}\right) \\ \left(-3600 \cdot E_n(\mathrm{SOC}_k - \mathrm{SOC}_{\min}) + \tau P_{e,k}\right) \leq K_f\left(-\mu\sigma + W_{f,k}\right) \end{cases}. \quad (18)$$

We can see that Eq. 18 expresses the inequality relationship among the BESS capacity margin, energy exchanged by $P_{e,k}$, and PFR energy. The uncertainty of PFR action is ultimately reflected in the parentheses at the right end of the inequality. At each step of DAS, SOC_k can be obtained based on known optimization results, so this constraint is built for the optimization of $P_{e,k}$ and K_f. Such two inequalities can constrain the SOC changes in both directions of the BESS at the same time. Eq. 18 can be further extended to the constraints of the BESS operation for a day, similar to Eq. 19:

$$\begin{cases} \left(3600 \cdot E_n(\mathrm{SOC}_{\max} - \mathrm{SOC}_0) + \tau\sum_{k=0}^{N-1} P_{e,k}\right) \geq K_f\left(N\mu\sigma + \sum_{k=0}^{N-1} W_{f,k}\right) \\ \left(-3600 \cdot E_n(\mathrm{SOC}_k - \mathrm{SOC}_{\min}) + \tau\sum_{k=0}^{N-1} P_{e,k}\right) \leq K_f\left(-N\mu\sigma + \sum_{k=0}^{N-1} W_{f,k}\right) \end{cases}. \quad (19)$$

The above equation indicates that after a day of PFR and charging or discharging behavior, the deviation between the final SOC of the BESS and the initial SOC_0 should be within the constraint conditions. This constraint contributes to the safety of the next day's initiation SOC of the BESS.

- Power constraints

The operation of the BESS and IS also needs to meet certain power constraints. First, for the BESS, its droop coefficient K_f should meet the requirements of the scheduling agency, i.e.,

$$0 \leq K_f \leq K_{f,\max}. \quad (20)$$

The output of the BESS must be within the allowable range of its rated power output $P_{b\mathrm{N}}$, so we have

$$-P_{b\mathrm{N}} \leq P_{e,k} \leq P_{b\mathrm{N}}, \quad (21)$$

$$-P_{b\mathrm{N}} \leq \frac{K_f W_{f,k}}{\tau} \leq P_{b\mathrm{N}}, \quad (22)$$

$$0 \leq |K_f \Delta f_{\max}| \leq P_{b\mathrm{N}}, \quad (23)$$

where $\Delta f_{\max}$ is the maximum frequency deviation of this region obtained from the historical data and $K_f \Delta f_{\max}$ refers to the possible maximum power demand by PFR. Eq. 21 is a constraint for the optimization of $P_{e,k}$. Eqs 22, 23 are constraints for PFR output. First, we consider that the average output for PFR cannot exceed the rated power of the BESS. Then, considering extreme situations, the maximum PFR output should also need to be constrained.

$P_{e,k}$ also needs to meet the following ramp constraint:

$$\left|P_{e,k+1} - P_{e,k}\right| \leq \Delta P_{b\max}, \quad (24)$$

where $\Delta P_{b\max}$ is the maximum power variation in the BESS.

Finally, it is necessary to impose constraint on the total output of the IS:

$$0 \leq P_{new,k} + P_{e,k} \leq P_{t\mathrm{N}}, \quad (25)$$

where $P_{t\mathrm{N}}$ is the maximum rated power for the IS. Except for the output in response to the PFR signal, the sum of all other outputs of the power station should be greater than zero, indicating that it should supply electricity to the grid at any time.

4 Hour-ahead scheduling

4.1 Objective function

HAS is an optimization process that corrects the results of DAS based on the latest SOC variation and PFR requirements to maintain the long-term operation capacity of the BESS. The goal of HAS is to improve the safety of SOC without changing the optimization results from DAS as much as possible. For running HAS before-hour, the following data should be available in advance.

(a) the DAS result $\{P_{e\mathrm{D},k}\}$ and droop coefficient K_f;
(b) the penalty coefficient c_{de};
(c) the updated SOC of the BESS SOC_i;
(d) the updated frequency integral $\{\hat{W}_{fh,k}\}$ and the standard deviation σ;
(e) the updated renewable energy power $\{P_{new,k}\}$.

Figure 3 shows the schematic diagram of HAS. Suppose that i represents the number of hours in a day (0, 1, 2, . . . , 23), $n = 3600/\tau$ is the number of scheduling periods within an hour, and k represents the number of scheduling periods in a day (in; $in + 1$,. . .,96). Suppose we run HAS in the first hour of the day ($i = 0$), and we already have the results from DAS $\{P_{e\mathrm{D},k}\}$. Then, we obtain the latest optimization results $\{P_{e,k}\}$ from HAS. Next, the BESS will work based on $\{P_{e,k}\}$ for n steps, and the SOC of the BESS will update according to real PFR actions and K_f. When it comes to $i = 1$, HAS gets scheduling for the rest of the day with SOC_i, and the process will repeat in the same way as the first hour. Only the results of one coming hour (CH) at ith hour will be put into the real operation of the BESS, and the results of the remaining hours (RH) of the day are just a subsidiary result for HAS.

The objective function of HAS in the ith hour is as follows:

$$J_{\mathrm{HAS},i} = \max_{\{P_{e,k}\},\mu_c,\mu_r} -c_{de}\sum_{k=in}^{N-1}\left|P_{e,k} - P_{e\mathrm{D},k}\right| + \left(\alpha_c\mu_c + \alpha_r\mu_r\right). \quad (26)$$

In Eq. 26, c_{de} is the penalty coefficient for the deviation of HAS and DAS results; α_c and α_r are the weight coefficients for CH and RH, respectively; and μ_c and μ_r are quantiles in probability constraints for CH and RH, respectively. The objective function of HAS optimization

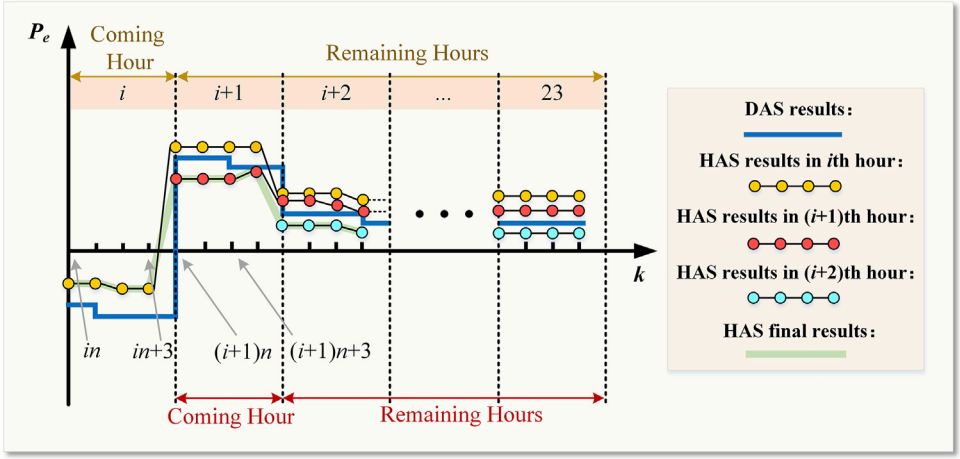

FIGURE 3
HAS example.

consists of two parts: one is the penalty for deviation from the *in* step to $N-1$ step between DAS and HAS optimization results, and the other is the SOC safety optimization index. The larger the value of $J_{\mathrm{HAS},i}$, the smaller the deviation of the optimization results between DAS and HAS, and $\alpha_c\mu_c + \alpha_r\mu_r$ should be larger. The larger the $\alpha_c\mu_c + \alpha_r\mu_r$ value, the safer the SOC of the BESS, which is discussed in Section 4.2.

4.2 Constraints

The SOC constraint set for HAS is as follows (CH and RH, respectively):

$$\begin{cases} \left(3600 \cdot E_n\left(\mathrm{SOC}_{\max} - \mathrm{SOC}_k\right) + \tau P_{e,k}\right) \geq K_f\left(\mu_c\sigma + W_{fh,k}\right) \\ \left(-3600 \cdot E_n\left(\mathrm{SOC}_k - \mathrm{SOC}_{\min}\right) + \tau P_{e,k}\right) \leq K_f\left(-\mu_c\sigma + W_{fh,k}\right) \end{cases}, \tag{27}$$

$$\mu_{\min} \leq \mu_c \leq \mu_{\max}, \tag{28}$$

$$\begin{cases} \left(3600 \cdot E_n\left(\mathrm{SOC}_{\max} - \mathrm{SOC}_k\right) + \tau P_{e,k}\right) \geq K_f\left(\mu_r\sigma + W_{fh,k}\right) \\ \left(-3600 \cdot E_n\left(\mathrm{SOC}_k - \mathrm{SOC}_{\min}\right) + \tau P_{e,k}\right) \leq K_f\left(-\mu_r\sigma + W_{fh,k}\right) \end{cases}, \tag{29}$$

$$\mu_{\min} \leq \mu_r \leq \mu_{\max}. \tag{30}$$

Eqs 27–30 are actually reformulations of Eq. 18, where μ and $W_{f,k}$ in the original formula are replaced with μ_c (μ_r) and $W_{fh,k}$. In DAS, such SOC constraints are implemented for a whole day, while in HAS, they are used separately in CH and RH. These constraints are all derived based on the probability constraints of the SOC offset (Eq. 11) to ensure that the SOC deviation of the BESS at each step is within a safe range. The objective of $J_{\mathrm{HAS},i}$ is to increase the values of μ_c and μ_r as they increase the probability of constraint Eqs 27–29 being satisfied. This can be seen from the calculation formula of μ. The value of μ that satisfies probability ρ is

$$\begin{cases} \Phi(\mu) = \dfrac{1}{\sqrt{2\pi}}\displaystyle\int_{-\infty}^{\mu} e^{-\frac{t^2}{2}}\mathrm{d}t \\ \Phi(\mu) = \dfrac{1}{2}(\rho + 1) \end{cases}, \tag{31}$$

where $\Phi(\cdot)$ represents the distribution function of the standard Gaussian distribution. We can then obtain the derivative of ρ as Eq. 32.

$$\frac{\mathrm{d}\rho}{\mathrm{d}\mu} = \frac{\sqrt{2}}{\pi}e^{-\frac{\mu^2}{2}}. \tag{32}$$

Clearly, $\frac{\mathrm{d}\rho}{\mathrm{d}t}$ is greater than zero. So, as the value of μ increases, the corresponding probability ρ, which refers to the possibility of Eqs 27–29 being valid, also increases. We add constraints for μ_c and μ_r in Eqs 28–30 to limit the range of possibilities that the constraint can satisfy. Therefore, we can ensure the durable operation of the BESS using the above constraints.

There is a contradiction between the two optimization objectives in Eq. 25. The results of DAS have already achieved economic optimality while maximizing the utilization of energy storage capacity. If we want to make the operation of energy storage more conservative, it will inevitably lead to an increase in the deviation of the optimization results between DAS and HAS. Therefore, the size of the three weight coefficients in Eq. 25 will significantly affect the difference in the final optimization results.

The power constraints for HAS are almost the same as those for DAS (i.e., Eqs 21–25) and will not be further elaborated here.

5 Simulation analysis

For the simulation part, first, we focus on a renewable energy power station that consists of 10 wind turbines with a rated capacity of 1.5 MW and a total rated output of 15 MW. Consider equipping these wind turbines with a BESS of 2MW/2 MW·h to provide PFR and peak-valley arbitrage services. We collected historical frequency fluctuation data measured from several stations in the power grid of Henan province, China. We selected several days of system frequency difference data as our simulation scenario and obtained the corresponding frequency regulation demand prediction using the AR model. The time-of-use electricity price released by Henan province is used as the value of $c_{t,k}$. Renewable

TABLE 1 Simulation parameters.

Parameter	Numerical value	Parameter	Numerical value
τ (s)	900	$\Delta P_{b\max}$ (MW)	2
f_N (Hz)	50	P_{tN} (MW)	18
c_{pfr} (CNY)	180	SOC_{max}	0.9
c_{de} (CNY/MW)	31.25	SOC_{min}	0.1
ρ	0.95	μ_{min} (ρ = 0.95)	1.69
$K_{f,\max}$	80	μ_{max} (ρ = 0.99)	2.58

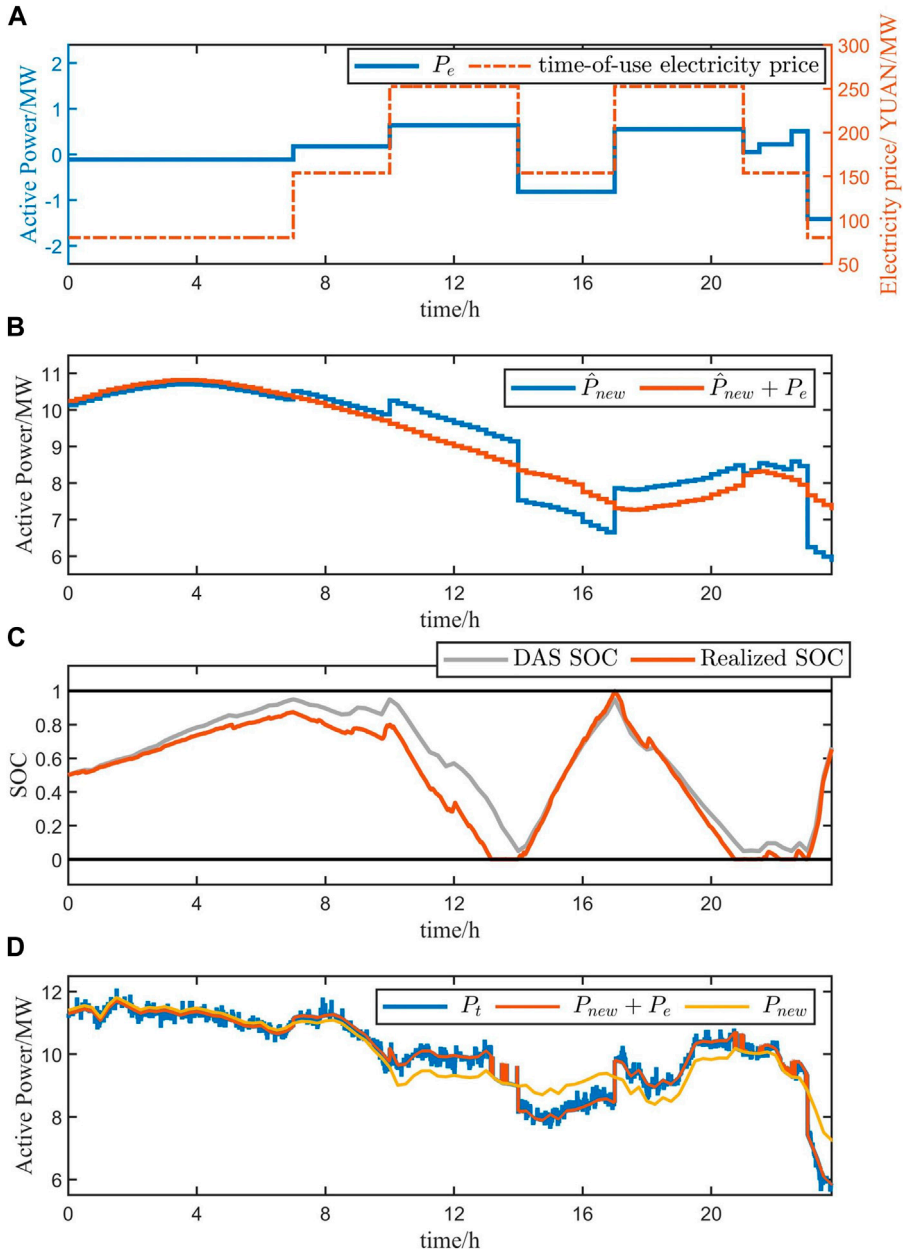

FIGURE 4
DAS results.

10.3389/fenrg.2024.1424389

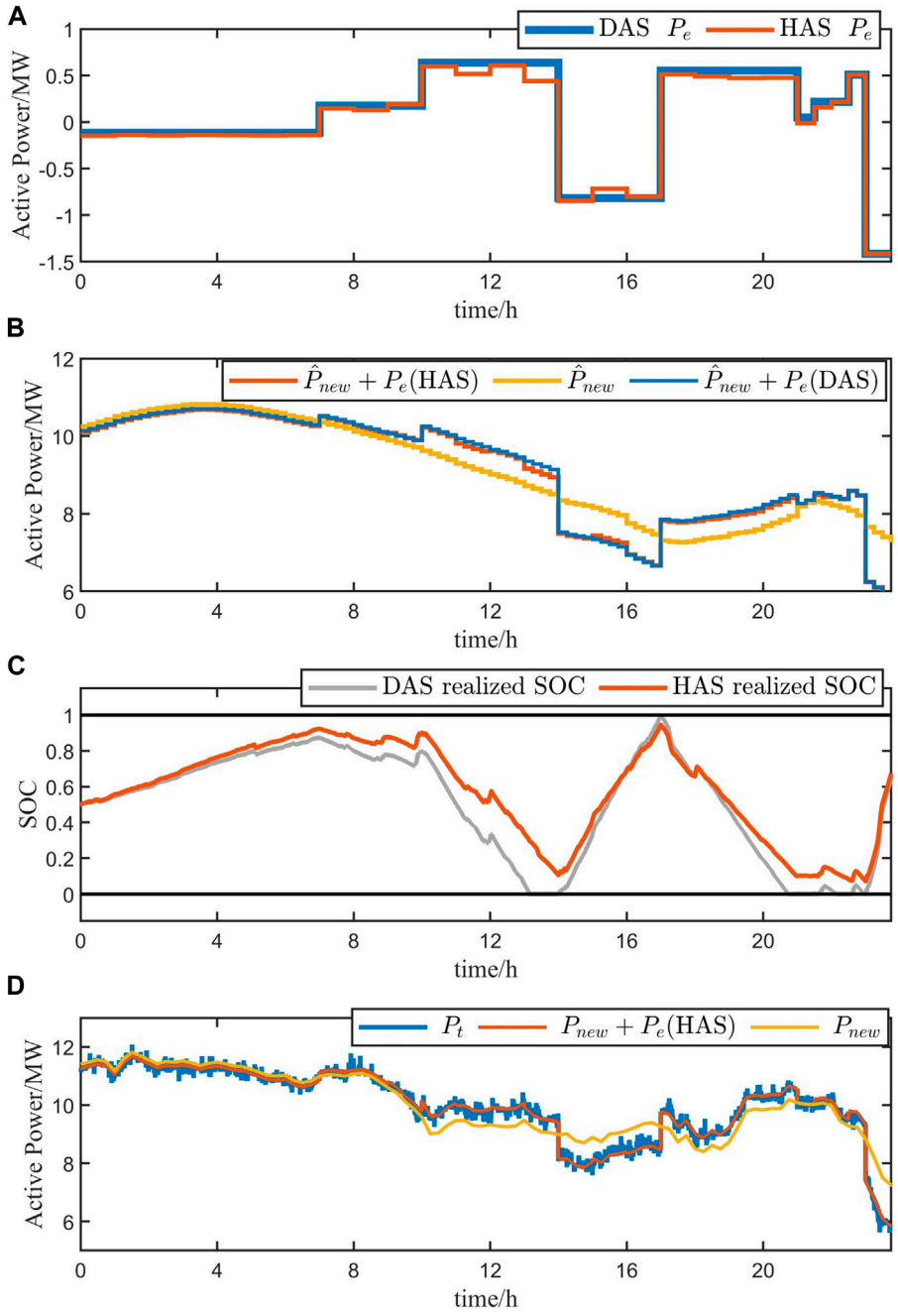

FIGURE 5
HAS results.

energy outputs are chosen from Elia Transmission Belgium. For the values of other parameters in our algorithm, please refer to Table 1. Additionally, the programming of DAS and HAS is written using the YALMIP toolbox and solved using CPLEX in MATLAB.

We first select the operation optimization of the BESS on a certain day as the first part of our simulation. The results of DAS and DAS and HAS will be shown separately. Figure 4 shows the simulation results using DAS optimization only. Figure 4A shows the scheduling result for DAS $\{P_{e,k}\}$ together with the time-of-use electricity price $\{c_{t,k}\}$, corresponding to the left and right coordinate axes, respectively. Figure 4B shows the renewable energy forecast $\{\hat{P}_{new,k}\}$ and the sum of $\{\hat{P}_{new,k}\}$ and $\{P_{e,k}\}$. The SOC variation curve calculated by DAS and the realized ones are displayed in Figure 4C. Figure 4D shows the real renewable energy output $\{P_{new,k}\}$ and the sum of $\{P_{new,k}\}$ and $\{P_{e,k}\}$, together with the real total power output $\{P_{t,k}\}$. First, Figure 4A shows that the trends of $\{P_{e,k}\}$ and $\{c_{t,k}\}$ are very similar. The BESS was charged and replenished during low-electricity prices (such as 0–7) and discharged during high-electricity prices (like 10–14) to generate revenue. Figure 4B shows that the economic output of BESS does not change the overall trend of renewable energy output but transfers energy from different periods according to electricity prices. From

10.3389/fenrg.2024.1424389

TABLE 2 Simulation result data.

Simulation setting		K_f	γ/%	PFR revenue (CNY)	Electricity revenue (CNY)	Total revenue (CNY)
BESS for PFR scenario 1	PFR only	28.55	0	5,056.43	—	5,056.43
	Arbitrage only	—			2,313.63	2,313.63
	DAS	55.51	7.50	6,515.56	3,216.81	9,732.37
	DAS and HAS		0	9,271.94	2,724.41	11,996.35
BESS for PFR scenario 2	PFR only	12.75	0	2,300.17	—	2,300.17
	Arbitrage only	—			2,527.01	2,527.01
	DAS	17.75	1.45	438.49	3,055.93	3,494.42
	DAS and HAS		0	3,194.87	2,208.50	5,403.37

Figure 4C, we can infer that during DAS, the SOC of the BESS is fully utilized, while in the realized situation, the SOC has crossed the safety boundary at certain hours. This is due to significant errors between the predicted and actual frequency differences, so the results of DAS may be aggressive in practical scenarios. This issue can be addressed through the updated SOC trajectory and frequency regulation requirements in HAS. When SOC exceeds the boundary, the BESS output is zero to ensure safety, as shown in Figure 4D (approximately 13): at a certain time, only renewable energy output constitutes the total output. The long-term operation of energy storage near the SOC boundary not only affects its own safety but also hinders its provision of PFR services. Such a situation should be avoided as much as possible.

Figure 5 shows the simulation results using DAS and HAS optimization. Figure 5A shows the scheduling results for DAS and HAS. Figure 5B contains the sum of two scheduling results and the prediction of renewable energy output separately. The realized SOC by DAS and HAS is displayed in Figure 5C. Figure 5D shows the real renewable energy output $\{P_{new,k}\}$, the sum of $\{P_{new,k}\}$ and $\{P_{e,k}\}$, together with the real total power output $\{P_{t,k}\}$ from HAS. We can find from the results of HAS that it comes from a little correction of DAS, which makes the output of BESS more conservative and does not change its overall trend with variation in electricity prices. Through the HAS, the SOC changes calculated based on actual frequency modulation actions did not exceed the upper and lower limits within a day. BESS can provide sufficient PFR services throughout the day. Therefore, HAS can ensure the reliability of the BESS operation.

Table 2 summarizes the data results from the above simulations as PFR scenario 1, and we add additional simulation results for another day's operation as PFR scenario 2. It mainly displays the optimization results of the BESS droop coefficient, PFR revenue, and electricity revenue under different simulation settings. We introduce γ% to describe the failure rate of the BESS providing primary frequency regulation, which is the proportion of the time when SOC exceeds the limit to the total time of a day. The PFR revenue is obtained by multiplying the original revenue by the actual duration of the PFR provided, and the electricity revenue is the product of the economic output of the BESS and the time-of-use electricity price. We have also imposed penalties for the inability of the BESS to participate in PFR in accordance with the Implementation Rules for Auxiliary Service Management of Central China Electric Power. For PFR scenario 1, it is obvious that the droop coefficient and PFR revenue of the BESS only participating in PFR are lower than those of DAS and HAS. This indicates that the economic output and PFR output within a day can partially offset each other, increasing more space for BESS PFR actions. When BESS output only includes economic output, the electricity price revenue is lower than the optimization results of DAS, which also indicates that our optimization algorithm can increase the freedom of the BESS to participate in PFR and peak-valley arbitrage simultaneously. The low profit of the PFR revenue from DAS is mainly due to the significant punishment it received, which was avoided during the intra-day optimization. The reduction in electricity price revenue through HAS compared to DAS alone is mainly due to the correction of DAS's overly aggressive charging and discharging behavior. HAS reduces the PFR failure time by 7.5%, and its total revenue is much greater than that of DAS. Therefore, the scheduling results optimized by DAS and HAS can ensure the reliability of PFR by the BESS and achieve maximum total revenue.

The optimization results for PFR scenario 2 show that the PFR task on the day is much heavier, so the optimized droop coefficient is small. We can see that there is still 1.45% of the time that the BESS cannot provide PFR, resulting in a decrease in PFR revenue in DAS. Due to the fact that the PFR penalty stipulated in the implementation rules for auxiliary service management in Central China is related to its rated capacity and the optimized droop coefficient is small, the PFR revenue of DAS is relatively low. We can see that in the current scenario, the total revenue after DAS and HAS is still optimal. The simulation results above show that the proposed optimization scheduling method can ensure that the BESS can provide PFR services stably, as well as increase the overall revenue of the power station.

To verify the adaptability of the proposed algorithm in various scenarios, we consider conducting the second simulation for a PV station with a rated capacity of 10 MW. Other simulation configurations remain unchanged. Figure 6 shows the simulation results after using DAS and HAS. Figure 6A shows the scheduling results for DAS and HAS. Figure 6B contains the sum of two scheduling results and the prediction of PV output separately. The realized SOC by DAS and HAS is displayed in Figure 6C. Figure 6D shows the real PV output $\{P_{new,k}\}$, the sum of $\{P_{new,k}\}$ and

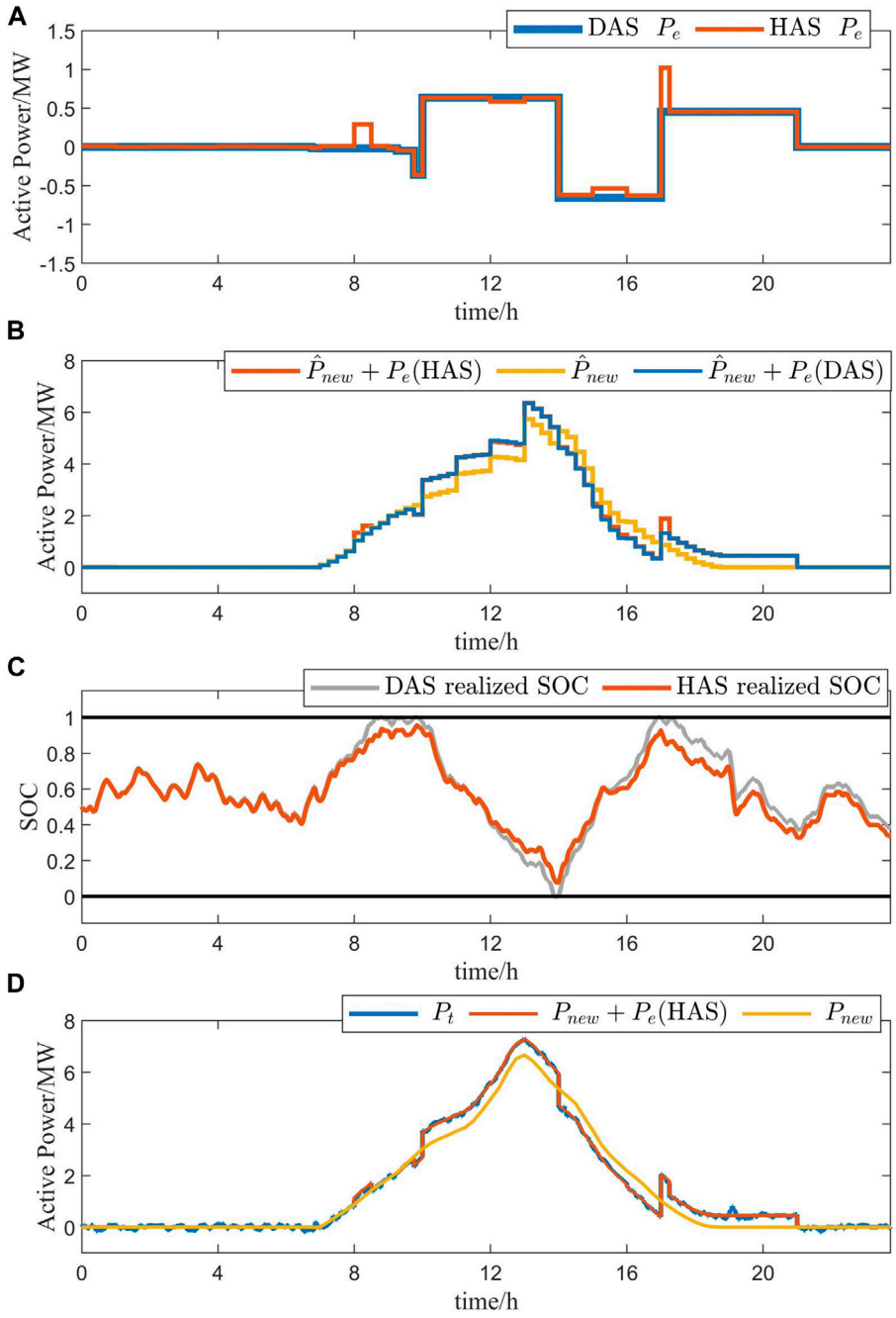

FIGURE 6
HAS results of the PV.

$\{P_{e,k}\}$, together with the real total power output $\{P_{t,k}\}$ from HAS. Because the output of the PV station at night is very low, our optimization results are mainly reflected between 7 and 21 o'clock. From Figure 6A, we can see that the BESS roughly goes through two rounds of charging and discharging based on the electricity price. Again, our HAS results are very similar to those of DAS. The DAS SOC curve also showed an out-of-bounds situation, which is improved during HAS. Finally, Figure 6D clearly shows that our optimization has caused a deviation in the trend of the real PV output: when the electricity price is high, the output of the power station is increased (from 10 to 13), while when the electricity price is low, the output of the power station is appropriately reduced (from 13 to 17). Furthermore, the BESS has extended the time for power transmission by the PV (from 18 to 21), achieving the migration of energy from the PV at different periods. These simulation results indicate that the method we proposed has shown good performance in different renewable energy generation scenarios.

6 Conclusion

In order to fully harness the potential of battery energy storage, it is essential to enhance its capability of supporting primary frequency regulation while simultaneously carrying out peak-valley arbitrage through the time-of-use electricity price. Thus, a day-ahead and hour-ahead optimal scheduling algorithm is proposed in this paper. The main conclusion of the context is as follows.

(1) The proposed algorithm can ensure the long-term operation ability of the energy storage and provide the primary frequency regulation service stably, indicating that the proposed probability constraints can ensure the safety of the energy storage state of charge.
(2) The proposed algorithm can adjust the charge and discharge plan of the energy storage in a day according to the time-of-use electricity price, thereby maximizing the utilization of the energy storage capacity and achieving the maximum energy storage profit.

Data availability statement

The data analyzed in this study are subject to the following licenses/restrictions: The operation data of the power network dispatching organization must not be disclosed. Requests to access these datasets should be directed to Yanzhao Ma, hebutmyz@163.com.

Author contributions

HH: writing–review and editing. YM: writing–original draft. XZ: writing–review and editing and data curation. CH: writing–original draft and investigation. YH: writing–original draft and software.

Funding

The author(s) declare that no financial support was received for the research, authorship, and/or publication of this article.

Conflict of interest

Author XZ was employed by State Grid Henan Electric Power Company, State Grid Corporation of China (SGCC).

The remaining authors declare that the research was conducted in the absence of any commercial or financial relationships that could be construed as a potential conflict of interest.

Publisher's note

All claims expressed in this article are solely those of the authors and do not necessarily represent those of their affiliated organizations, or those of the publisher, the editors, and the reviewers. Any product that may be evaluated in this article, or claim that may be made by its manufacturer, is not guaranteed or endorsed by the publisher.

References

Arrigo, F., Bompard, E., Merlo, M., and Milano, F. (2020). Assessment of primary frequency control through battery energy storage systems. *Int. J. Electr. Power Energy Syst.* 115, 105428. doi:10.1016/j.ijepes.2019.105428

Conte, F., Massucco, S., Schiapparelli, G. –P., and Silvestro, F. (2020). Day-ahead and intra-day planning of integrated BESS-PV systems providing frequency regulation. *IEEE Trans. Sustain. Energy* 11 (3), 1797–1806. doi:10.1109/TSTE.2019.2941369

Cristaldi, L., Faifer, M., Laurano, C., Ottoboni, R., Petkovski, E., and Toscani, S. (2022). "Reduced power model-based tracker for photovoltaic panels," in *2022 IEEE 16th international conference on compatibility, power electronics, and power engineering (CPE-POWERENG), birmingham, United Kingdom, 2022 (IEEE)*, 1–6. doi:10.1109/CPE-POWERENG54966.2022.9880905

Fang, C., Tang, Y., Ye, R., Lin, Z., Zhu, Z., Wen, B., et al. (2020). Adaptive control strategy of energy storage system participating in primary frequency regulation. *Processes* 8 (6), 687. doi:10.3390/pr8060687

Feng, C., Mai, Z., Wu, C., Zheng, Y., and Zhang, N. (2024). Advantage of battery energy storage systems for assisting hydropower units to suppress the frequency fluctuations caused by wind power variations. *J. Energy Storage* 78, 109989. doi:10.1016/j.est.2023.109989

Li, Z., Cheng, Z., Si, J., Zhang, S., Dong, L., Li, S., et al. (2021). Adaptive power Point tracking control of PV system for primary frequency regulation of AC microgrid with high PV integration. *IEEE Trans. Power Syst.* 36 (4), 3129–3141. doi:10.1109/TPWRS.2021.3049616

Li, Z., Duan, J., Qin, B., Xia, Y., and Chen, B. (2022) "Self-adaptive control strategy of battery energy storage for power grid primary frequency regulation," in *2022 IEEE/IAS industrial and commercial power system Asia I&CPS Asia*. IEEE: Shanghai, China.

Ma, R., Yuan, S., Li, X., Guan, S., Yan, X., and Jia, J. (2024). Primary frequency regulation strategy based on rotor kinetic energy of double-fed induction generator and supercapacitor. *Energies* 17 (2), 331. doi:10.3390/en17020331

Ma, Y., Hu, Z., and Song, Y. (2022). Hour-ahead optimization strategy for shared energy storage of renewable energy power stations to provide frequency regulation service. *IEEE Trans. Sustain. Energy* 13 (4), 2331–2342. doi:10.1109/TSTE.2022.3194718

Mahish, P., and Pradhan, A. K. (2020). Distributed synchronized control in grid integrated wind farms to improve primary frequency regulation. *IEEE Trans. Power Syst.* 35 (1), 362–373. doi:10.1109/TPWRS.2019.2928394

Meng, G., Lu, Y., Liu, H., Ye, Y., Sun, Y., and Tan, W. (2021). Adaptive droop coefficient and SOC equalization-based primary frequency modulation control strategy of energy storage. *Electronics* 10 (21), 2645. doi:10.3390/electronics10212645

Schiapparelli, G. P., Massucco, S., Namor, E., Sossan, F., Cherkaoui, R., and Paolone, M. (2018). "Quantification of primary frequency control provision from battery energy storage systems connected to active distribution networks," in *2018 power systems computation conference (PSCC)*, IEEE: Dubin, Ireland.

Turk, A., Sandelic, M., Noto, G., Pillai, J. R., and Chaudhary, S. K. (2019). Primary frequency regulation supported by battery storage systems in power system dominated by renewable energy sources. *J. Eng.* 2019, 4986–4990. doi:10.1049/joe.2018.9349

Wang, X., Ying, L., Wen, K., and Lu, S. (2022). Bi-le*vel non*-convex joint optimization model of energy storage in energy and primary frequency regulation markets. *Int. J. Electr. Power Energy Syst.* 134, 107408. doi:10.1016/j.ijepes.2021.107408

Xiong, L., Liu, L., Liu, X., and Liu, Y. (2021). Frequency trajectory planning based strategy for improving frequency stability of droop-controlled inverter based standalone power systems. *IEEE J. Emerg. Sel. Top. Circuits Syst.* 11 (1), 176–187. doi:10.1109/JETCAS.2021.3052006

Xiong, L., Liu, X., Liu, H., and Liu, Y. (2022). Performance comparison of typical frequency response strategies for power systems with high penetration of renewable energy sources. *IEEE J. Emerg. Sel. Top. Circuits Syst.* 12 (1), 41–47. doi:10.1109/JETCAS.2022.3141691

Xiong, L., Liu, X., Zhang, D., and Liu, Y. (2021). Rapid power compensation-based frequency response strategy for low-inertia power systems. *IEEE J. Emerg. Sel. Top. Power Electron.* 9 (4)), 4500–4513. doi:10.1109/JESTPE.2020.3032063

Zhang, Y. J. A., Zhao, C., Tang, W., and Low, S. H. (2018). Profit-maximizing planning and control of battery energy storage systems for primary frequency control. *IEEE Trans. Smart Grid* 9 (2), 712–723. doi:10.1109/TSG.2016.2562672

Zhao, P., Gu, C., Li, F., and Yang, X. (2022). Battery storage configuration for multi-energy microgrid considering primary frequency regulation and demand response. *Energy Rep.* 8 (10), 1175–1183. doi:10.1016/j.egyr.2022.06.086

Zhu, D., and Zhang, Y. A. (2019). Optimal coordinated control of multiple battery energy storage systems for primary frequency regulation. *IEEE Trans. Power Syst.* 34 (1), 555–565. doi:10.1109/TPWRS.2018.2868504

frontiers | Frontiers in Energy Research

TYPE Original Research
PUBLISHED 08 July 2024
DOI 10.3389/fenrg.2024.1427593

OPEN ACCESS

EDITED BY
Liansong Xiong,
Xi'an Jiaotong University, China

REVIEWED BY
Nan Chen,
University of Birmingham, United Kingdom
Gen Li,
Technical University of Denmark, Denmark

*CORRESPONDENCE
Jinjia Zhang,
epjinjiazhang@mail.scut.edu.cn

RECEIVED 04 May 2024
ACCEPTED 29 May 2024
PUBLISHED 08 July 2024

CITATION
Duan S, Zhang J, Yu L and Cai Z (2024), Development of an equivalent system frequency response model based on aggregation of distributed energy storage systems.
Front. Energy Res. 12:1427593.
doi: 10.3389/fenrg.2024.1427593

Development of an equivalent system frequency response model based on aggregation of distributed energy storage systems

Shuyin Duan[1], Jinjia Zhang[2]*, Lei Yu[1] and Zexiang Cai[2]

[1]State Key Laboratory of HVDC (Electric Power Research Institute), China Southern Power Grid Co., Ltd., Guangzhou, Guangdong, China, [2]School of Electric Power, South China University of Technology, Guangzhou, Guangdong, China

Energy storage systems (ESSs) installed in distribution networks have been widely adopted for frequency regulation services due to their rapid response and flexibility. Unlike existing ESS design methods which focus on control strategies, this paper proposes a new method based on an ESS equivalent aggregated model (EAM) for calculating the capacity and the droop of an ESS to maintain the system frequency nadir and quasi-steady state frequency using low-order functions. The proposed method 1) uses first-order functions to describe the frequency response (FR) of synchronous generators (SGs); 2) ignores the control strategies of SGs, making the method systematic and allowing it to avoid analyzing complex high-order functions; and 3) is suitable for low inertia systems. The applicability and accuracy of the method is demonstrated using a modified four-generator two-area (4G2A) system.

KEYWORDS

energy storage system (ESS), distribution network, synchronous generator (SG), frequency response (FR), capacity, droop

1 Introduction

Frequency is a crucial index for measuring power quality, representing the balance of active power in power systems (He and Wen, 2021). With the increasing penetration of renewable energy sources, the inertia of power systems is decreasing and the effective maintenance of the frequency nadir (f_{nadir}) and quasi-steady state frequency (f_{ss}) consequently becomes challenging, posing a threat to system stability.

Therefore, system operators all over the world are focused on setting a series of frequency response (FR) services. Among FR energy sources, energy storage systems (ESSs) installed in distribution networks have been widely used (GB/T 30370-2013, 2013; Rana et al., 2023). The National Grid in Britain has set various dynamic frequency control products (AEMO, 2023), the Australian Energy Market Operator (AEMO) has proposed a Contingency Frequency Control Ancillary Service (FCAS) and a Regulation FCAS (National Grid ESO, 2019), and in Guangdong, China, a $LiFePO_4$ (LFP) battery is also used as a frequency control product (Wang et al., 2023). However, the design of the aforementioned ESSs relies entirely on simulation analysis. Systematic methods for system operators to evaluate the frequency support ability of an ESS and calculate the main parameters of an ESS have not been proposed.

ESSs can function both as generators and loads. Existing research mainly focuses on the construction of the ESS FR model. In these studies, the classical FR model proposed by Anderson

and Mirheydar (1990) has been widely used. Based on the classical model, researchers have developed an ESS transfer function model (Aik, 2006; Yang et al., 2022). In Chen et al. (2016), the penetration rate of an ESS is considered to improve the FR model. However, ESS FR models based on the classical FR model only consider the reheat turbines of synchronous generators (SGs); thus, they are not suitable for systems with other types of gas/hydraulic turbines. To avoid this limitation, generic FR models have been proposed by Gao et al. (2021), Ju et al. (2021), and Zhang et al. (2021). In Ju et al. (2021) and Gao et al. (2021), the FR of an SG is described as an nth-order function, and in Zhang et al. (2021), all generation sources are presented as lead-lag functions, and the FR of the system can be described as the classical FR model. Nevertheless, generic FR models present the system frequency characteristics in an aggregated manner, making it difficult to distinguish the FR of an ESS.

To precisely evaluate the frequency support ability of an ESS, many ESS control strategies have been proposed. An ESS management strategy was proposed by Ben Elghali et al. (2019) to determine the optimal capacity of an ESS based on system frequency, and an ESS shaping strategy was introduced by Jiang et al. (2021) to maintain the f_{nadir} with the optimal cost of an ESS (Mustafa and Altinoluk H, 2023) and aging minimization (Wang et al., 2020). In Xiong et al. (2021), first-order functions were used to size an ESS based on the rate of change of frequency (RoCoF) to avoid dealing with high-order transfer functions. Recently, ESS control schemes employing robust control (Xiong et al., 2020), grid-tied inverter design (Xiong et al., 2016), self-adaptive control (Wu et al., 2020), predictive models based on the uncertainty of renewable sources (Zarei and Ghaffarzadeh, 2024), and ESS generation (Baker et al., 2017; Zarei and Ghaffarzadeh, 2024) have been used to design ESSs. However, these methods are only suitable for specific power grids, limiting their broader applicability. Moreover, the control strategies always ignore the capacity limit and droop limit of an ESS and regard the frequency response output of an ESS as a step change, resulting in significant errors in evaluating the frequency support ability of an ESS.

In this paper, an ESS equivalent aggregated model (EAM) is introduced and a new method named the Energy Storage Designing Method (ESDM) based on an EAM is proposed. An EAM consists of a multistep model named FM to maintain the f_{nadir} and a model named QM to maintain the f_{ss}. For both FM and QM, which include a first-order system FR model and a first-order ESS FR model, it is convenient for system operators to evaluate and analyze the frequency support ability of an ESS and lay the foundation of ESS sizing. Since renewable sources such as wind farms and photovoltaic (PV) panels always work in Maximum Power Point Tracking (MPPT) mode (Bai et al., 2015; Mohanty et al., 2016) and are strongly related to the weather, and the participation of renewable sources in frequency modulation is not mandatory at present (Guangfu, 2020; Guangfu, 2022), SGs and ESSs are still the main resources for frequency regulation. Therefore, the proposed ESDM can effectively calculate the capacity and the droop of an ESS based on a historical event and therefore accurately maintain the f_{nadir} and f_{ss} of the power system.

2 System equivalent frequency response model

When there is an imbalance in the active power of the power system, the system's primary frequency response (PFR) can be described in Figure 1, and it can also be described by the classical swing equation as shown in (Eq. 1).

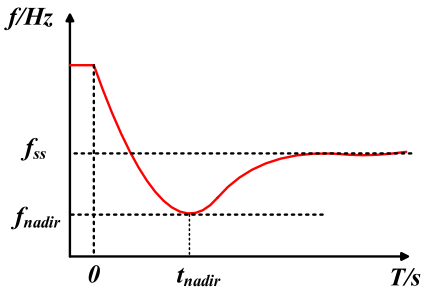

FIGURE 1
System PFR.

$$2H\frac{\partial \Delta f(t)}{\partial t} + D\Delta f(t) = \Delta P_m - \Delta P_d, \tag{1}$$

where H [s] is the inertia constant, D [p.u.] is the equivalent damping factor, ΔP_m [p.u.] is the mechanical power deviation from generators, and ΔP_d [p.u.] is the power disturbance. During a frequency event, the system frequency must have a nadir. Due to the monotone decreasing and converging of the step response of the first-order system, if only the f_{nadir} is considered, there must be a first-order power function with a minimum value that is equal to the f_{nadir} as shown in Figure 2A. Similar to the f_{nadir}, the f_{ss} can also be described as a first-order function as shown in Figure 2B.

In Figure 2, t_{nadir1} is the time at which the system reaches the frequency nadir at the maximum rate of the change of frequency ($RoCoF_{max}$), while t_{nadir} is the time at which the system reaches the f_{nadir}.

Therefore, the system equivalent FR (SEFR) model is depicted in Figure 3. If $K = K_1$, SEFR can be used to predict the f_{nadir} after a frequency event, with $\Delta f = \Delta f_{nadir}$ at t = ∞. Similarly, when $K = K_2$, SEFR is used to forecast the f_{ss} with $\Delta f = f_{ss}$ at t = ∞. According to Figure 3, the SEFR model can be shown as follows:

$$\frac{\Delta f(s)}{\Delta P_d(s)} = \frac{1}{2Hs + D + K} \tag{2}$$

Assuming that the load disturbance during a frequency event undergoes a step change, with an amplitude of ΔP_d, the time-domain expression of the system frequency can be obtained by solving (Eq. 3).

$$\begin{cases} \Delta f(s) = \dfrac{1}{2Hs + D + K} \cdot \dfrac{\Delta P_d}{s} \\ \Delta f^*(t) = L^{-1}[\Delta f(s)] = \dfrac{\Delta P_d}{D + K}\left(1 - e^{-\frac{D+K}{2H}t}\right) \end{cases} \tag{3}$$

$\Delta f^*(t)$ is the per unit system frequency. It is clear from (Eq. 3) that $\Delta f^*(t)$ is an increasing function, so its maximum value can be calculated as shown in (Eq. 4).

$$\Delta f^*_{\max} = \lim_{t\to\infty} \Delta f^*(t) = \frac{\Delta P_d}{D + K} \tag{4}$$

For a historical frequency event, the f_{nadir} and f_{ss} can be acquired from system operators so that K_1 and K_2 can be easily calculated.

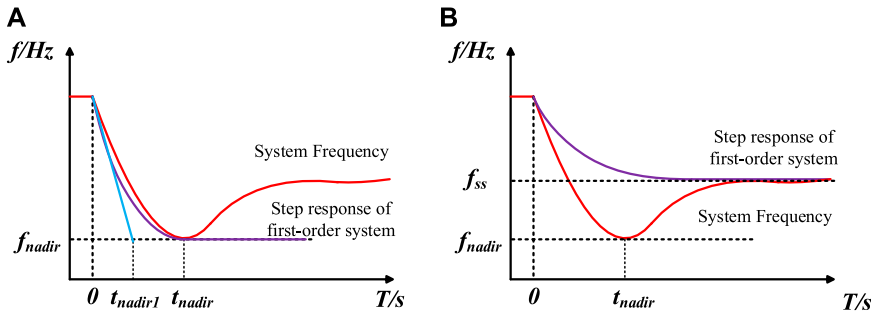

FIGURE 2
(A) Representation of f_{nadir} using the step response of the first-order system, and **(B)** Representation of f_{ss} using the step response of the first-order system.

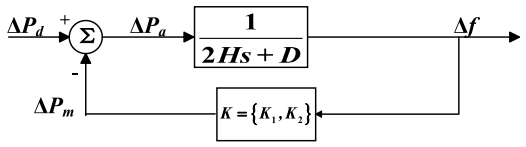

FIGURE 3
SEFR model.

$$\begin{cases} K_1 = \dfrac{\Delta P_d f_N}{f_N - f_{nadir}} - D \\ K_2 = \dfrac{\Delta P_d f_N}{f_N - f_{ss}} - D \end{cases}, \tag{5}$$

where f_N is the base of system frequency (i.e., 50 Hz or 60 Hz).

As for the f_{ss}, if only PFR is considered, SEFR can accurately symbolize the f_{ss} because both the actual value and SEFR value are calculated when the time approaches infinity, i.e., t = ∞. To analyze the accuracy of the SEFR in representing the f_{nadir}, a parameter named E is introduced to symbolize the error between the actual f_{nadir} and the SEFR value at t_{nadir}. E can be shown as

$$\begin{cases} E = \Delta f^*_{nadir} - \Delta f^*(t_{nadir}) = \Delta f^*_{nadir}\, e^{-\frac{\Delta P_d}{2H\Delta f^*_{nadir}} t_{nadir}} \\ \Delta f^*_{nadir} = \dfrac{f_N - f_{nadir}}{f_N} \end{cases}. \tag{6}$$

According to (1), $RoCoF_{max}$ can be described as (7), and if frequency continues to fall at $RoCoF_{max}$, t_{nadir1} can be calculated as follows:

$$RoCoF_{\max} = \frac{\Delta P_d}{2H}, \tag{7}$$

$$t_{nadir1} = \left| \frac{\Delta f^*_{nadir}}{RoCoF_{\max}} \right|. \tag{8}$$

A parameter named φ is proposed to describe the relationship between t_{nadir1} and t_{nadir}, so that E can be described as

$$\begin{cases} t_{nadir1} = \varphi \cdot t_{nadir} \\ E = \Delta f^*_{nadir} e^{-\frac{1}{\varphi}} \end{cases}, \tag{9}$$

where φ is a constant and $\varphi \le 1$.

According to Gao et al. (2021), t_{nadir} usually falls in 8.5 s–10 s, and in many areas, $RoCoF_{max}$ can be very large (Xiong et al., 2021); thus, φ can be very large so that E can be very small.

3 The proposed EAM

The parameters of an ESS are always designed based on the maximum power disturbance (ΔP_{dmax}), which means the utilization ratio of an ESS will be quite low, and an ESS with a large droop and capacity is not energy-efficient. Since ΔP_{dmax} is a small probability event, an ESS designed based on ΔP_{dmax} is not flexible in dealing with normal ΔP_d.

3.1 The proposed FM

A new model named FM is proposed to calculate the parameters of an ESS based on different levels of ΔP_d and different required frequency deviations as shown in Figure 4A.

V_{si} and δ_{si}, respectively, represent the equivalent capacity and droop of an ESS for addressing frequency events with a power disturbance level ΔP_{di}, and Δf_i is the system-required frequency maximum deviation at ΔP_{di}.

The principle of the ESS FM model is that different levels of power disturbances have different occurrence probabilities. For example, a% of disturbance lies in 0 to ΔP_{d1}, b% of disturbance lies in ΔP_{d1} to ΔP_{d2}, and others lie in ΔP_{d2} to ΔP_{dmax}. Therefore, according to the range of power disturbances that need to be addressed, system operators can design the V_{si} and δ_{si} of an ESS using the FM model, as depicted in Figure 5, and choose the appropriate combinations of V_{si} and δ_{si} based on their economic or technical needs.

The Δf_{max} shown in Figure 5 can be selected as load-shedding frequency deviation to deal with ΔP_{dmax} of the power system, and the frequency response characteristic of an ESS at ΔP_{di} should be divided into three parts to deal with different disturbance levels according to FM. The product of V_{si} and δ_{si} can be described as (10).

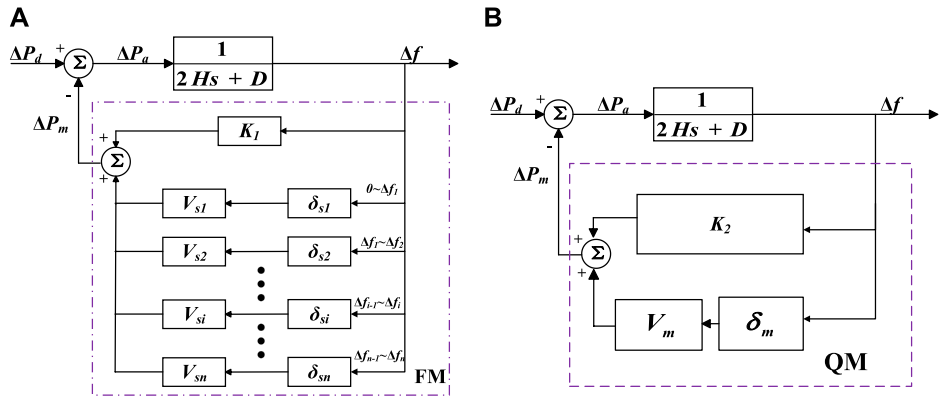

FIGURE 4
(A) The proposed FM, and **(B)** The proposed QM.

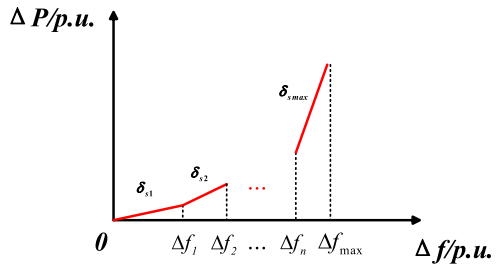

FIGURE 5
FR of ESS dealing with f_{nadir}.

$$\begin{cases} \dfrac{f_N \Delta P_{di}}{D + V_{si}\delta_{si} + K_1} \le \Delta f_i \\ V_{si}\delta_{si} \ge \dfrac{f_N \Delta P_{di}}{\Delta f_i} - D - K_1 \Leftrightarrow V_{si}\delta_{si}\Delta f_i + \dfrac{f_N \Delta P_{di}}{\Delta f_{nadiri}}\Delta f_i \\ \quad \ge f_N \Delta P_{di} \Rightarrow V_{si}\delta_{si} \ge f_N \Delta P_{di}\left(\dfrac{1}{\Delta f_i} - \dfrac{1}{\Delta f_{nadiri}}\right), \end{cases} \tag{10}$$

where Δf_i is the knee point of FR of an ESS and can also be illustrated as the system-required frequency maximum deviation at ΔP_{di} which can be selected by system operators. Δf_{nadiri} symbolizes the frequency deviation at ΔP_{di} from a historical frequency event which can be easily acquired from system operators. In applications, system operators can select the Δf_i based on their economic or technical needs of an ESS and the stability of the power grid.

3.2 The proposed QM

As the proposed FM model does not consider detailed governor-turbine dynamics, it cannot be used to represent frequency dynamics after the nadir. To address this limitation, the QM model is proposed to characterize the f_{ss}, as illustrated in Figure 4B.

The product of an ESS's capacity, V_m, and droop, δ_m, can be calculated as

$$\frac{\Delta P_{d\max} f_N}{D + K_2 + V_m\delta_m} \le \Delta f_{ss\max} \Rightarrow V_m\delta_m \ge \frac{\Delta P_{d\max} f_N}{\Delta f_{ss\max}} - (D + K_2). \tag{11}$$

System operators always set up a rigorous limitation of f_{ss} deviation (Δf_{ss}), so the calculation of V_m and δ_m can be based on the ΔP_{dmax}, where the Δf_{ssmax} is the required maximum Δf_{ss}.

3.3 The proposed EAM

The EAM includes the FM model and the QM model to deal with the f_{nadir} and f_{ss}, as mentioned above. The timing of switching between FM and QM depends on ξ and the time t_{nadir}. The t_{nadir} can be acquired from system operators and is smaller when an ESS takes part in FR; thus, it is suitable that the moment of switching should be greater than t_{nadir}. ξ is introduced to measure the f_{ss} without the QM mode's participation.

$$\xi = \frac{f_N \Delta P_{di}}{D + K_2 + V_{si}\delta_{si}} \tag{12}$$

3.4 Constraint condition in the ESDM

This section compares the energy efficiency of ESS designs based on different levels of ΔP_d and ΔP_{dmax} to establish the constraint conditions of the ESDM. If a power system experiences a disturbance ΔP_{dm}, according to the ESDM, the capacity and droop of an ESS are V_{sm} and δ_{sm}, respectively. The output power of an ESS, P_{m1}, is given by (Eq. 13).

$$P_{m1} = V_{sm}\delta_{sm}\frac{\Delta P_{dm} f_N}{D + K_1 + V_{sm}\delta_{sm}} = \frac{\Delta P_{dm} f_N}{\frac{\Delta P_{dm} f_N}{\Delta f_{nadir1} V_{sm}\delta_{sm}} + 1} \tag{13}$$

If $V_{sm}\delta_{sm} < V_{smax}\delta_{smas}$ (the product of V_{sm} and δ_{sm} is based on ΔP_{dm}), an ESS designed through the ESDM is more energy-saving.

4 Simulation results

The modified four-generator two-area (4G2A) system with PV penetration and an line commutated converter based High Voltage

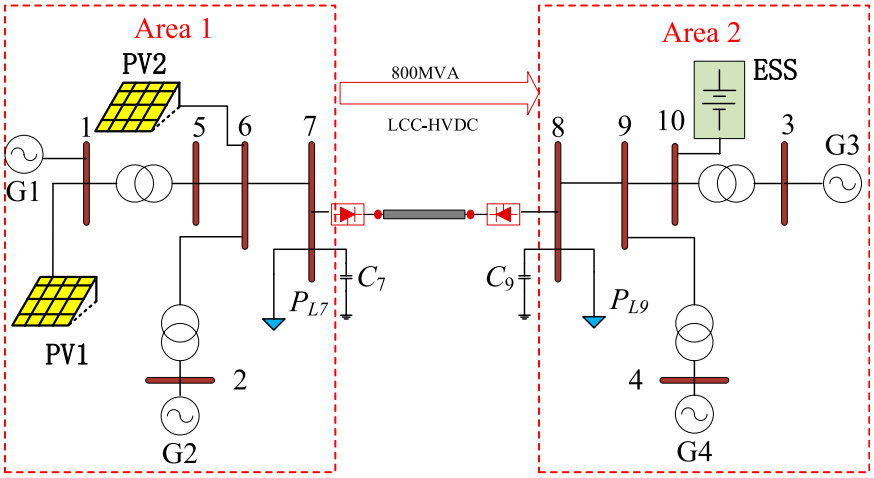

FIGURE 6
Modified four-generator two-area (4G2A) system.

TABLE 1 Simulation Scenario.

Scenario	ΔP_d		Δf_{nadir}/Hz	Δf_{ss}/Hz	Δf_{ssmax}/Hz
Scenario I	ΔP_{d1}	0.037	0.234	0.134	0.15
	ΔP_{d2}	0.046	0.325	0.18	
Scenario II	ΔP_{d1}	0.037	0.237	0.134	
	ΔP_{d2}	0.0468	0.395	0.187	
Scenario III	ΔP_{d1}	0.036	0.235	0.14	0.2
	ΔP_{d2}	0.05	0.683	0.236	
	ΔP_{d3}	0.06	1.95	0.346	

Direct Current (LCC-HVDC) connection is used for simulation in this section, as shown in Figure 6.

G1–G4 represent synchronous generators; P_{L7} and P_{L8} are the equivalent loads at bus 7 and bus 9, respectively; and C_7 and C_8 represent reactive compensations. A grid-connected ESS is connected to bus 10. Grid-connected PVs, named PV1 and PV2, are connected to bus 1 and 6. The power rating of each synchronous generator is 900 MVA, and the capacity of LCC-HVDC is 800 MVA, resulting in the power rating of the receiving system (Area 2) being 2600 MVA. The parameters of the simulation system are from Kundur (1994). The mechanical power gain factor is 1 p.u., the power generated by the high-pressure turbine is 0.4 p.u., the reheat time constant is 8 s, and the equivalent damping factor is 0. The system frequency characteristics are listed in Table 1.

4.1 Installed PV capacity of 33.3%

In scenario I, the power ratings of PV1 and PV2 are both 450 MVA. Furthermore, 90% of ΔP_d is below 0.037 p.u., and the system's ΔP_{dmax} is 0.046 p.u.

According to (10), if Δf_1 is selected as 0.2 Hz, and Δf_{max} is 0.3 Hz, V_{si}, δ_{si} should satisfy $V_{s1}\delta_{s1} \geq 1.613$ and $V_{s2}\delta_{s2} \geq 0.708$. According to (12), ξ = 0.172 Hz, and according to (11), $V_m\delta_m \geq 3.067$. The simulation results are shown in Figure 7.

It can be seen in Figure 7 that FM and QM can accurately describe the f_{nadir} and f_{ss}, respectively. The orange curve in Figure 7 shows that the ESDM effectively maintains f_{nadir} and f_{ss}. Considering that Δf_{ss} is smaller than Δf_{ssmax} when ΔP_d = 0.037, the ESS will not switch to f_{ss} maintaining mode.

4.2 Installed PV capacity of 66.7%

In scenarios II and III, G1 is replaced with PV1 and PV2, both with capacities of 900 MVA.

4.2.1 Scenario II

In scenario II, 90% of ΔP_d is below 0.037 p.u., and the system's ΔP_{dmax} is 0.0468 p.u.

According to (10), if Δf_1 is selected as 0.2 Hz, and Δf_{max} is 0.3 Hz, V_{si}, δ_{si} should satisfy $V_{s1}\delta_{s1} \geq 1.733$ and $V_{s2}\delta_{s2} \geq 2.251$. According to (12), ξ = 0.167 Hz, and according to (11), $V_m\delta_m \geq 3.704$. Taking ΔP_{dmax} as an example, simulation results are shown in Figure 8.

Figure 8 shows different switching times and combinations of capacity and droop of an ESS. It can be seen that FM and QM can accurately describe the f_{nadir} and f_{ss}, respectively. Additionally, the orange curve in Figure 8 shows that the ESDM effectively evaluates the frequency support ability of an ESS and maintains f_{nadir} and f_{ss}.

4.2.2 Scenario III

In scenario III, 40% of ΔP_d is below 0.037 p.u., 50% of ΔP_d lies between 0.037 p.u. and 0.05 p.u., and ΔP_{dmax} is 0.06 p. u. According to (10), if Δf_1 is selected as 0.2 Hz, Δf_2 is selected as 0.5 Hz, and Δf_{max} is 0.8 Hz, V_{si}, δ_{si} should satisfy $V_{s1}\delta_{s1} \geq 1.609$, $V_{s2}\delta_{s2} \geq 1.608$, and $V_{s3}\delta_{s3} \geq 2.654$.

Eq. 12 yields ξ = 0.21 Hz for ΔP_{d2} and ξ = 0.276 Hz for ΔP_{d3}, indicating that the ESS should be in f_{ss} maintaining mode and $V_m\delta_m \geq 7.595$ according to (11).

Figure 9 demonstrates that the ESDM maintains f_{nadir} and f_{ss} not only at ΔP_{dmax} but also at various ΔP_d levels (as shown in Figure 9A). For instance, in Figure 9A, the f_{nadir} is larger than 59.5 Hz but lower than 59.8 Hz, which means that ΔP_d is larger than 0.036 and smaller

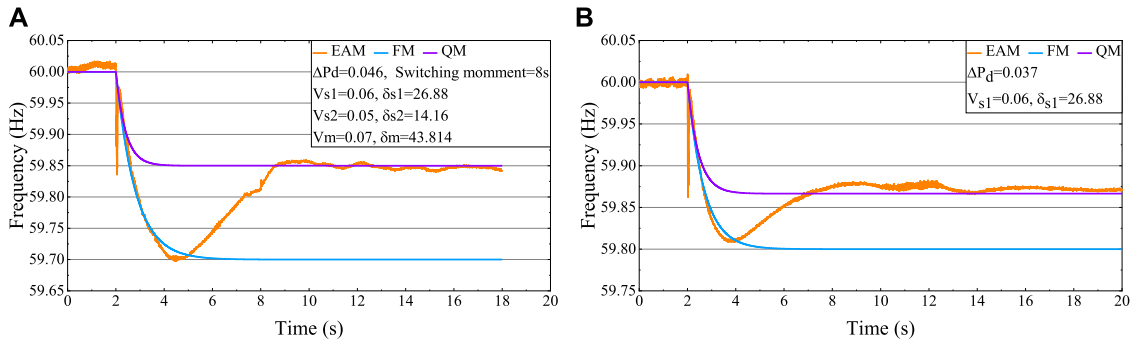

FIGURE 7
(A) FR of Scenario I at ΔP_d = 0.046, and **(B)** FR of Scenario I at ΔP_d = 0.037.

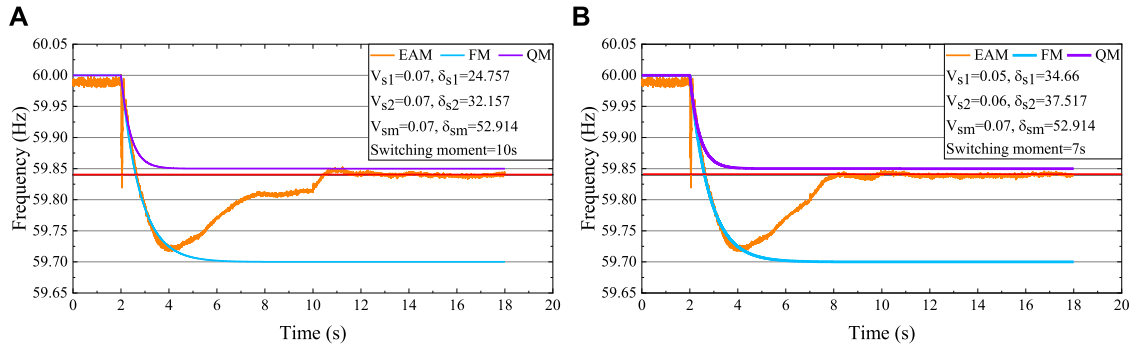

FIGURE 8
(A) FR of Scenario II at Switching moment = 10 s, and **(B)** FR of Scenario II at Switching moment = 7 s.

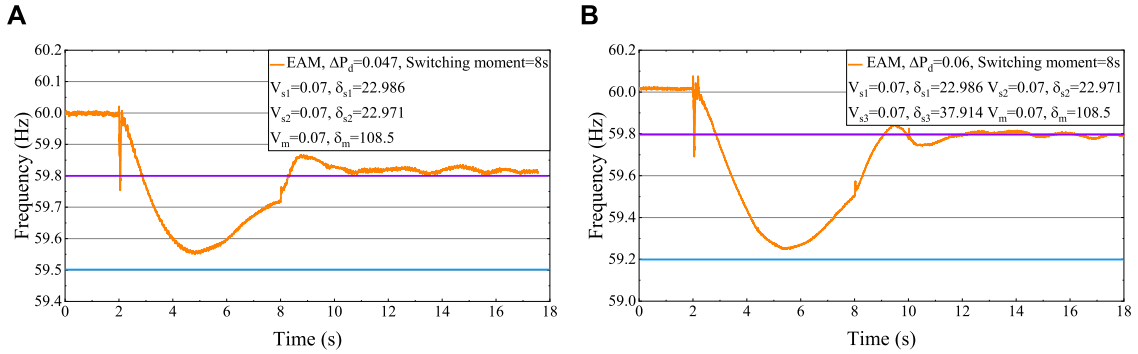

FIGURE 9
(A) FR of Scenario III at ΔP_d = 0.047, and **(B)** FR of Scenario I at ΔP_d = 0.06.

than 0.05. Therefore, the ESS should be switched to f_{ss} maintaining mode for added assurance.

4.3 Discussion

From Figures 7–9, it is evident that the ESS based on EAM is conservative at the f_{nadir} but exhibits some error at the f_{ss}. That is because of the neglect of the coupling relationship between active power and voltage in the model. With an increase in power disturbance, the active power support increases, leading to higher line losses and reduced load voltage. Taking the system load surge as an example, the active power of the system increases so that the load voltage decreases. As for the constant impedance load, active power is positively correlated with the voltage. Consequently, the actual power disturbance is lower than expected. With the frequency support provided by an ESS and SGs, the system frequency is recovered and the load voltage therefore increases. The increasing voltage increases the power disturbance, leading to tiny errors in maintaining the f_{ss} (as observed by the red lines (59.84 Hz) in 10; the

error of 0.01 Hz is smaller than the dead-band of 0.015 Hz (GB/T 40595-2021, 2021)). In simulation scenarios, D is set as zero but cannot be zero in reality. As for FM and QM models used for the ESS calculation, D is not one of the input parameters according to (10) and (11), and all input parameters are from system operators, so D will not influence the accuracy of the models.

5 Conclusion

This paper proposes a method for calculating the capacity and droop of an ESS based on historical frequency events to maintain the f_{nadir} and f_{ss}. The proposed method is convenient and accurate for system operators to evaluate the frequency support ability of an ESS and design ESSs. Furthermore, an ESS based on the ESDM proves to be energy-efficient. Given that all parameters are provided by system operators, the method holds significant practical applications. Moreover, the proposed method serves as a foundation for ESS sizing and control of distribution network ESSs.

Data availability statement

The raw data supporting the conclusion of this article will be made available by the authors, without undue reservation.

Author contributions

SD: Methodology, project administration, supervision, writing–original draft, and writing–review and editing. JZ: Data curation, investigation, methodology, validation, writing–original draft, and writing–review and editing. LY: Methodology, project administration, supervision, and writing–original draft. ZC: Methodology, project administration, supervision, and writing–review and editing.

Funding

The author(s) declare that financial support was received for the research, authorship, and/or publication of this article. The research is supported by State Key Laboratory of HVDC (Grant No. SKLHVDC-2022-KF-02).

Conflict of interest

Authors SD and LY were employed by China Southern Power Grid Co., Ltd.

The remaining authors declare that the research was conducted in the absence of any commercial or financial relationships that could be construed as a potential conflict of interest.

Publisher's note

All claims expressed in this article are solely those of the authors and do not necessarily represent those of their affiliated organizations, or those of the publisher, the editors, and the reviewers. Any product that may be evaluated in this article, or claim that may be made by its manufacturer, is not guaranteed or endorsed by the publisher.

References

AEMO (2023). Market ancillary service specification 8.1. Available at: https://aemo.com.au/media/files/stakeholder_consultation/consultations/nem-consultations/2023/primary-freq-resp-norm-op-conditions/market-ancillary-services-specification-v81.pdf?la=en.

Aik, D. L. H. (2006). A general-order system frequency response model incorporating load shedding: analytic modeling and applications. *IEEE Trans. Power Syst.* 21 (2), 709–717. doi:10.1109/tpwrs.2006.873123

Anderson, P. M., and Mirheydar, M. (1990). A low-order system frequency response model. *IEEE Trans. Power Syst.* 5 (3), 720–729. doi:10.1109/59.65898

Bai, Y., Kou, B., and Chan, C. C. (2015). A simple structure passive MPPT standalone wind turbine generator system. *IEEE Trans. Magnetics* 51 (11), 1–4. doi:10.1109/tmag.2015.2439043

Baker, K., Hug, G., and Li, X. (2017). Energy storage sizing taking into account forecast uncertainties and receding horizon operation. *IEEE Trans. Sustain. Energy* 8 (1), 331–340. doi:10.1109/tste.2016.2599074

Ben Elghali, S., Outbib, R., and Benbouzid, M. (2019). Selecting and optimal sizing of hybridized energy storage systems for tidal energy integration into power grid. *J. Mod. Power Syst. Clean Energy* 7 (1), 113–122. doi:10.1007/s40565-018-0442-0

Chen, S., Zhang, T., Gooi, H. B., Masiello, R. D., and Katzenstein, W. (2016). Penetration rate and effectiveness studies of aggregated BESS for frequency regulation. *IEEE Trans. Smart Grid* 7 (1), 167–177. doi:10.1109/pesgm.2016.7741318

Gao, H., Xin, H., Huang, L., Xu, T., Ju, P., Qin, X., et al. (2021). Common mode frequency analysis and characteristic quantification of new energy power system. *Chin. J. Electr. Eng.* 41 (3), 890–900. doi:10.13334/j.0258-8013.pcsee.201897

GB/T 30370-2013 (2013). *Guide of primary frequency control test and performance acceptance for thermal power generating units*. Beijing: China Standards Press.

GB/T 40595-2021 (2021). *Guide for technology and test on primary frequency control of grid-connected power resource*. Beijing: China Standards Press.

Guangfu (2020). State Grid is trying to solve the problem of high proportion of new energy consumption. Available at: https://guangfu.bjx.com.cn/news/20200930/1108031.shtml.

Guangfu (2022). The installed new energy capacity of East China power grid exceeded 100 million kilowatts. Available at: https://guangfu.bjx.com.cn/news/20220314/1210096.shtml.

He, Y., and Wen, Z. (2021) *Power system analysis*. Wuhan, China: Huazhong University of Science and Technology Press.

Jiang, Y., Cohn, E., Vorobev, P., and Mallada, E. (2021). Storage-based frequency shaping control. *IEEE Trans. Power Syst.* 36 (6), 5006–5019. doi:10.1109/tpwrs.2021.3072833

Ju, P., Zheng, Y., Jin, Y., Qin, C., Jiang, Y., and Cao, L. (2021). Analytic assessment of the power system frequency security. *IET Generation. Transm. Distribution* 15 (15), 2215–2225. doi:10.1049/gtd2.12171

Kundur, P. (1994) *Power system stability and control*. New York: McGraw-Hill Education.

Mohanty, S., Subudhi, B., and Ray, P. K. (2016). A new MPPT design using grey wolf optimization technique for photovoltaic system under partial shading conditions. *IEEE Trans. Sustain. Energy* 7 (1), 181–188. doi:10.1109/tste.2015.2482120

Mustafa, H., and Altinoluk H, S. (2023). Current and future prospective for battery controllers of solar PV integrated battery energy storage systems. *Front. Energy Res.* 11. doi:10.3389/fenrg.2023.1139255

National Grid ESO (2019). *Future of frequency response industry update*. Available at: https://www.nationalgrideso.com/document/138861/download.

Rana, M. M., Uddin, M., Sarkar, M. R., Meraj, S. T., Shafiullah, G. M., Muyeen, S. M., et al. (2023). Applications of energy storage systems in power grids with and without renewable energy integration — a comprehensive review. *J. Energy Storage* 68, 107811–152X. 107811. doi:10.1016/j.est.2023.107811

Wang, F., Li, B., Xia, T., Peng, M., Wang, S., et al. (2023). Economic research on energy storage auxiliary frequency regulation of lithium iron phosphate battery for 2×600 MW coal-fired unit in Guangdong. *South. Energy Constr.* 10 (06), 71–77. doi:10.16516/j.gedi.issn2095-8676.2023.06.008

Wang, S., Liu, S., Yang, F., Bai, X., and Yue, C. (2020). Novel power allocation approach in a battery storage power station for aging minimization. *Front. Energy Res.* 7. doi:10.3389/fenrg.2019.00166

Wu, Q., Song, X., Zhang, J., Yu, H., Huang, J., Dai, H., et al. (2020). Study on self-adaptation comprehensive strategy of battery energy storage in primary frequency regulation of power grid. *Power Grid Technol.* 44 (10), 3829–3836. doi:10.13335/j.1000-3673.pst.2019.1214

Xiong, L., Liu, X., Zhang, D., and Liu, Y. (2021). Rapid power compensation-based frequency response strategy for low-inertia power systems. *IEEE J. Emerg. Sel. Top. Power Electron.* 9 (4), 4500–4513. doi:10.1109/jestpe.2020.3032063

Xiong, L., Liu, X., Zhao, C., and Zhuo, F. (2020). A fast and robust real-time detection algorithm of decaying DC transient and harmonic components in three-phase systems. *IEEE Trans. Power Electron.* 35 (4), 3332–3336. doi:10.1109/tpel.2019.2940891

Xiong, L., Zhuo, F., Wang, F., Liu, X., Chen, Y., Zhu, M., et al. (2016). Static synchronous generator model: a new perspective to investigate dynamic characteristics and stability issues of grid-tied pwm inverter. *IEEE Trans. Power Electron.* 31 (9), 6264–6280. doi:10.1109/tpel.2015.2498933

Yang, Y., Peng, J. C.-H., Ye, C., and Ye, Z.-S. (2022). Optimal reserve allocation with simulation-driven frequency dynamic constraint: a distributionally robust approach. *IEEE Trans. Circuits Syst. II Express Briefs* 69 (11), 4483–4487. doi:10.1109/tcsii.2022.3184969

Zarei, A., and Ghaffarzadeh, N. (2024). Optimal demand response scheduling and voltage reinforcement in distribution grids incorporating uncertainties of energy resources, placement of energy storages, and aggregated flexible loads. *Front. Energy Res.* 12. doi:10.3389/fenrg.2024.1361809

Zhang, C., Liu, L., Cheng, H., Liu, D., Zhang, J., and Li, G. (2021). Frequency-constrained Co-planning of generation and energy storage with high-penetration renewable energy. *J. Mod. Power Syst. Clean Energy* 9 (4), 760–775. doi:10.35833/mpce.2020.000743

frontiers | Frontiers in Energy Research

TYPE Original Research
PUBLISHED 08 July 2024
DOI 10.3389/fenrg.2024.1404462

OPEN ACCESS

EDITED BY
Yonghui Liu,
Hong Kong Polytechnic University, Hong Kong SAR, China

REVIEWED BY
Jiejie Huang,
Nantong University, China
Kai Wang,
China University of Mining and Technology, China
Bowen Wang,
Kashgar University, China
M Emad Farrag,
Glasgow Caledonian University, United Kingdom

*CORRESPONDENCE
Yang Li,
liyangguizhou1018@163.com

RECEIVED 21 March 2024
ACCEPTED 10 June 2024
PUBLISHED 08 July 2024

CITATION
Yang L, Li Y, Zhang Y, Xie Z, Chen J, Qu Y and Shi G (2024), Low-voltage ride-through strategy for an integrated permanent magnet synchronous generator in a flexible interconnected distribution network. *Front. Energy Res.* 12:1404462. doi: 10.3389/fenrg.2024.1404462

Low-voltage ride-through strategy for an integrated permanent magnet synchronous generator in a flexible interconnected distribution network

Lin Yang[1,2], Yang Li[2]*, Yu Zhang[3], Zhongren Xie[2], Julong Chen[3], Yinlong Qu[3] and Gang Shi[4]

[1]School of Informatics, Xiamen University, Xiamen, China, [2]Xingyi Power Supply Bureau of Guizhou Power Grid Co., Ltd., Xingyi, China, [3]Guizhou Power Grid Co., Ltd., Power Grid Planning and Research Center, Guiyang, China, [4]Department of Electrical Engineering, Shanghai Jiao Tong University, Shanghai, China

For the permanent magnet synchronous generator (PMSG) integrated into the flexible interconnected distribution network (FIDN), its low-voltage ride-through (LVRT) strategy needs to be designed to enhance the transient operation capability of the FIDN. The design of the LVRT strategy also needs to take the fault location of the FIDN into consideration. To deal with faults occurring on the integrated feeder of the PMSG, the PMSG needs to realize successful LVRT using the hardware protection equipment. To deal with faults occurring on the feeder adjacent to the integrated feeder of the PMSG, the PMSG needs to release its stored energy to temporarily increase its active power output, which is then supplied to the loads on the faulted feeder that are isolated from the fault through the soft open point (SOP). In this paper, a novel LVRT strategy designed for the PMSG integrated into the FIDN is proposed, which includes dual operation modes that are separately applied to different fault locations. If PMSG is on the faulted feeder, the DC-link voltage of the PMSG is maintained with the controllable resistive fault current limiter (CRFCL), while the maximized stored kinetic energy is reserved to enhance the generation efficiency during the LVRT. If PMSG is on the feeder adjacent to the faulted feeder, the control strategy of the converters of the PMSG is adjusted in response to the power regulation goal at the SOP. Meanwhile, the maximum releasable kinetic energy of the PMSG is considered when increasing its active power output. The feasibility and effectiveness of the LVRT strategy for the PMSG are verified based on the numerical analysis.

KEYWORDS

low-voltage ride-through, permanent magnet synchronous generator, flexible interconnected distribution network, controllable resistive fault current limiter, q-axis stator current control, maximized stored kinetic energy, temporary increased active power output, maximum releasable kinetic energy

1 Introduction

With the increasing penetration of distributed generation within the distribution network, the operation state of the distribution network becomes increasingly variable and complicated. Thus, the novel structure of the distribution network incorporating the back-to-back converters, i.e., the flexible interconnected distribution network (FIDN), has attracted great attention with potential for wide-scale application (Ji et al., 2022; Yang et al., 2022; Liu Y. et al., 2023). The FIDN replaces the traditional interconnection switch that links two feeders with the soft open point (SOP). With the SOP, active power exchange between the two feeders can be flexibly controlled. Furthermore, the back-to-back converter at the SOP can provide reactive power to support the terminal voltage of the feeder. The control flexibility brought by the FIDN enhances the capability of distributed power generation integration into the distribution network. For example, the permanent magnet synchronous generator (PMSG) may be connected to the FIDN as part of the wind power integration (Yang et al., 2024; Pradhan et al., 2022). With the integration of distributed wind generation, low-voltage ride-through (LVRT) requirements, traditionally prescribed to wind turbine generators (WTGs) (Yao et al., 2018; He et al., 2020; Xie et al., 2021), become an issue to solve from the operation perspective of the FIDN rather than the WTG alone (Li et al., 2022).

In cases where a fault occurs on the feeder to integrate the PMSG, the PMSG needs to stay connected within the LVRT duration prescribed by grid codes to support the operation of the FIDN (Kim et al., 2013; Wu et al., 2019). To assist the LVRT of the PMSG, usually hardware protection equipment is applied, e.g., the chopper circuit (Xiong et al., 2016; Xing et al., 2018), the series braking resistor (Ji et al., 2014), and the fault current limiter (Huang et al., 2019; Okedu, 2022), to dissipate the redundant active power generation caused by the reduced active power output with the voltage dip at the point of common coupling (PCC) (Huang et al., 2020). The hardware protection scheme is easy to implement but has drawbacks caused by its fixed resistance. For example, multiple switch-ins and -outs of the chopper circuit may occur with inappropriate resistance values, leading to an intensified ripple of the DC-link voltage (Li et al., 2017). For the series braking resistor with comparatively high resistance, overvoltage may occur with minor voltage dips at the PCC (Firouzi et al., 2020). In view of these, the controllable resistive fault current limiter (CRFCL) is a feasible solution to avoid these shortcomings and is capable of providing adjustable resistance values in response to different fault scenarios (Behzad and Negnevitsky, 2015; Huang and Li, 2020). Moreover, instead of dissipating the redundant active power generation in the resistor, the active power output of the machine-side converter (MSC) of the PMSG may be regulated to store the excessive active power generation as the kinetic energy of the rotor (Alepuz et al., 2013; Marmouh et al., 2019). In this way, the generation efficiency of the PMSG during the LVRT may be improved, and the active power reserved may be utilized to provide support to system frequency at the fault-clearance stage (Xiong et al., 2021). In the existing research studies, the variable resistance of the CRFCL is mostly utilized to constrain the fault current during the LVRT. In this case, different levels of resistance values are applied under different voltage drop depths. The resistance of the CRFCL may also be controlled based on simple functions, e.g., the ramp function to realize smooth switch-in and -out of the CRFCL. To further regulate the active power dissipated on the CRFCL during the LVRT, delicate control of the CRFCL resistance is needed, which requires a more complicated control design.

To assist the LVRT of the PMSG, modification to the control of the converter is another widely adopted scheme, apart from hardware protection equipment. To reduce the active power imbalance between the MSC and grid-side converter (GSC), their active power control targets may be switched, i.e., the MSC is responsible for regulating the DC-link voltage during the LVRT (Hanson and Michalke, 2009; Yuan et al., 2009; Yassin et al., 2016). In this way, the active power output from the PMSG may be actively reduced to alleviate the DC-link voltage deviation during LVRT. Still, this scheme retains the outer-loop current control loop, which fails to provide a fast response at the comparatively short LVRT time scale. By eliminating the outer-loop control and applying the direct inner-loop current control (Li et al., 2017), the LVRT performance of the PMSG may be further enhanced.

On the other hand, in cases where the fault occurs on the adjacent feeder connected to the integration feeder of the PMSG through the SOP, the back-to-back converter at the SOP needs to adjust its control strategy to respond to the fault scenario. The converter at the side of the faulted feeder adjusts its current reference to provide the required reactive current injection for the voltage support (Geng et al., 2018; Liu J. et al., 2023) and utilizes the remaining current capacity to maximize the active power output during the LVRT to provide power supply to the loads on the faulted feeder that have been isolated from the fault during the reconfiguration process (Zhou et al., 2021). If the increased active power output is needed by the converter at the side of the faulted feeder, the PMSG at the adjacent feeder may temporarily increase its active power to reduce the transient active power imbalance of the back-to-back converter at the SOP. With the increased active power output, the rotating speed of the shaft is gradually decreasing. For the wind turbine (WT), its rotating speed needs to be regulated so as not to drop below the critical value that causes instability of the WT. Thus, the maximum value of the increased active power needs to be predetermined, and two-mass modeling of the shaft needs to be adopted to ensure a comparatively accurate estimation of the rotating speed of the WT (Yang et al., 2023).

In this paper, the LVRT strategy for the PMSG, especially in the application scenario with integration to the FIDN, is designed with two operation modes corresponding to different locations of the fault. For the fault on the integration feeder of the PMSG, the PMSG utilizes the CRFCL to realize satisfactory LVRT performances under various fault scenarios. The maximized kinetic energy is stored in the rotor with coordinated control between the converters and the CRFCL, which both improves the generation efficiency of the PMSG during the LVRT and reserves active power for the post-fault recovery of the FIDN. For the fault on the feeder adjacent to the integration feeder of the PMSG, the PMSG is controlled to provide active power support to the back-to-back converter at the SOP, in the case where additional active power output is needed at the faulted feeder, to provide power supply to loads isolated from the fault through the process of network reconfiguration. The tow-mass shaft model is adopted to analyze the dynamics of the rotating speed

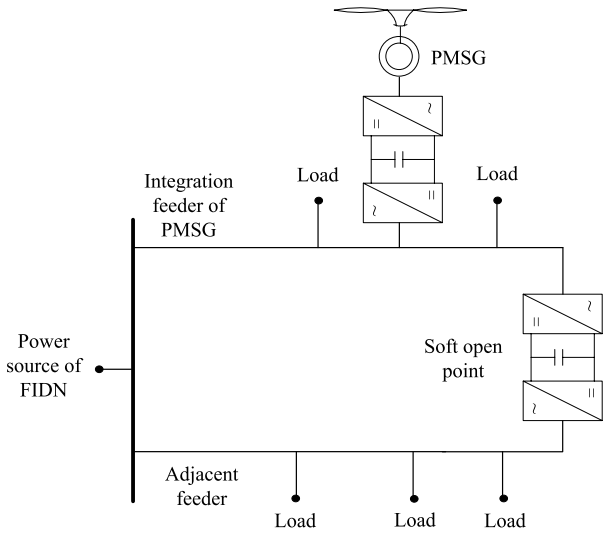

FIGURE 1
Configuration of the FIDN with the integration of the PMSG.

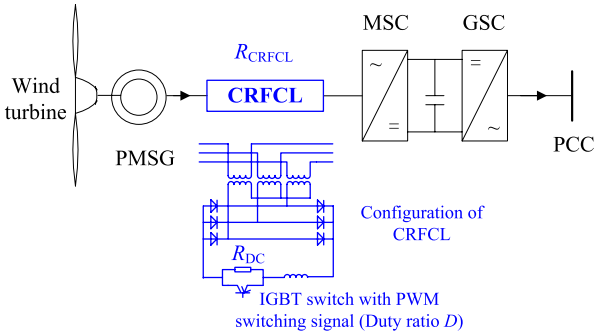

FIGURE 2
PMSG with implemented CRFCL at the stator side to assist the LVRT.

of the WT so as to avoid deacceleration below the critical rotating speed that causes the instability of the WT. Numerical analysis is carried out to verify the feasibility and effectiveness of the proposed LVRT strategy for the PMSG integrated into the FIDN.

The remainder of this paper is organized as follows. The literature review of research related to the LVRT of the PMSG and the FIDN is conducted in Section 1. In Section 2, the configuration of the studied system, i.e., the PMSG-integrated FIDN, is illustrated and modeled. The requirements during the LVRT process are also introduced. In Section 3, the LVRT strategy of the PMSG in the case of faults occurring on the integration feeder is developed. The coordinated control between the CRFCL and converter control is designed to maximize the kinetic energy storage of the rotor during the LVRT process while maintaining the DC-link voltage within security constraints. In Section 4, the LVRT strategy of the PMSG in the case of faults occurring on the adjacent feeder is developed. The control scheme of the PMSG to adjust its active power output based on the power demands of the back-to-back converter and its maximum releasable kinetic energy during the LVRT is presented. The numerical analysis is carried out in Section 5, and the resulting conclusions are presented in Section 6.

2 Configuration of FIDN with integrated PMSG and LVRT requirements

2.1 System configuration

The configuration of the FIDN with the integration of the PMSG is illustrated in Figure 1. The feeder that connects the PMSG to the FIDN is denoted as the integration feeder, and the adjacent feeder in the FIDN is connected to the integration feeder through the back-to-back converter at the SOP.

When faults occur on the integration feeder of the PMSG, the PMSG will suffer from a voltage drop at the PCC. In this case, the PMSG is required to realize LVRT during the fault. Here, the CRFCL is implemented at the stator side of the PMSG to dissipate the power imbalance between the MSC and GSC, as illustrated in Figure 2. Usually, the fault current limiter (FCL) is placed at the generator terminal to elevate the terminal voltage. Yet, in the case of the PMSG, the fault is partially isolated by the back-to-back converter, and the key to a successful LVRT is to mitigate the transient active power imbalance between the MSC and GSC. In view of this, the CRFCL is directly placed on the MSC side to dissipate the redundant active power output from the PMSG. Another choice to implement the CRFCL is to connect it to the DC-link capacitor to operate as the DC chopper circuit. However, the DC chopper circuit is a comparatively passive protection scheme that requires the DC-link voltage to reach its constraint in the first place. Thus, installing the CRFCL as the DC chopper circuit fails to fully utilize the controllability of the CRFCL.

The resistance of the CRFCL is controllable. When a fault occurs on the adjacent feeder, its resistance is reduced to zero, while the PMSG adjusts its active power output, which is transferred to the adjacent feeder through the SOP.

2.2 Modeling and control of the PMSG and CRFCL

For the PMSG, when assuming that its flux is aligned to the direct axis, the stator flux of the PMSG and its dynamic adopting the generator convention are modeled using Eq. 1.

$$\begin{cases} \psi_{s,d} = -L_{s,d} I_{s,d} + \psi_f \\ \psi_{s,q} = -L_{s,q} I_{s,q} \\ p\psi_{s,d} = 0 = V_{s,d} + \omega_r \psi_{s,q} + R_s I_{s,d} \\ p\psi_{s,q} = 0 = V_{s,q} - \omega_r \psi_{s,d} + R_s I_{s,q} \end{cases}, \quad (1)$$

where ψ, L, I, V, and R are the flux, inductance, current, voltage, and resistance, respectively; p is the differential operator; ψ_f is the flux of the permanent magnet; ω_r is the rotor speed; the subscript s denotes the stator; and subscripts d and q denote the direct and quadrature axes, respectively.

If the d-axis inductance of the stator is equal to its q-axis inductance, the steady-state output active power of the stator and the electromagnetic torque of the PMSG are derived based on Eq. 1, which is given by Eq. 2.

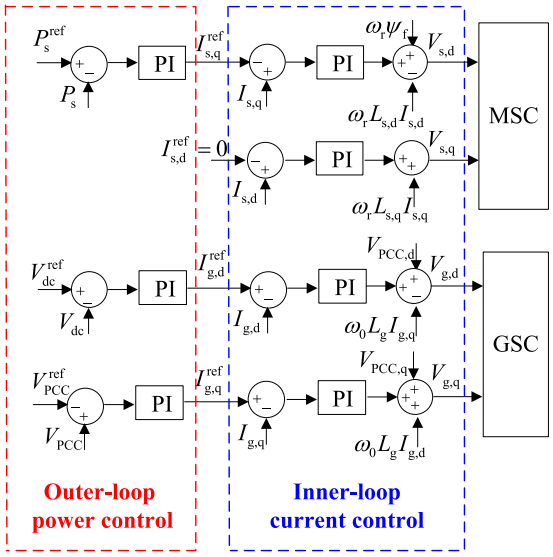

FIGURE 3
Traditional dual-loop PI control schemes for MSC and GSC.

$$\begin{cases} P_s = \omega_r \psi_f I_{s,q} - R_s I_s^2 \approx \omega_r \psi_f I_{s,q} \\ T_e = \psi_f I_{s,q} - \dfrac{R_s I_s^2}{\omega_r} \approx \psi_f I_{s,q} \end{cases}, \tag{2}$$

where P_s is the active power of stator and T_e is the electromagnetic torque of the PMSG.

It can be seen from Eq. 2 that the active power output of the PMSG is approximately proportional to the q-axis stator current, based on which the traditional dual-loop PI control schemes of the MSC and GSC are developed and illustrated in Figure 3, where subscripts PCC, dc, and g denote the point of common coupling, the DC-link capacitor, and the GSC, respectively; superscript ref denotes the reference value, and ω_0 is the synchronous electric angular speed of the power system.

For the MSC, since the stator output active power is approximately proportional to the q-axis stator current, the reference of the q-axis stator current is yielded by the outer-loop power control. On the other hand, for the GSC, its active power outer-loop control is responsible for the DC-link voltage regulation, and its reactive power outer-loop control is responsible for maintaining the PCC voltage (Xiong et al., 2020). Current references proportional to the active and reactive power output of the GSC are prescribed by the outer-loop power control and applied for the inner-loop current control.

As for the CRFCL, its equivalent resistance at the AC side is determined by the resistance value of the resistor placed at the DC side and the duty ratio of the switching signals applied to the parallel connected switch, as given by Eq. 3 (Behzad and Negnevitsky, 2015). Through control of the duty ratio of the switching signal, the CRFCL is capable of providing variable resistance. The switching signal is generated using the pulse width modulation (PWM) technique. To realize effective control over the equivalent resistance of the CRFCL, the frequency of the PWM signal does not need to be set to a high value. The frequency of the PWM signal is set to 500 Hz for the studied system illustrated in Figure 2.

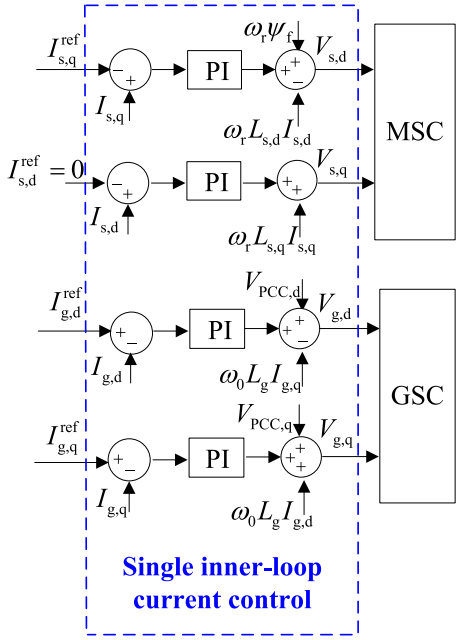

FIGURE 4
Modified converter control scheme for enhanced LVRT capability of the PMSG.

$$R_{CRFCL} = \frac{\pi^2}{18}(1 - D)R_{DC}, \tag{3}$$

where R_{CRFCL} is the equivalent resistance of the CRFCL, D is the duty ratio of the switching signal, and R_{DC} is the resistance value of the resistor at the DC side.

3 LVRT strategy of the PMSG with faults in the integration feeder

The designed LVRT scheme applies different strategies, with faults occurring at the integration and adjacent feeders, as shown in Figure 1, respectively. The controller collects protection information from the feeders to identify fault locations. With faults occurring on the integration feeder, the controller aims to ensure successful LVRT of the PMSG, and the active power output of the PMSG is reduced to avoid overvoltage of the DC-link capacitor. However, with faults occurring on the adjacent feeder, the active power output of the PMSG is increased to provide power supply through the soft open point to load nodes on the faulted feeder that have been isolated from the fault.

3.1 Control schemes of converters during LVRT

With faults occurring on the integration feeder, the coordinated operation of the converter control and the CRFCL come into action to assist the LVRT of the PMSG. Considering the short time scale of the LVRT transient, the single inner-loop current control scheme is applied to both the MSC and GSC in the modified converter control

10.3389/fenrg.2024.1404462

scheme to enhance the LVRT capability of the PMSG, as illustrated in Figure 4. The elimination of the outer-loop power control enables the converter to provide a faster response to the LVRT needs compared to the traditional dual-loop control scheme. To achieve the same control target, the current references need to be calculated based on the parameters of the outer-loop power control and then applied to the direct inner-loop current control, as given by Eq. 4.

$$\begin{cases} I_{s,q}^{ref} = P_s / \omega_r \psi_f \\ I_{s,d}^{ref} = 0 \\ I_{g,q}^{ref} = 2(0.9 - k_{PCC}) \\ I_{g,d}^{ref} = P_m / V_{g,d} \end{cases}, \tag{4}$$

where k_{PCC} is the voltage dip depth at the PCC and subscript m denotes the MSC.

One of the essential functions of the outer-loop power control is to maintain the DC-link voltage, which is a key requirement for successful LVRT and needs to be retained by setting up connections between the active current references of the MSC and GSC to indirectly maintain the active power balance. However, this balance is difficult to maintain since the active power output capability of the GSC is constrained by the voltage dip at the PCC. With severe voltage dips, assistance from the CRFCL is needed to dissipate the redundant active power from the stator.

The dynamic DC-link voltage of the PMSG is given in Eq. 5. For the GSC, its maximum active power output during the LVRT is determined by the remaining capacity of the GSC after the GSC injects reactive current to the PCC based on the voltage dip depth, as given by Eq. 6.

$$\mathrm{p}\left(\frac{1}{2}CV_{dc}^2\right) = P_m - P_g, \tag{5}$$

$$P_g = k_{PCC} V_{PCC} \sqrt{\left(I_g^{max}\right)^2 - [2(0.9 - k_{PCC})]^2}, \tag{6}$$

where C is the DC-link capacitance and the superscript max denotes the maximum feasible value.

With the CRFCL resistance taken into consideration, the input active power of the MSC is quantified using Eq. 7.

$$P_m = \omega_r \psi_f I_{s,q} - (R_s + R_{CRFCL}) I_{s,q}^2. \tag{7}$$

Combining Eqs 6, 7, the maximum variation in the stored energy in the DC-link capacitor during the LVRT yielded by the active power imbalance between the MSC and GSC is given by Eq. 8.

$$\begin{aligned} \Delta E &= \max\left[\int_0^t (P_m - P_g)\mathrm{d}t\right] = \max\left[\int_0^t \left(\omega_r \psi_f I_{s,q} - (R_s + R_{CRFCL}) I_{s,q}^2 - P_g\right)\mathrm{d}t\right] \\ &= \max\left[\psi_f I_{s,q} \int_0^t \omega_r \mathrm{d}t - t_f\left[(R_s + R_{CRFCL}) I_{s,q}^2 - P_g\right]\right], 0 \le t \le t_f, \end{aligned} \tag{8}$$

where ΔE is the maximum variation in the stored energy and t_f is the duration of the LVRT process.

As can be seen from Eq. 8, to solve ΔE, the integral of the rotor speed, i.e., the variation in the rotor speed during the LVRT duration, is needed. With the one-mass modeling of the PMSG shaft, i.e., the rotating speed of the PMSG rotor is equal to that of the WT, variation in the rotor speed is modeled using Eqs 9, 10. To solve the differential equation, the improved Euler method is applied to solve the rotor speed dynamic during the LVRT.

$$\frac{\mathrm{d}\omega_r}{\mathrm{d}t} = \frac{1}{2H_{eq}}\left(\frac{P_{WT}}{\omega_r} - \psi_f I_{s,q}\right), \tag{9}$$

$$\begin{cases} P_{WT} = \dfrac{\rho \pi r^2 v_w^3}{2} c_1 \left(\dfrac{c_2}{\lambda_i} - c_3\beta - c_4\beta^{c_5} - c_6\right) \mathrm{e}^{-\frac{c_7}{\lambda_i}} \\ \dfrac{1}{\lambda_i} = \dfrac{1}{\lambda + c_8\beta} - \dfrac{c_9}{\beta^3 + 1} \\ \lambda = \dfrac{\omega_{WT} r}{v_w} \end{cases}, \tag{10}$$

where H_{eq} is the equivalent inertia time constant of the PMSG shaft, P_{WT} is the mechanical power captured by the WT, ρ is the air density, v_w is the wind speed, c_1–c_9 are parameters of the C_p function, λ is the tip speed ratio, λ_i is the intermediate variable, ω_{WT} is the rotating speed of the WT, and r is the radius of the WT.

The process of solving Eq. 9 using the improved Euler method is given by Eq. 11, where Δt is the time step adopted to solve the rotating speed dynamic; superscripts (n) and $(n+1)$ denote the values at the beginning and ending instants of the nth time step, respectively; and the superscript pred denotes the prediction value obtained with the Euler method.

$$\begin{cases} \omega_r^{(n+1)} = \omega_r^{(n)} + \dfrac{\Delta t}{2} \dfrac{1}{2H_{eq}} \left[\dfrac{P_{WT}^{(n)}}{\omega_r^{(n)}} + \dfrac{P_{WT}^{(n+1),pred}}{\omega_r^{(n+1),pred}} - 2\psi_f I_{s,q}\right] \\ \omega_r^{(n+1),pred} = \omega_r^{(n)} + \Delta t \dfrac{1}{2H_{eq}} \left(\dfrac{P_{WT}^{(n)}}{\omega_r^{(n)}} - \psi_f I_{s,q}\right) \end{cases}. \tag{11}$$

In some cases, the variation in the mechanical power captured by the WT is ignored for the LVRT duration. This assumption is acceptable with no change to the active power control scheme of the MSC. As for the LVRT scheme in this paper, the active power of the stator is adjusted and the rotating speed of the WT varies with the significant change in the stored kinetic energy; thus, in this case, the impact of the rotating speed change on the mechanical power of the WT may not be ignored.

When solving the rotor dynamic during the LVRT based on Eqs 9, 10, the pitch angle of the WT is considered to be constant due to the short time scale of the LVRT duration. The allowable change rate of the pitch angle is usually constrained below 2° per second. With the limited response capability of the pitch angle regulation and further considering the postponed response due to control delay, the impact of the pitch angle regulation is ignored here to realize higher calculation efficiency without affecting the accuracy of the calculation results.

Considering the upper limit of the DC-link voltage, the maximum value of the stored energy variation is quantified using Eq. 12.

$$\Delta E^{max} = \frac{1}{2} C\left(V_{dc,upper}^2 - V_{dc,ini}^2\right) \tag{12}$$

where $V_{dc,upper}$ and $V_{dc,ini}$ denote the upper limit and the initial value of the DC-link voltage, respectively.

To realize successful LVRT of the PMSG, the key is to constrain the DC-link voltage within its security constraint. Based on calculations with Eqs 5–12, the DC-link voltage variation with the setting of the q-axis stator current reference is obtained to check its voltage constraint, and the required minimum CRFCL resistance to avoid the overvoltage of the DC-link can be

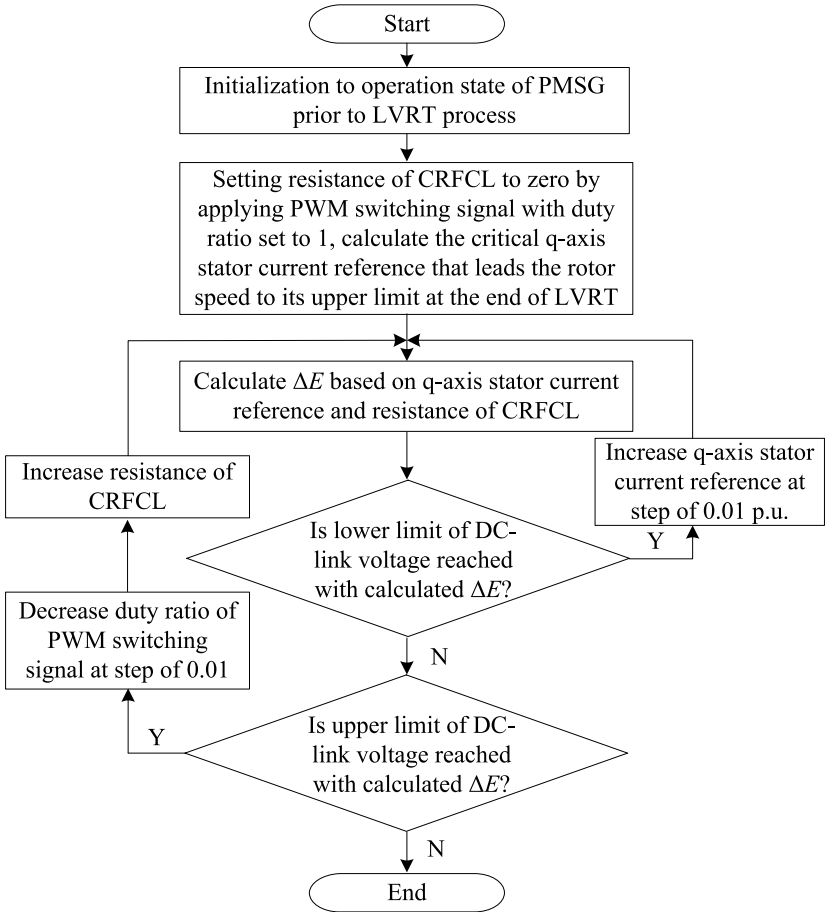

FIGURE 5
Coordinated operation of CRFCL and converter control with faults on the integration feeder.

determined. Meanwhile, the acceleration of the PMSG rotor may also cause violations of the upper constraint of the rotor speed. In that case, a larger reference of the q-axis stator current needs to be applied to increase the electromagnetic torque of the PMSG.

3.2 Coordinated operation of the CRFCL and converter control for the enhanced LVRT effect

As can be seen from Section 3.1, the current references of the converter control and the resistance of the CRFCL both affect the LVRT transient; thus, they need to be applied in a coordinated manner to realize the optimal LVRT effect. The optimization targets for the coordinated control are set to first maximize the kinetic energy stored in the PMSG rotor and then minimize the resistance of the CRFCL to reduce the active power dissipated in the resistor. The flowchart of the coordinated operation of the CRFCL and the converter control is shown in Figure 5.

As shown in Figure 5, first, the initial operation state of the PMSG needs to be solved. The PMSG may operate in the maximum power point tracking (MPPT) or power dispatch mode. The initialization of the PMSG under these two modes may be referred to in Li (2015). Normally, under the power dispatch mode, the operation point of the PMSG drifts away from the MPPT point to realize active power reserve for frequency regulation. If the overspeed control is adopted to reserve active power, the capacity of the kinetic energy that can be stored in the PMSG rotor will be decreased compared to the case of MPPT operation.

Based on the initial operation state, the critical q-axis stator current that leads the rotor speed to its upper limit at the ending instant of the LVRT duration, with the resistance of the CRFCL controlled to zero, is first determined. This q-axis stator current corresponds to the ideal LVRT transient, where the theoretical maximum kinetic energy is stored and no active power is dissipated in the CRFCL resistance. The variation in the DC-link voltage is then evaluated, and if the voltage constraint of the DC-link is violated, the q-axis stator current reference and the resistance of the CRFCL are correspondingly readjusted to ensure the successful LVRT of the PMSG.

If the prescribed q-axis stator current reference and CRFCL resistance yield an undervoltage of the DC-link, the active power output of the MSC needs to be increased by increasing the q-axis stator current reference. This situation may occur with minor voltage drops where the comparatively small value of the reactive current injection is required and a large amount of active current is provided to the integrated grid, and the undervoltage of the DC-link

will occur as the active power originally transmitted to the MSC now transforms into kinetic energy stored in the PMSG rotor.

In the other case, with the overvoltage of the DC-link, the active power imbalance may not be compensated merely through storing kinetic energy in the PMSG rotor; thus, the resistance of the CRFCL is increased to dissipate part of the active power imbalance. With the scheme of the CRFCL resistance control shown in Figure 5, the minimum resistance of the CRFCL is determined to minimize the transient active power consumption of the CRFCL during the LVRT. In this way, the active power loss is minimized.

After the fault clearance, the PMSG needs to realize a quick recovery to its initial operation state prior to the LVRT process. To realize the quick recovery of the DC-link voltage to its nominal value, the output of the integral link with the DC-link voltage difference as the input is adjusted to ensure that the q-axis stator current reference is set to its pre-fault value at the initial fault clearance stage. In this way, the active power imbalance between the MSC and GSC will be minimized as the PMSG enters the fault clearance stage. Then, using the outer-loop DC-link voltage control, the DC-link voltage may be quickly controlled to its nominal value.

4 LVRT strategy of the PMSG with faults on the adjacent feeder

4.1 Power control target of the PMSG for active power support

With faults occurring on the feeder adjacent to the integration feeder of the PMSG, first, the converters at the SOP need to respond to this LVRT scenario. For the back-to-back converters at the SOP, the converter at the PMSG side is denoted with the subscript int and the converter at the adjacent feeder is denoted with the subscript adj in this section. With the voltage dip depth k_{adj} at the adjacent feeder, the active power reference of the connected converter during the LVRT, $P_{adj,LVRT}$, is given by Eq. 13 in a similar manner to the transient LVRT control of the PMSG. The connected converter injects reactive current proportional to the voltage drop depth, and the remaining current capacity is utilized for the transient active power output.

$$P_{adj,LVRT} = k_{adj} V_{PCC} \sqrt{\left(I_{adj}^{max}\right)^2 - \left[2\left(0.9 - k_{adj}\right)\right]^2}. \quad (13)$$

Meanwhile, the converter at the PMSG side is currently responsible for maintaining the DC-link voltage at the SOP; thus, the additional active power need, ΔP_{int}, is incorporated into its outer-loop active power control based on the calculation of the increased active power output of the converter at the adjacent feeder side, as given by Eq. 14. The additional active power need is added as a compensation term to the output of the outer-loop PI control with the input of the DC-voltage control difference to ensure the quick response of the active control by the converter at the PMSG side.

$$\Delta P_{int} = P_{adj,LVRT} - P_{adj,ini}. \quad (14)$$

The increased active power demand from the converter at the integration feeder side may be partially or completely provided by the PMSG by releasing the kinetic energy in the PMSG rotor during the LVRT transient. Through the deacceleration process to release the kinetic energy of the PMSG, the rotating speed of the WT needs to be maintained above the critical value $\omega_{WT,cri}$ to prevent instability of the PMSG shaft, as shown in Figure 6.

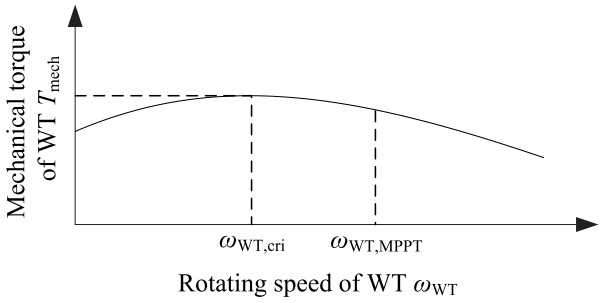

FIGURE 6
Critical rotating speed of the WT corresponding to the instability of the PMSG shaft.

As can be seen from Figure 6, the value of the critical rotating speed of the WT is smaller than its value corresponding to the MPPT operation mode $\omega_{WT,MPPT}$. At the critical rotating speed, the derivative of the mechanical torque of the WT to its rotating speed is zero. Thus, the critical rotating speed may be obtained by solving the mathematical equation given in Eq. 15.

$$\frac{\partial T_{mech}}{\partial \omega_{WT,cri}} = \frac{\partial \left(P_{WT}/\omega_{WT,cri}\right)}{\partial \omega_{WT,cri}} = \frac{\partial P_{WT}}{\partial \omega_{WT,cri}} \frac{1}{\omega_{WT,cri}} - \frac{P_{WT}}{\omega_{WT,cri}^2} = 0. \quad (15)$$

Once the rotating speed of the WT drops below the critical value, the mechanical torque of the WT also decreases, making the PMSG unable to recover to its initial operation state. Thus, increased active power output from the PMSG, ΔP_m, must be constrained to maintain the rotating speed of the WT above its critical value.

It should be noted that the mechanical power captured by the WT needs to be modeled based on the detailed C_p function, as given by Eq. 10, to solve Eq. 15, despite the complexity involved in the calculation process. One classically simplified model assumes that the mechanical power of the WT is proportional to the cube of the rotating speed, but this assumption is only valid for MPPT operation. As shown in Figure 6, at the critical rotating speed, the WT does not work under the MPPT mode; thus, the simplified model cannot be applied here.

4.2 Two-mass shaft model for dynamic rotating speed analysis

As stated in Section 4.1, the rotating speed of the WT needs to be maintained above its critical value when releasing the kinetic energy; thus, the two-mass shaft model is adopted to analyze the dynamic rotating speed of the WT to achieve higher accuracy and eventually obtain an appropriate reference for the increased active power output of the PMSG during the LVRT.

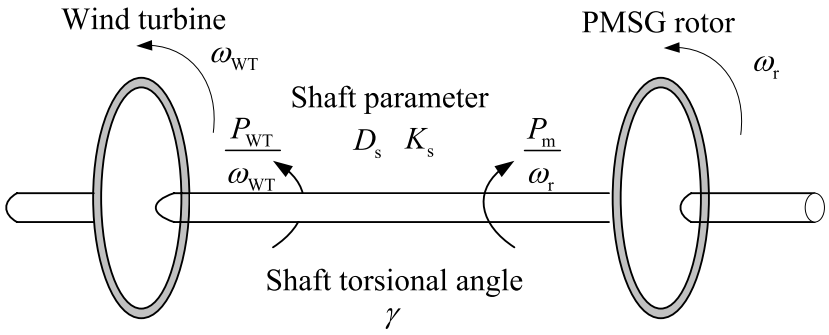

FIGURE 7
Two-mass model of the PMSG shaft.

With the increased active power reference of the PMSG, the rotating speeds of the WT and the rotor may be analyzed based on the two-mass shaft model, as given in Eq. 16. The two-mass model of the PMSG shaft is illustrated in Figure 7. The different inertias of the WT and PMSG rotors are considered in the two-mass model. When increasing the active power output of the PMSG, the electromagnetic torque increases, and the PMSG rotor quickly decreases due to its comparatively smaller inertia. As shown in Eq. 2, the active power control of the PMSG is affected by its rotor speed, and the improved accuracy of rotor speed modeling based on the two-mass shaft is beneficial to the transient power control of the PMSG.

$$\begin{cases} \dfrac{d\omega_{WT}}{dt} = \dfrac{1}{2H_{WT}}\left(\dfrac{P_{WT}}{\omega_{WT}} - D_s(\omega_{WT} - \omega_r) - K_s\gamma\right) \\ \dfrac{d\omega_r}{dt} = \dfrac{1}{2H_r}\left(K_s\gamma - \dfrac{P_m}{\omega_r} - D_s(\omega_r - \omega_{WT})\right) \\ \dfrac{d\gamma}{dt} = \omega_{WT} - \omega_r \\ P_m = P_{m,ini} + \Delta P_m \approx \omega_r \psi_f I_{s,q} \end{cases} \tag{16}$$

where H is the inertia time constant; D_s and K_s are constant coefficients describing the damping and stiffness of the shaft, respectively (Han et al., 2011; Mandic et al., 2012); and γ is the torsional angle of the shaft. With a larger stiffness coefficient, the torque generated by the torsional angle resulting from the difference between the rotating speeds of the WT and PMSG rotors will be increased, i.e., their difference tends to be decreased. On the other hand, with the larger damping coefficient, a similar damping torque is increased, also to reduce the difference between the rotating speeds of the WT and PMSG rotors. In conclusion, with the larger stiffness and damping coefficient, the two-mass shaft will behave more like the one-mass shaft.

With the improved Euler method applied to solve the differential equations in Eq. 16, the rotating speed of the WT at the ending instant of the LVRT process with increased active power output of the PMSG is calculated. Based on the calculation results, the maximized active power support capability of the PMSG is determined to obtain the appropriate active power reference during the LVRT. The solving process of Eq. 16 using the improved Euler method is given by Eq. 17. The flowchart describing the detailed LVRT scheme procedure is shown in Figure 8.

$$\begin{cases} \omega_{WT}^{(n+1)} = \omega_{WT}^{(n)} + \dfrac{\Delta t}{2}\dfrac{1}{2H_{WT}}\left[\dfrac{P_{WT}^{(n)}}{\omega_{WT}^{(n)}} + \dfrac{P_{WT}^{(n+1),pred}}{\omega_{WT}^{(n+1),pred}} - D_s\left(\omega_{WT}^{(n+1),pred} + \omega_{WT}^{(n)} - \omega_r^{(n+1),pred} - \omega_r^{(n)}\right) - K_s\left(\gamma^{(n+1),pred} + \gamma^{(n)}\right)\right] \\ \omega_{WT}^{(n+1),pred} = \omega_{WT}^{(n)} + \Delta t\dfrac{1}{2H_{WT}}\left[\dfrac{P_{WT}^{(n)}}{\omega_{WT}^{(n)}} - D_s\left(\omega_{WT}^{(n)} - \omega_r^{(n)}\right) - K_s\gamma^{(n)}\right] \\ \omega_r^{(n+1)} = \omega_r^{(n)} + \dfrac{\Delta t}{2}\dfrac{1}{2H_r}\left[K_s\left(\gamma^{(n+1),pred} + \gamma^{(n)}\right) - \left(\dfrac{P_m^{(n+1),pred}}{\omega_r^{(n+1),pred}} + \dfrac{P_m^{(n)}}{\omega_r^{(n)}}\right) - D_s\left(\omega_r^{(n+1),pred} + \omega_r^{(n)} - \omega_{WT}^{(n+1),pred} - \omega_{WT}^{(n)}\right)\right] \\ \omega_r^{(n+1),pred} = \omega_r^{(n)} + \Delta t\dfrac{1}{2H_r}\left[K_s\gamma^{(n)} - \dfrac{P_m^{(n)}}{\omega_r^{(n)}} - D_s\left(\omega_r^{(n)} - \omega_{WT}^{(n)}\right)\right] \\ \gamma^{(n+1)} = \gamma^{(n)} + \dfrac{\Delta t}{2}\left(\omega_{WT}^{(n+1),pred} + \omega_{WT}^{(n)} - \omega_r^{(n+1),pred} - \omega_r^{(n)}\right) \\ \gamma^{(n+1),pred} = \gamma^{(n)} + \Delta t\left(\omega_{WT}^{(n)} - \omega_r^{(n)}\right) \end{cases} \tag{17}$$

As shown in Figure 8, the initial active power setting applied to the PMSG is intended to fully compensate for the active power demand from the converter at the PMSG side of the SOP. However, if the calculation of the rotating speed of the WT based on the two-mass model indicates that the instability of the WT will occur with its rotating speed dropping below the critical value, the q-axis stator current reference is reduced to decrease the active power output of the PMSG to the optimal value that both fully utilizes the stored kinetic energy of the PMSG to provide active power support during the LVRT and prevents instability of the PMSG at the same time to enable the PMSG to recover to its initial operation state after the LVRT transient. In Figure 8, the q-axis stator current reference is adjusted to ensure that, at the end of the LVRT duration, the rotating speed of the WT is maintained above its critical value with a plus 3% margin, taking into account the calculation error caused by the improved Euler method to solve the differential equation, as well as the neglection of the pitch angle variation. To further ensure that the instability of the PMSG shaft will not occur, a backup protection scheme is employed that reduces the active power control goal of the PMSG to 80% of the current value of mechanical power captured by the WT, once the rotating speed approaches the critical value, to prevent further dropping of the rotating speed.

To maintain the rotating speed of the WT above its critical value, the speed control of the PMSG may be applied to replace the active power control of the MSC. This scheme is not adopted here for the following two reasons: on one hand, this scheme still contains the outer-loop PI control; thus, it may not provide a fast response during the LVRT transient. On the other hand, the parameters of the speed control require careful tuning to avoid the rotor speed dropping below its critical value during the control transient.

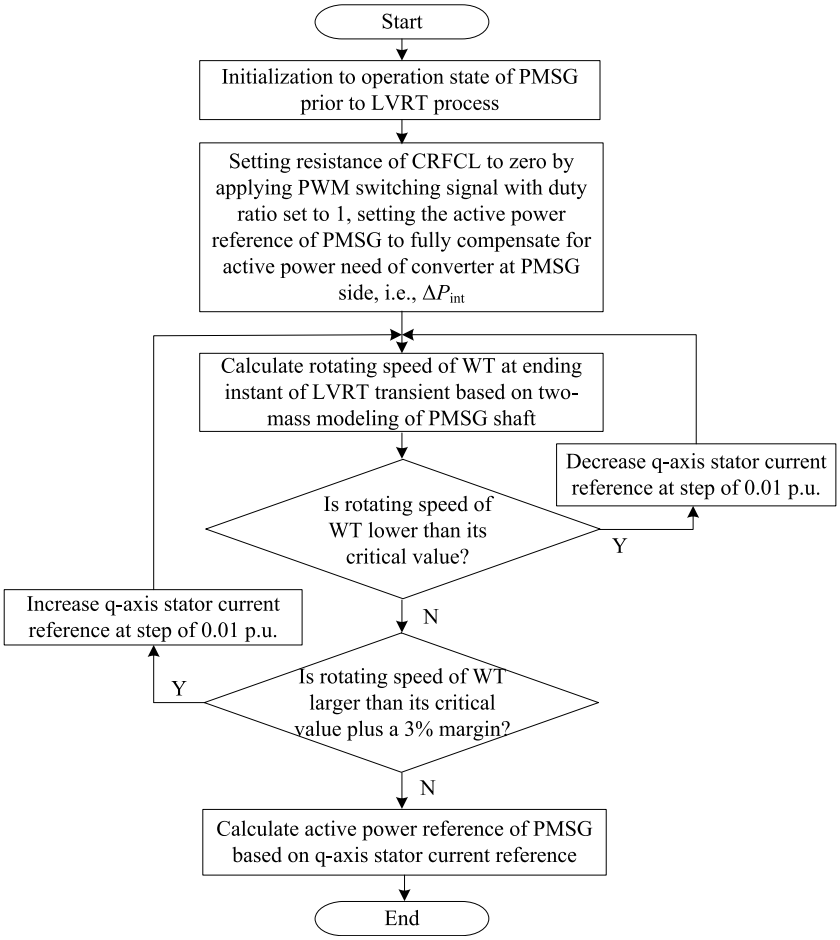

FIGURE 8
Flowchart to determine the active power reference of the PMSG with faults on the adjacent feeder.

TABLE 1 Parameters of the PMSG (Huang et al., 2021).

Variable	Description	Value (unit)
$L_{s,d}$	Direct-axis inductance of the stator	0.5 (p.u.)
$L_{s,q}$	Quadrature-axis inductance of the stator	0.5 (p.u.)
ψ_f	Flux of the PMSG	1 (p.u.)
R_s	Resistance of the stator	0.0025 (p.u.)
C	DC-link capacitance	0.21 (p.u.)
H_{eq}	Equivalent inertia time constant of the PMSG shaft	2.5 (s)
H_{WT}	Equivalent inertia time constant of the WT	2 (s)
H_r	Equivalent inertia time constant of the PMSG rotor	0.5 (s)
D_s	Shaft damping constant	25.5 (p.u)
K_s	Shaft stiffness constant	0.1 (p.u.)
ρ	Air density	1.225 (kg/m^3)
r	Radius of the WT	35.5 (m)

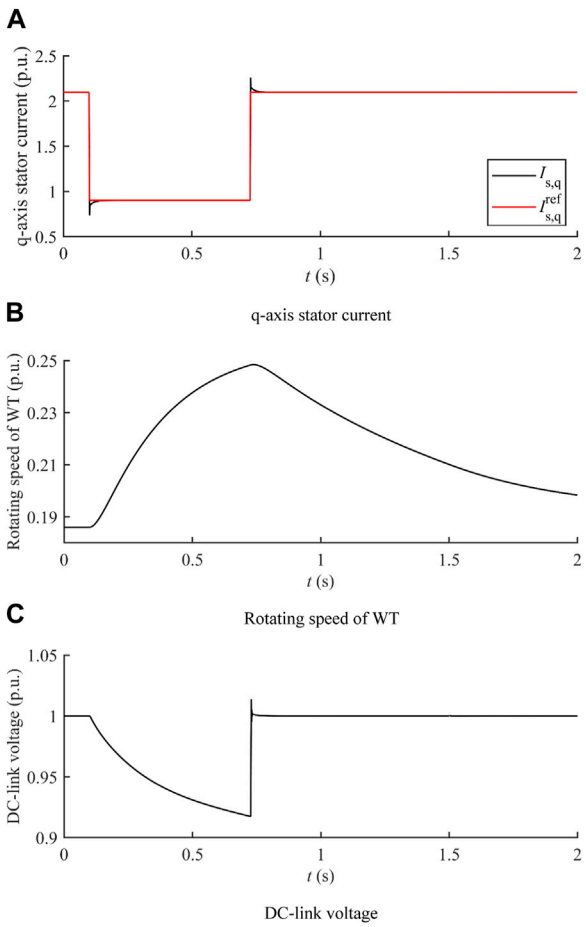

FIGURE 9
LVRT transient under a minor voltage dip with no CRFCL resistance. **(A)** q-axis stator current. **(B)** Rotating speed of the WT. **(C)** DC-link voltage.

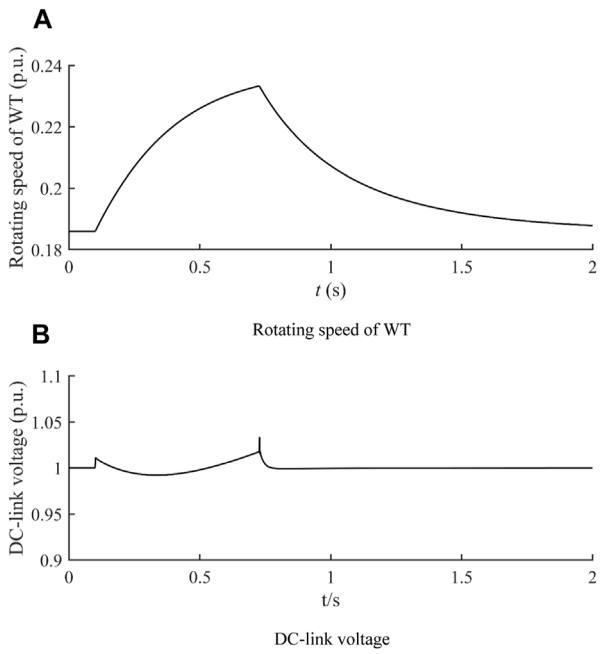

FIGURE 10
LVRT transient under a minor voltage dip with the DC-link voltage maintained close to the nominal value. **(A)** Rotating speed of the WT. **(B)** DC-link voltage.

5 Numerical analysis

5.1 Parameters of the simulation system

The detailed parameters of the PMSG used for the simulation analysis are provided in Table 1. The parameters of the C_p function are referred to in Li (2015). As for the LVRT analysis, the fault occurs at t = 0.1 s and lasts for 0.625 s.

5.2 Verification of the LVRT strategy of the PMSG with faults on the integration feeder

In this section, the effectiveness of the LVRT strategy with faults occurring on the integration feeder of the PMSG is verified.

5.2.1 Transient LVRT control with no need for CRFCL resistance

During the LVRT, the output active power of the GSC is reduced according to grid code requirements and the voltage dip depth, as given by Eq. 6. In this subsection, a minor voltage dip under a wind speed of 9 m/s is considered, and in this case, the active power output of the GSC is reduced to 70% of its pre-fault value. The calculated q-axis stator current that leads the rotating speed of the WT to its maximum value is 0.9 p. u., and no CRFCL resistance is applied. The transient q-axis stator current, rotating speed of the WT, and DC-link voltage are shown in Figure 9.

The quick response of the inner-loop current control is verified based on the transient stator q-axis current shown in Figure 9A. The q-axis stator current is capable of tracking its reference within a short duration of time, which enhances the transient active power control capability of the PMSG. Figure 9B shows that the calculated q-axis stator current reference can maximize the kinetic energy stored in the WT during the LVRT. With a minor voltage dip, the active power imbalance is comparatively small and can be solely compensated with kinetic energy stored in the WT. The reduced active power output of the MSC yields the voltage drop of the DC-link, as shown in Figure 9C. Generally, the DC-link voltage should not fall below 0.95 p. u. The setting value of the allowable DC-link voltage drop (0.05 p. u.) is smaller than that of the allowable DC-link voltage increase (0.2 p. u.) as the converter voltage control will be affected by the undervoltage of the DC-link. In this case, the q-axis stator current reference may be increased to the value that yields smaller deviations of the DC-link voltage.

By increasing the q-axis stator current reference, the power transmitted to the MSC is increased to reduce the deviation of the DC-link voltage. With the q-axis stator current reference increased to 1.25 p. u., the active power input of the MSC is increased, and the increment of the rotating speed during the LVRT is reduced due to the increased active power. Meanwhile, the undervoltage of the DC-link is avoided, with the DC-link voltage maintained close to its nominal value during the whole LVRT process, as verified by the results shown in Figure 10.

As the q-axis stator current reference further increases, the active power output of the MSC is also increased, and the upper

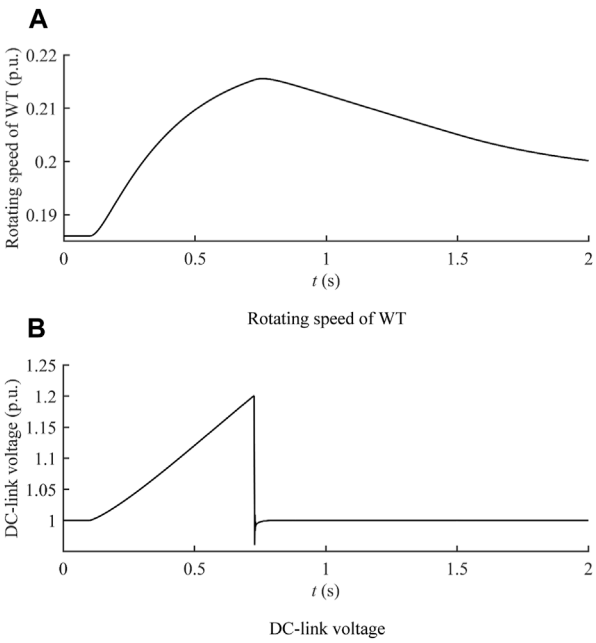

FIGURE 11
LVRT transient under a minor voltage dip with the maximum q-axis stator current reference. **(A)** Rotating speed of the WT. **(B)** DC-link voltage.

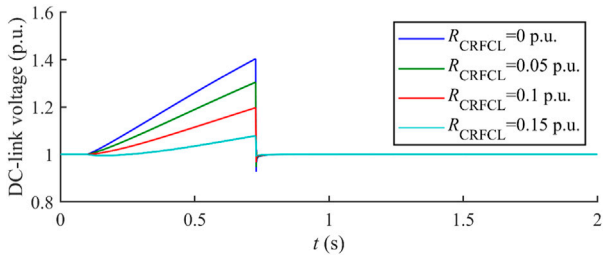

FIGURE 12
Comparison of transient DC-link voltage with different CRFCL resistance values.

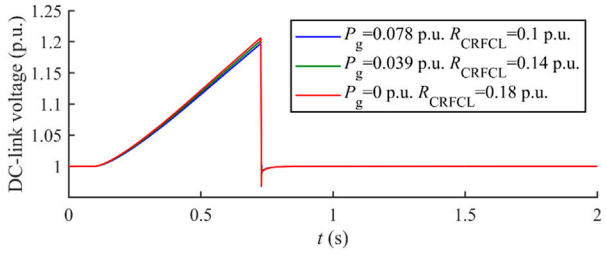

FIGURE 13
Optimal CRFCL resistance with different active power output values of the GSC during the LVRT.

limit of the q-axis stator current reference is reached once the DC-link voltage reaches its maximum feasible value at the ending instant of the LVRT transient, as shown in Figure 11.

As shown in Figure 11B, with the q-axis stator current reference increased to 1.4 p. u., the upper limit of the DC-link voltage is reached, which denotes the maximum active power output capability of the MSC during the LVRT. Figure 11A shows that, under the minor voltage drop, the active power output of the MSC can be increased to enhance the active power support capability of the PMSG, as long as the DC-link voltage does not increase above its upper constraint, instead of utilizing the full capacity of kinetic energy storage of the WT to reduce the active power imbalance between the MSC and GSC.

5.2.2 Transient LVRT control with coordinated CRFCL and converter control

In this subsection, a severe voltage dip under the wind speed of 9 m/s is considered, and in this case, the active power output of the GSC is reduced to 20% of its pre-fault value. The calculated q-axis stator current that leads the rotating speed of the WT to its maximum value is 0.98 p. u. However, with the greatly reduced active power output of the GSC under the severe voltage dip, the active power imbalance between the MSC and GSC needs to be partially dissipated in CRFCL resistance to avoid the overvoltage of the DC-link. The calculation result of the optimal CRFCL resistance in this case is 0.1 p. u. The comparison between different CRFCL resistances, as displayed in Figure 12, shows that the optimal resistance can avoid the overvoltage of the DC-link while minimizing the active power dissipated in the CRFCL resistance at the same time.

With the active power output of the GSC further dropping from 20% of its pre-fault value to 0% of its pre-fault value (0.078 p. u. to 0 p. u.), the active power imbalance between the MSC and GSC is increased; thus, the required CRFCL resistance to maintain the DC-link voltage within security constraints is increased alongside, as revealed by the optimal CRFCL resistance values with the decreasing active power output of the GSC during the LVRT shown in Figure 13.

5.2.3 Evaluation of LVRT effectiveness under different wind speeds

In this subsection, a severe voltage dip is considered, and in this case, the active power output of the GSC is reduced to 0% of its pre-fault value. Different wind speeds are considered, and with each wind speed, the q-axis stator current reference and the optimal CRFCL resistance are obtained based on the procedure illustrated in Figure 5. The transient rotating speed of the WT and DC-link voltage under different wind speeds with optimized q-axis stator current reference and CRFCL resistance are shown in Figure 14.

Figure 14A shows that the initial rotating speed of the WT is higher at high wind speeds; thus, the capacity for kinetic energy storage is smaller. In this case, the optimal q-axis stator current reference is increased to provide larger electromagnetic torque so as to avoid the overspeed of WT. Meanwhile, the optimal q-axis stator current reference is capable of fully utilizing the available capacity for kinetic energy storage as the rotating speeds of the WT all approach their upper limit under the different wind speeds. Based on the optimal q-axis stator current references, corresponding CRFCL resistance values that avoid overvoltage of the DC-link with the

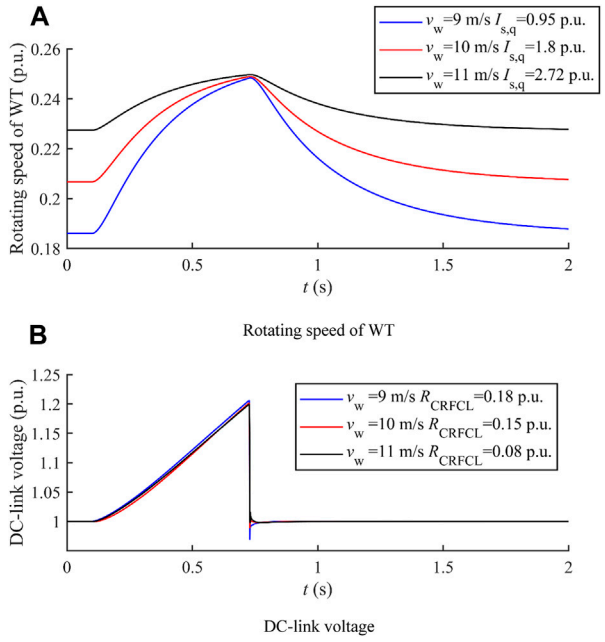

FIGURE 14
LVRT transient with optimized q-axis stator current and CRFCL resistance under different wind speeds. **(A)** Rotating speed of the WT. **(B)** DC-link voltage.

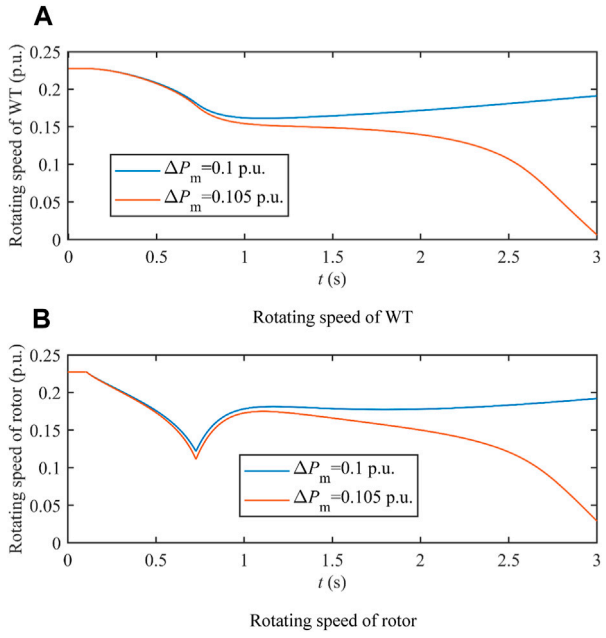

FIGURE 15
Transient rotating speeds of the WT and rotor with different active power increments. **(A)** Rotating speed of the WT. **(B)** Rotating speed of the rotor.

minimized active power consumed by the CRFCL are determined, and their effectiveness under different wind speeds is verified, as shown in Figure 14B.

5.3 Verification of the LVRT strategy of PMSG with faults on the adjacent feeder

In this section, the effectiveness of the LVRT strategy with faults occurring on the feeder adjacent to the integration feeder of the PMSG is verified.

5.3.1 Maximized active power support capability considering the stability of the PMSG shaft

With faults occurring on the adjacent feeder, the PMSG may provide active power support to the adjacent feeder through SOP during the LVRT. It needs to be ensured that, with an increased active power output of the PMSG, the rotating speed of the WT will not drop below the critical value related to shaft instability. Under wind speed 11 m/s, through a calculation based on the flowchart shown in Figure 8, it is determined that the maximum increase in the active power output of the PMSG during the LVRT duration (0.1 s–0.725 s) is 0.1 p.u. The transient rotating speeds of the WT and the rotor with different active power increments are compared in Figure 15.

The correctness of the calculated maximum active power increment of the PMSG (0.1 p.u.) is verified by the results shown in Figure 15. Even with the slightly larger active power increase (0.105 p.u.), the WT will deaccelerate to a rotating speed smaller than its critical value; thus, the WT keeps deaccelerating even after the active power output of the PMSG recovers to its pre-fault value.

5.3.2 Verification of the necessity to incorporate two-mass modeling of the PMSG shaft

As can be seen from Figure 15, the transient rotating speeds of the WT and rotor are different due to their different inertia and the stiffness and damping of the shaft. Given that the instability of the PMSG shaft is closely related to the rotating speed of the WT, the two-mass model of the shaft is capable of providing more accurate results of the rotating speeds of the WT and rotor. In this subsection, the necessity of adopting two-mass modeling is further verified. With the active power increment of the PMSG set to 0.105 p.u., the previous results shown in Figure 15 indicate that instability of the PMSG shaft will occur with analysis based on the two-mass model of the shaft. With the one-mass model of the shaft, the result of the rotating speed of the WT is shown in Figure 16, in comparison to results based on the two-mass model.

Figure 16 shows that, with the one-mass model, instability of the PMSG shaft will not occur. This is because the one-mass model combines the WT with the larger inertia and the rotor with the smaller inertia; thus, the rotor speed change is underestimated by the one-mass model. With the smaller inertia, a rotor speed deaccelerates at a faster speed. With the smaller rotor speed, the larger electromagnetic torque is required to maintain the active power output of the PMSG, which further leads to the deacceleration of both the WT and rotor. Based on the results shown in Figure 16, with the one-mass modeling of the PMSG shaft, the optimistic result of the deacceleration with the active power output increment is yielded, failing to prevent instability issues with the PMSG shaft. The results in Figure 17 show that, with the one-mass model of the shaft, it is estimated that instability of the shaft will

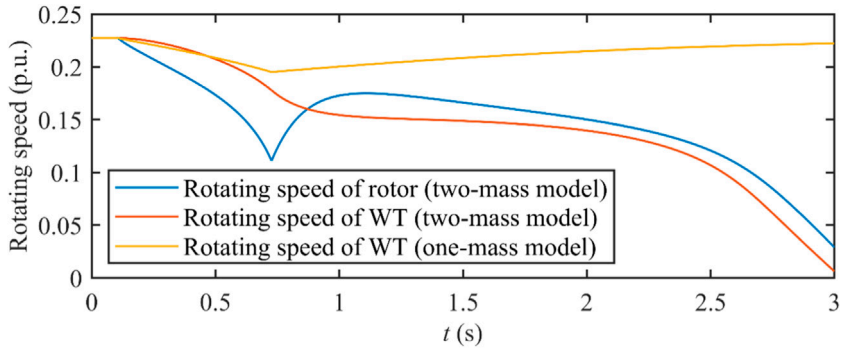

FIGURE 16
Rotating speeds of WT and the rotor with a 0.105 p. u. active power increment based on one-mass and two-mass modeling.

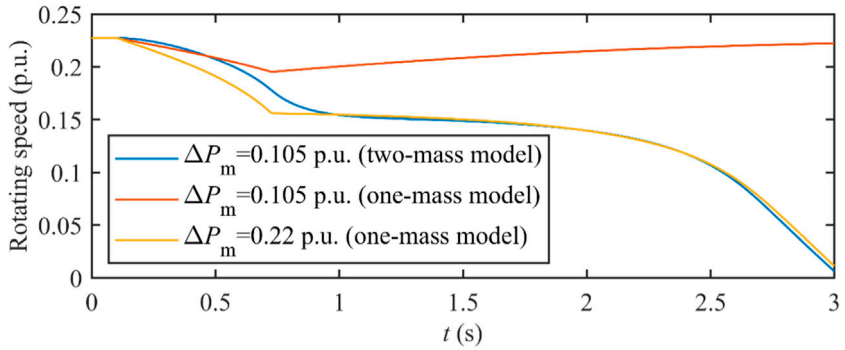

FIGURE 17
Evaluation results of the maximum active power output increment with different shaft models.

occur until the active power increment increases to approximately 0.22 p.u., which is far larger than the result obtained based on the more accurate two-mass modeling (0.105 p.u.), showing the necessity to incorporate two-mass shaft modeling.

6 Conclusion

In this paper, the LVRT strategy for the PMSG integrated into the FIDN is designed considering faults occurring on different feeders. With faults on the integration feeder of the PMSG, a coordinated scheme between control to the converters and CRFCL is developed, which is capable of realizing optimization targets, including storing imbalanced active power as kinetic energy of the PMSG, maintaining the DC-link voltage within its security constraints, and minimizing the active power dissipated in CRFCL resistance. With faults occurring on the feeder adjacent to the integration feeder of the PMSG, active power support is provided by the PMSG if needed, and the scheme to determine the maximum active power support capability is designed to avoid the instability of the PMSG shaft resulting from constant deacceleration. Based on the results of the numerical analysis, the following conclusions are drawn:

(i) During the LVRT with faults on the integration feeder of the PMSG, through optimization of its q-axis stator current reference, the capability of the PMSG to store the imbalanced active power as kinetic energy is fully utilized with the rotating speed of the WT controlled to its maximum value at the ending instant of the LVRT transient.

(ii) During the LVRT with faults on the integration feeder of the PMSG, through optimization of the resistance of the CRFCL, the minimized CRFCL resistance needed to keep the DC-link voltage within its security constraint is obtained to realize a successful LVRT with the minimum active power loss on the CRFCL.

(iii) During the LVRT with faults on the adjacent feeder, the maximum active power increment of the PMSG is determined based on the two-mass modeling of the shaft, which ensures that the rotating speed of the WT is kept within the stable operation range during the LVRT transient.

Data availability statement

The raw data supporting the conclusion of this article will be made available by the authors, without undue reservation.

Author contributions

LY: conceptualization, data curation, and writing–original draft. YL: conceptualization, project administration, resources, software, and writing–review and editing. YZ: data curation, formal analysis, investigation, methodology, and writing–review and editing. ZX: methodology, project administration, resources, and writing–review and editing. JC: data curation, investigation, resources, and writing–review and editing. YQ: resources, validation, and writing–review and editing. GS: writing–review and editing, methodology, validation, investigation.

Funding

The author(s) declare that financial support was received for the research, authorship, and/or publication of this article. This work is supported by the Science and Technology Project of Xingyi Power Supply Bureau of Guizhou Power Grid Co., Ltd (0606002023030103JH00011).

Conflict of interest

Authors LY, YL, and ZX were employed by Xingyi Power Supply Bureau of Guizhou Power Grid Co., Ltd.

Authors YZ, JC, and YQ were employed by Guizhou Power Grid Co., Ltd.

The remaining authors declare that the research was conducted in the absence of any commercial or financial relationships that could be construed as a potential conflict of interest.

The authors declare that this study received funding from Xingyi Power Supply Bureau of Guizhou Power Grid Co., Ltd. The funder had the following involvement in the study: preparation of the manuscript and decision to publish.

Publisher's note

References

Alepuz, S., Calle, A., Busquets-Monge, S., Kouro, S., and Wu, B. (2013). Use of stored energy in PMSG rotor inertia for low-voltage ride-through in back-to-back NPC converter-based wind power systems. *IEEE Trans. Ind. Electron.* 60 (5), 1787–1796. doi:10.1109/tie.2012.2190954

Behzad, N. S., and Negnevitsky, M. (2015). *Soft and fast starting induction motors using controllable resistive type fault current limiter*. Denver, CO, USA: IEEE Power and Energy Society General Meeting, 1–5.

Yang, D., Wang, X., Chen, W., and Yan, G. (2024). Adaptive Frequency Droop Feedback Control-Based Power Tracking Operation of a DFIG for Temporary Frequency Regulation. *IEEE Trans. Power Syst.* 39 (2), 2682–2692. doi:10.1109/TPWRS.2023.3277009

Firouzi, M., Nasiri, M., Senbouzid, M., and Gharehpetian, G. B. (2020). Application of multi-step bridge-type fault current limiter for fault ride-through capability enhancement of permanent magnet synchronous generator-based wind turbines. *Int. Trans. Electr. Energy Syst.* 30 (11), e12611. doi:10.1002/2050-7038.12611

Geng, H., Liu, L., and Li, R. (2018). Synchronization and reactive current support of PMSG-based wind farm during severe grid fault. *IEEE Trans. Sustain. Energy* 9 (4), 1596–1604. doi:10.1109/tste.2018.2799197

Han, X., Wang, P., Wang, P., and Qin, W. (2011). "Transient stability studies of doubly-fed induction generator using different drive train models," in *2011 IEEE power and* (Detroit, MI, USA: Energy Society General Meeting), 1–6.

Hanson, A. D., and Michalke, G. (2009). Multi-pole permanent-magnet synchronous generator wind turbines' grid support capability in uninterrupted operation during grid faults. *IET Renew. Power Gener.* 3 (3), 333–348. doi:10.1049/iet-rpg.2008.0055

He, Yu., Wang, M., and Xu, Z. (2020). Coordinative low-voltage-ride-through control for the wind-photovoltaic hybrid generation system. *IEEE J. Emerg. Sel. Top. Power Electron.* 8 (2), 1503–1514. doi:10.1109/jestpe.2019.2958213

Huang, C., Xiao, X. Y., Zheng, Z., and Wang, Y. (2019). Cooperative control of SFCL and SMES for protecting PMSG-based WTGs under grid faults. *IEEE Trans. Appl. Supercond.* 29 (2), 1–6. doi:10.1109/tasc.2019.2891908

Huang, C., Zheng, Z., Xiao, X., and Chen, X. (2020). Enhancing low-voltage ride-through capability of PMSG based on cost-effective fault current limiter and modified WTG control. *Electr. Power Syst. Res.* 185, 106358. doi:10.1016/j.epsr.2020.106358

Huang, J., and Li, S. (2020). Asymmetrical LVRT of DFIG incorporating feed-forward transient current control and controllable resistive-type fault current limiter. *IEEJ Trans. Elec. Electron. Eng.* 15, 1100–1108. doi:10.1002/tee.23155

Huang, J., Sang, S., Zhang, L., Xue, X., Yang, D., and Zhang, X. (2021). "Small signal stability analysis of PMSG with different orientations under pitch angle regulation," in 2021 IEEE Sustainable Power and Energy Conference, Nanjing, China, December 2021, 1438–1443.

Ji, H., Jian, J., Yu, H., Ji, J., Wei, M., Zhang, X., et al. (2022). Peer-to-peer electricity trading of interconnected flexible distribution networks based on distributed ledger. *IEEE Trans. Ind. Inf.* 18 (9), 5949–5960. doi:10.1109/tii.2021.3137220

Ji, T., He, X., Li, X., Liu, K., and Zhang, M. (2014). "Performance analysis and research on LVRT of PMSG wind power systems with SDBR," in Proceedings of the 33rd Chinese Control Conference, Nanjing, July 2014, 6953–6958.

Kim, S., Kang, B., Bae, S., and Park, J. (2013). Application of SMES and grid code compliance to wind/photovoltaic generation system. *IEEE Trans. Appl. Supercond.* 23 (3), 5000804. doi:10.1109/tasc.2012.2232962

Li, S. (2015). "Multiple solutions of PMSG with different orientations and reference powers," in *2015 IEEE power* (Denver, CO, USA: Energy Society General Meeting), 1–5.

Li, S., Huang, J., and Wang, Z. (2017). "Inner-loop current control for low-voltage ride-through of permanent-magnet synchronous generator," in 43rd Annual Conference of the IEEE Industrial Electronics Society, Beijing, China, October-November 2017, 2546–2551.

Li, Y., Chen, X., Li, W., Yu, S., Xu, S., Wei, T., et al. (2022). Research on interconnection structure and control technology of flexible distribution network based on soft open point in parallel with interconnection switch. *Proc. CSEE.* 42 (13), 4749–4759. doi:10.13334/j.0258-8013.pcsee.210479

Liu, J., Sun, K., Li, K., Li, Y., and Zhang, J. (2023b). A novel power injection priority optimization strategy for voltage support control of PMSG-based wind farm. *IEEE Trans. Ind. Appl.* 59 (2), 2152–2161. doi:10.1109/tia.2022.3228226

Liu, Y., Guan, L., Chen, J., Shi, G., Zheng, J., Wei, T., et al. (2023a). Over-current mechanism and suppression strategy of DC transformer in multiterminal interconnected flexible DC distribution network. *IEEE Syst. J.* 17 (2), 1785–1796. doi:10.1109/jsyst.2023.3241053

Mandic, G., Nasiri, A., Muljadi, E., and Oyague, F. (2012). Active torque control for gearbox load reduction in a variable-speed wind turbine. *IEEE Trans. Ind. Appl.* 48 (6), 2424–2432. doi:10.1109/tia.2012.2227131

Marmouh, S., Boutoubat, M., Mokrani, L., and Machmoum, M. (2019). A coordinated control and management strategy of a wind energy conversion system for a universal low-voltage ride-through capability. *Int. Trans. Electr. Energy Syst.* 29 (8), e12035. doi:10.1002/2050-7038.12035

Okedu, K. E. (2022). Improving the performance of PMSG wind turbines during grid fault considering different strategies of fault current limiters. *Front. Energy Res.* 10, 909044. doi:10.3389/fenrg.2022.909044

Pradhan, S., Singh, B., and Panigrahi, K. (2022). Adaptive position observer for multimode wind-BES based Microgrid interfaced to distribution network. *IEEE Trans. Ind. Appl.* 58 (4), 5081–5092. doi:10.1109/tia.2022.3170003

Wu, Y., Chang, S., and Mandal, P. (2019). Grid-connected wind power plants: a survey on the integration requirements in modern grid codes. *IEEE Trans. Ind. Appl.* 55 (6), 5584–5593. doi:10.1109/tia.2019.2934081

Xie, Q., Zheng, Z., Huang, C., and Dai, T. (2021). Coordinated fault ride through method for PMSG-based wind turbine using SFCL and modified control strategy. *IEEE Trans. Appl. Supercond.* 31 (8), 1–5. doi:10.1109/tasc.2021.3103730

Xing, P., Fu, L., Wang, G., Wang, Y., and Zhang, Y. (2018). A compositive control method of low-voltage ride through for PMSG-based wind turbine generator system. *IET Gener. Transm. Distri.* 12 (1), 117–125. doi:10.1049/iet-gtd.2017.0270

Xiong, L., Liu, X., Zhang, D., and Liu, Y. (2021). Rapid power compensation-based frequency response strategy for low-inertia power systems. *IEEE J. Emerg. Sel. Top. Power Electron.* 9 (4), 4500–4513. doi:10.1109/jestpe.2020.3032063

Xiong, L., Liu, X., Zhao, C., and Zhuo, F. (2020). A fast and robust real-time detection algorithm of decaying DC transient and harmonic components in three-phase systems. *IEEE Trans. Power Electron.* 35 (4), 3332–3336. doi:10.1109/tpel.2019.2940891

Xiong, L., Zhuo, F., Wang, F., Liu, X., Chen, Y., Zhu, M., et al. (2016). Static synchronous generator model: a new perspective to investigate dynamic characteristics and stability issues of grid-tied PWM inverter. *IEEE Tran. Power Electron.* 31 (9), 6264–6280. doi:10.1109/tpel.2015.2498933

Yang, H., Yuan, S., Wang, Z., Qiu, X., and Liang, D. (2022). Adaptive model predictive scheduling of flexible interconnected low-voltage distribution networks considering charging preferences of electric vehicles. *Front. Energy Res.* 10, 1009238. doi:10.3389/fenrg.2022.1009238

Yang, X., Zhou, Z., Zhang, Y., Liu, J., Wen, J., Wu, Q., et al. (2023). Resilience-oriented co-deployment of remote-controlled switches and soft open points in distribution networks. *IEEE Trans. Power Syst.* 38 (2), 1350–1365. doi:10.1109/tpwrs.2022.3176024

Yao, J., Pei, J., Xu, D., Liu, R., Wang, X., Wang, C., et al. (2018). Coordinated control of a hybrid wind farm with DFIG-based and PMSG-based wind power generation systems under asymmetrical grid faults. *Renew. Energy* 127, 613–629. doi:10.1016/j.renene.2018.04.080

Yassin, H. M., Hanafy, H. H., and Hallouda, M. M. (2016). Enhancement low-voltage ride through capability of permanent-magnet synchronous generator-based wind turbines using interval type-2 fuzzy control. *IET Renew. Power Gener.* 10 (3), 339–348. doi:10.1049/iet-rpg.2014.0453

Yuan, X., Wang, F., Boroyevich, D., Li, Y., and Burgos, R. (2009). DC-link voltage control of a full power converter for wind generator operating in weak-grid systems. *IEEE Trans. Power Electron.* 24 (9), 2178–2192. doi:10.1109/tpel.2009.2022082

Zhou, A., Li, Y. W., and Mohamed, Y. (2021). Mechanical stress comparison of PMSG wind turbine LVRT methods. *IEEE Trans. Energy Convers.* 36 (2), 682–692. doi:10.1109/tec.2020.3018093

frontiers | Frontiers in Energy Research

TYPE Brief Research Report
PUBLISHED 09 July 2024
DOI 10.3389/fenrg.2024.1425105

OPEN ACCESS

EDITED BY
Liansong Xiong,
Xi'an Jiaotong University, China

REVIEWED BY
Xiaokang Liu,
Polytechnic University of Milan, Italy
Meng Chen,
University of Cambridge, United Kingdom
Yonghui Liu,
Hong Kong Polytechnic University, Hong Kong, SAR China

*CORRESPONDENCE
Chao Wu,
wuchao@sjtu.edu.cn

RECEIVED 29 April 2024
ACCEPTED 04 June 2024
PUBLISHED 09 July 2024

CITATION
Wu C, Huang Z, Wang Y and Blaabjerg F (2024), A new transient phenomenon caused by active current dynamics of grid-following converters during severe grid faults.
Front. Energy Res. 12:1425105.
doi: 10.3389/fenrg.2024.1425105

A new transient phenomenon caused by active current dynamics of grid-following converters during severe grid faults

Chao Wu[1]*, Zhanqi Huang[1], Yong Wang[1] and Frede Blaabjerg[2]

[1]Renewable Energy and Automotive Electronics Laboratory, Department of Electrical Engineering, Shanghai Jiao Tong University, Shanghai, China, [2]AAU Energy, Aalborg University, Aalborg, Denmark

Existing transient stability analysis of grid-following (GFL) converters mainly focuses on the dynamics of the phase-locked loop (PLL), while current loop dynamics are usually neglected due to their faster response than PLL. However, this article reveals that active current may not be able to track its reference quickly during severe grid faults even with high current loop bandwidth, which leads to a non-negligible impact on the transient stability of GFL converters. Furthermore, this article discusses the intrinsic mechanism of why active current cannot track its reference quickly during severe grid faults and establishes a refined third-order transient synchronization model that offers a more accurate assessment of transient stability during severe grid faults than the conventional second-order model.

KEYWORDS

grid-following converter, severe grid fault, transient stability, active current dynamic, phase-locked loop

1 Introduction

With the continuous integration of renewable energy into modern power systems through grid-following (GFL) converters, the transient stability of GFL converters during grid faults is receiving increasing attention. It has been found that a GFL converter may experience loss of synchronization (LOS) during grid faults (Göksu et al., 2014; Xiong et al., 2020). Various analysis techniques have been applied to understand the synchronization instability mechanism, such as the equal-area criteria (He et al., 2021), phase portraits (Wu and Wang, 2020), and the energy function method (Tian et al., 2022).

The aforementioned studies mainly focus on the dynamics of the phase-locked loop (PLL), neglecting the current loop dynamics due to their faster response. However, it has been pointed out that ignoring current loop dynamics when the current loop bandwidth is not high enough may lead to incorrect transient stability assessment (Chen et al., 2020). Then, a high-order transient synchronization model considering the coupling effect between the PLL and current loop is established to analyze the impact mechanism of current loop dynamics (Hu et al., 2021). Furthermore, the work by Wu et al. (2024) gives a conservative bandwidth boundary that can ignore the current loop dynamics. The above studies suggest that the current loop dynamics may harm the transient stability of GFL converters. Nevertheless, the changes in the current reference are not considered, which could potentially invalidate the conclusion during severe grid faults.

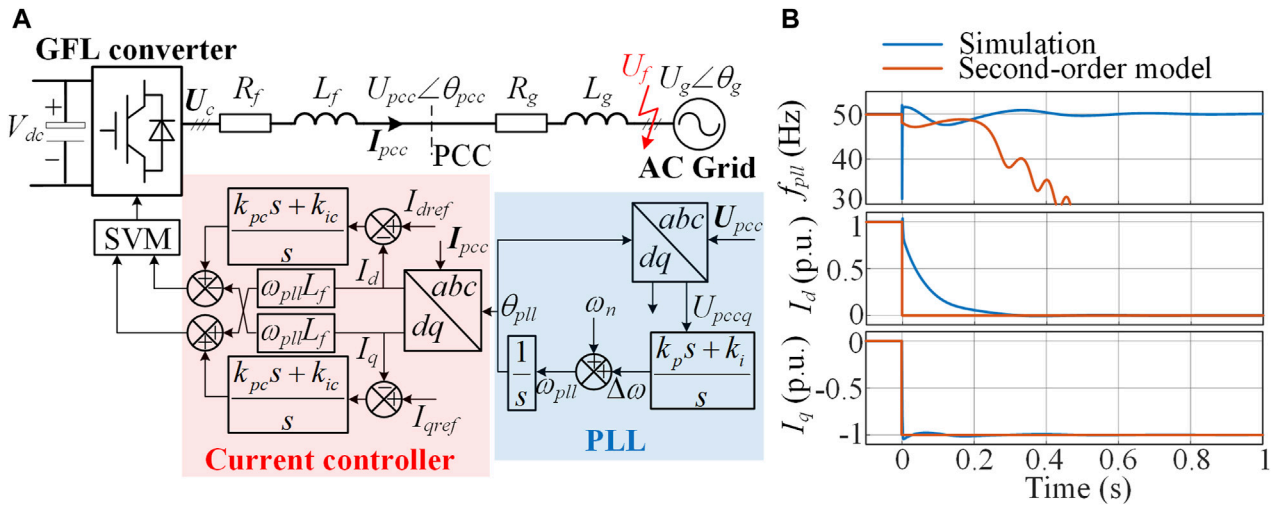

FIGURE 1
(A) Topology and control diagram of the GFL converter, and **(B)** simulation results and solutions of the second-order model with a grid fault voltage of U_f = 0.05 p.u.

In fact, according to the grid code requirements, GFL converters must inject reactive current to support the grid voltage during the low-voltage ride-through process. Particularly, GFL converters should inject pure reactive current during severe grid faults (Yuan et al., 2019). Under this situation, this article observes that although reactive current tracks its reference quickly, active current may undergo obvious dynamic attenuation even with high current loop bandwidth. This phenomenon challenges the assumption of treating the current loop as a unity gain in transient stability modeling, as the active current dynamics have a non-negligible impact on the transient stability. The zero-pole characteristics of the current loop are analyzed to reveal the intrinsic mechanism of why active current cannot track its reference quickly during severe grid faults. Then, a refined third-order transient synchronization model considering active current dynamics is established, which offers a more accurate assessment of the transient stability during severe grid faults than the conventional second-order model. Finally, the impact of active current dynamics is validated through experimental results.

2 Misjudgment of the second-order model

Figure 1A illustrates the topology and control diagram of the GFL converter. $\boldsymbol{U}_{pcc} = U_{pcc}\angle\theta_{pcc}$ represents the voltage of the point of common coupling (PCC). $\boldsymbol{U}_g = U_g\angle\theta_g$ represents the grid voltage. $\boldsymbol{U}_c$ represents the voltage at the converter port. $\boldsymbol{I}_{pcc}$ is the output current of the converter. L_f and R_f are the filter inductance and parasitic resistance. L_g and R_g are the grid inductance and resistance.

A synchronous reference frame PLL is used to extract the phase angle information of the point of common coupling (PCC) voltage, in which θ_{pll} and ω_{pll} are the output phase angle and angular frequency, respectively. ω_n is the norm angular frequency, which is a constant of 100π. k_p and k_i are the PI parameters of the PLL. The current control in Figure 1A is oriented by the PLL. The outer loop control is disconnected during grid faults, and the current references I_{dref} and I_{qref} are directly designated according to the grid code (Yuan et al., 2019; He et al., 2021). The PI parameters of the current control are denoted as k_{pc} and k_{ic}.

According to Tian et al. (2022), if the current loop is approximated as a unity gain, that is, $I_d \approx I_{dref}$ and $I_q \approx I_{qref}$, the transient synchronization process of the GFL converter during grid faults can be described by a second-order nonlinear model as (1), in which the phase error of the PLL is defined as $\delta = \theta_{pll} - \theta_g$.

$$\begin{cases} \dot{\delta} = \Delta\omega \\ \Delta\dot{\omega} = \dfrac{-U_f k_p \dot{\delta}\cos\delta + k_i\left(-U_f\sin\delta + \omega_{pll}L_g I_{dref} + R_g I_{qref}\right).}{1 - k_p L_g I_{dref}} \end{cases} \tag{1}$$

When a severe grid fault occurs with a fault voltage of U_f = 0.05 p.u., simulation results and solutions of the second-order model are as shown in Figure 1B. The solutions of the second-order model show that the PLL frequency f_{pll} is unable to converge, and LOS occurs. However, the simulation results demonstrate that only the reactive current I_q tracks its reference quickly, while active current I_d undergoes obvious dynamic attenuation even with a high current loop bandwidth of 500 Hz. The simulation system ultimately maintains synchronicity with the grid, which contradicts the results of the second-order model. The above results indicate that the second-order model cannot capture the dynamic process of active current during severe grid faults, leading to a misjudgment of transient stability.

3 Intrinsic mechanism of active current dynamics during severe grid faults

According to the main circuit structure in Figure 1A, the dq-axis voltage at the converter port can be obtained as (2), where $R = R_f + R_g$ represents the sum of the parasitic filter resistance and the grid

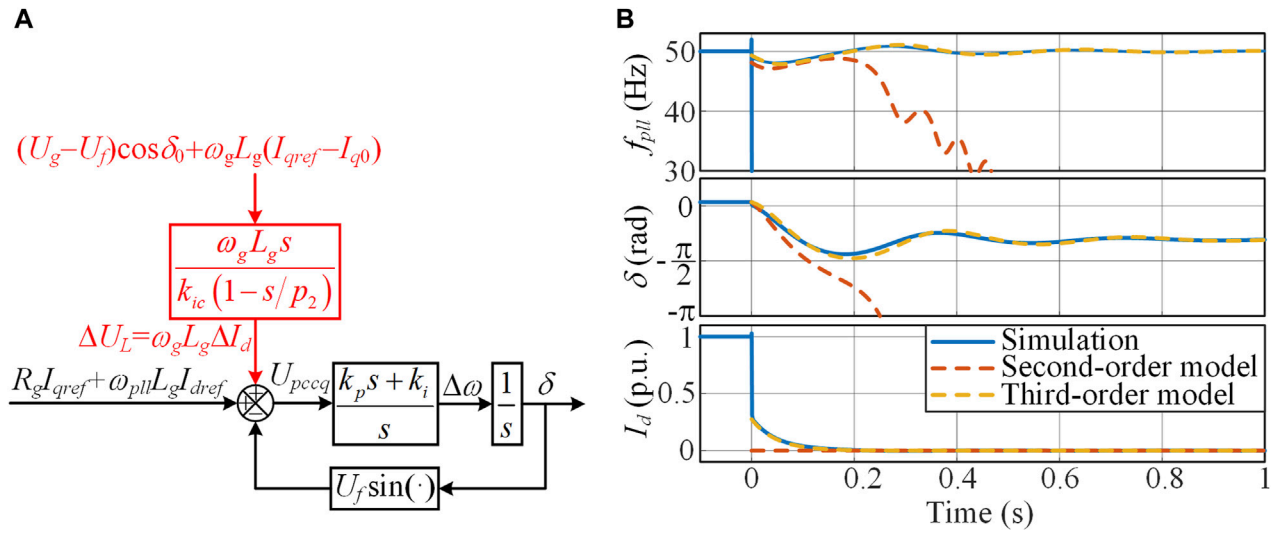

FIGURE 2
(A) Third-order transient synchronization model, and **(B)** transient response with a fault voltage of U_f = 0.05 p.u.

resistance and $L = L_f + L_g$ represents the sum of the filter inductance and the grid inductance. s is the Laplace operator.

$$\begin{cases} U_{cd} = U_g \cos\delta + RI_d - \omega_{pll} LI_q + sLI_d \\ U_{cq} = -U_g \sin\delta + RI_q + \omega_{pll} LI_d + sLI_q \end{cases}. \tag{2}$$

The output of the current controller is approximately equal to U_{cd} and U_{cq}. So, according to the control structure, the control equations for U_{cd} and U_{cq} are obtained as follows:

$$\begin{cases} U_{cd} = \frac{k_{pc}s + k_{ic}}{s}\left(I_{dref} - I_d\right) - \omega_{pll} L_f I_q \\ U_{cq} = \frac{k_{pc}s + k_{ic}}{s}\left(I_{qref} - I_q\right) + \omega_{pll} L_f I_d \end{cases}. \tag{3}$$

Combining (2) and (3), the dq-axis current can be derived as follows:

$$\begin{cases} I_d = G_1(s) I_{dref} + G_2(s)\left(\omega_{pll} L_g I_q - U_g \cos\delta\right) \\ I_q = G_1(s) I_{qref} + G_2(s)\left(U_g \sin\delta - \omega_{pll} L_g I_d\right) \end{cases}. \tag{4}$$

$$\begin{cases} G_1(s) = \frac{sk_{pc} + k_{ic}}{Ls^2 + \left(k_{pc} + R\right)s + k_{ic}} \\ G_2(s) = \frac{s}{Ls^2 + \left(k_{pc} + R\right)s + k_{ic}} \end{cases}. \tag{5}$$

According to Eqs 4, 5, the impact of grid voltage changes on the current dynamics is characterized by $G_2(s)$. Because $G_2(s)$ is a bandpass filter, the bandwidth of the current loop cannot reflect the speed of dynamic response caused by grid voltage changes. Therefore, even if the current loop bandwidth is large enough, it cannot guarantee that the current dynamics caused by grid voltage changes will be fast.

The zero-pole characteristics of the current loop are analyzed to reveal the intrinsic mechanism of why active current cannot track its reference quickly during severe grid faults. According to the zero-pole elimination approach, the parameters of the current loop are set as $k_{pc} = \omega_c L_f$ and $k_{ic} = \omega_c R_f$, where ω_c represents the open-loop crossover angular frequency. This configuration results in a non-dominant pole p_1 and a dominant pole p_2 on the negative real axis. The approximate expressions for the poles are given as Eqs 6, 7

$$p_1 = -\frac{k_{pc} + R + \sqrt{\left(k_{pc} + R\right)^2 - 4k_{ic}L}}{2L} \approx -\frac{k_{pc} + R}{L}. \tag{6}$$

$$p_2 = \frac{k_{ic}}{Lp_1} \approx -\frac{k_{ic}}{k_{pc} + R.} \tag{7}$$

The zero of $G_1(s)$ is $z_1 = -k_{ic}/k_{pc}$, which is approximately equal to the dominant pole p_2 because the P gain of the current controller k_{pc} is typically much larger than the resistance R. Hence, z_1 and p_2 are canceled out, leading to a fast response to changes in the current reference. However, the zero of $G_2(s)$ is located at the origin, which cannot be canceled by the dominant pole. Therefore, the response speed of $G_2(s)$ is much lower than that of $G_1(s)$.

Based on the above analysis, the current dynamics are dominated by p_2 and the zero of $G_2(s)$, while $G_1(s)$ and the non-dominant pole of $G_2(s)$ can be neglected. Consequently, the expressions for the current dynamics ΔI_{dq} can be formulated as (8), where δ_0 and I_{q0} represent the stable phase error and the reactive current prior to the grid fault, respectively.

$$\begin{cases} \Delta I_d = \frac{s}{k_{ic}\left(1 - \frac{s}{p_2}\right)}\left(\omega_{pll} L_g I_q - \omega_g L_g I_{q0} + U_g \cos\delta_0 - U_f \cos\delta\right) \\ \Delta I_q = \frac{s}{k_{ic}\left(1 - \frac{s}{p_2}\right)}\left(U_f \sin\delta - \omega_{pll} L_g I_d - R_g I_{q0}\right) \end{cases}. \tag{8}$$

From the expression of ΔI_q, the input includes three terms: $U_f \sin\delta$, $-\omega_{pll} L_g I_d$, and $-R_g I_{q0}$. During severe faults, the fault voltage U_f is small. The converter must output reactive current to support the grid voltage, so the active current I_d cannot be very large. In addition, the pre-fault reactive current I_{q0} is generally 0. Therefore,

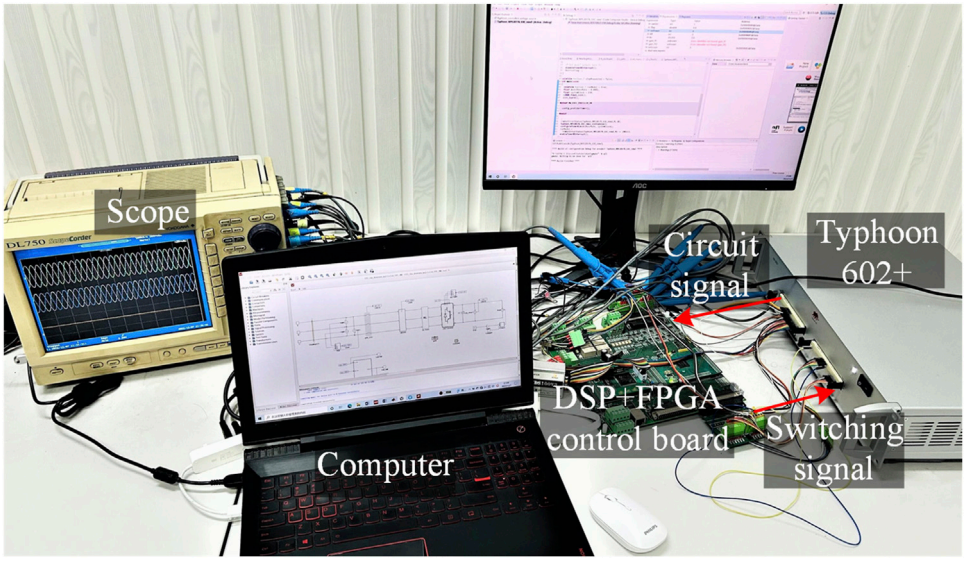

FIGURE 3
Hardware platform of the CHIL experiment.

the reactive current dynamics are small, that is, $\Delta I_q \approx 0$, which means that the reactive current can track its reference quickly. However, the input of the active current dynamics has two large terms $\omega_{pll} L_g I_q$ and $U_g \cos\delta_0$, leading to obvious active current dynamics.

4 Third-order transient synchronization model

According to the above analysis, the active current dynamics are much larger than the reactive current dynamics during severe grid faults. Additionally, the input voltage of the PLL includes the grid impedance voltage drop $R_g I_q + X_g I_d$. Typically, X_g is greater than R_g, so the active current dynamics have a dominant impact on the transient synchronization process, while the impact of the reactive current dynamics can be ignored.

Considering the active current dynamics, the q-axis component of the PCC voltage is corrected as

$$\begin{aligned} U_{pccq} &= -U_f \sin\delta + R_g I_{qref} + \omega_{pll} L_g I_{dref} + \left(\omega_g + \Delta\omega\right) L_g \Delta I_d \\ &\approx -U_f \sin\delta + R_g I_{qref} + \omega_{pll} L_g I_{dref} + \omega_g L_g \Delta I_d \end{aligned}. \quad (9)$$

According to Equation 8, voltage disturbances generate the active current dynamics through a high-pass filter. The grid voltage sag and switching of the reactive current reference have the main impact on the current dynamics, while the slow changes in the phase error δ and the PLL frequency ω_{pll} have a relatively small impact. Hence, the active current dynamics can be approximated as

$$\Delta I_d \approx \frac{s}{k_{ic}\left(1 - \frac{s}{p_2}\right)} \left[\left(U_g - U_f\right)\cos\delta_0 + \omega_g L_g \left(I_{qref} - I_{q0}\right)\right]. \quad (10)$$

According to the PLL structure in Figure 1A, the dynamics of the PLL are expressed as

$$\ddot{\delta} = k_p \dot{U}_{pccq} + k_i U_{pccq}. \quad (11)$$

Combining Equations 9–11 and taking the phase error δ, the angular frequency error $\Delta\omega$, and the active current dynamics ΔI_d as state variables, a third-order state space equation is derived as

$$\begin{cases} \dot{\delta} = \Delta\omega \\ \Delta\dot{\omega} = \dfrac{k_p\left(-U_f \dot{\delta}\cos\delta + \omega_g L_g \Delta\dot{I}_d\right)}{1 - k_p L_g I_{dref}} + \dfrac{k_i\left(-U_f \sin\delta + \omega_{pll} L_g I_{dref} + R_g I_{qref} + \omega_g L_g \Delta I_d\right).}{1 - k_p L_g I_{dref}} \\ \Delta\dot{I}_d = p_2 \Delta I_d \end{cases} \quad (12)$$

According to the Eq 12, a refined third-order transient synchronization model of the GFL converter is established, as illustrated in Figure 2A. The black part is a PLL-based second-order transient synchronization model, while the red part represents the impact of active current dynamics on PLL dynamics. The transient active current ΔI_d generates a transient voltage drop ΔU_L on the grid impedance, which affects the PCC voltage and subsequently affects the transient synchronization process.

5 Simulation and experimental verification

A full-order simulation model based on Figure 1A is constructed using MATLAB/Simulink to validate the correctness of the third-order transient synchronization model, and the simulation results are compared with the solutions of the reduced-order models. The rated voltage and rated power of the system are 690 V and 1.5 MW, respectively. The parameters related to the filter and grid impedance are L_f = 0.1 mH, R_f = 2.1 mΩ, L_g = 0.11 mH, and R_g = 13 mΩ. The

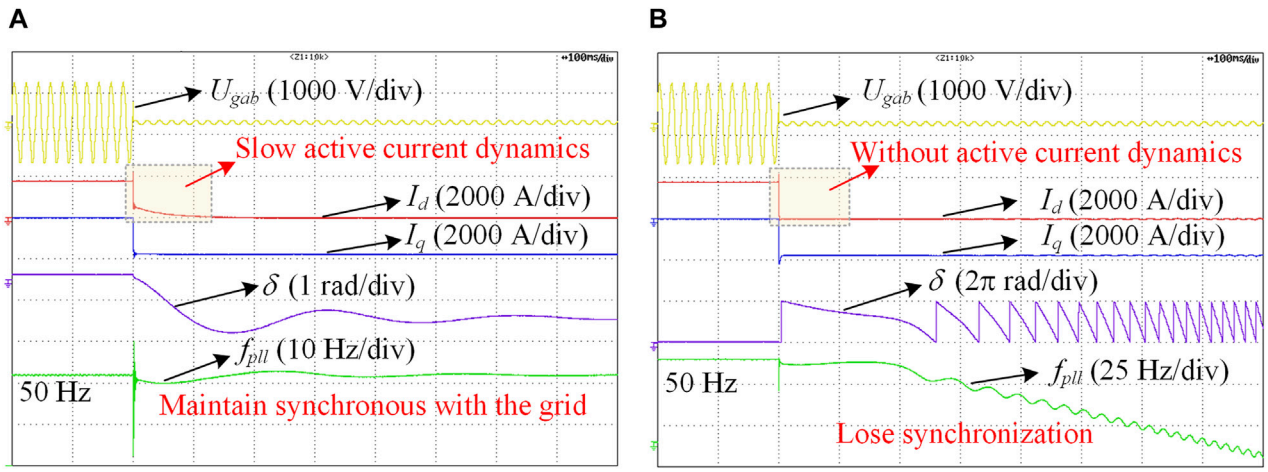

FIGURE 4
Experimental results. **(A)** With slow active current dynamics and **(B)** without active current dynamics.

damping ratio of the PLL is 1.2, and the bandwidth is approximately 50 Hz. The parameters of the current loop are k_{pc} = 0.95 and k_{ic} = 20.

With a fault voltage of U_f = 0.05 p.u., the transient response is shown in Figure 2B. The third-order model closely aligns with the simulation results, while the second-order model does not match the simulation results, validating the correctness of the third-order transient synchronization model.

Experiments are conducted in a control hardware-in-loop (CHIL) platform to verify the impact of active current dynamics. The detailed experimental platform is shown in Figure 3. The main circuit is developed in Typhoon 602+, and the system is controlled by a TMS320F28335/Spartan 6 XC6SLX16 DSP + FPGA control board. The sampling frequency is set as 5 kHz. Other parameters are consistent with the simulation parameters above.

The experimental results using the above parameters are shown in Figure 4A. The figure sequentially shows the waveforms of the grid line voltage U_{gab}, d-axis current I_d, q-axis current I_q, phase error δ, and PLL frequency f_{pll}. When the grid voltage drops from 1.0 p.u. to 0.05 p.u., the current reference switches quickly. The active current reference I_{dref} switches from 1.0 p.u. to 0, while the reactive current reference I_{qref} switches from 0 to −1 p.u. As the steady-state operating point changes, the system enters the transient synchronization process. During this process, the reactive current quickly tracks its reference and stabilizes at −1 p.u., while the active current undergoes a dynamic decay process of over 100 ms. As a result, the system maintains synchronicity with the grid, which is consistent with the theoretical analysis and simulation results.

Increasing k_{ic} can increase the absolute value of the dominant pole p_2, thereby accelerating the active current dynamics. In this case, the experimental results are shown in Figure 4B. Both active and reactive current can quickly track their references. However, without slow active current dynamics, the PLL frequency decreases continuously, and a loss of synchronization occurs. The experimental results demonstrate that the active current dynamics have a non-negligible impact on the transient stability of GFL converters.

6 Conclusion

This article discusses the intrinsic mechanism of why active current cannot track its reference quickly during severe grid faults. The transfer function from grid voltage disturbance to current output has a zero located at the origin and a dominant pole, resulting in a slow dynamic response. In addition, severe grid faults have a much greater impact on active current dynamics than reactive current dynamics. Therefore, active current will undergo obvious dynamic attenuation during severe grid faults. The coupling of active current dynamics and the grid impedance generates a transient voltage that affects the transient synchronization process. Accordingly, a refined third-order transient synchronization model is established, which offers a more accurate assessment of the transient stability of GFL converters during severe grid faults than the conventional second-order model.

Data availability statement

The raw data supporting the conclusion of this article will be made available by the authors, without undue reservation.

Author contributions

CW: validation, methodology, supervision, conceptualization, and writing–review and editing. ZH: software, investigation, and writing–original draft. YW: validation, supervision, and writing–review and editing. FB: supervision and writing–review and editing.

Funding

The author(s) declare that financial support was received for the research, authorship, and/or publication of this article. This work is

supported by the National Natural Science Foundation of China under Grant 52207063.

Conflict of interest

The authors declare that the research was conducted in the absence of any commercial or financial relationships that could be construed as a potential conflict of interest.

Publisher's note

All claims expressed in this article are solely those of the authors and do not necessarily represent those of their affiliated organizations, or those of the publisher, the editors, and the reviewers. Any product that may be evaluated in this article, or claim that may be made by its manufacturer, is not guaranteed or endorsed by the publisher.

References

Chen, J., Liu, M., O'Donnell, T., and Milano, F. (2020). Impact of current transients on the synchronization stability assessment of grid-feeding converters. *IEEE Trans. Power Syst.* 35, 4131–4134. doi:10.1109/tpwrs.2020.3009858

Göksu, Ö., Teodorescu, R., Bak, C. L., Iov, F., and Kjær, P. C. (2014). Instability of wind turbine converters during current injection to low voltage grid faults and PLL frequency based stability solution. *IEEE Trans. Power Syst.* 29, 1683–1691. doi:10.1109/tpwrs.2013.2295261

He, X., Geng, H., Xi, J., and Guerrero, J. M. (2021). Resynchronization analysis and improvement of grid-connected VSCs during grid faults. *IEEE J. Emerg. Sel. Top. Power Electron.* 9, 438–450. doi:10.1109/jestpe.2019.2954555

Hu, Q., Fu, L., Ma, F., Ji, F., and Zhang, Y. (2021). Analogized synchronous-generator model of PLL-based VSC and transient synchronizing stability of converter dominated power system. *IEEE Trans. Sustain. Energy.* 12, 1174–1185. doi:10.1109/tste.2020.3037155

Tian, Z., Tang, Y., Zha, X., Sun, J., Huang, M., Fu, X., et al. (2022). Hamilton-based stability criterion and attraction region estimation for grid-tied inverters under large-signal disturbances. *IEEE J. Emerg. Sel. Top. Power Electron.* 10, 413–423. doi:10.1109/jestpe.2021.3076189

Wu, C., Lyu, Y., Wang, Y., and Blaabjerg, F. (2024). Transient synchronization stability analysis of grid-following converter considering the coupling effect of current loop and phase locked loop. *IEEE Trans. Energy Convers.* 39, 544–554. doi:10.1109/tec.2023.3314095

Wu, H., and Wang, X. (2020). Design-oriented transient stability analysis of PLL-synchronized voltage-source converters. *IEEE Trans. Power Electron.* 35, 3573–3589. doi:10.1109/tpel.2019.2937942

Xiong, L., Liu, X., Zhao, C., and Zhuo, F. (2020). A fast and robust real-time detection algorithm of decaying DC transient and harmonic components in three-phase systems. *IEEE Trans. Power Electron.* 35, 3332–3336. doi:10.1109/tpel.2019.2940891

Yuan, H., Xin, H., Huang, L., Wang, Z., and Wu, D. (2019). Stability analysis and enhancement of type-4 wind turbines connected to very weak grids under severe voltage sags. *IEEE Trans. Energy Convers.* 34, 838–848. doi:10.1109/tec.2018.2882992

frontiers | Frontiers in Energy Research

TYPE Original Research
PUBLISHED 11 July 2024
DOI 10.3389/fenrg.2024.1429256

OPEN ACCESS

EDITED BY
Yonghui Liu,
Hong Kong Polytechnic University, Hong Kong SAR, China

REVIEWED BY
Jun Huang,
Hebei University of Technology, China
Shun Sang,
Nantong University, China
Huimin Wang,
Zhejiang Sci-Tech University, China

*CORRESPONDENCE
Xiaoke Zhang,
zxk5511@126.com

RECEIVED 07 May 2024
ACCEPTED 14 June 2024
PUBLISHED 11 July 2024

CITATION
Zhang X, Wang J, Gao Z, Zhang S and Teng W (2024), Advanced strategy of grid-forming wind storage systems for cooperative DC power support.
Front. Energy Res. 12:1429256.
doi: 10.3389/fenrg.2024.1429256

Advanced strategy of grid-forming wind storage systems for cooperative DC power support

Xiaoke Zhang[1]*, Jiaqi Wang[2], Zan Gao[2], Shaofeng Zhang[1] and Weijun Teng[1]

[1]State Grid Henan Electric Power Research Institute, Zhengzhou, China, [2]School of Electrical Engineering, Xi'an Jiaotong University, Xi'an, China

Grid-forming (GFM) wind storage systems (WSSs) possess the capability of actively building frequency and phase, enabling faster frequency response. The frequency regulation power of GFM WSSs is provided by both the rotor of wind turbine and the battery storage (BS) in parallel with DC capacitor. However, with existing control strategies, the energy storage immediately responds to both small and large grid disturbances. The frequent responses significantly decrease the lifespan of energy storage. To address this issue, a cooperative strategy between rotor and energy storage is necessary. This paper proposes an advanced strategy of GFM WSSs for cooperative DC power support. The cooperative principle is that for small disturbances, the BS is disabled and total frequency regulation power is provided by the rotor, while for large disturbances, the BS is enabled to cooperatively provide power support with the rotor. The proposed cooperative strategy can decrease the charging and discharging times of BS with a small range of rotor speed fluctuation, and then the service life of BS can be significantly extended. Simulation results validate the effectiveness and superiority of the proposed strategy.

KEYWORDS

wind storage system, cooperative power support, grid forming control, battery storage, frequency regulation

1 Introduction

With the development of wind power generation, its penetration in grids is increasing (Liu et al., 2021; Bao et al., 2022; Huang et al., 2023). Currently, the predominant control method for most wind turbines is grid-following (GFL) control, which relies on a phase-locked loop (PLL) to synchronize with the frequency/phase of the AC grid. However, this approach faces challenges in maintaining stable operation under weak grid conditions and lacks grid support capability Xiong et al. (2020). Consequently, wind power systems utilizing grid-forming (GFM) control have obtained wide attention due to their capability of rapid frequency regulation (FR), facilitated to autonomously forming frequency/phase (Jiao and Nian, 2020; Zhao et al., 2021).

The FR of GFM wind power systems takes a frequency regulation (FR) cost of the frequency response resources (Xiong et al., 2019). Releasing the rotational kinetic energy of the rotor can enhance grid frequency stability (Lin and Liu, 2020). However, utilizing rotor power for FR purposes requires sacrificing the maximum power point tracking

(MPPT) of the wind power system and tapping into the limited amount of stored energy, thus somewhat diminishing the FR effect (Xiong et al., 2015). Battery storage (BS) offers notable advantages such as rapid response times and precise tracking of active power commands. Through optimized control system designs, wind farms can attain swift inertia response capabilities and continuous active power support, underscoring the necessity of equipping wind farms with a certain percentage of BS (Astero and Evens, 2020).

For wind storage systems (WSSs), scholars both domestically and internationally have proposed various control methods. In Shadoul et al. (2022), flywheel energy storage is integrated on the DC side of WSSs. Here, the BS assumes control over the DC bus voltage during grid-connected operation, facilitating virtual synchronous control of the grid-side converter. This approach ultimately enhances system inertia responsiveness, smoothens the active output of WSSs, and ensures the stability of the DC bus voltage. Yang et al. (2023) addresses the practical constraints of wind farms and BS systems, using model prediction to design WSSs for small-scale grid-oriented FR control. However, this strategy necessitates the determination of the grid inertia time constant, a parameter often challenging to ascertain in large grids. Mohamed et al. (2022) integrates considerations of DC voltage maintenance on the energy storage side and virtual synchronization control of the grid-side converter (GSC). Furthermore, it accounts for the load state of the BS and coordinates main unit control, converter control, and BS side control to maintain energy balance. This is achieved through rotational speed control of the machine-side converter (MSC) and adjustment of blade pitch angles to ensure energy equilibrium. Zeng et al. (2021) establishes a connection between the BS and the wind farm exit bus. It devises a strategy based on fuzzy control for the BS to emulate the FR inertia of the wind farm. However, this strategy overlooks the utilization of the frequency support capability inherent in WSSs. Sang et al. (2021) proposes a voltage source-type configuration network control method that utilizes DC-side energy. It integrates the concepts of virtual synchronous control and DC capacitor inertial synchronous control within the grid-side converter for WSSs equipped with additional supercapacitors on the DC-side. Additionally, it introduces a virtual capacitor control strategy in the supercapacitor storage-side converter. Sun et al. (2022) uses fuzzy control to devise a strategy for superconducting BS to aid wind turbines in MPPT operation, aiming to conserve BS capacity allocation. However, this strategy overlooks the potential coordination between BS and rotor kinetic energy to provide frequency support. Ahsan and Mufti (2020) investigates the coordination strategy of BS and wind turbines to deliver FR response. It explores scenarios based on whether the frequency rate of change meets FR power demand. This involves designing load shedding operations for WSSs to participate in FR control using fuzzy control. Meng et al. (2023) proposes a virtual synchronous generator cooperative control scheme for wind farms and their GFM BS devices on the AC side. This scheme enables the WSSs to function as a voltage source, providing both system damping and inertia. Yao et al. (2024) developed a wind farm FR model and an adaptive primary FR control strategy for a BS system, utilizing the frequency change rate as the output conversion characteristic. In summary, existing control methods for GFM WSSs often result in frequent actions of the energy storage, with insufficient consideration for the service life of the battery. Notably, the general design life of batteries is typically 4–5 years, a duration often insufficient for high FR demand scenarios (Dhiman and Deb, 2020).

To address the aforementioned challenges, this paper investigates the cooperative principle of DC power support in GFM WSSs and introduces a cooperative control strategy. The fundamental principle of the proposed control is as follows: for small disturbances, the BS is disabled and total frequency regulation power is provided by the rotor, while for large disturbances, the BS is enabled to cooperatively provide power support with the rotor. This control approach aims to minimize the time of BS charging and discharging, consequently enhancing the service life of BS, while ensuring minimal fluctuations in rotor speed.

The remaining sections of this manuscript are as follows. Section 2 describes the control methods for GFM WSSs. Section 3 analyzes the cooperative principle of DC-side power support in GFM WSSs and introduces a cooperative control strategy tailored for these systems. Finally, Section 4 validates the effectiveness and superiority of the proposed control method.

2 Control strategy of GFM WSS

As shown in Figure 1, the typical PMSG based GFM WSSs consists of wind generation modules and BS modules. Wind generation module mainly consists of wind turbine (WT), PMSG, MSC, dc-capacitor, and GSC. The BS module mainly consists of battery, battery storage converter (BSC).

2.1 GFM control strategy for WTs

The power balance relationship on the DC side of the WSSs is given by

$$P_{wt} + P_{BS} = P_{dcout} = P_w \tag{1}$$

where P_{BS} is the BS output power; P_{dcout} is the power released by the DC capacitor; P_w is the WSSs output power and P_{wt} is the wind power captured by WT, which is shown in Eq. 2,

$$P_{wt} = \frac{1}{2}\rho\pi R_w^2 C_p(\lambda,\beta)\, v_m^3 \tag{2}$$

where ρ is the air density; R_w is the blade radius of the wind turbine; C_p is the wind energy utilization coefficient; λ is the blade tip speed ratio; β is the pitch angle; and v_w is the inlet wind speed.

The MSC uses DC-link voltage control to stabilize the DC voltage, as depicted in Figure 2. In dc-link voltage strategy, the d-axis current command value i_{rdref} is set to 0, while the q-axis current command value i_{rqref} is determined by the DC capacitor voltage loop.

The GSC uses droop control to construct the voltage and frequency, which realizes the grid-configuration operation, as depicted in Figure 3. It should be noted that for GFM WSSs, the GFM control is implemented by the GSC. Consequently, WSSs output power is no longer determined by P_{wt} captured by WT, but depends on the grid load.

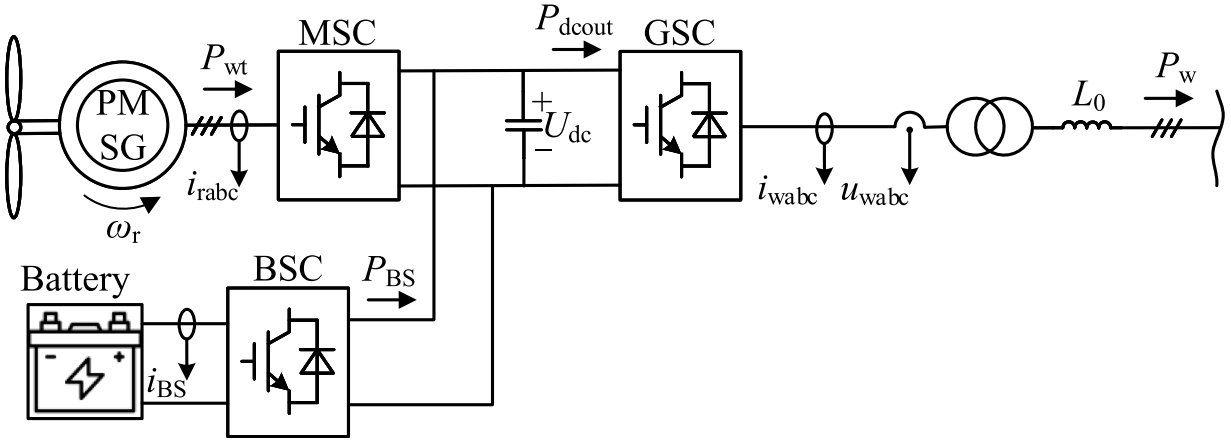

FIGURE 1
Circuit topology of GFM WSS.

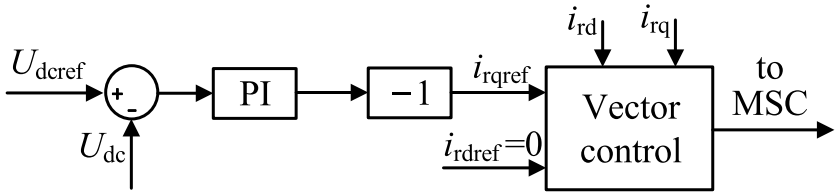

FIGURE 2
MSC control structure.

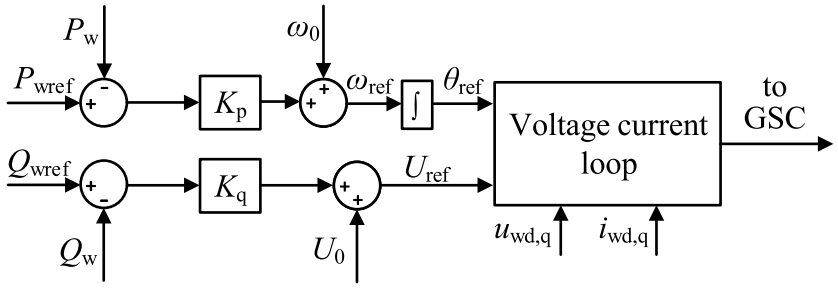

FIGURE 3
GSC control strategy.

Droop control simulates the active-frequency and reactive-voltage droop characteristics of a synchronous generator, and the control equations for its frequency and voltage are shown in Eq. 3,

$$\begin{cases} \omega_{ref} = \omega_0 + K_p(P_{wref} - P_w) \\ U_{ref} = U_0 + K_q(Q_{wref} - Q_w) \end{cases} \quad (3)$$

where ω_{ref} is the grid angular velocity reference value; ω is the grid angular velocity; ω_0 is the grid rated angular velocity; K_p is the active droop coefficient; P_{wref} is the WSSs rated output power; U_{wref} is the grid voltage reference value; U_0 is the rated grid voltage; K_q is the reactive droop coefficient; Q_w is the WSSs reactive power; Q_{wref} is the WSSs rated reactive power.

2.2 BS control strategy

GFM WSSs BS distribution methods include AC-side BS and DC-side BS. For the former, it can be considered as utilizing the BS system of GFM control to assist the operation of the wind generation systems, while the wind generation systems still adopt GFL control. The significant advantage of the DC-side BS in GFM WSSs is that the DC voltage can be stabilized with the help of an additional BS on the DC side, which effectively aids in realizing the GFM control of the turbine. Compared to the AC-side BS, the DC-side BS of WSSs can save one inverter, thus reducing the cost. Additionally, the DC-side BS is more integrated in structure and control, which

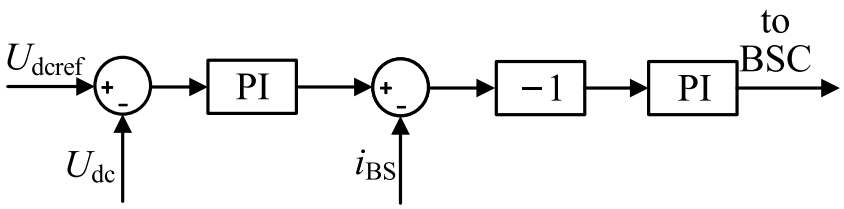

FIGURE 4
BSC control structure.

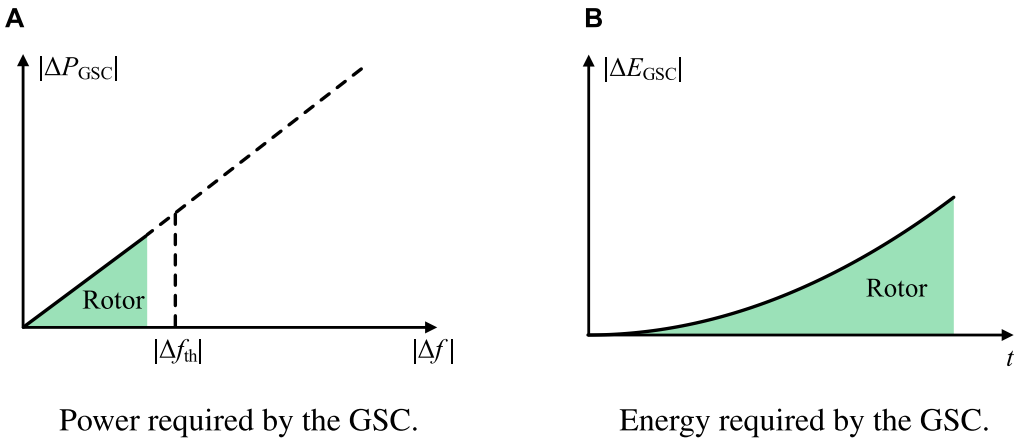

FIGURE 5
Small disturbance power support. **(A)** Power required by the GSC. **(B)** Energy required by GSC.

has the potential to enhance the transient and steady-state control capabilities of the unit and optimize its operational flexibility while meeting active support energy demand (Liu et al., 2020). Therefore, in this paper, the DC-side distribution BS is adopted to provide FR support power for the system.

The BSC control structure is shown in Figure 4. The current command value for the BS is derived from the DC capacitor voltage loop. Subsequently, the PWM control signal for the BSC is generated from the current loop.

2.3 Challenge of GFM WSSs

From Eq. 1, for wind generation systems without BS, in the event of a small disturbance, the system can respond by utilizing the wind turbine rotor to release or absorb energy, thereby adjusting rotational speed. However, during large disturbances, the spare power available from the rotor may not suffice to counteract the disturbance. Consequently, the energy supplied by the rotor to the DC capacitor may fail to match the energy it releases, resulting in instability of the capacitor voltage.

In conventional wind storage systems, the BS responds to disturbances of any magnitude, ensuring stabilization of the DC voltage and maintenance of rotor speed within normal ranges. However, frequent activation of the BS can lead to unnecessary wear and tear on the battery. Presently, the cycle life of Li-ion batteries ranges from 3,000 to 5,000 cycles. Excessive activation of the BS for each disturbance significantly shortens the battery's service life (Liu et al., 2020). Therefore, imprudent utilization of the BS can have adverse effects on the economic operation of the wind storage system.

In summary, to fulfill the system's power support requirements while minimizing the usage times of BS, there is a pressing need for a cooperative control strategy. This strategy aims to facilitate effective collaboration between the wind turbine rotor and the BS, enabling them to respond appropriately to varying degrees of disturbances encountered by the wind storage system within the power system.

3 Cooperative DC power support strategy of GFM WSS

3.1 Cooperative principle

From the analysis presented above, it becomes apparent that BS in WSSs should only be activated in response to large disturbances, while small disturbances do not necessitate their activation. It is not desirable for BS to respond to every disturbance encountered. Building upon this insight, this paper proposes a cooperative control strategy for DC-side power support in wind storage systems. This strategy utilizes frequency as a threshold to discern the size of the disturbance, determining when BS activation is warranted.

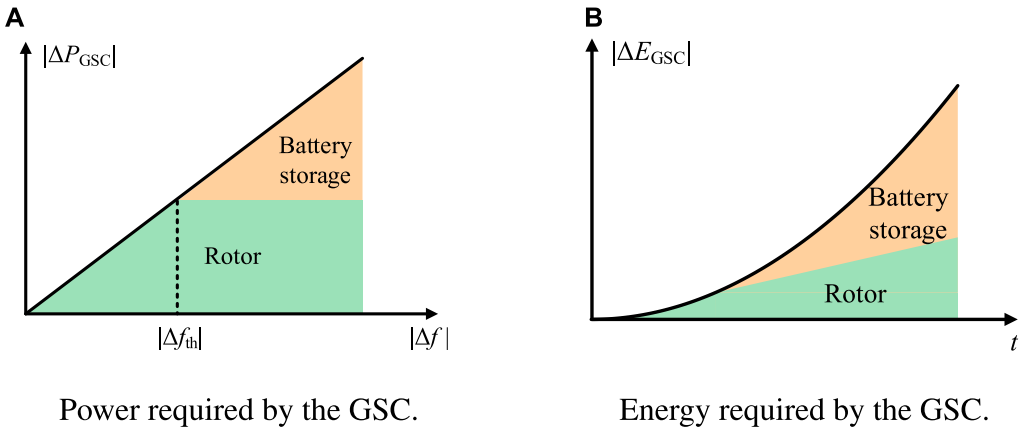

FIGURE 6
Large disturbance power support. **(A)** Power required by the GSC. **(B)** Energy required by GSC.

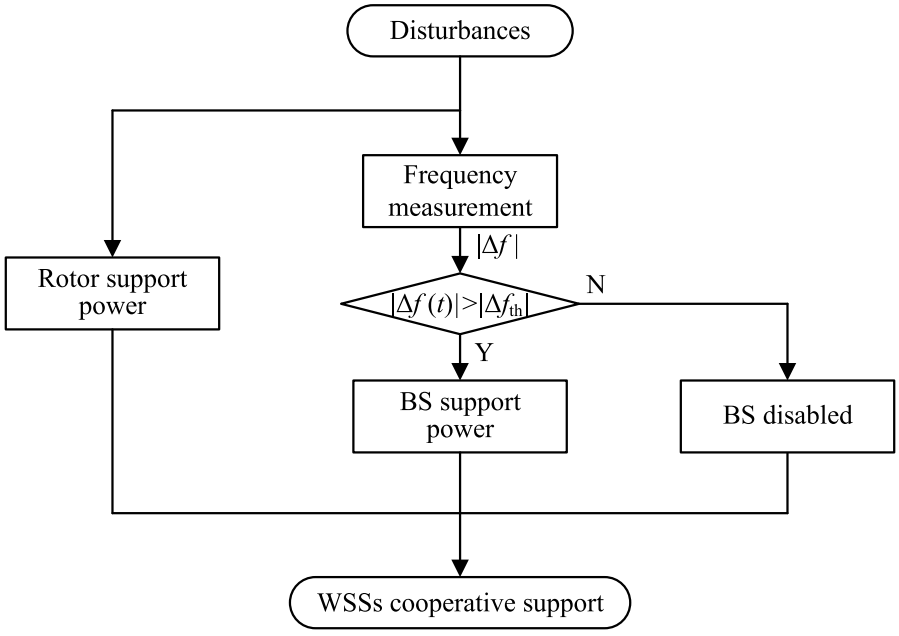

FIGURE 7
Cooperative principle of the cooperative control for GFM WSS.

When a disturbance results in a frequency deviation of the WSSs that is below the frequency threshold $|\Delta f_{th}|$, it is categorized as a small disturbance. In such cases, the BS does not respond, and the DC voltage is maintained stable solely by the rotor. Figure 5 illustrates the power and energy needed to support the GSC during small disturbances. As depicted in Figure 5A, the frequency deviation caused by small disturbances remains below the frequency threshold $|\Delta f_{th}|$, indicating that all the GSC power $|\Delta P_{GSC}|$ is sustained by the rotor. Figure 5B displays the corresponding GSC energy $|\Delta E_{GSC}|$ during small disturbances over time, revealing that the entire energy demand is sustained by the rotor throughout the disturbance period.

When the disturbance causes the frequency deviation of the WSSs to exceed the frequency threshold $|\Delta f_{th}|$, it is classified as a large disturbance. At this point, the DC voltage is stabilized by both the rotor and the BS to achieve cooperative support on the DC side. Since the system's frequency deviation resulting from large disturbances undergoes a process, the proposed control uses a different cooperative strategy before and after reaching the frequency triggering threshold. Figure 6 illustrates the support of power and energy required by the GSC during large disturbances. In Figure 6A, when the system is in state $|\Delta f| < |\Delta f_{th}|$, all the power required by the GSC is supplied by the rotor alone; however, in state $|\Delta f| > |\Delta f_{th}|$, both the rotor and the BS jointly provide

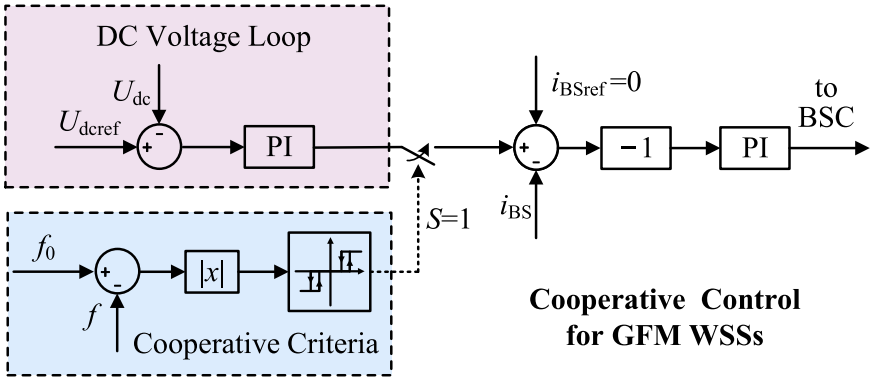

FIGURE 8
Block diagram of the cooperative control for GFM WSS.

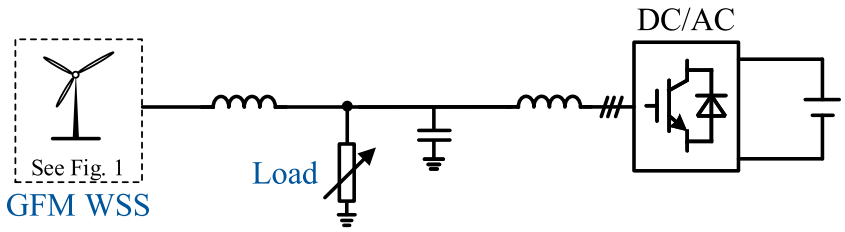

FIGURE 9
Test system of the cooperative control for GFM WSS.

TABLE 1 Main parameters of test system.

Description	Symbol	Value
Initial load power	P_{L0}	400 kW
Initial WSSs power	P_{w0}	200 kW
Initial grid power	P_{g0}	200 kW
Wind speed	v	12 m/s
Initial rotor speed	n_0	89.4 r/min
DC-capacitor	C_{dc}	20 mF
DC-link voltage	U_{dc}	1800 V
Droop coefficient	K_p	0.01 Hz/kW
Rated line voltage	E_N	690 Vrms
Rated frequency	f_N	50 Hz
Frequency deviation threshold upper limit	$\lvert\Delta f_{th}^{h}\rvert$	0.11 Hz
Frequency deviation threshold lower limit	$\lvert\Delta f_{th}^{l}\rvert$	0.09 Hz
Initial battery SOC	SOC	80%

power support for the DC capacitor. The corresponding energy required by the GSC during large disturbances over time is depicted in Figure 6B. In state $|\Delta f| < |\Delta f_{th}|$, all the energy is sourced from the rotor, whereas in state $|\Delta f| > |\Delta f_{th}|$, the BS is activated to supply energy to the DC capacitor in conjunction with the rotor.

The cooperative principle of the proposed cooperative FR control strategy for the wind storage system is shown in Figure 7. When the WSSs encounter disturbances, the rotor first provides FR support power for the DC capacitor, and at the same time, its frequency deviation is measured; if $|\Delta f| < |\Delta f_{th}|$, the BS is disabled and the rotor only supports the disturbed power by sacrificing the rotational speed; if $|\Delta f| > |\Delta f_{th}|$, the BS is enabled, and the rotor and the BS work together to maintain the stability of the DC voltage, which realizes the cooperative support of DC capacitance.

3.2 Cooperative control strategy

Building upon the cooperative principle described above, the control block diagram of the proposed DC side power support cooperative control strategy for GFM WSSs is depicted in Figure 8.

To achieve the control objective of determining whether the BS should be activated based on whether the frequency deviation reaches the frequency threshold $|\Delta f_{th}|$, the BS DC current i_{BS} can be selected as the controlled parameter. In the cooperative control

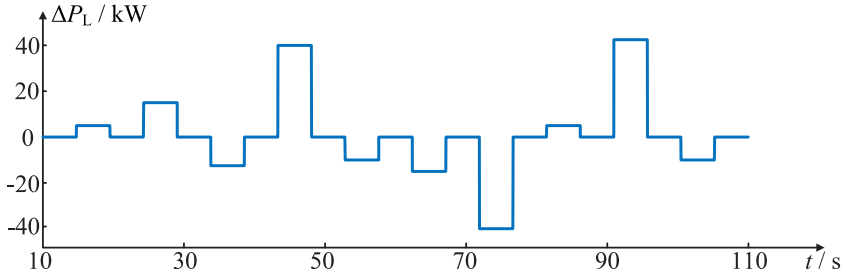

FIGURE 10
Stochastic disturbances.

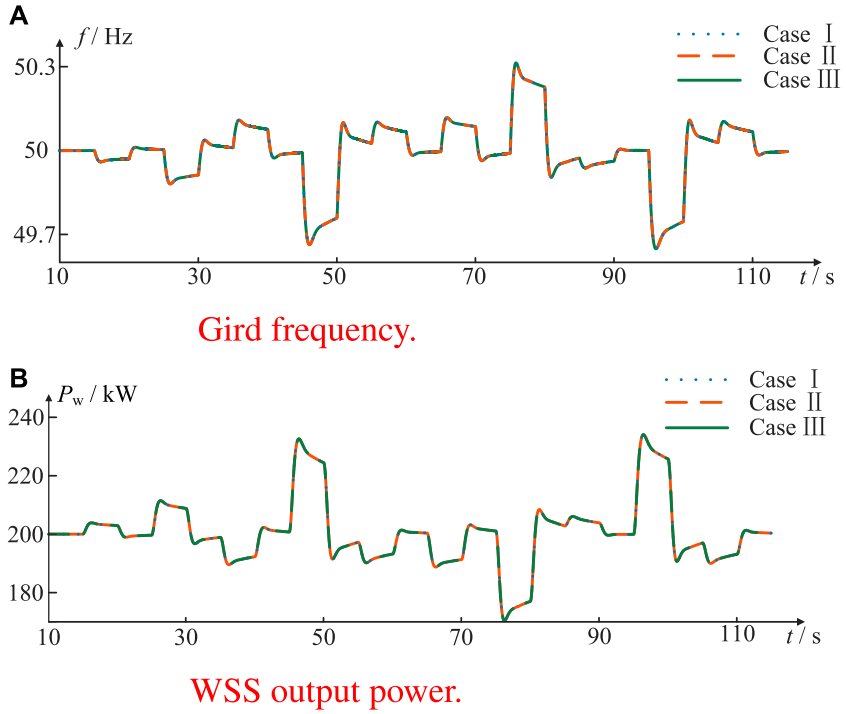

FIGURE 11
Gird-side results under stochastic disturbances. **(A)** Gird frequency. **(B)** WSS output power.

strategy, the reference value of the BS DC current, i_{BSref}, is initially set to 0 since the BS typically remains inactive. Activation of the BS occurs only when a disturbance causes the system deviation to exceed the frequency threshold $|\Delta f_{\mathrm{th}}|$, indicating a large disturbance. To address potential instability issues at the threshold boundary, a hysteresis loop module is implemented to define the cooperative criteria for large disturbances. The design logic of the hysteresis loop module is shown in Eq. 4,

$$S = \begin{cases} 0 & |\Delta f| < \left|\Delta f_{\mathrm{th}}^{\mathrm{l}}\right| \\ 1 & |\Delta f| \geq \left|\Delta f_{\mathrm{th}}^{\mathrm{h}}\right| \end{cases} \tag{4}$$

where S is the flag of the energy storage criterion; $\left|\Delta f_{\mathrm{th}}^{\mathrm{h}}\right|$ is the frequency deviation threshold upper limit and $\left|\Delta f_{\mathrm{th}}^{\mathrm{l}}\right|$ is the frequency deviation threshold lower limit.

When the hysteresis loop module S is at 0, the BS remains inactive; however, when the hysteresis loop module S transitions to 1, the DC voltage loop activates, thereby enabling the BS to provide power support for the DC capacitor.

4 Verification

To validate the effectiveness and superiority of the proposed DC power support cooperative control, this section integrates the GFM WSSs with the grid to evaluate the DC power support characteristics. The constructed test system is illustrated in Figure 9.

In this paper, the test system is constructed within the MATLAB/SIMULINK environment, and the specific parameters are outlined in Table 1. The detailed configuration of the tested

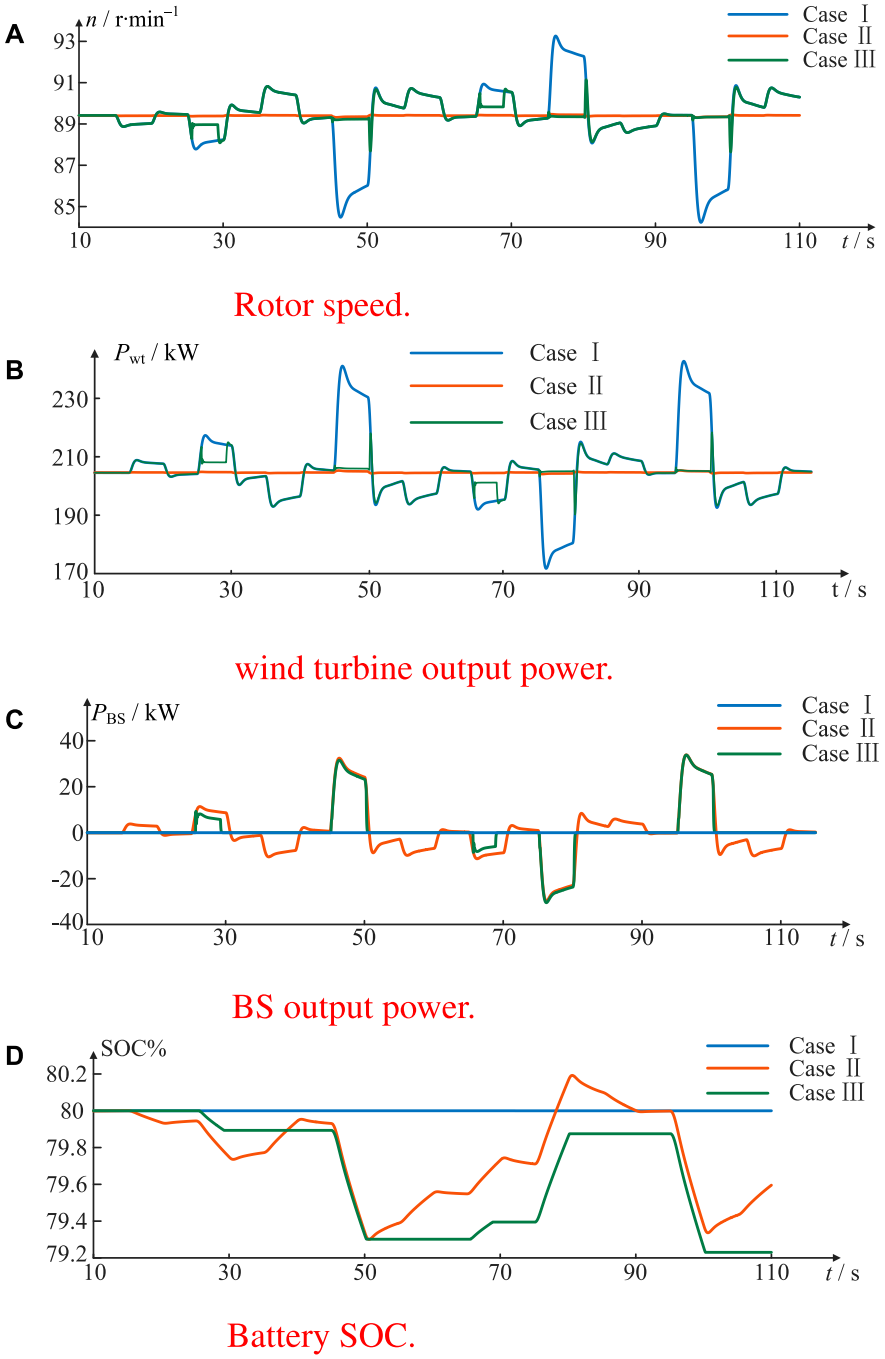

FIGURE 12
DC-side results under stochastic disturbances. **(A)** Rotor speed. **(B)** Wind turbine output power. **(C)** BS output power. **(D)** Battery SOC.

GFM WSSs is depicted in Figure 8. The grid's frequency response characteristics are emulated using an inverter, which is controlled using virtual synchronous generator control.

When a small disturbance occurs, the proposed cooperative control anticipates that the WSSs BS will remain inactive, with the rotor supplying all the necessary support power. Only in the event of a large disturbance causing the frequency deviation to surpass the frequency threshold $|\Delta f_{th}|$, does the BS become operational, collaborating with the rotor to stabilize the DC voltage and achieve cooperative power support on the DC side. To assess the effectiveness of the proposed cooperative control strategy, the control effects of the following three control methods are simulated and analyzed.

- Case I: The BS does not participate in FR and total FR power is provided by the rotor.
- Case II: Immediately upon the occurrence of a grid disturbance, both the rotor and the energy storage system respond promptly.
- Case III: The proposed cooperative control strategy.

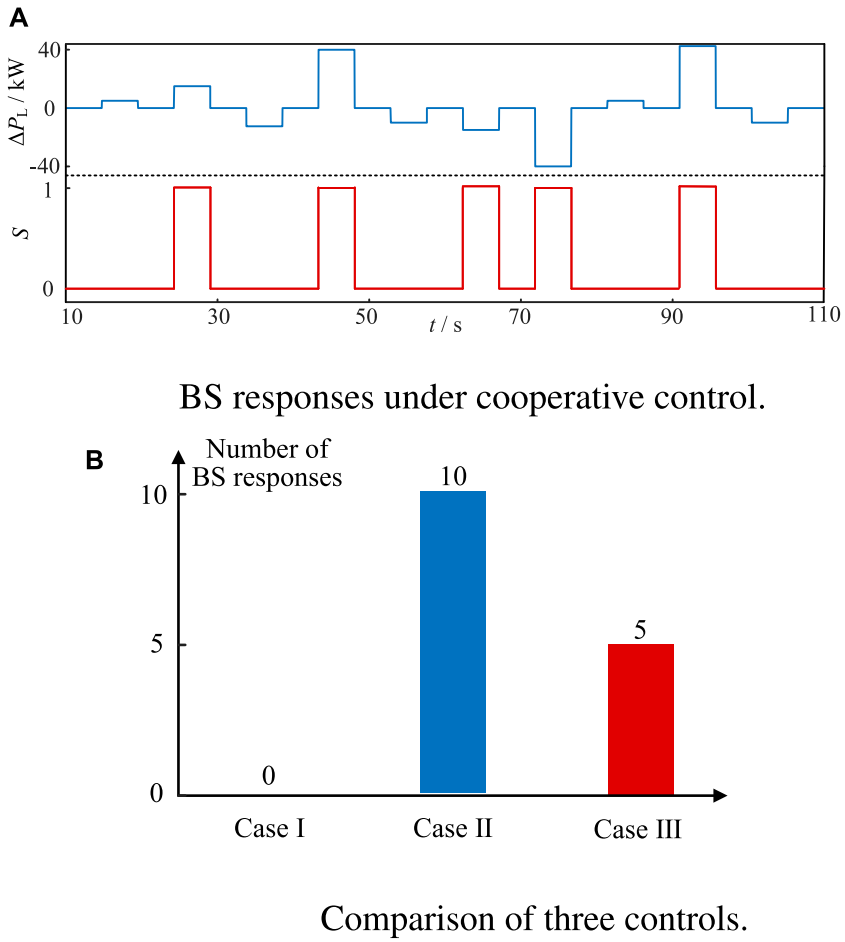

FIGURE 13
Comparison of WSSs BS responses under three controls. **(A)** BS responses under cooperative control. **(B)** Comparison of three controls.

In the initial conditions of the test system, the load power is jointly supported by the WSSs and the grid to ensure the stabilization of the system frequency. Random disturbances, including both large and small disturbances, are set between 10 s and 110 s. The values of these disturbances are in the range of −40 kW–40 kW, as illustrated in Figure 10.

As shown in Figure 11, the grid frequency f and the output power P_w of the WSSs remain consistent across all three control methods. This consistency is attributed to the uniform GSC control strategy employed by all three methods. Moreover, the output power of the WSSs, managed by the GSC to integrate with the grid, is contingent upon the grid-side loads and the GFM control methodology it employs.

In Figures 12A,B, the WSSs rotor speed n and BS power PBS are illustrated. In Case I, grid-side load changes are solely managed by the rotor, resulting in wide fluctuations in rotor speed and potential damage to its mechanical structure. In Case II, the BS responds faster than the rotor to grid-side load changes, leading to frequent charging and discharging cycles of the BS, thus reducing its service life and increasing WSSs' investment costs. However, in Case III, the proposed cooperative control method is employed. Here, the BS responses are minimized while ensuring stable rotor speed. This is achieved by activating the BS only when $|\Delta f| > |\Delta f_{th}|$, and the rotor provides all support power when $|\Delta f| < |\Delta f_{th}|$. Consequently, the proposed method enhances the BS's service life and improves the economic and technological benefits of WSSs, while safeguarding the rotor's mechanical integrity. Figure 12C displays the SOC% of the BS under the three control methods. The proposed cooperative control method notably reduces the time of BS charging and discharging compared to the method where the BS responds to every disturbance.

In Figure 13A, the response of the WSSs BS to load-side disturbances under cooperative control is depicted. It's evident that the BS only reacts to large disturbances under this control scheme. Additionally, Figure 13B compares the response times of the BS under the three control methods. It demonstrates that when confronted with identical disturbance scenarios, cooperative control significantly reduces the number of BS responses, thereby enhancing its service life.

5 Conclusion

This manuscript analyzes the principle of cooperative DC power support for GFM WSSs and proposes a cooperative strategy for GFM

WSSs. The simulation results verify that the proposed control can effectively reduce the number of BS responses. The main conclusions are as follows.

1) The cooperative principle of the GFM WSSs is as follows: for small disturbances, the BS is disabled and total frequency regulation power is provided by the rotor, while for large disturbances, the BS is enabled to cooperatively provide power support with the rotor.
2) Based on the cooperative principle, the proposed cooperative strategy can distinguish between large and small disturbances by using a frequency threshold. Additionally, it incorporates a hysteresis loop module into the cooperative criterion. This module facilitates the cooperative support of both the rotor and the BS on the DC side of the WSSs.
3) The simulation results indicate that the proposed strategy effectively can reduce the times of BS charging and discharging. This improvement contributes to extend the service life of BSs while ensuring that rotor speed remains stable without wide fluctuations.

Data availability statement

The original contributions presented in the study are included in the article/Supplementary Material, further inquiries can be directed to the corresponding author.

Author contributions

XZ: Conceptualization, Data curation, Formal Analysis, Funding acquisition, Investigation, Methodology, Project administration, Resources, Software, Supervision, Validation, Visualization, Writing–original draft, Writing–review and editing. JW: Conceptualization, Methodology, Software, Validation, Writing–original draft, Writing–review and editing, Data curation, Formal Analysis, Investigation. ZG: Data curation, Software, Writing–review and editing, Formal Analysis, Investigation, Methodology. SZ: Formal Analysis, Investigation, Writing–review and editing, Visualization. WT: Supervision, Writing–review and editing, Visualization.

Funding

The author(s) declare that no financial support was received for the research, authorship, and/or publication of this article.

Conflict of interest

The authors declare that the research was conducted in the absence of any commercial or financial relationships that could be construed as a potential conflict of interest.

Publisher's note

All claims expressed in this article are solely those of the authors and do not necessarily represent those of their affiliated organizations, or those of the publisher, the editors and the reviewers. Any product that may be evaluated in this article, or claim that may be made by its manufacturer, is not guaranteed or endorsed by the publisher.

References

Ahsan, H., and Mufti, M.-u. D. (2020). Systematic development and application of a fuzzy logic equipped generic energy storage system for dynamic stability reinforcement. *Int. J. Energy Res.* 44, 8974–8987. doi:10.1002/er.5606

Astero, P., and Evens, C. (2020). Optimum operation of battery storage system in frequency containment reserves markets. *IEEE Trans. Smart Grid* 11, 4906–4915. doi:10.1109/tsg.2020.2997924

Bao, W., Ding, L., Kang, Y. C., and Sun, L. (2022). Closed-loop synthetic inertia control for wind turbine generators in association with slightly over-speeded deloading operation. *IEEE Trans. Power Syst.* 38, 5022–5032. doi:10.1109/tpwrs.2022.3224431

Dhiman, H. S., and Deb, D. (2020). Wake management based life enhancement of battery energy storage system for hybrid wind farms. *Renew. Sustain. Energy Rev.* 130, 109912. doi:10.1016/j.rser.2020.109912

Huang, L., Wu, C., Zhou, D., Chen, L., Pagnani, D., and Blaabjerg, F. (2023). Challenges and potential solutions of grid-forming converters applied to wind power generation system—an overview. *Front. Energy Res.* 11, 1040781. doi:10.3389/fenrg.2023.1040781

Jiao, Y., and Nian, H. (2020). Grid-forming control for dfig based wind farms to enhance the stability of lcc-hvdc. *IEEE Access* 8, 156752–156762. doi:10.1109/access.2020.3019691

Lin, Z., and Liu, X. (2020). Wind power forecasting of an offshore wind turbine based on high-frequency scada data and deep learning neural network. *Energy* 201, 117693. doi:10.1016/j.energy.2020.117693

Liu, H., Li, M., Liu, L., and Shi, J. (2021). Frequency trajectory planning-based transient frequency regulation strategy for wind turbine systems. *IEEE J. Emerg. Sel. Top. Power Electron.* 10, 3987–4000. doi:10.1109/jestpe.2021.3113822

Liu, Y., Wu, X., Du, J., Song, Z., and Wu, G. (2020). Optimal sizing of a wind-energy storage system considering battery life. *Renew. Energy* 147, 2470–2483. doi:10.1016/j.renene.2019.09.123

Meng, J., Wang, D., Wang, Y., Guo, F., and Yu, J. (2023). An improved damping adaptive grid-forming control for black start of permanent magnet synchronous generator wind turbines supported with battery energy storage system. *IET Generation, Transm. Distribution* 17, 354–366. doi:10.1049/gtd2.12753

Mohamed, M. M., El Zoghby, H. M., Sharaf, S. M., and Mosa, M. A. (2022). Optimal virtual synchronous generator control of battery/supercapacitor hybrid energy storage system for frequency response enhancement of photovoltaic/diesel microgrid. *J. Energy Storage* 51, 104317. doi:10.1016/j.est.2022.104317

Sang, S., Pei, B., Huang, J., Zhang, L., and Xue, X. (2021). Low-voltage ride-through of the novel voltage source-controlled pmsg-based wind turbine based on switching the virtual resistor. *Appl. Sci.* 11, 6204. doi:10.3390/app11136204

Shadoul, M., Ahshan, R., AlAbri, R. S., Al-Badi, A., Albadi, M., and Jamil, M. (2022). A comprehensive review on a virtual-synchronous generator: topologies, control orders and techniques, energy storages, and applications. *Energies* 15, 8406. doi:10.3390/en15228406

Sun, M., Sun, Y., Chen, L., Zou, Z., Min, Y., Liu, R., et al. (2022). Novel temporary frequency support control strategy of wind turbine generator considering coordination with synchronous generator. *IEEE Trans. Sustain. Energy* 13, 1011–1020. doi:10.1109/tste.2022.3142914

Xiong, L., Liu, X., Zhang, D., and Liu, Y. (2020). Rapid power compensation-based frequency response strategy for low-inertia power systems. *IEEE J. Emerg. Sel. Top. Power Electron.* 9, 4500–4513. doi:10.1109/jestpe.2020.3032063

Xiong, L., Liu, X., Zhao, C., and Zhuo, F. (2019). A fast and robust real-time detection algorithm of decaying dc transient and harmonic components in three-phase systems. *IEEE Trans. Power Electron.* 35, 3332–3336. doi:10.1109/tpel.2019.2940891

Xiong, L., Zhuo, F., Wang, F., Liu, X., Chen, Y., Zhu, M., et al. (2015). Static synchronous generator model: a new perspective to investigate dynamic characteristics and stability issues of grid-tied pwm inverter. *IEEE Trans. Power Electron.* 31, 6264–6280. doi:10.1109/tpel.2015.2498933

Yang, J., Yang, T., Luo, L., and Peng, L. (2023). Tracking-dispatch of a combined wind-storage system based on model predictive control and two-layer fuzzy control strategy. *Prot. Control Mod. Power Syst.* 8, 58–16. doi:10.1186/s41601-023-00334-6

Yao, L., Wang, W., Liu, J., Wang, Y., and Chen, Z. (2024). Economic optimal control of source-storage collaboration based on wind power forecasting for transient frequency regulation. *J. Energy Storage* 84, 111002. doi:10.1016/j.est.2024.111002

Zeng, W., Li, R., Huang, L., Liu, C., and Cai, X. (2021). Approach to inertial compensation of hvdc offshore wind farms by mmc with ultracapacitor energy storage integration. *IEEE Trans. Industrial Electron.* 69, 12988–12998. doi:10.1109/tie.2021.3134092

Zhao, F., Wang, X., Zhou, Z., Harnefors, L., Svensson, J. R., Kocewiak, Ł. H., et al. (2021). Control interaction modeling and analysis of grid-forming battery energy storage system for offshore wind power plant. *IEEE Trans. Power Syst.* 37, 497–507. doi:10.1109/tpwrs.2021.3096850

frontiers | Frontiers in Energy Research

TYPE Original Research
PUBLISHED 15 July 2024
DOI 10.3389/fenrg.2024.1429713

OPEN ACCESS

EDITED BY
Yushuai Li,
Aalborg University, Denmark

REVIEWED BY
Xiang Li,
Zhengzhou University, China
Zheng Lan,
Hunan University of Technology, China
Zhongting Tang,
Aalborg University, Denmark

*CORRESPONDENCE
Zhengmei Lu,
luzhengmei@csu.edu.cn

RECEIVED 08 May 2024
ACCEPTED 17 June 2024
PUBLISHED 15 July 2024

CITATION
Li J, Wan D, Lu Z and Xu G (2024), A modified two-stage isolated bidirectional buck-DAB converter with a full-load ZVS range.
Front. Energy Res. 12:1429713.
doi: 10.3389/fenrg.2024.1429713

A modified two-stage isolated bidirectional buck-DAB converter with a full-load ZVS range

Jinliang Li[1,2], Dai Wan[1,2], Zhengmei Lu[3]* and Guo Xu[3]

[1]State Grid Hunan Electric Power Company Limited Research Institute, Changsha, China, [2]State Grid Joint Laboratory for Intelligent Application and Key Equipment in Distribution Network Institute, Changsha, China, [3]School of Automation, Central South University, Changsha, China

A modified two-stage buck-DAB (MBDAB) converter is proposed to improve the performance of the traditional two-stage buck-DAB (TSBDAB) converter. In the MBDAB converter, the DAB can work with fixed voltage gain and voltage-matched condition under a wide input voltage range. The voltage gain of the converter is adjusted through the added front-end stage, which is similar to a buck converter. Compared with the TSBDAB converter, only part of the transmitted power flows through the front-end stage, so the loss of the buck stage and the burden of zero-voltage switching (ZVS) can be reduced. Detailed analysis of the working principle, partial power characteristics, and the full-load ZVS range design are presented. To verify the effectiveness of the proposed MBDAB converter, experimental results are obtained from a prototype with a rated power of 1 kW.

KEYWORDS

isolated DC/DC converter, modified two-stage, buck-DAB converter, zero-voltage switching, bidirectional converter

1 Introduction

Bidirectional DC/DC converters play a crucial role in various applications like DC microgrids and energy storage systems to provide electrical isolation and voltage gain regulation capability (Inoue and Akagi, 2007; Masrur et al., 2018; Tu et al., 2019). In the domain of traditional IBDC converters, there are two key types: resonant converters and dual active bridge (DAB) converters (Zhao et al., 2014). DAB converters have gained significant interest due to their numerous benefits, such as electrical isolation, high efficiency, the ability to transfer energy bidirectionally, and soft-switching characteristics (Shao et al., 2019).

The single phase shift (SPS) control has only one degree of freedom, which is very simple (Doncker et al., 1988). However, the efficiency of the SPS-controlled DAB converter is low when the voltage gain is far away from the unity gain due to the large current stress and backflow power, and the zero-voltage switching (ZVS) cannot be achieved under full range. Therefore, to improve the efficiency of the DAB converter under a wide voltage range, modulation strategies with more control variables have been proposed. Extended phase shift (EPS) control and dual phase shift (DPS) control are two common two-degree-of-freedom control methods (Zhao et al., 2012; Sun et al., 2020). An inner phase-shift angle is introduced to reduce the RMS inductance current and the backflow power under a wide voltage range. Triple phase shift (TPS) control (Everts, 2017; Guo, 2020) is designed to further improve the performance of the DAB. There are three degrees of freedom in TPS control, which results in increased

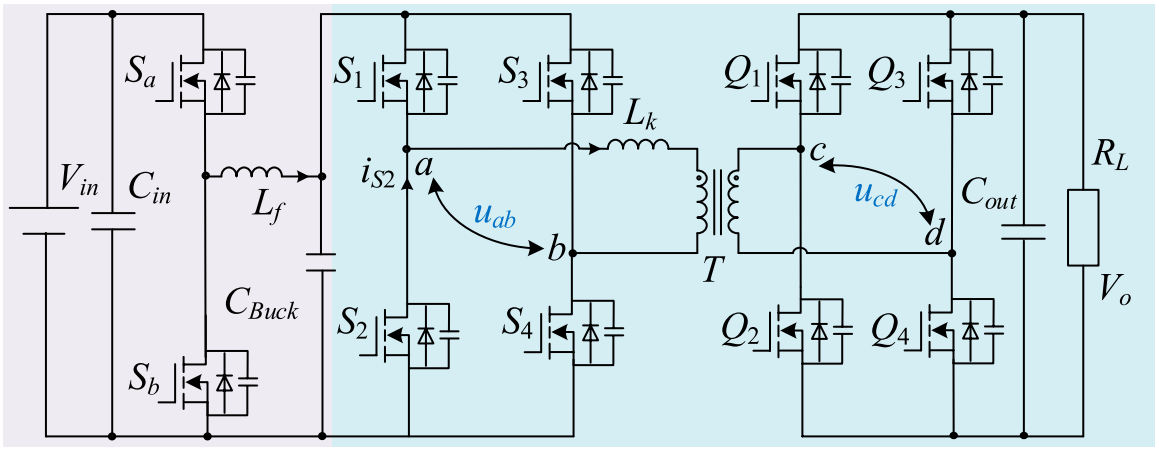

FIGURE 1
Topology of the TSBDAB converter.

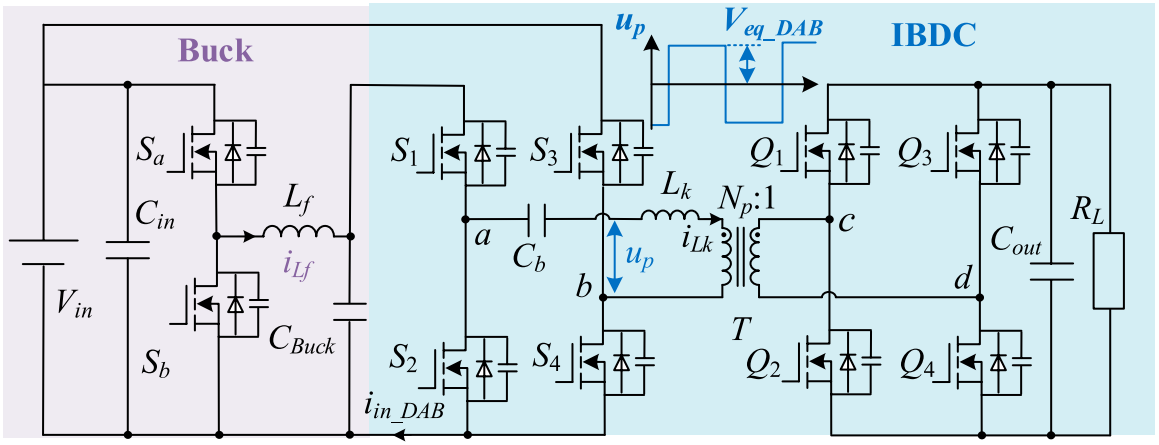

FIGURE 2
Topology of the proposed MBDAB converter.

complexity in both the operation modes and control strategy due to the added degree of freedom.

Another effective and simple solution for improving the performance of the converter under a wide voltage range is the restructuring of its topology (Alou et al., 2001; Lee et al., 2011; Fu et al., 2020; Xu et al., 2020; Liao et al., 2022; Lin et al., 2022). The core concept of this technique is to enable the DAB converter to operate under a unity gain condition across a wide voltage range by restructuring the topology. One straightforward way is the two-stage cascade solution. To achieve high performance, the IBDC converter operates under fixed voltage gain in the two-stage cascade scheme. The two-stage structure includes two DC/DC converters, and one of them has isolation properties, as detailed in Alou et al. (2001), Lee et al. (2011), Fu et al. (2020), and Xu et al. (2020). Figure 1 illustrates the configuration of the TSBDAB converter. Fu et al. (2020) enhanced the efficiency by combining the IBDC converter with a non-isolated boost converter. ZVS of all switches is achieved, and the overall losses are reduced. Xu et al. (2020) combined a DAB converter and a buck–boost converter to achieve superior performance under a wide voltage gain range. Lin et al. (2022) described the combination of the DAB and the

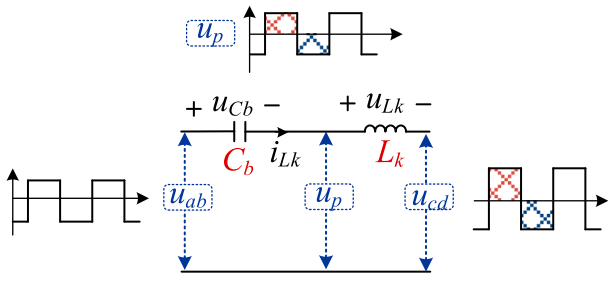

FIGURE 3
Equivalent circuit.

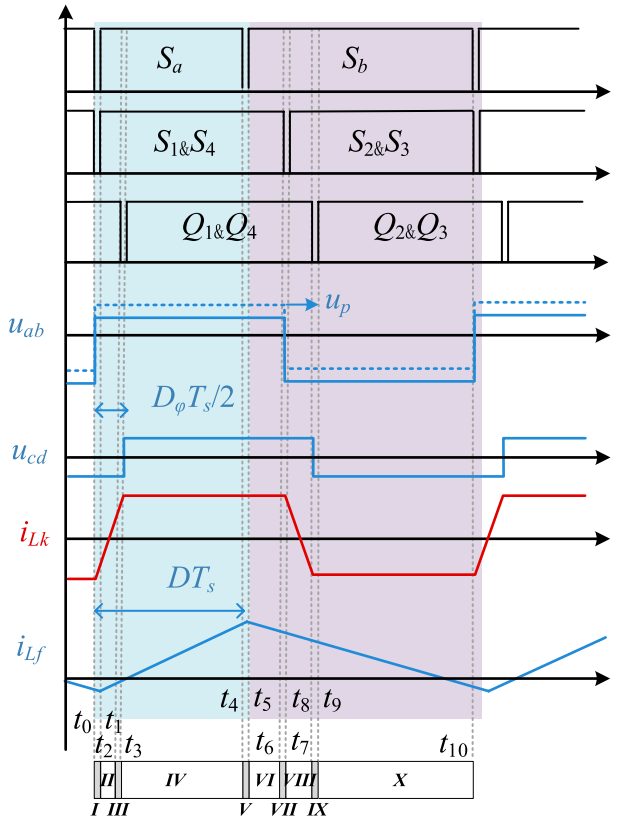

FIGURE 4
Key waveforms of the MBDAB converter.

boost converter in input-series configuration. High efficiency can be achieved by power-sharing adjustments between the two converters.

All of the power should be transferred by the front-end stage in the existing two-stage scheme, which leads to increased conversion loss. To improve the efficiency of the two-stage scheme and reduce the front-end-stage-transferred power, a partial power converter (PPC) approach as mentioned in Sun et al. (2008), Zientarski et al. (2019), and Liao et al. (2022) can be used. The PPC concept involves integrating the PPC submodule alongside the main power converters, either in parallel or in series. It is important to note that the PPC solution typically does not provide electrical isolation, as it often uses buck or buck/boost converters for the DC–DC conversion with partial power characteristics, as explained in Sun et al. (2008).

In this article, a modified isolated bidirectional buck-DAB converter is proposed to construct partial power transmission characteristics of the front-stage converter and further improve the efficiency of the two-stage converter under a wide voltage range. The proposed converter only requires a simple change in the connection architecture of the TSBDAB converter. In the MBDAB converter, when the input voltage changes, the front-end buck stage performs a gain adjustment, whereas DAB operates under a fixed voltage gain condition. In addition, the buck stage can only transmit part of the output power, which is due to the change in the connection architecture of the TSBDAB scheme. All the switches of the proposed converter can achieve the ZVS operation.

2 Proposed MBDAB converter and operation principles

2.1 Proposed modified buck-DAB converter

Figure 2 illustrates the proposed MBDAB converter. Compared with the TSBDAB converter in Figure 1, to achieve the partial power conversion, the source of S_1 is disconnected from the source of S_3, and the source of S_3 is directly connected to the input voltage. In addition, a blocking capacitor C_b is added to ensure that the voltages on both sides of the leakage inductor L_k are matched. The buck stage consists of two switches (S_a-$_b$), an inductor (L_f), and a capacitor (C_{Buck}). The DAB stage consists of two full bridges in the primary side and the secondary side, connected by a high-frequency transformer T with the turns ratio of N_p:1, an inductor (L_k), and a capacitor (C_b).

2.2 Mechanism of DC block capacitor C_b

The equivalent circuit of the DAB stage is shown in Figure 3. When the DAB stage is under the SPS control, the voltages on both sides of the leakage inductor are in volt–second equilibrium, which ensures that the inductor current i_{Lk} does not diverge. According to Figure 3, the relationship can be calculated as Eq. 1:

$$L_k \frac{d\bar{i}_{Lk}}{dt} = \bar{u}_{Lk} = \bar{u}_{ab} - \bar{u}_{cb} - \bar{u}_{cd}. \tag{1}$$

The steady state of the converter means that the average voltage of inductor L_k is 0. The relationship between the u_{ab}, u_p and u_{cd} is shown in Figure 3, the average values of u_{cd} and u_{ab} are 0 and $(V_{in}-V_{Buck})/2$, then the voltage on DC block capacitor C_b can be deduced as Eq. 2:

$$|\bar{u}_{cb}| = |\bar{u}_{ab}| = \frac{V_{in} - V_{Buck}}{2}. \tag{2}$$

2.3 Modulation strategies and operation principles

Figure 4 illustrates the modulation strategy and theoretical operating waveforms of the proposed MBDAB converter. According to Figure 4, switches S_a and S_b are driven complementarily, and pulse width modulation is applied to the buck converter. As for the DAB stage, the conventional SPS modulation is applied. It is very simple with a fixed 50% duty ratio.

The duty cycle D of S_a is to regulate the voltage across C_{Buck}. The half-cycle phase shift ratio D_φ is used to regulate the output power of

10.3389/fenrg.2024.1429713

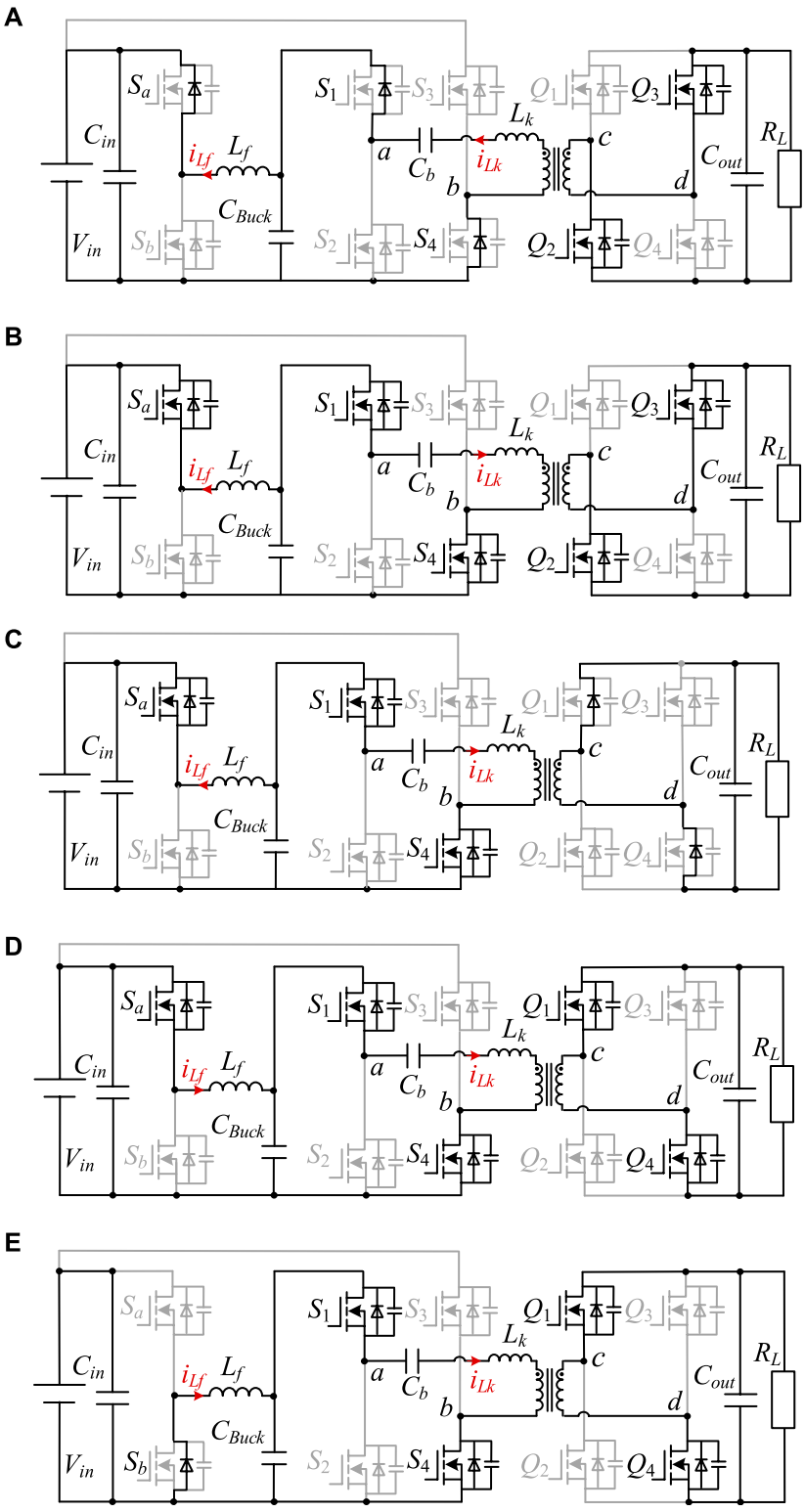

FIGURE 5
(Continued).

10.3389/fenrg.2024.1429713

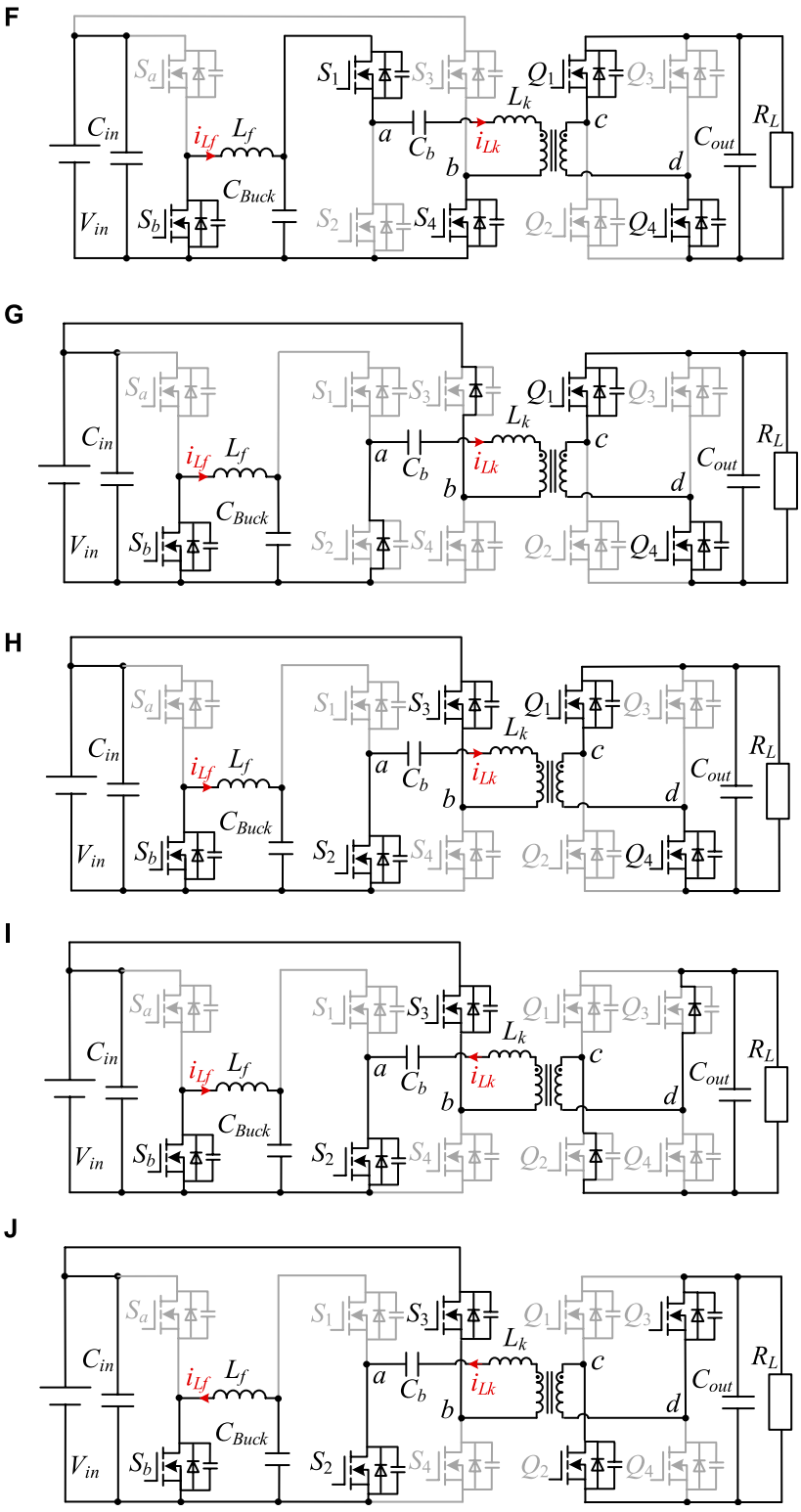

FIGURE 5
(Continued). Operational principles of the proposed converter: **(A)** *stage I* (t_0–t_1); **(B)** *stage II* (t_1–t_2); **(C)** *stage III* (t_2–t_3); **(D)** *stage IV* (t_3–t_4); **(E)** *stage V* (t_4–t_5); **(F)** *stage VI* (t_5–t_6); **(G)** *stage VII* (t_6–t_7); **(H)** *stage VIII* (t_7–t_8); **(I)** *stage IX* (t_8–t_9); and **(J)** *stage X* (t_9–t_{10}).

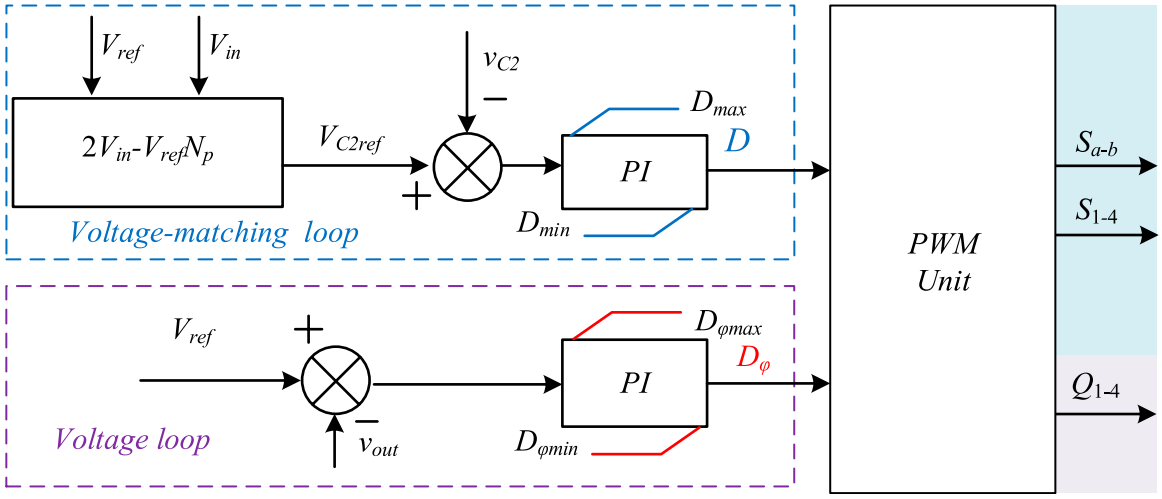

FIGURE 6
Control diagram of the proposed MBDAB converter.

TABLE 1 Specific parameters.

Parameter	Value
V_{in}	250–450 V
V_o	48 V
V_{eq_DAB}	240 V
N_p:1	5:1
L_k	39 μH
P	1,000 W
fs	100 kHz
C_{Buck}	25 μF
C_{in}/C_{out}	250 μF

DAB. It is worth pointing out that S_a and S_1 do not have to be turned on at the same time.

The 10 operating intervals are analyzed as follows and shown in Figure 5.

Stage I (t_0–t_1): At t_0, switches S_b, S_2, and S_3 are turned off. During stage I, since the currents i_{Lf} and i_{Lk} are negative, respectively, the body diodes of S_a, S_1, and S_4 are turned on. The conduction of diodes provides the conditions for the ZVS of the corresponding switches.

Stage II (t_1–t_2): At t_1, switches S_a, S_1, and S_4 are turned on under the ZVS condition. The voltage across inductors L_f and L_k is kept constant, and the currents i_{Lf} and i_{Lk} increase linearly. The inductor currents i_{Lf} and i_{Lk} are expressed in Eqs 3, 4:

$$L_f \frac{di_{Lf}}{dt} = V_{in} - DV_{in}, \tag{3}$$

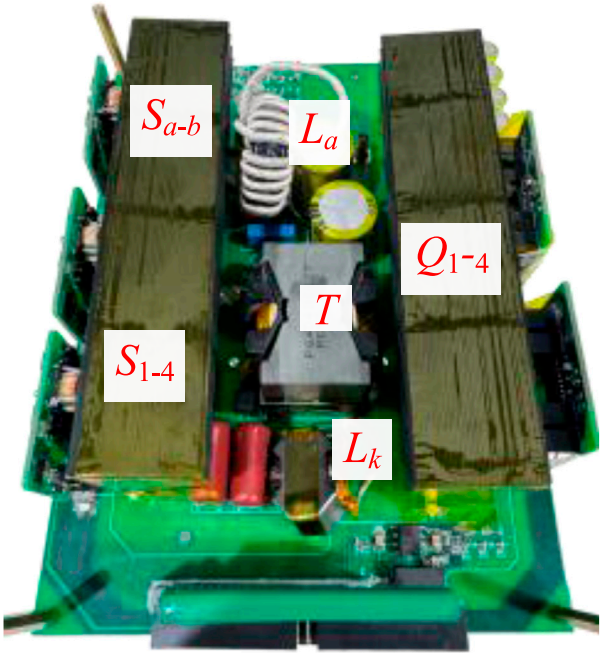

FIGURE 7
Prototype of the proposed MBDAB converter.

$$L_k \frac{di_{Lk}}{dt} = \frac{V_{in}(1+D)}{dt} = N_P + V_O. \tag{4}$$

Stage III (t_2–t_3): At t_2, switches Q_2 and Q_3 are turned off. During stage III, since the current i_{Lk} is positive, the body diodes of Q_1 and Q_4 are turned on. The conduction of diodes provides the conditions for the ZVS of the corresponding switches.

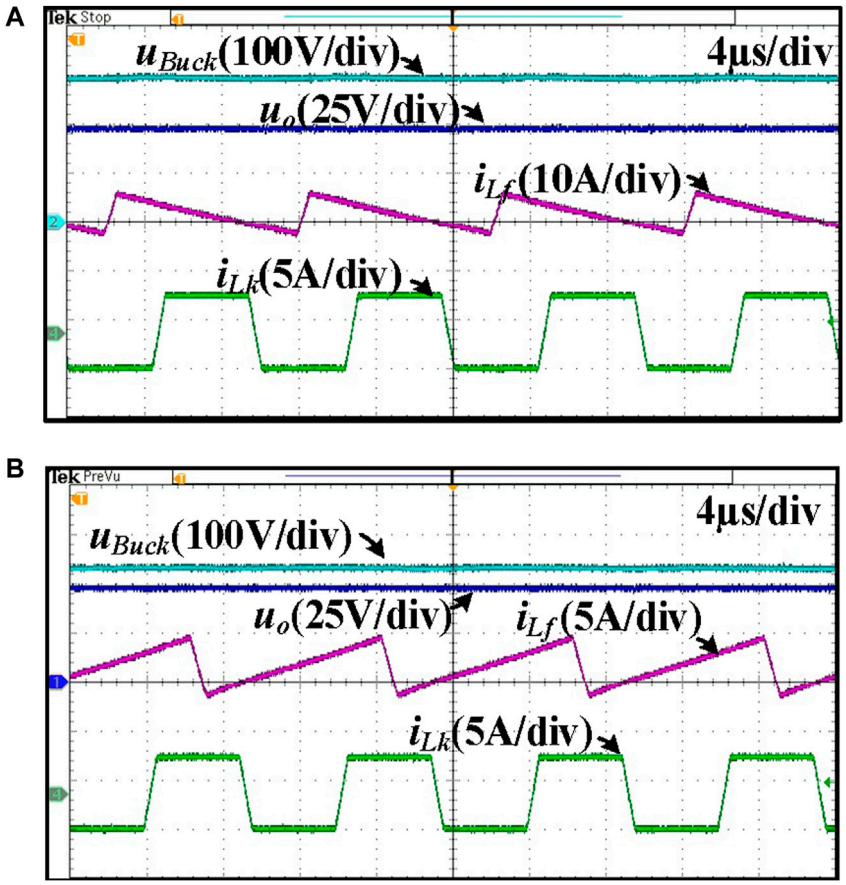

FIGURE 8
Steady-state waveforms of **(A)** V_{in} = 250 V; **(B)** V_{in} = 450 V.

Stage IV (t_3–t_4): At t_3, switches Q_1 and Q_4 are turned on under the ZVS condition. Since the voltage across the inductor Lk is zero under the voltage-matching condition, i_{Lk} keeps constant.

Stage V (t_4–t_5): At t_4, the switch S_a is turned off. Since the inductor current i_{Lf} is positive during stage V, the body diodes of S_b are turned on, which provides the conditions for ZVS of S_b.

Stage VI (t_5–t_6): At t_5, the switch S_b is turned on under the ZVS condition. The voltage across the inductor L_f is kept constant, and the current i_{Lf} decreases linearly which is expressed in Eq. 5:

$$L_f \frac{di_{Lf}}{dt} = -DV_{in}. \tag{5}$$

Stage VIII (t_7–t_8): At t_7, switches S_2 and S_3 are turned on under the ZVS condition. The voltage across the inductor L_k is kept constant, and the current i_{Lk} decreases linearly, which is expressed in Eq. 6:

$$L_k \frac{di_{Lk}}{dt} = -\frac{V_{in}(1+D)}{dt} = N_P V_O. \tag{6}$$

Stage IX (t_8–t_9): At t_8, switches Q_1 and Q_4 are turned off. During stage IX, since the current i_{Lk} is negative, the body diodes of Q_2 and Q_3 are turned on. The conduction of diodes provides the conditions for the ZVS of the corresponding switches.

Stage X (t_9–t_{10}): At t_9, switches Q_2 and Q_3 are turned on under the ZVS condition. Since the voltage across the inductor L_k is zero under the voltage-matching condition, the current i_{Lk} keeps constant.

3 Steady-state analysis of the proposed MBDAB converter

3.1 Analysis of the voltage gain ratio of the MBDAB converter

Under the SPS modulation strategy, the output power of DAB in the MBDAB converter can be expressed as Eq. 7:

$$P_{out} = \frac{N_p V_{eq} V_{out} D_\varphi \left(1 - D_\varphi\right)}{2L_k f_s}, \tag{7}$$

where N_p is the ratio of the high-frequency transformer and fs is the switching frequency of the converter. V_{eq} is one half of the peak-to-peak value of the voltage u_p, which can also be regarded as the

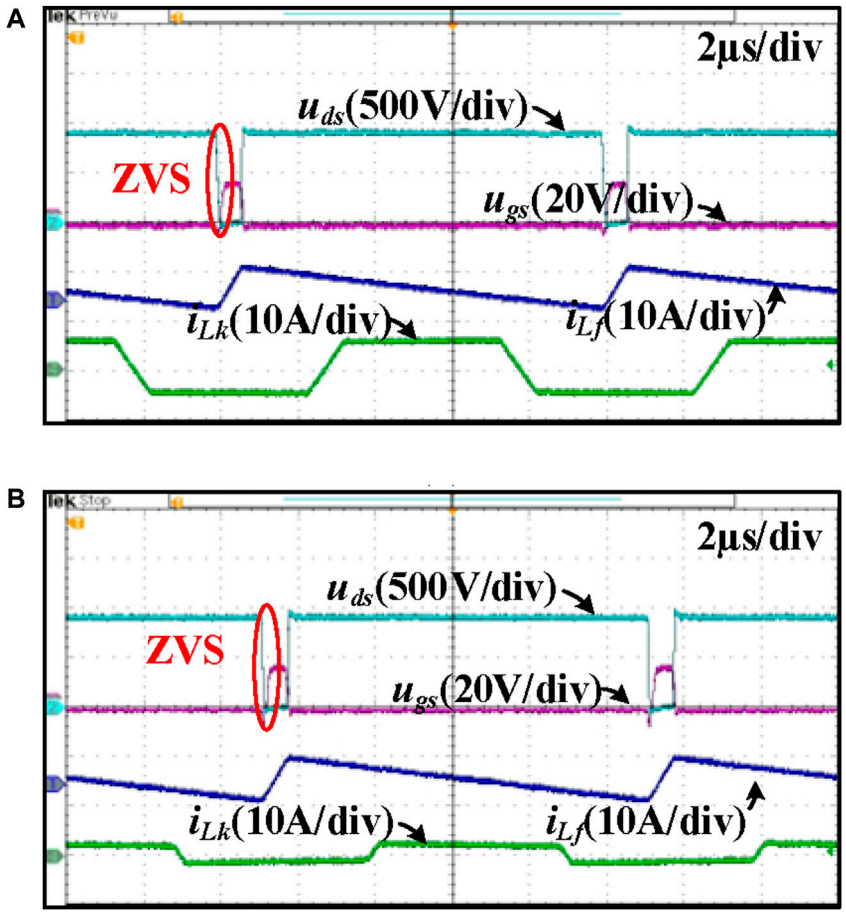

FIGURE 9
ZVS waveforms of S_a when V_{in} = 250 V: **(A)** light load; **(B)** heavy load.

equivalent input voltage of DAB. The expression of V_{eq} can be deduced as Eq. 8:

$$V_{eq} = \frac{V_{in} + V_{Buck}}{2}. \tag{8}$$

Therefore, the voltage gain of the DAB circuit in the modified buck-DAB converter can be derived as follows:

$$\begin{aligned} P_{out} &= \frac{N_p V_{eq} V_{out} D_\varphi (1 - D_\varphi)}{2 L_k f_s} = \frac{{V_{out}}^2}{R_L} \\ \Rightarrow M_1 &= \frac{V_{out}}{V_{eq}} = \frac{N_p D_\varphi (1 - D_\varphi) R_L}{2 L_k f_s} \end{aligned}, \tag{9}$$

where R_L is the resistance value of the load resistance and M_1 is the voltage gain of the DAB circuit. In order to achieve the voltage-matched condition of the DAB primary and secondary sides, the normalized gain of DAB is controlled to be constant at 1 in this converter, that is, $N_p M_1 = 1$.

The voltage gain of the buck circuit is expressed as Eq. 10:

$$\frac{V_{Buck}}{V_{in}} = D. \tag{10}$$

Considering the voltage gain of the buck part yields Eq. 11:

$$M_2 = \frac{V_{eq}}{V_{in}} = \frac{1 + D}{2}. \tag{11}$$

The voltage gain of the MBDAB converter can be expressed as Eq. 12:

$$M = M_1 M_2 = \frac{V_{out}}{V_{in}} = \frac{1 + D}{2N_p}. \tag{12}$$

It can be known from Eq. 9 that the voltage gain ratio is related to D of the buck stage and N_p. When D is within the range of [0,1], the normalized voltage gain ratio (MN_p) is within the range of [0.5,1].

3.2 Transferred power of the buck stage

In the proposed MBDAB converter, the buck stage only transfers power when S_1 is on, so the transferred power of it is always smaller than the output power of the system. In addition, the power is directly transferred from the input voltage V_{in} when the switch S_3 is on. Then, the inductor current of the buck stage has a smaller offset

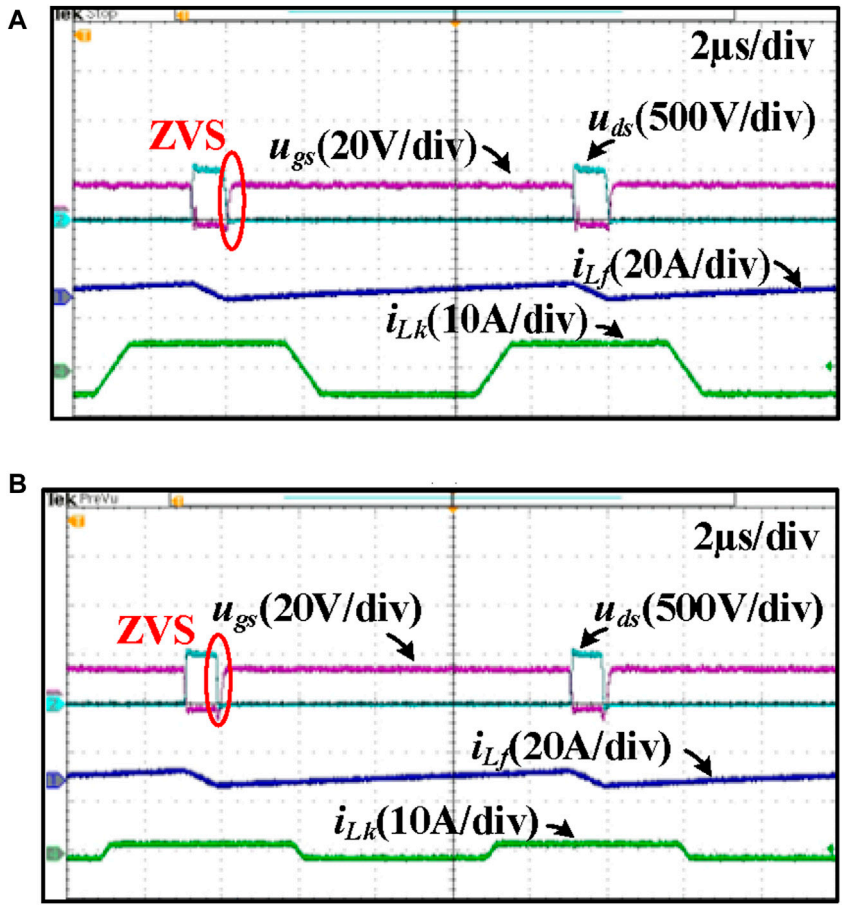

FIGURE 10
ZVS waveforms of S_a when V_{in} = 450 V: **(A)** light load; **(B)** heavy load.

and RMS value. It will reduce the loss and size of the buck inductor and help meet the ZVS condition of the buck switches.

The power of the MBDAB converter can be expressed as Eq. 13, according to power transmission characteristics of the DAB stage.

$$P = \frac{N_p V_{eq\_DAB} V_o D_\varphi \left(1 - D_\varphi\right)}{L_k f_s}. \tag{13}$$

Because the average inductor current is equal to half of the average DAB stage input current, the load current of the buck circuit can be expressed as Eq. 14:

$$i_{Load\_Buck} = \frac{1}{2} i_{in\_DAB} = \frac{N_p V_o D_\varphi \left(1 - D_\varphi\right)}{2L_k f_s}. \tag{14}$$

The transferred power of the buck stage can be expressed as Eq. 15:

$$P_{Buck} = V_{buck} i_{Load\_Buck=} = \frac{N_p V_o D_\varphi \left(1 - D_\varphi\right) D V_{in}}{4L_k f_s}. \tag{15}$$

The power transfer ratio for the buck stage to the DAB stage can be expressed as Eq. 16:

$$\frac{P_{Buck}}{P} = \frac{D}{1 + D} \leq 1. \tag{16}$$

3.3 Analysis of the ZVS condition

First, the ZVS conditions of the DAB circuit are analyzed. It can be seen from Figure 4 that before the switches S_1 and S_4 are turned on, the inductor current i_{Lk}<0 should be ensured to discharge the junction capacitor of the switches and make their body diodes turn on. Before the switches Q_1 and Q_4 are turned on, the inductor current i_{Lk} >0 should be ensured. The situation is similar when switches S_{2-3} and Q_{2-3} are switched on.

Therefore, the conditions for all switches of the DAB circuit to realize ZVS can be summarized as Eq. 17:

$$\begin{cases} i_{Lk}(t_1) < 0, \\ i_{Lk}(t_3) > 0. \end{cases} \tag{17}$$

To simplify the calculation, the change in the current in the dead time is ignored in the deduction. According to Formulas 4, 6 and the voltage-matching condition, the leakage inductor current at times t_1 and t_3 in the modified buck-DAB converter can be obtained as Eqs 18, 19:

$$i_{Lk}(t_1) = \frac{D_\varphi N_p v_{out}}{2L_k f_s}, \tag{18}$$

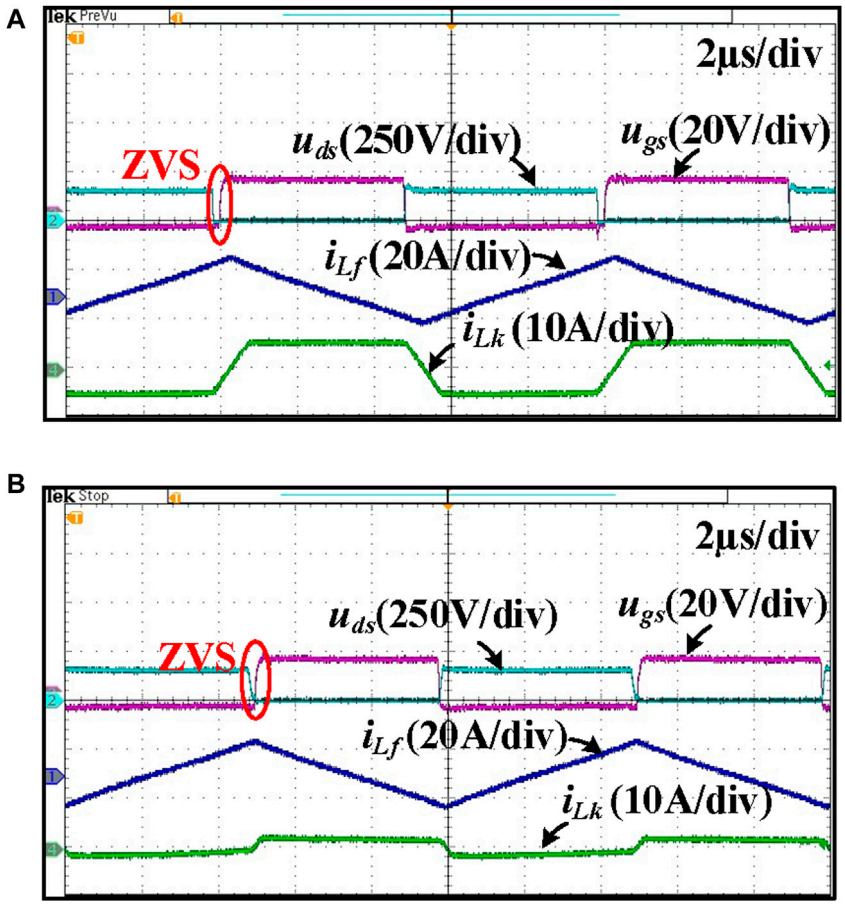

FIGURE 11
ZVS waveforms of S_1 under **(A)** light load; **(B)** heavy load.

$$i_{Lk}(t_3) = -\frac{D_\varphi N_p v_{out}}{2L_k f_s}. \tag{19}$$

It can be seen from the equation that when the modified buck-DAB satisfies the voltage-matched conditions, all switches in the DAB circuit can achieve the ZVS condition under any voltage gain and any load conditions.

As for the buck stage, the polarity of i_{Lf} before S_a and S_b are turned on determines the ZVS realization. The ZVS can always be achieved for S_a since $i_{Lf}(t) < 0$ are always feasible. By properly designing the inductance value of L_f, $i_{Lf}(t_2)<0$ can be ensured. Then, Sb can achieve ZVS turn on. The condition of S_b to realize ZVS turn on is shown in Eq. 20:

$$\frac{P}{V_{in}(D+1)} - \frac{D(1-D)V_{in}}{2f_s L_f} < 0. \tag{20}$$

3.4 Control strategy of the MBDAB converter

Based on the voltage-matched principle, the converter control strategy is designed as follows. The control block diagram is shown in Figure 6. The converter has two control degrees of freedom, D and D_φ, which are the output of the voltage-matching control loop and the output of the voltage-regulating loop, respectively. In the voltage control loop, the direction of the output voltage and transmission power is changed by adjusting the phase shift ratio D_φ.

4 Experimental verifications

To validate the effectiveness of the proposed MBDAB converter, a 1-kW prototype is designed. The main parameters of the prototype are presented in Table 1. In addition, the prototype of the MBDAB converter is shown in Figure 7.

The steady-state experimental waveforms of the MBDAB converter under V_{in} = 250 V and V_{in} = 450 V are shown in Figure 8. The voltage across the auxiliary capacitor C_{Buck}, the output voltage of the MBDAB converter, the buck inductor current i_{Lf}, and the DAB leakage inductor current are shown in the figure. As can be seen, the output voltage of the MBDAB converter can be stabilized at 48 V. The DAB leakage

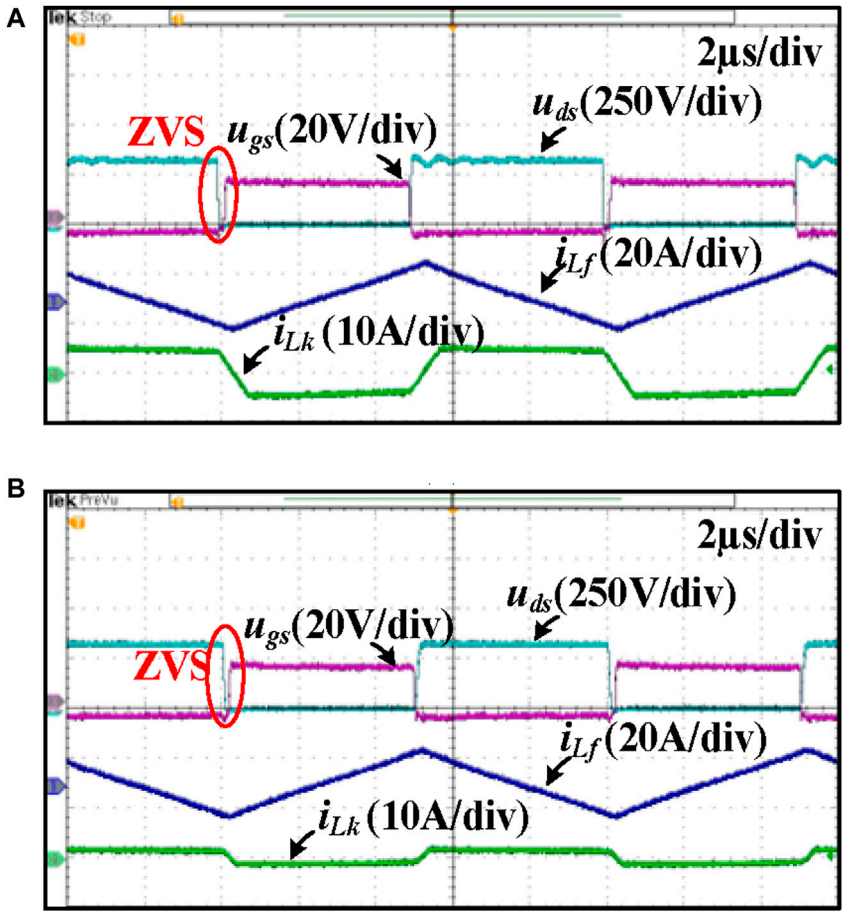

FIGURE 12
ZVS waveforms of S_2 under **(A)** light load; **(B)** heavy load.

inductor current iLk indicates that the voltage-matched condition is achieved. The waveforms of the currents are consistent with the theoretical analysis when input voltage varies.

The ZVS waveforms of S_a under 250 V input voltage and different loads are shown in Figure 9. The drain–source voltage across S_a, the driving signal of S_a, the buck inductor current, and the DAB leakage inductor current are shown in the figure. As can be seen, drain–source voltage across S_a has dropped to zero before the driving signal arises. As shown in the experimental results, S_a of the buck stage realizes ZVS under 250 V input voltage at both light and heavy loads. The heavy load condition is 1,000 W, and the light load condition is 300 W.

The ZVS waveforms of S_a under 450 V input voltage and different loads are shown in Figure 10. The drain–source voltage across S_a, the driving signal of S_a, the buck inductor current, and the DAB leakage inductor current are shown in the figure. As can be seen, the drain–source voltage across S_a has dropped to zero before the driving signal arises. As shown in the experimental results, S_a of the buck stage realizes ZVS under 450 V at both light and heavy loads.

The ZVS waveforms of S_1 under both light and heavy loads are shown in Figure 11. The drain–source voltage across S_1, the driving signal of S_1, the buck inductor current, and the DAB leakage inductor current are shown in the figure. As can be seen, the drain–source voltage across S_1 has dropped to zero before the driving signal arises. As shown in the experimental results, S_1 of the DAB stage realizes ZVS under a wide voltage range at both light and heavy loads.

The ZVS waveforms of S_2 under both light and heavy loads are shown in Figure 12. As can be seen, the drain–source voltage across S_2 has dropped to zero before the driving signal arises. As shown in the experimental results, S_2 of the DAB stage realizes ZVS under a wide voltage range at both light and heavy loads.

The experimental results of bidirectional power transfer are shown in Figure 13. As can be seen, under forward power transmission mode, the phase of u_{ab} is ahead of the phase of u_{cd}, as shown in Figure 13A. In addition, under backward power transmission mode, the phase of u_{ab} lags behind the phase of u_{cd}, as shown in Figure 13B.

The measured efficiency comparisons of the proposed MBDAB converter and the TSBDAB converter are shown in Figure 14. It includes experimental results under different loads and different input voltages. To ensure the fairness of comparison, the input and output voltage and the circuit parameters of the DAB circuit of the TSBDAB converter are

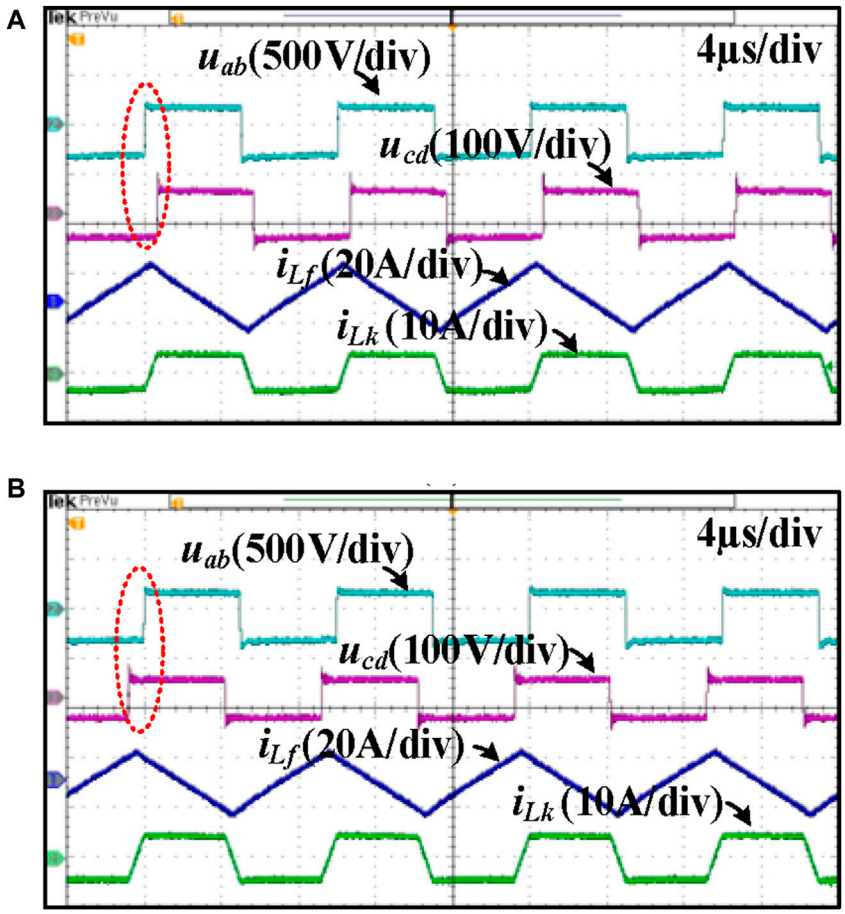

FIGURE 13
Bidirectional waveforms under 1,000 W: **(A)** forward mode; **(B)** backward mode.

the same as the MBDAB converter. In addition, to make a comparison under the same magnetic component, the inductance of the buck inductor in the TSBDAB converter is also designed the same as that in the MBDAB converter. This means that the ZVS condition of the buck part cannot be achieved under some load conditions in the TSBDAB converter. At lower input voltage, the proposed MBDAB converter has a higher efficiency than buck-DAB under a full-load range due to the partial power transmission characteristic. At medium input voltage, the two converters have similar efficiencies due to the similar current of i_{Lf}. At higher voltage, the proposed MBDAB converter has a higher efficiency than the buck-DAB converter due to the lower inductor current.

The loss breakdown of the proposed MBDAB converter under different input voltages and different loads is shown in Figure 15. The C3M0045065D of CREE is adopted as the MOSFETs of the primary and secondary switches of the converter. The PQ40-40 and RM10 are used as the inductor and transformer core of DAB. In addition, the inductor type of buck used for the prototype is Kool Mμ Toroid of 77071A7.

As shown in the figure, the total loss of the MBDAB converter under 350 V input voltage is higher than that of the input voltages at 250 V and 450 V, which is mainly caused by the increased inductor L_f iron loss. The peak-to-peak and RMS values of the buck inductor current under this operating point are larger. In addition, it can be seen from Figure 13 that the estimated efficiency is basically consistent with the measured efficiency with slightly mismatching. For example, at the output power of 200 W, the estimated losses are 9.4 W, 41.5 W, and 17.8 W at the input voltages of 250 V, 350 V, and 450 V, which are close to the measured efficiencies of 95.3%, 79.2%, and 91.1%, respectively.

5 Conclusion

In this article, a modified two-stage isolated bidirectional buck-DAB converter is proposed. When the input voltage of the MBDAB changes, the front-end buck stage performs gain adjustment, whereas DAB operates under a fixed voltage gain condition. The buck stage can only transmit part of the output power, which is due to the change in the TSBDAB scheme. All the switches of the proposed converter can achieve the ZVS condition. Working principle, voltage gain ratio analysis, power transfer

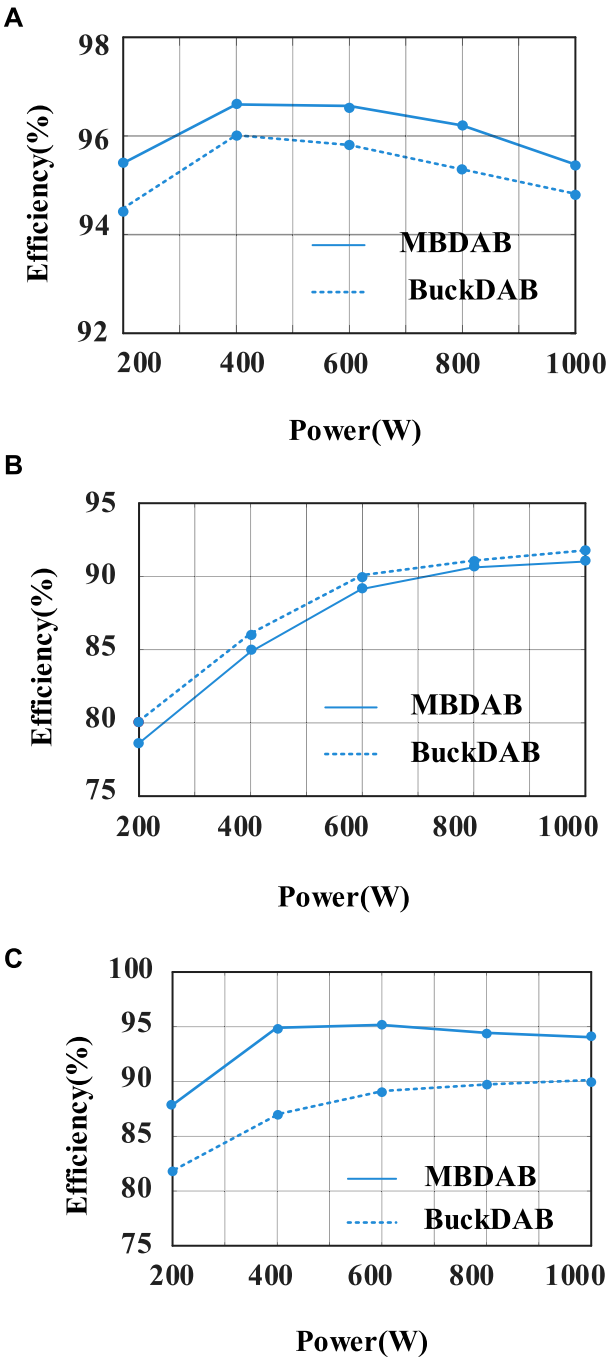

FIGURE 14
Comparison of measured efficiency of the proposed MBDAB and TSBDAB converters: **(A)** 250 V; **(B)** 350 V; and **(C)** 450 V.

characteristic, and ZVS analysis are introduced for the MBDAB converter.

The experimental results show that the proposed MBDAB converter can realize partial power transmission of the buck stage and ZVS of all switches, which reduces losses of the MBDAB converter effectively.

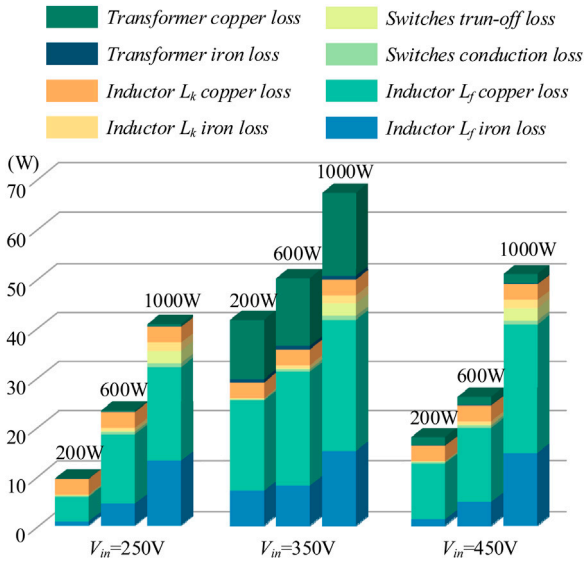

FIGURE 15
Loss breakdown of the proposed MBDAB converter under different input voltages and different loads.

Data availability statement

The raw data supporting the conclusions of this article will be made available by the authors, without undue reservation.

Author contributions

JL: software and writing–original draft. DW: investigation and writing–review and editing. ZL: methodology and writing–review and editing. GX: validation and writing–review and editing.

Funding

The author(s) declare that financial support was received for the research, authorship, and/or publication of this article. This work was financially supported by the Science and Technology Project of State Grid Hunan Electric Power Company Limited (5216A522000M).

Conflict of interest

Authors JL and DW were employed by State Grid Hunan Electric Power Company Limited Research.

The remaining authors declare that the research was conducted in the absence of any commercial or financial relationships that could be construed as a potential conflict of interest.

The authors declare that this study received funding from State Grid Hunan Electric Power Company Limited. The funder had the following involvement in the study:Thesis preparation, theoretical analysis and design.

Publisher's note

References

Alou, P., Oliver, J., and Cobos, J. A. (2001) "Buck + half bridge (d = 50%) topology applied to very low voltage power converters," in Annual IEEE Applied Power Electronics Conference and Exposition (APEC).

Doncker, R. W. D., Divan, D. M., and Kheraluwala, M. H. (1988)."A three-phase soft-switched high power density dc/dc converter for high power ap-plications," in Conference Record of the 1988 IEEE Industry Applications Society Annual Meeting, January-February, 1991 (IEEE), 1, 796–805.

Everts, J. (2017). Closed-form solution for efficient ZVS modulation of DAB converters. *IEEE Trans. Power Electron.* 32 (10), 7561–7576. doi:10.1109/tpel.2016.2633507

Fu, M., Fei, C., Lee, F. C., and Li, Q. (2020). A GaN-based DC–DC module for railway applications: design consideration and high-frequency digital control. *IEEE Trans. Ind. Electron.* 67 (2), 1638–1647. doi:10.1109/tie.2019.2896279

Guo, Z. (2020). Modulation scheme of dual active bridge converter for seamless transitions in multi-working modes compromising ZVS and conduction loss. *IEEE Trans. Ind. Electron.* 67 (9), 7399–7409. doi:10.1109/tie.2019.2945270

Inoue, S., and Akagi, H. (2007). A bidirectional DC–DC converter for an energy storage system with galvanic isolation. *IEEE Trans. Power Electron.* 22 (6), 2299–2306. doi:10.1109/tpel.2007.909248

Lee, J., Jeong, Y., and Han, B. (2011). An isolated DC/DC converter using high-frequency unregulated LLC resonant converter for fuel cell applications. *IEEE Trans. Ind. Electron.* 58 (7), 2926–2934. doi:10.1109/tie.2010.2076311

Liao, Y., Xu, G., Peng, T., Sun, Y., Yang, Y., and Xiong, W. (2022). Power-estimation-Based synchronous rectification solution for bidirectional DAB-LLC converter. *IEEE Trans. Circuits Syst. II Express Briefs* 69 (3), 1213–1217. doi:10.1109/TCSII.2021.3104884

Lin, N., Zhao, Z., Diao, F., Zhao, Y., and Balda, J. C. (2022). A current-fed dual-half-bridge-based composite converter with improved light-load efficiency through a multi-variable optimization. *IEEE Trans. Transp. Electrification* 8 (2), 3008–3020. doi:10.1109/tte.2021.3126726

Masrur, M. A., Skowronska, A. G., Hancock, J., Kolhoff, S. W., McGrew, D. Z., Vandiver, J. C., et al. (2018). Military-based vehicle-to-grid and vehicle-to-vehicle microgrid—system architecture and implementation. *IEEE Trans. Transp. Electrific* 4 (1), 157–171. doi:10.1109/tte.2017.2779268

Shao, S., Chen, H., Wu, X., Zhang, J., and Sheng, K. (2019). Circulating current and zvs-on of a dual active bridge dc-dc converter: a review. *IEEE Access* 7, 50 561–650 572. doi:10.1109/access.2019.2911009

Sun, J., Sun, Q., and Wang, P. (2020). Improved dynamic response strategy with dual phase-shift control for dual-active-bridge DC-DC converter. *IET Power Electron.* 13 (12), 2671–2674. doi:10.1049/iet-pel.2020.0076

Sun, J., Xu, M., Reusch, D., and Lee, F. C. (2008). "High efficiency quasi-parallel voltage regulators," in Proc. 23rd annu. IEEE appl. Power electron. Conf. Expo, Austin, TX, USA, February 24–28, 2008 (IEEE), 811–817.

Tu, H., Feng, H., Srdic, S., and Lukic, S. (2019). Extreme fast charging of electric vehicles: a technology overview. *IEEE Trans. Transp. Electrific* 5 (4), 861–878. doi:10.1109/tte.2019.2958709

Xu, C., Liu, S., and Guo, X. (2020) "A novel converter integrating buck-boost and DAB converter for wide input voltage," in The 46th Annual Conference of the IEEE Industrial Electronics Society (IECON), Singapore, October 18–21, 2020 (IEEE).

Zhao, B., Song, Q., Liu, W., and Sun, Y. (2014). Overview of dual-active-bridge isolated bidirectional DC–DC converter for high-frequency-link pow-er-conversion system. *IEEE Trans. Power Electron.* 29 (8), 4091–4106. doi:10.1109/tpel.2013.2289913

Zhao, B., Yu, Q., and Sun, W. (2012). Extended-phase-shift control of isolated bidirectional DC-DC converter for power distribution in microgrid. *IEEE Trans. Power Electron.* 27 (11), 4667–4680. doi:10.1109/tpel.2011.2180928

Zientarski, J. R. R., da Silva Martins, M. L., Pinheiro, J. R., and Hey, H. L. (2019). Evaluation of power processing in series-connected partial-power converters. *IEEE J. Emerg. Sel. Top. Power Electron.* 7 (1), 343–352. doi:10.1109/jestpe.2018.2869370

frontiers | Frontiers in Energy Research

TYPE Original Research
PUBLISHED 24 July 2024
DOI 10.3389/fenrg.2024.1426902

OPEN ACCESS

EDITED BY
Haitao Zhang,
Xi'an Jiaotong University, China

REVIEWED BY
Xingxing Chen,
Hong Kong Polytechnic University, Hong Kong SAR, China
Fangzhou Zhao,
Aalborg University, Denmark
Yang Peng,
China Academy of Railway Sciences, China

*CORRESPONDENCE
Mingli Ping,
ml1232011@163.com

RECEIVED 02 May 2024
ACCEPTED 03 July 2024
PUBLISHED 24 July 2024

CITATION
Ping M, Niu C, Liu X, Yang M and Wang X (2024), AC fault ride-through control strategy of MMC-UHVDC system with hierarchical connection mode.
Front. Energy Res. 12:1426902.
doi: 10.3389/fenrg.2024.1426902

AC fault ride-through control strategy of MMC-UHVDC system with hierarchical connection mode

Mingli Ping[1,2]*, Chong Niu[2], Xinhe Liu[1], Meijuan Yang[2] and Xianwei Wang[3]

[1]XJ Electric Corporation, Xuchang, China, [2]Xi'an Xuji Power Electronics Technology Co., Ltd., Xi'an, China, [3]China Electrical Equipment Group Co., Ltd., Shanghai, China

The ultra-high voltage direct current (UHVDC) transmission composed of modular multilevel converters (MMC) is an important technology for large-scale centralized transmission of renewable energy. In UHVDC system, temporary faults in the AC power grid system are a high probability fault, and the fault control strategy affects the safety and reliability of system operation. This paper studies on the condition of AC power grid faults occurring at the receiving converter station. Firstly, study the system characteristics after the occurrence of AC faults, and use theoretical analysis to derive the trend of DC voltage changes of each converter valve. Then, an AC fault ride-through control strategy with high power transmission capability is proposed with hierarchical connection structure, the strategy controls the system to synchronously reduce DC voltage and AC active power after a fault, maximizing the retention of the system's transmission capacity during the occurrence of faults, thereby reduce power shock in the system. Finally, a simulation model of the dual ended system has built based on the PSCAD simulation platform. The simulation results show that when a single-phase ground fault and a three-phase ground fault occur in the high valve group at the receiving station, the system can retain about 83% and 50% of the transmission capacity during the fault period, respectively. Meanwhile, there is no serious overvoltage or overcurrent phenomenon in the system. The simulation results verified the effectiveness of the proposed control strategy.

KEYWORDS

MMC-UHVDC, hierarchical connection mode, AC fault ride-through, reducing DC voltage, high power transmission capability

1 Introduction

With the profound transformation of the global energy structure and the urgent need for sustainable development, the position of renewable energy, such as solar energy, wind energy, etc., in the energy field is increasingly prominent due to their environmentally friendly and sustainable characteristics (Liu et al., 2021; Xiong et al., 2021; Rokicki et al., 2022; Alghamdi et al., 2023). The distance between load centers and renewable energy power stations is usually far, so the efficient transmission technology of large-scale renewable energy has become a research hotspot in the field of transmission.

The high-voltage direct current (HVDC) transmission system composed of MMC has many key technological advantages, such as large transmission capacity, low losses, long

transmission distances, the ability to connect to isolated and weak AC systems, and strong support for the power grid system (Wang and Redfern, 2010; Lei et al., 2019; Vercellotti, 2019; Saadeh et al., 2023). The MMC-UHVDC transmission system has a higher voltage level and larger transmission capacity, therefore it has greater advantages in the application scenarios of large-scale renewable energy transmission. In the process of building a new type of power system in the future, the technology of large-scale renewable energy transmission through MMC-UHVDC systems will play an important role.

At present, there is only one MMC-UHVDC project in operation worldwide, in which the receiving station is connected to the AC power grid through centralized access, with a maximum capacity of 5,000 MW (Baoan et al., 2021). In the future, with the increasing demand for optimizing the power grid structure and dispersedly consuming system power, the MMC-UHVDC system can refer to the line commutated converter based high-voltage direct current (LCC-HVDC) system and adopt the structure of hierarchical connection to the AC power grid. In recent years, most of the LCC-HVDC projects put into operation in China have adopted this hierarchical connection structure (Li et al., 2017). This structure gives the system a large short-circuit ratio and voltage support capacity, which helps optimize the power grid structure, balance power flow distribution, and improve the safety and stability level of the receiving end AC power grid (Jia et al., 2016; Qi et al., 2018; Ying et al., 2018; Ding et al., 2020).

This paper mainly studies the AC Fault ride-through control strategy of MMC-UHVDC system with hierarchical connection mode. In MMC-HVDC systems, there are two solutions to solve the power surplus problem caused by AC grid faults at the receiving station:

The first solution is to install additional energy consuming devices in the system to absorb surplus power. For application scenarios where onshore renewable energy transmission through MMC-HVDC systems, AC energy consumption devices are generally installed on the AC side of the transmitting station (Nian et al., 2020; Boning et al., 2020). For offshore wind power systems transmitted through MMC-HVDC, DC energy dissipation devices are generally installed on the DC side of the receiving station (Nentwig et al., 2016; Xu et al., 2021; Sixuan et al., 2023; Wang and Li, 2023). However, this solution requires additional equipment, which increases the system's footprint and investment cost.

The second solution is to use control strategies to reduce the power delivered to the DC system. This solution is suitable for the application scenario of the MMC-HVDC system's transmitting station connecting to the AC power grid. In this scenario, the active power is usually controlled by the transmitting station and the DC voltage is controlled by the receiving station. When a fault occurs in the AC power grid at the receiving end, control the transmitting station to reduce the active power, thereby ensuring power balance in the HVDC system (Ma et al., 2020).

For the application scenario where renewable energy is connected in parallel with the AC power grid and then sent out by MMC-UHVDC system, neither of the above two AC fault handling solutions is fully applicable to this system. Due to the fact that the AC side of the transmitting station in this system is equivalent to connecting to the power grid, the transmitting station can actively control the magnitude of AC power, so there is no need for the first costly solution. The second solution of using control strategies to reduce active power is usually applied in scenarios where the receiving station is centrally connected to the AC power grid. This solution significantly reduces the transmission capacity of the system during faults, causing significant power shocks in the system. At present, there is no literature proposing a better AC fault ride-through control strategy when MMC-UHVDC's receiving station hierarchical connected to the AC power grid.

In order to reduce the power shock of MMC-UHVDC system with hierarchical connection mode during AC fault ride-through process, this paper proposes an AC fault ride-through strategy with high power transmission capability that synchronously reduces DC voltage and active power during the fault period. This paper first analyzes the topology structure and steady-state control strategy of the MMC-UHVDC system. Then, study the system fault characteristics in the case of AC power grid faults occurring in a single valve group at the receiving station. Next, based on the characteristics of the system, an AC fault ride-through strategy with high power transmission capability is proposed. Finally, a dual end system simulation model is built on the PSCAD simulation platform, and the effectiveness of the proposed fault ride-through strategy is verified based on the simulation model.

This paper is organized as follows: Section 2 introduces the topology and steady-state control strategy of the MMC-UHVDC system. Section 3 establishes the equivalent circuit of the system after the AC fault to describe the system fault characteristics. Section 4 proposes a cost-effective AC fault ride-through strategy. Section 5 analyzes the effectiveness of control strategies using the simulation method. Section 6 introduces the conclusion.

2 Topology structure and steady-state control strategy of MMC-UHVDC system

2.1 Topology structure

The MMC-UHVDC system generally adopts a symmetrical bipolar topology structure. The parameters of each MMC in the same pole are consistent. Each pole is composed of high valves and low valves in series, thereby raising the DC voltage of the system. In order to enable the system to have DC fault ride-through capability, the MMC in the system is usually designed as the hybrid MMC composed of full bridge sub modules (FBSM) and half bridge sub modules (HBSM) (Fu et al., 2022; Han et al., 2023). This paper conducts research on the MMC-UHVDC system with hierarchical connection mode. The basic topology of the dual ended MMC-UHVDC system is shown in Figure 1.

2.2 Basic control strategy and operational characteristics

For the MMC-UHVDC system, the stability of DC voltage is the foundation for power transmission, so it is necessary to have a converter station to control the DC voltage of the system, and the other converter stations to control the active power of the system.

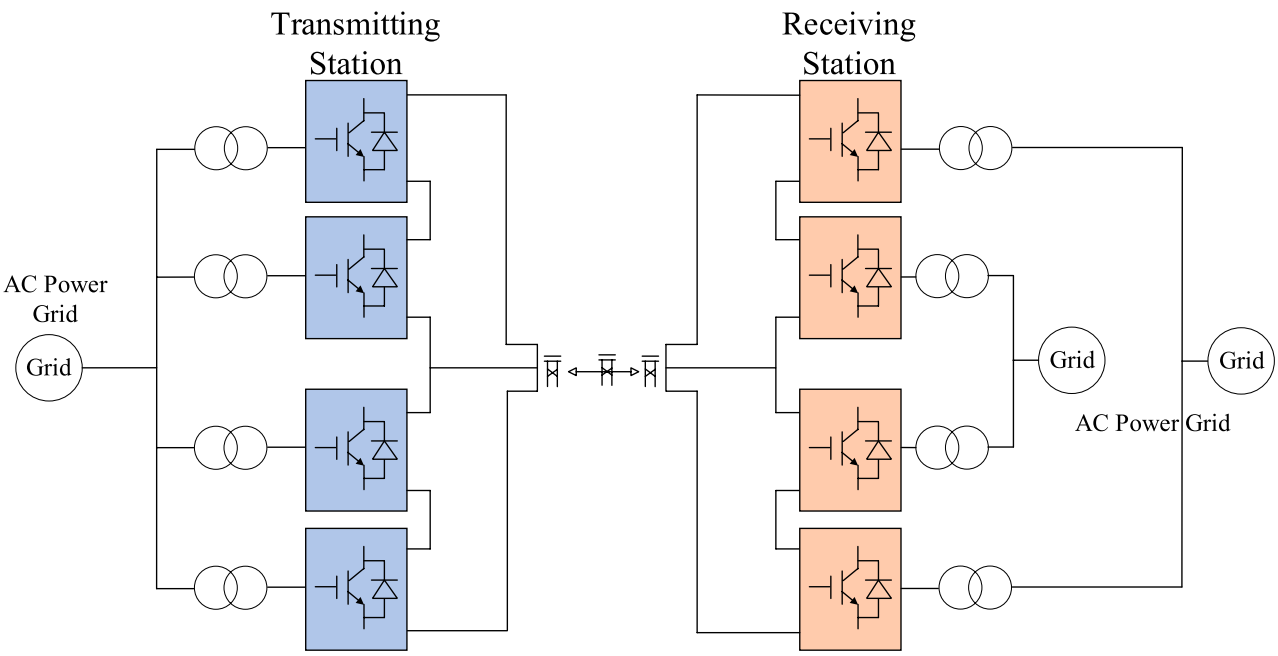

FIGURE 1
The topology of the dual ended MMC-UHVDC system.

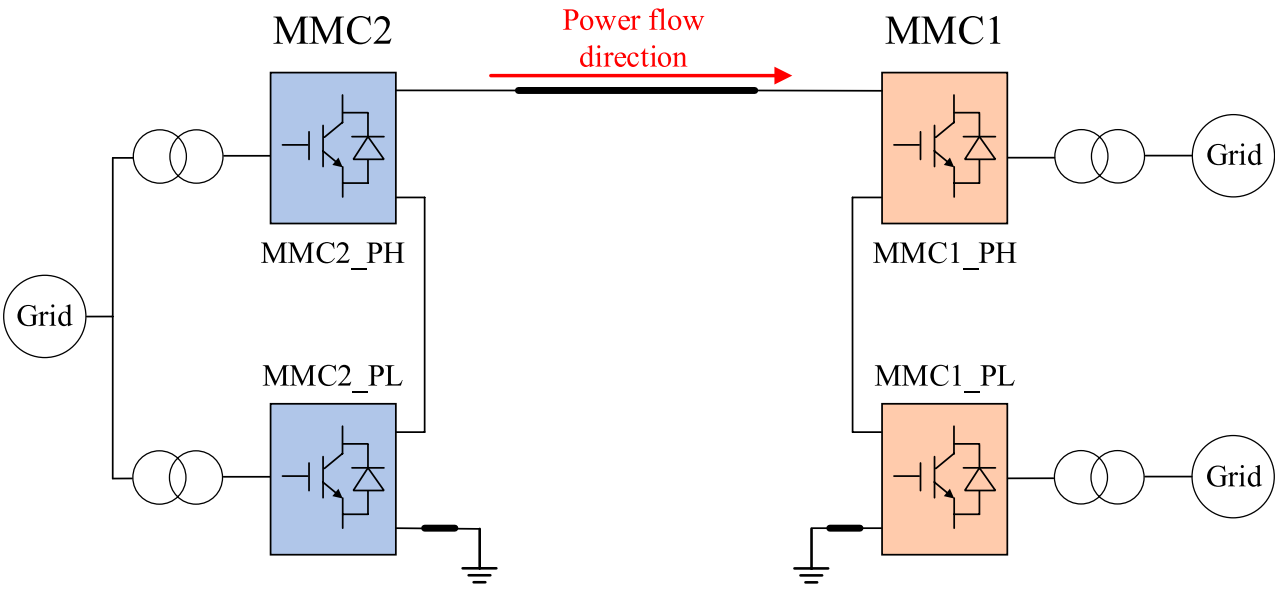

FIGURE 2
The topology of the positive electrode system.

Due to the consistent control strategies of the positive and negative electrode systems, the steady-state control strategy is analyzed using the positive electrode system as an example. The topology of the dual ended positive electrode system is shown in Figure 2, where the receiving station is called MMC1 and the transmitting station is called MMC2.

For a dual ended DC transmission system, the transmission capacity is determined by the transmitting station, so the active power is generally controlled by the transmitting station and the DC voltage of the system is controlled by the receiving station.

In this control mode, the high MMC at receiving station (MMC1_PH) and low MMC at receiving station (MMC1_PL) control their own DC voltage to be stable, and the DC voltage of both MMC is controlled to the rated value Udc0, that is, $U_{dc1\_PH} = U_{dc1\_PL} = U_{dc0}$. Due to the series structure of each MMC in the station, the DC current I_{dc} of each MMC is equal, indicating that the

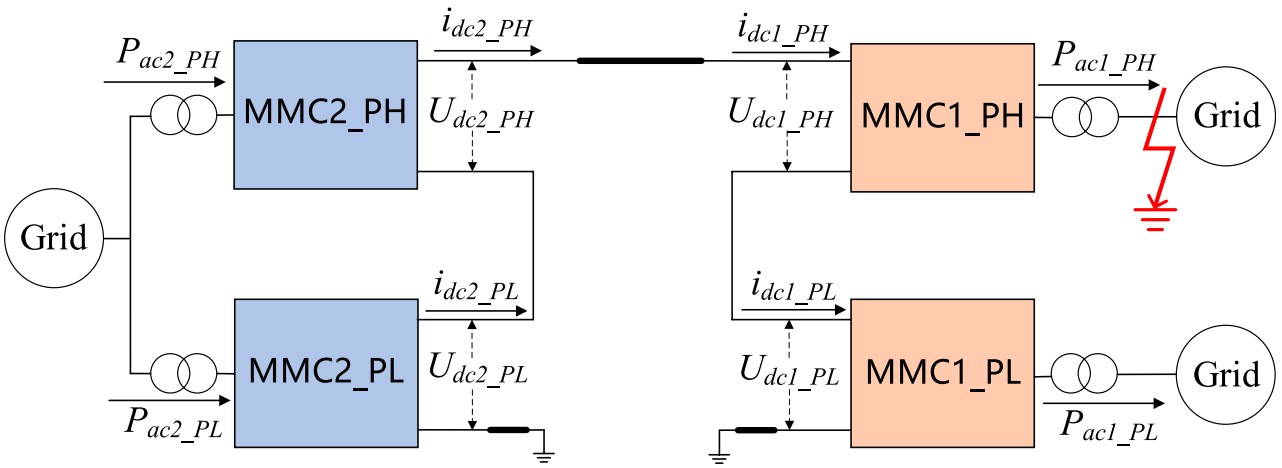

FIGURE 3
Schematic diagram of the system when the AC fault occurring in MMC1_PH.

DC input power of the 2 MMCs in the receiving station is equal. Because the power inside each MMC is balanced during steady state, the output AC power of MMC1_PH and MMC1_PL is also equal.

In the transmitting station, the high MMC at transmitting station (MMC2_PH) and low MMC at transmitting station (MMC2_PL) control their own AC active power, and the AC active power of the two MMC is equal. If there is no disturbance in the system, the DC voltage of both MMC will remain stable at the rated value Udc0. When a small disturbance occurs in the system, causing a small deviation $\triangle Udc$ in the DC voltage of the two MMC, if this disturbance causes the DC voltage U_{dc2_PH} of MMC2_PH being higher than that of MMC2_PL, this relationship can be expressed as Eq. 1:

$$\begin{cases} \boldsymbol{U_{dc2\_PH} = U_{dc0} + \Delta U_{dc}} \\ \boldsymbol{U_{dc2\_PL} = U_{dc0} - \Delta U_{dc}} \end{cases} \tag{1}$$

Then the DC side output power P_{dc2_PH} of MMC2_PH will increase, and the P_{dc2_PH} can be expressed as Eq. 2:

$$\boldsymbol{P_{dc2\_PH} = I_{dc} \times (U_{dc0} + \Delta U_{dc})} \tag{2}$$

At this point, due to the constant input power P_{ac2_PH} on the AC side of MMC2_PH, there will be a power imbalance phenomenon in the converter valve, the relationship can be expressed as Eq. 3:

$$\boldsymbol{P_{ac2\_PH} < P_{dc2\_PH}} \tag{3}$$

There is a power loss phenomenon in MMC2_PH, which leads to a decrease in its DC voltage and gradually decreases to near the rated value U_{dc0}.

Similarly, if the small disturbance in the system causes the DC voltage of MMC2_PH being lower than that of MMC2_PL, under the inherent relationship between the power and DC voltage of the MMC, the DC voltage of the MMC will also gradually recover to the rated value. Finally, the DC voltage of the MMC2_PH and MMC2_PL in the transmitting station will also be in an automatic equilibrium state, that is, $U_{dc2\_PH} = U_{dc2\_PL}$.

Based on the above analysis, when the transmitting station controls the active power of the system and the receiving station controls the DC voltage, the DC voltage and active power of the high and low converter valves in the receiving and transmitting stations can automatically maintain a balanced state in steady state.

3 System characteristics after fault occurring

This section mainly studies the system characteristics after a temporary AC power grid fault occurring. Considering that under the same type of fault conditions, the DC overvoltage caused by faults in the receiving station is the most severe. Therefore, this section takes the most severe three-phase metallic grounding fault (named ABCG fault) on the AC grid side of MMC1_PH in the receiving station as an example to analyze the system characteristics after the fault occurring. The schematic diagram of the positive electrode system fault is shown in Figure 3.

For the receiving station, after the occurrence of ABCG fault, the amplitude of the three-phase voltage on the AC side of MMC1-PH drops to zero, so the output power of MMC1_PH on the AC side drops to zero. Meanwhile, due to the fact that the DC side of MMC1_PH can be seen as composed of the capacitors of MMC submodules in series and parallel. Therefore, MMC1_PH can be equivalent to a capacitor *Ceq1_PH* connected in series to the DC side of the system. For MMC1_PL in the receiving station, due to the hierarchical connection of MMC1_PL and faulty MMC1_PH to different AC power grids, so the AC active power output by MMC1_PL is not affected by the fault, and the DC voltage control capability of MMC1_PH remains unchanged. Therefore, MMC1_PL can be equivalent to a DC voltage power supply, with a voltage source amplitude of U_{dc1_PL}.

For the transmitting station, both MMC2_PH and MMC2_PL maintain the control mode of controlling AC active power, and the active power of these 2 MMCs is equal, that is, $P_{ac2\_PH} = P_{ac2\_PL}$. According to the analysis in Section 2.2, it can be seen that the DC voltage of these 2 MMCs is also equal, that is, $U_{dc2\_PH} = U_{dc2\_PL}$. Therefore, the DC current of these 2 MMCs is also equal, with a current value of $i_{dc2\_PH} = i_{dc2\_PL}$. At the same time, the parameters of the MMC2_PH and MMC2_PL are exactly the same, so their DC

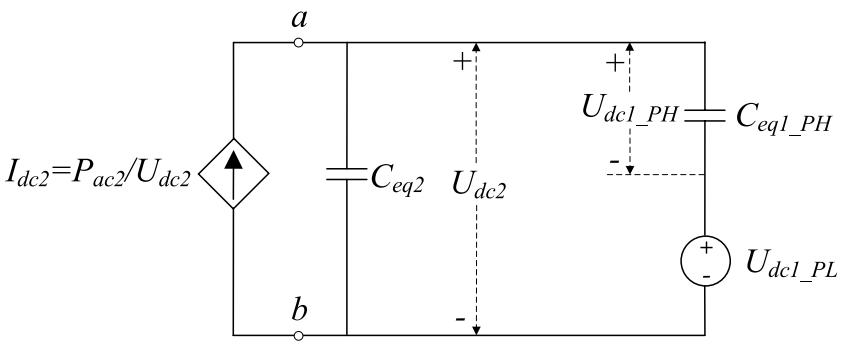

FIGURE 4
Equivalent circuit of positive electrode system after the ABCG fault occurs on MMC1_PH AC grid side.

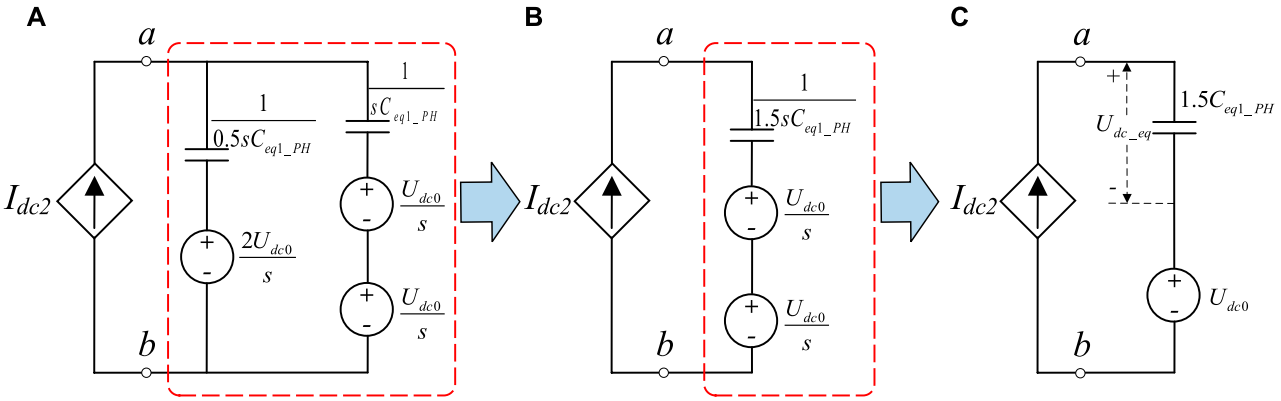

FIGURE 5
Further equivalent circuit after the ABCG fault occurs on MMC1_PH AC grid side. **(A)** Operational circuit **(B)** Thevenin equivalent circuit **(C)** Final equivalent circuit.

side can be equivalent to equal capacitance. Therefore, the transmitting station can be equivalent to a controlled current source i_{dc2} and an equivalent capacitor *Ceq2* in parallel as a whole. The amplitude i_{dc2} of the controlled current source is equal to the total active power P_{ac2} divided by the total DC voltage U_{dc2} at the transmitting station, and the equivalent capacitance *Ceq2* is equal to the series value of the equivalent capacitance of MMC2_PH and MMC2_PL.

Based on the above analysis, the circuit of positive electrode system after the ABCG fault occurs on the AC grid side of MMC1_PH can be equivalent to the topology shown in Figure 4.

Before the fault occurred, the DC voltage of MMC1_PH and MMC1_PL in the receiving station is equal. Therefore, in Figure 4, the initial voltage of the equivalent capacitance *Ceq1_PH* of MMC1_PH is equal to the equivalent DC voltage source amplitude U_{dc1_PL} of MMC1_PL, both of which are rated values U_{dc0}. Similarly, in Figure 4, the initial voltage of the equivalent capacitance *Ceq2* in the transmitting station is $U_{dc2} = 2^*U_{dc0}$. Due to the fact that in the MMC-UHVDC system studied in this paper, the parameters of each MMC at the transmitting and receiving stations are equal, so the relationship between the equivalent capacitance *Ceq1_PH* and *Ceq2* is: *Ceq2* = *Ceq1_PH*/2.

Perform Laplace transform on the right circuit of port ab in Figure 4 to obtain the operational circuit shown in Figure 5A. Then using the Thevenin's theorem, equivalent the circuit on the right side of port ab in Figure 5A to obtain the Thevenin equivalent circuit shown in Figure 5B. Finally, perform Laplace inverse transformation on the circuit in Figure 5B to obtain the time-domain circuit shown in Figure 5C, where the initial voltage of the equivalent capacitance of 1.5*Ceq1_PH* is U_{dc0}.

As shown in Figure 5C, the voltage of capacitor 1.5*Ceq1_PH* is U_{dc_eq}, and the capacitor voltage can generally be equivalent to a historical voltage source and an equivalent resistance related to the capacitance value and calculation step (Gnanarathna et al., 2011). Therefore, U_{dc_eq} can be expressed as Eq. 4:

$$\begin{aligned} U_{dc\_eq}(t) &= \frac{1}{1.5C_{eq1\_PH}}\int i_{dc2}(t)dt \approx U_{dc\_eq}(t-\Delta T) \\ &\quad + \frac{\Delta T}{1.5C_{eq1\_PH}}\left[\frac{i_{dc2}(t-\Delta T)+i_{dc2}(t)}{2}\right] \\ &= \frac{\Delta T}{2\times 1.5C_{eq1\_PH}} i_{dc2}(t) \\ &\quad + \left[\frac{\Delta T}{2\times 1.5C_{eq1\_PH}} i_{dc2}(t-\Delta T) + U_{dc\_eq}(t-\Delta T)\right] \end{aligned} \quad (4)$$

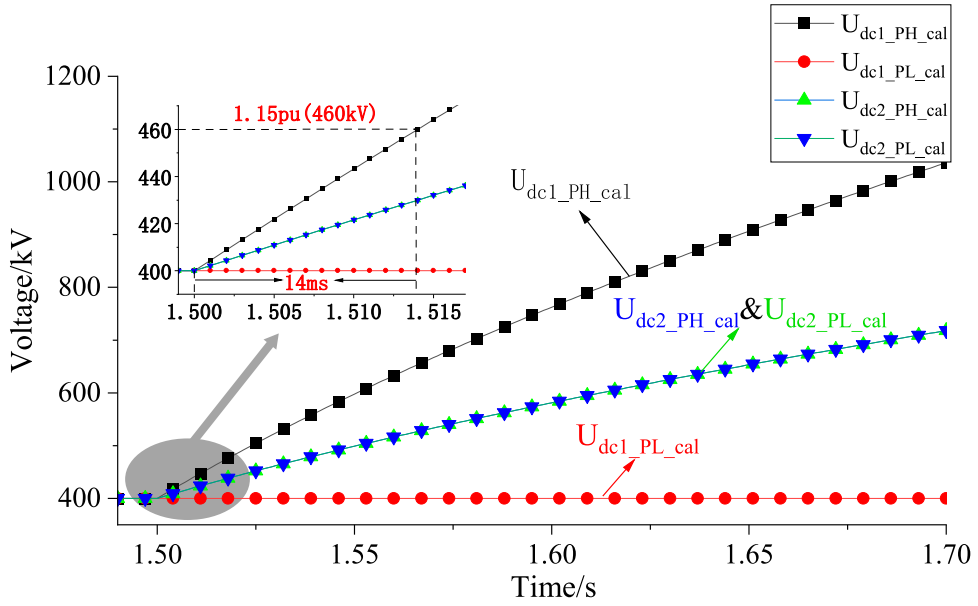

FIGURE 6
Calculation results of DC voltage variation trends for all MMCs after the fault.

In the above formula, $\triangle T$ is the calculation step size, and $U_{dc\_eq}(t\text{-}\triangle T)$ is the voltage of $1.5C_{eq1\_PH}$ at the previous calculation time. $i_{dc2}(t\text{-}\triangle T)$ is the current flowing through the equivalent capacitor $1.5C_{eq1\_PH}$ at the previous calculation time.

After the system completes the calculation of the capacitor voltage $U_{dc\_eq}(t)$ at this time, the calculation result at this time is stored for the next calculation time.

The calculation formula for the current $i_{dc2}(t+\triangle T)$ flowing through the equivalent capacitor $1.5C_{eq1\_PH}$ in the next calculation time of the system is:

$$i_{dc2}(t+\Delta T) = P_{ac2}/U_{dc2} = P_{ac2}/\left(U_{dc\_eq}(t)+U_{dc0}\right) \quad (5)$$

By replacing the current $i_{dc2}(t)$ in Eq. 4 with the calculated value $i_{dc2}(t+\triangle T)$ in Eq. 5, and the equivalent capacitor voltage $U_{dc\_eq}(t+\triangle T)$ at the next calculation time can be obtained. By iteratively calculating, the trend of the capacitor voltage $U_{dc\_eq}(t)$ over time in the equivalent circuit of Figure 5C can be obtained.

The following text derives the voltage of the high-end and low-end MMCs in the transmitting and receiving stations based on the calculated voltage $U_{dc\_eq}(t)$.

From Figures 4, 5C, it can be seen that the voltage at port ab is the total voltage U_{dc2} of the positive electrode system. Due to the fact that the DC voltage of MMC2_PH and MMC2_PL in the transmitting station is equal, the calculation formula for the DC voltage of these 2 MMCs is:

$$U_{dc2\_PH} = U_{dc2\_PL} = U_{dc2}/2 = \left(U_{dc\_eq}(t)+U_{dc0}\right)/2 \quad (6)$$

From Figure 4, it can be seen that for MMC1_PL in the receiving station, its DC voltage U_{dc1_PL} is equal to U_{dc0}. Therefore, the formula for calculating the DC voltage of MMC1_PH in the receiving station is shown in Eq. 7.

$$U_{dc1\_PH} = U_{dc2} - U_{dc1\_PL} = U_{dc\_eq}(t) \quad (7)$$

Figure 6 shows the trends of voltage variation over time for $U_{dc1\_PH}(t)$, $U_{dc1\_PL}(t)$, $U_{dc2\_PH}(t)$, and $U_{dc2\_PL}(t)$ after the fault occurring, with C_{eq1_PH} = 750uF, $\triangle T$ = 50us, P_{ac2} = 4000 MW, and U_{dc0} = 400 kV as the initial variables.

From Figure 6, it can be seen that when a three-phase grounding fault occurs in the MMC1_PH of the receiving station, due to the system output power being blocked while the input power remains unchanged, the DC voltage of the system will rapidly increase. Among them, the DC voltage $U_{dc1\_PH}(t)$ of the faulty MMC rises the fastest, and it rises to 1.15pu (460 kV) within 14 ms after the fault occurring. In order to avoid equipment damage caused by overvoltage in MMC, it is recommended that the system quickly take fault handling measures in a short period of time to protect the safety of the system equipment.

4 AC fault ride-through control strategy

Section 3 has studied the system characteristics after an AC power grid fault occurring at the receiving station. The research results show that the DC voltage of the faulty MMC will rapidly increase, and the effective measure need to be taken in a timely manner to suppress overvoltage. Therefore, this section mainly studies the AC fault ride-through control strategy of the receiving station after the fault occurring.

4.1 Basic AC fault ride-through control strategy

In a dual ended MMC-UHVDC system, when an AC grid fault occurs in the MMC1_PH of the receiving station, so the output power on the AC side is blocked, resulting in surplus power in this

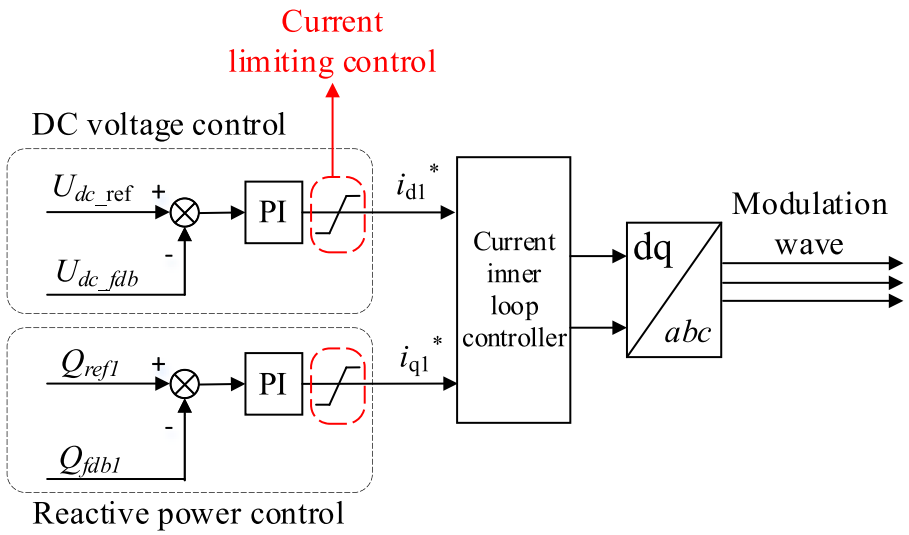

FIGURE 7
Basic control strategy of high-end MMC at the receiving station.

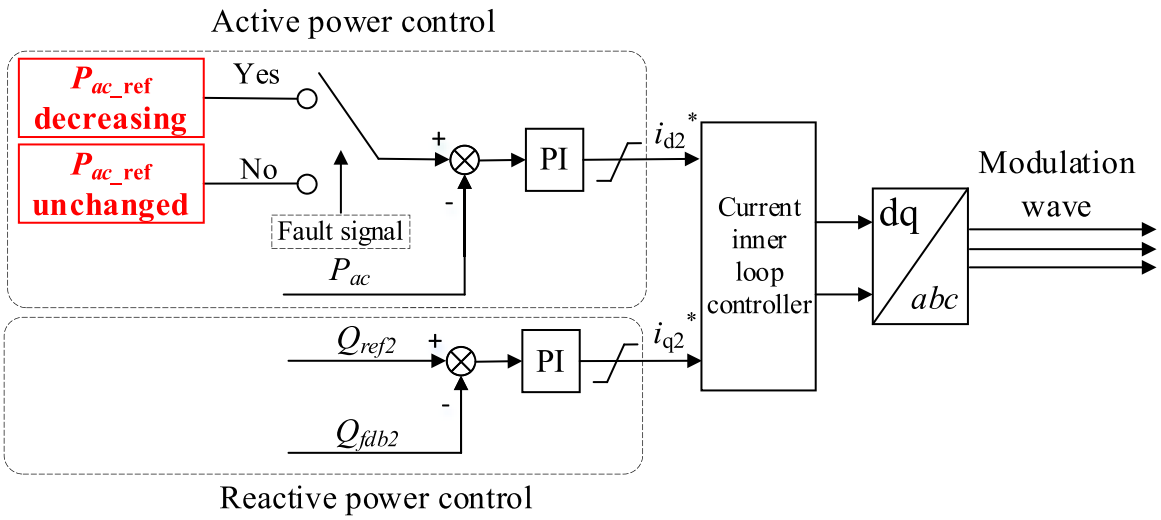

FIGURE 8
Basic control strategy of high-end MMC at the transmitting station.

MMC. The surplus power in the faulty MMC can be reduced by reducing the AC power of the transmitting station.

For the receiving station, during the fault ride through process, the control strategy of its high-end MMC and low-end MMC is the same, maintaining a constant DC voltage control strategy and adopting a current limiting control strategy to avoid serious overcurrent phenomena. The control strategy of MMC in the receiving station is shown in Figure 7.

In Figure 7, U_{dc_ref} is the DC voltage command value of MMC in the receiving station, and U_{dc_fdb} is the DC voltage feedback value. Q_{ref1} is the reactive power command value, and Q_{fdb1} is the reactive power feedback value; I_{d1}* and I_{q1}* are the command values for the d-axis component and q-axis component of the current inner loop, respectively.

For the transmitting station, since the DC current of the high-end MMC and the low-end MMC are the same, and the DC voltage of the 2 MMCs are also in an automatic balancing state, so the AC power of the 2 MMCs must also be consistent. After the fault occurring, the active power of the high-end MMC and the low-end MMC need to be synchronously reduced. The control strategy for the MMCs in the transmitting station is consistent, as shown in Figure 8. When the transmitting station receives the fault signal, its MMCs synchronously reduce the active power command value, so that the active power absorbed by the MMC-UHVDC system from the AC power grid will be reduced, avoiding serious overvoltage in the system.

In Figure 8, P_{ac_ref} is the AC active power command value of MMC in the transmitting station, and P_{ac_fdb} is the AC active power

feedback value. Q_{ref2} is the reactive power command value of MMC, and Q_{fdb2} is the reactive power feedback value. I_{d2}* and I_{q2}* are the command values for the d-axis and q-axis components of the current inner loop of MMC, respectively.

When an ABCG fault occurs on the AC side of the high-end MMC in the receiving station, the active power output on the AC side of the MMC drops to zero. In order to ensure power balance of the faulty MMC, the DC current of the system should be reduced to zero. Under the control of the basic AC fault ride-through strategy, the active power of both the high-end MMC and low-end MMC in the transmitting station is reduced to zero. Meanwhile the active power of the low-end MMC in the receiving station that without fault is also reduced to zero due to the decrease in DC current.

According to the above analysis, there is certain problem when using the basic AC fault ride-through strategy. In order to reduce the surplus power in the faulty MMC, it is necessary to synchronously reduce the active power of all MMCs in the same pole to avoid serious overvoltage in the faulty MMC. So, it can be said that adopting this basic control strategy significantly reduces the power transmission capacity of the system during faults, leading to significant power shocks in the system.

Therefore, it is necessary to study the AC fault ride-through strategy with high power transmission capacity during the fault occurring.

4.2 Optimized AC fault ride-through strategy for high power transmission capability

In order to maximize the power transmission capacity of the system after a fault occurs, this paper proposes a strategy to reduce the surplus power in the faulty MMC by reducing its DC voltage while keeping the DC current of the system unchanged. At the same time, the transmitting station synchronously reduces a portion of active power. The following text provides a detailed explanation of the AC fault ride-through control strategy with high power transmission capability.

In MMC, electrical variables such as active power, DC voltage, and reactive power are controlled by adjusting the magnitude and phase of the bridge arm voltage. The expression of the a-phase bridge arm voltage in MMC is shown in Eq. 8 (Saeedifard and Iravani, 2010), and there is also the similar electrical variable relationship in b-phase and c-phase.

$$\begin{cases} v_{arm\_pa} = 0.5 \times U_{dc} - e_a \\ v_{arm\_na} = 0.5 \times U_{dc} + e_a \end{cases} \tag{8}$$

In the formula, v_{arm_pa} and v_{arm_na} are the voltages of the upper and lower bridge arms of a-phase in MMC, respectively; U_{dc} is the DC voltage of MMC; e_a is the voltage of phase A on the AC side of the MMC.

In the conventional basic control strategy of MMC, MMC is usually regarded as a single input control system as shown in Figure 9A, which only controls MMC by adjusting the valve side AC voltage e_{abc}. In order to fully utilize the control freedom of MMC, MMC can be seen as a dual input control system as shown in Figure 9B, which can control the power balance in MMC by simultaneously adjusting the valve side AC voltage e_{abc} and DC voltage U_{dc}.

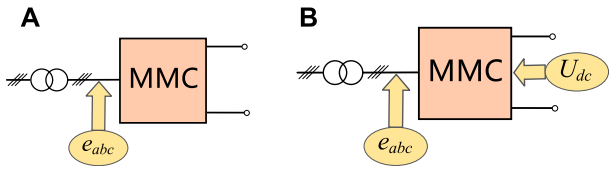

FIGURE 9
Equivalent control system of MMC. **(A)** Equivalent single input control system **(B)** Equivalent dual input control system.

When an AC fault occurs in the high-end MMC of the receiving station, the output active power on the AC side is blocked, and the AC side control ability of the faulty MMC is weakened. In order to quickly reduce the surplus power in the faulty MMC, the DC input power P_{dc} of the MMC can be reduced. And P_{dc} is directly related to the DC voltage U_{dc} and DC current I_{dc}, as shown in Eq. 9.

$$P_{dc} = I_{dc} \times U_{dc} \tag{9}$$

Due to the equal I_{dc} of each MMC in the same pole system, in order to reduce the impact of faults on other MMCs without fault, it is chosen to reduce the surplus power by reducing the DC voltage U_{dc} of the faulty MMC. The amount of surplus power in the faulty MMC will be reflected by the sub-module voltage. Therefore, a controller is designed between the submodule voltage and the DC voltage U_{dc}. When the submodules' average voltage v_{sm_ave} increases and is higher than the rated value of the submodules' average voltage v_{sm_rated} in the faulty MMC, the DC modulation voltage U_{dc_m} is decreased to reduce the input active power on the DC side, thereby controlling the power balance inside the faulty MMC. The control strategy on the AC side is the same as the basic strategy in Section 4.1, and the modulation voltage v_{abc} on the AC side is obtained through dual closed-loop control. The overall control strategy of the faulty MMC is shown in Figure 10. The low-end MMC of the receiving station maintains the original control strategy unchanged.

For the transmitting station, due to the fact that the input active power remains unchanged for a short period of time after the fault occurring, the system's DC current will increase with the decrease of the receiving station's DC voltage. In order to control the DC current near the rated value, a controller needs to be designed in the transmitting station between the DC current I_{dc_fdb} and the active power reference value P_{ac_ref}. Under the action of the controller, P_{ac_ref} will decrease with the increase of I_{dc_fdb}.

At the same time, in order to control the submodule voltage of the MMC in the transmitting station within a stable range, it is also necessary to control the DC voltage of the MMC. Therefore, a controller is designed between the submodules' average voltage v_{sm_ave2} and the DC modulation voltage U_{dc_m2}. Under the action of this controller, when v_{sm_ave2} decreases, U_{dc_m2} is decreased to reduce the output power on the DC side, thereby controlling the power balance within the MMC. Setting only one MMC as the power reducing MMC in the transmitting station can achieve the control goal. In this paper, the high-end MMC in the transmitting station is set to reduce active power. The control strategy of this MMC is shown in

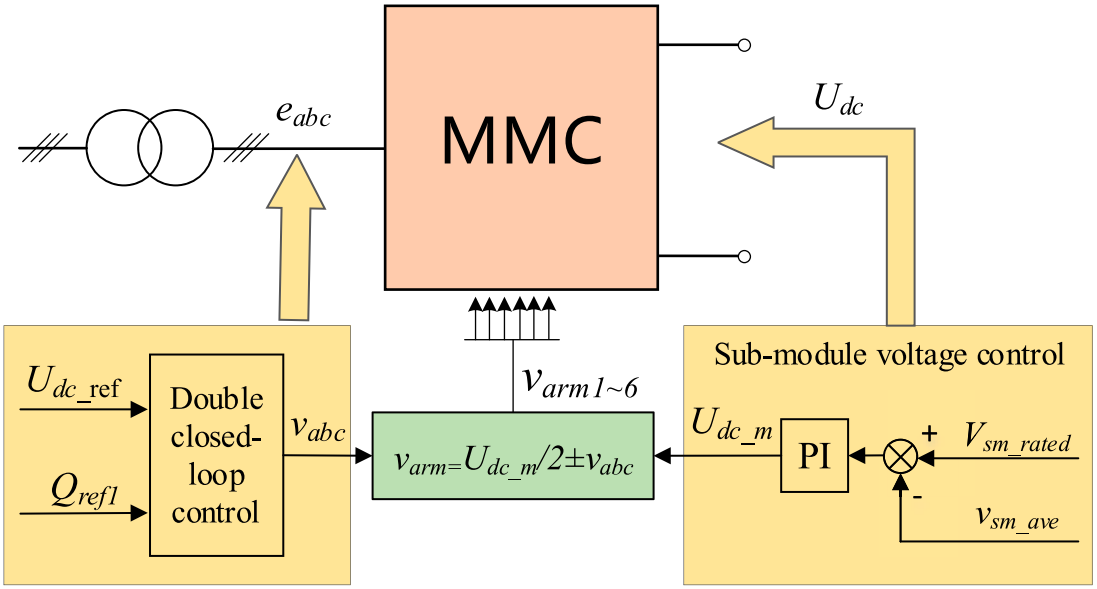

FIGURE 10
Control strategy of high-end MMC at the receiving station.

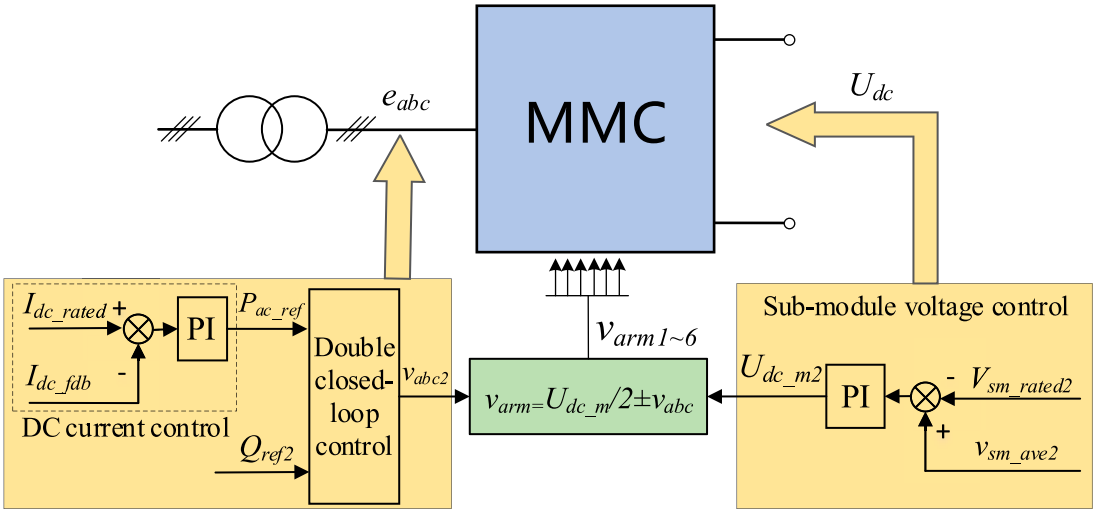

FIGURE 11
Control strategy of high-end MMC at the transmitting station.

Figure 11, while the low-end MMC maintains the original control strategy.

5 Simulation analysis

5.1 System parameters

To verify the effectiveness of the proposed AC fault ride-through strategy, a simulation model of the dual ended system is built based on the PSCAD/EMTDC simulation platform, as shown in Figure 1. The parameters of each MMC in the system are the same, and Table 1 provides the system parameters and the parameters of a single MMC.

5.2 Simulation of the system fault characteristics

This section takes the ABCG fault on the AC power grid side of the high-end MMC in the receiving station as an example, and analyzes the system fault characteristics without adopting fault ride-through strategy. As the parameters and control strategies of the positive and negative electrode systems are the same, only the

TABLE 1 Main parameters of the MMC-UHVDC transmission system.

Object	Parameters	Value (unit)
MMC-UHVDC system	Active power (bipolar)	8,000 MW
	Reactive power (bipolar)	2,400 Mvar
	DC voltage	±800 kV
	DC current	5 kA
Modular multilevel converter (MMC)	Active power	2,000 MW
	Reactive power	600 Mvar
	DC voltage	400 kV
	DC current	5 kA
	AC voltage on valve side	208 kV
	Number of sub-modules	192 + 10
		FBSM: 116, HBSM: 86
	Rated operating voltage of sub-modules	2.1 kV
	Sub-module capacitance	24 mF
	Bridge Arm Inductors	20 mH

simulation results of the positive electrode system are provided in this paper.

Set the fault to occur at 1.5 s, record the waveforms of the DC voltages U_{dc1_PH} and U_{dc1_PL} of MMC1_PH and MMC1_PL in the receiving station, as well as the waveforms of the DC voltages U_{dc2_PH} and U_{dc2_PL} of MMC2_PH and MMC2_PL in the transmitting station. The simulation results are shown in Figure 12. In this figure, data from the theoretical calculations in Section 3, including $U_{dc1\_PH\_cal}$, $U_{dc1\_PL\_cal}$, $U_{dc2\_PH\_cal}$, and $U_{dc2\_PL\_cal}$, were also added for comparison.

From Figure 12, it can be seen that after the fault occurring, the DC voltage U_{dc1_PH} of the faulty MMC1_PH rapidly increases, while the DC voltage U_{dc1_PL} of MMC1_PL stabilizes around the rated value. For the transmitting station, the DC voltage of MMC2_PH and MMC2_PL increases synchronously, but the rising speed is lower than the DC voltage of the faulty MMC. The simulation results are consistent with the theoretical calculation results, verifying the correctness of the theoretical analysis results in Section 3.

5.3 Simulation of AC fault ride-through control strategy

This section analyzes the effectiveness of the fault ride-through control strategy proposed in Section 4.2 based on a dual end simulation model. The fault conditions are: single-phase ground fault and three-phase ground fault occur on the AC grid side of the high-end MMC in the receiving station. The fault time settings for the two types of faults are the same. The system runs in a stable state before 1.5 s, and the fault occurs between 1.5 s and 2.0 s. The fault is cleared after 2.0 s.

As the parameters and control strategies of the positive and negative electrode systems are the same, only the simulation results of the positive electrode system are provided in this paper. The variables of MMC1_PH and MMC1_PL in the receiving station were recorded, including DC voltage U_{dc1_PH} and U_{dc1_PL}, average voltage of all sub-modules $v_{sm\_ave1\_PH}$ and $v_{sm\_ave1\_PL}$, AC side output active power P_{ac1_PH} and P_{ac1_PL}, as well as the DC current I_{dc} of the system. For the transmitting station to record the variables of MMC1_PH and MMC2_PH, including DC voltage U_{dc2_PH} and U_{dc2_PL}, average voltage of all sub-modules $v_{sm\_ave2\_PH}$ and $v_{sm\_ave2\_PL}$, AC side input active power P_{ac2_PH} and P_{ac2_PL}.

5.3.1 Simulation of single-phase ground fault

The simulation results of a single-phase ground fault occurring on the AC grid side of MMC1_PH in the receiving station are shown in Figures 13, 14.

As can be seen from Figure 13D, after the fault occurring, the output active power P_{ac1_PH} of MMC1_PH rapidly decreased to around 1,300 MW. Due to the obstruction of the active power output of MMC1_PH, there will be surplus power in the MMC shortly after the fault occurring, resulting in an increase in the voltage of its submodule $v_{sm\_ave1\_PH}$, as shown in Figure 13C. As shown in Figures 13A, B, when the system detects the fault, it begins to execute the fault ride-through strategy, and the DC voltage of MMC1_PH is controlled to decrease to around 250 kV. The decrease in DC voltage of the system leads to the increase in DC current I_{dc} of the system.

For the transmitting station, as shown in Figure 14C, in order to control the system DC current near the rated value, under the action of the AC fault ride-through strategy, the input active power of the MMC2_PH is reduced to about 1,300 MW. At the same time, in order to stabilize the voltage of the sub-module near the rated value, MMC2_PH controls its DC voltage U_{dc2_PH} to decrease with the decrease of the voltage of the sub-module $v_{sm\_ave2\_PH}$. After the fault enters steady state, U_{dc2_PH} drops to about 250 kV, as shown in Figures 14A, B.

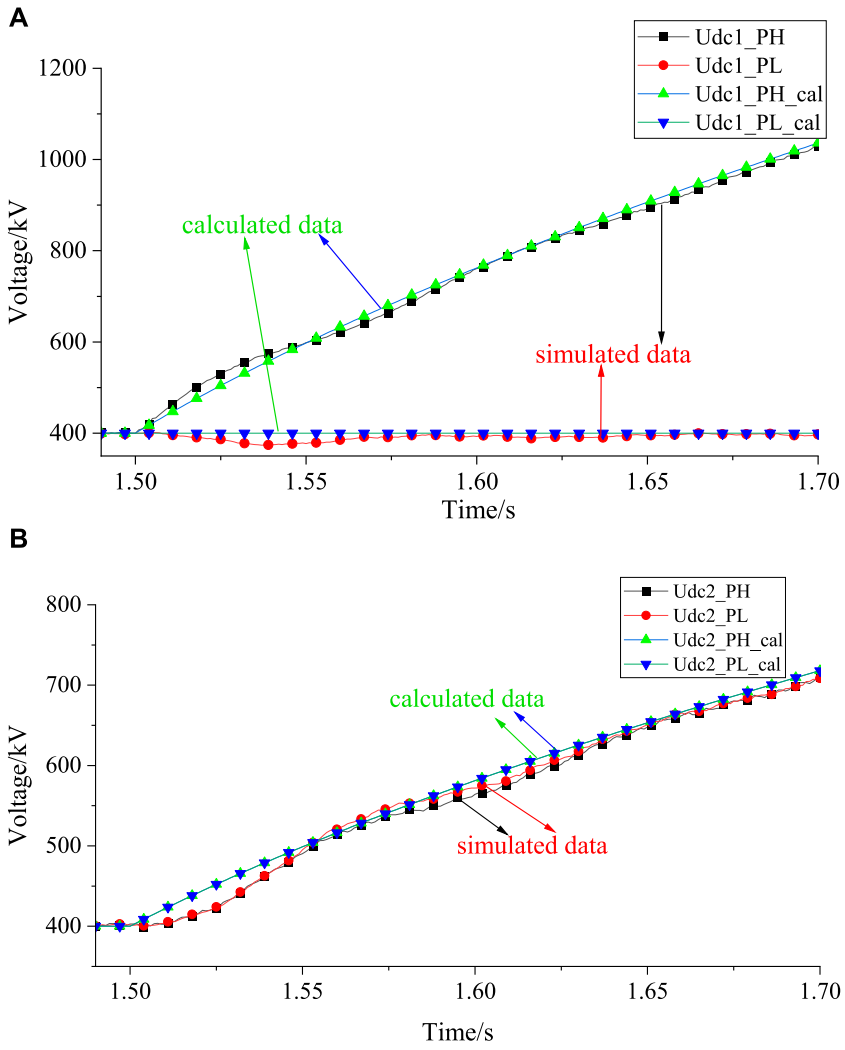

FIGURE 12
DC voltage after a three-phase ground fault occurs in MMC1_PH. **(A)** Calculation and simulation results of DC voltage for MMC1_PH and MMC1_PL **(B)** Calculation and simulation results of DC voltage for MMC2_PH and MMC2_PL.

During the entire fault process, the active power and DC voltage of the high-end MMC in the receiving and transmitting stations decrease synchronously, which can stably control the DC current of the system near the rated value. The AC active power, DC voltage, and sub-module voltage of all MMCs in the system are controlled within a stable range, and there is no serious overvoltage or overcurrent phenomenon in the system. Based on the above analysis, it can be concluded that after the single-phase ground fault occurs in MMC1_PH, the system can still retain about 83% of its power transmission capacity, which verifies the effectiveness of the AC fault ride-through strategy proposed in this paper.

5.3.2 Simulation of three-phase ground fault

The simulation results of a three-phase ground fault occurring on the AC grid side of MMC1_PH in the receiving station are shown in Figures 15, 16.

As can be seen from Figure 15D, after the fault occurring, the output active power P_{ac1_PH} of MMC1_PH rapidly decreased to 0 MW. In the short period after the fault occurring, there will be a large amount of surplus power in this MMC, resulting in an increase in the voltage of its submodule $v_{sm\_ave1\_PH}$, as shown in Figure 15C. As shown in Figures 15A, B, when the system detects the fault, it begins to execute the fault ride-through strategy, and the DC voltage of MMC1_PH is controlled to decrease to around 0 kV. The decrease in DC voltage of the system leads to the increase in DC current I_{dc} of the system.

For the transmitting station, as shown in Figure 16C, in order to control the system DC current near the rated value, under the action of the AC fault ride-through strategy, the input active power of the MMC2_PH is reduced to 0 MW. At the same time, in order to stabilize its voltage of the sub-module near the rated value, MMC2_PH controls its DC voltage U_{dc2_PH} to decrease with the decrease of the voltage of the sub-module $v_{sm\_ave2\_PH}$. After the fault enters steady state, U_{dc2_PH} drops to about 0 kV, as shown in Figures 16A, B.

During the entire fault process, the active power and DC voltage of the high-end MMC in the receiving and transmitting stations synchronously decreased to zero, which can stably control the DC

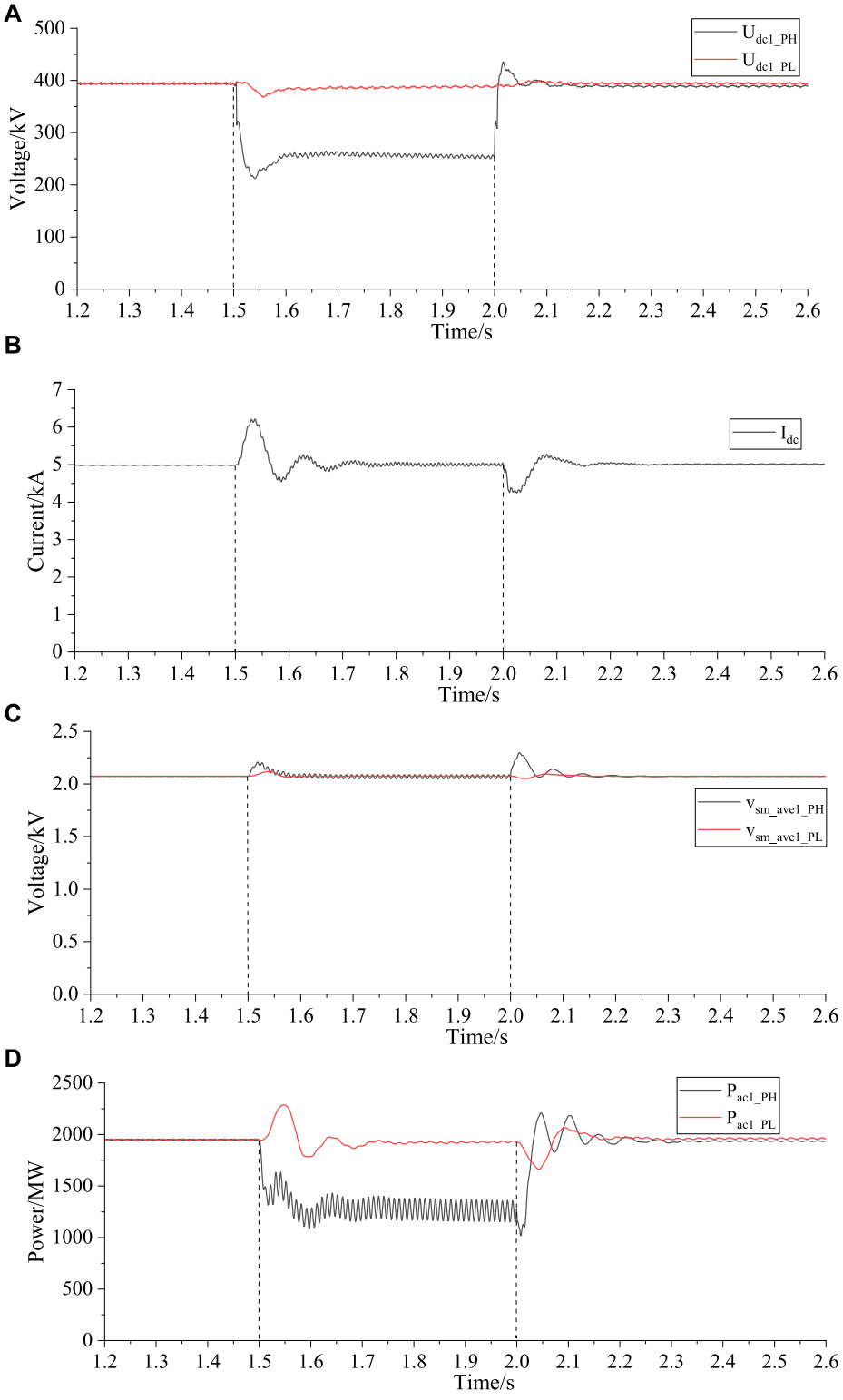

FIGURE 13
Simulation waveforms of receiving station during single-phase ground fault. **(A)** DC voltage of MMC1_PH and MMC1_PL **(B)** DC current of the system **(C)** Average voltage of submodules of MMC1_PH and MMC1_PL **(D)** AC side active power of MMC1_PH and MMC1_PL.

current of the system near the rated value. The AC active power, DC voltage, and sub-module voltage of all MMCs in the system are controlled within a stable range, and there is no serious overvoltage or overcurrent phenomenon in the system. Based on the above analysis, it can be concluded that after the three-phase ground fault occurs in MMC1_PH, the system can still retain about 50% of its power transmission capacity, which verifies the effectiveness of the AC fault ride-through strategy proposed in this paper.

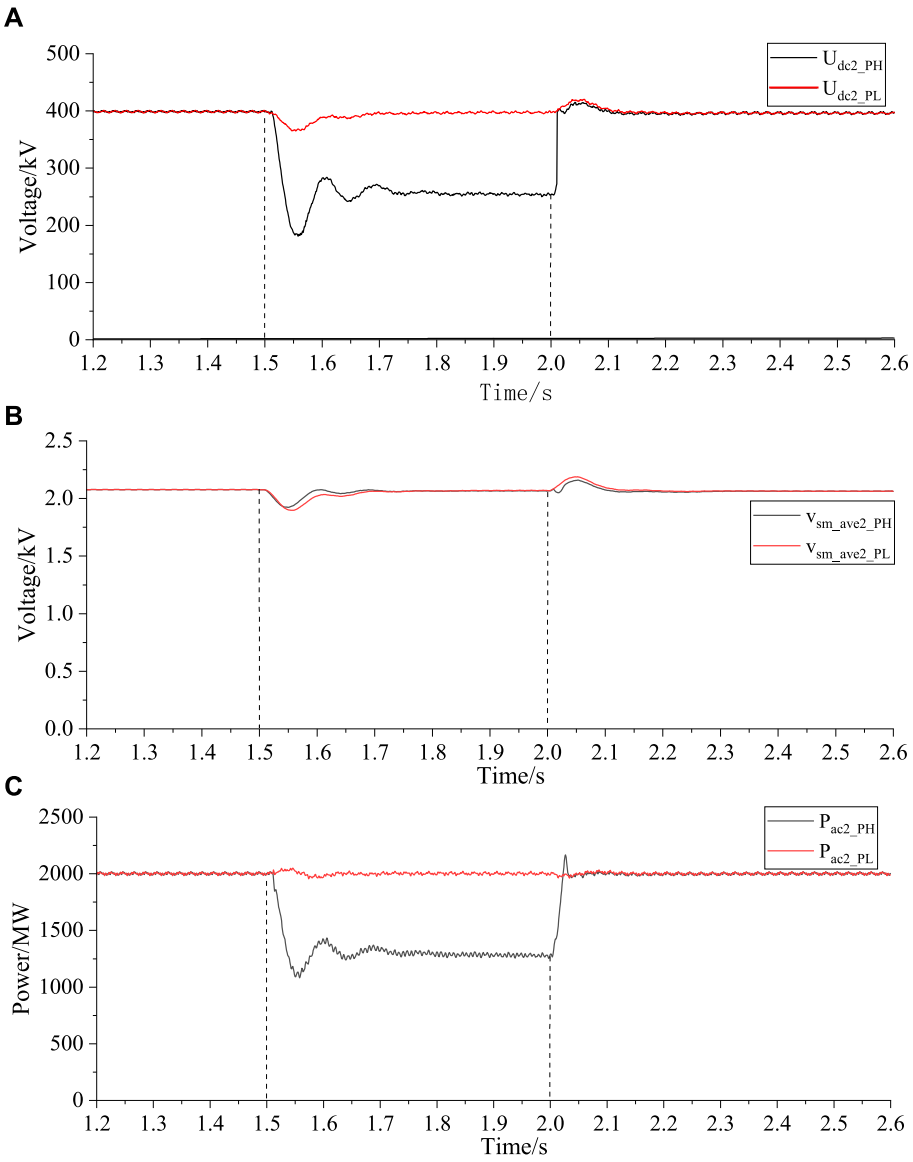

FIGURE 14
Simulation waveforms of transmitting station during single-phase ground fault. **(A)** DC voltage of MMC2_PH and MMC2_PL **(B)** Average voltage of submodules of MMC2_PH and MMC2_PL **(C)** AC side active power of MMC2_PH and MMC2_PL.

6 Conclusion

Addressing the current absence of an AC fault ride-through control strategy with robust power transmission capabilities for the MMC-UHVDC system with hierarchical connection mode, this paper first analyzes the characteristics of the system when a fault occurs in the AC power grid. Subsequently, it introduces an innovative AC fault ride-through control strategy with high power transmission capability. Finally, conduct simulation analysis on the proposed strategy. The conclusions are as follows:

(1) Based on theoretical analysis, this paper obtains the equivalent circuit of the high-end MMC in the receiving station after a three-phase ground fault occurring on the AC power grid side, and uses theoretical calculation methods to obtain the trend of DC voltage changes of the all MMCs in the transmitting station and receiving station after the fault occurring. According to the calculation results, it can be concluded that the DC voltage of the faulty MMC rises the fastest, and it rises to 1.15pu (i.e. 460 kV) within 14 ms after the fault occurring. And the simulation results have verified the correctness of the theoretical analysis. To protect the safety of system equipment, it is recommended that the system quickly take fault handling measures in a short period of time after a fault occuring.

(2) An AC fault ride-through control strategy with high power transmission capability has been proposed based on the characteristics of the system. The implementation of this control strategy requires coordination and

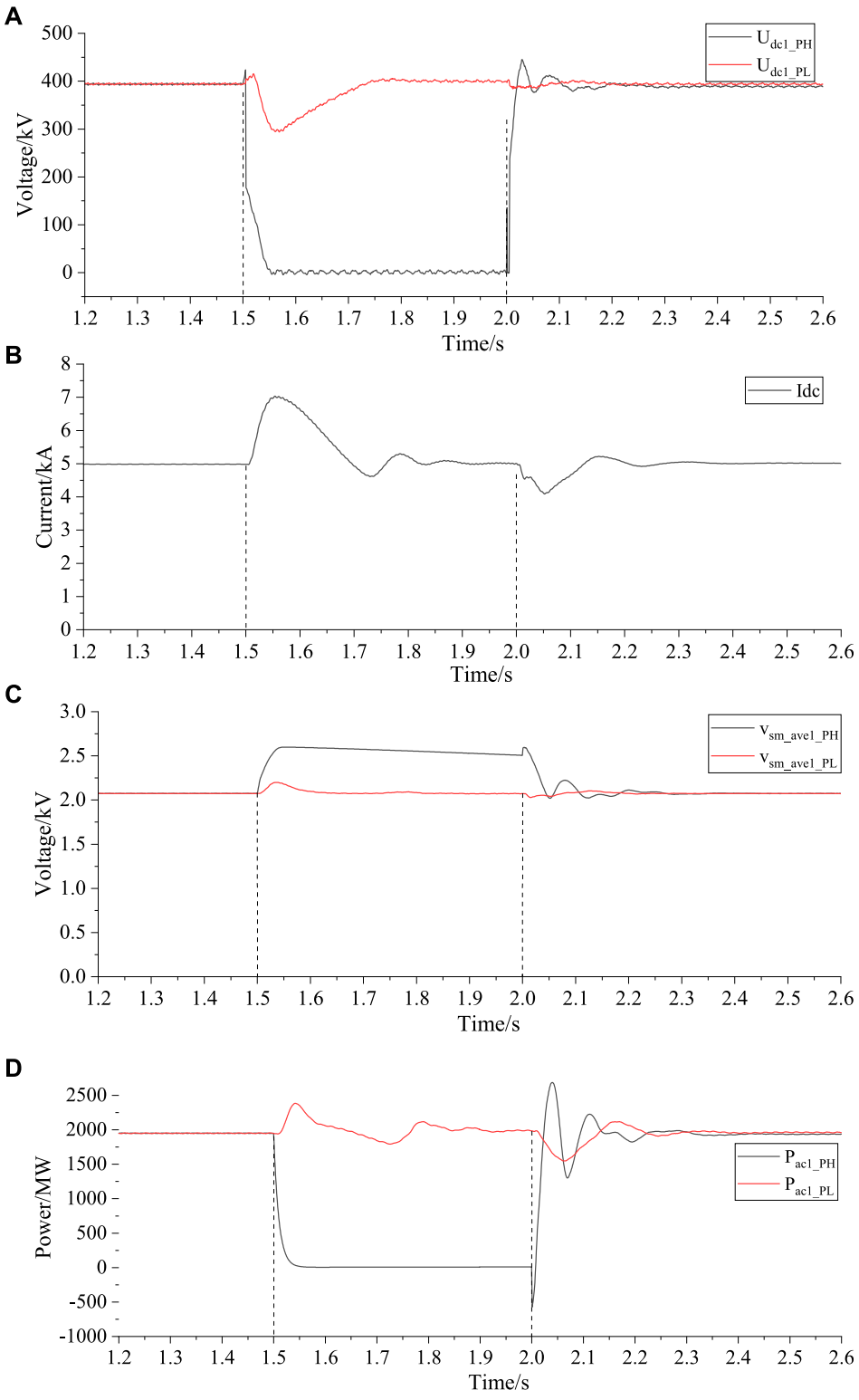

FIGURE 15
Simulation waveforms of receiving station during three-phase ground fault. **(A)** DC voltage of MMC1_PH and MMC1_PL **(B)** DC current of the system **(C)** Average voltage of submodules of MMC1_PH and MMC1_PL **(D)** AC side active power of MMC1_PH and MMC1_PL.

cooperation between the transmitting station's MMC and the receiving station's MMC. In order to maintain the stability of the system's DC current, this strategy requires synchronous reduction of the DC voltage of the faulty MMC and the partial active power of the transmitting station, so as to reduce the impact of system fault ride-

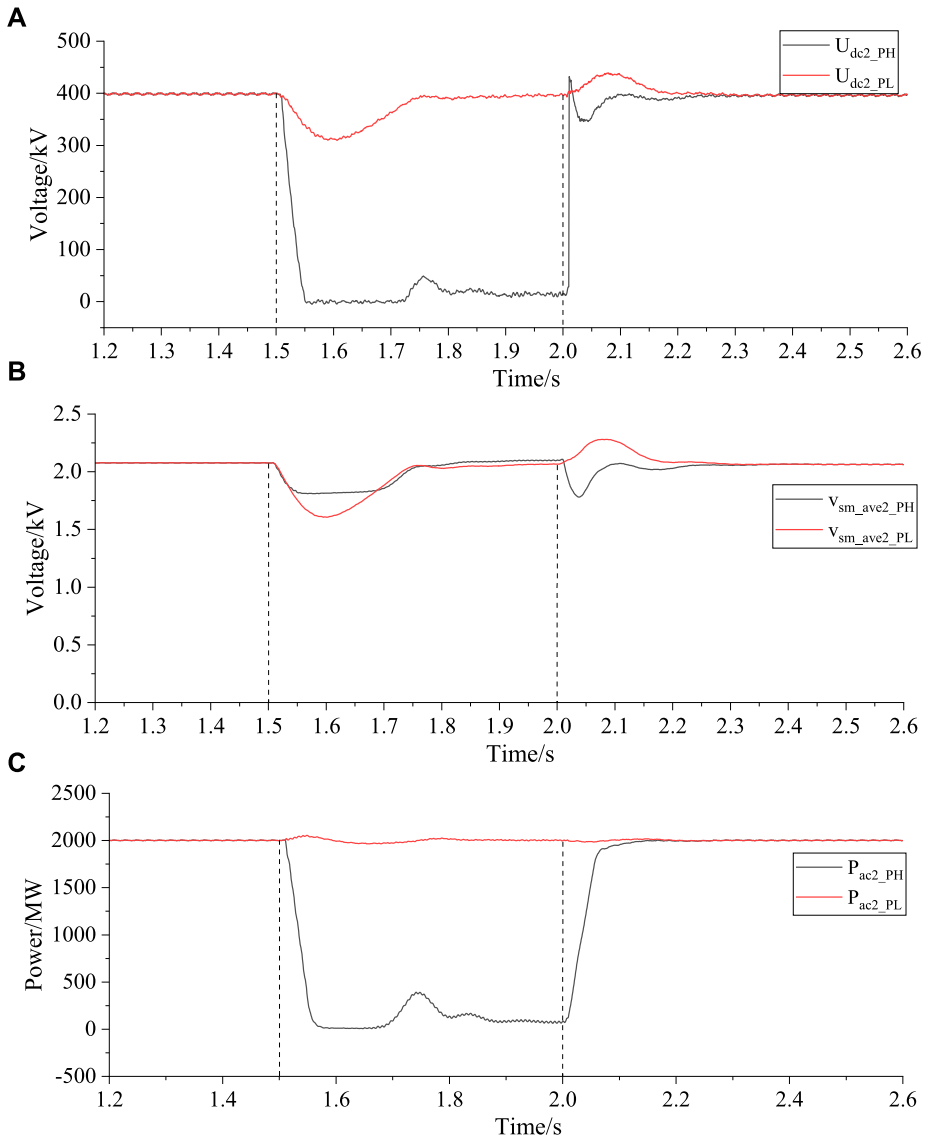

FIGURE 16
Simulation waveforms of transmitting station during three-phase ground fault. **(A)** DC voltage of MMC2_PH and MMC2_PL **(B)** Average voltage of submodules of MMC2_PH and MMC2_PL **(C)** AC side active power of MMC2_PH and MMC2_PL.

through strategy on MMC that has not experienced faults. This strategy can maximize the retention of the system's power transmission capacity during failures and reduce power shock in the system.

(3) Based on the PSCAD simulation platform, simulate the fault conditions of single-phase ground fault and three-phase ground fault in the high-end MMC at the receiving station. The simulation results show that when a single-phase ground fault occurs, the system can still maintain about 83% of its power transmission capacity during the fault period. When a three-phase grounding fault occurs, the system can maintain approximately 50% of its power transmission capacity during the fault period. The simulation results have verified the effectiveness of the proposed AC fault ride-through control strategy.

Data availability statement

The original contributions presented in the study are included in the article/Supplementary Material, further inquiries can be directed to the corresponding author.

Author contributions

MP: Conceptualization, Data curation, Formal Analysis, Investigation, Methodology, Project administration, Resources, Software, Supervision, Validation, Writing–original draft, Writing–review and editing. CN: Conceptualization, Formal Analysis, Methodology, Writing–review and editing. XL: Conceptualization, Methodology, Writing–review and editing.

MY: Software, Supervision, Validation, Writing–review and editing.
XW: Software, Validation, Writing–review and editing.

Funding

The author(s) declare that financial support was received for the research, authorship, and/or publication of this article. This research work was supported by the China Electrical Equipment Science and Technology Project (CEE-2023-B-01-01-013-XJ).

Conflict of interest

Authors MP and XL were employed by XJ Electric Corporation.

Authors MP, CN, and MY were employed by Xi'an Xuji Power Electronics Technology Co., Ltd.

Author XW was employed by China Electrical Equipment Group Co., Ltd.

Publisher's note

References

Alghamdi, O. A., Alhussainy, A. A., Alghamdi, S., AboRas, K. M., Rawa, M., Abusorrah, A. M., et al. (2023). Optimal techno-economic-environmental study of using renewable energy resources for Yanbu city. *Front. Energy Res.* 10. doi:10.3389/fenrg.2022.1115376

Baoan, X., Mingqun, G., Shaowu, W., et al. (2021). Friendly HVDC transmission Technologies for large-scale renewable energy and their engineering practice [J]. *Automation Electr. Power Syst.* 45 (22), 1–8. (In Chinese). doi:10.7500/AEPS20210302001

Boning, Y., Tianxin, Z., Ming, D., and Ming, R. (2020). "Simulation research on operation characteristics of AC energy consuming device in VSC-HVDC system," in The 16th IET international conference on AC and DC power transmission (ACDC 2020), Online Conference, July 02–03, 2020 (IET), 2315–2318.

Ding, Y., Wang, F., Wang, W., Wang, G., Xiong, J., and Fu, J. (2020). "Analysis of DC line fault characteristics with the UHVDC hierarchical integration into AC power grid," in 2020 5th asia conference on power and electrical engineering, Chengdu, China, June 04–07, 2020 (IEEE), 1539–1543.

Fu, F., Pan, H., and Jia, X. (2022). "A hybrid MMC with low FBSM ratio for DC fault," in 2022 4th international conference on power and energy technology (ICPET), Beijing, China, July 28–31, 2022 (IEEE), 456–461.

Gnanarathna, U. N., Gole, A. M., and Jayasinghe, R. P. (2011). Efficient modeling of modular multilevel HVDC converters (MMC) on electromagnetic transient simulation programs. *IEEE Trans. Power Deliv.* 26 (1), 316–324. doi:10.1109/TPWRD.2010.2060737

Han, Y., Wang, Q., Liu, P., Peng, Z., and Tong, X. (2023). "Research on DC fault clearance speed of hybrid MMC full bridge submodule ratio," in 2023 2nd international conference on power systems and electrical technology (PSET), Milan, Italy, Auguest 25–27, 2023, 18–22.

Jia, N., Qi, W., Yi, T., and Chen, B. (2016). "Study on the characteristics of AC/DC hybrid system under UHVDC hierarchical connection mode," in 2016 IEEE PES asia-pacific power and energy engineering conference (APPEEC), Xi'an, China, October 25–28, 2016 (IEEE), 1013–1017.

Lei, Y., He, X., Duan, J., and Li, H. (2019). "Boundary protection scheme for HVDC transmission system," in 2019 IEEE 8th international conference on advanced power system automation and protection (APAP), Xi'an, China, October 21–24, 2019 (IEEE), 75–79.

Li, X., Pu, Y., Ma, Y., Xiong, L., and Guo, Q. (2017). "DC voltage balance control of UHVDC system with hierarchical connection mode," in IECON 2017 - 43rd Annual Conference of the IEEE Industrial Electronics Society, Beijing, China, October 29–November 01, 2017 (IEEE), 3003–3008.

Liu, W., Fan, W., Hong, Y., and Chen, C. (2021). A study on the comprehensive evaluation and analysis of China's renewable energy development and regional energy development. *Front. Energy Res.* 9. doi:10.3389/fenrg.2021.635570

Ma, H., Ping, M., Li, D., Yang, M., Liu, X., and Zhou, Y. (2020). "Optimized AC Fault Ride-through strategy for back-to-back VSC-HVDC system," in 2020 IEEE 4th conference on energy internet and energy system integration (EI2), Wuhan, China, October 30–November 01, 2020 (IEEE), 794–799.

Nentwig, C., Haubrock, J., Renner, R. H., and Van Hertem, D. (2016). "Application of DC choppers in HVDC grids," in 2016 IEEE international energy conference (ENERGYCON), Leuven, Belgium, April 04–08, 2016 (IEEE), 1–5.

Nian, M., Yang, Z., Tan, L., and Bian, Y. (2020). Energy consumption method for power surplus in zhangbei VSC-based DC grid. *Power Syst. Technol.* 44 (05), 1991–1999. (In Chinese). doi:10.13335/j.1000-3673.pst.2019.1946

Qi, W., Jun, Y., Lei, W., Tiezhu, W., Lingkuan, W., and Yucheng, G. (2018). "Study on operation characteristics of UHVDC power system with hierarchical connection to AC grid," in 2018 international conference on power system technology (POWERCON), Guangzhou, China, November 6–8, 2018, 3158–3165.

Rokicki, T., Koszela, G., Ochnio, L. B., Perkowska, A., Bórawski, P., Bełdycka-Bórawska, A., et al. (2022). Changes in the production of energy from renewable sources in the countries of Central and Eastern Europe. *Front. Energy Res.* 10. doi:10.3389/fenrg.2022.993547

Saadeh, O., Sba, B. A., Dalala, Z., and Bashaireh, A. (2023). "Comparative performance analysis of HVDC and HVAC transmission systems in the presence of PV generation: a case study using the IEEE-5-bus network," in 2023 AEIT HVDC international conference (AEIT HVDC), Rome, Italy, May 25–26, 2023 (IEEE), 1–5.

Saeedifard, M., and Iravani, R. (2010). Dynamic performance of a modular multilevel back-to-back HVDC system. *IEEE Trans. Power Deliv.* 25 (4), 2903–2912. doi:10.1109/TPWRD.2010.2050787

Sixuan, X., Feifei, Z., Guojing, L., Quanquan, W., and Lu, W. (2023). "Fault ride-through strategy of new energy through flexible DC based on wind power shedding and energy consumption device," in 2023 2nd asian conference on frontiers of power and energy (ACFPE), Chengdu, China, October 20–22, 2023, 706–710.

Vercellotti, U. (2019). "HVDC links at increased voltage, CESI experience on extruded cable systems up to 525kV," in 2019 AEIT HVDC international conference (AEIT HVDC), Florence, Italy, May 9–10, 2019, 1–5.

Wang, D., and Li, Q. (2023). "Research on cooperative Fault Ride-through strategy of offshore wind power grid-connected system via VSC-HVDC system," in 2023 international conference on power energy systems and applications (ICoPESA), Nanjing, China, February 24–26, 2023, 96–103.

Wang, H., and Redfern, M. A. (2010). "The advantages and disadvantages of using HVDC to interconnect AC networks," in 45th international universities power engineering conference UPEC2010, Cardiff, Wales, 1–5.

Xiong, L., Liu, X., Zhang, D., and Liu, Y. (2021). Rapid power compensation-based frequency response strategy for low-inertia power systems. *IEEE J. Emerg. Sel. Top. Power Electron.* 9 (4), 4500–4513. doi:10.1109/jestpe.2020.3032063

Xu, B., Wang, X., Wang, G., Ning, Z., Li, J., and Zhou, J. (2021). "The state of art of energy consumption devices for offshore wind power system," in 2021 international conference on power system technology (POWERCON), Haikou, China, December 08–09, 2021 (IEEE), 1510–1514.

Ying, P., Lingfei, X., Xun, G., Yajun, L., Qidi, Z., Jian, Y., et al. (2018). "Study on control strategies for UHVDC system with 500kV/1000kV AC hierarchical connection at receiving end," in 2018 international conference on power system technology (POWERCON), Guangzhou, China, November 6–8, 2018, 2306–2312.

frontiers | Frontiers in Energy Research

TYPE Original Research
PUBLISHED 29 July 2024
DOI 10.3389/fenrg.2024.1439210

OPEN ACCESS

EDITED BY
Haitao Zhang,
Xi'an Jiaotong University, China

REVIEWED BY
Jun Cong Ge,
Jeonbuk National University, Republic of Korea
Zhaoyang Jin,
Shandong University, China
Jiejie Huang,
Nantong University, China

*CORRESPONDENCE
Gang Shi,
peresearcher@yeah.net

RECEIVED 28 May 2024
ACCEPTED 12 July 2024
PUBLISHED 29 July 2024

CITATION
Chen Q, Shi G, Lu Y, Qiu P, Zhou J, Yang R and Zhang J (2024), Droop control-based fast frequency support of wind power generation integrated grid-forming VSC-HVDC system. *Front. Energy Res.* 12:1439210. doi: 10.3389/fenrg.2024.1439210

Droop control-based fast frequency support of wind power generation integrated grid-forming VSC-HVDC system

Qian Chen[1], Gang Shi[2]*, Yi Lu[1], Peng Qiu[1], Jianqiao Zhou[2], Renxin Yang[2] and Jianwen Zhang[2]

[1]Electric Power Research Institute of State Grid Zhejiang Electric Power Corporation, Hangzhou, China, [2]Department of Electrical Engineering, Shanghai Jiao Tong University, Shanghai, China

Current researches mainly focus on the participation of wind farms in primary frequency regulation, including overspeed load shedding control, propeller control and their coordinated control, etc. The frequency support is realized by reserving reserve capacity of wind turbines, but the influence of the dynamic characteristics of maximum power point tracking (MPPT) on the overall frequency regulation characteristics of wind turbines during frequency support is ignored. To this end, firstly, the frequency response model of the system is constructed, and the main factors that affect the frequency dynamic characteristics are revealed. Secondly, the principle of the grid-forming VSC with the function of self-inertial synchronization is introduced, the influence of the dynamic characteristics of MPPT on the frequency regulation characteristics of the wind turbine generator is clarified. Finally, based on the PSCAD/EMTDC electromagnetic transient simulation software platform, the influence of the dynamic characteristics of MPPT on the frequency regulation characteristics are verified by combining the inertia self-synchronous network control technology. The simulation results indicate that with the increase of setting of droop control, the decrease of output power of MPPT becomes large so as to weaken the frequency support capability.

KEYWORDS

grid forming VSC, VSC-HVDC, droop control, fast frequency support, selfsynchronizing

1 Introduction

The global energy landscape has undergone a significant transformation, with wind energy evolving into an indispensable component of the power industry in Europe, China, and worldwide over the past few decades (Eto et al., 2010). The wind power industry, as a vital force in clean energy, will assume greater responsibilities. China's commitment to global "carbon peak" and "carbon neutrality" will further propel wind power to become one of the most important pillars in achieving energy transition and addressing global climate change (Rezaei and Kalantar, 2015). Therefore, it is evident that wind power generation will continue to see significant development in the foreseeable future, with further effective harnessing and utilization of wind energy resources (Yang et al., 2024).

The large-scale integration of wind power into the grid will have a significant impact on the transient stability of grid frequency, with the most prominent issue being the deterioration of frequency transient support capability due to the lack of inertia and

primary frequency control (Yang et al., 2018; Qin et al., 2021; Xiong et al., 2021; Arévalo Soler et al., 2023). Conventional VSC-HVDC control methods decouple wind farms from grid frequency, rendering them unable to perceive changes in AC grid frequency (Flourentzou et al., 2009; Castro and Acha, 2016). Consequently, wind farm grid-side flexible systems cannot provide transient power support to the grid. It is necessary for wind turbine units to autonomously perceive changes in grid frequency, akin to traditional synchronous generators, and autonomously respond to system frequency changes to provide transient support capabilities (Bianchi and Domnguez-Garca, 2016; Adeuyi et al., 2017).

To address this issue, it is necessary to transmit information about grid frequency changes to the wind farm side. Literature (Bianchi and Domnguez-Garca, 2016) utilizes communication means to transmit information about grid frequency changes, which is subject to limitations in terms of communication costs and stability. This approach in Bianchi and Domnguez-Garca (2016) requires detecting AC grid frequency and controlling DC voltage to track its changes, with the voltage variations reflected on the wind farm side frequency changes by the sending converter station. This method of Arghir et al. (2018) places high demands on the frequency tracking capability of phase-locked loops and the adjustment speed of DC voltage, particularly in weak grid scenarios, where it can lead to system instability issues.

In research on providing inertia support through VSC-HVDC grid integration with wind farms, methods based on communication or actively controlling DC bus voltage are often used to transmit grid frequency changes to the wind farm (Li et al., 2014). However, due to the existence of delays in control, communication, etc., wind farms cannot perceive the actual grid frequency in real-time, making it challenging to ensure inertia support effectiveness (Li et al., 2017). VSC-HVDC still exhibits current-source characteristics to the grid, posing a series of stability issues in parallel with weak grids (Aouini et al., 2016). Although the application of virtual synchronous control at converter stations can avoid stability issues caused by current vector control and weak grids, it is not suitable for occasions with original power fluctuations such as wind farms.

When wind turbines sense changes in the frequency of the AC system, they can adjust their speed, increase or release the rotational energy stored in the blades and rotor, to provide transient power support to the grid. When necessary, they can also provide primary frequency regulation through active power reserves, enhancing grid stability (Markovic et al., 2021; Groß et al., 2022). Literature (Zhong et al., 2022) proposes adding an auxiliary control loop directly coupled with the grid frequency (frequency deviation and rate of change) in the power control loop of wind turbines, to respond to dynamic changes in grid frequency. However, as it still relies on phase-locked loop (PLL) for grid synchronization, it is challenging to ensure stable operation of the control strategy in weak grids. Literature (Subotić and Groß, 2022) suggests using virtual synchronous control (grid-forming technology) in the grid-side converter of wind turbines, simulating the rotor motion equation and excitation equation of traditional synchronous generators to eliminate the dependence on PLL. Externally, it exhibits voltage source characteristics, autonomously responding to grid frequency changes, providing inertia response, and further participating in primary frequency regulation. However, such control methods require the wind turbine's converter to control the DC bus voltage, leading to significant changes in torque control strategy and requiring evaluation of their impact on the stable operation of wind turbines, with high upgrade costs. Literature (Sang et al., 2022) utilizes the DC bus capacitance of wind turbine converters to simulate the rotor of a synchronous generator, achieving the grid-side converter's ability to self-synchronize without PLL, automatically tracking the DC bus voltage with grid frequency, so as to achieve grid-forming VSC function.

Current research mainly focuses on wind farms participating in primary frequency regulation, including overspeed load reduction control, pitch control, and coordinated control of both, all utilizing the reserved capacity of wind turbines to provide frequency support. However, they overlook the dynamic characteristics of maximum power point tracking during frequency support, which affects the overall turbine frequency response. In the context of accelerating the construction of new power systems, it is necessary to further explore the control potential of offshore wind power through flexible direct connection systems, making the overall system the dominant power source and taking responsibility for supporting system frequency. In this context, this paper first constructs a system frequency response model to reveal the main factors affecting frequency dynamic characteristics, then the principle of the grid-forming VSC with the function of self-inertial synchronization is introduced, after that this paper clarifies the influence of MPPT dynamic characteristics on the overall turbine frequency response. Finally, based on the PSCAD/EMTDC electromagnetic transient simulation software platform, it establishes an electromagnetic transient simulation model of wind farm clusters connected to the grid via AC/DC, combined with inertia self-synchronization grid construction technology, to verify the influence of MPPT dynamic characteristics on the overall turbine frequency response.

2 Structure of large-scale wind power transmission system through HVDC and principle of grid-forming VSC for self-inertial synchronization

2.1 System structure of large-scale wind power transmission through HVDC and mechanical power modeling

The structure of large-scale wind power transmission system through HVDC is shown in Figure 1, in which WTG uses wind turbines to capture wind energy. Rotor-side converter realizes decoupling control of constant voltage and frequency and power; the grid-side converter is used to maintain the DC voltage constant and adjust the power factor (Xiong et al., 2016).

Figure 2 shows the control strategies for the sending-end converter (SEC) and receiving-end converter (REC). The control strategy of the sending-end converter station has a similar active part to the receiving-end converter station. However, since the wind farm connected to the AC side of the sending-end converter station can quickly lock its frequency and phase angle through a phase-locked loop, changes in the output AC frequency will not directly affect the

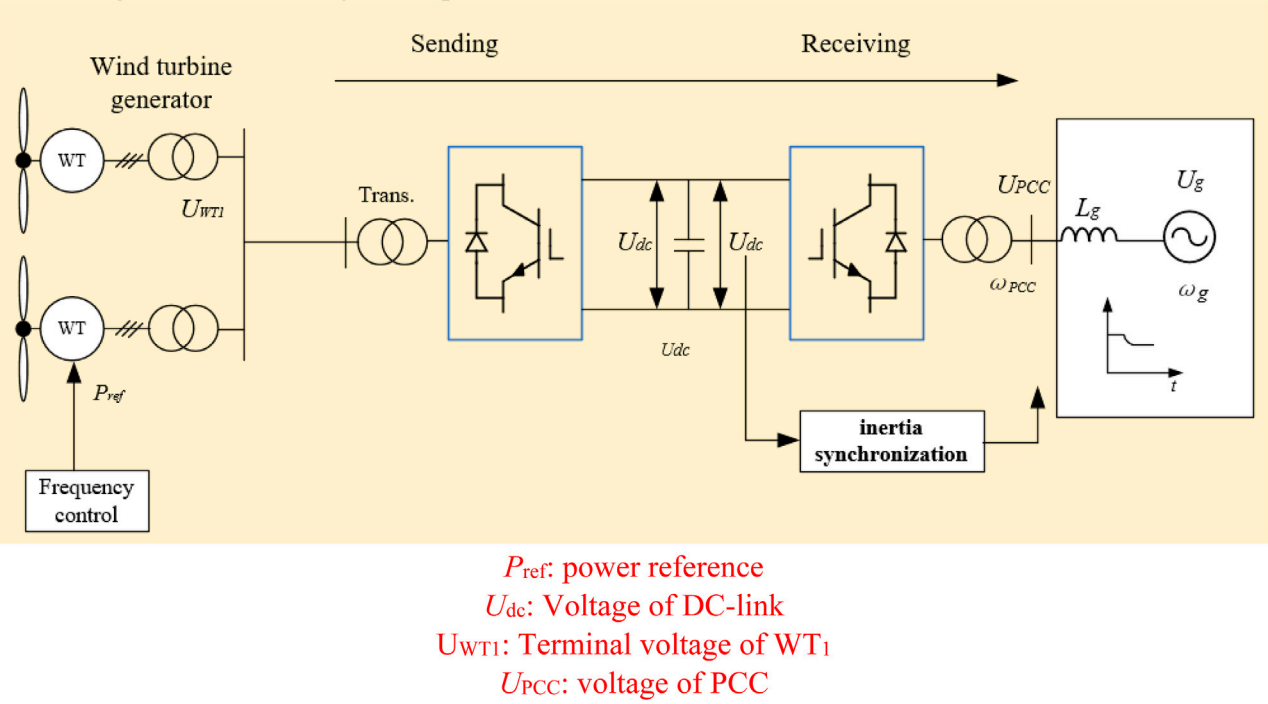

FIGURE 1
VSC-HVDC system for wind farm integration.

power output of the wind farm, but only serve to transmit information. The control object of the reactive part is the amplitude of the AC voltage on the wind farm side, which needs to be maintained stable by the sending-end converter station (Yang et al., 2020).

As the penetration rate of offshore wind power continues to increase, the receiving-end AC grid shows increasingly obvious characteristics of low inertia and weak damping. When the traditional backup plan of synchronous generator units cannot meet the requirements for grid frequency regulation capacity and speed, it may lead to problems such as large rate of change of grid frequency and frequency exceeding limits. Therefore, it is urgent to explore the potential of offshore wind power regulation, so that it can actively support system inertia, participate in frequency stability control, and improve the system's safety and stability.

The mechanical power (P_m) is described as a nonlinear function of various parameters, including air density (ρ), rotor radius (R), pitch angle (β), wind speed (v_w), tip-speed ratio (λ), and power coefficient (c_p), as in Formula 1.

$$P_m = \frac{1}{2}\rho\pi R^2 v_{wind}^3 c_P(\lambda,\beta) \tag{1}$$

where c_p could be represented in Formulas 2–4.

$$c_P(\lambda,\beta) = 0.645\left\{0.00912\lambda + \frac{-5-0.4(2.5+\beta)+116\lambda_i}{e^{21\lambda_i}}\right\} \tag{2}$$

$$\lambda_i = \frac{1}{\lambda + 0.08(2.5+\beta)} - \frac{0.035}{1+(2.5+\beta)^3} \tag{3}$$

$$\lambda = \frac{\omega_r R}{v_w}. \tag{4}$$

2.2 Principle of grid-forming VSC for self-inertial synchronization

Common grid-forming inverters employ virtual synchronous generation (VSG) technology to simulate the characteristic features of synchronous generators, introducing inertia and damping into the frequency control system to enhance the system's active support capability and compensate for the lack of inertia in phase-locked loops (PLLs). However, the grid-forming VSG technology exhibits weak responsiveness to grid loads and poor system stability, posing instability risks in weak grid scenarios. Additionally, significant modifications to the inverter structure incur high retrofitting costs. Without altering the structure and control strategy of the machine-side inverter, by modifying the control structure of the grid-side inverter, the voltage phase θ of the output grid-side converter voltage ug is modulated using the integral of the normalized DC capacitor voltage u_{dc} measured in its control loop with a gain ω_n, achieving real-time correlation between the DC bus voltage u_{dc} and the output angular frequency ω_g of the grid-side converter. This allows direct observation of grid frequency variations based on changes in the DC bus voltage, presenting the grid with external characteristics of a SG, as "voltage source". This approach mitigates instability issues caused by PLLs and inaccurate frequency measurements due to voltage fluctuations, facilitating upgrades and improvements in grid-connected wind turbine control structures.

Figure 3 illustrates motion feature similarity between SG and GSC. The relationship between the angular frequency of AC voltage output by grid-side converter and DC voltage is shown in Formula 5

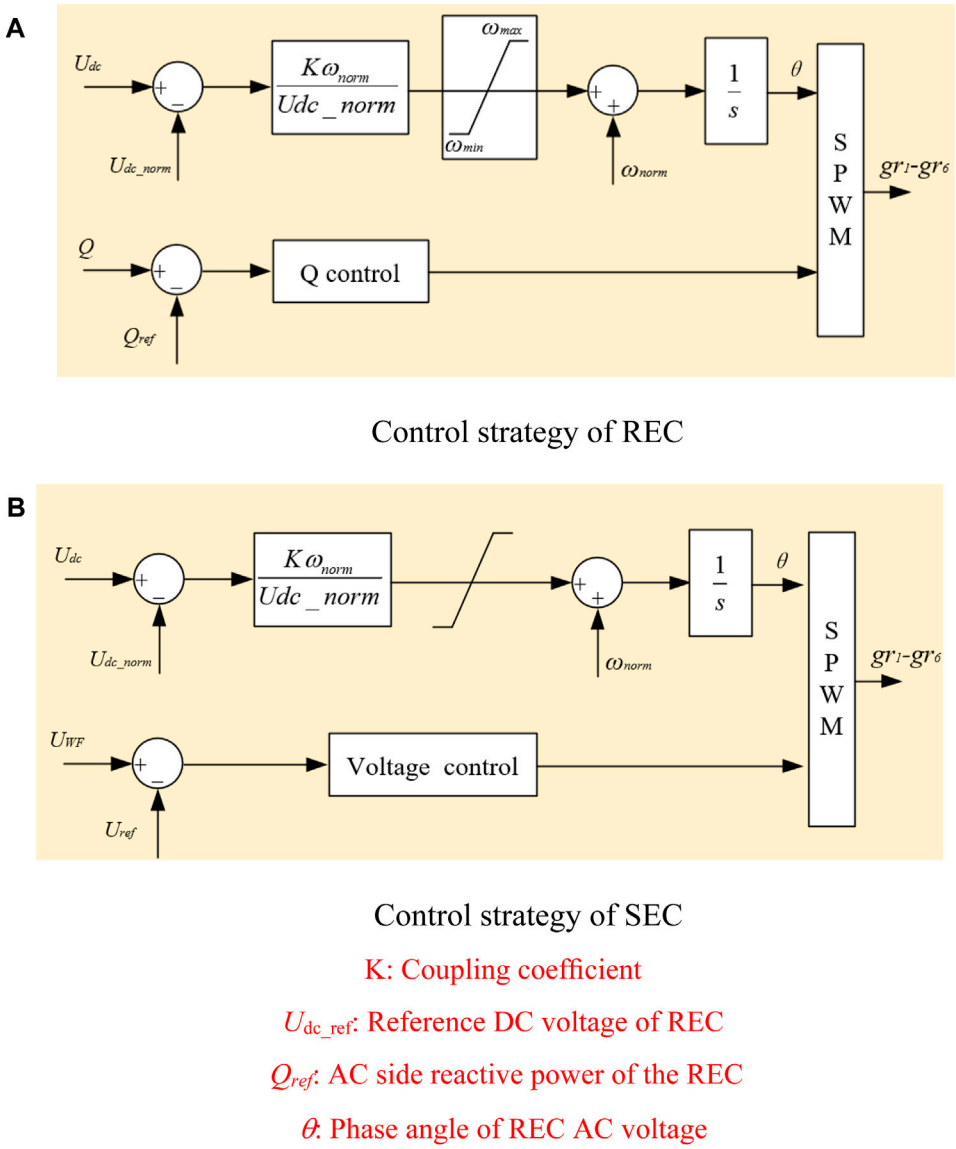

FIGURE 2
Control strategies of SEC and RES. **(A)** Control strategy of REC, **(B)** Control strategy of SEC.

$$\omega_g^* = u_{dc}^* \tag{5}$$

where: ω_g is the angular frequency of AC voltage output and u_{dc} is the DC bus voltage.

The dynamic equation of u_{dc} is given in Formula 6.

$$2H_C u_{dc}^* \frac{du_{dc}^*}{dt} = P_m^* - P_g^* \tag{6}$$

where: P_m^* and P_g^* are the nominal values of the output power of the permanent magnet direct driver and the input power of the grid-side converter respectively; HC is the inertia time constant of DC capacitor.

H_C of DC capacitor is given in Formula 7.

$$H_C = \frac{CU_{dcn}^2}{2S_n} \tag{7}$$

where: C is the DC capacitance; U_{dcn} is the reference value of DC voltage; S_n is the rated power of the wind turbine.

Ignoring the loss of the grid-side converter, the output power of the WTG can be expressed as in Formula 8.

$$P_g^* = \frac{U_t^* E_g^*}{x_g^*} \sin\delta \tag{8}$$

where: E_g^* is the unit value of the regulation voltage of the grid-side converter; U_t^* is the nominal value of grid voltage; x_g^* is the unit value of reactance between grid-side converter and grid synchronous generator; δ is the phase where the output voltage vector of the grid-side converter leads the grid voltage.

Figure 4 shows the response characteristic curves of the frequency and DC capacitor voltage of HVDC system under over-frequency disturbance. After being disturbed, the change of

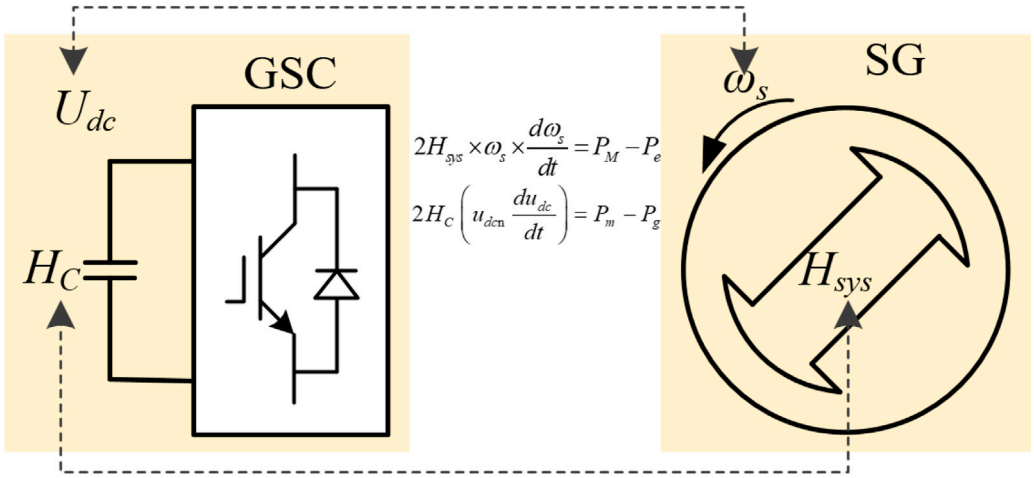

FIGURE 3
Motion feature similarity between SG and GSC.

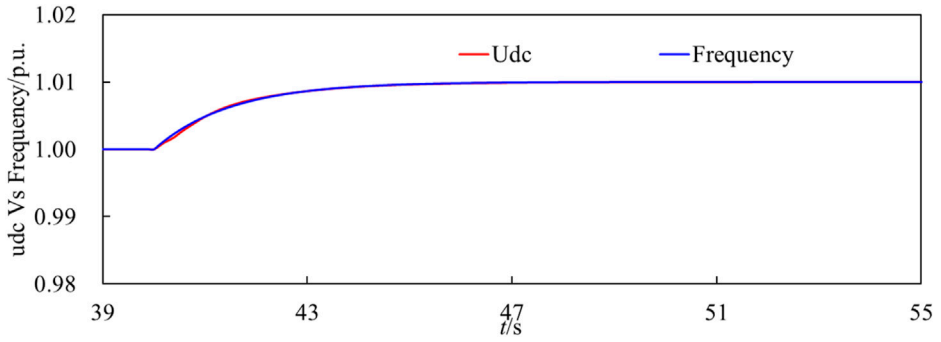

FIGURE 4
DC voltage and frequency under over-frequency disturbance.

grid-connected power of wind turbines will cause the natural response of DC bus voltage, and this response is positively related to the grid frequency. Taking the frequency increase as an example, that is, the grid frequency increases, the delta angle decreases, the grid-connected power decreases, and the DC side voltage increases, the natural linkage between DC side voltage and grid frequency is realized by the grid-forming VSC with the function of inertial synchronization and the amplitude change of AC side grid frequency is converted into the amplitude change of DC side voltage, thus realizing the frequency information transmission function and avoiding the need of converter phase-locked loop and communication. Which are highly consistent, and the DC capacitor voltage can be used to characterize the frequency change of the power grid.

2.3 Droop control-based fast frequency support of wind power generation

For large-scale wind power transmission via high-voltage direct current (HVDC) systems, active participation of wind turbines in system frequency support is the future development trend. Currently, the primary frequency regulation resources in the power system are still traditional synchronous generator units, which exhibit significant differences in response speed and control capability compared to wind turbines. After disturbances, the spare capacity of traditional synchronous generator units is sufficient to absorb unbalanced power. However, due to the decreasing proportion of synchronous generator units in the power system, the inertia response capability of the sending-end system weakens. During the initial disturbance, the excessive rate of frequency variation in low-inertia AC systems may trigger wind turbine protection actions, leading to disconnection accidents and causing larger active power deficits, thereby threatening the safety and stability of the system operation.

A comprehensive system frequency response control diagram considering the frequency support characteristics of doubly-fed induction generator (DFIG) and traditional synchronous generator units is shown in Figure 5. Here, H represents the inertia time constant of the sending-end grid; D is the equivalent damping coefficient; T_G is the time constant of the synchronous generator governor; F_{HP} represents the proportion of steady-state

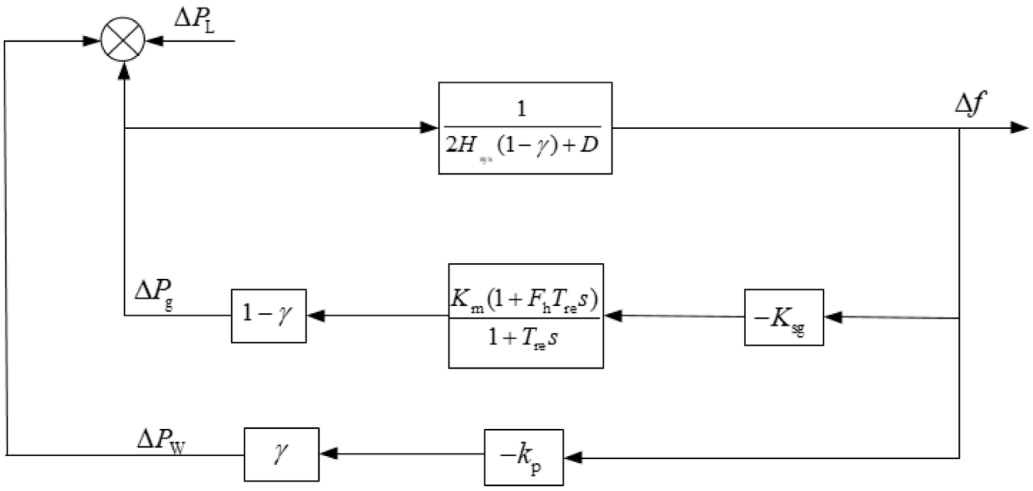

FIGURE 5
Simplified system frequency response model considering high wind power penetrated power gird.

output power of the prime mover high-pressure cylinder; T_{RH} is the time constant of the prime mover reheating; and s is the Laplace operator (Shi et al., 2018). Referring to the simplified conditions of the traditional system frequency response model, considering the much smaller time constants of fast frequency support strategies (virtual control and droop control) of wind turbine units compared to the time constants of reheating coefficients of synchronous generators, the fast frequency support control loop of wind turbine units is directly introduced into the traditional system frequency response model in Figure 5.

According to Figure 5, when the system is faced with active power deficiency (ΔP_L), the frequency domain expression of system frequency deviation with wind power frequency regulation can be arranged as in Formulas 9, 10.

$$\Delta f(s) = \left(-\gamma k_d s - (1-\gamma)\Delta f \frac{K_m(1+F_h T_{re} s)}{1+T_{re} s} - \Delta P_L - \Delta f k_p\right) \times \left(\frac{1}{2H_{sys}(1-\gamma)+D}\right) \tag{9}$$

$$\Delta f(s) = \left(\frac{K_{sg}\omega_n^2}{(D+\gamma k_P)K_{sg}+k_m}\right)\left(\frac{(1+T_{re}s)\Delta P_L}{s^2+2\xi\omega_n s+\omega_n^2}\right) \tag{10}$$

where K_m is the mechanical power gain coefficient, F_h is a part of the high-pressure turbine power, T_{re} is the reheat time constant, H_{sys} is the system inertia time constant, D is the damping coefficient, and ω_n and ζ are the intermediate variables (Shi et al., 2018).

ω_n and ζ are as in Formulas 11, 12.

$$\omega_n = \sqrt{\frac{(D+\gamma k_P)K_{sg}+K_m}{(2H_{sys}+\gamma k_d)K_{sg}T_{re}}} \tag{11}$$

$$\xi = \left(\frac{(2H_{sys}+\gamma k_d)K_{sg}+\left((D+\gamma k_P)K_{sg}+K_m F_h\right)T_{re}}{2\left((D+\gamma k_P)K_{sg}+K_m\right)}\right)\omega_n \tag{12}$$

Performing inverse Laplace transform on the Formula 10, The expression of Δf in time domain can be obtained as in Formula 13.

$$\Delta f(t) = -\frac{K_{sg}\Delta P_L \omega_n^2}{\left[(D+\gamma k_P)K_{sg}+K_m\right]}\left[1+\alpha e^{-\zeta\omega_n t}\sin(\omega_d t+\phi)\right] \tag{13}$$

where α, ω_d and φ can be expressed by Formulas 14–16.

$$\alpha = \sqrt{\frac{1-2T_{re}\xi\omega_n+T_{re}^2\omega_n^2}{1-\xi^2}} \tag{14}$$

$$\omega_d = \omega_n\sqrt{1-\xi^2} \tag{15}$$

$$\phi = \tan^{-1}\left(\frac{\omega_d T_{re}}{1-\xi\omega_n T_{re}} - \tan^{-1}\left(\frac{\sqrt{1-\xi^2}}{-\xi}\right)\right) \tag{16}$$

After a disturbance, the imbalance power in the system causes the grid frequency to exceed the primary frequency regulation deadband of synchronous generator units. Subsequently, the speed control system of the prime mover automatically decreases or increases the mechanical power of synchronous generator units in response to the grid frequency variation, weakening the imbalance in active power and restraining frequency changes. The primary frequency regulation of synchronous generator units is automatically completed under the action of the prime mover's speed control system. To ensure the safe operation of the units, the imbalance power response of primary frequency regulation is generally limited to within 6% of rated load. Additionally, since the input signal of inertia control is the frequency change rate, which may contain various degrees of noise, it can easily induce system instability. Therefore, based on droop control, this paper conducts research on droop control on the characteristics of the fast frequency support.

After a disturbance, WTG starts the fast frequency support strategy with frequency deviation f as input, and releases the rotational kinetic energy to respond to the frequency change, which is injected into the AC power grid through the DC transmission system. The additional power, ΔP, is:

$$\Delta P = -K_P \Delta f \tag{17}$$

TABLE 1 Parameters of WTG.

Parameters	Value/unit
Stator resistance	0.0048 p.u.
Rotor resistance	0.0055 p.u.
Leakage inductance coefficient	0.0468 p.u.
Excitation reactance	3.954 p.u.
Wind turbine inertia	3.5 p.u.
Generator inertia	1.2 p.u.
DC bus capacitance	0.003 p.u.

TABLE 2 Comparison results low-frequency disturbance.

	Kp = 0	Kp = 10	Kp = 30
Rotor speed	0.847	0.821	0.63
Minimum output power (p.u.)	0.761	0.841	0.985
Maximum frequency deviation (Hz)	0.34	0.33	0.29

With the kinetic energy output of DFIG rotor, ω_r decreases. According to Eq. 17, MPPT output is affected, and the change amount of DFIG output ΔP_{MPPT} is:

$$\Delta P_{MPPT} = k_g(\omega_0 + \Delta\omega_r)^3 - k_g\omega_0^3 \approx 3k_g\omega_0^2\Delta\omega_r \quad (18)$$

where ω_0 is the initial rotational speed of DFIG, $\Delta\omega_r$ is the speed deviation after DFIG frequency regulation.

After integrating Eqs 17, 18, ΔP_e would be represented as

$$\Delta P_e = 3k_g\omega_0^2\Delta\omega_r - K_P\Delta f \quad (19)$$

As shown in Eqs 18, 19 of the revised manuscript, the decrease of ΔPMPPT depends on two factors: initial rotor speed of wind turbine and variation of rotor speed. This means that in a high wind speed condition or the rotor speed variation is large during the frequency support period, the decrease of ΔP_{MPPT} is serious, which would give significant negative impact on the frequency support. In the simulation analysis, the coupling relationship between the maximum power tracking power variation, rotor speed of WTG and system frequency will be analyzed.

3 Simulation results

To investigate the influence of the dynamic characteristics of MPPT on the frequency regulation characteristics, the model shown in Figure 4 is employed based on PSCAD/EMTDC. The droop control is implemented in the WTG with the input of deviation of voltage of DC-link. Three scenarios are selected with the setting of Kp for 0, 10, and 30. The parameters of WTG are shown in Table 1 The other parameters are referred to (Yang et al., 2020) As disturbance.

TABLE 3 Comparison results over-frequency disturbance.

	Kp = 0	Kp = 10	Kp = 30
Rotor speed	0.847	0.852	0.867
Minimum output power (p.u.)	0.761	0.730	0.673
Maximum frequency deviation (Hz)	0.21	0.20	0.17

3.1 Case 1: 2.5-MW load is connected to the grid

Figure 6 shows comparison results with various control coefficient under low-frequency disturbance. The simulation results show that the DC voltage changes by 0.005 p.u. for no frequency regulation strategy and the frequency changes by 0.005 p.u. This means that the self-synchronization strategy is confirmed, as shown the results of frequency and voltage in Figures 6A, B. When the WTG adopts no additional frequency regulation control, the rotor speed remains constant, and the WTG does not participate in frequency regulation. The maximum frequency deviation is 0.34 Hz due to the large load connection. When kp is set to 10 and 30, respectively, the maximum frequency deviation could be improved to 0.33 Hz and 0.29 Hz, respectively, as shown in Table 2. With the increase of droop coefficient, the maximum frequency deviation gradually decreases, the rotor speed reduction gradually increases, and the active output of the WTG gradually decreases. As in Figure 6C, the rotor speed reduction of kp = 10 is much more than that of kp = 10, the frequency support improvement is not significant clear due to the rapid change of output power in Figure 6D.

3.2 Case 2: 1-MW load is disconnected from the grid

Figure 7 shows comparison results with various control coefficient under over-frequency disturbance. The simulation results show that the DC voltage changes by 0.003 p.u. and the frequency changes by 0.003 p.u. The mirror image relationship between frequency and voltage is confirmed, as shown in Figures 7A, B. According to the mirror image relationship between the system frequency and DC voltage, the fluctuation of DC voltage is consistent with the frequency. Among them, the highest frequencies of kp = 0, kp = 10, and kp = 30 are 50.21, 50.20, and 50.17 Hz, respectively, as shown in Table 3. With the increase of droop coefficient, the maximum frequency deviation gradually decreases, the rotor speed reduction gradually increases, and the active output of the WTG gradually decreases. When kp is set to 30, the maximum frequency deviation can be significantly improved and the frequency regulation effect is obvious. kp = 0, kp = 10, and kp = 30 correspond to the highest rotational speeds of 0.847, 0.852, and 0.867 pu, respectively; the corresponding active output is 0.7608, 0.753, and 0.756 pu respectively. As in Figure 7C, the rotor speed increase of kp = 10 is much more than that of kp = 10, the frequency support improvement is not significant clear because of the fast variation of output, as shown in Figure 7D.

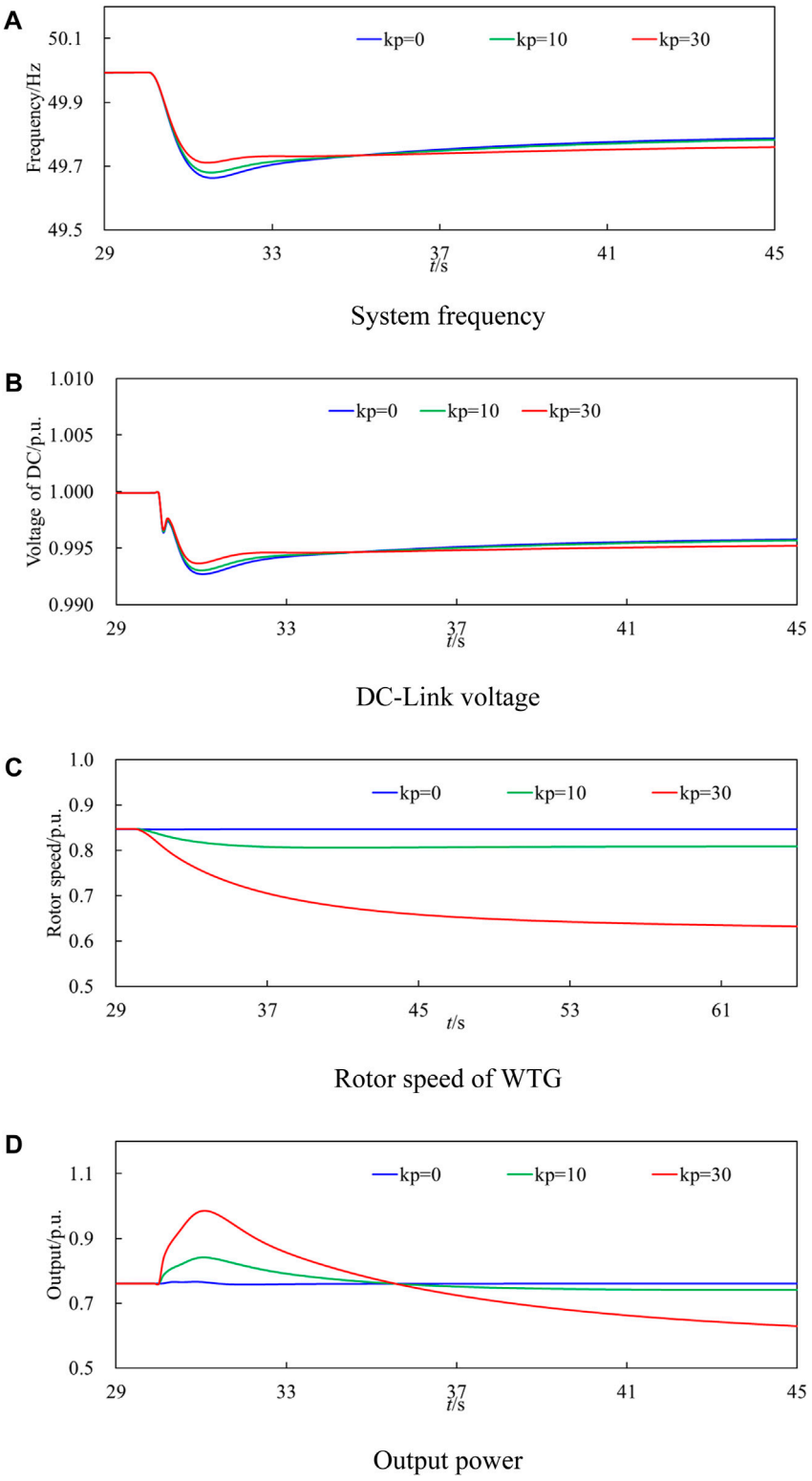

FIGURE 6
Comparison results with various control coefficient under low-frequency disturbance. **(A)** System frequency, **(B)** DC-Link voltage, **(C)** Rotor speed of WTG, **(D)** Output power.

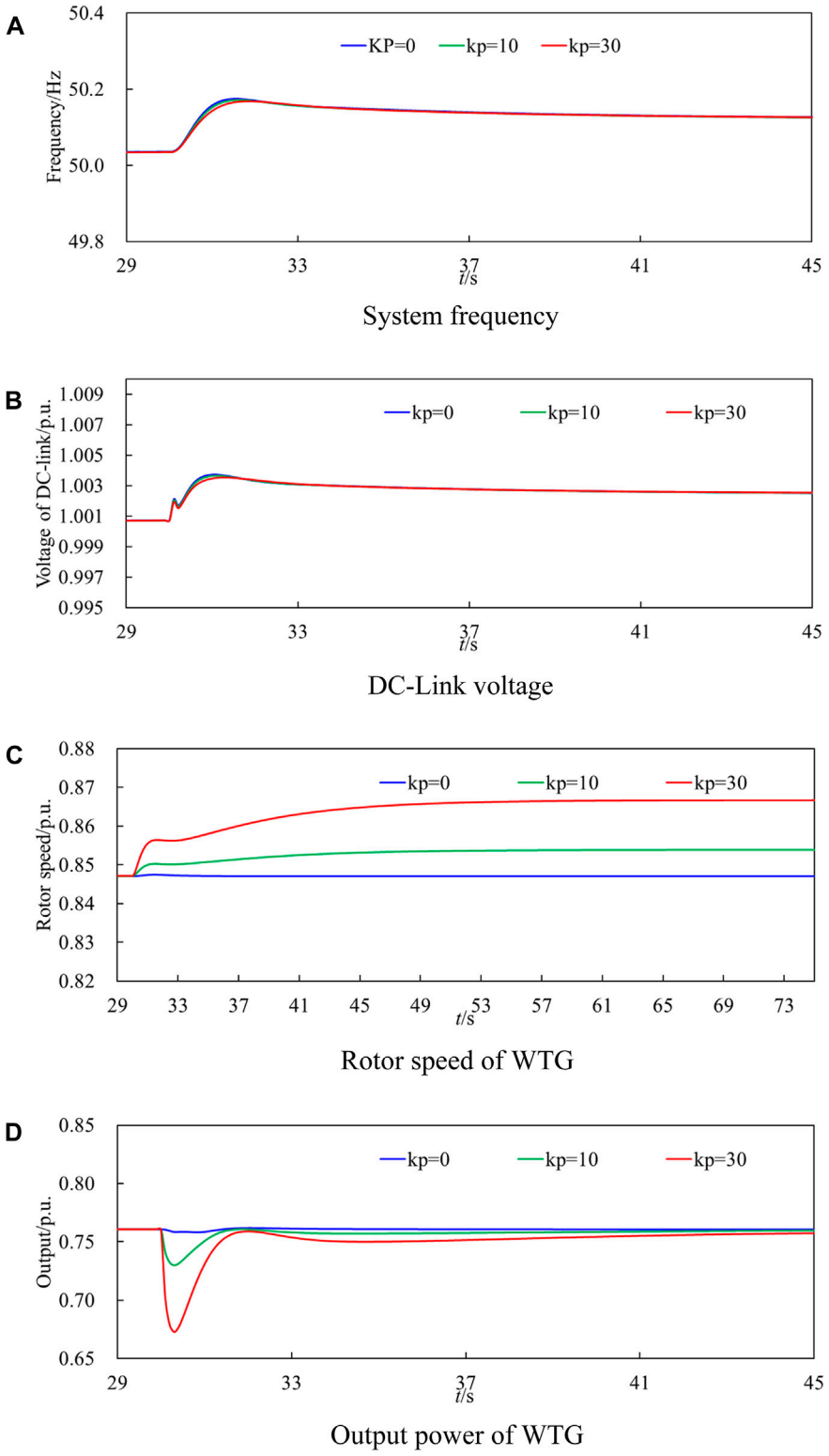

FIGURE 7
Comparison results with various control coefficient under over-frequency disturbance. **(A)** System frequency, **(B)** DC-Link voltage, **(C)** Rotor speed of WTG, **(D)** Output power of WTG.

4 Conclusion

The frequency support is realized by reserving reserve capacity of wind turbines, but the influence of the dynamic characteristics of MPPT on the overall frequency regulation characteristics of wind turbines during frequency support is ignored. To further tap the regulation potential of offshore wind power through flexible direct interconnection system, firstly, the frequency response model of the system is constructed, and the main factors that affect the frequency dynamic characteristics are revealed. Secondly, the principle of the grid-forming VSC with the function of self-inertial synchronization is introduced and the influence of the dynamic characteristics of MPPT on the frequency regulation characteristics of the WTG is clarified. Finally, based on the PSCAD/EMTDC electromagnetic transient simulation software platform, the electromagnetic transient simulation model of wind farms connected to AC/DC grid is established, and the influence of the dynamic characteristics of MPPT on the frequency regulation characteristics are verified by combining the grid-forming control technology. The simulation results indicate that with the increase of setting of droop control, the decrease of output power of MPPT becomes large so as to weaken the frequency support capability. The contribution of this research is to investigate the influence of the dynamic characteristics of MPPT on the frequency regulation characteristics. In future, the coordinated frequency support strategy between the WTG and energy storage system would be addressed.

Data availability statement

The raw data supporting the conclusions of this article will be made available by the author, without undue reservation.

Author contributions

QC: Conceptualization, Investigation, Methodology, Writing–original draft, Writing–review and editing. GS: Funding acquisition, Investigation, Writing–original draft, Writing–review and editing. YL: Project administration, Resources, Software, Writing–review and editing. PQ: Software, Supervision, Validation, Visualization, Writing–review and editing. JoZ: Conceptualization, Funding acquisition, Methodology, Project administration, Writing–original draft, Writing–review and editing. RY: Investigation, Project administration, Resources, Writing–original draft. JnZ: Methodology, Project administration, Resources, Software, Writing–review and editing.

Funding

The author(s) declare that financial support was received for the research, authorship, and/or publication of this article. This work is supported by the Science and Technology Project of State Grid Zhejiang Electric Power Co., Ltd., (5211DS230005), and partly by the National Natural Science Foundation of China (No.52107201).

Conflict of interest

Authors QC, YL, and PQ were employed by Electric Power Research Institute of State Grid Zhejiang Electric Power Corporation.

The remaining authors declare that the research was conducted in the absence of any commercial or financial relationships that could be construed as a potential conflict of interest.

Publisher's note

References

Adeuyi, O. D., Cheah-Mane, M., Liang, J., and Jenkins, N. (2017). Fast frequency response from offshore Multiterminal VSC–HVDC schemes. *IEEE Trans. Power Del.* 32 (6), 2442–2452. doi:10.1109/tpwrd.2016.2632860

Aouini, R., Marinescu, B., Kilani, K. B., and Elleuch, M. (2016). Synchronverter-based emulation and control of HVDC transmission. *IEEE Trans. Power Syst.* 31 (1), 278–286. doi:10.1109/tpwrs.2015.2389822

Arévalo Soler, J., Groß, D., Araujo, E. P., and Bellmunt, O. G. (2023). Interconnecting power converter control role assignment in grids with multiple ac and dc subgrids. *IEEE Trans. Power Del.* 38, 2058–2071. doi:10.1109/tpwrd.2023.3236977

Arghir, C., Jouini, T., and Dörffer, F. (2018). Grid-forming control for power converters based on matching of synchronous machines. *Automatica* 95, 273–282. doi:10.1016/j.automatica.2018.05.037

Bianchi, F. D., and Domnguez-Garca, J. L. (2016). Coordinated frequency control using MT-HVDC grids with wind power plants. *IEEE Trans. Sustain. Energy* 7 (1), 213–220. doi:10.1109/tste.2015.2488098

Castro, L. M., and Acha, E. (2016). On the provision of frequency regulation in low inertia AC grids using HVDC systems. *IEEE Trans. Smart Grid* 7 (6), 2680–2690. doi:10.1109/tsg.2015.2495243

Eto, J. H., Undrill, J., Mackin, P., Daschmans, R., Williams, B., Haney, B., et al. (2010). *Use of frequency response metrics to assess the planning and operating requirements for reliable integration of variable renewable generation*. Berkeley, CA: Lawrence Berkeley National Laboratory.

Flourentzou, N., Agelidis, V. G., and Demetriades, G. D. (2009). VSC-based HVDC power transmission systems: an overview. *IEEE Trans. Power Electron.* 24 (3), 592–602. doi:10.1109/tpel.2008.2008441

Groß, D., Sa´nchez-Sa´nchez, E., Prieto-Araujo, E., and GomisBellmunt, O. (2022). Dual-port grid-forming control of mmcs and its applications to grids of grids. *IEEE Trans. Power Del.* 37, 4721–4735. doi:10.1109/tpwrd.2022.3157249

Li, Y. J., Zhang, Z. R., Yang, Y., Chen, H., and Xu, Z. (2014). Coordinated control of wind farm and VSC-HVDC system using capacitor energy and kinetic energy to improve inertia level of power systems. *Int. J. Electr. Power and Energy Syst.* 59 (59), 79–92. doi:10.1016/j.ijepes.2014.02.003

Li, Y. J., Xu, Z., Ostergarrd, J., and Hill, D. J. (2017). Coordinated control strategies for offshore wind farm integration via VSC-HVDC for system frequency support. *IEEE Trans. Energy Convers.* 32 (3), 843–856. doi:10.1109/tec.2017.2663664

Markovic, U., Stanojev, O., Aristidou, P., Vrettos, E., Callaway, D., and Hug, G. (2021). Understanding small-signal stability of low-inertia systems. *IEEE Trans. Power Syst.* 36 (5), 3997–4017. doi:10.1109/tpwrs.2021.3061434

Qin, Y., Wang, H., Shao, H., Yang, R., Cai, X., and Cao, Y. (2021) "Self-synchronization and frequency response control of PMSG-based wind turbine

generator," in IEEE energy conversion congress and exposition-Asia, Singapore, 24–27 May 2021, IEEE. doi:10.1109/ECCE-Asia49820.2021.9479272

Rezaei, N., and Kalantar, M. (2015). Smart microgrid hierarchical frequency control ancillary service provision based on virtual inertia concept: an integrated demand response and droop controlled distributed generation framework. *Energy Convers. Manage* 92, 287–301. doi:10.1016/j.enconman.2014.12.049

Sang, S., Zhang, C., Zhang, J., Shi, G., and Deng, F. (2022). Analysis and stabilization control of a voltage source controlled wind farm under weak grid conditions. *Front. Energy* 16 (6), 943–955. doi:10.1007/s11708-021-0793-5

Shi, Q., Li, F., and Cui, H. (2018). Analytical method to aggregate multi-machine SFR model with applications in power system dynamic studies. *IEEE Trans. Power Syst.* 33 (6), 6355–6367. doi:10.1109/tpwrs.2018.2824823

Subotić, I., and Groß, D. (2022). Power-balancing dual-port grid-forming power converter control for renewable integration and hybrid ac/dc power systems. *IEEE Trans. Control Netw. Syst.* 9, 1949–1961. doi:10.1109/tcns.2022.3181551

Xiong, L., Zhuo, F., Wang, F., Liu, X., Chen, Y., Zhu, M., et al. (2016). Static synchronous generator model: a new perspective to investigate dynamic characteristics and stability issues of grid-tied PWM inverter. *IEEE Trans. Power Electron.* 31 (9), 6264–6280. doi:10.1109/tpel.2015.2498933

Xiong, L., Liu, X., Zhang, D., and Liu, Y. (2021). Rapid power compensation-based frequency response strategy for low-inertia power systems. *IEEE J. Emerg. Sel. Top. Power Electron.* 9 (4), 4500–4513. doi:10.1109/jestpe.2020.3032063

Yang, R., Zhang, C., Cai, X., and Shi, G. (2018). Autonomous grid-synchronising control of VSC-HVDC with real-time frequency mirroring capability for wind farm integration. *IET Renew. Power Gener.* 12 (13), 1572–1580. doi:10.1049/iet-rpg.2017.0824

Yang, R., Shi, G., Cai, X., Zhang, C., Li, G., and Liang, J. (2020). Autonomous synchronizing and frequency response control of multi-terminal DC systems with wind farm integration. *IEEE Trans. Sustain. Energy* 11, 2504–2514. doi:10.1109/TSTE.2020.2964145

Yang, D., Jin, Z., Jin, E., Wang, X., Chen, W., Yan, G.-G., et al. (2024). Adaptive frequency droop feedback control-based power tracking operation of a DFIG for temporary frequency regulation. *IEEE Trans. Power Syst.* 39 (2), 2682–2692. doi:10.1109/tpwrs.2023.3277009

Zhong, C., Li, H., Zhou, Y., Lv, Y., and Chen, J. (2022). Virtual synchronous generator of PV generation without energy storage for frequency support in autonomous microgrid. *Int. J. Electr. Power and Energy Syst.* 134, 107343. doi:10.1016/j.ijepes.2021.107343

frontiers | Frontiers in Energy Research

TYPE Original Research
PUBLISHED 31 July 2024
DOI 10.3389/fenrg.2024.1416785

OPEN ACCESS

EDITED BY
Yonghui Liu,
Hong Kong Polytechnic University, Hong Kong SAR, China

REVIEWED BY
Xiaokang Liu,
Polytechnic University of Milan, Italy
Yuting Gao,
Wuhan University, China
Pu Liu,
Zhengzhou University of Light Industry, China
Godwin Norense Osarumwense Asemota,
University of Rwanda, Rwanda
Delong Zhang,
Tianjin University of Technology, China

*CORRESPONDENCE
Shuhuai Shi,
shishuhuai@126.com

RECEIVED 13 April 2024
ACCEPTED 11 July 2024
PUBLISHED 31 July 2024

CITATION
Zhao Z, Li H, Sun F, Shi S, Wang D, Zhang J and Wu C (2024), Power quality improvement of unipolar-input-bipolar-output DC transmission system via load power balancing.
Front. Energy Res. 12:1416785.
doi: 10.3389/fenrg.2024.1416785

Power quality improvement of unipolar-input-bipolar-output DC transmission system via load power balancing

Zhuan Zhao[1], Haoran Li[2], Fei Sun[3], Shuhuai Shi[4]*, Di Wang[1], Jingxian Zhang[1] and Chaoyang Wu[5]

[1]Zhengzhou Electric Power College, Zhengzhou, China, [2]State Grid Zhoukou Electric Power Supply Company, Zhoukou, China, [3]Henan Jiuyu Epri Electric Power Technology Co., Ltd., Zhengzhou, China, [4]State Grid Henan Electric Power Research Institute, Zhengzhou, China, [5]China Power New Life Town Technology Co., Ltd., Beijing, China

In DC transmission and distribution systems, both unipolar and bipolar transmission modes exist, and DC transformers used in these systems are also available in either unipolar or bipolar configurations. In actual systems, due to requirements such as economy, land occupation, and reliability, there is a tendency to use a system with unipolar input and bipolar output. However, the bipolar loads, if unbalanced, will lead to increased equipment costs and voltage imbalance, causing power quality problems. This paper defines the Power Unbalance Factor (PUF) to describe the power quality of the studied DC transmission system and presents an improved DC transformer topology based on a power balancing system. This topology realizes bipolar voltage balance and improves the power quality of the DC transmission system when the load is unbalanced. The influence of the proposed solution on the power design of the DC system is demonstrated through theoretical analysis, and its effectiveness for improving the DC power quality is verified by both simulations in MATLAB/Simulink environment and physical experiments. When the power electronic transformer needs to be overloaded, the proposed topology can reduce the design power of the two branches by using the difference power, which is economical.

KEYWORDS

DC transmission system, load power balancing, DC power quality, unipolar to bipolar, power unbalance factor

1 Introduction

The need to adjust the energy structure and develop sustainable green energy on a large scale is imperative due to the exhaustion of mainstream fossil energy and the serious problem of environmental pollution (Chen et al., 2013). The application of new renewable energies, such as water, wind, light, and geothermal energy, is an important measure to achieve environmental protection and sustainable economy development worldwide. The European Union has set a higher development goal, requiring renewable energy consumption to reach 20.0% of energy consumption and 30.0% of total power generation by 2020 (Wang et al., 2018; Yao et al., 2014). To reduce the use of fossil energy, promote multi-energy complementation, and achieve comprehensive energy utilization of the power system, it is necessary to develop new technologies related to

power grid equipment (Wang et al., 2013; Xiong et al., 2021a, Xiong et al., 2021b) and reduce the loss and transformation of each link of power generation, transmission, and distribution (Zhang et al., 2018; Xiong et al., 2021a, Xiong et al., 2021b). One effective complement to the AC system can be seen in the DC system, which has advantages such as low loss, less reactive power, and convenient access to new energy, especially with the continuous development of fully-controlled semiconductor devices such as insulated-gate bipolar transistors (IGBTs) (Zhao et al., 2008; Engel et al., 2014). DC power electronic transformer has the advantages of electrical isolation, efficient energy conversion, fast dynamic response, flexible control, small size, light weight and easy expansion and integration (Lin, 2016; Xiong et al., 2020). These advantages make DC power electronic transformers have a wide range of applications in distributed power systems, renewable energy access, DC micro-grid and other fields.

However, power quality is a key issue in the transmission, distribution, and consumption of power systems that affects the stability, security, and economy of the system (Kenzelmann et al., 2014; Xiong et al., 2021a, Xiong et al., 2021b). In comparison with the AC system, the power quality of the DC transmission and distribution system is usually better, as the DC voltage does not change as frequently as in the AC system but is maintained approximately at a rated value, and there are no traditional power quality problems caused by harmonics and interference (Akagi and Kitada, 2011). However, if the rationale behind the definition of power quality is considered to be describing the quality of the power supply, either in the form of AC or DC, with a special focus on the waveforms of voltages and currents, then the power quality of a DC system can be reflected similarly by the deviation between the ideal and real-time waveforms in such a system. Under such a premise, the power quality in a DC transmission and distribution system is closely related to the topology, control, modulation method, and application scenarios of power electronic converters, which are important elements to form the DC system.

Unipolar and bipolar hybrid transmission is one of the typical application scenarios for DC transmission and distribution systems (Jovcic and Ool, 2010). Specifically, unipolar transmission is used on the medium-voltage side of medium-voltage DC distribution networks to reduce transmission costs and the land area used (Gowaid et al., 2015). Meanwhile, bipolar transmission is used on the low-voltage side as it can maximize the reliability of the power supply and reduce the insulation design requirements of the system (Li et al., 2012). Such systems mostly adopt two DC transformers in series on the input side and in parallel on the output side, forming an input-series output-parallel (ISOP) topology (Ooi and Wang, 1991; Xiong et al., 2016; Falcones S et al., 2013), which requires double the cost of equipment. Moreover, the voltage instability caused by the load imbalance of the two poles is the biggest problem faced by this application scenario, which is a great challenge to the power quality of DC transmission systems.

Focusing on the aforementioned issues, this paper uses the degree of voltage imbalance between the two poles as an indicator of the DC system's power quality. Such an indicator is crucial for evaluating and improving the power transmission in the DC system. On this basis, a novel topology is proposed for enhancing the power quality of the unipolar-input-bipolar-output system, by forcing load power balancing. Such a balance is implemented by properly controlling the dual active bridge (DAB) circuit in parallel with the two loads on different poles. Theoretical analysis proves the improvement of DC system power design by adopting the topology in the case of unbalanced loads, which are commonly encountered in practical applications. This paper introduces the structure and control method of the topology in detail, and sets the boundary conditions of the scene in detail, and gives the detailed design parameters of the design capacity of the topology according to the boundary conditions. By comparing the design parameters in different scenarios, the economy of the topology is proved. Finally, the feasibility of the new topology is verified by simulation results in the MATLAB/Simulink environment as well as experimental results based on a physical platform.

2 Studied system and power unbalance factor

Figure 1 illustrates the most well-established topology for unipolar to bipolar conversion. This topology utilizes two DC transformers connected in parallel at a single pole, with their outputs connected in series to two loads, while the ground wire is led out from the middle. With reference to Figure 1, Load 1 and Load 2 represent two load units, which may consist of a single load, a load group, or a power supply line of the same voltage level. As seen from the diagram, the power of Load 1 is transmitted by DC transformer 1, and the power of Load 2 is transmitted by DC transformer 2. Both loads are independent of each other, and there is no power coupling between the two DC transformers. The two DC transformers share the same input side with input voltage V_{in}, i.e., the unipolar input is used, while the two loads on the output side are grounded with no power interaction between them, forming a positive pole (with voltage $U_{dc}/2$) and a negative pole (with voltage $-U_{dc}/2$). This topology is equivalent to two separate monopole-to-monopole power transformation legs.

Power imbalance refers to the imbalance of power output or consumption among various parts or components in a system. In a three-phase power system, if the three-phase current or voltage is not balanced, it will lead to power imbalance. In the DC system, if two circuits are connected in parallel, the situation similar to the AC system will also occur. When both loads are balanced, the rated power per pole yields $P_{out+} = P_{out-} = P$. The maximum total power of the load on the bipolar side is designed to be $2P$, considering the unbalance of the DC system. Then, the power imbalance between the two load ports is defined to reflect the power quality in the DC system. Since Load 1 and Load 2 are connected in series, the imbalance of load, voltage, and power is equivalent. If the voltage balance between the positive and negative poles is achieved, it also means that the power of the two poles is equal. To this end, in this paper, the power unbalance factor (PUF) is defined as Eq. 1

$$\eta = \frac{P_{load} - P}{P} \times 100\% \tag{1}$$

where P_{load} is the load power of the pole (either positive or negative).

The PUF value indicates the degree of power imbalance in the system, with $\eta = 0$ representing perfect balance. When the value of

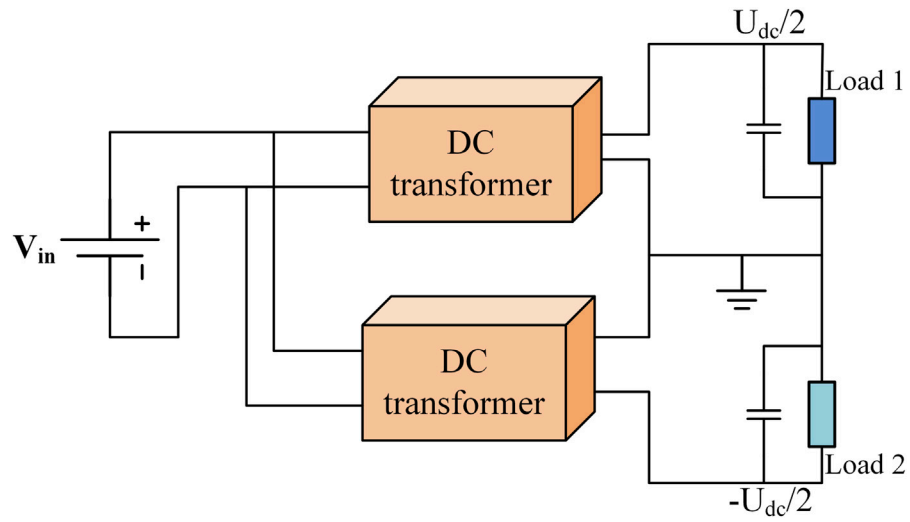

FIGURE 1
Principle diagram of the studied unipolar-input-bipolar-output DC system.

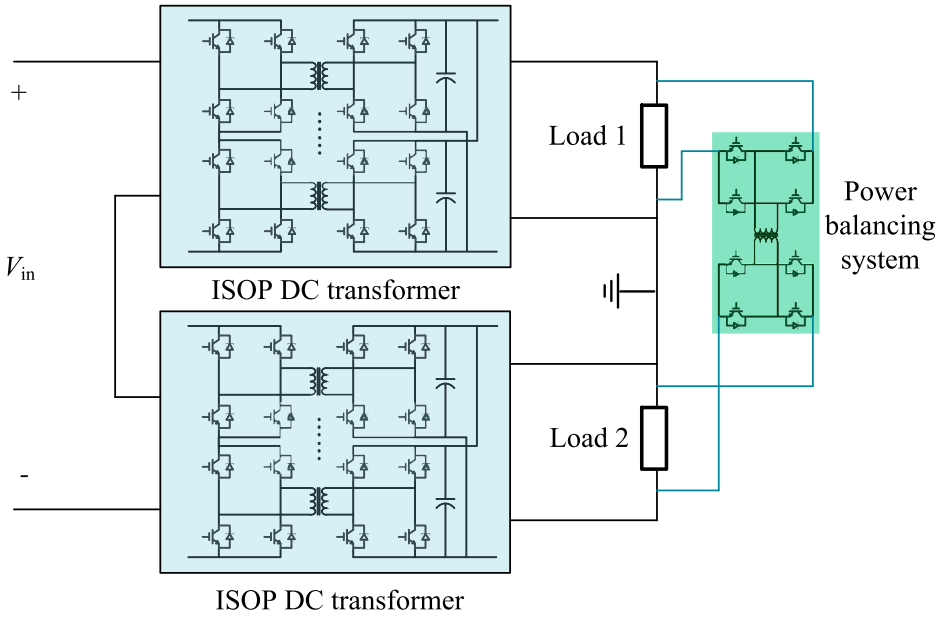

FIGURE 2
Proposed topology with power balance system.

η is positive, it means that the power of the load exceeds the rated power at load balance; when it is negative, it means that the power of the load is lower than the rated power at load balance. The PUF value can be used as an essential indicator of the system's stability and efficiency, enabling effective management of the system's performance. By utilizing this topology and PUF value, we can establish a more stable and efficient power conversion system, reducing power loss and ensuring reliable and consistent operation.

It is noted that though such a DC system is usually designed to be symmetrical in order to maximize power delivery efficiency and reduce cost, in practice, it is common that loads are unbalanced. In those cases, the PUF value is different than 0, and the power quality is compromised.

3 Research on topology and control method of DC transformer

In this Section, a novel configuration is developed to improve the power quality of the unipolar-to-bipolar power conversion under unbalanced load conditions, by incorporating a system that enables

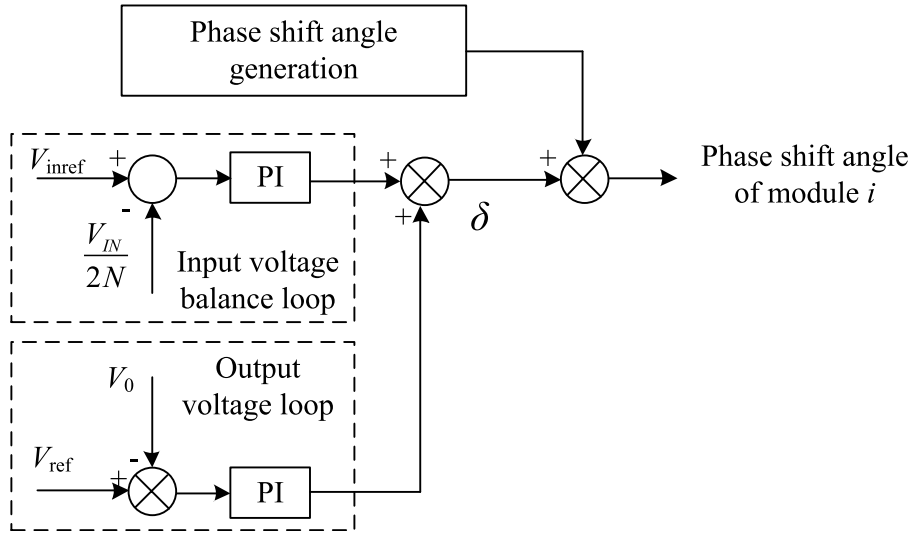

FIGURE 3
Control diagram of DC transformer.

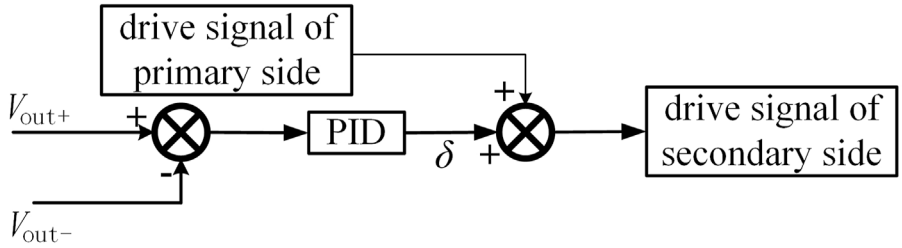

FIGURE 4
Control diagram of proposed PBS.

TABLE 1 Comparison of system design power between two topologies.

	Scenario 1	Scenario 2
Topology without PBS	$2P$	$P_{all} = 2P + (\max\{\lvert\eta'_{L1}\rvert, \lvert\eta'_{L2}\rvert\} + \max\{\lvert\eta''_{L1}\rvert, \lvert\eta''_{L2}\rvert\})P$
Topology with PBS	$P_{all} = 2P + \frac{\lvert\eta_{L1}-\eta_{L2}\rvert}{2}P$	$P_{all} = 2P + \max\left\{\frac{\lvert\eta'_{L1}-\eta'_{L2}\rvert}{2}, \frac{\lvert\eta''_{L1}-\eta''_{L2}\rvert}{2}\right\}P$

load power balancing. A detailed analysis of the physical implementation and control principles is performed in the following section.

3.1 Physical implementation

Figure 2 shows the detailed implementation of DC transmission system, realizing the principle diagram in Figure 1 and incorporating a power balance system to tackle the possible presence of load imbalance. The input side (medium-voltage side) is powered by a voltage source converter, while the two loads correspond to the positive and negative poles on the output side. The DC transformer for each pole consists of multiple DAB modules that are connected in series on the input side and in parallel on the output side, with the number of DAB modules determined by the voltage level and required power. The medium-voltage DC network transfers power to the load through the DC transformers, keeping the voltages of the two loads equal under the nominal condition with balanced loads. However, when the loads are imbalanced, the voltages of the two ports become unequal.

To address this issue, the proposed topology incorporates a power balancing system (PBS) that enables power balancing between loads. As shown in Figure 2, such a PBS is implemented by connecting a DAB, whose ports are in parallel with the two loads, into the original system. This allows for bidirectional power flow

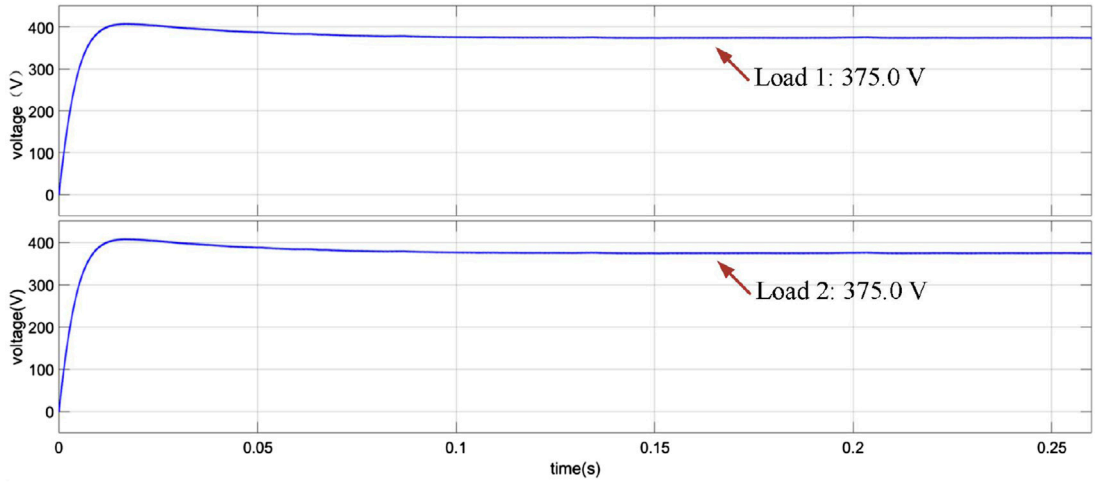

FIGURE 5
Simulated voltage waveforms in the absence of the PBS when Load 1 and Load 2 have the same impedance of 10.0 Ω.

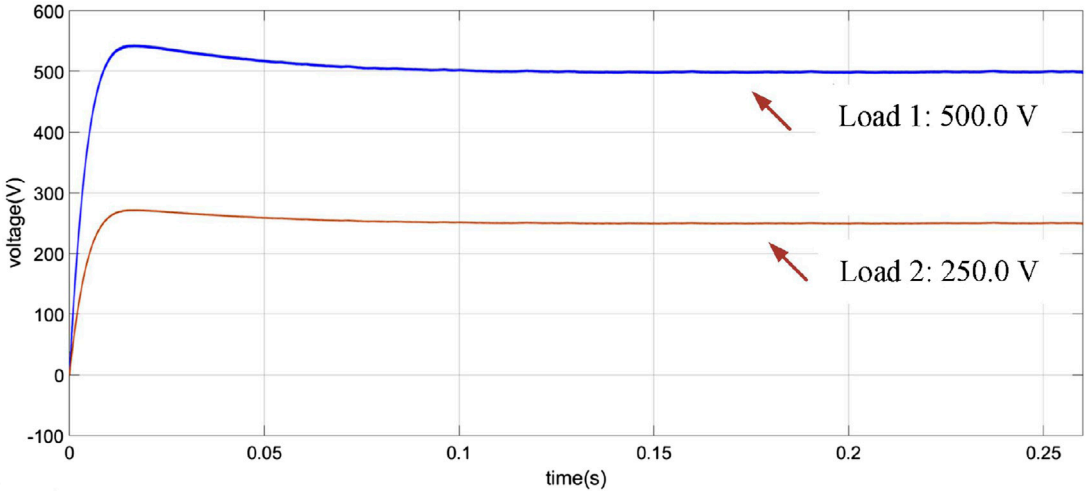

FIGURE 6
Simulated voltage waveforms in the absence of the PBS when Load 1 is 20.0 Ω while Load 2 is 10.0 Ω.

between the two loads. Specifically, the PBS transfers power from the high-voltage port to the low-voltage one, achieving voltage balance between the two ports. Since the PBS handles the power difference between the two ports, its design capacity only needs to be half the power difference between the two.

3.2 Control method

3.2.1 DC transformer control

The main circuit topology of the DC transformer features an ISOP structure, with multiple DAB circuits connected in series on the input side to reduce the withstand voltage of each module and in parallel on the output side to reduce the current of each module. The phase shift control strategy is employed in DAB modules, with each module controlled separately. Given that each module on the input side is connected in series, it is essential to ensure that all modules are voltage balanced. Therefore, the phase shift angle of each module is adjusted by the input voltage and the output voltage, as shown in Figure 3. Specifically, the control system of the ISOP DC transformer comprises an input voltage loop and an output voltage loop, each adopting a proportional-integral (PI) controller, in order to generate the phase shift angle of each module. Finally, the gate signals of the pertinent switches are generated based on the real-time phase shift angle (not shown here for brevity).

3.2.2 Power balancing control

To achieve voltage balance between the two ports, the proposed PBS is used to transfer unbalanced power. Given that the two loads are connected in series, the power balance system needs to meet the two conditions of bidirectional power flow and electrical isolation. To this end, the DAB is employed to implement the power balance system, with the control diagram shown in Figure 4.

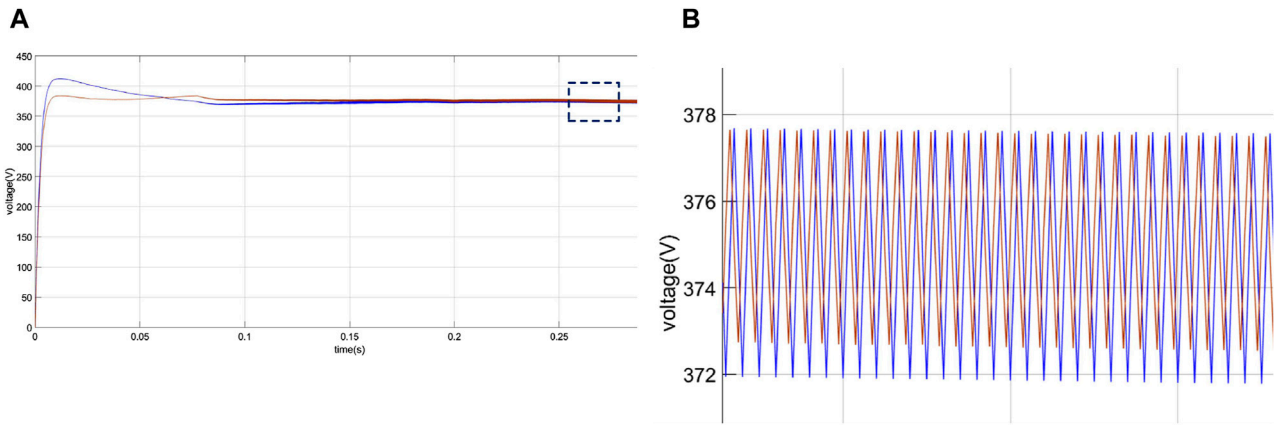

FIGURE 7
Simulated voltage waveforms in the presence of the PBS when Load 1 is 20.0 Ω while Load 2 is 10.0 Ω. **(A)** Overall waveforms. **(B)** Zoomed-in waveforms.

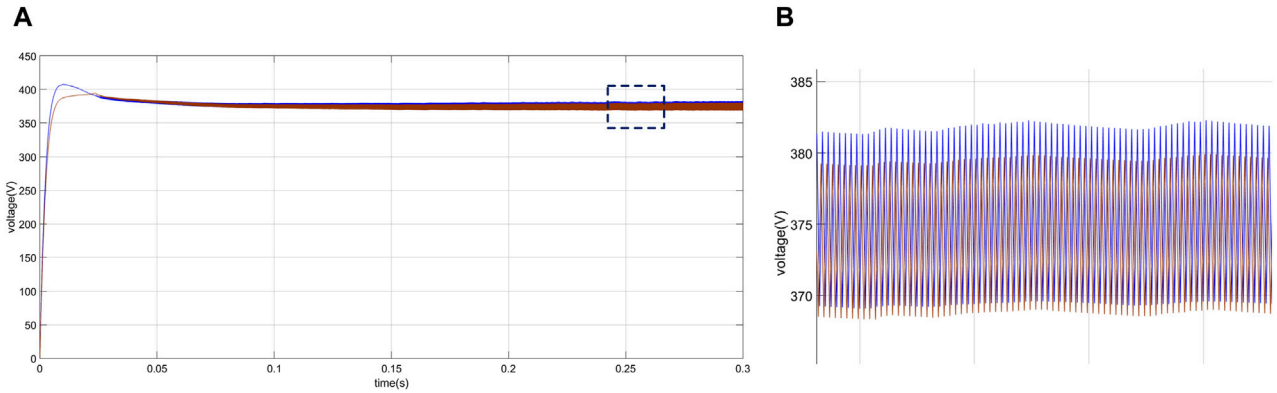

FIGURE 8
Simulated voltage waveforms in the presence of the PBS when Load 1 is 10.0 Ω while Load 2 is 20.0 Ω. **(A)** Overall waveforms. **(B)** Zoomed-in waveforms.

Unlike the control strategy of the main circuit that aims to transfer the power from the input to the output, the power balance system needs to achieve voltage balancing of the two ports. As such, the phase shift angle is determined by the voltage difference between the two ports, using a proportional-integral-derivative (PID) controller. Following this, the drive signal of the DAB secondary side can be generated.

4 System power design

In this Section, the system power design is discussed for the sample system in Figure 2, with two scenarios being used to reveal the impact of the proposed PBS. In Scenario 1, the loads operate within their respective set intervals, and it will be shown that the topology with PBS does not offer any advantage in terms of power design compared to the topology without PBS. However, in Scenario 2, where the operating power of one load may exceed the rated power, the topology with PBS has significant advantages in power design. For both cases, the total operating power of Load 1 and Load 2 will not exceed the rated power of the system.

4.1 Scenario 1: $0 \le P_{out+} \le P$, $0 \le P_{out-} \le P$

The topology in Figure 2 contains two DC transformers, each of which is constructed from ISOP structures, but neither of them is loaded with power more than P, namely, neither P_{out+} nor P_{out-} will exceed the power rating of their respective lines. Therefore, both Load 1 and Load 2 only operate within their respective set intervals, and the two lines will not be standby for each other, nor will they be overloaded.

At this time, the design power of each ISOP of the DC transformer in the topology is P, and the design power of the DC transformer is $2P$. Additionally, if the proposed scheme with the PBS is used, the PBS is required to handle the differential power. Hence, the total equipment design power of the system, including the DC transformer and the PBS, is Eq. 2:

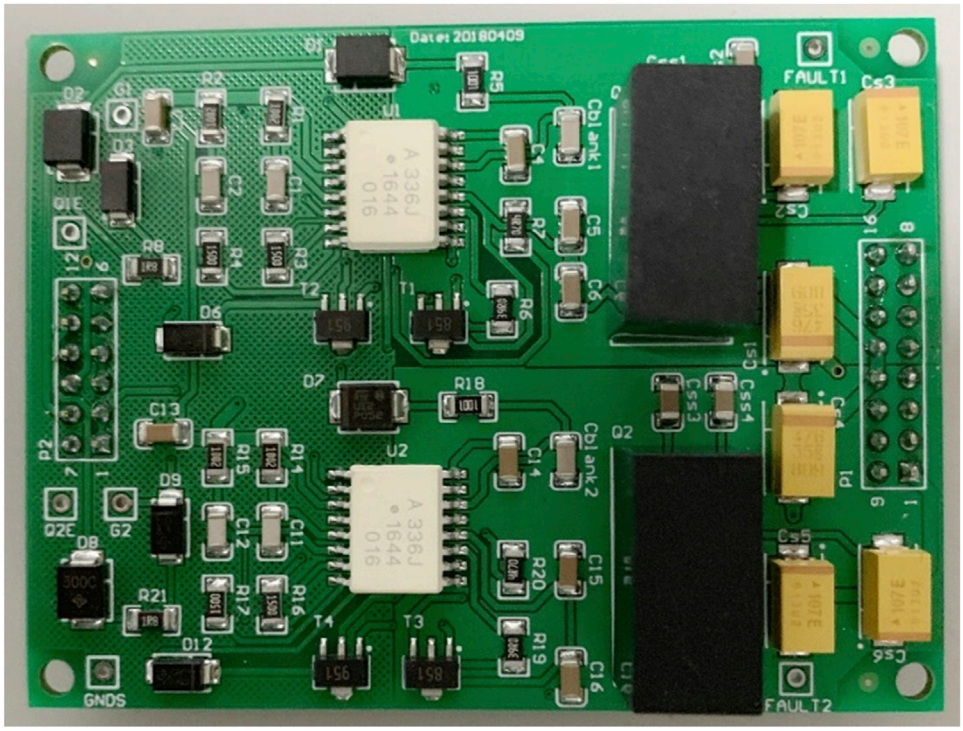

FIGURE 9
H-bridge submodule circuit board.

TABLE 2 Devices and parameters used in the experiment.

Device	Model	Parameter
IGBT	IKW75N60TA	600.0V/75.0A
Voltage Hall sensor	LV25-P	10.0V~500.0V
Current Hall sensor	LA25-NP	−25.0A~+25.0A
IGBT driver chip	ACPL-336J	15.0V~30.0V
IGBT drive power module	QA241	24.0V to +15.0V/-8.0V
Programmable DC sources	IT6726B	160.0V/40.0A/3000.0W
DC electronic load 1	IT8514C	120.0V/240.0A/1500.0W
DC electronic load 2	IT8512	120.0V/30.0A/300.0W

$$P_{all} = 2P + \frac{|\eta_{L1} - \eta_{L2}|}{2} P \tag{2}$$

where η_{L1} is the PUF value of Load 1, and η_{L2} is the PUF value of Load 2.

It is seen that in the setting of scenario 1, since the two loads are not overloaded, there will always be an extra PBS handling the unbalanced power, and the total design power of the system will be greater than that without the proposed PBS ($2P$). The proposed PBS in this scenario has no advantage in terms of system power design.

4.2 Scenario 2: $0 \le P_{out+} + P_{out-} \le 2P$, $0 \le P_{out+} \le 2P$, $0 \le P_{out-} \le 2P$

In this scenario, the upper power limits of both Load 1 and Load 2 are $2P$, indicating a certain load may be overloaded with the elapse of operating time. In practice, this suggests that a line will suddenly increase its load, or that two lines will be standby for each other.

In the first case, when the traditional topology without the proposed PBS is used, the design power of ISOP modules in each DC transformer needs to be designed to meet the overload power, considering the upper power limit of loads. When $P_{out+} \ge P$ and $P_{out-} \le P$, the positive DC transformer is overloaded, and its power is given by Eq. 3

$$P_{+} = P + \max\left\{\left|\eta'_{L1}\right|, \left|\eta'_{L2}\right|\right\} P \tag{3}$$

where η'_{L1} is the PUF value of Load 1, and η'_{L2} is the PUF value of Load 2, when the power of positive pole exceeds P.

Similarly, when $P_{out+} \le P$ and $P_{out-} \ge P$, the negative DC transformer is overloaded, and its corresponding power is Eq. 4

$$P_{-} = P + \max\left\{\left|\eta''_{L1}\right|, \left|\eta''_{L2}\right|\right\} P \tag{4}$$

where η''_{L1} is the PUF value of Load 1, and η''_{L2} is the PUF value of Load 2, when the power of negative pole exceeds P.

The total design power of the device needs to be the sum of the positive and negative poles, yielding Eq. 5

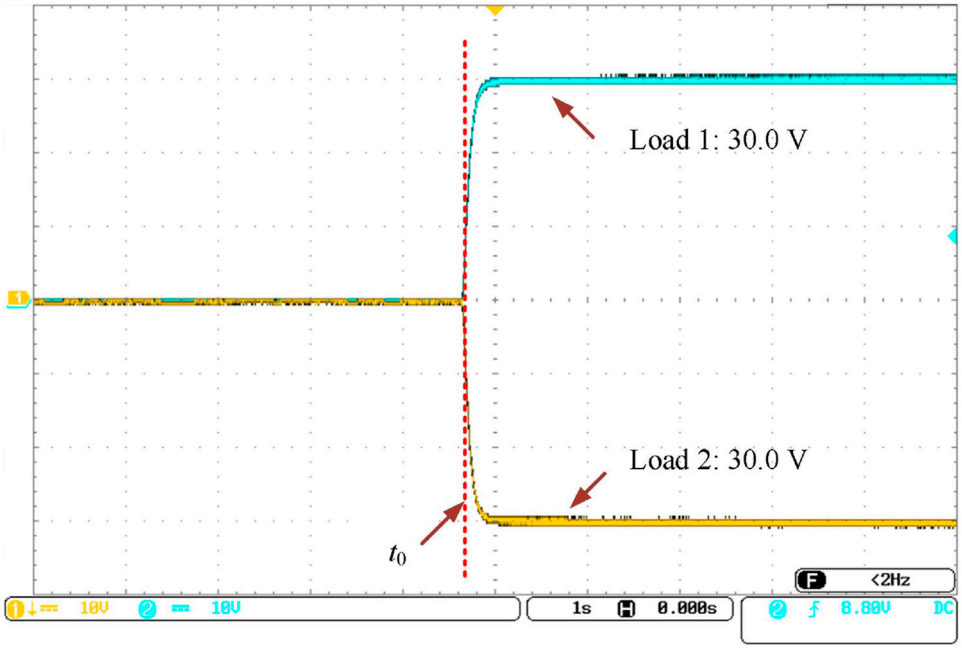

FIGURE 10
Experimental voltage waveforms of loads in the presence of the PBS when Load 1 is 75.0 Ω while Load 2 is 150.0 Ω.

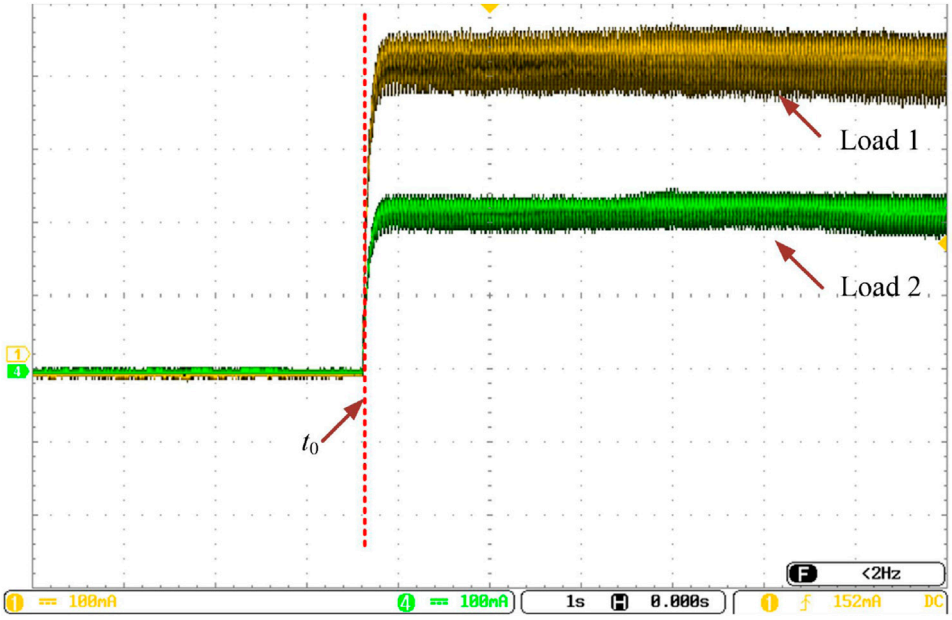

FIGURE 11
Experimental current waveforms of loads in the presence of the PBS when Load 1 is 75.0 Ω while Load 2 is 150.0 Ω.

$$P_{all} = 2P + \left(\max\left\{\left|\eta'_{L1}\right|, \left|\eta'_{L2}\right|\right\} + \max\left\{\left|\eta''_{L1}\right|, \left|\eta''_{L2}\right|\right\}\right)P \quad (5)$$

In the second case, when the proposed scheme is used, since the sum of the power of Load 1 and Load 2 does not exceed 2*P*, the design power of each ISOP is just half of the total power, namely, *P*. The PBS handles the power difference between the positive and negative poles. Accordingly, when $P_{out+} \geq P$ and $P_{out-} \leq P$, the design power of the system is Eq. 6

$$P_{all} = 2P + \frac{\left|\eta'_{L1} - \eta'_{L2}\right|}{2}P \quad (6)$$

When $P_{out+} \leq P$ and $P_{out-} \geq P$, the design power of the system is Eq. 7

$$P_{all} = 2P + \frac{\left|\eta''_{L1} - \eta''_{L2}\right|}{2}P \quad (7)$$

Since the system needs to meet the demand of the maximum differential power, we have Eq. 8

$$P_{all} = 2P + \max\left\{\frac{\left|\eta'_{L1} - \eta'_{L2}\right|}{2}, \frac{\left|\eta''_{L1} - \eta''_{L2}\right|}{2}\right\}P \quad (8)$$

Comparing Eqs 5, 8, it is seen that the PBS system in Scenario 2 has obvious advantages in terms of power design. Besides, with the increase of load imbalance, this advantage becomes more obvious, as illustrated by Table 1.

5 Verification

In this Section, simulation results based on MATLAB/Simulink, as well as experimental results on a physical platform, have been used to demonstrate the effectiveness of the PBS in balancing the voltage across two loads and thus improving the power quality of the DC system.

5.1 Simulation verification

Simulations were carried out using MATLAB/Simulink to verify the performance of the PBS. With reference to the system topology in Figure 1, the simulation setup involved a unipolar input voltage of 20.0 kV on the medium-voltage side of the system, while the low-voltage side was bipolar with an output voltage of ±375.0 V. The simulation results depicted in Figure 5 showed that when both loads 1 and 2 were equal and set to 10.0 Ω, the system functioned correctly without the need for the PBS. However, when Load 1 was increased to 20.0 Ω while Load 2 remained at 10.0 Ω, the voltage of Load 1 was twice that of Load 2 in the absence of the proposed PBS, causing the system to become voltage unbalanced, as shown in Figure 6.

After the proposed PBS was added, the system topology becomes Figure 2, and the simulation results depicted in Figure 7A show that the voltages of two ports were initially inconsistent when Load 1 was 20.0 Ω while Load 2 was 10.0 Ω. However, after an adjustment period of 0.15 s, the voltage of both ports approached the same value, which was 375.0 V. Figure 7B shows an enlarged portion of the waveforms in Figure 7A, where the voltage fluctuation after the system was stabilized was within 1.0%, showing the effectiveness of the proposed PBS in this situation.

Similarly, the simulation results shown in Figure 8, corresponding to the case the case where Load 1 is 10.0 Ω and Load 2 is 20.0 Ω, demonstrate again the effect of the proposed PBS on system voltage balancing. Moreover, the PBS could achieve bidirectional flow of power, since in this case power flowed to the upper port through the PBS. The voltage of the two ports approached the same value after a period of adjustment.

5.2 Experimental verification

To validate the effectiveness of the PBS, experimental tests were conducted on a physical platform comprising a dSPACE system, DC transformer hardware circuits, a DC power supply, and DC loads. The experimental setup involved using a programmable DC source with protection as the DC power supply and pure resistive DC electronic loads as the output port loads. The single-stage input side, the bipolar output side, and the PBS, are composed of H-bridge submodules and isolation transformers (see circuit board in Figure 9). Each H bridge independently uses a circuit board including the power modules and driver modules, and the number of H bridges in the cascaded H bridges can be flexibly selected. The experimental platform parameters are shown in Table 2.

Specifically, the H-bridge structure and its front-end half-bridge protection circuit are composed of upper and lower IGBT half-bridge units. The H-bridge circuit used discrete IGBT components, IKW75N60TA of Infineon. The driving circuit was designed to provide IGBT turn-on voltage and ensure IGBT turn-off voltage. A plurality of H-bridge modules formed the structure shown in Figure 2.

During the experiment, Load 1 was set to 75.0 Ω and Load 2–150.0 Ω. An input voltage of 50.0 V was supplied at time t_0. Due to the different loads, when there is no power balance system, the voltage of the two ports will be inconsistent, that is, the power imbalance problem of the DC system defined in this paper. According to the waveforms of Figures 10, 11, the system incorporates a power balancing system. The experimental results depicted in Figures 10, 11 showed that the PBS system was capable of bipolar balanced output. After a short transient, the output voltages of the two loads become equal in magnitude (30.0V). At this time, the positive current was 0.4 A, and the negative current was 0.2 A, which was consistent with the ratio of the two loads.

In summary, both the simulation and experimental results demonstrated the effectiveness of the PBS in balancing the voltage across two loads and improving the power quality of the DC system. The experimental setup and simulation model could be used as a reference for future research on power balancing systems.

6 Conclusion

In this paper, a novel DC transformer and power balance topology is proposed to address the problem of load imbalance possibly present in a DC distribution network. Our proposed topology achieves voltage/power balancing through an actively-controlled PBS, and its feasibility has been verified. Specifically, in the DC/DC conversion scenario where the input is unipolar and the output is bipolar, the proposed topology balances the output voltage of the positive and negative poles and effectively mitigates the impact of load imbalance on the system operation. The proposed topology is robust and able to maintain power balance under various operating conditions. Overall, the findings demonstrate the potential of the proposed topology to address one of the major challenges faced by the DC transmission and distribution system. In the second scenario, the proposed topology can reduce the design difference power by 50.0%, which means that the greater the difference between the output of the two poles, the greater the advantage of the topology.

Data availability statement

The original contributions presented in the study are included in the article/Supplementary Material, further inquiries can be directed to the corresponding author.

Author contributions

ZZ: Formal Analysis, Software, Supervision, Writing–original draft, Writing–review and editing. HL: Conceptualization, Supervision, Writing–review and editing. FS: Data curation, Investigation, Writing–review and editing. SS: Conceptualization, Formal Analysis, Methodology, Project administration, Software, Validation, Visualization, Writing–original draft, Writing–review and editing. DW: Formal Analysis, Investigation, Validation, Writing–review and editing. JZ: Data curation, Project administration, Writing–original draft. CW: Conceptualization, Validation, Writing–review and editing.

Funding

The author(s) declare that no financial support was received for the research, authorship, and/or publication of this article.

Conflict of interest

Author HL was employed by State Grid Zhoukou Electric Power Supply Company. Author FS was employed by Henan Jiuyu Epri Electric Power Technology Co., Ltd. Author CW was employed by China Power New Life Town Technology Co., Ltd.

The remaining authors declare that the research was conducted in the absence of any commercial or financial relationships that could be construed as a potential conflict of interest.

Publisher's note

All claims expressed in this article are solely those of the authors and do not necessarily represent those of their affiliated organizations, or those of the publisher, the editors and the reviewers. Any product that may be evaluated in this article, or claim that may be made by its manufacturer, is not guaranteed or endorsed by the publisher.

References

Akagi, H., and Kitada, R. (2011). Control of a modular multilevel cascade BTB system using bidirectional isolated DC/DC converters. *IEEE Trans. Power Electron.* 26, 2457–2464. doi:10.1109/ECCE.2010.5617703

Chen, D., Xu, L., and Yao, L. (2013). DC voltage variation based autonomous control of DC microgrids. *IEEE Trans. Power Deliv.* 28, 637–648. doi:10.1109/TPWRD.2013.2241083

Engel, S. P., Stieneker, M., Soltau, N., Rabiee, S., Stagge, H., and Doncker, R. W. D. (2014). Comparison of the modular multilevel DC converter and the dual-active bridge converter for power conversion in HVDC and MVDC grids. *IEEE Trans. Power Electron.* 30, 124–137. doi:10.1109/TPEL.2014.2310656

Falcones, S., Ayyanar, R., and Mao, X. (2013). A DC–DC multiport-converter-based solid-state transformer integrating distributed generation and storage. *IEEE Trans. Power Electron.* 28 (5), 2192–2203. doi:10.1109/TPEL.2012.2215965

Gowaid, I. A., Adam, G. P., Massoud, A. M., Ahmed, S., Holliday, D., and Williams, B. W. (2015). Quasi two-level operation of modular multilevel converter for use in a high-power DC transformer with DC fault isolation capability. *IEEE Trans. Power Electron.* 30 (1), 108–123. doi:10.1109/TPEL.2014.2306453

Jovcic, D., and Ooi, B. T. (2010). Developing DC transmission networks using DC transformers. *IEEE Trans. Power Deliv.* 25 (4), 2535–2543. doi:10.1109/TPWRD.2010.2052074

Kenzelmann, S., Rufer, A., Dujic, D., Canales, F., and Novaes, Y. R. D. (2014). Isolated DC/DC structure based on modular multilevel converter. *IEEE Trans. Power Electron.* 30, 89–98. doi:10.1109/TPEL.2014.2305976

Li, Z., Wang, P., Zhu, H., Chu, Z., and Li, Y. (2012). An improved pulse width modulation method for chopper-cell-based modular multilevel converters. *IEEE Trans. Power Electron.* 27 (8), 3472–3481. doi:10.1109/TPEL.2012.2187800

Lin, W. (2016). DC-DC autotransformer with bidirectional DC fault isolating capability. *IEEE Trans. Power Electron.* 31, 5400–5410. doi:10.1109/TPEL.2015.2491781

Ooi, B., and Wang, X. (1991). Boost-type PWM HVDC transmission system. *IEEE Trans. Power Deliv.* 6 (4), 1557–1563. doi:10.1109/61.97692

Wang, S., Li, Z., Lei, W., Shahidehpour, M., and Li, Z. (2013). New metrics for assessing the reliability and economics of microgrids in distribution system. *IEEE Trans. Power Syst.* 28, 2852–2861. doi:10.1109/TPWRS.2013.2249539

Wang, Y., Qiu, Y., Bian, Q., Guan, Y., and Xu, D. (2018). A single switch quadratic boost high step up DC-DC converter. *IEEE Trans. Industrial Electron.* PP, 4387–4397. doi:10.1109/TIE.2018.2860550

Xiong, L., Liu, L., Liu, X., and Liu, Y. (2021a). Frequency trajectory planning based strategy for improving frequency stability of droop-controlled inverter based standalone power systems. *IEEE J. Emerg. Sel. Top. Circuits Syst.* 11 (1), 176–187. doi:10.1109/JETCAS.2021.3052006

Xiong, L., Liu, X., Zhang, D., and Liu, Y. (2021b). Rapid power compensation-based frequency response strategy for low-inertia power systems. *IEEE J. Emerg. Sel. Top. Power Electron.* 9 (4), 4500–4513. doi:10.1109/JESTPE.2020.3032063

Xiong, L., Liu, X., Zhao, C., and Zhuo, F. (2020). A fast and robust real-time detection algorithm of decaying DC transient and harmonic components in three-phase systems. *IEEE Trans. Power Electron.* 35 (4), 3332–3336. doi:10.1109/TPEL.2019.2940891

Xiong, L., Zhuo, F., Wang, F., Liu, X., Chen, Y., Zhu, M., et al. (2016). Static synchronous generator model: a new perspective to investigate dynamic characteristics and stability issues of grid-tied pwm inverter. *IEEE Trans. Power Electron.* 31 (9), 6264–6280. doi:10.1109/TPEL.2015.2498933

Yao, L., Jing, W. U., Wang, Z., Yan, L. I., and Zongxiang, L. U. (2014). Pattern analysis of future HVDC grid development. *Proc. Csee* 34, 6007–6020. doi:10.13334/j.0258-8013.pcsee.2014.34.001

Zhang, J., Wang, J., and Xu, C. (2018). Active thermal control based anti-condensation strategy in paralleled wind power converters by adjusting reactive circulating current. *IEEE J. Emerg. Sel. Top. Power Electron.* 6, 277–291. doi:10.1109/JESTPE.2017.2741447

Zhao, C., Round, S. D., and Kolar, J. W. (2008). An isolated three-port bidirectional DC-DC converter with decoupled power flow management. *IEEE Trans. Power Electron.* 23, 2443–2453. doi:10.1109/TPEL.2008.2002056

frontiers | Frontiers in Energy Research

TYPE Brief Research Report
PUBLISHED 31 July 2024
DOI 10.3389/fenrg.2024.1443626

OPEN ACCESS

EDITED BY
Liansong Xiong,
Xi'an Jiaotong University, China

REVIEWED BY
Zhenjia Lin,
Hong Kong Polytechnic University, Hong Kong SAR, China
Sheng Cai,
Nanjing University of Science and Technology, China
Fuqi Ma,
Xi'an University of Technology, China
Chaoran Zhuo,
Xi'an University of Technology, China

*CORRESPONDENCE
Juan Wei,
weijuanba@hnu.edu.cn

RECEIVED 04 June 2024
ACCEPTED 10 July 2024
PUBLISHED 31 July 2024

CITATION
Ma K, Chen Y, Wang S, Wang Q, Sun K, Fan W, Nian H and Wei J (2024), Coordinated voltage control for large-scale wind farms with ESS and SVG based on MPC considering wake effect. *Front. Energy Res.* 12:1443626.
doi: 10.3389/fenrg.2024.1443626

Coordinated voltage control for large-scale wind farms with ESS and SVG based on MPC considering wake effect

Kuichao Ma[1,2], Yinpeng Chen[1], Shuaifeng Wang[3], Qiang Wang[4], Kai Sun[4], Wei Fan[1], Heng Nian[2] and Juan Wei[3]*

[1]Huadian Electric Power Research Institute Co., Ltd., Hangzhou, China, [2]College of Electrical Engineering, Zhejiang University, Hangzhou, China, [3]College of Electrical and Information Engineering, Hunan University, Changsha, China, [4]Inner Mongolia Huadian Huitengxile Wind Power Co., Ltd., Hohhot, China

The wake effect reduces the wind speed at downstream wind turbines (WTs), making it necessary for the central controller to collect wind power generation data from each WT. However, wind farms (WFs) face a more complex problem in maintaining the voltage stability at the WT terminal while following the transmission system operator (TSO) instructions due to the information collection as well as the possible data loss during transmission. Therefore, this study proposes a coordinated control method for WTs and multiple power sources based on model predictive control under wake disturbance conditions, aiming to reduce the average voltage deviation in WT terminals and go close to the rated voltage and ensure effective compliance with TSO commands in large-scale WFs. Accordingly, the Jensen wake model was utilized to accurately calculate the available active and reactive power limits for each WT. Energy storage systems and static Var generators were modeled to coordinate and maintain the voltage in all WT terminals within the feasible range, providing peak shaving and valley filling support to reduce wind energy waste and shortfall, thereby enhancing the economic and operational reliability of WF. Further, the effectiveness of the proposed method was validated in MATLAB/Simulink.

KEYWORDS

wind farm, voltage control, energy storage system (ESS), static var generator (SVG), model predictive control (MPC), wake effect

1 Introduction

The development of wind farms (WFs) demonstrates a rapid growth and globalization trend (Huang et al., 2020). The continuous expansion of the installed capacity of WFs, with the consistent emergence of new projects, highlights the significant role of wind energy as a clean source (Lei et al., 2022; Li et al., 2022; Shang et al., 2022) showed the immense power generation potential of wind energy, which makes it a crucial component in future energy transition. Therefore, wind energy system technologies are continuously advancing, with WFs emerging both onshore and offshore, showcasing a trend toward diversification and sustainable development. These advancements provide important technological solutions and pathways for addressing energy security and climate change issues, thus promoting global energy industry transformation (Glasson et al., 2019).

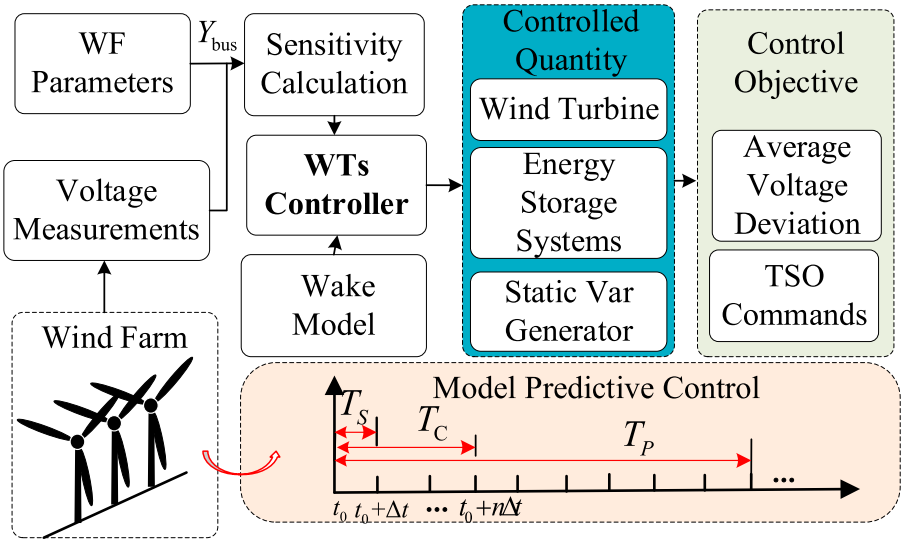

FIGURE 1
Coordinated voltage control framework for WF with ESS and SVG considering wake effect.

Voltage control in WFs is crucial for the stable operation and reliability of power systems (Zhao et al., 2020). Proposed a voltage control strategy utilizing doubly fed induction generators in WF, which adjusted wind turbine (WT) parameters and control strategies to achieve stable voltage control, thereby enhancing the grid integration capability and operational reliability of WF (Li et al., 2018). Addressed voltage control and reactive power optimization issues in large-scale wind power integration scenarios, presenting voltage control strategies for various operating scenarios and achieving coordinated operation between WF and the grid through optimized reactive power allocation, thereby improving grid stability and efficiency (Huang et al., 2019). Proposed a novel coordinated voltage control strategy for WF by integrating wind speed and active power fluctuations, dynamically adjusting voltage control parameters, and optimizing control strategies to effectively reduce voltage fluctuations at grid connection points, thereby enhancing the stability of power systems. Focusing on the impact of reactive power fluctuations on WF voltage stability (Guo et al., 2017), introduced a voltage control strategy based on doubly fed induction generators, optimizing control parameters and strategies to effectively mitigate reactive power fluctuations and improve voltage control performance in WF (Ouyang et al., 2019). Proposed a novel coordinated voltage control strategy for WF using doubly fed induction generators, considering grid constraints, and dynamically adjusting voltage control parameters while accounting for network constraints, thus achieving coordinated operation between WF and the grid as well as enhancing grid stability and reliability. Although various voltage control strategies have been proposed for WFs, to the best of our knowledge, none of them have addressed schemes involving energy storage systems (ESS) (Shang et al., 2022; Liu et al., 2023; Wu et al., 2023) and static Var generators (SVG) for voltage control. However, ESS and SVG, as flexible power electronic devices, can potentially enhance voltage control in WFs.

Wake effects decrease the wind speed behind WTs, thereby reducing their power generation capacity. This affects the overall power output of WFs, especially large-scale WFs, where this impact may be more significant. The wake effect also results in an uneven distribution of wind speed among WTs in a WF, thereby affecting its operational stability. This necessitates the adoption of additional control strategies to adjust the operation of WTs and mitigate the impact of wake effects (Zhang et al., 2016). proposed a voltage control strategy based on DFIGs, considering the wake effect between WTs in WF, aimed at improving the voltage stability and responsiveness of WFs (Feijoo and Villanueva, 2017). Integrated the wake effect between WTs and characteristics of WTs, and proposed a novel voltage control method that achieved stability and power control in WF voltage through dynamic and wake models (Tian et al., 2017). Considered the wake effect and grid constraints, and proposed a comprehensive voltage control strategy that optimized the control parameters of WTs in WFs, aiming to achieve coordinated operation with the grid and voltage stability. Further, the wake also has a broader impact on wind farm power generation under time-varying wind speeds. Sensor measurement biases, including wind speed and wind direction biases, may exist in real systems. Ignoring these biases reduces the overall performance of the wind farm and may even be inferior to the tracking capability of a single radar (Ren et al., 2024). Therefore, under various wind conditions and grid interactions (Xiao et al., 2024), emphasizing the flexibility and variability of energy delivery based on different wind speeds and operating conditions, the overall output of the wind farm and the consistency of the Transmission System Operator's (TSO) directives are needed.

Therefore, considering the wake effect, a coordinated voltage control method is proposed in this study for WTs and multiple power sources in WFs to follow the TSO command, which reduced the wind speed and increased the downstream turbulence, resulting in a loss in power generation. By utilizing model predictive control (MPC) and the Jensen wake model, the proposed method aimed to

reduce voltage deviation at WT terminals and ensure compliance with TSO commands. Moreover, ESS and SVG were employed to maintain stable voltage, optimize power utilization, and enhance operational reliability. The main contributions of this study are summarized below:

1) A coordinated control method for WTs and multiple power sources, based on MPC and tailored for wake disturbance conditions, was proposed to reduce the average voltage deviation at WT terminals in large-scale WFs and ensure compliance with TSO commands. The control problem can be formulated as a quadratic programming problem based on MPC and sensitivity, which can be real-time optimization.
2) The Jensen wake model was employed to calculate the available active and reactive power limits for all WTs, enabling them to follow TSO commands without the need for local wind power sensors. Compared to existing method by measuring wind power the by local sensors, this approach can help in mitigating the adverse effects of inaccurate power data collection and data loss during information transmission.
3) Considering the impact of wake-induced losses on downstream WT electricity generation, WFs face challenges in maintaining stable turbine-end voltages while adhering to TSO commands. The ESS and SVG were modeled to coordinate and maintain voltage levels within feasible ranges for all WTs. Compared to transitional WFs without ESS and SVG, the proposed method can facilitate peak shaving and valley filling to reduce wind energy waste and shortfall, and thus enhancing the economic viability and reliability of WF.

2 Voltage control architecture for wind farm

Figure 1 displays the control framework for WF with ESS and SVG considering the significant wake effect. The core of the control strategy employs the Jensen wake model in conjunction with MPC. The Jensen model predicts how downstream turbines are affected by the wake of upstream turbines, which includes both reductions in wind speed and increases in turbulence. The MPC method utilizes this predictive capability to dynamically adjust the active and reactive power outputs of individual WTs. First, the WT controller collected voltage information from all nodes and obtained the nodal admittance matrix for calculating the voltage sensitivity matrix. Based on the Jensen wake model and MPC method, it controlled the active and reactive power outputs of WTs. This ensured optimal performance even under varying wind speed and direction conditions, thereby maximizing the energy yield of WF. Simultaneously, it coordinated ESS and SVG to minimize the average voltage deviation. By continuously optimizing these outputs based on real-time and predicted wind conditions, the system ensures that the available wind power of each WTG is captured in the face of changing wind speeds and directions. This strategic approach not only enhanced the operational stability, but also ensured adherence to the operational guidelines set forth by the TSO.

3 Wind farm model with ESS and SVG

3.1 Wake effect model

Traditional voltage control methods require the collection of wind speeds from all WTs in a WF to calculate the available wind power for each WT. However, data loss and errors frequently occur in large-scale WFs during data collection and transmission. Additionally, the wind speed across the WF is not uniform owing to the influence of wake effects. The wake effect, observed in fluid dynamics and aerodynamics, occurs when an object moving through a fluid leaves behind a disturbance characterized by altered flow patterns, pressure changes, and turbulence. This phenomenon impacts the efficiency and performance of WT systems. Therefore, this study proposed the use of wake models to calculate the power output of all WTs. In this approach, only the wind speed and direction across the entire WF need to be measured, thus eliminating the need for sensors to measure local wind speeds and transmitting local power availability information to a central controller.

The Jensen wake model is a simplified mathematical tool used to predict the wake effects of WTs in a WF. Its advantages include its simplicity and computational efficiency, making it suitable for large-scale simulations.

$$[X, Y] = [x, y]\begin{bmatrix} \cos\theta & \sin\theta \\ -\sin\theta & \cos\theta \end{bmatrix} \tag{1}$$

Equation 1 describes how to decompose a given wind direction into two predefined directions in a WF, where (X) and (Y) represent the two predefined directions in the WF, differing by 90 degrees. This decomposition aims to better understand and simulate the variations in wind speed in the WF.

$$\alpha = \arccos\left(\frac{R_s^2 + D_{ij}^2 - R_0^2}{2R_s D_{ij}}\right) \tag{2}$$

$$\beta = \arccos\left(\frac{R_0^2 + D_{ij}^2 - R_s^2}{2R_s D_{ij}}\right) \tag{3}$$

$$A_s^{ij} = \frac{1}{2}R_s^2(2\alpha - \sin(2\alpha)) + \frac{1}{2}R_0^2(2\beta - \sin(2\beta)) \tag{4}$$

Equations 2–4 can be used to calculate the area affected by wake on WT j due to WT i. Where R_s, D_{ij} and R_0 represent the radius of expansion of the wake, distance between upstream and downstream turbines, rotor radius, respectively. A_s^{ij} represents the area affected by wake on WT j due to WT i.

$$v_{ij} = v_i\left[1 - \sqrt{1 - C_i}\left(1 + \frac{kD_{ij}}{R}\right)^{-2}\frac{A_s^{ij}}{A_0}\right] \tag{5}$$

Equation 5 describes the influence of WT i on the wind speed experienced by WT j. Where C_i, v_i, v_{ij}, k, A_0 and R represent the thrust coefficient, wind speed, the wind speed affected by wake on WT j due to WT i, wake expansion coefficient, swept area of the WT and rotor radius respectively. A_s^{ij} represents the area affected by wake on WT j due to WT i.

$$v_j = \sqrt{v_0^2 - \sum_{j \in I_i}\left(v_i^2 - v_{ij}^2\right)} \tag{6}$$

The issue of mutual influence among WTs is discussed in Eq. 6. Typically, downstream WTs are affected by multiple upstream WTs. To estimate the inflow wind speed of one of

these WTs, denoted as (WT) [where (n >2)], the wake superposition model was proposed. In this model, i represents the set of WTs that produce wake effects on a specific WT, while v denotes the free stream wind speed. The model considered the combined impact of multiple upstream WTs on the wind conditions experienced by downstream WTs, which is crucial for optimizing the layout and efficiency of WFs.

3.2 Voltage sensitivity analysis

Sensitivity coefficients are used to estimate the changes in voltage and phase angles in the dynamic process of WF control systems. To improve the computational efficiency, an analytical computation method was developed for calculating the sensitivity coefficients. The link between bus voltages and power injections was established based on fundamental physical principles and network topology of the power system (Christakou et al., 2013). This connection enabled us to infer power injections in the grid by monitoring changes in the bus voltage, allowing dynamic adjustments and optimizations in the WF control system. Equations 7-8 are the voltage sensitivity calculation equations.

$$\frac{\partial \underline{S}_i}{\partial P_l} = \frac{\partial \underline{V}_i}{\partial P_l} \sum_{j \in \mathcal{S} \cup \mathcal{N}} \bar{Y}_{\mathrm{bus},ij} \bar{V}_j + \underline{V}_i \sum_{j \in \mathcal{N}} \bar{Y}_{\mathrm{bus},ij} \frac{\partial \bar{V}_j}{\partial P_l} = \begin{cases} 1, & \text{for } i = l \\ 0, & \text{for } i \neq l \end{cases} \tag{7}$$

$$\frac{\partial \underline{S}_i}{\partial Q_l} = \frac{\partial \underline{V}_i}{\partial Q_l} \sum_{j \in \mathcal{S} \cup \mathcal{N}} \bar{Y}_{\mathrm{bus},ij} \bar{V}_j + \underline{V}_i \sum_{j \in \mathcal{N}} \bar{Y}_{\mathrm{bus},ij} \frac{\partial \bar{V}_j}{\partial Q_l} = \begin{cases} -j1, & \text{for } i = l \\ 0, & \text{for } i \neq l \end{cases} \tag{8}$$

The voltage magnitude and phase angle sensitivity can be computed by analyzing the changes in these parameters relative to variations in system conditions or control inputs. The control inputs are only relative to the active and reactive outputs of power components. Equations 9-10 represent the voltage magnitude and phase angle sensitivity can be computed by analyzing the changes in these parameters relative to variations in system conditions or control inputs.

$$\frac{\partial V_i}{\partial P_l} = \frac{1}{\partial V_i} \mathrm{Re}\left(\underline{V}_i \frac{\bar{V}_i}{\partial P_l} \right), \quad \frac{\partial \theta_i}{\partial P_l} = \frac{1}{\partial V_i^2} \mathrm{Im}\left(\underline{V}_i \frac{\bar{V}_i}{\partial P_l} \right) \tag{9}$$

$$\frac{\partial V_i}{\partial Q_l} = \frac{1}{\partial V_i} \mathrm{Re}\left(\underline{V}_i \frac{\bar{V}_i}{\partial Q_l} \right), \quad \frac{\partial \theta_i}{\partial Q_l} = \frac{1}{\partial V_i^2} \mathrm{Im}\left(\underline{V}_i \frac{\bar{V}_i}{\partial Q_l} \right) \tag{10}$$

where $\frac{\partial V_i}{\partial P_l}$ is the sensitivity of voltage magnitude of bus i to the active power injected at bus l, $\frac{\partial \theta_i}{\partial P_l}$ is the sensitivity of voltage phase angle of bus i to the active power injected at bus l, $\frac{\partial V_i}{\partial Q_l}$ is the sensitivity of voltage magnitude of bus i to the reactive power injected at bus l, and $\frac{\partial \theta_i}{\partial Q_l}$ is the sensitivity of voltage phase angle of bus i to the reactive power injected at bus l. $\bar{V}_i$ is the voltage at bus i, $\underline{V}_i$ is the conjugation of voltage at bus i, $\underline{S}_i$ is the conjugation of power at bus i.

3.3 WT and SVG model

In the standard double-closed loop control structure of WTs, owing to the rapid dynamic behavior of the inner current loop, it can be approximated as a first-order lag function. Therefore, the incremental state-space model of WTs can be obtained by considering communication delay. Equations 11-12 represent the transfer function of WTs with a first-order lag function.

$$\Delta P_{\mathrm{wt}} = \frac{1}{1 + sT_{\mathrm{P}}} \Delta P_{\mathrm{wt}}^{\mathrm{ref}} \tag{11}$$

$$\Delta Q_{\mathrm{wt}} = \frac{1}{1 + sT_{\mathrm{Q}}} \Delta Q_{\mathrm{wt}}^{\mathrm{ref}} \tag{12}$$

where $\Delta P_{\mathrm{wt}}^{\mathrm{ref}}$ and $\Delta Q_{\mathrm{wt}}^{\mathrm{ref}}$ denote the incrementations in the reference of active and reactive power outputs of WT, respectively; ΔP_{wt} and ΔQ_{wt} are the incrementations in the active and reactive power outputs of WT, respectively; and T_{P} and T_{Q} are the active and reactive time constants, respectively.

Then, we obtained Equations 11-12 represent the incremental state-space model of WTs with a first-order lag function.

$$\Delta \dot{P}_{\mathrm{wt}} = -\frac{1}{T_{\mathrm{P}}} \Delta P_{\mathrm{wt}} + \frac{1}{T_{\mathrm{P}}} \Delta P_{\mathrm{wt}}^{\mathrm{ref}} \tag{13}$$

$$\Delta \dot{Q}_{\mathrm{wt}} = -\frac{1}{T_{\mathrm{Q}}} \Delta Q_{\mathrm{wt}} + \frac{1}{T_{\mathrm{Q}}} \Delta Q_{\mathrm{wt}}^{\mathrm{ref}} \tag{14}$$

where $\Delta \dot{P}_{\mathrm{wt}}$ and $\Delta \dot{Q}_{\mathrm{wt}}$ are the derivative of incrementations in the active and reactive power outputs of WT, respectively.

We can also obtain the incremental state-space model of the SVG with a first-order lag function. Equations 11-12 represent the transfer function of SVG with a first-order lag function.

$$\Delta Q_{\mathrm{svg}} = \frac{1}{1 + sT_{\mathrm{svg}}} \Delta Q_{\mathrm{svg}}^{\mathrm{ref}} \tag{15}$$

where $\Delta Q_{\mathrm{svg}}^{\mathrm{ref}}$, ΔQ_{svg}, and T_{svg} denote the incrementation in the reference of reactive power output of SVG, incrementation in the reactive power output of SVG, and reactive time constant, respectively.

Then, we obtain Equations 11-12 represent the incremental state-space model of SVG with a first-order lag function.

$$\Delta \dot{Q}_{\mathrm{svg}} = -\frac{1}{T_{\mathrm{svg}}} \Delta Q_{\mathrm{svg}} + \frac{1}{T_{\mathrm{svg}}} \Delta Q_{\mathrm{svg}}^{\mathrm{ref}} \tag{16}$$

where $\Delta \dot{Q}_{\mathrm{svg}}$ is the derivative of incrementation in the reactive power output of SVG.

3.4 ESS model

ESS plays a crucial role in WFs. Through energy storage systems, WFs can effectively smooth out wind fluctuations, provide frequency regulation services, respond to sudden load changes, and quickly meet grid demands, thereby enhancing grid stability and reliability. This increase in flexibility and controllability helps in optimizing the utilization of renewable energy sources and promotes the development of energy systems toward greater sustainability.

Constraints (17)–(21) represent the operating behavior of an ESS. Constraints (17) is the charging/discharging state constraint of ESS, which ensures that the ESS can only work at either charging or discharging condition. Constraints (18) and (19) confine the maximum power during charging or discharging. Constraints Eqs 20, 21 represents state-of-charge (SOC) operation of ESS.

$$u^c + u^s \leq 1 \tag{17}$$

$$0 \leq x^c \leq P^{\max} u^c \tag{18}$$

$$0 \leq x^s \leq P^{\max} u^s \tag{19}$$

$$SOC_t \cdot \Delta t = SOC_{t-1} \cdot \Delta t + \eta_c x^c - \eta_s x^s \tag{20}$$

$$\varepsilon \leq \mathrm{SOC} \leq 1 \tag{21}$$

where x^c and x^s represent the charge and discharge power of ESS at time t, respectively; u^c and u^s are binary variables defining the charging/discharging status of ESS (for example, if $u_t^c = 1$, the ESS is charging from the grid); η_c and η_s are the efficiency coefficients of ESS during charging and discharging, respectively, which were both set to 0.9; and ε is the minimum stored energy of ESS, which was set to 0.1.

The SOC can be defined as follows,

$$SOC = E_t / E^{cap} \tag{22}$$

where E_t represents the stored energy of ESS at time t and E^{cap} is the maximum capacity of ESS.

4 Coordinated voltage control optimization problem

4.1 Cost function

MPC generates control actions by predicting future system behavior over a specified prediction horizon. This predictive capability allows MPC to optimize control actions in real-time, achieving superior performance compared to traditional controllers. After the quadratic key between power and voltage based sensitivity is linearized, the wind farm voltage control optimization problem can be solved based on quadratic programming. A coordinated control method for WTs and multiple power sources based on MPC under wake disturbance conditions was proposed to reduce the average voltage deviation at WT terminals and ensure effective compliance with TSO commands. It improved the stability and reliability of WFs, optimized the wind energy utilization efficiency, and promoted the application and development of intelligent control technologies. Equation 23 represents the voltage sensitivity coefficients with respect to power.

$$\begin{bmatrix} \Delta V \\ \Delta \theta \end{bmatrix} = \begin{bmatrix} \frac{\partial V}{\partial P} & \frac{\partial V}{\partial Q} \\ \frac{\partial \theta}{\partial P} & \frac{\partial \theta}{\partial Q} \end{bmatrix} \begin{bmatrix} \Delta P \\ \Delta Q \end{bmatrix} \tag{23}$$

where ΔV, $\Delta\theta$, ΔP, and ΔQ are the increments in voltage amplitude, voltage phase angle, active power, and reactive power, respectively. $\frac{\partial \theta}{\partial P}$, $\frac{\partial V}{\partial P}$, $\frac{\partial \theta}{\partial Q}$, and $\frac{\partial V}{\partial Q}$ are the voltage sensitivity coefficients with respect to power, which were used to linearize the WF model.

Accordingly, the continuous state-space model of WF can be discretized as,

$$\Delta \dot{x} = \mathbf{A}\Delta x + \mathbf{B}\Delta u \tag{24}$$

where

$$\begin{aligned} \Delta x &= \left[\Delta P_{ess}, \Delta P_{wt,1}, \ldots, \Delta P_{wt,|\mathcal{N}_T|}, \Delta Q_{svg}, \Delta Q_{wt,1}, \ldots, \Delta Q_{wt,|\mathcal{N}_T|}\right]^T, \\ \Delta u &= \left[\Delta P_{ess}^{ref}, \Delta P_{wt,1}^{ref}, \ldots, \Delta P_{wt,|\mathcal{N}_T|}^{ref}, \Delta Q_{svg}^{ref}, \Delta Q_{wt,1}^{ref}, \ldots, \Delta Q_{wt,|\mathcal{N}_T|}^{ref}\right]^T, \\ \mathbf{A} &= \mathrm{diag}\left[-1/T_{ess}^{P}, -1/T_{wt,1}^{P}, \ldots, -1/T_{wt,|\mathcal{N}_T|}^{P}, -1/T_{svg}^{Q}, -1/T_{wt,1}^{Q}, \ldots, -1/T_{wt,|\mathcal{N}_T|}^{Q}\right], \\ \mathbf{B} &= \mathrm{diag}\left[1/T_{ess}^{P}, 1/T_{wt,1}^{P}, \ldots, 1/T_{wt,|\mathcal{N}_T|}^{P}, 1/T_{svg}^{Q}, 1/T_{wt,1}^{Q}, \ldots, 1/T_{wt,|\mathcal{N}_T|}^{Q}\right]. \end{aligned} \tag{25}$$

then, the discrete state-space model can be expressed as,

$$\Delta x(k+1) = \mathbf{A}_d \Delta x(k) + \mathbf{B}_d \Delta u(k) \tag{26}$$

the objective function to minimize the average voltage deviation in WT terminal can be expressed as,

$$\min \sum_{i=1}^{|\mathcal{N}_T|} \|\Delta V_{wt}\|^2 \tag{27}$$

the terminal voltage of each WT, ΔV_{wt}, can be calculated based on sensitivity as,

$$\Delta V_{wt}(k) = V_{wt}^0 + \frac{\partial V_{wt}}{\partial Q_{wt}} \Delta Q(k) - V_{wt}^{rated} \tag{28}$$

4.2 Constraint

The voltage constraints at WT terminals, as well as constraints on the active and reactive power outputs of WTs are expressed below,

$$\underline{V}_i \le V_i \le \bar{V}_i \tag{29}$$

$$0 \le P_{W_i} \le \bar{P}_{W_i} \tag{30}$$

$$\underline{Q}_{W_i} \le Q_{W_i} \le \bar{Q}_{W_i} \tag{31}$$

Equation 29 represents the voltage constraints, ensuring that the voltage at WT terminals remains within a feasible range and does not exceed the allowable upper and lower limits. Eq. 30 denotes the active power constraints, which limit the output of active power from WTs to ensure that it does not exceed the available maximum wind power. Eq. 31 signifies the reactive power constraints, restricting the output of reactive power from WTs to ensure that the power output does not surpass the capacity of WTs.

WFs dynamically adjust the power generation of WTs to ensure that their output satisfies TSO instructions. Equation 32 represent that WFs dynamically adjust the power generation of WTs to ensure that their output satisfies TSO instructions.

$$\sum_{i=1}^{N} P_i^{ref} = P_{WF}^{ref} \tag{32}$$

In summary, the aforementioned optimal control problem based on MPC can be formulated as a quadratic programming problem, which is well-suited for real-time implementation. MPC considers predictive models of the system dynamics and optimizes control actions over a finite time horizon, balancing performance objectives and constraints. Given the advancements in computational techniques, existing solvers can efficiently solve these quadratic programming problems within milliseconds. This capability ensures rapid decision-making and enables effective mitigation of voltage control issues in large-scale wind power systems.

5 Casy study

A WF model, comprising 32 5 MW DFIG-based WTs, was created in MATLAB/Simulink to validate the proposed control strategy. Each WT was linked to the feeder via a 0.9/33 kV transformer. Four feeders were connected to the medium voltage (MV) bus, with eight WTs in each feeder positioned every 4 km. All WTs were aggregated at the point of connection (POC) and transmitted to external grids through the 155/

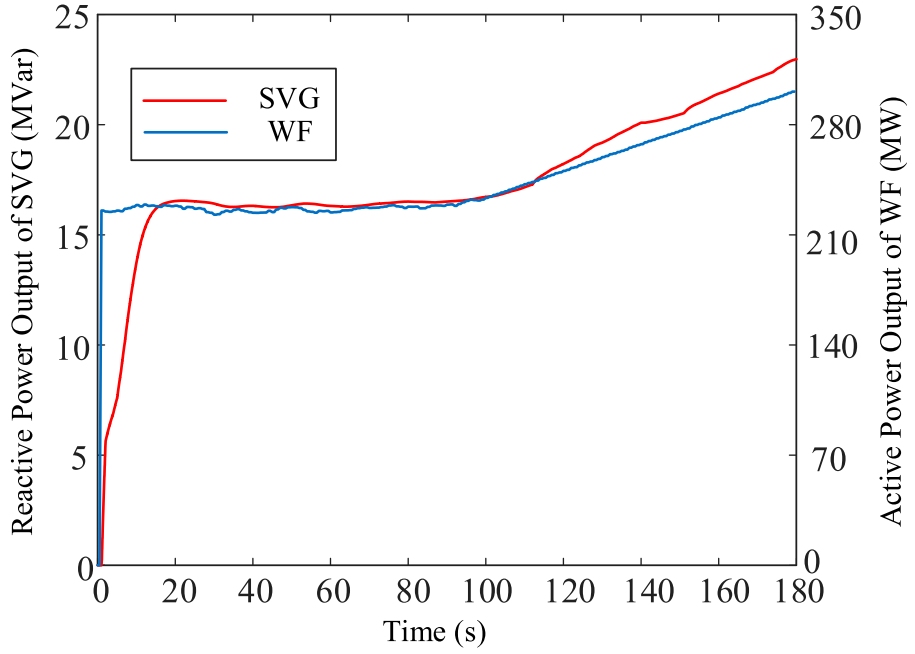

FIGURE 2
Power output of SVG and WF.

380 kV main transformer. The WF had a rated power of 160 MW, with individual WTs rated at 5 MW each. For the 33 kV cable, the resistance, inductance, and capacitance were 0.108 Ω/km, 0.3915 mH/km, and 0.13 μF/km, respectively. Similarly, for the 155 kV cable, the resistance, inductance, and capacitance were 0.158 Ω/km, 0.47 mH/km, and 0.13 μF/km, respectively. The rated capacity, resistance, and reactance of the 0.9/33 kV transformer were 6.25 MVA, 0.008 p.u., and 0.06 p. u. respectively; those of the 33/155 kV transformer were 100 MVA, 0.01 p. u., and 0.06 p. u. respectively; while those of the 155/380 kV transformer were 500 MVA, 0.01 p. u., and 0.06 p. u. respectively. The thrust coefficient of each WT C_i, wake expansion coefficient k and rotor radius R are set as 0.8, 0.04, and 63 m, respectively. The local WT terminal voltages as well as active and reactive power output from WTs, active power output from ESS, and reactive power output from SVG to the central controller were recorded. The central controller measured the wind speed and direction in the WF; it then calculated the wind power for each WT and voltage sensitivity matrix of the system, and determined the optimal output power for both WTs and multiple power sources. The configured ESS capacity and SVG capacity were both observed to be 30% of the wind farm capacity.

Figure 2 displays the reactive output power of SVG and active output power of WF. The output energy of the WF was 400 MW when all turbines operated at maximum capacity. However, factors such as the wake effect and fluctuating wind speeds inevitably reduced the WF output energy below the 400 MW threshold. During the initial period from 1 to 100 s, the WF output power was stabilized at approximately 230 MW, while the SVG contributed to around 16 MVar of reactive power. Subsequently, between 100 and 180 s, the available power output of WF gradually increased. Consequently, the TSO adjusted the active power command upward in tandem with this increase. Therefore, the WF output power gradually increased. To mitigate the impact of rising active power on the WT terminal voltage, the SVG incrementally ramped up its reactive power output. This adjustment ensured a smoother transition in the system's overall operation.

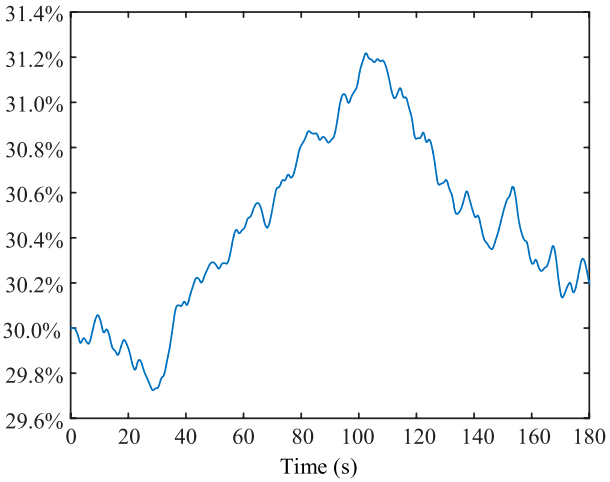

FIGURE 3
SOC of ESS.

Figure 3 illustrates the SOC of ESS. The role of the energy storage element involved peak shaving. When the available power of the WF was larger than the TSO instruction, the energy storage element absorbed energy. Meanwhile, when the available power of the WF was smaller than the TSO instruction, the energy storage element released energy. During 1–100 s, the charging state of the storage element exhibited an increasing trend, and during 100–180 s, it demonstrated a decreasing trend. This

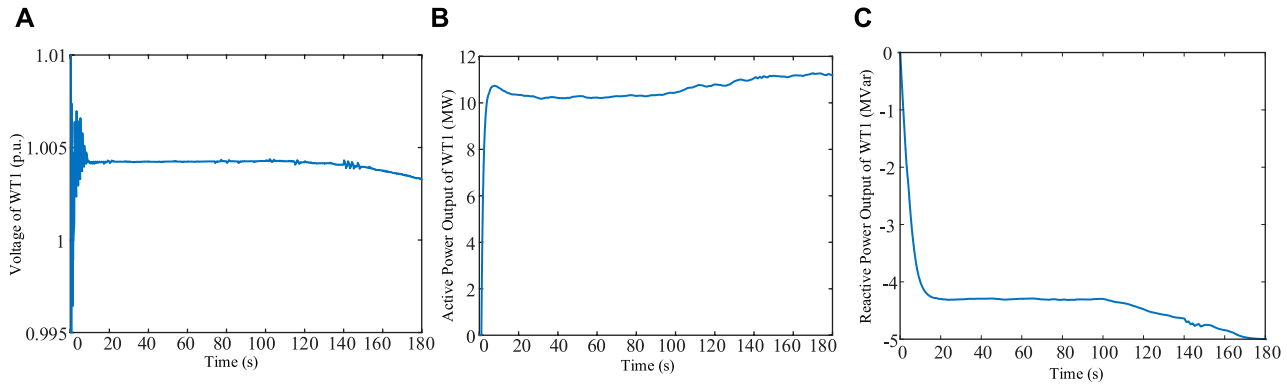

FIGURE 4
(A) Voltage of WT1. **(B)** Active power output of WT1. **(C)** Reactive power output of WT1.

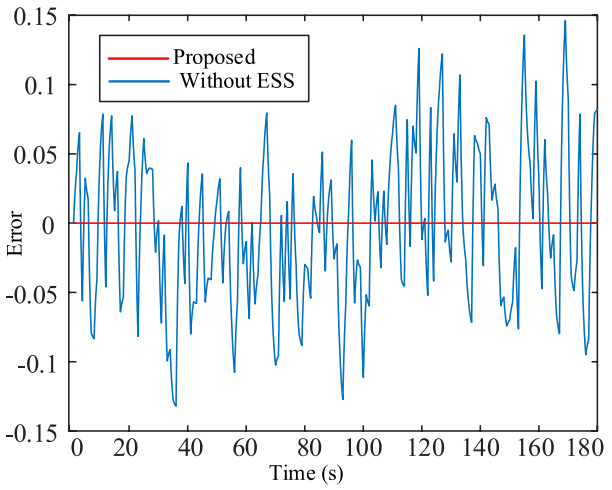

FIGURE 5
Comparison of the errors of the two methods for following the TSO command.

dynamic behavior highlights the role of the ESS in maintaining grid stability by balancing fluctuations during renewable energy generation against demand.

Figure 4 illustrates the terminal voltage and active and reactive power output of WT1. The purpose of controlling the power output from the WT is to maintain the turbine terminal voltage and to track the TSO command. Therefore, the main role of the active power output from the turbine is to track the TSO command, and the main role of the reactive power output is to regulate the voltage fluctuation due to the fluctuation of the active power. During the period 0–100 s, the voltage at terminal 1 of the WT is basically at a constant value, and the active and reactive power output from the turbine fluctuates less. During the period 100–180 s, the active power output from the WT rises and therefore the reactive power absorbed by the WT rises.

Figure 5 illustrates the comparison of the errors of the two methods for following the TSO command. At high wind speeds, the WTs will deliver as much power as possible in order to avoid wasting energy. Meanwhile, at low wind speeds, the available power of the WTs cannot meet the power demanded by the TSO command. Therefore, WFs without ESS have errors in the tracking effect of the TSO command.

6 Conclusion

In WF operations, the wake effect not only reduces the electricity generation efficiency of downstream WTs, but also leads to an overall loss in power generation. Additionally, the inaccuracies in wind power information and data loss during transmission increase the uncertainty in WF control. With the objective to address these challenges, this study proposed a scheduling method based on MPC to optimize the stability of WT terminal voltage and ensure that WFs can effectively respond to system TSO commands. By accurately calculating the power boundaries of turbines using the Jensen wake model and introducing coordinated control through ESS and SVGs, the stability and reliability of WFs could be improved. This research outcome provides profound insights for addressing practical issues in WF operations and lays a crucial foundation for the intelligent operation of future WFs.

Data availability statement

The original contributions presented in the study are included in the article/Supplementary Material, further inquiries can be directed to the corresponding author.

Author contributions

KM: Conceptualization, Data curation, Formal Analysis, Funding acquisition, Investigation, Methodology, Project administration, Resources, Software, Supervision, Validation, Visualization, Writing–original draft, Writing–review and editing. YC: Formal Analysis, Project administration, Validation, Writing–review and editing. SW: Data curation, Formal Analysis, Methodology, Writing–original draft, Writing–review and editing.

QW: Writing–original draft, Resources, Validation, Visualization. KS: Data curation, Methodology, Project administration, Validation, Writing–original draft. WF: Data curation, Methodology, Project administration, Validation, Writing–original draft. HN: Data curation, Formal Analysis, Methodology, Writing–original draft. JW: Data curation, Formal Analysis, Methodology, Project administration, Writing–original draft, Writing–review and editing.

Funding

The author(s) declare that financial support was received for the research, authorship, and/or publication of this article. This work received the funding from the Huadian Corporation Ltd. (No. CHDKJ-21-01-98) and the National Natural Science Foundation of China (52207050).

Conflict of interest

Authors KM, YC, and WF were employed by Huadian Electric Power Research Institute Co., Ltd. Authors QW and KS were employed by Inner Mongolia Huadian Huitengxile Wind Power Co., Ltd.

The remaining authors declare that the research was conducted in the absence of any commercial or financial relationships that could be construed as a potential conflict of interest.

The authors declare that this study received funding from Huadian Corporation Ltd. The funder had the following involvement in the study: Conceptualization, Data curation, Formal Analysis, Funding acquisition, Investigation, Methodology, Project administration, Resources, Software, Supervision, Validation,Visualization, Writing–original draft, Writing–review and editing.

Publisher's note

References

Christakou, K., LeBoudec, J. -Y., Paolone, M., and Tomozei, D. -C. (2013). Efficient computation of sensitivity coefficients of node voltages and line currents in unbalanced radial electrical distribution networks. *IEEE Trans. Smart Grid* 4 (2), 741–750. doi:10.1109/TSG.2012.2221751

Feijoo, A., and Villanueva, D. (2017). Contributions to wind farm power estimation considering wind direction-dependent wake effects. *Wind Energy* 20 (2), 221–231. doi:10.1002/we.2002

Glasson, J., Durning, B., Welch, K., and Olorundami, T. (2019). The local socio-economic impacts of offshore wind farms. *Environ. Impact Assess. Rev.* 192, 106783. doi:10.1016/j.eiar.2022.106783

Guo, Y., Gao, H., Wu, Q., Zhao, H., Østergaard, J., and Shahidehpour, M. (2017). Enhanced voltage control of VSC-HVDC-connected offshore wind farms based on model predictive control. *IEEE Trans. Sustain. Energy* 9 (1), 474–487. doi:10.1109/TSTE.2017.2743005

Huang, S., Wu, Q., Guo, Y., Chen, X., Zhou, B., and Li, C. (2019). Distributed voltage control based on ADMM for large-scale wind farm cluster connected to VSC-HVDC. *IEEE Trans. Sustain. Energy* 11 (2), 584–594. doi:10.1109/TSTE.2019.2898102

Huang, S., Wu, Q., Guo, Y., and Rong, F. (2020). Hierarchical active power control of DFIG-based wind farm with distributed energy storage systems based on ADMM. *IEEE Trans. Sustain. Energy* 11 (3), 1528–1538. doi:10.1109/TSTE.2019.2929820

Lei, S., Hua, Z., Liu, C., and Dong, X. (2022). Amplitude-phase-locked-loop-based power injection strategy for wind power generation under three-phase grid fault. *IEEE Trans. Energy Conv.* 37 (4), 2952–2961. doi:10.1109/TEC.2022.3207285

Li, M., Yang, M., Yu, Y., and Lee, W. -J. (2022). A wind speed correction method based on modified hidden markov model for enhancing wind power forecast. *IEEE Trans. Ind. Appl.* 58 (1), 656–666. doi:10.1109/TIA.2021.3127145

Li, Y., Xu, Z., Zhang, J., and Meng, K. (2018). Variable droop voltage control for wind farm. *IEEE Trans. Sustain. Energy* 9 (1), 491–493. doi:10.1109/TSTE.2017.2726355

Liu, K., Sheng, W., Li, Z., Liu, F., Liu, Q., Huang, Y., et al. (2023). An energy optimal schedule method for distribution network considering the access of distributed generation and energy storage. *IET Generation, Transm. Distribution* 17 (13), 2996–3015. doi:10.1049/gtd2.12855

Ouyang, J., Tang, T., Yao, J., and Li, M. (2019). Active voltage control for DFIG-based wind farm integrated power system by coordinating active and reactive powers under wind speed variations. *IEEE Trans. Energy Conv.* 34 (3), 1504–1511. doi:10.1109/TEC.2019.2905673

Ren, B., Jia, T., Liu, H., Wang, Y., and Yan, J. (2024). Efficient estimation for sensor biases and target states in the presence of sensor position errors. *IEEE Sensors J.* 24 (10), 16551–16562. doi:10.1109/JSEN.2024.3384810

Shang, L., Dong, X., Liu, C., and Gong, Z. (2022). Fast grid frequency and voltage control of battery energy storage system based on the amplitude-phase-locked-loop. *IEEE Trans. Smart Grid* 13 (2), 941–953. doi:10.1109/TSG.2021.3133580

Tian, J., Zhou, D., Su, C., Chen, Z., and Blaabjerg, F. (2017). Reactive power dispatch method in wind farms to improve the lifetime of power converter considering wake effect. *IEEE Trans. Sustain. Energy* 8 (2), 477–487. doi:10.1109/TSTE.2016.2607146

Wu, S., Ma, H., Alharbi, A. M., Wang, B., Xiong, L., Zhu, S., et al. (2023). Integrated energy system based on isolation forest and dynamic orbit multivariate load forecasting. *Sustainability* 15 (20), 15029. doi:10.3390/su152015029

Xiao, D., Lin, Z., Chen, H., Hua, W., and Yan, J. (2024). Windfall profit-aware stochastic scheduling strategy for industrial virtual power plant with integrated risk-seeking/averse preferences. *Appl. Energy* 357, 122460. doi:10.1016/j.apenergy.2023.122460

Zhang, B., Hou, P., Hu, W., Soltani, M., Chen, C., and Chen, Z. (2016). A reactive power dispatch strategy with loss minimization for a DFIG-based wind farm. *IEEE Trans. Sustain. Energy* 7 (3), 914–923. doi:10.1109/TSTE.2015.2509647

Zhao, H., Wu, Q., Guo, Q., Sun, H., Huang, S., and Xue, Y. (2020). Coordinated voltage control of a wind farm based on model predictive control. *IEEE Trans. Sustain. Energy* 7 (4), 1440–1451. doi:10.1109/TSTE.2016.2555398

frontiers | Frontiers in Energy Research

TYPE Original Research
PUBLISHED 01 August 2024
DOI 10.3389/fenrg.2024.1429295

OPEN ACCESS

EDITED BY
Yonghui Liu,
Hong Kong Polytechnic University, Hong Kong SAR, China

REVIEWED BY
Xiaokang Liu,
Polytechnic University of Milan, Italy
Hong Cencen,
Nanjing Institute of Technology (NJIT), China
Huimin Wang,
Zhejiang Sci-Tech University, China
Tong Wang,
Hubei University of Economics, China

*CORRESPONDENCE
Qun Li,
qun_li@sina.com
Weijia Tang,
tang_jsepc@126.com

RECEIVED 07 May 2024
ACCEPTED 08 July 2024
PUBLISHED 01 August 2024

CITATION
Li Q, Li Q, Tang W and Wang C (2024), Voltage response characterization of grid-forming wind power systems.
Front. Energy Res. 12:1429295.
doi: 10.3389/fenrg.2024.1429295

Voltage response characterization of grid-forming wind power systems

Qun Li*, Qiang Li, Weijia Tang* and Chenggen Wang

State Grid Jiangsu Electric Power Co., Ltd., Research Institute, Nanjing, China

The widespread integration of wind turbines poses voltage stability challenges to power systems. To enhance the ability of wind power systems to actively support grid voltage, grid-forming control techniques are increasingly being employed. However, current research primarily focuses on voltage stability challenges at the point of common coupling in wind power systems, lacking thorough investigation into system voltage response characterization. This paper establishes the voltage response model of a grid-forming wind power system. Based on this model, mathematical derivation and theoretical analysis are conducted, and the effect factors of the voltage at the point of common coupling are investigated. Furthermore, a voltage stabilization method is explored by adjusting the above effect factors. Finally, based on the MATLAB/Simulink platform, the simulation verification of each effect factor is carried out. The results indicate that voltage response characterization obtained by the theoretical analysis and simulation is similar and that the proposed method is valid.

KEYWORDS

grid-forming, wind power systems, voltage response, droop control, voltage stability

1 Introduction

Constructing a novel power system characterized by a significant share of renewable energy sources and a high proportion of converters (Kang and Yao, 2017) represents a pivotal approach toward achieving the objectives of carbon peaking and carbon neutrality (Yang et al., 2023). With wind power (Ouyang et al., 2019), photovoltaic power (Kim et al., 2023), and other new energy power sources connected to the grid on a large scale, the traditional power system dominated by synchronous machines is undergoing a transformation. The extensive access of new energy power sources induces the characteristics of low inertia and weak damping for the new power system (Leon et al., 2024), which is difficult for actively supporting the safe and stable operation of the power system (Shang et al., 2022).

To provide the converter with the ability to actively support the grid frequency and voltage and increase the immunity of the grid during load disturbances, grid-forming (GFM) control techniques are widely used (Rosso et al., 2021; Wu and Wang, 2021). Xiong et al. (2021) proposed a rapid power compensation-based frequency response strategy, which can maximize the suppression of frequency deviation and the rate of change of frequency (ROCOF) simultaneously, yet avoiding the limitations due to unknown grid parameters. Xi et al. (2021) presented a decoupling control scheme to optimize the frequency response characteristics of virtual synchronous generator (VSG) (Fang et al., 2018) control using wind power plants as a research object. Shao et al. (2019) proposed

a double-fed induction generator model based on equivalent electromotive force and equivalent power angle and evaluated the inertial response characteristics of the system. Verma et al. (2023) proposed a self-regulating configuration strategy and analyzed the frequency characteristics of the system. However, the existing papers related to the GFM system are more focused on the problem of frequency support (Xiong et al., 2016; Xiong et al., 2020; Li et al., 2022), and there is less research on the voltage support problem of the GFM wind power system, but with the change in the load side of the wind power system, the voltage support problem is also subject to severe challenges. Therefore, it is necessary to study the voltage response characteristics of GFM wind power systems.

In order to analyze the problem of voltage support in grid-forming wind power systems (GFM WPSs), Pal et al. (2023) proposed a new current saturation strategy for grid-forming inverters, which provides a solution to the low-voltage ride-through problem of grid-forming inverter systems. Liu and Wang (2021) proposed a voltage–magnitude control scheme and analyzed the system transient stability. Luo et al. (2023) proposed an adaptive-output–voltage-regulation-based solution to mitigate the dc-link undervoltage problem and confirmed it by experimental tests. Shang et al. (2021) presented a novel fast-frequency and voltage regulation method for a battery energy storage system (BESS) based on the amplitude-phase-locked-loop. Most of the above analyses of the voltage response characteristics of the GFM WPS focus on the improvement of the control structure and lack a generalized voltage response model of the GFM WPS to describe it. At the same time, the above studies are not accurate on the influencing factors of the voltage response of GFM WPSs, and a detailed study on the influencing factors of the voltage response is needed.

In summary, this study centers on investigating the voltage response characteristics of GFM WPSs. It establishes a voltage response circuit model and mathematical model of the system, analyzing the influencing factors on voltage at the point of common coupling (PCC). Furthermore, the study explores voltage stabilization strategies at the PCC. Finally, simulation verification is conducted using the MATLAB/Simulink platform, providing a theoretical foundation for addressing the voltage support issue in GFM WPSs.

2 Modeling of grid-forming wind power systems

Taking wind permanent-magnet synchronous generators as an example, the structure of a typical GFM WPS is shown in Figure 1, which mainly consists of a wind turbine (WT), machine-side converter (MSC), dc-capacitor, and grid-side converter (GSC). The GFM WT machine-side control is usually in the form of constant voltage control, where the reference values of the rotor d-axis and q-axis currents are controlled by means of dc-capacitor voltage. The control structure used by the GSC is more complex, and the common control structures are droop control, VSG control, and adaptive control. Although the control structures adopted by the GSCs of GFM WT are quite different, their reactive power–voltage control parts and active power–frequency control parts can all be equated with the classical *P-f* droop control and *Q-U* droop control (Liu et al., 2022). In the next section, the voltage response of GFM WPSs will be modeled using the *Q-U* droop control as an example.

2.1 The *Q-U* droop control of GFM WPSs

When the sum of the inverter equivalent output impedances in GFM WPSs is inductive, the reactive power output from the inverter becomes a primary function of the bus voltage magnitude, so the *Q-U* droop characteristic equation for GFM WPSs can be described as follows:

$$E = E_0 + D(Q_0 - Q), \tag{1}$$

where E_0 is the reference value of the turbine terminal voltage, E is the value of the turbine terminal voltage, Q_0 is the reference value of reactive power on the load side, Q is the value of output reactive power on the load side, and D is the *Q-U* droop coefficient, which indicates the slope of the *Q-U* droop curve.

The value of D needs to be selected such that when the reactive power changes by ΔQ, the voltage amplitude changes within ΔE, i.e., and the expression for ΔE is shown in Equation 2.

$$D = \frac{\Delta E}{\Delta Q}. \tag{2}$$

2.2 Equivalent circuit

In order to analyze the effect of the GFM wind turbine on the grid voltage, the GFM wind turbine is equated to the form of a three-phase AC voltage source with the phase of the GFM wind turbine as the initial phase while focusing only on the external characteristics of the wind turbine. For the grid side, it can also be equated to the form of a three-phase AC source and disassembled into the form of a superposition of active and reactive power, and the power system can be equated to a single system of GFM wind turbines, as shown in Figure 2, under the premise of considering only the GFM wind turbines and the grid. In Figure 2, $\dot{V}_{\mathrm{PCC}}$ is the system voltage phase; $\dot{I}$ is the system current phase; P and Q are the active and reactive power on the load side, respectively; and X is the equivalent output reactance of the inverter, which is shown in Equation 3.

$$X = 2\pi f L, \tag{3}$$

where f is the system frequency and L is the equivalent inductance value of the inverter. According to Equation 1, the wind turbine-side terminal voltage magnitude can be expressed in Equation 4.

$$E = E_0 + D(Q_0 - Q). \tag{4}$$

3 Modeling of voltage response

According to Kirchhoff's voltage law (KVL), the equivalent circuit voltage equation is

$$\dot{E} - \dot{V}_{\mathrm{PCC}} = \mathrm{j}\dot{I}X. \tag{5}$$

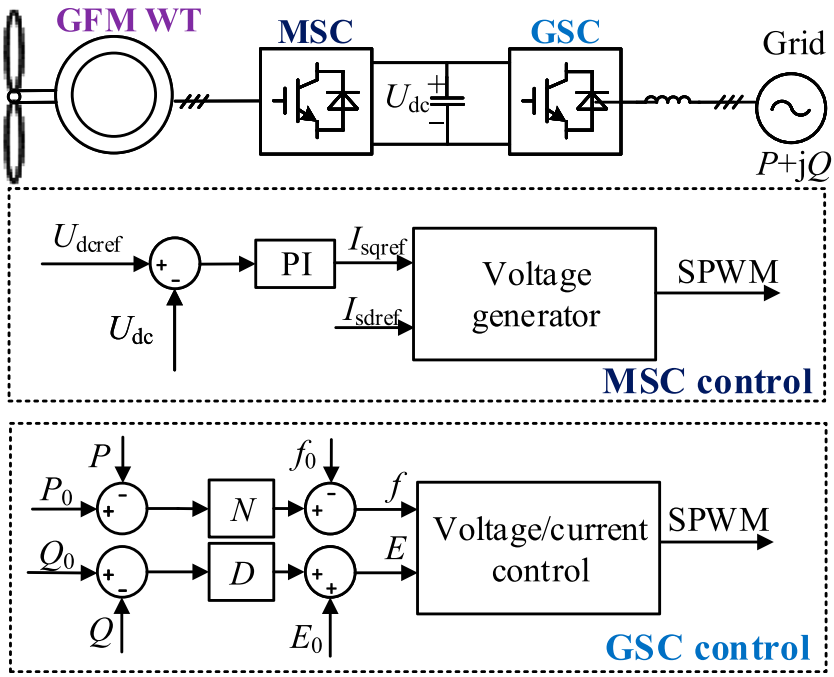

FIGURE 1
Schematic structure of a typical GFM WPS.

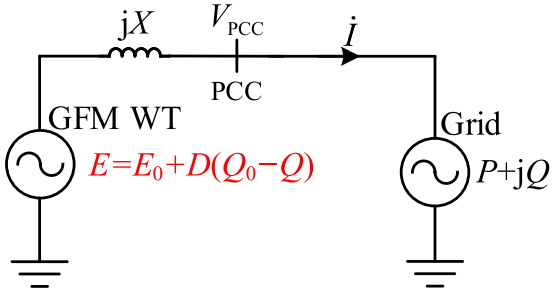

FIGURE 2
Equivalent circuit of the GFM WPS.

Taking the phase angle of the voltage at the PCC as a reference and assuming that the phase angle of the terminal voltage at the turbine-side is δ, then, Equation 6 can be obtained through Equation 5.

$$E\cos\delta + jE\sin\delta - V_{PCC} = jX\dot{I}. \tag{6}$$

The equivalent current can be expressed in Equation 7.

$$\dot{I} = \frac{E\sin\delta}{X} + j\frac{V_{PCC} - E\cos\delta}{X}. \tag{7}$$

For the load-side satisfying Equation 8

$$P + jQ = V_{PCC}\left(\frac{E\sin\delta}{X} + j\frac{E\cos\delta - V_{PCC}}{X}\right). \tag{8}$$

Then, the active and reactive power at the load-side can be expressed in Equation 9.

$$\begin{cases} P = \dfrac{EV_{PCC}\sin\delta}{X} \\ Q = \dfrac{EV_{PCC}\cos\delta - V_{PCC}^2}{X} \end{cases}. \tag{9}$$

Further organizing leads to the following expression which is shown in Equation 10.

$$\begin{cases} XP = EV_{PCC}\sin\delta \\ XQ + V_{PCC}^2 = EV_{PCC}\cos\delta \end{cases}. \tag{10}$$

Combined with the trigonometric theorem, the above expression can be which is shown in Equation 11.

$$X^2P^2 + (XQ + V_{PCC}^2)^2 = E^2V_{PCC}^2. \tag{11}$$

Furthermore, the square of the voltage magnitude V_{PCC} at the point of common coupling may be expressed in Equation 12.

$$V_{PCC}^2 = \frac{E^2 - 2XQ \pm \sqrt{(2XQ - E^2)^2 - 4X^2(P^2 + Q^2)}}{2}. \tag{12}$$

Mathematically, the following expression needs to be satisfied in order to keep the calculations correct:

$$(2XQ - E^2)^2 - 4X^2(P^2 + Q^2) \geq 0. \tag{13}$$

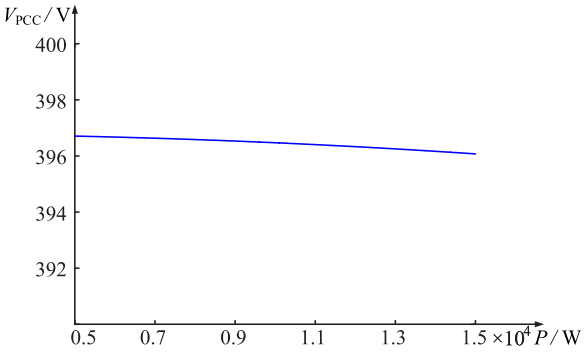

FIGURE 3
Curve of voltage amplitude at PCC with varying active power.

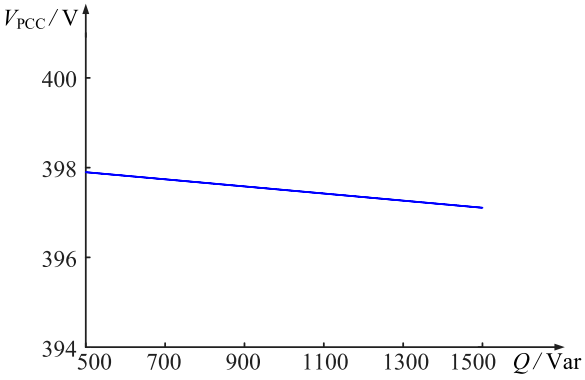

FIGURE 4
Curve of voltage amplitude at PCC with varying reactive power.

Further collation yields the following results which is shown in Equation 14.

$$\begin{cases} 2XQ - E^2 \geq 2X\sqrt{P^2+Q^2} & 2XQ \geq E^2 \\ E^2 - 2XQ \geq 2X\sqrt{P^2+Q^2} & 2XQ \leq E^2 \end{cases}. \tag{14}$$

Combining the above determining conditions, the square of the voltage magnitude V_{PCC} at the point of common coupling can be expressed in Equation 15.

$$2V_{PCC}^2 = \begin{cases} E^2 - 2XQ + \sqrt{(E^2-2XQ)^2 - 4X^2(P^2+Q^2)} & 2XQ \geq E^2 \\ E^2 - 2XQ - \sqrt{(E^2-2XQ)^2 - 4X^2(P^2+Q^2)} & 2XQ \leq E^2 \end{cases}. \tag{15}$$

The above expression is determined by the establishment condition, i.e., $2V_{PCC}^2 \geq 0$, and Equation 16 can be obtained:

$$\begin{cases} E^2 - 2XQ + \sqrt{(E^2-2XQ)^2 - 4X^2(P^2+Q^2)} & \geq 0 \\ E^2 - 2XQ - \sqrt{(E^2-2XQ)^2 - 4X^2(P^2+Q^2)} & \geq 0 \end{cases} \Rightarrow \begin{cases} 2XQ \leq E^2 \\ 2XQ \leq E^2. \end{cases} \tag{16}$$

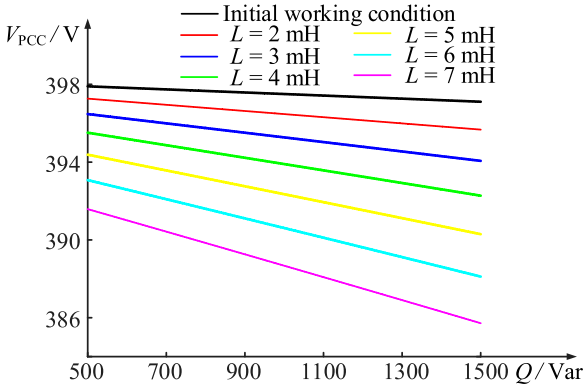

FIGURE 5
Curve of voltage amplitude at PCC with varying equivalent reactance.

Combining the above condition criteria, the calculation result needs to satisfy $2XQ \leq E^2$; the above calculation is rounded off, and the square of the dot voltage magnitude V_{PCC} only has the following expression:

$$\begin{cases} 2V_{PCC}^2 = E^2 - 2XQ - \sqrt{E^4 - 4XQE^2 - 4X^2P^2} & 2XQ \leq E^2 \\ E = E_0 + k(Q_0 - Q) \end{cases}. \tag{17}$$

Substituting Equation 1 into Equation 17 yields the following expression for the voltage magnitude at the point of common coupling which is shown in Equation 18.

$$\begin{cases} 2V_{PCC}^2 = [E_0 + D(Q_0 - Q)]^2 - 2XQ \\ \qquad\qquad \pm\sqrt{\{[E_0 + D(Q_0 - Q)]^2 - 2XQ\}^2 - 4X^2(P^2+Q^2)} \\ 2XQ \leq [E_0 + D(Q_0 - Q)]^2 \end{cases} \tag{18}$$

Combining the above expressions and assuming initial operating conditions where the droop coefficient $D = 0$, reactive power $Q = Q_0$, active power $P = P_0$, and initial operating conditions of the voltage amplitude of the grid point can be calculated as shown in Equation 19.

$$\begin{cases} 2V_0^2 = E_0^2 - 2XQ_0 \pm \sqrt{(E_0^2 - 2XQ_0)^2 - 4X^2(P_0^2 + Q_0^2)} \\ 2XQ \leq E_0^2 \end{cases}. \tag{19}$$

Under the condition that the initial working condition is known, in order to facilitate the calculation of voltage magnitude under different working conditions, the expression of voltage magnitude at the point of common coupling is normalized, which can be expressed as follows:

$$\begin{cases} \left(\frac{V_{PCC}}{V_0}\right)^2 = \frac{1}{2}\left[\frac{E_0 + k(Q_0 - Q)}{V_0}\right]^2 - \frac{XQ}{V_0^2} \\ \qquad \pm\sqrt{\left\{\frac{1}{2}\left[\frac{E_0 + k(Q_0 - Q)}{V_0}\right]^2 - \frac{XQ}{V_0^2}\right\}^2 - \left(\frac{X}{V_0}\right)^2(P^2+Q^2)} \\ 2V_0^2 = E_0^2 - 2XQ_0 \pm \sqrt{(E_0^2 - 2XQ_0)^2 - 4X^2(P_0^2 + Q_0^2)} \end{cases} \tag{20}$$

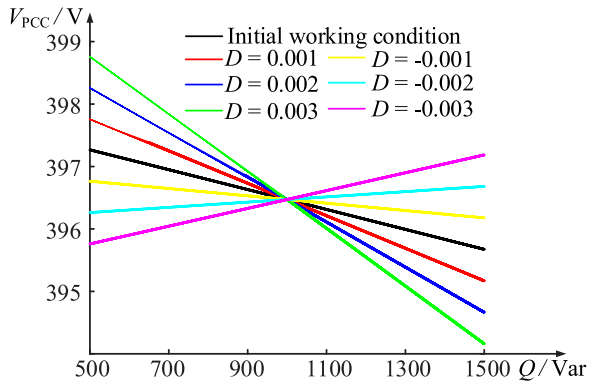

FIGURE 6
Curve of voltage amplitude at PCC with varying droop coefficient.

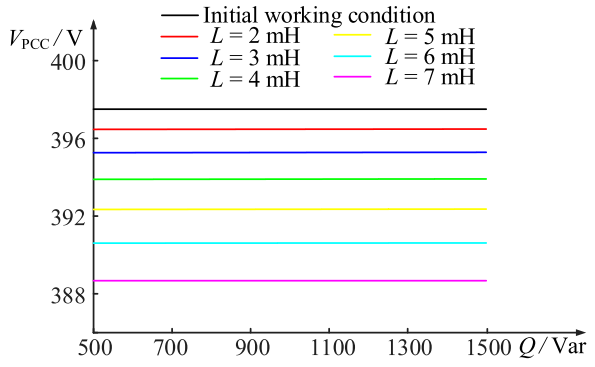

FIGURE 7
Curve of voltage amplitude at PCC with equivalent reactance and droop coefficient interacting cooperatively.

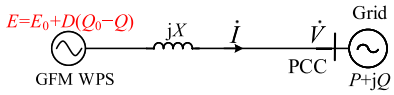

FIGURE 8
Circuit structure of the tested WPS.

4 Voltage response influencing factors and mechanism analysis

According to Equation 20, the voltage amplitude V_{PCC} is related to four parameters: P, Q, X, and D. The effects and mechanisms of these parameters are analyzed subsequently, respectively.

4.1 Effect of active power on voltage magnitude at PCC

According to Figure 3, it can be seen that with the increase in active power P, the voltage magnitude V_{PCC} stays floating at approximately 396.7 V, which is approximated to be unchanged. This is because in the GFM wind turbine inverter control, the active power P is related to the wind turbine frequency but not to the wind turbine terminal voltage, so the increase in the active power P does not affect the common coupling point voltage magnitude, i.e., the active power does not participate in the GFM WPS voltage response process.

TABLE 1 Simulation model structural parameters of case 1.

Parameter	Value	Parameter	Value
E_0	398.37 V	D	0.001
Q_0	1 kVar	L	1 mH
P	10 kW	Q	1 kVar

TABLE 2 Simulation model structural parameters of case 2.

Parameter	Value	Parameter	Value
E_0	398.37 V	D	0.001
Q_0	20 kVar	L	1 mH
P	200 kW	Q	20 kVar

4.2 Effect of reactive power on voltage magnitude at PCC

According to Figure 4, it can be seen that as the reactive power Q increases from 500 Var to 1,500 Var, the voltage magnitude V_{PCC} shows an overall decreasing trend. This phenomenon arises from the control mechanism of the GFM wind turbine inverter, which is governed by the Q-U droop control relationship. As the reactive power Q increases, the wind turbine terminal voltage decreases, consequently reducing the voltage magnitude at the point of common coupling. The slope of the overall curve is directly linked to the droop coefficient D.

4.3 Effect of equivalent reactance on voltage magnitude at PCC

In order to investigate the effect of the X value on the magnitude of voltage at the point of common coupling, the equivalent inductance value L of the inverter is gradually increased from 1 mH to 7 mH, and the waveform of V_{PCC} is obtained, as shown in Figure 5.

According to Figure 5, it can be seen that with the increase in the value of L, the voltage V_{PCC} shows an overall decreasing trend. This is because the increase in the L value leads to an increase in the voltage divider on the equivalent reactance of the inverter, while the voltage at the end of the GFM turbine remains unchanged, which results in a gradual decrease in the voltage at the grid point.

4.4 Effect of droop coefficient on voltage magnitude at PCC

In order to study the effect of the D value on the magnitude of the voltage at the point of common coupling, different values of D were taken and the waveform of V_{PCC} was obtained, as shown in Figure 6.

According to Figure 6, it can be seen that V_{PCC} shows a complex trend under the influence of D: before the image intersection, V_{PCC} and D are in a positive relationship, i.e., with the increase in D, V_{PCC} is also increased gradually. After the image intersection, V_{PCC} and D are in an inverse relationship, i.e., with the increase in D, V_{PCC} is decreased gradually. This is because before the intersection point, $Q < Q_0$, and after the intersection point, $Q > Q_0$; the above conclusion can be obtained from the droop relation analysis.

Moreover, in order to achieve better voltage stabilization and explore the reasonableness of the value of D, the partial derivative of Equation 5 is taken, i.e.,

$$\frac{dV_{PCC}}{dQ} \to 0. \tag{21}$$

Predicting the value of D that satisfies the relation of Equation 13 for different X, the waveform of V_{PCC} under the joint action of D and X is shown in Figure 7.

From Figure 7, it can be seen that under the influence of D and X, the waveform of V_{PCC} is more stable compared to that in Figure 5, and the slope of the waveform is smaller, which plays a role in stabilizing the voltage.

5 Verification

A single WPS was built in the MATLAB/Simulink platform to verify the influence of each influencing factor on the voltage at the point of common coupling in Figure 8. Two simulation conditions were set up to prove the correctness of the above analysis. The specific parameters under the initial working condition are shown in Tables 1, 2.

Combined with Figures 9, 10, it can be seen that the change in load reactive power P does not have a significant effect on the voltage magnitude V_{PCC}, and it can be assumed that P does not participate in the system voltage response process; however, the change in the three parameters of Q, X, and D causes the voltage magnitude V_{PCC} to have a different change, and it can be assumed that Q, X, and D participate in the voltage response process of the system.

Specifically, in the case of constant inverter equivalent output reactance X and droop coefficient D, the voltage magnitude V_{PCC}

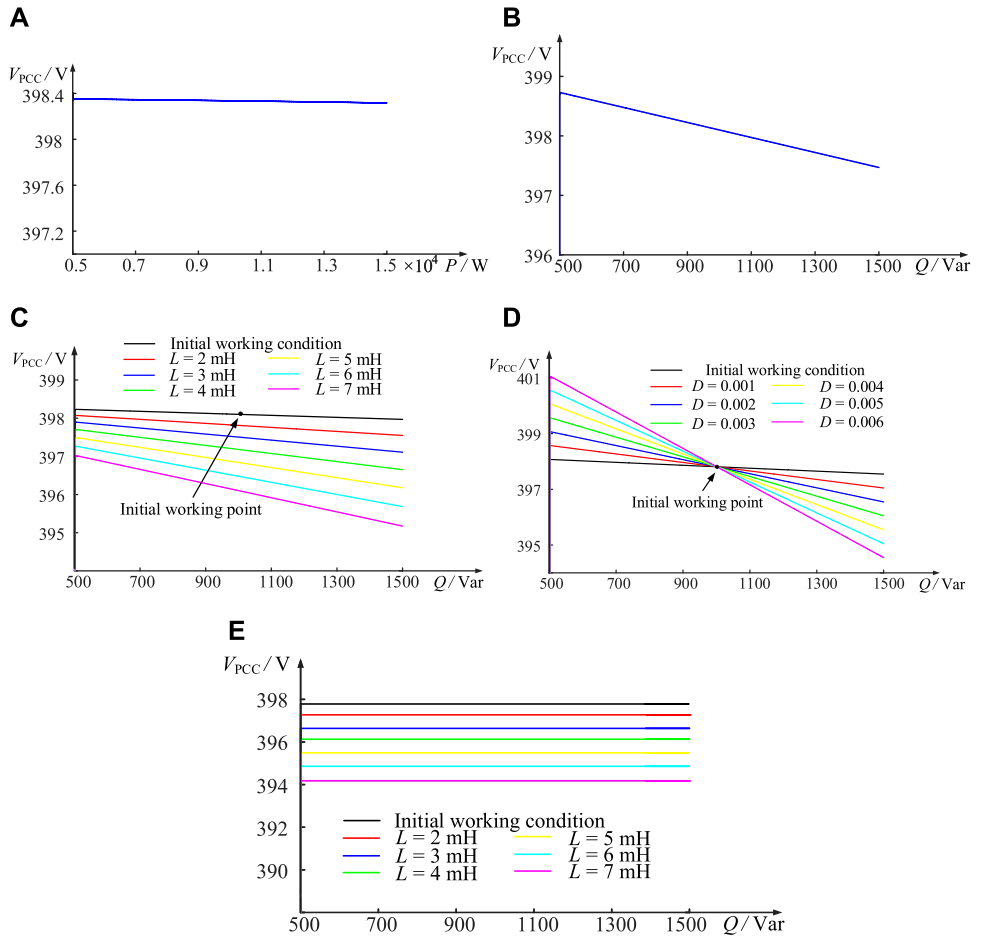

FIGURE 9
Curve of PCC voltage with different effect factors of case 1. **(A)** Active power. **(B)** Reactive power. **(C)** Equivalent reactance. **(D)** Droop coefficient. **(E)** Equivalent reactance and droop coefficient interacting cooperatively.

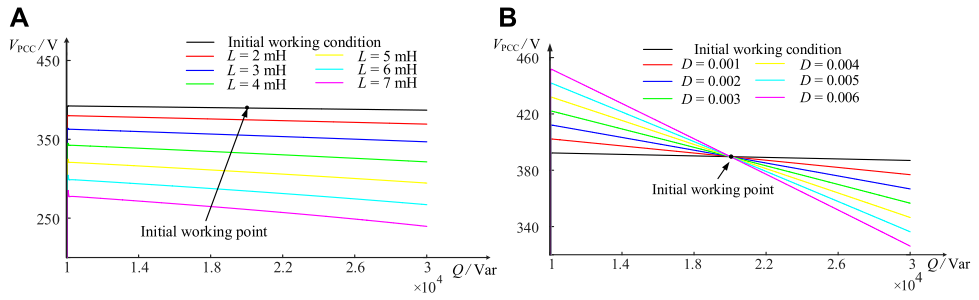

FIGURE 10
Curve of PCC voltage with different effect factors of case 2. **(A)** Equivalent reactance. **(B)** Droop coefficient.

TABLE 3 Impact of effect factors on V_{PCC}.

Effect factor	Influence
P	Irrelevant
Q	Negative correlation
X	Negative correlation
D	Before IWP: positive correlation; after IWP: negative correlation

gradually decreases with the increase in *Q*. In the case of constant load reactive power *Q* and droop coefficient *D*, V_{PCC} gradually decreases with the increase in *X*. In the case of constant load reactive power *Q* and inverter equivalent output reactance *X*, V_{PCC} exhibits a complicated trend.

These phenomena are inextricably linked to the *Q*-*U* droop control relationship of the GFM wind turbine. From Equation 1, it can be seen that with the increase in *Q*, the turbine end voltage *E* gradually decreases, which indirectly causes the decrease in V_{PCC}. At the same time, with the increase in *Q*, the more partial voltage on *X* further aggravates the drop of V_{PCC}; in the case of the same reactive power *Q*, the larger the value of *X*, the more the partial voltage on it. The droop coefficient has a more complex impact on V_{PCC}, and unreasonable *D* will lead to the fluctuation of V_{PCC} becoming larger. Specifically, before the initial working point (IWP), the amplitude of V_{PCC} increases as *D* increases because $Q < Q_0$, and after the IWP, the amplitude of V_{PCC} decreases instead as *D* increases because $Q > Q_0$. To ensure that the V_{PCC} maintains stability, the setting of the droop coefficient should satisfy Equation 21, and its simulation results are shown in Figure 9E. Under the effect of droop control, V_{PCC} can remain stable when the reactive power *Q* changes.

In order to better reflect the impact of the effect factors on V_{PCC}, the effect factors were organized into a table, as shown in Table 3.

6 Conclusion

In this study, the voltage response characteristics of the system at the point of common coupling and the voltage stabilization strategy are investigated by modeling analysis and simulation verification with GFM WPS as the research object. The main conclusions are as follows:

1) The voltage response circuit model and mathematical model of the system are established; the expression for the voltage magnitude V_{PCC} at the point of common coupling is derived, and the affecting components *P*, *Q*, *X*, and *D* in the expression are examined. It is discovered that the voltage at the point of common coupling is mainly affected by *Q*, *X*, and *D*, where the voltage magnitude V_{PCC} is inversely proportional to *Q* and *X*, while the effect of *D* is related to the IWP.
2) The voltage stabilization method is further investigated by analyzing the expression for the voltage magnitude V_{PCC} at the point of common coupling, and its feasibility is theoretically analyzed. Furthermore, the stabilization of V_{PCC} is achieved by adjusting the droop coefficient *D*.
3) The simulation verification of the influencing elements and voltage stabilization method is performed using the MATLAB/Simulink platform, and the above influencing factors and the proposed voltage stabilization strategy were verified, which proved the reliability of the analysis. At the same time, it provides a theoretical foundation for solving the voltage stabilization support problem in a new energy GFM system.

Data availability statement

The original contributions presented in the study are included in the article/Supplementary Material; further inquiries can be directed to the corresponding authors.

Author contributions

QuL: conceptualization, data curation, formal analysis, funding acquisition, investigation, methodology, project administration, resources, software, supervision, validation, visualization, writing–original draft, and writing–review and editing. QiL: conceptualization, data curation, investigation, software, validation,

and writing–review and editing. WT: formal analysis, investigation, project administration, and writing–review and editing. CW: supervision, visualization, and writing–review and editing.

Funding

The author(s) declare that financial support was received for the research, authorship, and/or publication of this article. This work was supported by the science and technology project of the State Grid Jiangsu Electric Power Co., Ltd. (J2023021).

Acknowledgments

The authors wish to thank the science and technology project of the State Grid Jiangsu Electric Power Co., Ltd., for the project funding (J2023021).

Conflict of interest

Authors QuL, QiL, WT, and CW were employed by State Grid Jiangsu Electric Power Co., Ltd.

The authors declare that this study received funding from State Grid Jiangsu Electric Power Co., Ltd. The funder had the following involvement in the study: the study design, collection, analysis, interpretation of data, and the writing of this article.

Publisher's note

References

Fang, J., Li, H., Tang, Y., and Blaabjerg, F. (2018). Distributed power system virtual inertia implemented by grid-connected power converters. *IEEE Trans. Power Electron.* 33, 8488–8499. doi:10.1109/tpel.2017.2785218

Kang, C., and Yao, L. (2017). Key scientific issues and theoretical research framework for power systems with high proportion of renewable energy. *Dianli Xit. Zidonghua/Automation Electr. Power Syst.* 41, 2–11.

Kim, G. G., Hyun, J. H., Choi, J. H., ahn, S.-H., Bhang, B. G., and Ahn, H.-K. (2023). Quality analysis of photovoltaic system using descriptive statistics of power performance index. *IEEE Access* 11, 28427–28438. doi:10.1109/access.2023.3257373

Leon, A. E., Nozal, Ã. R. d., and Mauricio, J. M. (2024). Frequency support strategy for fast response energy storage systems. *IEEE Trans. Power Syst.* 39, 5439–5442. doi:10.1109/tpwrs.2024.3358631

Li, Y., Hu, J., Wen, W., Wang, Q., Ma, S., and Guo, J. (2022). Concept and definition of dynamic symmetrical components with time-varying amplitude and frequency. *IEEE Trans. Energy Convers.* 37, 2737–2748. doi:10.1109/tec.2022.3188864

Liu, T., Chen, A., Gao, F., Liu, X., Li, X., and Hu, S. (2022). Double-loop control strategy with cascaded model predictive control to improve frequency regulation for islanded microgrids. *IEEE Trans. Smart Grid* 13, 3954–3967. doi:10.1109/tsg.2021.3129220

Liu, T., and Wang, X. (2021). Transient stability of single-loop voltage-magnitude controlled grid-forming converters. *IEEE Trans. Power Electron.* 36, 6158–6162. doi:10.1109/tpel.2020.3034288

Luo, C., Ma, X., Liu, T., and Wang, X. (2023). Adaptive-output-voltage-regulation-based solution for the dc-link undervoltage of grid-forming inverters. *IEEE Trans. Power Electron.* 38, 12559–12569. doi:10.1109/tpel.2023.3298468

Ouyang, J., Li, M., Zhang, Z., and Tang, T. (2019). Multi-timescale active and reactive power-coordinated control of large-scale wind integrated power system for severe wind speed fluctuation. *IEEE Access* 7, 51201–51210. doi:10.1109/access.2019.2911587

Pal, A., Pal, D., and Panigrahi, B. K. (2023). A current saturation strategy for enhancing the low voltage ride-through capability of grid-forming inverters. *IEEE Trans. Circuits Syst. II Express Briefs* 70, 1009–1013. doi:10.1109/tcsii.2022.3221134

Rosso, R., Wang, X., Liserre, M., Lu, X., and Engelken, S. (2021). Grid-forming converters: control approaches, grid-synchronization, and future trends—a review. *IEEE Open J. Industry Appl.* 2, 93–109. doi:10.1109/ojia.2021.3074028

Shang, L., Dong, X., Liu, C., and Gong, Z. (2021). Fast grid frequency and voltage control of battery energy storage system based on the amplitude-phase-locked-loop. *IEEE Trans. Smart Grid* 13, 941–953. doi:10.1109/tsg.2021.3133580

Shang, L., Hua, Z., Liu, C., and Dong, X. (2022). Amplitude-phase-locked-loop-based power injection strategy for wind power generation under three-phase grid fault. *IEEE Trans. Energy Convers.* 37, 2952–2961. doi:10.1109/tec.2022.3207285

Shao, H., Cai, X., Zhou, D., Li, Z., Zheng, D., Cao, Y., et al. (2019). Equivalent modeling and comprehensive evaluation of inertia emulation control strategy for dfig wind turbine generator. *IEEE Access* 7, 64798–64811. doi:10.1109/access.2019.2917334

Verma, P., K, S., and Dwivedi, B. (2023). A self-regulating virtual synchronous generator control of doubly fed induction generator-wind farms. *IEEE Can. J. Electr. Comput. Eng.* 46, 35–43. doi:10.1109/icjece.2022.3223510

Wu, H., and Wang, X. (2021). Passivity-based dual-loop vector voltage and current control for grid-forming vscs. *IEEE Trans. Power Electron.* 36, 8647–8652. doi:10.1109/tpel.2020.3048239

Xi, J., Geng, H., and Zou, X. (2021). Decoupling scheme for virtual synchronous generator controlled wind farms participating in inertial response. *J. Mod. Power Syst. Clean Energy* 9, 347–355. doi:10.35833/mpce.2019.000341

Xiong, L., Liu, X., Zhang, D., and Liu, Y. (2021). Rapid power compensation-based frequency response strategy for low-inertia power systems. *IEEE J. Emerg. Sel. Top. Power Electron.* 9, 4500–4513. doi:10.1109/jestpe.2020.3032063

Xiong, L., Liu, X., Zhao, C., and Zhuo, F. (2020). A fast and robust real-time detection algorithm of decaying dc transient and harmonic components in three-phase systems. *IEEE Trans. Power Electron.* 35, 3332–3336. doi:10.1109/tpel.2019.2940891

Xiong, L., Zhuo, F., Wang, F., Liu, X., Chen, Y., Zhu, M., et al. (2016). Static synchronous generator model: a new perspective to investigate dynamic characteristics and stability issues of grid-tied pwm inverter. *IEEE Trans. Power Electron.* 31, 6264–6280. doi:10.1109/tpel.2015.2498933

Yang, B., Li, Y., Yao, W., Jiang, L., Zhang, C., Duan, C., et al. (2023). Optimization and control of new power systems under the dual carbon goals: key issues, advanced techniques, and perspectives. *Energies* 16, 3904. doi:10.3390/en16093904

frontiers | Frontiers in Energy Research

TYPE Original Research
PUBLISHED 01 August 2024
DOI 10.3389/fenrg.2024.1428748

OPEN ACCESS

EDITED BY
Yonghui Liu,
Hong Kong Polytechnic University, Hong Kong, SAR China

REVIEWED BY
Chaoran Zhuo,
Xi'an University of Technology, China
Pu Liu,
Zhengzhou University of Light Industry, China
Dongqi Liu,
Changsha University of Science and Technology, China

*CORRESPONDENCE
Kai Li,
2018129@hebut.edu.cn

RECEIVED 07 May 2024
ACCEPTED 02 July 2024
PUBLISHED 01 August 2024

CITATION
Sun X, Cai J, Wang D, Lin J and Li K (2024), Small-disturbance stability analysis and control-parameter optimization of grid-connected virtual synchronous generator.
Front. Energy Res. 12:1428748.
doi: 10.3389/fenrg.2024.1428748

Small-disturbance stability analysis and control-parameter optimization of grid-connected virtual synchronous generator

Xianshan Sun[1], Jinming Cai[1], Dongsheng Wang[1], Jinwei Lin[1] and Kai Li[2]*

[1]State Grid Zhejiang Electric Power Co., Ltd., Deqing Power Supply Company, Huzhou, China, [2]School of Electrical Engineering, Hebei University of Technology, Tianjin, China

The virtual synchronous generator (VSG) has been widely used to improve the system inertia and damping in the renewable energy generation system. However, the in-depth understanding of VSG's stability under disturbances on different control parameters is lacked. In order to solve the problem, the small-signal model of single-VSG is established at first. The influences of key control parameters on the stability of system are analyzed by using the eigenvalue analysis method in detail. On this basis, a novel optimization strategy for control parameters is proposed based on the Particle Swarm Optimization (PSO) algorithm. The control parameters are optimized to realize excellent damping and stability of VSG system. Finally, the simulation and experimental results verify the effectiveness of stability analysis and parameter optimization strategy.

KEYWORDS

virtual synchronous generator (VSG), small-signal model, small-disturbance stability, control-parameter optimization, particle swarm optimization (PSO) algorithm

1 Introduction

With the development of new energy sources, many new energy units are connected to the grid by traditional inverters (Du et al., 2020; Zhang et al., 2021). However, traditional grid-connected inverters cannot participate in grid regulation. This will result in a decrease in the overall inertia and damping of the power system, which brings serious challenges to the stable operation of system (Pattabiraman et al., 2018). In order to ensure the stable operation of the power system under the high penetration rate of new energy, related literature have proposed the concept of Virtual Synchronous Generator (VSG) by referring to the operating characteristics and principles of the traditional synchronous generator, and carried out extensive researches on the control strategy, stability analysis, and parallel connection of multiple machines (Xiong et al., 2016; Choopani et al., 2020).

In the study of grid-connected stability of VSG, a VSG and an SG were connected in (Baruwa and Fazeli, 2021) for analyzing the low-frequency oscillation phenomenon after the VSG replaces the SG, as well as the characteristics and main modes of low-frequency oscillations. Literature (Lu et al., 2022) analyzes the impacts of VSG parameter changes by eigenvalue analysis method. But it does not give any advice on how the parameters should be designed.

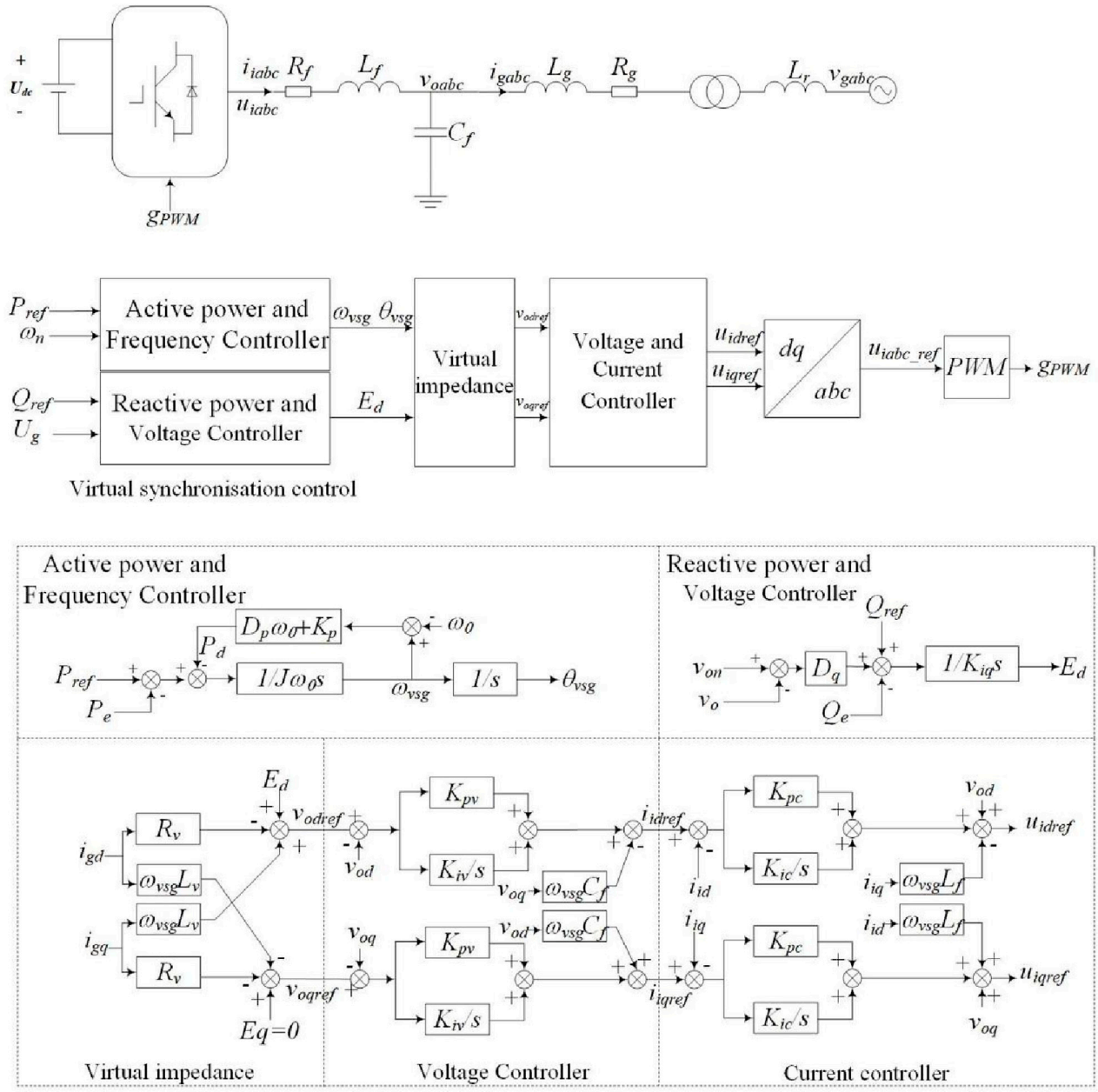

FIGURE 1
Topology diagram of VSG.

The parameters design of the VSG has been discussed (Du et al., 2013), Due to the equivalence of the VSG and droop control, the parameters design methods of droop control also provide the design guidance for the VSG(Coelho et al., 1999; Guerrero et al., 2007; Guerrero et al., 2004). The root-locus design method was used in literature (Du et al., 2013), but it is just the design of a separate power loop, thus the designed parameters may not be good enough and they are needed to be further adjusted to obtain the optimized results. Literature (D'Arco and Suul, 2014) derives the closed-loop characteristic equations of the power loop with droop control. However, due to the coupling effect between the active and reactive power loops the parameter design of the two loops is very difficult and the control parameters are partially tuned by trial and error. Similarly, Literature (Wu et al., 2016) has developed a small-signal model of the VSG power loop and proposed a step-by-step parameter design methodology that takes into account the stability and dynamic performance of the VSG. However, there is no detailed study of VSG parameter variations on its stability. Literature (Wu et al., 2019; Xu et al., 2021) provide impedance modeling and stability analysis for virtual synchronous control of permanent magnet wind turbines. However, the impedance characteristic curve can only reflect the external characteristics of the system, and the relationship with each internal controller or parameter is not clear. Literature (D'Arco et al., 2015; D'Arco et al., 2013) indicate that there are interactions between the cascade control loops contained in the VSG system, and the VSG system dynamics

TABLE 1 Parameters of single-VSG system.

Parameter	Value	Parameter	Value
L_f/H	0.0008	K_p	1,592
R_f/Ω	0.03	K_q	34
C_f/F	0.0001	J	1
R_g/Ω	0.03	D_P	30
L_g/H	0.0006	K_{iq}	195
E_{gd}/V	311.127	K_{pc}	4
ω_g/(rad/s)	314.159	K_{ic}	1,500
L_v/H	0.0006	K_{pv}	2
ω_0/(rad/s)	314.159	K_{iv}	133
R_v	0	L_v	0

equations are relatively complex. For these reasons, it can be seen that the current literature on the parameter design method for VSGs is only designed independently for each control loop and does not consider the coupling effect of the overall parameters. Classical tuning methods to this scheme are difficult to use.

Therefore, small-signal modeling of a stand-alone grid-connected system is carried out in this paper. Meanwhile, the effect of each control loop on the small-signal stability of the system is comprehensively considered in this paper. A detailed analysis of the active power loop control parameters, virtual impedance, and voltage loop of a single-unit grid-connected system is presented in this paper. Based on the above analysis, this paper proposes a PSO-based global control parameter optimization algorithm for multiple operating points. The optimized control parameters are used to provide better dynamic performance and stability at different grid strengths.

The rest of this paper is organized as follows: Section 2 provides a brief description of VSG control strategy and small-signal model of single-VSG grid-connected System. In Section 3, Eigenvalue analysis based on the small signal model of the system reveals that power loops, virtual impedances, and voltage loops have a large impact on system stability. Therefore, the influences of control parameters of active power loop, virtual impedance and voltage loop on the stability of the system are analyzed in detail. Section 4 presents a coordinated optimization strategy of control parameters based on PSO. In Section 5, the above analysis is verified by PSCAD simulation, and then Section 6 presents the experimental results obtained with coordinated optimization method and stability analysis. Finally, conclusions are presented in Section 7.

2 Small-signal model of Single-VSG grid-connected system

2.1 Control strategy

The control block diagram of VSG is shown in Figure 1. The control strategy of VSG can be divided into four parts. The first part is the power loop controller, which is composed of active-power-frequency control and reactive-power-voltage control. Active-power-frequency control can simulate the inertia and damping of synchronous generators. Reactive-power-voltage control can simulate the primary regulation of synchronous generators. The second part is the virtual impedance control, which is used to reshape the output impedance of VSG. The third part is the voltage-current double closed-loop controller, which consists of outer voltage and inner current closed-loop modules. The fourth part contains the dq/abc transformation as well as sinusoidal pulse width modulation.

In Figure 1, u_{dc} is the ideal DC voltage on the DC side, R_f is filter resistance, L_f is filter inductance, and C_f is filter capacitance. R_g and L_g are the resistance and inductance of the connecting line. v_{iabc} are the output voltage of the inverter. v_{oabc} are the voltage across filter capacitance. i_{iabc} are the output currents of the inverter. i_{gabc} are the currents of the line inductance. u_{gabc} are the AC power grid voltages. P_{ref} is the active power reference, and Q_{ref} is the reactive power reference. ω_{vsg} is the virtual angular frequency. ω_0 is the rated angular frequency of VSG. K_d is the active frequency regulation coefficient of the governor. P_e is the measured electrical power. J is the virtual inertia of VSG, D_p is the virtual damping coefficient, and θ_{vsg} is the phase angle that is the integral of the virtual angular frequency. K_q is the regulation coefficient of reactive-power-voltage. v_{oref} is voltage amplitude reference. v_o is the amplitude of capacitor voltage. The variables with subscripts d or q indicate variables in dq coordinates.

2.2 Modelling

The detailed modeling process of VSG has been described in Literature (Pogaku et al., 2007; Li et al., 2023). Therefore, this paper will not repeat the details. A non-linear model of the single-VSG grid-connected system can be established by Eq. (1).

$$
\begin{cases}
J\omega_0\dfrac{d\omega_{vsg}}{dt} = P_{ref} - P_e - \left(D_p\omega_0 + K_p\right)\left(\omega_{vsg} - \omega_0\right) \\
K_{iq}\dfrac{dE_d}{dt} = Q_{set} + K_q\left(v_{on} - v_o\right) - Q_e \\
v_{odref} + jv_{oqref} = E_d - i_{gd}R_v + i_{gq}w_{vsg}L_v + j\left(-i_{gq}R_v - i_{gd}w_{vsg}L_v\right) \\
i_{idref} + i_{iqref} = K_{pv}\left(v_{odref} - v_{od}\right) + K_{iv}x_{ud} - v_{oq}w_{vsg}C_f \\
\qquad\qquad + j\left(K_{pv}\left(v_{oqref} - v_{oq}\right) + K_{iv}x_{uq} + v_{od}w_{vsg}C_f\right) \\
\dfrac{dx_{ud}}{dt} + j\dfrac{dx_{uq}}{dt} = v_{odref} - v_{od} + j\left(v_{oqref} - v_{oq}\right) \\
u_{idref} + ju_{iqref} = v_{od} + K_{pc}\left(i_{idref} - i_{id}\right) + K_{ic}x_{id} - i_{iq}w_{vsg}L_f \\
\qquad\qquad + j\left(v_{oq} + K_{pc}\left(i_{iqref} - i_{iq}\right) + K_{ic}x_{iq} + i_{id}w_{vsg}L_f\right) \\
\dfrac{dx_{id}}{dt} + j\dfrac{dx_{iq}}{dt} = i_{idref} - i_{id} + j\left(i_{iqref} - i_{iq}\right) \\
\dfrac{di_{id}}{dt} + j\dfrac{di_{iq}}{dt} = -\dfrac{R_f}{L_f}i_{id} + w_{vsg}i_{iq} + \dfrac{1}{L_f}v_{id} - \dfrac{1}{L_f}v_{od} + j\left(-\dfrac{R_f}{L_f}i_{iq} - w_{vsg}i_{id} + \dfrac{1}{L_f}v_{iq} - \dfrac{1}{L_f}v_{oq}\right) \\
\dfrac{dv_{od}}{dt} + j\dfrac{dv_{oq}}{dt} = w_{vsg}v_{oq} + \dfrac{1}{C_f}i_{id} - \dfrac{1}{C_f}i_{gd} + j\left(-w_{vsg}v_{od} + \dfrac{1}{C_f}i_{id} - \dfrac{1}{C_f}i_{gd}\right) \\
\dfrac{di_{gd}}{dt} + j\dfrac{di_{gq}}{dt} = -\dfrac{R_g}{L_g}i_{gd} + w_{vsg}i_{gq} + \dfrac{1}{L_g}v_{od} - \dfrac{1}{L_g}v_{bd} + j\left(-\dfrac{R_g}{L_g}i_{gq} - w_{vsg}i_{gd} + \dfrac{1}{L_g}v_{oq} - \dfrac{1}{L_g}v_{bq}\right) \\
v_{bd} + jv_{bq} = E_{gd}\cos\left(\delta\right) + jE_{gd}\sin\left(\delta\right) \\
\dfrac{d\delta}{dt} = w_g - w_{vsg}
\end{cases}
\tag{1}
$$

The above nonlinear equations can be simplified and linearized at the steady state point. Consequently, the small-signal model of single-VSG grid-connected system can be obtained as Eq. (2)

TABLE 2 Eigenvalues of single-VSG system.

Eigenvalue	Real part	Imaginary Part	Oscillation Frequency/Hz	Dominant Related state Variables
1,2	−2156.5	±10,276.1	1,636	i_{id}、i_{iq}、v_{od}、v_{oq}
3,4	−2081.4	±9942.4	1,583	i_{id}、i_{iq}、v_{od}、v_{oq}
5,6	−420.6	±297.3	47	i_{gd}、i_{gq}
7,8	−382.5	±34.5	5.41	x_{id}、x_{iq}
9,10	−33.3	±13.3	2.01	x_{ud}、x_{uq}、ω_{vsg}、σ
11	−6.5	0	—-	E_d
12,13	−2.5	±36.3	5.82	x_{ud}、x_{uq}、ω_{vsg}、σ

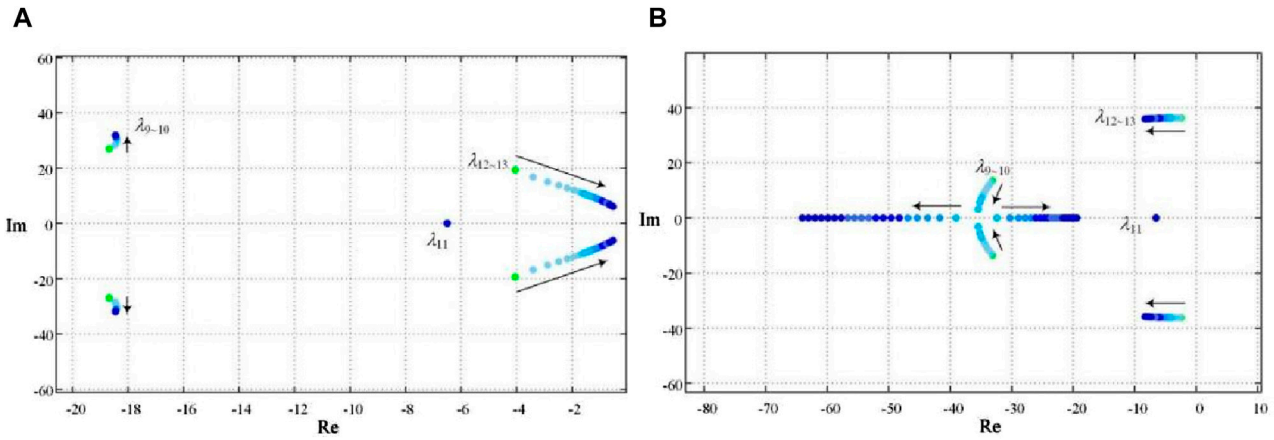

FIGURE 2
The eigenvalue trajectories under different control parameters of active-power-frequency loop. **(A)** Eigenvalue trajectories of the system under different inertias. **(B)** Eigenvalue trajectories of the system under different damping coefficients.

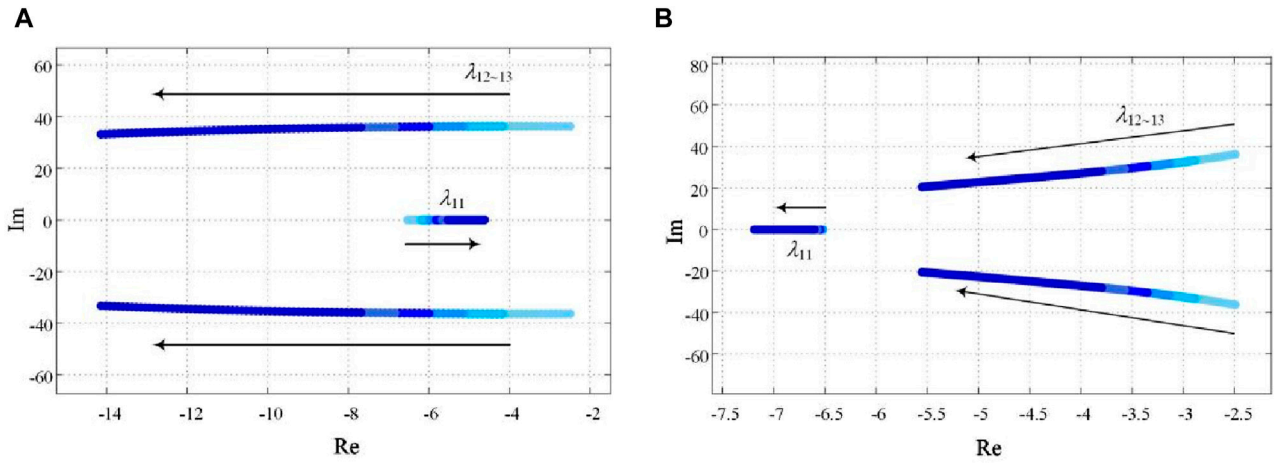

FIGURE 3
The eigenvalue trajectories under different virtual impedance parameters. **(A)** Eigenvalue trajectories of the system under different virtual inductor. **(B)** Eigenvalue trajectories of the system under different virtual resistor.

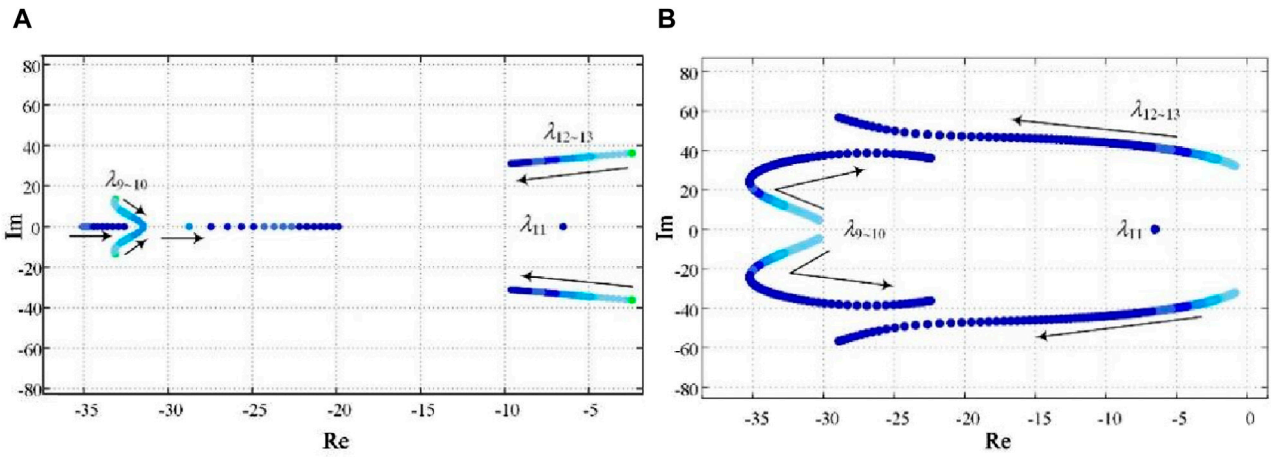

FIGURE 4
The eigenvalue trajectories under different voltage loop controller parameters. **(A)** Eigenvalue trajectories of the system under different proportionality coefficient. **(B)** Eigenvalue trajectories of the system under different integrity coefficient.

$$\frac{d\Delta x_{sys}}{dt} = \mathbf{A}\Delta x_{sys} + \mathbf{B}\Delta u \tag{2}$$

In Eq. (2), Δx_{sys} is the state variable vector of the system, Δu is the input variable vector of the system, and the elements of matrices A and B are related to the steady state point. Matrices A and B are given in Supplementary Materia S1–S3.

3 Stability analysis of Single-VSG grid-connected system

3.1 Oscillation mode analysis of Single-VSG system

According to the small-signal model described by Eq. (2), all eigenvalues of the system matrix A are obtained based on the system parameters in Table 1. The oscillation modes of system and the effect of parameter variations on the stability can be obtained by analyzing the eigenvalue distribution.

The system eigenvalues are shown in Table 2. It can be concluded that the system has thirteen eigenvalues, corresponding to seven oscillation modes. There are 6 pairs of conjugate complex eigenvalues and 1 real eigenvalue. They correspond to 7 oscillation modes. The system is stable on condition that the eigenvalues of the system are in the left half plane of the complex plane. By using the participation factor analysis, it can be obtained that $\lambda_{1\sim4}$ are mainly associated with the state variables i_{id}, i_{iq}, v_{od}, and v_{oq} generated by the LC filters. However, the distances between the eigenvalues $\lambda_{1\sim4}$ and the imaginary axis are much greater than the distances between other eigenvalues and the imaginary axis. As a result, $\lambda_{1\sim4}$ have little influence on the system stability and can be ignored. $\lambda_{5\sim6}$ are mainly associated with the state variables i_{gd} and i_{gq}. $\lambda_{7\sim8}$ are mainly associated with the state variables x_{id} and x_{iq} generated by the current loop control. $\lambda_{9\sim10}$ and $\lambda_{12\sim13}$ are mainly associated with the state variables x_{ud} and x_{uq} generated by the voltage loop control as well as the state variables ω_{vsg} and δ generated by the active-power-frequency control. The influences of various controller parameters on system stability are presented in the following parts of this section.

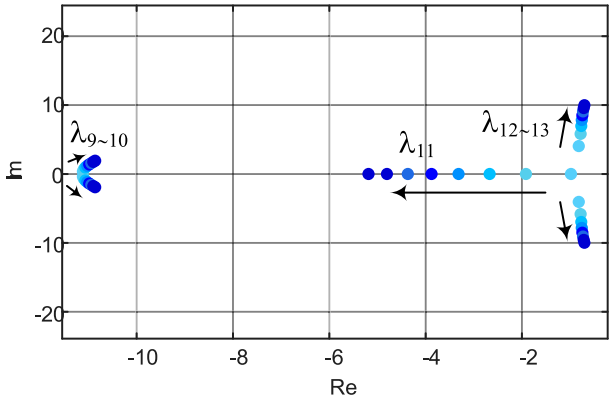

FIGURE 5
The eigenvalue trajectories under different short circuit ratio.

3.2 Controller parameters of active-power-frequency loop

The control parameters of active-power-frequency loop include the virtual inertia J and the virtual damping coefficient D_p. The eigenvalue trajectories with the changes of parameter are shown in Figure 2.

When the virtual inertia J changes from 4 to 40 and other parameters remain unchanged, the eigenvalue trajectories are shown in Figure 2A. With the increase in virtual inertia, the eigenvalues $\lambda_{1\sim10}$ have slight changes. However, the

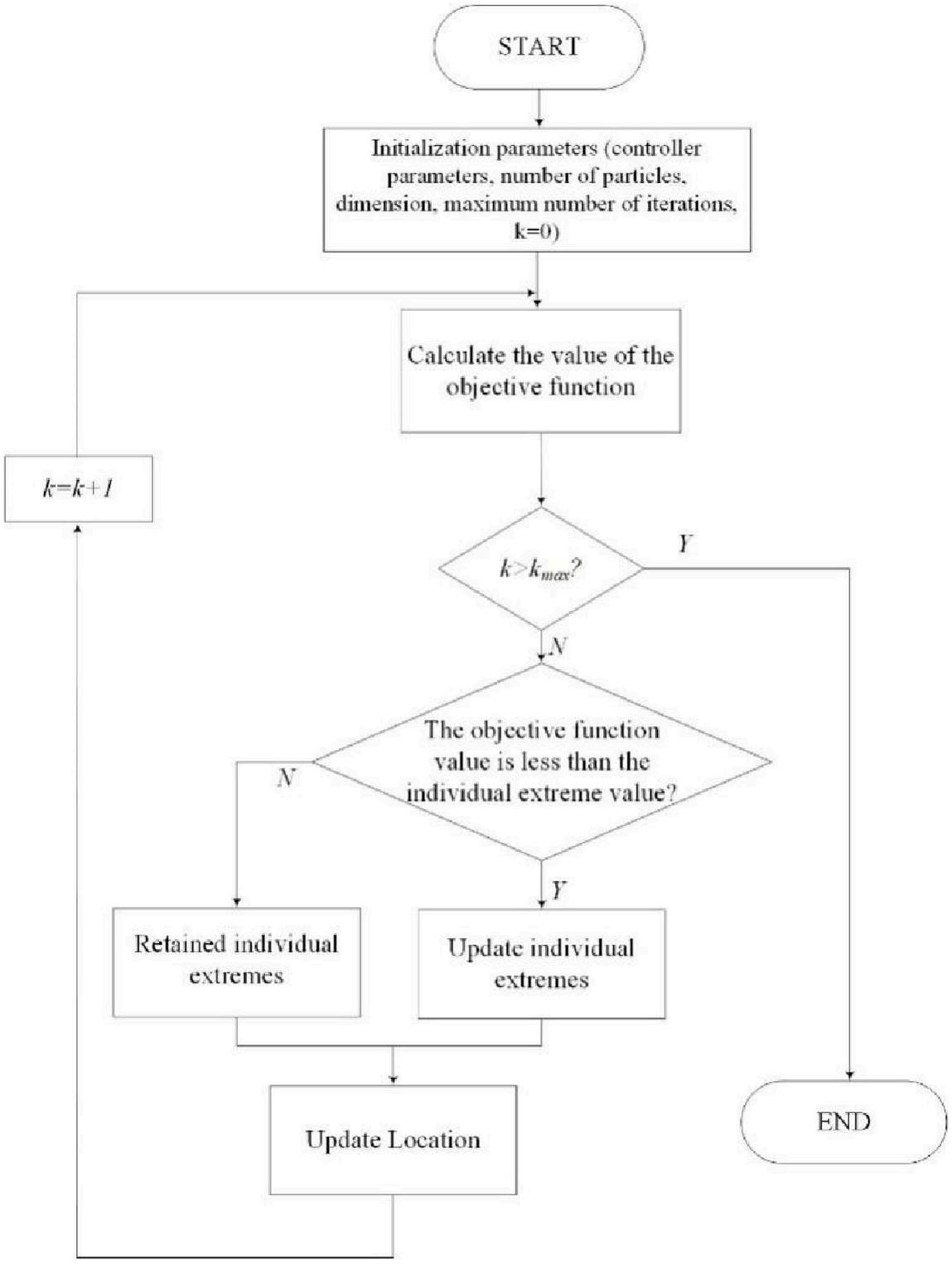

FIGURE 6
Flowchart of PSO algorithm.

eigenvalues λ_{12-13} move towards the imaginary axis rapidly. It is evident that the damping ratio of the corresponding oscillation mode decreases rapidly while the oscillation frequency decreases slightly. As a result, the system stability is deteriorated.

When the virtual damping coefficient D_p changes from 30 to 60 and other parameters remain unchanged, the eigenvalue trajectories are shown in Figure 2B. With the increase in virtual damping coefficient, the eigenvalues λ_{1-8} and λ_{10} have slight changes. The eigenvalues λ_{12-13} move to the left of the

complex plane and the movement speed away from the imaginary axis is much higher than that away from the real axis. It can be concluded that the damping ratio of the corresponding oscillation mode increases, the overshoot gradually decreases, the oscillation frequency increases slightly, and the system stability is improved. However, the eigenvalues λ_{9-10} firstly move away from the right half plane and towards the real axis; then moves to the right half plane along the real axis. Therefore, the virtual damping coefficient D_p should not be too large, otherwise the system stability will be deteriorated.

3.3 Virtual impedance parameters

The virtual impedance parameters include the virtual resistor R_v and the virtual inductor L_v. The eigenvalue trajectories with the parameter changes are shown in Figure 3.

When the virtual inductor L_v changes from 0 to 0.0005, other parameters remain unchanged, and the eigenvalue trajectories is shown in Figure 3A. With the increase in virtual inductor L_v, the eigenvalues λ_{1-10} has little changed. However, the eigenvalues λ_{12-13} move rapidly away from the imaginary axis, the damping ratios of the corresponding oscillation attenuation mode increase rapidly, the oscillation frequency decreases slightly, and the system stability improved. Meanwhile, the eigenvalues λ_{11} gradually approaches the imaginary axis, and the system will be slightly worse for stability.

When the virtual resistor R_v changes from 0 to 0.3, other parameters remain unchanged, and the eigenvalue trajectories is shown in Figure 3B. With the increase in virtual resistor R_v, the eigenvalues λ_{1-10} has little changed. However, the eigenvalues λ_{12-13} move rapidly away from the imaginary axis, the damping ratios of the corresponding oscillation attenuation mode increase rapidly, the oscillation frequency decreases slightly, and the system stability improved. Unlike the trajectory of the eigenvalues when the virtual inductor changes, the eigenvalues λ_{11} also moves away from the imaginary axis, and the stability of the system will be further improved.

3.4 Control parameters of voltage loop

The voltage loop controller parameters include proportionality coefficient K_{pv} and the integrity coefficient K_{iv}. The eigenvalue trajectories with the parameter changes are shown in Figure 4.

When the proportionality coefficient K_{pv} changes from 2 to 20, other parameters remain unchanged, and the eigenvalue trajectories is shown in Figure 4A. With the increase in proportionality coefficient K_{pv}, the eigenvalues λ_{12-13} move rapidly away from the imaginary axis, the damping ratios of the corresponding oscillation attenuation mode increase rapidly, the oscillation frequency decreases slightly, and the system stability improved. However, the eigenvalues λ_{9-10} gradually approaches the right half plane after changing to the real axis from a pair of conjugate complex roots, and the system will be slightly worse for stability. Therefore, the proportionality coefficient should not be too large.

When the integrity coefficient K_{iv} changes from 100 to 400, other parameters remain unchanged, and the eigenvalue trajectories is shown in Figure 4B. With the increase in integrity coefficient K_{iv}, the eigenvalues λ_{12-13} also move rapidly away from the imaginary axis, the damping ratios of the corresponding oscillation attenuation mode increase rapidly, the oscillation frequency decreases slightly, and the system stability improved. However, the eigenvalues λ_{9-10} first moves away from the imaginary axis and then gradually moves closer to the imaginary axis. Therefore, the integrity coefficient also should not be too large.

3.5 Different short circuit ratios

The eigenvalue trajectories with different short circuit ratios are shown in Figure 5.

When the short circuit ratio changes from 1 to 8 and other parameters remain unchanged, the eigenvalue trajectories are shown in Figure 5. With the increase in short circuit ratio, the eigenvalues λ_{12-13} move towards the right-half plane rapidly. It is evident that the damping ratio of the corresponding oscillation mode decreases rapidly while the oscillation frequency increase slightly. Although the eigenvalue λ_{11} is moving to the left half plane, the eigenvalue λ_{12-13} is closer to the right half plane. As the short-circuit ratio is increasing, the system becomes less stable.

4 Optimization strategy for control parameters based on PSO

4.1 PSO algorithm

The basic idea of the PSO algorithm is to assume that there are N1 particles in the D-dimensional space, and the particles update their velocities and positions according to Eq. (3).

$$\begin{cases} v_{ij}^{k+1} = wv_{ij}^{k} + r_1 a_1\left(p_{ij} - x_{ij}^{k}\right) + r_2 a_2\left(p_{kj} - x_{ij}^{k}\right) \\ x_{ij}^{k+1} = x_{ij}^{k} + v_{ij}^{k} \end{cases} \tag{3}$$

In Eq. (3), w is the inertia weight; $r1$ and $r2$ are uniform random numbers in the range of [0, 1]; $a1$ and $a2$ are the learning factors; v^k_{ij} and x^k_{ij} are the velocity and position of particle i in the kth iteration, respectively, and both of them are restricted to be movable; p_{ij} is the optimal position experienced by the ith particle; and p_{gj} is the optimal position experienced by all particles of the particle swarm.

4.2 The objective function

It can be known from the above: the stability performance of the system depends on the distribution of the eigenvalues, which depends on the design of the controller parameters. Therefore, the optimization objectives designed in this paper are as follows:

(1) All eigenvalues as far away from the right half plane as possible.

TABLE 3 Comparison of control parameters before and after optimization.

Parameter	Before optimization	After optimization
J	1	0.83
D_p	30	35.1
K_{iq}	195	207.64
L_v	0	0.00014
R_v	0	0.011
K_{pc}	4	2.64
K_{ic}	1,000	2148.4
K_{pv}	2	16.94
K_{iv}	133	260.24

(2) The damping ratio of each oscillation mode should be as large as possible to minimize the number of oscillation cycles during the transient process.

According to the optimization objective, the objective function of the system under a single operating point is defined as Eq. (4).

$$\min E_j = \sum_{i=1}^{N} w_i f(\lambda_i) + \sum_{i=1}^{N} k_i h(\lambda_i)$$
$$f(\lambda_i) = \begin{cases} 0 & \mathrm{Re}(\lambda_i) \le \sigma \\ \mathrm{Re}(\lambda_i) - \sigma & \mathrm{Re}(\lambda_i) > \sigma \\ \inf & \mathrm{Re}(\lambda_i) \ge 0 \end{cases}$$
$$h(\lambda_i) = \begin{cases} 0 & \frac{|\mathrm{Re}(\lambda_i)|}{|\lambda_i|} \ge \xi, \mathrm{Re}(\lambda_i) < 0 \\ \xi - \frac{|\mathrm{Re}(\lambda_i)|}{|\lambda_i|} & \frac{|\mathrm{Re}(\lambda_i)|}{|\lambda_i|} < \xi, \mathrm{Re}(\lambda_i) < 0 \\ \inf & \mathrm{Re}(\lambda_i) \ge 0 \end{cases} \tag{4}$$

In Eq. (4), N is the number of eigenvalues. Re (λ_i) is the real part of the eigenvalue λ_i. $|\lambda_i|$ is the value of the modulus of the eigenvalue λ_i. ξ is the desired damping ratio. σ is the desired real part value. w_i is the weight of $f(\lambda_i)$. k_i is the weight of $h(\lambda_i)$. In this paper, we take $\sigma = -15$, $\xi = 0.707$ and w_i and k_i are taken as shown in Eq. (5).

$$w_i = \begin{cases} 0.01 & \mathrm{Re}(\lambda_i) < \delta \\ 0.1 & \delta < \mathrm{Re}(\lambda_i) < 0.5\delta \\ 0.8 & 0.5\delta < \mathrm{Re}(\lambda_i) < 0 \\ 1 & \mathrm{Re}(\lambda_i) > 0 \end{cases}, k_i = \begin{cases} 0.01 & \frac{|\mathrm{Re}(\lambda_i)|}{|\lambda_i|} > \xi \\ 10 & 0.5\xi < \frac{|\mathrm{Re}(\lambda_i)|}{|\lambda_i|} < \xi \\ 30 & \frac{|\mathrm{Re}(\lambda_i)|}{|\lambda_i|} < 0.5\xi \end{cases} \tag{5}$$

Considering different grid strengths as well as different output powers in practice, the VSG can be linearized at different steady state operating points, and then the eigenvalues corresponding to each operating point can be solved separately. Therefore, in order to consider the effectiveness of the control parameters under multiple operating points, the objective function is changed to Eq. (6) based on a single operating point.

TABLE 4 Voltage source type D-PMSG with different operating conditions.

Work point serial number	Output power (kW)	SCR
1	10	2
2	20	2
3	30	2
4	10	4
5	20	4
6	30	4

$$\min E = \sum_{j=1}^{M} p_j E_j \tag{6}$$

where p_j is the probability of the jth operating point, E_j is the optimization objective function at the jth operating point. In this way, the control parameters can be globally optimized for multiple operating conditions.

4.3 Optimization process

In the PSO algorithm, the objective function represents the fitness value of the particle, the controller parameter represents the position, the change value of the controller parameter represents the speed, the individual extreme value represents the optimal fitness value of each particle, the global extreme value represents the optimal fitness value searched by all the particles, and the position corresponding to the particle with the global extreme value is the optimal control parameter value. The algorithm flow is shown in Figure 6. Firstly, the particle velocity and particle position are initialized. The particle position is the main control parameter of the VSG and is represented by the vector [J D_p L_v R_v K_{pv} K_{iv} K_{pc} K_{ic}]. Secondly, the above control parameters are brought into the system eigenmatrix to obtain the system eigenvalues. The system eigenvalues are brought into the objective function to get the individual objective value for each particle. Updating the group historical optimum with the individual optimum based on the current individual objective function values. Update the particle positions by learning factor and inertia factor for several iterations. Finally, the particle positions corresponding to the population historical optimal values are the optimal control parameters of the VSG.

4.4 Example analysis

The control parameters of the system are optimized by using a PSO-based multiple operating point optimization algorithm. And the control parameters of the system before and after

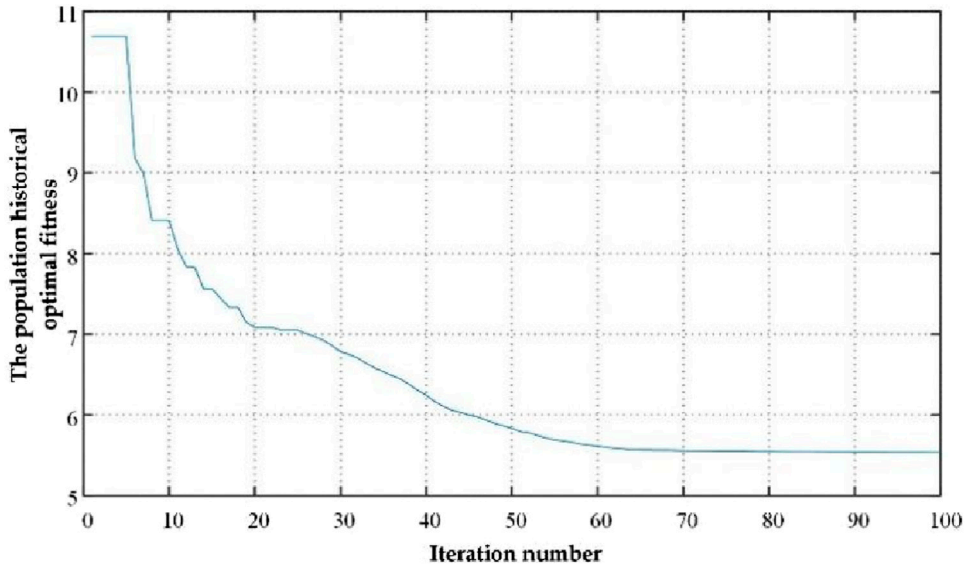

FIGURE 7
Population optimal fitness convergence curve.

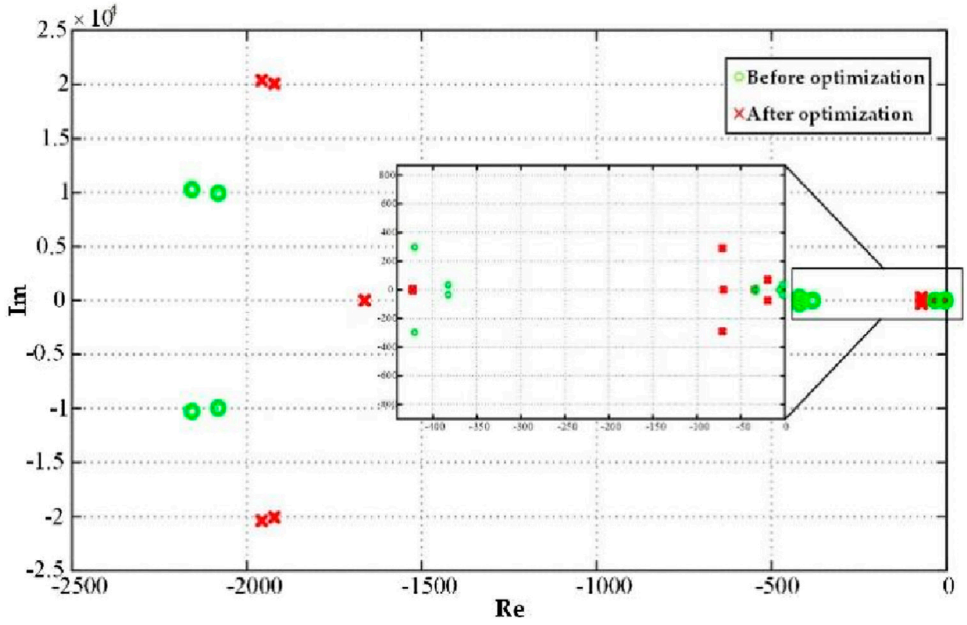

FIGURE 8
The distribution of eigenvalues before and after optimization.

optimization are shown in Table 3. The different work points are shown in Table 4 The population historical optimal fitness and the number of iterations is shown in Figure 7. As the number of iterations increases, the population historical optimal fitness rapidly converges. The distribution of eigenvalues before and after optimization is shown in Figure 8. The PSO algorithm was run several times. the population historical optimal fitness all converge to the optimal value relatively quickly, and the average number of convergence is about 65 times, which indicates that the optimization strategy of the PSO algorithm has a good convergence property, and the optimization results can be obtained within a limited number of iterations. The distribution of eigenvalues after optimization is further away from the imaginary axis than before optimization. However, the complex eigenvalue closest to the imaginary axis after optimization is close to the optimal damping ratio.

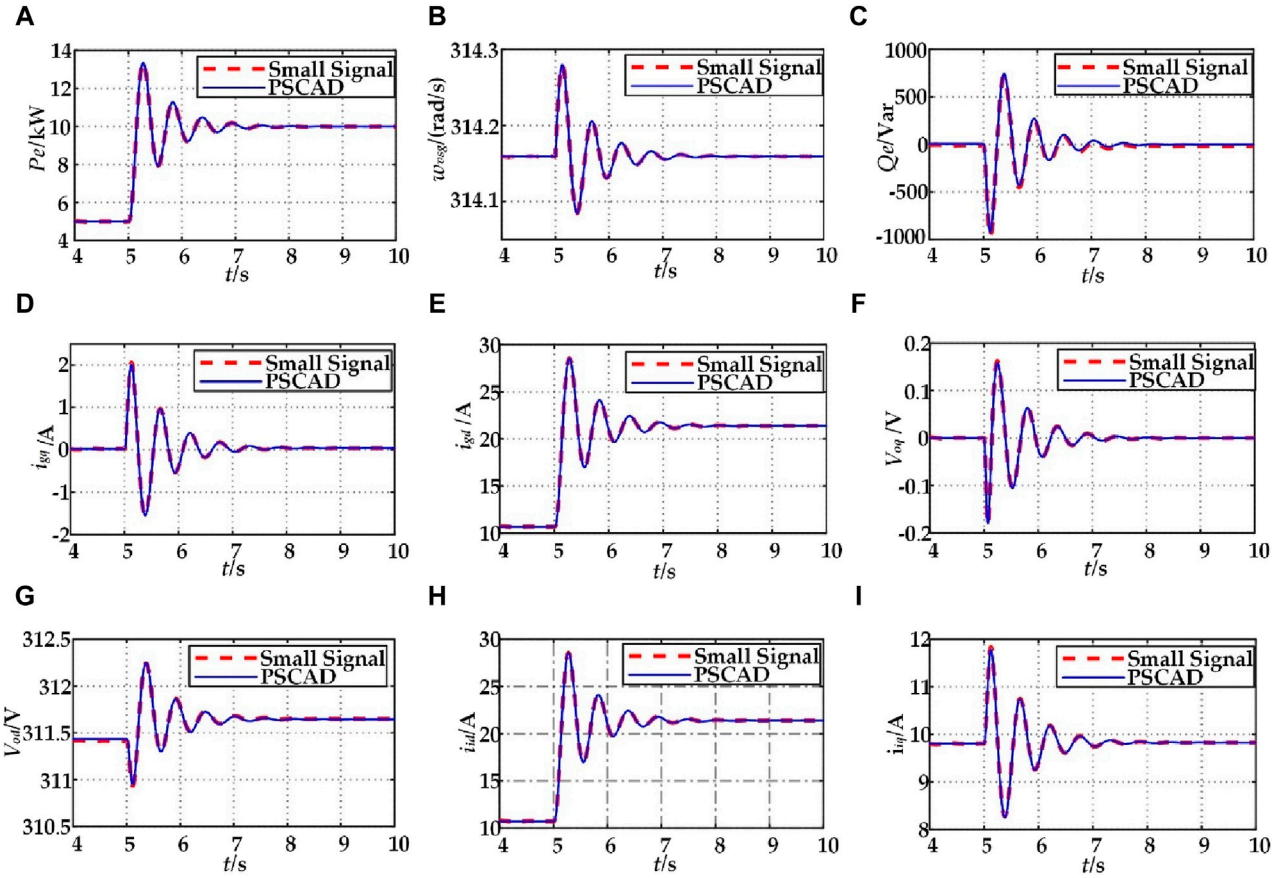

FIGURE 9
Comparison of simulation results between small signal model and PSCAD model: **(A)** Pe; **(B)** wvsg; **(C)** Qe; **(D)** igq; **(E)** igd; **(F)** voq; **(G)** vod; **(H)** iid; **(I)** iiq.

5 Simulation verification

5.1 Small-signal model verification

To verify the correctness of the small-signal model derived above, the actual model was built in PSCAD according to the parameters in Table 1.

The change curves of each variable in the two models are shown in Figure 9 by comparing the change curves of each variable in the two models at 5 s for the active power reference value P_{ref} from a step of 5kW–10 kW. It can be observed that the dynamic process of the small-signal model basically overlaps with the PSCAD simulation model, which verifies the accuracy of the small-signal model established in this paper.

5.2 Stability analysis verification

To verify the correctness of the analysis of the above variable parameters on the change law of eigenvalue trajectories, a time domain simulation model of a VSG grid-connected system was built in PSCAD. With the same other parameters (as shown in Table 1), when the power is stepped, the response simulation waveforms under different virtual moments of inertia, virtual damping coefficients, virtual inductor, virtual resistor, voltage proportionality coefficients and voltage integration coefficients are shown in Figure 10A–E respectively.

As can be seen from Figures 10A,B, increasing the virtual inertia J or decreasing the virtual damping coefficient D_p will make the system unstable under a power stepping. Increasing the virtual inertia J influences the number of oscillations of active power and frequency under power stepping, increasing the regulation time of the system. Increasing the virtual damping coefficient D_p reduces the amplitude of oscillations of active power and frequency and shortens the time for the system to reach stability.

As can be seen from Figures 10C,D, decreasing the virtual inductor L_v or decreasing the virtual resistor R_v will make the system unstable under a power stepping. Decreasing the virtual inductor L_v influences the number of oscillations of active power and frequency under power stepping, increasing the regulation time of the system. Increasing the virtual resistors R_v reduces the amplitude of oscillations of active power and frequency and shortens the time for the system to reach stability.

As can be seen from Figures 10E,F, decreasing the voltage proportionality coefficients K_{pv} or decreasing the voltage integrity coefficients K_{iv} will make the system unstable under a power stepping. Decreasing the voltage proportionality coefficients K_{pv} influences the number of oscillations of active power and

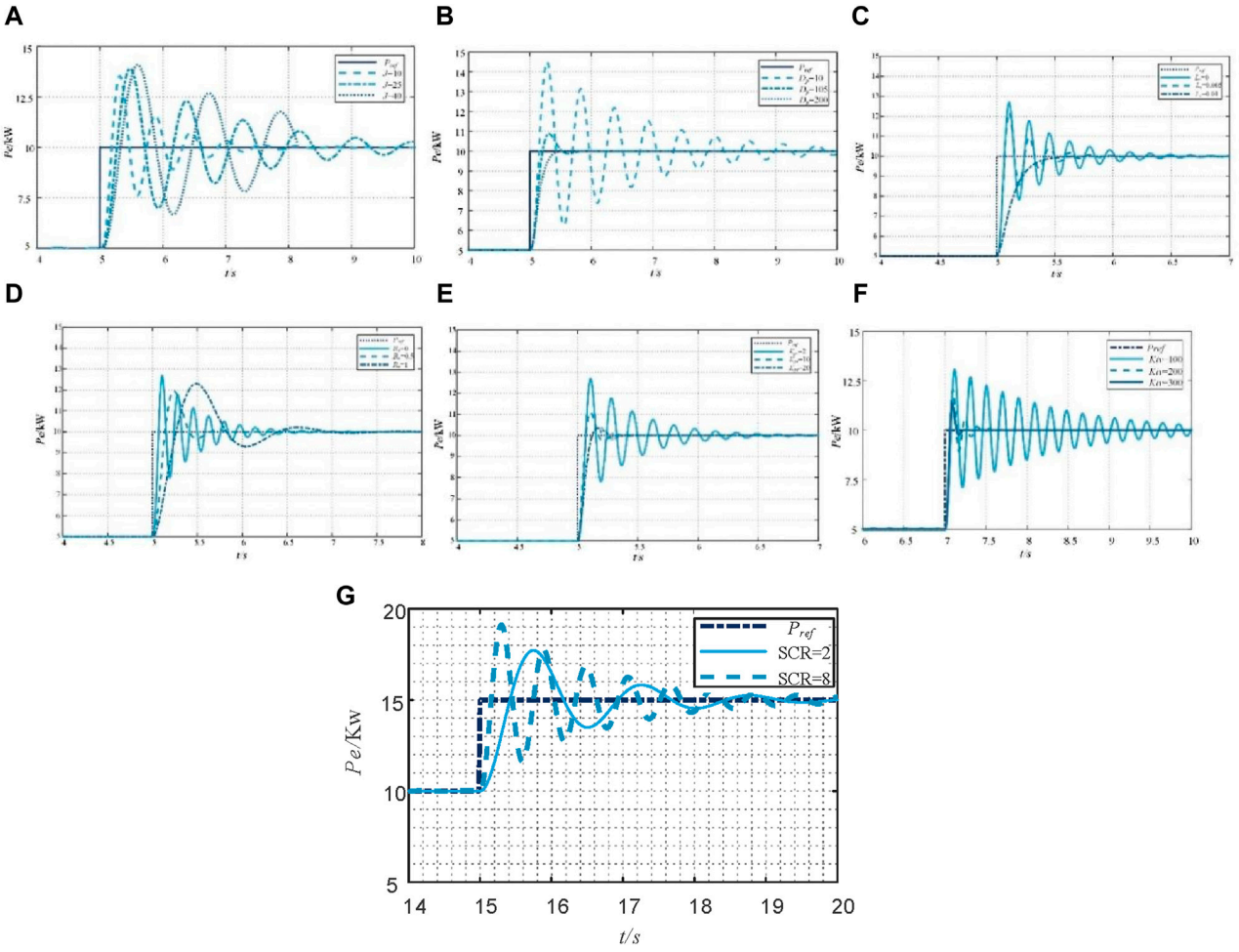

FIGURE 10
Simulation waveforms with parameters: **(A)** different virtual inertias; **(B)** different damping coefficients; **(C)** different virtual inductor; **(D)** different virtual resistors; **(E)** different proportionality coefficients; **(F)** different integrity coefficients; **(G)** different short circuit ratio.

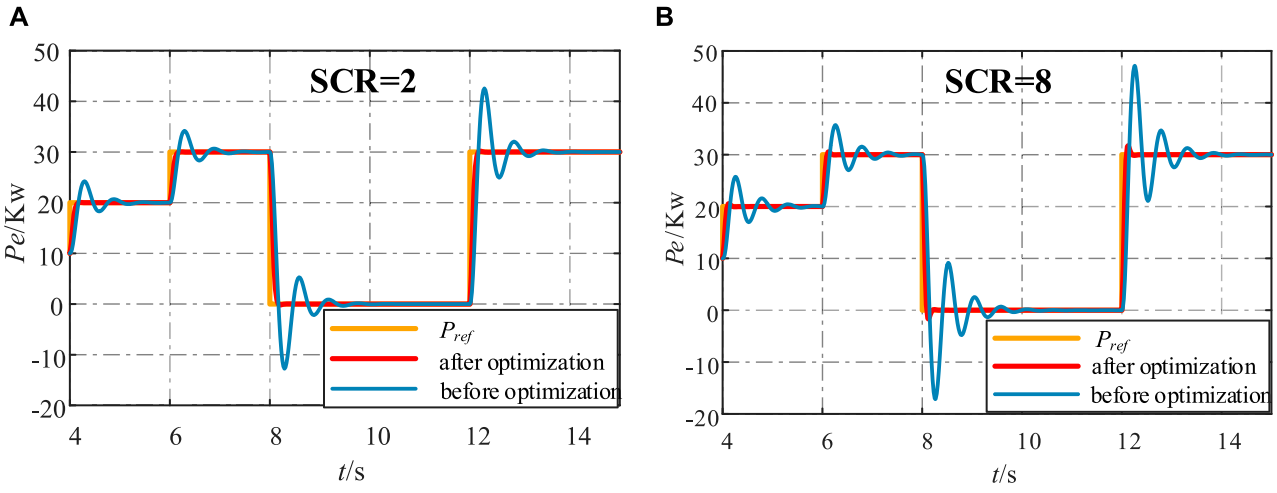

FIGURE 11
Simulation waveforms of active power before and after optimization for different short circuit ratios (SCR): **(A)** SCR = 2; **(B)** SCR = 8.

TABLE 5 VSG critically stabilized system parameters.

Parameter	Value	Parameter	Value
L_f/H	0.0008	K_p	1,592
R_f/Ω	0.03	K_q	321
C_f/F	0.0001	J	1
R_g/Ω	0.03	D_P	30
L_g/H	0.0006	K_{iq}	100
E_{gd}/V	311.127	K_{pc}	4
ω_g/(rad/s)	314.159	K_{ic}	1,500
L_r/H	0.001	K_{pv}	1.2
ω_0/(rad/s)	314.159	K_{iv}	70
R_v	0	L_v	0

frequency under power stepping, increasing the regulation time of the system. Increasing the voltage integrity coefficients K_{iv} reduces the amplitude of oscillations of active power and frequency and shortens the time for the system to reach stability.

As can be seen from Figure 10G, increasing short circuit ratio will make the system unstable under a power stepping. Increasing short circuit ratio influences the number of oscillations of active power and frequency under power stepping. And it will increase the regulation time of the system.

5.3 Parameter optimization

To verify the validity of optimization strategy derived above, the actual model was built in PSCAD according to the parameters in Table 3. In order to simulate the large perturbation, the active power reference value Pref changes rapidly from 10Kw to 20Kw at t = 4 s, 20Kw to 30Kw at t = 6 s, 30Kw to 0Kw at t = 8 s, 0 to 30Kw at t = 12 s. The active power response curves at different short circuit ratios are shown in Figure 11A, B. It can be found that the stability of the system is improved even under large disturbances after using the optimization of multiple operating points. And the optimized system performs well at different short circuit ratios.

As can be seen from Figure 11A ~ Figure 11B, Parameter optimization not only improves response speed, but also reduces oscillation amplitude. As a result, the system with optimized parameters has better response characteristics under different grid strengths and disturbances.

6 Experimental verification

To further verify the reliability and accuracy of the above theoretical analysis, a virtual synchronous machine model is built based on RT-LAB semi-physical simulation platform. And for the observation and verification, the parameters of the critically stabilized system are selected as shown in Table 5.

RT-LAB real-time simulation platform consists of an upper computer, a lower computer and a controller. The upper computer is an PC, the lower computer consists of OP5600 module produced by Opal-RT Canada, and the controller used TMS320F28379d DSP control chip. The detailed experimental platform is shown in Figure 12A. The experimental schema is shown in Figure 12B. The simulation model built in MATLAB/Simlink is put into the OP5600 real-time simulator for real-time operation, and the DSP controller receives the analog signals output from the OP5600 through the ADC module and executes the algorithmic procedures in the DSP to generate the corresponding PWM signals to be sent back to the main circuit through the digital port of the OP5600. The model realizes the complete control.

Figure 13A illustrates the variation of the eigenvalues nearest to the imaginary axis when the virtual inertia coefficient J is changed.

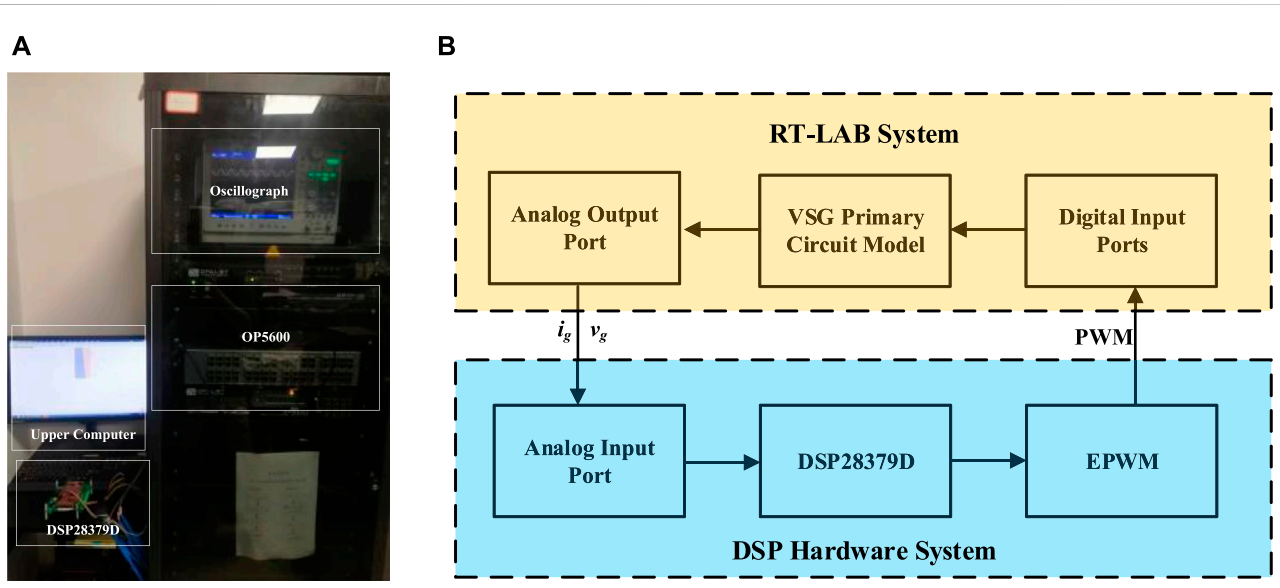

FIGURE 12
Experimental device and principle: **(A)** Experimental device; **(B)** The experimental schema.

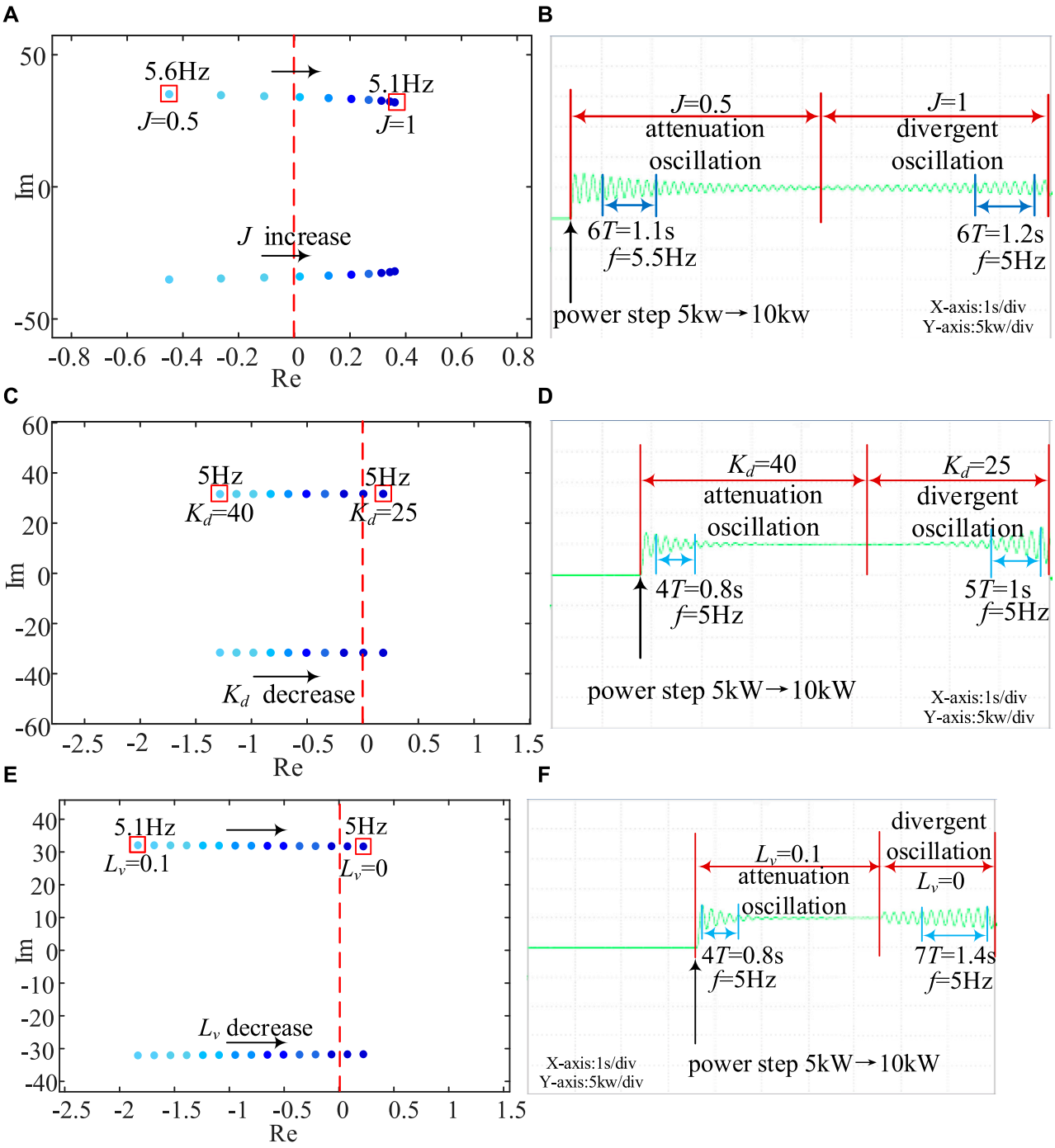

FIGURE 13
(Continued).

From the figure, it can be found that when J = 0.5, the eigenvalues are located in the left half plane and the system is in a stable state, corresponding to an oscillation frequency of 5.6 Hz for the eigenmode, and when J = 1, the eigenvalues are located in the right half plane and the system is in an unstable state, corresponding to an oscillation frequency of 5.1 Hz for the eigenmode. The experimental results in Figure 13B demonstrate this process; when J = 0.5, an active power step is applied and the output power undergoes decaying oscillations at an oscillating frequency of 5.5 Hz and the system is in a steady state. After 5 s, J is changed to 1, the output power oscillates with a 5 Hz oscillation frequency for divergence oscillation, and the system is in a destabilized state. The experimental results are the same as the theoretical analysis, which further proves that the stability of the system deteriorates with the increase of the virtual inertia coefficient J in a certain range.

Figure 13C illustrates the variation of the eigenvalues nearest to the imaginary axis during the reduction of the virtual damping

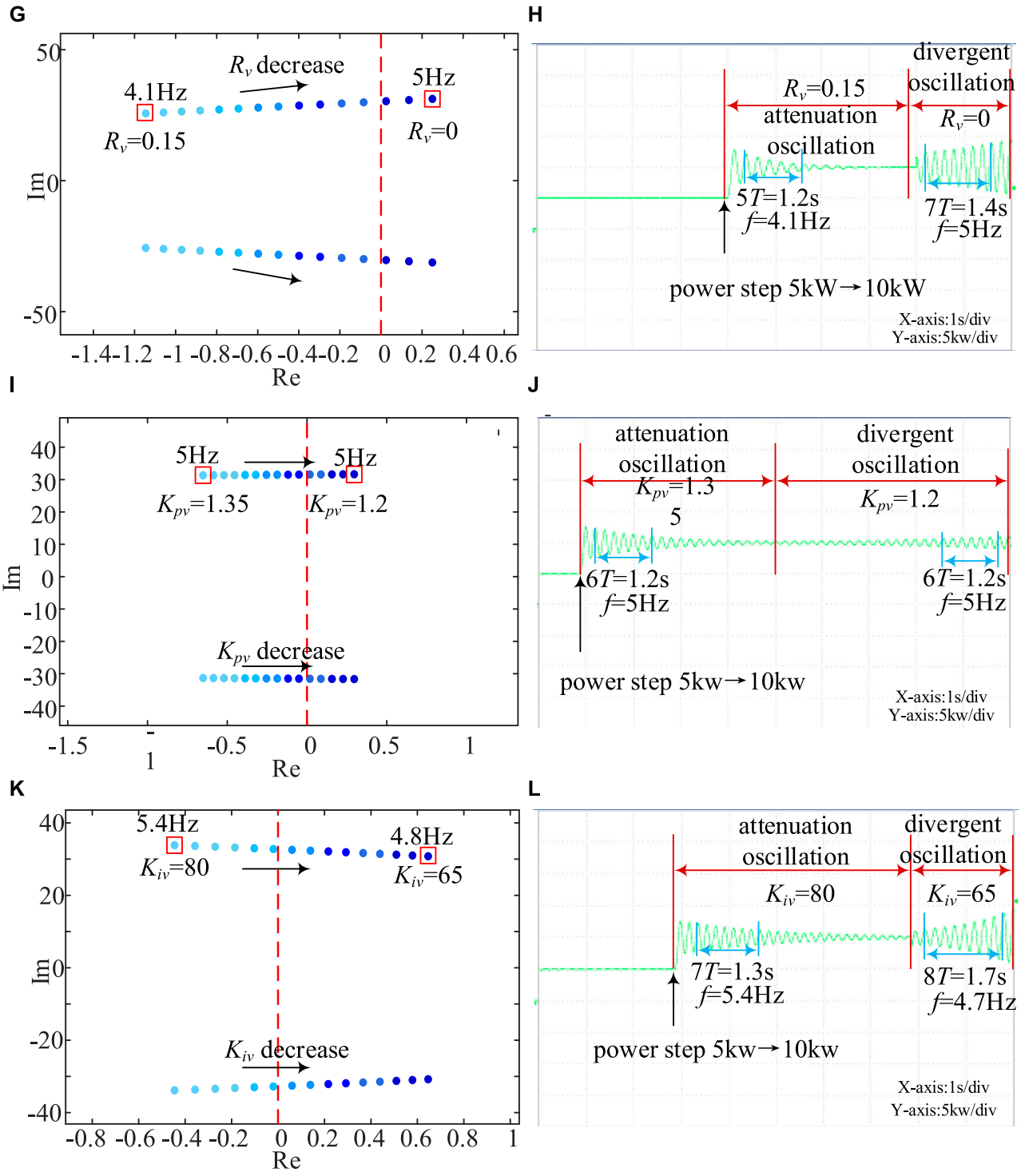

FIGURE 13
(Continued). Experimental waveform and analysis with different parameters: **(A)** Eigenvalue $\lambda_{12\sim13}$ trajectories with different J;**(B)** Active power experiment waveform with different J; **(C)** Eigenvalue $\lambda_{12\sim13}$ trajectories with different D_p;**(D)** Active power experiment waveform with different D_p; **(E)** Eigenvalue $\lambda_{12\sim13}$ trajectories with different L_v;**(F)** Active power experiment waveform with different L_v; **(G)** Eigenvalue $\lambda_{12\sim13}$ trajectories with different R_v; **(H)** Active power experiment waveform with different R_v; **(I)** Eigenvalue $\lambda_{12\sim13}$ trajectories with different K_{pv};**(J)** Active power experiment waveform with different K_{pv}; **(K)** Eigenvalue $\lambda_{12\sim13}$ trajectories with different K_{iv}; **(L)** Active power experiment waveform with different K_{iv}.

coefficient K_d from 40 to 25. From the figure, it can be found that when K_d = 40 the eigenvalues are located in the left half-plane and the system is in a stable state, which corresponds to an oscillation frequency of 5 Hz for the eigenmodes, and when K_d = 25 the eigenvalues are located in the right half-plane and the system is in a destabilized state, which corresponds to an oscillation frequency of

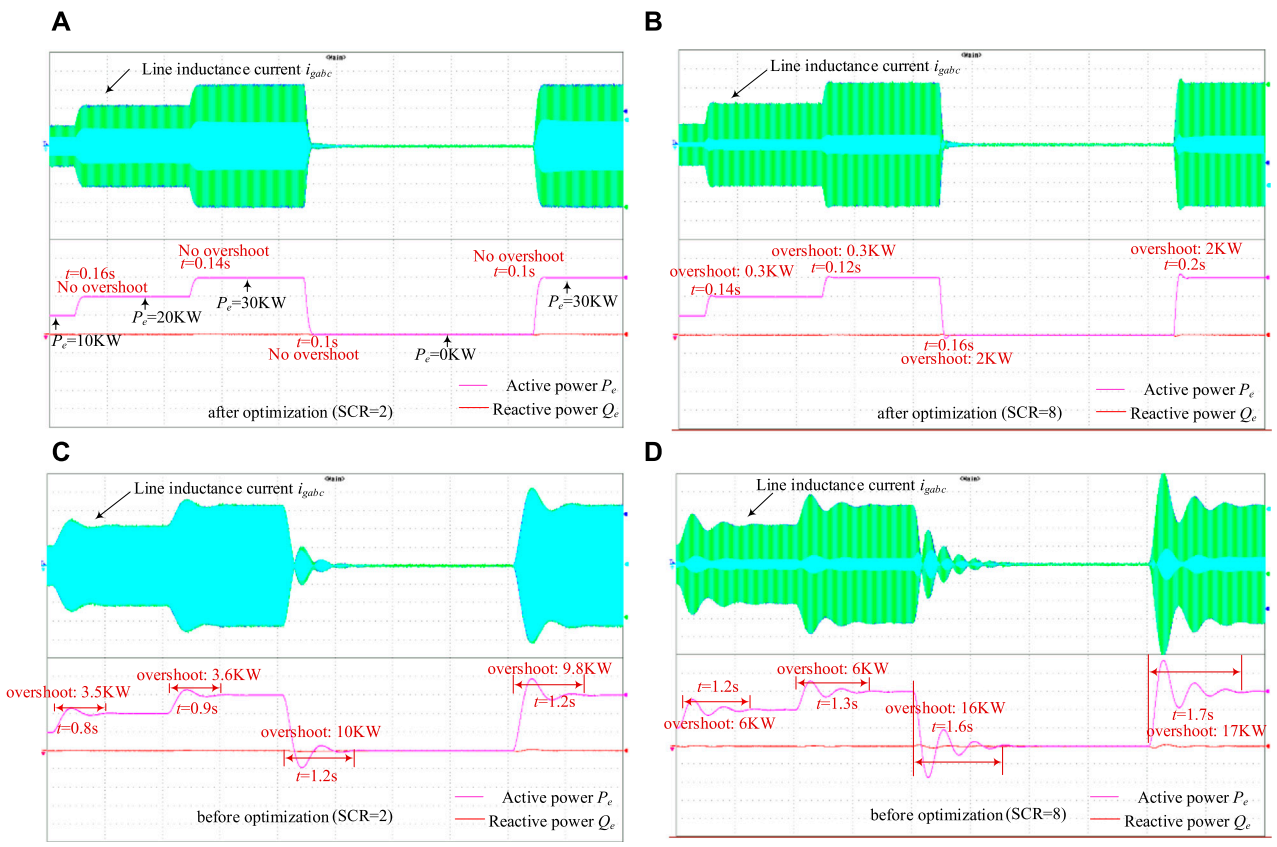

FIGURE 14
Experimental waveforms of active power before and after optimization for different short circuit ratios (SCR) **(A)** SCR = 2, after optimization **(B)** SCR = 8, after optimization **(C)** SCR = 2, before optimization **(D)** SCR = 8, before optimization.

5 Hz for the eigenmodes. The experimental results in Figure 13D demonstrate this process; when K_d = 40, an active power step is applied and the active power oscillates with a decaying frequency of 5 Hz and the system is in a steady state. After 5 s, K_d is changed to 25, the active power oscillates with 5 Hz oscillation frequency for divergence oscillation, and the system is in the destabilized state. The experimental results are the same as the theoretical analysis, which further proves that the stability of the system deteriorates with the decrease of the virtual damping coefficient K_d in a certain range.

Figure 13E illustrates the variation of the eigenvalues nearest to the imaginary axis during the reduction of the virtual reactance L_v from 0.1 to 0. From the figure, it can be found that when L_v = 0.1 the eigenvalues are located in the left half plane and the system is in a stable state, corresponding to an oscillation frequency of the eigenmode of 5.1 Hz, and when L_v = 0 the eigenvalues are located in the right half plane and the system is in a destabilized state, corresponding to an oscillation frequency of the eigenmode of 5 Hz. The experimental results in Figure 13F demonstrate this process; when L_v = 0.1, an active power step is applied and the active power undergoes decaying oscillations at an oscillating frequency of 5 Hz and the system is in a steady state. After 5 s, L_v is changed to 0, the active power oscillates with a 5 Hz oscillation frequency for divergence oscillation, and the system is in a destabilized state. The experimental results are the same as the theoretical analysis, which further proves that the stability of the system deteriorates with the decrease of the virtual reactance L_v in a certain range.

Figure 13G illustrates the variation of the eigenvalues nearest to the imaginary axis during the reduction of the virtual resistance R_v from 0.15 to 0. From the figure, it can be found that when R_v = 0.15 the eigenvalues are located in the left half-plane and the system is in a steady state, corresponding to the eigenmode with an oscillation frequency of 4.1 Hz, and when R_v = 0 the eigenvalues are located in the right half-plane and the system is in a destabilized state, corresponding to the eigenmode with an oscillation frequency of 5 Hz.The experimental results in Figure 13H demonstrate this process, when R_v = 0.15, the application of the active power step, the active power decays and oscillates at an oscillation frequency of 4.1 Hz and the system is in a steady state. After 5 s, R_v is changed to 0, and the active power oscillates with a 5 Hz oscillation frequency for divergence oscillation, and the system is in a destabilized state. The experimental results are the same as the theoretical analysis, which further proves that the stability of the system deteriorates with the decrease of the virtual resistance R_v in a certain range.

Figure 13I illustrates the variation of the eigenvalues nearest to the imaginary axis during the reduction of the net-side voltage loop

proportionality coefficient K_{pv} from 1.35 to 1.2. It can be found from the figure that the eigenvalues are located in the left half-plane when K_{pv} = 1.35, the system is in a stable state, and the corresponding eigenmode oscillates at a frequency of 5.4 Hz, and the eigenvalues are located in the right half-plane when K_{pv} = 1.2 and the system is in a destabilized state, and the oscillation frequency of the corresponding eigenmode is 5.4 Hz. The experimental results in Figure 13J demonstrate this process; when K_{pv} = 1.35, an active power step is applied and the active power undergoes decaying oscillations at an oscillating frequency of 5 Hz and the system is in a steady state. After 5 s, K_{pv} is changed to 1.2, the active power oscillates with 5 Hz oscillation frequency for divergence oscillation, and the coefficients are in a destabilized state. The experimental results are the same as the theoretical analysis, which further proves that the stability of the system deteriorates with the decrease of the proportionality coefficient K_{pv} of the grid-side voltage loop in a certain range.

Figure 13K illustrates the variation of the eigenvalue closest to the imaginary axis during the reduction of the grid-side voltage loop integration coefficient K_{iv} from 80 to 65. From the figure, it can be found that the eigenvalues are located in the left half-plane when K_{iv} = 80 and the system is in a stable state, corresponding to an oscillation frequency of the eigenmode of 5.4 Hz, and the eigenvalues are located in the right half-plane when Kiv = 65 and the system is in a destabilized state, corresponding to an oscillation frequency of the eigenmode of 4.8 Hz. The experimental results in Figure 13L demonstrate this process, when K_{iv} = 80, an active power step is applied and the active power oscillates decaying at a frequency of 5.4 Hz and the system is in a steady state. After 5 s, K_{iv} is changed to 0, the active power oscillates with a frequency of 4.7 Hz for divergence oscillation, and the system is in a destabilized state. The experimental results are the same as the theoretical analysis and simulation results, which further proves that the stability of the system deteriorates in a certain range with the decrease of the loop proportionality coefficient K_{iv} of the grid-side voltage.

The control parameters before and after optimization as shown in Table 3 were applied to the semi-physical simulation platform for experimental verification. We can compare the dynamic performance of the system by setting the power stepping with different short-circuit ratios. The experimental results are shown in Figure 14. From Figure 14, it can be seen that the unoptimized system has longer regulation times with larger overshoots for different grid strengths and different levels of disturbance. Moreover, the oscillations increase significantly with increasing short-circuit ratio. The optimized system shows better dynamic performance under different disturbances and different grid strengths.

7 Conclusion

The stability of single-VSG Grid-Connected system and global parameter optimization are studied in this paper. The system stability and parameter optimization methods are verified by experiments, and the following conclusions can be obtained:

(1) In the single-VSG grid-connected system, increasing the virtual inertia coefficient will rapidly reduce the damping ratio of the corresponding oscillation attenuation mode and deteriorate the system stability. Increasing the virtual damping coefficient, the virtual impedance parameters, the voltage loop proportionality coefficient and the voltage loop integration coefficient will increase the damping ratio and improve the system stability.

(2) The PSO algorithm is able to optimize all controller parameters of the system at the same time. that the optimized system has high control accuracy under different grid strengths and large disturbances, and the steady state and transient characteristics of the system are greatly improved.

Data availability statement

The raw data supporting the conclusions of this article will be made available by the authors, without undue reservation.

Author contributions

XS: Conceptualization, Writing–original draft, Writing–review and editing, Methodology. JC: Writing–review and editing, Software. DW: Writing–review and editing, Validation. JL: Writing–review and editing, Formal Analysis. KL: Writing–review and editing.

Funding

The author(s) declare that no financial support was received for the research, authorship, and/or publication of this article.

Conflict of interest

Authors XS, JC, DW, and JL were employed by Deqing Power Supply Company.

Publisher's note

All claims expressed in this article are solely those of the authors and do not necessarily represent those of their affiliated organizations, or those of the publisher, the editors and the reviewers. Any product that may be evaluated in this article, or claim that may be made by its manufacturer, is not guaranteed or endorsed by the publisher.

Supplementary material

The Supplementary Material for this article can be found online at: https://www.frontiersin.org/articles/10.3389/fenrg.2024.1428748/full#supplementary-material

References

Baruwa, M., and Fazeli, M. (2021). Impact of virtual synchronous machines on low-frequency oscillations in power systems. *IEEE Trans. Power Syst.* 36, 1934–1946. doi:10.1109/TPWRS.2020.3029111

Choopani, M., Hosseinian, S. H., and Vahidi, B. (2020). New transient stability and LVRT improvement of multi-VSG grids using the frequency of the center of inertia. *IEEE Trans. Power Syst.* 35, 527–538. doi:10.1109/TPWRS.2019.2928319

Coelho, E. A. A., Cortizo, P. C., and Garcia, P. F. D. (1999). "Small signal stability for single phase inverter connected to stiff AC system," in Conference Record of the 1999 IEEE Industry Applications Conference. Thirty-Forth IAS Annual Meeting (Cat. No.99CH36370), Phoenix, AZ, USA, 03-07 October 1999, 2180–2187. doi:10.1109/IAS.1999.798756

D'Arco, S., and Suul, J. A. (2014). Equivalence of virtual synchronous machines and frequency-droops for converter-based MicroGrids. *IEEE Trans. Smart Grid* 5, 394–395. doi:10.1109/TSG.2013.2288000

D'Arco, S., Suul, J. A., and Fosso, O. B. (2013). "Control system tuning and stability analysis of Virtual Synchronous Machines," in 2013 IEEE energy conversion congress and exposition, Denver, CO, USA, 15-19 September 2013 (IEEE), 2664–2671. doi:10.1109/ECCE.2013.6647045

D'Arco, S., Suul, J. A., and Fosso, O. B. (2015). Small-signal modeling and parametric sensitivity of a virtual synchronous machine in islanded operation. *Int. J. Electr. Power & Energy Syst.* 72, 3–15. doi:10.1016/j.ijepes.2015.02.005

Du, W., Fu, Q., and Wang, H. (2020). Damping torque analysis of DC voltage stability of an MTDC network for the wind power delivery. *IEEE Trans. Power Deliv.* 35, 324–338. doi:10.1109/TPWRD.2019.2933641

Du, Y., Guerrero, J. M., Chang, L., Su, J., and Mao, M. (2013). "Modeling, analysis, and design of a frequency-droop-based virtual synchronous generator for microgrid applications," in 2013 IEEE ECCE Asia downunder, Melbourne, VIC, Australia, 03-06 June 2013, 643–649. doi:10.1109/ECCE-Asia.2013.6579167

Guerrero, J. M., de Vicuna, L. G., Matas, J., Castilla, M., and Miret, J. (2004). A wireless controller to enhance dynamic performance of parallel inverters in distributed generation systems. *IEEE Trans. Power Electron.* 19, 1205–1213. doi:10.1109/TPEL.2004.833451

Guerrero, J. M., Matas, J., Garcia de Vicuna, L., Castilla, M., and Miret, J. (2007). Decentralized control for parallel operation of distributed generation inverters using resistive output impedance. *IEEE Trans. Industrial Electron.* 54, 994–1004. doi:10.1109/TIE.2007.892621

Li, C., Yang, Y., Cao, Y., Aleshina, A., Xu, J., and Blaabjerg, F. (2023). Grid inertia and damping support enabled by proposed virtual inductance control for grid-forming virtual synchronous generator. *IEEE Trans. Power Electron.* 38, 294–303. doi:10.1109/TPEL.2022.3203049

Lu, S., Zhu, Y., Dong, L., Na, G., Hao, Y., Zhang, G., et al. (2022). Small-signal stability research of grid-connected virtual synchronous generators. *Energies* 15, 7158. doi:10.3390/en15197158

Pattabiraman, D., Lasseter, R. H., and Jahns, T. M. (2018). "Comparison of grid following and grid forming control for a high inverter penetration power system," in 2018 IEEE power & energy society general meeting (PESGM), Portland, OR, USA, 05-10 August 2018 (IEEE), 1–5. doi:10.1109/PESGM.2018.8586162

Pogaku, N., Prodanovic, M., and Green, T. C. (2007). Modeling, analysis and testing of autonomous operation of an inverter-based microgrid. *IEEE Trans. Power Electron.* 22, 613–625. doi:10.1109/TPEL.2006.890003

Wu, H., Ruan, X., Yang, D., Chen, X., Zhao, W., Lv, Z., et al. (2016). Small-signal modeling and parameters design for virtual synchronous generators. *IEEE Trans. Ind. Electron.* 63, 4292–4303. doi:10.1109/TIE.2016.2543181

Wu, W., Zhou, L., Chen, Y., Luo, A., Dong, Y., Zhou, X., et al. (2019). Sequence-impedance-based stability comparison between VSGs and traditional grid-connected inverters. *IEEE Trans. Power Electron.* 34, 46–52. doi:10.1109/TPEL.2018.2841371

Xiong, L., Zhuo, F., Wang, F., Liu, X., Chen, Y., Zhu, M., et al. (2016). Static synchronous generator model: a new perspective to investigate dynamic characteristics and stability issues of grid-tied PWM inverter. *IEEE Trans. Power Electron.* 31, 6264–6280. doi:10.1109/TPEL.2015.2498933

Xu, Y., Nian, H., Hu, B., and Sun, D. (2021). Impedance modeling and stability analysis of VSG controlled type-IV wind turbine system. *IEEE Trans. Energy Convers.* 36, 3438–3448. doi:10.1109/TEC.2021.3062232

Zhang, H., Xiang, W., Lin, W., and Wen, J. (2021). Grid forming converters in renewable energy sources dominated power grid: control strategy, stability, application, and challenges. *J. Mod. Power Syst. Clean Energy* 9, 1239–1256. doi:10.35833/MPCE.2021.000257

frontiers | Frontiers in Energy Research

TYPE Original Research
PUBLISHED 07 August 2024
DOI 10.3389/fenrg.2024.1437287

OPEN ACCESS

EDITED BY
Yonghui Liu,
Hong Kong Polytechnic University, Hong Kong SAR, China

REVIEWED BY
Yuqing Dong,
The University of Tennessee, United States
Zhenxiong Wang,
Xi'an Jiaotong University, China
Huangqing Xiao,
South China University of Technology, China

*CORRESPONDENCE
Gang Shi,
peresearcher@yeah.net

RECEIVED 23 May 2024
ACCEPTED 19 July 2024
PUBLISHED 07 August 2024

CITATION
Lu Y, Shi G, Chen Q, Qiu P, Zhou J, Yang R and Zhang J (2024) Stability analysis and stabilization control of a grid-forming VSC-HVDC system.
Front. Energy Res. 12:1437287.
doi: 10.3389/fenrg.2024.1437287

Stability analysis and stabilization control of a grid-forming VSC-HVDC system

Yi Lu[1], Gang Shi[2]*, Qian Chen[1], Peng Qiu[1], Jianqiao Zhou[2], Renxin Yang[2] and Jianwen Zhang[2]

[1]Electric Power Research Institute of State Grid Zhejiang Electric Power Corporation, Hangzhou, China, [2]Department of Electrical Engineering, Shanghai Jiao Tong University, Shanghai, China

As the penetration of the integrated intermittent and fluctuating new energy (e.g., wind and photovoltaic power) increases, the conventional grid-following voltage source converter (VSC)-based high voltage direct current (HVDC) transmission system faces the problem of interactive instability with the grid. A novel grid-forming control strategy is proposed to overcome these issues, which adopts the dynamics of a DC capacitor to realize the function of self-synchronization with the grid. Moreover, the per-unit DC voltage can automatically track the grid frequency, acting as a phase-locked loop. Next, the small-signal model of the grid-forming VSC-HVDC system is established, and the stability of the system is analyzed using the eigenvalue analysis method and the complex power coefficient method. In addition, the stabilization controller is proposed for the grid-forming (GFM) control structure, which further enhances the grid-forming VSC-HVDC system's stability and helps it operate stably under both stiff and weak grid conditions. Research results show that the VSC-HVDC system under the proposed grid-forming control can work stably in both stiff and weak grids. The grid-forming VSC-HVDC system is robust and can maintain stable operations with a large range variation of the parameters in the current and voltage control loop. Simulations are carried out on the PSCAD/EMTDC platform to verify the proposed grid-forming control strategy.

KEYWORDS

grid-forming control, VSC-HVDC, state-space modeling, interaction stability, weak grid, stabilization control

1 Introduction

In recent years, new energy sources, including wind and photovoltaic power, have developed rapidly in response to the energy crisis (Liu et al., 2024). The proportion of new energy integrated into the grid and the proportion of power electronic converters in the power system have been continuously increasing (Ma et al., 2024). The renewable energy-based power system is forming a "dual high" development trend (Zhang et al., 2023). At the same time, the power grid tends to exhibit weak grid characteristics (Sang et al., 2018; Zhu et al., 2020), which can cause problems such as low inertia and abnormal interaction phenomena (Wu Q. et al., 2019), posing severe challenges to the stability of renewable power generation.

The VSC-based high voltage direct current (HVDC) system is an effective way to solve the transmission issues of high-ratio new energy. As a key component of the HVDC system, the control strategy of the VSC plays a significant role in ensuring system stability and the

quality of output power. At present, the control modes of grid-connected VSCs mainly include the grid-forming (GFM) control and the grid-following (GFL) control (Zhang et al., 2021). Under these two control modes, the grid-connected VSCs reflect the external characteristics of the current source and voltage source, respectively (Zhang et al., 2023; Pawar et al., 2021). The conventional VSC adopts the GFL control strategy, where the phase-locked loop (PLL) is employed to measure the voltage phase in the point of common connection (PCC) and adjust the output current to control the grid-connected power. However, due to the abnormal interference between the PLL and the grid's impedance, the interactive stability margin of the grid-connected VSC gradually decreases with the reduction of the short-circuit ratio (SCR), triggering oscillation instability. Wang et al. (2020) and Wang et al. (2019) noted that the dynamic coupling between the PLL and grid impedance occurs under weak grid conditions, and the coupling degree will exacerbate with the increase of the PLL's bandwidth. To improve the stability of the GFL VSC, Huang et al. (2022) present a voltage regulation control strategy that improves the synchronous operating performance of GFL VSC by automatically adjusting the input of PLL. Shao et al. (2021) proposed a modified design method of the PLL's parameters to reduce the negative impact of PLL dynamics under weak grid conditions.

Compared with the GFL VSC, the VSC under the GFM control has better stability in a weak grid (Fu et al., 2021). Unlike the GFL strategy, the GFM control strategy does not need PLL and realizes the autonomous synchronization with the grid according to the power or DC-link voltage synchronization principle. The GFM control strategies mainly include the virtual synchronous generator (VSG) control, the droop control, and the matching control (Pan et al., 2020). Meng et al. (2019) proposed a generalized droop control strategy, where the inverter can offer virtual damping and virtual inertia without large overshoot and oscillation by adding an auxiliary controller. In addition, Meng et al. (2019) also noted that the generalized droop control can be equivalent to the droop control or VSG control strategy by adjusting the parameters. Aiming at the problem of low inertia and lacking frequency fluctuation caused by the renewable energy integration, Zha et al. (2021) adopted the electric torque model to analyze the inertia support characteristics and the system stability and noted that the VSC had better inertia support characteristics under the generalized droop control. Ge et al. (2023) established the model of the VSG-based VSC, and the support effect of VSG-based VSC was deeply studied with different inertia parameters. The sequence impedance model of VSG-based VSC was built and compared with that of the conventional VSC by Wu W. et al. (2019) through the harmonic linearization method, and the analysis results indicated the VSG-based VSC's sequence impedance is essentially the same as the grid impedance, which means the VSG-based VSC is more stable than the conventional VSC under weak grid conditions. Li et al. (2022) analyzed the voltage and frequency stability of VSG-based VSC by establishing the small-signal model and proposed an improved control method to enhance the inertia and damping. However, these above droop and VSG control strategies Wu W. et al. (2019), Meng et al. (2019), Pan et al. (2020), Zha et al. (2021), Li et al. (2022), and Ge et al. (2023) take the active power as control targets and are applicable to grid-connected VSCs with stable and controllable motive power. With respect to the receiving end converter (REC), that is, the grid-connected VSC in the HVDC transmission system with intermittent and fluctuating input motive power, it is still essential to investigate a novel GFM control strategy with the DC-side voltage as the control target.

Recently, a kind of GFM control method with the DC-side voltage as the control objective has been proposed. A GFM control method called inertia synchronization control (ISynC) was presented by Sang et al. (2019) based on the matching principle between the DC voltage and the synchronous generator (SG). In Shao et al. (2019a) and Shao et al. (2019b), the ISynC-based GFM control strategy was applied to the doubly fed induction generator (DFIG)-based wind turbine, which makes the DC-side voltage track the grid frequency instantaneously, thus, the inertia response of the DFIG-based wind turbine can be achieved. Yang et al. (2018) utilized the ISynC-based GFM control method in the VSC-HVDC system, and the frequency tracking capability was useful in realizing the function of inertia support. Moreover, in Yang et al. (2020), the ISynC-based GFM control method was further expanded to the multi-port VSC-HVDC, which was able to establish the DC grid based on the droop control. Nevertheless, there is no current control loop in the ISynC-based GFM VSC (Shao et al., 2019a; Shao et al., 2019b; Sang et al., 2019), which cannot limit the output current and is not conducive to practical engineering applications.

Oriented to the VSC-HVDC transmission system with intermittent and fluctuating input motive power, a novel GFM control method taking the DC-side voltage as the control target is proposed in this article, which has the function of autonomously synchronizing the grid. The internal current control loop is added to the GFM structure; thus, the function of limiting the output current can be achieved, which makes the proposed GFM control strategy suitable for practical engineering applications. The GFM VSC-HVDC's small-signal model is built, and the stability of the system is analyzed using the eigenvalue analysis method and the complex power coefficient method. In addition, the stabilization controller is proposed for the GFM control structure, which further enhances the GFM VSC-HVDC's stability and helps it operate stably under both stiff and weak grid conditions.

2 Configuration of VSC-HVDC and grid-forming control

2.1 System configuration

Figure 1 presents the configuration of the VSC-HVDC transmission system, where renewable energy (e.g., wind farm) is integrated into the sending-end converter (SEC). The DC line is between the SEC and the REC, the voltage of the DC-side equivalent capacitor is u_{dc}, the SEC is integrated into the utility grid via an LC filter, and R_d is the damping resistor.

As seen in Figure 1, the dynamic equation of the REC's capacitor voltage can be expressed in Eq. 1 as

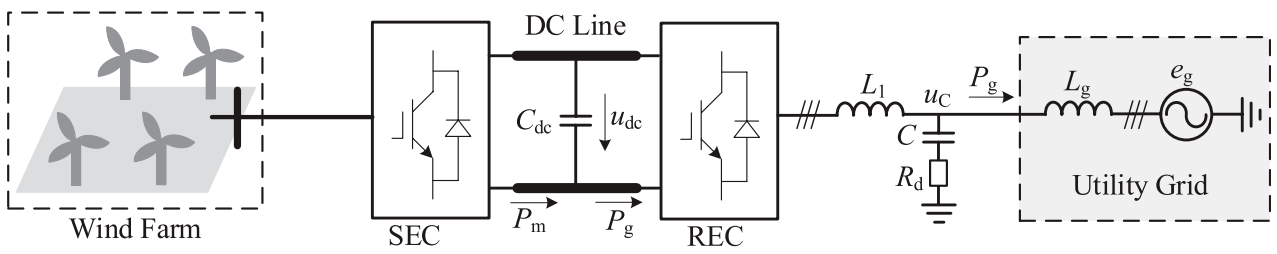

FIGURE 1
Configuration of the VSC-HVDC transmission system.

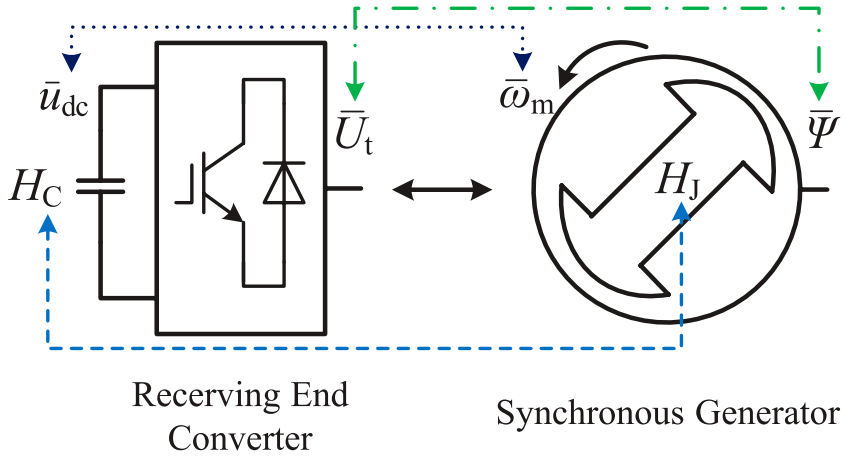

FIGURE 2
Matching relationship between the REC and the SG.

$$2H_C\left(\bar{u}_{dc0}\frac{d\bar{u}_{dc}}{dt}\right) = \bar{P}_m - \bar{P}_g, \tag{1}$$

where $\bar{P}_g$ is the REC's output per-unit active power, $\bar{P}_{\mathrm{m}}$ is the SEC's output per-unit active power, $\bar{u}_{\mathrm{dc}}$ is the DC-side voltage in the per-unit form, $\bar{u}_{\mathrm{dc0}}$ is the steady-state DC-side voltage in the per-unit form, and H_C is the DC-side capacitor's equivalent time constant.

The REC's output active power $\bar{P}_g$ is derived in Eq. 2 by

$$\bar{P}_g = \frac{\bar{u}_{\mathrm{dc}}\bar{U}_{\mathrm{t}}\bar{E}_{\mathrm{g}}}{\bar{x}_{\mathrm{g}}}\sin\delta, \tag{2}$$

where $\bar{U}_{\mathrm{t}}$ is the SEC's modulation voltage amplitude in the per-unit form, $\bar{E}_{\mathrm{g}}$ is the grid voltage amplitude in the per-unit form, $\bar{x}_{\mathrm{g}}$ is the grid line inductance in the per-unit form, and δ is the power angle.

With respect to SG in the grid, the motion equation of the rotor is represented in Eq. 3 as

$$2H_J\left(\bar{\omega}_m\frac{d\bar{\omega}_m}{dt}\right) = \bar{P}_M - \bar{P}_e, \tag{3}$$

where $\bar{P}_M$ is the SG's input active power in the per-unit form, $\bar{P}_e$ is the SG's electromagnetic power in the per-unit form, $\bar{\omega}_m$ is the SG's rotor speed in the per-unit form, and $\mathrm{H_J}$ is the equivalent time constant of the SG's rotor.

The SG's input active power $\bar{P}_M$ is expressed in Eq. 4 as

$$\bar{P}_M = \frac{\bar{\psi}\bar{\omega}_{\mathrm{m}}\bar{E}_{\mathrm{g}}}{\bar{x}_{\mathrm{g}}}\sin\delta_G, \tag{4}$$

where $\bar{\psi}$ is the SG's per-unit flux linkage and δ is the power angle of the SG.

Comparing (1) with (3) shows that the dynamical equation of the REC's capacitor voltage is similar to the motion equation of the SG's rotor. According to the similarity principle, the analogy relationship between the REC and the SG can be obtained, as shown in Figure 2. Comparing (2) with (4), the REC's per-unit modulation voltage amplitude $\bar{U}_t$ is analogized to the SG's per-unit flux linkage $\bar{\psi}$, and the time constant H_C of the DC-link equivalent capacitor is analogized to the time constant H_J.

2.2 Grid-forming control strategy

The control target of the presented grid-forming control method is the converter's DC-side voltage. Currently, according to different control objectives, existing grid-forming control methods can be divided into two groups, namely, the GFM control under the active power control mode and the GFM control under the DC-side voltage control mode. The VSG control belongs to the GFM control under the active power

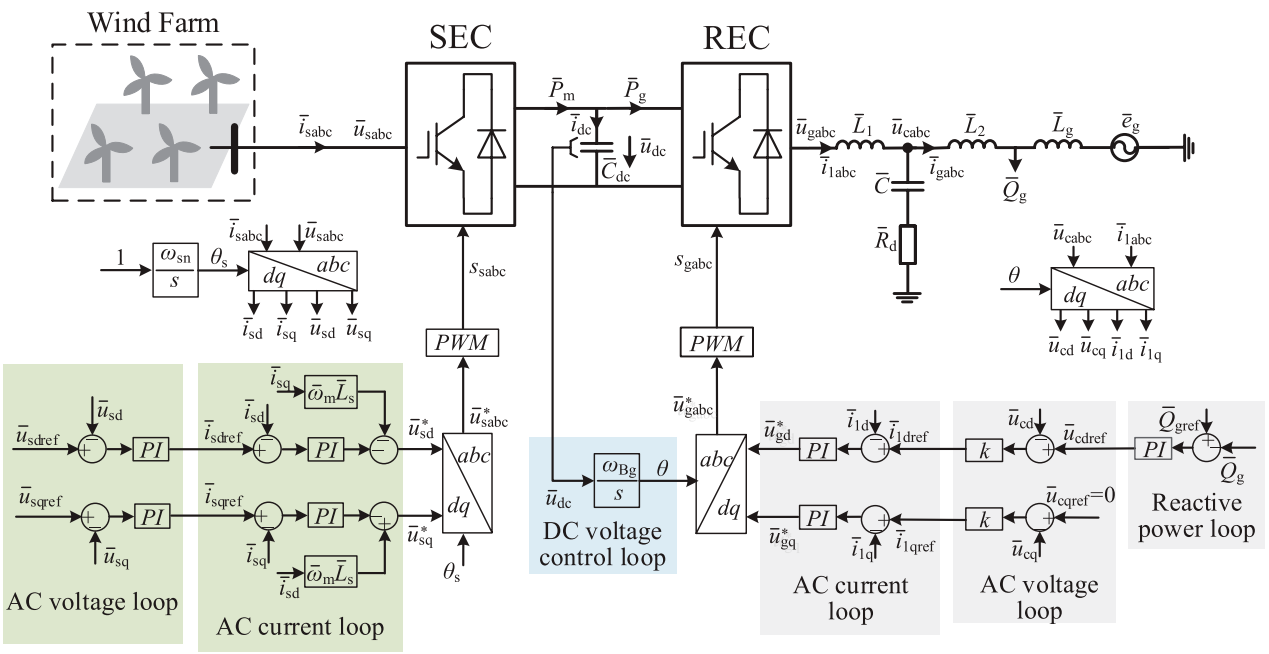

FIGURE 3
Grid-forming control structure of the VSC-HVDC system.

control mode, which is suitable for scenarios with a controllable input source, such as energy storage. Different from the VSG control, the proposed GFM control takes the DC voltage as the control objective, which is suitable for the two-stage conversion scenario with intermittent and fluctuating input motive power.

Figure 3 gives the VSC-HVDC system's grid-forming control structure, where the REC adopts the grid-forming control strategy with three cascaded loops, and the SEC utilizes the conventional two cascaded loops. The REC takes the DC-side voltage and the reactive power as the control objectives. In the REC's control diagram, the DC-side voltage of the REC passes through an integrator whose gain is the rated value of the grid's angular frequency ω_{Bg}, and the output is the phase θ of the REC's modulation voltage.

According to the matching relationship in Figure 2, the DC-side voltage of the REC can be analogized to the SG's rotor speed. The linkage between the AC-side angular frequency of the REC and the DC voltage is established so that it meets the following conditions:

$$\bar{\omega}_{REC} = \bar{u}_{dc,} \tag{5}$$

where $\bar{\omega}_{REC}$ is the AC-side angular frequency of the REC.

Based on the control principle given by Equation 5, when the active power sent by the SEC to the DC capacitor increases, the DC-side voltage increases. According to the relationship in Equation 5, the AC-side angular frequency $\bar{\omega}_{REC}$ of the REC increases, corresponding to an increase in the power angle δ, thus increasing the REC's output active power and maintaining the DC-side voltage constant. This method achieves self-synchronization according to the DC-side capacitor's inertia.

In the outer reactive power control loop of the REC, the difference between the reactive power reference $\bar{Q}_{gref}$ and the feedback-reactive power $\bar{Q}_g$ passes through a PI regulator to obtain the d-axis reference $\bar{u}_{cdref}$ of the AC capacitor voltage. The q-axis reference $\bar{u}_{cqref}$ of the AC capacitor voltage is 0. In the middle AC voltage control loop of the REC, the differences between the d-axis and q-axis reference of the AC capacitor voltage and the feedback value, respectively, multiplied by the virtual impedance coefficient k are the d-axis and q-axis references of the REC's output current. In the inner AC current control loop of the REC, the difference between the d-axis and q-axis references of the AC current and the feedback value, respectively, passes through the PI regulator, and the output is the d-axis and q-axis components of the REC's modulation voltage.

Different from the ISynC-based GFM control (Wu W. et al., 2019; Li et al., 2022; Ge et al., 2023), the inner current loop is added to the GFM structure in this article, which can limit the output current. The control structure shown in Figure 3 can enable the REC to provide frequency support and realize the grid-forming function.

The SEC takes the AC voltage as the control objective. In the control diagram of the REC, the rated per-unit value of the SEC's AC frequency, that is, 1 p.u., passes through an integrator whose gain is the rated value of the SEC's rated angular frequency ω_{sn}, and the output is the phase θ_s of the SEC's modulation voltage. In the outer AC voltage control loop of the SEC, the difference between the d-axis reference $\bar{u}_{sdref}$ and the q-axis reference $\bar{u}_{sqref}$ of the SEC's AC voltage and the feedback value, respectively, multiplied by the PI regulator are the d-axis reference $\bar{i}_{sdref}$ and the q-axis reference $\bar{i}_{sqref}$ of the SEC's input current. In the inner AC current control loop of the SEC, the difference between the d-axis reference $\bar{i}_{sdref}$ and the q-axis reference $\bar{i}_{sqref}$ of the AC current and the feedback value,

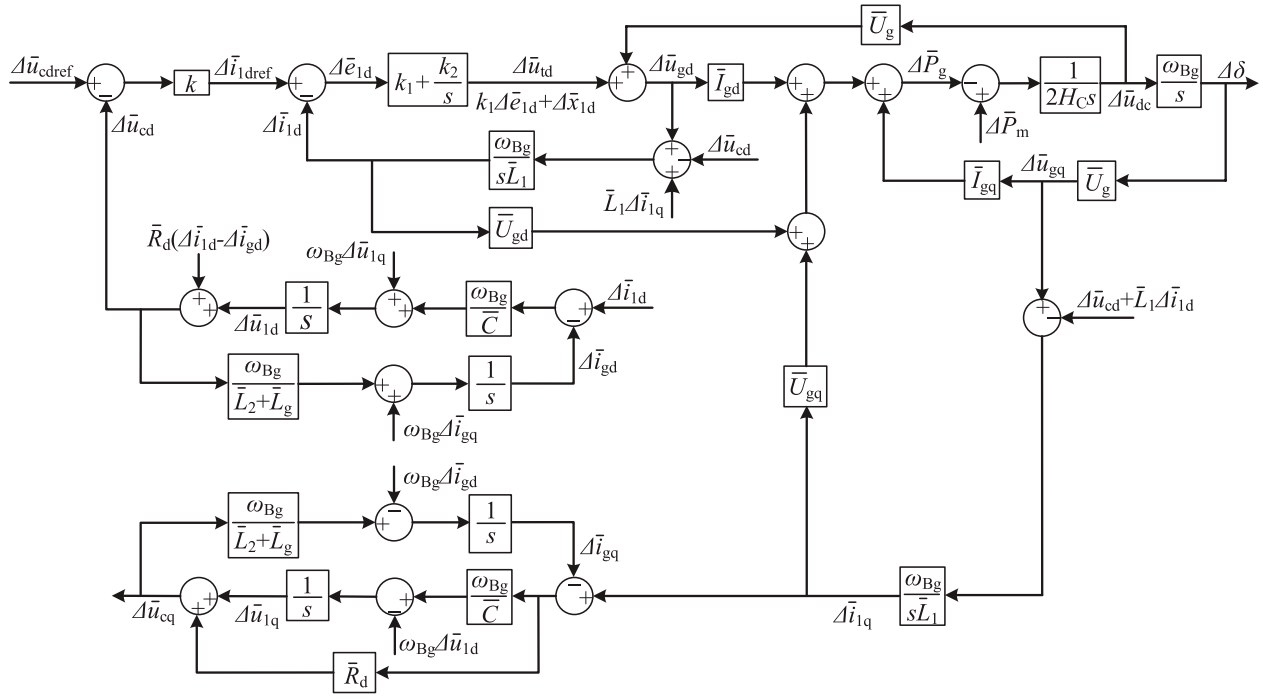

FIGURE 4
Small-signal control diagram of the VSC-HVDC system under the GFM control.

respectively, passes through the controller, and the output is the d-axis component and q-axis component of the SEC's modulation voltage.

Other variable symbols in Figure 3 are explained as follows. $\bar{u}_{cabc}$ is the AC capacitor's voltage in the per-unit form. $\bar{u}_{cd}$ and $\bar{u}_{cq}$ are the d-axis and q-axis voltages, respectively, of the AC capacitor in the per-unit form. $\bar{i}_{1abc}$ is the filter inductor's current in the per-unit form. $\bar{i}_{1d}$ and $\bar{i}_{1q}$ are the d-axis and q-axis current of the filter inductor in the per-unit form, respectively. $\bar{u}_{gabc}$ is the REC's voltage in the per-unit form. $\bar{u}^*_{gabc}$is the modulation voltage of the REC in the per-unit form. $\bar{u}^*_{gd}$ and $\bar{u}^*_{gq}$ are the d-axis and q-axis modulation voltages of the REC in the per-unit form, respectively. $\bar{i}_{1dref}$ and $\bar{i}_{1qref}$ are the d-axis and q-axis reference currents of the inductor's current in the per-unit form, respectively. $\bar{u}_{sabc}$ is the SEC's AC voltage in the per-unit form. $\bar{u}_{sd}$ and $\bar{u}_{sq}$ are SEC's d-axis and q-axis AC voltages in the per-unit form, respectively. $\bar{i}_{sabc}$ is the three-phase current of the SEC in the per-unit form. $\bar{i}_{1d}$ and $\bar{i}_{1q}$ are the d-axis and q-axis currents of the SEC in the per-unit form, respectively. $\bar{u}^*_{sabc}$ is the three-phase modulation voltage of the SEC in the per-unit form. $\bar{u}^*_{sd}$ and $\bar{u}^*_{sq}$ are the d-axis and q-axis modulation voltages of the SEC in the per-unit form, respectively.

3 Small-signal modeling and stability analysis

In this article, the state-space model-based analysis method is utilized to research the interaction stability between the grid-forming VSC-HVDC system.

3.1 State-space modeling

After linearizing the grid-forming VSC-HVDC system's control structure, as shown in Figure 3, the small-signal control block diagram shown in Figure 4 can be obtained. For the SEC of the GFM VSC-HVDC system, due to the application of compensation modulation, the SEC's AC voltage is not relevant to the DC voltage. Thus, the small-signal control diagram of the VSC-HVDC in Figure 4 only covers the REC.

The state variable Δx is selected in Eq. 6 as

$$\Delta x = \left[\Delta\bar{u}_{dc}, \Delta\delta, \Delta\bar{i}_{1d}, \Delta\bar{i}_{1q}, \Delta\bar{i}_{gd}, \Delta\bar{i}_{gq}, \Delta\bar{u}_{cd}, \Delta\bar{u}_{cq}, \Delta\bar{x}_{1d}\right], \quad (6)$$

where $\Delta\bar{u}_{dc}$ is the variation of the DC-side voltage in the per-unit form, $\Delta\delta$ is the phase variation of the REC's AC-side voltage, $\Delta\bar{i}_{1d}$ is the variation of the per-unit d-axis output current, $\Delta\bar{i}_{1q}$ is the variation of the q-axis output current in the per-unit form, $\Delta\bar{i}_{gd}$ is the variation of the d-axis current in the per-unit form, $\Delta\bar{i}_{gq}$ is the variation of the q-axis current in the per-unit form, $\Delta\bar{u}_{cd}$ is the variation of per-unit d-axis capacitor voltage, $\Delta\bar{u}_{cq}$ is the variation of the per-unit q-axis capacitor voltage, and $\Delta\bar{x}_{1d}$ is the variation of the per-unit d-axis current integral regulator's output.

Based on the small-signal diagram in Figure 4, the state-space equation of the grid-forming VSC-HVDC system is derived in Eq. 7 as

$$\frac{d\Delta x}{dt} = H\Delta x, \quad (7)$$

where H is the state-space matrix of a grid-forming VSC-HVDC system.

TABLE 1 Parameters of the grid-forming VSC-HVDC system.

Variable	Description	Value
e_{gL}	Effective value of the grid line voltage	100 kV
f_n	Rated frequency of the grid	50 Hz
f_s	Switching frequency of the converter station	2 kHz
U_{dc}	Rated DC-link voltage	200 kV
C_{dc}	DC-link capacitance	70 μF
P_{gn}	Rated output active power	200 MW
Q_{gn}	Rated output reactive power	0 Var
k_{qp}	Reactive power control loop's proportional gain	0.01
k_{qi}	Reactive power control loop's integral gain	10
k	Virtual impedance coefficient	0.75
k_1	Current control loop's proportional gain	0.05
k_2	Current control loop's integral gain	1

The state-space matrix H can be represented in Eqs 8–11 as

$$H = A + BC, \tag{8}$$

where

$$A = \begin{bmatrix} -\frac{\bar{I}_{gd}\bar{U}_g}{2H_C} & -\frac{\bar{I}_{gq}\bar{U}_g}{2H_C} & -\frac{\bar{U}_g}{2H_C} & 0 & 0 & 0 & 0 & 0 & 0 \\ \omega_{Bg} & 0 & 0 & 0 & 0 & 0 & 0 & 0 & 0 \\ \frac{\omega_{Bg}\bar{U}_g}{\bar{L}_1} & 0 & -\frac{\omega_{Bg}\bar{R}_d}{\bar{L}_1} & \omega_{Bg} & \frac{\omega_{Bg}\bar{R}_d}{\bar{L}_1} & 0 & -\frac{\omega_{Bg}}{\bar{L}_1} & 0 & 0 \\ 0 & \frac{\omega_{Bg}\bar{U}_g}{\bar{L}_1} & -\omega_{Bg} & -\frac{\omega_{Bg}\bar{R}_d}{\bar{L}_1} & 0 & \frac{\omega_{Bg}\bar{R}_d}{\bar{L}_1} & 0 & -\frac{\omega_{Bg}}{\bar{L}_1} & 0 \\ 0 & 0 & \frac{\omega_{Bg}\bar{R}_d}{\bar{L}_2+\bar{L}_g} & 0 & -\frac{\omega_{Bg}\bar{R}_d}{\bar{L}_2+\bar{L}_g} & \omega_{Bg} & \frac{\omega_{Bg}}{\bar{L}_2+\bar{L}_g} & 0 & 0 \\ 0 & 0 & 0 & \frac{\omega_{Bg}\bar{R}_d}{\bar{L}_2+\bar{L}_g} & -\omega_{Bg} & -\frac{\omega_{Bg}\bar{R}_d}{\bar{L}_2+\bar{L}_g} & 0 & \frac{\omega_{Bg}}{\bar{L}_2+\bar{L}_g} & 0 \\ 0 & 0 & \frac{\omega_{Bg}}{\bar{C}} & 0 & -\frac{\omega_{Bg}}{\bar{C}} & 0 & 0 & \omega_{Bg} & 0 \\ 0 & 0 & 0 & \frac{\omega_{Bg}}{\bar{C}} & 0 & -\frac{\omega_{Bg}}{\bar{C}} & -\omega_{Bg} & 0 & 0 \\ 0 & 0 & -k_2 & 0 & 0 & 0 & 0 & 0 & 0 \end{bmatrix}, \tag{9}$$

$$B = \begin{bmatrix} 0 & 0 & 0 & 0 & 0 & 0 & 0 & 0 & k_2 \\ \frac{\bar{I}_{gd}}{2H_C} & 0 & \frac{\omega_{Bg}}{\bar{L}_1} & 0 & 0 & 0 & 0 & 0 & 0 \end{bmatrix}^T, \tag{10}$$

$$C = \begin{bmatrix} 0 & 0 & -k\bar{R}_d & 0 & k\bar{R}_d & 0 & -k & 0 & 0 \\ 0 & 0 & -k_1 - kk_1\bar{R}_d & 0 & kk_1\bar{R}_d & 0 & -kk_1 & 0 & 1 \end{bmatrix}. \tag{11}$$

3.2 Small-signal stability analysis

The characteristic equation of the grid-forming VSC-HVDC system is derived in Eq. 12 as

$$f = \det(\lambda I - H), \tag{12}$$

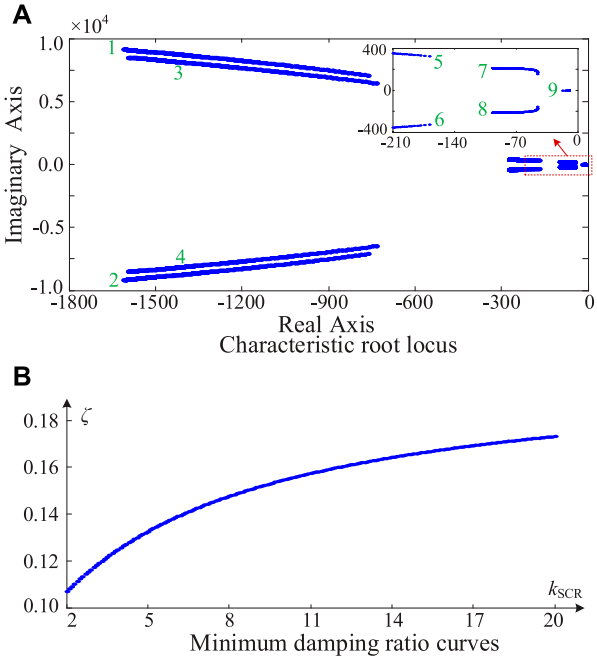

FIGURE 5
Characteristic root locus and minimum damping ratio curves with the change of SCR. **(A)** Characteristic root locus. **(B)** Minimum damping ratio curves.

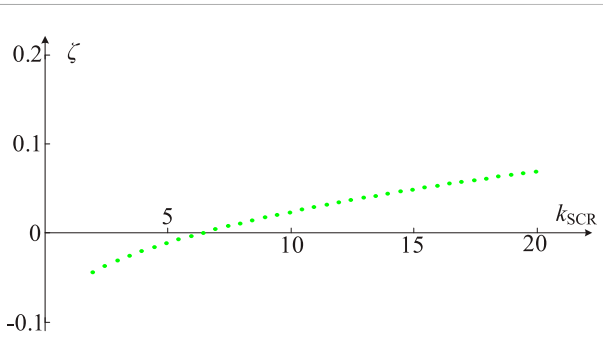

FIGURE 6
Minimum damping ratio curves of the grid-following VSC-HVDC with the change of SCR.

where λ is the eigenvector, and I is the identity matrix.

The eigenvalues $\lambda_1, \lambda_2, ., \lambda_n$ of the GFM VSC-HVDC system can be derived by setting the value of (12) to 0. The quantitative index of small-signal stability margin for the grid-forming VSC-HVDC system is obtained as

$$\zeta = \min_{i=1\longrightarrow n}\left[-\frac{real(\lambda_i)}{|\lambda_i|}\right], \tag{13}$$

where real (λ_i) represents the real part of the eigenvalues λ_i, and $|\lambda_i|$ represents the amplitude of the eigenvalues λ_i.

It can be seen from Equation 13 that the quantitative index ζ represents the system's characteristics of electrical damping, which can measure the small-signal stability margin. If the value of λ is

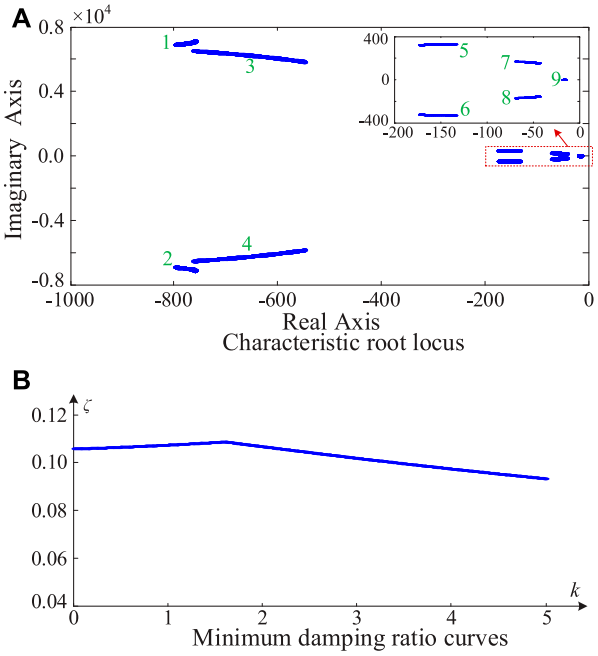

FIGURE 7
Characteristic root locus and minimum damping ratio curves as the virtual impedance coefficient changes. **(A)** Characteristic root locus. **(B)** Minimum damping ratio curves.

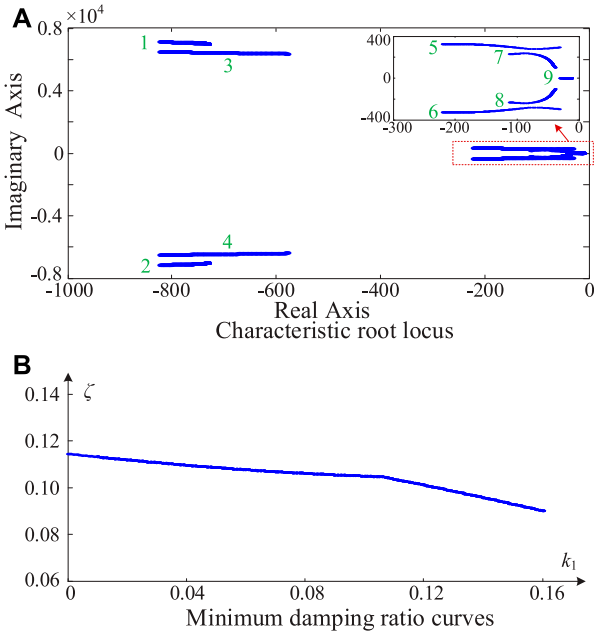

FIGURE 8
Characteristic root locus and minimum damping ratio curves as the current control loop's proportional gain changes. **(A)** Characteristic root locus. **(B)** Minimum damping ratio curves.

greater than 0, the GFM VSC-HVDC system can work stably. If the value of λ is negative, the GFM VSC-HVDC system cannot work stably.

Based on parameters in Table 1 and the state-space model, Figure 5 presents the characteristic root locus and minimum damping ratio curves with the change of the short-circuit ratio (SCR) k_{SCR}, where k_{SCR} is equal to the reciprocal of the grid line inductance $\bar{L}_g$ in the per-unit form. In Figure 5A, with the change of k_{SCR} from 20 to 2, the nine root trajectories are all located in the left half plane, which means the grid-forming VSC-HVDC system can work stably in both stiff and weak grids. In Figure 5B, the quantitative index ζ of the small-signal stability margin for the grid-forming VSC-HVDC system decreases slowly as k_{SCR} declines from 20 to 2, but the value of ζ is still greater than 0.1. Research results in Figure 5 indicate that the presented grid-forming method has good grid adaptability, which can guarantee the stable working of the VSC-HVDC system.

For the grid-following VSC-HVDC system (Yang et al., 2020), Figure 6 presents the minimum damping ratio curves as the SCR changes, where the REC adopts the conventional vector control, the outer DC voltage loop's control bandwidth is 20 Hz, the inner current loop's control bandwidth is 200 Hz, and the PLL's control bandwidth is 50 Hz. It can be seen from Figure 6 that with the decrease of the SCR from 20 to 2, the minimum damping ratio curves of the grid-following VSC-HVDC gradually decrease below 0, which shows that the grid-following VSC-HVDC can operate stably under the stiff grid condition and will lose stability in a weak grid. Comparing Figures 5, 6 demonstrates that the proposed grid-forming control strategy in this article has better stability than the conventional grid-following VSC-HVDC.

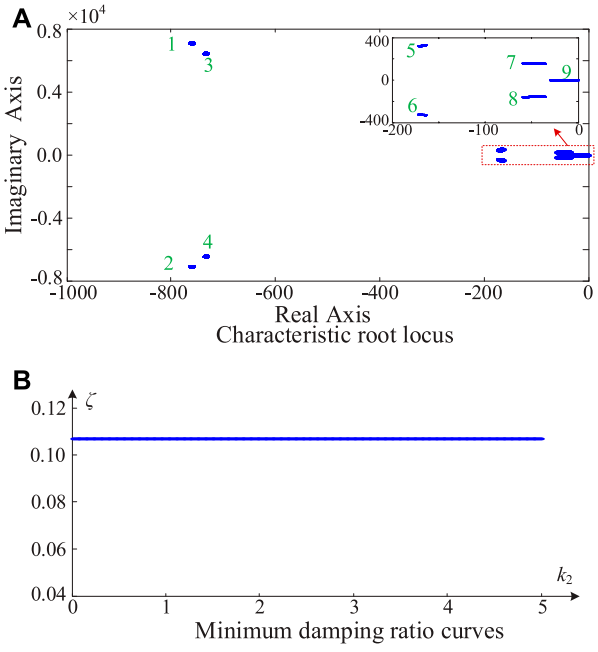

FIGURE 9
Characteristic root locus and minimum damping ratio curves with the change of the current control loop's integral gain. **(A)** Characteristic root locus. **(B)** Minimum damping ratio curves.

Figure 7 presents the characteristic root locus and minimum damping ratio curves with the change of the virtual impedance coefficient, where the SCR is 2, the current loop's proportional gain k_1 is 0.05, and the current loop's integral gain k_2 is 1. It can be seen

from Figure 7A that when the virtual impedance coefficient k increases from 0 to 5, the nine root trajectories of the system are all distributed in the left half plane, corresponding to the stable operations of the grid-forming VSC-HVDC system. Furthermore, when the virtual impedance coefficient k increases from 0 to 5, the minimum damping ratio of the system first increases and then decreases, but it is always greater than 0. Research results shown in Figure 7 illustrate that the VSC-HVDC system under the proposed grid-forming control is robust and can maintain stable operations with a large range variation of the voltage loop parameters.

Figure 8 presents the characteristic root locus and minimum damping ratio curves as the proportional gain k_1 of the current control loop changes, where the SCR is 2, the virtual impedance coefficient k is 0.75, and the current loop's integral gain k_2 is 1. In Figure 8A, when the current loop's proportional gain k_1 increases from 0 to 0.16, the nine root trajectories of the system are all distributed in the left half plane, corresponding to the stable operations of the grid-forming VSC-HVDC system. Moreover, in Figure 8B, when the current control loop's proportional gain k_1 increases from 0 to 0.16, the minimum damping ratio of the system decreases, but it is always greater than 0. Research results in Figure 8 demonstrate that the VSC-HVDC system under the proposed grid-forming control is robust and can maintain stable operations with a large range variation of the current control loop's proportional gain.

Figure 9 presents the characteristic root locus and minimum damping ratio curves as the current control loop's integral gain k_2 changes, where the SCR is 2, the virtual impedance coefficient k is 0.75, and the current loop's proportional gain k_1 is 0.05.

Figure 9A shows that when the current loop's integral gain k_2 increases from 0 to 5, the nine root trajectories of the system are all located in the left half plane and almost remain unchanged, corresponding to the stable operations of the grid-forming VSC-HVDC system. In addition, in Figure 9B, when the current control loop's integral gain k_2 increases from 0 to 5, the minimum damping ratio of the VSC-HVDC almost remains unchanged and is always greater than 0.1. Research results shown in Figure 9 demonstrate that the VSC-HVDC system under the proposed grid-forming control is robust and can maintain stable operations with a large range variation of the current control loop's integral gain.

4 Mechanism analysis and stabilization control

4.1 Interaction mechanism analysis

This article utilizes the complex power coefficient method (Sang et al., 2019) to reveal the interaction mechanism between the grid-forming VSC-HVDC system and the grid. First, the REC's grid-connected active power of the VSC-HVDC system can be derived in Eq. 14 by

$$\bar{P}_{\mathrm{g}} = \frac{\bar{u}_{\mathrm{dc}}\bar{U}_{\mathrm{t}}\bar{E}_{\mathrm{g}}}{\bar{X}_{\mathrm{f}} + \bar{X}_{\mathrm{g}}} \sin\delta, \tag{14}$$

where $\bar{X}_{\mathrm{f}}$ is the per-unit inductive reactance of the REC's filter inductor, $\bar{X}_{\mathrm{g}}$ is the inductive reactance of the line inductor in the per-unit form, $\bar{U}_{\mathrm{t}}$ is the per-unit modulation voltage's amplitude of the REC, and $\bar{E}_{\mathrm{g}}$ is the amplitude of the grid voltage in the per-unit form. δ is the phase of the REC's output voltage leading the grid voltage.

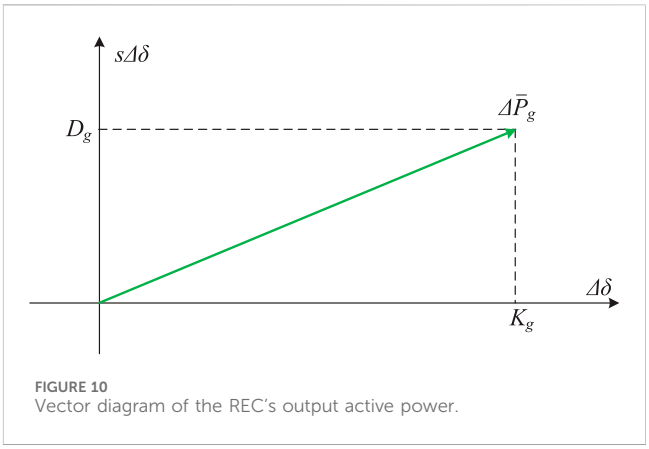

FIGURE 10
Vector diagram of the REC's output active power.

Linearizing the grid-connected active power of the REC in (14) gives

$$\begin{aligned}\Delta\bar{P}_{\mathrm{g}} &= \frac{\bar{u}_{\mathrm{dc0}}\bar{U}_{\mathrm{t0}}\bar{E}_{\mathrm{g}}}{\bar{X}_{\mathrm{f}} + \bar{L}_{\mathrm{g}}} \cos\delta\Delta\delta + \frac{\bar{U}_{\mathrm{t}}\bar{E}_{\mathrm{g}}}{\omega_{\mathrm{Bg}}\left(\bar{X}_{\mathrm{f}} + \bar{L}_{\mathrm{g}}\right)} \sin\delta s\Delta\delta, \\ &= K_{\mathrm{g}}\Delta\delta + D_{\mathrm{g}}s\Delta\delta\end{aligned} \tag{15}$$

where $\bar{u}_{\mathrm{dc0}}$ is per-unit steady-state DC voltage of the REC, $\bar{U}_{\mathrm{t0}}$ is per-unit steady-state modulation voltage's amplitude of the REC, K_{g} is the synchronous power coefficient of the REC, and D_{g} is the damping power coefficient of the REC.

According to the linearized output active power in Eq. 15, the vector diagram of the REC's output active power can be obtained in Figure 10. The synchronous power coefficient K_{g} of the REC is greater than 0, and the damping power coefficient D_{g} of the REC is greater than 0. Because the SEC's output active power is not related to the DC voltage, the variation of the SEC's output active power $\Delta\bar{P}_{\mathrm{m}}$ is independent of $\Delta\delta$. Substituting $\Delta\bar{P}_{\mathrm{g}}$ and $\Delta\bar{P}_{\mathrm{m}}$ into (1), the characteristic equation of the grid-forming VSC-HVDC system is derived as

$$\frac{2H_{\mathrm{C}}}{\omega_{\mathrm{Bg}}}s^2\Delta\delta + D_{\mathrm{g}}s\Delta\delta + K_{\mathrm{g}}\Delta\delta = 0. \tag{16}$$

It can be seen from Equation 16 that the characteristic equation of the grid-forming VSC-HVDC system is a second-order equation, and the stability of the system is decided by the damping coefficient D_{g}. Because the value of D_{g} is greater than 0, the VSC-HVDC system under the proposed grid-forming control is always stable, whether the grid is weak or stiff. The above mechanism analysis results are in accordance with the conclusions of numerical analysis in Section 3, further validating the correctness of the conclusion.

4.2 Stabilization control strategy

Although the minimum damping ratio ζ of the grid-forming VSC-HVDC system is greater than 0, the value of ζ is not big enough; that is, the stability margin is inadequate. Therefore, it is essential to propose a stabilization controller to further improve the system's small-signal stability. As is well known, a power system

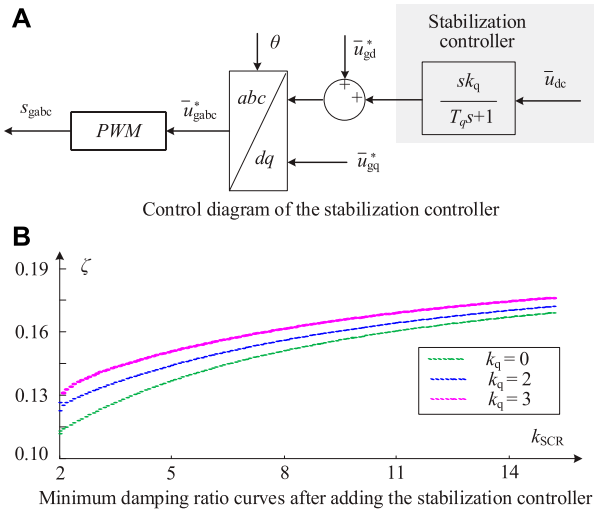

FIGURE 11
Stabilization controller. **(A)** Control diagram. **(B)** Minimum damping ratio curves after adding the stabilization controller.

stabilizer (PSS) can be added to the excitation system of the SG. The PSS usually takes the rotational speed of the SG as the input signal, and its output is superimposed on the excitation signal to increase the electrical damping. In the proposed GFM control structure of the REC, the modulation voltage amplitude can be analogized to the flux linkage of the SG. Therefore, imitating the stabilization mechanism of the PSS, this section proposes a damping injection strategy according to the DC voltage feedback to change the modulation voltage amplitude of the REC.

Figure 11 presents the control diagram of the stabilization controller and minimum damping ratio curves after adding the stabilization controller. In Figure 11A, a stabilization controller is added to the original grid-forming structure. The input of the stabilization controller is the DC-side capacitor voltage, and the output of the stabilization controller is superimposed on the per-unit d-axis modulation voltage $\bar{u}^*_{gd}$. The per-unit d-axis modulation voltage $\bar{u}^*_{gd}$ and per-unit q-axis modulation voltage $\bar{u}^*_{gq}$ are transferred to $\bar{u}^*_{gabc}$ by the rotation transformation. The stabilization controller's transfer function is given in Eq. 17 as

$$H(s) = \frac{sk_q}{T_q s + 1}, \tag{17}$$

where s is the Laplace operator, k_q is the stabilization controller's gain, and T_q is the stabilization controller's time constant.

Figure 11B presents the minimum damping ratio curves of the grid-forming VSC-HVDC system after adding the stabilization controller, where T_q is 0.1. It can be seen that with the increasing of the stabilization gain, k_q, from 0 to 2 and 3, the small-signal stability quantitative index ζ is promoted overall. The research result shown in Figure 11B illustrates that the proposed stabilization controller can further enhance the grid-forming VSC-HVDC's stability, whether under stiff or weak grid conditions.

Figure 11A shows that the parameters needed to be designed are k_q and T_q. The high-pass filter in the stabilization controller can pass through signals with a frequency greater than $1/T_q$ rad/s. When designing the time constant T_q, it is essential to enable the signal of resonant frequency to pass through. Increasing the value of the stabilization controller's gain k_q can improve the stability of the GFM VSC-HVDC. Because increasing the DC-side voltage during the dynamic process will increase the modulation ratio of the REC after adding the stabilization controller, the REC's modulation ratio m is represented in Eq. 18 as

$$m = \frac{k_q \Delta \bar{u}_{dc} U_{dcb} + \bar{U}_g U_b}{\bar{u}_{dc0} U_{dcb}}, \tag{18}$$

where $\bar{U}_g$ is the AC voltage amplitude of the REC in the per-unit form, U_b is the base value of the AC voltage, U_{dcb} is the base value of the DC-side voltage, and $\Delta\bar{u}_{dc}$ is the variation of the DC-side voltage.

Because the per-unit DC-side voltage can track the per-unit grid frequency, the variation of the DC-side voltage $\Delta\bar{u}_{dc}$ is taken as 0.01 p.u. in this article. The maximum value k_{qmax} of the stabilization controller's gain is limited by the maximum modulation ratio of the REC. According to (18), the maximum value k_{qmax} can be obtained in Eq. 19 as

$$k_{qmax} = \frac{m_{max} - \bar{U}_g U_b \big/ (\bar{u}_{dc0} U_{dcb})}{0.01}, \tag{19}$$

where m_{max} is the maximum value of the REC's modulation ratio.

According to the range of k_q and T_q, designing the gain and time constant of the stabilization controller follows the steps below.

Step 1. he potential resonant frequency of the GFM VSC-HVDC system can be derived by building the GFM VSC-HVDC's state-space model.

Step 2. he time constant T_q of the stabilization controller is tuned based on the derived potential resonant frequency.

Step 3. A value for the stabilization controller's gain k_q is provided and substituted into the state-space model of the GFM VSC-HVDC system.

Step 4. If the electrical oscillation is suppressed and the stability margin is big enough, the design of the stabilization controller is completed. Otherwise, return to step 2 and redesign the parameters.

In contrast, as shown in Figure 11A, a variation related to $\bar{u}_{dc}$ is superimposed on the amplitude of the modulation voltage $\bar{U}_t$. After adding the stabilization controller, linearizing the output active power of the REC in (14) yields

$$\begin{aligned} \Delta\bar{P}_g &= K_g \Delta\delta + D_g s\Delta\delta + \frac{\bar{u}_{dc0}\bar{E}_g}{\bar{X}_f + \bar{X}_g} \sin\delta \Delta\bar{U}_t, \\ &= K_g \Delta\delta + \left(D_g + D_s\right) s\Delta\delta \end{aligned} \tag{20}$$

where D_s is the system's damping coefficient provided by the stabilization controller.

According to the control diagram of the stabilization controller in Figure 11A, because the stabilization controller's time constant is fixed, the variation of the modulation voltage's amplitude $\bar{U}_t$ is related to the stabilization gain k_q and the DC-side voltage. Thus, the damping coefficient D_s provided by the stabilization controller is proportional to the stabilization gain k_q. Combining Eq. 1 and the linearized active power in Eq. 20, the damping power coefficient of

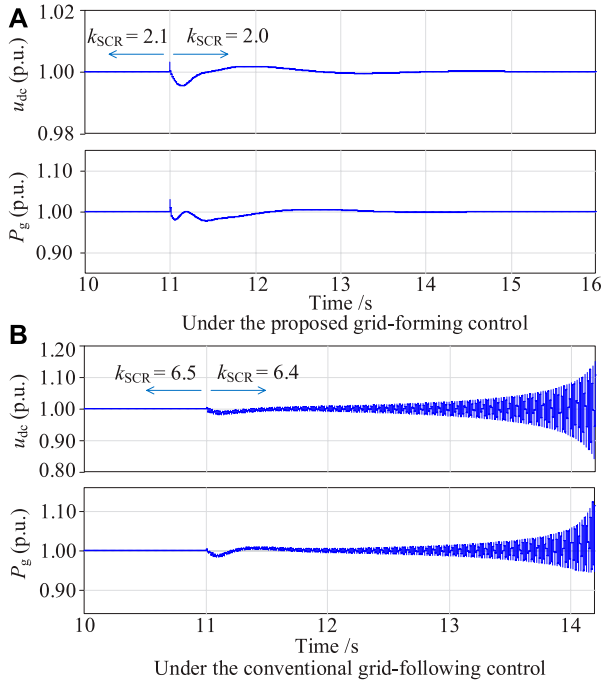

FIGURE 12
Simulation results of the VSC-HVDC as the SCR changes. **(A)** Under the proposed grid-forming control. **(B)** Under the conventional grid-following control.

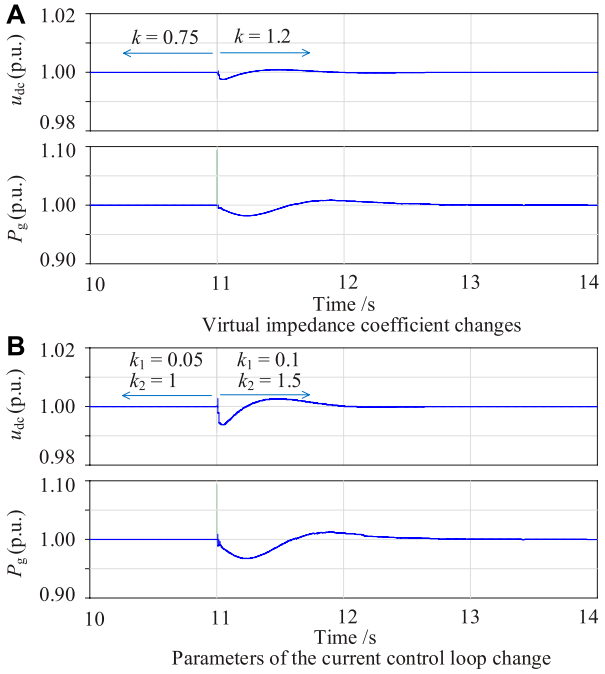

FIGURE 13
Simulation waveforms of the grid-forming VSC-HVDC as control parameters change. **(A)** Virtual impedance coefficient changes. **(B)** Parameters of the current control loop change.

the GFM VSC-HVDC system can be obtained as (D_g + D_s). In addition, adding stabilization control and properly adjusting the stabilization gain k_q can increase the value of (D_g + D_s), therefore improving the stability margin of the grid-forming VSC-HVDC. The above mechanism analysis results are in accordance with the research results in Figure 11B.

5 Simulation verification

To further prove the practicability of the presented GFM strategy for the VSC-HVDC system and demonstrate the correctness of stability analysis, simulations have been carried out based on the PSCAD/EMTDC. The electrical and control parameters of the simulation system are shown in Table 1.

Figure 12 presents the simulation results of the VSC-HVDC transmission system as the SCR changes. In Figure 12A, where the VSC-HVDC adopts the presented grid-forming control in this article, and the grid's short-circuit ratio k_{SCR} decreases from 2.1 to 2.0, the DC-side voltage fluctuates and then returns to a stable state. The VSC-HVDC system's grid-connected active power fluctuates and then recovers stability. Simulation results in Figure 12A show that the VSC-HVDC under the proposed grid-forming control can work stably in weak grids. In Figure 12B, where the VSC-HVDC utilizes the conventional grid-following control, the bandwidth of the outer DC voltage control loop is 20 Hz, the inner current loop's control bandwidth is 200 Hz, and the control bandwidth of the PLL is 50 Hz. The DC-side voltage and the grid-connected active power of the VSC-HVDC gradually oscillate and diverge with the grid's short-circuit ratio k_{SCR} decreasing from 6.5 to 6.4, demonstrating that the stability of the conventional grid-following VSC-HVDC deteriorates when the grid's stiffness decreases. Simulation results in Figure 12A illustrate that the VSC-HVDC under the proposed GFM control can work stably when the SCR decreases from 2.1 to 2.0, which is in accordance with the numerical analysis conclusions shown in Figure 5. The critically stable value of the SCR in Figure 12B is 6.5, which is approximately equal to the value shown in Figure 6. The simulation results shown in Figure 12B are in accordance with the numerical analysis conclusions in Figure 6. Furthermore, comparing Figure 12B with Figure 12A, the VSC-HVDC under the presented GFM control has better stability than that under the conventional GFL control in weak grids.

Figure 13 shows the simulation results of the grid-forming VSC-HVDC as control parameters change. In Figure 13A, where the SCR is 2, the current control loop's proportional gain k_1 is 0.05, the integral gain k_2 of the current control loop is 1, and the voltage control loop's virtual impedance coefficient k changes from 0.75 to 1.2. The DC-side voltage and the grid-connected active power of the GFM VSC-HVDC system fluctuate slightly and then recover. No oscillations occur in the DC-side voltage and the grid-connected active power, demonstrating that the VSC-HVDC under the presented GFM control is robust and can maintain stable operations with a large range variation of the voltage loop parameters. Simulation results in Figure 13A illustrate that the VSC-HVDC under the proposed GFM control can work stably when the virtual impedance

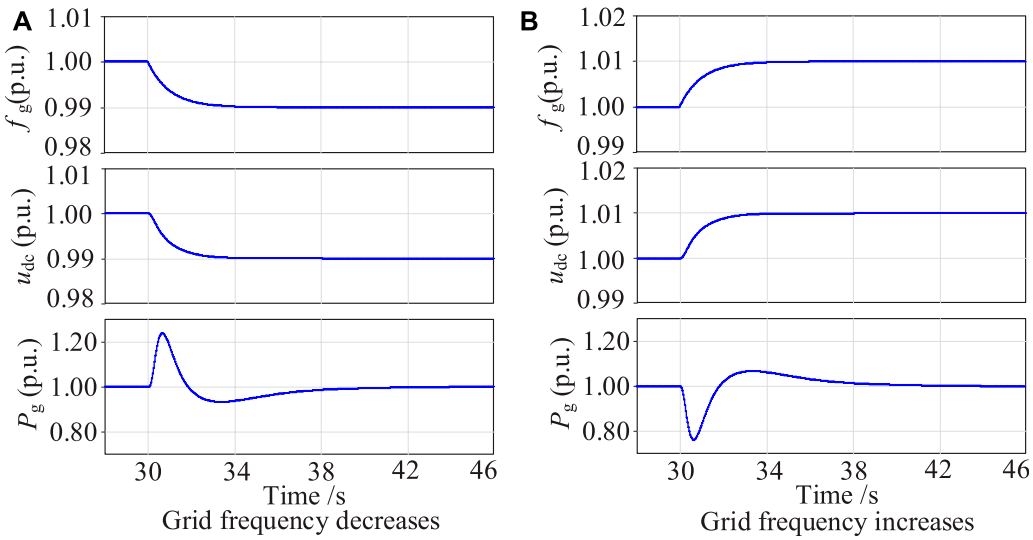

FIGURE 14
Simulation waveforms of the grid-forming VSC-HVDC system when providing the inertia response. **(A)** Under the proposed grid-forming control. **(B)** Under the conventional forming control.

coefficient k increases from 0.75 to 1.2, which is in accordance with numerical analysis conclusions in Figure 7. In Figure 13B, where the SCR is 2, the virtual impedance coefficient *k* is 0.75, the current control loop's proportional gain k_1 changes from 0.05 to 0.1, and the current control loop's integral gain k_2 changes from 1 to 1.5. Small-amplitude oscillations occur in the DC-side voltage and grid-connected active power of the grid-forming VSC-HVDC system, indicating that the VSC-HVDC system under the proposed grid-forming control is robust and can maintain stable operations with a large range variation of the current control loop's integral gain. Simulation results in Figure 13B illustrate that the VSC-HVDC under the proposed GFM control can work stably when the parameters of the current control loop change, which is in accordance with numerical analysis conclusions in Figure 8.

Figure 14 presents simulation waveforms of the grid-forming VSC-HVDC system when providing inertia response, where the SCR is 2, the current control loop's proportional gain k_1 is 0.05, the current control loop's integral gain k_2 is 1, and the virtual impedance coefficient *k* of the voltage control loop is 0.75. In Figure 14A, when the grid frequency falls from the rated value to 99% of the rated value, the DC voltage of the grid-forming VSC-HVDC can automatically track grid frequency, acting as the PLL. Based on the DC-side voltage in the per-unit form, the source renewable energy (e.g., wind farm) increases the output active power to provide inertia response to the grid. The grid-connected active power P_g of the grid-forming VSC-HVDC increases by 0.24 p.u. and then recovers. In Figure 14B, the DC-side voltage of the grid-forming VSC-HVDC can automatically track the grid frequency as the grid frequency increases from the rated value to 101% of the rated value. According to the DC-side voltage in the per-unit form, the source of the renewable energy (e.g., wind farm) reduces the output active power to provide inertia support to the grid. The output active power P_g of the REC grid-forming VSC-HVDC system decreases by 24% and then recovers. Simulation results in Figure 14 demonstrate that the presented grid-forming control can make the VSC-HVDC automatically sense the grid frequency and realize the function of inertia response.

6 Conclusion

A novel grid-forming control strategy with the function of limiting the output current is proposed to deal with the interaction instability issues between a conventional grid-following VSC-HVDC system and the grid. A state-space model of the grid-forming VSC-HVDC system is established to research the small-signal stability, and the eigenvalue analysis method is adopted. Moreover, the complex power coefficient method is utilized to reveal the interaction mechanism between the grid-forming VSC-HVDC system and the grid. To further improve the stability margin of the grid-following VSC-HVDC system, a stabilization controller is proposed for the original grid-forming structure, which can introduce positive electrical damping. Conclusions are obtained as follows:

1) The grid-forming control strategy makes the REC realize the function of self-synchronization with the grid through the dynamics of the DC capacitor. The per-unit DC voltage can automatically track the grid frequency, acting as a phase-locked loop.
2) Different from the conventional grid-following VSC-HVDC, which loses stability in a weak grid, the VSC-HVDC system under the proposed grid-forming control can work stably in both stiff and weak grids.
3) The VSC-HVDC system under the proposed grid-forming control is robust and can maintain stable operations with a large range variation of the parameters in the current and voltage control loop.

Data availability statement

The raw data supporting the conclusions of this article will be made available by the authors, without undue reservation.

Author contributions

YL: formal analysis, writing–original draft, and writing–review and editing. GS: validation, writing–original draft, and writing–review and editing. QC: investigation, resources, and writing–original draft. PQ: software and writing–review and editing. JZ: Investigation, supervision, and writing–review and editing. RY: project administration and writing–review and editing. JZ: funding acquisition and writing–review and editing.

Funding

The author(s) declare financial support was received for the research, authorship, and/or publication of this article. This work is supported by the Science and Technology Project of State Grid Zhejiang Electric Power Co., Ltd (5211DS230005) and partly by the National Natural Science Foundation of China (No. 52107201).

Conflict of interest

Authors YL, QC, and PQ were employed by the Electric Power Research Institute of State Grid Zhejiang Electric Power Corporation.

The remaining authors declare that the research was conducted in the absence of any commercial or financial relationships that could be construed as a potential conflict of interest.

The authors declare that this study received funding from State Grid Zhejiang Electric Power Co., Ltd. The funder had the following involvement in the study: investigation and resources.

Publisher's note

References

Fu, X., Sun, J., Huang, M., Tian, Z., Yan, H., Iu, H. H. C., et al. (2021). Large-signal stability of grid-forming and grid-following controls in voltage source converter: a comparative study. *IEEE Trans. Power Electron.* 36 (7), 7832–7840. doi:10.1109/tpel.2020.3047480

Ge, P., Tu, C., Xiao, F., Guo, Q., and Gao, J. (2023). Design-oriented analysis and transient stability enhancement control for a virtual synchronous generator. *IEEE Trans. Industrial Electron.* 70 (3), 2675–2684. doi:10.1109/tie.2022.3172761

Huang, S., Yao, J., Pei, J., Chen, S., Luo, Y., and Chen, Z. (2022). Transient synchronization stability improvement control strategy for grid-connected VSC under symmetrical grid fault. *IEEE Trans. Power Electron.* 37 (5), 4957–4961. doi:10.1109/tpel.2021.3131361

Li, C., Yang, Y., Cao, Y., Wang, L., and Blaabjerg, F. (2022). Frequency and voltage stability analysis of grid-forming virtual synchronous generator attached to weak grid. *IEEE J. Emerg. Sel. Top. Power Electron.* 10 (3), 2662–2671. doi:10.1109/jestpe.2020.3041698

Liu, D., Jiang, K., Ji, X., Cao, K., Xu, C., Sang, S., et al. (2024). Improved VSG strategy of grid forming inverters for supporting inertia and damping. *Front. Energy Res.* 11, 1331024. doi:10.3389/fenrg.2023.1331024

Ma, J., Su, N., and Shen, Y. (2024). Stability analysis for direct-drive wind farm transmitted via flexible DC system based on dynamic energy. *CSEE J. Power Energy Syst.* doi:10.17775/CSEEJPES.2022.07150

Meng, X., Liu, J., and Liu, Z. (2019). A generalized droop control for grid-supporting inverter based on comparison between traditional droop control and virtual synchronous generator control. *IEEE Trans. Power Electron.* 34 (6), 5416–5438. doi:10.1109/tpel.2018.2868722

Pan, D., Wang, X., Liu, F., and Shi, R. (2020). Transient stability of VoltageSource converters with grid-forming control: a design-oriented study. *IEEE J. Emerg. Sel. Top. Power Electron.* 8 (2), 1019–1033. doi:10.1109/jestpe.2019.2946310

Pawar, B., Batzelis, E. I., Chakrabarti, S., and Pal, B. C. (2021). Grid-forming control for solar PV systems with power reserves. *IEEE Trans. Sustain. Energy* 12 (4), 1947–1959. doi:10.1109/tste.2021.3074066

Sang, S., Gao, N., Cai, X., and Li, R. (2018). A novel power-voltage control strategy for the grid-tied inverter to raise the rated power injection level in a weak grid. *IEEE J. Emerg. Sel. Top. Power Electron.* 6 (1), 219–232. doi:10.1109/jestpe.2017.2715721

Sang, S., Zhang, C., Cai, X., Molinas, M., Zhang, J., and Rao, F. (2019). Control of a type-IV wind turbine with the capability of robust grid synchronization and inertial response for weak grid stable operation. *IEEE Access* 7, 58553–58569. doi:10.1109/access.2019.2914334

Shao, B., Zhao, S., Yang, Y., Gao, B., and Blaabjerg, F. (2021). Sub-synchronous oscillation characteristics and analysis of direct-drive wind farms with VSC-HVDC systems. *IEEE Trans. Sustain. Energy* 12 (2), 1127–1140. doi:10.1109/tste.2020.3035203

Shao, H., Cai, X., Li, Z., Zhou, D., Sun, S., Guo, L., et al. (2019b). Stability enhancement and direct speed control of DFIG inertia emulation control strategy. *IEEE Access* 7, 120089–120105. doi:10.1109/access.2019.2937180

Shao, H., Cai, X., Zhou, D., Li, Z., Zheng, D., Cao, Y., et al. (2019a). Equivalent modeling and comprehensive evaluation of inertia emulation control strategy for DFIG wind turbine generator. *IEEE Access* 7, 64798–64811. doi:10.1109/access.2019.2917334

Wang, X., Taul, M. G., Wu, H., Liao, Y., Blaabjerg, F., and Harnefors, L. (2020). Grid-synchronization stability of converter-based resources—an overview. *IEEE Open J. Industry Appl.* 1, 115–134. doi:10.1109/ojia.2020.3020392

Wang, X., Yao, J., Pei, J., Sun, P., Zhang, H., and Liu, R. (2019). Analysis and damping control of small-signal oscillations for VSC connected to weak AC grid during LVRT. *IEEE Trans. Energy Convers.* 34 (3), 1667–1676. doi:10.1109/tec.2019.2915680

Wu, Q., Huang, Y., Li, C., Gu, Y., Zhao, H., and Zhan, Y. (2019a). Small signal stability of synchronous motor-generator pair for power system with high penetration of renewable energy. *IEEE Access* 7, 166964–166974. doi:10.1109/access.2019.2953514

Wu, W., Zhou, L., Chen, Y., Luo, A., Dong, Y., Zhou, X., et al. (2019b). Sequence impedance-based stability comparison between VSGs and traditional grid-connected inverters. *IEEE Trans. Power Electron.* 34 (1), 46–52. doi:10.1109/tpel.2018.2841371

Yang, R., Shi, G., Cai, X., Zhang, C., Li, G., and Liang, J. (2020). Autonomous synchronizing and frequency response control of multi-terminal DC systems with wind farm integration. *IEEE Trans. Sustain. Energy* 11 (4), 2504–2514. doi:10.1109/tste.2020.2964145

Yang, R., Zhang, C., Cai, X., and Shi, G. (2018). Autonomous grid-synchronising control of VSC-HVDC with real-time frequency mirroring capability for wind farm integration. *IET Renew. Power Gener.* 12 (13), 1572–1580. doi:10.1049/iet-rpg.2017.0824

Zha, Y., Lin, J., Li, G., Wang, Y., and Zhang, Yi (2021). Analysis of inertia characteristics of photovoltaic power generation system based on generalized droop control. *IEEE Access* 9, 37834–37839. doi:10.1109/access.2021.3059678

Zhang, H., Xiang, W., Lin, W., and Wen, J. (2021). Grid forming converters in renewable energy sources dominated power grid: control strategy, stability, application, and challenges. *J. Mod. Power Syst. Clean Energy* 9 (6), 1239–1256. doi:10.35833/mpce.2021.000257

Zhang, N., Jia, H., Hou, Q., Zhang, Z., Xia, T., Cai, X., et al. (2023). Data-driven security and stability rule in high renewable penetrated power system operation. *Proc. IEEE* 111 (7), 788–805. doi:10.1109/jproc.2022.3192719

Zhu, D., Zhou, S., Zou, X., and Kang, Y. (2020). Improved design of PLL controller for LCL-type grid-connected converter in weak grid. *IEEE Trans. Power Electron.* 35 (5), 4715–4727. doi:10.1109/tpel.2019.2943634

frontiers | Frontiers in Energy Research

TYPE Original Research
PUBLISHED 09 August 2024
DOI 10.3389/fenrg.2024.1413910

OPEN ACCESS

EDITED BY
Yushuai Li,
Aalborg University, Denmark

REVIEWED BY
Yibin Zhang,
Eaton, United States
Bingyu Wang,
North China Electric Power University, China

*CORRESPONDENCE
Pan Lei,
panlei199905@163.com

RECEIVED 08 April 2024
ACCEPTED 03 June 2024
PUBLISHED 09 August 2024

CITATION
Lei P and Zhao J (2024), The analysis of the threshold value of the complex short-circuit ratio index and its significance in the context of static voltage stability.
Front. Energy Res. 12:1413910.
doi: 10.3389/fenrg.2024.1413910

The analysis of the threshold value of the complex short-circuit ratio index and its significance in the context of static voltage stability

Pan Lei* and Jinquan Zhao

College of Electrical Engineering, Shanghai University of Electric Power, Shanghai, China

The short-circuit ratio index (SCR) can effectively quantify the voltage support strength in traditional DC grid-connected scenarios, yet it cannot reasonably describe the voltage support strength in diverse device grid connection scenarios. This paper introduces a new calculation method of the complex short-circuit ratio index ($\widetilde{SCR}$) and derives the threshold value of the complex short-circuit ratio index to enable a comprehensive quantitative assessment of grid voltage support strength across diverse device grid connection scenarios. Firstly, critical short-circuit ratio (CSCR) under different assumed conditions were derived based on the short-circuit ratio index. Secondly, the calculation method of the complex short-circuit ratio index was introduced, considering both the equivalent impedance angle of the device and the Thevenin equivalent impedance angle. This was followed by the determination of the threshold value of the complex short-circuit ratio ($\widetilde{CSCR}$), enabling a precise quantitative evaluation of power grid voltage support strength in diverse device grid connection scenarios. Finally, the example analysis proves the accuracy and efficacy of the complex short-circuit ratio index in assessing the voltage support strength of diverse devices in grid-connected scenarios.

KEYWORDS

power grid strength, short-circuit ratio index, critical short-circuit ratio, complex short-circuit ratio index, the threshold value of the complex short-circuit ratio

1 Introduction

With the integration of new energy generation devices such as wind and photovoltaic power into the grid, a new type of power system dominated by renewable energy has been formed. This shift has led to profound changes in both internal mechanisms and external characteristics governing the stable operation of the AC grid (Zhou et al., 2014; Chen et al., 2017). In order to accurately assess the voltage restoration capability during grid faults, the concept of "voltage support strength" has been proposed. To effectively describe this abstract concept of grid voltage support strength, appropriate index need to be employed. In the context of traditional DC grid-connected systems, the short-circuit ratio index (IEEE Standards Board IEEE Std 1204-1997, 1997) can reasonably indicate the grid's voltage support strength.

Abbreviations: SCR, Short Circuit Ratio; CSCR, Critical Short Circuit Ratio; $\widetilde{SCR}$, Complex Short Circuit Ratio; $\widetilde{CSCR}$, The Threshold Value Of The Complex Short Circuit Ratio.

SCR is used in DC planning problems (IEEE Standards Board IEEE Std 1204-1997, 1997) to measure the AC system's acceptance capacity of the DC system. When multiple DC lines connect to the same point to form a multi-infeed system, the concept of Multi-Infeed Short-Circuit Ratio (MISCR) was derived based on the short-circuit ratio index through power conversion (Lin et al., 2008). As SCR continues to evolve and improve, its application scenarios are expanding, with widespread applications in power system steady-state voltage stability, transient voltage stability, and harmonic resonance. For example, references (Sun et al., 2023a) and utilize SCR to characterize voltage support strength, quantitatively analyzing the impact of voltage support (Sun et al., 2023b) strength in new energy grid-connected systems on post-fault steady-state voltage security issues and quantifying the effect of voltage support strength on transient overvoltage in new energy grid-connected systems. Reference (Yin et al., 2019) analyzes the relationship between reactive power short-circuit ratio and transient overvoltage from the perspective of parallel resonance.

In the current power grid, the dynamic interplay between device-side components and the AC power grid undergoes constant evolution due to the integration of diverse reactive power compensation technologies and new energy grid interfaces. As a result, the mechanisms of mutual influence between the device and the AC grid are continually changing. To accurately assess the voltage support strength of the contemporary power grid, scholars have refined the short-circuit ratio index in response to these developments. Reference (Sun et al., 2021), building upon the physical principles of the short-circuit ratio, introduces the concept of the Multiple Renewable Energy Station Short-Circuit Ratio (MRSCR), considering interactions between sites and substations. This includes the provision of analytical expressions for calculating different impedance ratio ranges based on the relationship between system impedance ratio and short-circuit ratio. Furthermore, Reference (Kim et al., 2022) proposes the Hybrid Multi-Infeed Effective Short-Circuit Ratio (HMESCR) by evaluating the reactive power control capability of VSC-HVDC systems composed of power electronic fully controlled elements, elucidating the relationship between transient overvoltage and HMESCR through comparative studies. Additionally, Reference (Huang et al., 2023) proposes the Multi-Infeed Transient Short-Circuit Ratio (MITSCR) by leveraging the characteristics of stochastic variations in both the amplitude and phase of short-circuit currents from new energy sources and terminal voltages. This is used to quantitatively evaluate the voltage support strength of multi-input HVDC transmission systems accommodating a high proportion of new energy grid connections.

In the new energy power system, the methodology for quantifying grid voltage support strength using the short-circuit ratio index differs significantly from that of traditional power grids. In traditional DC grid-connected systems, the value 2 is commonly regarded as the critical threshold of the short-circuit ratio index. When the index falls below 2, the system is classified as extremely weak and unstable. However, in the case of new energy grid integration systems, ensuring stable operation does not necessarily mandate SCR exceeding 2. Reference (Sun et al., 2021) conducted electromechanical transient simulation analysis on the proposed SCR of new energy substations to ascertain critical instability phenomena within the system. It was observed that when

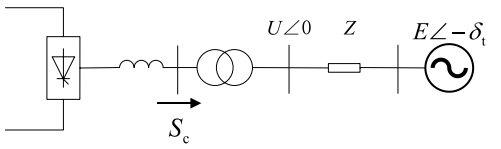

FIGURE 1
Simplified model of single device grid-connected system.

SCR of multiple new energy substations within the network range between 1.7 and 2.1, they can adequately fulfill the operational requirements of the connected new energy generation device. With a prudent engineering margin factored in, it is deemed reasonable for CSCR of new energy substation network nodes to fall within the range of 2.0–2.5. Reference (Kang et al., 2020) derives the transmission limit of static voltage instability and integrates it into SCR to obtain a critical short-circuit ratio value of $\sqrt{2}$. Reference (Wu et al., 2018) derived CSCR of new energy grid-connected system as 1 by means of modal analysis and listing Jacobian matrix.

Based on the analysis above, it is evident that in assessing the current voltage support strength of the power grid using SCR, a novel index is commonly introduced building upon the existing short-circuit ratio index. Subsequently, the critical threshold of this new index is determined based on the system's critical conditions to quantitatively evaluate the voltage support strength of the power grid.

The main contributions of this paper are summarized below.

1. This paper illustrates that critical short-circuit ratios vary under different assumed conditions, as deduced from the derivation of threshold values for the short-circuit ratio index. The critical value of 2 is derived under specific hypothesis conditions.
2. The calculation method of the complex short-circuit ratio index which can take into account the equivalent impedance angle and Thevenin equivalent impedance angle of device is proposed. Then, according to the critical condition of static voltage stability of the system, the threshold value of the complex short-circuit ratio is derived to quantitatively evaluate the voltage support strength under grid-connected scenario. The accuracy and rationality of the complex short-circuit ratio index to evaluate the voltage support strength in grid-connected scenario are verified by the example analysis.

2 Analysis of the short-circuit ratio index

Figure 1 shows a simplified model of the grid-connected system for any device:

In Figure 1, S_c represents the injected power of the device; $U\angle 0^0$ represents the AC bus voltage of the junction point; Z represents the Thevenin equivalent impedance of the AC system; $E\angle -\delta_t$ represents the equivalent potential of the AC system.

With the assumption that the input power of the device equals the rated DC power, the short-circuit ratio index is defined as the

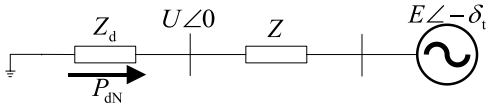

FIGURE 2
Equivalent circuit of DC grid-connected system.

ratio between the short-circuit capacity of the converter station's AC bus and the rated DC power (Xu, 1997), namely,:

$$SCR = \frac{S_{ac}}{P_{dN}} = \frac{U_N{}^2}{P_{dN}} \cdot \frac{1}{|Z|} \tag{1}$$

Where, S_{ac} represents Short-circuit capacity; P_{dN} represents the rated DC power; U_N represents rated voltage at the grid connection point.

If the reference voltage of the AC system is set to the rated value of the AC bus voltage, and the reference power is set to the rated DC power, then SCR can be expressed as:

$$SCR = \frac{1}{|Z_{pu}|} \tag{2}$$

Where, Z_{pu} represents the Thevenin equivalent impedance of AC system in per unit.

The critical short-circuit ratio index is derived from the critical stability conditions of the system and serves as a quantitative measure to evaluate the critical threshold of voltage support strength within the power grid. In traditional power systems primarily driven by synchronous machines, a short-circuit ratio value of 2 is employed as the critical threshold for classifying system strength. Systems with the short-circuit ratio index below 2 are categorized as very weak, those with values between 2 and 3 are considered weak, and systems with a short-circuit ratio value exceeding 3 are classified as strong.

If Figure 1 is a DC grid-connected system, it can be equivalent to the equivalent circuit shown in Figure 2.

In Figure 2, Z_d represents the DC equivalent impedance. It can be calculated from the injected power of the device and the grid voltage. Assuming that the equivalent potential of the AC system is equal to the rated voltage of the AC bus, the short circuit capacity of the AC system can be expressed as:

$$S_{ac} = \frac{U_N E}{|Z|} = \frac{E^2}{|Z|} \tag{3}$$

Ignore internal control strategies of the device, the rated DC power can be expressed as:

$$P_{dN} = I^2 R_d = \frac{E^2}{|Z + Z_d|^2} \cdot R_d \tag{4}$$

Where, P_{dN} represents the rated DC power.

In Eq. 4: $Z_d = R_d + jX_d$, $Z = R + jX$; the short-circuit ratio index at the junction can be obtained as follows:

$$SCR = \frac{S_{ac}}{P_{dN}} = \frac{E^2}{|Z|} \cdot \frac{|Z_d + Z|^2}{E^2 R_d} = \frac{|Z_d + Z|^2}{|Z| R_d} \tag{5}$$

Where, R_d and X_d represent the resistance and reactance of the DC equivalent impedance; R and X represent the resistance and reactance of the Thevenin equivalent impedance of the AC system.

TABLE 1 Table I CSCR under different assumptions.

Assumed condition	CSCR
$X_d = 0$, $R = 0$	2
$X_d = 0$, $X = \sqrt{3}R$	3
$X_d = 0$, $R = X$	3.414
$X_d = 0$, $X = 0$	4

When the system is critically stable, the two equivalent impedance modes in Figure 2 are equal (Liu, 2000):

$$|Z_d| = |Z| \tag{6}$$

Assume that when the $X_d = 0$, $R = 0$, Eq. 6 can be obtained:

$$|R_d| = |X| \tag{7}$$

Equivalent to:

$$R_d = \pm X \tag{8}$$

In Eq. 8, the negative equivalent resistance solution corresponds to the DC power feeding scenario, while the positive equivalent resistance solution corresponds to the load scenario. CSCR can be obtained:

$$CSCR = \frac{|Z_d + Z|^2}{|Z| \cdot R_d} = 2 \tag{9}$$

It can be seen that the critical short-circuit ratio is equal to 2 only under certain hypothetical conditions; Similarly, based on different assumptions, the short-circuit ratio threshold can be obtained, as shown in Table 2.

It can be seen from Table 1 that the critical short-circuit ratio is affected by the equivalent impedance and Thevenin equivalent impedance of the AC system. Under different impedance, the critical short-circuit ratio is different. Therefore, the critical short-circuit ratio of 2 is not suitable as the critical value for dividing the strength of any device grid-connected system, and it only applies to specific assumptions. This also reflects the limitations of using short-circuit ratio index to divide the power grid voltage support strength. The critical short-circuit ratio of 2 can only be used to analyze whether the system is stable and cannot determine the strength of the system.

3 Complex short-circuit ratio index

The analysis in the second section reveals that a critical short-circuit ratio of 2 is well-suited for evaluating the voltage support strength of DC grid systems. However, for grid-connected systems incorporating reactive compensation devices and integrating modern renewable energy sources, the conventional short-circuit ratio index proves inadequate for accurately quantifying the voltage support strength of these grids. To address this limitation and provide a more comprehensive assessment of voltage support across different grid-connected systems, this chapter introduces the complex short-circuit ratio index. This index takes into account the impedance angle information of both the equivalent

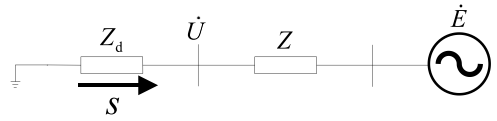

FIGURE 3
Equivalent circuit of single device grid-connected system.

impedance angle of the grid-connected devices and the Thevenin equivalent impedance angle of the AC system, thereby offering a more nuanced approach to evaluating voltage support strength.

3.1 Calculation of complex short-circuit ratio index

The single-device grid-connected system depicted in Figure 1 can be effectively represented by the equivalent circuit illustrated in Figure 3.

For the grid-connected system illustrated in Figure 3, it expands beyond the scope of a singular DC grid connection scenario. As a result, the power injected at the grid connection point is represented in complex power terms. In order to accurately quantify the voltage support strength of the AC grid when integrating diverse devices, the ratio between the short-circuit complex power of the AC system and the injected complex power of the device is introduced as the complex short-circuit ratio index for grid-connected systems.

$$\widetilde{SCR} = \frac{\tilde{S}_{ac}}{\tilde{S}} \tag{10}$$

Where, $\tilde{S}_{ac}$ represents Short-circuit complex power for the system; $\tilde{S}$ represents power injection for the device.

The complex short-circuit ratio index shares a similar form of expression with the short-circuit ratio index. However, as the complex short-circuit ratio index represents the ratio of two complex powers, it evolves beyond being a one-dimensional variable. It transforms into a two-dimensional variable capable of considering both phase angle and magnitude concurrently. Through this computational approach, the complex short-circuit ratio index is liberated from the constraints that limit the traditional short-circuit ratio index to the singular scenario of DC feed-in to the grid.

3.2 Calculation of $\widetilde{SCR}$

For the grid-connected system shown in Figure 3, assuming that the rated voltage of the AC bus is equal to the equivalent potential of the AC system. Assuming a three-phase fault occurs at the grid connection point, the short-circuit complex power (short-circuit capacity) of the system can be obtained as follows:

$$\tilde{S}_{ac} = \frac{E^2}{|Z|^2} Z \tag{11}$$

The system injection power can be expressed as:

$$\tilde{S} = \dot{U}\dot{I}^* = \dot{I}Z_d\dot{I}^* = I^2 Z_d = \frac{E^2}{|Z + Z_d|^2} Z_d \tag{12}$$

Substituting Eqs 11, 12 into Eq. 10, the complex short-circuit ratio index at the junction can be obtained as follows:

$$\widetilde{SCR} = \frac{\tilde{S}_{ac}}{\tilde{S}_N} = \frac{E^2}{|Z|^2} Z \frac{|Z + Z_d|^2}{E^2 Z_d} = \frac{|Z + Z_d|^2}{|Z|^2} \frac{Z}{Z_d} \tag{13}$$

From Formula 13, it can be seen that only the calculation of Z and X is needed to compute the complex short-circuit ratio index. The variables required for calculating Z and X are also needed when calculating the short-circuit ratio index, so there is no need to introduce new variables, and their computation speed and memory consumption are the same as that of the short-circuit ratio index.

Assuming that: $\dot{Z}_d = Z_d\angle\varphi_d$, $\dot{Z} = Z\angle\varphi$; φ_d and φ represent the equivalent impedance Angle of the device and Thevenin equivalent impedance Angle of the AC system. And $\alpha = |Z + Z_d|^2/|Z|^2$; Then the complex short-circuit ratio index can be expressed as:

$$\widetilde{SCR} = \frac{|Z + Z_d|^2}{|Z|^2} \frac{Z}{Z_d} = \alpha \frac{|Z|}{|Z_d|} \angle(\varphi - \varphi_d) \tag{14}$$

Where, α represents the constant term of the complex short-circuit ratio index.

Suppose that: $\theta = \varphi - \varphi_d$, θ represents the complex short-circuit ratio angle; In this case, $\widetilde{SCR}$ can be expressed as:

$$\widetilde{SCR} = \alpha \frac{|Z|}{|Z_d|} \angle(\theta) \tag{15}$$

It can be seen from Eq. 15 that the complex short-circuit ratio index is a two-dimensional index, which contains two kinds of information, one is amplitude information and the other is phase Angle information. For diverse devices grid-connected scenarios, different complex short-circuit ratio angles can be obtained, and then different complex short-circuit ratio index modulus can be calculated.

4 Threshold value of $\widetilde{SCR}$ under static voltage stability

The threshold value of the complex short-circuit ratio is utilized to quantitatively assess the stability of the device interconnection system. System stability is achieved only when the system's complex short-circuit ratio index surpasses its threshold value. This chapter establishes the threshold value of the complex short-circuit ratio index through derivation.

4.1 Calculation of threshold value of the short-circuit ratio

α can be further expressed as follows:

$$\alpha = \frac{|Z + Z_d|^2}{|Z|^2} = \left|\frac{(Z + Z_d)^2}{Z^2}\right| = \left|1 + 2\frac{Z_d}{Z} + \left(\frac{Z_d}{Z}\right)^2\right| \tag{16}$$

Combining Eqs 15, 16, the following can be obtained.

$$\widetilde{SCR} = \left|1 + 2\frac{Z_d}{Z} + \left(\frac{Z_d}{Z}\right)^2\right| \frac{|Z|}{|Z_d|} \angle(\theta) \tag{17}$$

When the system is critical and stable, the equivalent impedance of the device is equal to the impedance mode of the Thevenin equivalent impedance of the AC system, that is:

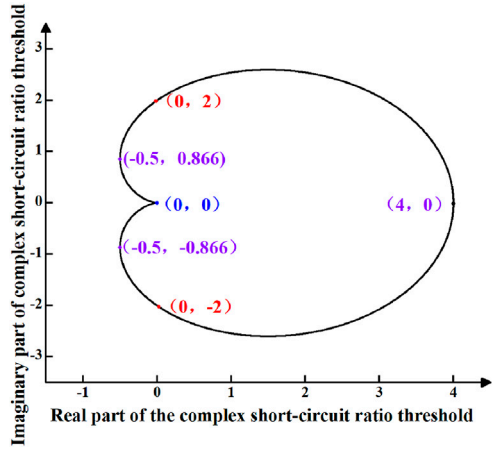

FIGURE 4
Threshold value distribution of complex short circuit ratio for single device grid-connected system.

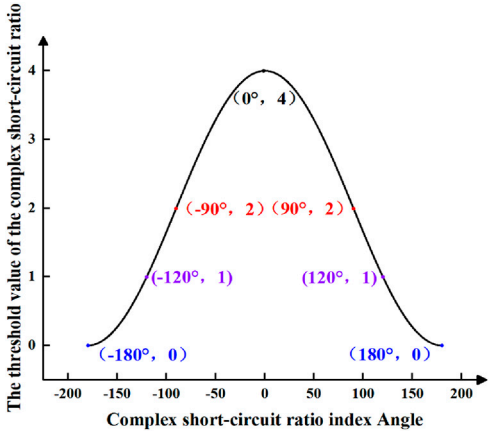

FIGURE 5
The amplitude of the threshold value of the complex short-circuit ratio.

$$|Z_d| = |Z| \tag{18}$$

Under the condition of Eq. 18, it can be obtained that:

$$\alpha = \left|1 + 2\angle(\varphi_d - \varphi) + (1\angle(\varphi_d - \varphi))^2\right|$$
$$= \left|1 + 2\angle(-\theta) + (1\angle(-\theta))^2\right|$$
$$= |1 + 1\angle(-\theta)|^2 \tag{19}$$

According to Eq. 19, the threshold value of system complex short-circuit ratio can be obtained as follows.

$$\widetilde{CSCR} = |1 + 1\angle(-\theta)|^2\angle\theta = (2 + 2\cos\theta)\angle\theta \tag{20}$$

Where, $\widetilde{CSCR}$ represents the threshold value of the complex short-circuit ratio.

Eq. 20 demonstrates a strong correlation between the threshold value of the complex short-circuit ratio index and its angle. Since the equivalent impedances of the device and the impedance angle of the AC system's Thevenin equivalent are not constant, the angle of the complex short-circuit ratio index is a dynamic quantity. Consequently, the numerical value of the threshold value for the complex short-circuit ratio index also fluctuates. By computing different angles of the complex short-circuit ratio within the context of static voltage stability, it becomes possible to derive the threshold value of the complex short-circuit ratio index. This approach facilitates a quantitative evaluation of the power grid's voltage support strength.

4.2 Threshold value analysis of the complex short circuit ratio

Based on Eq. 20, assuming that the angle values of the complex short-circuit ratio fall within the range of $(-\pi, \pi)$, a distribution map depicting the threshold values of the complex short-circuit ratio in the complex plane can be generated for a single-device interconnected system. The critical complex short-circuit ratio map for such a system is illustrated in Figure 4.

From Figure 4, it can be observed that the threshold value of the complex short-circuit ratio form a closed shape on the complex plane, rather than a fixed value. Similar to the short-circuit ratio index, a system can only be classified as strong when its complex short-circuit ratio index exceeds its critical complex short-circuit ratio. Figure 4 delineates the boundaries of the threshold value of the complex short-circuit ratio in the complex plane. A system can be deemed strong only when the numerical value of the complex short-circuit ratio index lies outside the boundary of the threshold value. Additionally, Eq. 20 facilitates the plotting of the magnitude diagram of the threshold value of the complex short-circuit ratio, as illustrated in Figure 5.

From Figure 5, it is evident that the range of value for the complex short-circuit ratio threshold falls within the interval of 0–4.

The critical value of short-circuit ratio was also derived in references (Yu and Sun, 2022; Yamada et al., 2023). These two papers, similar to this paper, derived the critical value by considering the external characteristics of the device and performed a Thevenin equivalent for the AC system. While the two references approached the device side from a power perspective, this paper took an impedance perspective. Nevertheless, the critical value derived in this paper align numerically with those derived in the two references.

The expression of critical short-circuit ratio given by reference (Yu and Sun, 2022) can be divided into two cases:

When the Thevenin impedance ratio of the AC system approaches 0:

$$CSCR = 2 - 2P/|S| \tag{21}$$

When the Thevenin impedance ratio of the AC system approaches infinity:

$$CSCR = 2 - 2Q/|S| \tag{22}$$

Where, S represents the apparent power injected by the device; P and Q represent active and reactive power. It can be seen from the above two equations that the value range of CSCR is also (0, 4).

The expression of critical short-circuit ratio given in reference (Yamada et al., 2023) is as follows:

$$CSCR = 2(1 - \cos(\varphi - \eta)) \tag{23}$$

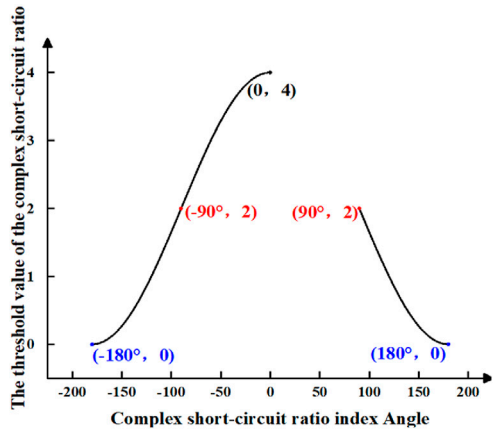

FIGURE 6
The threshold value amplitude of complex short circuit ratio is assumed under condition 1.

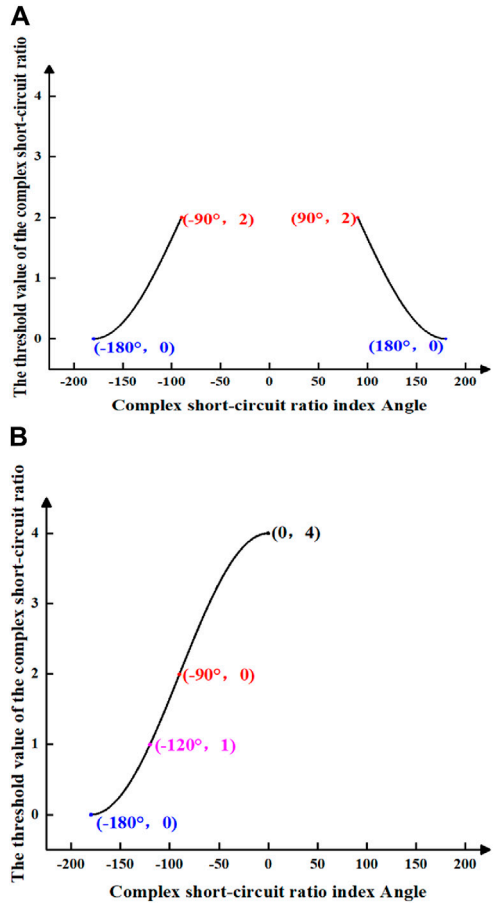

FIGURE 7
The threshold value amplitude of complex short circuit ratio is assumed under condition 2. **(A)** shows the threshold value amplitude of the complex short-circuit ratio when the index Angle of the complex short-circuit ratio is from −180° to −90° and when the index Angle of complex short-circuit ratio is from 90° to 180°. **(B)** shows the threshold value amplitude of the complex short-circuit ratio when the index Angle of the complex short-circuit ratio is from −180° to 0°.

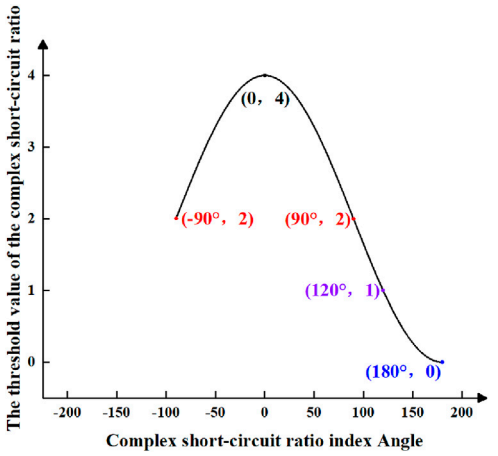

FIGURE 8
The threshold value amplitude of complex short circuit ratio is assumed under condition 3.

Where, φ represents Thevenin impedance Angle of AC system, η represents the power factor Angle. It can be seen from Eq. 23 that the value range of CSCR is also (0, 4).

The CSCR calculated in this paper is found to be numerically consistent with the findings reported in references (Yu and Sun, 2022; Yamada et al., 2023). This validation serves to verify the accuracy of the conclusions drawn in this paper regarding the calculation of the CSCR. In comparison to references (Yu and Sun, 2022; Yamada et al., 2023), which derive the critical values based on assumed input power, this paper takes a different approach by deriving the critical values based on the equivalent impedance angle and Thevenin equivalent impedance angle of the AC system. In contrast to references (Yu and Sun, 2022; Yamada et al., 2023), this paper provides a detailed explanation of the CSCR for different connected equipment and presents a range of values for the CSCR. This analysis allows for a more precise assessment of the voltage support strength of the power grid, presenting a refined study of the CSCR.

In reference (Xu, 2019), K_{vtg} is used as a new voltage support strength index based on the short-circuit ratio index. In this paper, K_{vtg} is considered to be related to short-circuit ratio index and operating short-circuit ratio index, and the relationship is shown as follows:

$$\frac{SCR}{OSCR} = \frac{S_{ac}/S_{device}}{S_{ac}/S} = \frac{S}{S_{device}} = \frac{U_{sys}^2/Z_{device}}{U_{sys0}^2/Z_{device}} = \frac{U_{sys}^2}{U_{sys0}^2} = \left(K_{vtg}\right)^2 \quad (24)$$

Where, S_{ac}, S_{device}, and S represent the short-circuit capacity, the rated capacity of the connected device and the actual capacity of the connected device when it is operating; U_{sys} and U_{sys0} represent the voltage at the junction and the no-load voltage at the junction; Z_{device} represents impedance of device.

From Eq. 24, it is evident that the square of the voltage stiffness index represents the ratio between the short-circuit ratio index and the operational short-circuit ratio index. This elucidates the correlation between the short-circuit ratio index and the practical short-circuit ratio during operation.

Several typical points of complex short-circuit ratio thresholds are marked in Figure 4 and Figure 5, which are analyzed as follows:

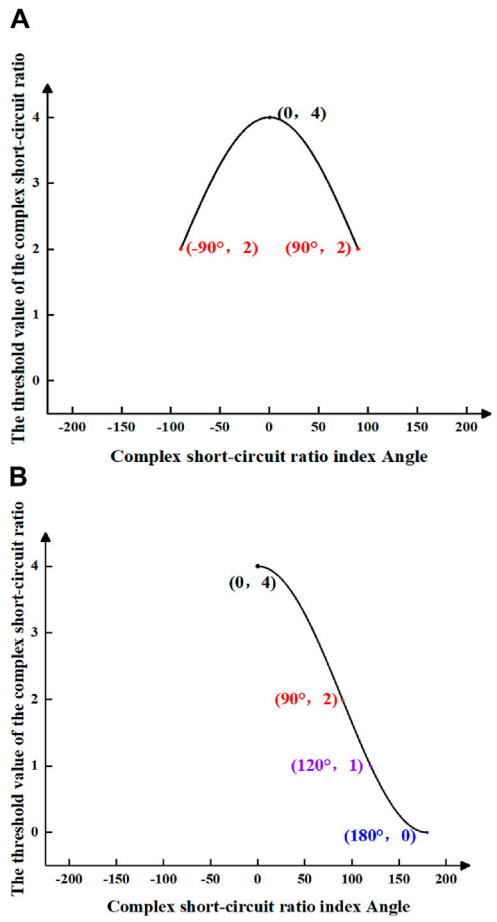

FIGURE 9
The threshold value amplitude of complex short circuit ratio is assumed under condition 4. **(A)** shows the threshold value amplitude of the complex short-circuit ratio when the index Angle of the complex short-circuit ratio is from −90° to 90°. **(B)** shows the threshold value amplitude of the complex short-circuit ratio when the index Angle of the complex short-circuit ratio is from 0° to 180°.

(1) Point (4, 0) in Figure 4 corresponds to point (0°, 4) in Figure 5. At this juncture, the complex short-circuit ratio threshold is 4, with the angle of the complex short-circuit ratio index being 0°. This implies that the condition is met when the equivalent impedance of the device and the Thevenin impedance of the system share the same phase angle.

(2) Point (0, ±2) in Figure 4 corresponds to point (±90°, 2) in Figure 5. At this juncture, the complex short-circuit ratio threshold is 2. The complex short-circuit ratio index angle can take on two values of ±90°, leading to the existence of the following two special cases:

1) The equivalent impedance of the device is a pure resistance (which can be positive or negative), while the system's Thevenin impedance is purely reactive. A negative resistance can be understood as the scenario commonly assumed in conventional LCC-DC analysis, whereas a positive resistance corresponds to the typical assumption made in load analysis.

2) The equivalent impedance of the device is a pure reactance (which can be positive or negative), while the system's Thevenin impedance is purely resistive. A negative reactance can be understood as the scenario commonly assumed in parallel capacitor or SVC analysis, whereas a positive reactance corresponds to the typical assumption made in parallel reactance compensation.

Assuming that the Thevenin equivalent impedance angle of the AC system is 70° and the equivalent impedance angle of the device is −20° (indicating some reactive compensation), the threshold value is 2. If reactive compensation on the device side is increased at this point, with the assumed equivalent impedance angle becoming −50°, the critical complex short-circuit ratio will be less than 2. This scenario can be likened to the integration of new energy sources through VSC grid connection.

(3) Point (−0.5, ±0.866) in Figure 4 corresponds to point (±120°, 1) in Figure 5. At this juncture, the threshold value of the complex short-circuit ratio is 1, with an angle index of 120°. This criterion is met when there is a 120° difference between the angles of the system's Thevenin equivalent impedance and the equivalent impedance of the device.

(4) Point (4, 0) in Figure 4 corresponds to point (±180°, 0) in Figure 5. At this juncture, the threshold value of the complex short-circuit ratio is 0, with two scenarios for the angle index of ±180°. In this unique case, where only reactance is considered for both the device's equivalent impedance and the system's Thevenin equivalent impedance, one exhibiting positive reactance while the other negative reactance, it signifies an extreme scenario within the power grid.

In the actual power grid, the Thevenin equivalent impedance of the system is $R \geq 0$ and $X \geq 0$, so it is more reasonable to set the Thevenin equivalent impedance Angle of the AC system at (0, 90°).

Assuming Condition 1: In scenarios involving conventional DC or new energy grid integration on the device side, when the device injects positive active power into the system, the angle of the device's equivalent impedance ranges from (−180°, −90°) to (90°, 180°). Consequently, the angle range for the complex short-circuit ratio is (−180°, 0) and (90°, 180°). Following Eq. 20, one can generate the magnitude plot of the threshold value of the complex short-circuit ratio as illustrated in Figure 6.

Assuming Condition 2: When the device injects positive reactive power into the system, such as in the case of phase reversal failure during the operation of the LCC, there will be significant changes in the reactive power consumption by the LCC (Yin and Li, 2021). It will cease to consume excess reactive power and instead feed the surplus reactive power into the AC system. At this juncture, the impedance angle of the device ranges from (−180°, −90°), allowing for the calculation of the angle of the complex short-circuit ratio within the ranges of (90°, 180°) and (−180°, −90°). Subsequently, the threshold value of the complex short-circuit ratio becomes (0, 2), leading to the generation of the magnitude plot illustrating the threshold value of the complex short-circuit ratio, as depicted in Figure 7A.

When the device injects negative reactive power into the system, thereby absorbing excess reactive power from the system. For example, a

TABLE 2 Parameters of the single device grid-connected system.

R	Equivalent impedance of AC system	Short-circuit capacity
R = 0	$Z = 0.2i$	$S_{ac} = 5$
R≠0	$Z = 0.1 + 0.2i$	$S_{ac} = 4.472$

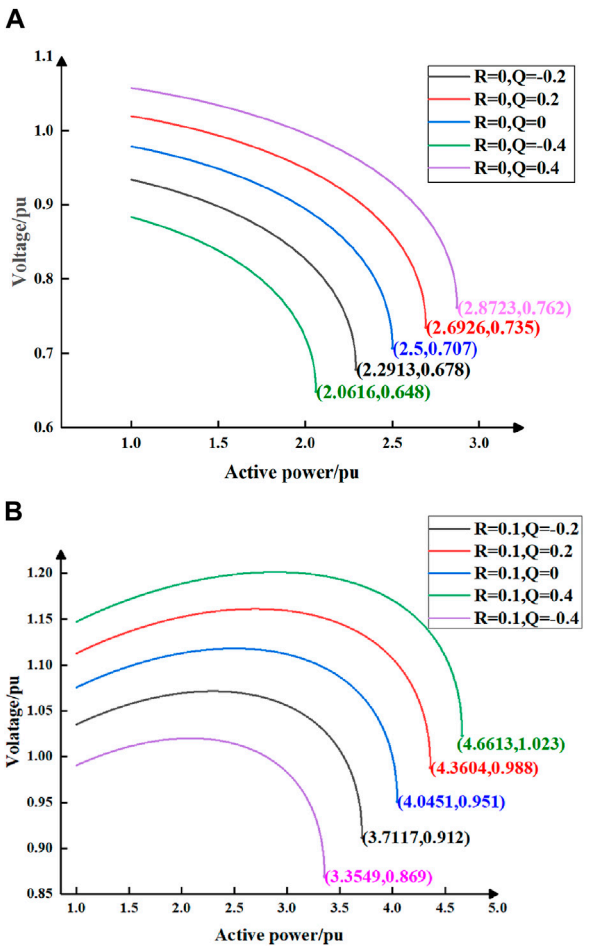

FIGURE 10
P-V curve of single device grid-connected system. **(A)** shows the P-V curve of the single device grid-connected system when R = 0. **(B)** shows the P-V curve of the single device grid-connected system when R = 0.1.

generator can decrease excitation current to operate at a leading power factor, thereby absorbing excess reactive power from the system (He and Wen, 2016). At this juncture, the impedance angle of the device ranges from (90°, 180°), facilitating the computation of the angle of the complex short-circuit ratio as (−180°, 0). The threshold value of the complex short-circuit ratio at this stage is (0, 4), leading to the graphical representation of the threshold value of the complex short-circuit ratio, as illustrated in Figure 7B.

Figures 7A,B both share a common element of (−90°, 0), which is associated with the magnitude of the equivalent impedance angle under the assumed conditions and the impedance angle of the equivalent device.

TABLE 3 CSCR of single device grid-connected system.

R	R = 0				
Q	−0.4	−0.2	0	0.2	0.4
CSCR	2.381	2.174	2	1.852	1.724
R	R≠0				
Q	−0.4	−0.2	0	0.2	0.4
CSCR	1.324	1.203	1.106	1.025	0.956

TABLE 4 $\widetilde{CSCR}$ of single device grid-connected system.

R	R = 0				
Q	−0.4	−0.2	0	0.2	0.4
θ	−79°	−85°	−90°	−94.3°	−97.9°
$\widetilde{CSCR}$	2.381	2.174	2	1.852	1.724
R	R≠0				
Q	−0.4	−0.2	0	0.2	0.4
θ	−109.8°	−113.5°	−116.6°	−119.2°	−121.5°
$\widetilde{CSCR}$	1.324	1.203	1.156	1.025	0.956

Assumption 3. In the scenario where the device operates under load conditions and injects negative active power into the system, the impedance angle of the equivalent device ranges from −90° to 90°. Consequently, the complex short-circuit ratio angle falls within the range of −90°–180°, and a graphical representation of the threshold value of the complex short-circuit ratio can be constructed using Eq. 20 as depicted in Figure 8.

Assumption 4. When the device introduces negative reactive power into the system, the impedance angle of the device spans from 0° to 90°, resulting in a complex short-circuit ratio angle of −90°–90°. In this case, the threshold value of the complex short-circuit ratio ranges from 2 to 4, leading to the magnitude plot shown in Figure 9A. On the other hand, if the device injects positive reactive power, the impedance angle of the device ranges from 0 to −90°, yielding a complex short-circuit ratio angle of 0°–180°. The corresponding The corresponding the threshold value of the complex short-circuit ratio is between 0 and 4 is between 0 and 4, resulting in the magnitude plot shown in Figure 9B.

Both Figures 9A,B exhibit a common element of (0, 90°), which is related to the magnitude of the Thevenin equivalent impedance angle and the device equivalent impedance angle under the assumed conditions.

This section presents the derivation of the threshold value of the complex short-circuit ratio in diverse scenarios, taking into account the complex short-circuit ratio angle. As a result, the critical value of the complex short-circuit ratio are not simply specific values under certain assumed conditions, as is the case with the short-circuit ratio index. Consequently, the use of the complex short-circuit ratio index

to analyze voltage support issues in power grids is no longer confined to the traditional scenario of DC injection into an AC grid, as with the short-circuit ratio index.

5 Example analysis

The Matlab model was employed to calculate the system's maximum power transmission using the continuous load flow method. The equivalent impedance model of the AC system, which considers different reactive power injections, was devised, accounting for both reactance and impedance. Through simulating a single-feed system when a three-phase fault occurs at the grid connection point, the correlation between the threshold value of the complex short-circuit ratio and the critical short-circuit ratio is validated.

Table 2 presents the equivalent impedance of the AC system for the single-device grid system depicted in Figure 3. Furthermore, Figure 10 demonstrates the P-V curve of the single-device grid system under different reactive power injections.

Based on Figure 10, the critical short-circuit ratios for the single-device grid system depicted in Figure 3 under different reactive power injections can be computed and are presented in detail in Table 3.

By calculating the angle of the complex short-circuit ratio index and combining it with Eq. 20, we can obtain the threshold value of the complex short-circuit ratio for the single-feed-in system depicted in Figure 3 under different reactive power injections, as presented in Table 4.

For grid-connected systems with varying reactive power injections, their P-V curves exhibit differences, resulting in distinct critical stability points and, consequently, varying critical short-circuit ratio index. The angles of the complex short-circuit ratio index, vary under different reactive power injections, leading to unique numerical values for the calculated the threshold value of the complex short-circuit ratio. By integrating data from Tables 3, 4, it becomes apparent that the threshold value of the complex short-circuit ratio in Table 4 correspond to the numerical values of the critical short-circuit ratio in Table 3. This correspondence illustrates that the complex short-circuit ratio index can effectively quantify and evaluate the voltage support strength of the power grid in a systematic manner.

Analysis of Table 4 reveals that when both active and reactive powers are injected positively, the angle of the complex short-circuit ratio falls exactly within the range of Figure 7A. Conversely, when injecting positive active power alongside negative reactive power, the angle of the complex short-circuit ratio falls within the range shown in Figure 7B.

From Tables 3, 4, it can be observed that the threshold value of the complex short-circuit ratio equals 2 only when active power is injected at the equipment side and the system side considers only reactance. Additionally, these tables highlight a considerable disparity in the threshold value of the complex short-circuit ratio when factoring in the influence of resistance compared to disregarding it at the same level of reactive power injection. Therefore, when quantitatively assessing voltage support strength, the influence of resistance cannot be ignored.

6 Conclusion

This paper mainly conducts relevant research on the influencing factors of the critical short-circuit ratio, the construction method of the complex short-circuit ratio index, and the calculation analysis method of the threshold value of the complex short-circuit ratio under the static voltage stability. The following conclusions can be drawn:

(1) Through the derivation of the critical short-circuit ratio, it can be proved that the threshold value of 2 is obtained under specific assumptions, and can only be applied to the traditional DC grid-connected scenario.
(2) The proposed the complex short-circuit ratio index integrates considerations both the magnitude and phase angle of the equivalent impedance of the device and the Thevenin equivalent impedance of the AC system. This makes the complex short-circuit ratio index a two-dimensional metric, facilitating a quantitative assessment of voltage support strength in the grid-connected scenario of diverse devices.
(3) By considering the angle of the complex short-circuit ratio index, this paper establishes a linkage between the device side and the AC power grid side of the grid-connected system. Leveraging the criteria of static voltage stability, the paper derives the threshold value of the complex short-circuit ratio. Notably, variations in the threshold value of the complex short-circuit ratio across diverse devices grid-connected configurations are evident from the analysis.

Data availability statement

The original contributions presented in the study are included in the article/Supplementary Material, further inquiries can be directed to the corresponding author.

Author contributions

PL: Writing–original draft, Writing–review and editing. JZ: Conceptualization, Formal analysis, Methodology, Resources, Writing–original draft, Writing–review and editing.

Funding

The author(s) declare that no financial support was received for the research, authorship, and/or publication of this article.

Conflict of interest

The author declares that the research was conducted in the absence of any commercial or financial relationships that could be construed as a potential conflict of interest.

Publisher's note

References

Chen, G., Li, M., Xu, T., Zhang, J., and Wang, C. (2017). Practice and challenge of Chinese power grid supporting the development of renewable energy. *Power Grid Technol.* 41 (10), 3095–3103. doi:10.13335/j.1000-3673.pst.2017.1780

He, Y., and Wen, Z. (2016). *Power system analysis*. Wuhan: Huazhong University of Science and Technology Press.

Huang, Q., Cao, S., Wu, Y., Lin, X., Wei, F., Yang, D., et al. (2023). New multi-feed short-circuit ratio index taking into account new energy amplitude-phase characteristics. *Proc. CSEE*. Available at: http://kns.cnki.net/kcms/detail/11.2107.TM.20230711.0838.002.html.

IEEE Standards Board IEEE Std 1204-1997 (1997). *IEEE guide for planning DC links terminating at AC locations having low short-circuit capacities*. New York: IEEE.

Kang, Y., Lin, X., Zheng, Y., Quan, X., Hu, J., Yuan, X., et al. (2020). Static stability limit and static stability working area of new energy grid-connected converter single-machine infinite bus system. *Proc. CSEE* 40 (14), 4506–4515+4730. doi:10.13334/j.0258-8013.pcsee.190906

Kim, Y.-K., Lee, G. S., Kim, C. K., and Moon, S. I. (2022). An improved AC system strength measure for evaluation of power stability and temporary overvoltage in Hybrid multi-infeed HVDC systems. *IEEE Trans. Power Deliv.* 37 (1), 638–649. doi:10.1109/tpwrd.2021.3068153

Lin, W., Tang, Y., and Bu, G.-Q. (2008). Definition and application of Short-circuit ratio in multi-feed AC-DC system. *Proc. CSEE* 28 (31), 1–8. doi:10.13334/j.0258-8013.pcsee.2008.31.001

Liu, Z. (2000). Impedance analysis of heavy load node in voltage stability problem. *Proc. CSEE* 20 (4), 36–40. doi:10.13334/j.0258-8013.pcsee.2000.04.008

Sun, H., Xu, S., and Xu, T. (2021). Definition and index of Short-circuit ratio of new energy multi-station. *Proc. CSEE* 41 (02), 497–506. doi:10.13334/j.0258-8013.pcsee.202112

Sun, H., Lin, Y., and Zhao, B. (2023a). Quantitative Analysis Method of voltage support Strength for new energy grid-connected Systems based on steady-state voltage safety constraints after faults. *Proc. CSEE* 43 (09), 3322–3332. doi:10.13334/j.0258-8013.pcsee.220466

Sun, H., Yu, L., and Zhao, B. (2023b). Quantitative Analysis Method of voltage support Strength for new energy grid-connected Systems based on transient overvoltage constraints. *Proc. CSEE* 43 (11), 4207–4218. doi:10.13334/j.0258-8013.pcsee.220468

Wu, D., Milad, J., Malyscheff, A. M., Hong, M., and Jiang, J. N. (2018). Assessing impact of renewable energy integration on system strength using site-dependent short circuit ratio. *IEEE Trans. Sustain. Energy* 9 (3), 1072–1080. doi:10.1109/tste.2017.2764871

Xu, Z. (1997). Study on DC transmission Characteristics of weak AC System: transmission power of DC transmission. *Power Grid Technol.* 21 (1), 12–16. doi:10.13335/j.1000-3673.pst.1997.01.004

Xu, Z. (2019). Reasonable definition and calculation method of power grid strength under the background of new power system. *High. Volt. Technol.* 48 (10), 3805–3819. doi:10.13336/j.1003-6520.hve.20221327

Yamada, Y., Tsusaka, A., Nanahara, T., and Yukita, K. (2023). A study on short-circuit-ratio for an inverter-based resource with power-voltage curves. *IEEE Trans. Power Syst.*, 1–10. doi:10.1109/tpwrs.2023.3347574

Yin, C., Li, F., and Zhou, S. (2019). Dc lock-in transient Overvoltage calculation method based on reactive Power Short-circuit Ratio. *Automation Electr. Power Syst.* 43 (10), 150–154. doi:10.7500/AEPS20181114006

Yin, C., and Li, F. (2021). Analytical expression on transient overvoltage peak value of converter bus caused by DC faults. *IEEE Trans. Power Syst.* 36 (3), 2741–2744. doi:10.1109/tpwrs.2021.3062218

Yu, L., and Sun, H. (2022). A critical system strength evaluation of a power system with high penetration of renewable energy generations. *CSEE J. Power Energy Syst.* 8 (3), 710–720. doi:10.17775/CSEEJPES.2021.03020

Zhou, X., Lu, Z., Liu, Y., and Chen, S. (2014). Development mode and key technologies of China's future power grid. *Proc. CSEE* 34 (29), 4999–5008. doi:10.13334/j.0258-8013.pcsee.2014.29.001

frontiers | Frontiers in Energy Research

TYPE Original Research
PUBLISHED 30 August 2024
DOI 10.3389/fenrg.2024.1430580

OPEN ACCESS

EDITED BY
Yonghui Liu,
Hong Kong Polytechnic University, Hong Kong SAR, China

REVIEWED BY
Chaoran Zhuo,
Xi'an University of Technology, China
Cencen Hong,
Nanjing Institute of Technology (NJIT), China
Huimin Wang,
Zhejiang Sci-Tech University, China
Kenneth E. Okedu,
Melbourne Institute of Technology, Australia

*CORRESPONDENCE
Gao Ningyu,
gao_ningyu_ntu@163.com

RECEIVED 10 May 2024
ACCEPTED 16 August 2024
PUBLISHED 30 August 2024

CITATION
Zhengwan D, Ningyu G and Yali Z (2024) Improved droop control strategy for distributed photovoltaic power generation systems. *Front. Energy Res.* 12:1430580. doi: 10.3389/fenrg.2024.1430580

Improved droop control strategy for distributed photovoltaic power generation systems

Deng Zhengwan[1], Gao Ningyu[2]* and Zhu Yali[1]

[1]Department of Electronics and Information, Jiangsu Vocational College of Business, Nantong, Jiangsu, China, [2]School of Electrical Engineering, Nantong University, Nantong, Jiangsu, China

The control strategy of a distributed photovoltaic (PV) power generation system within a microgrid consists of an inner-loop controller and an outer-loop controller. The inner-loop controller is divided into two types, namely, the maximum power point tracking (MPPT) control strategy and DC bus voltage support strategy. Switching between these two control strategies results in issues such as DC bus overvoltage, system oscillations, or even PV system failure. An improved droop control strategy with a novel inner-loop controller is proposed, incorporating an output power derivative regulator. The control system unifies MPPT and DC bus voltage support strategy without switching the controller structure. A simulation model is built to validate the effectiveness of the proposed control strategy, and the results show that the ripple of DC bus voltage decreases by more than 60%.

KEYWORDS

output power differential control strategy, distributed photovoltaic power generation system, droop control, maximum power point tracking, DC bus voltage support strategy

1 Introduction

The photovoltaic (PV) power generation system can reduce fossil energy consumption and carbon emissions (Manoj Kumar et al., 2023; Dhinesh and Vijayakumar, 2022). The installed capacity of PV systems has the most spectacular growth all over the world. Because of the features of microgrids and PV systems, it is essential for PV systems to be connected to microgrids through power electronic devices on a large scale (Hu et al., 2022; Shao et al., 2023).

In order to maximize the utilization of solar energy, most available PV systems always adopt the maximum power point tracking (MPPT) control strategy (Xiong et al., 2021; Xuan et al., 2022). Due to the volatility of PV power, which creates an imbalance between generation and local load power, and the lack of DC bus voltage support, additional energy storage devices are required (Shen et al., 2023). As high-density distributed PV systems with increasing capacity are connected to microgrids, there are still problems such as DC bus overvoltage and undervoltage, which result in energy storage devices being overcharged or undercharged (Hadjidj et al., 2019; Xiong et al., 2020). While increasing the capacity of energy storage devices may solve the problem, it also leads to higher maintenance costs.

In order to apply MPPT, the PV controller requires steady and reliable DC bus voltage with small fluctuation and high capacity for proper functioning (Shavolkin et al., 2023; Raj and Kos, 2022; Harag et al., 2022). In island mode, the microgrid is disconnected from the major power grid, so it loses the reliable and stable DC voltage support ability from the bulk power grid. Thus, the power balance between the local load and power generation should be governed within the microgrid itself (Rezaei et al., 2022; Liu et al., 2023). To some extent, a high-capacity energy storage device in the microgrid can support the DC bus voltage (He

et al., 2022). Nevertheless, energy storage devices increase construction and maintenance costs, and there are still problems such as overcharging and undercharging (De et al., 2023).

Cai et al. (2018) proposed a control strategy for PV systems in the island mode, which consists of two control loops. The inner control loop is the output voltage loop, and the outer control loop is divided into two categories, namely, MPPT control strategy and DC bus voltage support strategy. When the charging and discharging powers of energy storage devices and the load and output powers of PV systems are unbalanced, the outer loop adopts the DC bus voltage support strategy. Conversely, when these are balanced, the outer loop adopts MPPT. However, switching between MPPT and DC bus voltage support strategies will lead to voltage and power oscillations and may even cause the PV system to crash.

Thus, an advanced and reliable control strategy for PV should meet the following criteria. In island mode, a steady DC bus voltage should be achieved without requiring additional efforts in software and hardware design (Li et al., 2023). In grid-connected mode, PV applies MPPT to maximize the utilization of solar energy (Shubham Kumar and Anshul, 2023). The control strategy can implement MPPT and DC bus voltage support without switching the control configurations (Vijayshree and Sumathi, 2023), and for distributed PV systems in microgrids, the control strategy algorithm is decentralized to reduce the influence of communication systems (Zhu et al., 2022).

The mathematical formulas for describing photovoltaic arrays tend to be nonlinear. It can be divided into two regions, namely, region I and region II. In region I, dP_{pv}/dv_{pv} is positive. P_{pv} is the output power of the PV array, and v_{pv} is the output voltage of the PV array. In region II, dP_{pv}/dv_{pv} is negative; as P_{pv} increases beyond the load power, v_{pv} decreases to maintain a steady DC bus voltage. On the basis of theoretical analysis, an improved droop control strategy is proposed.

The proposed control strategy also consists of two loops. The outer control loop is the droop control loop, and the inner control loop is used to control dP_{pv}/dv_{pv}. By controlling dP_{pv}/dv_{pv} to be 0, the proposed control strategy becomes equivalent to MPPT. By controlling dP_{pv}/dv_{pv} to be negative, the proposed control strategy becomes equivalent to the DC bus voltage support strategy. Thus, with the novel control strategy, the PV system can switch control targets naturally without switching the control strategy.

Since dP_{pv}/dv_{pv} and P_{pv} tend to be nonlinear, the droop coefficients for each distributed PV change to distribute the local power balanced to each PV. A parametric design method for droop coefficients is also proposed.

To verify the feasibility of the proposed control strategy, a simulation model with three distributed PV systems is built, and the results show its effectiveness.

2 PV model

2.1 Mathematics model of photovoltaic arrays

PVs are always connected to the DC bus through a DC/DC converter. The DC/DC converter adopts a control strategy with two control loops, and the outer-loop controller applies MPPT, the inner-loop controller is the output voltage of the photovoltaic array controller. Figure 1 shows the structure diagram of the PV.

Here, i_{pv} and v_{pv} are the output current and output voltage of the photovoltaic array. v_{dc} and i_{dc} are the DC bus voltage and the DC bus current, respectively. L_f is the filter inductance. C_{pv} and C_b are the output capacitance and DC bus capacitance, respectively. v_i and i_i are the output voltage and output current of the DC/AC converter, respectively.

The DC/DC converter can adopt the Boost converter if the serial number of photovoltaic arrays is relatively small, and the DC/DC converter can adopt the Buck converter if the serial number of photovoltaic arrays is relatively large, and the DC/DC converter can adopt the Buck/Boost converter, if the serial number of photovoltaic arrays is reasonable.

The output current of the PV is expressed as

$$i_{pv} = N_p I_{sc,n} - \frac{N_p I_{sc,n}}{e^{\frac{V_{oc,n}}{aV_t}} - 1}\left(e^{\frac{V_{pv}}{N_s a V_t}} - 1\right), \tag{1}$$

where N_p is the number of parallel photovoltaic arrays and N_s is the number of serial photovoltaic arrays. $V_{oc,n}$ and $I_{sc,n}$ are, respectively, the open-circuit voltage and short-circuit current of photovoltaic arrays at 298.16 K and 1,000 W/m^2. a is an equivalent constant of the ideal diode. V_t in Equation 1 is the thermal voltage of the photovoltaic panel, and it is expressed as

$$V_t = \frac{NkT}{q}, \tag{2}$$

where k is the Boltzmann's constant, T is the environmental temperature, q is the number of elementary charge, and N is the serial number of the photovoltaic power generation unit.

Based on Equations 1, 2, the output power of photovoltaic arrays is expressed as

$$P_{pv} = i_{pv} v_{pv} = N_p I_{sc,n} v_{pv}\left(1 - e^{\left(\frac{v_{pv}}{N_s a V_t} - \frac{V_{oc,n}}{aV_t}\right)}\right). \tag{3}$$

The relational expression of the output voltage ripple and the output capacitance is

$$C_{pv}\frac{dv_{pv}}{dt} = i_{pv} - i. \tag{4}$$

According to Equation 4, the lager capacitance can reduce the output voltage ripple.

2.2 Control strategy of the PV

The PV system operates in three different modes, namely, "islanding mode," "grid-connected mode," and "switching mode."

In switching mode, once the interconnecting tie of the PV and large power grid breaks, the PV system should switch its operation mode from grid-connected mode to islanding mode. After the fault is cleared, the PV system should switch back to grid-connected mode.

In grid-connected mode, with the support of voltage and frequency from bulk power systems, the PV system always adopts MPPT. In islanding mode, due to the lack of DC bus voltage support, the PV system should be configured with energy storage devices to adopt MPPT. There is still a risk of overcharging energy storage devices if P_{pv} is larger than the local load and the

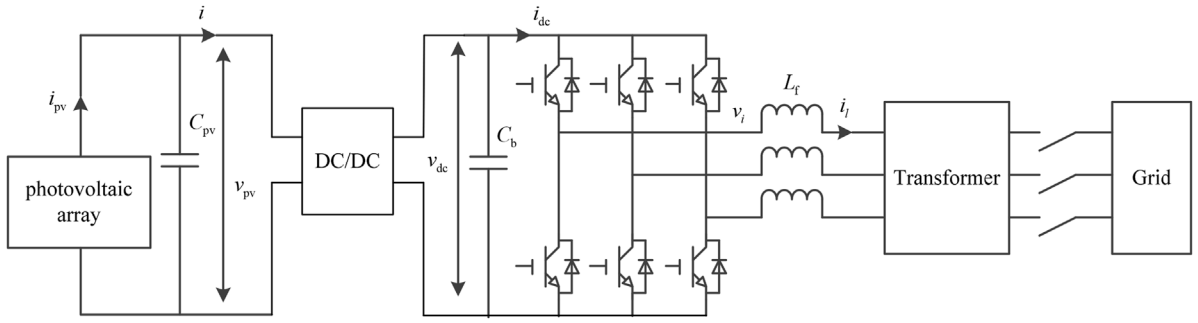

FIGURE 1
Structure diagram of the PV system.

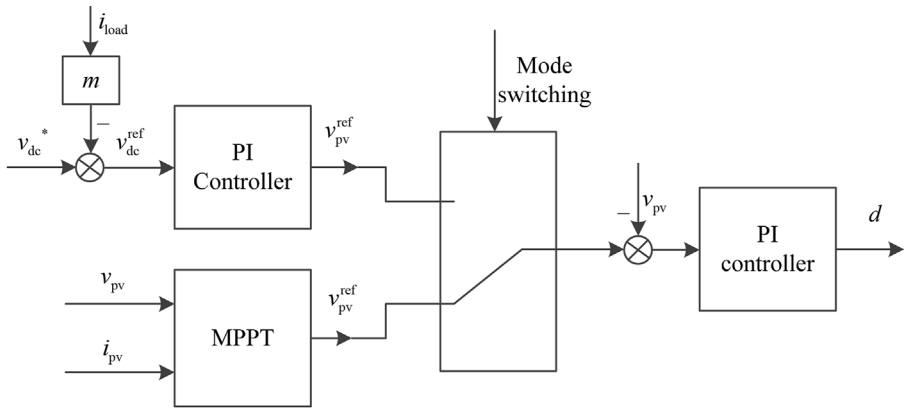

FIGURE 2
Control strategy.

charging power of the energy storage device, leading to DC bus overvoltage and even system failure. In addition, incorporating the energy storage devices increases the construction and maintenance costs.

Thus, in islanding mode, the control strategy of the PV system can be divided into two categories, namely, MPPT and DC bus voltage support strategy. According to the operating condition, the control system switches the control strategy to meet the performance requirement. Figure 2 shows the control strategy of the PV system.

As shown in Figure 2, the control system of the PV needs to switch between the two types of control strategies according to the operating condition. The construction of the control system is complicated, and the hardware and software costs increase. The toughest problems caused by switching control strategies are voltage and power fluctuations, which result in poor reliability of the control system. The severe voltage and power fluctuations will result in PV system failure.

Here, d is the duty cycle of the DC/DC converter, i_{load} is the load current, $v_{\mathrm{dc}}{}^{*}$ is the reference value of DC bus voltage, $v_{\mathrm{dc}}^{\mathrm{ref}}$ is the reference value of the DC bus voltage controller, and $v_{\mathrm{pv}}^{\mathrm{ref}}$ is the reference value of the controller for v_{pv}.

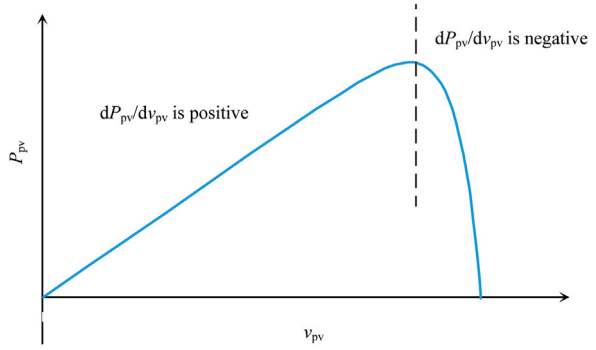

FIGURE 3
Output characteristics of the photovoltaic array.

2.3 Output characteristics of photovoltaic arrays

Figure 3 shows the schematic diagram describing P_{pv} varying with v_{pv} of the PV array.

As shown in Figure 3, it is divided into two regions, namely, region I and region II. In region I, dP_{pv}/dv_{pv} is positive, and in region II, dP_{pv}/dv_{pv} is negative. MPPT is equivalent to $dP_{pv}/dv_{pv} = 0$.

As the local load power increases, the DC bus voltage decreases. While in region II, as v_{pv} decreases, P_{pv} increases. So, the local load power and P_{pv} are balanced again. In region I, as v_{pv} decreases, P_{pv} decreases, which results in a worse decrease in DC bus voltage. Hence, region II is more stable than region I. By controlling dP_{pv}/dv_{pv} to be negative, the DC bus voltage support strategy is achieved.

3 Proposed control strategy

3.1 dP_{pv}/dv_{pv}

Based on Equation 3, dP_{pv}/dv_{pv} can be calculated using the micro-increment of conductance di_{pv}/dv_{pv}, and it is expressed as

$$\frac{dP_{pv}}{dv_{pv}} = \frac{d(v_{pv}i_{pv})}{dv_{pv}} = i_{pv} + v_{pv}\frac{di_{pv}}{dv_{pv}}. \tag{5}$$

A low-pass filter is adopted to reduce the influence of noise on i_{pv}, v_{pv}, and P_{pv}. In addition, the micro-increments of i_{pv} and v_{pv} are calculated using the low-pass filter. The output voltage and output current of the low-pass filter are expressed as

$$i_f(s) = \frac{1}{Ts+1}i_{pv}(s), \tag{6}$$

$$v_f(s) = \frac{1}{Ts+1}v_{pv}(s), \tag{7}$$

where s is the differential operator and $i_{pv}(s)$ and $v_{pv}(s)$ are Laplace transform from $i_{pv}(t)$ and $v_{pv}(t)$, respectively. T is the time constant of the low-pass filter. $i_f(s)$ is the output of the low-pass filter for $i_{pv}(s)$. $v_f(s)$ is the output of the low-pass filter for $v_{pv}(s)$.

The deviations from Equations 6, 7 are expressed as

$$si_f(s) = \frac{i_{pv}(s) - i_f(s)}{T}, \tag{8}$$

$$sv_f(s) = \frac{v_{pv}(s) - v_f(s)}{T}. \tag{9}$$

According to Equations 8, 9 and inverse Laplace transformation theory, di_f/dv_f is expressed as

$$\frac{di_{pv}}{dv_{pv}} \approx \frac{di_f}{dv_f} = \frac{i_{pv} - i_f}{v_{pv} - v_f}. \tag{10}$$

Based on Equation 10, the time constant of the low-pass filter has no influence on di_{pv}/dv_{pv}. Thus, the time constant of the low-pass filter is designed to reduce the noise. T is set based on the cut-off frequency of the low-pass filter. The cut-off frequency is 1,000 Hz, so T is equal to $1/2000\pi$.

According to Equations 5, 10, dP_{pv}/dv_{pv} is expressed as

$$\frac{dP_{pv}}{dv_{pv}} = i_{pv} + v_{pv}\frac{i_{pv} - i_f}{v_{pv} - v_f}. \tag{11}$$

According to Equation 11, Figure 4 shows the schematic diagram illustrating the computational method of dP_{pv}/dv_{pv}.

In Figure 4, the limit of dP_{pv}/dv_{pv} is equal to y (v_{oc_i}).

3.2 Improved droop control

To distribute the local power to multiple PV systems, an improved droop control strategy is proposed. It consists of two control loops, namely, the inner-loop controller, which adopts the dP_{pv}/dv_{pv} control strategy, and the outer-loop controller, which adopts droop control with adaptive droop coefficients.

Figure 5 shows the schematic diagram of the improved droop control strategy for the PV system.

Here, $[dP_{pv}/dv_{pv}]_{ref}$ is the input reference of the inner-loop controller, and it is expressed as

$$\left[\frac{dP_{pv}}{dv_{pv}}\right]_{ref} = \frac{dP_{pv}^{*}}{dv_{pv}} - m(v_{dc} - v_{dc-ref}), \tag{12}$$

where $(dP_{pv}/dv_{pv})^*$ is the reference value of dP_{pv}/dv_{pv}. If $(dP_{pv}/dv_{pv})^*$ is equal to 0, the proposed control system of the PV is equivalent to MPPT for the maximum utilization of solar energy, and m is the droop coefficient. v_{dc_ref} is the reference value of DC bus voltage.

As shown in Figure 5, if the difference between the real-time v_{dc} and v_{dc_ref} is smaller than the dead band, $[dP_{pv}/dv_{pv}]_{ref}$ is 0. If P_{Load} is smaller than P_{pv}–P_c, v_{dc} decreases; thus, v_{dc}-v_{dc_ref} is negative, which leads to $[dP_{pv}/dv_{pv}]_{ref}$ being negative. Hence, the control system of the PV is equivalent to the DC bus voltage support strategy.

Because of line impedance, power allocation among all PV systems can have errors when using the traditional droop control. To achieve accurate power allocation, a controller with a consensus algorithm in the second layer is necessary. Using the simplified and linear model affects the accuracy of the control system, but power allocation in the first layer is implemented.

3.3 Multiple operating modes of PV

In grid-connected mode, the DC bus voltage is adjusted using the grid-connected converter, and the DC/DC converter adopts MPPT. Thus, $(dP_{pv}/dv_{pv})^*$ is set to 0.

In isolating mode, the comparison expressions between the local load power P_{Load}, P_{pv}, the charging power of energy storage devices P_c, and the discharging power of energy storage devices P_D are presented as follows:

Once $P_{Load} < P_{pv}$–P_c, P_{pv} is excessive. Thus, to obtain a steady DC bus voltage, P_{pv} should decrease, and dP_{pv}/dv_{pv} is controlled to be negative.

Once P_{pv}–$P_c < P_{Load} < P_{pv} + P_D$, the DC bus voltage is supported by energy storage devices, dP_{pv}/dv_{pv} is controlled to be 0 so that MPPT is adopted.

Once $P_{Load} > P_{pv} + P_D$, dP_{pv}/dv_{pv} is controlled to be 0 so that MPPT is adopted. If the DC bus voltage continues to decrease, the fractional local load should be cut off to obtain a steady and limited DC bus voltage.

3.4 Calculation method of the droop coefficient

The output power of each PV system to support the local load is dependent on the droop coefficients. To simplify the analysis and

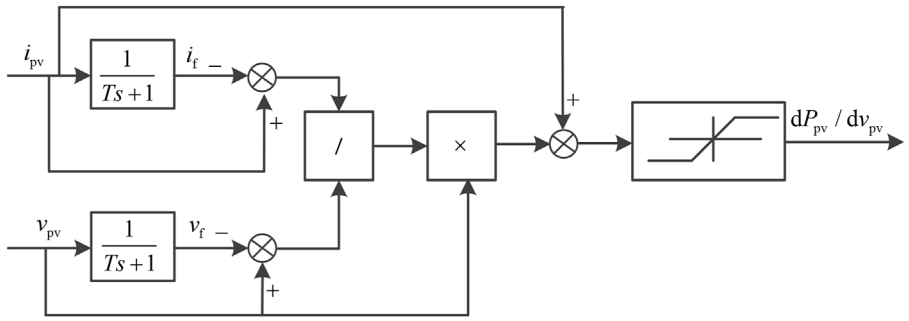

FIGURE 4
Schematic diagram illustrating the computational method of dP_{pv}/dv_{pv}.

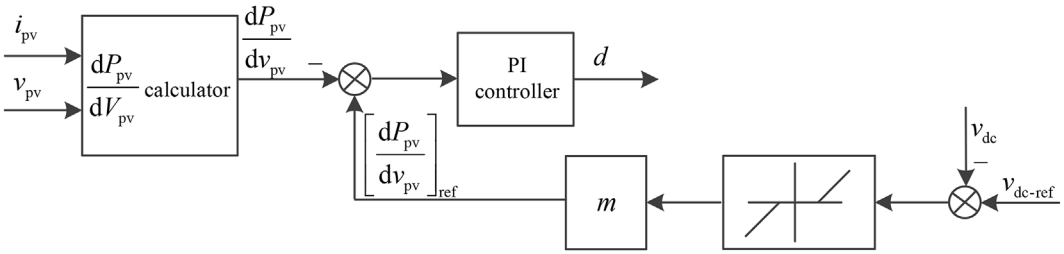

FIGURE 5
Improved control strategy of the PV system.

calculation, the relationship between P_{pv} and dP_{pv}/dv_{pv} of each PV system is simplified as a linear relation, which is expressed as

$$\hat{P}_{pv\_i} = f\left(\frac{dP_{pv-i}}{dv_{pv\_i}}\right) = \frac{P_{max\_i}}{y(v_{oc\_i})} \times \frac{dP_{pv-i}}{dv_{pv\_i}} + P_{max\_i}, \tag{13}$$

where P_{max_i} is the maximum output power of the ith PV, v_{oc_i} is the open-circuit output voltage of the ith PV, $y(v_{oc\_i})$ is dP_{pv}/dv_{pv} when the ith PV is an open circuit. $\hat{P}_{pv\_i}$ is the output power of the ith PV on the linear curve between P_{pv} and dP_{pv}/dv_{pv}.

The control system should distribute local power to each PV system as a rated ratio, which is expressed as

$$\frac{\hat{P}_{pv\_i}}{\hat{P}_{pv\_j}} = \frac{P_{max\_i}}{P_{max\_j}}. \tag{14}$$

By applying MPPT and according to Equations 12, 13, with $dP_{pv}/dv_{pv} = 0$, Equation 14 can be expressed as

$$\frac{\hat{P}_{pv\_i}}{\hat{P}_{pv\_j}} = f\left(\frac{dP_{pv\_i}}{dV_{pv\_i}}\right) \Big/ f\left(\frac{dP_{pv\_j}}{dV_{pv\_j}}\right) = \frac{\frac{P_{max\_i}}{y(v_{oc\_i})} \cdot m_i \cdot \Delta v + P_{max\_i}}{\frac{P_{max\_j}}{y(v_{oc\_j})} \cdot m_j \cdot \Delta v + P_{max\_j}}, \tag{15}$$

where Δv is expressed as

$$\Delta v = v_{dc\_ref} - v_{dc}. \tag{16}$$

According to Equations 15, 16, the droop coefficient of each PV system is expressed as

$$m_i = \frac{y(v_{oc\_i})}{v_{dc\_max} - v_{dc\_ref}}, \tag{17}$$

where m_i is the droop coefficient of the ith PV and u_{dc_max} is the upper limit value of DC bus voltage.

4 Parameters of the control system

4.1 Proposed control system

Figure 6 shows the whole control system. The inner-loop controller of PV applies a proportional–integral (PI) controller, while the outer-loop controller employs the droop control strategy. And m in Figure 6 is calculated by Equation 17.

4.2 Parameter design method

Figure 7 shows the small-signal model of the inner-loop controller.

Here, $G_{v_{pv}d}(s)$ is the transfer function of Δd to Δv_{pv}, and K_{pv} is expressed as Equation 18, and it is obtained by the linear small-signal model of the PV system, which is expressed as

$$K_{pv} = \frac{\Delta i_{pv}}{\Delta v_{pv}} = \frac{N_p \cdot I_{sc,n}}{e^{\frac{v_{oc,n}}{a \cdot v_t}} - 1 \cdot a \cdot N_s \cdot v_t} e^{\frac{v_{pv}}{a \cdot N_s \cdot v_t}}. \tag{18}$$

The small-signal model of the Buck converter is expressed as

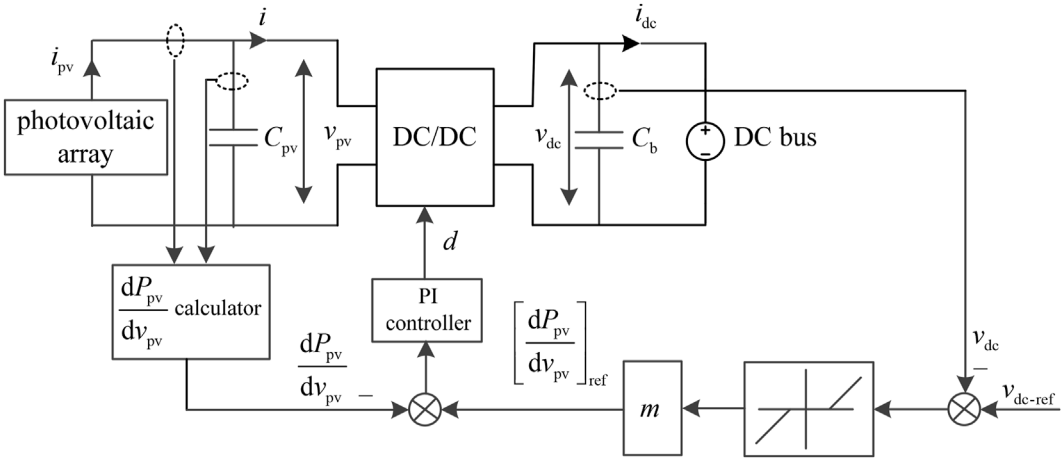

FIGURE 6
Whole control system.

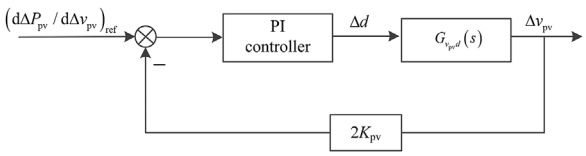

FIGURE 7
Small-signal model of the inner-loop controller.

$$L\frac{\mathrm{d}\Delta i_l}{\mathrm{d}t} = v_{\mathrm{pv}} \times \Delta d + d \times \Delta v_{\mathrm{pv}} - \Delta v_{\mathrm{dc}}, \tag{19}$$

$$C\frac{\mathrm{d}\Delta v_{\mathrm{dc}}}{\mathrm{d}t} = \Delta i_l - \frac{\Delta v_{\mathrm{dc}}}{R}, \tag{20}$$

$$C_{\mathrm{pv}}\frac{\mathrm{d}\Delta v_{\mathrm{pv}}}{\mathrm{d}t} = K_{\mathrm{pv}} \times \Delta v_{\mathrm{pv}} - d \cdot \Delta i_l - I_l \cdot \Delta d, \tag{21}$$

where L is the inductance of the Buck converter, d is the duty cycle of IGBT in the Buck converter, C is the output capacitor in the Buck converter, R is the equivalent load impedance, C_{pv} is the output capacitor of the photovoltaic array, and Δd is the variation in the duty cycle.

According to Equation 5, the small-signal model of the photovoltaic array is expressed as

$$\frac{\mathrm{d}\Delta P_{\mathrm{pv}}}{\mathrm{d}\Delta v_{\mathrm{pv}}} = \Delta i_{\mathrm{pv}} + K_{\mathrm{pv}}\Delta v_{\mathrm{pv}} = 2K_{\mathrm{pv}}\Delta v_{\mathrm{pv}}. \tag{22}$$

According to Equations 19–21, the transfer function between Δd and Δv_{pv} is achieved by Laplace transform, which is expressed as

$$G_{v_{\mathrm{pv}}d}(s) = \frac{\Delta v_{\mathrm{pv}}}{\Delta d} = -\frac{I_l \times L \times s + D \times v_{\mathrm{pv}}}{C_{\mathrm{pv}} \times L \times s^2 - K_{\mathrm{pv}} \times L \times s + d^2}. \tag{23}$$

According to Equations 22, 23, the transfer function between Δv_{pv} and $(\mathrm{d}P_{\mathrm{pv}}/\mathrm{d}v_{\mathrm{pv}})_{\mathrm{ref}}$ is expressed as

$$G_1(s) = \frac{\Delta v_{\mathrm{pv}}}{\left(\frac{\mathrm{d}P_{\mathrm{pv}}}{\mathrm{d}V_{\mathrm{pv}}}\right)_{\mathrm{ref}}} = \frac{G_{vpvd}(s) \times T_1(s)}{G_{vpvd}(s) \times T_1(s) \times 2 \times K_{\mathrm{pv}} + 1}, \tag{24}$$

where $T_1(s)$ is the transfer function of the PI controller shown in Figure 6, and it is expressed as

$$T_1(s) = K_{\mathrm{P1}} + \frac{K_{\mathrm{I1}}}{s}, \tag{25}$$

where K_{P1} and K_{I1} are the proportional and integral coefficients of the inner-loop controller, respectively.

In this paper, the phase margin of the inner-loop controller is set to 76°, and the bandwidth of the inner-loop controller is set to 580 Hz. And according to the tranfer function expressed by Equations 24, 25 is expressed as

$$T_1(s) = 0.001 + \frac{0.1}{s}. \tag{26}$$

5 Analysis of the results

5.1 Parameters of the simulation model

To verify the proposed control strategy, a simulation model is built. The parameters of the distributed PV system are shown in Table 1. The output capacitance of each PV system is 2,000 μF, the equivalent impedance of the transmission line is 0.002 Ω, the equivalent inductance of the transmission line is 0.2 mH, the output capacitance of the DC/DC converter is 10,000 μF, the rated DC bus voltage is 550 V, and the maximum charging and discharging powers are both 280 kW.

5.2 Influence of load in island mode

To verify the DC bus voltage support capability of the proposed control strategy, the DC bus voltage support capability of energy storage devices is neglected. The local load is set to 706 kW in the first stage, and the load impedance is 0.46 Ω. The local load is set to 899 kW in the second stage, and the load impedance is 0.35 Ω. The local load is set to 1,038 kW in the third stage, and the load impedance is 0.24 Ω.

10.3389/fenrg.2024.1430580

TABLE 1 Parameters of distributed PV systems.

Parameter	PV1	PV2	PV3
a	1.428	1.643	1.820
Short-circuit current	8.2 A	8.3 A	5.4 A
Open-circuit voltage	32.9 V	36.3 V	44.2 V
Serial number of electricity generation units	54	60	72
Serial number of photovoltaic arrays	30	25	22
Parallel number of photovoltaic arrays	84	55	66
Rated output power	504 kW	302 kW	251 kW
Droop coefficient	150	120	75
K_{P1}	0.001	0.001	0.001
K_{I1}	0.1	0.1	0.1
Phase margin of the dP_{pv}/dv_{pv} regulator	76°	76°	76°
Bandwidth of the dP_{pv}/dv_{pv} regulator	580 Hz	580 Hz	580 Hz
Switching frequency of IGBT	10 kHz	10 kHz	10 kHz

Figure 8 shows the response to a step change in load: a) DC bus voltage waveform, b) output power waveform of each PV system, and c) output voltage waveform of each PV system.

As shown in Figure 8, in the first and second stages, the local power is less than the maximum output power of PV, so PV applies the DC bus support strategy. Moreover, since dP_{pv}/dv_{pv} is controlled to be negative, the output voltage of the photovoltaic array is relatively high. In the third stage, the local load power is more than the maximum output power of PV, so PV applies MPPT, and the DC bus voltage is maintained at 500 V.

In addition, the droop coefficients of each distributed PV system are designed as the rated output power ratio, so the output power of each distributed PV is always 1.67:1:0.83.

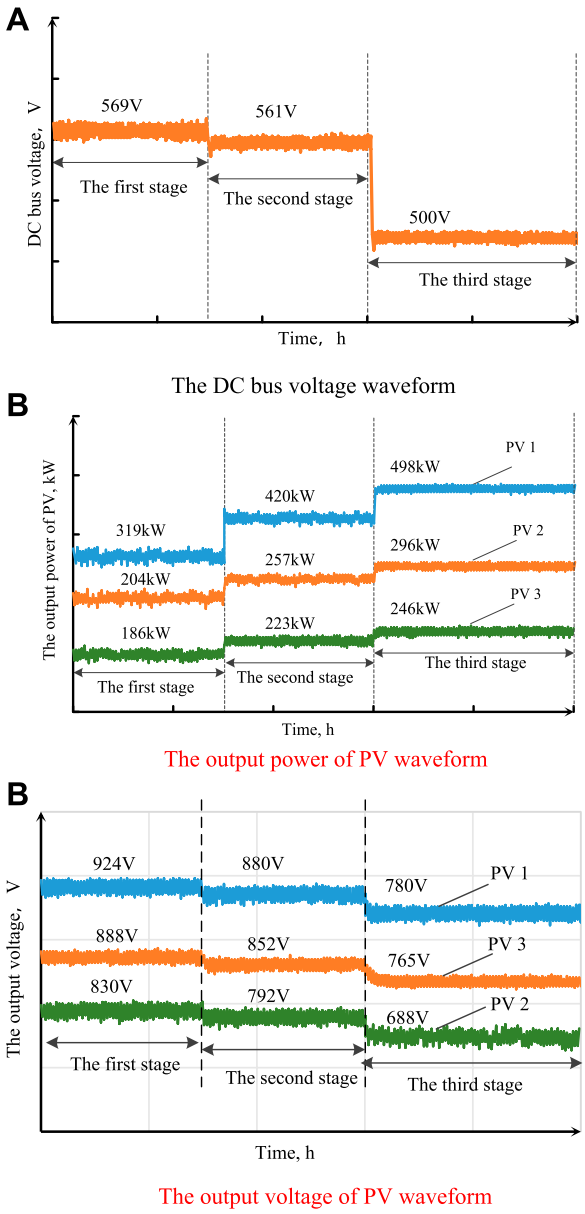

FIGURE 8
Operation performance of the PV system under different loads. **(A)** DC bus voltage of the waveform, **(B)** output power of the PV waveform, and **(C)** output voltage of the PV waveform.

5.3 Influence of irradiance in island mode

The local load is set as a constant and equal to 0.6 Ω. In the first stage, irradiance is set to 600 W/m^2. In the second stage, irradiance is set to 800 W/m^2. In the third stage, irradiance is set to 1,000 W/m^2. Figure 9 shows the response to a step change in irradiance: a) DC bus voltage waveform, b) output voltage waveform of each PV, and c) output power waveform of each PV.

As shown in Figure 9, the local load power is smaller than the maximum output power of PV, so the control strategy of PV becomes equivalent to the DC bus voltage support strategy to maintain a steady DC bus voltage.

Since PV operates in region II, dP_{pv}/dv_{pv} is negative. Thus, the output voltage increases as the output power decreases.

5.4 Performance of the improved control strategy

The initial state-of-charge of energy storage is set to 20% to consider the influence of the energy storage system. Furthermore, the local load power is set to 605 kW in the first stage, it is set to 316 kW in the second stage, and it is reset to 605 kW in the third stage.

By the proposed control strategy, in the first and third stages, the local load power and the charging power of the energy storage device are more than the maximum output power of the PV, so the inner-loop controller adjusts dP_{pv}/dv_{pv} to be 0, which is equivalent to MPPT. In the second stage, the local load power and the charging power of the energy storage device are less than the maximum output power of the PV, so the inner-loop controller adjusts dP_{pv}/dv_{pv} to be a negative value, which is equivalent to the DC bus voltage support strategy.

10.3389/fenrg.2024.1430580

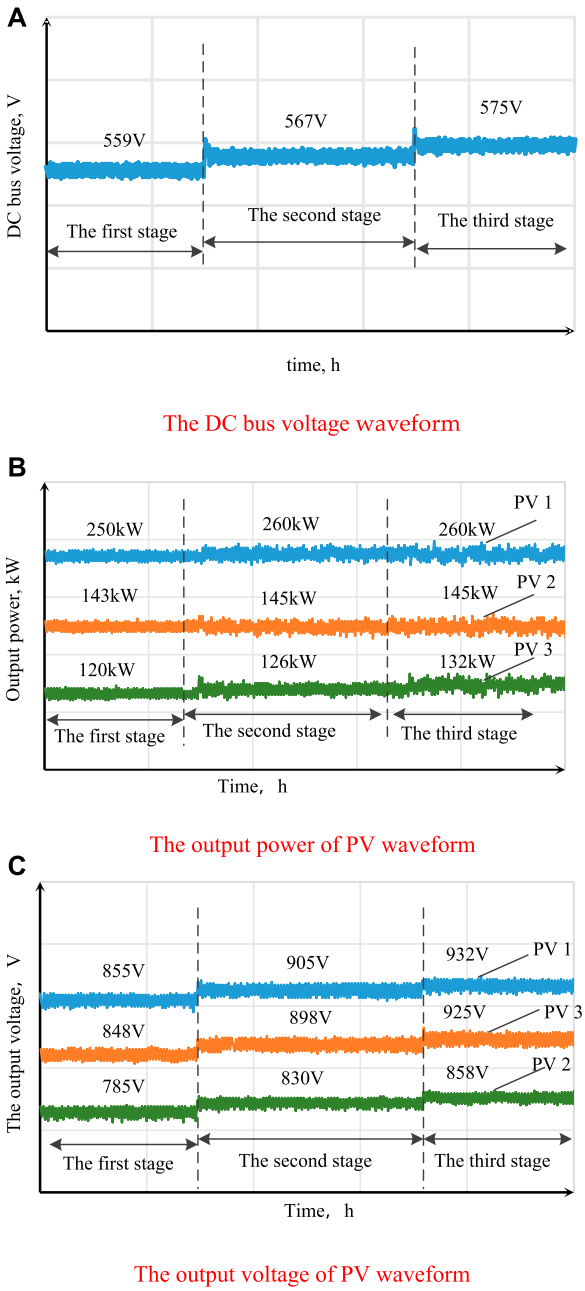

FIGURE 9
Operation performance of the PV system under different irradiance values. **(A)** DC bus voltage of the waveform, **(B)** output power of the PV waveform, and **(C)** output voltage of the PV waveform.

By the traditional control strategy, in the first and third stages, the inner-loop controller applies MPPT, and in the second stage, the inner-loop controller applies the DC bus voltage support strategy.

Hence, the proposed control strategy adjusts dP_{pv}/dv_{pv} to obtain a different control objective, while the traditional control strategy switches the control system to obtain a different control objective.

Figure 10 shows the DC bus voltage waveform using the proposed and traditional control strategies.

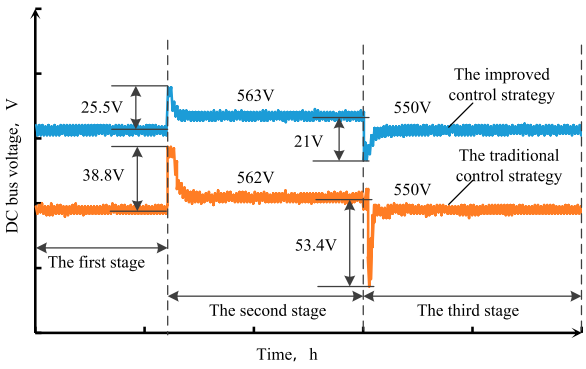

FIGURE 10
DC bus voltage waveform.

Figure 10 shows that both the improved and traditional control strategies can maintain the stability of DC bus voltage. In addition, for both control strategies, the ripples of DC bus voltage satisfy PV system requirements. With the proposed control strategy, the ripple of DC bus voltage is relatively small, thereby decreasing the influence of switching the control system on the PV system.

6 Conclusion

An improved droop control strategy for distributed PV systems is proposed; the inner-loop controller adjusts dP_{pv}/dv_{pv}, and the outer-loop controller applies droop control with adaptive droop coefficients to allocate local power scientifically to each distributed PV system. Using the proposed inner-loop controller, the PV system can achieve the maximum output power and provide DC bus support without changing the control configurations.

The proposed inner-loop controller can suppress the DC bus voltage oscillation. In the inner-loop controller, if dP_{pv}/dv_{pv} is regulated to be 0, the inner-loop controller is equivalent to MPPT. If dP_{pv}/dv_{pv} is regulated to be a negative value, the inner-loop controller is equivalent to the DC bus voltage support strategy. Using the proposed droop control strategy, both the maximum available output power of distributed PV systems and the steady DC bus voltage can be obtained.

Data availability statement

The original contributions presented in the study are included in the article/Supplementary Material; further inquiries can be directed to the corresponding author.

Author contributions

DZ: conceptualization, methodology, validation, writing–original draft, and writing–review and editing. GN: data

curation, formal analysis, funding acquisition, resources, writing–original draft, and writing–review and editing. ZY: conceptualization, formal analysis, software, supervision, validation, and writing–original draft.

Funding

The author(s) declare that financial support was received for the research, authorship, and/or publication of this article. This research was funded by the Nantong Natural Science Foundation Project (grant number JCZ2023029) and the Nantong City Social Livelihood Science and Technology Project (grant number MS2023062).

Conflict of interest

The authors declare that the research was conducted in the absence of any commercial or financial relationships that could be construed as a potential conflict of interest.

Publisher's note

References

Cai, H., Xiang, J., and Wei, W. (2018). Decentralized coordination control of multiple photovoltaic sources for DC bus voltage regulating and power sharing. *IEEE Trans. industrial Electron.* 65 (7), 5601–5610. doi:10.1109/tie.2017.2779412

De, P. J., Ruy, I., Galhardo, B., Costa, T., Pinho, J., Williamson, S., et al. (2023). Influence of photovoltaic microgeneration on the demand profile and its effects on the grid power quality. *Electr. Power Syst. Res.* 214 (Jan.Pt.B), 1–8. doi:10.1016/j.epsr.2022.108935

Dhinesh, V., and Vijayakumar, G. (2022). A switched quasi Z-source three-port (SqZSTP) DC-DC converter for a photovoltaic power generation system. *Semicond. Sci. Technol.* 37, 045014–45014.22. doi:10.1088/1361-6641/ac419d

Hadjidj, S., Bibi-Triki, N., and Faouzi, D. (2019). Analysis of the reliability of photovoltaic-micro-wind based hybrid power system with battery storage for optimized electricity generation at Tlemcen, north west Algeria. *Archives Thermodyn.* 40 (1), 161–185.

Harag, N., Imanaka, M., Kurimoto, M., Sugimoto, S., Bevrani, H., and Kato, T. (2022). Autonomous dual active power-frequency control in power system with small-scale photovoltaic power generation. *J. Mod. Power Syst. Clean Energy* 10 (04), 941–953. doi:10.35833/mpce.2020.000700

He, H., Lu, Z., Guo, X., Shi, C., Jia, D., Chen, C., et al. (2022). Optimized control strategy for photovoltaic hydrogen generation system with particle swarm algorithm. *Energies* 15 (4), 1472–1472.17. doi:10.3390/en15041472

Hu, Z., Cao, Wu, Sha, J., and Minhui, Q. (2022). "Improved frequency response model for power system with photovoltaic generation," in *2022 IEEE 5th international electrical and energy conference (CIEEC), nangjing, China*, 2929–2933. doi:10.1109/CIEEC54735.2022.9846523

Li, F., Yu, Y., and Yue, S. (2023). Study on characteristics of photovoltaic and photothermal coupling compressed air energy storage system. *Trans. Institution Chem. Eng. Process Saf. Environ. Prot.* 178, 147–155.

Liu, L., Zhai, R., Hu, Y., and Liu, S. (2023). Operation performance analysis of a novel renewable energy-driven multienergy supply system based on wind, photovoltaic, concentrating solar power, proton exchange membrane electrolyzers, and proton exchange membrane fuel cell. *Energy Technol. Gener. Convers. Storage, Distrib.* 11, 2–17. doi:10.1002/ente.202300291

Manoj Kumar, S., Chittaranjan, P., and Kaur, C. R. (2023). A computational intelligence based maximum power point tracking for photovoltaic power generation system with small-signal analysis. *Optim. Control Appl. Methods* 44 (2), 617–636. doi:10.1002/oca.2798

Raj, R., and Kos, A. (2022). A novel method of islanding detection in a distributed power generation system integrated with photovoltaic-array. *Przeglad Elektrotechniczny* 98 (7), 88–94.

Rezaei, J., Golshan, M. E. H., and Alhelou, H. H. (2022). Impacts of integration of very large-scale photovoltaic power plants on rotor angle and frequency stability of power system. *IET Renew. power Gener.* 16 (11), 2384–2401. doi:10.1049/rpg2.12529

Shao, B., Qi, X., Xiong, L., Wang, L., Yang, Y., Chen, Z., et al. (2023). Power coupling analysis and improved decoupling control for the VSC connected to a weak AC grid. *Int. J. Electr. Power and Energy Syst.* 145, 108645, Feb. doi:10.1016/j.ijepes.2022.108645

Shavolkin, O., Shvedchykova, I., Kolcun, M., Dusan, M., and Svitlana, D. (2023). Implementation of planned power generation for a grid-tied photovoltaic system with a storage battery for self-consumption of local object. *Przeglad Elektrotechniczny* 99 (1), 18–27. doi:10.15199/48.2023.01.04

Shen, Fu, Zhang, Y., Qiu, G., Yang, Z., Li, S., and Yang, G. (2023). Generalized discrete-time equivalent model for interfacing the grid-connected photovoltaic system. *IET generation, Transm. and distribution* 17 (5), 1070–1080. doi:10.1049/gtd2.12656

Shubham Kumar, S., and Anshul, A. (2023). A comparative analysis of artificial neural network algorithms to enhance the power quality of photovoltaic distributed generation system based on metrological parameters. *Mapan J. Metrology Soc. India* 38 (3), 607–618. doi:10.1007/s12647-023-00649-7

Vijayshree, G., and Sumathi, S. (2023). Power quality improvement in distributed generation system under varying load conditions using PWM and hysteresis controller. *Przeglad Elektrotechniczny* 99 (3), 142–147.

Xiong, L., Liu, X., Zhang, D., and Liu, Y. (2021). Rapid power compensation-based frequency response strategy for low-inertia power systems. *IEEE J. Emerg. Sel. Top. Power Electron.* 9 (4), 4500–4513. doi:10.1109/jestpe.2020.3032063

Xiong, L., Liu, X., Zhao, C., and Zhuo, F. (2020). A fast and robust real-time detection algorithm of decaying DC transient and harmonic components in three-phase systems. *IEEE Trans. Power Electron.* 35 (4), 3332–3336. doi:10.1109/tpel.2019.2940891

Xuan, Y., Sun, Ke, Wang, J., Yin, J., Fang, X., and Wang, G. (2022). Optimal allocation of energy storage capacity of high-permeability photovoltaic power generation system based on elastic neural network. *J. Nanoelectron. Optoelectron.* 17 (12), 1641–1647. doi:10.1166/jno.2022.3351

Zhu, Y., Wen, H., Chu, G., Wang, X., Peng, Q., Hu, Y., et al. (2022). Power-rating balance control and reliability enhancement in mismatched photovoltaic differential power processing systems. *IEEE Trans. Power Electron.* 37, 879–895. doi:10.1109/tpel.2021.3094220

frontiers | Frontiers in Energy Research

TYPE Original Research
PUBLISHED 04 September 2024
DOI 10.3389/fenrg.2024.1447094

OPEN ACCESS

EDITED BY
Yonghui Liu,
Hong Kong Polytechnic University, Hong Kong SAR, China

REVIEWED BY
Jun Cong Ge,
Jeonbuk National University, Republic of Korea
Xiaokang Liu,
Polytechnic University of Milan, Italy

*CORRESPONDENCE
Feng Yu,
yufeng628@ntu.edu.cn

RECEIVED 11 June 2024
ACCEPTED 14 August 2024
PUBLISHED 04 September 2024

CITATION
Xue S, Yin Z, Wang Z, Yu F and Chen H (2024) Reactive power regulation strategy for WTGs based on active disturbance rejection control. *Front. Energy Res.* 12:1447094.
doi: 10.3389/fenrg.2024.1447094

Reactive power regulation strategy for WTGs based on active disturbance rejection control

Shuilian Xue[1], Zhilong Yin[2], Zhiguo Wang[2], Feng Yu[3]* and Hailiang Chen[1]

[1]Nanjing Moral Testing and Certification Co., Ltd., Nanjing, China, [2]Xi'an Dynamic Inspection and Testing Co., Ltd., Xi'an, China, [3]School of Electrical Engineering and Automation, Nantong University, Nantong, China

With the large-scale interconnection of wind power generation, the voltage problem of the power system becomes more and more prominent. Compared with adding external reactive power compensation devices, it is more economical and responsive for fans to adjust their control strategies to provide reactive power support. To make full use of reactive power supported by wind turbines, a mathematical model of doubly fed induction generator (DFIG) wind turbines is constructed to characterize the reactive power boundary of wind turbines. Then, active disturbance rejection control (ADRC) is used to generate a voltage control signal to effectively improve the unit's reactive response speed; in addition, a variable gain coefficient is used to adjust the reactive power output of the unit, which effectively improves the reactive power response speed and its control adaptability and robustness under changing power grid conditions. Finally, a wind turbine generator (WTG) simulation model is built using MATLAB/Simulink simulation software, different fault locations are perturbed, and the effectiveness of reactive power support of the proposed ADRC-based strategy is simulated and verified. The proposed ADRC-based strategy could inject more reactive power to the grid to improve the voltage.

KEYWORDS

wind power integration, doubly fed induction generators (DFIGs), reactive power support, ADRC, voltage control

1 Introduction

An important form of clean energy, the installed capacity of wind power has increased rapidly worldwide in recent years, and it has become a considerable industry. With the increasing proportion of new energy sources installed in China and the weak overcurrent characteristics of new energy power electronic equipment, a situation of large-scale new energy stations connecting to weak electricity networks has gradually appeared in some areas of China. It is foreseeable that with the comprehensive construction of large-scale renewable energy, there will be more and more situations of new energy connecting to the weak power grid in the future, and it will gradually become the development trend of new energy grid-connected power generation in the northwest and north China. However, in the scenario of weak voltage support on the system side, the system voltage will drop sharply during the fault period, which may lead to large-scale off-grid renewable energy sources and secondary chain accidents. Therefore, during a period of weak current network failure, the new energy station should not only ensure its own safe ride-through but also make full use of controllable resources to provide safe, fast, and flexible transient voltage support for the system. Generally,

with the increasing proportion of renewable energy in power systems, the demand for transient control of new energy stations in weak power network environments will become increasingly prominent, and research into the application of more flexible and efficient multi-objective control methods will be an important development direction (Wang et al., 2020; Zhu et al., 2024; Yang et al., 2024).

Because wind turbines often operate at unit power factor, the reactive power regulation potential of wind turbines has not been utilized (LÓpez et al., 2008; Pannell et al., 2010; Lima et al., 2010). However, due to the low power density of wind energy, wind turbines operate under light load most of the time, and wind turbines have great reactive power potential. The doubly fed induction generator (DFIG) has been widely utilized in wind power systems due to its high efficiency and reliability (Chang et al., 2023). However, the long-distance connection between wind turbine generators (WTGs) and the main power grid results in relatively weak grid strength in the areas where WTGs are located, making them more susceptible to grid fluctuations (Gui et al., 2019; Tsili and Papathanassiou, 2009; Wu et al., 2023). Therefore, wind power grid integration standards require wind turbines to have fault ride-through capability to ensure they remain connected when grid voltage drops and to provide reactive power support to assist in rapid grid voltage recovery (Hu et al., 2014; Zou et al., 2018).

Several studies have proposed solutions to address this issue. One study proposes a voltage control strategy for coordinated static reactive power generators in DFIG that effectively suppresses grid voltage fluctuations. However, this solution may entail additional costs. Another study suggests a model predictive control-based strategy for reactive power voltage control in WTGs to enhance their rapid reactive power regulation capability. However, this method requires high-quality data and may suffer from overfitting issues. Another study proposes a DFIG wind turbine field reactive power output control based on low-voltage ride-through capability assessment, providing a reactive power evaluation index (Xu et al., 2015). However, this strategy may lack precision in reactive power control, and wind turbines need to provide grid reactive power support.

Traditional proportional-integral (PI) controllers struggle to achieve ideal control effects when facing external disturbances. In contrast, active disturbance rejection control (ADRC), developed further from traditional PI control theory, is a control strategy that does not rely on precise system models (Qiming et al., 2024). It offers fast tracking response, low overshoot, and strong disturbance rejection capabilities and has been widely applied in inverter control. For instance, some studies have combined ADRC with fuzzy PI control to improve droop control, achieving stable voltage and frequency through control of the voltage outer loop (Xia et al., 2022; Zhu et al., 2024). Another study introduced linear ADRC into current inner loop control, resulting in better suppression of sub-synchronous oscillations under various conditions. Additionally, applying ADRC in the current inner loop can weaken the coupling between dq currents, while applying it in the outer loop can enhance system disturbance rejection capabilities. Because the focus of wind power system control lies primarily on inverter control within wind turbines, ADRC methods show significant applicability in voltage control. Chang et al. (2023) divided the fault ride-through (FRT) configuration into three parts. A reactive current distribution strategy of DFIG is proposed, considering grid code requirements and stress (Wu et al., 2023). Zhu et al. (2015) addressed the virtual damping flux-based LVRT strategy for DFIG to improve the FRT performance.

To improve the transient response characteristics of wind farms under grid faults, this article introduces ADRC into the wind farm controller and proposes a hierarchical reactive power support strategy based on ADRC for DFIG. First, a mathematical model of DFIG wind turbines is constructed to characterize the reactive power boundary of wind turbines. Second, ADRC is used to generate voltage control signals to effectively improve the unit's reactive response speed; in addition, a variable gain coefficient is used to accurately adjust the reactive power output of the unit. Finally, simulations are conducted under different short-circuit position conditions to verify the effectiveness of the proposed strategy.

2 Modeling of a wind turbine generator

The expression of a wind turbine blade model that captures the mechanical power from the wind is as in Equation 1

$$P_m = c_p(\lambda,\beta)\frac{A}{2}\rho v_w^3 \tag{1}$$

where c_p, λ, and β are the power coefficient, tip-speed ratio, and pitch angle, respectively; ρ is the air density; A represents the swept area by the wind blade; and v_w is the wind speed (Rafiee et al., 2022; Dejian et al., 2024).

c_p is a non-linear function given by Equations 2–4:

$$c_P(\lambda,\beta) = 0.645\left\{0.00912\lambda + \frac{-5-0.4(2.5+\beta)+116\lambda_i}{e^{21\lambda_i}}\right\} \tag{2}$$

where

$$\lambda_i = \frac{1}{\lambda + 0.08(2.5+\beta)} - \frac{0.035}{1+(2.5+\beta)^3} \tag{3}$$

$$\lambda = \frac{\omega_r R}{v_w} \tag{4}$$

where ω_r is the rotor speed of WTG.

The power reference for maximum power point tracking (MPPT) operation, P_{MPPT}, is expressed as in Equation 5:

$$P_{MPPT} = c_{p,\max}\frac{\pi R^2}{2}\rho\left(\frac{\omega_r R}{\lambda_{opt}}\right)^3 = k_g\omega_r^3 \tag{5}$$

where k_g is a constant coefficient, λ_{opt} represents the optimal value of λ, and $c_{p,\max}$ is the maximum value of c_P.

3 Characterization of the reactive power boundary of a DFIG and ADRC-based reactive power strategy

3.1 Characterization of DFIG reactive power boundary

The reactive power of DFIG is mainly determined by its reactive power control scheme. If this scheme is improperly set, and the

reactive power control setting exceeds the reactive power limit of the wind turbine generator, excessive heating of the stator will lead to the shutdown of the wind turbine generator (Xiao et al., 2019; Kayikci and Milanovic, 2007). Therefore, it is crucial to understand and characterize the reactive power boundary of the unit so that its reactive support potential can be effectively utilized during grid faults.

The primary boundary of DFIG reactive power depends on rotor current, stator current, and rotor voltage. Given the active power of the DFIG, these three physical quantities can be used as constraints to determine the maximum reactive power that the unit can absorb or generate. This boundary is depicted using a P-Q curve diagram.

The power flow on the stator winding and rotor winding is typically described in the P-Q curve diagram. Assuming the wind turbine operates in maximum power point tracking (MPPT) mode and neglecting the impedance of the step-up transformer, the stator voltage is considered as 1 per unit (pu) or normalized value.

By thoroughly understanding and characterizing the reactive power boundary of the DFIG, wind turbine operation in the grid can be effectively managed, ensuring its stability and reliability. Additionally, appropriate reactive power support can be provided when necessary to maintain stable grid operation.

(1) When considering the constraint of rotor current, the power on the stator side is expressed by rotor current, as shown in Equation 6:

$$S_{s\_I_r} = -U_s\left(\frac{U_s - Z_m I_r}{Z_s + Z_m}\right)^* \tag{6}$$

where U_S is the stator side voltage, I_r is the rotor side current, and * is the conjugate. Z_s is the stator side impedance, and Z_m is the magnetization impedance.

To highlight the influence of rotor current on power, I_r is extracted, and Equation 6 is rewritten as Equation 7:

$$S_{s\_I_r} = -|U_s|^2\left(\frac{1}{Z_s + Z_m}\right)^* + I_r{}^* U_s\left(\frac{Z_m}{Z_s + Z_m}\right)^* \tag{7}$$

Assuming that the amplitude of the rotor current is constant and the angle changes, Equation 7 can be expressed as a circle on the complex plane. The center c of the circle is shown in Equation 8, and the radius r is shown in Equation 9.

$$c = -|U_s|^2\left(\frac{1}{Z_s + Z_m}\right)^* \tag{8}$$

$$r = |I_r||U_s|\left|\frac{Z_m}{Z_s + Z_m}\right| \tag{9}$$

The DFIG active power and reactive power can be expressed as:

$$P = P_r + P_s \approx (1 - s)P_s \tag{10}$$

$$Q \approx Q_s \tag{11}$$

where s is slip, and P_r and P_s are the output power of the rotor and stator, respectively.

Substituting Equations 10, 11, the total power can be obtained as in Equation 12:

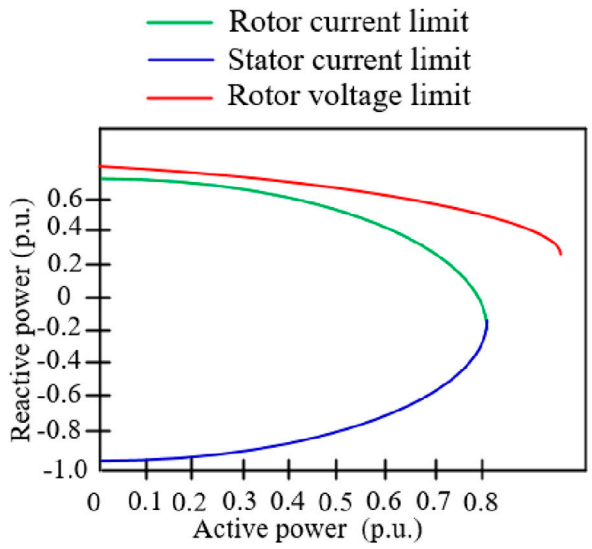

FIGURE 1
Reactive power limitation with different active power boundaries.

$$P + jQ = -|U_s|^2\left(\frac{1}{Z_s + Z_m}\right)^* + |I_r||U_s|\left|\frac{Z_m}{Z_s + Z_m}\right| \times \left((1 - s)\cos(\gamma) + j\sin(\gamma)\right) \tag{12}$$

where γ is the angle of the rotor current.

Considering the constraint of the rotor current, the amplitude of the rotor current is constant, and the angle changes. The image of the total power is an ellipse on the complex plane. Due to the first term on the right of the equal sign, the reactive power boundary moves down, as shown in the green curve of Figure 1.

(2) Considering the stator current constraint, the power of the stator side and the rotor side are expressed by the stator current, respectively, as in Equations 13, 14:

$$S_{s\_I_s} = -U_s I_s{}^* \tag{13}$$

$$S_{r\_I_s} = -\left\{\left(\frac{Z_r}{Z_m} + 1\right)U_s - \left(Z_r + \frac{Z_s Z_r}{Z_m} + Z_s\right)I_s\right\} \cdot s\left(I_s + \frac{U_s - I_s Z_s}{Z_m}\right) \tag{14}$$

Under the representation of the stator current, the center of the reactive power image is close to the origin, so the stator current is the limiting factor of the boundary on the constructed P-Q diagram, as in the blue curve of Figure 1.

(3) When considering the constraint of rotor voltage, the power on the stator and rotor sides is expressed by rotor voltage, respectively, as shown in Equations 15, 16:

$$S_{s\_V_r} = -U_s\left(\frac{U_s(Z_r + Z_m) - \frac{V_r}{s}Z_m}{(Z_r + Z_s)Z_m + Z_s Z_r}\right)^* \tag{15}$$

$$S_{r\_V_r} = -U_r\left(\frac{-U_s Z_m - \frac{V_r}{s}(Z_r + Z_m)}{(Z_r + Z_s)Z_m + Z_s Z_r}\right)^* \tag{16}$$

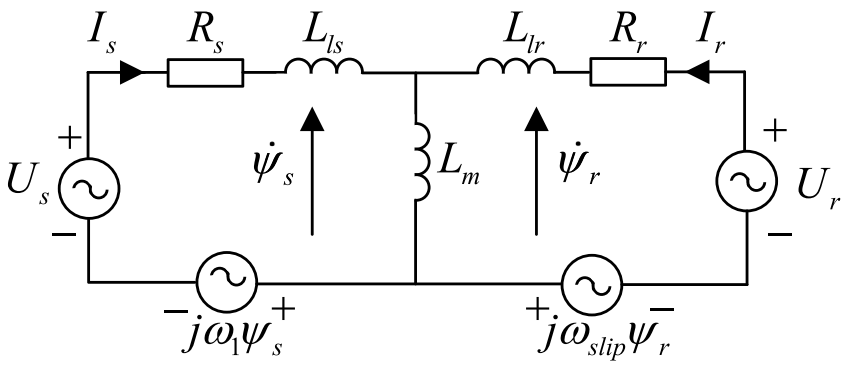

FIGURE 2
DFIG equivalent circuit.

The centers of Equations 15, 16 have great negative deviation on the imaginary axis of the complex plane, and the radius is inversely proportional to the absolute value of the slip. Therefore, the rotor voltage only limits the upper boundary of the P-Q diagram when the absolute value of the slip is very high, as shown by the red dotted line in Figure 1.

Figure 1 shows the reactive power boundary of the 3 MW doubly fed wind turbine used in this article, that is, the P-Q curve. The rotor current is the dominant factor limiting the maximum generated reactive power, and the stator current is the dominant factor limiting the maximum absorbed reactive power. Compared with the curve, the reactive power boundary under different active working points can be obtained.

This article proposes a reactive power support strategy for WTGs. ADRC is used to generate a voltage control signal to effectively improve the unit's reactive response speed; in addition, a variable gain coefficient is used to accurately adjust the reactive power output of the unit. Thus, it could achieve reactive power support for the wind farm.

3.2 Reactive power support strategy of a station based on an active disturbance rejection controller

A traditional station controller uses PI controllers to deal with the change in voltage, so it is difficult to find a balance between response speed and stability. In this article, a station controller based on ADRC is proposed.

The response speed and robustness of the control system are improved by actively estimating and compensating for the internal and external disturbances of the system. There are vector DFIG voltage equations and flux linkage equations in the dq coordinate system rotating at synchronous speed, as in Equations 17, 18:

$$\begin{cases} U_s = R_s I_s + \dfrac{d\psi_s}{dt} + j\omega_1\psi_s \\ U_r = R_r I_r + \dfrac{d\psi_r}{dt} + j\omega_{slip}\psi_r \end{cases} \tag{17}$$

$$\begin{cases} \psi_s = L_s I_s + L_m I_r \\ \psi_r = L_m I_s + L_r I_r \end{cases} \tag{18}$$

where L_s, L_m, and L_r are the inductance of the stator, magnetizing, and rotor, respectively. ψ_s and ψ_r are the flux linkage of the stator and rotor, respectively. R_r and R_s are the resistance of the stator and rotor, respectively.

The DFIG equivalent circuit in vector form can be derived using the above equation, as shown in Figure 2.

When connecting the grid, because the DFIG stator is directly connected to the grid, the stator voltage Us is equal to the grid voltage (U_g). Therefore, voltage could be expressed as in Equation 19:

$$U_g = R_s I_s + L_s\frac{dI_s}{dt} + L_m\frac{dI_r}{dt} + j\omega_1\psi_s \tag{19}$$

In the DFIG system, power transmission is mainly carried out through the stator side, so the fluctuation of the stator current directly reflects the change in the power output. Because the power transfer is proportional to the product of voltage and current and depends on the phase angle between them, the dynamic characteristics of voltage and current on the stator side are very important for the power control and stability of the system. In this article, the fluctuation of grid voltage is evaluated by the change of the stator current, as in Equation 20:

$$k\frac{dU_g}{dt} = U_g - R_s I_s - L_m\frac{dI_r}{dt} - j\omega_1\psi_s \tag{20}$$

Selecting U_g as the state variable yields $x_1 = U_g$, $x_2 = f_w = U_g/k\text{-}L_m dI_r/dkt\text{-}j\omega_1\Psi_s/k$, $u = I_s$. As a result, Equation 18 can be rewritten as:

$$\dot{x}_1 = x_2 + b_0 u \tag{21}$$

where f_w is the external disturbance, including current disturbance, power disturbance, and error disturbance of model parameters of the system.

To design a linear extended state observer (LESO)-based voltage control strategy conveniently, the system state vector x = [x1, x2]^T is defined, and Equation 21 could be expressed in matrix form, as shown in Figure 3.

$$\dot{x} = Ax + Bu + Eh. \tag{22}$$

where A, B, E and h could be expressed as in Equation 23

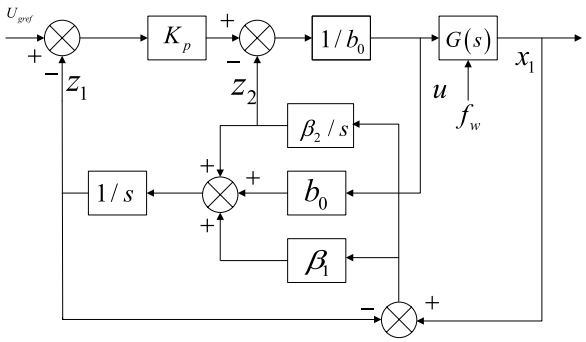

FIGURE 3
ADRC-based reactive power control diagram.

$$\begin{cases} A = \begin{bmatrix} 0 & 1 \\ 0 & 0 \end{bmatrix} \\ B = \begin{bmatrix} b_0 & 0 \end{bmatrix}^T \\ E = \begin{bmatrix} 0 & 1 \end{bmatrix}^T \\ h = \dot{f}_w \end{cases} \tag{23}$$

Defining $z = [z_1, z_2]^T$ as the state vector of LESO, where z_1 is the observed value of x_1, and z_2 is the observed value of x_2, the corresponding first-order LESO equation for Equation 22 can be designed as in Equation 24:

$$\begin{cases} \dot{z} = Az + Bu + L(y - \hat{y}) \\ \hat{y} = Cz \end{cases} \tag{24}$$

where C = (Wu et al., 2023); u is the input control variable; $\hat{y}$ is the input of LESO; y is the observed value of LESO; and $L = [\beta_1, \beta_2]^T$ is the error feedback gain matrix of LESO, which is designed according to the bandwidth of LESO.

3.3 Definition of a control coefficient for the reactive power controller

The reactive power control is used to respond to the transient voltage change, and the specific formula is as in Equation 25:

$$Q_{ref} = k_Q \Delta u \tag{25}$$

where Q_{ref} is the reactive power command of WTG, and Δu is the deviation between the grid voltage and the reference voltage, respectively. k_Q of the wind turbine is the gain coefficient of WTG, which determines the reactive power output by the wind turbine during the fault. Under the constant gain coefficient, it is difficult to make full use of the reactive power support capacity of WTG.

Considering the different reactive power output capabilities of various operating conditions, a variable gain coefficient, as shown in Equation 26, is proposed to realize the adaptive control of the unit:

$$k_Q = \alpha \frac{u_{\max} - u_{\min}}{Q_{\max} - Q_{\min}} \tag{26}$$

where Q_{max} and Q_{min} represent the maximum reactive power that WTG can emit and absorb under a certain active output, and $u_{\max}$ and $u_{\min}$ represent the voltage of the grid connection point when the wind turbine generator absorbs the maximum reactive power and emits the maximum reactive power. α is the regulating factor. In this article, $u_{\max}$ is set to 1.10, and $u_{\min}$ is set to 0.9.

4 Characterization model system and case studies

To verify the feasibility of the control strategy proposed in this article, a simulation example system with a wind farm is built based on MATLAB/Simulink software, as shown in Figure 4. The wind farm consists of 20 sets of 3 MW-DFIGs. The wind farm is connected to the power grid through 110 kV transmission lines of 10 km. The parameters of the ADRC and PI controller are shown in Table 1, and the parameters of the model system are shown in Table 2.

When the fault location, fault duration, and fault degree are different, the voltage drop degree of the grid point of the wind farm is different, and the reactive power demand for supporting the grid point voltage system is different. The reactive power support capacity of wind turbines is different under different operating conditions. The effectiveness of the proposed strategy is verified under various sizes of fault, durations of fault, and operating conditions by comparing the following two schemes: Scheme #1: ADRC-based reactive power support strategy and Scheme 2: PI-based reactive power support strategy.

4.1 Impact of fault duration

In Case 1 (Fault duration = 0.3 s, Wind speed = 10 m/s), with the rapid intervention of the ADRC controller, each wind turbine can inject reactive power more quickly. At 6.2 s, the grid-connected voltages of the ADRC control strategy and PI control strategy reach 0.613 p.u. and 0.593 p.u., respectively, as shown in Figure 5, because the ADRC controller has better response characteristics than the PI controller. Before the fault is cleared (6.3 s), the reactive power output of the wind farm with ADRC control strategy and PI control strategy is 0.270 p.u. and 0.077 p.u., respectively, as shown in Figure 5.

In Case 2 (Fault duration = 0.5 s, Wind speed = 10 m/s), the fault duration was increased from 0.3 s to 0.5 s, and the reactive power support of the ADRC controller and PI controller was close to the maximum after 0.3 s, so the two control strategies showed similar voltage levels during 6.3 s–6.5 s, as shown Figure 6. The ADRC-based Q control strategy shows better support performance under various fault durations than the PI-based Q control strategy.

4.2 Impact of sizes of fault

In Case 3 (Fault duration = 0.3 s, Wind speed = 10 m/s, Severe Fault), the grounding resistance is reduced from 17 Ω to 10 Ω, the voltage level of the grid connection point of the wind farm is further

10.3389/fenrg.2024.1447094

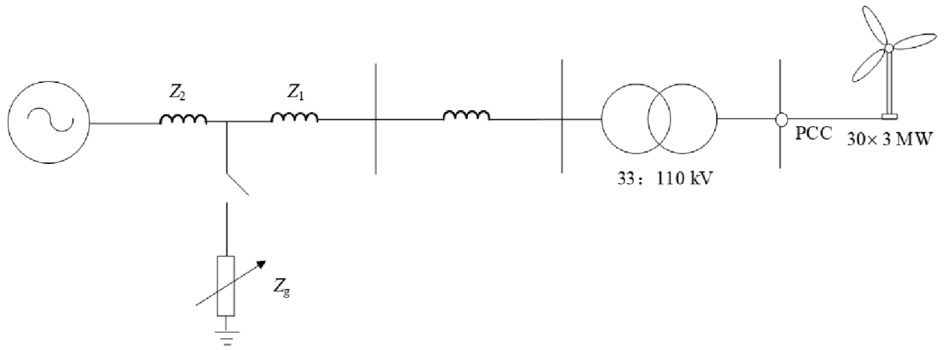

FIGURE 4
Model system.

TABLE 1 Control parameters of the ADRC and the PI controller.

Parameters	Values
K_p	200
b_0	30
β_1	90
β_2	270
K_p of PI	0.01
K_i of PI	10

TABLE 2 Parameters of model system.

Parameters	Values
P	20 × 3 MW
V	2.3 kV
V_{dc}	4,600 V
p	4
R_s	0.020 Ω
L_{ls}	0.159 mH
R_r	0.014 Ω
L_{lr}	0.141 mH
L_{md}	2.557 mH
L_{mq}	2.557 mH
Z_1	0.003 + j6.588 Ω
Z_2	0.014 + j26.351 Ω
Z_1	0.003 + j6.588 Ω
Z_2	0.008 + j16.469 Ω
R_g	17.567 Ω

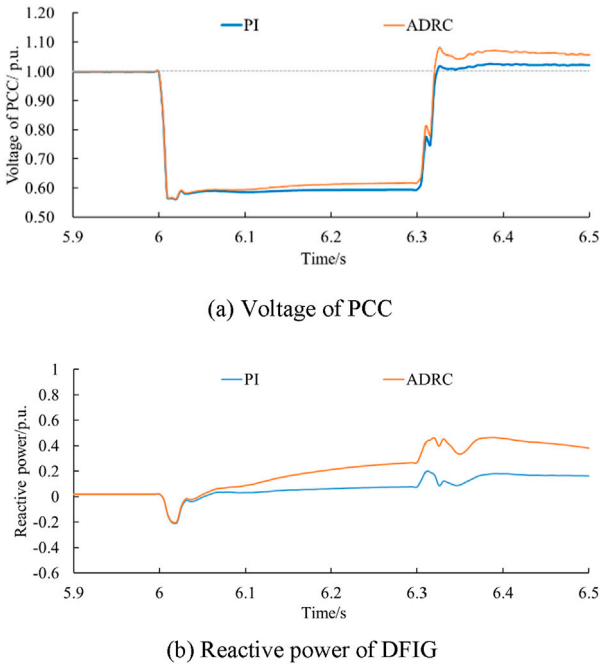

FIGURE 5
Results for Case 1. **(A)** Voltage of point of common coupling (PCC), and **(B)** reactive power of DFIG.

reduced under the condition of increasing disturbance, and the minimum voltage is reduced from 0.563 p.u. to 0.357 p.u., as shown Figure 7. The ADRC-based Q control strategy shows better support performance under various sizes of faults than those of the PI-based Q control strategy.

4.3 Impact of operating conditions

In Case 4 (Fault duration = 0.3 s, Wind speed = 9 m/s) and Case 5 (Fault duration = 0.3 s, Wind speed = 8 m/s), the received wind speed of the wind farm decreased from 10 ms to 1–9 m s^{-1} and 8 m

10.3389/fenrg.2024.1447094

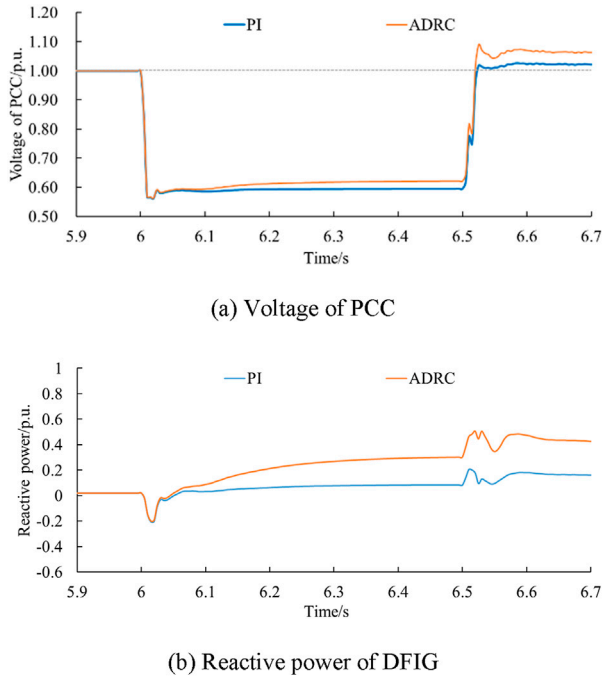

FIGURE 6
Results for Case 2. **(A)** Voltage of PCC, and **(B)** reactive power of DFIG.

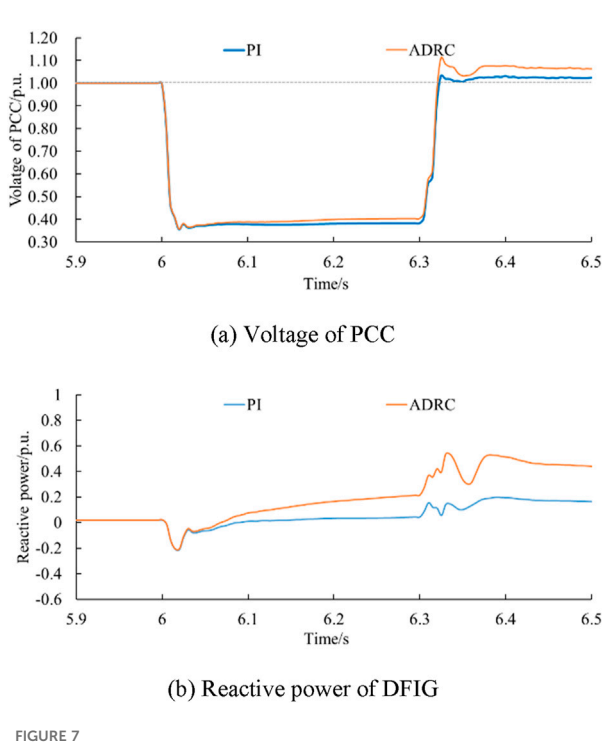

FIGURE 7
Results for Case 3. **(A)** Voltage of PCC, and **(B)** reactive power of DFIG.

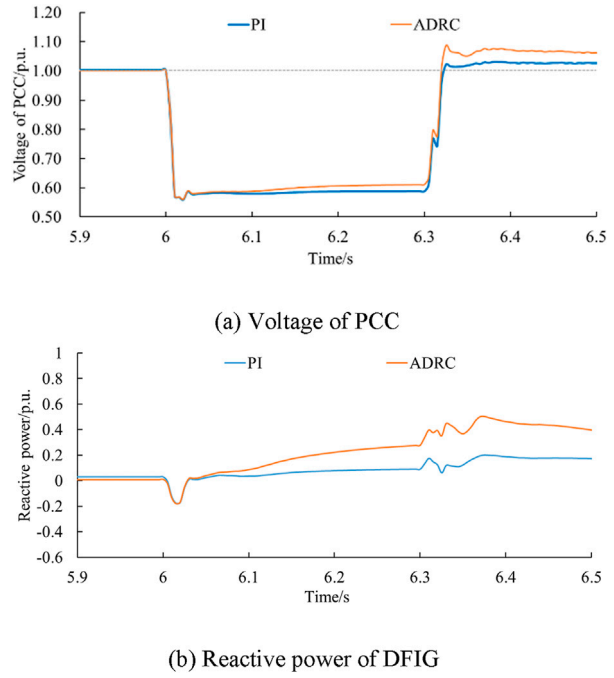

FIGURE 8
Results for Case 4. **(A)** Voltage of PCC, and **(B)** reactive power of DFIG.

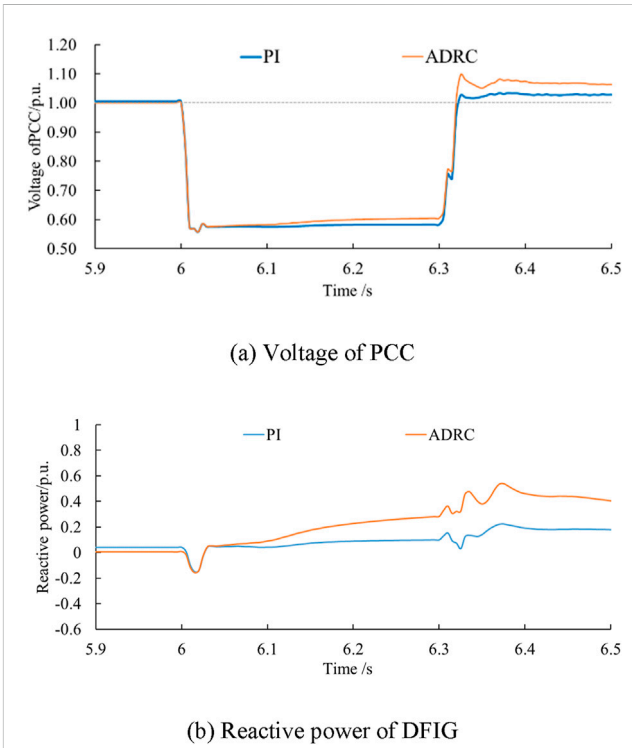

FIGURE 9
Results for Case 5. **(A)** Voltage of PCC, and **(B)** reactive power of DFIG.

s^{-1}. With the decrease of wind speed, the highest voltage levels during the fault period gradually decreased, which were 0.617 p.u., 0.610 p.u., and 0.603 p.u. in turn, as shown in Figures 8, 9. At various wind speeds, the ADRC-based Q control strategy shows better response characteristics than the PI control strategy.

5 Conclusion

To improve the transient response characteristics of DFIGs under grid fault, this article characterizes the DFIG reactive power boundary and proposes a reactive power control strategy for wind turbines based on ADRC. Through simulation and analysis, the following conclusions are drawn:

1) The reactive power boundaries are investigated, which can tap the reactive power support potential of units at different wind speeds.
2) Considering the characteristics of ADRC, the use of an ADRC-based Q control strategy instead of a PI controller has a faster response and injects more reactive power to compensate for the voltage dip during fault under various fault sizes, fault durations, and operating conditions.

Future research could address fault clearing, the transient overvoltage problem, the lack of a cooperative control strategy with reactive power support components, improving reactive power support capacity, and restraining transient overvoltage.

Data availability statement

The raw data supporting the conclusions of this article will be made available by the authors, without undue reservation.

Author contributions

SX: writing–original draft, writing–review and editing, methodology. ZY: methodology, writing–original draft, writing–review and editing, conceptualization, data curation, formal analysis, investigation, resources. ZW: data curation, formal analysis, resources, visualization, writing–original draft. FY: data curation, resources, supervision, validation, writing–original draft, writing–review and editing. HC: writing–original draft.

Funding

The author(s) declare that no financial support was received for the research, authorship, and/or publication of this article.

Conflict of interest

Authors SX and HC were employed by the Nanjing Moral Testing and Certification Co., Ltd. Authors ZY and ZW were employed by the Xi'an Dynamic Inspection and Testing Co., Ltd.

The remaining author declares that the research was conducted in the absence of any commercial or financial relationships that could be construed as a potential conflict of interest.

Publisher's note

References

Chang, Y., Kocar, I., Farantatos, E., Haddadi, A., and Patel, M. (2023). Short-circuit modeling of DFIG-based WTG in sequence domain considering various fault-ride-through requirements and solutions. *IEEE Trans. Power Deliv.* 38 (3), 2088–2100. doi:10.1109/tpwrd.2023.3235985

Dejian, Y., Li, J., Jin, Z., Gangui, Y., Xin, W., Lei, D., et al. (2024). Sequential frequency regulation strategy for DFIG and battery energy storage system considering artificial deadbands. *Int. J. Electr. Power and Energy Syst.* 155, 1–14. doi:10.1016/j.ijepes.2023.10950

Gui, Y., Wang, X., Blaabjerg, F., and Pan, D. (2019). Control of grid-connected voltage-source converters: the relationship between direct-power control and vector-current control. *IEEE Ind. Electron. Mag.* 13 (2), 31–40. doi:10.1109/mie.2019.2898012

Hu, S., Zou, X., and Kang, Y. (2014). A novel optimal design of DFIG crowbar resistor during grid faults. *Int. Power Electron. Conf. Hiroshima, Jpn.*, 555–559.

Kayikci, M., and Milanovic, J. V. (2007). Reactive power control strategies for DFIG-based plants. *IEEE Trans. Energy Convers.* 22 (2), 389–396. doi:10.1109/tec.2006.874215

Liang, X., Tianfu, S., Xinyu, L., Xianfeng, T., and Denghua, D. (2022). Research on double closed-loop ADRC control strategy of wind power grid-connected inverter. *Shandong Electr. Power Technol.* 49 (11), 70–77.

Lima, F. K. A., Luna, A., Rodriguez, P., Watanabe, E. H., and Blaabjerg, F. (2010). Rotor voltage dynamics in the doubly fed induction generator during grid faults. *IEEE Trans. Power Electron.* 25 (1), 118–130. doi:10.1109/tpel.2009.2025651

López, J., Gubía, E., Sanchis, P., Roboam, X., and Marroyo, L. (2008). Wind turbines based on doubly fed induction generator under asymmetrical voltage dips. *IEEE Trans. Energy Convers.* 23 (1), 321–330. doi:10.1109/tec.2007.914317

Pannell, G., Atkinson, D. J., and Zahawi, B. (2010). Minimum-threshold crowbar for a fault-ride-through grid-code-compliant DFIG wind turbine. *IEEE Trans. Energy Conver* 25 (3), 750–759. doi:10.1109/tec.2010.2046492

Qiming, C., Zhou, W., Cheng, Y., and Lei, Z. (2024). Study on suppression of subsynchronous oscillation of doubly-fed fan based on linear active disturbance rejection control. *Electr. Power Constr.* 1-14 -01-27.

Rafiee, Z., Heydari, R., Rafiee, M., Aghamohammadi, M. R., and Blaabjerg, F. (2022). Enhancement of the LVRT capability for DFIG-based wind farms based on short-circuit capacity. *IEEE Syst. J.* 16 (2), 3237–3248. doi:10.1109/jsyst.2022.3153887

Tsili, M., and Papathanassiou, S. (2009). A review of grid code technical requirements for wind farms. *IET Renew. Power Gener.* 3 (3), 308–332. doi:10.1049/iet-rpg.2008.0070

Wang, X., Taul, M. G., Wu, H., Liao, Y., Blaabjerg, F., and Harnefors, L. (2020). Grid-synchronization stability of converter-based resources an overview. *IEEE Open J. Ind. Appl.* 1, 115–134. doi:10.1109/ojia.2020.3020392

Wu, H., Xu, H., Li, Z., Zhao, R., and Hu, J. (2023). Reactive current distribution strategy of DFIG's RSC and GSC considering electromagnetic stress and grid codes requirement. *IEEE Trans. Energy Conver* 38 (1), 273–283. doi:10.1109/tec.2022.3218708

Xiao, X., Yang, R., Zheng, Z., and Wang, Y. (2019). Cooperative rotor-side SMES and transient control for improving the LVRT capability of grid-connected DFIG-based wind farm. *IEEE Trans. Appl. Super.* 29 (2), 1–5. doi:10.1109/tasc.2018.2881315

Xu, H., Ma, X., and Sun, D. (2015). Reactive current assignment and control for DFIG based wind turbines during grid voltage sag and swell conditions. *J. Power. Electron.* 15 (1), 235–245. doi:10.6113/jpe.2015.15.1.235

Yang, D., Wang, X., Chen, W., Jin, Z., Jin, E., Gangui, Y., et al. (2024). Adaptive frequency droop feedback control-based power tracking operation of a DFIG for temporary frequency regulation. *IEEE Trans. Power Syst.* 39, 2682–2692. doi:10.1109/tpwrs.2023.3277009

Zhu, D., Wang, Z., Hu, J., Zou, X., Kang, Y., and Guerrero, J. M. (2024). Rethinking Fault ride-through control of DFIG-based wind turbines from new perspective of rotor-port impedance characteristics. *IEEE Trans. Sustain. Energy* 15, 2050–2062. doi:10.1109/TSTE.2024.3395985

Zhu, J. R., Chen, Z., Wu, X., and Deng, F. (2015). Virtual damping flux-based LVRT control for DFIG-based wind turbine. *IEEE Trans. Energy Convers.* 30 (1), 714–725. doi:10.1109/tec.2014.2385966

Zou, X., Zhu, D., Hu, J., Zhou, S., and Kang, Y. (2018). Mechanism analysis of the required rotor current and voltage for DFIG-based WTs to ride-through severe symmetrical grid faults. *IEEE Trans. Power Electron.* 33 (9), 7300–7304. doi:10.1109/tpel.2018.2799218

frontiers | Frontiers in Energy Research

TYPE Opinion
PUBLISHED 11 September 2024
DOI 10.3389/fenrg.2024.1414068

OPEN ACCESS

EDITED BY
Anant Kumar Verma,
Universidad de O'Higgins, Chile

REVIEWED BY
Ziqing Zhu,
Hong Kong Polytechnic University, Hong Kong, SAR China
Jian Zhao,
Shanghai University of Electric Power, China
Xiang Huo,
Texas A&M University, United States

*CORRESPONDENCE
Xiang Gao,
gaoxiang@szpu.edu.cn

RECEIVED 08 April 2024
ACCEPTED 27 August 2024
PUBLISHED 11 September 2024

CITATION
Bao J, Gao X and Yan X (2024) Opinions on the multi-grade pricing strategy for emergency power supply of mobile energy storage systems.
Front. Energy Res. 12:1414068.
doi: 10.3389/fenrg.2024.1414068

Opinions on the multi-grade pricing strategy for emergency power supply of mobile energy storage systems

Jieying Bao[1], Xiang Gao[2]* and Xin Yan[1]

[1]College of Electrical and Information Engineering, Hunan University, Changsha, China, [2]Industrial Training Centre, Shenzhen Polytechnic University, Shenzhen, China

KEYWORDS

bi-level optimization, emergency power supply, mobile energy storage, multi-grade pricing, Stackelberg game

1 Introduction

As a typical spatial–temporal flexible resource, mobile energy storage can respond promptly to ensure uninterrupted power supply in case of life safety issues and economic loss due to the consequences of electricity outages (Sun et al., 2022; Sun et al., 2017; Chuangpishit et al., 2023). In addition to emergency power supply, mobile energy storage systems can also provide various ancillary services, including peak shaving and valley filling (Li et al., 2023; Manojkumar et al., 2021; Li X. et al., 2021), distributed renewable energy consumption (Li X. et al., 2021; Zhou et al., 2021; Zhong et al., 2023), and power quality management (Xiong et al., 2020; Cao et al., 2024; Naderi et al., 2021). Nevertheless, energy storage mostly stays in a standby state, thus failing to fully leverage its multiple spatiotemporal applications, leading to low utilization and long investment payback periods (Li et al., 2022). Moreover, the existing literature studies (Wang et al., 2023a; Yang, 2021; Wang et al., 2023b) on the research of power supply trading models mainly focus on the economic efficiency, and the presented charging standards of power supply are uniform. This results in customers with significantly different power supply demands paying the same electricity price, severely undermining customers' enthusiasm for purchasing emergency supply services. Consequently, this paper aims to offer insightful opinions and discussions on a multi-grade pricing strategy for mobile energy storage systems providing emergency power supply services that meet the differentiated demands of customers.

The main contributions of this paper are twofold, as listed: (1) a hierarchical trading framework is presented for mobile energy storage systems to provide emergency power supply services, and three metrics, namely, power supply capacity, duration of power supply, and response time, are formulated to evaluate the reliability of emergency power supply. (2) A bi-level pricing optimization model based on Stackelberg game is proposed to obtain tiered prices of emergency power supply and customer purchase capacity of emergency power supply, thereby increasing the revenue of mobile energy storage and reducing the emergency power supply cost of customers.

2 Multi-grade metrics of emergency power supply services

Currently, there is no established pricing mechanism for MESS to provide emergency power supply services in China (Yang et al., 2023). Shang (2021) selected power supply

10.3389/fenrg.2024.1414068

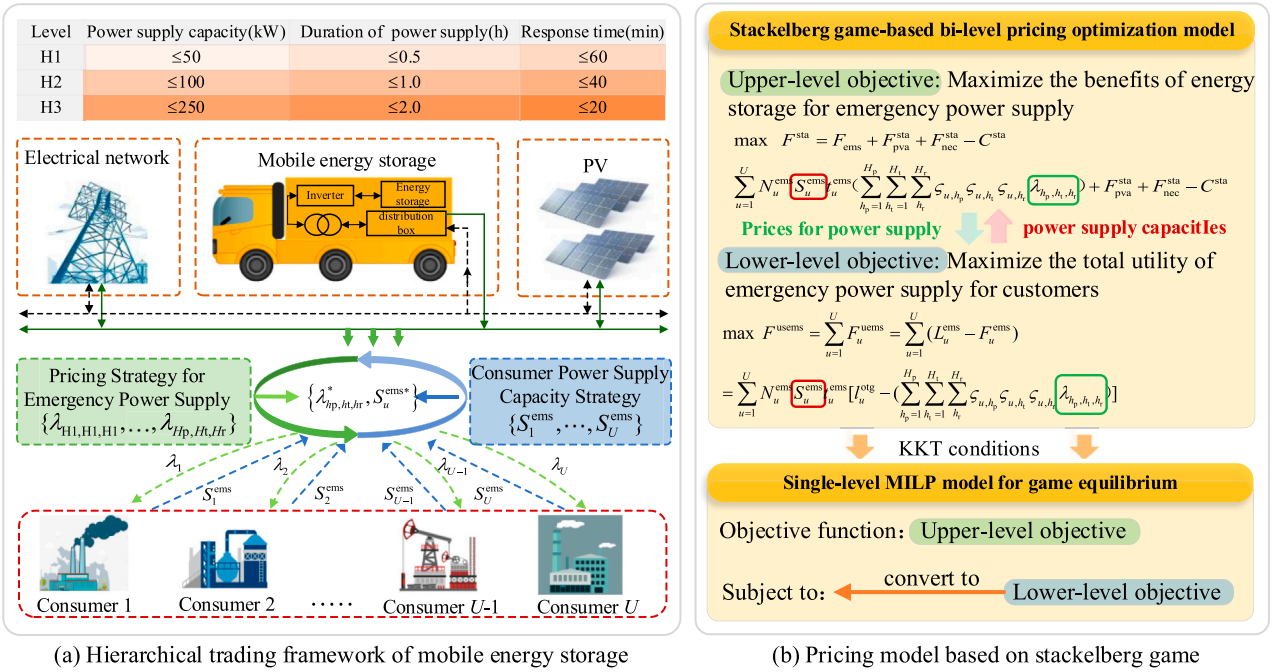

(a) Hierarchical trading framework of mobile energy storage

(b) Pricing model based on stackelberg game

FIGURE 1
Multi-grade pricing strategy for emergency power supply of mobile energy storage. **(A)** Hierarchical trading framework of the mobile energy storage. **(B)** Pricing model based on Stackelberg game.

duration as the standard to divide emergency power supply subsidy tariffs. Meanwhile, Yu (2015) suggested that the significance of energy storage in offering differentiated emergency power supply services is primarily demonstrated by the magnitude of emergency standby capacity and response speed. It is known that the higher the emergency power supply capacity and the longer the duration of the emergency power supply, the greater the investment cost of energy storage equipment will be. In addition, the mobile cost of energy storage increases with the amplification of response speed (Sun et al., 2022; Lei et al., 2019). Consequently, power supply capacity, duration of power supply, and response time were selected as the three metrics to delineate the classification of power supply levels in this paper. Based on the typical capacity of mobile energy storage and the historical downtime of customers (Xiao, 2021), three levels have been classified, with higher levels indicating a greater demand for emergency power supply (Zhu and Si, 2023; Zhang et al., 2021). This is shown in detail in Figure 1A, where H1 represents the lowest power supply level, while H3 represents the highest power supply level. Hence, the unit price of emergency power supply λ_{h_p,h_t,h_r} is composed of a basic electricity price and an additional electricity price, which is expressed as Equation 1:

$$\lambda_{h_p,h_t,h_r} = \lambda_{h_p}^{\text{base}} + \Delta\lambda_{h_t} + \Delta\lambda_{h_r}, \tag{1}$$

where $\lambda_{h_p}^{\text{base}}$ is the basic price of emergency power supply with capacity at the h_p level and duration and response time at the H1 level; $\Delta\lambda_{h_t}$ and $\Delta\lambda_{h_r}$ are the additional electricity price of emergency power supply with duration at the h_t level and response time at the h_r level, respectively.

3 Hierarchical trading framework of the mobile energy storage system

According to the analysis of the interactive mechanism between energy storage and customers, the hierarchical trading framework for energy storage providing emergency power supply services is established, as depicted in Figure 1A. On one hand, mobile energy storage strategically sets electricity prices to maximize the benefits for emergency power supply, but on the other hand, power supply customers optimize the emergency power supply capacity to achieve the maximum utility during power outages. Therefore, it is a sequential decision process, thereby constituting a Stackelberg game relationship dominated by energy storage, which can be expressed as a bi-level mathematical optimization model (Sun et al., 2022; Xu et al., 2023). The upper level of this model aims to maximize the revenue of mobile energy storage providing emergency power supply services, considering the energy storage investment constraint, individual rational constraint, and premium pricing constraint. The lower level takes the purchase decision constraint into account to maximize the customer utility of emergency power supply. As the leader in this game relationship, mobile energy storage takes the initiative to make electricity price decisions. Meanwhile, customers functioning as followers in the model adapt their electricity purchase strategies in response to the pricing decisions. Subsequently, the leader revises the initial decision framework, creates new decisions, and shares them with all the followers. Then, the followers adjust their power supply strategy again based on the latest electricity prices. This iterative process continues until equilibrium is achieved, resulting in optimal tiered pricing of emergency power supply and optimal power supply capacity purchase strategies of customers.

(a) The utility function of customers purchasing emergency power supply considering outage loss.

The utility function of emergency power supply on the customer's side is determined by calculating the difference between the reduced economic losses after choosing the power supply service and the emergency power supply service fee paid, which is formulated as Equation 2:

$$F_u^{\text{uems}} = L_u^{\text{ems}} - F_u^{\text{ems}}, \tag{2}$$

where L_u^{ems} and F_u^{ems} are the reduced economic losses and the emergency power supply service fee paid of customer u, respectively. They can be defined as Equations 3, 4:

$$L_u^{\text{ems}} = N_u^{\text{ems}} S_u^{\text{ems}} t_u^{\text{ems}} l_u^{\text{otg}}, \tag{3}$$

$$\begin{aligned} F_u^{\text{ems}} &= N_u^{\text{ems}} S_u^{\text{ems}} t_u^{\text{ems}} \lambda_u \\ &= N_u^{\text{ems}} S_u^{\text{ems}} t_u^{\text{ems}} \left(\sum_{h_{\text{p}}=1}^{H_{\text{p}}} \sum_{h_{\text{t}}=1}^{H_{\text{t}}} \sum_{h_{\text{r}}}^{H_{\text{r}}} \varsigma_{u,h_{\text{p}}} \varsigma_{u,h_{\text{t}}} \varsigma_{u,h_{\text{r}}} \lambda_{h_{\text{p}},h_{\text{t}},h_{\text{r}}} \right), \end{aligned} \tag{4}$$

where N_u^{ems} is the annual emergency power supply times of customer u; S_u^{ems} and t_u^{ems} are emergency power supply capacity and emergency power supply duration of customer u, respectively; l_u^{otg} is outage losses per unit electricity consumption of customer u; λ_u is the unit price of emergency power supply paid for customer u; $\varsigma_{u,h_{\text{p}}}$, $\varsigma_{u,h_{\text{t}}}$, and $\varsigma_{u,h_{\text{r}}}$ are Boolean variables representing customer u's choice of the power capacity level, power supply duration level, and response time level, respectively, with a value of 1 indicating customer u's selection of that emergency power supply level.

(b) The income function of mobile energy storage providing emergency power supply services.

Mobile energy storage is typically kept in a standby state, only being utilized to provide an emergency power supply in the event of a power outage (Cao et al., 2024; Jiang et al., 2021). Considering energy storage resource reuse strategies to enhance its capacity utilization efficiency, the standby capacity for emergency power supply can be used for peak–valley arbitrage and distributed renewable energy consumption in electricity trading to maximize revenue (Li et al., 2023) (Zhong et al., 2023). Therefore, the income function of mobile energy storage is composed of the emergency power supply service income, peak–valley arbitrage income, distributed renewable energy consumption income, and power supply service cost, which is formulated as Equation 5:

$$F^{\text{sta}} = F_{\text{ems}} + F_{\text{pva}}^{\text{sta}} + F_{\text{nec}}^{\text{sta}} - C^{\text{sta}}, \tag{5}$$

where F_{ems}, $F_{\text{pva}}^{\text{sta}}$, and $F_{\text{nec}}^{\text{sta}}$ are the revenue of emergency power supply, peak–valley arbitrage, and distributed renewable energy consumption by mobile energy storage; C^{sta} is the total annual cost of energy storage providing emergency power supply services. They can be defined as Equations 6–9:

$$F_{\text{ems}} = \sum_{1}^{U} F_u^{\text{uems}} = \sum_{1}^{U} N_u^{\text{ems}} S_u^{\text{ems}} t_u^{\text{ems}} \left(\sum_{h_{\text{p}}=1}^{H_{\text{p}}} \sum_{h_{\text{t}}=1}^{H_{\text{t}}} \sum_{h_{\text{r}}}^{H_{\text{r}}} \varsigma_{u,h_{\text{p}}} \varsigma_{u,h_{\text{t}}} \varsigma_{u,h_{\text{r}}} \lambda_{h_{\text{p}},h_{\text{t}},h_{\text{r}}} \right), \tag{6}$$

$$F_{\text{pva}}^{\text{sta}} = \sum_{i=1}^{D} \left(\eta_{\text{dis}} \lambda_{\text{F}} - \frac{\lambda_{\text{G}}}{\eta_{\text{cha}}} \right) T_{\text{rat}} S^{\text{sta}} + \left(\eta_{\text{dis}} \lambda_{\text{F}} - \frac{\lambda_{\text{G}}}{\eta_{\text{cha}}} \right) (T_{\text{rat}} S^{\text{sta}} - P_{\text{nec},i}), \tag{7}$$

$$F_{\text{nec}}^{\text{sta}} = \sum_{i=1}^{D} (\eta_{\text{cha}} \eta_{\text{dis}} \lambda_{\text{F}} P_{\text{nec},i} - \lambda_{\text{S}} P_{\text{nec},i}), \tag{8}$$

$$C^{\text{sta}} = C_{\text{inv}} + C_{\text{op}} + C_{\text{ch}} + C_{\text{car}} + C_{\text{oil}} + C_{\text{lab}}, \tag{9}$$

where U is the number of customers; D is the annual operating days of energy storage; η_{cha} and η_{dis} are the charging and discharging efficiencies of energy storage, respectively; λ_{F}, λ_{G}, and λ_{S} are the peak price, the valley price, and the on-grid price, respectively; T_{rat} is rated charging and discharging time of energy storage; S^{sta} is the energy storage battery capacity to provide emergency power supply services; $P_{\text{nec},i}$ is the releasing power absorbed by energy storage on day i; C_{inv} is the investment cost of energy storage equipment; C_{op} is the annual operating cost of energy storage equipment; C_{ch} is the annual charging cost; C_{car} is the vehicle acquisition cost; C_{oil} is the annual fuel cost; C_{lab} is the annual labor cost.

4 Stackelberg game-based bi-level pricing optimization strategy

The multi-grade pricing of a mobile energy storage system is designed as a one-leader-multi-follower bi-level optimization problem in Figure 1B, where the mobile energy storage is the leader in the upper-level problem and the multi-type customers are the followers in the lower-level problem (Ding et al., 2023). In the upper-level problem, the energy storage aims to maximize its operating income by optimizing the expected revenue from emergency power supply services, with multi-grade electricity price $(\lambda_{h_{\text{p}},h_{\text{t}},h_{\text{r}}}^{*})$as the decision variable. In the lower-level problem, customers tend to mitigate economic losses caused by power outages by expecting lower fees of emergency power supply services, with the customer power supply purchase strategy $(S_u^{\text{ems}*})$ as the decision variable. Thus, energy storage and the users are in a strong game relationship. The bi-level pricing optimization model of emergency power supply is established in this paper based on the Stackelberg game, as detailed below.

(a) Upper-level problem: maximize the benefits of energy storage for emergency power supply, which can be defined in Equations 10–13.

$$\begin{aligned} \max \ F^{\text{sta}} = &\sum_{u=1}^{U} N_u^{\text{ems}} S_u^{\text{ems}} t_u^{\text{ems}} \left(\sum_{h_{\text{p}}=1}^{H_{\text{p}}} \sum_{h_{\text{t}}=1}^{H_{\text{t}}} \sum_{h_{\text{r}}}^{H_{\text{r}}} \varsigma_{u,h_{\text{p}}} \varsigma_{u,h_{\text{t}}} \varsigma_{u,h_{\text{r}}} \lambda_{h_{\text{p}},h_{\text{t}},h_{\text{r}}} \right) + F_{\text{pva}}^{\text{sta}} \\ &+ F_{\text{nec}}^{\text{sta}} - C^{\text{sta}}. \end{aligned} \tag{10}$$

s.t. (11)–(13)

$$F_{h_{\text{p}},h_{\text{t}},h_{\text{r}}}^{\text{ems}} \geq C_{h_{\text{p}},h_{\text{t}},h_{\text{r}}}^{\text{sta}}, \tag{11}$$

$$\begin{cases} E_u \lambda_u \leq k_u^{\text{able}} C_u^{\text{buy}} \\ F_u^{\text{ems}} \leq k_u{}^{\text{exp}} L_u^{\text{ems}} \end{cases}, \tag{12}$$

TABLE 1 Economic benefits of mobile energy storage under different cases (yuan/year).

Economic indicator	Case 1	Case 2	Case 3
Revenue of emergency power supply	166,822.87	144,952.32	0.00
Revenue of peak–valley arbitrage	347,545.76	347,545.76	347,545.76
Revenue of distributed renewable energy consumption	10,037.46	10,037.46	10,037.46
Total cost of energy storage	442,795.23	430,113.62	319,767.01
Total revenue	81,610.86	72,421.93	37,816.21

$$\begin{cases} \lambda^{\text{base}}_{h_{\text{p}}+1} > \lambda^{\text{base}}_{h_{\text{p}}} \\ \Delta\lambda_{h_{\text{t}}+1} > \Delta\lambda_{h_{\text{t}}} \\ \Delta\lambda_{h_{\text{r}}+1} > \Delta\lambda_{h_{\text{r}}} \end{cases}. \tag{13}$$

Constraints (11)–(13) are the energy storage investment constraint, individual rational constraint, and premium pricing constraint, respectively. Here, $F^{\text{ems}}_{h_{\text{p}},h_{\text{t}},h_{\text{r}}}$ and $C^{\text{sta}}_{h_{\text{p}},h_{\text{t}},h_{\text{r}}}$ are the revenue and investment cost of mobile energy storage providing emergency power supply service with capacity at the h_{p} level, duration at the h_{t} level, and response time at the h_{r} level; E_u is the annual amount of power outage of customer u; λ_{u} is the unit price of emergency power supply paid by customer u; C^{buy}_u is the total annual cost of self-funded energy storage equipment by customer u; k^{able}_u and $k_u{}^{\text{exp}}$ are the expected discount coefficient and expected utility coefficient, respectively.

(b) Lower-level problem: maximize the utility of emergency power supply for customers, which can be defined in Equations 14, 15.

$$\max F^{\text{usems}} = \sum_{u=1}^{U} N^{\text{ems}}_u S^{\text{ems}}_u t^{\text{ems}}_u \left[l^{\text{otg}}_u - \left(\sum_{h_{\text{p}}=1}^{H_{\text{p}}} \sum_{h_{\text{t}}=1}^{H_{\text{t}}} \sum_{h_{\text{r}}=1}^{H_{\text{r}}} \varsigma_{u,h_{\text{p}}} \varsigma_{u,h_{\text{t}}} \varsigma_{u,h_{\text{r}}} \lambda_{h_{\text{p}},h_{\text{t}},h_{\text{r}}} \right) \right], \tag{14}$$

$$s.t. S^{\text{ems}}_{u,\min} \le S^{\text{ems}}_u \le S^{\text{ems}}_{u,\max}, \tag{15}$$

where $S^{\text{ems}}_{u,\min}$ is the minimum power supply capacity of customer u. Constraint (15) is the customer purchase electricity strategy constraint.

It is evident that the objective function involves the multiplication of decision variables, but a bi-level nonlinear optimization problem cannot be directly solved by the available commercial solver. Since the objective functions for energy storage and customers are all in the linear space for their decision variables, Karush–Kuhn–Tucker (KKT) theory is used to transform the lower-level problem into constraints of the upper-level problem (Zhou et al., 2023). Therefore, the bi-level multi-grade pricing problem can be converted into the game equilibrium single-level MILP model (Chuangpishit et al., 2023), which can be optimized by the Gurobi solver based on MATLAB.

Since the maximum power supply capacity standard is 250 kW in Section 2, this paper selects the lithium iron phosphate batteries as the energy storage battery, with an energy storage inverter capacity of 250 kW. The cost of the energy storage vehicle body is 150,000 yuan, with an annual labor cost of 100,000 yuan (Gong et al., 2022). Basic parameters and other energy storage parameters are explained in Fang et al. (2023). The scenario considers 20 emergency power supply customers, and parameters for power supply customers are referenced in the literature (Wang et al., 2023b; Fang et al., 2023; Chen, 2015; Li J. et al., 2021). In order to evaluate the effectiveness of the multi-grade pricing method for emergency power supply of mobile energy storage, this paper designs three cases to conduct a comparative analysis of energy storage economics. Case 1 is the multi-grade pricing strategy proposed in this paper. In case 2, mobile energy storage provides emergency power supply without considering grading. In case 3, energy storage only engages in peak–valley arbitrage and distributed renewable energy consumption, and customers independently configure energy storage as backup power at their own expense in case of blackout. Furthermore, based on the parameters provided above, calculations are performed according to formulas 4 to 8, and the results of the economic benefits (Fang et al., 2023) of mobile energy storage under different cases are shown in Table 1.

Compared with cases 2 and 3, the total revenue of case 1 is the highest, while the total cost is the highest in Table 1, as the increased revenue of emergency power supply in case 1 far outweighs the increase in cost. This demonstrates that emergency power supply services can significantly increase the annual operating income of energy storage and that emergency power supply services provided by energy storage have strong commercial prospects.

5 Discussion and conclusions

Mobile energy storage plays a crucial role in peak shaving and valley filling, distributed renewable energy consumption, and power quality management, especially in ensuring the reliability of power supply. In this paper, a comprehensive overview of the multi-grade pricing strategy for emergency power supply of the mobile energy storage system is conducted. The key findings of this paper can be summarized as follows: 1) the hierarchical pricing metrics of the emergency power supply service provided by mobile energy storage are proposed, which consist of the power supply capacity, power supply duration, and response time. These metrics achieve a precise delineation of emergency power supply levels, having specific significance for the formulation of customized power service grade standards in the future. 2) A bi-level pricing optimization model based on Stackelberg game is proposed to obtain optimal tiered pricing of emergency power supply and optimal power supply capacity purchase strategies of customers, achieving interest equilibrium between mobile energy storage and consumers.

Numerous studies (Wang et al., 2023a; Yang, 2021; Xiao, 2021; Jiang et al., 2021) have been conducted on the configuration of mobile energy storage. The power emergency center optimizes and schedules mobile energy storage based on customers' demand for power supply within the emergency mechanism (Xiao, 2021). Therefore, combining

the configuration of energy storage and the emergency power supply needs of customers within a certain region, the tiered pricing model proposed in this paper can be applied to calculate the electricity prices for different levels of emergency power supply. In the existing power market, energy storage can profit by providing multiple customized power services (Fang et al., 2023). Thus, according to the results of the emergency power supply price and customers' demand for power supply, the emergency power supply service can be paid on a per-use basis.

During the process of mobile energy storage transporting to designated power supply points, the traffic network is highly complex. The multi-grade pricing model in this paper does not take into account real-time scheduling issues of mobile energy storage, only calculating the annual operational costs but ignoring daily or real-time operational conditions. The next step could integrate real-time scheduling of mobile energy storage into the multi-grade pricing model.

Author contributions

JB: writing–original draft and writing–review and editing. XG: conceptualization and writing–original draft. XY: data curation, formal analysis, and writing–review and editing.

Funding

The author(s) declare that financial support was received for the research, authorship, and/or publication of this article. This work was sponsored by the Guangdong Basic and Applied Basic Research Foundation (2023A1515110105) and the Scientific Research Startup Fund for Shenzhen High-Caliber Personnel of SZPT (No. 6022310042k).

Conflict of interest

The authors declare that the research was conducted in the absence of any commercial or financial relationships that could be construed as a potential conflict of interest.

Publisher's note

References

Cao, Y., Zhou, B., Chung, C. Y., Wu, T., Ling, Z., and Shuai, Z. (2024). A coordinated emergency response scheme for electricity and watershed networks considering spatio-temporal heterogeneity and volatility of rainstorm disasters. *IEEE Trans. Smart Grid* 15, 3528–3541. doi:10.1109/TSG.2024.3362344

Chen, J. (2015). Research on reducing power loss of important power users in power distribution network. *Telecom Power Technol.* doi:10.19399/j.cnki.tpt.2015.06.011

Chuangpishit, S., Katiraei, F., Chalamala, B., and Novosel, D. (2023). Mobile energy storage systems: a grid-edge technology to enhance reliability and resilience. *IEEE Power Energy Mag.* 21, 97–105. doi:10.1109/MPE.2023.3246899

Ding, Y., Xu, Q., Hao, L., and Xia, Y. (2023). A stackelberg game-based robust optimization for user-side energy storage configuration and power pricing. *Energy* 283, 128429. doi:10.1016/j.energy.2023.128429

Fang, J., He, D., Pei, Z., Peng, Z., Bao, J., Liu, W., et al. (2023). A multi-grade pricing strategy for distributed energy storage considering default risks of customized power services. *J. Shanghai Jiaot. Univ.* doi:10.16183/j.cnki.jsjtu.2023.481

Gong, C., Wu, M., and Sun, L. (2022). Economic benefit analysis of mobile energy storage based on improved genetic algorithm. *Electr. Eng.* doi:10.19768/j.cnki.dgjs.2022.05.003

Jiang, X., Chen, J., Zhang, W., Wu, Q., Zhang, Y., and Liu, J. (2021). Two-step optimal allocation of stationary and mobile energy storage systems in resilient distribution networks. *J. Mod. Power Syst. Clean Energy* 9, 788–799. doi:10.35833/MPCE.2020.000910

Lei, S., Chen, C., Zhou, H., and Hou, Y. (2019). Routing and scheduling of mobile power sources for distribution system resilience enhancement. *IEEE Trans. Smart Grid* 10, 5650–5662. doi:10.1109/TSG.2018.2889347

Li, J., Han, J., Liu, X., Zhang, Y., Zhang, Y., Zhang, X., et al. (2021b) "Optimal capacity allocation of anti-disaster mobile power vehicles based on dynamic programming," in *2021 IEEE 4th international Conference on renewable Energy and power engineering (REPE)*. doi:10.1109/REPE52765.2021.9617024

Li, J., Mu, G., Zhang, J., Li, C., Yan, G., Zhang, H., et al. (2023). Dynamic economic evaluation of hundred megawatt-scale electrochemical energy storage for auxiliary peak shaving. *Prot. Control Mod. Power Syst.* 8, 50. doi:10.1186/s41601-023-00324-8

Li, L., Cao, X., and Zhang, S. (2022). Shared energy storage system for prosumers in a community: investment decision, economic operation, and benefits allocation under a cost-effective way. *J. Energy Storage* 50, 104710. doi:10.1016/j.est.2022.104710

Li, X., Wang, L., Yan, N., and Ma, R. (2021a). Cooperative dispatch of distributed energy storage in distribution network with PV generation systems. *IEEE Trans. Appl. Supercond.* 31, 1–4. doi:10.1109/TASC.2021.3117750

Manojkumar, R., Kumar, C., Ganguly, S., and Catalão, J. P. S. (2021). Optimal peak shaving control using dynamic demand and feed-in limits for grid-connected PV sources with batteries. *IEEE Syst. J.* 15, 5560–5570. doi:10.1109/JSYST.2020.3045020

Naderi, E., K. C., B., Ansari, M., and Asrari, A. (2021). Experimental validation of a hybrid storage framework to cope with fluctuating power of hybrid renewable energy-based systems. *IEEE Trans. Energy Convers.* 36, 1991–2001. doi:10.1109/TEC.2021.3058550

Shang, B. (2021). *Study on optimal configuration and operation method of user side energy storage*. Beijing, China: Beijing Jiaotong University. doi:10.1016/j.ijepes.2022.108621

Sun, S., Yang, Q., and Yan, W. (2017). Optimal temporal-spatial PEV charging scheduling in active power distribution networks. *Prot. Control Mod. Power Syst.* 2, 34. doi:10.1186/s41601-017-0065-x

Sun, W., Liu, W., Zhang, J., and Tian, K. (2022). Bi-level optimal operation model of mobile energy storage system in coupled transportation-power networks. *J. Mod. Power Syst. Clean Energy* 10, 1725–1737. doi:10.35833/MPCE.2020.000730

Wang, F., Ou, Y., and Xin, X. (2023a) "Operation strategy analysis of power supply ensuring microgrid with photovoltaic and energy storage," in *Electric power automation equipment*. doi:10.16081/j.epae.202210020

Wang, F., Ou, Y., and Xin, X. (2023b). Optimal configuration of user-side energy storage considering power supply transaction mode and capacity market. *High. Volt. Eng.* doi:10.13336/j.1003-6520.hve.20230205

Xiao, K. (2021). *Mobile energy storage planning and scheduling under different scenario in distribution network*. Hangzhou, China: Zhejiang University. doi:10.27461/d.cnki.gzjdx.2021.000453

Xiong, L., Liu, X., Zhao, C., and Zhuo, F. (2020). A fast and robust real-time detection algorithm of decaying DC transient and harmonic components in three-phase systems. *IEEE Trans. Power Electron.* 35, 3332–3336. doi:10.1109/TPEL.2019.2940891

Xu, C., Xu, C., Zhang, T., Si, L., Yang, J., Yu, H., et al. (2023). Stackelberg game-based three-stage optimal pricing and planning strategy for hybrid shared energy storage. *Front. Energy Res.* 11. doi:10.3389/fenrg.2023.1273929

Yang, T. (2021). *Research on power boosting and operation strategy of charging pile based on distributed mobile energy storage*. Beijing, China: Beijing Jiaotong University. doi:10.26944/d.cnki.gbfju.2021.001979

Yang, Z., Gao, T., Liu, Y., Huang, X., Gao, S., Zhao, Q., et al. (2023). A two-stage pricing strategy for electric vehicles participating in emergency power supply for

important loads. *Electr. Power Syst. Res.* 218, 109239. doi:10.1016/j.epsr.2023.109239

Yu, L. (2015). *Energy storage system service and value assessment in smart grid*. Beijing, China: North China Electric Power University. doi:10.7666/d.Y2879251

Zhang, H., Ma, S., Ding, T., Lin, Y., and Shahidehpour, M. (2021). Multi-Stage multi-zone defender-attacker-defender model for optimal resilience strategy with distribution line hardening and energy storage system deployment. *IEEE Trans. Smart Grid* 12, 1194–1205. doi:10.1109/TSG.2020.3027767

Zhong, J., Li, Y., Cao, Y., Tan, Y., Peng, Y., Zhou, Y., et al. (2023). Robust coordinated optimization with adaptive uncertainty set for a multi-energy microgrid. *IEEE Trans. Sustain. Energy* 14, 111–124. doi:10.1109/TSTE.2022.3203299

Zhou, B., Fang, J., Ai, X., Cui, S., Yao, W., Chen, Z., et al. (2023). Storage right-based hybrid discrete-time and continuous-time flexibility trading between energy storage station and renewable power plants. *IEEE Trans. Sustain. Energy* 14, 465–481. doi:10.1109/TSTE.2022.3215839

Zhou, B., Zou, J., Chuang, C., Wang, H., Liu, N., Voropai, N., et al. (2021). Multi-microgrid energy management systems: architecture, communication, and scheduling strategies. *J. Mod. Power Syst. Clean Energy* 9, 463–476. doi:10.35833/MPCE.2019.000237

Zhu, X., and Si, Y. (2023). Multi-Period dynamic power supply recovery strategy for distribution networks considering cyber-physical-traffic network coupling. *IEEE Trans. Power Deliv.* 38, 4454–4464. doi:10.1109/TPWRD.2023.3317278

frontiers | Frontiers in Energy Research

TYPE Original Research
PUBLISHED 12 September 2024
DOI 10.3389/fenrg.2024.1429241

OPEN ACCESS

EDITED BY
Yonghui Liu,
Hong Kong Polytechnic University, Hong Kong, SAR China

REVIEWED BY
Bi Liu,
Sichuan Agricultural University, China
Xiaokang Liu,
Polytechnic University of Milan, Italy
Bin Zhang,
Aalborg University, Denmark

*CORRESPONDENCE
Wentao Feng,
1179623991@qq.com

RECEIVED 07 May 2024
ACCEPTED 12 June 2024
PUBLISHED 12 September 2024

CITATION
Feng W, Deng B, Chen T, Zhang Z, Fu Y, Zheng Y, Zhang L and Jing Z (2024), Probabilistic net load forecasting based on sparse variational Gaussian process regression.
Front. Energy Res. 12:1429241.
doi: 10.3389/fenrg.2024.1429241

Probabilistic net load forecasting based on sparse variational Gaussian process regression

Wentao Feng[1]*, Bingyan Deng[1], Tailong Chen[1], Ziwen Zhang[1], Yuheng Fu[1], Yanxi Zheng[1], Le Zhang[1] and Zhiyuan Jing[2]

[1]State Grid Sichuan Information & Telecommunication Company, Chengdu, China, [2]School of Mechanical and Electrical Engineering, University of Electronic Science and Technology of China, Chengdu, China

The integration of stochastic and intermittent distributed PVs brings great challenges for power system operation. Precise net load forecasting performs a critical factor in dependable operation and dispensing. An approach to probabilistic net load prediction is introduced for sparse variant Gaussian process based algorithms. The forecasting of the net load is transferred to a regression problem and solved by the sparse variational Gaussian process (SVPG) method to provide uncertainty quantification results. The proposed method can capture the uncertainties caused by the customer and PVs and provide effective inductive reasoning. The results obtained using real-world data show that the proposed method outperforms other best-of-breed algorithms.

KEYWORDS

net load forecasting, power system, Gaussian process, uncertainties, probabilistic forecasting

1 Introduction

Distributed generation such as photovoltaic (PV) has become an important component with the increasing demand for low-carbon power systems (Zhu et al., 2023). In addition, electric vehicles are becoming increasingly popular around the world due to their clean and economic properties (Cao et al., 2020a; Dhawale et al., 2024). The adjustability of EV power enables them to be the focus of research in load management. However, the intermittent nature of PVs and the uncertainty of the commuting and charging behaviors of EV bring more uncertainties to both the generation and demand sides, which pose great challenges for a reliable and safe operation of power systems (Cao et al., 2020b; Xiong et al., 2021).

Accurate load forecasting contributes to the reliability and security of smart grid performance. (Zhao et al., 2023; Zulfiqar et al., 2023; Zhao et al., 2024). Conventional load forecasting researches focus on forecasting the aggregate load demand in a given area based on historical load demand data, weather and geographic information, which can be divided into two subcategories: point forecasting methods and probabilistic methods. Various point forecasting methods have been proposed. A short-term loading prediction model based on multivariate linear regression is presented in Saber and Alam, (2017). In the face of complicated nonlinear systems, multivariate linear regression approaches possibly fail to provide high-precision forecasting results. An autonomy regressive integrative moving averaging (ARIMA)-based intradaily load predicting model is introduced (Cao et al., 2015). The principle of the ARIMA method is to build a model by using the historical load data sampled in the previous period. The primal loading is considered as a stochastic variation of the model, and the variation procedure of those primal loads is derived from the statistical

laws (Taieb et al., 2016). However, the ARIMA method does not deal well with time-series data with high randomness and non-stationary features. Neural network (NN)-based approaches have been extensively employed in the literature for load prediction in recent years for the power of their nonlinear matching capacity. A load forecasting method combining the backpropagation NN (BPNN) and radial basis function NN is proposed for day-ahead load prediction. Xu et al. (2018) proposes a NN based load forecasting model and adopts an enhanced Levenberg-Marquardt method for training the NN. The NNs utilized in the aforementioned studies are fully-connected, which ignores the temporal correlation between input data that contains valuable information. Recurrent NN is a kind of network structure that has the ability of memory. It considers both the current input and what it learned previously when utilized for prediction. Various RNNs have been proposed, such as long-short term memory (LSTM), just-another net (Gao et al., 2018), and gated recurrent unit. Among them, LSTM is the most widely used. An LSTM-based short-term residential load forecasting method is proposed. An ensemble load forecasting method based on LSTM is developed in (Tan et al., 2020). Simulation tests demonstrate that the proposed method can achieve state-of-the-art performance on open datasets. In addition to the methods mentioned above, extreme learning machines (Li et al., 2023) and k-nearest neighbor methods (Prasad et al., 2023) are also employed to forecast loads and obtain gratifying outcomes.

Those approaches are point predictions where only one value is supplied at each step. However, due to increasing penetration of renewable energy sources and competitive markets, point forecasting approaches are becoming obsolescent and probabilistic prediction approaches are growing in necessity for system operators. Probabilistic prediction approaches allow quantification of indeterminacy through interaction intervals, quantity, or probability density functions, enabling applications in unit commitment, dependability programming, and competitive tendering in the electricity market. The various probabilistic prediction approaches presented can be classified into two types (Feng et al., 2020): one-step approaches (He et al., 2016; Zhang et al., 2019) and two-step approaches (Xie and Hong, 2018; Wang et al., 2019).

While there are extensive researches on load prediction, there are very rarely researches on the prediction of net load, which is defined as the discrepancy between electricity consumption and power generation. The reliability and security of smart grid operations can be increased by accurately predicting net loads. However, net load forecasting is fraught with substantially more challenges than conventional load forecasting due to the intermittency and stochastic character of renewable energy. Over the past several years, a couple of researches have concentrated on the prediction of net loads. (Liu et al., 2014; Kaur et al., 2016; Sepasi et al., 2017; Wang et al., 2018; Sun et al., 2020). Liu et al. (2014) presents a BPNN-based point prediction approach for net loads. The performance comparison between the combined net load predicting model and the additive model is provided in Kaur et al. (2016). A complex-valued NN-based net load prediction model is proposed in Sepasi et al. (2017). The above studies belong to the deterministic net load forecasting methods, which cannot capture the multiple uncertainties caused by the behind-meter PV and load demand. Probabilistic forecasting methods Wang et al. (2018) are proposed to quantify the uncertainties. The work (Sun et al., 2020) presents a Probability forecasting model which is supported by Bayesian theoretic and LSTM. Experimental findings indicate that excellent properties can be obtained with both determination and probability Metrics. Although LSTM alleviates the gradient explosion problem via the introduction of the gate mechanism, it cannot calculate in parallel, which unusually leads to a long calculation time.

Sparse Gaussian processes (SGP) fit complex non-linear relationships using flexible probabilistic models to accurately predict future data. In this context, an algorithm of sparsely variant Gaussian process based probabilistic net load forecasting model is introduced. The forecasting of load demand is cast to a regression problem and the sparse variational Gaussian process (SVPG) (Hu et al., 2024) method is applied to estimate the prediction values as well as to provide the uncertainty quantification. Comparative tests using real field data among various point and probabilistic forecasting methods illustrate the superior performance of the proposed method in terms of both deterministic and probabilistic results. The main contributions are as follows:

1) A prediction model based on a sparse variational Gaussian process is constructed;
2) The proposed SVGP model accurately captures load uncertainty;
3) The proposed SVGP model gives excellent performance in both point load prediction and probabilistic prediction.

The rest of the paper is formulated as follows: the problem formulation and proposed method are given in Section II, followed by simulation results in Section III. Section IV concludes this paper.

2 Proposed methodology

In this section, the probabilistic load predicting issue is firstly presented, followed by detailed information on the Gaussian process regression method and the SVPG regression method. Finally, the details of the training procedure are provided.

2.1 Formulation of the probabilistic load predicting issue

In power systems, the net load data captured by intelligent meters is typically considered as a time series $\{P_{i,t}\}$. To anticipate the prospect $P_{i,t}$, the training dataset was constructed by obtaining historically net load data and other parameters (e.g., meteorological data and time indices). Specifically, the dataset was consisted of the following output variables y_t, which denotes the projections of future net loads, and the input variables x_t that is a collection of variables associated with $P_{i,t}$. The aim of net load predicting is to learn the mapping relationship $y_t = f(x_t)$ depending on the trained set $T = \{(x_t, y_t), t = 1, 2, \ldots, n$, where n indicates the amount of examples in the trained set. Direct evaluation of the function $f(\cdot)$ produces a definitive net load prediction. Nevertheless, historic data on net load includes uncertainty on the generating side and the

demanding side, where determination prediction results could be subject to larger prediction errors. To this end, a Bayesian theory-based prediction approach is introduced in this paper, that allows the estimation of the distribution of the function $f(\cdot)$ to improve the capability of capturing the unpredictability of the net load and to produce probabilistic prediction results. The details of the proposed method are given below.

2.2 Gaussian process regression

Assuming that (X, Y) and (X^*, Y^*) indicate the training and test sets, where $X \in R^{N\times Q}$ and $Y \in R^{N\times 1}$ are the inputs and outputs of the trained sets; $X^* \in R^{N^*\times Q}$ and $Y^* \in R^{N^*\times 1}$ are the inputs and outputs of the test sets. So that can derive (1) and (2)

$$Y = f(X) + \varepsilon \tag{1}$$

$$Y^* = f(X^*) + \varepsilon \tag{2}$$

where $\varepsilon \sim N(0, \sigma_n^2)$ represents Gaussian white noise; $f(\cdot)$ denotes a Gaussian process matching from inputs to outputs (3):

$$f(x) = GP(m(x), K(x, x')) \tag{3}$$

where $x, x' \in X$; $m(\cdot)$ denotes the average value function, which can typically be regarded as 0 when little *a priori* information is available; $K(\cdot)$ represents the covariance function as (4), of which the most frequently employed is the radial basis function (RBF):

$$k(x, x') = \sigma^2 exp\left(-(x - x')^2 / 2\right) \tag{4}$$

Then the prior distribution of y can be acquired as (5):

$$y \sim N(0, K(X, X) + \sigma_n^2 I_n) \tag{5}$$

and Joint distributed of observations y and forecast value f_* can be obtained as (6)

$$\begin{bmatrix} y \\ f_* \end{bmatrix} \sim N\left(0, \begin{bmatrix} K(X,X) + \sigma_n^2 I_n & K(X, x^*) \\ K(x^*, X) & K(x^*, x^*) \end{bmatrix}\right) \tag{6}$$

The posterior distribution of the forecast values will then be represented as f_* which can be described as (7–9)

$$f_* | X, y, x_* \sim N(\bar{f}_*, \mathrm{cov}(f_*)) \tag{7}$$

where

$$f^* = K(x^*, X)\left(K(X, X) + \sigma_n^2 I_n\right)^{-1} y \tag{8}$$

$$\mathrm{cov}(f_*) = K(x^*, x^*) - K(x^*, X) \times \left(K(X, X) + \sigma_n^2 I_n\right)^{-1} K(X, x^*) \tag{9}$$

If we can obtain all the hyper-parameter Θ, which contains the parameters σ_n in Gaussian white noise ε and the parameters σ in kernel function $K(\cdot)$, The mean and variance of the testing sites are obtained based on (8) and (9), respectively. Generally, the most used method to obtain hyper-parameters of GPR is a maximum likelihood estimate based on a gradient that makes the negative logarithm marginal likelihood $\ell = -\log p(Y|X)$ maximum:

$$\frac{\partial \ell}{\partial \Theta} = -\frac{\partial \log p(Y|X, \Theta)}{\partial \Theta} \tag{10}$$

$$\hat{\Theta} = \underset{\Theta}{\mathrm{argmax}}\left(-\log p(Y|X, \Theta)\right) \tag{11}$$

The hyper-parameters are updated based on gradient according to (10) until finding the optimal in (11). Where there is a drawback that the complexity of this training process is $O(N^3)$, which means it will take a lot of time to train the model and it is not suitable for the scenario in which the data is large.

2.3 Sparse variational Gaussian process regression

To solve the problem above, a useful method called sparse Gaussian process regression (SGPR) is proposed. SGPR can reduce the complexity of the training process to $O(NM^2)$ (M << N) by introducing M auxiliary inputs $Z \in R^{M\times Q}$ and the corresponding outputs $u \in R^{M\times 1}$ to approximate the original N-dimensional Gaussian process. And the joint density of y, f and u is:

$$p(y, f, u) = \underbrace{p(f, u; X, Z)}_{\text{GP prior}} \underbrace{p(y|f)}_{\text{likelihood}} \tag{12}$$

In (12) the joint density is factorized into GP prior and likelihood where the likelihood can be expressed as (13):

$$p(y|f) = N(y|f, \sigma_n^2 I_n) \tag{13}$$

and GP prior can be factorized into the prior $p(u|Z)$ and conditional $p(f|u; X, Z)$ (14):

$$p(f, u; X, Z) = \underbrace{p(u|Z)}_{\text{prior}} \underbrace{p(f|u; X, Z)}_{\text{conditional}} \tag{14}$$

and the prior and conditional parts can be expressed as (15, 16):

$$p(u; Z) = N(u \,|\, 0, K(Z, Z)) \tag{15}$$

$$p(f|u; X, Z) = N(f|K_{nm}K_{mm}^{-1}u, K_{nn} - K_{nm}K_{mm}^{-1}K_{mn}) \tag{16}$$

where K_{nn}, K_{nm}, K_{mn} and K_{mm} represent $K(X,X)$, $K(X,Z)$, $K(Z,X)$ and $K(Z,Z)$, respectively.

An approximate posterior $q(f,u) = p(f|u)q(u)$ is introduced to replace the true posterior $p(f,u)$, where $q(u) = N(\mu,\Sigma)$. Variational inference seeks the variational posterior by minimizing the Kullback-Leibler divergence between variational posterior q and true posterior p, where a lower Kullback-Leibler divergence represents a closer similarity between two distributions. Equivalently, we can maximize the evidence lower bound (ELBO) to seek the variational posterior:

$$\mathcal{L}_{\mathrm{SGPR}} = \log p(y) \geq E_{q(f,u)} \log \frac{p(y, f, u)}{q(u, f)} \tag{17}$$

where $p(y, f, u)$ is expressed in (12) and $q(u, f)$ is the variational posterior. And the ELBO can be simplified from (17) as (18):

$$\mathcal{L}_{\mathrm{SGPR}} \geq E_{q(f,u)}\left[\log p(y|f)\right] - KL(q(u, f) \| p(u, f)) \tag{18}$$

where the latter part can be expressed as (19):

$$\begin{aligned} KL(q(u, f) \| p(u, f)) &= KL(q(u)p(f|u) \| p(u)p(f|u)) \\ &= KL(q(u) \| p(u)) \end{aligned} \tag{19}$$

So, the ELBO can be simplified as (20):

$$\mathcal{L}_{\mathrm{SGPR}} \geq \mathrm{E}_{q(f)} \log p\left(y|f\right) - KL\left(q(u)\|p(u)\right) \tag{20}$$

The Gaussian marginal likelihood $q(f)$ can be expressed as (21):

$$q(f) = \int p\left(f|u\right)q(u)du = N\left(f|\mu', \Sigma'\right) \tag{21}$$

where $p(f|u)$ is expressed in (20) and $q(u) = N(\mu,\Sigma)$, so the μ' and Σ′ be calculated as (22, 23):

$$\mu' = K_{nm}K_{mm}^{-1}u \tag{22}$$

$$\Sigma' = K_{nn} + K_{nm}K_{mm}^{-1}(\Sigma - K_{mm})K_{mm}^{-1}K_{mn} \tag{23}$$

All parts in (20) are known, so we can calculate the ELBO and then obtain all the hyper-parameters by maximizing the ELBO. Besides the model hyper-parameter Θ which is the same as that in GPR, there is another kind of parameters called variational parameters θ, which contain the mean μ and variance Σ of variational posterior $q(u)$ and the auxiliary inputs Z. All the hyper-parameters can be expressed as (24, 25):

$$\Theta = \{\sigma_n, \sigma\} \tag{24}$$

$$\theta = \left\{\{\mu\}_{m=1}^{M}, \{\Sigma\}_{m=1}^{M}, Z\right\} \tag{25}$$

After obtaining both the model and variational parameters, we can predict the new points via as (26).

$$q(f^*) = \int p(f^*|u)q(u)du \tag{26}$$

where $q(f^*)$ is the distribution of new points.

The detailed training and testing procedure of the proposed algorithm is shown in Algorithm 1.

Require: train data-set: Tr=(X,Y); test data-set: Te=(X*,Y*)
Require: model parameters: Θ; variational parameters: θ; training iterations: T; amount of sparse point: m
procedure Train(Tr, Θ, θ, T)
  Initialize all parameters
    for epoch t = 1, 2, ... T **do**
      obtain the variational posterior $q(u)$ according to the variational parameters μ and Σ
      obtain the conditional $p(f|u;X,Z)$ according to (16)
      obtain the marginal $q(f)$ according to (21)
      obtain the ELBO L_{SGPR} according to (20)
      update model parameters: $\theta \leftarrow \theta - \nabla_{\theta}L_{SGPR}$
      update variational parameters: $\Theta \leftarrow \Theta - \nabla_{\Theta}L_{SGPR}$
    end
end procedure
procedure Test(Te, Θ,θ)
    obtain marginal $q(f^*)$ of test point according to (26)
end procedure

Algorithm 1. Details of the training and test procedure.

3 Case study

3.1 Data description

Comparative numerical testing is performed with authentic on-site smart meter data. These data have been measured on the Ausgrid distribution network which contains load demand and photovoltaic (PV) generation data from 300 residential households (Ausgrid 2014, 2015). The time period for recording values is 0.5 h. The purpose of this research is to provide a probabilistic prediction of the net load, which is derived by adding the differential of each consumer's load demand and PV production. The reader is directed to Ausgrid 2014, 2015 for additional details about the dataset.

Since the dataset contains some low-quality data (Ratnam et al., 2017), we delete some original data for better illustration and fair comparison. The data are divided into the training samples and test samples, which contain 11,739 and 480 pairs of data, respectively. The training samples have been applied to train the predictive models while the testing samples have been performed to estimate the performance of the different models. The net load of the training and testing sets are shown in Figures 1, 2, respectively. The characteristics picked comprise the below variables: 1) the time index, which includes messages for hour of the day, day of the week, and month of the year. A single coding technique is employed in this research to encode the time message; 2) the historical load demand data, which include load data from the previous 2 days with the same time-steps; 3) the historical PV generation data, which contain data on PV generation at the same point in time for the last 3 days and 1 week ago on the same day.

3.2 Experimental setup

Comparative tests among a series of load forecasting methods are carried out to access the performance of the proposed approach. Comparison methods fall into two categories: point prediction approaches and probabilistic approaches. The point prediction approaches involve: 1) multiple linear regression (MLR); 2) support vector regression (SVR), where RBF is specified to be the kernel function with hyper parameters adjusted following the grid search approach.; 3) back-propagation neural network (BPNN), where a three-layer model is built. The numbers of the hidden layers are 64, 64, and 32, respectively; 4) LSTM method, where a model with two hidden layer is built. The hidden nodes of the two hidden layer are set to 30 and 30, respectively. For the probabilistic forecasting method, quantile regression (QR) is selected as the benchmark method.

3.3 Evaluation metrics

In order to assess the performance of various approaches for point prediction results, three extensively adopted deterministic prediction assessment metrics and two probabilistic prediction metrics are adopted in this research.

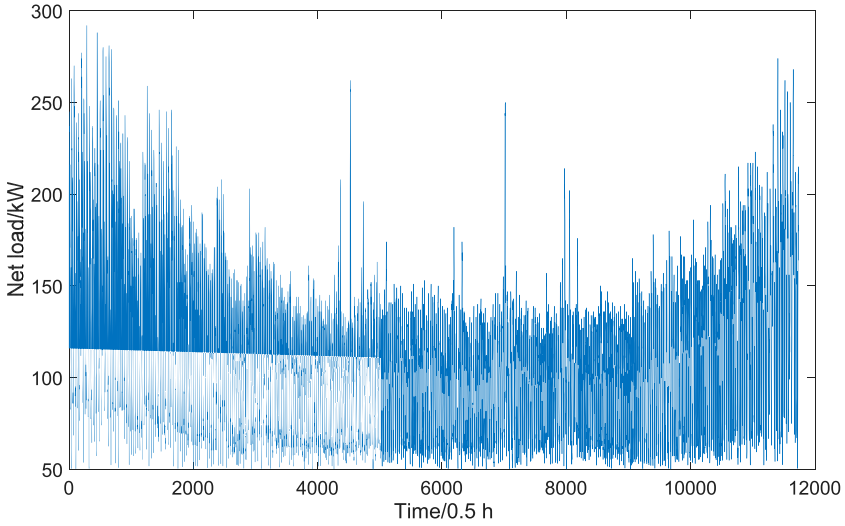

FIGURE 1
Net load of the training set.

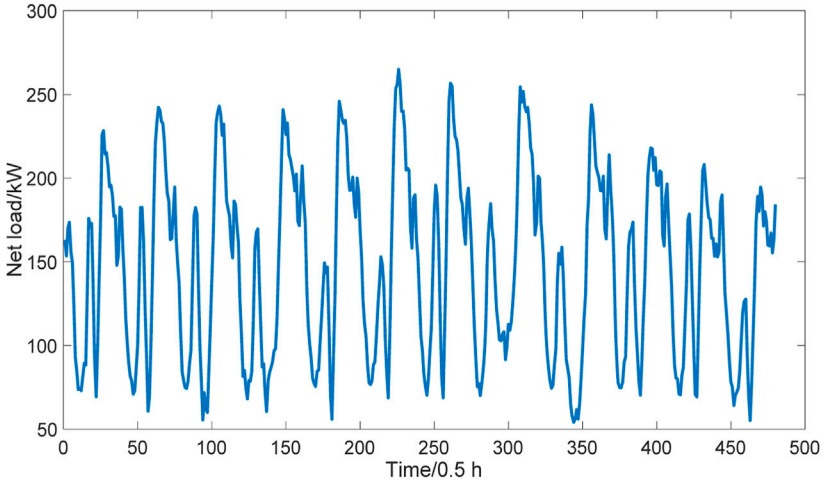

FIGURE 2
Net load of the test set.

3.3.1 Metrics for deterministic prediction

Three point forecasting metrics are utilized, that are, mean absolute error (MAE), root mean square error (RMSE), and mean absolute percentage error (MAPE) which present as (27–29):

$$MAE = \frac{1}{N}\sum_{i=1}^{N}\left|\widehat{y}_i - y_i\right| \tag{27}$$

$$RMSE = \sqrt{\frac{1}{N}\sum_{i=1}^{N}\left(\widehat{y}_i - y_i\right)^2} \tag{28}$$

$$MAPE = 100\% \times \frac{1}{N}\sum_{i=1}^{N}\frac{\left|\widehat{y}_i - y_i\right|}{y_i} \tag{29}$$

where y_i and $\widehat{y}_i$ represent the real value and projected f value of the ith sample; N denotes the sampling size in the test set.

3.3.2 Metrics for probabilistic prediction

Two probabilistic prediction metrics are employed in this study, that is, Pinball loss and PINAW. The most commonly used metrics for evaluating probability forecasting results are reliability, sharpness and resolution. Pinball is a comprehensive metric which allows for the assessment of the aforementioned metrics, where the definition of the metrics is (30):

$$Pinball = \begin{cases} (1-q)\left(\widehat{y}_{i,q} - y_i\right), y_i < \widehat{y}_{i,q} \\ q\left(y_i - \widehat{y}_{i,q}\right), y_i \geq \widehat{y}_{i,q} \end{cases} \tag{30}$$

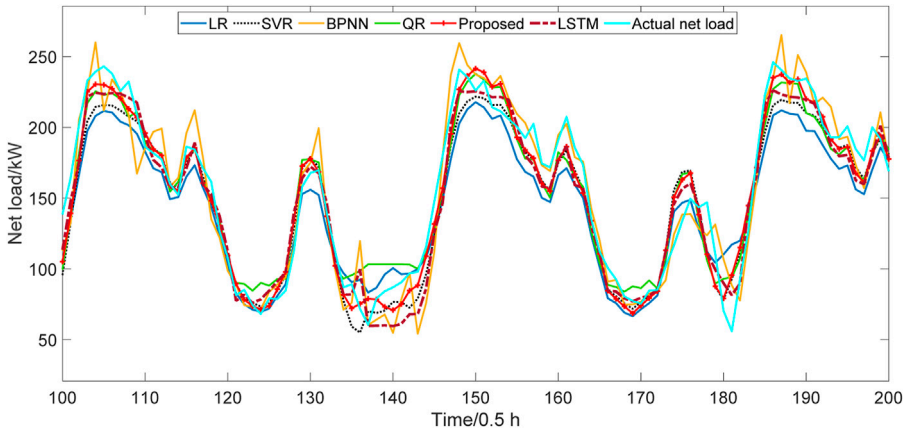

FIGURE 3
Point prediction results for different approaches.

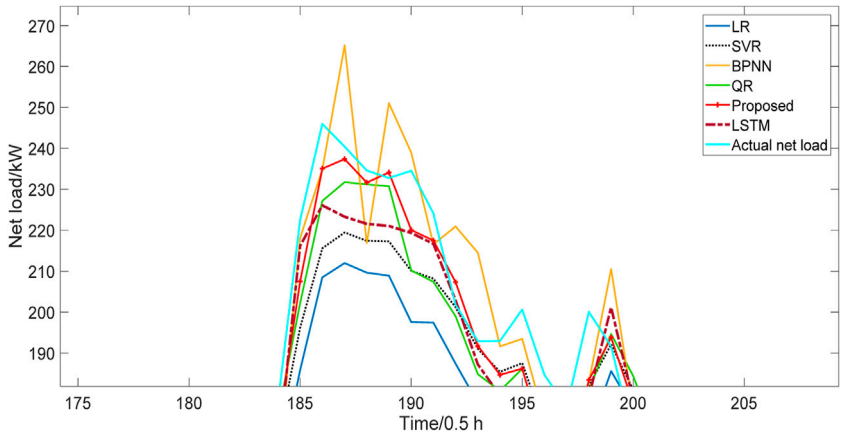

FIGURE 4
Prediction results for different approaches at the curve peak in Figure 3.

TABLE 1 Point forecasting results of different forecasting models.

Method	MAE	MAPE (%)	RMSE
LR	17.0	13.5	22.5
SVR	13.9	10.5	19.0
BPNN	14.9	12.2	20.9
LSTM	14.5	11.8	19.2
QR	14.2	12.1	18.4
Proposed	**12.8**	**10.2**	**17.4**

where q $(q = 0.01, 0.02, ..., 0.99)$ denotes order of magnitude and $\widehat{y}_{i,q}$ indicates the forecast value of the qth quantitative value. A lower Pinball value indicates a better prediction performance.

PINAW is a measurement of the prediction horizon width which is determined as (31):

$$PINAW = \frac{1}{N*D}\sum_{i=1}^{N}(U_i^{\alpha} - L_i^{\alpha}) \tag{31}$$

where U_i^{α} and L_i^{α} represent the upper bound and lower bound of the forecasting interval when the confidence level is set to α. A lower PINAW value indicates a narrower forecasting interval and a better performance.

3.4 Point forecasting results

To illustrate the superiority of the proposed model, several approaches will be employed in this section for comparison. The MAE, MAPE and RMSE of each prediction approach are displayed in Table 1. The results of QR are forecasting values when the quantile is set to 50%. The units of MAE and RMSE are kW and of MAPE is PU. The best performance cases of each metrics are shown in bold. That when the proposed method is utilized, its performance outperforms that of the LR method by 24.7%, 24.4%,

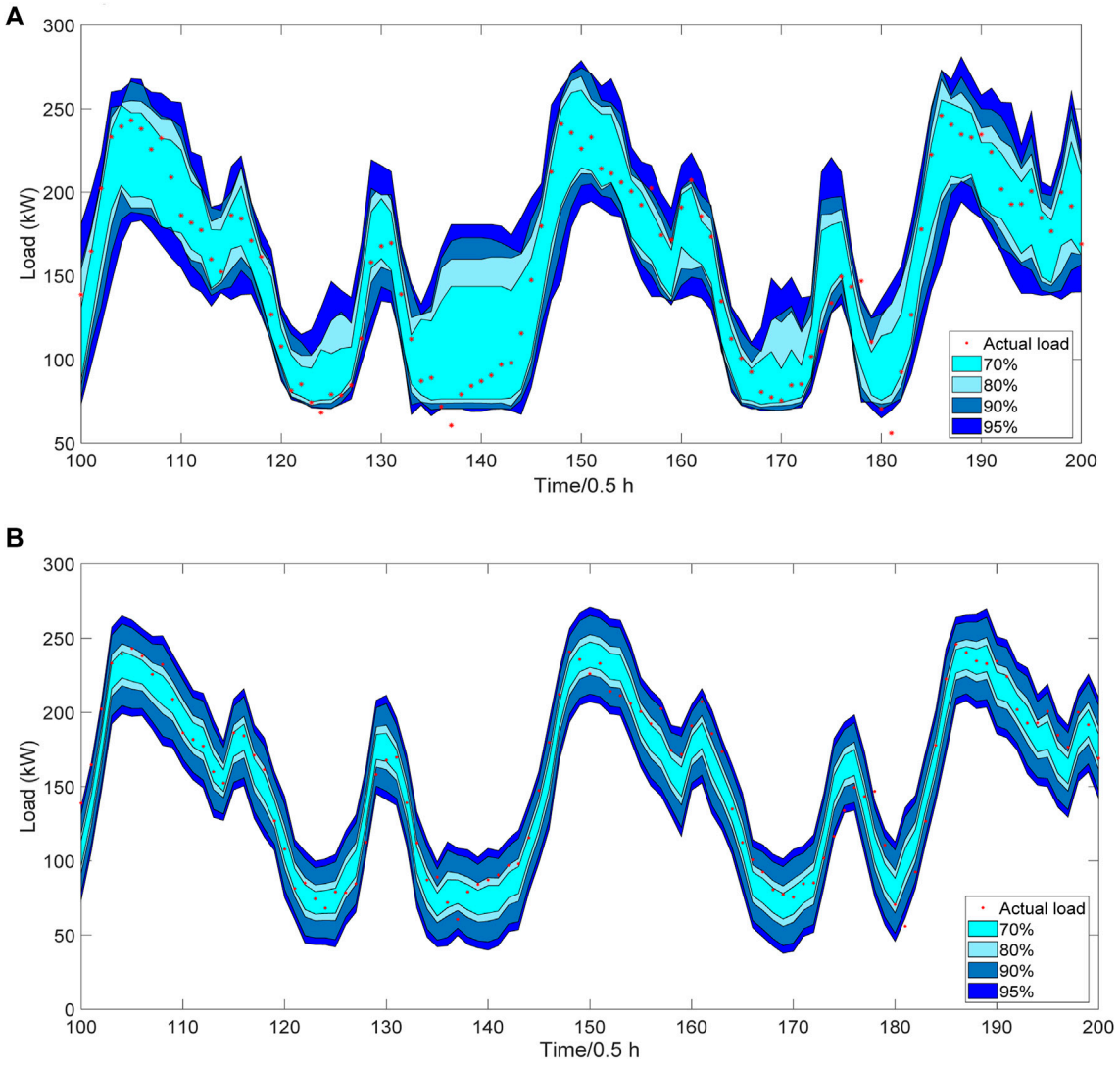

FIGURE 5
Forecasting intervals of different methods. **(A)** QR. **(B)** proposed method.

TABLE 2 Probabilistic forecasting results of different methods.

Method	Pinball	PINAW (%)
QR	5.12	30.14
Proposed	**5.03**	**24.59**

TABLE 3 The PINAW achieved by various methods under different confidence levels.

Method	90 (%)	80 (%)	70 (%)	60 (%)
QR	30.14	24.76	18.55	14.72
Proposed	**24.59**	**19.31**	**15.74**	**12.83**

and 22.7% in MAE, MAPE, and RMSE, respectively. The BPNN achieves better performance than the LR method owing to its strong nonlinear approximation capability. However, since BPNN ignores the temporal relationship between the input data, the performance of BPNN is worse than the proposed approach. LSTM has high computational complexity and requires a large amount of training data. SVR requires a high time during the training process and cannot handle the linear problem perfectly The performance of the proposed approach also outperforms that obtained by a kernel based SVR method and a recurrent NN based LSTM method, and demonstrating its effectiveness.

For analyzing the performing of the proposed model additionally, the prediction results for different approaches for 100–200 instants in the test set are displayed in Figure 3. The proposed approach is the one that comes nearest to the real load values, which demonstrates the supremacy of the proposed approach. The predicted results for each approach at peak values, which are more difficult to predict, are shown in Figure 4. It can be observed from the figure that the peak value is difficult to predict for all methods owing to the high uncertainty. The deviation between the real net load and the value forecasted by the LR method is even

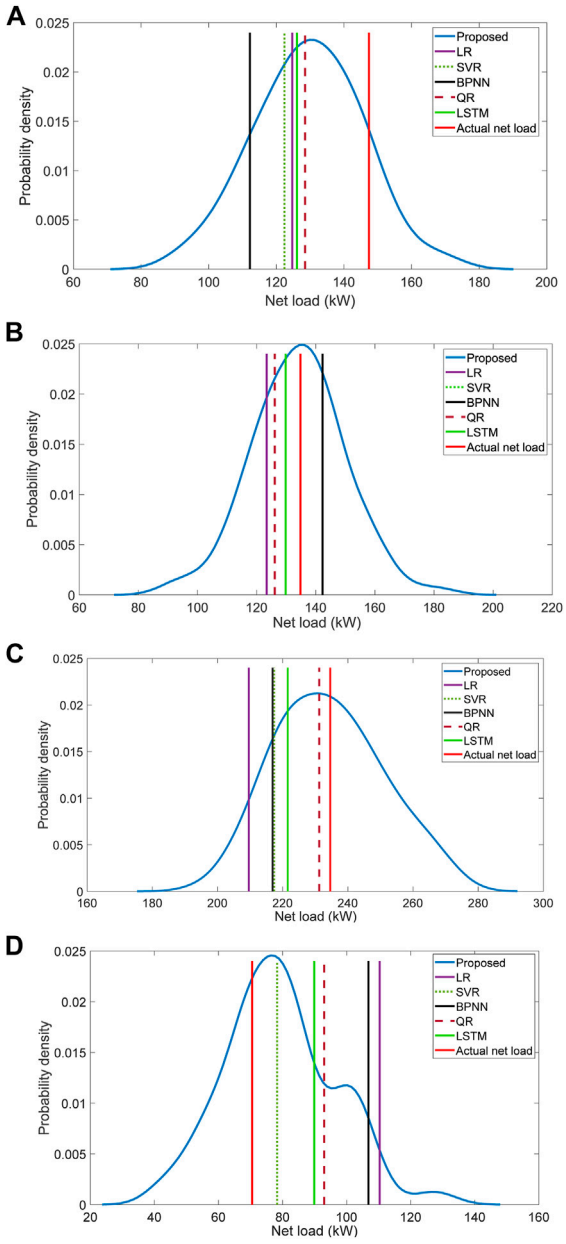

FIGURE 6
Forecasting results at different periods of the load curve. **(A)** Forecasting results at the rising stage of the curve. **(B)** Forecasting results at the falling stage of the curve. **(C)** Forecasting results at the curve peak. **(D)** Forecasting results at the curve valley.

larger than 10% of the real value. The BPNN tends to over-predict the peak value and has large fluctuations. The SVR and LSTM also fail to provide accurate forecasting values at the peak of the curve. The predicted values derived from the presented methodology appear to be the closest to the actual values, demonstrating the excellence of the proposed methodology.

The PINAW is a metric to evaluate the width of the forecasting interval. That the PINAW achieved by the proposed method is 18.4% lower than that of the QR method, demonstrating that the proposed method can achieve a better performance with narrower forecasting interval.

To further evaluate the uncertainty quantification capability of various methods, the PINAW obtained by different methods under different quantiles are listed in Table 3. It can be observed from the table that the width of the forecasting interval increases when we gradually improve the confidence level. However, the forecasting intervals obtained by the proposed method are always narrower than that of the QR method. The PINAW of the proposed method is 12.8%, 15.1%, 22.0%, and 18.4% lower than that of the QR method when the quantile is set to 60%, 70%, 80%, and 90%, respectively. This further illustrates the strength of the proposed model.

The predicted intervals for 100–200 instants in the test set for the various approaches are shown in Figure 5 when the quantile is configured as 70%, 80%, 90%, 95%, separately. It can be observed from Figure 5A that the physical net loads for some valley values fall outside the 95% credibility intervals of the QR approach, while the prediction intervals of the proposed approach will be capable of covering majority of the prediction intervals, demonstrating a higher reliability of the proposed method. Visually inspecting the probabilistic results of the two methods, the width of the proposed model is narrower than the QR approach under various quantile settings. This is consistent with the results shown in Table 2, 3, illustrating a better sharpness of the proposed method. From the perspective of the resolution, the width of the forecasting interval should be different at different periods of the curve. The forecasting interval is narrow at the rising and falling stage of the curve, while the width is large at the peak and valley of the curve. Since the value of the net load at the curve valley is mainly decided by the PV generation, which has larger uncertainty than the load demand, the width of the interval is the largest at the curve valley. This can be observed from both figures. However, the presented approach catches the uncertainty at the peak curve with a narrower interval, illustrating its effectiveness.

The prediction from various approaches at different stages of the load profile is shown in Figure 6 for deeper validation of the capability of the proposed approach. The forecasting results of different methods at the rising and falling period of the load curve are shown in Figures 6A,B. The forecasting values of various methods are not far from the actual net load at the falling stage. In addition, the density curve of the proposed method is relatively steep, demonstrating that the uncertainty level is low at the falling stage of the curve. The forecasting results of different methods at the curve peak are shown in Figure 6C. All the methods tend to underestimate the net load. The predicted values of QR and the proposed approach in the test set are more similar to the actual values as compared to the other methods. The proposed methodology quantifies the unpredictability of the net load, which provides informative implications for the system operator's planning. Visually inspecting the forecasting results at curve valley in Figure 6D, all methods tend to overestimate the net load. By contrast, the presented approach catches the uncertainty caused by the PV generation, which is curial for the operation of power systems.

4 Conclusion

This paper proposes a probabilistic prediction model for the prediction of net load based on a SVPG regression algorithm.

Comparative tests with several point forecasting and probabilistic forecasting methods utilizing real-world historical data illustrate that: 1) the proposed model can achieve better point forecasting results than benchmarking methods. The performance achieved by the proposed approach can at most outperform that of other methods by 21.8%, 20.0%, and 19.6% in MAE, MAPE, and RMSE, respectively; 2) the proposed approach has better uncertainty quantification capability compared to the baseline methodology. It is more reliable and its PINAW value is 22.0% lower than the benchmark method at most. In our future research, how to obtain predictions quickly and accurately becomes the focus of the study.

Data availability statement

The original contributions presented in the study are included in the article/Supplementary material, further inquiries can be directed to the corresponding author.

Author contributions

WF: Conceptualization, Investigation, Methodology, Software, Supervision, Writing–original draft, Writing–review and editing. BD: Conceptualization, Data curation, Investigation, Methodology, Writing–original draft. TC: Investigation, Methodology, Software, Writing–original draft. ZZ: Conceptualization, Data curation, Investigation, Writing–original draft. YF: Formal Analysis, Investigation, Project administration, Software, Writing–original draft. YZ: Data curation, Methodology, Software, Writing–review and editing. LZ: Conceptualization, Data curation, Formal Analysis, Investigation, Methodology, Software, Writing–original draft. ZJ: Investigation, Methodology, Validation, Writing–original draft, Writing–review and editing, Data curation.

Funding

The author(s) declare that financial support was received for the research, authorship, and/or publication of this article. This work was supported by the Science and Technology Project of State Grid Sichuan Electric Power Company (B7194723R001).

Conflict of interest

Authors WF, BD, TC, ZiZ, YF, YZ, and LZ were employed by State Grid Sichuan Information & Telecommunication Company.

The remaining authors declare that the research was conducted in the absence of any commercial or financial relationships that could be construed as a potential conflict of interest.

The authors declare that this study received funding from State Grid Sichuan Electric Power Company. The funder had the following involvement in the study: study design, data collection and analysis.

Publisher's note

All claims expressed in this article are solely those of the authors and do not necessarily represent those of their affiliated organizations, or those of the publisher, the editors and the reviewers. Any product that may be evaluated in this article, or claim that may be made by its manufacturer, is not guaranteed or endorsed by the publisher.

References

Ausgrid 2014 (2015). Solar home electricity data [DB/OL]. Available at: https://www.ausgrid.com.au/-/media/Documents/Reports-andResearch/Solar-Home-Electricity-Data/20112012-Solar-homeelectricity-data-v2.

Cao, D., Hu, W. H., Zhao, J. B., Huang, Q., Chen, Z., and Blaabjerg, F. (2020b). A multi-agent deep reinforcement learning based voltage regulation using coordinated PV inverters. *IEEE Trans. Power Syst.* 35 (5), 4120–4123. doi:10.1109/tpwrs.2020.3000652

Cao, D., Hu, W. H., Zhao, J. B., Zhang, G. Z., Zhang, B., Liu, Z., et al. (2020a). Reinforcement learning and its applications in modern power and energy systems: a review. *J. Mod. Power Syst. and Clean Energy* 8 (6), 1029–1042. doi:10.35833/mpce.2020.000552

Cao, X., Dong, S., Wu, Z., and Jing, Y. (2015). "A data-driven hybrid optimization model for short-term residential load forecasting, in "*Proceeding IEEE international conference on computer and information Technology; ubiquitous computing and communications; dependable, autonomic and secure computing; pervasive intelligence and computing*, Liverpool, UK, October 26-28, 2015 (IEEE), 283–287.

Dhawale, P. G., Kamboj, V. K., Bath, S. K., Raboaca, M. S., and Filote, C. (2024). Integrating renewable energy and plug-in electric vehicles into security constrained unit commitment for hybrid power systems. *Energy Rep.* 11, 2035–2048. doi:10.1016/j.egyr.2024.01.027

Feng, C., Sun, M., and Zhang, J. (2020). Reinforced deterministic and probabilistic load forecasting via Q -learning dynamic model selection. *IEEE Trans. Smart Grid* 11 (2), 1377–1386. doi:10.1109/tsg.2019.2937338

Gao, X. Y., Wang, Y., Gao, Y., Sun, C. Z., Xiang, W., and Yue, Y. M. (2018). Short-term load forecasting model of GRU network based on deep learning framework. *2018 2nd IEEE Conf. Energy Internet and Energy Syst. Integration* EI2, 1–4. doi:10.1109/EI2.2018.8582419

He, Y., Xu, Q., Wan, J., and Yang, S. (2016). Short-term power load probability density forecasting based on quantile regression neural network and triangle kernel function. *Energy* 114, 498–512. doi:10.1016/j.energy.2016.08.023

Hong, T., and Shu, F. (2016). Probabilistic electric load forecasting: a tutorial review. *Int. J. Forecast.* 32 (3), 914–938. doi:10.1016/j.ijforecast.2015.11.011

Hu, J. X., Hu, W. H., Cao, D., Sun, X. W., Chen, J. J., Huang, Y. H., et al. (2024). Probabilistic net load forecasting based on transformer network and Gaussian process-enabled residual modeling learning method. *Renew. Energy* 225, 120253. doi:10.1016/j.renene.2024.120253

Kaur, A., Nonnenmacher, L., and Coimbra, C. F. (2016). Net load forecasting for high renewable energy penetration grids. *Energy* 114, 1073–1084. doi:10.1016/j.energy.2016.08.067

Kong, W. C., Dong, Z. Y., Jia, Y., Hill, D. J., Xu, Y., and Zhang, Y. (2017). Short-term residential load forecasting based on LSTM recurrent neural network. *IEEE Trans. Smart Grid* 10 (1), 841–851. doi:10.1109/tsg.2017.2753802

Li, S. Y., Ma, H. Y., Zhang, Y. D., Wang, S., Guo, R., He, W., et al. (2023). Emergency evacuation risk assessment method for educational buildings based on improved extreme learning machine. *Reliab. Eng. Syst. Saf.* 238, 109454. doi:10.1016/j.ress.2023.109454

Liu, J., Dong, C., Liu, G. Y., and Yu, J. L. (2014) "Short-term net feeder load forecasting of microgrid considering weather conditions," in *2014 IEEE international energy conference (ENERGYCON)*, 1205–1209.

Prasad, R. K., Sarmah, R., Chakraborty, S., and Sarmah, S. (2023). NNVDC: a new versatile density-based clustering method using k-Nearest Neighbors. *Expert Syst. Appl.* 227, 120250. doi:10.1016/j.eswa.2023.120250

Ratnam, E. L., Weller, S. R., Kellett, C. M., and Murray, A. T. (2017). Residential load and rooftop PV generation: an Australian distribution network dataset. *Sustain. Energy* 36 (8), 787–806. doi:10.1080/14786451.2015.1100196

Saber, A. Y., and Alam, A. K. M. R. (2017). "Short term load forecasting using multiple linear regression for big data," in *2017 IEEE symposium series on computational intelligence (SSCI)*, 1–6.

Sepasi, S., Reihani, E., Howlader, A. M., Roose, L. R., and Matsuura, M. M. (2017). Very short term load forecasting of a distribution system with high PV penetration. *Renew. Energy* 106, 142–148. doi:10.1016/j.renene.2017.01.019

Sun, M., Zhang, T., Wang, Y., Strbac, G., and Kang, C. (2020). Using Bayesian deep learning to capture uncertainty for residential net load forecasting. *IEEE Trans. Power Syst.* 35 (1), 188–201. doi:10.1109/tpwrs.2019.2924294

Taieb, S. B., Huser, R., Hyndman, R. J., and Genton, M. G. (2016). Forecasting uncertainty in electricity smart meter data by boosting additive quantile regression. *IEEE Trans. Smart Grid* 7 (5), 2448–2455. doi:10.1109/tsg.2016.2527820

Tan, M., Yuan, S., Li, S., Su, Y., Li, H., and He, F. (2020). Ultra-short-term industrial power demand forecasting using LSTM based hybrid ensemble learning. *IEEE Trans. Power Syst.* 35 (4), 2937–2948. doi:10.1109/tpwrs.2019.2963109

Wang, Y., Zhang, N., Chen, Q., Kirschen, D. S., Li, P., and Xia, Q. (2018). Data driven probabilistic net load forecasting with high penetration of behind the-meter PV. *IEEE Trans. Power Syst.* 33 (3), 3255–3264. doi:10.1109/tpwrs.2017.2762599

Wang, Y., Zhang, N., Tan, Y., Hong, T., Kirschen, D. S., and Kang, C. (2019). Combining probabilistic load forecasts. *IEEE Trans. Smart Grid* 10 (4), 3664–3674. doi:10.1109/tsg.2018.2833869

Xie, J. R., and Hong, T. (2018). Temperature scenario generation for probabilistic load forecasting. *IEEE Trans. Smart Grid* 9 (3), 1–1687. doi:10.1109/tsg.2016.2597178

Xiong, L. S., Liu, X. K., Zhang, D. H., and Liu, Y. H. (2021). Rapid power compensation-based frequency response strategy for low-inertia power systems. *IEEE J. Emerg. and Sel. Top. Power Electron.* 9 (4), 4500–4513. doi:10.1109/jestpe.2020.3032063

Xu, F., Cun, X., Yan, M., Yuan, H., Wang, Y., and Lai, L. (2018). Power market load forecasting on neural network with beneficial correlated regularization. *IEEE Trans. Industrial Inf.* 14 (11), 5050–5059. doi:10.1109/tii.2017.2789297

Zhang, W., Quan, H., and Srinivasan, D. (2019). An improved quantile regression neural network for probabilistic load forecasting. *IEEE Trans. Smart Grid* 10 (4), 4425–4434. doi:10.1109/tsg.2018.2859749

Zhao, P. F., Cao, D., Hu, W. H., Huang, Y. H., Hao, M., Chen, Z., et al. (2023). Geometric loss-enabled complex neural network for multi-energy load forecasting in integrated energy systems. *IEEE Trans. Power Syst.*, 1–13. doi:10.1109/tpwrs.2023.3345328

Zhao, P. F., Hu, W. H., Cao, D., Zhang, Z. Y., Huang, Y. H., Dai, L. C., et al. (2024). Probabilistic multienergy load forecasting based on hybrid attention-enabled transformer network and Gaussian process-aided residual learning. *IEEE Trans. Industrial Inf.* 20, 8379–8393. doi:10.1109/tii.2024.3366946

Zhu, X. X., Xue, J. F., Hu, M., Liu, Z. T., Gao, X. X., and Huang, W. J. (2023). Low-carbon economy dispatching of integrated energy system with P2G-HGT coupling wind power absorption based on stepped Carbon emission trading. *Energy Rep.* 10, 1753–1764. doi:10.1016/j.egyr.2023.08.023

Zulfiqar, M., Kamran, M., Rasheed, M. B., Alquthami, T., and Milyani, A. H. (2023). A hybrid framework for short term load forecasting with a navel feature engineering and adaptive grasshopper optimization in smart grid. *Appl. Energy* 338, 120829. doi:10.1016/j.apenergy.2023.120829

frontiers | Frontiers in Energy Research

TYPE Original Research
PUBLISHED 06 November 2024
DOI 10.3389/fenrg.2024.1423199

OPEN ACCESS

EDITED BY
Haitao Zhang,
Xi'an Jiaotong University, China

REVIEWED BY
Chunyang Liu,
Shandong University, China
Jiaxing Lei,
Southeast University, China
Shenquan Liu,
South China University of Technology, China

*CORRESPONDENCE
Shaoyan Jiang,
jiangshaoyan_csg@163.com

RECEIVED 25 April 2024
ACCEPTED 25 June 2024
PUBLISHED 06 November 2024

CITATION
Jiang S, Du L, Li Y, Yang L and Luo B (2024), LCL APF control strategy based on model predictive control.
Front. Energy Res. 12:1423199.
doi: 10.3389/fenrg.2024.1423199

LCL APF control strategy based on model predictive control

Shaoyan Jiang*, Lifeng Du, Yongjian Li, Le Yang and Binbin Luo

Zhongshan Power Supply Bureau of Guangdong Power Grid Co., Ltd., Zhongshan, China

In order to further control harmonic current in distribution network, a LCL APF control strategy based on model predictive control is proposed. Firstly, APF mathematical model is established. Then, a multi-objective optimization model predictive control strategy (MPC) is proposed, which comprehensively considers the performance of AC side and DC side of APF. This strategy solves the delay problem existing in the existing MPC strategy: while improving the performance of APF, there is no need to set weight factor; Then, Kalman filter is used to predict the inverter current, thus simplifying the APF measurement system. Finally, the simulation results show that the proposed control strategy can simplify the measurement system and make APF have stronger harmonic suppression ability when it only participates in power conversion and better active filter performance when it participates in harmonic control.

KEYWORDS

LCL filter, active filter, finite set model predictive control, Kalman filtering, harmonic control

1 Introduction

With the continuous progress of power electronic technology, a large number of power electronic devices have been applied to the source, network, load and storage of power system, which not only improves the operation and control flexibility of power system, but also brings the problem of broadband harmonics of power grid (Shi et al., 2020). On the one hand, the power electronic device itself constitutes a harmonic source, and its internal power semiconductor switching action will bring considerable high-frequency harmonics; On the other hand, the mechanism of harmonic transmission and evolution is more complex due to the interaction between devices, which shows the characteristics of wide area and wide frequency (Xiong et al., 2021). The existence of harmonics will lead to the deterioration of power quality, accelerated aging of equipment, interference in measurement communication and other problems, which must be suppressed (Liu et al., 2023).

At the distribution network level, passive filters are commonly used to achieve harmonic control (Xie et al., 2013), but passive filters are usually configured in band-stop mode and have limited frequency bands, which is difficult to meet the challenge of harmonic broadband. The active power filter (APF) based on power electronics technology has the characteristics of flexible operation control and can realize the tracking and compensation of dynamic harmonics, and the filter bandwidth is high, which has attracted much attention in recent years (Xiong et al., 2020). However, due to the high cost of APF, it has not been widely promoted and applied. At the hardware level, the circuit structure of APF is a three-phase voltage source rectifier/inverter, which is the same as the grid-connected converter structure in other devices such as new energy units and electric vehicle charging facilities. Therefore, in recent years, many scholars have proposed to use three-phase grid-connected inverters as active filters (APF) to participate in harmonic

governance (L. Yang et al., 2020). However, there is still room for improvement in performance: 1) Absorb harmonic current in distribution network as much as possible; 2) At the same time, ensure that no new harmonic current is introduced. The high performance APF control strategy needs to be further studied.

However, because the grid-connected converter is designed to realize the power conversion of the frequency segment, the control structure and strategy used are difficult to meet the functional requirements of APF (Xiong et al., 2016). The double closed-loop linear control strategy usually adopted by grid-connected converters has limited bandwidth, and the current control bandwidth is generally set at 300 Hz, which makes it difficult to track and adjust the current harmonics of higher frequencies (Cheng et al., 2017). Therefore, nonlinear control strategies such as repetitive control, sliding mode control and model predictive control with faster dynamic response and stronger tracking performance are more suitable. The repetitive control that accumulates the error to the output signal period by period has good steady-state performance, but the embedded delay link causes the output current to lag the reference value by one power frequency cycle (Liang et al., 2018). Although the addition of proportional integration can effectively improve the dynamic performance of repetitive control, the complex compensation function makes it difficult to implement in engineering applications (Zhang et al., 2014). The sliding mode control with error switching function as the core has a large current control bandwidth, which can ensure that the electrical volume in APF converges to the balance point error determined by the output current reference value (Guo et al., 2022). However, because the system will jitter near the preset sliding mode state, additional output current will be chattered, which will affect the control accuracy and stability of the system and increase the energy loss (Li and Hong, 2012). Finite set Model Predictive Control (MPC) is good at solving nonlinear control problems by selecting the optimal switching state through traversal algorithm. With the progress of computing power of embedded control chip, it effectively compensates for the defect of large calculation amount of MPC, so it has been applied more and more in power electronic device control (Falkowski and Sikorski, 2018; Zhang et al., 2023). For grid-connected converters, in order to overcome the problem that MPC method cannot directly control the current on the grid side of LCL filter (Zhang et al., 2022), the traditional MPC strategy introduces damping ratio to calculate the corresponding current reference value on the inverter side, but the control effect of the current on the grid side is poor (Chico-Villegas et al., 2023). In recent years, two new MPC strategies have emerged: 1) The optimal switching combination3 (PCi1i2uc) is selected by predicting the current on the grid side, the current on the inverter side and the filter capacitance voltage at the next time according to the equation of state of LCL-type APF (Falkowski and Sikorski, 2018). 2) On this basis, the state equation is used to predict two steps, and then the optimal switch combination is selected. Longer prediction steps can obtain higher control accuracy, but correspondingly the calculation steps are more complicated and the calculation amount is larger (PCi1i2uc-2steps) (Falkowski and Sikorski, 2018). The above two have defects: 1) In the process of deriving the current reference value of the inverter side and the capacitor voltage reference value from the current reference value of the grid side, the delay problem under the discrete control system is ignored, resulting in the deterioration of the control performance of the current on the grid side; 2) In order to make up for this defect, two more items are added to the value function for correction, thus introducing weight factors that need to be artificially set. The selection of factors has a great impact on APF performance, but it can only rely on experience value, which is not reliable; 3) The premise of using the equation of state is to measure all variables involved in the equation, resulting in a complex measurement system.

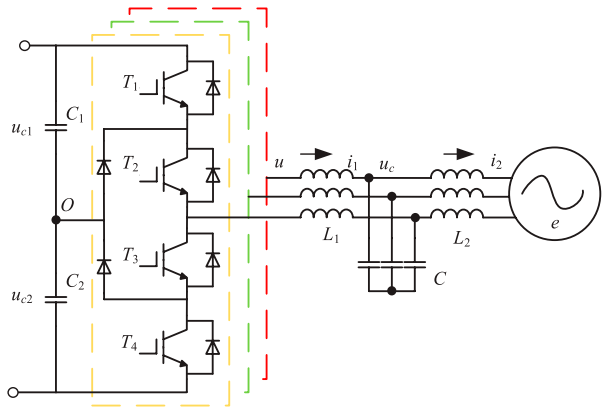

FIGURE 1
Topology of three-level LCL inverter.

Faced with the complex measurement system of APF, some scholars use extended state observer to reduce the impact of measurement errors (Zheng et al., 2023), or adopt periodic model parameter adjustment strategy to correct device parameter errors (Xie et al., 2021), but it is still necessary to sample up to 11 electrical volumes. The Kalman filter can reduce the measurement sensor and reduce the hardware cost while ensuring the measurement accuracy. At present, this method has been applied to the control of modular multilevel converters (Pizarro et al., 2023). This method can be applied to APF control for reference.

To solve these problems, this paper proposes a LCL APF control strategy based on model predictive control.By analyzing the LCL-type APF mathematical model, the multi-objective optimization model predictive control strategy considering the time delay problem of discrete systems is established. The Kalman filter is used to predict the APF inverter current, thus simplifying the measurement system.

2 APF mathematical model

2.1 Analytic relationship on the AC side

Figure 1 shows the main circuit topology of APF. APF connects capacitors C_1 and C_2 with voltages u_{C1} and u_{C2} respectively in series to provide DC voltage V_{DC} with O as the neutral point on the DC side. The LCL filter composed of inductor L_1 on the inverter side, filter capacitor C and inductor L_2 on the grid side is connected to the system containing power supply, line and load.

After the Parker transformation, u_d, u_q is the direct axis component of the inverter voltage. i_{1d}, i_{1q} are the direct axis and

quadrature axis components of the inverter side current. i_{2d} and i_{2q} are the direct axis components of the current on the network side. u_{cd} and u_{cq} are the direct axis and cross-axis components of the filter capacitor voltage. e_d, e_q are the direct axis quadrature axis components of APF network side voltage; The positive direction of the signal is shown by the arrow in the figure. According to Kirchhoff's law, the electric volume on the AC side has the following relationship in the dq rotating coordinate system:

$$\frac{d}{dt}\boldsymbol{i}_1+\begin{pmatrix}0&-\omega\\ \omega&0\end{pmatrix}\boldsymbol{i}_1=\frac{1}{L_1}\boldsymbol{u}-\frac{1}{L_1}\boldsymbol{u}_c \tag{1}$$

$$\frac{d}{dt}\boldsymbol{u}_c+\begin{pmatrix}0&-\omega\\ \omega&0\end{pmatrix}\boldsymbol{u}_c=\frac{1}{C}\boldsymbol{i}_1-\frac{1}{C}\boldsymbol{i}_2 \tag{2}$$

$$\frac{d}{dt}\boldsymbol{i}_2+\begin{pmatrix}0&-\omega\\ \omega&0\end{pmatrix}\boldsymbol{i}_2=\frac{1}{L_2}\boldsymbol{u}_c-\frac{1}{L_2}\boldsymbol{e} \tag{3}$$

where, ω is the angular velocity corresponding to the system frequency, $\mathbf{i}_1=[i_{1d}\ i_{1q}]^{\mathrm{T}}$, $\mathbf{i}_2=[i_{2d}\ i_{2q}]^{\mathrm{T}}$, $\mathbf{u}_c=[u_{cd}\ u_{cq}]^{\mathrm{T}}$, $\mathbf{u}=[u_d\ u_q]^{\mathrm{T}}$, $\mathbf{e}=[e_d\ e_q]^{\mathrm{T}}$, respectively, are the direct axis component and the quadrative axis component of the corresponding electrical volume. In order to discretize Equations 1–3, the forward difference method is used for any electrical quantity x as shown in Equation 4.

$$\frac{dx}{dt}=\frac{1}{T_s}\left(x(k+1)-x(k)\right) \tag{4}$$

where, T_s is the period corresponding to the switching frequency. The spatial state equation of APF under the dq coordinate axis after discretization is shown in Equations 5–9.

$$\boldsymbol{x}(k+1)=\boldsymbol{A}\boldsymbol{x}(k)+\boldsymbol{B}\boldsymbol{v}(k) \tag{5}$$

$$\boldsymbol{A}=\begin{pmatrix}1&\omega T_s&-\frac{T_s}{L_1}&0&0&0\\ -\omega T_s&1&0&-\frac{T_s}{L_1}&0&0\\ \frac{T_s}{C}&0&1&\omega T_s&-\frac{T_s}{C}&0\\ 0&\frac{T_s}{C}&-\omega T_s&1&0&-\frac{T_s}{C}\\ 0&0&\frac{T_s}{L_2}&0&1&\omega T_s\\ 0&0&0&\frac{T_s}{L_2}&-\omega T_s&1\end{pmatrix} \tag{6}$$

$$\boldsymbol{B}=\begin{pmatrix}\frac{T_s}{L_1}&0&0&0\\ 0&\frac{T_s}{L_1}&0&0\\ 0&0&0&0\\ 0&0&0&0\\ 0&0&-\frac{T_s}{L_2}&0\\ 0&0&0&-\frac{T_s}{L_2}\end{pmatrix} \tag{7}$$

$$\boldsymbol{x}(k)=\left(\boldsymbol{i}_1(k)^{\mathrm{T}}\ \ \boldsymbol{u}_c(k)^{\mathrm{T}}\ \ \boldsymbol{i}_2(k)^{\mathrm{T}}\right)^{\mathrm{T}} \tag{8}$$

$$\boldsymbol{v}(k)=\left(\boldsymbol{u}(k)^{\mathrm{T}}\ \ \boldsymbol{e}(k)^{\mathrm{T}}\right)^{\mathrm{T}} \tag{9}$$

The formula shows that at the time k+1, the state variable x (k+1), which consists of the inverter side current, filter capacitor voltage and network side current, is determined by the state variable $x(k)$ at the time k, the input state $u(k)$ and the interference quantity $e(k)$. Where **A** is the state matrix and **B** is the input matrix.

2.2 Analytic relationship on the DC side

APF adopts the neutral point clamp (NPC) topology that can output three levels. The output voltage of any phase can be described by the switching state function S_x (x = a, b, c) as shown in Equation 10. Take phase A as an example: when S_a = 1, switch tubes T_1 and T_2 are on, T_3 and T_4 are off, $u_a=V_{DC}/2$; when S_a = 0, T_2 and T_3 are on, T_1 and T_4 are off, u_a = 0. When S_a = −1, T_3 and T_4 are on, T_1 and T_2 are off, and $u_a=-V_{DC}/2$.

$$\underset{x\in\{a,b,c\}}{S_x}=\begin{cases}1\\ 0\\ -1\end{cases} \tag{10}$$

As shown in Table 1, considering ABC three-phase, there are 27 kinds of switch combinations in APF, constituting 19 kinds of vector states.

Among them, V_1 ~ V_6 are large vectors, V_7 ~ V_{12} are medium vectors, and each vector only corresponds to one type of switch combination. V_{13} ~ V_{18} are small vectors, and each small vector has positive and negative switching combinations, respectively called positive small vector and negative small vector. The zero vector V_{18} corresponds to three switching states. In order to avoid a series of problems such as damage to the switching device due to excessive pressure, it is necessary to maintain the neutral point balance, that is, the upper and lower capacitor voltage difference $\Delta u_o=u_{C1}$-u_{C2} on the DC side is about 0. The direction and magnitude of the neutral current can be controlled by adjusting the action time of the positive and negative small vectors with redundant relationship, so as to achieve the upper and lower capacitor voltage balance on the DC side (Liu et al., 2018) as shown in Equations 11, 12.

$$i_o(k+1)=-\sum_{x\in\{a,b,c\}}|S_x(k+1)|i_{2x}(k+1) \tag{11}$$

$$\Delta u_o(k+2)=u_{C1}(k+1)-u_{C2}(k+1)+i_o(k+1)T_s/C \tag{12}$$

3 Model predictive control strategy considering multi-objective optimization

The MPC algorithm can control multiple variables at the same time only through a single value function, and the proposed strategy is realized: on the AC side, the control i_2 outputs according to the given current command value i_2*; on the DC side, the maintenance Δu_o is about 0.

By type (5)–(8), u (k + 1) only can directly control i_1 (k + 2), and indirectly affect the u_c (k + 3) and i_2 (k + 4). To track the output of i_2*, i_2* can be used to calculate the current reference value i_1* on the inverter side, and then select the optimal switch combination u (k + 1). In the case of discrete system control delay, the calculation process is as follows:

TABLE 1 Three-level APF vector table.

Space vector	Switching state (S_A, S_B, S_C)	Vector definition
V_1	(1,0,−1)	$(V_{DC}/\sqrt{3})e^{j\pi/6}$
V_2	(0,1,−1)	$(V_{DC}/\sqrt{3})e^{j\pi/2}$
V_3	(−1,1,0)	$(V_{DC}/\sqrt{3})e^{j5\pi/6}$
V_4	(−1,0,1)	$(V_{DC}/\sqrt{3})e^{j7\pi/6}$
V_5	(0,−1,1)	$(V_{DC}/\sqrt{3})e^{j3\pi/2}$
V_6	(1,−1,0)	$(V_{DC}/\sqrt{3})e^{j11\pi/6}$
V_7	(1,−1,−1)	$2V_{DC}/\sqrt{3}$
V_8	(1,1,−1)	$(2V_{DC}/\sqrt{3})e^{j\pi/3}$
V_9	(−1,1,−1)	$(2V_{DC}/\sqrt{3})e^{j2\pi/3}$
V_{10}	(−1,1,1)	$(2V_{DC}/\sqrt{3})e^{j\pi}$
V_{11}	(−1,−1,1)	$(2V_{DC}/\sqrt{3})e^{j4\pi/3}$
V_{12}	(1,−1,1)	$(2V_{DC}/\sqrt{3})e^{j5\pi/3}$
V_{13}	(1,0,0)、(0,-1,-1)	$V_{DC}/3$
V_{14}	(1,1,0)、(0,0,-1)	$(V_{DC}/3)e^{j\pi/3}$
V_{15}	(0,1,0)、(-1,0,-1)	$(V_{DC}/3)e^{j2\pi/3}$
V_{16}	(0,1,1)、(-1,0,0)	$(V_{DC}/3)e^{j\pi}$
V_{17}	(0,0,1)、(-1,-1,0)	$(V_{DC}/3)e^{j4\pi/3}$
V_{18}	(1,0,1)、(0,-1,0)	$(V_{DC}/3)e^{j5\pi/3}$
V_{19}	(1,1,1)、(0,0,0)、(-1,-1,-1)	0

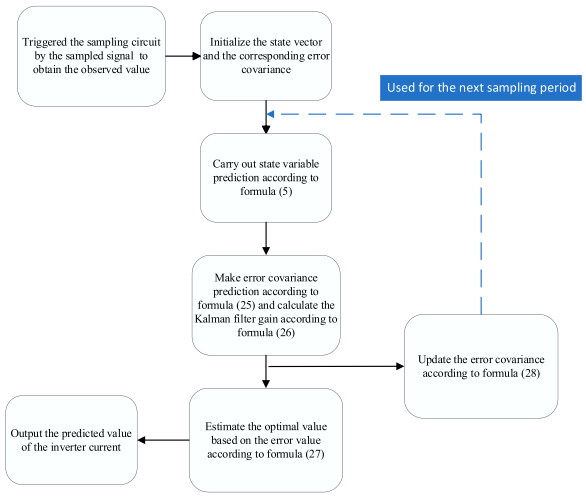

FIGURE 2
Kalman filter calculation flow.

1) The reference values also follow the mathematical relationship of Equations 5–8, and the Equations 13, 14 can be obtained by a certain transformation, and the reference value of the filter capacitor voltage $u_c^*(k+3)$ at $k+3$ can be calculated. Considering that the grid voltage changes slowly on the time scale of the switching frequency, if T_S is small enough, the sampling value $e(k)$ at the current time k can replace the sampling value $e(k+3)$ at the future time. Similarly, $u_c^*(k+2)$ can be calculated according to Equations 15, 16. Then, based on $u_c^*(k+3)$ and $u_c^*(k+2)$, the reference value $i_1^*(k+1)$ of the inverter current at $k+1$ is calculated according to Equations 17, 18, which is also obtained by the transformation of Equations 5–8.

$$u_{cd}^*(k+3) = \frac{L_2}{T_s}\left(i_{2d}^*(k+4) - i_{2d}^*(k+3) - \omega T_s i_{2q}^*(k+3)\right) + e_d(k+3) \tag{13}$$

$$u_{cq}^*(k+3) = \frac{L_2}{T_s}\left(i_{2q}^*(k+4) - i_{2q}^*(k+3) + \omega T_s i_{2d}^*(k+3)\right) + e_q(k+3) \tag{14}$$

$$u_{cd}^*(k+2) = \frac{L_2}{T_s}\left(i_{2d}^*(k+3) - i_{2d}^*(k+2) - \omega T_s i_{2q}^*(k+2)\right) + e_d(k+2) \tag{15}$$

$$u_{cq}^*(k+2) = \frac{L_2}{T_s}\left(i_{2q}^*(k+3) - i_{2q}^*(k+2) + \omega T_s i_{2d}^*(k+2)\right) + e_q(k+2) \tag{16}$$

$$i_{1d}^*(k+2) = \frac{C}{T_s}\left(u_{cd}^*(k+3) - u_{cd}^*(k+2) - \omega T_s u_{cq}^*(k+2)\right) + i_{2d}^*(k+2) \tag{17}$$

$$i_{1q}^*(k+2) = \frac{C}{T_s}\left(u_{cq}^*(k+3) - u_{cq}^*(k+2) + \omega T_s u_{cd}^*(k+2)\right) + i_{2q}^*(k+2) \tag{18}$$

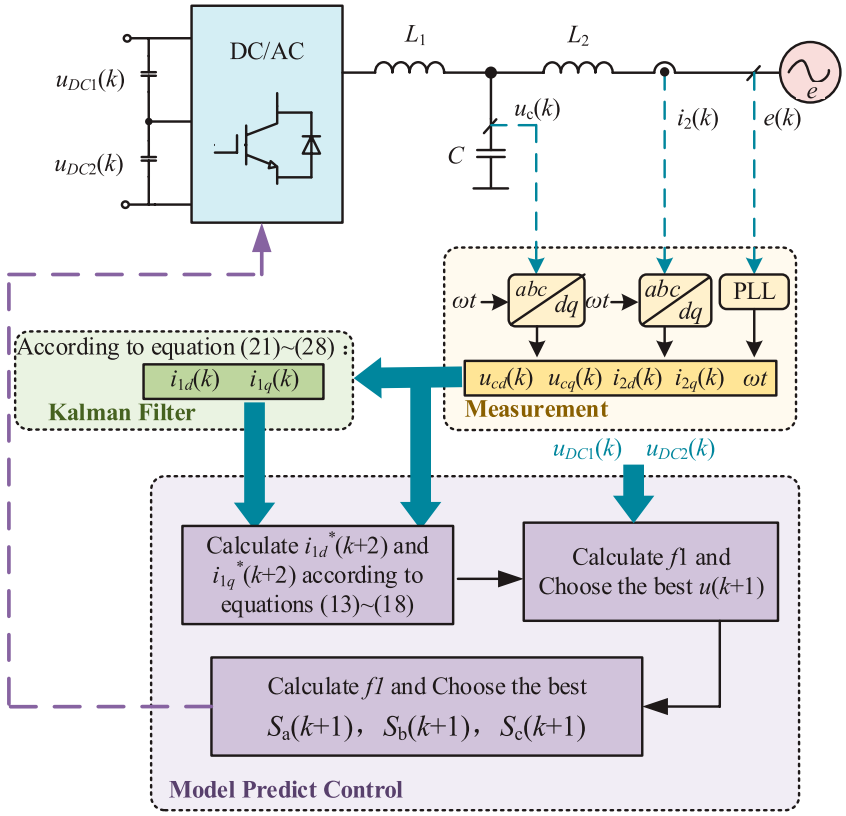

FIGURE 3
Schematic diagram of control strategy.

TABLE 2 Device parameters and control parameters.

Parameter	Symbol	Value	unit
Inverter inductance	L_1	1.8	mH
Net side inductance	L_2	0.6	mH
Filter capacitor	C	5	uF
DC side voltage	V_{DC}	800	V
DC capacitance	$C_1(C_2)$	4.7	mF
Sample frequency	f_s	100	kHz
Policy 2 to 3 Weight 1	ω_1^2	400	—
Policy 2 to 3 Weight 2	ω_2^2	0.5	—
Strategy 1 damping coefficient	Ad	0.6	—
System frequency (angular velocity)	ω	100π	rad/s

2) Based on u $(k + 1)$, the corresponding i_1 $(k + 2)$ can be predicted. The value function f_1, which represents the future error of i_1, is calculated according to Equation 19.

$$f_1 = \left(i_{1d}^{ref}(k+2) - i_{1d}(k+2)\right)^2 + \left(i_{1q}^{ref}(k+2) - i_{1q}(k+2)\right)^2 \quad (19)$$

Go through 19 vector states and select the u $(k+1)$ that minimizes f_1. Equations 13–18 shows that when the switch combination makes f_1 the lowest, the difference between the actual output network current and i_2* can be minimized, and the resonance can be suppressed.

3) If u $(k + 1)$ belongs to large vector or medium vector, corresponding switch combinations $S_a(k + 1)$, $S_b(k + 1)$, $S_c(k + 1)$ can be obtained directly. If u $(k + 1)$ belongs to the zero vector, set $S_a(k + 1) = 0$, $S_b(k + 1) = 0$, $S_c(k + 1) = 0$. If u $(k + 1)$ is a small vector, the value function $f2$ that characterizes the future size of Δuo is calculated according to Equation 20.

$$f_2 = |\Delta u_o(k+2)| \quad (20)$$

Select S_a $(k + 1)$, $S_b(k + 1)$, $S_c(k + 1)$ from the positive and negative small vectors that make f_2 take a smaller value.

4) Continue to cycle steps 1)~3), so that i_2 follows the output of i_2*, and maintains Δu_o in a small range.

4 Inverter side current prediction method based on Kalman filter

According to the electric quantity relationship of AC side in Equations 5–8, the current value of inverter side can be derived by using the current of grid side and the filter capacitor voltage. Therefore, the measurement system can be simplified to measure only i_2 and u_c to make real-time

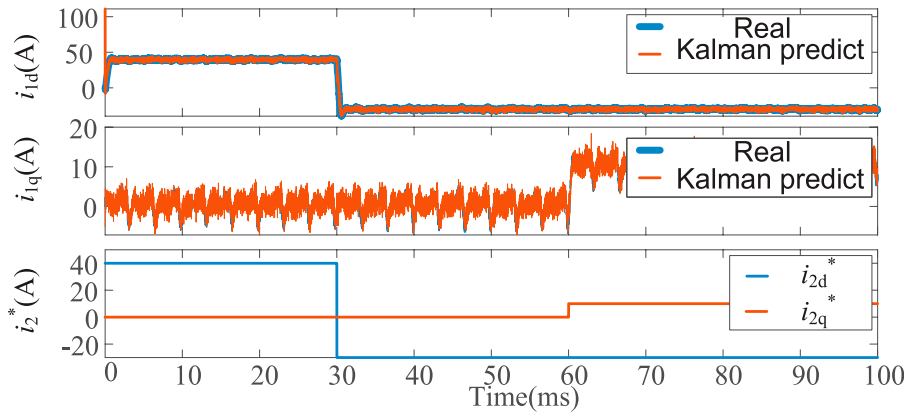

FIGURE 4
Prediction Error of i_1.

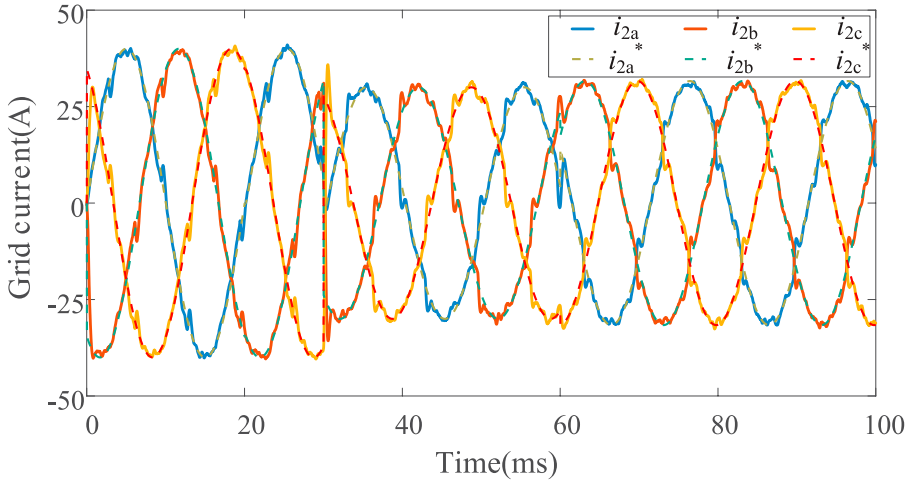

FIGURE 5
i_2* and i_2.

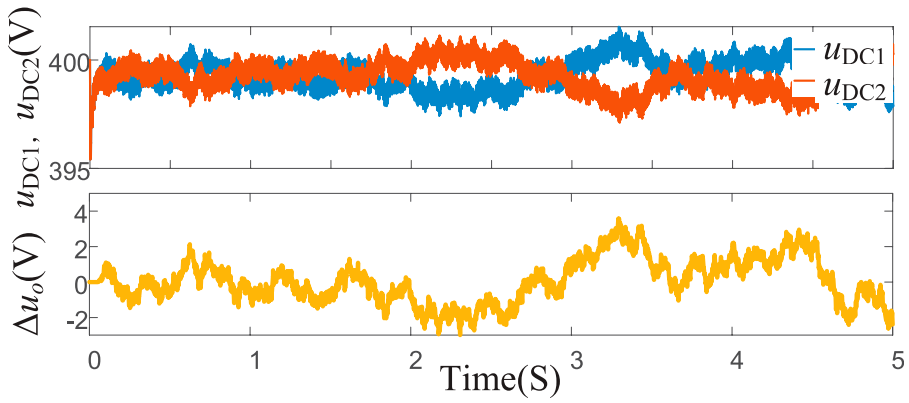

FIGURE 6
u_{DC1}、u_{DC2} and Δu_o.

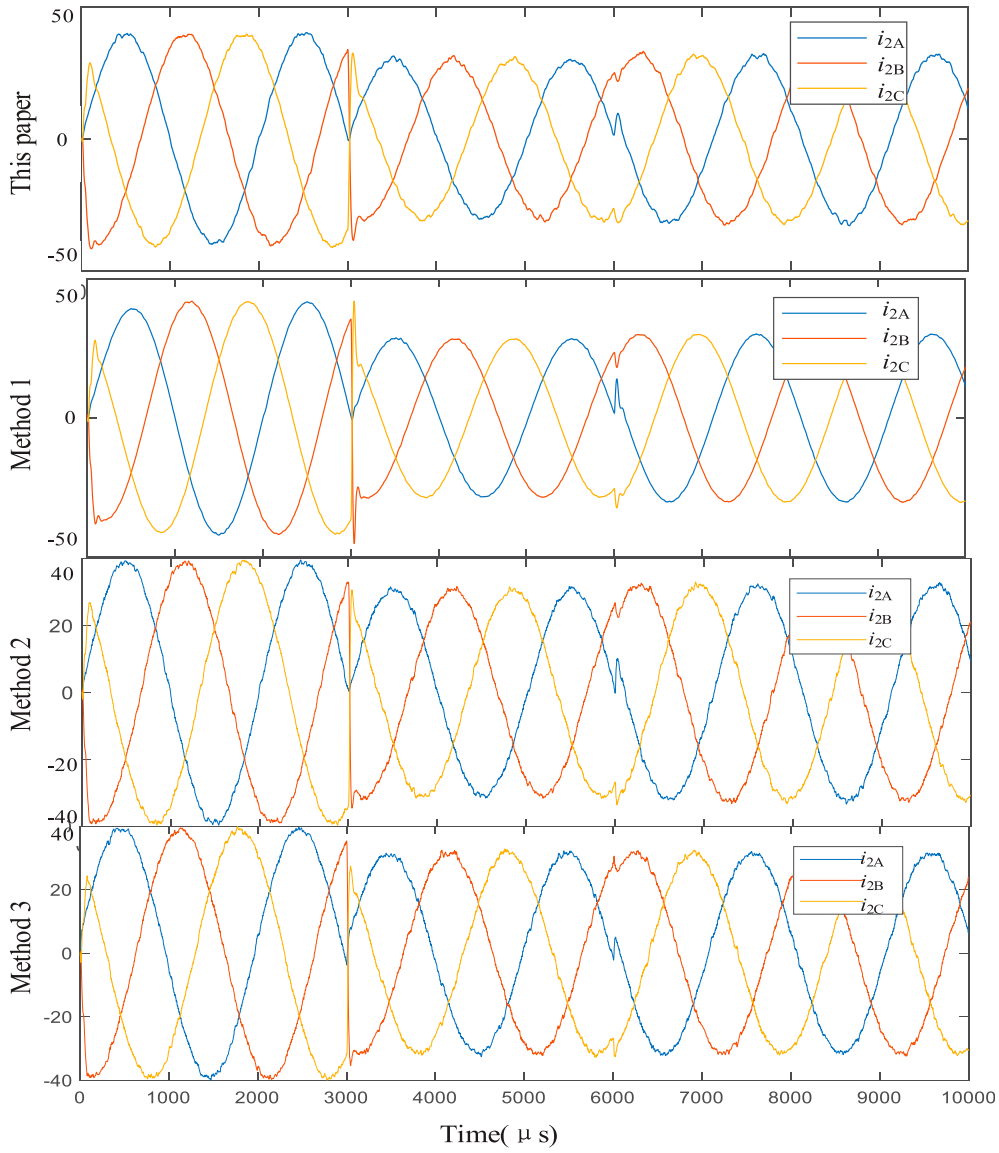

FIGURE 7
i_2 under four control strategies.

closed-loop prediction of i_1, eliminating part of the current sensor structure. Specifically, measurement i_2 and u_c constitute measurement matrix $z(k)$, as defined in Equations 22, 23. Real-time prediction of i_1 is performed based on Kalman filter state observer. As a closed-loop prediction scheme with strong adaptability to the system, Kalman filter algorithm can extract the estimator information from the measurement information to obtain the online estimate, which has a significant advantage in eliminating the impact of measurement noise caused by the sensor. The steps to build a Kalman filter state observer are as follows:

Firstly, the Kalman filter state observation equation is established on the basis of Equation 5:

$$\boldsymbol{x}^{-}(k) = \boldsymbol{A}\boldsymbol{x}(k-1) + \boldsymbol{B}\boldsymbol{v}(k-1) + \boldsymbol{R} \tag{21}$$

$$z(k) = \boldsymbol{H}\boldsymbol{x}(k) + \boldsymbol{Q} \tag{22}$$

$$z(k) = \left(\boldsymbol{u}_c(k)^{\mathrm{T}} \;\; \boldsymbol{i}_2(k)^{\mathrm{T}}\right)^{\mathrm{T}} \tag{23}$$

where, $z(k)$ is the output matrix of the state observer at k time; **H** is the observation matrix; **R** is the state noise variance matrix, and **Q** is the measurement noise variance matrix. A prior estimate x-(k) of the state variable can be calculated by Equation 21. According to Equations 24–28, the error between x-(k) and the actual value $x(k)$ is defined as the prior error e-(k), and the covariance of e-(k) is the prior error matrix P-(k). In the actual calculation, e-(k) is unknown, so the posterior error matrix $P(k)$ at k-1 time is needed to calculate.

$$\boldsymbol{e}^{-}(k) = \boldsymbol{x}(k) - \boldsymbol{x}^{-}(k) \tag{24}$$

$$\boldsymbol{P}^{-}(k) = \mathrm{E}\left[\boldsymbol{e}^{-}(k)\boldsymbol{e}^{-}(k)^{T}\right] = \boldsymbol{A}\boldsymbol{P}(k-1)\boldsymbol{A}^{\mathrm{T}} + \boldsymbol{Q} \tag{25}$$

Then, combining **H** and P-(k), the Kalman filter gain matrix **K**(k) is obtained.

$$\boldsymbol{K}(k) = \boldsymbol{P}^{-}(k)\boldsymbol{H}^{T}\left(\boldsymbol{H}\boldsymbol{P}^{-}(k)\boldsymbol{H}^{T} + \boldsymbol{R}\right)^{-1} \tag{26}$$

Based on $\mathbf{K}(k)$ and observation matrix $z(k)$, the posterior estimator $x^{kal}(k)$ can be obtained by modifying x-(k).

$$\boldsymbol{x}^{kal}(k) = \boldsymbol{x}^{-}(k) + \boldsymbol{K}(k)(\boldsymbol{z}(k) - \boldsymbol{H}\boldsymbol{x}^{-}(k)) \quad (27)$$

In order to continuously update the covariance p-(k) of the prior estimate, a posterior error matrix is calculated after modifying the state variable:

$$\boldsymbol{P}(k) = (\boldsymbol{I} - \boldsymbol{K}(k)\boldsymbol{H})\boldsymbol{P}^{-}(k) \quad (28)$$

Where $\mathbf{I}$ is the identity matrix.

The specific operation flow chart of Kalman filtering is shown in Figure 2:

To sum up, the overall control strategy of the strategy proposed in this paper is shown in Figure 3:

(1) Input u_c and i_2 sampling values to Kalman filter to obtain real-time closed-loop prediction value of i_1;
(2) The optimal switch combination is calculated based on model predictive control considering multiple objectives.

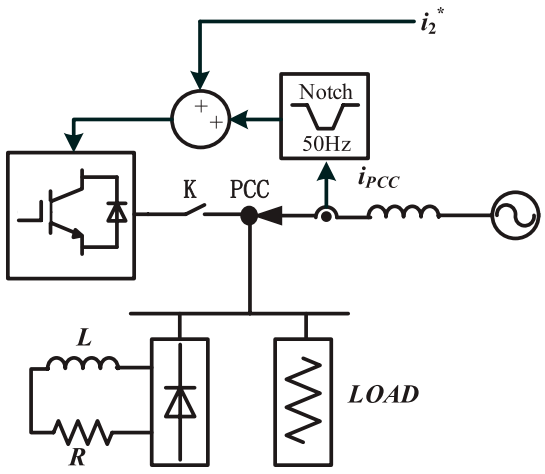

FIGURE 8
Active filter application scenario.

5 Simulation

5.1 Simulation parameter

Through modeling and simulation in Matlab/Simulink, it is verified that the proposed strategy can accurately predict the inverter current and effectively suppress the neutral voltage deviation. The active filtering performance of the proposed method is compared with the PC-iAD method in reference (Chico-Villegas et al., 2023), and the PC-$i_1i_2u_c$ and PC$i_1i_2u_c$-2steps in reference (Falkowski and Sikorski, 2018) (referred to as strategies 1, 2, and 3, respectively). Device parameters and control parameters are shown in Table 2. In particular, in order to simulate the voltage and current sensor errors in the actual device, the measurement errors of u_c, i_2 and e are set to ±0.5 V, ±0.5 V, and ±0.2A respectively in the simulation.

5.2 APF is only involved in electrical energy conversion

The basic function of APF is to participate in electric energy conversion and realize inverter or rectification. For this reason, the D-axis reference value of the current at the network side is set to 40A at the beginning, and the step changes to −30A after 0.03 s. The reference value of the q axis is initially 0A, and the step transition after 0.06 s is 10A. Comparing the control strategies proposed in this paper with strategies 1, 2, and 3, the control effects of the four control strategies only participate in electric energy conversion.

Firstly, it is verified that the proposed strategy can accurately predict the inverter current. As shown in Figure 4, when i_{2d}^* is constant and unchanged, the predicted value of Kalman filter is basically similar to the actual value for the D-axis component of the current on the inverter side, and the error is about ± 2A. After the mutation of i_{2d}^*, the error between the predicted value and the actual value can reach 10A, but the process only lasts tens of microseconds and ends. Similarly, for the Q-axis component of the current on the inverter side, the predicted value of Kalman filter is basically consistent with the actual value.

Converted back to the stationary three-phase coordinate system, the mean square error of the current prediction error on the inverter side of phase A, B and C is 0.93A, 0.92A, and 0.93A, respectively, and the error is all within 2%. Obviously, Kalman filter can accurately predict the inverter current. And as shown in Figure 5, the current on the network side can be accurately and quickly output following the reference value. Therefore, the inverter side current sensor can be omitted, thus simplifying the measurement system.

Secondly, it is verified that the proposed strategy can effectively inhibit Δu_o. As shown in Figure 6, although Δu_o fluctuates, it can always be maintained in the range of [−4V, 4V], and the deviation is only 1.5% of the capacitor voltage.

Finally, the output effect of APF side current is considered. As shown in Figure 7, the current waveforms of the four strategies at the network side are basically the same, and the total harmonic distortion (THD) of the four strategies within 80 ms–100 ms is also 1.26%, showing similar performance.

5.3 APF participates in harmonic control

The common application scenario is shown in Figure 8. The APF is connected to the connecting point (PCC) after the switch K, and is in parallel with the load containing nonlinear components. In this paper, the load inductor of the rectifier is 2 mH, and the load resistance of the rectifier is 5Ω. APF needs to cooperate with the distribution network to provide fundamental current for the load, so set i_{2d}^* to 30A and i_{2q}^* to 0A. At the same time, APF should actively filter out the harmonic current in the distribution network. To this end, additional sampling of the current i_{pcc} flowing from the distribution network into the PCC point is needed, and the harmonic component is obtained through the 50 Hz notch, which is added as the grid side current command, and the harmonic current similar to the rectifier is output, thus reducing THD (i_{pcc}) to achieve active filtering.

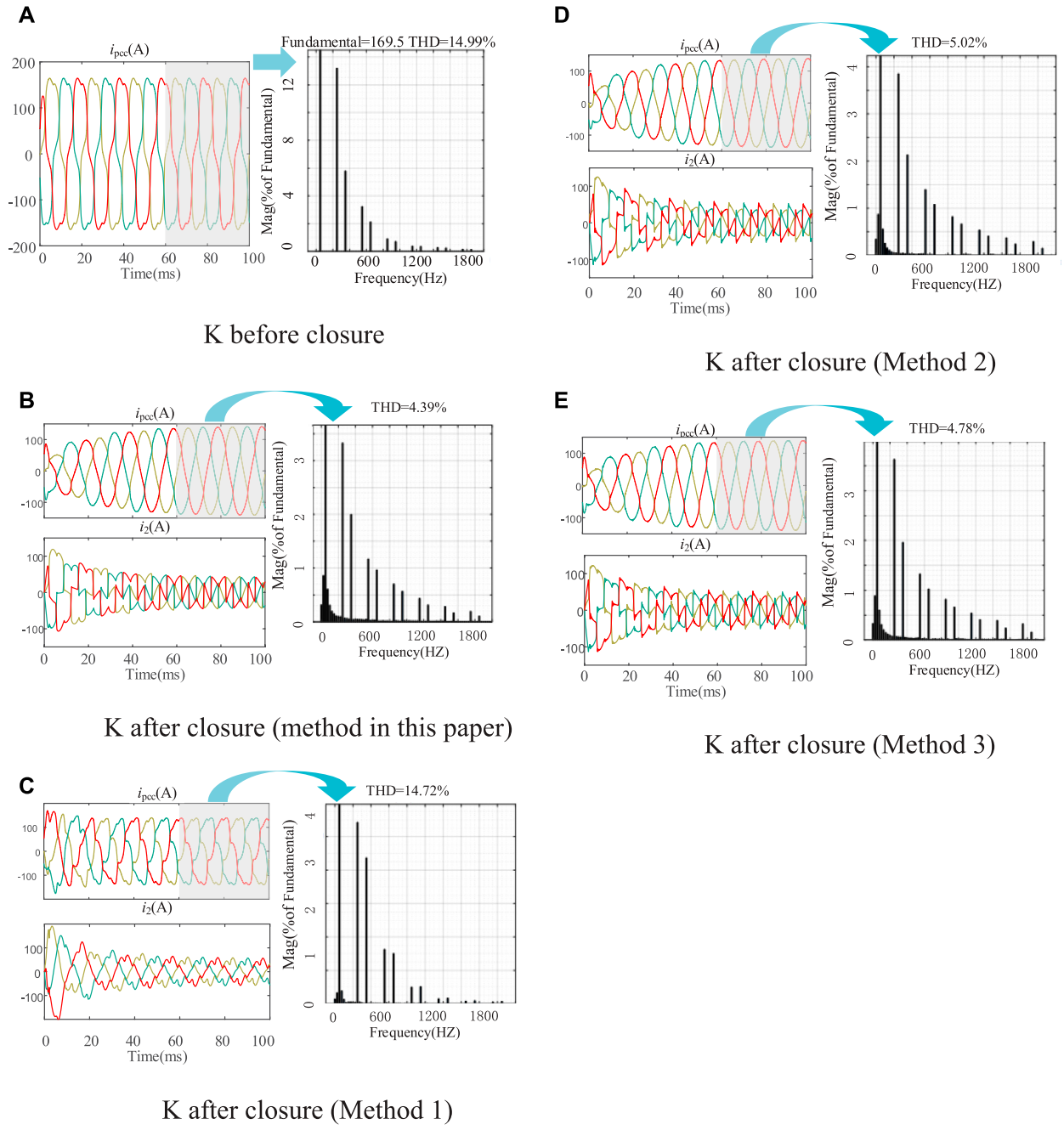

FIGURE 9
Harmonic analysis diagram. **(A)** K before closure, **(B)** K after closure (method in this paper), **(C)** K after closure (Method 1), **(D)** K after closure (Method 2), **(E)** K after closure (Method 3).

TABLE 3 THD comparative analysis table.

Switching frequency (kHz)	THD (i_2) (Only involved in electrical energy convers)	THD (i_{pcc}) (Participate in harmonic control)
20	3.35	6.01
50	2.56	5.83
80	1.59	5.02

As shown in Figure 9A, before APF participated in harmonic control, the existence of nonlinear loads caused a large amount of harmonic current in i_{pcc}: THD was about 15%. As shown in Figures 9B–E, after adopting the proposed strategy in this paper, the harmonic control effect of APF is the best: THD decreases by 10.60% compared with that before treatment; THD decreased by 10.33% compared with method 1. Compared with method 2, THD decreased by 0.63%. THD decreased by 0.39% compared with method 3.

5.4 Sensitivity analysis

Considering that the sampling delay caused by analog-to-digital conversion and signal filtering processing is $1/f_s$, the performance of THD (i_2) and THD (i_{pcc}) in the two scenarios becomes 1.3% and 4.56% respectively, which still has a good performance.

The performance of the proposed method at different switching frequencies is listed in Table 3. Although the performance of the proposed method decreases with the decrease of switching frequency in both scenarios, it still maintains a high level. It can be seen that the switching frequency band adapted by the proposed method is relatively wide.

6 Conclusion

Based on the discrete mathematical model of LCL APF, this paper proposes a control strategy of LCL APF based on model predictive control, which can solve the delay problem caused by LCL filter. Combined with Kalman filter, the APF performance can still be improved under the condition of simplifying the measurement system. Simulation verification is as follows:

1) Kalman filter can accurately predict the APF inverter current, and the error is less than 2%. After the predicted value is used, the current on the network side can change accurately and quickly with the reference value. Therefore, it can save the current sensor and simplify the measurement system.
2) The newly proposed MPC strategy improves the performance of APF: THD decreases by about 10% compared with that before treatment. It can also achieve lower THD than existing MPC strategies. This strategy does not need to change the weight factor according to the device parameters, so it is easy to use.

The control method proposed in this paper is verified by Matlab/Simulink simulation. There are stray parameters in the power device in the actual device, and the sampling and calculation delay also affect the control performance. Therefore, the next step is to build a physical platform to further test the proposed method.

Data availability statement

The original contributions presented in the study are included in the article/Supplementary Material, further inquiries can be directed to the corresponding author.

Author contributions

SJ: Writing–original draft, Writing–review and editing. LD: Writing–original draft, Writing–review and editing. YL: Writing–original draft, Writing–review and editing. LY: Writing–original draft, Writing–review and editing. BL: Writing–original draft, Writing–review and editing.

Funding

The author(s) declare that financial support was received for the research, authorship, and/or publication of this article. This research was funded by China Southern Power Grid Corporation Science and Technology Project under Grant 032000KK52222025.

Conflict of interest

Authors SJ, LD, YL, LY, and BL were employed by Zhongshan Power Supply Bureau of Guangdong Power Grid Co., Ltd.

Publisher's note

References

Cheng, N., Wang, Y., and Lei, W. (2017). Resonance characteristics of multiple converters in parallel and optimal virtual damping method. *Proc. CSEE* 37 (05), 1467–1478. doi:10.13334/j.0258-8013.pcsee.160216

Chico-Villegas, J.-P., Guzman, R., de Vicuña, L. G., Miret, J., Castilla, M., and Komurcugil, H. (2023) "Model predictive control for an LCL voltage source inverter with active damping capability and current limitation," in IECON 2023- 49th Annual Conference of the IEEE Industrial Electronics Society, Singapore, October 19, 2023, 1–5. doi:10.1109/IECON51785.2023.10312716

Falkowski, P., and Sikorski, A. (2018). Finite control set model predictive control for grid-connected AC–DC converters with LCL filter. *IEEE Trans. Industrial Electron.* 65 (4), 2844–2852. doi:10.1109/TIE.2017.2750627

Guo, L., Zheng, M., Li, Y., Zhu, H., and Jin, N. (2022). Parametric sliding mode predictive control strategy for three-phase LCL grid-connected inverter. *Power Syst. Prot. Control* 50 (18), 72–82. doi:10.19783/j.cnki.pspc.211576

Li, J., and Hong, Z. (2012). Sliding mode variable structure control of three phase photovoltaic grid-connected system. *Power Syst. Prot. Control* 40 (12), 83–87.

Liang, G., Xu, J., and Wang, Y. (2018). Research on three-level modular intelligent power quality compensation device. *Adv. Technol. Electr. Eng. Energy* 37 (05), 45–50.

Liu, W., Lv, Z., and Liu, H. (2023). A review of the development of form and operation control technology of electric power distribution area. *Proc. CSEE* 43 (13), 4899–4922. doi:10.13334/j.0258-8013.pcsee.220890

Liu, Y., Hu, C., Ma, D., and Chen, Q. (2018). Three-level ANPC converter midpoint voltage balance MPC. *Power Electron.* 52 (8), 110–113.

Pérez-Estévez, D., and Doval-Gandoy, J. (2020). A finite-control-set linear current controller with fast transient response and low switching frequency for grid-tied inverters. *IEEE Trans. Industry Appl.* 56 (6), 6546–6564. doi:10.1109/TIA.2020.3012923

Pizarro, G., Poblete, P., Droguett, G., Pereda, J., and Núñez, F. (2023). Extended kalman filtering for full-state estimation and sensor reduction in modular multilevel converters. *IEEE Trans. Industrial Electron.* 70 (2), 1927–1938. doi:10.1109/TIE.2022.3165286

Shi, L., Jia, Q., and Lin, L. (2020). Global optimal governance strategy of harmonic distribution in electronic power distribution network. *Proc. CSEE* 40 (09), 2914–2924. doi:10.13334/j.0258-8013.pcsee.191844

Xie, H., Wang, K., and Jiang, Z. (2013). Optimization design of passive filter banks based on three-point working condition. *Power Syst. Technol.* 37 (06), 1713–1718. doi:10.13335/j.1000-3673.pst.2013.06.008

Xie, Y., Liu, L., and Guan, Y. (2021). Adaptive model predictive control strategy for three-phase LCL grid-connected inverter. *Electr. Mach. Control* 25 (4), 40–51. doi:10.15938/j.emc.2021.04.006

Xiong, L., Liu, X., Zhang, D., and Liu, Y. (2021). Rapid power compensation-based frequency response strategy for low-inertia power systems. *IEEE J. Emerg. Sel. Top. Power Electron.* 9 (4), 4500–4513. doi:10.1109/JESTPE.2020.3032063

Xiong, L., Liu, X., Zhao, C., and Zhuo, F. (2020). A fast and robust real-time detection algorithm of decaying DC transient and harmonic components in three-phase systems. *IEEE Trans. Power Electron.* 35 (4), 3332–3336. doi:10.1109/TPEL.2019.2940891

Xiong, L., Zhuo, F., Wang, F., Liu, X., Chen, Y., Zhu, M., et al. (2016). Static synchronous generator model: a new perspective to investigate dynamic characteristics and stability issues of grid-tied pwm inverter. *IEEE Trans. Power Electron.* 31 (9), 6264–6280. doi:10.1109/TPEL.2015.2498933

Yang, L., Yang, J., Gao, M., Chen, Y., and Zhang, X. (2020). A systematic approach via IIR filters for enhancing the robustness of LCL-type shunt active power filters to grid impedance. *IEEE Trans. Industry Appl.* 56 (5), 5095–5107. doi:10.1109/TIA.2020.2999273

Zhang, B., Wu, W., Yang, Y., Gao, N., Chen, J., Koutroulis, E. G., et al. (2023). A novel simplified finite control set repeat model predictive control for grid-connected inverters. *IEEE Trans. Industrial Electron.* 70 (11), 11324–11333. doi:10.1109/TIE.2022.3231252

Zhang, B., Wu, W., Gao, N., Koutroulis, E., Chen, J., Lu, G., et al. (2022) "An improved DBC-MPC strategy for LCL-filtered grid-connected inverters," in IECON 2022 – 48th Annual Conference of the IEEE Industrial Electronics Society, Brussels, Belgium, October 20, 2022, 1–6. doi:10.1109/IECON49645.2022.9968666

Zhang, X., Wang, Y., and Yu, C. (2014). Improved repetitive control strategy for LCL grid-connected inverter. *Automation Electr. Power Syst.* 38 (20), 101–107.

Zheng, S., He, G., and Dong, Y. (2023). Robust model predictive current control for three-phase grid-connected inverters. *Control Eng. China* 30 (7), 1233–1241. doi:10.14107/j.cnki.kzgc.20220698

Frontiers in
Energy Research

Advances and innovation in sustainable, reliable and affordable energy

Explores sustainable and environmental developments in energy. It focuses on technological advances supporting Sustainable Development Goal 7: access to affordable, reliable, sustainable and modern energy for all.

Discover the latest Research Topics

See more →

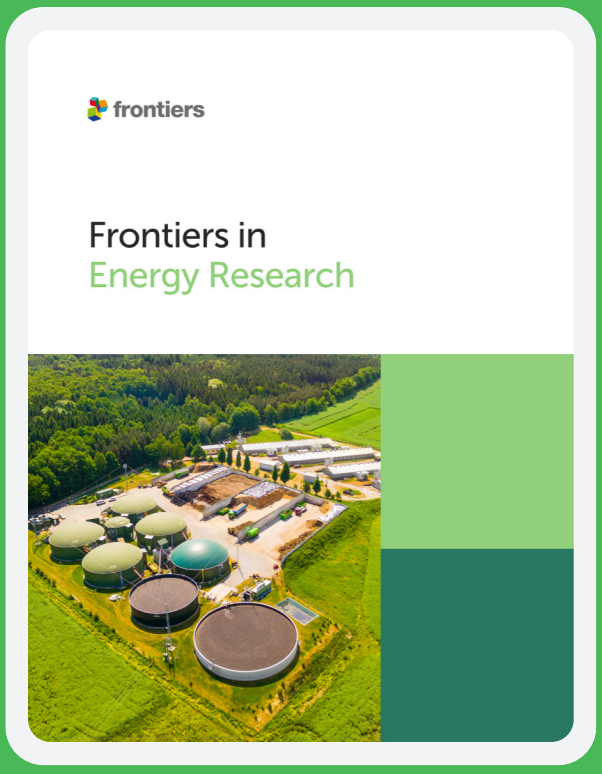

Frontiers

Avenue du Tribunal-Fédéral 34
1005 Lausanne, Switzerland
frontiersin.org

Contact us

+41 (0)21 510 17 00
frontiersin.org/about/contact